Advances in Compressible Turbulent Mixing

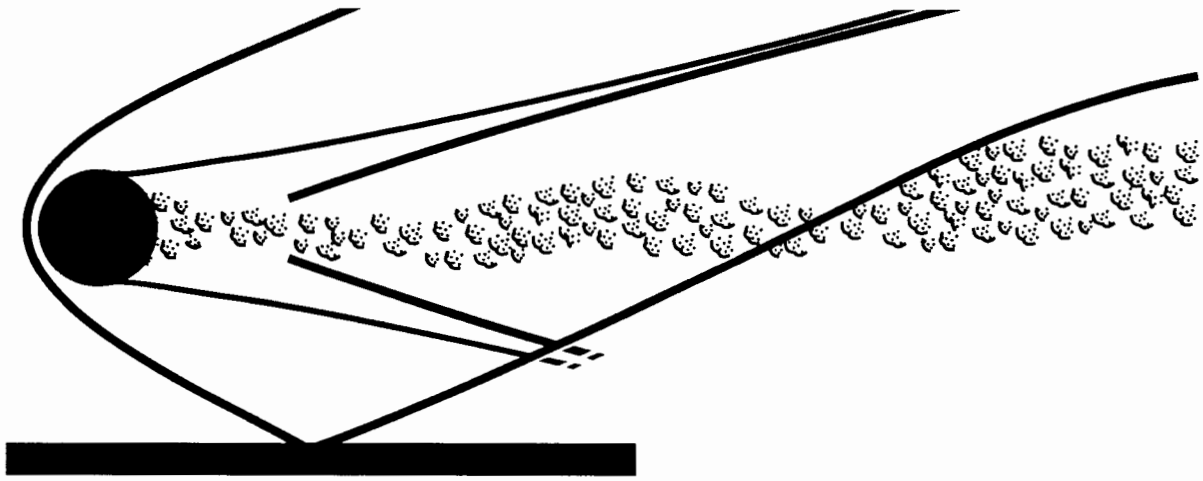

W. P. Dannevik
A. C. Buckingham
C. E. Leith
Editors

January 1, 1992

Conf-8810234

This document is based primarily on contributions from the International Workshop on the Physics of Compressible Turbulent Mixing held at the Princeton University in Princeton, New Jersey, on October 24-27, 1988. Some contributions and updates were added subsequently.

FOREWORD

On October 24-27, 1988, an international workshop was held at Princeton University, Princeton, New Jersey, on the physics of compressible turbulent mixing. The idea for the workshop originated with David L. Youngs at Aldermaston, Reading, United Kingdom, in 1986. Organization of the workshop was begun in late spring, 1987, by Youngs, his Aldermaston colleagues, and a small group of scientists at the Lawrence Livermore National Laboratory in California. Immediate and enthusiastic response from scientists in Europe, the Soviet Union, Canada, and the United States confirmed the timeliness and appropriateness of the subject matter.

For the workshop content, the organizers sought a balance between experimental and theoretical investigations of high-speed compressible turbulent mixing in free shear layers, wakes, jets, and boundary layers. With the exception of a few selected presentations on flow instabilities at low Mach Number, the organizers purposely sought contributions on supersonic flow with developing turbulence as opposed to transitional flows. Particular emphasis was given to the influence of high-speed compressibility, including the influence of shock waves on turbulence rather than combustion flow situations because the latter appear to have a substantial forum, whereas the physics of high-speed flow mixing and transport have a limited forum.

There were over 150 workshop participants. A single daily session of talks was scheduled, supplemented by scheduled poster sessions. Each day, panel discussions were summarized by the organizers. A good cross section of current understanding and research in compressible turbulent mixing was provided by participants from Canada, the United Kingdom, the Federal Republic of Germany, France, the then Soviet Union, and the United States.

In addition to the three editors of this volume, all from Lawrence Livermore National Laboratory, the organizers of this workshop included: C. David Levermore, University of Arizona; Steven A. Orszag, Princeton University; Raold Z. Sagdeev, Space Research Institute, Academy of Sciences of the USSR; and David L. Youngs, Atomic Weapons Establishment, Aldermaston, Reading, United Kingdom.

The editors gratefully acknowledge the sponsorship for this Workshop provided by the Department of Energy's Lawrence Livermore and Los Alamos National Laboratories, Princeton University, the National Science Foundation, the U.S. Army Research Office, the Office of Naval Research, and the Air Force Office of Scientific Research.

W. P. Dannevik, A. C. Buckingham, and C.E. Leith
Editors
Livermore, California
January, 1992

Contents

III. Strongly Coupled Compressibility

INTRODUCTION

This volume, ***Advances in Compressible Turbulent Mixing,*** includes some recent additions to original material prepared for the *Princeton International Workshop on the Physics of Compressible Turbulent Mixing*, held in 1988. The Princeton Workshop was organized to exchange views, collect available data, and report on work in progress and planned research in the topical area of compressible turbulent mixing. Workshop participants were asked to emphasize the physics of the compressible mixing process rather than measurement techniques or computational methods. To this end, actual experimental results and their meaning were given precedence over discussions of new diagnostic developments. Similarly, theoretical interpretations and understanding were stressed rather than the exposition of new analytical model developments or advances in numerical procedures.

By design, compressibility influences on turbulent mixing were discussed—almost exclusively—from the perspective of supersonic flow field studies. This distinction unfortunately, but purposely, excludes contributions from the turbulent combustion community. However, at the characteristically lower combustion flow speeds usually encountered, the role of acoustic propogation in turbulent field evolution is much less significant than is is in supersonic flow. In addition, the reactive complexity of turbulent combustion flows reduces the opportunity for unambiguous isolation and investigation of fundamental questions in the dynamics of compressible turbulent flow processes. For example, Workshop emphasis was placed on questions about the interactively coupled influences of entropy, vorticity, and acoustic field fluctuations on turbulent mixing and transport development, evolution, and dissipation. An additional consideration is that combustion necessarily introduces added turbulent production complications associated with reactive energy release, as well as multicomponent species production/annihilation influences on density fluctuations. While these added complications are of great importance in combustion analysis, they are substantially beyond the range of physical processes chosen for special emphasis in this Workshop. Consequently, in the organizers view, the inclusion of turbulent combustion contributions would unnecessarily dilute the primary emphasis and goals established for the Workshop.

The papers are arranged in three topical categories: **Foundations**, **Vortical Domination**, and **Strongly Coupled Compressibility.**

The **Foundations** category is a collection of fundamentally seminal studies that may be considered a bridge connecting what currently is under study in compressible turbulent mixing with the compressible, high-speed turbulent flow research that, unfortunately, almost completely vanished about two decades ago in apparent response to a shift in national programmatic interests. Based on this seminal role, a number of contributions are included on flow instability initiation, evolution, and transition between the states of unstable flow onset through those descriptive of fully developed turbulence.

The **Vortical Domination** category includes theoretical and experimental studies of coherent structures, vortex pairing, vortex-dynamics-influenced pressure focusing, and associated studies of the consequences of such focusing: e.g., possible incipient shocklet formation and the relationship of these flow field structure changes to significant alteration of basic mixing and transport processes. Also included in this category are experimental, theoretical, and numerically modeled contributions on both shocked as well as shock-free compressible and physically illuminating (albeit nearly incompressible) results of studies on wakes, free shear layers, and boundary layers.

In the **Strongly Coupled Compressibility** category the organizers included the high-speed turbulent flow investigations in which the interaction of shock waves could be considered an important source for production of new turbulence or for the enhancement of pre-existing turbulence. The words *Strongly Coupled* have been adopted here to refer to the shockwave-turbulence interactive states developing at sufficiently high Mach Number so as to require simultaneous consideration of three inherently compressible fluctuating energy partition modes: acoustical, vortical, and entropy production.

One of the Workshop's most significant outcomes was the unusual level of cooperation that began at the workshop and was subsequently pursued by participants despite their very different perspectives, backgrounds, and work motivations. Typical cooperative efforts included the informal but well-attended experimental and theoretical discussion groups that formed during intervals in the Workshop schedule. A prominent example was the development of an informal planning group that first met at Princeton to establish a common basis for prescribing a common and consistent set of shock-tube flow conditions for future investigations and later compressible turbulent mixing workshops. These plans included the important identification of facilities appropriate for undertaking the experiments simultaneously at several sites in the United States, the United Kingdom, France, Germany, and the then Soviet Union.

An Experimental Study of Turbulent Mixing by Rayleigh-Taylor Instabilities and a Two-Fluid Model of the Mixing Phenomena

M.J.Andrews

Mechanical and Aerospace Engineering Department

Princeton University

ABSTRACT

A simple experiment has been used to quantitatively investigate turbulent mixing at an unstable interface when the interface is subject to a large two-dimensional disturbance. The introduction of a small amplitude long wavelength does little to alter the early time development of a planar mixed region, but at late times causes a large overturning motion that tends to thin the planar mixed region and accelerate the overall mixing process. Data have been collected from the experiment by way of image analysis of experimental photographs. These data serve as a source of information for the development of a "two-fluid" model of the mixing process.

A "two-fluid" model has been developed to describe the turbulent mixing by Rayleigh-Taylor instabilities of the two different density fluids investigated in the experimental study above. A one-dimensional model was employed for the planar mixing experiments; here attention is focused on the development of a physically plausible equation to describe the length-scale development within the mixed region. The one-dimensional model was then extended to two-dimensions for the overturning experiments, and terms are added to account for thinning of the mixing region at late times. Data collected from the experiments are used to validate the model and to determine several model constants. The two-fluid model successfully simulates the experimental results and is recommended for further application to turbulent mixing processes in buoyant environments.

1. INTRODUCTION

1.1. The Rayleigh-Taylor Instability

The Rayleigh-Taylor instability occurs when a heavy fluid is placed above a light one in a gravitational field. The interface becomes increasingly distorted and small wavelength disturbances degenerate finally into a turbulent mixing process.

Such mixing is of current interest because of its deleterious effect during the laser implosion of fusion targets, it is also important in meteorology, oceanography, astronomy and elsewhere.

1.2. Objectives of the present investigation

* To devise a simple experiment for the investigation of Rayleigh-Taylor mixing, and its deformation by large-scale motions.
* To collect data from the experiment for the validation of a new *two−fluid* model of the mixing process.
* To perform computer simulations for several experiments to validate the new turbulence model.

1.3. Outline of the poster

The experimental arrangement is described in the next section. This is followed by the densitometer analysis of photographic records.

Section 4 presents some theoretical considerations for the phenomena of interest.

Section 5 describes the use of the Euler equations for *direct* simulation of the experiments, and section 6 the new *two−fluid* model.

Sections 7 and 8 present the results of two experiments, and their simulation on the computer.

The poster closes with conclusions and references.

2. EXPERIMENTAL ARRANGEMENT

A heavy fluid, brine ($\rho_b = 1.1 \times 10^3 kg/m^3$) is situated above a light one, water ($\rho_w = 1.0 \times 10^3 kg/m^3$), by inverting a slim perspex tank, of dimensions $360 \times 250 \times 5mm$, containing the unmixed fluids. Gravity then drives Rayleigh-Taylor mixing.

The tank pivoted on an axle that could be tilted to impose an initial 2-D disturbance on the density interface, as may be seen on the video tape that accompanies this poster.

An experimental run was performed in three steps:

(1) The tank was filled with clear brine to the level of the axle, and then water (dyed blue to allow densitometer analysis) was added to completely fill the tank. At this stage there was no mixing.

(2) Rotation springs were attached to the tank. Removing a holding pin then released the tank which then rotated through 180^o, situating the clear brine above the dyed water.

(3) Once mixing was complete the tank was drained and cleaned by flushing with water.

3. DENSITOMETER ANALYSIS

A data collection technique has been developed based on densitometer analysis of photographic records. The technique gives a volume-fraction measurement of brine at a point, and then forming sub-domain averages a mixing contour may be drawn for direct comparison with results from *two−fluid* simulations.

The densitometer scans a photographic negative taking light absorption measurements expressed on a grey scale. Typically 340×500 measurements covered the flow domain. After subtracting non-uniform lighting from the absorption measurements well defined bi-modal grey level histograms were obtained with an estimated error of 7%. The histogram peak values were used to define the measurement of pure brine as $I_{\max}$ and pure water as $I_{\min}$.

Figure 1 shows that there is a linear relationship between the grey scale measurements, I, and dye concentration. The volume-fraction of brine is determined from:

$$r_b = \frac{I - I_{\min}}{I_{\max} - I_{\min}} \tag{1}$$

Averaging over a sub-domain containing 100 measurements provided a set of 34×50 averaged volume-fractions from which the mixing contours shown in the figures were obtained.

4. THEORETICAL CONSIDERATIONS

Using a linear analysis G.I.Taylor (1950) predicted the growth of a disturbance of amplitude, A, and wavelength, λ, as:

$$A = A_0 \cosh(n_\lambda t), \quad n_\lambda^2 = \frac{2\pi g}{\lambda} \frac{\rho_w - \rho_b}{\rho_w + \rho_b} \tag{2}$$

where g is the gravitational acceleration. According to (2) as $\lambda \to 0, n_\lambda \to \infty$. Chandrasekhar (1962) demonstrated that viscosity acts as a stabilizing mechanism, giving a 'most unstable' wavelength:

$$\lambda_m = 4\pi \left[\frac{4\mu^2}{\rho_w^2 - \rho_b^2} \frac{1}{g} \right]^{\frac{1}{3}} \tag{3}$$

for the present case of brine-water $\lambda_m = 1.56mm$.

Experiments by D.J.Lewis (1950), performed in conjunction with Taylor's theory, showed that the penetration rate of the disturbance reaches a limiting velocity.

The development of turbulent Rayleigh-Taylor mixing from an initial random disturbance may be expected to occur in three stages:

(1) The appearance of λ_m.

(2) The most unstable wavelength reaches its limiting velocity and longer wavelengths overtake because of their continuing exponential growth.

(3) Non-linear interactions and continued engulfment cause an expanding turbulent mixing region with loss of memory of the initial conditions.

The depth of the tank ($5mm$) restricts the larger turbulent motions to two-dimensions. The height ($360mm$) and width ($250mm$) of the tank are $>> \lambda_m$ and so viscosity may be expected to play a significant roll only in the early stages of the experiment.

5. DIRECT SIMULATIONS

Several 'direct' (no turbulence model) simulations have been performed for the overturning motion in the 'tilted' experiments. The simulations solved the 2-D Euler equations with the initial conditions shown in Figure 2.

The solution procedure used was the fully-implicit, finite-volume scheme embodied in the PHOENICS84 computer code, Spalding (1985a). An explicit interface-tracking procedure was attached to the computer code to both visualize the brine-water interface, and to provide an accurate determination of fluid density for the solution algorithm.

6. A TWO-FLUID MODEL

6.1. The need for a two-fluid model

The wide range of length-scales, $1mm \rightarrow 1m$, associated with Rayleigh-Taylor mixing necessitates the use of a turbulence model, e.g. the $k-\varepsilon$ model. The use of such a model involves a 'gradient diffusion' hypothesis. Stafford (1982) demonstrated that reversing gravity causes partial de-mixing, showing a non-diffusive mixing process.

6.2. The two-fluid concept

These experiments suggest that the Rayleigh-Taylor mixture comprises fragments from different density fluids. Gravity induces different accelerations in the different density fragments, causing different velocities. The velocity separation is limited by drag. This is an example of 'sifting' Spalding (1985b), and suggests the use of the two-phase flow equations for the motion of the different fluids.

6.3. Mathematical equations of the two-fluid model

$$Continuity: \frac{\partial(r_i\rho_i)}{\partial t}+\frac{\partial(r_i\rho_i u_i)}{\partial x}+\frac{\partial(r_i\rho_i v_i)}{\partial y}=0$$

$$u-momentum: \frac{\partial(r_i\rho_i u_i)}{\partial t}+\frac{\partial(r_i\rho_i u_i^2)}{\partial x}+\frac{\partial(r_i\rho_i u_i v_i)}{\partial y}=-r_i\frac{\partial p}{\partial x}+r_i\rho_i g_x+F_i(u_w-u_b)$$

$$v-momentum: \frac{\partial(r_i\rho_i v_i)}{\partial t}+\frac{\partial(r_i\rho_i v_i u_i)}{\partial x}+\frac{\partial(r_i\rho_i v_i^2)}{\partial y}=-r_i\frac{\partial p}{\partial y}+r_i\rho_i g_y+F_i(v_w-v_b)$$

$$Completeness: r_w+r_b=1$$

where $i=w$ *or* b, for water or brine; r the fluid volume-fraction; u and v fluid velocities; p pressure. The drag coefficient is given by:

$$F_w=-F_b=C_f r_w r_b(r_w\rho_w+r_b\rho_b)\,|\underline{u}_b-\underline{u}_w|/L\,,\quad C_f=5.75.$$

(note: if $\underline{u}_b=\underline{u}_w$ then the sum of the separate fluid equations gives the Euler equations)

$$Length-scale: \frac{\partial L}{\partial t}+\frac{\partial(u_L L)}{\partial x}+\frac{\partial(v_L L)}{\partial y}=\underline{n}\cdot(\underline{u}_b-\underline{u}_w)-\frac{1}{2}\bar{S}\,L$$

$$where\ \underline{n}=\begin{cases}\nabla r/|\nabla r| & \text{if } |\nabla r|>0\\ or & \\ 0 & otherwise\end{cases},\quad \bar{S}=\left\{\frac{1}{2}S_{ij}S_{ji}\right\}^{\frac{1}{2}},\quad u_L=r_w u_b+r_b u_w,$$

$$v_L=r_w v_b+r_b v_w,\ \text{and } S_{ij}\ \textit{is the mean flow strain tensor.}$$

The value of the drag coefficient, C_f, was determined by matching one-dimensional two-fluid simulations with plane Rayleigh-Taylor mixing observed in zero

tilt experiments, Andrews (1986).

6.4. Two-fluid simulations

Computer simulations have been performed using the two-fluid model given above for the 'tilted' experiments shown on the video accompanying this poster and displayed in the figures that follow.

The two-fluid equations were solved using the two-phase flow solver in the PHOENICS computer code. To reduce numerical diffusion, accurate explicit schemes were constructed for the calculation of two-phase convective transport. The explicit schemes use the Van-Leer method to prevent spurious oscillations, and have been employed in the calculation of volume-fraction, momenta and length-scale.

7. RESULTS FOR A TILT OF 55′

Examination of the photographs shown in Figure 3 reveals two distinct phenomenon; Rayleigh-Taylor mixing along the brine-water interface; and wall plumes associated with an overturning motion.

The photographs show the mixing length-scale developing during the experiment. In the latter stages of the experiment an overturning motion rotates the mixing region, elongating the mixing interface and slowing the expansion of the mixture. The appearance of wall plumes may be attributed to the rapid growth of short wavelength Fourier components that make up the initial tilted (saw-tooth) disturbance.

Comparison of the direct simulation in Figure 3 with the photographs shows that the overturning motion is well represented. Mixing at the density interface does not appear in the simulation, a turbulence model being necessary to account for the range of length-scales.

The densitometer mixing contours shown in Figure 4 compare well with the corresponding photographs in Figure 3. At the early time the contours are smooth, but later they become irregular. The irregular contours are caused by fluid fragments of the same scale as the averaged measurement sub-domain. Ensemble averaging over several experiments would be required for a smooth contour.

Comparison of the two-fluid model simulation shown in Figure 4 with the densitometer contours, shows that the two-fluid calculation simulates well the mixing process.

8. RESULTS FOR A TILT OF $3^o21'$

Examination of the photographs in Figure 5 reveals the Rayleigh-Taylor mixing and wall plume phenomena observed in the photographs of the 55′ tilt experiment.

The higher tilt angle gives a greater amplitude to the initial disturbance, and as a consequence the overturning motion envelops the mixing more quickly. An interesting effect shown in the photographs is the contraction of the width of the Rayleigh-Taylor mixing region as the overturning motion stretches the mixing interface.

The direct simulations of the $3^o21'$ experiment well represent the overturning motion, but cannot show the mixing phenomena.

Reduction of the spacing between the densitometer contours shown in Figure 6 reinforces the observed contraction of the mixing region by the deformation mechanism.

Comparison of the two-fluid simulations shown in Figure 6 with the densitometer contours of the $3^o21'$ experiment shows that the simulation is in good agreement with the experiment. Is is particularly satisfying to note that the two-fluid model correctly simulates the contraction of the mixing region.

9. CONCLUSIONS

* A simple experiment has been devised to investigate the Rayleigh-Taylor instability.

* Two experiments have been presented; one for an axle tilt angle of 55′ and the other for $3^o21'$. Two distinct phenomena have been observed in the experiments; Rayleigh-Taylor mixing along the brine-water interface; and the growth of an overturning motion that at the higher tilt angle thins the mixing region.

* Densitometer analysis of photographic records from the experiments has been successfully used to collect data for comparison with two-fluid simulations.

* Direct simulations (i.e. no turbulence model) of the experiments, which used the 2-D Euler equations, successfully demonstrated the overturning motion observed in the experiments.

* A new two-fluid model of Rayleigh-Taylor mixing, that incorporates an equation for fragment size, has been described. The model is based on the mathematical

equations that govern two-phase flow. When the separation velocity of the fluids is zero, the model equations reduce to the Euler equations.

* Two-fluid simulations for the experiments agree well with the densitometer results, and correctly predict the contraction of the Rayleigh-Taylor mixture observed at the higher tilt angle.

10. REFERENCES

1. Chandrasekhar, S (1960)
"Hydrodynamic and Hydromagnetic Stability", O.U.P.

2. Lewis, DJ (1950)
"The Instability of Liquid Surfaces when Accelerated in a Direction Perpendicular to their Planes, II", Proc Roy Soc, 202A, 81, 1950.

3. Spalding, DB (1985a)
"The Numerical Computation of Multi-Phase Flows", Computational Fluid Dynamics Report, CFDU/85/7, Imperial College, 1985.

4. Spalding, DB (1985b)
"Two-Fluid Models of Turbulence", Computational Fluid Dynamics Report, CFDU/85/4, Imperial College, 1985.

5. Stafford, LG (1982)
"An Experimental Investigation of Turbulent Mixing due to Buoyancy Forces in Unstably Stratified Media", Computational Fluid Dynamics Report, CFDU/82/10, Imperial College, 1982.

6. Taylor, GI (1950)
"The Instability of Liquid Surfaces when Accelerated in a Direction Perpendicular to their Planes, I", Proc Roy Soc, 201A, 192-196, 1950.

7. Andrews, MJ (1986)
"Turbulent Mixing by Rayleigh-Taylor Instability", PhD Thesis, Imperial College of Science and Technology, London University, UK, 1986.

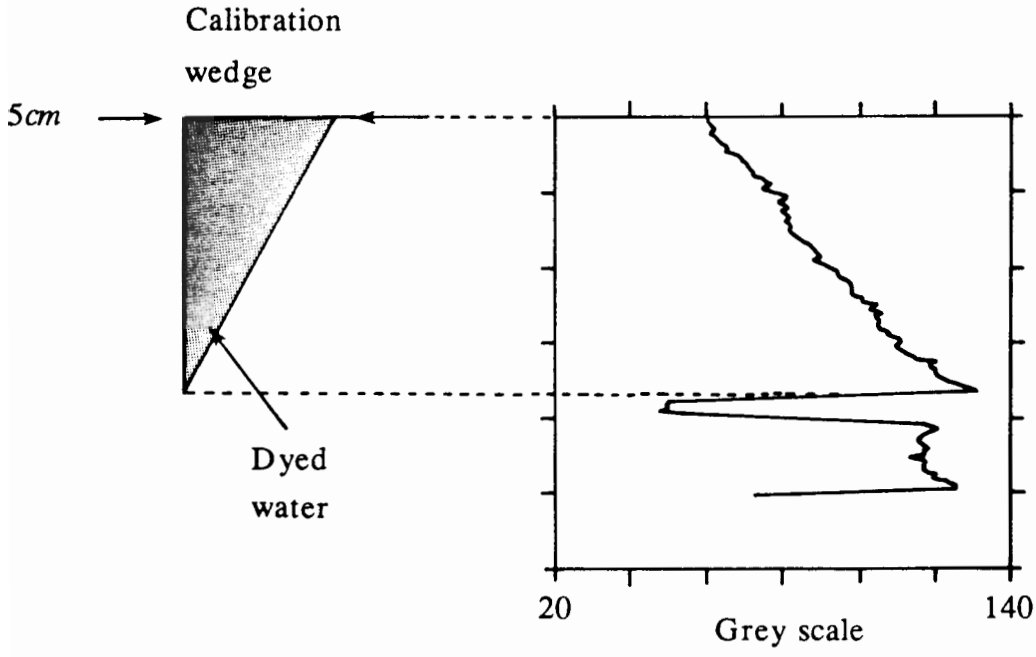

Figure 1. Calibration of dye concentration.

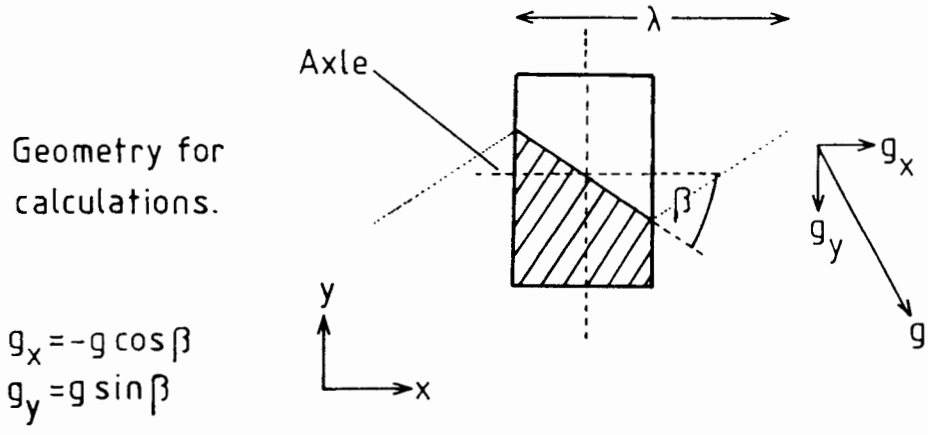

Figure 2. Initial conditions in the 'tilted' experiments.

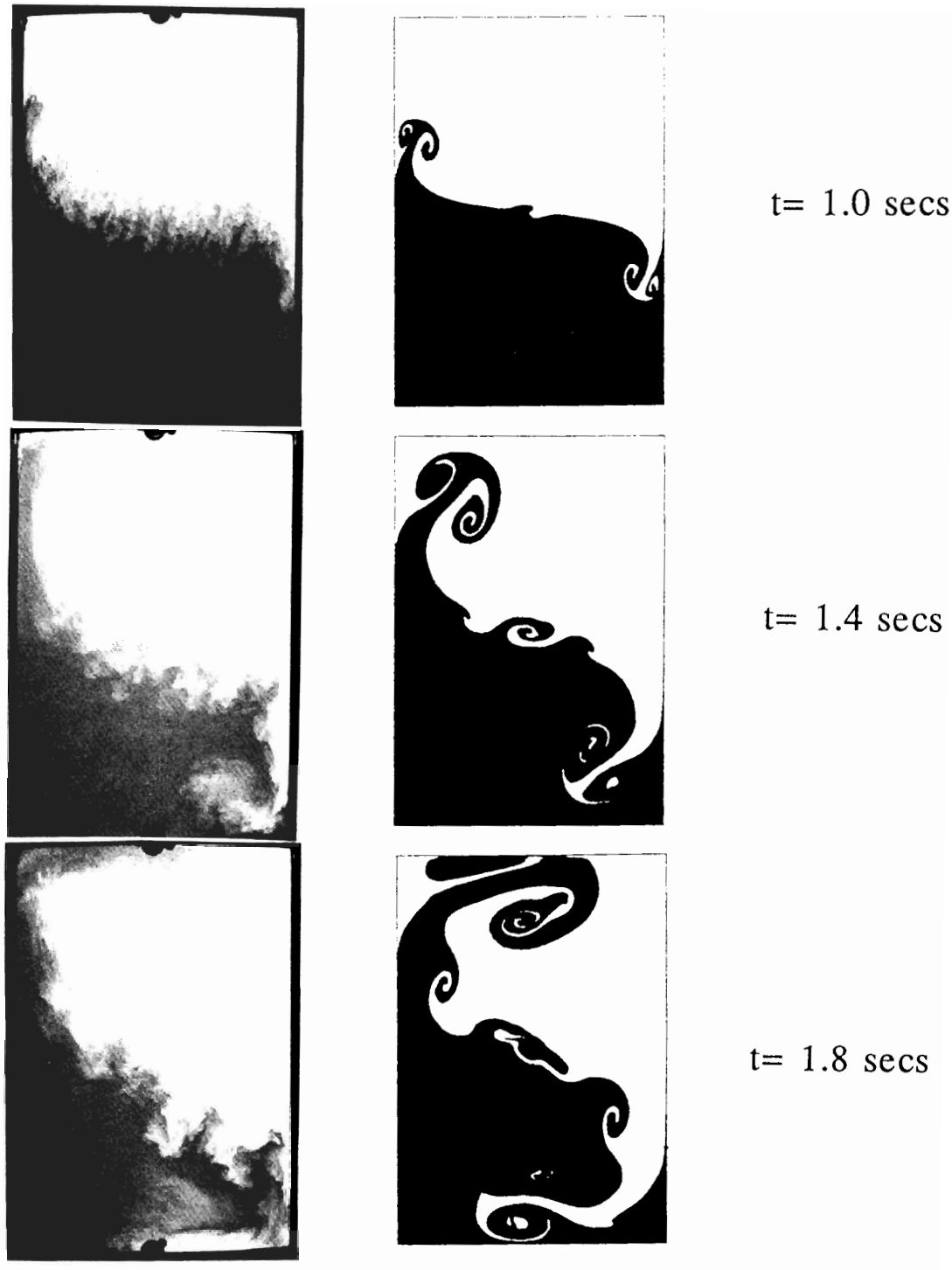

Figure 3. Photographs and direct simulations of the 55′ tilt experiment.

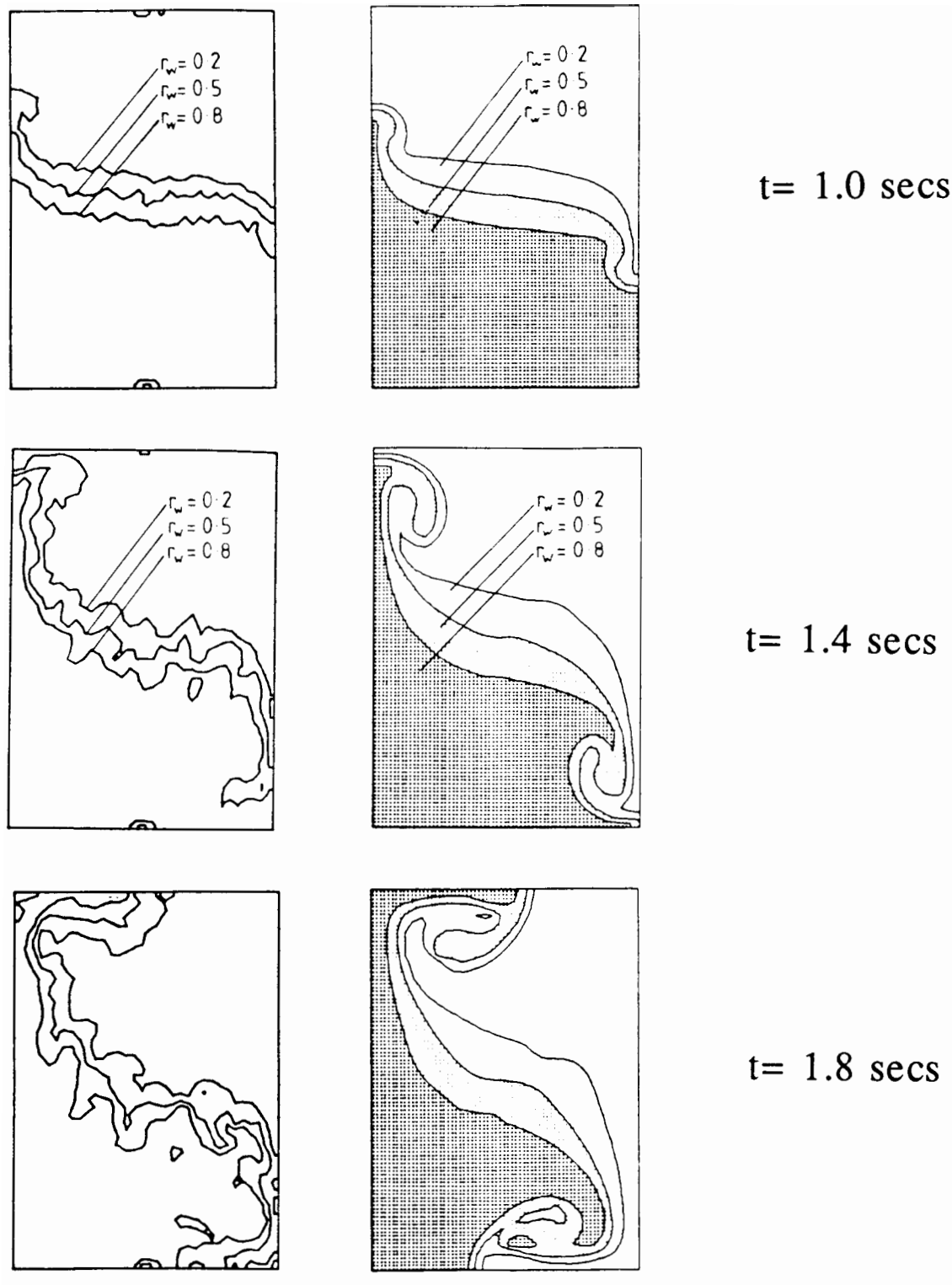

Figure 4. Densitometer contours and two-fluid simulations of the 55′ tilt experiment.

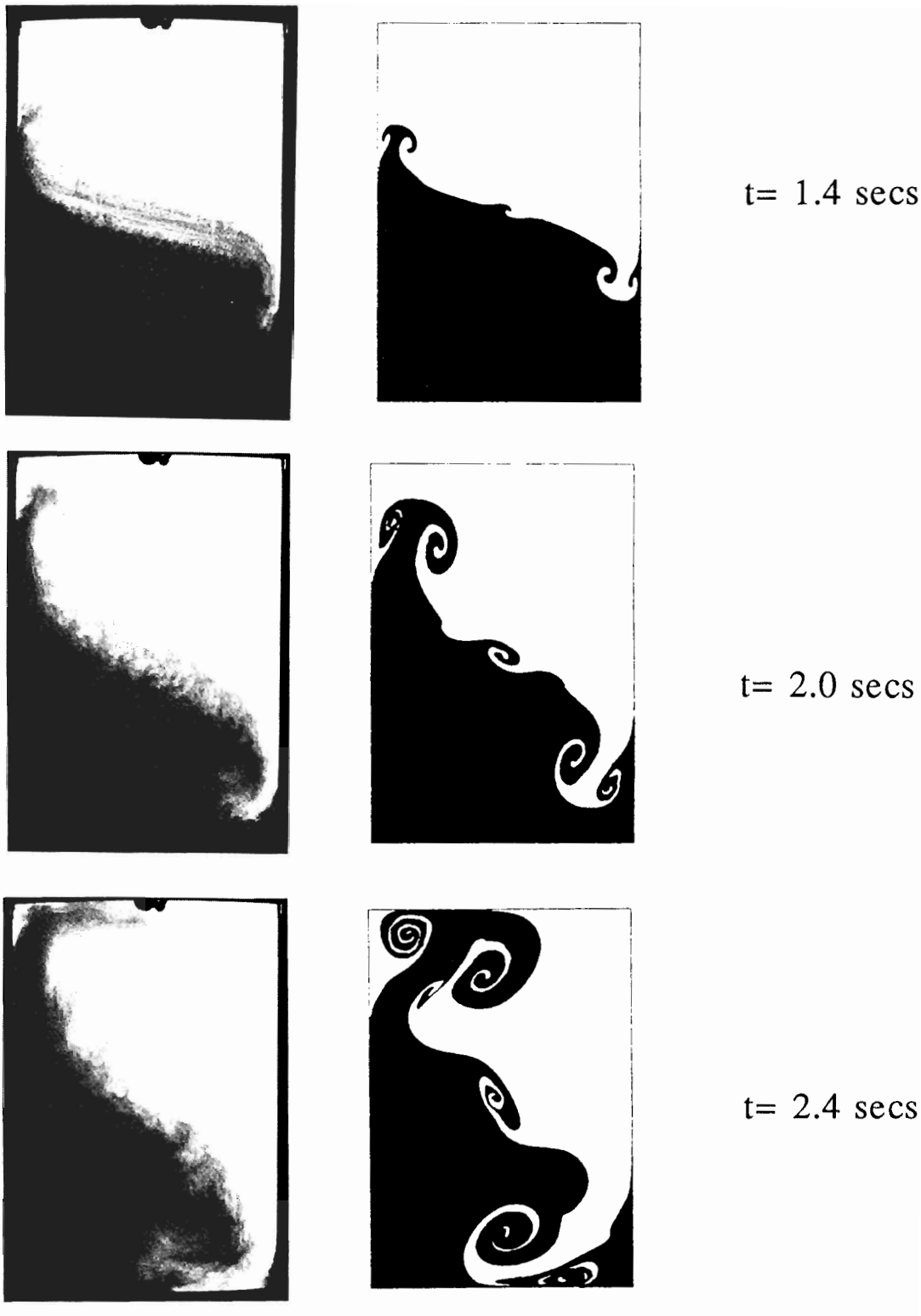

Figure 5. Photographs and direct simulations of the $3^{o}21'$ tilt experiment.

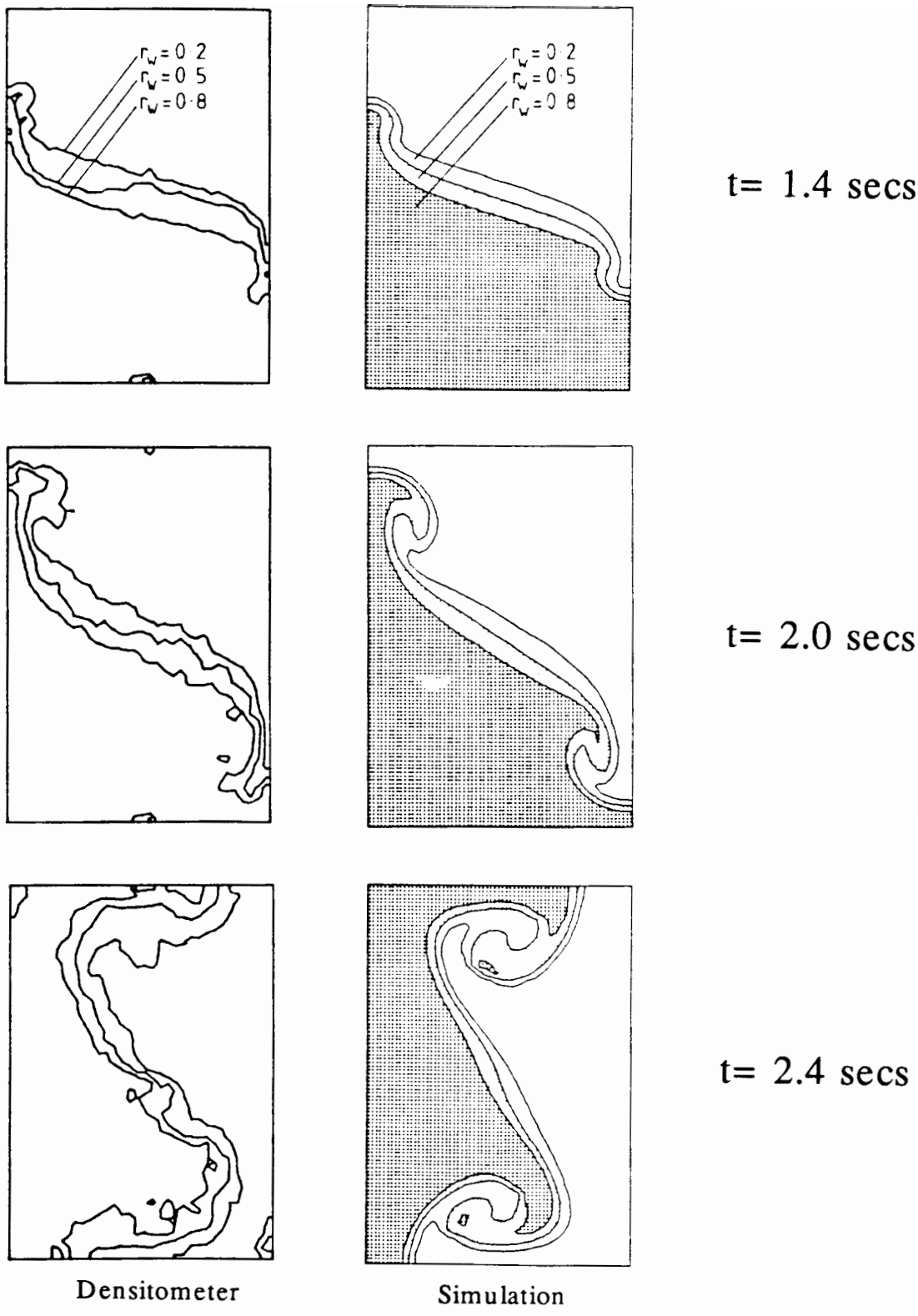

Figure 6. Densitometer contours and two-fluid simulations of the $3^o 21'$ tilt experiment.

COMPRESSIBILITY INFLUENCES ON BOUNDARY-LAYER TRANSITION

by

Dennis M. Bushnell and Mujeeb R. Malik
NASA Langley Research Center
Hampton, VA 23665-5225

Invited Paper
Physics of Compressible Turbulent Mixing
October 25-27, 1988
Princeton, New Jersey

Compressibility Influences on Boundary-Layer Stability and Transition

Dennis M. Bushnell and Mujeeb R. Malik
NASA Langley Research Center
Hampton, VA 23665-5225

Abstract

Paper briefly summarizes the influences of increasing Mach number upon the various stages of boundary-layer transition including body flow field processing of incident stream disturbances and normal mode amplification. Other compressibility unique or altered phenomena discussed include (a) outward movement of the critical layer and the related "precursor" transition, (b) flow chemistry, (c) shock waves, and (d) the all pervasive roughness issue. Paper concludes with consideration of ground simulation and prediction of high-speed transition.

Introduction

In general, transition is an important design consideration for moderate Reynolds numbers, whether achieved through small bodies, high altitudes or with short distances at conventional flight conditions. In the absence of large initial disturbance fields and/or the cross flow and Gortler modes, transition at hypersonic speeds may occur at Reynolds numbers as large as 80×10^6 (Ref. 1) and therefore the definition of moderate Reynolds number in the present context can at high speeds subsume major portions of a vehicle's trajectory. High-speed applications for which the location and extent of transition is a major issue include: (a) space shuttles; (b) aerospace planes or transatmospheric vehicles; (c) re-entry vehicles; (d) laminar flow control for high-speed civil transports; (e) radomes on high-speed fighters and missiles; (f) inlets and leading edges of all types; (g) supersonic compressor blades; (h) high angle-of-attack vortex dynamics; and (i) gas dynamic lasers. Phenomena influenced by transition at high speeds include drag, surface heating and attendant thermal stresses, surface dynamic loading, control effectiveness, propulsion efficiency,and vehicle dynamics (Ref. 2).

The canonical transition process consists of six serially occurring stages (Ref. 3), starting with some initial disturbance field (stream particulates, stream velocity, concentration, temperature or pressure fluctuations, body vibration or, in the limit, Brownian motion). This disturbance field is modified or "processed" initially by the body inviscid flow field (e.g. via shock processing and "rapid distortion" processes) and subsequently by the body viscous flow field, the latter usually termed the "receptivity" process. The resultant internalized disturbance field is then amplified by the linear or normal mode processes. For low amplitude initial background disturbances this linear amplification can entail huge (order of a thousand-fold) increases in amplitude. The final stages in this concatenation are the (usually brief) non-linear "end game" and (finally) rapid spectral broadening and

formation of Emmons spots or at least wall region transport elevated above usual laminar levels.

In the absence of large background disturbances inferential evidence indicates that the linear amplification region constitutes the rate-limiting critical physics. Parametric sensitivities of the linear region include variables which can influence the mean viscous field including (a) Mach number, (b) pressure gradient, (c) wall temperature, (d) angle of attack, (e) wall mass transfer, (f) sweep, (g) flow history, (h) roughness and waviness, (i) streamline curvature/body geometry, (j) body rotation/dynamics, (k) flow chemistry and surface catalicity, (l) bluntness, (m) shock waves, and (n) Reynolds number. The present paper provides a brief summary of several of the influences of increasing Mach number upon these various stages of the boundary-layer transition process, along with the attendant issues of ground simulation and estimation of high-speed transition location. Previous and in some cases more detailed summaries of the high-speed transition physics include References 4-10.

High-Speed Aspects of Body Flow Field-Incident Disturbance Interactions

The incident disturbances of interest for high-speed atmospheric flight include particulates and stream fluctuations of velocity, pressure, concentration, and temperature. For subsonic speeds the influence of the body inviscid flow field upon these incident disturbance fields is governed primarily by rapid distortion theory. (Also, incident stream pressure fluctuations are augmented by vehicle-produced propulsion and airframe noise.) Several aspects combine to compound and alter the problem at high speeds. The heating problem at high speeds causes (either by design or inadvertently) a finite bluntness in the vehicle nose region and consequent body bow shock formation about this blunted nose. The nose shock creates an embedded subsonic flow region immediately preceeded by the shock (which acts as a disturbance modifier).

Therefore, the following can occur (for the high-speed case). First, consider stream particulates of an intermediate size, neither too small so that their Knudsen number is high and thus non-continuum, nor so large that the particle impacts the nose region. Such intermediate particles will typically traverse the shock without immediately slowing down and therefore downstream of the shock but within the body flow field the particles can be traveling supersonically compared to the local flow and produce "inverted" or "reversed" embedded dynamic shocks which can strafe the body boundary layer, creating a strong disturbance. From Reference 11 the distances required for the particles to attain local gas velocity can be the order of 10 cm. This uniquely high-speed disturbance production by particle induction can be particularly worrisome for the flight case because (a) the effective wavelength of the induced disturbance is a function of particle concentration as well as size and can easily be the order of the wavelength of linearly unstable waves; (b) the disturbance can be produced by particles in the nominally inviscid flow field (as

opposed to the usual low-speed case where the particle must be entrained into the viscous flow to produce a worrisome disturbance); (c) the amplitude of the disturbance can be quite large initially so that even if sub-critical decay occurs resulting initial levels at the start of amplification can be significant; and (d) the atmosphere is particularly rich in particulate content of various sizes including cosmic and terrestial dust, rocket exhaust products from previous flights and volcanic and water-based particles. Large particles can impact the body and rebound, in some cases retraversing through the bow shock thereby producing extremely large amplitude flow perturbations of potentially dangerous scale. These high-speed mechanisms overlay the usual low-speed particle disturbance mechanisms including particle adhesion/interaction with the surface (various roughness effects) and particle wake/rotation due to motions within the viscous layer.

Typically, atmospheric perturbation/turbulence scales are large compared to body viscous flow dimensions, and of such small amplitude that conventional wisdom holds that, to first order, transition is not influenced by stream disturbance fields in free flight. However, the aforementioned presence at high speeds of bow shocks and embedded subsonic regions may possibly alter this conjecture. This problem was considered by Morkovin (Ref. 12) and exhibits the following essential features. Due to the intermodal coupling inherent in the Rankine-Hugoniot equations, stream disturbances which traverse the bow shock will engender downstream acoustic waves even if the incident field does not initially have an acoustic component. Such post shock acoustic fields can reflect and re-reflect between the body and the bow shock (as can acoustic fields produced by nose region body vibration) as well as possibly interact with waves having other incidence angles, wave numbers, and phase.

For the stream disturbances to couple into the boundary-layer transition problem to first order, mechanisms must be present for these low-wave number disturbances to shift energy content to higher wave number. Whether the high-speed nose region interactions just described can, perhaps through either sums and differences of (possibly resonating) frequencies, or through wavelength shifts and wave trapping in the subsonic region (see Ref. 13), yield such wave number shifts is the subject of current research at ICASE. Another possible mechanism involves the interaction of shock wave/shock layer oscillations due to long wavelength stream fluctuations with body roughness/waviness and/or dynamic shock oscillations associated with instability waves. Such a combination of "flow-field processed" stream perturbations and roughness may both amplify and wave number shift the incident perturbation. At the highest speeds (high hypersonic) incident concentration fluctuations may induce chemical reaction/"flame front" induced oscillations in the nose shock region (depending upon incident species) possibly providing other wave-number shifting mechanisms. This area of atmospheric disturbance-body flow-field interactions is virtually untouched and obviously requires considerable further research.

Compressibility Influence Upon Linear Amplification

The influence of Mach number upon the linear amplification modes for flat-plate boundary layers is well known and well documented. The pioneering and still current work of Mack (Ref. 14) identified the major intrinsically compressible phenomena in the linear theory area, the second or acoustic mode which becomes dominant (most unstable) in two-dimensional zero pressure gradient flows above Mach numbers the order of 4 to 5. This mode was experimentally verified by Kendall (Ref. 22). Therefore, at high speeds the three low-speed instability modes, Gortler, crossflow, and Tollmien-Schlichting (T-S), are joined by the Mack second mode at higher Mach numbers. The influence of compressibility upon these various modes can be conveniently and simplistically summarized as follows: For the first or viscous (T-S) mode the amplification rate decreases with Mach number while the most unstable wave angle increases. The most unstable second mode waves are two-dimensional and at higher frequency than the first mode case. Also, for the second mode, the critical layer moves to the outer part of the boundary layer and the amplification rate decreases with Mach number (after an initial increase above first mode values). See Reference 14 for detailed discussion of these behaviors. The movement of the critical layer to the outer part of the boundary is depicted in Figure 1 where the disturbance eigenfunctions are plotted for M = 0 (first mode) and M = 10 (second mode), respectively. For the latter case temperature fluctuations are dominant.

Of particular interest when comparing the first and second modes is their different sensitivity to wall cooling. Cooling stabilizes the first mode, but the second mode is actually destabilized by cooling (Fig. 2). This is because the first mode amplified disturbances require the existence of a generalized inflection point $(\frac{d}{dy}\ (\rho\ \frac{du}{dy}) = 0)$ which is present in all insulated wall boundary layers. This inflection point may be eliminated by sufficient wall cooling, thus stabilizing the boundary layer to first-mode disturbances. The second mode, on the other hand, does not require the presence of a generalized inflection point and only the condition that $\bar{M}^2 > 1$ (where $\bar{M} = (u-c)M_e/\sqrt{T}$) is sufficient for inviscid disturbances to exist. The boundary-layer region in which this condition is satisfied expands with cooling, thus enhancing instability of the cold wall flow. The influences of pressure gradient, wall suction/injection, etc., have been little studied at high speeds (e.g., Refs. 15 and 16) but the trends are as would be expected from low speeds, at least up to low-hypersonic conditions. Wall suction and favorable pressure gradients stabilize both the first- and second-mode disturbances.

The other linear modes, crossflow and Gortler, are usually more unstable than the conventional (two-dimensional, flat surface) cases just discussed and are therefore to be avoided for transition delay (as in the low-speed case). The influence of increasing Mach number upon Gortler vortices is shown in Figure 3. The effect of compressibility is stabilizing (Refs. 17 and 18), though weak. This centrifugal instability is hard to control by wall suction or heat transfer (Refs. 17

and 19). The effect of adverse pressure gradient on Gortler instability in hypersonic boundary layers is found to be destabilizisng (Ref. 19). Figure 4 shows that the computed growth rates are significantly higher in the presence of adverse pressure gradient. The inflow Mach number for this calculation is 8. For the adverse pressure gradient case, the Mach number drops from 8 to about 6.5 towards the end of the computational domain. Since compressibility has been shown to have a stabilizing effect, part of the increase of the growth rates may be attributed to decreasing Mach numbers due to adverse pressure gradients.

Crossflow instability in subsonic and low supersonic Mach number flows has also been studied. The effect of compressibility on this inflectional instability is rather weak. This instability may be controlled by wall suction but wall cooling has only a weak stabilizing effect (Refs. 20 and 21). Detailed experimental verification of the influence of Mach number upon the T-S and Mack modes is available from Kendall in Reference 22. Disturbance-amplification data for high speeds are somewhat questionable due primarily to gross facility acoustic contamination as discussed subsequently (see Refs. 23-29, see also Ref. 30). Detailed compressible disturbance amplification data for the cross flow and Gortler modes are not yet available.

Some Additional Compressibility-Related or Accentuated Transition Physics

Outward Movement of the Critical Layer, Effect on Transition Process

As just noted, with increasing Mach numbers the critical layer moves to the outer portion of the boundary layer. Visualization on cones indicates that at high Mach number the disturbance growth in the outer region can become highly non-linear without grossly affecting the wall transport (Refs. 31-33) and there is some indication that "turbulence" can set in above the wall in a manner more analogous to the free shear layer case (spectral broadening) than the conventional Emmons spot "fully turbulent patch" wall production of turbulence (Ref. 34). Early attempts at modeling such behavior (Ref. 35 using the results of Ref. 36) improved the prediction of the transitional phase of the flow.

Flow Chemistry - Essentially nothing is yet known concerning the detailed physics of the influence of flow chemistry upon the transition process. Plots of transition Reynolds number against Mach number for cones in free flight do not exhibit any unusual behavior as the ideal gas-reacting gas boundary is crossed at high-edge Mach number (Ref. 1). Figure 5 from Reference 37 is one of the first attempts to include the effects of equilibrium gas chemistry in linear stability calculations and a slight destabilization is indicated along with a shift in unstable frequencies. Some changes would be expected, as the mean profiles are obviously altered. Whether any new, chemistry specific modes will arise can only be determined from further research. The area is wide open.

Shock Waves - The presence of shock waves constitutes an obvious and important difference between low- and high-speed flows. For the boundary-layer case the disturbance characteristics are such that, at least thus far, dynamic eddy shocklets do not seem to form/alter the amplification processes, e.g., Reference 38. However, quasi-steady shock waves can and do affect high-speed transition in several ways. The zeroth order effect is due to the curved bow shock which produces mean vorticity which in turn alters particularly the mean flow and thus the amplification characteristics of the tender external portion of the boundary layer and may cause instability of the outer inviscid but rotational flow in the region preceeding entropy swallowing (Refs. 24 and 39-41). In fact, at high speeds stability computations should be carried out using inputs from PNS or full NS rather than separate inviscid and boundary-layer codes to ensure that this effect is correctly incorporated. A transition reversal is observed in the experiments in which transition Reynolds number first increases with bluntness but then begins to decrease beyond a critical bluntness. This may be explained by considering the effect of bluntness on competing boundary and entropy layer instability modes (e.g., Ref. 39).

Another possible manifestation of the effect of bluntness is the possibility of a wave structure between the bow shock and a blunt face (Ref. 13). Such a wave structure, if linked to an instability mechanism, perhaps through surface-irregularity interactions, may provide a "receptivity" link for the boundary-layer disturbances. The shock wave also constitutes an altered external boundary condition which can affect the instability process (Ref. 42). In addition, the interaction of disturbances within a boundary layer with a quasi-steady shock wave, either impinging upon a surface or generated thereon can significantly amplify the disturbances and also cause intermodal energy transfer (e.g., Refs. 43 and 44). Such a process can be an integral part of the influence of adverse pressure gradients upon transition at high speeds where adverse pressure gradients can be accompanied by both concavely curved streamlines (which could induce a concomitant Gortler instability) and coalescing shock waves.

Roughness - Roughness and/or waviness are obviously not unique to the high-speed transition problem but unfortunately their importance as well as the richness of the associated physics is accentuated by increasing Mach number. This increased importance is due to the increasing aerodynamic heating which accompanies high-speed flight and induces large thermal stresses. In many cases these thermal stresses exceed the aerodynamic loading and dictate the design of the structure, particularly the surface region. Several techniques have historically been employed to handle this heat load and/or accompanying thermal stresses, including sublimation/ablation, tiles/expansion joints/shingles and merely letting the surface deform into "waffles" or corrugations. As an adjunct to this problem various dissimilar structural and material joints exist,

including antenna interfaces, handling plugs, field joints and fibers associated with some surface materials which give rise to additional steps and surface mismatches and irregularities. All of these approaches to surface survivability at high speeds produce "non-smooth" surfaces, i.e., roughness and waviness are endemic to high-speed atmospheric flight and the transition problem in particular.

The possible influences of roughness/waviness upon transition are manifold and include (a) altering the mean flow locally and downstream, thereby changing local amplification rates/eigenvalues, (b) affecting receptivity of external disturbance fields by providing spatial gradients which can readily couple certain disturbances into the local viscous flow, (c) introduction of streamwise vorticity into both mean and fluctuating local fields, (d) direct production of dynamic vorticity through element "eddy shedding" (at low speeds), and (e) at high speeds, influences of roughness/waviness induced embedded shock waves. These latter influences include the aforementioned direct amplification through the shock as well as the direct production of dynamic vorticity via shock unsteadiness and even possible delay of transition due to shock-induced Reynolds number diminution (Refs. 45 and 46). As a typical example of the importance of roughness in high-speed flight the U.S. space shuttle windward surface transition problem is dominated by tile-induced roughness, with transition Reynolds numbers in the 2 to 5 x 10^6 range rather than the 40 x 10^6 plus values one would normally expect at shuttle conditions (high angle of attack, edge Mach number of order 2 (first mode disturbances, cold wall). Reference 47 indicates the decreased sensitivity due to roughness which occurs at higher Mach numbers. This may be partly due to the shift to the second mode and movement of the critical layer to the outer region of the boundary layer. It should be noted that the roughness sensitivity of the cross flow and Gortler modes is evidently not significantly diminished at high Mach numbers.

Experimental Simulation and Prediction of High-Speed Transition

The influence of free-stream vorticity fluctuations upon transition location in low-speed facilities is well known. This source of facility stream disturbance diminishes at high Mach number but is replaced by a much more insidious and tenacious disturbance source - pressure fluctuations radiated from the turbulent nozzle wall boundary layer (Refs. 48 and 49). Extensive research at the NASA Langley Research Center over the past 15 years has indicated that in general this noise field alters both the level and magnitude of parametric trends of the transition location and that the only known approach to the replication of high-speed flight transition behavior in wind tunnels is the attainment of laminar flow on the nozzle walls of the facility (Ref. 49). This has been accomplished at NASA Langley by performing massive suction upstream of the throat to relaminarize the turbulent boundary layer incoming from the upstream piping

and stagnation chamber wall. The resultant thin laminar boundary layer which grows downstream of the suction slot is kept laminar through a combination of ultra-smooth walls and favorable pressure gradient until it is destabilized by the Gortler process in the nozzle reflex (concave curvature) region. This approach has provided a sufficient run of quiet test flow to allow duplication of flight transition behavior in the Langley pilot facility at a stream Mach number of 3.5. Suction laminarization on the high speed portion of the nozzle cannot be used as weak shocks are produced as the flow is turned into suction slots or holes and these weak shocks can cause greater disturbances than the original turbulent boundary-layer noise.

Additional pilot quiet facilities at Mach numbers of 6 and 20, to allow experimental study of second mode physics at high Mach number, are currently under development at NASA Langley. As an indication of the importance to transition of the stream asoustic disturbance field present in conventional tunnels, recent studies in the M ~ 3.5 pilot quiet tunnel indicate an order of magnitude difference in transition Reynolds number on flat plates for noisy and quiet free-stream flows (Ref. 50). It should be noted that successful duplication of flight transition behavior involves not only the maintenance of laminar nozzle wall flow but also control of other untoward disturbance fields such as gross particulates, small scale vorticity fluctuations, model vibration, and (uncontrolled) roughness. Transition data at high hypersonic cold-wall conditions in conventional, large facilities tends to approach flight-observations, perhaps due to a partial decoupling of the disturbance scale between the thick facility wall boundary layer and the thin model viscous flow (e.g., Ref. 8).

The current status of the prediction of hypersonic transition is wholly unsatisfactory, as it rests entirely upon engineering correlations of flight data taken over a very limited and often ill-defined parameter space. The high-speed experimental data from conventional facilities simply cannot be trusted (except perhaps at high hypersonic, cold wall, large scale conditions), either as to trend or level, due to the stream acoustic disturbances just discussed. Therefore, at the present time, at best, the location of high-speed transition can be estimated to within a factor of 5 to 10. Research at Langley over the past 12 years in the laminar flow control area indicates that the e^N method, which utilizes the linear stability theory to estimate transition location, may be applicable to the high-speed area (in the absence of roughness/waviness and Morkovin "bypasses") with an N value of the order of 10 (the usual low-speed value), Reference 3. Such an approach allows transition prediction within the order of 20 percent and parameterization for quantities which influence the mean flow such as (a) Mach number, (b) pressure gradient, (c) wall temperature, (d) angle of attack, (e) wall mass transfer, (f) sweep, (g) flow history, (h)

geometry/curvature, (i) body dynamics, (j) flow chemistry, and (k) bluntness. This extension of the e^N approach to high-speed flows (Ref. 3) should, except for roughness, elevated stream disturbances or perhaps shock interaction effects, allow a more accurate near-term estimation of transition location for design purposes.

Concluding Remarks

Paper sketches briefly the current state of the art in the understanding of high-speed boundary-layer transition. Of the 6 stages of the transition process the weakest links in the long term are the specification of stream-disturbance fields, including particulates, as a function of latitude, longitude, altitude and time (as well as body-generated disturbances), and the body processing and viscous internalization of this disturbance field as an initial condition for normal mode amplification. The basic normal mode processes are largely understood for the basic case with cleanup for bluntness, pressure gradient, and real gas effects currently underway. The non-linear end game is currently being attacked numerically and this approach, in fact in many cases the same codes, could also be used to study the receptivity problem. For most flight conditions with low-background disturbances the initial, internalized disturbance levels appear to be, to first order, the same order of magnitude. This is inferred from the fact that the e^N method, which addresses only the normal mode/linear amplification (as a ratio) appears thus far to be capable of estimating high-speed transition location within engineering accuracy (O(20%)).

The major research frontiers in high-speed transition, in the opinion of the present authors, include: (a) initial disturbance specification and internalization; (b) transition in other than conventional boundary-layer flows including two- and three-dimensional free shear layers, vortex boundary-layer interactions and separated flows; (c) roughness effects; and (d) influences of shock waves and chemistry.

References

1. Wright, R. L.; and Zoby, E. V.: Flight Boundary Layer Transition Measurements on a Slender Cone at Mach 20. Presented at the AIAA 10th Fluid and Plasmadynamics Conference, Albuquerque, NM, June 27-29, 1977. AIAA Paper No. 77-719.
2. Ericsson, L. E.: What About Transition Effects? Presented at the AIAA 26th Aerospace Sciences Meeting, Reno, Nevada, January 11-14, 1988. AIAA Paper No. 88-0564.
3. Bushnell, D. M.; Malik, M. R.; and Harvey, W. D.: Transition Prediction in External Flows Via Linear Stability Theory. Presented at the IUTAM Symposium Transsonicum III, Gottingen, West Germany, May 24-27, 1988.
4. Morkovin, Mark V.: Critical Evaluation of Transition from Laminar to Turbulent Shear Layers with Emphasis on Hypersonically Traveling Bodies. Technical Report AFFDL-TR-68-149, March 1969.

5. Morkovin, Mark V.: Transition at Hypersonic Speeds. NASA CR-178315, May 1987.
6. Mack, Leslie M.: Linear Stability Theory and the Problem of Supersonic Boundary-Layer Transition. AIAA Journal, Vol. 13, No. 3, March 1975, pp. 278-289.
7. Reshotko, Eli; Bushnell, Dennis M.; and Cassidy, Mell D.: Report of the Task Force for Boundary Layer Transition. NASP Technical Memorandum 1007, April 1987.
8. Stetson, Kenneth F.: On Predicting Hypersonic Boundary Layer Transition. AFWAL-TM-87-160-FIMG, March 1987.
9. Gaponov, S. A.; and Maslov, A. A.: "Razvitie Vozmushchenii V Szhimaemykh Potokakh," Otvetstvennyi Redaktor Kand. Tekhin. Nauk V. Ya. Levchenko, Izdatel-Stvo, Nauka, Sibirskoe Otdelenie, Novosibirsk, 1980.
10. Arnal, D.: Laminar-Turbulent Transition Problems in Supersonic and Hypersonic Flows. AGARD/FDP/VKI Special Course "Aerothermodynamics of Hypersonic Vehicles," Rhode-St-Genese, Belgium, May 30-June 3, 1988.
11. Walsh, Michael J.: Influence of Particle Drag Coefficient on Particle Motion in High-Speed Flow With Typical Laser Velocimeter Applications. NASA TN D-8120, February 1976.
12. Morkovin, M. V.: Note on the Assessment of Flow Disturbances at a Blunt Body Traveling at Supersonic Speeds Owing to Flow Disturbances in Free Stream. Journal of Applied Mechanics, June 1960, pp. 223-229.
13. Canning, Thomas N.; and Sommer, Simon C.: Investigation of Boundary-Layer Transition on Flat-Faced Bodies of Revolution at High Supersonic Speeds. NACA RM A57C25, June 1957.
14. Mack, Leslie M.: Boundary-Layer Linear Stability Theory. AGARD-R-709, June 1984, pp. 3-1 - 3-81.
15. Malik, M. R.: Prediction and Control of Transition in Hypersonic Boundary Layers. Presented at the AIAA 19th Fluid Dynamics, Plasma Dynamics and Lasers Conference, Honolulu, Hawaii, June 8-10, 1987. AIAA Paper No. 87-1414.
16. Lysenko, V. I.: The Role of the First and Second Modes in Compressible Boundary-Layer Transition. Journal of Applied Mechanics and Technical Physics, Vol. 26, No. 6, November-December 1985, pp. 809-812.
17. El-Hady, N.; and Verma, A. K.: Growth of Gortler Vortices in Compressible Boundary Layers Along Curved Surfaces. Presented at the AIAA 14th Fluid and Plasma Dynamics Conference, Palo Alto, California, June 23-25, 1981, AIAA Paper No. 81-1278.
18. Hall, P.; and Malik, M. R.: The Growth of Gortler Vortices in Compressible Boundary Layers. NASA CR-178369, 1987.
19. Spall, R. E.; and Malik, M. R.: Gortler Vortices in Supersonic Boundary Layers. Presented at the AIAA First National Fluid Dynamics Congress, Cincinnati, Ohio, July 25-28, 1988. AIAA Paper No. 88-3678.
20. Lekoudis, S.: The Stability of the Boundary Layer on a Swept Wing with Wall Cooling. Presented at the AIAA 12th Fluid and Plasma Dynamics Conference, July 1979, Williamsburg, Virginia. AIAA Paper No. 79-1495.
21. Bushnell, D. M.; and Malik, M. R.: Supersonic Laminar Flow Control. Presented at NASA Langley Symposium on Research in Natural Laminar Flow and Laminar-Flow Control, Hampton, Virginia, March 16-19, 1987. NASA CP-2487, Part 3, pp. 923-946.
22. Kendall, J. M.: Wind Tunnel Experiments Relating to Supersonic and Hypersonic Boundary Layer Transition. AIAA Journal, Vol. 13, No. 3, pp. 290-299, March 1975.
23. Stetson, K. F.; Thompson, E. R.; Donaldson, J. C.; and Siler, L. G.: Laminar Boundary Layer Stability Experiments on a Cone at Mach 8, Part 1: Sharp Cone. AIAA Paper No. 83-1761, July 1983.
24. Stetson, K. F.; Thompson, E. R.; Donaldson, J. C.; and Siler, L. G.: Laminar Boundary Layer Stability Experiments on a Cone at Mach 8, Part 2: Blunt Cone. AIAA Paper No. 84-0006, January 1984.
25. Stetson, K. F.; Thompson, E. R.; Donaldson, J. C.; and Siler, L. G.: Laminar Boundary Layer Stability Experiments on a Cone at Mach 8, Part 3: Sharp Cone at Angle of Attack. AIAA Paper No. 85-0492, January 1985.

26. Stetson, K. F.; Thompson, E. R.; Donaldson, J. C.; and Siler, L. G.: Laminar Boundary Layer Stability Experiments on a Cone at Mach 8, Part 4: On Unit Reynolds Number and Environmental Effects. AIAA Paper No. 86-1087, May 1986.
27. Demetriades, Anthony: New Experiments on Hypersonic Boundary Layer Stability Including Wall Temperature Effects. Proceedings of the 1978 Heat Transfer and Fluid Mechanics Institute, Stanford University Press, 1978.
28. Kosinov, A. D.; and Maslov, A. A.: Growth of Artificially Induced Disturbances in a Supersonic Boundary Layer. Novosibirsk. Translatted from Izvestiya Akademii Nauk SSSR, Mekhanika Zhidkosti i Gaza, No. 5, September-October 1984, pp. 37-43.
29. Laufer, John; and Vrebalovich, Thomas: Stability of a Supersonic Laminar Boundary Layer on a Flat Plate. JPL Report No. 20-116, December 1958.
30. Mack, Leslie M.: Stability of Axisymmetric Boundary Layers on Sharp Cones at Hypersonic Mach Numbers. Presented at the AIAA 19th Fluid Dynamics, Plasma Dynamics and Lasers Conference, Honolulu, Hawaii, June 8-10, 1987. AIAA Paper No. 87-1413.
31. Fischer, Michael C.; and Weinstein, Leonard M.: Cone Transitional Boundary-Layer Structure at $M_e = 14$. AIAA J., Vol. 10, No. 5, May 1972, pp. 699-701.
32. Demetriades, Anthony: Hypersonic Viscous Flow Over a Slender Cone. Part III: Laminar Instability and Transition. AIAA Paper No. 74-535, June 1974.
33. Owen, F. K.: Fluctuation Measurements in Compressible Boundary Layers. Report No. 1,076,69, Dep. Eng. Sci., Univ. Oxford, March 1969.
34. Fischer, Michael C.: Turbulent Bursts and Rings on a Cone in Helium at $M_e = 7.6$. AIAA J., Vol. 10, No. 10, October 1972, pp. 1387-1389.
35. Bushnell, D. M.; and Alston, D. W.: Calculation of Transitional Boundary-Layer Flows. AIAA J., Vol. 11, No. 4, April 1973, pp. 554-556.
36. Fischer, Michael C.: Spreading of a Turbulent Disturbance. AIAA J., Vol. 10, No. 7, July 1972, pp. 957-959.
37. Malik, M. R.: Real Gas Effects on Hypersonic Boundary Layer Stability. To be published.
38. Hussaini, M. Y.; Collier, F.; and Bushnell, D. M.: Turbulence Alteration due to Shock Motion. Turbulent Shear Layer/Shock Wave Interactions IUTAM Symposium Palaiseau 1985, Springer, Berlin Heidelberg 1986, pp. 371-381.
39. Reshotko, Eli; and Khan, M. M. S.: Stability of the Laminar Boundary on a Blunted Plate in Supersonic Flow. Laminar-Turbulent Transition, IUTAM Symposium, R. Eppler and H. Fasel (eds.), Springer-Verlag 1980, pp, 186-200.
40. Young, C. H.; Reda, D. C.; and Roberge, A. M.: Hypersonic Transitional and Turbulent Flow Studies on a Lifting Entry Vehicle. Journal of Spacecraft and Rockets, V. 9, December 1972, pp. 883.
41. Morkovin, M. V.: Instability, Transition to Turbulence and Predictability. AGARDograph AG-236, 1978.
42. Petrov, G. V.: Stability of Thin Viscous Shock Layer on a Wedge in Hypersonic Flow of a Perfect Gas, Laminar Turbulent Transition, (Ed. V. V. Kozlov), Springer-Verlag, 1985, pp. 487-493.
43. Anyiwo, J. C.; and Bushnell, D. M.: Turbulence Amplification in Shock Wave-Boundary Layer Interactions. AIAA Journal, Vol. 20, No. 7, July 1982, pp. 893-899.
44. Zang, T. A.; Hussaini, M. Y.; and Bushnell, D. M.: Numerical Computations of Turbulence Amplification in Shock-Wave Interactions. AIAA Journal, Vol. 22, No. 1, January 1984, pp. 13-22, also ICASE report; NASA TM-85413.
45. James, Carlton S.: Boundary Layer Transition on Hollow Cylinders in Supersonic Free Flight as Affected by Mach Number and a Screwthread Type of Surface Roughness. NASA Memorandum 1-20-59A, February 1959.
46. Sterrett, James R.; and Holloway, Paul F.: Effects of Controlled Roughness on Boundary Layer Transition at a Mach Number of 6. AIAA Journal, Vol. 1, No. 8, August 1963, pp. 1951-1953.
47. Braslow, Albert L.: A Review of Factors Affecting Boundary-Layer Transition. NASA TN D-3384, August 1966.
48. Laderman, A. J.: Review of Wind-Tunnel Freestream Pressure Fluctuations. AIAA Journal, Vol. 15, No. 4, April 1977, pp. 605-608.

49. Beckwith, Ivan E.; Creel, Theodore R., Jr.; Chen, Fang-Jenq; and Kendall, James M.: Free-Stream Noise and Transition Measurements on a Cone in a Mach 3.5 Pilot Low-Disturbance Tunnel. NASA TP-2180, September 1983.
50. Chen, F.-J.; Malik, M. R.; and Beckwith, I. E.: Comparison of Boundary Layer Transition on a Cone and Flat Plate at Mach 3.5. Presented at the AIAA 26th Aerospace Sciences Meeting, Reno, Nevada, January 11-14, 1988. AIAA Paper No. 88-0411.

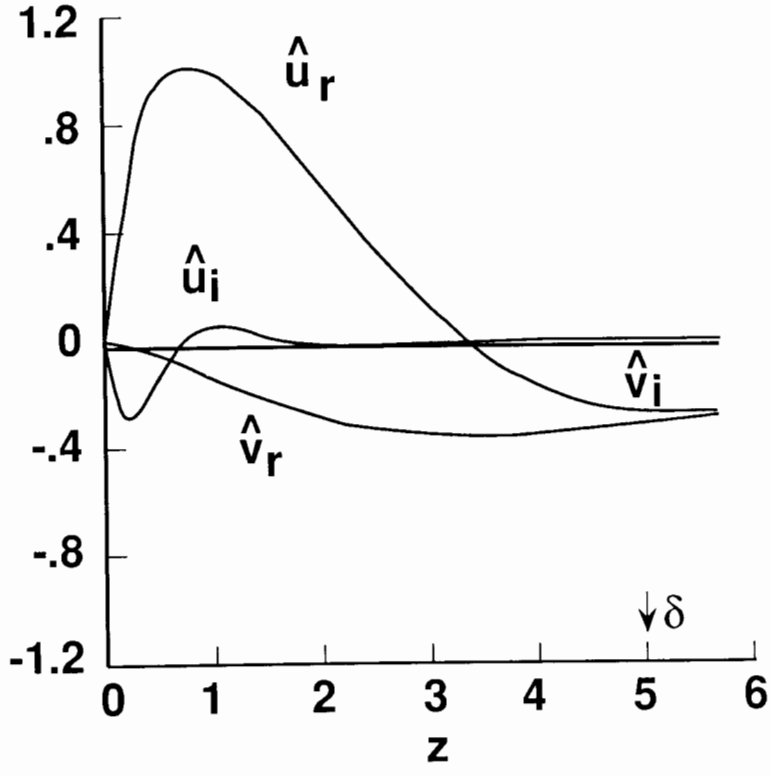

Figure 1. - Real and imaginary parts of the disturbance eigenfunctions for incompressible and Mach 10 (adiabatic wall) boundary layers.

(a) M = 0

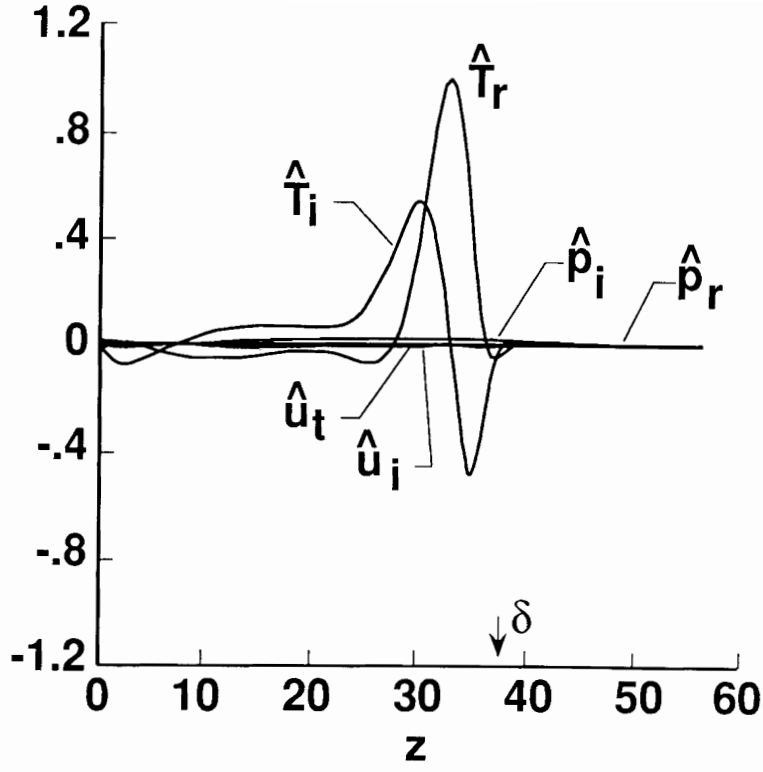

(b) M = 10

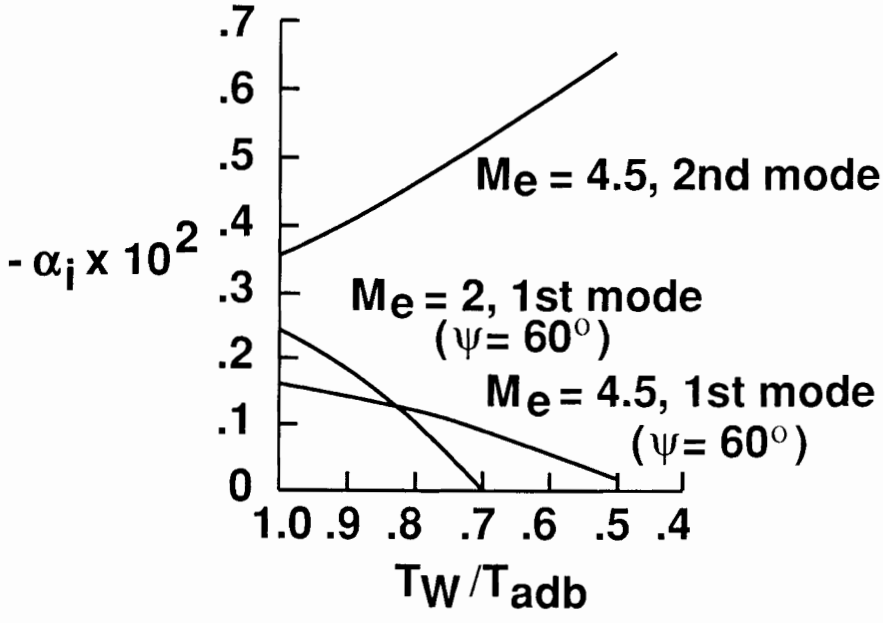

Figure 2. - Effect of wall cooling on the most amplified first- and second-mode disturbances in a flat-plate boundary layer at R = 1500.

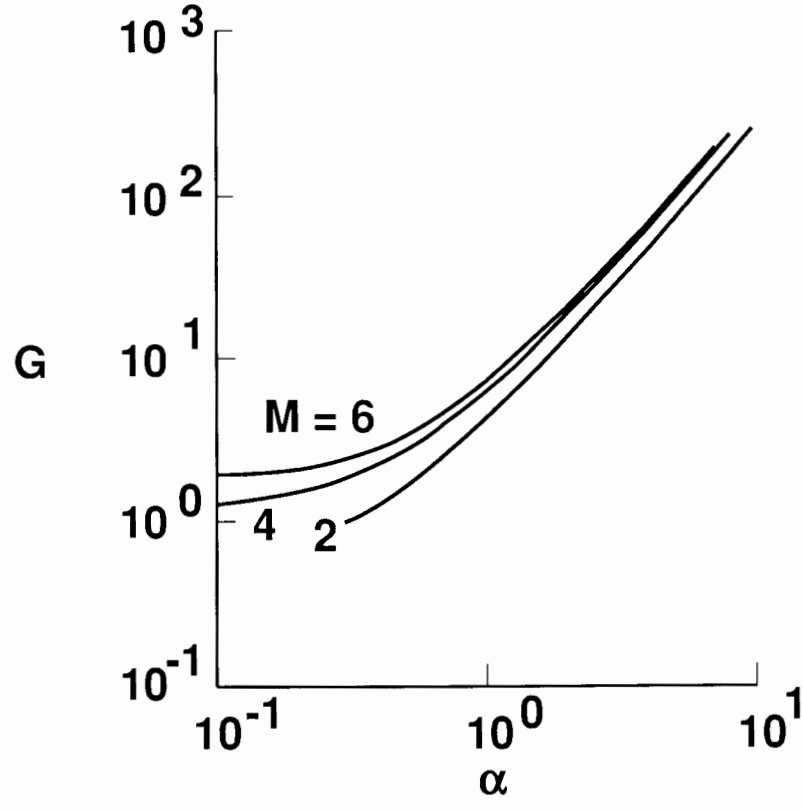

Figure 3. - Effect of compressibility on neutral curves for Gortler instability.

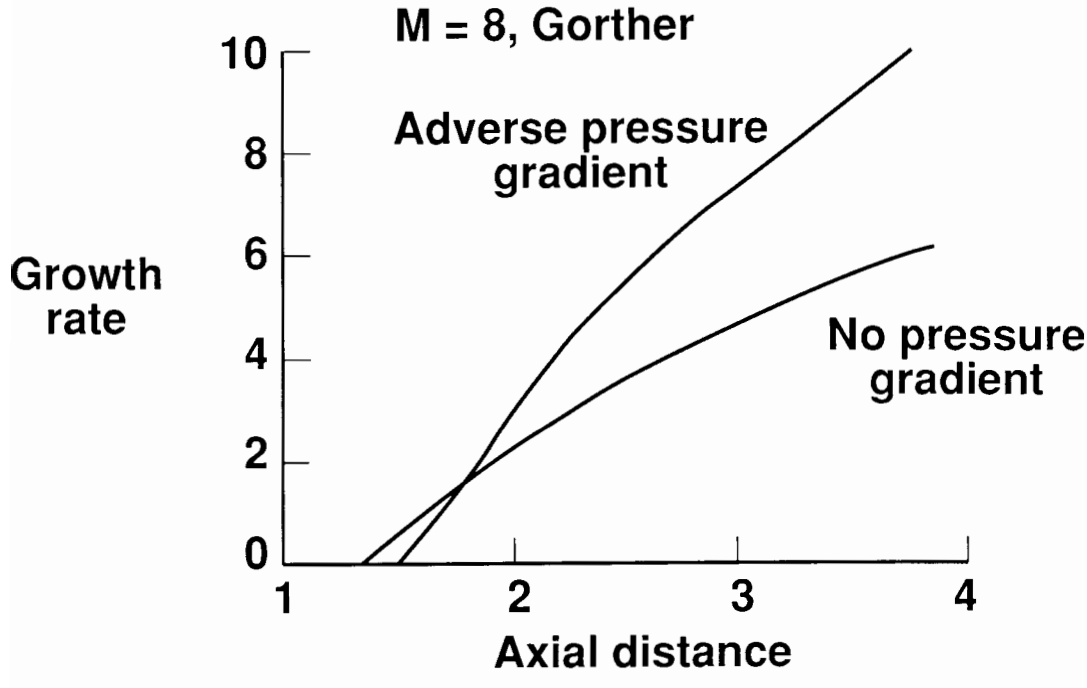

Figure 4. - Effect of adverse pressure gradient on Gortler instability in a Mach 8 boundary layer (growth rates for the most amplified wavelengths).

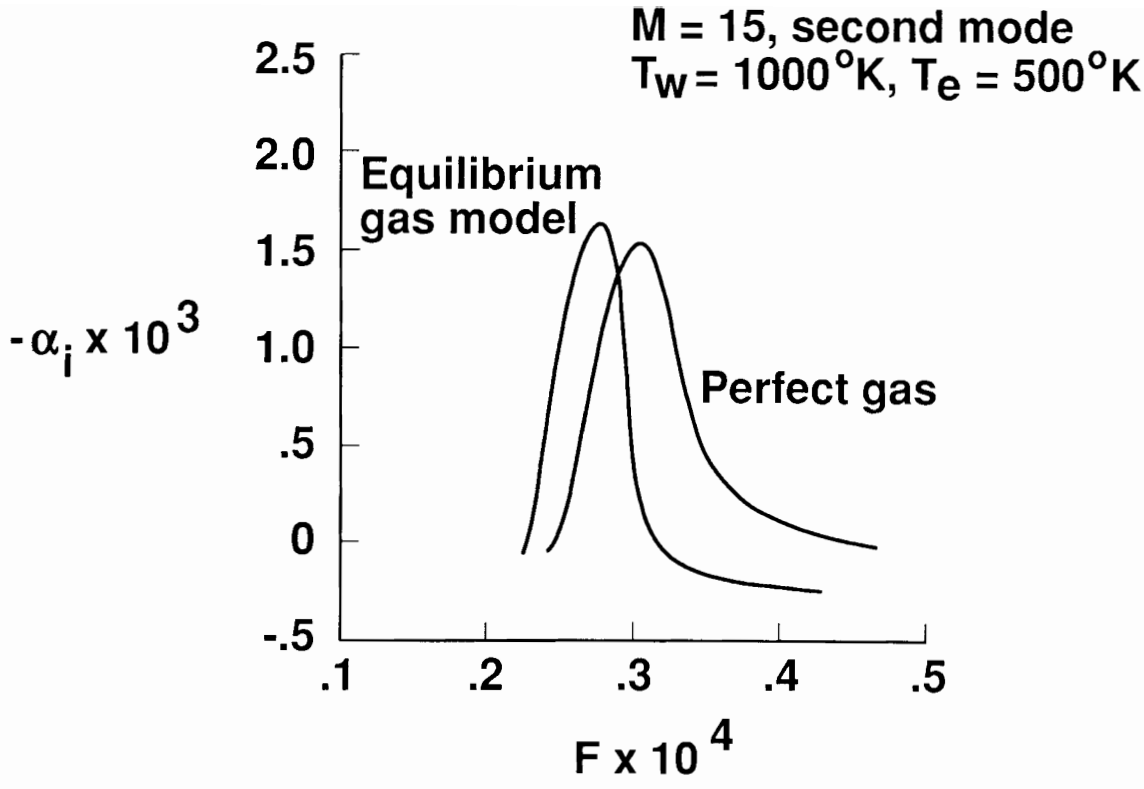

Figure 5. - Effect of equilibrium gas chemistry on second-mode growth rates in a Mach 15 boundary layer.

QUASISYMMETRY OF FLOWS AND CHAOS OF STREAMLINES

A. A. Chernikov, R. Z. Sagdeev, G. M. Zaslavsky
Space Research Institute, Academy of Sciences
of the USSR, Profsoyuznaya 84/32, Moscow 117810 USSR

1. INTRODUCTION

The onset of turbulence may be preceded by development of ordered spatial structures. Such structures play a prominent role in mixing and advection processes. Presence of these structures can lead to chaotic spatial distribution of streamlines and to random walk of passive particles along the streamlines. Examples of such particle mixing are well known, they are the ABC-flow [1], and the flow between rotating cylinders [2,3]. In connection with these phenomena some general questions arise concerning the "structural mixing": (1) which kinds of structures are admissible; (2) which structures can lead to mixing of streamlines; (3) what are the laws of transport of passive particles? Here we discuss the first two questions which are tightly connected with modern problems of nonlinear dynamics. The part of the paper devoted to symmetry of the structures is restricted to incompressible flows. This provides the simplest way to deduce possible types of flow organization. We further restrict ourselves to the Beltrami-type flows. Special interest in such flows is associated with instability of large-scale modes obeying the Beltrami condition in fluids with strongly developed turbulence [4,5]. It is plausible that extended regions occupied by Beltrami flows can be present in turbulent flows [6]. It is possible to say that flows can be "beltramized." We have shown that stationary hydrodynamic Beltrami flows can possess an arbitrary symmetry of quasi-crystallic type. Not withstanding the regular character of the structures, the flow also includes elements of irregularity, stochasticity. In some regions of space, the streamlines are distributed chaotically. The second group of our

results is associated with investigation of this property. The concluding part of the paper is devoted to chaos of streamlines in stationary Rayleigh-Benard convection. It is shown that three-dimensional stationary flow with hexagonal cells produces a spatial web of finite thickness within which the chaotic streamlines are concentrated.

2. STATIONARY STRUCTURES AND SYMMETRY OF PLANAR FLOWS

For planar incompressible flows, the Navier-Stokes equation is reduced to the following scalar equation:

$$\frac{\partial}{\partial t}\nabla^2\psi + \frac{\partial(\psi, \nabla^2\psi)}{\partial(x,y)} = \nu\nabla^4\psi + F(x,y,t) \tag{1.1}$$

where ψ is the stream function, F is the pumping that excites the medium. In two dimensions the solenoidality of the velocity field x allows expressing it in terms of the stream function as

$$v_x = -\frac{\partial\psi}{\partial y};\quad v_y = \frac{\partial\psi}{\partial x} \tag{1.2}$$

Now we specify the pumping in (1.1) by choosing the external force F in the form

$$F(x,y,t) = F_o(t)\cos k(x\cos\omega t + y\sin\omega t) \tag{1.3}$$

where the pumping wave number is $k = 2\pi/L$ and the frequency is $\omega = 2\pi/T$, and F_o is the amplitude of external force that generally depends on time.

We have solved Eq. (1.1) numerically on a 128 x 128 grid in a unit square. At the square boundary Q the boundary conditions are given by

$$\psi(t, \Gamma) = \text{const} = \psi_o \tag{1.4}$$

Initial conditions are chosen in a similar way, $\psi(O,x,y) = \text{const} = \psi_o$. Figure 1 shows the results for the case when the amplitude $F_o(t)$ is a sequence of short pulses of duration τ with period $T_o = 2\pi/\Omega$. In our computations, the length of an individual pulse, τ, is much shorter than remaining characteristic times. As was revealed by numerical integration [7], the flow patterns under the resonance $\Omega = N\omega$ (with integer N) is qualitatively different from the corresponding patterns far from the resonance. Under the resonance and for $\omega/\nu k >> 1$, the flow eventually evolves to stationary structures of N-fold quasi-crystallic symmetry. Figure 1a shows the stationary flow structure under the resonance $\Omega = 10\ \omega$ which possesses the quasi-crystallic symmetry, while Fig. 1b shows the pattern of streamlines for the eighth-order resonance.

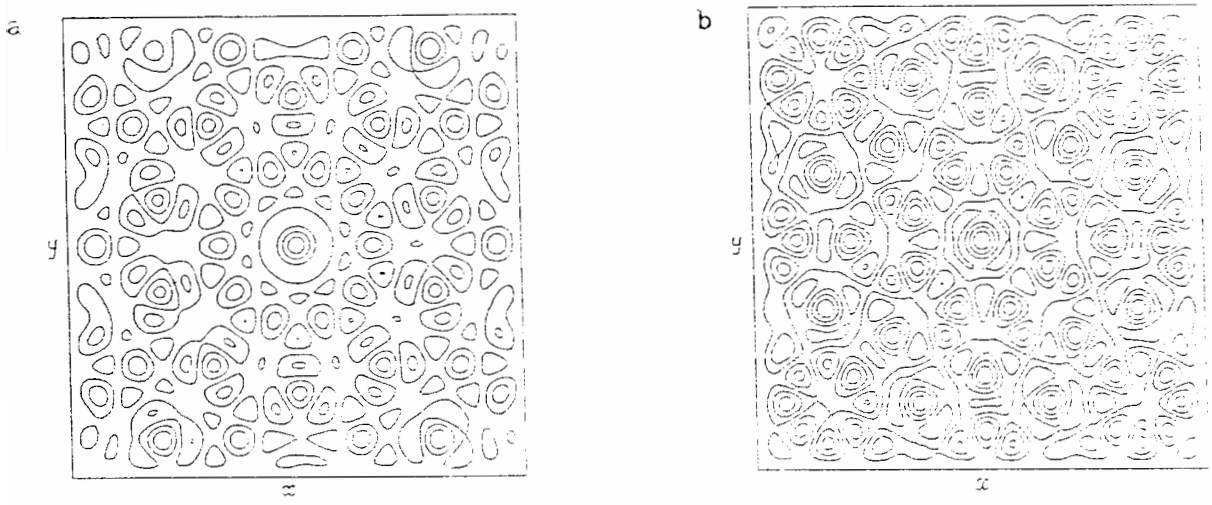

Figures 1a and 1b.

The approximate analytical expression for the stationary stream function ψ can be obtained as follows. Let us approximate the amplitude of the pumping $F_o(t)$ by a sequence of delta functions

$$F(x,y,t) = F_o \sum_{n=-\infty}^{+\infty} \delta\left(\frac{t}{T_o} - n\right) \cos k\left(x \cos \omega t + y \sin \omega t\right) \qquad (1.5)$$

With use of the representation

$$\sum_{n=-\infty}^{+\infty} \delta(t/T_o - n) = \frac{1}{N} \sum_{j=1}^{N} \sum_{m=-\infty}^{+\infty} \exp\left[2\pi i m \frac{t/T_o - j}{N}\right] \tag{1.6}$$

it can easily be shown [8] that

$$F = \bar{F} + \tilde{F}$$

$$\bar{F} = \frac{F_o}{N} \sum_{j=1}^{N} \cos \xi_j$$

$$\tilde{F} = \frac{2F_o}{N} \sum_{k=1}^{N} \cos \xi_j \sum_{m=1}^{\infty} \cos\left[\frac{2\pi m}{N}(t/T_o - j)\right] \tag{1.7}$$

where $\xi_j = j\left(x \cos \frac{2\pi j}{N} + y \sin \frac{2\pi j}{N}\right)$ or $\xi_j = k\underset{\sim}{\rho}\underset{\sim}{e}_j$ with $\underset{\sim}{\rho}$ the radius-vector on the plane (x, y) and $\underset{\sim}{e}_j$ the unit vector that determines a vertex of the regular N-agon. Since the function $\bar{F}(x,y)$ in (1.7) is the exact solution of the Helmholtz equation

$$\nabla^2 \bar{F} + k^2 \bar{F} = 0 \tag{1.8}$$

for the stream function

$$\bar{\psi} = -\frac{F_o}{\nu k^4 N} \sum_{j=1}^{N} \cos k\left[x \cos \frac{2\pi j}{N} + y \sin \frac{2\pi j}{N}\right] \tag{1.9}$$

the nonlinear term on the left-hand side of Eq. (1.1) vanishes. Therefore, the stream function (1.9) is the exact solution to the Navier-Stokes equation with stationary pumping F(x, y).

3. CHAOS OF STREAMLINES IN STATIONARY THREE-DIMENSIONAL FLOWS

Above we have discussed only two-dimensional quasi-symmetric flows. Quasi-symmetric structures can be present also in three-dimensional flows described by the Euler equation

$$\frac{\partial}{\partial t}\underset{\sim}{v} + \underset{\sim}{v} \times \mathrm{rot}\,\underset{\sim}{v} = -\nabla\left(P + v^2/2\right) \quad ; \quad \mathrm{div}\,\underset{\sim}{v} = 0 \tag{2.1}$$

where P is the pressure. If Beltrami condition

$$\underset{\sim}{v} = \alpha\ \mathrm{rot}\,\underset{\sim}{v} \tag{2.2}$$

with α = const is also imposed, these velocity fields $\underset{\sim}{v}$ are the stationary solutions of the Euler equation. It was shown in [9,10] that the velocity field

$$v_x = -\frac{\partial \psi}{\partial y} + \varepsilon \sin z \quad ; \quad v_y = \frac{\partial \psi}{\partial x} - \varepsilon \cos z \quad ; \quad v_z = \psi \tag{2.3}$$

with ε the perturbation parameter and $\psi = \psi(x, y)$ obeys two-dimensional Helmholtz Eq. (1.8). We call such flow quasi-symmetric when the function ψ is determined by (1.9) up to a constant factor. The flow (2.3) is solenoidal and is of Beltrami type, $\nabla \times \underset{\sim}{v} = -\underset{\sim}{v}$, i.e., this flow is a stationary solution of the Euler Eq. (2.1).

Equations

$$\frac{dx}{v_x} = \frac{dy}{v_y} = \frac{dz}{v_z} \tag{2.4}$$

determine the pattern of streamlines of the velocity field $v(\underset{\sim}{x},y,z)$. For a quasi-symmetric flow (2.3) the system of Eqs. (2.4) reduces to

$$\frac{dx}{dz} = -\frac{1}{\psi}\frac{\partial H}{\partial y} \quad ; \quad \frac{dy}{dz} = \frac{1}{\psi}\frac{\partial H}{\partial x} \tag{2.5}$$

where

$$H = \psi + eV \quad ; \quad V = - x \cos z - y \sin z \quad ;$$

$$\psi = \psi_0 \sum_{j=1}^{N} \cos\left[x \cos\frac{2\pi j}{N} + y \sin\frac{2\pi j}{N}\right] \tag{2.6}$$

Reduction of (2.4) to the form (2.5) indicates that we actually deal with a "nonstationary" problem formulated for a dynamic system in two-dimensional phase space (x,y). The variable z stands for the time variable. Since Eqs. (2.5) have Hamiltonian form we can readily apply some results of the theory of dynamic systems. Let us recall them briefly. The unperturbed part of the system (2.5) with Hamiltonian (2.6) for $\varepsilon = 0$ has a set of singular trajectories (separatrices) which pass through singular points of saddle type. For instance, for N = 4 or N = 3, 6, when the stream function is given by

$$\psi_{N=4} = \psi_0 (\cos x + \cos y) \tag{2.7}$$

or

$$\psi_{N=3} = \frac{1}{2}\psi_6 = \psi_0 \left\{\cos x + \cos\left(\frac{x}{2} + \frac{\sqrt{3}}{2} y\right) + \cos\left(\frac{x}{2} - \frac{\sqrt{3}}{2} 2\right)\right\} \tag{2.8}$$

respectively, all separatrices belong to the same value of the stream function ψ and thereby form single square or hexagonal network. Any arbitrarily weak periodic perturbation in z (i.e., arbitrary ε) leads to disruption of separatrices and to occurrence in their vicinity of a finite region of stochastic streamline dynamics. In the considered case this means development in the space (x,y,z) of a stochastic web with square or hexagonal cells. Examples of such a web are given in Fig. 2. Within the web cells, small regions (islands) are preserved where the streamline dynamics are stable. This means that streamlines are regularly wound around some invariant surface. In the case considered, such surfaces are periodically meandering stream tubes orientated at different angles to the plane,

z = const. Cross sections of these tubes are actually the windows in the stochastic web of Fig. 2. The whole remaining region occupied by the web is filled by only a single trajectory and is essentially a fractal set occupying a finite volume in the (x,y,z) space.

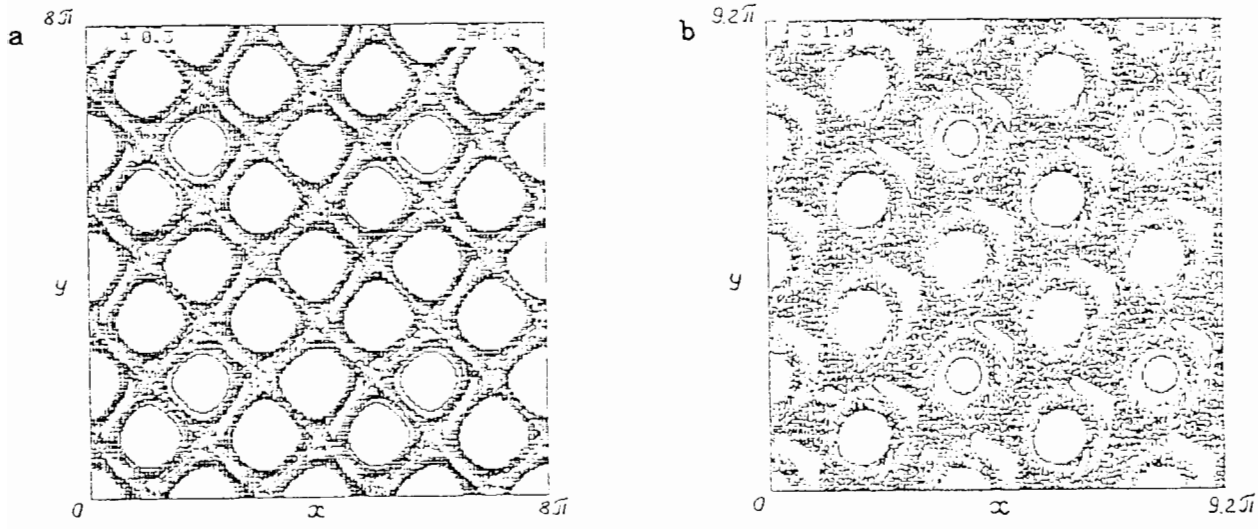

Figures 2a and 2b.

The stochastic web with square (a) and hexagonal (b) symmetry formed by streamlines.

When approaching the spatial rest points (saddles) that lie on intersections of separatrices, a streamline randomly chooses the direction of further motion. As a result, a spatial diffusion arises that is similar to Brownian motion of particles on square or hexagonal lattice. Two examples of such diffusion for N = 4 and N = 3 are obtained numerically and shown in Fig. 3. A streamline sometimes passes a considerable interval along the plane z = const, then turns and follows the plane x = const which produces a rather complicated loop and returns to the same plane z = const. This is why the diffusion alternates with "jumps" of streamlines along the same plane z = const. This feature is seen particularly clear in the case of the harmonics obtained by expansion of the solution into Fourier series and truncation. Any finite sum of harmonics possesses the quasi-symmetry. In three- dimensional problems the quasi-symmetry corresponds to streamline equations with 3/2

degrees of freedom. Therefore, stochasticity of streamlines must be typical of generic three-dimensional flows.

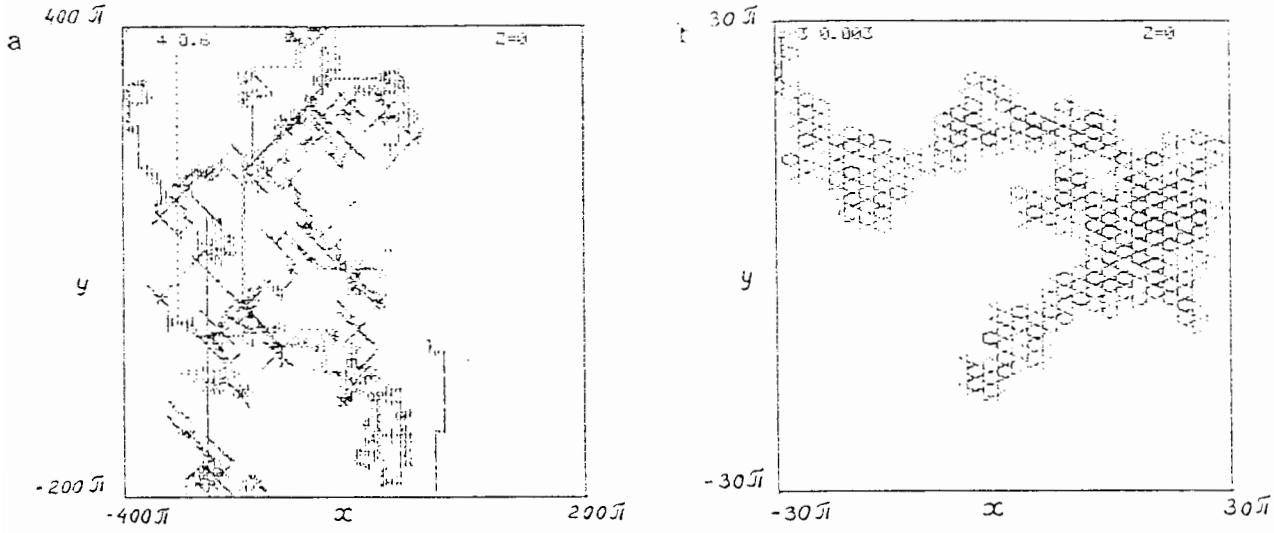

Figures 3a and 3b.

"Lagrangian turbulence" as contrasted to ordinary "Euler turbulence." As long as for stationary flows trajectories of Lagrangian particles coincide with streamlines, the chaos of streamlines implies also an anomalous diffusion of admixture particles along the channels of the stochastic web.

Let us make these arguments more specific, using as example the streamlines of stationary Rayleigh-Benard convection in horizontal infinite fluid layer. When the Rayleigh number, which is a dimensionless measure of temperature difference across the layer, exceeds certain threshold value R_c, the fluid motion is self-organized into hexagonal Benard cells. Slightly above the threshold, for $\varepsilon = (R - R_c)^{0.5} << 1$, the spatial dependence of the velocity field $\underset{\sim}{v}$ is given by

$$\underset{\sim}{v} = \varepsilon \text{ rot rot } \underset{\sim}{z}\psi \qquad (3.1)$$

With accuracy up to ε^2, where

$$\psi = \left\{\cos x + \cos\left(\frac{x}{2} + \frac{\sqrt{3}}{2}y\right) + \cos\left(\frac{x}{2} - \frac{\sqrt{3}}{2}y\right)\right\}\left(\sin z + a\varepsilon \sin 2z\right)$$

$$+ b\varepsilon\left\{\cos\sqrt{3}\,y + \cos\left(\frac{\sqrt{3}}{2}y + 3x\right) + \cos\left(\frac{\sqrt{3}}{2}y - 3x\right)\right\}(\sin z) \qquad (3.2)$$

Explicit expressions for the coefficients a and b as functions of the problem parameters are obtained in [11].

Introducing parameter, t, we obtain the following equations that describe dynamics of impurity in the field (3.1) - (3.2):

$$\frac{dx}{dt} = -\left(\sin x + \sin\frac{x}{2}\cos\frac{\sqrt{3}}{2}y\right)\left(\cos z + 2\varepsilon_1 \cos 2z\right)$$

$$- 2\varepsilon_2 \cos\frac{\sqrt{3}}{2}y \sin\frac{3}{2}X \cos 2z$$

$$\frac{dy}{dt} = -\sqrt{3}\cos\frac{x}{2}\sin\frac{\sqrt{3}}{2}y\left(\cos z + 2\varepsilon_1 \cos 2z\right)$$

$$-\frac{2\sqrt{3}}{3}\varepsilon_2\left(\sin\sqrt{3}\,y + \sin\frac{\sqrt{3}}{2}y\cos\frac{3}{2}x\right)\cos 2z$$

$$\frac{dz}{dt} = \left(\cos x + 2\cos\frac{x}{2}\cos\frac{\sqrt{3}}{2}y\right)\left(\sin z + \varepsilon_1 \sin 2z\right)$$

$$+\varepsilon_2\left(\cos\sqrt{3}\,y + 2\cos\frac{\sqrt{3}}{2}y\cos\frac{3}{2}x\right)\sin 2z \qquad (3.3)$$

here $\varepsilon_1 = a\varepsilon$ and $\varepsilon_2 = 2b\varepsilon$. To the first approximation in ε, i.e., for $\varepsilon_1 = 0$ and $\varepsilon_2 = 0$, the streamline pattern forms in a hexagonal so-called ABC flow (Fig. 3a).

Thus, the streamlines divide the whole coordinate space occupied by the flow into a system of cells which can have either a simple crystallic pattern (N = 3,4,6) or be very complicated, as is the case for five-fold or higher quasi-symmetry. These cells are

separated by layers of turbulent streamlines whose thickness is of the order of ε [9,10]. This phenomenon is sometimes described also by the notion of "Lagrangian turbulence" as contrasted to ordinary "Euler turbulence." As long as, for stationary flows, trajectories of Lagrangian particles coincide with streamlines, the chaos of streamlines also implies an anomalous diffusion of admixture particles along the channels of the stochastic web.

4. STOCHASTICITY OF STREAMLINES IN RAYLEIGH-BENARD CONVECTION

The picture described previously seems to be of rather universal character and therefore well-known structures in other stationary motions of fluid, gas or plasma must also possess similar properties. This means that the structures that arise in fluids before transition to turbulence also form a stochastic web of streamlines. Moreover, spatial orientation of this web naturally reflects the structure form. This conclusion is motivated by the following arguments. Let us use any suitable method of analysis of a hydrodynamic medium in a preturbulent state. Such a state, which can be described by a finite collection of cells, was obtained in [12]. These streamlines are closed and lie on vertical cylindrical surfaces.

To the next approximation in ε, i.e. for $\varepsilon_2 \neq 0$, but small $\varepsilon_2 << 1$, the picture changes. The majority of streamlines now become unclosed and wind around toroidal surfaces. Figure 4a illustrates the results of numerical integration of the system (3) for $\varepsilon_1 = 0$ and $\varepsilon_2 = 0.2$. Shown is cross section of one of the tori in the plane $z = \pi/2$. However, near the cell boundary such surfaces turn out to be destroyed. Figure 4b shows the chaos of streamlines in one of the sectors of a hexagonal cell. We should note that, to the second approximation in ε, fluid cannot diffuse between the cells because the normal velocity vanishes at the cell boundaries, even though the streamlines are chaotic. In contrast to the case of square cells [13], development of a global stochastic web in this case can be associated with only higher-order terms in Galerkin's approximation.

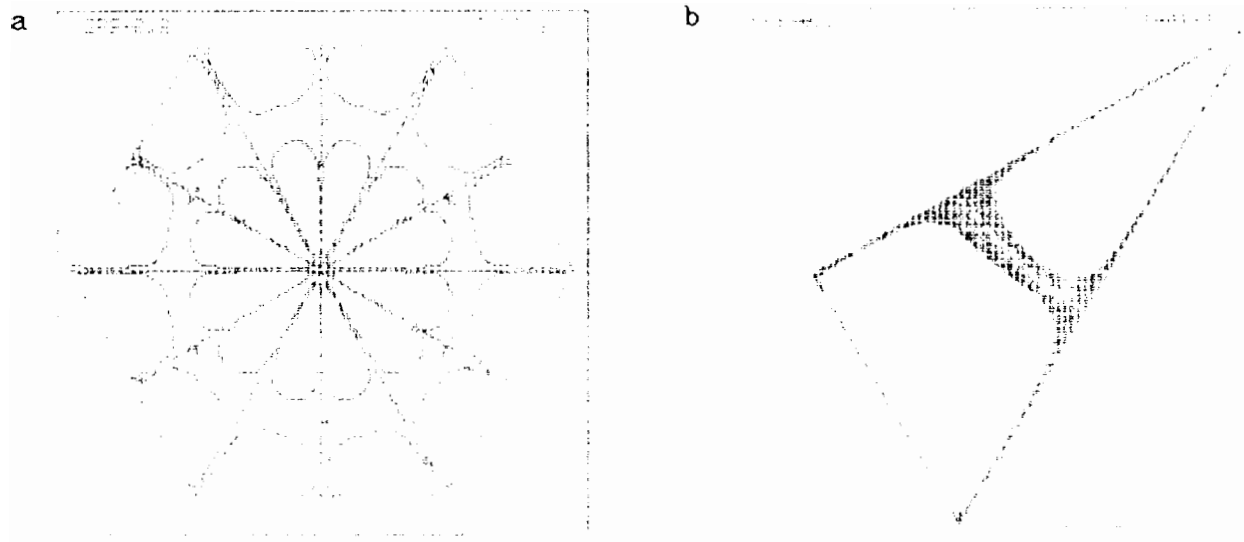

Figures 4a and 4b.

5. CONCLUSIONS

Hydrodynamic structures do not always have the property of symmetry or quasi-symmetry. The previous discussion refers only to such structures. Nevertheless, our results underline an urgent need to clarify connection between Lagrangian and Eulerian turbulence. The difference between them directly affects the character of particle mixing in a flow, even though in both cases the mixing process is of clearly turbulent nature.

REFERENCES

1. Dombre, T., Frisch, U., Green, J. M., et al., J. Fluid Mech. **167**, 353 (1986).

2. Aref, H., J. Fluid Mech. **143**, 1 (1984).

3. Ottino, J. M., Leong, C. W., Rising, H., and Swanson, P. D., Nature **333**, 419 (1988).

4. Moiseev, S. S., Sagdeev, R. Z., Tur, A. V., Khomenko, G. A., and Yanovskii, V. V., Zh. Eksp. Teor. Fis. **85**, 1979 (1983).

5. Frisch, U., She, Z. S., and Sulem, P. L., Physica **28D**, 382 (1987).

6. Moffatt, H. K., J. Fluid Mech. **159**, 359 (1985).

7. Beloshapkin, V. V., Chernikov, A. A., Sagdeev, R. Z., and Zaslavsky, G. M., Phys. Letters A (1988).

8. Chernikov, A. A., Usikov, D. A., Sagdeev R. Z., and Zaslavsky, G. M., Phys. Letters **125A**, 101 (1987).

9. Zaslavsky, G. M., Sagdeev, R. Z., and Chernikov, A. A., Zh. Eksp. Teor. Fiz. **94**, 102 (1988).

10. Beloshapkin, V. V., Chernikov, A. A., Natenzon, M. Ya., et al. (submitted).

11. Palm, E., J. Fluid Mech. **8**, 183 (1960).

12. Stuart, J. T., J. Fluid Mech. **18**, 481 (1964).

13. Arter, W., Phys. Letters **97A**, 171 (1983).

EVOLUTION OF THE LASER ABLATIVELY DRIVEN RAYLEIGH-TAYLOR MIX LAYER

Mark H. Emery and John H. Gardner
Laboratory for Computational Physics and Fluid Dynamics
U.S. Naval Research Laboratory
Washington, DC 20375-5000

The Rayleigh-Taylor[1] (RT) instability occurs whenever a dense fluid is accelerated by a fluid of lower density. Perturbations on the interface between the two fluids are predicted to grow exponentially in time with a growth rate $\gamma = (\mathrm{Akg})^{1/2}$, where the Atwood number A $= (\rho_h - \rho_l)/(\rho_h + \rho_l)$, ρ_h (ρ_l) is the density of the heavy (light) fluid, the wavenumber k $= 2\pi/\lambda$, λ is the wavelength of the perturbation and g is the acceleration. When the amplitude of the perturbation (η) becomes of order of $\lambda/2\pi$, the sinusoidal surface disturbance mutates to rounded columns of "light" fluid rising into the "heavy" fluid which, in turn, is funneled downward.[2-4] This is the classical bubble-and-spike structure. It is at about this amplitude that the RT exponential growth transitions into a nonlinear "free-fall" regime.[4,5] The evolution of the bubble (spike) is now well described by $\eta_b = \alpha_b g t^2/2$ ($\eta_s = \alpha_s g t^2/2$), where η_b (η_s) is the amplitude of the bubble (spike) and α_b (α_s) is the free-fall reduction factor for the bubble (spike). Typically $\alpha_b \leq \alpha_s \leq 1$. In addition, the velocity[4] of the bubble rise is $\propto (g\lambda)^{1/2}$. Thus for classical, incompressible RT in the presence of many perturbation wavelengths, the shortest wavelength modes will grow the fastest, saturate the earliest and then the larger bubbles will subsume the smaller bubbles and larger and larger structures will dominate the flow.[4] This tendency for the bulk of the energy to concentrate in the long wavelength modes means that fluid elements with like signed vorticity must tend to group together; in no other way is it possible for the scale of the velocity distribution to increase.[5]

Classical, incompressible, inviscid turbulence theory predicts that in two-dimensions both the kinetic energy and the enstrophy, the integrated square of the vorticity, are constants of the motion.[6] As a result, the excitation of a wide spectrum of middle wavenumbers in the presence of some dissipation results in the "inverse cascade" of energy to lower wavenumbers and a cascade of enstrophy to higher wavenumbers. Both this process and the process of "selective decay" of enstrophy with respect to energy in undriven dissipative systems[7] leads to the eventual dominance of the largest spatial scales of the system. This inverse cascade process has been observed in carefully prepared 2-dimensional numerical simulations of constant density fluids[8], electrostatic guiding-center plasmas[9] and magnetohydrodynamic fluids[10]. There is

both experimental[11] (in 2D and 3D) and numerical[12] evidence (in 2D) that this process occurs during the nonlinear evolution of the classical two-fluid multimode RT instability. We present here the first evidence of this 2D inverse cascade process in the compressible, ablative environment of the laser implosion scenerio.

In laser driven ablation, the inward flow of thermal energy from the hot laser absorption region is roughly balanced by the outward flow of plasma kinetic energy and pdV work from the target, or ablation, surface. As the newly heated material at the target surface expands outward, the cold, dense shell is accelerated inward as a result of conservation of momentum. In effect, a cold dense material is being accelerated by a hot, low density plasma and the ablation surface; i.e., the interface, is subject to the RT instability. The RT instability is a potential obstacle to inertial confinement fusion in that small perturbations on the ablation layer may grow large enough to destroy the spherical implosion symmetry of high aspect ratio pellets. Recent theoretical[13], numerical[14-17] and experimental[18] investigations of the RT instability in laser ablatively accelerated targets are in general agreement and indicate that the RT growth rate is about 1/2 of the classically predicted (non-ablative) value. With the exception of a 5 mode study in Ref. 15 and a 2 mode study in Ref. 14, all of the above investigations have concentrated on single wavelength perturbations. In reality, RT will develop from initial perturbations where many different wavelengths are present.

The evolution of the multimode RT instability in laser ablatively accelerated targets is modeled with our FAST2D Laser Matter Interaction Code. This is a fully two-dimensional, Cartesian, compressible hydrodynamics code with a sliding Eulerian grid with variable grid spacing. There are periodic boundary conditions in the direction transverse to the laser. This model has been extensively compared with experimental results[18,19] and is discussed in some detail in Ref. 16. Although the flux-corrected-transport (FCT) algorithms do not require artifical viscosity for stability and ensure that the large scale features are treated inviscidly, the nonlinear properties of the FCT algorithms ensure that energy in wavelengths smaller than a few computational cells is (numerically) dissipated. The small residual numerical viscosity of the algorithm mimics the behavior of physical viscosity.[20] The laser energy is absorbed by classical inverse Bremsstrahlung absorption with a 10% dump at critical. For the results presented here, the code is initially run in a one-dimensional mode with a laser pulse that has a 2 ns Gaussian rise after which the intensity is held constant at its peak value. The peak laser intensity is 3×10^{14} W/cm^2 with a wavelength of 1/4 μm. These steady-state profiles then serve as initial conditions in the two-dimensional model. At the start of the RT simulation, these profiles are perturbed at the ablation front with multiple wavelength perturbations of equal amplitudes and random phases; this gives rise to an initial mass perturbation of $\sim 0.1\%$.

The laser intensity is held constant throughout the evolution of the RT instability. The growth rate of the instability is obtained by Fourier transformation of the summed mass of the foil. The mass of the target (ρ X) is integrated from the rear of the foil (the side away from the laser) to the ablation front for each transverse coordinate.

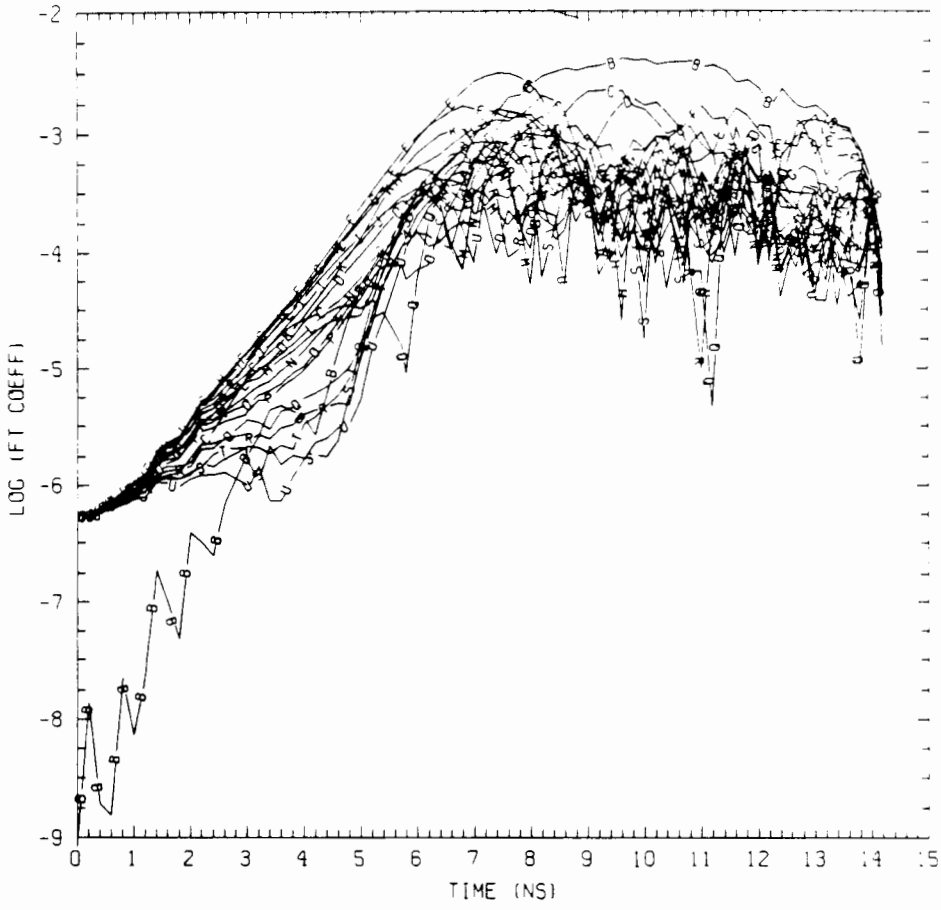

FIG. 1. Log of the Fourier transform coefficient of the areal mass density as a function of time (ns) for all 20 modes. The areal mass of the target (ρx) is integrated from the rear of the target (the side away from the laser) to the ablation front for each transverse coordinate. Modes 2 - 20 ("C" - "U", 75 μm - 7.5 μm) are perturbed initially. Mode "B" (150 μm) is not perturbed initially.

The target is a 200 μm thick planar slab of plastic (CH). After compression, at the time the target is perturbed, the target thickness is $\approx$ 40 μm. The transverse dimension is 150μm and modes 2 - 20 (7.5 $\mu m \leq \lambda \leq$ 75.0 μm) are perturbed with equal amplitudes and random phases. The wavelengths range from nearly 4 times the inflight target thickness to 1/5 of the inflight target thickness. The time evolution of the amplitude of the mass variation of all 20 modes is shown in Fig. 1. There is much information to be gained from this figure. The longest wavelength mode in the system ("B", 150 μm), which is not perturbed initially, undergoes rapid oscillatory growth with a growth rate $\approx$ 2 ns^{-1}. This wavelength becomes the dominant mode in the system by about 8 ns, after all the other modes have saturated, and reaches a saturation level nearly an order of magnitude larger than the other modes. The growth of this mode stems directly from the nonlinear interaction between the smaller wavelength modes. The shortest wavelength modes in the system ("Q" - "U", 9.375 μm - 7.5 μm) exhibit very little growth until about 5 ns when they begin to grow at an increased rate. They are apparently being fed by the longer wavelength modes which are saturating at about this time. Modes "Q" - "U" saturate at about 6.5 ns. Note that the long wavelength modes ("B" - "J", 75 μm - 15 μm) initially grow at nearly the same growth rate. It is quite clear that nonlinear mode coupling is occuring very early in the evolution of the instability. The growth rates of the individual modes (square symbols), measured in the 1.5 - 5 ns time

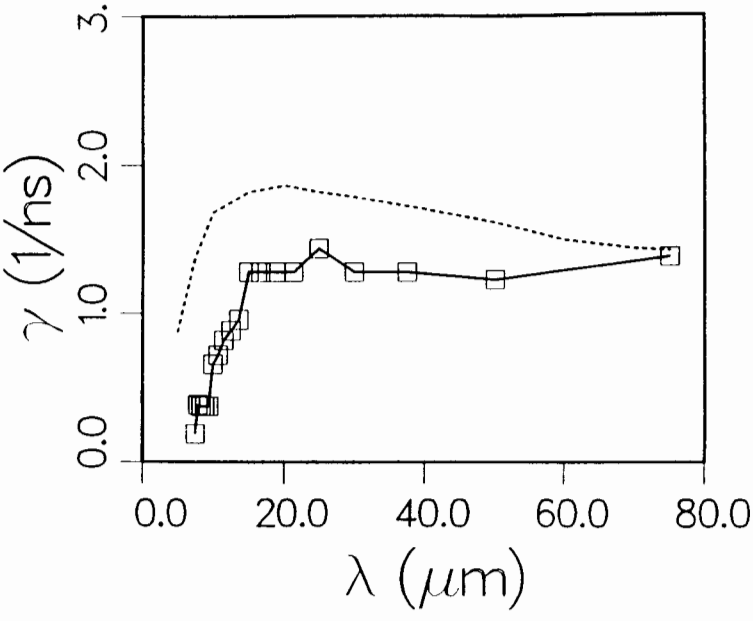

FIG. 2. Plot of the numerical growth rates (squares) as a function of perturbation wavelength. Also shown are the growth rates when only single modes are perturbed (dashed line).

interval, are shown in Fig. 2. Also shown are the growth rates obtained when only single modes were perturbed (dashed line). During the exponential growth phase of the instability, the multimode behavior is strikingly different from the single mode behavior. The intermediate and long wavelength modes grow at nearly the same rate and, for $\lambda \leq 75\mu m$, at rates substantially below the single mode behavior. The growth rates for $\lambda \leq 15\mu m$ are strongly suppressed.

The inverse cascade process which results in the eventual dominance of large scale motion can also be observed by examination of the isodensity contours. Fig. 3 shows the evolution of the target surface at four different times during the development of the mix layer. The instability is well developed by 5 ns. At 8 ns five well-developed spikes are evident; the fourth and fifth modes have just saturated. Note the two large bubbles at the top and bottom of the density contours. By 9 ns, these bubbles have expanded to cover over half of the target surface. This rapid spreading of the vortex pairs in each of the two largest bubbles, coupled with the strong ablative flow, shears off several of the spikes (at the top and bottom), which are then convected back towards the laser. In addition, this spreading and shearing process causes the four central spikes to collapse into one spike and by 14 ns, the system has evolved to a single spike and the bulk of the target is relatively flat. In effect, the evolution to the long wavelength modes coupled with the strong ablative flow causes the target to be "self-healing"; i.e., the bubbles are not observed to break through the target in this case. This late time spreading and shearing process has been observed over a wide range of modes (from 6 to 20) and system lengths (from 42 μm to 150 μm). The rapid bubble spreading begins when the bubble diameter $\approx \eta/2$.

The transition from a many mode structure to a single mode structure occures in two distinct phases. The initial phase, up to about 7 ns, is qualitatively similar to what is predicted by the inverse cascade theory and large amplitude RT theory. There is a gradual evolution to longer wavelength modes as vertex merging, or bubble amalgamation, appears to dominate. When the amplitude of the perturbation becomes large, $O(\lambda/2\pi)$, the spike and bubble enter a free-fall regime. The time evolution of the mix layer is shown in Figure 4; plotted is the height of the bubble rise (h_b) and the depth of the spike fall (h_s) as a function of time. After $\approx$ 4 ns, the spike begins to fall much faster than the spike rises. After 7 ns, the rate of bubble rise rapidly slows and h_b approaches a $ln(t)$ dependence by 9 ns. There is reduction in the free-fall rate in the 5 - 7 ns time interval. With g = 2.0 x 10^{15} cm/s^2, we find $\alpha_b = 0.08$ and $\alpha_s = 0.17$. This is 70% of the free-fall reduction factor for the multimode, nonablative RT case.[17] In the nonablative mix layer, as the bubbles grow, the vortices on either side of the spikes (of unlike magnitude) induce a net rotational flow on one another. The vortices tend

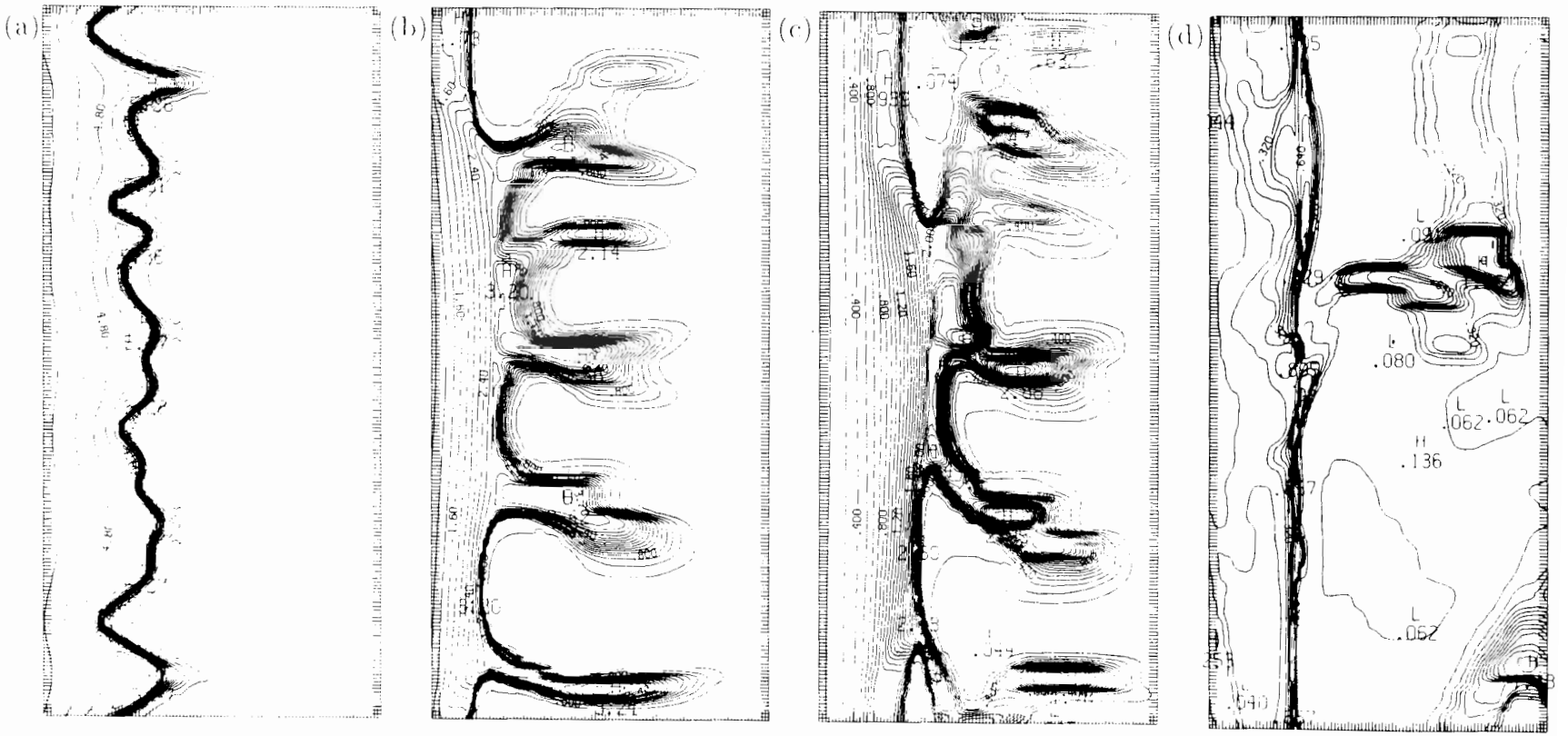

FIG. 3. Isodensity contours showing the late time evolution of the unstable mix layer. The lateral dimension is 150 μm and the laser is impinging the target from the right. The times and horizontal dimensions are: (a) 5 ns, 27 μm, (b) 8 ns, 195 μm, (c) 9 ns, 342 μm, (d) 14.3 ns, 482μm.

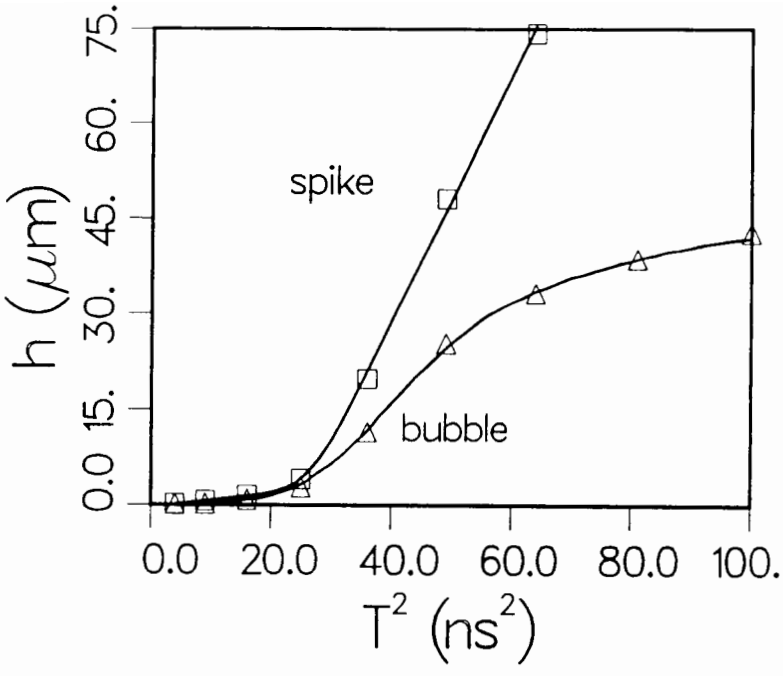

FIG. 4. Plot of the height of the bubble rise (squares, h_b) and the depth of the spike fall (triangles, h_s) in μm as a function of time^2 (ns^2). These distances are measured on the ablation front, the point of steepest density gradient, at the center of the largest bubble and the longest spike.

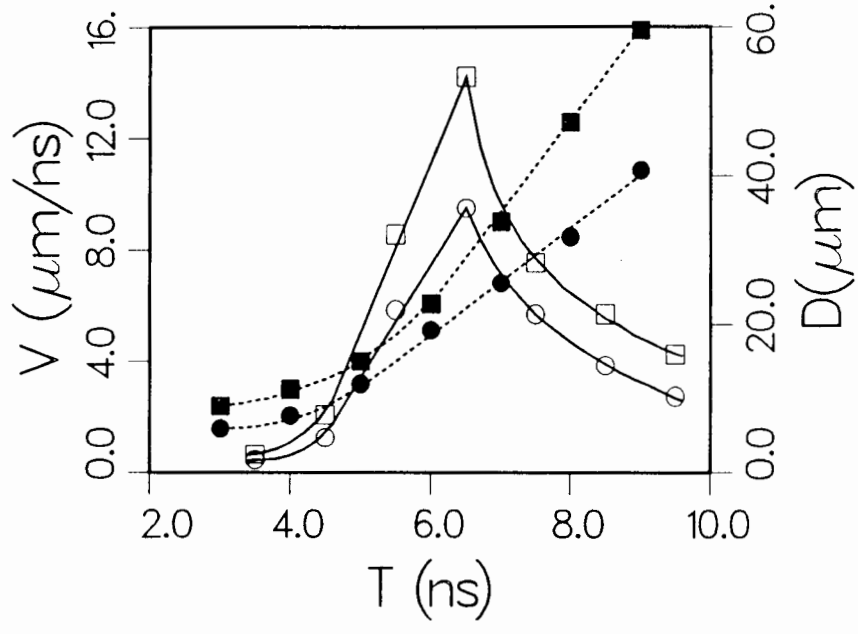

FIG. 5. Plot of the bubble diameters (solid symbols) of the two largest bubbles (square:upper bubble, triangle:lower bubble) and the rise velocities (open symbols) of the same two bubbles as a function of time.

to rotate about one another, further entraining the heavy and light fluids and extending the mix layer.[17,18] This secondary rotation is not observed in the laser driven case.

The second phase of the transition to the fundamental mode, from 8 ns - 14 ns, is governed by the evolution of spreading, buoyant vortex pairs. As the largest spikes enter the free-fall regime, the vortex pairs, in the corresponding bubbles, are convected away from the steep, unstable density gradient and reside in the nearly constant density fluid making up the bubble. By 8 ns, isovorticity contours and streamline plots (not shown) indicate that the vortex pairs comprising the two largest bubbles are centered in the nearly constant density fluid of the bubble. The isodensity contours at 9 ns, Fig. 3, show the nearly constant density in the largest bubbles. For a buoyant, vortex pair it has been shown[20] that if the circulation remains constant while the buoyancy force acts to increase the momentum of the pair, then the buoyant pair spreads linearly in time and rises at a rate $\propto 1/t$. The rate of change of circulation $\dot{\Gamma} = -\oint dp/\rho \rightarrow 0$ for nearly constant density. The rise velocity of the vortex pair is $V = \Gamma/(2\pi D)$, where D is the vortex separation distance. The constant buoyancy force (F_b) is equal to the rate of change of upward momentum, $F_b = d(MV)/dt$, where M is the total mass of the vortex ($M \propto D^2$). Then the separation distance $D \propto t$ and the rise velocity $V \propto 1/t$. Figure 5a shows the diameters of the two largest bubbles as a function of time. The bubble diameters follow a linear time dependence for $t \geq 6.5$ ns. The bubble rise velocities, Fig. 5b, follow a linear time dependence for $4.5\text{ns} \leq t \leq 6.5$ ns, corresponding to the free-fall regime, but there is a sharp transition into a $1/t$ dependence for times ≥ 6.5 ns. The bubble diameter ($D \propto t$) is increasing at a much faster rate than the bubble height ($h_b \propto \ln(t)$). This rapid expansion coupled with the strong ablative flow essentially scours the perturbations off the surface of the target. This causes an enhanced erosion of the target surface; by 14 ns, only 30% of the initial target mass remains.

In summary, the results indicate that nonlinear mode coupling occurs very early in the evolution of the ablative RT mix layer. The nonlinear process, the inverse cascade of energy towards the larger spatial scales, drives the RT instability toward progressively longer wavelengths and limits the growth of the shorter wavelength perturbations, as evidenced by: (1) the early appearance of an initially unperturbed long wavelength mode, and (2) the strong reduction in the wavenumber dependence on the growth rate as compared to the single mode perturbation case. The rate of development of the vortical mix layer is smaller than that observed in the nonablative case. Subsequent late time development of the mix layer appears to be well described by the phenomena of buoyant vortex pairs; the bubbles rise much slower than the linear time dependence predicted by large amplitude bubble theory. Although the inverse cascade mechanism may be particular to two dimensions, the nonlinear mode coupling

which severely reduces the wavenumber dependence of the RT growth in the multimode case will most likely not depend on the dimensionality of the problem. If buoyant vortex rings are formed in three dimensions, they are predicted to rise at a rate[20] $\propto 1/t^{1/2}$, which is less than the large amplitude steady state prediction ($V \propto t$).

One of the authors (MHE) wishes to thank J. P. Dahlburg for several stimulating conversations during the course of this work. This work was supported by the U. S. Department of Energy, the Office of Naval Research and by a grant of computer time on the NRL CRAY-XMP by the Director of Research of the Naval Research Laboratory.

REFERENCES

1. Lord Rayleigh, *Theory of Sound*, 2nd. ed. (Dover, New York, 1894), Vol. 2; G. I. Taylor, Proc. R. Soc. London Ser. **A 201**, 192(1950).

2. H. Helmholtz, Philos. Mag. Ser. 4, **36**, 337(1868); Lord Kelvin, *Hydrodynamics and* **General Dynamics**(Cambridge University, Cambridge, 1910), p.69ff.

3. D. J. Lewis, Proc. Roy. Soc. **A 202**, 81(1850).

4. M. H. Emery et al., Appl. Phys. Lett. **41**, 808(1982).

5. G. K. Batchelor, *Theory of Homogeneous Turbulence* (Cambridge University, Cambridge, 1953).

6. R. H. Kraichnan and D. Montgomery, Rept. Prog. Phys. **43**, 547(1980).

7. D. K. Lilly, Geo. Fluid Dyn. **3**, 289(1972.

8. D. Montgomery and G, Joyce, Phys. Fluids **17**, 1139(1974).

9. W. H. Matthaeus and D. Montgomery, Ann. NY Acad. Sci. **357**, 203(1980).

10. K. I. Read, Physica **12D**, 45(1984).

11. D. L. Youngs, Physica **12D**, 32(1984).

12. Y. -M. Wang and J. A. Robertson, Astro. J. **299**, 85(1985).

13. S. E. Bodner, Phys. Rev. Lett. **33**, 761(1974); W. M. Manheimer and D. G. Colombant, Phys. Fluids **27**, 983(1984); H. J. Kull and S. I. Anisimov, Phys. Fluids **29**, 2067(1986).

14. C. P. Verdon et al., Phys. Fluids **25**, 1653(1982).

15. M. H. Emery et al., Phys. Rev. Lett. **48**, 677(1982).

16. R. G. Evans, Phys. Rev. Lett. **49**, 1639(1982).

17. M. H. Emery et al., Phys. Rev. Lett. **57**, 703(1986); also, M. H. Emery et al., Phys. Fluids **31**, 1007(1988).

18. A. J. Cole et al., Nature (London) **299**, 329(1982); R. R. Whitlock et al., Phys. Rev. Lett. **52**, 819(1984); J. Grun et al., Phys Rev. Lett. **53**, 1352(1984); J. Grun et al. **58**, 2672(1987).

19. M. J. Herbst et al., *Laser Int. and Rel Phenomena*, (Plenum, New York, 1984) **6**, 317; J. H. Gardner et al., Phys. Fluids **29**, 1305(1986); P. G. Burkhalter et al., Phys. Fluids **26**, 3650(1983).

20. J. P. Boris and D. L. Book, Methods of Comp. Phys. **16**, 85(1976).

21. J. S. Turner, J. Fluid Mech. **7**, 419(1959).

Similarity Theory of Incompressible Random Rayleigh-Taylor Instability

N. Freed, D. Ofer, D. Shvarts, Physics Department,

NRCN, P.O. Box 9001, Beer-Sheva, Israel

and

Steven A. Orszag, Applied and Computational Mathematics,

Princeton University, Princeton, NJ 08544-1000

In this Note, we show how a detailed analysis of recent high resolution two-dimensional numerical simulations[1] of low Mach number (incompressible) random Rayleigh-Taylor instability allows the formulation and explicit perturbative solution of a mathematical model that embodies key features of these flows. The results are in good agreement with both the numerical simulations and with experiment[2]. Some typical interfacial contours from the numerical simulations of Rayleigh-Taylor instability at density ratios $\alpha = 2:3, 1:3, 1:20$ [(Atwood ratios $A = (1-\alpha)/(1+\alpha)$ of $\frac{1}{5}, \frac{1}{2}, \frac{19}{21}$, respectively)] are given in Figure 1; the numerical results are obtained using an ALE (Arbitrary Lagrangian-Eulerian) compressible flow code, supplemented by a novel and accurate interface tracking scheme, at a spatial resolution of 200x200 cells (run on a superworkstation).

Our analytical model is based on the two-fluid model of Youngs[3]. The dependent variables of the model equations are horizontally averaged velocity, pressure, volume fraction, etc. We denote the direction of gravity as $+\mathbf{z}$. The dependent variables are $u_r(z,t), f_r(z,t), p(z,t), \rho_r$ $(r = 1, 2)$ where u_r is the average velocity in fluid r at z, t, f_r

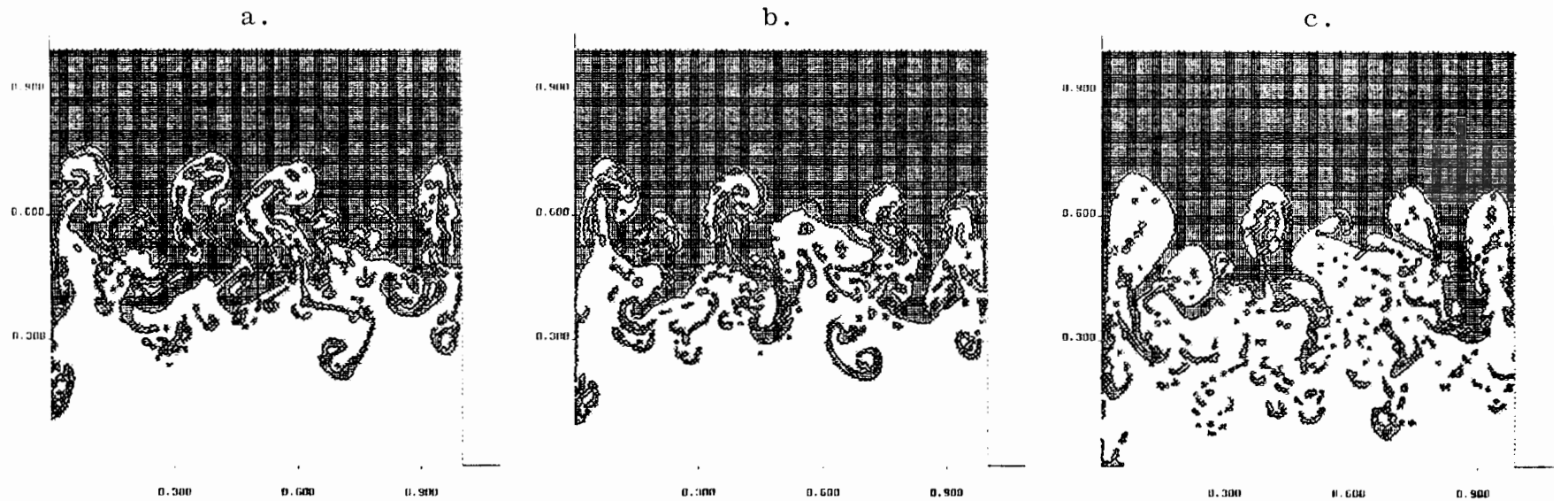

Fig. 1. Two dimensional hydrodynamic simulations of a Rayleigh Taylor mixing layer obtained using our interface tracking code. The ratio of the densities of the lower fluid to the upper one is 2:3 in (a)[t=5.0], 1:3 in (b)[t=3.0], and 1:20 in (c)[t=2.0].

is the average volume fraction, p is the pressure, and ρ_r is the (constant) density. We assume that at $t = 0$, the heavy fluid of density ρ_1 occupies $z < 0$ while the light fluid of density ρ_2 occupies $z > 0$.

Conservation of mass requires that

$$\frac{\partial}{\partial t} f_r \rho_r + \frac{\partial}{\partial z} f_r \rho_r u_r = 0 \qquad (r = 1, 2) \tag{1}$$

$$\frac{\partial}{\partial t} f_r \rho_r u_r + \frac{\partial}{\partial z} f_r \rho_r u_r^2 = -f_r \frac{\partial p}{\partial z} + K(u_{3-r} - u_r) + f_r \rho_r g \qquad (r = 1, 2) \tag{2}$$

where g is the (constant) gravitational acceleration and K is an interphase drag coefficient. These two equations should be viewed as defining relations for the effective pressure p and drag coefficient K. Furthermore, the fluid is space filling so

$$f_1(z,t) + f_2(z,t) = 1 \tag{3}$$

for all z, t. Eqs. (1)-(3) are closed by a relation for the friction coefficient K. Following Youngs we assume that K depends only on the local properties (f_r, ρ_r, u_r) of the flow, that it vanishes if either $f_1 = 0$ or $f_2 = 0$; dimensional analysis then gives the relation

$$K = C \frac{f_1 f_2 (f_1 \rho_2 + f_2 \rho_2)}{L} |u_2 - u_1|$$

where $L(z,t)$ is a new length scale, an effective mixing length for the Rayleigh-Taylor instability.

Finally, we assume that the scale length L is independent of space and grows with time according to the velocity jump at the original interface location (say $z = 0$),

$$\frac{dL}{dt} = |u_2 - u_1|_{z=0} \tag{4}$$

so L qualitatively measures the average bubble-spike separation.

We solve the model (1)-(4) using the following additional approximations. First, we assume that the statistical behavior of the random Rayleigh-Taylor unstable interface

is independent of the details of the (random) initial conditions; this suggests a self-similar solution to (1)-(4) in which the non-dimensional dependent variables $f_r, v_r = u_r/gt, q = p/(\rho_1 + \rho_2)g^2t^2, \ell = L/gt^2$ depend only on the non-dimensional variable

$$s = z/gt^2$$

and on the density ratio $\alpha = \rho_2/\rho_1$. This assumption may be checked from the numerical simulations; in Fig. 2, we plot f_1 as a function of s at various times as well as a smooth second-order polynomial fit. The results plotted in Fig. 2 suggest that self-similarity is a good approximation at the level of 5-10% errors[4].

Transforming (1), (2) to the non-dimensional similarity variables gives the ordinary differential equations

$$-2sf_r' + (f_r v_r)' = 0 \tag{1'}$$

$$\rho_r(f_r v_r - f_r'(2s - v_r)^2) = -f_r(\rho_1 + \rho_2)q' + f_r\rho_r + \frac{C}{\ell} f_1 f_2(f_1\rho_1 + f_2\rho_2)|v_{3-r} - v_r|(v_{3-r} - v_r) \tag{2'}$$

where the prime indicates differentiation with respect to the scaling variable s.

From (1') and (3), we obtain

$$f_1 v_1 + f_2 v_2 \equiv 0 \tag{5}$$

for all s. Then, eliminating q from (2') for $r = 1, 2$ gives

$$(v_1 - v_1'(2s - v_1)) - \alpha(v_2 - v_2'(2s - v_2)) = 1 - \alpha - \frac{C}{\ell}(f_1 + \alpha f_2)(v_1 - v_2)^2 \tag{6}$$

Another critical test of the model is gotten by using Eq. (6), together with the polynomial fits to $f_r(s), v_r(s)$ (see Fig. 2) to evaluate ℓ as a function of s; the result is

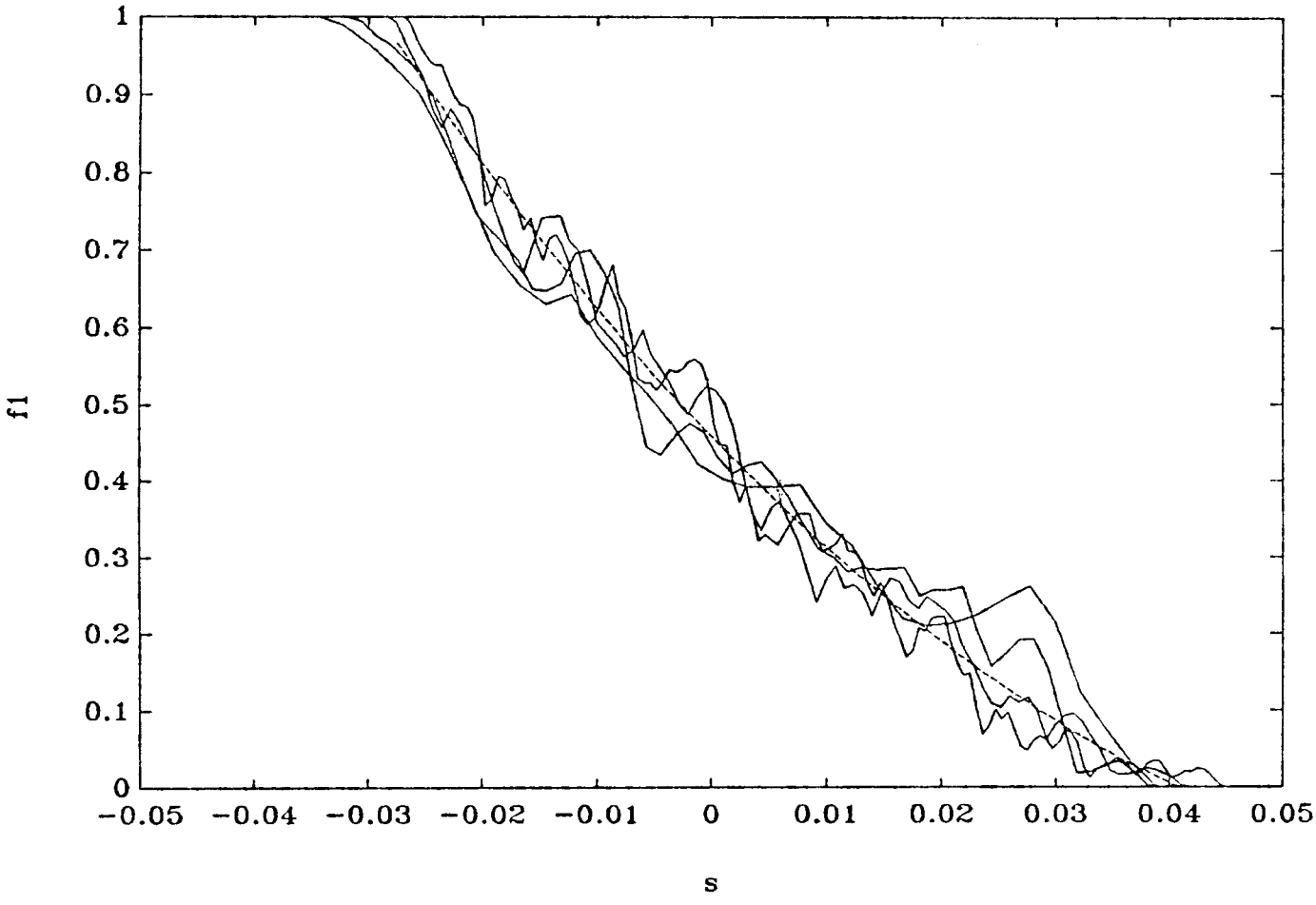

Fig. 2. Check of the self-similarity of the profiles of the heavy fluid volume fraction f_1 vs. the reduced coordinate $s = z/gt^2$ obtained from the simulation of Fig. 1(a) at the times t = 1.5, 2, 2.5 and 3. Also shown is a polynomial approximation to the curve (dashed line) used for eliminating numerical noise.

plotted in Fig. 3, which shows (with an error of order 20%) that ℓ is nearly independent of s (as it must be if L depends only on t). In this case, (4) becomes

$$\ell = \frac{1}{2}|v_2 - v_1|_{s=0} \tag{4'}$$

The results plotted in Fig. 3 also show that $\ell/C = 0(5\text{x}10^{-3})$ so the interphase drag coefficient C may be expected to be a large parameter.

We could now proceed by solving the ordinary differential equations (4'), (5), (6) numerically. However, we believe that it is more instructive to solve these equations *analytically* by expanding in powers of $1/C$. Guided by the numerical simulation results and the form of (4'), (5), (6), we assume that ℓ and v_r are first-order in $1/C$ while f_r is zeroth-order in $1/C$. Then the left-side of (6) may be neglected to leading order so, noting (5),

$$v_1 = \left(\frac{\ell}{C}\right)^{\frac{1}{2}} (1 - f_1)\left[f_1 + \frac{\alpha}{1-\alpha}\right]^{-\frac{1}{2}} \tag{7}$$

This result for v_1 as a function of f_1 together with (3) and (5) may be inserted into (1') with the result

$$s = \left(\frac{\ell}{C}\right)^{\frac{1}{2}} \left[\frac{1}{2} - f_1 - \frac{1}{4}\frac{f_1(1-f_1)}{f_1 + \frac{\alpha}{1-\alpha}}\right]\left(f_1 + \frac{\alpha}{1-\alpha}\right)^{-\frac{1}{2}} \tag{8}$$

which shows that s is also of order $1/C$ over the region of significant mixing.

To determine ℓ from (4'), we first find f_1 at $s = 0$ by solving (8)

$$f_1|_{s=0} = \frac{1 - 5\alpha + (\alpha^2 + 14\alpha + 1)^{\frac{1}{2}}}{6(1-\alpha)} \tag{9}$$

where the sign of the square root is chosen so that $f_1|_{s=0} \to \frac{1}{2}$ when $\alpha \to 1-$. Eqs. (3), (4'), (5) give $\ell = \frac{1}{2}v_1/(1 - f_1)|_{s=0}$ so (7) and (9) imply that

$$\ell = \frac{3(1-\alpha)}{2C[1 + \alpha + (\alpha^2 + 14\alpha + 1)^{\frac{1}{2}}]} \tag{10}$$

Eqs. (3), (5), (7)-(10) give the analytic model.

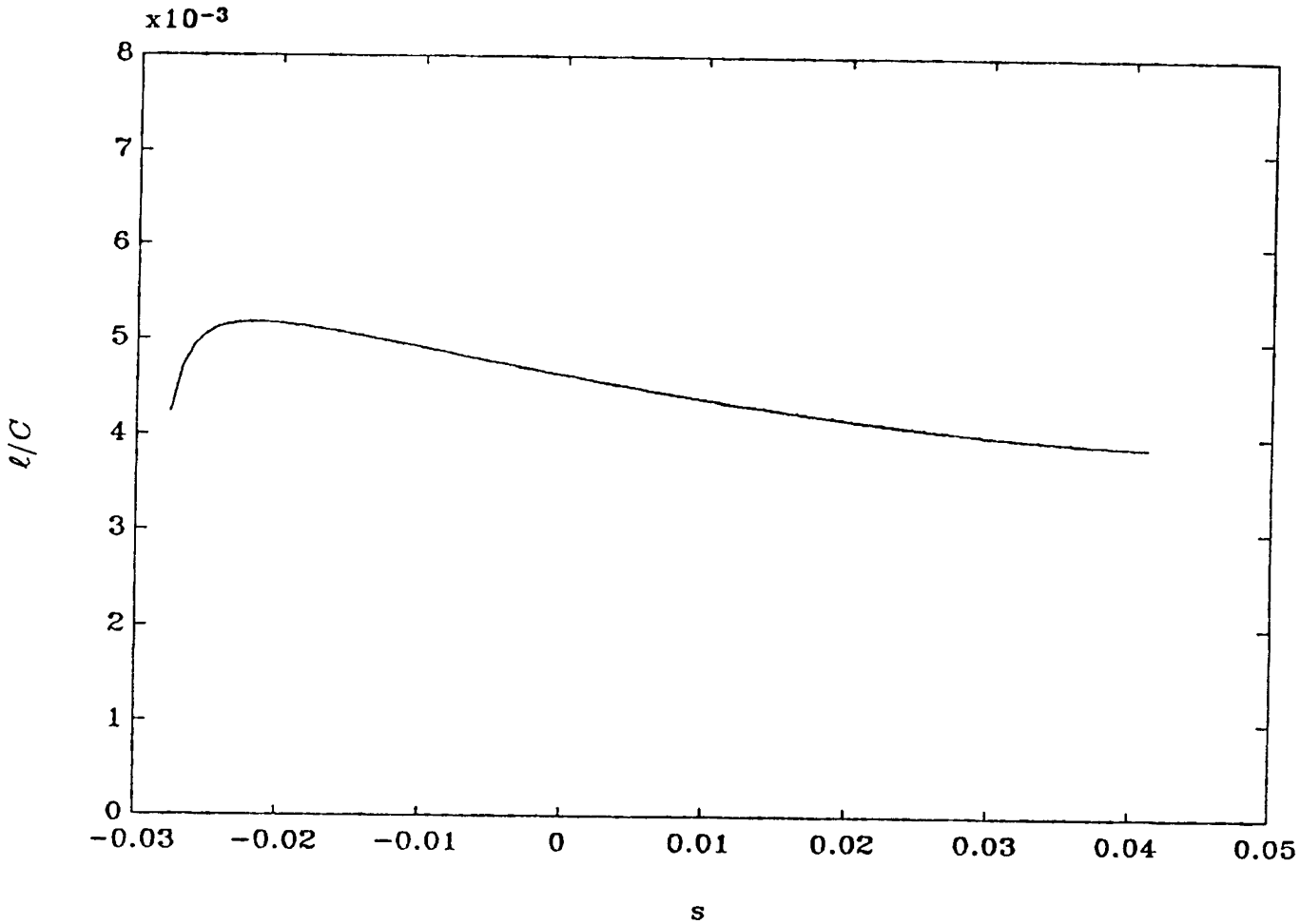

Fig. 3. The effective scale length as obtained from the simulation vs. the (reduced) spatial coordinate. The two-phase flow model (1)-(4) assumes the scale length is independent of space as shown here to be approximately true.

We now compare the predictions of this analytically solvable model with the results of our numerical simulations of the two-dimensional random Rayleigh-Taylor flow. The only adjustable parameter of the similarity flow model is the dimensionless friction coefficient C. The volume fraction $f_1(s)$ for Atwood ratio $A = \frac{1}{2}$ is fit well by the analytic result (8) with $C = 7.5$ [see Fig. 4]; for the other Atwood ratio runs plotted in Fig. 1, the best choice of C is between 7 and 8. The results plotted in Fig. 4 show the modelling error in f_1 and v_1 is only about 10%, except where the numerical noise is large (near the rarely occurring far-reaching spikes).

Let us now consider a few global parameters of the mixing layer, since this facilitates both comparison with experiments and a clear view of the dependence of the results on the Atwood ratio A. The maximum excursion of the bubbles in the model is

$$-s|_{f_1=1} = \left[\frac{\ell}{4C}(1-\alpha)\right]^{1/2} \tag{11}$$

while for the spikes it is

$$s|_{f_1=0} = \left(\frac{\ell}{4C}\frac{1-\alpha}{\alpha}\right)^{1/2} \tag{12}$$

In Fig. 5, we plot the dependence of the bubble excursion on A. The fit to the simulation data is good and is very near to the straight line $0.057Agt^2$ for the whole parameter range.

The ratio of spike to bubble excursion equals the inverse square root of the density ratio α and does not depend on the drag parameter C. This is impossible for very small density ratios (high Atwood numbers) since it gives a spike excursion which might exceed $\frac{1}{2}gt^2$. Inspection of Eq. (6) shows that when both α and f_1 are small (of the order of $1/C$ or less), the neglect of all terms on the left hand side is not justified. Luckily, it can be shown that only the first term, v_1, on the left side is important in this case. Retaining v_1 on the left side of (6) complicates the analytic expressions but poses no new difficulties. We shall give here only the maximum excursion results for the corrected

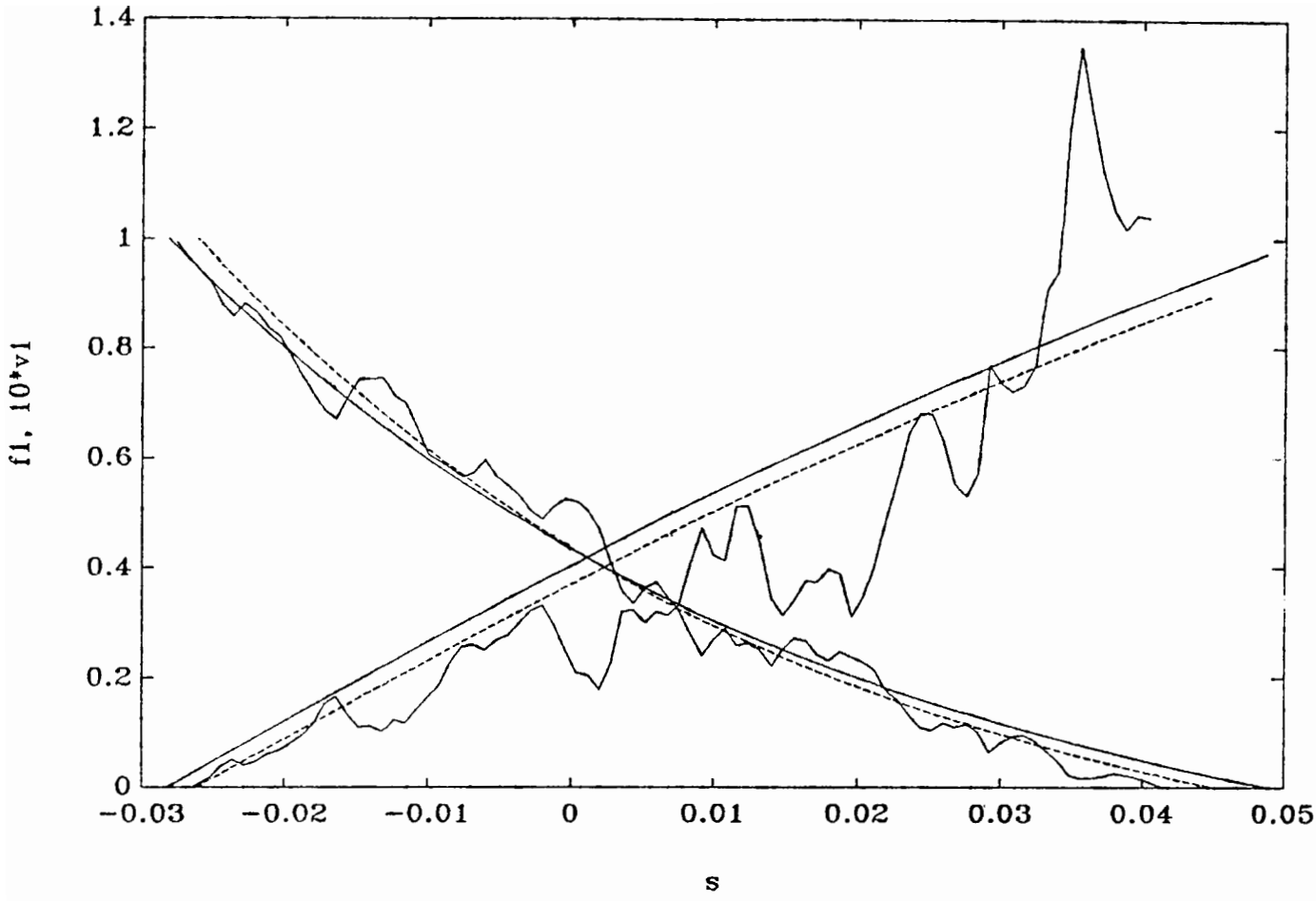

Fig. 4. Comparison of profiles of the volume fraction (decreasing to the right) and velocity (increasing to the right) of the heavy fluid, from the model and the simulation (with density ratio 1:3). Both the simple analytic approximation (continuous lines) and the numerical solution of the model differential equations (dashed lines) are given, and all agree within the accuracy of the direct simulation (continuous lines with numerical noise). The plots are done at t = 2.5.

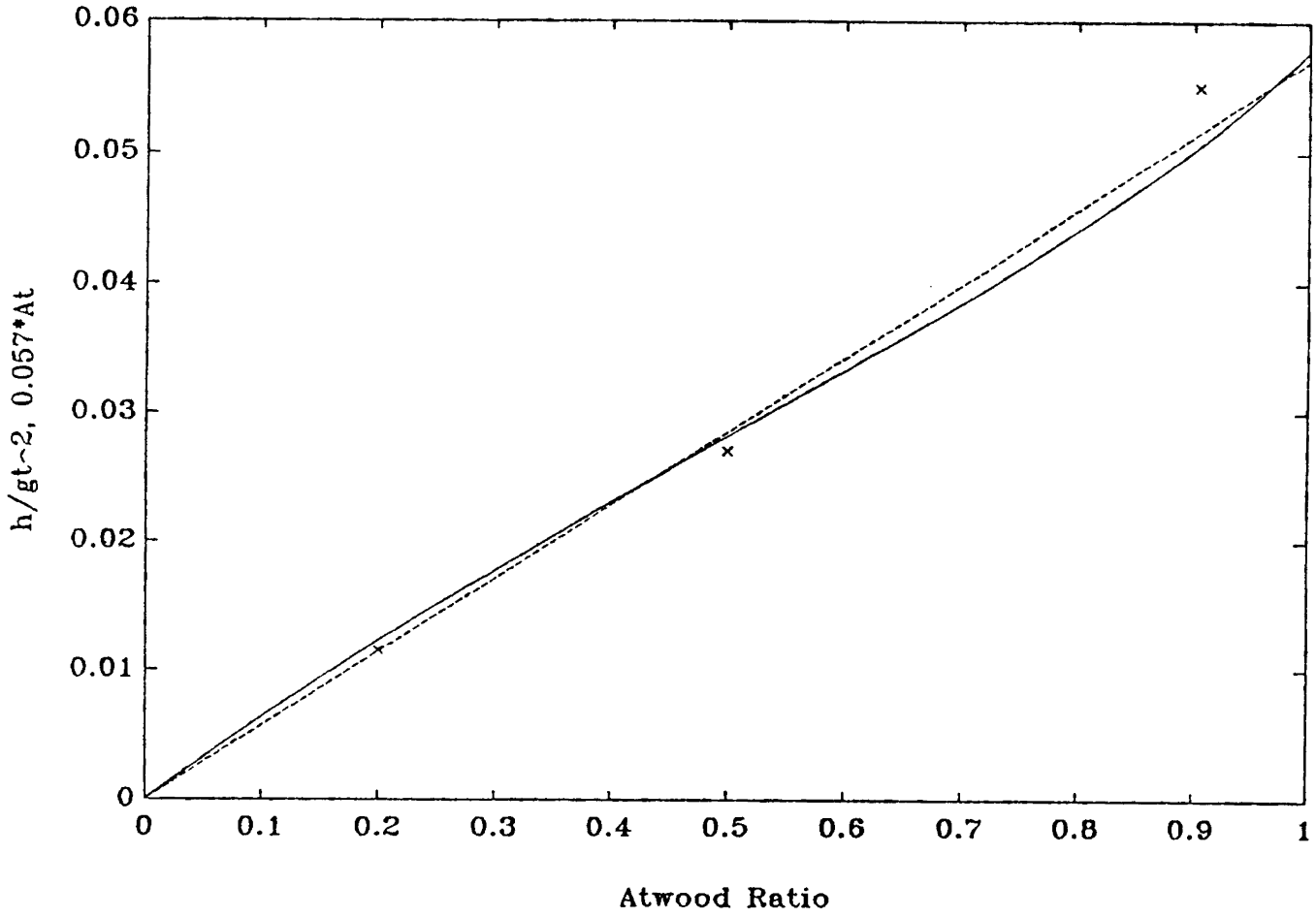

Fig. 5. The maximum penetration of the heavy fluid by bubbles of the light fluid (scaled by gt^2), as a function of the Atwood ratio (or density ratio). The analytic model results (continuous line) roughly agree with a straight line (dashed), which is the familiar expression γAgt^2 with $\gamma = 0.057$. Also shown are the results from the simulations [indicated by x's].

model which, for the spikes, is

$$s|_{f_1=0} = \frac{\ell}{4C\alpha}\left(\left[1+\frac{4C\alpha}{\ell}(1-\alpha)\right]^{1/2}-1\right) \tag{13}$$

and (11) unchanged for the bubbles. This expression is close to the previous result (12) for large density ratios, and tends to $s = \frac{1}{2}$($z = \frac{1}{2}gt^2$ in dimensional units) for very small α.

Further results can be obtained from this analytic model, for example, the global energetics of the flow. Only global energy results can be easily obtained since differential energy conservation equations would necessitate the introduction of a new inter-fluid interaction term, thereby complicating the model. Computing the change in potential energy relative to the initial state, and normalizing it by $(\rho_1+\rho_2)g^3t^4$, the simple version of our model gives

$$E_{pot} = -\frac{1-\alpha}{1+\alpha}\int_0^1 \frac{s^2}{2}df_1 = -\frac{\ell}{32C}\left(1-\frac{1-4\alpha+\alpha^2}{1-\alpha^2}log\,\alpha\right) \tag{14}$$

while for the kinetic energy of the average flow (calculated from the mean velocities within each fluid) we obtain

$$E_{kin} = \int \frac{f_1v_1^2+\alpha f_2v_2^2}{2(1+\alpha)}ds = \frac{2}{15}\left(\frac{\ell}{C}\right)^{3/2}\left(\frac{1-\sqrt{\alpha}}{1+\sqrt{\alpha}}\right)^{3/2}\frac{(1-\sqrt{\alpha}+\alpha)(1+3\sqrt{\alpha}+\alpha)}{\sqrt{\alpha}(1+\alpha)} \tag{15}$$

The ratio of the kinetic energy to the absolute potential energy can be regarded as an energy conversion efficiency factor (with the "wasted" energy going to turbulence and possibly heat); this quantity is plotted in Fig. 6. It is seen that the efficiency factor is low for moderate density ratios, and only rises when the density ratio becomes very small ($A\gtrsim 0.9$). In fact, it is also clear from this result that the simple model cannot hold for extremely small α because it implies negative turbulent kinetic energy. We already know that for small α we must use the corrected model, which necessitates numerical

integration; these results are also given in Fig. 6. The sudden change of slope for $A \gtrsim 0.9$ suggests that the analytic model has limited validity for Atwood ratios higher than about 0.9, since the behavior there is a different flow regime with relatively organized spikes and bubbles. For example, it is possible that the scale length is not absolutely constant and decreases for low α in the far reaching spikes (which would lead to better agreement with experiments).

A more complete summary of this work will be published elsewhere[1].

One of us (SAO) would like to acknowledge support under DARPA contract number N00014-86-K-0759, by the US Air Force under contract number F08635-89-C-0383, by the Office of Naval Research under contract number N00014-82-C-0451.

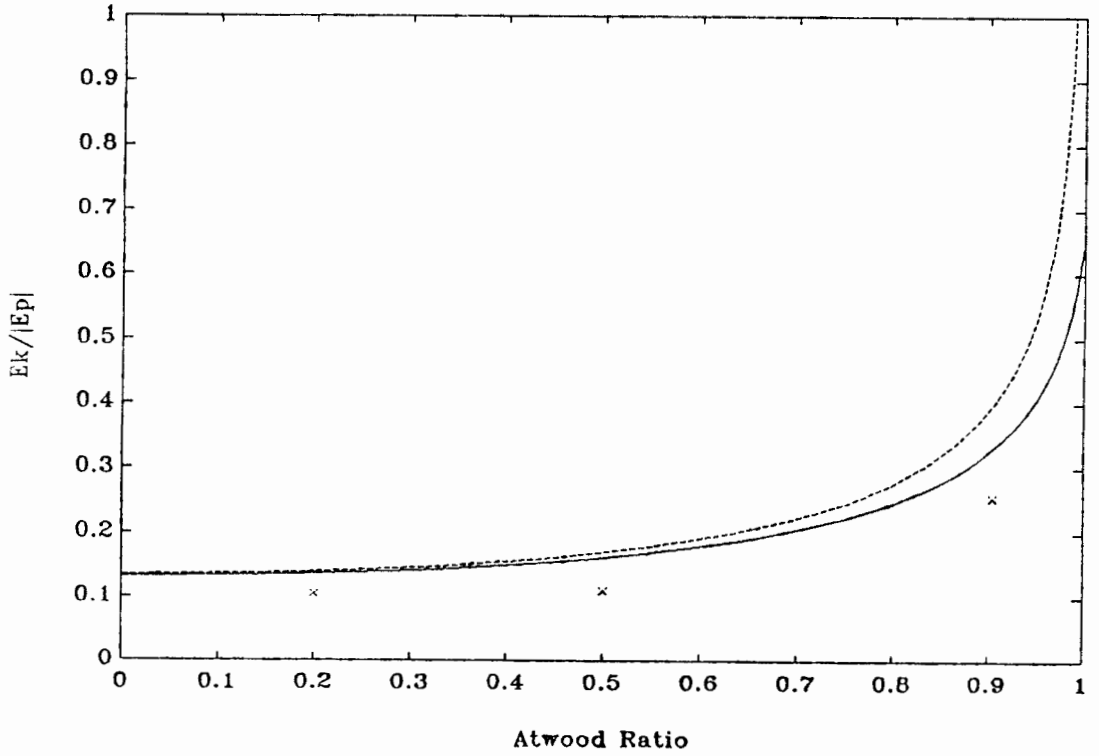

Fig. 6. Ratio of mean kinetic energy to available potential energy gained from the gravitational field for the simple analytic approximation (dashed line) and the corrected analytic results (continuous line). Also shown are the results from the simulations [indicated by x's]. The sharp changes at Atwood ratios above 0.9 indicate that these flows may be in a different regime.

References

1. N. Freed, D. Ofer, D. Shvarts and S. Orszag, to be published (1990).
2. K. I. Read, Physica **12D**, 45 (1984).
3. D. L. Youngs, Physica **12D**, 32 (1984); also **37D**, 270 (1989).
4. A word of caution about using the self-similarity argument is in order: usually, when a nearly self-similar situation occurs with scale length L and initial noise of the order of d, corrections to the self-similar description are of the order of a power of d/L. In our case, the interface is unstable, and if the initial perturbations are at amplitude d in a wavelength λ which is of the order of the scale length $L = \ell g t^2$, it may grow exponentially and reach an appreciable amplitude at times of the order of $(\lambda/g)^{\frac{1}{2}} log(L/d)$, which may be near t. This may lead to logarithmic corrections, or at least to high coefficients for power law corrections. Indeed, indications of appreciable deviations from self-similarity at $d/\lambda \approx 1\%$ do exist (see Ref. 3). In fact, there have even been claims that all experimental results could be explained as arising from single modes in the initial conditions, without any self-similar growth at all [S. W. Haan, UCRL-98206 (1988)].

PSEUDO-SPECTRAL NUMERICAL SIMULATIONS OF SUB AND SUPERSONIC COMPRESSIBLE VISCOUS FLOWS

Serge Gauthier
Centre d'Etudes de Limeil-Valenton, BP 27
94190 Villeneuve-St-George,FRANCE.

I-INTRODUCTION:

Stability and transition to turbulence have been the object of a considerable interest in the past fifteen years. However, the mechanism by which a flow becomes chaotic has been studied, essentially, for thermal convection of incompressible fluids. Numerical simulations of such flows are usually carried out with the spectral methods owing to their high accuracy [1-2]. The Boussinesq approximation, used in these studies, holds for a compressible fluid provided that the vertical extent of the fluid is small enough. In some situations, for example in stellar convection or in laser driven fusion, the stratification of the fluid can no longer be ignored and we have to use the full Navier-Stokes equations. Since the pioneering work of Graham [3], some papers have been devoted to the simulation of compressible convection [4-5]. In the special case of fixed heat flux Yamaguchi [6] found supersonic solutions even at low Rayleigh numbers. From a numerical point of view, viscous compressible flows involve very different time scales which lead to long time runs. It is then necessary to use numerical schemes more implicit than those used in incompressible flow simulations, in order to overcome, as far as possible, time step restriction due to convective terms.

In view of this, we have developed a 2D pseudo-spectral code for the full Navier-Stokes equations [7], which has been used so far to numerically simulate the compressible Rayleigh-Bénard convection. A Fourier expansion is used in the horizontal direction. The expansion in the Chebyshev polynomials used in the inhomogeneous direction leads to severe time step constraints due to the high resolution on the boundaries. However, in compressible flows, viscous and thermal diffusion terms are nonlinear. This nonlinearity leads to use iterative methods such as suggested by Orszag [8]. In the first version of the code, only vertical diffusion terms were solved implicitly by an iterative method preconditioned by the time independent Chebyshev approximation of the diffusion operator.

In this paper we present a more implicit version where convective terms are treated semi-implicitly and all diffusion terms are handled with an iterative method preconditioned by the finite difference approximation of the diffusion operator. We used both numerical schemes to compute sub and supersonic steady state solutions obtained with radiative boundary conditions.

The next section II poses the physical problem, section III is devoted to detail the numerical scheme and numerical applications are described in section IV.

II-THE PHYSICAL PROBLEM:

The motion takes place in a two-dimensional rectangular cavity of width L_x and height d. The z-axis is directed downward so that the gravity, represented by the vector $\underline{g}=(0,0,g)$, is positive along this direction.

The equations of motion for a compressible, viscous, thermally conducting gas are as follows:

$$\partial\rho/\partial t+\partial\rho u_i/\partial x_i=0, \tag{2.1}$$

$$\partial\rho u_i/\partial t + \partial\, \rho u_i u_j/\partial x_j=-\partial P / \partial x_i+\partial\, \tau_{ij}/ \partial\, x_j - g_i\rho, \tag{2.2}$$

and

$$\partial\rho E/\partial t + \partial\, (\rho E+Pr)u_j/\partial x_j= \partial\, \tau_{ij}\, u_i/ \partial\, x_j +\partial / \partial\, x_i\, K\, \partial T / \partial\, x_i, \tag{2.3}$$

where E is the total energy

$$E = 1/2\, (\, u_1^2 + \, u_2^2\,) + e - \, g\, x_2\,, \tag{2.4}$$

and τ_{ij} the viscous stress tensor given by

$$\tau_{ij}= \mu(\, \partial u_i/\partial\, x_j + \partial u_j/\partial\, x_i -2/3\, \delta_{ij}\, \partial u_l/\partial\, x_l)\,, \tag{2.5}$$

where i,j,l=1,2. The Stokes' relation between the first and the second viscosity coefficients has been used. The coordinates x_1 and x_2 stand for the x and z coordinates respectively.

This set of equations is closed by the equation of state for the perfect gas,

$$P = R_*\, \rho T \qquad \text{and} \qquad e = C_v\, T. \tag{2.6}$$

P, ρ, T and e are pressure, density, temperature and internal energy respectively; the u_i are the components of the velocity. The thermal conductivity and the dynamic viscosity are taken as constants. R_* is the gas constant and C_v the specific heat at constant volume.

We use slippery boundary conditions for the velocity and radiative boundary conditions for the temperature. This set of boundary conditions is a reasonable approximation for stellar convection zones. The boundary conditions for the velocity read

$$u_2 = 0 \text{ and } \partial u_1/\partial z = 0 \text{ at } \qquad z = z_o,\, z_o + d. \tag{2.7}$$

We impose the heat flux at the upper boundary to be fixed by the radiative energy of a black body

$$K\, dT/dz = \sigma^{sb}\, T^4 \tag{2.8}$$

where σ^{sb} is the Stefan Boltzmann's constant. Taking into account the fluctuations of the thermal conductivity up to the first order with respect to the density and the temperature and linearizing the equation (2.8) gives the following relation at the upper boundary:

$1/S_f\, d\theta/dz + 1/K_o(\delta K/\delta\rho)\rho + 1/K_o(\delta K/\delta\theta)\theta = 4\,\theta$

where $\delta/\delta\rho$ is the derivative with respect to ρ and the Stefan number $S_f = \sigma^{sb}\, T^3 d/K_o$ has been used. If the thermal conductivity K is of the form T^3/ρ, the temperature fluctuations satisfie an inhomogeneous time-dependent Robin type boundary condition at the top of the layer.

$$1/S_f\, d\theta(x,z_o,t)/dz \; - \theta(x,z_o t) = \rho\,(x,z_o,t) \qquad (2.9)$$

$$\text{and } T(z_o+d) = T_1 \qquad \text{at the bottom of the layer.} \qquad (2.10)$$

Periodic boundary conditions are used in the horizontal direction for all variables. With these boundary conditions, the static state reads

$$T(z) = S_f z + 1 - S_f Z^{-1}, \qquad (2.11a)$$

$$\rho(z) = [S_f z + 1 - S_f Z^{-1}]^m, \qquad (2.11b)$$

$$P(z) = [S_f z + 1 - S_f Z^{-1}]^{m+1}. \qquad (2.11c)$$

The coordinate z goes from Z^{-1} to $Z^{-1}+1$, where $Z=d/z_0$. The index of the polytrope is

$$m = g/R_* \beta_0 - 1 \qquad \text{where} \qquad \beta_0 = T(z_0+d) - T(z_0).$$

In Eqs.(2.11), we have used the following units: d, $d^2\rho(z_0)/\mu$, $\mu(z_0)$ and $T(z_0)$ for length, time, density and temperature respectively. The two-dimensional compressible convection problem is characterized by seven dimensionless parameters which are the aspect ratio A, the Prandtl number σ, the ratio of specific heats γ, the normalized layer thickness Z, the polytropic index m, the Stefan number S_f and the Rayleigh number R. The parameters σ and γ are given by the thermodynamical properties of the fluid. Z characterizes the stratification of the configuration while the Stefan number measures the magnitude of the radiative diffusion with respect to the thermal conductivity and the Rayleigh number measures the degree of the instability. Their expressions are

$$A = L_x/d, \qquad \sigma = C_p\mu/K, \qquad Z = d/z_0, \qquad \gamma = C_p/C_v,$$

and

$$R = (g/T_u)d^4\,[(T_l - T_u)/d - g/C_p]/(K/\rho_u C_p)(\mu/\rho_u),$$

where the subscripts l and u refer to the lower and upper layer boundaries.

III - DESCRIPTION OF THE PSEUDO-SPECTRAL CODE :

Density, velocity and total energy are expanded in a Fourier-Chebyshev basis as

$$u(x,z,t)= \Sigma_{l=-N/2}^{l=N/2} \Sigma_{m=0}^{M} u_{lm}(t) \; e^{2i\pi lx/L_x} \; T_m(2z), \qquad (3.1)$$

where T_m is the Chebyshev polynomial of degree m, and L_x is the horizontal periodicity.

We use a collocation method where spatial derivatives are computed in the spectral space and nonlinear products are performed in the physical space. Time marching is performed in the physical space by means of a finite difference technique. As already stated, a simple numerical scheme consists of the Adams-Bashforth predictor of order two and the third order Adams-Moulton corrector for all terms but the vertical diffusion terms. Such terms are handled by an iterative procedure preconditioned by the time independent Chebyshev approximation of the diffusion operator. This spectral preconditioning appears to be very efficient both in term of the number of iterations needed to achieve a given accuracy and in term of CPU time. However, in this approach, the time step obeys the CFL condition and then it is of interest to test more implicit numerical method in order to overcome this constraint. Harned and Kerner [9] have investigated a possible way within the finite difference framework by stabilizing convective terms with a diffusive term handled semi-implicitly. More precisely, they first notice that fast modes are described by the following equation

$$\partial^2 V / \partial t^2 = \gamma P_o/\rho_o \nabla (\nabla.V) \qquad (3.2)$$

obtained by linearizing the Euler's equation and the energy equation written for the pressure. Consequently, they add the term $A_o^2 \Delta t^2 \nabla (\nabla.V)$ in the velocity equations and handle it implicitly. Coupled with the second order Runge-Kutta numerical scheme, they show that unconditional stability is ensured provided that

$$A_o^2 > 1/4 \;\; \gamma P_o/\rho_o \qquad (3.3)$$

In other words the constant A_o is of the order of the sound velocity.

Second order Runge-Kutta numerical scheme with Chebyshev approximation are known to be weakly stable. So we turned to the third order Runge-Kutta such as used by Hussaini and coworkers [2, 10].This scheme reads

$$\partial u/\partial t = F(u) + G(u) \qquad (3.4a)$$

where the terms in F are treated by the third order Runge-Kutta and those in G by Crank Nicholson.

$$H_1 = \Delta t \, F(u^n) \qquad (3.4b)$$

$$[\, 1 - \Delta t^2 A_o^2 \nabla \nabla.] \, u^1 = u^n + H_1/3 + \Delta t /6(G_n + G_1) - \Delta t^2 A_o^2 \nabla \nabla.u^n \qquad (3.4c)$$

$$H_2 = \Delta t\, F(u^1) - 5/9\, H_1 \qquad (3.4d)$$

$$[\, 1 - \Delta t\, A_o^2 \nabla\nabla. \,]\, u^2 = u^1 + 15/16\, H_2 + 5/24\, \Delta t\, (G_n + G_2) - \Delta t^2\, A_o^2 \nabla\, \nabla.u^1 \qquad (3.4e)$$

$$H_3 = \Delta t\, F(u^2) - 153/128\, H_2 \qquad (3.4f)$$

$$[\, 1 - \Delta t\, A_o^2 \nabla\nabla.]\, u^{n+1} = u^2 + 8/15\, H_3 + 1/8\, \Delta t\, (G_2 + G_{n+1}) - \Delta t^2 A_o^2\, \nabla\, \nabla.u^2 \qquad (3.4g)$$

In this approach, diffusion terms are iteratively solved with the Chebyshev method in the Fourier space. The two velocity components are coupled by the second viscosity term. Then we have to solve

$$L\, u_k = F_k,$$

where the right hand side F_k is given by the convection and pressure terms of the Navier-Stokes equations. The operator L is given by

$$L\, u = \begin{pmatrix} 1 + (Dt + 1)\, k^2\, \rho(z) - \rho^{-1}(z)\, \partial^2/\partial z^2 & -\rho^{-1}(z)\, Dt\, i\, k\, \partial/\partial z \\ -\rho^{-1}(z)\, Dt\, i\, k\, \partial/\partial z & 1 + k^2\, \rho^{-1}(z) - \rho^{-1}(z)\, (Dt + 1)\, \partial^2/\partial z^2 \end{pmatrix}$$

with $Dt = \Delta t^2 A_o^2 + 1/3$

We use the Chebyshev iterative method preconditioned by the diagonal part of L.

IV-NUMERICAL APPLICATIONS:

We have computed convection solutions for different Stefan number values. The aspect ratio is fixed to 4 and the Rayleigh number to 11500 for all studied cases. The Prandtl number is fixed to the value σ=0.1 and the ratio of specific heats is chosen to the value of a monoatomic gaz γ=1.67. The polytopic index is equal to the value m=1.

In Table I we give the final steady values of characteristic quantities such as the maximum of the velocity, the Mach number and the relative thermodynamical fluctuation quantities. They are defined by

$$\rho_{max} = \mathrm{Max}\, (\, \rho(x,z)/\rho(z)\,)$$

where the maximum is taken over the two dimensional domain.

Table I

Stefan number	1.	1.5	2.	2.5	2.73
Velocity maxi.	487.	478.	461.	439.	428.
Mach max.	0.37	0.53	1.02	1.23	1.31
Nusselt number	1.82	2.42	3.06	3.69	3.99
ρ_{max}	0.217	0.536	1.05	1.91	2.70
T_{max}	0.174	0.269	0.365	0.457	0.496
P_{max}	0.324	0.656	1.08	1.53	1.76

On Fig.1 we have plotted the velocity field when the Stefan number is equal to 1. The asymmetry between the rising and sinking flows is clearly revealed by the iso-vorticity contour on Fig.1b. This asymmetry is a feature of compressible convection in comparison with the Boussinesq case where there is a symmetry with respect to the center of the cell. On Fig1.c the divergence of the velocity field shows positive values where the flow is ascending and negative ones in the downward-directed plume. In this solution, the ratio of densities between the top and the bottom is equal to 2 while the same ratio for the pressures is equal to 4.

In a steady state the total energy flux becomes independent of depth and is written as

$$F_T = F_c + F_K + F_R + F_v$$

where F_c is the convective heat flux, F_K is the kinetic flux, F_R is the radiative flux and F_V is the viscous flux defined by the following relations.

$$F_c = -\overline{\rho\, C_p\, w\, T'}$$

$$F_K = -1/2\, \overline{\rho\, u_i\, u_i\, w}$$

$$F_R = K\, \partial\overline{T}/\partial z$$

$$F_V = \overline{u_i\, \tau_{3i}}$$

In the latter the overbar denotes the horizontal average and the prime denotes the fluctuation about the mean.

We also define the pressure flux by $F_P = w\ P'$ and the rates of working done by buoancy, pressure and viscous forces. They are given by

$$E_B = g\ \overline{\rho' w}$$

$$E_P = \overline{P' \partial u_i / \partial x_i}$$

$$E_V = \overline{\tau_{ij}\ \partial u_i / \partial x_j}$$

On Fig.1-c, we have displayed these five fluxes. The dominant ones are the convective and the radiative fluxes. Kinetic and pressure fluxes are always less than 10% when all fluxes are normalized to the total flux. Viscous flux is negligible throughout the layer. Fig.1-d shows the rates of working done by buoancy, pressure and viscous forces. The work done by pressure fluctuations are clearly dominant at the bottom of the fluid layer where both pressure fluctuations and velocity gradients are large.

For a Stefan value parameter equal or larger than 2 we obtain supersonic regions at the top of the fluid layer. The size of this domain is increasing with the stratification parameter value. On Fig.2 we displayed the velocity field for a Stefan number equal to 2.73. As expected, the cell centers are shifted to the bottom and to the sinking flow. The maximum of the relative thermodynamical quantities also increases with the Stefan number. For the largest parameter stratification value used the density and pressure fluctuations respectively reach 2.7 and 1.76 times the density and pressure of the static state. Both convective heat flux and radiative flux reach larger values while the viscous flux and the corresponding rate of working remain very small.

V- CONCLUSION :

We have developed a numerical algorithm to simulate the thermal convection of a two-dimensional fully compressible fluid; the third order Runge-Kutta numerical scheme and a semi-implicit treatment of the convective terms have been used. All diffusion terms were handled by the Chebyshev iterative method in the Fourier space. Fourier functions in the horizontal direction and Chebyshev polynomials in the inhomogeneous direction have been used. The fluid is a perfect gas with constant dynamic viscosity and thermal conductivity. Both sub and supersonic steady state solutions have been reached with radiative boundary conditions for the temperature, they reveal the features of compressible convection even in the case of a weak value of the stratification parameter.

ACKNOWLEDGMENTS I would like to thank A. Grimaldi for her help in preparing the manuscript.

REFERENCES

1. R. G. Voigt, D. Gottlieb and M. Y. Hussaini, Proceedings of the symposium on Spectral Methods for PDE , (SIAM Monograph, Philadelphia,1984).
2. C. Canuto, M. Y. Hussaini, A. Quarteroni, T.A. Zang, "Spectral Methods in Fluid Dynamics" (Springer-Verlag, New-york, 1988)
3. E. Graham, J. Fluid Mech., **70**, 689, (1975).
4. K. L. Chan and C. L. Wolff, Astrophys. J., **263** ,935, (1982).
5. N. E. Hurlburt, J. Toomre and J. Massaguer, Astrophys. J. **282**, 557-573, (1984).
6. S. Yamaguchi, Publ. Astron. Soc. Japan **37**, 735 (1985).
7. S. Gauthier, J. Comp. Phys., **75**, 217 (1988).
8. S. A. Orszag , J. Comput. Phys., **37**, 70-92, (1980).
9. D. S. Harned and W. Kerner, J. Comp. Phys. **60**, 62-75 (1985).
10. J. H. Williamson, J. Comp. Phys., **35**, 48-56 (1980).

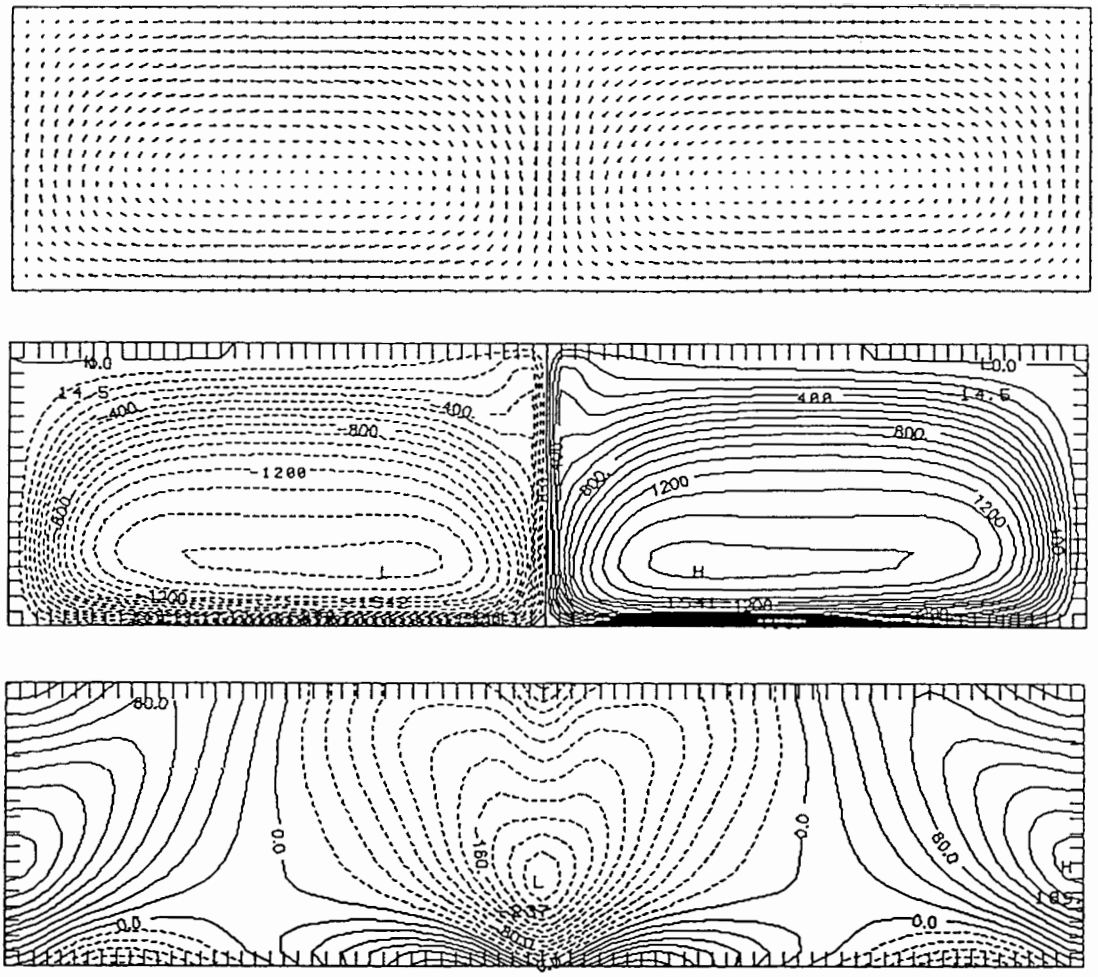

Fig.1-a-b-c: Velocity field, isovorticity contour and iso-velocity divergence contour for a Stefan number value equal to 1.

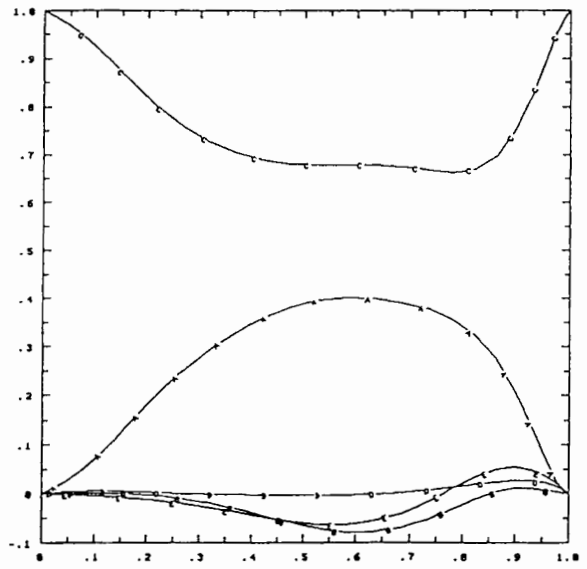

Fig.1-c: Convective heat, kinetic, radiative, viscous and pressure fluxes for a Stefan number value equal to 1.

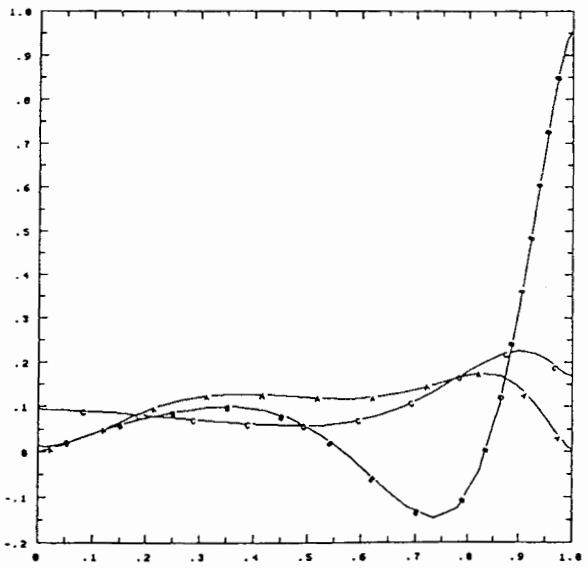

Fig.1-d: Rates of working by buoyancy, pressure and viscous forces.

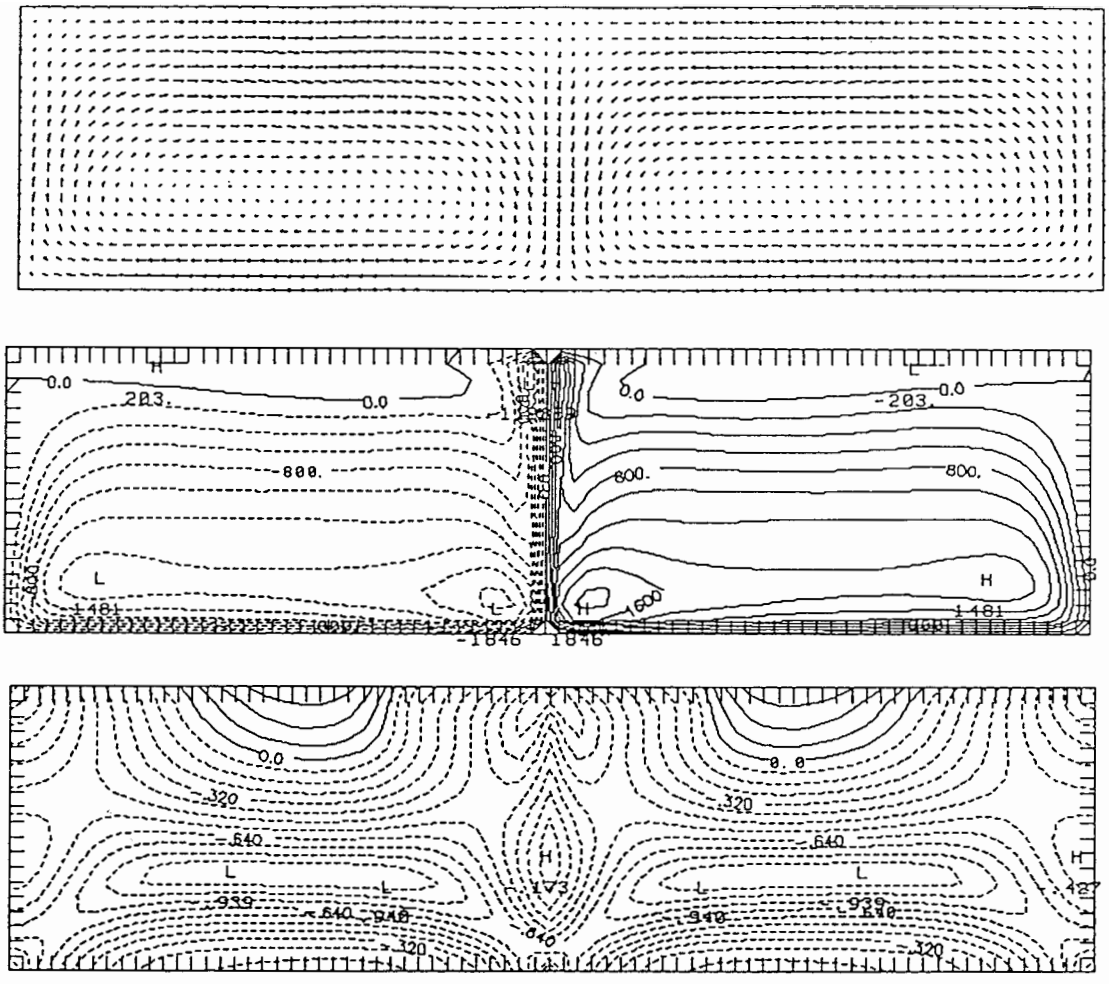

Fig.2a-b-c: Velocity field, isovorticity contour and iso-Mach number -1 contour for a Stefan number value equal to 2.73.

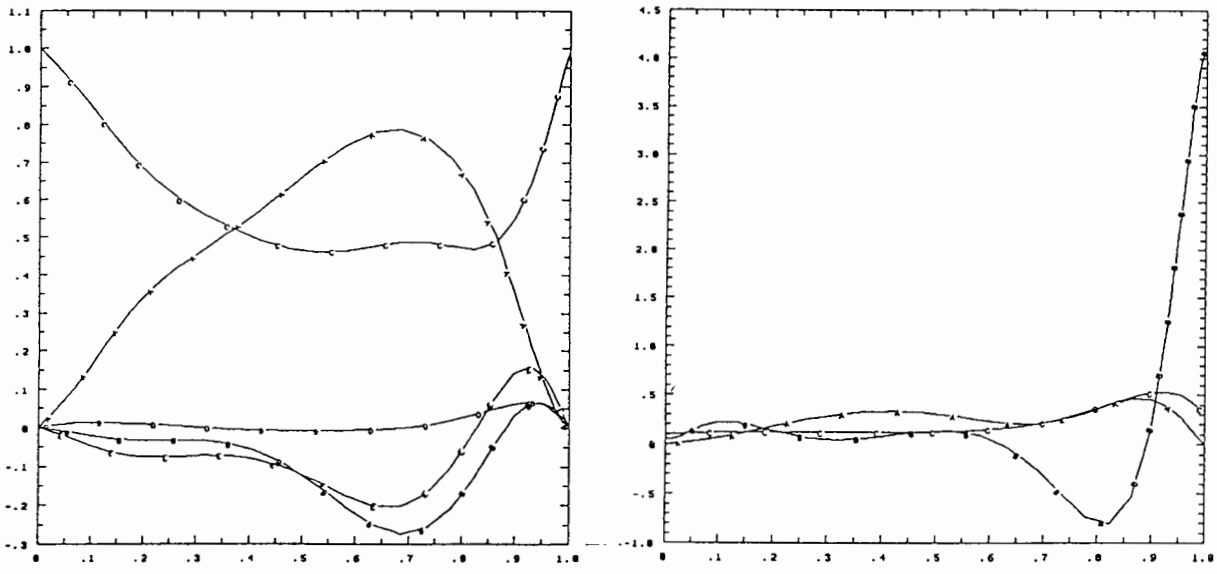

Fig.2-c: Convective heat, kinetic, radiative, viscous and pressure fluxes for a Stefan number value equal to 2.73.

Fig.2-d: Rates of working by buoyancy, pressure and viscous forces.

STATISTICAL THEORIES OF RAYLEIGH-TAYLOR INSTABILITY FOR COMPRESSIBLE FLUIDS

J.Glimm [1,2]
X. L. Li [1,3]
Q. Zhang [1]

Courant Institute of Mathematical Sciences
New York University
New York, NY 10012

R. Menikoff [4]
D. Sharp [4]

Theoretical Division
Los Alamos National Laboratory
Los Alamos, NM 87545

ABSTRACT

Statistical theories for the outer envelope of the Rayleigh-Taylor mixing layer refer to a simplified dynamics of fundamental modes and their interactions. These modes are bubbles of light fluid entrained in the mixing layer between the undisturbed light and heavy fluids. The dynamics can be understood in terms of the motion of a single mode and the interactions between modes. The single mode dynamics has to be solved self-consistently in a background field of random bubbles. The dominant interaction is bubble merger, i. e. the spreading of larger bubbles at the bubble envelope. Merger leads to dynamically increasing length scales, and thus to a dynamic renormalization of scaling dimensions. The mechanism for bubble merger is the differential motion of physically adjacent single bubble modes.

This paper is focused on the above topics: single bubble motion, bubble interactions and statistical models.

1. Introduction

Density gradients at an accelerated interface result in Rayleigh-Taylor instability. At late times, the interface evolves into a chaotic regime characterized by a mixing layer and the entrainment of one fluid in the other. Sensitivity to the initial conditions and to random heterogeneities as well as the complexity of the mixing process call for statistical descriptions. Here we focus on statistical theories for the outer envelope

1. Supported in part by the U. S. Department of Energy, contract DE-AC02-76ER03077.
2. Supported in part by the National Science Fundation, grant DMS-83-1229.
3. Address: Department of Mathematics, New Jersey Institute of Technology, Newark, NJ 07102.
4. Supported by the U. S. Department of Energy.

for the penetration of the light fluid into the heavy, i.e. the boundary of the mixing layer.

As with mixing theories in general, the issues discussed here fall within the area of nonequilibrium statistical mechanics. The essential issue is to determine transport behavior in the nonlaminar, chaotic regime. In this chaotic regime, macroscopic continuum events (i.e. interactions between coherent structures) rather than molecular collisions are the driving mechanisms. Pursuing this analogy, our current investigation could be viewed as an effort to characterize the two body potential of this process.

The elementary modes for the description of the outer envelope of the Rayleigh-Taylor mixing layer are bubbles of light fluid penetrating into undisturbed heavy fluid. §2 describes a recent refinement [8] of the single mode (bubble) theory developed previously [1]. An extension of this theory, based on superposition, describes the interaction of a single bubble with a random background field in the limit of small compressibility. §3 reviews current statistical theories and develops ingredients which may be needed in a new generation of statistical theories. Extending earlier work [1] using the Sharp-Wheeler model, we find a greater variability in α than was observed in the Read experiments [4]. This variability may be due to the smaller sample size in our computation as well as the ability to vary initial condition systematically.

2. Single Bubble Theory

2.1. The Periodic Array

The periodic array of bubbles, or equivalently the single bubble with periodic boundary conditions allows a detailed study of the long time behavior of a single mode. In this regime, the bubble goes through three successive time periods of exponential growth, bounded acceleration and approach to a constant (terminal) velocity. There are four parameters which effectively describe the entire motion, and in [8], the four parameter ODE for the velocity v

$$\frac{dv}{dt} = \frac{\sigma v (1 - \frac{v}{v_\infty})}{\frac{\sigma}{b}\frac{v}{v_\infty} + (1 - \frac{v}{v_\infty}) + [\frac{\sigma v_\infty}{g_R} - (1 + \sqrt{\frac{\sigma}{b}})^2] \frac{v}{v_\infty}(1 - \frac{v}{v_\infty})} \tag{2.1}$$

is proposed as a model for the single bubble dynamics. Here σ, g_R, v_∞ and b are the linear growth rate, the renormalized gravity, the terminal velocity and the decay constant to terminal velocity respectively. The reason for generalizing our previous three parameter ODE for single bubble motion was the realization that it contained an ansatz or prediction concerning the decay rate to terminal velocity which seemed to be lacking a physical basis. The solution for Eq. (2.1) is

$$t - t_0 = \frac{1}{\sigma}\ln(\frac{v_t}{v_0}) + [\frac{1}{g_R} - (\frac{1}{\sqrt{\sigma}} + \frac{1}{\sqrt{b}})^2 \frac{1}{v_\infty}] (v_t - v_0) - \frac{1}{b}\ln(\frac{v_\infty - v_t}{v_\infty - v_0}). \tag{2.2}$$

Extensive computations with the compressible two fluid Euler equations show a good fit for a range of Atwood numbers A and compressibilities $M^2 = \lambda g/c^2$ [8] for the equation (2.2). Here we give an intuitive, or physical interpretation for these parameters. We also note that two of the four parameters have been effectively determined and the remaining two must be obtained as a function of A and M^2 through explicit numerical solution of the single bubble problem to complete this theory. This determination has been made for a limited range of these variables only.

The two parameters which are known govern the initial period of bubble growth. The exponential growth rate σ is a solution of a transcendental equation, and its dependence on A and M^2 has been partially explored [1,8]. The constant which gives the maximum acceleration is $g_R = \frac{1}{2}Ag$ on the basis of the examination of a large number of numerical solutions to the two fluid Euler equations [1]. The final two parameters specify the terminal velocity v_∞ and the rate b of approach to v_∞.

2.2. The Superposition Hypothesis

The bubble velocity for the periodic case does not agree with the experimentally observed values for chaotic flow [2]. The essential idea we propose is to consider the bubble as a short wave length mode. Then an envelope is constructed through the tips of adjacent bubbles. This envelope defines a long wave length mode in the interface motion. We consider a bubble which is further advanced than its neighbors. Then its location can be regarded as a bubble on the long wave length envelope. In other words the long and short wavelengths are in phase in this case. Similarly, a bubble which is less advanced than its neighbors is a spike on the long wave length envelope, or in other words, the long and short wave lengths are phase reversed.

The superposition hypothesis states that the bubble velocity is the sum of the single bubble velocity plus the single bubble (or spike) velocity of the envelope. These two velocities are determined from the single bubble model of §2.1, using only the bubble radius and amplitude as geometrical parameters and so finally the bubble in a chaotic flow also has a velocity depending only on long and short wavelength radii and amplitudes (and dimensionless physical parameters A and M^2).

Experiment	34 A = 1			36 A = 0.5	104 A = 0.946		
t (ms)	23.6	29.2	34.8	60.8	46.6	57.6	68.6
V_{exp}	117	145	170	161	76.1	95.5	110
V_{th}	106	142	168	152	84.1	106	127
$\Delta V/V$	9%	2%	1.2%	5.9%	9.5%	9.8%	13.5%

Table 1. Verification of the superposition hypothesis from experiments of Read [4]. The hypothesis is satisfactory for those experiments in which envelopes can be clearly identified. In all these cases, $A \geq 0.5$.

The superposition hypothesis has been confirmed for the incompressible case by analysis of Read's experiments. Only cases with clearly formed bubbles and envelopes were analyzed. In the remaining cases (presumably with small surface tension) the interface was too irregular to define a long wave length envelope. The results are shown in Table 1.

Numerical solution of the two fluid Euler equation by the front tracking method shows agreement with the superposition hypothesis for $M^2 \approx 0$ in cases with clearly formed bubbles (no bubble splitting secondary instability). We find disagreement as M^2 is increased, see Table 2. We observe three cases of disagreement, all outside the range of experiments. Our proposed explanation in this case concerns the density stratification of the fluids in the gravitational field. In hydrostatic isothermal equilibrium, the density of the heavy fluid decreases exponentially with height. The density profile is more strongly stratified as M^2 increases. As a result, when the light fluid penetrates the stratified heavy fluid, the effective density ratio will be less than it was initially, thereby decreasing the velocities. We also observe disagreement with superposition in cases where bubble splitting occured presumably due omission of high frequency bubble splitting modes in the envelope description. Finally we observe disagreement with superposition for small Atwood number, for reasons not presently understood.

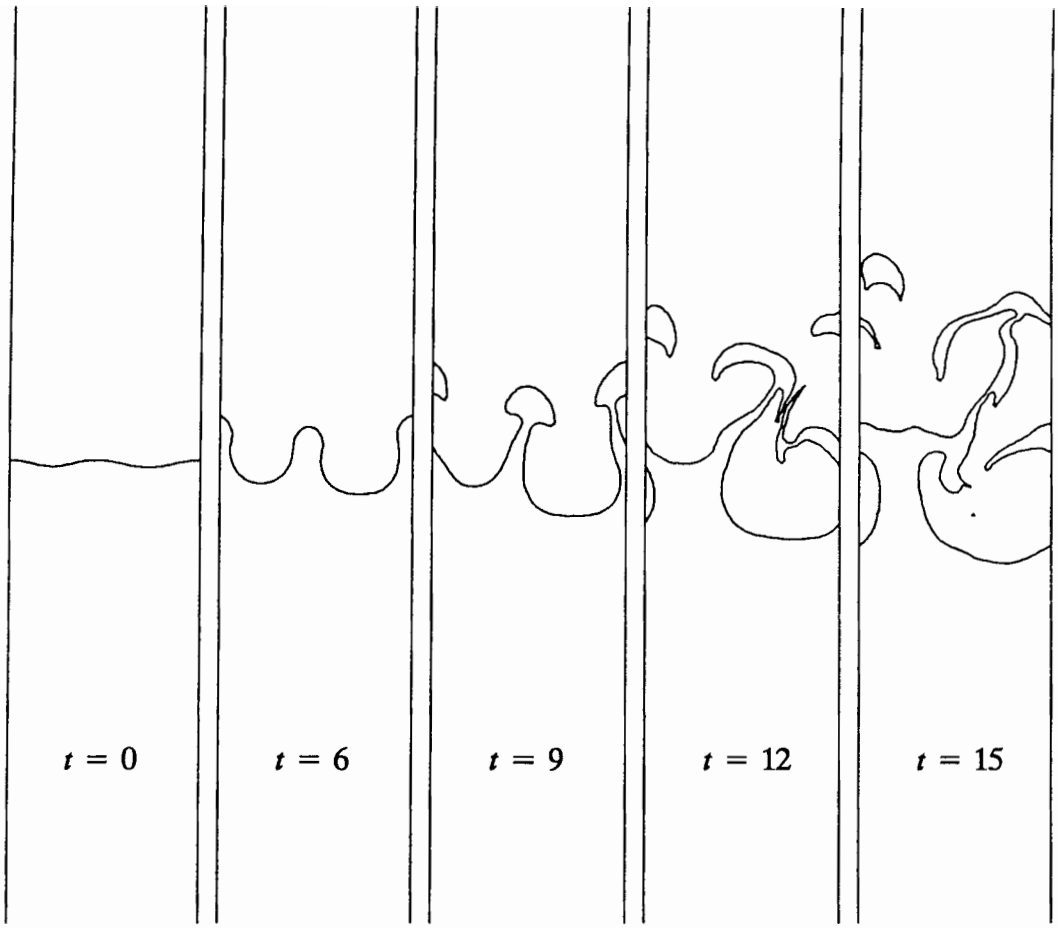

Figure 1. Successive times in a two bubble merger process. The compressibility and density ratio for this case are $M^2 = 0.1$ and $D = 5$ respectively. It can be seen that the large bubble overtakes the smaller one at $t = 12$. The velocity of the large bubble is accelerated during the merger while the velocity of the small bubble is reversed, see Figure 2.

Case	D	M^2	Error
Experiment	3−600	0.001-0.005	1.2-13.5%
Simulation	5−10	.1	1-19%
Simulation	2−10	0.5	72-105%

Table 2. The deviation of experimental and numerical results from the superposition hypothesis.

2.3. Mode Mode Interaction

The bubble merger process appears to have two stages. As illustrated in §2.2 with the superposition hypothesis, smaller bubbles develop a negative envelope velocity (contributions out of phase with their single bubble velocity), and at sufficient envelope amplitude, their total velocity becomes negative. At this point, they move rapidly away from the bubble envelope, and the position they previously occupied can be regarded as an oversized spike between the remaining larger bubbles. The second stage of the merger process involves an equilibration of radii, whereby the remaining (large) bubbles increase in size, while the spike region between them reduces to its equilibrium value. Fig. 1 shows the interface evolution of the two bubble interface during merger and Fig. 2 is the plot of the velocities of the two bubbles.

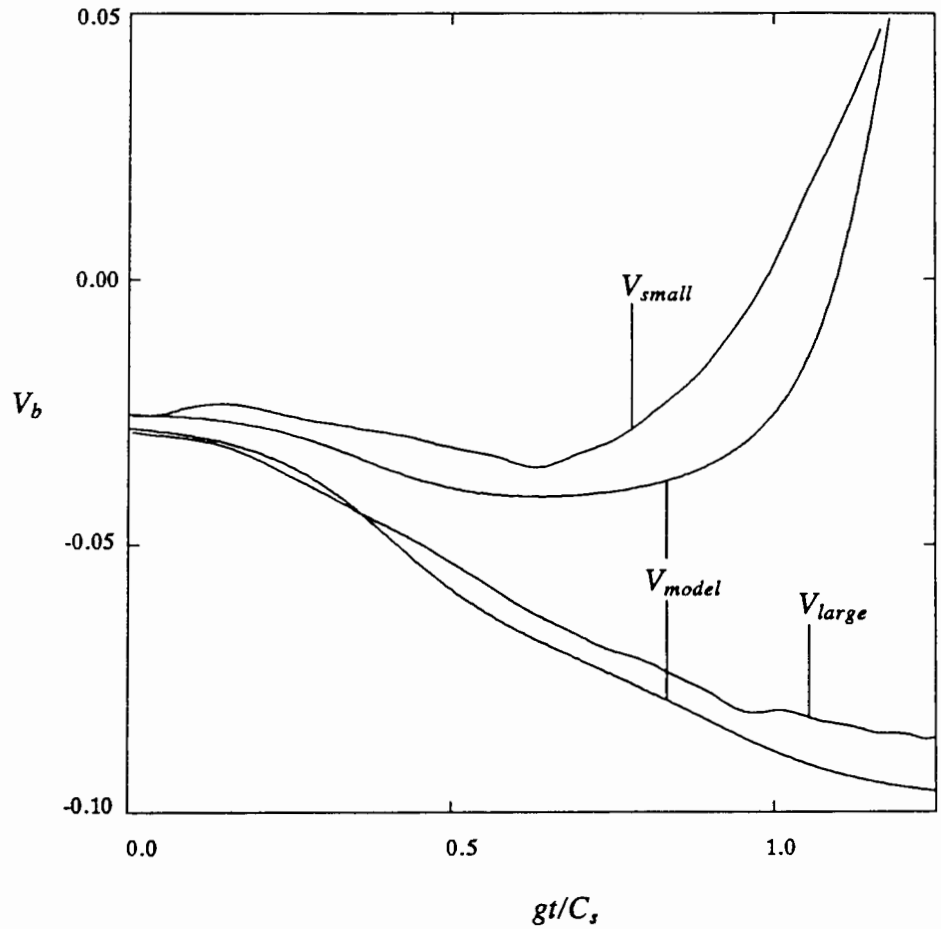

Figure 2. The plots of bubble velocities vs. time for the two bubble merger simulation. The result shows that the small bubble is accelerated at the beginning and is then decelerated after about $t = 5$. The small bubble is washed out downstream after its velocity is reversed. The large bubble is under constant acceleration. The smooth curves represent the bubble motion as predicted by the superposition hypothesis.

3. Statistical Theories

Let $h(t)$ be the distance from the initial bubble interface to the outer bubble envelope. Then

$$h(t) = \alpha A g t^2 \tag{3.1}$$

and in two dimensions, $\alpha = .06$ (experiment) [4].

Computations of the acceleration constant α have been given by several authors, based on the full two fluid Euler equations with a random interface. Youngs [7] used an incompressible MAC code with van Leer advection. Special interface enhancements (e.g. the method of LeBlanc) which minimize diffusive mixing were not used, and the computation presents considerable diffusive mixing of the two fluids. His computations used small amounts of viscosity. He considered initial configurations of 12 bubbles with 200 horizontal mesh blocks, or about 16 blocks per bubble. He used a variety of initial conditions and Atwood numbers, and obtained values for α in the range .04 to .05.

Zufiria [9] used a vortex-in-cell code for the incompressible case. He considered only $A = 1$, with small surface tension. His initial conditions were various 4 bubble configurations, and he used a range of mesh sizes, the coarest of which was 16 grid cells per bubble. His result was $\alpha = .05$ to .06.

We report here on recent compressible front tracking computations. A wide range of physical parameters have been varied in our simulation. Those include the Atwood number A, the compressibility M and a variation in the number and size of bubbles on the initial front. For these simulations, we have traced the height of the largest bubble during the run. We have two methods for analyzing the acceleration coefficient α, namely from plots of h vs. t^2 and from plots of v vs. t. The first type of analysis is similar to Read's analysis and is close to the experimental data. This first method gives integrated time averaged acceleration, α_h, relative to the instanteous acceleration, α_v, in the second method and is consequently more regular. We find that α_h in most cases is nearly time independent, and varies in the range 0.05 to 0.065 in agreement with Read [4]. However, some initial conditions give rise to significantly smaller values of α; namely extreme values $\alpha_h = 0.038$ were recorded. α_v shows even larger fluctuations, both between different runs and also at different times within a single run. In Figs. 3 and 4 we examine a case for which $\alpha_h = .066$. The bubble motion can be observed to have three stages, as recorded in Fig. 3b. The sharp increase in α_v in the time period $7.5 \le t \le 10$ is associated with the collision of two spikes which lie above the bubble interface and are falling into the larger bubble. Upon collision, they create a jet, which accelerates the bubble. The sign reversal for $10 \le t \le 14$ appears to be due to the formation of a secondary bubble splitting instability. This detail of structure is missing in the plots of Fig. 3a, which are once integrated from Fig. 3b. The more regular quantities plotted in Fig. 3a are the same as measured and plotted by Read, which provides a partial explanation of the regularity of his results in comparison to ours. A further explanation is that Read has about 10 times the number of initial bubbles in his experiments; if 10 of our runs were combined into an ensemble of 50 bubbles, we would obtain the same leading bubble behavior for α_h as Read.

None of the above computations or experiments have examined many generations of bubble merger. Computations have been limited to one or two generations of bubble merger. The experiments contain one observable generation of merger. According to the theory of the most unstable wavelength, the experiments have an additional one to two generations of bubble merger which is not directly observable from the experimental pictures. The fact that initial conditions can play an important role after one or two generations is not surprising.

The number of generations of bubble merger in the laser fusion application can be bounded as follows. The theory of the most dangerous wave length [3,6] gives an estimate of the final bubble size in terms of the aspect ratio of the spherical shell of the container; the initial bubble size could be fixed by (a) photon wave length, (b) surface tension, (c) surface finish, and (d) asymmetries of the driving source. An order of

magnitude estimate of the number of bubble merger generations from the initial bubbles set by these sources would be (a) 5 generations, (b) unknown but presumed very large, (c) at most 5 generations, (d) 0 to 1 generation. From this analysis we conclude that, aside from the driving source asymmetries, there is a potential for more generations of bubble merger in the laser fusion application than in present computations or experiments. We turn next to statistical models, and the possibility of universal behavior independent of initial conditions.

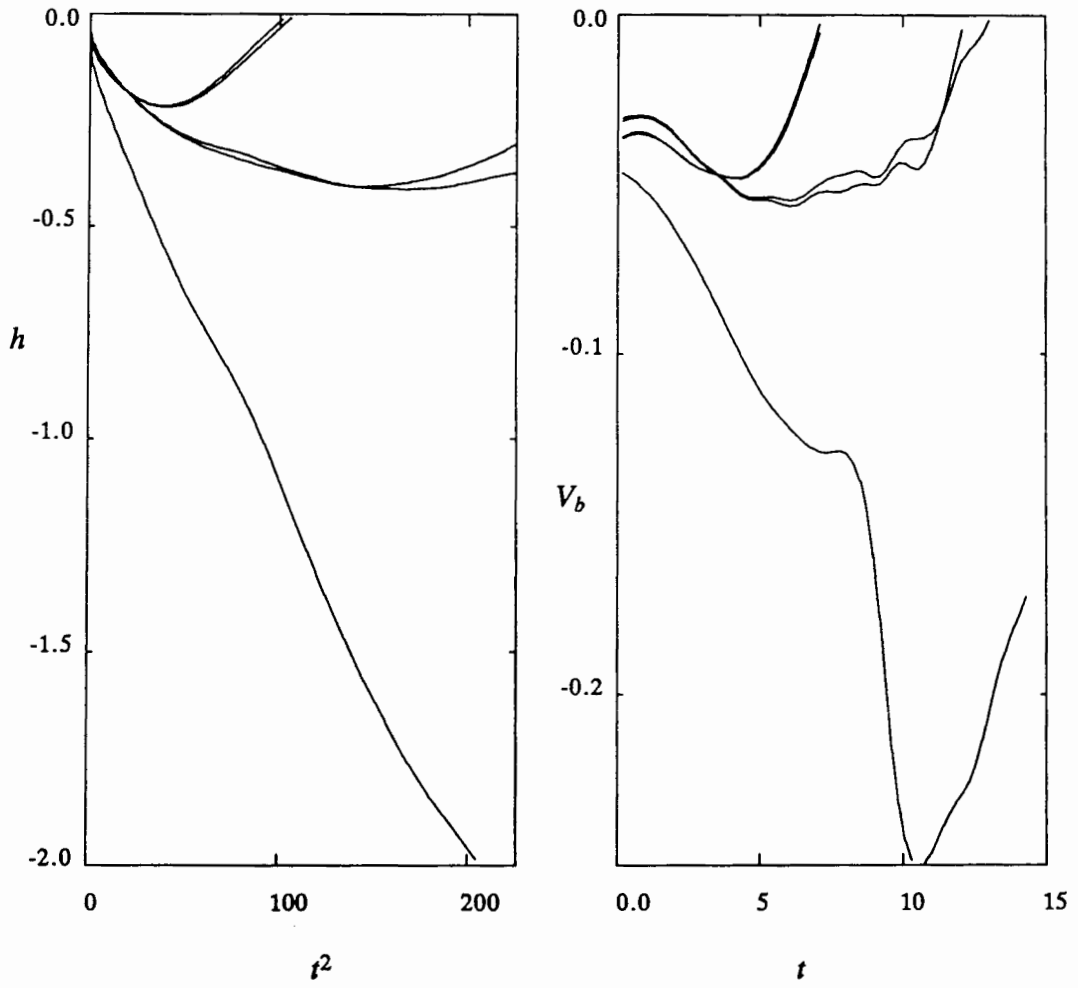

Figure 3. The left plot displays bubble heights vs. t^2 in a simulation with 5 initial bubbles. The Atwood number in this case is $A = 0.818$, and the compressibility $M^2 = 0.1$. The right picture shows the velocity vs. t in the same case.

Two statistical models for the bubble envelope have been proposed [5,10]. These models are coupled systems of differential or difference equations for the bubble growth and merger. The essential differences between these models are: The Zufiria model has no free parameters and is limited to the case $A = 1$, $M^2 = 0$. It allows continuous relaxation of bubble width, as an aspect of bubble merger. The Sharp-Wheeler model has two emiprical parameters and appears to be applicable to a range of values of A and M^2. Merger in this model is discrete in all its aspects. They both result in a constant acceleration, with an acceleration constant α in reasonable agreement with experiment.

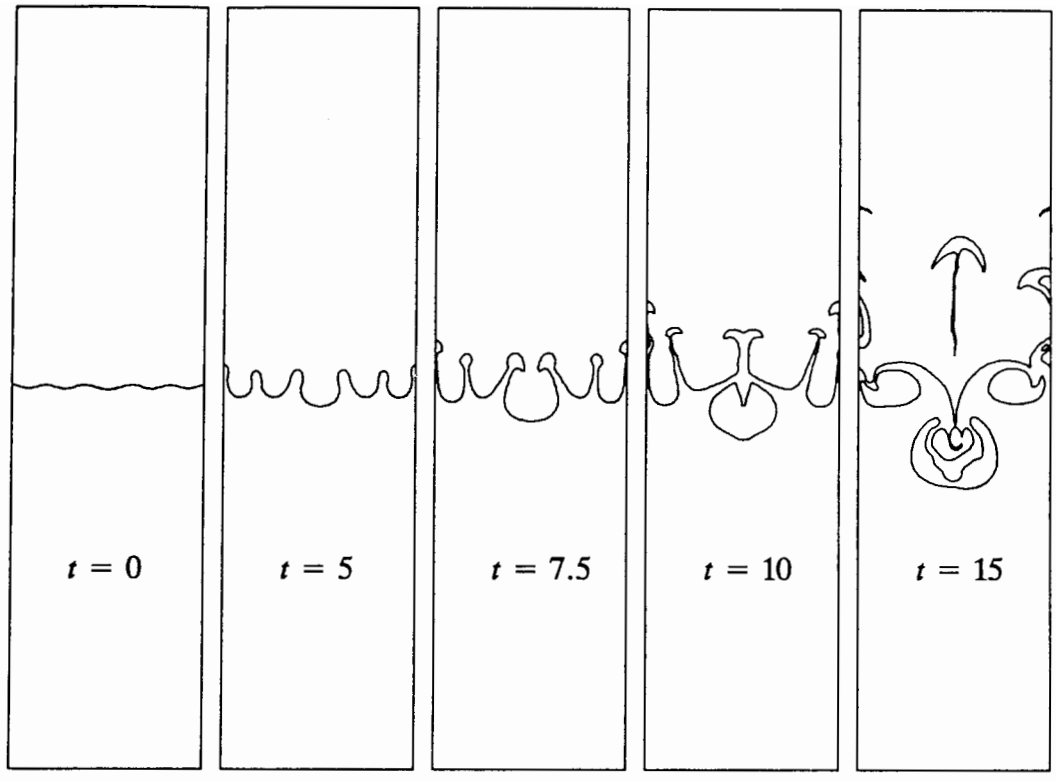

Figure 4. The interface positions at successive times in a computation with five initial bubbles. The physical parameters of this run are the same as in Figure 3.

Two phenomena have been observed in our random interface computations which are not contained in the above statistical models. One is the role of stratified initial conditions, which implies that for times large in proportion to the compressibility, the light fluid bubbles rise into a rarefied portion of the heavy fluid, to an extent that the effective Atwood number is diminished or even becomes zero. This observation raises the question of initial conditions which are not density stratified. It appears to be related to the breakdown of superposition for small Atwood numbers and moderate or large compressibilities. Also note that the increase in wave number due to bubble merger leads to an increase in the effective compressibility. A second phenomena is a change of flow regime to a bubbly, frothy or slug flow regime in the mixing layer, in which the light fluid spatially disconnected. This multiphase regime also reduces the effective Atwood number at the interface. The occurence of a slug flow regime is dependent on initial conditions, in particular on the relative size of adjacent bubbles. It could also depend on the distinction between exactly two-dimensional computations as opposed to approximately two-dimensional experiments.

References

1. C. Gardner, J. Glimm, O. McBryan, R. Menikoff, D. H. Sharp, and Q. Zhang, "The Dynamics of Bubble Growth for Rayleigh-Taylor Unstable Interfaces," *Phys. of Fluids*, vol. 31, pp. 447-465, 1988.

2. J. Glimm and X.L. Li, "Validation of the Sharp-Wheeler Bubble Merger Model from Experimental and Computational Data," *Phys. of Fluids*, vol. 31, pp. 2077-2085, 1988.

3. J. D. Lindl and W. C. Mead, "Two-dimensional Simulation of Fluid Instability in Laser-Fusion Pellets," *Phys. Rev. Letters*, vol. 34, pp. 1273-1276, 1975.

4. K. I. Read, "Experimental Investigation of Turbulent Mixing by Rayleigh-Taylor Instability," *Physica 12D*, pp. 45-48, 1984.

5. D. H. Sharp and J. A. Wheeler, "Late Stage of Rayleigh-Taylor Instability," Institute for Defense Analyses, 1961.

6. C. P. Verdon, R. L. McCrory, R. L. Morse, G. R. Baker, D. I. Meiron, and S. A. Orszag, "Nonlinear effects of multifrequency hydrodynamic instabilities on ablatively accelerated thin shells," *Phys. Fluids*, vol. 25, pp. 1653-1674, 1982.

7. D. L. Youngs, "Numerical Simulation of Turbulent Mixing by Rayleigh-Taylor Instability," *Physica 12D*, pp. 32-44, 1984.

8. Q. Zhang, *A Model for the Motion of Single Bubble and Spike in Rayleigh-Taylor Instability*, To appear.

9. Juan Zufiria, *Vortex-in-Cell simulation of Bubble competition in Rayleigh-Taylor instability.*

10. Juan A. Zufiria, "Bubble competition in Rayleigh-Taylor instability," *Phys of Fluids*, vol. 31, pp. 440-446, 1988.

MOLECULAR MIXING IN RAYLEIGH-TAYLOR INSTABILITY

P.F.Linden, J.M.Redondo & C.P.Caulfield

Department of Applied Mathematics and Theoretical Physics
University of Cambridge, Silver Street, Cambridge CB3 9EW, U.K.

Abstract

The amount of mixing at the molecular level at various stages during the growth of Rayleigh-Taylor instability is investigated in a series of laboratory experiments. Instability is produced at an interface between two miscible liquids, brine and fresh water, with zero surface tension. The brine, density $\rho + \Delta\rho$ with $\Delta\rho \geq 0$, is placed on top of a layer of fresh water, density ρ, and separated from it by a horizontal barrier. Both liquid layers are initially at rest, and the instability is initiated by removing the barrier horizontally.

Measurements consist of visual observations of the flow using fluorescent dye and shadowgraphs. Quantitative measurements of the amount of mixing are obtained from analysis of dye intensities profiles during the growth of the instability. These measurements give an integrated value (across the width of the mixing region) of the amount of mixing. A conductivity probe has been used to make point measurements of the salinity. These have been correlated with visual observations of relate changes in salinity with specific mixing processes.

1. Introduction

Rayleigh-Taylor (RT) instability is the name given to the motion that develops when light fluid is accelerated into a heavy fluid. This can occur, for example, during laser implosion of deuterium-tritium fusion targets, or as a result of local density inversions of a stratified fluid. Linear stability theory dates back to Taylor(1950), Chandrasekhar(1961) and a recent review of the development to finite amplitude is given by Sharp(1984). The characteristic of the instabilities observed at high density ratios is the production of 'bubbles' and 'spikes'. Secondary phenomena include the development of Kelvin-Helmholtz instability on the side of the 'spikes', amalgamation of bubbles and the production of small turbulent scales. The motion is essentially three-dimensional in character, with the interface having a fractal quality as the instability develops. For lower density ratios, the difference between bubbles and spikes disappears leaving two symmetric turbulent fronts marking the mixed region.

Much of the previous work (see e.g. Read(1984)) has considered the RT instability of immiscible liquids. Surface tension affects the production of small scales, and no mixing at the molecular scale is possible. In this paper we report some results of laboratory studies of RT instability between miscible fluids (brine and water) at low density differences. The aim of the work is to determine how the two fluids mix.

In section 2 the experimental method is outlined and the results are presented in section 3. The conclusions are given in section 4.

2. The experiments

The experiments were carried out in a perspex tank 500 mm deep, 400 mm long and 200 mm wide. The tank had a removable aluminium sheet 1.5 mm in thickness which separated a layer of brine from a layer of fresh water below (see figure 1). The two layers of fluid were initially at rest and the experiment was initiated by sliding the aluminium sheet horizontally through a slit in one end wall of the tank. Flow visualization was either by shadowgraph or by adding dye to one of the layers. Laser induced fluorescence was also used, with illumination provided by a thin (2mm) sheet of light from a 2W argon laser. Records of the flow were made using video and still photography. The video images were digitised to obtain quantitative estimates of dye

concentration. Measurements were also made of the salt concentration with a conductivity probe placed in the tank.

All the experiments were conducted with two layers of equal depth, with a range of initial density differences $\frac{\Delta\rho}{\rho}$ from 0.0005 to 0.098 . Only the experiments with $\frac{\Delta\rho}{\rho}$ between 0.005 and 0.065 are considered fully representative of the RT instability since for lower values of the density difference the initial disturbance caused by the plate removal caused considerable uncertainties (see setion 3.2.1) and at high values the growth rate of the instability was comparable with the velocity of the plate. There also remain regions near the side walls which exhibit some anomalous behaviour and are excluded from the subsequent analysis.

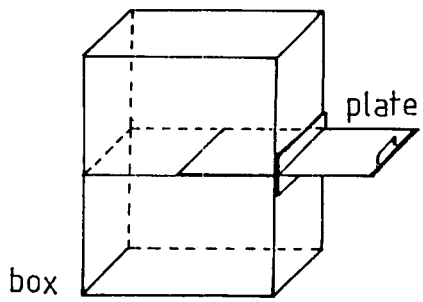

Figure 1: *Schematic diagram of the apparatus*

3. Experimental results

3.1 Qualitative results

The structure of the mixing region at two times after the removal of the plate is shown in figure 2. These shadowgraph images show that the front grows symmetrically about the original interface position, and that motion develops over a range of lengthscales. There is some variation in the thickness of the mixing region during the early stages which results from removing the plate through one end of the tank (see figure 2a) and there are strong flows generated in the immediate vicinity of the end walls of the tank. In the central region of the tank the mixing region is of approximately uniform thickness. Views from the end of the tank confirm that there are no significant mean variations in the thickness of the mixing region in the direction normal to the plane of these photographs.

The lengthscales which appear initially are those produced by vortices shed from the trailing edge of the plate. These are typically 100mm in length. Superimposed on these vortices are small scale instabilities, associated with RT instability (see section 3.2.2.). At later times the lengthscales of the dominant motions increase by vortex pairing. Eventually the whole system overturns on the scale of the tank. Denser fluid reaches the bottom and a stable stratification develops. This stratification supports internal gravity waves(see section 3.2.3.)

3.2. Quantitative results

3.2.1 Growth of the mixing region

The thickness δ of the mixing region was determined from flow visualization. If we assume that the rate of advance of the mixing front depends only on

$$g' = g\frac{\Delta\rho}{\rho}$$

and the instantaneous thickness, dimensional analysis gives

$$\frac{d\delta}{dt} = 2(cg'\delta)^{1/2}$$

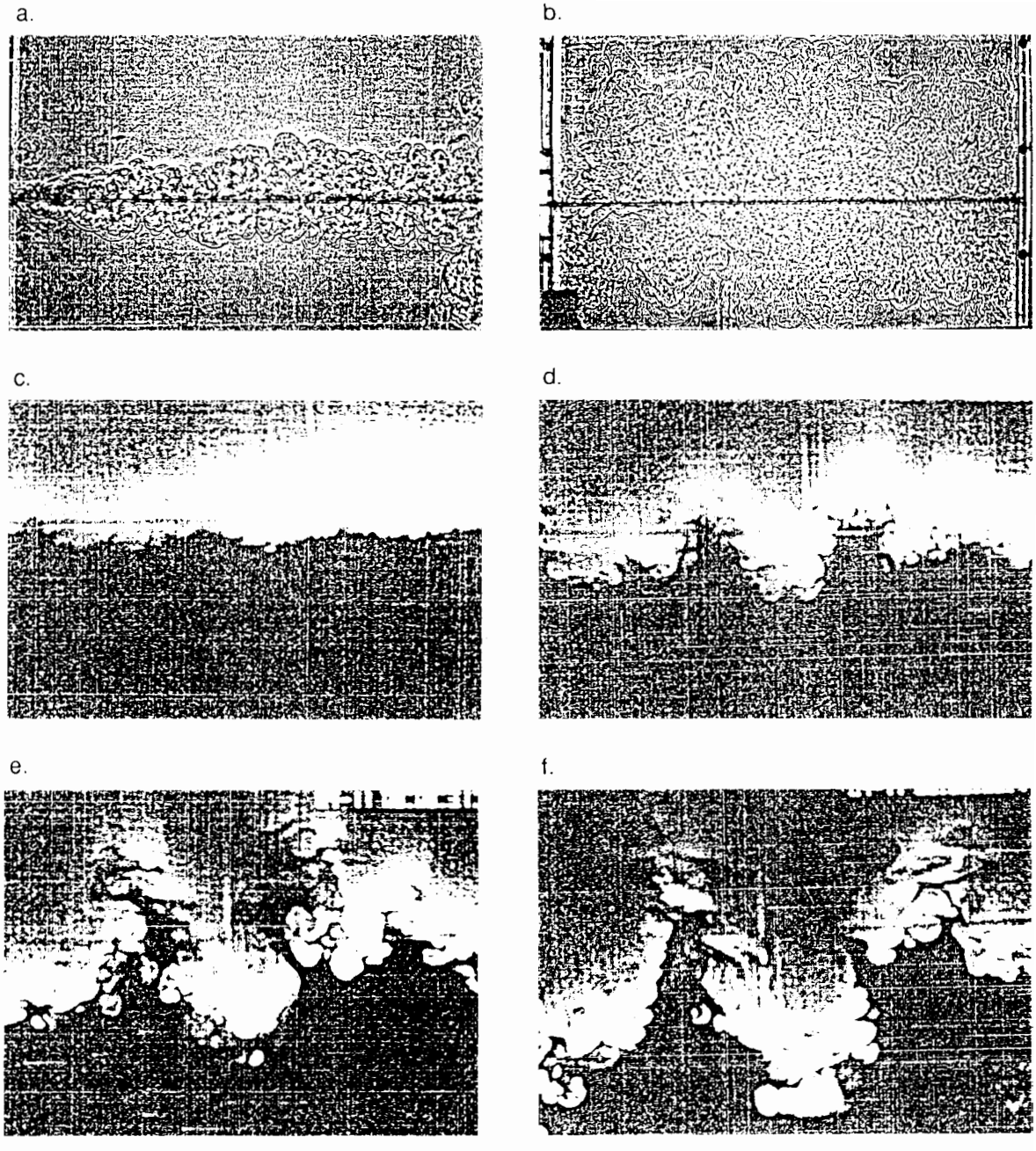

Figure 2: *Visualisation of the flow , a),b) Shadowgraph of a low density difference experiment. c),d),e),f) Laser induced fluorescence , KH billows can be seen in the sides of the bubbles.*

Integration and application of the boundary condition $\delta = \delta_0$ at $t = 0$ shows

$$\delta^{1/2} = (\delta_0)^{1/2} + (cg')^{1/2}t$$

Thus δ_0 represents a 'virtual origin' corresponding to the initial displacement produced by withdrawal of the plate. At large times, when $\delta \gg \delta_0$,the above formula is equivalent to the result given by Youngs(1984)

$$\delta = cg't^2$$

A typical plot of $\delta^{1/2}$ against $g'^{1/2}t$ for one experiment is shown in figure 3. The straight line is a least squares fit of the form given above. We see that it represents the data well, and from fits to all the experiments the values of δ_0 and c are determined.

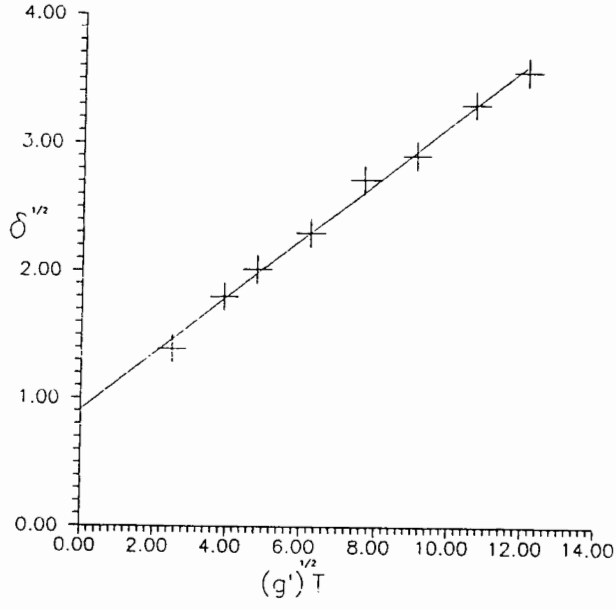

Figure 3: *Plot of the advance of the front with time. g' is 0.186 ms^{-2}.*

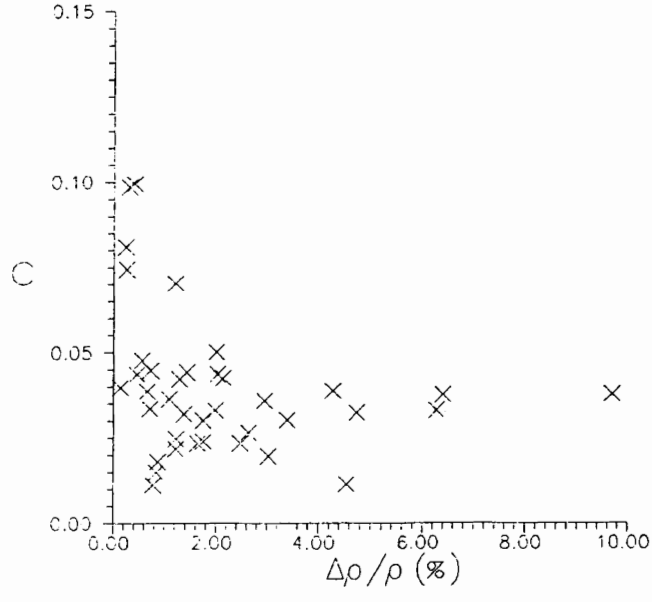

Figure 4: *Plot of the constant c versus $\frac{\Delta\rho}{\rho}$.*

Figure 4 shows the values of c plotted against the density differene $\frac{\Delta\rho}{\rho}$. Although the data are somewhat scattered, particularly at low values of $\frac{\Delta\rho}{\rho}$, they are consistent with a constant value of $c = 0.035 \pm 0.005$. This value is in agreement with those obtained at large density differences ($\Delta\rho/\rho$) by Read and Youngs(1984), Smeeton and Youngs(1988). The virtual origin δ_0 is plotted against $\frac{\Delta\rho}{\rho}$ on figure 5. As expected there is an increase in δ_0 at low density differences with values as high as 40mm being observed. At these large values we expect the effect of the initial disturbance caused by the plate to be significant throughout the measurement period and this may account for the increased scatter and larger values of c at low $\frac{\Delta\rho}{\rho}$.

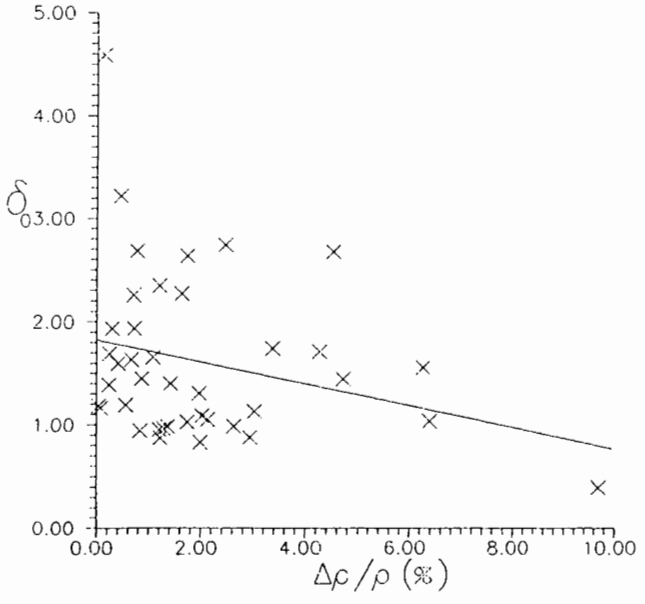

Figure 5: *Plot of the virtual origin, δ_0, with the initial non- dimensionalised density difference.*

3.2.2 Lengthscales

A range of lengthscales occurred during the RT process ranging from 5mm to the scale of the tank. The behaviour was similar for all of the densities analysed. Initially small disturbances could be seen which corresponded with the most unstable lengthscale λ_m between 3mm and 1.5mm (see figure 2c) . Superimposed on this scale 4 to 6 wavelengths of the order of 50 to 100 mm developed due to the removal of the barrier. As the RT instability front advanced new small scales could be seen developing (figures 2d, 2e). Some could be identified as KH billows and some as small vortex pairs (figure 2f). The large disturbances merged as the RT front advanced leaving one or two larger protuberances by the time the RT front reached the bottom of the tank. After that time a rotational overturning motion of the size of the box took over.

3.2.3. Conductivity measurements

Measurements made with a conductivity probe placed centrally within the tank and just above the plate for three initial $\frac{\Delta\rho}{\rho}$ are shown on figure 6 . These figures show the density ρ measured by the probe normalized by the initial density difference so that the upper layer corresponds to $\rho = 1$ and the lower layer to $\rho = 0$, as a function of time. Since the probe is in the upper layer, $\rho = 1$ before the plate is released and then ρ decreases as lower layer fluid mixes upward.

The overall behaviour is the same at all values of $\frac{\Delta\rho}{\rho}$,with a rapid decrease in the density being observed followed by oscillations which eventually decay, when the probe records a density intermediate between the upper and lower values. All records show fine scale fluctuations superimposed on longer timescale oscillations . There are significant differences between the way in which this final state is reached, depending on the initial density difference.

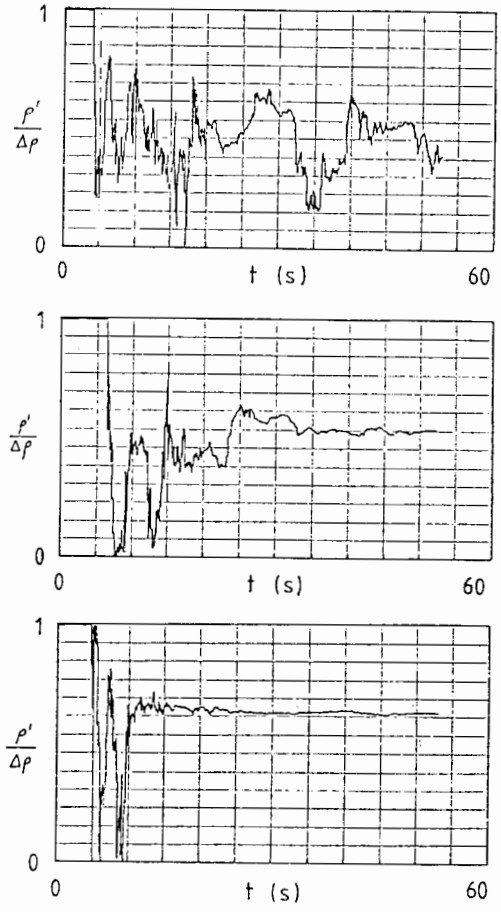

Figure 6: *Point density fluctuations with time for three different experiments , $\frac{\Delta\rho}{\rho}$ values are : a) 0.0078 ,b) 0.0251 ,c) 0.0647.*

As $\frac{\Delta\rho}{\rho}$ increases the oscillations on both timescales decrease more rapidly. This is associated with the formation of stable stratification as the two layers overturn causing a rapid damping of the turbulent motion.

Timescales for the decay of these fluctuations are shown in figures 7 and 8 . Figure 7 shows the e-folding time obtained by fitting an exponential decay to the peaks of the slow time oscillations plotted against $\frac{\Delta\rho}{\rho}$. These peak values provide a measure of the mixing into the large scale structures observed in the mixing region.

The timescale for the decay of these oscillations decreases with increasing initial density difference. The decay of the short timescale fluctuations is shown in figure 8. These values were obtained by visual inspection of the traces, such as shown in figure 6. These values also decrease with increasing $\frac{\Delta\rho}{\rho}$, and the values are, in general, larger than those in figure 7.

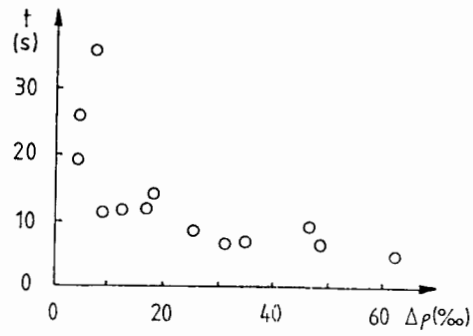

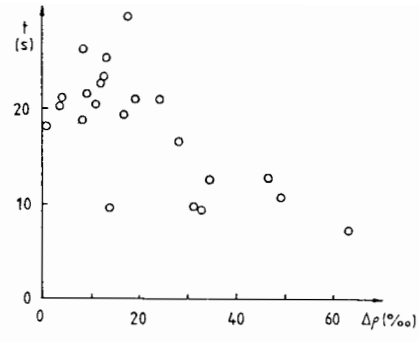

Figure 7 (left): *Decay e-folding time for the large scales associated with internal waves.*

Figure 8 (right): *Decay time for the small scale fluctuations recorded with a conductivity probe.*

3.2.4. Light intensity measurements

Figure 9 shows profiles of dye concentration in the lower half of the tank determined by digitisation of video images. These profiles give integrated values across the width of the tank, and are normalized so that initially the upper layer corresponds to unit concentration and the lower layer to zero concentration. The advance of the mixing region is clearly shown with a mean decrease in dye concentration. There are also considerable fluctuations about the mean, and there is clear evidence of regions of dense fluid falling as coherent entities.

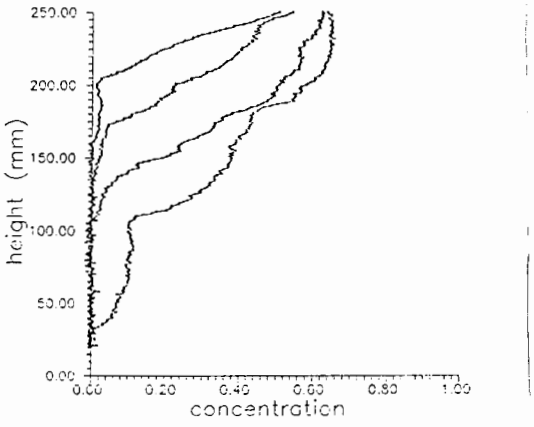

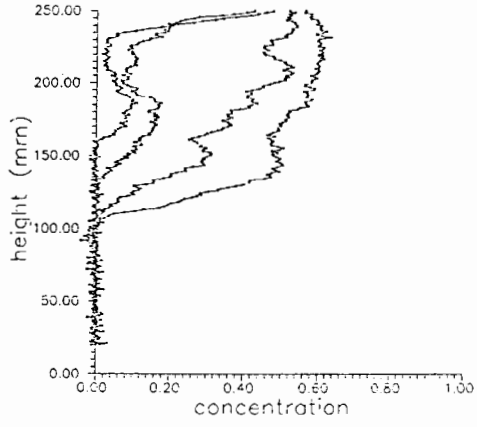

Figure 9 (left): *Averaged light intensity profiles ,normalized with the concetration of the upper layer. Volume fraction of dense fluid across the whole tank .The profiles were taken at times t= 0.5 , 0.8 ,2.3 and 3.7 sec.*

Figure 10 (right): *Same as figure 9 for the volume fraction of dense fluid near a single bubble in the same experiment with* $\frac{\Delta\rho}{\rho} = 0.02$

These measurements show that the front of the advancing disturbances is mantained sharp throughout the mixing process. This means that most of the mixing occurs through the sides of the falling bubbles. Figure 10 shows a similar averaged light intensity profiles as in figure 9, or the same experiment,but here the averaging has been done only over a single protuberance. It is seen that the averaged concentration gets sharper as the disturbance advances.

3.2.5. Final state

Vertical profiles made with the conductivity probe after all motion has ceased (see figure 11) show that there is a stable density stratification in the tank. If no molecular mixing had taken place, all of the upper layer fluid would ultimately lie beneath the original lower layer fluid and a two-layer stable stratification with the initial density difference would result.

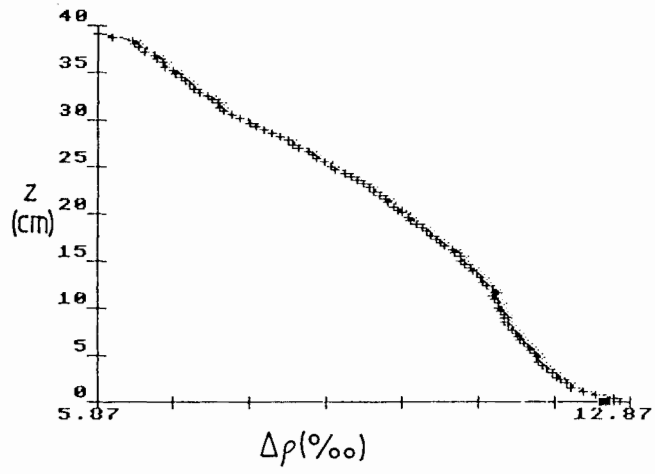

Figure 11: *Stable density profile after mixing has taken place for an initial density difference of* $0.023 gcm^{-3}$.

On the other hand, if complete molecular mixing occurred the tank would be uniform with no density variations. The observed density stratification lies between these two extremes and may be interpreted as a mixing efficiency.

A numerical estimate of mixing efficency is given by the final potential energy of the mixed fluid

$$PE_{final} = g \int_0^H z\rho(z)_{final}\, dz - \frac{g\Delta\rho H^2}{8}$$

associated with raising the centre of mass above the zero-mixing case. This is plotted on figure 12 normalized by the available potential energy that can be used for mixing. This is the initial potential energy

$$PE_{initial} = \frac{3g\Delta\rho H^2}{8}$$

minus the zero-mixing case potential energy ,

$$\frac{g\Delta\rho H^2}{8}$$

This curve increases from zero with increasing $\frac{\Delta\rho}{\rho}$, reaches a maximum of 0.46 and then decreases again at high $\frac{\Delta\rho}{\rho}$.

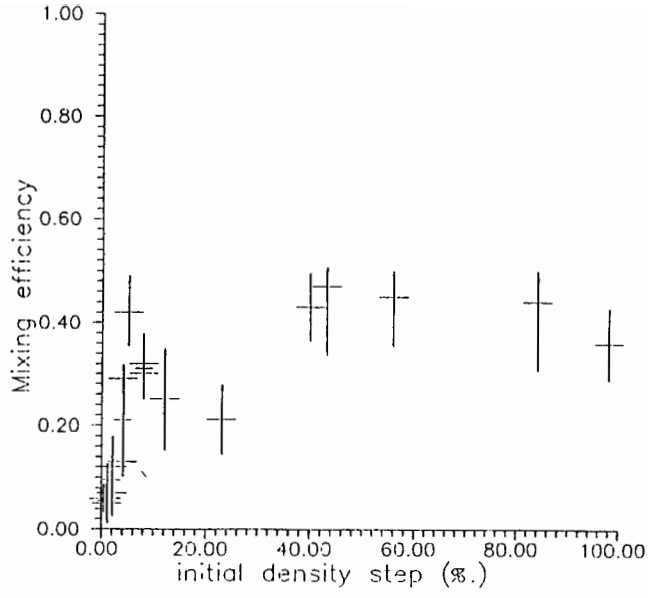

Figure 12: *Mixing efficiency versus* $\frac{\Delta\rho}{\rho}$.

This curve is characteristic of mixing processes in stratified fluids (Linden(1979,1980)). The maximum mixing efficiency, when the final profile is totally mixed is $\frac{1}{2}$, and if the profile were linearly stratified with slope $\frac{\Delta\rho}{H}$ then the mixing efficiency is $\frac{1}{6}$.

4. Conclusions

The experiments show that RT instability involves a number of interacting scales and processes. Small scale instabilities (consistent in scale and growth rate to those predited by linear theory) occur and are superimposed on a larger scale instability of the interface. This larger instability leads to the formation of blobs of fluid which penetrate into the layers on either side. Secondary instabilities in the form of Kelvin-Helmholtz billows form on the sides of the blobs. There appears to be little mixing across the leading edge of the blob, but fluid is entrained around the sides in a manner reminiscent of a falling plume or thermal, described in Turner(1973). The volume fraction profiles of dense fluid as it falls and mixes within the lower layer are similar to the ones obtained in the numerical calculations of Youngs(1984). The stepwise structure seen in the plan averaged volume fraction is due to the reduced mixing at the leading edge of the instabilities.

5. Acknowledgements

We would like to thank D.Youngs for many interesting discussions on this work and R.Perkins for his help with the digitiser. This work was supported by the Ministry of Defence. C.P.C. also acknowledges the support of a Robert Gardiner Memorial scholarship.

References

Chandrasekhar,S.(1961) "Hydrodynamic and Hydromagnetic Stability", (Oxford Univ. Press,Oxford).

Linden,P.F.(1979) "Mixing in stratified fluids", Geophys. Astrophys. Fluid Dyn. vol 13, 3-23.

Linden,P.F.(1980) " Mixing across a density interface produced by grid turbulence" J. Fluid Mech. 100, 691-703.

Read,K.I.(1984)"Turbulent mixing by Rayleigh-Taylor instability" A.W.E. Report 002/84.

Read,K.I. and Youngs,D.L.(1983) "Experimental Investigation of turbulent Mixing by Rayleigh-Taylor instability", AWRE Report 001/83.

Sharp,D.H.(1984) "An overview of Rayleigh-Taylor Instability", Physica 12D , 3-18.

Smeeton,V.S. and Youngs,D.L.(1988) "Experimental Investigation of Turbulent mixing by Rayleigh-Taylor instability, part 3" A.W.E. Report O 35/87.

Taylor,G.I.(1950) "The instability of liquid surfaces when accelerated in a direction perpendicular to their planes. I", Proc. Royal Soc. A,vol. CCI, 192-196.

J.S.Turner(1973) "Buoyancy effects in fluids", Cambridge University Press.

Youngs,D.L.(1984) "Numerical similation of turbulent mixing by Rayleigh-Taylor instability", Physica 12D, 32-44.

IS A LAMINAR FLAME FRONT A PASSIVE SCALAR SURFACE OF THE TURBULENT FIELD?

J. Mantzaras, P. G. Felton, and F. V. Bracco
Department of Mechanical and Aerospace Engineering
Princeton University, Princeton NJ 08544

ABSTRACT

The three–dimensional structure of the turbulent flame in premixed propane/air charges was examined by visualizing simultaneously four parallel planar sections through the flame with a time resolution of 10 ns and a spatial resolution as low as 200 μm. The ratio of the turbulent intensity u' to the laminar flame speed S_ℓ ranged from 0.5 to 25 and the ratio of the Kolmogorov length scale to the laminar flame thickness from 0.2 to 5.

The interface between reactants and products is: highly wrinkled; continuous; without islands of reactants and products; with only few cusps; with some "fingers" of products; and of fractal geometry. The fractal dimension increases with u'/S_ℓ but seems to tend to a maximum value of about 2.38. This is also the value measured in non–reacting turbulent flows, thus suggesting that the interface between reactants and products may act as a constant property passive scalar surface under certain conditions. If the local and instantaneous turbulent flame speed is related to the fractal dimension, then significant inhomogeneities in this speed are found even though the turbulent field is rather homogeneous and isotropic.

INTRODUCTION

The structure of the turbulent premixed flame is of fundamental importance. Since turbulent combustion is an interplay of turbulence, chemistry, and thermodynamics, the parameters of the turbulence influence the structure of the flame front and, consequently, the regime of turbulent combustion. Thus measurements of turbulent intensities with and without combustion [1,2] and of length scales without combustion [3,4] were also made in our apparatus, that happens to be a ported reciprocating engine, and in [5] an assessment of the regimes of turbulent combustion in engines is given. In [1–4] it was established that the turbulence field away from walls is roughly homogeneous and isotropic when the chamber volume is around its minimum and that is when the visualization measurements of this paper, most of which are three–dimensional, were made. Earlier two–dimensional visualization results [6–8] had given direct information on the flame structure and helped identify the regime of turbulent combustion in premixed–charge engines.

The quantification of the two–dimensional flame structure information, and its relation to fundamental turbulence and combustion quantities, was just initiated in [8]. A main obstacle to this quantification is that the flame front can be highly fragmented and therefore difficult to measure using classical geometrical concepts. But theories based on fractals have begun to emerge for the characterization of turbulent flame fronts [9], and in [10] the fractal nature of premixed engine flames was established. Very recently the first three–dimensional images of turbulent

engine flames were also obtained [11]. In this paper we summarize our conclusions from our two and three–dimensional imaging work and present some new data that explore the maximum value of the fractal dimension of the interface between reactants and products. Obviously such an interface is an extreme example of density change in a turbulent field.

The paper is organized as follows. The regimes of turbulent combustion are reviewed and fractal concepts are listed that will be used later for the fractal analysis of the data. Then, the results are considered. First we position our specific conditions within the regimes of turbulent combustion, next we examine the fundamental issue, that can be addressed only with three–dimensional measurements, of the presence of islands of reactants and products. Fractal dimensions are then considered initiating a discussion of whether the flame front acts as a passive scalar surface of the turbulent field and of homogeneity of the geometrical properties of the wrinkles as may be assessed by analyzing changes in fractal dimensions. Our main conclusions are summarized at the end.

THEORY

Turbulent Combustion Regimes

The regimes of turbulent combustion are discussed with the help of Fig. 1 [5] which is a plot of the Damkohler number Da_Λ versus the turbulence Reynolds number R_Λ [12]. The Damkohler number is the ratio of the characteristic turnover time, τ_t, of an eddy of the size of the integral length scale, Λ, to the characteristic transit time through the laminar flame, τ_ℓ:

$$Da_\Lambda = \frac{\tau_t}{\tau_\ell} = \frac{\Lambda}{u'} \frac{S_\ell}{\delta_\ell} \tag{1}$$

where δ_ℓ is the laminar flame thickness, u' the turbulent intensity and S_ℓ the laminar flame speed. The turbulence Reynolds number is:

$$R_\Lambda = \frac{u'\Lambda}{\nu} \tag{2}$$

with ν the kinematic viscosity. Relevant parameters appearing in this plot are the ratio of the Kolmogorov scale, η, to the laminar flame thickness, and the ratios Λ/δ_ℓ and u'/S_ℓ. Some understanding of the structure of turbulent flames exists in two regimes; the regimes of reaction sheets and of distributed reactions. In the regime of reaction sheets, turbulence does not affect chemistry and the residence time in the laminar flame is much smaller than the characteristic turnover time of the smallest eddies. In this regime, the propagating laminar flame fronts are wrinkled and convoluted by the turbulence. In the distributed reaction regime, chemical reactions proceed together with, or after, turbulent mixing and the concept of a laminar flame does not apply. The lower bound of the reaction sheet regime can be set at $\eta/\delta_\ell = 1$ (the quantity η^2/δ_ℓ^2 is a measure of the stretch to which the laminar flame is subjected in a turbulent flow [13]) and $\Lambda/\delta_\ell = 1$ is the upper bound of the distributed reaction regime. In the intermediate regions, $\eta < \delta_\ell < \Lambda$, the structure of the turbulent flame has not yet been identified. The reaction sheet regime is divided in two subregimes. For $u'/S_\ell << 1$, turbulence is weak and a single continuous reaction sheet can be identified; at higher turbulence intensities it had been thought that adjacent sheets could collide and cut off pockets of reactants, forming multiply–connected reaction sheets.

The line $u'/S_\ell = 1$ may be taken as the boundary between these subregimes. The rectangle in Fig. 1 indicates the combustion regimes for various engine operating conditions as estimated in [5]. It is seen that a survey of important regimes of turbulent combustion can be made by changing the operating conditions of an engine.

Fractals

The analysis of rough surfaces or curves has followed an independent mathematical route which is known as fractal analysis, largely advanced by Mandelbrot [14,15]. Fractals are objects that display self–similarity (in the statistical sense) over a wide range of scales. For a fractal curve, its measured length L will have a power law dependence on the measuring yardstick ϵ:

$$L \alpha \epsilon^{1-D_2} \tag{3}$$

The exponent D_2 is called the fractal dimension of the curve ($1 < D_2 < 2$) and is a measure of the roughness and fragmentation of the curve. An expression similar to Eq. 3 applies for fractal surfaces: the measured area A of the fractal three–dimensional object depends on the size, ϵ^2, of the square used to resolve it:

$$A \alpha \epsilon^{2-D_3} \tag{4}$$

The exponent D_3 is the fractal dimension of the surface ($2 < D_3 < 3$). For a fractal object with an isotropic surface (a surface with a degree of wrinkling independent of orientation), a plane cut intersecting this object defines a curve with fractal dimension D_2 such that $D_3 = D_2 + 1$.

The main thrust for the application of fractals in the field of turbulence and combustion came when Mandlebrot [16] suggested that constant property surfaces of passive scalars in homogeneous and isotropic turbulent flows possess fractal character within a certain range of scales, the lower being the Kolmogorov scale and the upper being of the order of the integral scale. Fractal dimensions in turbulent flows have been measured; in [17] the fractal dimension D_3 of the interface between turbulent and laminar parts of an incompressible jet was found to be between 2.3 and 2.4 and in [18] the fractal dimension of clouds was found to be 2.37.

In [9] Gouldin proposes that turbulent flame surfaces are fractals. He suggests that when $u'/S_\ell >> 1$ and $\eta/\delta_\ell > 1$ (the second condition is necessary to define a thin flame front unambiguously) the flame front behaves as a constant property passive scalar surface where the theory of [16] is applicable; in this case the same fractal dimension of the turbulent field is assumed to be obtained, with the only difference that the range of fractal behavior may start at a scale higher than the Kolmogorov scale due to the smoothening effect of the flame propagation. For lower values of u'/S_ℓ the effects of flame propagation are significant and the fractal dimension may differ from that of the non–reacting turbulent flow [9]. In [9] a theory based on fractals was also developed for the prediction of the turbulent flame speed.

The fractal analysis was applied to the flame fronts in engines in [10,11]. It was found that they exhibit fractal character between scales as small as 200 μm (the highest resolution of the measurements in [10]) and as large as 4.5 mm. The values of D_3 obtained in [10,11] are shown in Fig. 2. The turbulence intensity was increased by increasing the engine speed and the laminar flame speed was changed by varying the equivalence ratio ϕ i.e. the mass of propane for mass of air. Note the tendency for D_3 to increase with u'/S_ℓ and that the maximum value of D_3 is around

2.38, i.e. in the range observed in non–reacting turbulent flows [17,18]. However the trend of the data leave open the possibility that for $1.0 > \phi > 0.59$ the maximum value of D_3 may exceed 2.38. Thus for this paper additional two–dimensional measurements were made for $\phi = 0.7, 0.8, 0.9$.

RESULTS AND DISCUSSION

Table 1 shows the parameters of the six three–dimensional cases and the three two–dimensional ones. The experimental arrangement and the data processing are described in detail in [11]. Figure 3 shows typical three–dimensional flame images for cases 1 to 6; each set consists of four images corresponding to four planes. The top plane is in the upper–left side of the image and the direction from top to bottom is counterclockwise; the field of view in each plane is 16x16 mm and the total separation between top and bottom planes is 3.4 mm. Figure 4 shows typical two–dimensional flame images for cases 7–9, with field of view 20x20 mm. For each of the nine cases 100 flames were analyzed. In the discussion of our results, we shall first identify the regimes of premixed–charge turbulent combustion that correspond to our nine cases, and then we will consider the question of the presence or absence of islands of reactants and products, the values of D_3 and of the turbulent flame speed, the existence and significance of the asymptotic value of D_3, and the subject of homogeneity.

Turbulent–Combustion Regimes of Our Data

To identify the regimes of premixed–charge turbulent combustion of our data we refer again to Fig. 1. This figure is obtained using the definitions of Eqs 1, 2 as well as the following:

$$S_\ell \, \delta_\ell = D_T = \nu \tag{5}$$

$$\eta = \Lambda / R_\Lambda^{0.75} \tag{6}$$

where in Eq. 5 the thermal diffusivity D_T was taken to be equal to the kinematic viscosity ν. The four definitions can be combined to give Da_Λ versus R_Λ at constant S_ℓ / u':

$$Da_\Lambda = (S_\ell / u')^2 R_\Lambda;$$

Da_Λ versus R_Λ at constant (Λ / δ_ℓ):

$$Da_\Lambda = (\Lambda / \delta_\ell)^2 R_\Lambda^{-1};$$

and Da_Λ versus R_Λ at constant (η / δ_ℓ):

$$Da_\Lambda = (\eta / \delta_\ell)^2 R_\Lambda^{0.5}$$

which are the three functions plotted in Fig. 1.

In the application of Eqs 1, 2, 5, and 6 there are two types of problems: one must estimate the values of Λ, u', S_ℓ, δ_ℓ, and ν that appear in Eqs 1 and 2; such quantities, in reality, are not necessarily related to each other exactly as postulated by the equalities of Eqs 5 and 6. In other words, Fig. 1 and all of its information pertain to order–of–magnitude estimates, not to uniquely–defined, precise quantities. Thus in order to position within it our nine cases, we have taken the same qualitative approach of [5]: we have estimated the maximum and minimum values of Λ, u', S_ℓ, δ_ℓ, and ν and combined them to give the maximum and minimum values of of Da_Λ, R_Λ using Eqs 1 and 2. The estimated quantities are given in Table 1. They were obtained as

follows.

The values of the turbulence intensity u' at the time at which the flame images were taken were measured in [1]. For the ϕ = 1.0, 0.9 and 0.8 cases the values of the laminar flame speed S_ℓ was estimated from the high–pressure high–temperature correlations of [19]. For the ϕ = 0.7 and 0.59 cases, S_ℓ were estimated from the high pressure correlations of [20] and using the high temperature corrections of [19]. It should be pointed out that there is significant scatter in the measurements of the laminar flame speeds, particularly at very lean conditions, as illustrated for example in Fig. 5. For all cases, a lower bound for the laminar flame thickness δ_ℓ was estimated from the relation $\delta_\ell = D_{T,u}/S_\ell$ where $D_{T,u}$ is the thermal diffusivity in the reactants. For the ϕ = 0.59 case the upper bound for δ_ℓ was set by the measurements of [8], whereas for each of the other cases the upper bound for δ_ℓ was estimated from laminar flame structure computations [5] and using the distance between the 5% and the 95% temperature rise across the flame. The integral length scale Λ was measured in [4] to be 2.1 mm (lateral ensemble integral length scale) at 600 rpm and was assumed to be independent of engine speed. A range of values for the kinematic viscosity ν was obtained for each case by calculating ν in the reactants and the products. The ranges of R_Λ and Da_Λ are shown in Fig. 6 which is an enlarged portion of Fig. 1; for cases 7–9 only the average position is shown, to avoid crowding of the figure.

Figure 6 shows that we estimate our stoichiometric flames to be mostly in the reaction sheet regime and our lean flames in the more difficult, less understood intermediate regime but close to the reaction sheet regime. Thus the structure of at least the lean laminar flames can be expected to be perturbed by the turbulence [22].

Flame Structure and Islands of Reactants and Products

Figure 3 shows that flame fronts with larger values of u'/S_ℓ are more convoluted than the ones with lower values of u'/S_ℓ. In case 1 with the lowest u'/S_ℓ (= 0.5), cusps are often found pointing towards the product side (white); no such cusps occur at higher u'/S_ℓ. This is in agreement with the theory of [23] that predicts cusps for $u'/S_\ell < 1$ and no cusps for $u'/S_\ell \geq 1$; it should be mentioned however that the theory of [23] was developed for flames with $\eta/\delta_\ell > 1$ and this condition is met only by some of our cases (see Table 1).

We can now consider one of the fundamental questions of premixed–charge turbulent combustion: the existence of islands of reactants and of products. It was expected that islands of reactants exist in the reaction sheet regime (due to collision of the laminar flame fronts and subsequent cutoff of pockets of reactants) and islands of products (due to flame stretching and extinction) exist in the intermediate regime in which, presumably, there would still be islands of reactants also [24–26]. All 600 sets of three–dimensional flames were examined for islands. In addition, more than a thousand sets of flames were viewed in cases 5 and 6, which are the best candidates for the occurrence of islands; No instance was found in which one could unambiguously recognize a disruption of the flame contiguity. In addition to the experiments with 3.4 mm total vertical separation, case 6 was examined with a total separation of 5.2 mm. The increased separation should increase the chance of finding islands if they existed. No island was found in this case either indicating that the flame surface is composed of a continuous flame sheet.

However it is interesting that several instances of "fingers" of products were found especially in

the lean cases; it would appear that thin fingers are responsible for the connectedness of the flame whenever the intercepts of the four planes with the flame define small islands in some of the planes.

Fractal Dimension and Turbulent Flame Speed

The fractal dimension D_2 was calculated for each of the four images of a set; 100 sets were used for each of the six three–dimensional cases and the results were analyzed in several ways. The ensemble average and the standard deviation of D_2 in each plane was computed. There is a 2% to 3% difference in $\bar{D}_2$ between the various planes for a given case. This systematic difference appears to be small and may be due to systematic differences in the measuring technique. Thus one may be justified in neglecting the systematic differences and in considering an average value of D_2 over the four planes. The six values of $\bar{D}_3$ ($= \bar{D}_2 + 1$) are shown in Fig. 7 together with those of cases 7–9. In addition Fig. 7 shows results at low values of u'/S_ℓ obtained from burner studies [27]. The vertical error bars represent a two–standard deviation error on the mean ($2\sigma_{D_3}/N^{0.5}$ where N is the statistical population). Note that the difference in the horizontal scale between Figs 2 and 7 is due to the more accurate estimate of the laminar burning velocity at $\phi = 0.59$ in the current study. The results of Fig. 7 suggest that the fractal dimension reaches an asymptotic limit of 2.38 and that this limit is reached monotonically.

Theories are beginning to emerge that attempt to connect fractal data to turbulent flame speed. For $\eta/\delta_\ell > 1$ and $u'/S_\ell >> 1$, Gouldin [9] extrapolating from Mandelbrot [16], has suggested

$$S_t/S_\ell = (\Lambda/\eta)^{D_3-2} \sim R_\Lambda^{0.75(D_3-2)} \tag{7}$$

where $\Lambda = \eta R_\Lambda^{0.75}$ for isotropic turbulence. Peters [28] has argued in favor of

$$S_t/S_\ell = (u'/S_\ell)^{3(D_3-2)} \tag{8}$$

As can be seen from Fig. 6, cases 2 and 3 come closer to satisfying the conditions $\eta/\delta_\ell > 1$ and $u'/S_\ell >> 1$. The turbulent flame speeds obtained with Eq. 8 for cases 2 and 3 are shown in Fig. 8 together with correlations proposed by various authors [29,30], and data from [31]. Also shown in Fig. 8 are the values of S_t/S_ℓ obtained in [8] after correcting them [11] for the now–established fractal geometry of our wrinkled laminar flames. It is to be pointed out that in determining the four solid symbols of Fig. 8 from Eq. 8 and references [8,11], the turbulence intensity was obtained after filtering out the low frequency components of the measured velocity fluctuations to reduce the effect of systematic trends [3]. If the standard ensemble averaging technique without filtering is used, the four solid symbols may move as far as indicated by the arrows. Conversely the data of [31] could move to the left if a trend analysis of the results were to show systematic trends.

Constant Property Passive Scalar Surface

We can now address the question as to whether the wrinkled flame fronts act as a constant property scalar surface of the turbulent field. The limit value of $\bar{D}_3$ is 2.38 ± 0.5% and is approached for flame fronts with values of $u'/S_\ell > 4$. This value of D_3 happens to coincide with those measured in non–reacting turbulent fields. Thus, as far as the fractal dimension is concerned, the flame surfaces of our lean turbulent flames act as if they were constant property

scalar surfaces of the turbulent field. If confirmed, this behavior must result from a rather special balance of events since for our lean flames we have estimated $\eta/\delta_\ell < 1$ and hence we expect the structure of the laminar flame itself to be altered by turbulence. In [32] it is proposed that the value of the fractal dimension of the flame front is irrelevant to that of the turbulent field.

Homogeneity

In general, if two curves have the same fractal dimension and in addition the inner and outer cutoffs of the fractal region are the same, they both have (statistically) the same degree of wrinkling. Homogeneity of a random field implies translational invariance of all its statistical quantities. D_2 is one characteristic parameter of the "long–space average" of the flame front. For homogeneity of the flame front structure the values of D_2 in all planes should be the same at each time. This is equivalent to the homogeneity of turbulence, where a long–time average of the velocity is taken at different spatial locations to yield the turbulence intensity u'. Then for the turbulence to be homogeneous the turbulence intensity u' at the various spatial locations should be the same. It is important to note that D_2 is an average quantity, like u', and neglecting all errors of the fractal analysis (finite spatial domain, etc.) for homogeneity of the flame front wrinkling, D_2 should be the same in all planes at each time.

Then a measure of the inhomogeneity of the fractal dimension for each of cases 1–6 may be derived from the distribution of the instantaneous differences in D_2 between any two of the four planes over the 100 realizations. Each difference distribution will have a mean and a standard deviation, the mean representing a systematic difference between the ensemble distributions of the fractal dimension in each plane, which is between 2% and 3%, and the standard deviation representing the stochastic differences in fractal dimension between the two planes.

The wrinkles of the flame surfaces do show inhomogeneity and the magnitude of the random difference between D_2 in any two planes has a standard deviation of less than 9.1% in all cases (in [33] the turbulence intensity was found homogeneous within 15%). In [11] the detailed statistical analysis is presented. The next question is how significant this inhomogeneity is. Eq. 8 is sufficiently descriptive of the enhancement of the turbulent flame speed by wrinkling and that the flame surface is isotropic, a 10% change in D_2 would result in a 50% change in S_t/S_ℓ. But the effective turbulent flame speed would be some spatial and temporal average and the effects of local and instantaneous variations would be smoothed out. Nonetheless, it seems likely that significant instantaneous variation in the flame propagation rate exists over the surface of the flame, particularly for small flames.

The cross correlation of D_2 between various planes was also examined and found to decrease with increasing distance; the correlation distance is of the order of the measured integral length scale.

CONCLUSIONS

1) No island of reactants or products was observed in any of the flames. However, in about 10% of the lean flames "fingers" of products were found; it would appear that thin fingers of products are responsible for the connectedness of the flame surface in flames that would seem to

be highly fragmented in previous two–dimensional imaging studies. Such fingers were also observed in stoichiometric flames at higher engine speeds but were less frequent.

2) The flame wrinkles exhibit fractal behavior. The fractal dimension of the flame fronts averaged over all planes at each condition was found to have a minimum value of 2.15 and to approach the value of 2.38.

3) As far as the fractal dimension is concerned, it would appear that the laminar flame surfaces act as if they were constant property scalar surfaces of the turbulent field, under appropriate conditions.

4) Turbulent flame speed models based on fractals were examined and compared with correlations of turbulent–to–laminar flame speed ratios (S_t/S_ℓ) of various researchers. Even though the comparison shows general agreement in trends, the simple fractal models for S_t/S_ℓ we have considered are not totally satisfactory.

5) The question of homogeneity in the geometry of the flame wrinkles was then addressed by examining the instantaneous differences between any two of the four planes for the 100 realizations of each condition. The degree of inhomogeneity is less than 9% for all pairs of planes. Such degrees of inhomogeneity in fractal dimension were assessed to be significant in that a 10% change in fractal dimension could possibly produce a 50% change in S_t/S_ℓ . The wrinkling however could change with time, which may smooth out the effect of the instantaneous differences between planes, and would have to be averaged over some space as well.

6) The correlation of the fractal dimension in various planes was found to decrease with increasing separation of the planes; the correlation distance is of the order of the measured integral length scale.

ACKNOWLEDGEMENTS

Support for this work was provided by the Department of Energy, Office of Energy Utilization Research, Program of Energy Conservation and Utilization Technologies (Contract DE–AS–04–86AL33209), General Motors Corp., Ford Motor Corp., and Cummins Engine Co.

REFERENCES

1. Liou, T.M., Hall, M., Santavicca, D.A, and Bracco, F.V., "Laser Doppler Velocimetry Measurements in Valved and Ported Engines", SAE Paper No. 840375, 1984.
2. Hall, M.J., "A Study of Velocities and Turbulence Intensities Measured in Firing and Motored Engines", Ph.D. Thesis No. 1764, Princeton University, 1986.
3. Fraser, R.A. and Bracco, F.V., "Cycle–Resolved LDV Integral Length Scale Measurements in an I.C. Engine", SAE Paper No. 880381, 1988.
4. Fraser, R.A. and Bracco, F.V., "Measurements of Integral Length Scales in an I.C. Engine", Modelado en Motores de Combustion Interna, Universidad Politecnica de Valencia, Spain, CMT 8736, pp. 197–205, June 8–11, 1987.
5. Abraham, J., Williams, F.A., and Bracco, F.V., "A Discussion of Turbulent Flame Structure in Premixed Charges", SAE Paper No. 850345, 1985.
6. zur Loye, A.O., Santavicca, D.A, and Bracco, F.V., "Preliminary Study of Flame Structure in an Internal Combustion Engine Using 2–D Flow Visualization", COMODIA 85 Symposium, Tokyo, pp. 249–258, September 1985.
7. Baritaud, T. and Green, R., "A 2–D Flame Visualization Technique Applied to an I.C. Engine", SAE Paper No. 860025, 1986.
8. zur Loye, A.O. and Bracco, F.V., "Two–Dimensional Visualization of Premixed Charge

Flame Structure in an I.C. Engine", SAE Paper No 870454, 1987.
9. Gouldin, F.C., "An Application of Fractals to Mcdeling Premixed Turbulent Flames", Combustion and Flame, 68: 249–266, 1987.
10. Mantzaras, J., Felton, P.G., and Bracco, F.V, "Fractals and Turbulent Engine Flames", to appear in Combustion and Flame.
11. Mantzaras, J., Felton, P.G., and Bracco, F.V., "3–D Visualization of Premixed–Charge Engine Flames: Islands of Reactants and Products; Fractal Dimensions; and Homogeneity", SAE Paper No. 881635 [SP–759], 1988.
12. Bray, K.N.C., "Turbulent Flows with Premixed Reactants", in Turbulent Reacting Flows (Libby, P.A. and Williams, F.A., eds), Springer–Verlag, Berlin, W. Germany 1980.
13. Williams, F.A., Combustion Theory, 2nd Edition, Benjamin–Cummings, Menlo Park, CA, 1985.
14. Mandelbrot, B.B., "Fractals", W.H. Freeman, San Francisco 1977.
15. Mandelbrot, B.B., "The Fractal Geometry of Nature", W.H. Freeman, San Francisco 1982.
16. Mandelbrot, B.B., "On the Geometry of Homogeneous Turbulence, with Stress on the Fractal Dimension of the Iso–Surfaces of Scalars", J. Fluid Mechanics, 72: 401–416, 1975.
17. Sreenivasan, K.R. and Meneveau, C., "The Fractal Facets of Turbulence", J. Fluid Mechanics, 173: 357–386, 1986.
18. Lovejoy, S., "Area–Perimeter Relation for Rain and Cloud Areas", Science, 216: 185–187, 1982.
19. Metghalchi, M., and Keck, J.C., "Laminar Burning velocity of Propane–Air Mixtures at High Temperature and Pressure", Combustion and Flame, 38: 143–154, 1980.
20. Okajima, S., Iinuma, K., Yamaguchi, S., and Kumagai, S. "Measurements of Slow Burning Velocities and Their Pressure Dependence Using a Zero–Gravity Method", 20th Symposium (International) on Combustion, the Combustion Institute, 1951–1956, 1984.
21. Lewis, B., and von Elbe, G., Combustion Flames and Explosions of Gases, Third Edition , Academic Press Inc., London 1987.
22. Bracco, F.V., "Structure of Flames in Internal Combustion Engines", in Calculations of Turbulent Reactive Flows (So, R.M.C., Whitelaw, J.H. and Mongia, H.L., editors), ASME Publication AMD–Vol. 81, 1986.
23. Ashurst, W.T., Sivashinsky, G.I., and Yakhot, V., "Flame Front Propagation in Nonsteady Hydrodynamic Fields", to appear in Combustion Science and Technology.
24. Shchelkin, K.I, and Troshin, Y.K., "Gasdynamics of Combustion", Mono Book Corp., Baltimore 1965.
25. Howe, N.M., and Shipman, C.W., "A Tentative Model for Rates of Combustion in Confined Turbulent Flames", Tenth Symposium (International) on Combustion, the Combustion Institute, 1139–1149, 1965.
26. Blizard, N.C., and Keck, J.C., "Experimental and Theoretical Investigation of a Turbulent Burning Model for Internal Combustion Engines", SAE Paper No. 740191, 1974.
27. Santavicca, D.A., Personal Communication.
28. Peters, N., "Laminar Flamelet Concepts in Turbulent Combustion", 21st Symposium (International) on Combustion, the Combustion Institute, 1231–1250, 1986.
29. Klimov, A.M., "Premixed Turbulent Flames–Interplay of Hydrodynamic and Chemical Phenomena", in Flames, Lasers and Reactive Systems, Vol. 88 of Progress in Astronautics and Aeronautics, (J.R. Bowen, N. Manson, A.K. Oppenheim, R.I. Soloukhin, eds.) American Institute of Aeronautics and Astronautics, New York, 133–146, 1983.
30. Yakhot, V., "Propagation Velocity of Premixed Turbulent Flame: The Renormalization Group Approach", to appear in Combustion Science and Technology.
31. Abdel–Gayed, R.G., Al–Khishali, K.J., and Bradley, D., "Turbulent Burning Velocities and Flame Straining in Explosions", Proc. R. Soc. London, A 391, 393–414, 1984.
32. Kerstein, A.R., "Fractal Dimension of Turbulent Premixed Flames", to appear in Combustion Science and Technology.
33. Hall, M.J., and Bracco, F.V., "A Study of Velocities and Turbulence Intensities in Firing and Motored Engines", SAE paper No 870453, 1987.

TABLE 1
EXPERIMENTAL CONDITIONS

CASE	ϕ	RPM	u' (m/s)	S_ℓ (m/s)	u'/S_ℓ	Λ (mm)	η (μm)	δ_ℓ (μm)	$\overline{\eta/\delta_\ell}$
1	1.0	300	0.6	1.25	0.5	2.1	30–150	10–50	3
2	1.0	1200	2.5	1.25	2.0	2.1	9–50	10–50	1
3	1.0	2400	5.0	1.25	4.0	2.1	6–30	10–50	0.8
4	0.59	300	0.6	0.22–0.34	1.7–3	2.1	30–150	50–200	1
5	0.59	1200	2.5	0.22–0.34	7–12	2.1	9–50	50–200	0.3
6	0.59	2400	5.0	0.22–0.34	14–26	2.1	6–30	50–200	0.2
7	0.9	2400	5.0	1.11	4.5	2.1	6–30	11–56	0.5
8	0.8	2400	5.0	0.88	5.7	2.1	6–30	14–70	0.4
9	0.7	2400	5.0	0.50–0.80	6.3–9	2.1	6–30	21–120	0.3

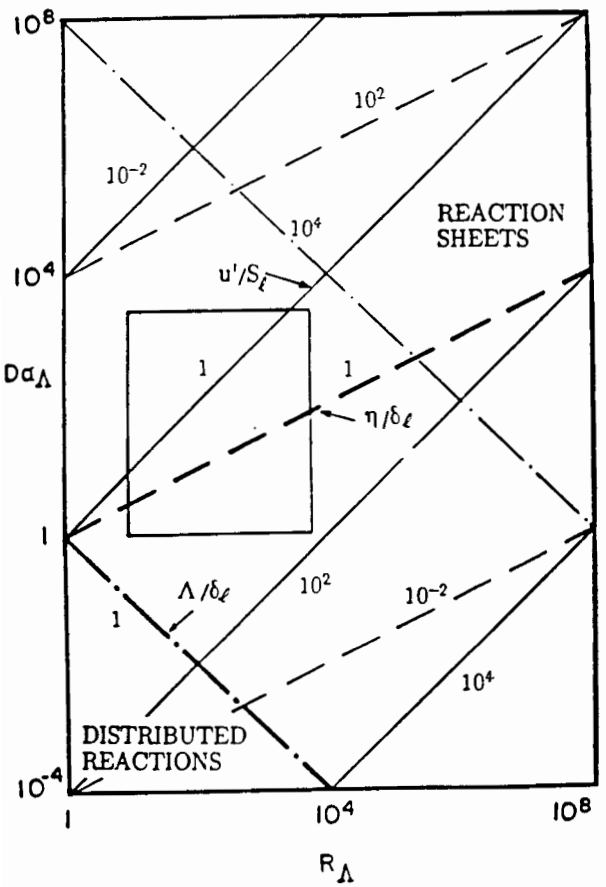

Fig. 1 Regimes of turbulent combustion. The rectangle is an estimate of the regimes applicable to internal combustion engines [5].

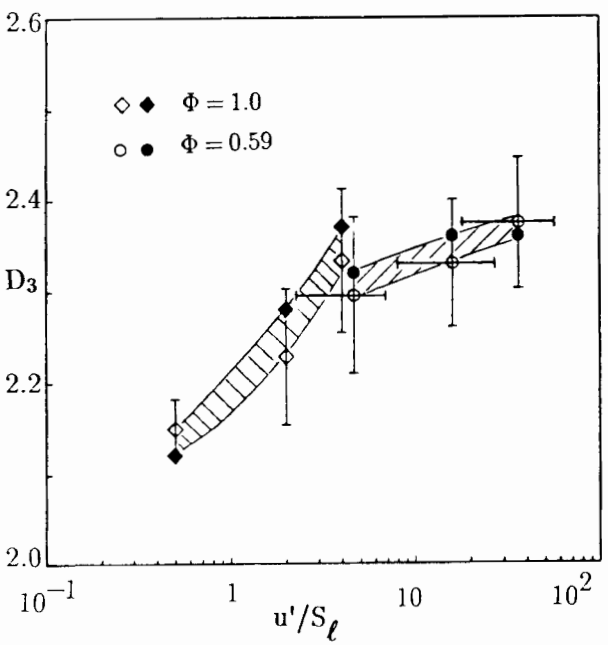

Fig. 2 Fractal dimension D_3 versus u'/S_ℓ. Filled symbols are from [10] and open symbols are from [11]. The vertical bars extend plus and minus a standard deviation of the distribution of D_3 [11].

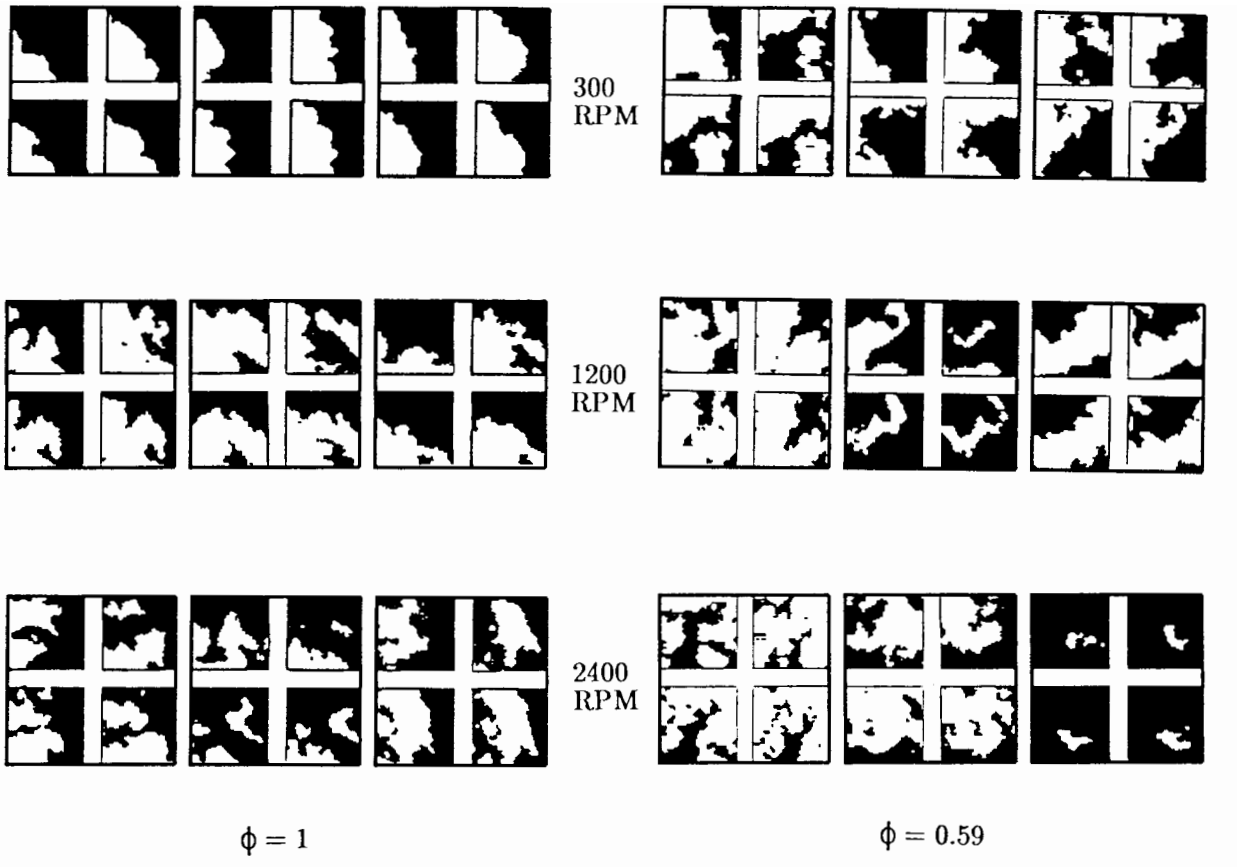

Fig. 3 Sets of three–dimensional flame images; 3 sets are shown for each of the cases 1–6 of Table 1.

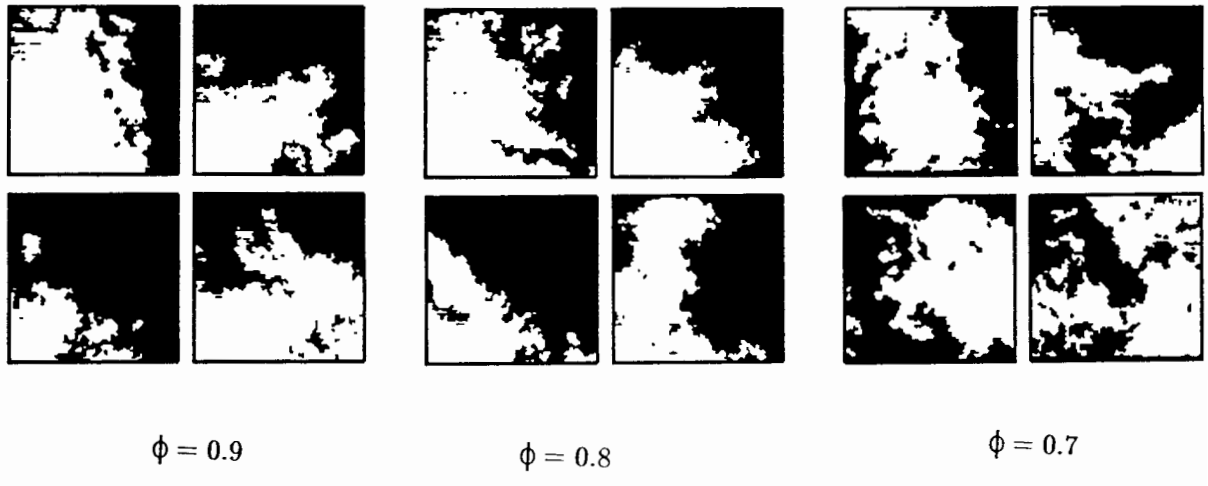

Fig. 4 Two–dimensional flame images at 2400 rpm; 4 flame images are shown for each of the cases 7–9 of Table 1.

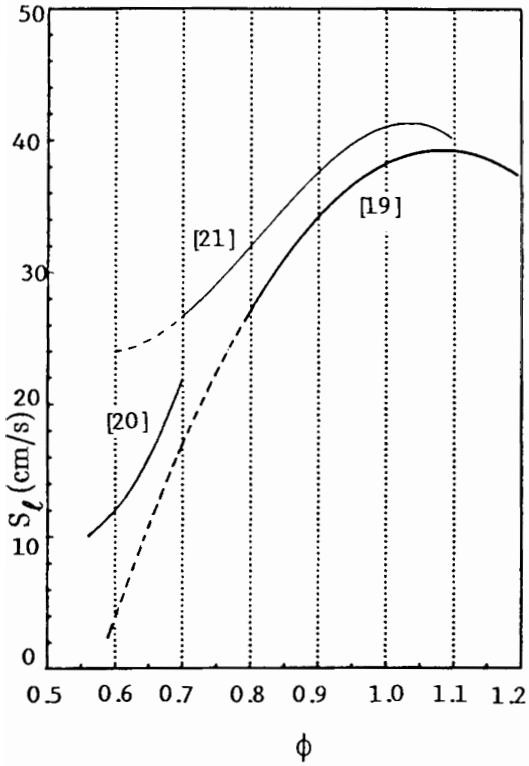

Fig. 5 Laminar flame speed for propane air mixtures at standard conditions by various authors [19–21].

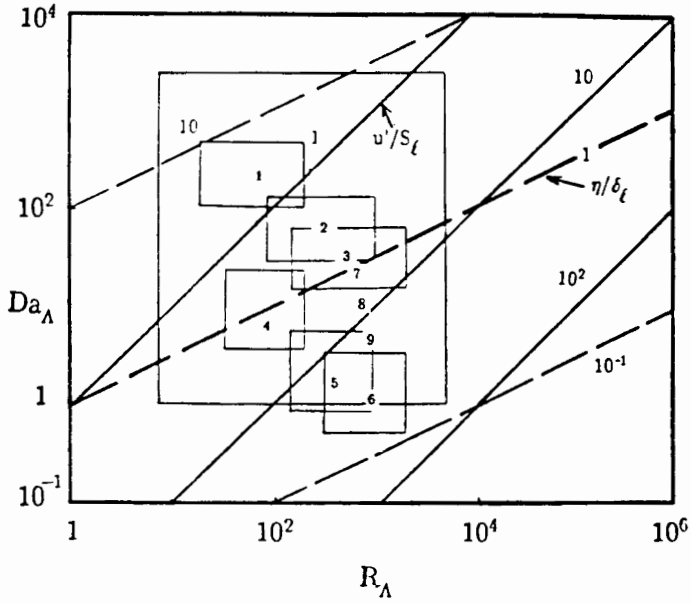

Fig. 6 Estimated regimes of turbulent combustion for cases 1–9 of Table 1. The larger rectangle is the range estimated in [5] for premixed–charge engine combustion.

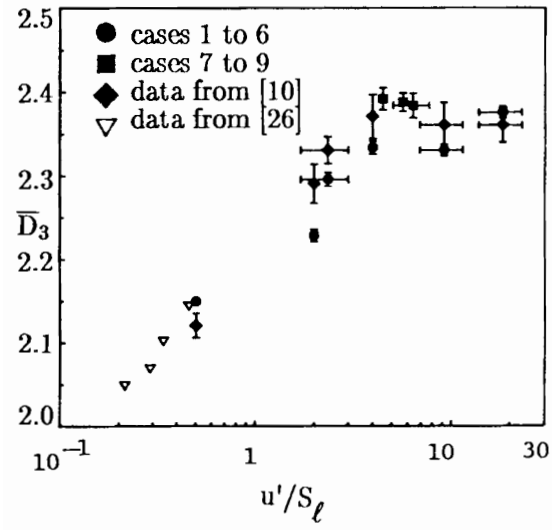

Fig. 7 Fractal dimension $\overline{D}_3$ versus u'/S_ℓ.

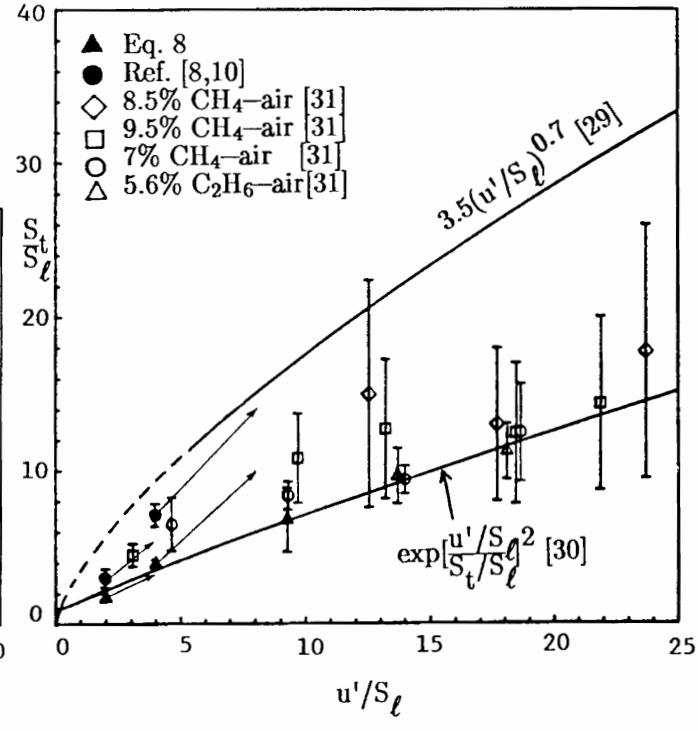

Fig. 8 Turbulent flame speeds for cases 2 and 3 of Table 1 estimated from Eq. 8 and from [8,10], correlations proposed by various authors and data from [31].

THE STABILITY OF VORTEX ARRAYS

P.G. Saffman
217–50 Applied Mathematics
California Institute of Technology
Pasadena California 91125

1. Laminar Models of the Mixing Layer

The seminal observations by Brown & Roshko (1974) of large scale coherent structures in the turbulent mixing layer have stimulated large amounts of work on the question of the extent to which turbulent flows can be modelled by inviscid laminar dynamics. We wish to know if such modelling can lead to quantitative predictions as well as provide qualitative insights into the mechanisms of the evolution of the turbulent flows. The jury is still out on this question, and more problems have been raised than have been solved, but whatever the final conclusions, there is no doubt that a significant increase in the understanding of vortex dynamics has resulted from the effort. As an aside, it is said that the eye of the artist can see deeper into nature than the trained scientist. The drawings by Leonardo da Vinci of coherent structures and van Gogh's painting "Starry Night", which resembles closely the pairing process of coherent structures in the mixing layer, illustrate this adage.

The simplest laminar model of the turbulent mixing layer consists of an infinite array of uniform, identical, finite area vortex patches in an unbounded incompressible, inviscid fluid. The existence, uniqueness and stability of such an array was first addressed by Pierrehumbert & Widnall (1981) and Saffman & Szeto (1981). Using the 'water bag method' of plasma physics (introduced into uniform vortex patch calculations by Deem & Zabusky 1978), the determination of the steady states can be reduced to the solution of an integro-differential equation. An alternative method due to J. Jimenez (private communication) employs the method of Schwarz functions and has been utilised by Kamm (1987). The latter method offers some distinct advantages for study of the two-dimensional linear stability properties of the array. An approximate method to calculate shapes (Moore & Saffman 1975a) is to approximate the shapes by ellipses, and use the exact solution of Moore & Saffman (1971) for a vortex in a uniform strain to determine the ellipticity and orientation of the ellipse. This method can be extended to unsteady flow (Saffman 1979), and has been developed more extensively, systematically and comprehensively by Melander et al (1986), who have obtained the Hamiltonian for the equations. (See also, Kamm 1987). The use of a cloud of point vortices to model the uniform vortex patches is a quick and easy way to obtain approximations, but it fails if the steady states are unstable (Moore & Saffman 1975a).

The calculations show that there is a one parameter family of solutions, the parameter being $\alpha = A^{1/2}/L$, where A is the area of each vortex and L is the longitudinal distance between the

centers of the patches. For small α, the vortices are nearly circular as is intuitively obvious. As α increases, the vortices become more deformed, and remarkably there is a maximum value of α. This is a limit point or fold of the family, which actually continues through more deformed shapes (of smaller area) until a limit is reached at which the vortices touch. The family then continues into a continuous varicosely deformed vortex sheet of finite thickness and finally ends at a uniform vortex sheet, whose bifurcation into a deformed sheet was studied by Rayleigh.

We mention in passing two alternative models for which steady states can be found in closed form. Baker, Saffman & Sheffield (1976) solved for the case of hollow or stagnant vortices. The behavior is very similar to that of the uniform cored vortices, except that the family does not change into a deformed connected vortex sheet of finite thickness but continues smoothly into a vortex sheet of zero thickness. The other model is the Stuart (1967) vortices which is a continuous family with a smooth vorticity distribution going from a tanh profile to a vortex sheet of zero thickness. This model seems less relevant as a model of the evolution of a mixing layer, as it does not possess limit point behavior. On the other hand it appears to offer the possibility of applying methods of global analysis to study two-dimensional finite amplitude stability, and is convenient for 'brute force' numerical investigations of three-dimensional linear stability (Pierrehumbert & Widnall 1982).

The existence of families of solutions means that application to the mixing layer requires a selection principle, in order to determine which members of a family are appropriate models. Stability is a criterion which is often tried, either to determine possible states or to model by the unstable modes the evolution of the flow. There are at least three approaches to the stability problem.

The first method, which we call spectral, finds the eigenvalues of infinitesimal disturbances to a steady state, and associates instability with existence of eigenvalues with non-zero real part. Since the system is inviscid, the eigenvalues come in pairs or quartets, so the existence of a non-zero real part implies an eigenvalue with positive real part. (We adopt the convention that the disturbance is proportional to $e^{\sigma t}$.) If all the eigenvalues are pure imaginary, the state is linearly stable, but can of course be non-linearly unstable. The spectral method gives little information about this matter. On the other hand, it is straightforward in principle and can be applied to both two and three dimensional disturbances. The main drawback is the need for large scale computing resources, as the eigenvalue problem can be multidimensional. Also for flows evolving in space there can be open questions about the boundary conditions.

The second method is initial value evolution. A disturbance is followed numerically to see if it grows or decays. Growth implies instability, provided one can distinguish between physical and numerical instability. Non-linear instability can be detected if the appropriate initial condition is given. The drawbacks are that the computing needs are greater than those for method 1, and that demonstrations of stability are not conclusive as the wrong class of disturbance may be chosen. (An example is the Karman vortex street, where initial value evolution calculations showed that finite core area stabilized the street because only disturbances of wavelength twice the separation distance were considered, and the unstable disturbances have a different wavelength as was found

by spectral calculations.)

The third method is global and gives general criteria for stability. The ideas are modern developments and extensions of Kelvin's observation that the equilibrium states are characterised by maxima or minima of energy. So far, the method is limited to two-dimensional disturbances and there is usually a restriction to a space which lacks physical significance. For example, the circular vortex can be shown to be L^1 stable, but appears to be L^∞ unstable (see the discussion below on filamentation).

There are two distinct classes of instability, which it is convenient to label as superharmonic and subharmonic. Superharmonic disturbances are those where the wavelength is the longitudinal spacing between the vortices, and every vortex behaves in the same way. Subharmonic disturbances have wavelength greater than the spacing and neighboring vortices behave differently. The major case is the pairing instability in which neighboring vortices interact. The vortex array is superharmonically stable when α is small, and becomes unstable when α reaches the critical value. This is the change of stability associated with the fold in the family of solutions. If a superharmonic disturbance is applied to the array at a state beyond the fold, the individual vortices break up; i.e. fission takes place (Moore & Saffman 1971). The subharmonic instability is always present for an array. It is easily calculated in the point vortex approximation (Lamb 1932), and the most unstable disturbance is the pairing one. When the vortices are of finite size, initial value evolution calculations show that the vortices rotate around each other and fusion takes place.

The superharmonic class can have a subharmonic component, and effects of finite size on the subharmonic disturbances can be worked out. Kamm (1987) has studied these questions, and finds that the modifications are generally slight. (See also Saffman 1988).

These considerations have led to a model of the mixing layer evolution proposed by Saffman (1981). The excess energy E of the array relative to that of a zero thickness vortex sheet is calculated. The mixing layer is represented at some station by one of the steady exact solutions of the Euler equations. Then the actual effects of turbulence can be modelled by an increase in the area of the vortices, the separation between them staying constant. The state of the mixing layer can be represented by points on the E *vs* α curve. There are two possibilities, which can be categorized as pairing or tearing. In the pairing mode, we assume that the energy of the layer is conserved during the entire evolution, which case it is necessary that $E = 0$ and the state is described by the array with this property. From details of the solution, it is found that in this case

$$a/b = 1.45, \qquad \delta_\omega/L = 0.28 \tag{1.1}$$

where a/b is the axis ratio of the vortex, and δ_ω is the vorticity width of the layer. In this case, the vortices would not grow between pairings, i.e. there is no turbulent entrainment or 'nibbling' and in the pairing process the vortices would have to ingest or 'gulp' a volume of fluid fluid equal to themselves in order to maintain the similarity with $A \propto L^2$. The time scale of the evolution would be the pairing time, which could be estimated from the exact solution for point vortices if there were a reliable way of estimating the stage at which coalescence takes place.

The second possibility is the tearing process, according to which the system moves from some state X by nibbling until the maximum area is attained at M. The steady state can no longer exist and something catastrophic occurs; presumably the vortices disintegrate and reform into a new array with double the spacing. The state X can be estimated by the assumption that energy is conserved during the rearrangement. It follows from the details that there is then a 35% increase in volume during the evolution from state X to state M, and the remaining 65% is gulped during the reformation. The dimensions are

$$\left(\frac{a}{b}\right)_X = 1.54, \qquad \left(\frac{a}{b}\right) = 2.4 \tag{1.2}$$

$$\left(\frac{\delta_\omega}{L}\right)_X = .30, \qquad \left(\frac{\delta_\omega}{L}\right)_M = .27. \tag{1.3}$$

These values are not inconsistent with the experimental data, and seem to agree with the idea that both pairing and tearing take place. It is possible that pairing is dominant wihen the layer is young, and tearing becomes more important as the layer ages, because once a significant amount of energy is lost, the pairing process would have to dissipate energy suddenly in order to preserve the similarity as the negative excess energy is doubled. Of course, the analysis does not explain why the vortices form in the first place or survive the numerous interactions rather than forming an amorphous cloud. Deeper understanding of the physics is called for to answer these questions.

So far the discussion only concerns two-dimensional disturbances. Three-dimensional disturbances are clearly also of interest and possible importance, but are more difficult to analyse. However, the various results for three-dimensional behavior suggest that only superharmonic instabilities are physically relevant for the mixing layer (this is not so for the wake and boundary layer), and they can be modelled satisfactorily by considering a single vortex in a uniform straining field (which is in the real situation produced by the other vortices in the array). There appear to be three instabilty mechanisms, which can be identified as (i) Biot-Savart (see Robinson & Saffman 1982), (ii) WBT (Widnall, Bliss & Tsai 1974), and (iii) Pierrehumbert (1986), and are distinguished by different axial length scales.

The Biot-Savart is the three-dimensional perturbation of the pairing instability with an axial scale long compared to the core radius. The three-dimensionality reduces the growth rate in general, so this instability does not appear to be too significant. The WBT is a parametric instability caused by interactions between Kelvin waves in the presence of strain (Moore & Saffman 1975b). Robinson & Saffman (1984) studied the effect of finite strain on this instability. The axial length scale is now comparable to the core radius. Finally, the Pierrehumbert (1986) instability, with a length scale small compared with the core radius, is an instability of elliptical streamlines in an almost two-dimensional flow. Bayly (1986) produced an analytical treatment based on exact solutions of Kelvin, and Landman & Saffman (1987) included the effects of viscosity. All three mechanisms have the same time scale A/Γ, where Γ is the strength of the vortices in the array,and it is not possible at present to decide what determines the actual axial scale of observed disturbances.

According to the ideas so far discussed, the mechanisms of mixing in the turbulent layer will be associated with the ingestion of fluid by the vortices in the pairing and/or tearing processes. Recent work has shown that there is another mechanism related to non-linear instability of a vortex which may play an important role in the mixing of fluid between the two streams, and this is the phenomenon of filamentation. Actually this was seen in the numerical calculations of Roberts & Christiansen (1972) of the fusion of two vortices. Deem & Zabusky (1978) saw it in the evolution of a circular vortex patch, and Melander, McWilliams & Zabusky (1987) have carried out a detailed study for the evolution of an elliptical vortex. Pullin (1981) observed filamentation in the evolution of a constant vorticity layer at a wall. Dritschel (1988) has done extensive calculations demonstrating repeated filamentation at the rim of a circular vortex patch.

Filamentation is not unexpected when the vortices are linearly unstable (Polvani et al 1988). The interesting phenomenon is that the process occurs for vortices that are linearly stable and provides a mechanism for the ingestion of fluid into a stable vortex. We would like to understand its basic cause, and determine if it always occurs. Numerical calculations by Shelley & Baker (1988) of the evolution of a vortex sheet of finite thickness show the formation of elliptical cores but no filamentation (which could be suppressed in this case by the sheet outside the cores which can be thought of as backwardly evolving filaments.) Further, it appears that filamentation can be either extrusive (e.g. Melander et al 1987) with filaments of vorticity entering the irrotational fluid, or intrusive (Pullin 1981) with filaments of irrotational fluid entering the vortex. Pullin, Jacobs, Grimshaw & Saffman (1988) have proposed a theory which attempts to explain these properties, it is based on the idea that filamentation is due to non-linear instability. When the vortex is stable, waves of finite amplitude exist on the interface. These waves can, however, be unstable and this instability will cause the generation of hyperbolic stagnation points in a frame of reference moving with the disturbance to the finite amplitude wave. Filamentation then occurs as the edge of the vortex is swept past the stagnation point. According to the details of the calculation, the time for filamentation to occur can be estimated as

$$t_f \approx -\omega^{-1}\Delta^{-2}\log\Delta \tag{2.1}$$

where ω is the magnitude of the vorticity in the layer, and Δ is the amplitude of the non-linear wave.

The approach by Pullin et al provides some insight into uncertainaties concerning aspects of the filamentation phenomenon. One is the requirement for a minimum steepness. The results suggest that a minimum steepness is required in the sense that the amplitude of the total interface perturbation must be sufficient to reach the critical layer, where stagnation points are present in the appropriate frame of reference. Pullin (1981) used disturbances of initially sufficient large amplitude to produce filamentation. On the other hand, an initial minimum steepness may not be required, provided a dynamical mechanism exists for the amplification of disturbances from arbitrarily small values. Such a mechanism is identified and shown by Pullin et al to be capable

of producing growths in interfacial amplitude sufficient to cause filamentation.

The real issue of filamentation of uniform vortex equilibria appears to focus on the question of the growth mechanism. This may be quite different for different classes of first disturbance to the same equilibrium state and also for similar disturbances to geometrically differing vortex equilibria. For example, the growth mechanism for waves on a circular vortex may differ from that found for plane interfaces. Also, external length scales may play a crucial role.

With regard to the phenomenon of different types of filamentation, consider filamentation of a uniform circular vortex of radius r_0 and vorticity ω. When subject to perimeter shape disturbances of the form

$$r = r_0 + \delta \exp\left[i(M\theta - \sigma_M t)\right] \tag{2.2}$$

where $\delta \ll r_0$ and M is integral, then to $O(\delta)$, the wave crests move with angular velocity

$$\sigma_M / M = \frac{(M-1)}{M}\frac{1}{2}\omega. \tag{2.3}$$

In a frame of reference moving with this angular velocity, the tangential velocity distribution for the mean flow is

$$v_\theta = \frac{\omega r}{2M}, \qquad r \leq r_0, \tag{2.4}$$

$$v_\theta = \frac{\omega}{2}\left[\frac{r_0^2}{r} - (1 - \frac{1}{M}r\right], \qquad r \geq r_0. \tag{2.5}$$

In this reference frame the flow is rotational in $r > r_0$. There is thus an effective critical layer, where $v_\theta = 0$, at $r = r_c$, where from (2.5)

$$r_c = r_0\left(1 + \frac{1}{2M} + \cdots\right). \tag{2.6}$$

In the rotating frame of reference in which to $O(\delta)$) the wave crests are stationary, stagnation points would be expected at at $r \simeq r_c$, $\theta = m\delta\theta$, $m = 1 \cdots M$ on the true irrotational side of the interface. It is then expected that filamentation would be extrusive in $r > r_0$. If $\omega > 0$, the filaments would be expected to grow in an anticlockwise direction, and at a radial displacement from $r = r_0$ given from (2.6) by

$$\frac{r_c - r_0}{r_0} = \frac{1}{2M} + O\left(\frac{1}{M^2}\right). \tag{2.7}$$

This formula gives reasonable quantitative agreement with Dritschel's calculations.

Finally, note that if the vorticity were of opposite sign on either side of a plane interface, there would be two critical layers and double filamentation would then be expected.

Acknowledgement

My work on vortex dynamics and interactions has been supported by the Department of Energy under contract DE-AS03-76ER72012, Applied Mathematical Sciences KC-07-01-01, and by the Office of Naval Research N00014-85-K-0205 SRO.

References

Baker, G.R., Saffman, P.G. and Sheffield, J.S. 1976 Structure of a linear array of hollow vortices of finite cross section. J. Fluid Mech., 74, 469:

Brown, G.L. and Roshko, A. 1974 On density effects and large structures in turbulent mixing layers. J. Fluid Mech. 64, 775:816.

Bayly, B.J. 1986 Three-dimensional instability of elliptical flow. Phys. Rev. Lett. 57, 2160:2163.

Deem, G.S.and Zabusky, N.J. 1978 Vortex waves: Stationary "V states," interactions, recurrence, and breaking. Phys. Rev. Lett. 40, 859:862.

Dritschel, D.G. 1988 The repeated filamentation of two-dimensional vorticity interfaces. J. Fluid Mech. (to appear).

Kamm, J.R. 1987 Shape and stability of two-dimensional uniform vorticity regions. Ph.D. thesis. California Institute of Technology.

Lamb, H. 1932 Hydrodynamics (6th edition). Cambridge University Press.

Landman, M.J. and Saffman, P.G. 1987 On the three-dimensional instability of vortices in a viscous fluid. Phys. Fluids 30, 2339:2342.

Melander, M.V., McWilliams, J.C. and Zabusky, N.J. 1987 Axisymmetrization and vorticity-gradient intensification of an isolated two-dimensional vortex through filamentation. J. Fluid Mech. 178, 137:159.

Melander, M.V., Zabusky, N.J. and Styczek, A.S. 1986 A moment model for vortex interactions fo the two-dimensional Euler equations. Part1. Computational validation of a Hamiltonian elliptical representation. J. Fluid Mech. 167, 95:115.

Moore, D.W. and Saffman, P.G. 1971 Structure of a line vortex in an imposed strain. Aircraft wake turbulence and its detection. Plenum press. 339:354.

Moore, D.W. and Saffman, P.G. 1975a The density of organized vortices in a turbulent mixing layer. J. Fluid Mech. 69, 465:473.

Moore, D.W. and Saffman, P.G. 1975b The instability of a straight vortex filament in a strain field. Proc. R. Soc. Lond. A 346, 413:425.

Pierrehumbert, R.T. 1986 A universal short wave instability of two-dimensional eddies in an inviscid fluid. Phys. Rev. Lett. 57, 2157:2159.

Pierrehumbert, R.T. and Widnall, S.E. 1981 The structure of organized vortices in a free shear layer. J. Fluid Mech. 102, 301:313.

Pierrehumbert, R.T. and Widnall, S.E. 1982 The two- and three- dimensional instabilities of a spatially periodic shear layer. J. Fluid Mech. 114, 59:82.

Polvani, L.M., Flierl, G.R. and Zabusky, N.J. 1988 Filamentization of unstable vortex structures via separatrix crossings: a quantitative estimate of onset time. (preprint)

Pullin, D.I. 1981 The nonlinear behavior of a constant vorticity interface at a wall. J. Fluid Mech. 108, 401:421.

Pullin, D.I., Jacobs, P.A., Grimshaw, R.H.J. and Saffman, P.G. 1988 Instability and filamentation of finite-amplitude waves on vortex layers of finite thickness. J. Fluid Mech. (sub judice).

Roberts, K.V. and Christiansen, J.P. 1972 Topics in computational fluid mechanics. Comput. Phys. Commun. 3, (suppl) 14:32.

Robinson, A.C. and Saffman, P.G. 1982 Three-dimensional stability of vortex arrays. J. Fluid Mech. 125, 411:427.

Robinson, A.C. and Saffman, P.G. 1984 Three-dimensional stability of an elliptical vortex in a straining field. J. Fluid Mech. 142, 451:466.

Saffman, P.G. 1979 The approach of a vortex pair to a plane surface in inviscid fluid. J. Fluid Mech. 92, 497:503.

Saffman, P.G. 1981 Vortex interactions and coherent structures in turbulence. Transition and Turbulence (Ed. R.E. Meyer). Academic Press. p149:166.

Saffman, P.G. 1988 The stability of vortex arrays to two and three dimensional disturbances. Fluid Dynamics Research (to appear).

Saffman, P.G. and Szeto, R. 1981 Structure of a linear array of uniform vortices. Stud. App. Math. 65, 223:248.

Shelley,M.J. and Baker, G.R. 1988 On the connection between thin vortex layers and vortex sheets. Part II Numerical Study. (Preprint)

Stuart, J.T. 1967 On finite amplitutde oscillations in laminar mixing layers. J. Fluid Mech. 29, 417:436.

Widnall, S.E., Bliss, D.B. and Tsai, C-Y. 1974 The instability of short waves on a vortex ring. J. Fluid Mech. 66, 35:47.

VORTEX FORMATION IN THE WAKE OF A FLAT PLATE FOR SUBSONIC AND SUPERSONIC FREESTREAM MACH NUMBERS

W. Althaus, W. Limberg, E. Krause
Aerodynamisches Institut RWTH Aachen, W. Germany

I. Introduction

The interaction of a straight oblique shock with a supersonic turbulent wake of a flat plate was studied experimentally by means of Laser-Doppler-Anemometry and Mach-Zehnder interferometry. Investigated were the changes of the time-averaged velocity, the Reynolds stresses, the turbulence intensity across the shock and instantaneous density profiles. After completion of the experiments with a smooth plate, the investigation was extended to flows about flat plates with rough surfaces. The roughening of the surfaces was achieved by pasting sandpaper on to both sides of the plate. It was found that a detectable vortex street was formed in the wake in subsonic and supersonic flow, if the following three conditions are met: First, the relative roughness had to exceed a certain critical value, second, the trailing edge had to be sharp, i.e. no rounded corners, and third, the sandpaper should not extend to the trailing edge, but should end at a certain distance upstream from it.
In a second series of experiments the shedding frequency was measured with Laser-Schlieren optics and the density drop in the vortex cores was evaluated with holographic interferometry in two wind tunnels.
In addition, the time averaged velocity profiles were measured as before for undisturbed and shock-disturbed flow.
The comparison of the results is discussed in this paper.
Finally, an attempt was made to explain the formation of the vortex street in terms of absolute and convective instability. In order to do so, the Raleigh-equation was solved on the basis of time-averaged velocity profiles, measured in the near wake. First results indicate that the predicted Strouhal number is in rather close agreement with the one observed in the corresponding experiment.

II. Experimental setup and instrumentation

The experimental setup for the investigation of the interaction between a shock wave and a wake is shown in Fig.1. The flat plate was pastenend with smooth paper or sandpaper. In the following figures the distance between the trailing edge and the beginning of the paper is expressed by the symbol PHK followed by a number between 0 and 9 indicating the distance in mm.
The densitiy distribution was measured by Mach-Zehnder interferometry, holographic interferometry and differrential interferometry, whereas the time-averaged flow quantities, as the velocity, the turbulence intensity and the Reynolds stresses were measured by a two component Laser-Doppler-Anemometer.
The vortex shedding frequency was determined by Laser-Schlieren optic. The experiments were carried out in the 15x15 cm^2 and the 40x40 cm^2 windtunnel of the Institute for subsonic and supersonic Mach numbers.

III. Interaction between a turbulent wake and a shock wave

The experiments were carried out for a freestream Mach number of Ma=2.2 and a Reynols number of $Re_d = 7 \cdot 10^4$ based on the thickness of the plate. The turbulent wake was generated with a smooth flat plate (Fig.2). The time-averaged profiles of the velocity, the turbulence intensity and the Reynolds stress component of the undisturbed turbulent wake are similar to those in incompressible wakes behind a circular cylinder. When the flow is disturbed by a shock, the wake broadens, the minimum velocity decreases and the turbulence intensity increases with the shock intensity. Also the Reynolds stress grows strongly due to the shock wave (Fig.3 and /3/)

In order to study the influence fo the boundary layer characteristics on the wake the surface of the plate was roughenend. With the appropriate combination of the distance between the trailing edge and the beginning of the sandpaper, the relative roughness of the sandpaper and the shape of the trailing edge a vortex street develops in the wake. Otherwise a turbulent wake develops.
First the existence of the vortex street for subsonic and supersonic freestream Mach numbers up to Ma=2.8 was confirmed by means of differential interferometry. The density distribution of the vortex street was measured by holographic interferometry. An example for the density profile is given in Fig.5 for Ma=1.9 for a rough plate with the beginning of the sandpaper 8 mm upstream from the trailing edge. The alternating form of a regular vortex street can be seen clearly. Fig.6 indicates a decrease of the minimum density of the vortex street as a function of the Mach number.
The most important parameters which influence the formation of the vortex street are the distance between the beginning of the sandpaper and the trailing edge and the roughness of the sandpaper. Holographic interferograms were taken for a flat plate with smooth paper pasted on to it (GP), with sandpaper of an average roughness of 0.18 mm (S80) and sandpaper of an average roughness of 0.43 mm (S40). The evaluation of these interferograms reveals that no vortex street develops in the wake of the smooth plate. For the flat plate with sandpaper S80 there was no vortex street for trailing edge distances of 0 and 1 mm. For a distance of 3, 5, 7, and 9 mm a vortex street had developed. The wake of the plate with sandpaper S40 shows a vortex street for every investigated distance except for zero. The location where the vortex street appears to be fully developed was shifted upstream when the distance of the paper from the trailing edge was enlarged up to 5 mm. For greater distances the location remains constant. Fig.7 shows the dependence of the minimum density on this distance. It is evident that the wake of the plate with sandpaper S40 and a distance of the paper from the trailing edge of 5 mm contains the strongest vortices. A similar but attenuated effect is found with sandpaper S80. Extending or shortening the distance of the paper from the trailing edge reduces the strenght of the vortices until the vortex street dimishes. This means that there are optimum conditions for the formation of a vortex street in the wake of a plate and indicates a simple possibility of

controlling the strenght of the vortices.
The effect of the formation of a vortex street on the defect velocity is seen in Fig.8. It shows a histogram of the minimum velocities in the wake at 47 and 107 mm downstream from the trailing edge. When the roughness is increased, the minimum velocity decreases for every distance of the paper from the trailing edge. This means that the loss of kinetic energy increases with the roughness of the paper.
If the roughness is held constant and the distance of the paper from the trailing edge is increased, the defect of velocity decreases in the wakes of the rough plates. This is explained by the stronger lateral exchange of momentum of a wake with a vortex street compared to a turbulent wake. Another result is a broadening of the wake which can be seen clearly in Fig.9. As a conclusion it can be said, that the stronger the vortices are, the greater becomes the half-width of the wake.
A decent comparison of the profiles of the mean velocity, the turbulence intensity and the Reynolds stress between the turbulent and the vortical wake is shown in Fig.10. As expected, the wake is broadened and the turbulence intensity as well as the Reynolds stress are increased by the vortex street.

V. Interaction between a wake containing a vortex street and a shock wake

As in the case of the turbulent wake, the defect of velocity and the half-width of the vortical wake disturbed by shock waves of various strenght is increased with the shock intensity. The same is true for the turbulence intensity and the Reynolds stress (Fig.11). The increase of the latter flow quantities is not as strong as the increase in a turbulent wake disturbed by shocks of variable intensities (see also /1/ and /2/).

VI. Calculation of the vortex shedding frequency

With a Laser-Schlieren optic the vortex shedding frequency was measured as a function of the Mach number. For subsonic Mach numbers the Strouhal number is nearly constant while for supersonic Mach numbers the Strouhal number seems to approach the value of an incompressible cylinder wake (Fig.12). In order to calculate the vortex shedding frequency, a linear stability analysis of the near wake profiles at Mach number Ma=0.4 was carried out on the basis of measured velocity profiles. The basic equations are the two-dimensional instationary Euler equations. They are simplified by the parallel flow approximation, linearisation and a plane wave as a disturbance function. This results in the following disturbance diffential equation (/3/):

$$[\omega + M(y)\alpha]\left[\frac{d^2p}{dy^2} + p\{[\omega + M(y)\alpha]^2 - \alpha^2\}\right] - \frac{2\,dM(y)}{dy}\,\alpha\,\frac{dp}{dy} = 0$$

where p is the complex disturbance pressure and M(y) is the measured Mach number profile.

With the boundary conditions $\frac{dp}{dy} = 0$ for y at the boundary of the wake and p(y=0)=0 this differential equation defines an eigenvalue problem for the complex values of ω and α.
Applying the resonance criterion as suggested by W. Koch (/3/), a bifurcation point of the dispersion relation with the imaginary part of ω equal to zero has to be searched. At this bifurcation point which is associated with a specific frequency, the group velocity of disturbance wave packets is zero. Physically, the existence of such a bifurcation point means that there is a transition point between an absolute and a convective instability. This point acts as a partial reflector for waves with that specific frequency. The trailing edge of the plate acts as a second broad-band reflector, so that a strong self-sustained feedback loop is possible. Fig.13 shows the complex eigenvalues α, where each α is associated with a real frequency ω. The bifurcation point can be identified as the saddle point in Fig.13 and results in a Strouhal number of Sr=0.112. The corresponding measured Strouhal number is Sr=0.12, which is only about 6.7 % higher. If the curve fitting of the measured velocity profiles could be made more accurate, the difference between the measured and the calculated Strouhal number might be less.

As a conclusion it can be said, that the concept of absolute and convective instability can describe some aspects of the formation of the vortex street in the wake of a flat plate sufficiently well.

VII. Outlook

The calculations of the Strouhal number will be continued for other Mach numbers in the subsonic and supersonic range.
Admitting nonlinear terms for the derivation of the disturbance differential equation would allow to calculate the disturbance pressure p more realistically and to compare it with measurements.
Further investigation will be conducted to clarify the important role of the distance of the paper from the trailing edge.

[1] Marenbach, G. : Störung ebener turbulenter Mischzonen durch Stoßwellen. Diss. RWTH Aachen, 1982.
[2] Tang, M.Z. : Wirbelstraßen im Überschallnachlauf einer rauhen ebenen Platte. Diss. RWTH Aachen, 1983.
[3] Koch, W. : Local Instability Chracteristics And Frequency Determination Of Self-Exited Wake Flows Journal Of Sound And Vibration (1985) 99, 55-58

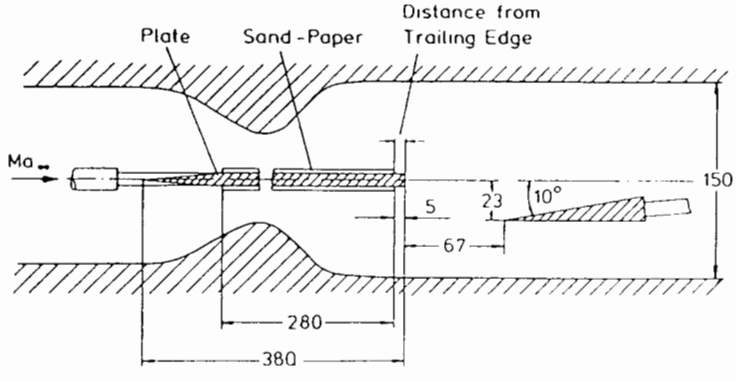

Fig.1. Experimental setup

Fig.2. Interferogram of the turbulent wake

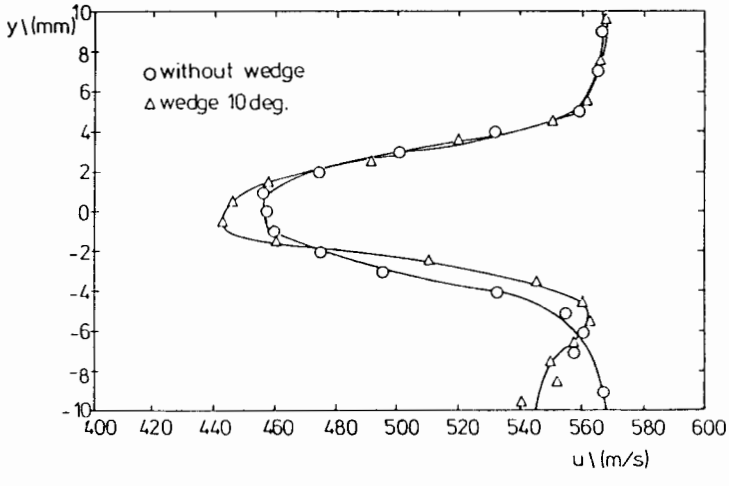

Fig.3a. Profile of the velocity

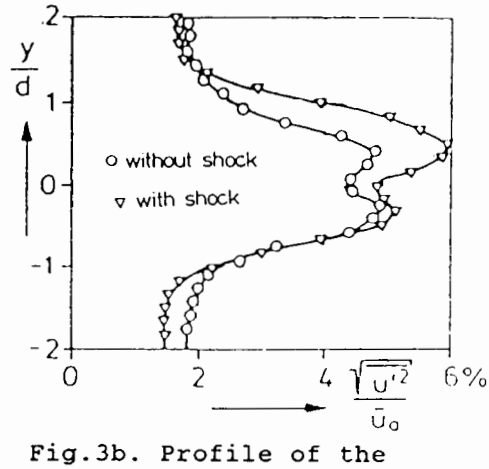

Fig.3b. Profile of the turbulence intensity

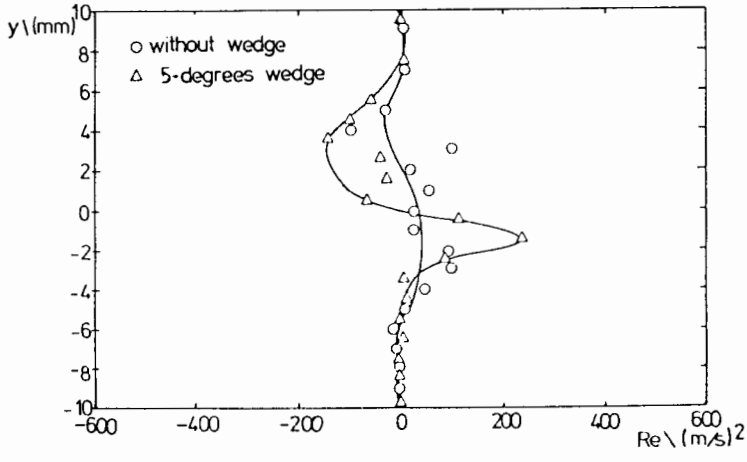

Fig.3c. Profile of the Reynolds stress

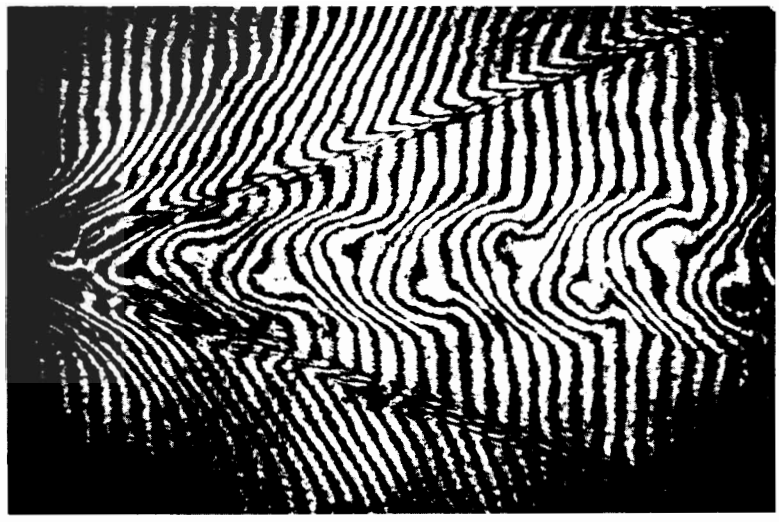

Fig.4. Interferogram of the vortical wake

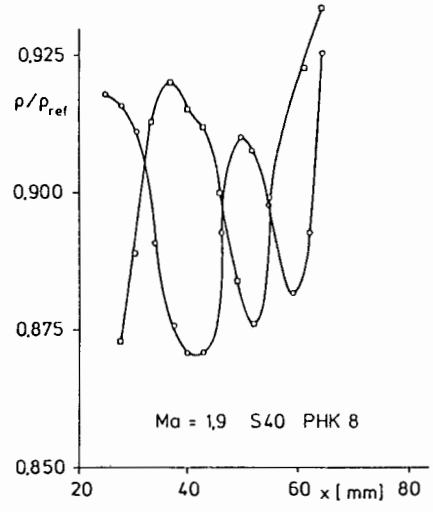

Fig.5. Density distribution of the vortical wake

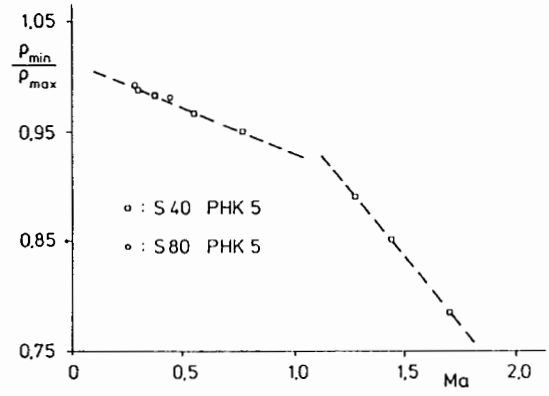

Fig.6. Density of the vortex core as a function of the Mach number

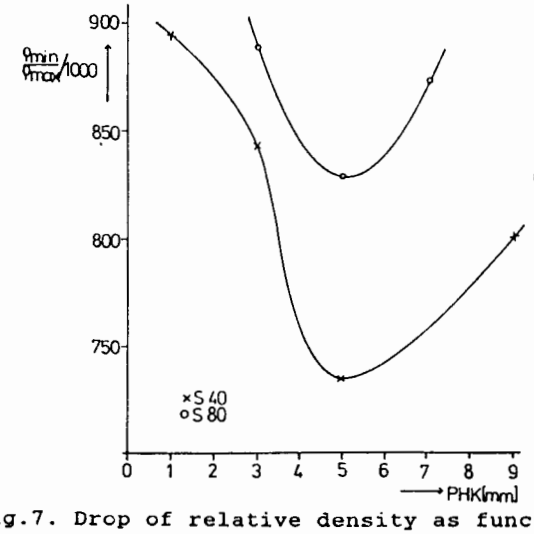

Fig.7. Drop of relative density as function the trailing edge of the distance from

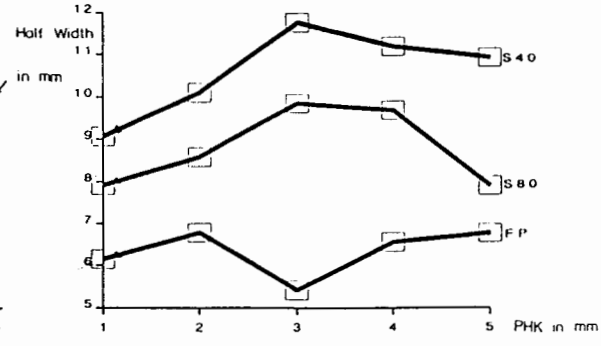

Fig.8. Histogram of centerline velocities

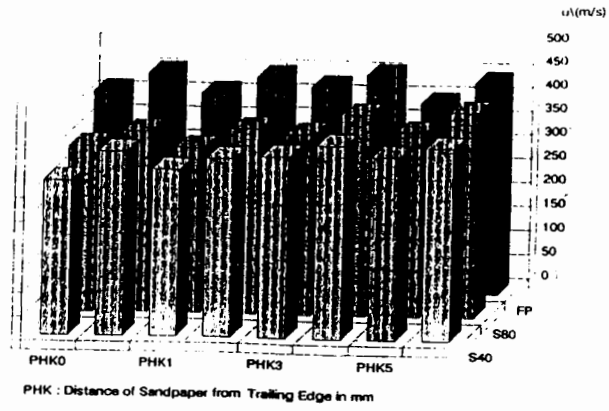

Fig.9. Half-width of the wake of a flat plate

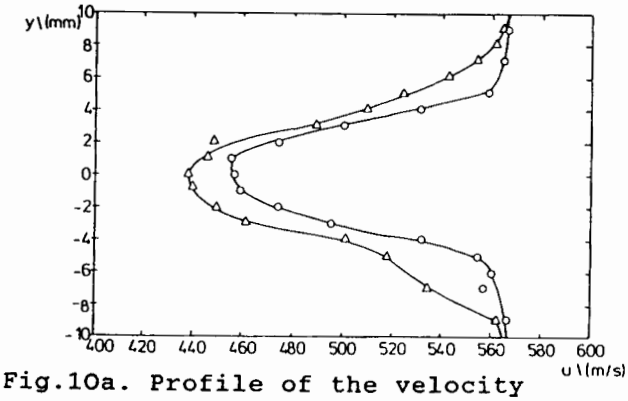

Fig.10a. Profile of the velocity

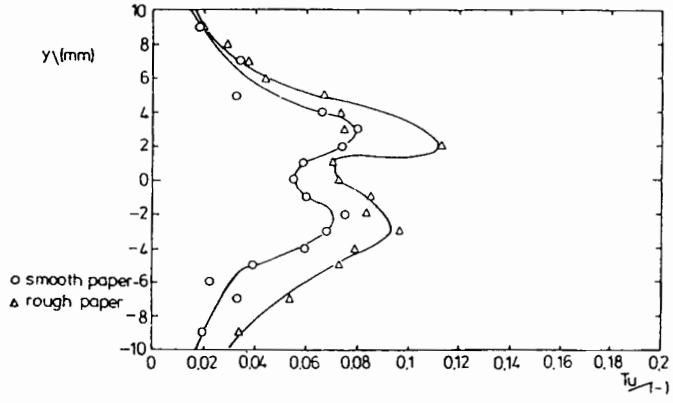

Fig.10b. Profile of the turbulence intensity

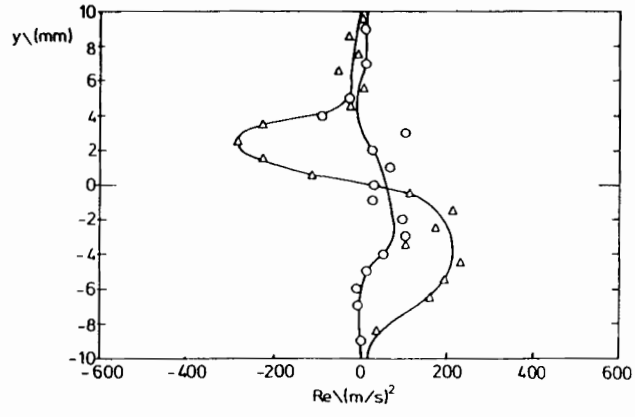

Fig.10c. Profile of the Reynolds stress

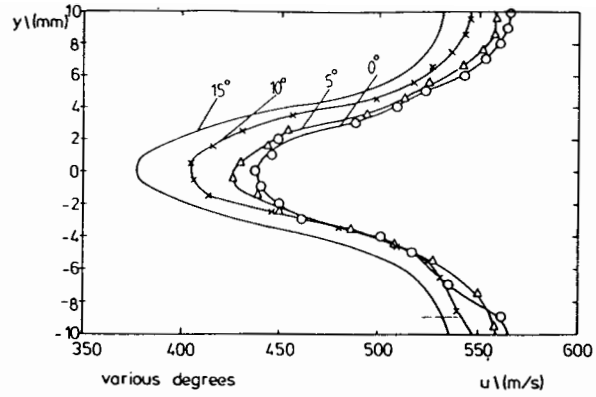

Fig.11a. Profile of the velocity

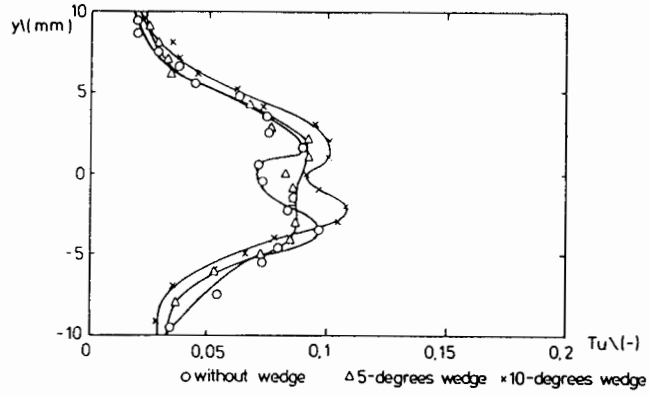

Fig.11b. Profile of the turbulence intensity

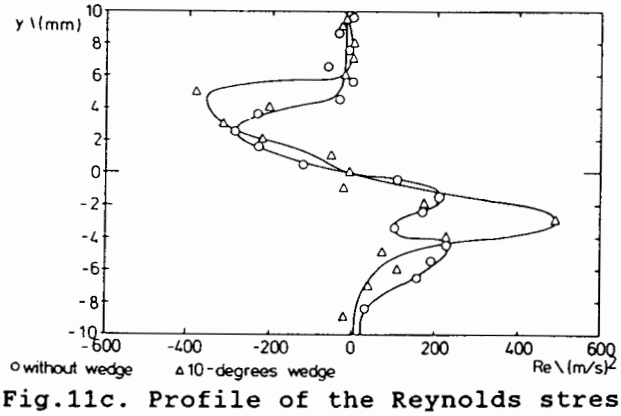

Fig.11c. Profile of the Reynolds stress

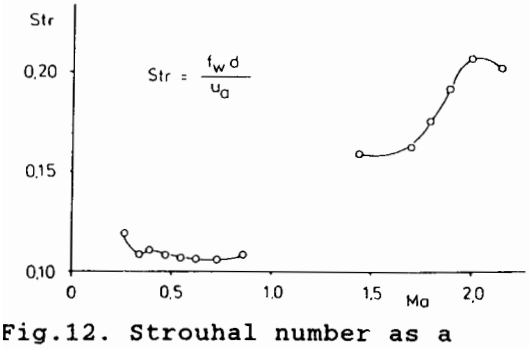

Fig.12. Strouhal number as a function of Mach number

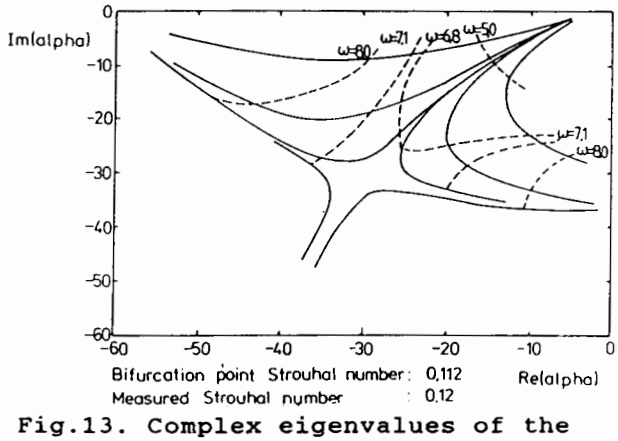

Fig.13. Complex eigenvalues of the disturbance differential equation

COMPRESSIBILITY IN TURBULENCE GENERATION AND MIXING

Jay P. Boris
Laboratory for Computational Physics and Fluid Dynamics
Naval Research Laboratory, Code 4400
Washington, D.C. 20375

Abstract

This paper considers some of the physical mechanisms by which fluid compressibility causes the generation of turbulence and affects turbulent mixing. All fluid velocity fields are composed of a rotational component, the curl of the velocity, a compressional component, the divergence of the velocity, and a potential component which is both curl and divergence free. In studying the physics of compressibility in turbulent mixing, different situations are distinguished by categorizing not only the curl and divergence currently in the flow but also by the existence of other properties induced by the prior effects of both rotation and compression. In this paper I will use the term "passive" to describe the integrated effects of prior compressibility which is currently influencing the flow from "active" compressibility effects stemming from compression or expansion accelerations occurring dynamically in the system.

These active and passive compressional interactions with rotational flow feed on each other in a dynamic three-stage cycle where fluid dynamic instabilities cascade through spatial and spectral scales to create a very complex flow field. These complex flows then distort and stretch physically meaningful surfaces in the flow such as fuel-oxidizer interfaces or vorticity layers. These convoluted surfaces in turn enhance molecular diffusion and transport between the separate materials, thus changing the overall energy balance in the system. This changed energy balance, in turn feeds back into the fluid dynamic channels of instability, closing the cycle.

In our earlier work involving compressible systems, which is reviewed elsewhere (eg. [1-4]), these passive and active roles of compressibility were encountered primarily in the context of reactive flows with turbulence. Combustion, reactive shocks and detonation, as sources of strong and rapid compressibility effects, naturally are associated with compressible turbulence, empowering such relatively passive expansion-driven phenomena as bouyancy and vortex bursting as well as the more active, shock-driven situations. This paper considers a somewhat broader class of compressible mixing and turbulence generation mechanisms including shock-vortex interactions, expansion generated turbulence and aspects of Rayleigh-Taylor instability.

Keynote Address & Proceedings, International Workshop on Physics of Compressible Turbulent Mixing, Princeton, NJ, 24–27 October 1988.

Introduction

Three broad (and loose) classes of flow mechanisms couple together in an interactive cycle to give a simple conceptual way to view compressible turbulent mixing. The first class of mechanisms in this dynamic mixing cycle involve the rearrangement of the available energy in the system by mechanisms other than pure fluid dynamic convection. The mechanisms of interest here depend on the interaction of a compressible phenomenon with convoluted density or material interfaces in the fluid or with the rotational flows that bring them about. These mechanisms include shock and acoustic wave propagation through density and vorticity structures in the flow, the local introduction of energy into the system by chemical reactions or external deposition. This energy rearrangement promotes expansion (compression), giving rise to short term accelerations and long term motions in the flow. The available energy, via the accelerations and their associated pressure gradients, feeds into a number of possible channels of fluid dynamic instability leading to turbulence.

The second class of mechanisms concerns these dynamic channels for instability and turbulence. It is useful to view turbulence as beginning in a fluid instability of a laminar macroscopic flow. The vorticity generated or released in this instability then cascades through additional fluid dynamic channels, spreading convectively over a broader spatial and spectral range. Thus turbulent mixing can be viewed as a cascade of systems of distinct instabilities [5]. The third class of mechanisms concerns mixing directly and relate to the contortion of interfacial surfaces in the flow which originally separate identifiably different phases or components of the fluid. We must follow and then predict the behavior of these surfaces as they move and stretch. It is here that the currently popular fractal notions have their greatest applicability. Figure 9, for example, shows the highly convoluted interface separating two gas species of different mass when the mixing due to a Rayleigh-Taylor instability has reached a very late stage.

Steady increase of the interfacial surface area enhances molecular mixing and in the case of reactive flow, speeds reactions. With density gradients at these interfaces in the presence of gravity or pressure gradients, vorticity will actually be generated as well as rearranged convectively. Since energy generation and/or rearrangement results from these contorted interfaces, the three-stage compressible mixing cycle is closed.

This cycle is shown in Figure 1 as specialized to the case of reactive flow turbulence where the energy feedback into the mixing cycle is particularly immediate. This view of the mixing cycle is two-dimensional. Using this framework, however, an additional way to characterize the roles of fluid compressibility is needed. Any fluid velocity field is composed of a rotational component, expressed mathematically through the curl of the velocity, a compressional component, expressed as the divergence, and a potential component which is both curl and divergence free. Different situations should be distinguished by categorizing not only the curl and divergence currently in the flow but also by the rates of change of these quantities induced by the current presence of or by prior effects of both rotation and compression on the fluid.

In this paper I will use the term "passive" to differentiate prior flow field compressions or expansions which are having current effects from "active" compressibility phenomena which are

occurring dynamically in the system. Figure 2 shows two important examples schematically in which an existing density gradient interacts with accelerations in the fluid. The first case is an active compressibility effect in since the density gradient is driven unstable by the adverse accelerations associated with an expanding region of gas. The second case shown is passive because the driving acceleration field arises from sources other than the fluid compressibility.

In this taxonomy the phenonemon is highly active when the accelerations associated with the compressiblity are the mechanism of vorticity generation or energy rearrangement. Such is the case in the upper panel of Figure 2. When velocities resulting from the integrated effect of compressibility-related accelerations play a major role, the mechanism is moderately active. When the main effect of compressibility arises from density gradients in the flow attributable to time-integrated displacements of the compression- or expansion-induced velocities, the mechanism will be characterized as passive as in the lower panel of Figure 2.

The characterization of compressibility effects using this active-to-passive scale determines a third dimension for the turbulent mixing cycle illustrated in Figure 1. This composite characterization of compressibility mechanisms in turbulence generation and mixing is illustrated schematically as the surface of a cylinder in Figure 3. On this figure a number of mechanisms of each class are indicated with successive 120 degree rotations in the top, middle and bottom panels. These mechanisms will be discussed further in the paragraphs below. In this taxonomy shock generation of turbulence is an active role for compression whether it occurs in a beam-heated channel [6,7] where geometric asymmetries in the heating induce a residual turbulent flow or in a supersonic shear layer where existing vorticity is moved about [8–10] by shocks.

Existing density gradients, which drive Rayleigh-Taylor and Richmyer-Meshkov modes, exemplify passive roles in the sense that the gradients were generated in the past by local compressible effects such as heating whose related flows have since decayed away. In vorticity generation by the Raylor-Taylor mechanism, the pressure gradients which drive the baroclinic source term often arise from pre-existing vortices in the the flow on a larger scale than the passive density gradients as indicated in Figure 2. In the classical Richtmyer-Meshkov scenario, the role of compression through the incident shock is highly active, causing the generation of turbulence through the shock associated accelerations of the fluid. At the same time compression is playing a passive role through the pre-existing density gradients.

The fact that aspects of both passive and active mechanisms can be present at the same time in some situations complicates and confuses the taxonomy somewhat. This isn't surprising since turbulence is a complex and often confusing subject. There are no hard and fast rules for this categorization but the approach is nevertheless instructive. It is also noteworthy that the passive mechanisms can often be stronger and more important than the active ones. In Figure 2, for example, the accelerations associated with a pocket of fuel-ozidizer mixture burning are relatively weak and short lived though they are classed as active. The persistence of passive accelerations due to large scale vortices in the flow, even though they may be weaker instantaneously, can often lead to much larger long-term effects.

In all of these compressible turbulent mixing cases, vorticity can actually be produced away

from boundaries and boundary layers in flows that are initially irrotational through the inviscid equation for the evolution of vorticity ω:

$$\frac{D\omega}{Dt} + \omega\nabla\cdot\mathbf{v} = \omega\cdot\nabla\mathbf{v} + \frac{\nabla\rho\times\nabla P}{\rho^2}\ . \tag{1}$$

Here $\mathbf{v}$ is the fluid velocity, P is the pressure, and ρ is the mass density. When the pressure and density gradients are misaligned, the source term on the right hand side of Eq.(1) is nonzero and generation of vorticity occurs. Direct integration of Eq.(1) in two dimensions with some simplifying assumptions has yielded useful expressions for the circulation or vortex strength for each of the phenomena that have been studied [see 7].

Since we are considering a cycle, any of the three classes of compressibility mechanisms could be used as a starting point for the discussion. Because I plan to finish with a discussion of an idealized type of Rayleigh-Taylor mixing problem, we will start by considering specific mechanisms which involve energy transport and rearrangement.

Compressibility, Energy Transport and Rearrangement

Energy can be transported fluid dynamically in two ways, convectively and through waves, both acoustic and gravitational. It also can be deposited externally or rearranged from internal degrees of freedom as in combustion or in temperature-controlled phase changes. In deposition of energy from external sources, the deposition is often determined by the local density and temperature of the fluid or by other properties which are influenced by the compressibility. Since the subsequent heating changes then feed back into the density via the compressibility runaway situations are possible. Cooling or condensation modes are also possible in which the radiated energy from a region depends on the square of the local density. a slight local reduction in the temperature causes an increased density in pressure balance situations. This increased density accelerates radiative cooling when the temperature dependence of the radiation efficiency has the proper slope. Phenomena of this sort are seen in several circumstances on the Sun and in other astrophysical situations.

Reactive flows such as flames, reactive shocks and detonations, major systems involving highly active compressiblity effects in turbulence, are reviewed in this volume by Elaine Oran [8]. In many reactive flow systems the mixing of fuel and oxidizer is a turbulent process. The subsequent fluid dynamic motions in reactive flows are then energized by the accelerations of active expansion resulting from chemical energy release. Detonations are complex reacting flows in which a leading shock is driven through a combustible material by local chemical energy released by the temperature rise associated with the shock. In the gas phase, detonations leave behind product gases that are often turbulent and noisy. In detonations compressibility plays a very active role because the pressures, accelerations, and velocities, more so than the resulting displacements, are the dominant effect.

A supersonic shear layer is a case where compressibility effects play a very active role in energy transfer and rearrangement [9-13]. The stability in compressible shear flows is affected by a number of parameters including the stream densities, their temperatures and their Mach numbers.

The experimentally determined growth rates seem to correlate well with the convective Mach number, determined by measuring the speed of the individual streams relative to the convecting coherent vortex structures.

There are intrinsically nonlinear phenomena as well which dominate the collective behavior of supersonic shear layers. As a shear layer separating high Mach number flows begins to deform, for example, growing spannwise vortices begin to stick out of the layer into the supersonic streams above or below. The embryonic roll generates a bow shock by partially blocking the supersonic fluid. The increased pressures in this bow shock iron the shear layer flat again, thus interfering substantially with the shear mixing [13].

The flow physics of vortex bursting is show in Figure 4. This mechanism, identified by Chomiak in 1977, and discussed recently [14,15], magnifies the already large rotational velocity of stretched vortex cores substantially. A small radial displacement of the relatively dense rotating vortex material creates room for a very rapid axial filling of the core by any hot, low density gas which comes into contact with the core somewhere along its length. A flame ignited at one point of a combustible vortex ring, for example, will engulf the entire ring one to two orders of magnitude faster by vortex bursting than by simple laminar propagation of the flame. Thus in vortex bursting, compressibility effects generate velocities which are greatly magnified by interaction with vortices, leading to rather rapid flows compared to what either the divergence or the curl component of the flow would cause by itself.

Bouyant convection in a highly stratified medium such as the Sun, where the density of a rising plume drops by about six orders of magnitude, is a passive ramification of compressibility. The density changes resulting from integrated expansion-based displacements are the major contributor to the changing energy situation. The entire temperature structure of the Sun, however, is controlled by this convection which transports orders of magnitude more heat out of the core than could be accomplished by thermal conduction or radiation transport [16,17]. The strongly time-dependent compressible flows are found to be highly asymmetric. There appear to be concentrated plumes and sheets of downflow with broader, weaker upflowing regions. Furthermore, coherence is seen in simulations over a number of scale heights. This situation is another prime example of the great importance "passive" compressibility effects can have.

Finally, shock-vortex interactions are an example where the passage of a shock can actually be considered a passive phenomenon. Here compression of the vortex coupled with conservation of angular momentum determines the configuration after the shock has passed. Though most previous attention has been focussed on perturbations of the passing shock, the vorticity pattern left in fact undergoes a larger transformation as discussed elsewhere in this volume, see eg. [18]. This resulting vorticity distortion depends on the resulting shock displacements and overall compression more than on the accelerations or velocities as long as the passage of the shock is fast compared to the velocities in the vortex.

Compressiblity, Fluid Dynamic Channels and Instabilities

Compressibility mechanisms affect a number of fluid dynamic instabilities in the linear regime

as well as the nonlinear and these effects range from destabilization of otherwise stable flows through partial or complete stabilization of otherwise highly unstable flows [19–20]. An appealing argument, often used, is that the incompressible limit is maximally unstable because the energy available to the instability goes entirely into the unstable modes without any fraction be sidetracked into compressing the fluid [22]. This argument is not entirely correct because compressibility also allows fluid perturbations which are mathematically prohibited in the rather singular incompressible limit. Thus, for example, the usual incompressible modes will actually be slightly stabilized while the acoustic modes, essentially absent in any incompressible treatment, may be unstable.

In boundary layers of high speed flows the presence of acoustic waves actually destabilizes the boundary layer faster than would otherwise occur [23]. Compressibility in these circumstances is usually thought of in terms of acoustics. An acoustic boundary layer, as well as a viscous boundary layer exists. In addition, new flow phenomena [24,25 and references therein] appear in the bulk of the fluid when acoustic phenomena and convective flow occur simultaneously. These include refraction phenomena of the sound waves and flow turning phenomena. There is, for example, a mechanism called Richardson's annular effect which describes an interaction between the mean and acoustic flow fields inside the acoustic boundary layer and which results in a mean flow velocity at the edge of the acoustic boundary layer.

In Rayleigh-Taylor instability driven by laser ablation [26,27] thermal energy deposited in the plasma by the laser conducts thermally through a low density plasma to the material surface where it heats cold target material very rapidly. The result is a high pressure region accelerating the cold dense material in one direction and accelerating the hot, ablated, "blowoff" material in the other direction. In the accelerating frame of reference of the solid or near solid target, the acceleration appears as an external gravity and the low density blowoff plasma appears to be supporting the heavier material in a Rayliegh-Taylor unstable configuration.

This situation is shown in Figure 5 where the laser beam enters the fluid region from below and the effective gravity is downward. The two solid wavy lines across the figure mark the 0.1 times solid and the 0.8 times solid contours of the dense target material. The upper part of the figure is essentially solid target material in which essentially no vorticity has been generated. The positive and negative regions of vorticity are shown as solid and dashed contours in the ablation region between the two wavy lines and in the blowoff plasma being driven out of the system to the bottom of the figure toward the incident laser beam.

This laser-driven configuration deviates from the classical Rayleigh-Taylor situation because of the rapid fluid expansion in the ablation layer where vorticity is being generated by misaligned pressure and density gradients. The velocity of the expanding gas drags the instability-generated vorticity away from the unstable solid–gas interface, as can be seen in Figure 5. This flow reduces the growth rates of the modes appreciably and thus the tendency of a thin shell of target material to fragment. The multimode and late-time nonlinear evolution of this dynamic system are considered in some detail by Emery and Gardner elsewhere in this volume [27].

The last example of continuum fluid instability interactions involving compressibility and

rotational flow to be considered in this section are the acoustic-vortex interactions. Small acoustically-driven displacements of a thin vortex layer provide seed perturbations on which the usual Kelvin-Helmholtz instability and its compressible counterparts [19–21] can build. These mechanisms are generally passive in the sense that compressiblity acts principally through the integrated positional displacements of the thin shear layer arising at a corner or splitter plate. They can be important both for the initial linear growth and rollup of a shear layer and for the regular nonlinear reinitiation of coherent vortex structures in open systems. These mechanisms appear even stronger in driven systems where a particular frequency acoustic mode is imposed [30,31].

Kailasanath et al. [32] discuss these acoustic-vortex interaction mechanisms elsewhere in this volume. A choked dump combustor configuration with a rearward facing step and cold flow is used for a number of these studies [31,33] because it closely resembles a reasonable ramjet configuration and yet is simple enough for careful numerical and experimental analysis. Complex but quite regular vortex shedding and merging patterns often appear at a subharmonic frequency near the center of the range of basic shedding frequencies of the rearward facing step which is present in a ramjet to hold the flame. The complicated subharmonic patterns are controlled by quarter wave modes of the relatively narrow inlet pipe.

The acoustic frequencies of the chamber appear to be most important in low Mach number flow, probably because the chamber acoustic modes do not match the vortex shedding frequencies well when the flow velocities are high. However, even in the higher Mach number flows, acoustic effects become important once several mergings of the basic vortex shedding bring the characteristic frequencies closer together. It is significant and interesting that acoustic compressibility effects can be most important at low Mach number when a superficial look at the problem suggests that the importance of compressibility should diminish.

Compressibility Effects in Interface Dynamics

In the previous section instability mechanisms occuring in the bulk of the flow and in constant entropy regions were considered. The existence of interfaces in the fluid between different types or phases of material or simply regions of different temperature and density provide another class of mechanisms where compressibility and turbulence can interact. Figure 6 shows schematically why interfaces are so important to reacting flows. The turbulent interpenetration of two materials greatly increases the area of the interface and it stretches the flow, steepening gradients of species concentrations in many regions. Both of these effects tend to increase the rate of molecular diffusion of the two materials into each other. This increases the rate of chemical reactions and feeds back into the energy transport and rearrangement portion of the three-stage compressible turbulent mixing cycle.

The generation of vorticity at convoluted interfaces is of particular interest because it provides a way that strong turbulence can feed on previous mixing in the flow actually generating additional turbulence in place. In incompressible constant-density turbulence, the vorticity arises only at boundaries and in boundary layers and has to be convected into the bulk of the flow. It can be rearranged in these incompressible cases but new vorticity is not as easily generated.

Several categories of compressible vorticity-generation by shocks and compressibility-related expansions can be identified:
(1) irregular reflections of shock waves from surfaces or nonlinear interactions among shocks,
(2) gas expansion into or shock wave propagation through a region of nonuniform mass density, e.g. shock-bubble interactions and Richtmyer-Meshkov modes, and
(3) expansion of an irregular volume of gas, produced for example by asymmetric energy deposition in a gas.

Mechanisms in category 1 and the highly active shock generation of turbulence via Richtmyer-Meshkov planar interfaces in category 2 are considered elsewhere in this volume and will not be considered in detail here. The Richtmyer-Meshkov generation of turbulence occurs in a very short interval as the driving shock passes through the nearly planar interface. It is hardly compressible during most of its subsequent evolution but the presence of strong density gradients means that the remnants of compressibility are always present. In this sense these three categories of vorticity generation must be viewed as simultaneously active and passive in our taxonomy.

An important example of vorticity (turbulence) generation which has received much attention lately is the propagation of shocks through a slow laminar flame [36] or through light and heavy bubbles in an ambient gas. The passage of the external diffracted shock and the internal refracted shock over and through the bubble produces residual vorticity at the interface of the bubble. The vorticity then rolls into a vortex ring, inducing a jet of ambient gas along the bubble axis. The simulations and theory [38] have agreed closely with recent experiments by Haas and Sturtevant [37].

Expansion-driven turbulence generation mechanisms of the third type are classed as moderately active because the strength of the coherent vortex structures which result depend on characteristic expansion velocities. As shown by Picone and Boris [6,7 and references therein], the vorticity evolution equation specialized to two dimensions can be integrated in a Lagrangian frame of reference. It is usually found that the velocities and hence displacements associated with the vorticity being generated are quite small compared to the shock- or expansion-related velocities driving the system. Thus the calculation of the strength of vortex pairs generated by the baroclinic source term on the right side of Eq. (1) can proceed with reasonable accuracy ignoring the accumulating rotation during the vorticity generation process. This means that the path of fluid particles, their acceleration from rest, their deceleration back to rest, and their asymptotic displacement (in the absence of the rotational component of the flow) can be approximated quite accurately.

Integration of Eq. (1) under these assumptions gives the following expression for the strength of the vortices generated (usually in pairs):

$$\kappa = U[R(\tau) - R(0)] \ln[\rho_\infty/\rho_0]\ f. \tag{2}$$

Here U is a characteristic velocity of expansion to pressure equilibrium, $R(\tau)$ and $R(0)$ are the final and initial characteristic scale sizes of the expanding region, ρ_∞ is the ambient unexpanded

density, ρ_0 is the relatively low density left at the center of the expanded channel, and the form factor f, between zero and unity, is related to the asymmetry of the energy deposition.

Problems to which this theory applies include turbulent cooling of lightning, laser, and laboratory discharge channels in a gas, shock-flame interactions, and shock propagation through inhomogeneous, compressible fluids. Reference 7 shows examples of experiments and numerical simulations of this mechanism. Subsequent experiments confirm the predictions of Eq. (2) in a wide variety of circumstances when numerical experiments are performed to evaluate the geometric form factor and characteristic velocity appearing.

A Rayleigh-Taylor Problem and the Numerical Model

Strong bouyancy driven convection, as described above and the nonlinear evolution of the Rayleigh-Taylor instability are examples of turbulent mixing involving passive compressibility effects if we assume that the driving density variations arise as the integrated result of compression or expansion effects. The existing density gradients "originally" embedded in the flow interact baroclinically with pressure gradients, whatever their source, to generate and rearrange vorticity. The very late time interpenetration of two compressible fluids of different density is the last example we will consider, discussing some new calculations incorporating a rather novel approach to the late-time Rayleigh-Taylor problem. Since the nonlinear stage of the R–T problem is usually viewed as an intrinsically unsteady situation, the study of an R–T problem, no matter how idealized, which has a dynamical steady state, is extremely interesting.

To limit the computational scope of the problem, doubly periodic geometry is attractive but the problem definition requires some manipulation to remove the secular pressure gradient which characterizes the equilibrium configuration of a heavy fluid unstably supported by a light fluid. This average pressure gradient can be removed by studying a problem which has no net force. The two fluids are accelerated in opposite directions with two different "gravitational" forces which are inversely proportional to the mass density. This could be be viewed as two oppositely charged fluids in an electrostatic field or as the usual Rayleigh-Taylor problem in an accelerated frame of reference. By ensuring that the total force on the system is zero, the net momentum of the system is constant for all time and can be taken as zero though the two fluids are being pulled through each other and will have a nonzero net interpenetration drift.

The fluids can be expected to reach this terminal interpenetration velocity when their average rate of extraction of energy from the opposed "gravities" equals the dissipation of flow kinetic energy into heat due to viscous heating at small scales.

Four scalar ideal gasdynamic equations are solved for conservation of mass, two components of momentum and energy. Two additional fluid equations,

$$\frac{\partial f_1(x,y,t)}{\partial t} + \mathbf{v} \cdot \nabla f_1 = 0 \tag{3}$$

$$\frac{\partial f_2(x,y,t)}{\partial t} + \mathbf{v} \cdot \nabla f_2 = 0, \tag{4}$$

are solved for the advective transport of the two distinct species number density fractions, $f_1(x,y,t) = n_1/(n_2+n_1)$ and $f_2(x,y.t) = n_2/(n_2+n_1)$. f_1 and f_2 clearly sum to unity and are advected without the compression term. The overall mass density, $\rho(x,y,t)$, is defined by

$$\rho(x,y,t) = \rho_1 n_1 + \rho_2 n_2 \tag{5}$$

where

$$n(x,y,t) = n_1(x,y,t) + n_2(x,y,t). \tag{6}$$

A series of simulations of this problem have been performed using Flux-Corrected Transport algorithms [39] on the LCP&Fd's parallel processing Graphical and Array Processing System in a doubly periodic square domain. FCT algorithms are conservative and monotone with fourth-order phase accuracy. During a convective transport timestep, FCT first modifies the linear properties of a high-order algorithm by adding diffusion. This prevents dispersive ripples from arising, and it ensures that all conserved quantities remain monotonic and positive. Then FCT subtracts out the added diffusion unless nonphysical oscillations in the computed solution would reappear. This antidiffusive step is necessary to maintaining the sharp gradients between the two fluids in the calculations shown below and it maintains a high order of accuracy while enforcing positivity and monotonicity.

Results of the Simulations

Several cases have been run varying the density ratio between the two fluids, the strength of the opposed accelerations acting on the two fluids, and the system size. Figure 7 shows the spatially averaged upward velocity of the light fluid, ${V_y}^{avg}$ - the solid line, and the root mean square vertical velocity, ${V_y}^{rms}$ - the dashed line, as a function of time. In this case the light density averages 1 kg/m^3 with the heavier density averaging 10 kg/m^3. The lighter fluid feels an upward acceleration of $G_1 = 10^5 m/s^2$; the heavier fluid is accelerated downward with $G_2 = 10^4 m/s^2$. The system size for this calculation was 100 × 100 cells of size 1 cm by 1 cm.

The horizontal solid line marks the light fluid vertical drift of 20.0 m/s averaged over the 30,000 timesteps of this simulation. Significant fluctuations in the system averaged vertical drift are observed with short periods when the lighter fluid actually moves downward on average throughout the system. The accelerations are ten thousand and one thousand times the normal acceleration of gravity, enough to accelerate the heavier fluid to a velocity of three or four times the speed of sound and the light fluid much faster. Nevertheless, the Kelvin-Helmholtz interactions between the oppositely moving fluids keeps the interpenetration drift velocity orders of magnitude smaller.

The light fluid velocity does show large excursions about the average drift, typically with an rms speed of 100 to 150 m/s. Thus transient local flows with Mach number over 0.3–0.5 are not uncommon. This means that the average interpenetration drift of the two fluids is much smaller than the speed at which most of the fluid is moving. Strong vortices and shear flows occur on all

scales in this problem but the mixing of the two fluids is correspondingly fine grained so almost as much light fluid is moving downward as upward at any time. Shear of the two fluids at an interface tends to mix the two fluids in a coarse-grained way, as shown in Figure 8 for three different system sizes. This tendency to mix on finer and finer scales is counterbalanced by a tendency for like fluids to coagulate under the influence of the opposed accelerations. One forcing factor in this coagulation is the radial pressure and density gradients in a strong vortex which tend to spin the heavier fluid out. Thus coherent vortex structures tend to drift in the direction of the lighter fluid.

When the gravity and the density ratio are varied, the resulting situation is very similar. The mass ratio was varied in three runs using values 2:1, 10:1 and 50:1 with the lower density held fixed at 1.0 kg/m^3. The system size was taken as 100 × 100 cells and $G_1 = 10^4\ m/s^2$. The corresponding interpenetration drifts, averaged over 30,000 timesteps, are 5.2 m/s, 7.8 m/s, and 10.7 m/s. A set of three 100 × 100 runs were performed using a species mass ratio of 10 : 1 with the acceleration of the light fluid taking the values $10^4\ m/s^2$, $3 \times 10^4\ m/s$, and $10^5\ m/s^2$. The corresponding light fluid drift velocities, 11 m/s, 14 m/s, and 20 m/s, roughly support a square root scaling of the interpenetration drift with gravitational acceleration. Another series of three runs, with the species mass ratio of 1 : 2 and with corresponding accelerations fixed at $10^4\ m/s^2$ and $-5 \times 10^3\ m/s^2$, were performed with system sizes of 100 × 100 cells, 200 × 200 cells, and 400 × 400 cells. The corresponding drift velocities were 5.2 m/s, 8 m/s and 12 m/s, also supporting a square root scaling of interpenetration drift speed with system size.

This approximate square root scaling cannot be viewed as surprizing since the only characteristic velocity which can be constructed out of the one spatial scale in the problem, the system size, and the acceleration is

$$V_{char} = (G_1 L_{sys})^{1/2} \tag{7}$$

What is surprizing is that the velocity actually calculated from this expression for the 400 × 400 cell case mentioned above, $V_{char} = (10^4 \times 4)^{1/2} = 200\ m/s$, is a factor of twenty larger than actually measured from the simulations.

This disparity can only be explained by the near uniform coarse-grained mixing indicated above and is well illustrated in the heavy species number density plots of Figure 8. The overall macroscopic interaction seems to involve slightly denser mixtures moving in one direction with slightly less dense mixtures drifting the other way. The density imbalance results in a much smaller effective differential acceleration which reduces the interpenetration drift appreciably. The Atwood number, $A = (\rho_2 - \rho_1)/(\rho_2 - \rho_1)$, is the wrong non-dimensional number to describe this effect. Since the two fluids are accelerated separately, the effect still exists even when the Atwood number is zero.

Figure 9 shows vertical fluid velocity color encoded with green–yellow–orange hues indicating downward velocities and the blue–magenta–red hues indicating upward velocities on the figure. The saturated green (and blue) regions show a velocity in excess of 80 m/s. This flow field corresponds to the density distribution of Figure 8. In these figures, the direction of the opposed

accelerations are such that the denser fluid 2 is actually pulled upward. As can be seen, there are relatively extensive regions of up and down flowing fluid within which very detailed density structure is evident. Further, the characteristic scales lengths and general character of the structures is similar in the three cases even though the system size varies greatly in the three cases shown.

Further work on this problem will be aimed at developing a model to explain these slow relative drifts quantitatively.

Summary

A number of mechanisms involving the interaction of compressibility and rotational flows including turbulence have been discussed. A framework for organizing this discussion was built out of the obvious cycle of energization, fluid dynamic instability, and evolution of convoluted material interfaces. This cycle characterizes each stage of the cascade of energy which occurs in turbulence and in turbulent mixing. The effects of compressibility on the three stages of the cycle were categorized on a more or less continuous scale ranging from "active" effects where the accelerations associated with the compression or expansion of the fluid are of paramount importance to "passive" effects which depend primarily on the integrated compression or expansion displacements and resulting density gradients in the fluid.

While useful, this taxonomy is hardly rigorous. Some problems of how to categorize a given phenomenon clearly arose above. Since the velocity is an integral of the acceleration and the displacement is an integral of the velocity, where on the scale from passive to active a given mechanism lies sometimes depends on what timescale is used to measure the process. In other cases, for example when both active shock accelerations and passive density gradients interact as in the Richtmyer–Meshkov instability, the characterization again depends on the point of view.

What is most interesting is the diversity of phenomena involved. In some cases the predominant compressibility mechanisms are destabilizing, again as in the Richtmyer–Meshkov instability or in a supersonic boundary layer. In others, i.e. the free supersonic shear layer or in laser ablation, compressibility can significantly reduce the growth of otherwise highly unstable fluid dynamic modes. It becomes clear, however, that compressibility, even in rather low Mach number flows usually plays a surprizing important role. Extremely low amplitude acoustics can dominate vortex shedding in important simple cases. In flames the pressure is also essentially constant and yet multidimensional propagation and extinction of flames depends critically on compressibility.

Acknowledgements

Research on the various fluid systems reported here was supported by a number of sponsors including the Office of Naval Research, the Naval Research Laboratory, the Naval Air Systems Command, DARPA and DOE. The author also wishes to acknowledge the varied and creative contributions of his co-authors to the NRL material reviewed above and indicated in the references listed below.

References

1. J.P. Boris, E.S. Oran, Modelling Turbulence: Physics or Curve Fitting?, Presentation & Proceedings, 7th International Colloquium on Gasdynamics of Explosions and Reactive Systems (ICOGER), Gottingen, W. Germany, 20–24 August 1979, in *Combustion in Reactive Systems*, J.R. Bowen, et al. (eds), AIAA Progress in Astronautics and Aeronautics, Vol 76, pg 187–210, 1981.
2. E.S. Oran, J.P. Boris, Detailed Modelling of Combustion Systems, *Progress In Energy and Combustion Sciences*, Vol 7, pg 1–72, 1981.
3. E.S. Oran, J.P. Boris, *Numerical Simulation of Reactive Flow*, (Elsevier Science Publishing Company, New York, 1987).
4. J.P. Boris, E.S. Oran, and K. Kailasanath, The Numerical Simulation of Compressible and Reactive Turbulent Structures, Invited Presentation & Proceedings, Joint US/France Workshop on Turbulent Reactive Flows, Rouen, France, 7–10 July 1987, Springer-Verlag, Eds. B.G. Murthy and R. Borghi, 1988.
5. H.L. Swinney and J.P. Gollub, The Transition to Turbulence, *Physics Today*, pp. 41–49, August 1978.
6. J.M. Picone, J.P. Boris, Vorticity Generation by Asymmetric Energy Deposition in a Gaseous Medium, *Physics of Fluids*, Vol 26 (2), pg 365–382, February 1983.
7. J.M. Picone and J.P. Boris, Shock Generated Turbulence, Proceedings, International Workshop on the Physics of Compressible Turbulent Mixing, Princeton University, Princeton NJ, 24–27 October 1988.
8. E.S. Oran, J.P. Boris, and K. Kailasanath, Computations of Supersonic Flows: Shears, Shocks and Detonations, Proceedings, International Workshop on the Physics of Compressible Turbulent Mixing, Princeton University, Princeton NJ, 24–27 October 1988.
9. D.W. Bogdanoff, Compressible Effects in Turbulent Shear Layers, *AIAA Journal*, Vol 21 No 6, pp 926–927, June 1983.
10. D. Papamoschou and A. Roshko, Observations of Supersonic Free Shear Layers, AIAA Paper 86–0162, AIAA 24th Aerospace Sciences Meeting, Reno NV, 6–9 January 1986, also The Compressible Turbulent Shear Layer: An Experimental Study.
11. R.H. Guirguis, F.F. Grinstein, T.R. Young, E.S. Oran, K. Kailasanath, and J.P. Boris, Mixing Enhancement in Supersonic Shear Layers, AIAA paper 87-0373, AIAA 25th Aerospace Sciences Meeting, Reno NV, January 1987.
12. S.A. Ragab and J.L. Wu, Instabilities in the Free Shear Layer Formed by Two Supersonic Streams, AIAA Paper 88–0038, AIAA 26th Aerospace Sciences Meeting, Reno NV, 11–14 January 1988.
13. J.P. Boris, E.S. Oran, J.H. Gardner, K. Kailasanath, T.R. Young, Jr., Computational Studies of a Localized Supersonic Shear Layer, AIAA Paper 89–????, 27th AIAA Aerospace Sciences Meeting, Reno NV, 9–12 January 1989.
14. S. Ishizuka, On the Flame Propagation in a Rotating Flow Field, Proceedings, 22nd International Symposium on Combustion, Seattle WA, 14–19 August 1988, (Combustion Institute, Pittsburg PA, 1989).
15. J. Jarosinski, J.H.S. Lee, and R. Knystautis, Interaction of a Vortex Ring and a Laminar Flame, Proceedings, 22nd International Symposium on Combustion, Seattle WA, 14–19 August 1988, (Combustion Institute, Pittsburg PA, 1989).
16. P. Gilman, Global Circulation and the Solar Dynamo, *The Sun as a Star*, NASA Publication SP–450, 1981.
17. J. Toomre, Simulations of Compressible Solar Convection, Invited Presentation, Workshop on Computational Fluid Dynamics, Topical Group on Computation Physics & Fluid Dynamics Division of the American Physical Society, 41st Annual Meeting, Buffalo NY, 19 November 1988.

18. J.L. Ellzey and E.S. Oran, Simulation of Shock and Vortex Interactions, Proceedings, International Workshop on the Physics of Compressible Turbulent Mixing, Princeton University, Princeton NJ, 24–27 October 1988.
19. W. Blumen, Shear Layer Instability of an Inviscid Compressible Fluid, *Journal of Fluid Mechanics*, Vol 40, Part 4, pp 769–781, 1970.
20. W. Blumen, P.G. Drazin, and D.F. Billings, Shear Layer Instability of an Inviscid Compressible Fluid. Part 2, *Journal of Fluid Mechanics*, Vol 71, Part 2, pp 305–316, 1975.
21. C.K.W. Tam, Excitation of Instability Waves in a Two-Dimensional Shear Layer by Sound, *Journal of Fluid Mechanics*, vol 89, No 2, pp 357–371, 1979.
22. H. Furth, J. Killeen, and M. Rosenbluth, *Physics of Fluids*, Vol 6, p 459, 1953.
23. D.W. Dunn and C.C. Lin, The Stability of the Laminar Boundary Layer in a Compressible Fluid for the Case of Three Dimensional Disturbances, *Journal of Aerospace Sciences*, Vol 19, p 491, 1952.
24. J.D. Baum and J.N. Levine, Numerical Investigation of Acoustic Refraction, *AIAA Journal*, Vol 25, No 12, pp 1577–1586, December 1987.
25. J.D. Baum, Investigation of Flow Turning Phenomenon; Effect of Upstream and Downstream Propagation, AIAA paper 88-0544, AIAA 26th Aerospace Sciences Meeting, Reno NV, 11–14 January 1988.
26. M.H. Emery, J.H. Gardner, J.P. Boris, A.L. Cooper, Vortex Shedding Due to Laser Ablation, *Physics of Fluids*, Vol 27 (5), pp 1338–1340, May 1984.
27. M.H. Emery, and J.H. Gardner, Evolution of the Laser Ablatively Driven Rayleigh-Taylor Mix Layer, Proceedings, International Workshop on the Physics of Compressible Turbulent Mixing, Princeton University, Princeton NJ, 24–27 October 1988.
28. F.F. Grinstein, E.S. Oran and J.P. Boris, Direct Simulation of Asymmetric Mixing in Planar Shear Flows, *Journal of Fluid Mechanics*, Vol 165, pp 201–220, 1986.
29. F.F. Grinstein, E.S. Oran and J.P. Boris, Numerical Simulation of Compressible Spatially-Evolving Shear Layers, Proceedings, SIAM, Boston MA, 21–25 July 1986.
30. K.B.M.Q. Zaman and A.K.M.F. Hussain, Vortex Pairing in a Circular Jet Under Controlled Excitation. Part 1. General Jet Response, *Journal of Fluid Mechanics*, Vol 101, pp 441–449, 1980.
31. K.C. Schadow, K.J. Wilson, J.E. Crump, J.B. Foster and E. Gutmark, Interaction Between Acoustics and Subsonic Ducted Flow with Dump, AIAA paper 84-0530, 22nd AIAA Aerospace Sciences Meeting, January 1984.
32. K. Kailasanath, J.H. Gardner, E.S. Oran and J.P. Boris, Vortex Shedding and Merging in High-Speed Confined Shear Flows, Proceedings, International Workshop on the Physics of Compressible Turbulent Mixing, Princeton University, Princeton NJ, 24–27 October 1988.
33. K. Kailasanath, J. Gardner, J. Boris, and E. Oran, Interactions Between Acoustics and Vortex Structures in a Central Dump Combustor, AIAA paper 86-1609, also see *J. Prop. Power*, Vol 3, Nov-Dec 1987, pp 525-533.
34. R.D. Richtmyer, *Commun. Pure and Appl. Math.*, Vol 23, p 297, 1960.
35. Y.Y. Meshkov, NASA TT F–13, 074, 1970.
36. G.H. Markstein, *Journal of Aerospace Sciences*, Vol 24, p 238, 1957.
37. J.-F.L. Haas and B. Sturtevant, *Journal of Fluid Mechanics*, Vol 181, p 41, 1987.
38. J.M. Picone and J.P. Boris, Vorticity Generation by Shock Propagation Through Bubbles in a Gas, *Journal of Fluid Mechanics*, Vol 189, pp 23–51, April 1988.
39. J.P. Boris, D.L. Book, Solution of Continuity Equations by the Method of Flux Corrected Transport, in *Methods of Computational Physics*, , Vol 16, Chap 11, Academic Press, New York, 1976.

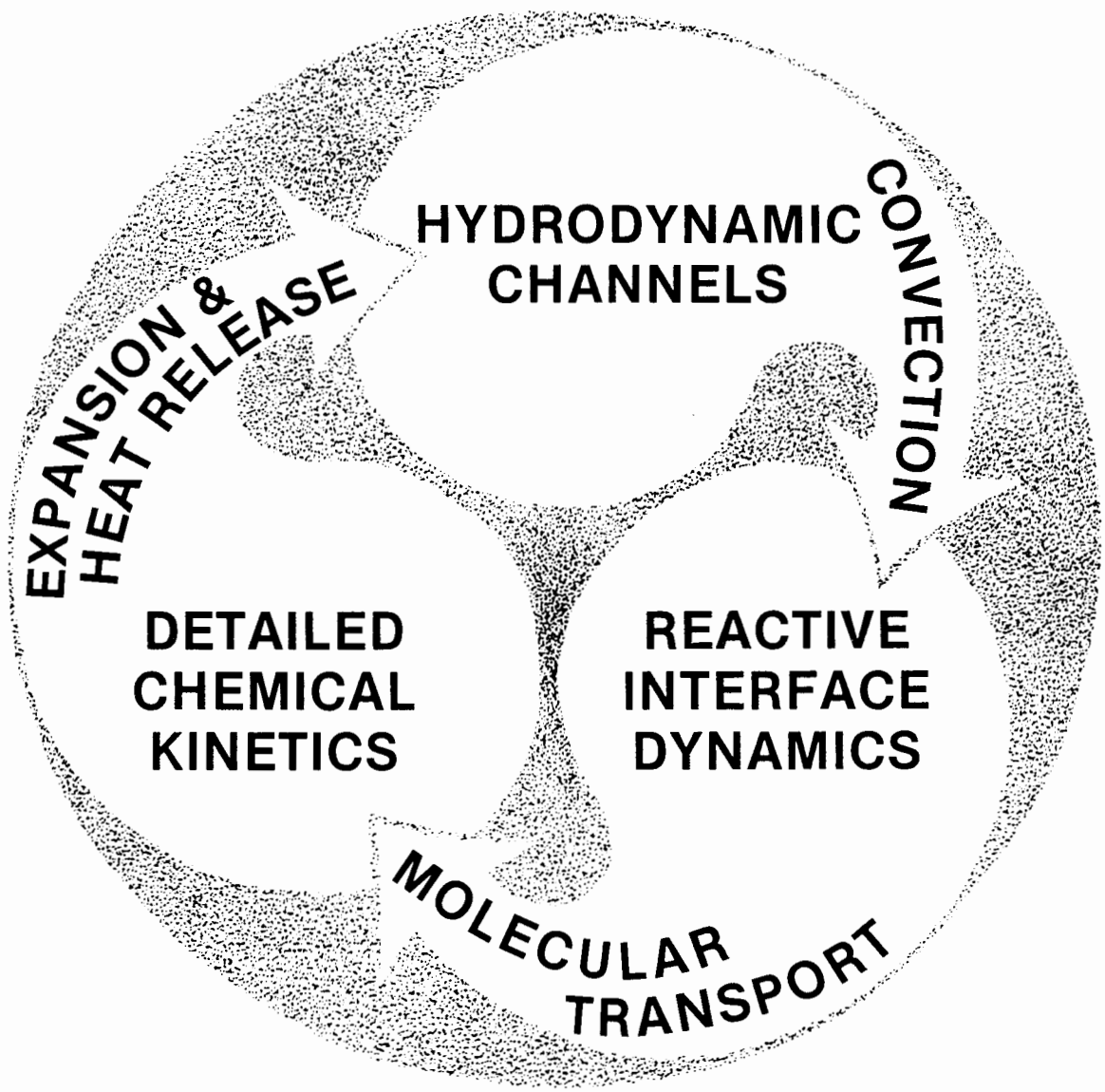

Figure 1. The three cyclic aspects of reactive flow turbulence, the classic model for compressibility effects in turbulence and mixing.

ROLES OF COMPRESSIBILITY IN MIXING & GENERATION OF TURBULENCE

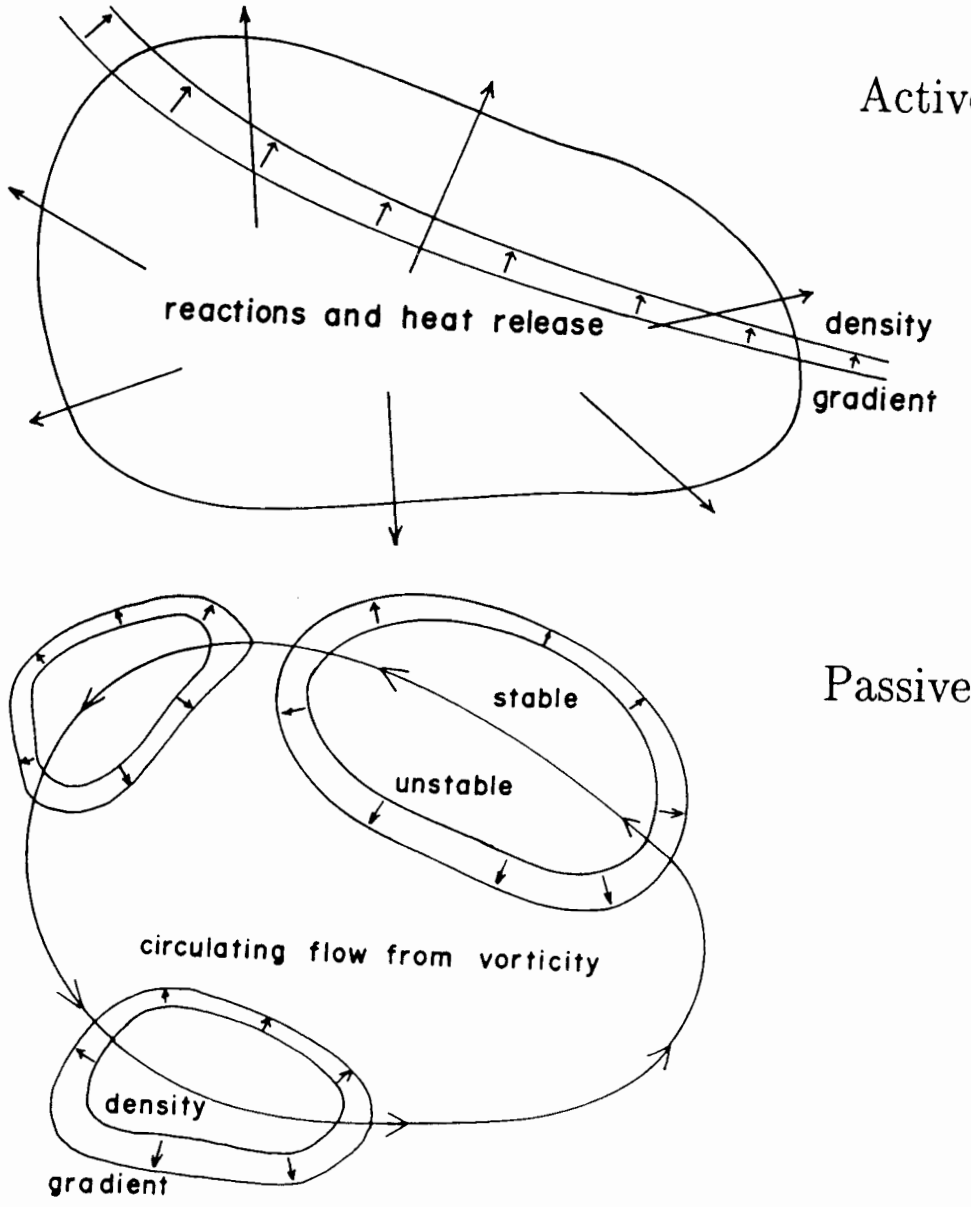

Figure 2. The active and passive roles of compressibility in mixing and in the generation of turbulence. A passive density gradient interacts unstably with expansion driven (active) accelerations and with rotationally-induced (passive) accelerations.

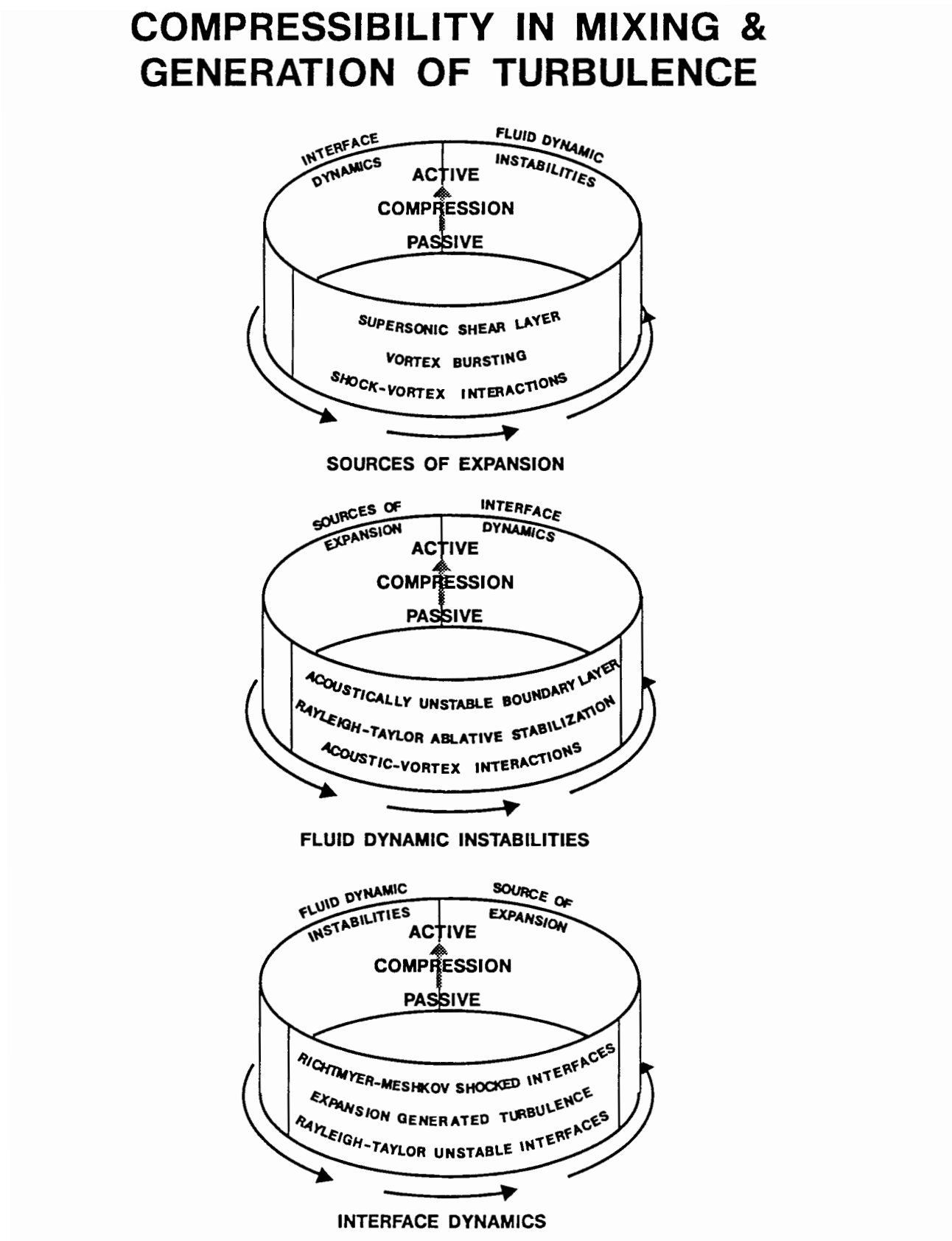

Figure 3. A schematic characterization of compressibility in mixing and the generation of turbulence is shown as a combination of the information in Figs. 2 and 3.

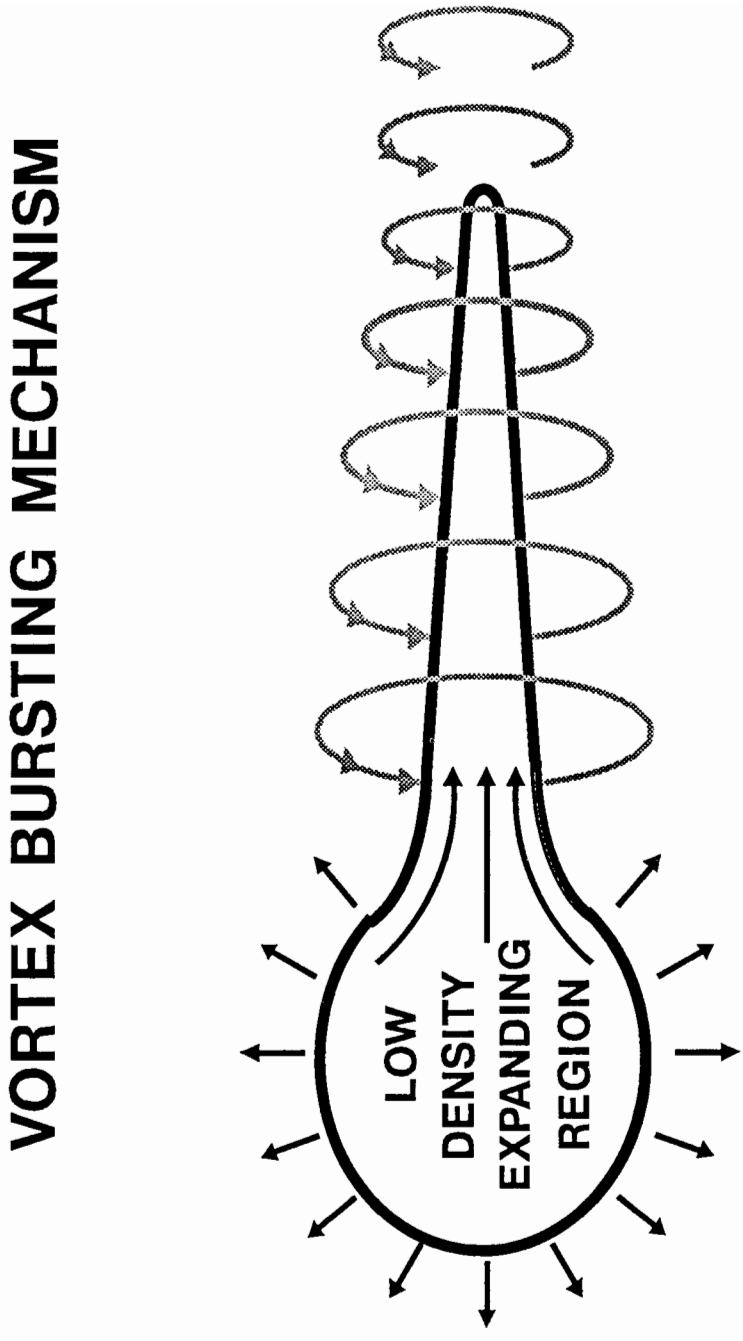

Figure 4. A schematic diagram of vortex bursting as enabled by compressibility in the flow. The azimuthal flow kinetic energy in the tight vortex core is converted to a rapid axial flow of low density material when expansion occurs near the vortex core.

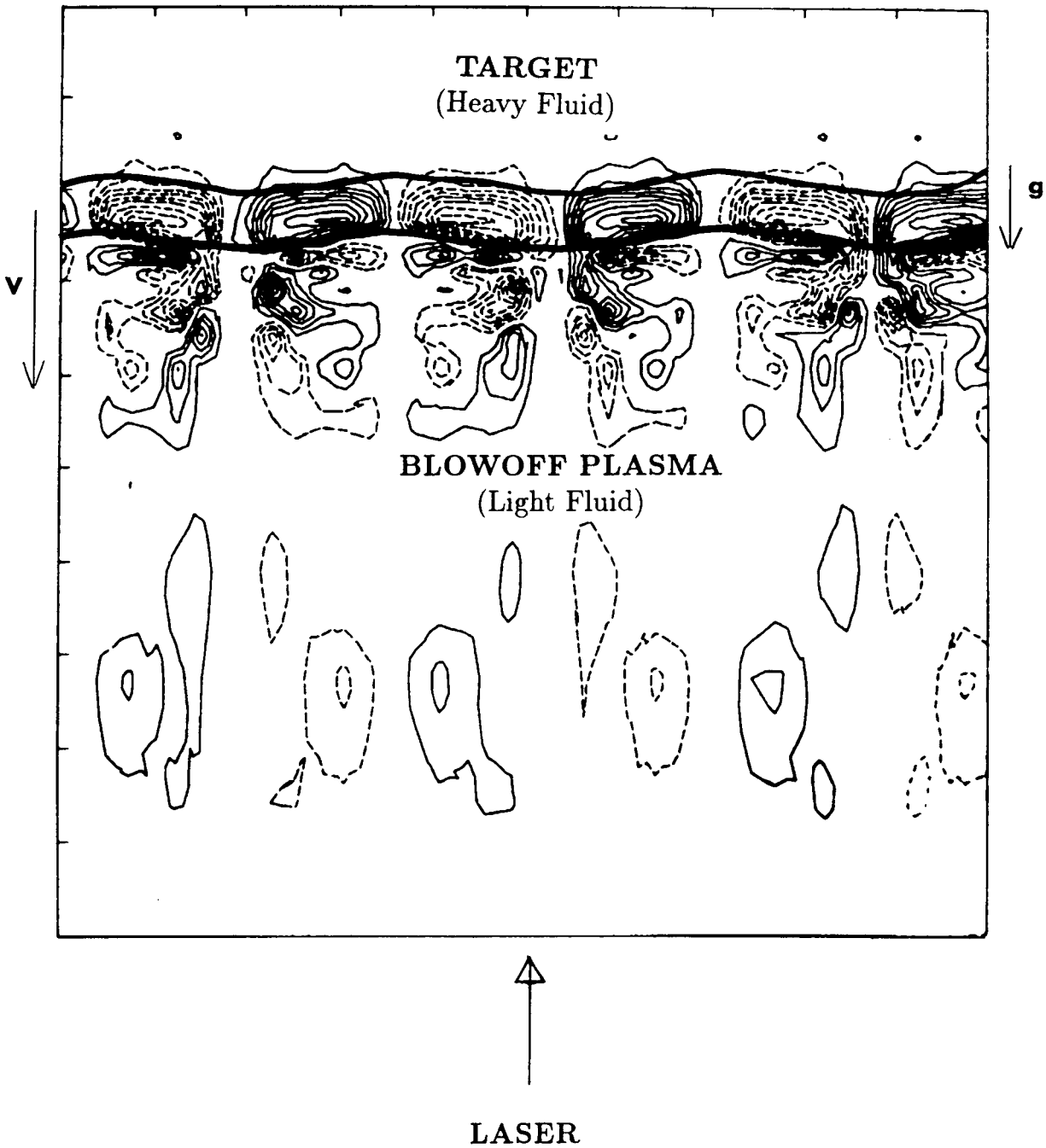

Figure 5. In the ablative Rayleigh-Taylor instability, here driven by a laser beam from below, the convection of vorticity away from the ablation layer by the strong expansion significantly reduces the Rayleigh-Taylor growth rate.

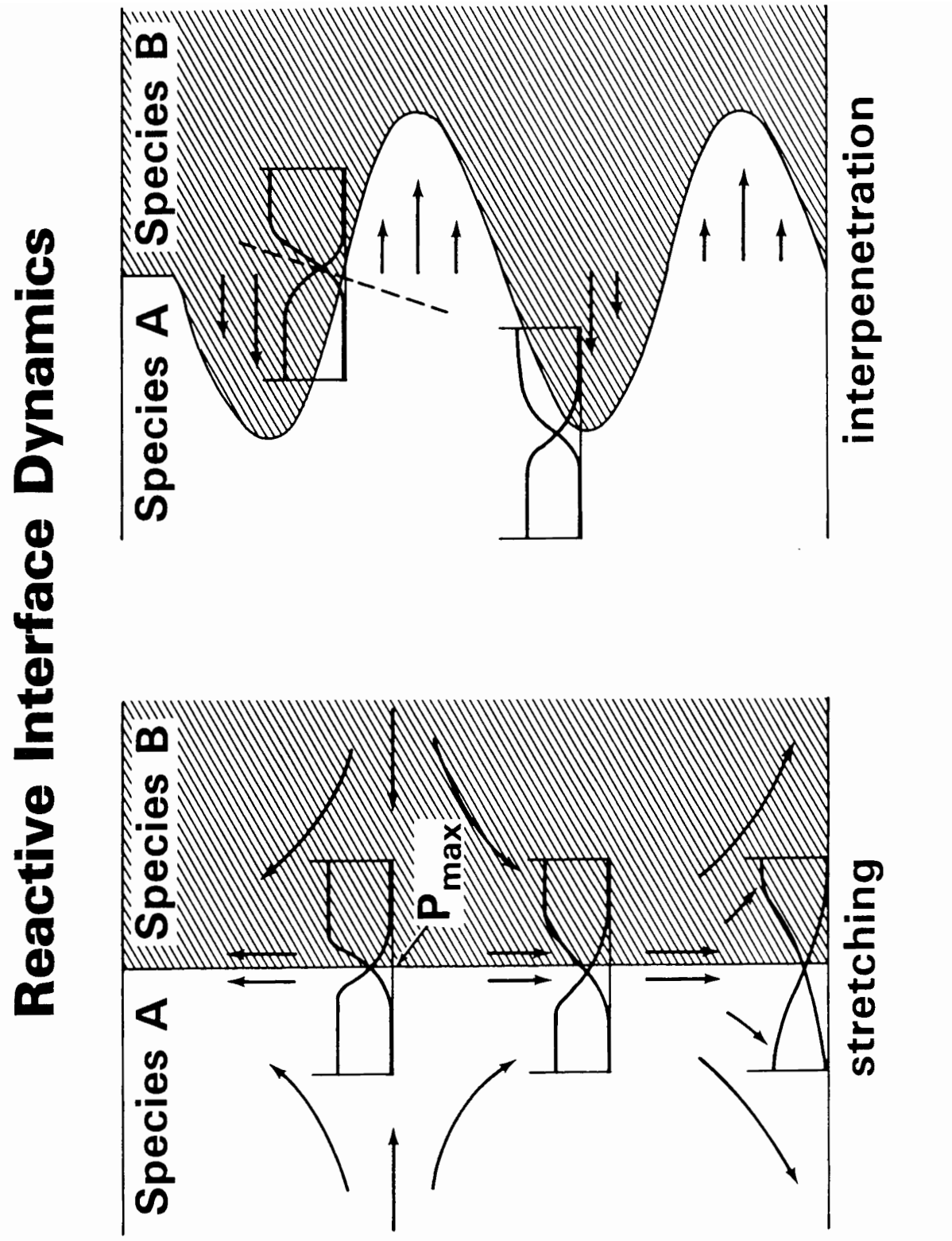

Figure 6. Reactive interface dynamics enhance molecular mixing both through stretching phenomena which increase local gradients and convection interpenetration which creates a larger interfacial surface area.

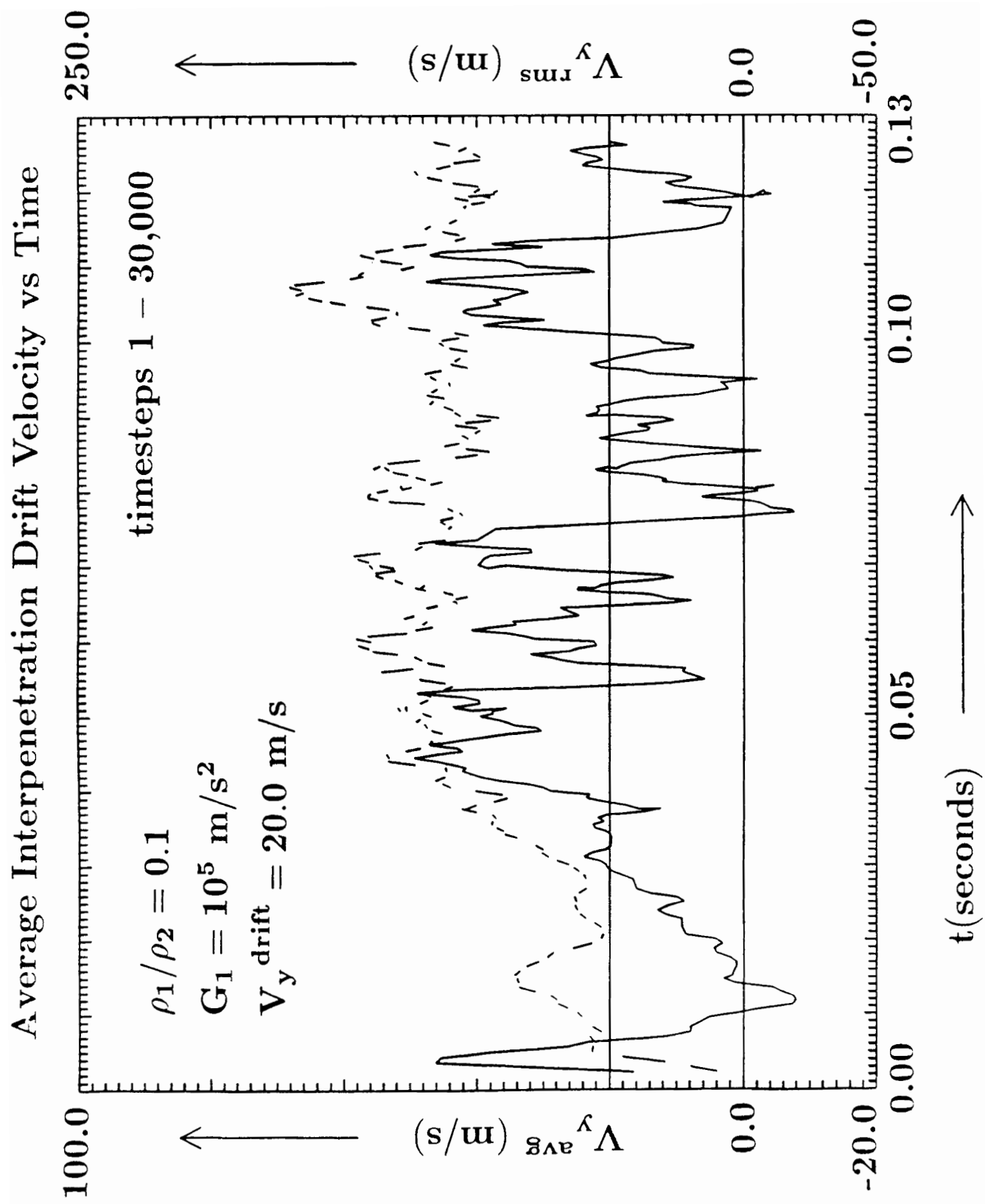

Figure 7. Average interpenetration drift velocity versus time for differentially accelerated fluids in a doubly periodic geometry.

Figure 8. Heavy species number density contours for a doubly periodic simulation of the asymptotic Rayleigh-Taylor interpenetration of two fluids.

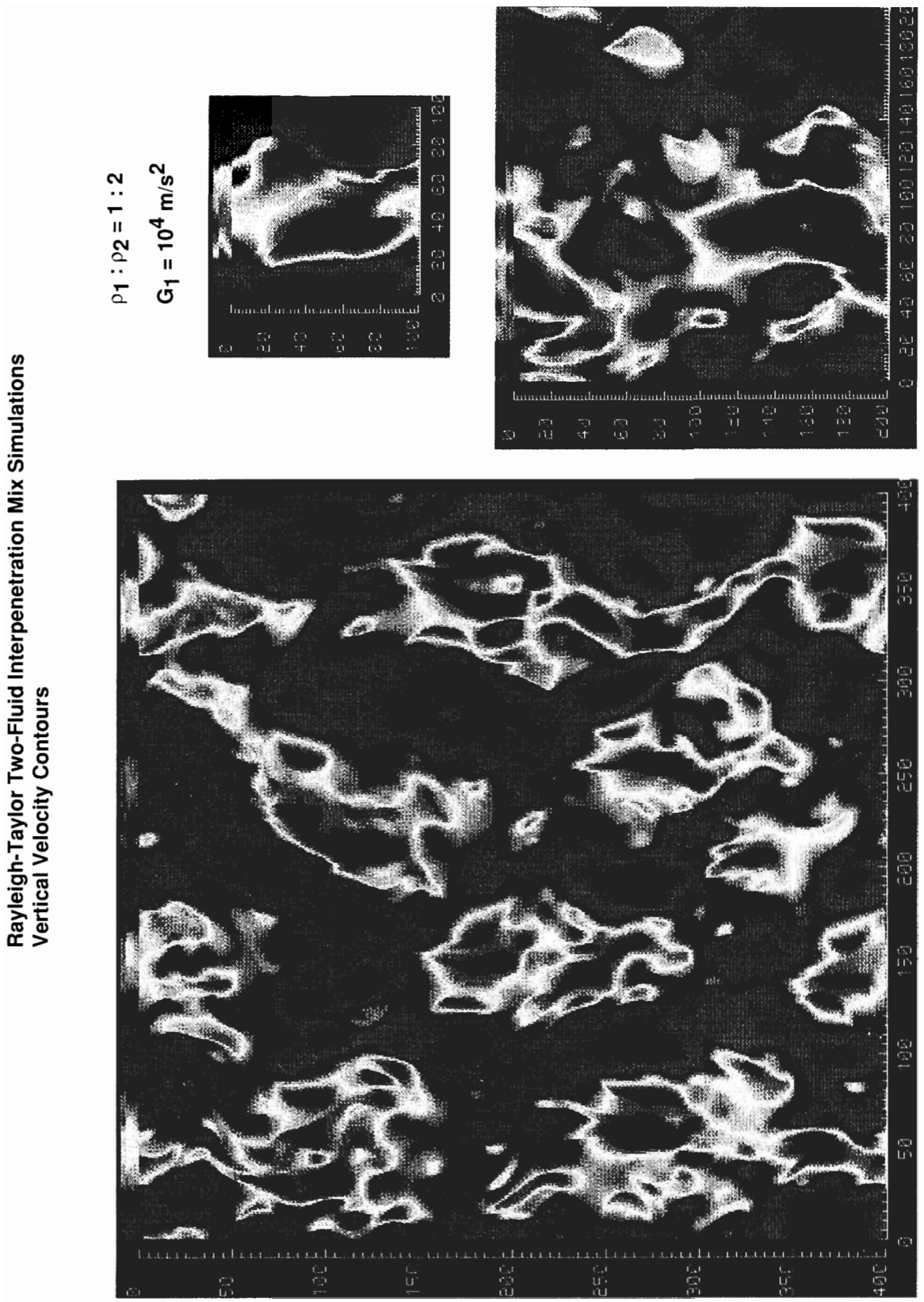

Figure 9. Vertical velocity contours for a doubly periodic simulation of the asymptotic Rayleigh-Taylor interpenetration of two fluids.

INVISCID SIMULATIONS OF TURBULENT SHEAR LAYERS - MEAN FLOW ANALYSIS

K.-Y. Chien, and R.E. Ferguson
Naval Surface Warfare Center
Silver Spring, MD 20903-5000

A.L. Kuhl
R & D Associates
Marina del Rey, CA 90295

H.M. Glaz
University of Maryland
College Park, MD 20742

P. Colella
Lawrence Livermore National Laboratory
Livermore, CA 94550

ABSTRACT

Effects of density and velocity variations between two streams of an unconfined, spatially-developing shear layer are studied by numerical solutions of the time-dependent Euler equations using a second-order Godunov scheme. The inviscid calculations duplicate quite well the major flow features that have been observed in the experiments of Brown and Roshko and of Oster and Wygnanski. These include the visual spreading rates and the mean-flow velocity and density profiles. This study suggests then that the mean-flow evolution is dominated by two-dimensional, inviscid effects.

INTRODUCTION

This paper presents results of numerical simulations of unconfined, unsteady, spatially developing, two-dimensional shear layer with large density variations between the two streams. This work is motivated by the experimental studies of Brown and Roshko [1] who showed clearly the effects of density on the rate of growth of large-scale vortex structures which are the intrinsic features of a turbulent shear layer. There have been many recent numerical studies of turbulent shear layers [2–4]. However, these efforts were mainly devoted to the computation of the development and evolution of those vortex structures in a constant-ambient-density environment. The present paper is an extension of our previous work [5,6] to study specifically the effects of large density variations between the two streams and to provide quantitative comparisons with the experimental data.

FORMULATION

The governing equations used are the unsteady, inviscid conservation laws of gasdynamics. In contrast with the vortex methods [2,3], there is no large-Mach-number limit with this approach and the baroclinic generation of vorticity is automatically included. Numerical results were

obtained by means of an explicit second-order Godunov scheme [7] that gives nondiffusive solutions for gasdynamics. Hence, this approach represents a large-Reynolds-number approximation to the flow. This numerical scheme has produced accurate solutions to a variety of blast wave reflection problems [8] and constant-ambient-density shear layer problems [5,6].

The computational grid consisted of 500 fine cells in the streamwise (x) direction and 80 fine cells in the transverse (y) direction across the shear layer ($\Delta x = \Delta y = 1$); a few coarse zones were used above, below and to the right (downstream) of the fine mesh to cover a large computational domain of 8800 by 3000. Typically, 10,000 to 20,000 time steps were run in one calculation so that reliable quantitative statistics can be obtained from the computed unsteady results. Tracer particles introduced into the flow field from the origin were tracked to follow the distortion of the interface. A typical calculation was run for about 10 hours on the LANL CRAY XMP computer. The initial shear layer was represented on the computational grid by Tanh(y) velocity and density profiles:

$$U(y) = [1 + \lambda \mathrm{Tanh}(y)](U_1 + U_2)/2 \tag{1}$$

$$\rho(y) = [1 + \lambda_\rho \mathrm{Tanh}(y)](\rho_1 + \rho_2)/2 \tag{2}$$

where the shear layer parameters are:

$$\lambda = (U_1 - U_2)/(U_1 + U_2) \tag{3}$$

$$r = U_2/U_1 \tag{4}$$

$$\lambda_\rho = (\rho_1 - \rho_2)/(\rho_1 + \rho_2) \tag{5}$$

Note that these profiles have the proper asymptotes (U_1, ρ_1 at $y = \infty$ and U_2, ρ_2 at $y = -\infty$).

The left-hand boundary of the grid was then driven by these same profiles with sinusoidal perturbations on the streamwise velocity only (and no pressure perturbations). Their frequencies corresponded to the frequency of maximum amplification rate (according to linear stability theory) and its first nine subharmonics. The maximum perturbation amplitude was one percent. A more complete description of this calculational approach may be found in [9].

RESULTS AND DISCUSSION

The shear layer parameters for the three cases presented in this study are listed in Table 1. Case 1 corresponds to the high velocity helium flow over a low velocity nitrogen flow as studied by Brown and Roshko [1], where the dynamic pressures of the two streams are equal; case 2 uses the same velocity profile but inverts the density profile. Case 3 corresponds to a constant density shear layer studied by Oster and Wygnanski [10].

TABLE 1. Calculational Matrix

CASE	λ	r	λ_ρ
1 – Brown & Roshko [1]	0.451	0.378	−0.75
2 – Brown & Roshko [1]	0.451	0.378	0.75
3 – Oster & Wygnanski [10]	0.250	0.600	0

The calculated material interface plots are shown in Figures 1(a), (c) and (e). For comparison, the shadowgraphs of the helium-nitrogen interface recorded during the experiment [1] are presented in Figures 1(b) and 1(d). Similarities between the calculated and experimental interface are remarkable. The shape and wavelength of these large-scale vortex structures are quite similar. Comparing Figures 1(a), (c) and (e), we see graphically the effect of density on the rate of growth of large-scale vortex structures.

In Figure 2, the calculated visual spreading rates δ'_{vis} are compared with the experimental data given in Figure 7 of Brown and Roshko [1]. We have also included in Figure 2 the results based on our earlier calculations [5] at $\lambda = 1$ for $\lambda_\rho = 0$. The bars over the calculated results represent the variation in the visual spreading rate over time. The calculated results and the experimental data are seen to be in good agreement.

Monitoring stations located at three constant x locations were used to store the flow field time histories. These were then integrated in time to establish the mean shear layer profiles. The mean velocity and density profiles are depicted in Figures 3, 4 and 5. The three stations for each case are compared by means of the scaling variable

$$\eta_{SL} = y/(x - x_o)$$

where x_o denotes the effective origin of the breakdown of the shear layer (x_o = 25, -42, 25 for cases 1, 2 and 3, respectively). As can be seen from these figures, the profiles seem to collapse reasonably well with this scaling.

The shaded regions in these figures denote the mean profiles as measured by Brown and Roshko (Figures 13(b) and (c) of [1]) and Oster and Wygnanski (Figure 6(d) of [10]). The calculated density and velocity profiles are seen to agree well with the measured profiles.

We have also computed r.m.s. time averages about the mean values. The peak values of the fluctuating quantities are given in Table 2. The present peak $u'$and shear stress values for case 3 are quite close to the experimental data of Oster and Wygnanski [10], but the peak v' value is about two times larger than the data because of our two-dimensional flow approximation. A detailed discussion of the r.m.s. profiles will be given in a forthcoming paper [11].

TABLE 2. Comparison of Peak Fluctuating Quantities (10^{-2}) at x = 400.

CASE	u'/U_1	v'/U_1	w'/U_1	$\overline{-u'v'}/U_1^2$	ρ'/ρ_{max}
1	14.5	18.8	--	0.69	35
2	14.3	17.1	--	0.57	32
3	8.6	11.2	--	0.24	0.2
data [10]	7.2	6.1	5.8	0.21	--

CONCLUSIONS

The present inviscid calculations seem to capture the major flow features that have been observed in experiments. These include the formation and growth of vortex structures, the visual spreading rates and the mean-flow velocity and density profiles. Therefore, this study suggests that the mean-flow evolution of unstable shear layers is dominated by inviscid effects. The principal limitation of the present calculations is the two-dimensional flow approximation.

REFERENCES

1. Brown, G.L. and Roshko, A., On density effects and large structure in turbulent mixing layers, *J. Fluid Mech.* **64**, 775-816, 1974.

2. Inoue, O., Vortex simulation of a turbulent mixing layer, *AIAA J.* **23**, 367-373, 1985.

3. Inoue, O. and Leonard, A., Vortex simulation of forced/unforced mixing layers, *AIAA J.* **25**, 1417-1418, 1987.

4. Grinstein, E.F., Oran, E.S. and Boris, J.P., Numerical simulations of asymmetric mixing in planar shear layers, *J. Fluid Mech.* **165**, 201-220, 1986.

5. Chien, K.-Y., Collins, J.P., Ferguson, R.E., Glaz, H.M. and Kuhl, A.L., Simulation of vortex merging in shear layers by an inviscid code, 10th U.S. National Congress of Applied Mech., June 1986.

6. Chien, K.-Y., Ferguson, R.E., Collins, J.P., Glaz, H.M. and Kuhl, A.L., A study of mixing in forced shear layers with an Euler code, AIAA Paper No. 87-1318, 1987.

7. Colella, P. and Glaz, H.M., Efficient solution algorithm for the Riemann problem for real gases, *J. Comp. Phys.* **59**, 264-289, 1985.

8. Glaz, H.M., Colella, P., Glass, I.I. and Deschambault, R.L., A numerical study of oblique shock-wave reflections with experimental comparisons, *Proc. Roy. Soc. London*, Ser. A., **398**, 117-140, 1985.

9. Kuhl, A.L., Chien, K.-Y., Ferguson, R.E., Glaz, H.M. and Colella, P., *Inviscid dynamics of unstable shear layers*, RDA-TR-161604-006, R & D Associates, Marina del Rey, CA, 1988.

10. Oster, D. and Wygnanski, I., The forced mixing layer between parallel streams, *J. Fluid Mech.* **123**, 91- 130, 1982.

11. Chien, K.-Y., Kuhl, A.L., Ferguson, R.E., Glaz, H.M., Colella, P., Inviscid simulations of turbulent shear layers - fluctuating flow profiles (in preparation).

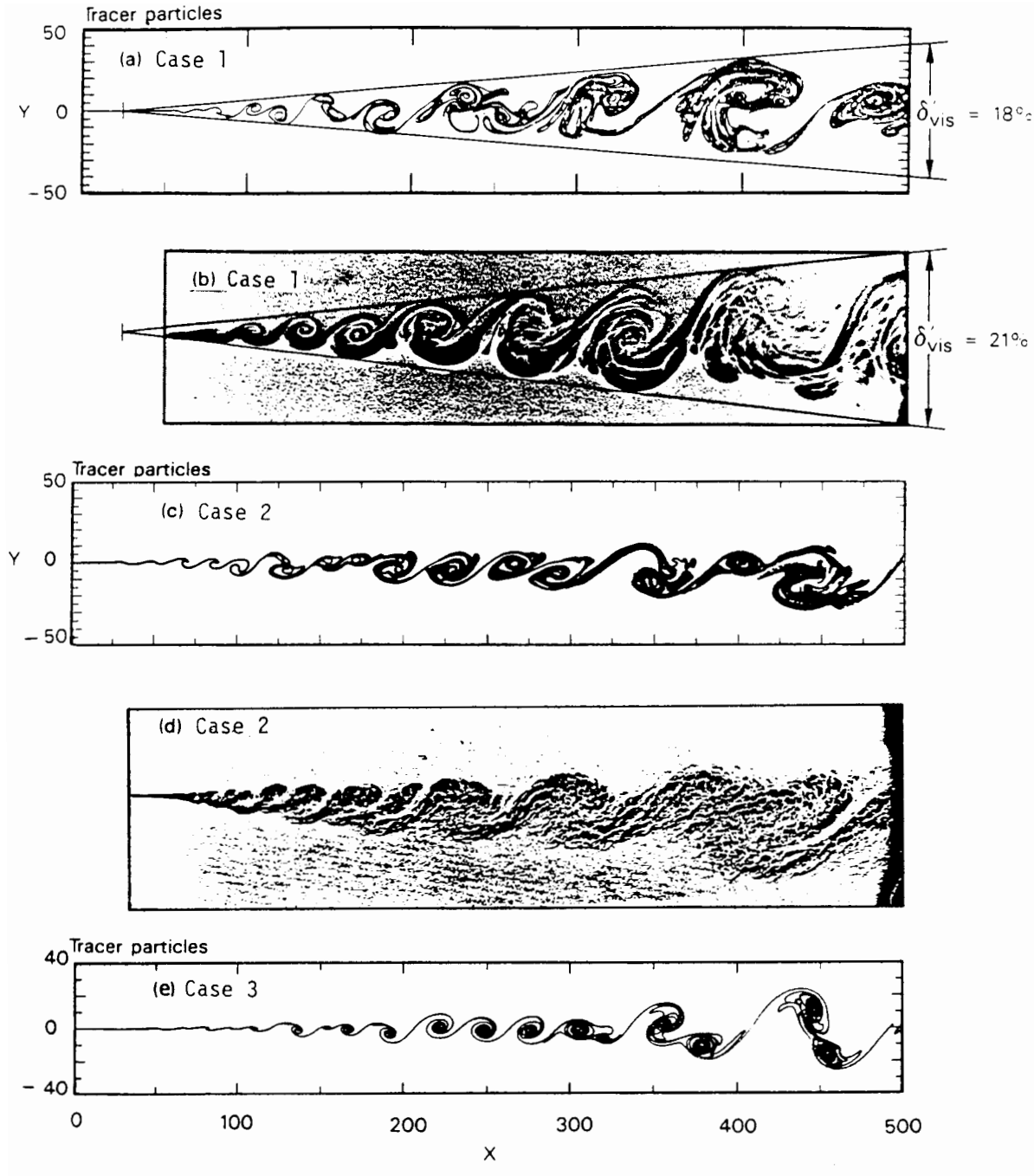

Figure 1. Material interface plots showing the development of rotational structures: (a) and (b) Case 1; (c) and (d) Case 2; (e) Case 3. Photographs (b) and (d) courtesy of Brown and Roshko (1974).

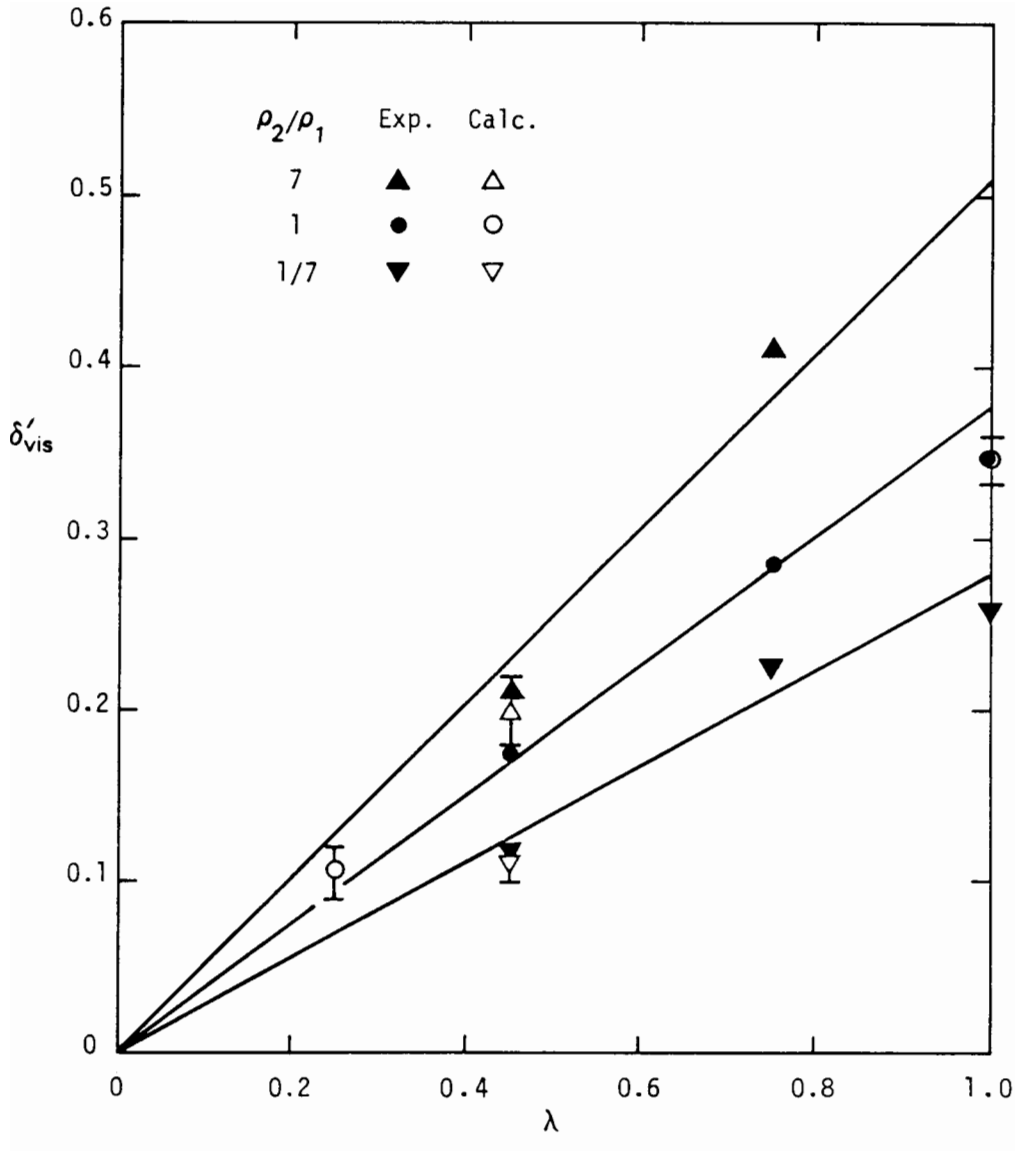

Figure 2. Visual spreading rate, δ'_{vis}, versus λ.

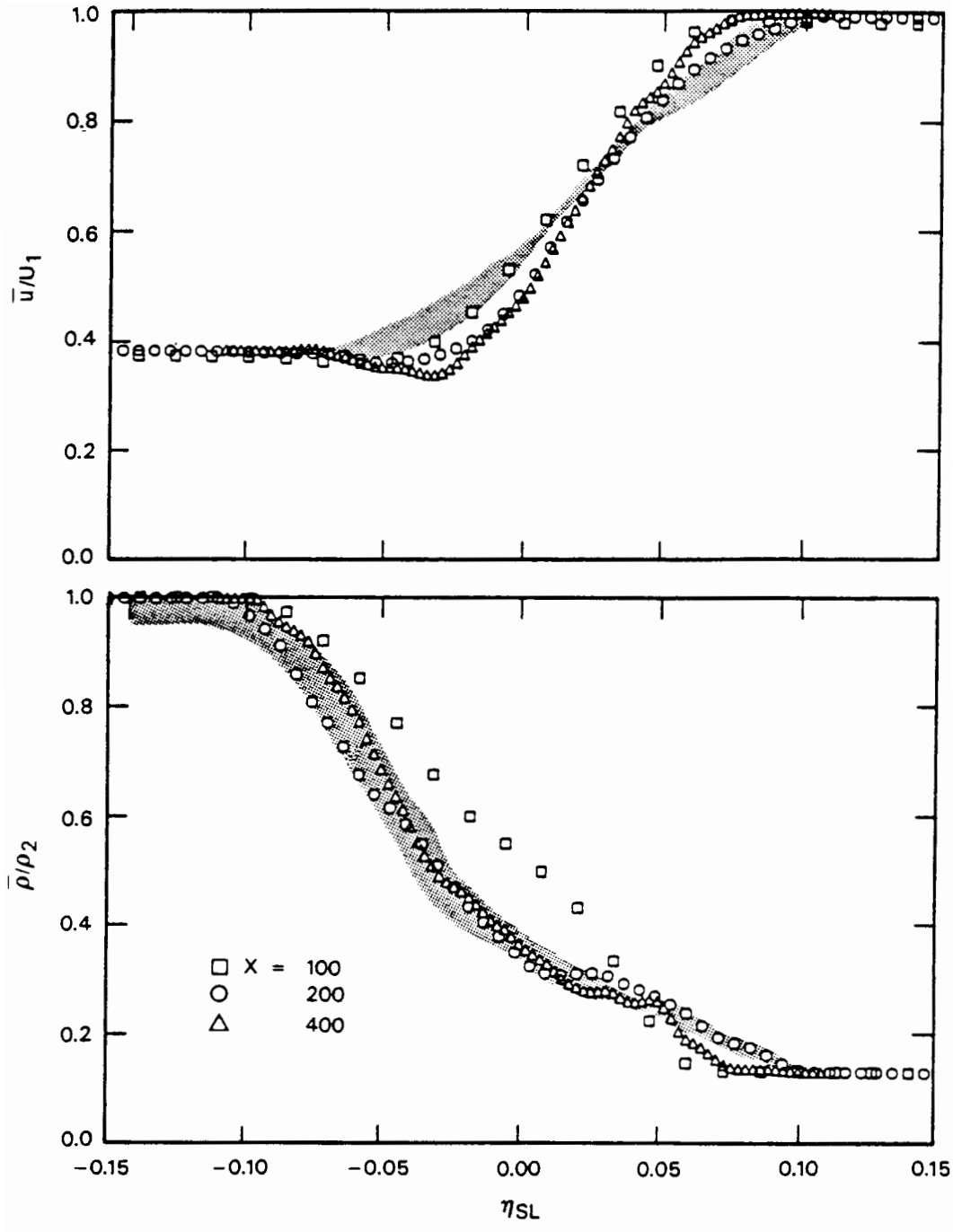

Figure 3. Mean velocity and density profiles for Case 1 ($\lambda = 0.45$, $r = 0.38$, $\rho_1/\rho_2 = 1/7$); shaded region denotes the data band of Brown and Roshko (1974).

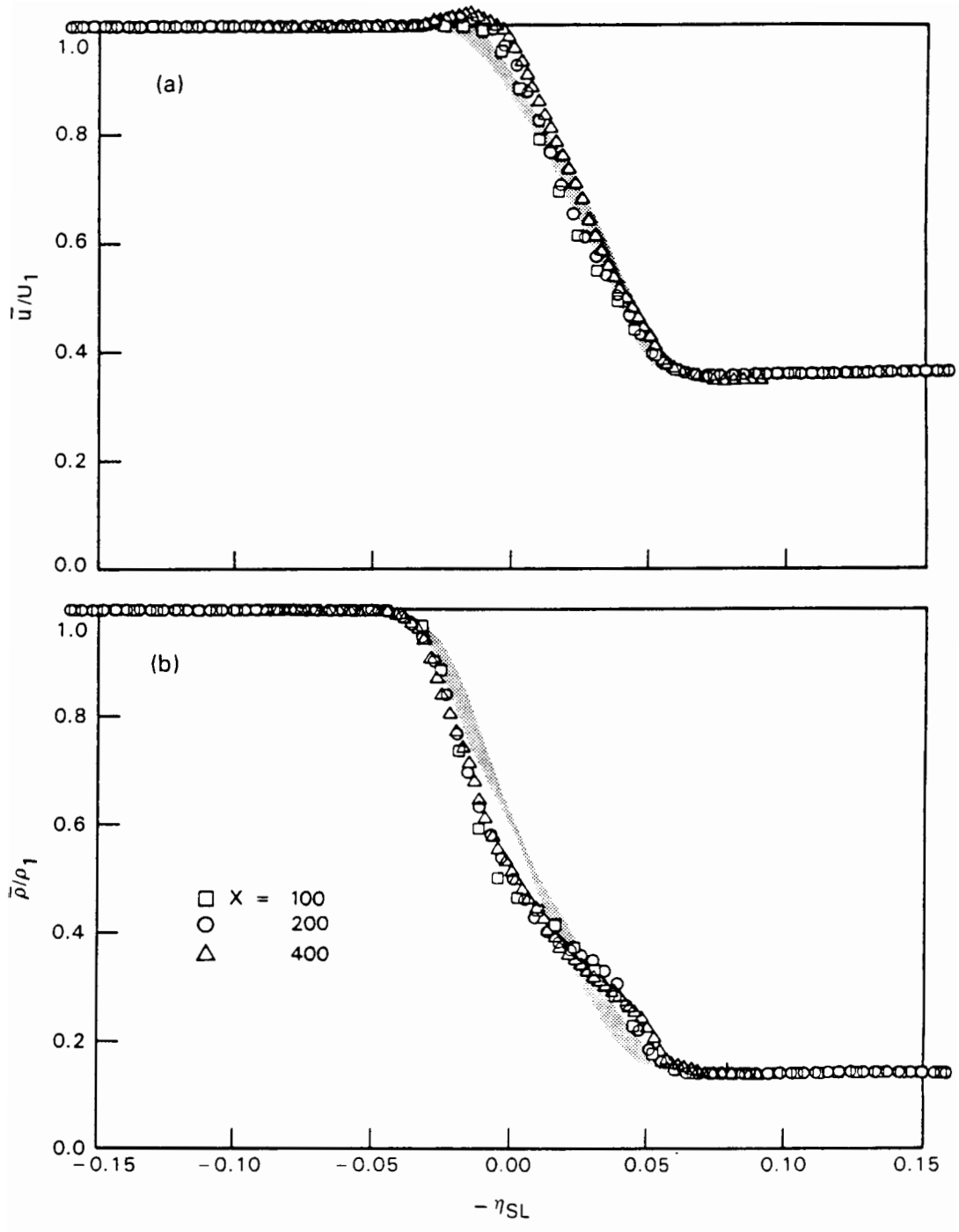

Figure 4. Mean velocity and density profiles for Case 2 ($\lambda = 0.45$, $r = 0.38$, $\rho_1/\rho_2 = 7/1$); shaded region denotes the data band of Brown and Roshko (1974).

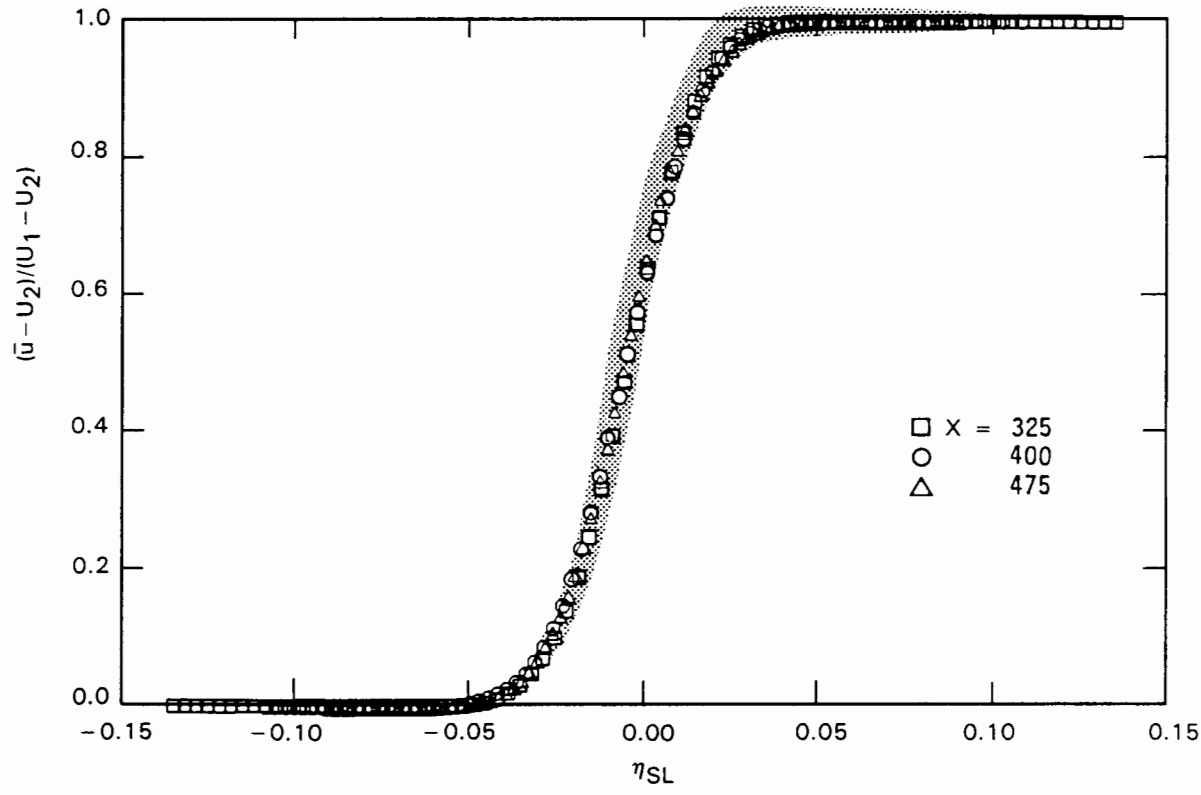

Figure 5. Mean velocity profile for Case 3 (λ = 0.25, r = 0.6, ρ_1/ρ_2 = 1); shaded region denotes the data band of Oster and Wygnanski (1982).

APPLICATION OF A TWO-EQUATION TURBULENCE MIX MODEL†

W.P. Crowley
Lawrence Livermore National Laboratory

Introduction

A mass averaged k-epsilon model was derived by Leith[1,2] using a moment expansion and appropriate closure models. Moving the mesh with the mass averaged velocity results in a Lagrangian model with constant mass in each zone. In this paper Leith's model is transformed into an "Almost Lagrangian"[3] model by taking the mesh velocity to be the ensemble averaged fluid velocity. Here the mass in each zone may change with time. The resulting 1-D model is used to simulate the Smits and Muck[4] supersonic wind tunnel experiment in which pre-existing turbulence is amplified by a shock wave. From the model results we deduce a simplified k-ε model that is applicable to the Smits and Muck (S&M) experiment. In the analytic solution for the simplified model we find the shock thickness to be increased by a factor of 10^5; behind the shock the turbulent energy decays as t^{-1}.

Leith introduces an ensemble average <f> and a mass average {f} where the mass average is defined by

$$\langle \rho f \rangle = \langle \rho \rangle \{f\}$$

Each average has its own associated fluctuations defined by

$$f = \langle f \rangle + f'' = \{f\} + f'$$

For velocity, the component averages are related by

$$\{u_i\} = \langle u_i \rangle + \langle \rho'' u_i'' \rangle / \langle \rho \rangle$$

and the eddy mass flux is defined to be

$$m_i = \langle \rho'' u_i'' \rangle$$

He derives the following equations in an Eulerian coordinate system:

$$\frac{\partial \rho}{\partial t} + \frac{\partial \rho \{u_k\}}{\partial x_k} = 0$$

$$\frac{\partial \rho \{u_i\}}{\partial t} + \frac{\partial \rho \{u_k\}\{u_i\}}{\partial x_k} = -\frac{\partial (p + p_T)}{\partial x_i} + \frac{\partial \mu_T S^*_{ik}}{\partial x_k}$$

$$\frac{\partial \rho e}{\partial t} + \frac{\partial \rho e \{u_k\}}{\partial x_k} = \frac{\partial (\frac{\mu_T}{\sigma_h} \frac{\partial h}{\partial x_k})}{\partial x_k} - p \frac{\partial \{u_k\}}{\partial x_k} - \rho (S - \varepsilon)$$

$$\frac{\partial \rho k}{\partial t} + \frac{\partial \rho k \{u_i\}}{\partial x_i} = \frac{\partial (\frac{\mu_T}{\sigma_k} \frac{\partial k}{\partial x_i})}{\partial x_i} - p_T \frac{\partial \{u_i\}}{\partial x_i} + \mu_T S^*_{ji} \frac{\partial \{u_j\}}{\partial x_i} + \rho (S - \varepsilon)$$

$$S^*_{ik} = \frac{\partial \{u_i\}}{\partial x_k} + \frac{\partial \{u_k\}}{\partial x_i} - \frac{2}{3} \frac{\partial \{u_j\}}{\partial x_j} \delta_{ik}$$

$$\rho S = m_k \frac{1}{\rho} \frac{\partial p}{\partial x_k}$$

---

†Work performed under the auspices of the U.S. Department of Energy by the Lawrence Livermore National Laboratory under Contract No. W-7405-ENG-48.

$$m_k = -\frac{\nu_T}{\sigma_m}\frac{\partial \rho}{\partial x_k}$$

$$\mu_T = \rho \nu_T = C_\mu \rho k^2/\varepsilon$$

Here ρ is mass density, p is fluid pressure, e is specific internal energy, h is specific enthalpy, k is specific turbulent energy, and ε is the dissipation rate of specific turbulent energy. In one dimension the Reynolds stress tensor becomes

$$Q_T = -\mu_T S^*_{11} = -\frac{4}{3}\mu_T \frac{\partial \{u\}}{\partial x}$$

Almost-Lagrangian k-ε Equations

Consider a conservation law in an Eulerian coordinate system where e represents some intensive quantity, say internal energy [ergs/gm]:

$$\frac{\partial \rho e}{\partial t} + \frac{\partial \rho e u_k}{\partial x_k} = R_e$$

We transform to a coordinate system moving with velocity s_k and the conservation law becomes

$$\frac{\delta \rho e}{\delta t} + \frac{\partial \rho e (u_k - s_k)}{\partial x_k} + \rho e \frac{\partial s_k}{\partial x_k} = R_e$$

or

$$\frac{\delta e}{\delta t} + (u_k - s_k)\frac{\partial e}{\partial x_k} = R_e/\rho$$

where

$$\frac{\delta x}{\delta t} = s$$

s_k is arbitrary and, if we choose s_k to be $\{u_k\}$, then the mass in a zone is constant and the eddy mass flux, m_k, must be chosen accordingly. To eliminate the constraint on m_k we let

$$s_k = \langle u_k \rangle$$
$$u_k = \{u_k\}$$

and then

$$u_k - s_k = \{u_k\} - \langle u_k \rangle = m_k/\rho = n_k$$

Under this choice of mesh velocity the mass in a zone can change with time, and in 1D, the preferred equations are then:

Mass flux due to turbulent diffusion

$$m_k = -D\frac{\partial \rho}{\partial x_k} \quad , D = C_1 k^2/\varepsilon$$

diffusion velocity

$$n_k = m_k/\rho$$

momentum

$$\rho\left(\frac{\delta \{u_i\}}{\delta t} + n_k \frac{\partial \{u_i\}}{\partial x_k}\right) = -\frac{\partial (p + Q + p_T + Q_T)}{\partial x_i}$$

mesh velocity = fluid velocity - diffusion velocity

$$\langle u_k \rangle = \{u_k\} - n_k$$

mesh kinematics

$$\frac{\delta x_k}{\delta t} = \langle u_k \rangle$$

$$\frac{1}{V}\frac{\delta V}{\delta t} = \frac{\partial \langle u_i \rangle}{\partial x_i}$$

mass

$$\frac{\delta \rho}{\delta t} + \rho \frac{\partial \langle u_k \rangle}{\partial x_k} = -\frac{\partial m_k}{\partial x_k}$$

specific internal energy

$$\frac{\delta \rho e}{\delta t} + \rho e \frac{\partial \langle u_i \rangle}{\partial x_i} = -\frac{\partial e m_i}{\partial x_i} + \frac{\partial \left(\frac{\mu_T}{\sigma_h}\frac{\partial h}{\partial x_i}\right)}{\partial x_i} - (p + Q)\frac{\partial \{u_i\}}{\partial x_i} - \rho(S - \varepsilon)$$

turbulent kinetic energy

$$\frac{\delta \rho k}{\delta t} + \rho k \frac{\partial \langle u_i \rangle}{\partial x_i} = -\frac{\partial k m_i}{\partial x_i} + \frac{\partial \left(\frac{\mu_T}{\sigma_k}\frac{\partial k}{\partial x_i}\right)}{\partial x_i} - (p_T + Q_T)\frac{\partial \{u_i\}}{\partial x_i} + \rho(S - \varepsilon)$$

turbulent dissipation rate

$$\frac{\delta \rho \varepsilon}{\delta t} + \rho \varepsilon \frac{\partial \langle u_i \rangle}{\partial x_i} = -\frac{\partial \varepsilon m_i}{\partial x_i} + \frac{\partial \left(\frac{\mu_T}{\sigma_\varepsilon}\frac{\partial \varepsilon}{\partial x_i}\right)}{\partial x_i} - C_{16}\frac{\varepsilon}{k}(p_T + Q_T)\frac{\partial \{u_i\}}{\partial x_i} + \rho\frac{\varepsilon}{k}(C_{\varepsilon 1}S - C_5\varepsilon)$$

The epsilon equation is "derived" from the k-equation by multiplying the k-equation by ε/k, forgetting the rules of algebra and introducing three constants that may be adjusted to fit experimental data. We also have introduced an artificial viscosity[5].

$$Q = C_0^2 \rho \left(\frac{\partial \{u\}}{\partial x}\Delta x\right)^2 \quad \text{if } \Delta u < 0$$

RESULTS

In this section we compare results from the model with results from the wind tunnel experiments. The "2-D" experimental setup is rotated into a 1-D configuration normal to the shock as suggested in Appendix A. The simulations are done with this k-ε model embedded in a 1-D Lagrangian hydrodynamics code which is based on the artificial viscosity method of Richtmyer and von Neumann[5]. To compare with the laboratory data we trade laboratory distance for (shock speed)x(time).

Figure 1 shows S&M data for three wedges. Figure 2 shows the turbulent energy, k, in a "zone" of the fluid as a function of time for different initial conditions for the test problem based on the 16° wedge (Appendix A). Figure 1 shows only the streamwise component of turbulent energy and

the model calculates the total turbulent energy so there is some ambiguity here on comparing the increase of k across the shock. We can, however, compare the full-width, half-max (FWHM) value of each curve and compare these values. For S&M, FWHM ~ 12.5 cm, and this translates into 4×10^{-4} seconds.

The baseline problem has an initial turbulent energy of 1.82e7 ergs/gm (about 1% of the initial internal energy) and an initial value for ε of 4.55e10 ergs/gm/sec. Using an experimental setup similar to that used by S&M, Settles, Fitzpatrick and Bogdonoff[6] estimate the incoming boundary layer to be 2.3 cm thick. Using this value for a length scale, and the above value for k, we compute ε to be 3.4e10 ergs/gm/sec.

Figure 2 shows the evolution of k for different initial values of k and ε. We conclude that there are values of k_0 and ε_0 within a factor of four that allow us to match model results with experimental results.

Figure 3 shows the relative importance of the different components of energy in zone 109. The matter energy is greater than the mean kinetic energy which is greater than the turbulent energy. The turbulent pressure is always an order of magnitude less than the matter pressure.

In Figure 4 we plot the time integral of various terms in the k-equation vs time in zone 109. We see that the dominant terms are the work term (curve E) and the dissipation term (curve C). This reduces the complexity of the model and suggests that an analytic solution may be possible in this situation. It also leads to questions about the sensitivity of the model to the coefficient of the work term, C16, in the ε-equation

Rapid Distortion Theory suggests that C16 = 2. Figure 5 shows k and ε vs time in zone 109 for C16 = 1, 2 and 4. From k and ε are derived a time scale, k/ε and a length scale, $k^{1.5}/\varepsilon$ and these quantities are plotted vs time in Figs. 6 and 7.

Figure 6 shows the time-scale vs time. If we think of k/ε as the age of the turbulence, then we expect the passage of a shock to create new (young) turbulence. Figure 6 thus suggests that a value for C16 greater than 1 is called for.

Figure 7 shows the turbulent length-scale. The rapid passage of a shock cannot create new, large-scale turbulence immediately. In fact, the shock probably creates new, small-scale turbulence and compresses the existing turbulence by the compression ratio of the shock. For the

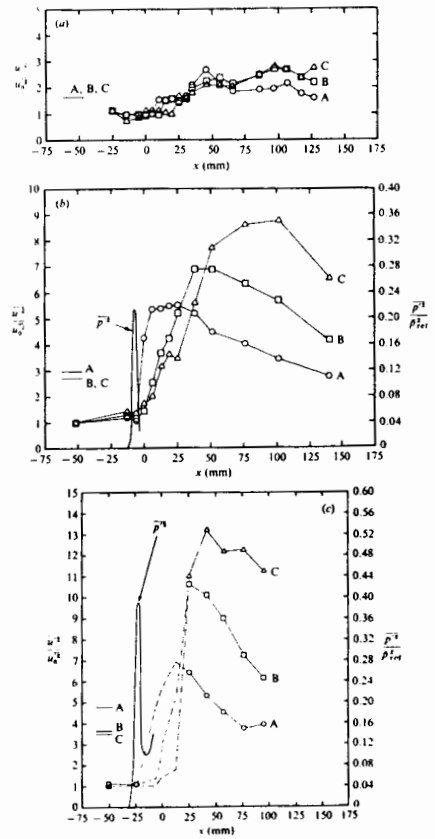

Figure 1

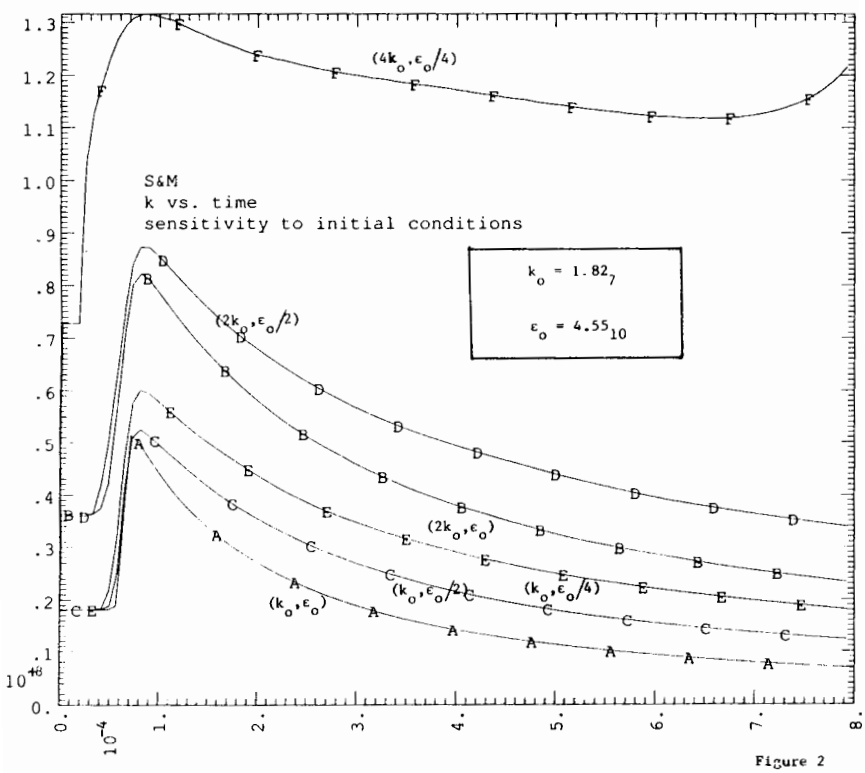

Figure 2

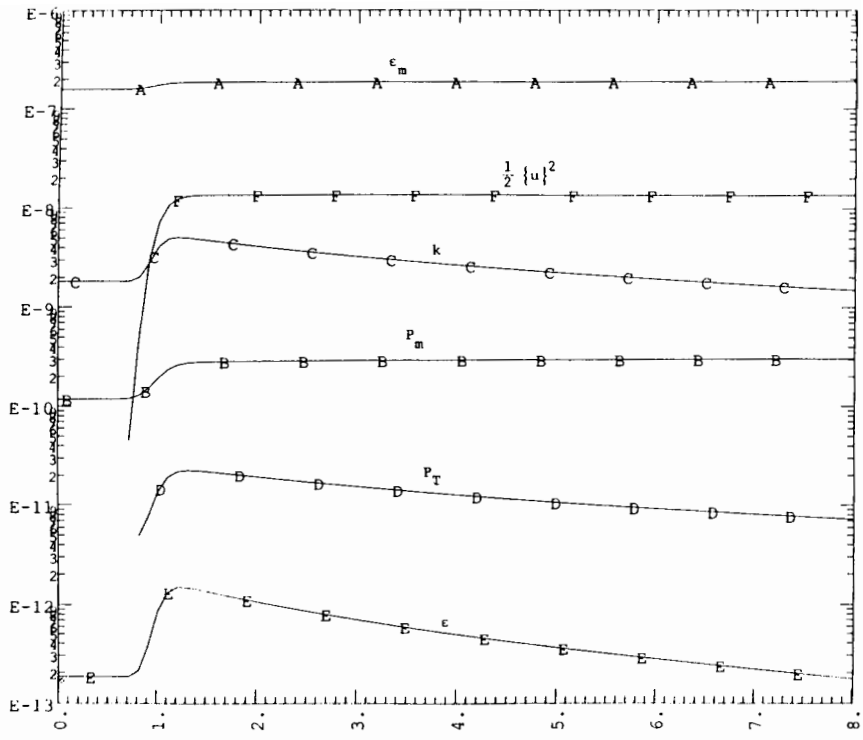

Figure 3

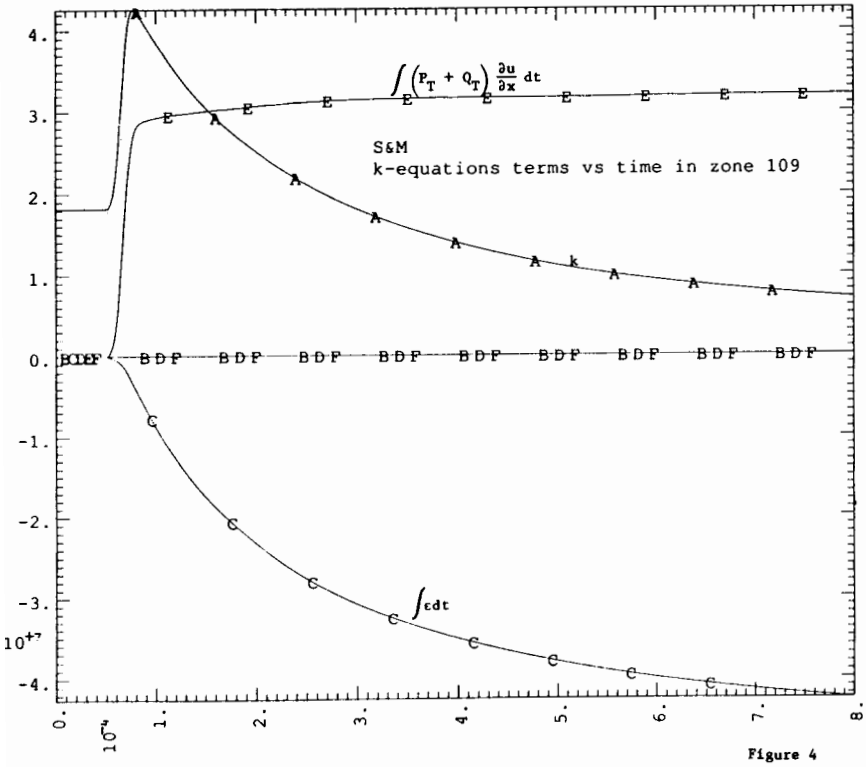

Figure 4

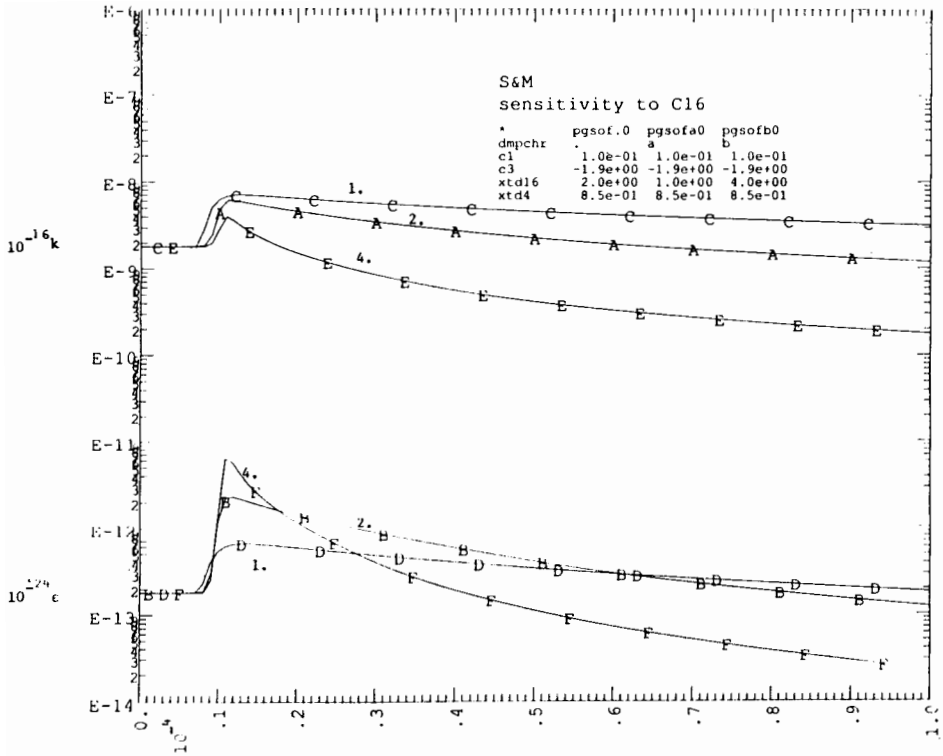

Figure 5

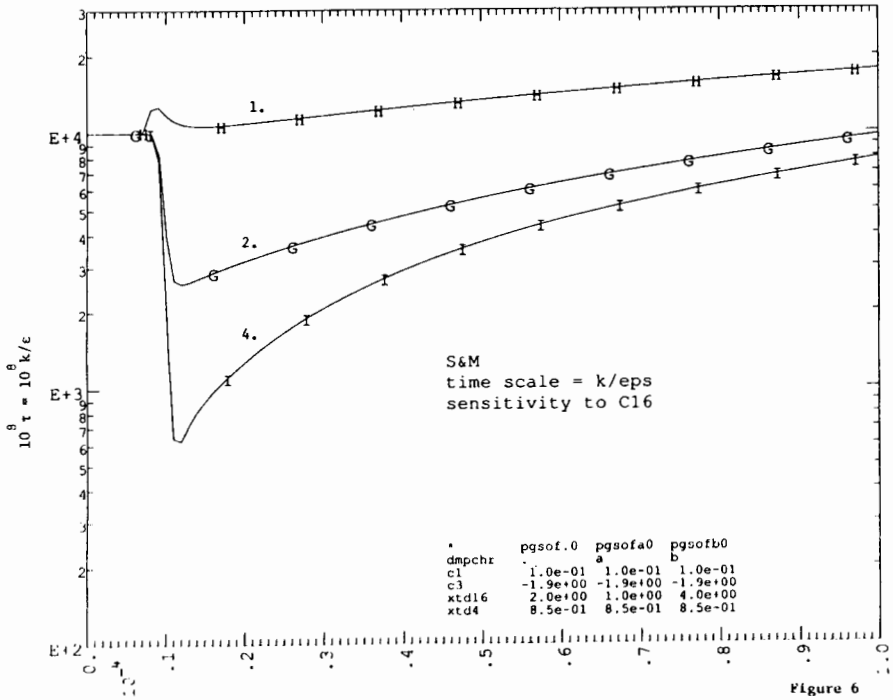

Figure 6

16° wedge, the normal compression is 2.1, and Figure 7 suggests that a choice of 2 for C16 is not unreasonable.

Figure 8 shows k and ε vs time in zone 109 for the 16° wedge (dashed line) and for the 8° wedge (solid line). For these model parameters, we see no growth in the 8° wedge case which seems to agree with experiment.

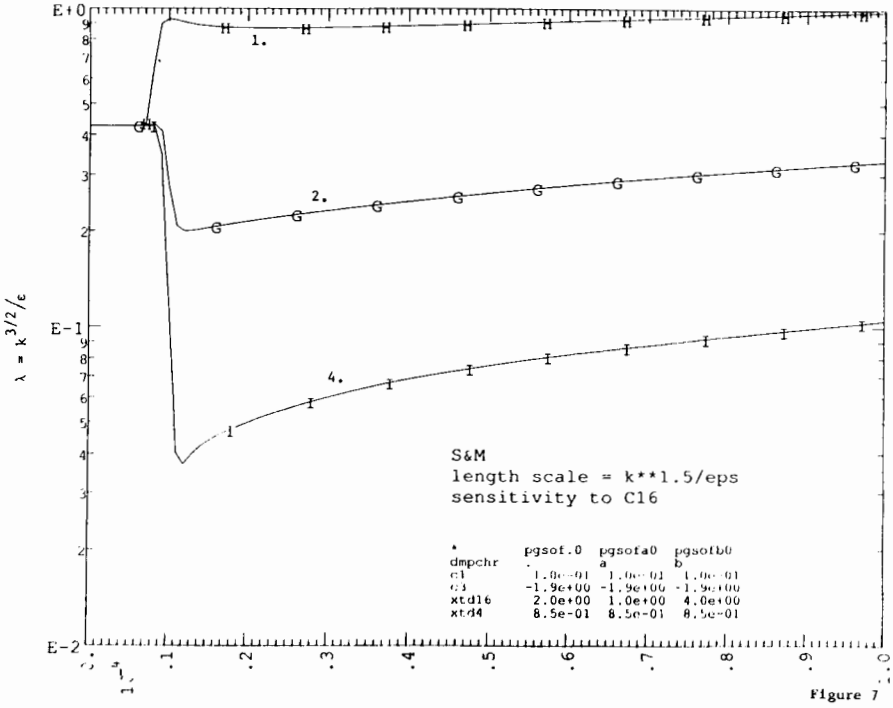

Figure 7

Figure 9 shows k, P_T and Q_T vs time in zone 109 for the 16° wedge (P_T and Q_T have both been multiplied by 100). We see that the process of turbulent energy generation is initiated by an almost delta-function Q_T.

ANALYTIC SOLUTION

From the numerical solutions we see that the dominant terms are turbulent work, dissipation, and the time derivative. Ignoring other terms, the equations become

$$\frac{dk}{dt} = -Ak + Bk^2/\varepsilon - D\varepsilon$$

$$\frac{d\varepsilon}{dt} = -\alpha\varepsilon + \beta k - \gamma\varepsilon^2/k$$

and the ratio produces an homogeneous equation of degree 3. We change variables, $k = \tau\varepsilon$ and obtain

$$\frac{d\varepsilon}{\varepsilon} = \frac{(\gamma + \alpha\tau - \beta\tau^2)d\tau}{(D-\gamma)\tau + (A-\alpha)\tau^2 - (B-\beta)\tau^3}$$

This equation is integrated to give

$$\varepsilon(\tau) = \varepsilon_0 f(\tau)/f_0$$

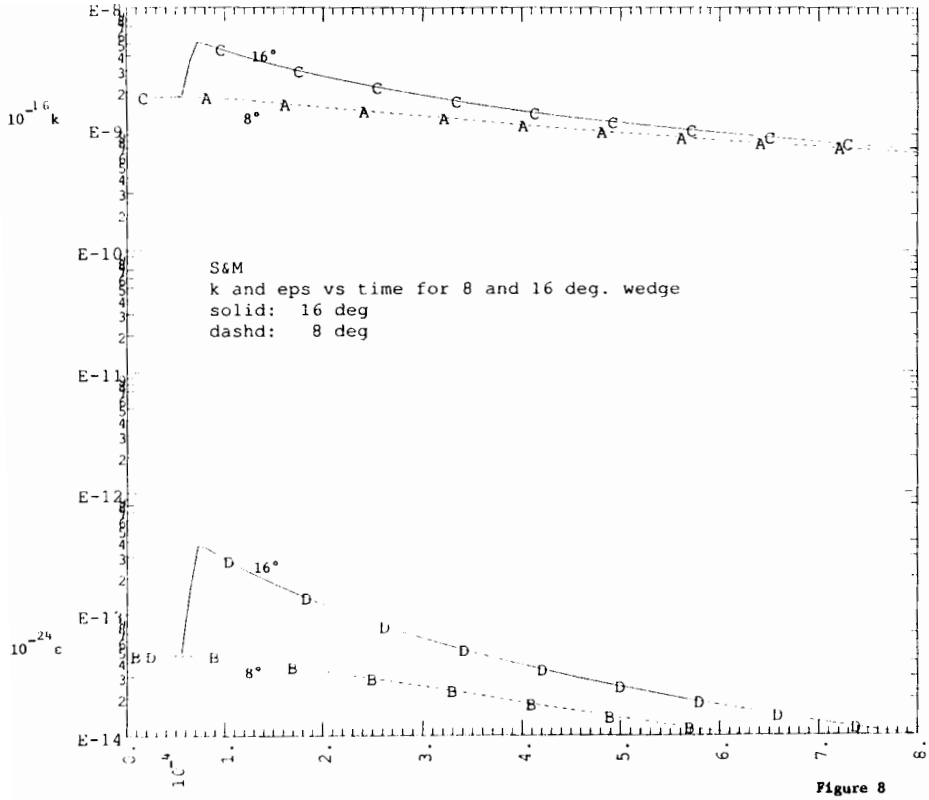

Figure 8

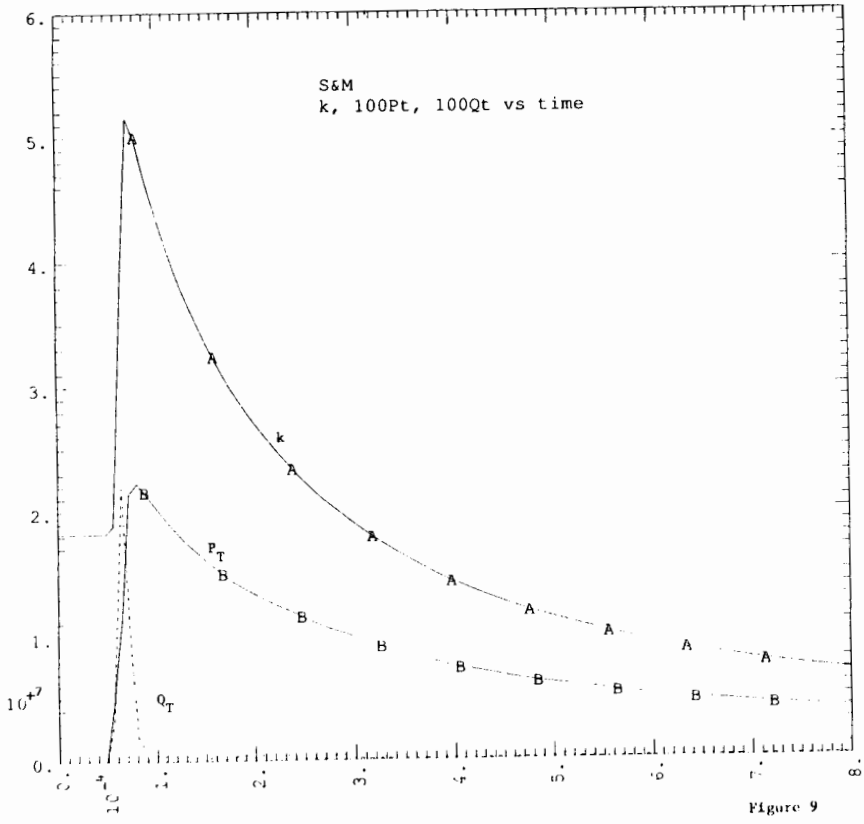

Figure 9

where

$$f(\tau) = \tau^{E2} X^{-E3} \left(\frac{2c\tau + b - \sqrt{-q}}{2c\tau + b + \sqrt{-q}} \right)^{E4}$$

For commonly used model constants (C_1 = 0.125, C_5 = 1.833, C_{13} = 0.7, C_{16} = 2) the three exponents evaluate to E2 = -2.2, E3 = -0.1, E4 = -1.6 and for large τ, we thus expect to find $\varepsilon \sim \tau^{-2}$ and $k \sim \tau^{-1}$

The equation for $d\varepsilon/\varepsilon$ is singular and we examine the behavior in this region. Setting the denominator to zero and substituting, we have

$$4C_1C_{13}\omega\tau_c = 1 \pm \sqrt{1 + 12C_1C_{13}\frac{1 - C_5}{1 - C_{16}}}$$

For the above model constants, this results in

$$\tau_c = \frac{1 \pm 1.369}{0.35\omega}$$

In a shock, ω $(=\partial u/\partial r) < 0$ and so $\omega\tau_C \sim 1$ and τ_C thus corresponds to the time scale of the shock. Estimating ω from the experiment, for the 16° wedge,

$$\frac{(3.14 - 1.49)\text{x}10^2}{0.1\text{x}10^{-2}} > \omega = \frac{\Delta u}{\Delta r} > \frac{(3.14 - 1.49)\text{x}10^2}{0.5\text{x}10^{-2}}$$

which gives a time scale between $6.6\text{x}10^{-6}$ and $33\text{x}10^{-6}$ sec, which is less than the FWHM of $4\text{x}10^{-4}$ sec observed by S&M but it is much greater than the time scale associated with a classical nonturbulent shock. The collisional mean-free-path in air is about 10^{-7} m and if the shock speed is 300 m/s, the characteristic classical shock time is about $3\text{x}10^{-10}$ sec. Thus the simplified model predicts a broadening of the shock wave due to turbulence by a factor of 10^5 or more.

ACKNOWLEDGMENTS

Thanks, and happy anniversary, Chuck.

APPENDIX A: 1D PROBLEM DEFINITION

For the 16° we take γ = 1.22 and a shock angle, σ = 33.0°. From these we have a normal Mach number M_{1n} = 1.55, $\rho_2 = 2.107\rho_1$, $p_2 = 2.539p_1$. S&M provide upstream conditions of stagnation pressure = $6.9\text{x}10^5 N/m^2$ = 6.9atm, Mach number = 2.85, reference velocity = V_1 = 576m/s. These conditions and gamma provide p_1 = 1.174atm, ρ_1 = 3.45e-3 and V_{1n} =

314m/s.For the shocked gas, p_2 = 2.9808atm, ρ_2 = 7.269e-3g/cc and V_{2n} = 149m/s.

To simulate this situation on a Lagrangian code, we subtract V_{1n} from all velocities so that the shock is moving into quiet turbulent gas. With $u = V - V_{1n}$, we have $u_1 = 0$, $u_2 = -165$, and the shock speed is $S = \rho_2 u_2/(\rho_2-\rho_1) = 314$.

The 8° wedge has a somewhat ambiguous shock angle. We somewhat arbitrarily choose M_{1n} = 1.1 which then gives a shock angle of 22.7°. For EOS purposes, we choose γ = 1.22. The upstream conditions are: p_1 = 1.174atm, ρ_1 = 3.45e-3g/cc and V_{1n} = 222m/s. The jump conditions are: $\rho_2 = 1.185\rho_1$, $p_2 = 1.231p_1$. For the shocked gas, p_2 = 1.445atm, ρ_2 = 4.088e-3 and V_{2n} = 187. Subtracting, $u_2 = V_{2n} - V_{1n} = -34.6$, and we have a shock velocity of 222m/s.

REFERENCES

[1] Leith, C. E.,1988: personal notes.

[2] Leith, C. E.,1986: "Two-Equation Turbulent Mix Model",.UCRL 96036.

[3] Crowley, B.K.,1967: "An 'Almost-Lagrangian' gasdynamic calculation for pipe flows with mass entrainment", J. Comp. Physics, **7**, 61-86

[4] Smits, A.J., and K.-C. Muck, 1987: "Experimental study of three shock wave/turbulent boundary layer interactions", J. Fluid Mech., **182**, 291-314.

[5] Von Neumann, J. and R. D. Richtmyer, 1957: "A Method for the Numerical Calculation of Hydrodynamic Shocks", J. Appl. Phys., **21**, 232

[6] Settles, G.S., T.J. Fitzpatrick and S.M. Bogdonoff, 1979: "Detailed Study of Attached and Separated Compression Corner Flowfields in High Reynolds Number Supersonic Flow", AIAA J., **17**, 579-585.

A Numerical Study of Inviscid, Supersonic Mixing Layers*

Scott Eberhardt,† James J. Riley,‡ Moeljo Soetrisno,§ and Jeffrey A. Greenough¶
University of Washington, Seattle, Washington

Abstract

The purpose of this research is to understand the physical processes associated with turbulent mixing in supersonic shear layers. Specifically, the evolution of instabilities in two and three-dimensional, confined and unconfined, temporal shear layers are studied. Both linear stability theory and direct numerical simulation are used. For the two-dimensional, supersonic, confined layer, two distinct modes of instability are found, a symmetric and an asymmetric mode. In both cases the instability grows nonlinearly with large amplitude disturbances that never roll up like the classical Kelvin-Helmholtz instability. Another mode of instability is found for the confined, transonic layer where a higher mode is excited from a nonlinear interaction of the walls with the fundamental mode. The most unstable modes for the three-dimensional layer at supersonic relative Mach numbers is purely three-dimensional, i.e. oblique to the flow direction.

Introduction

Efficient supersonic mixing is a key requirement in the development of supersonic combustion ramjets (Scramjets). To date, very little is understood about supersonic mixing except that supersonic flows are more stable than their subsonic counterparts. Only by understanding these flows can we expect to devise techniques to enhance the mixing in a supersonic mixing layer. In this study, an attempt is made to understand the behavior of two and three-dimensional supersonic shear layers.

Subsonic shear layers have been the focus of attention for many years. In 1974 a fundamental break-through was made when Brown and Roshko[1] discovered that the layer is partially composed of discrete, quasi-two-dimensional, organized structures. These structures are large and roll up in a coherent manner. Winant and Browand[2], also in 1974, showed that the growth of the layer is governed by the pairing mechanism of these structures.

What little that is known about supersonic shear layers has been learned in the last few years, particularly regarding the relationship of Mach number to growth. Brown and Roshko[1] showed that slower growth of supersonic mixing layers is not due to density effects alone, a departure from previous theories. Papamoschou and Roshko[3] introduced a "convective" Mach number, obtained by treating braids as stagnation points in the transverse flow, and found that compressibility effects dominate only above convective Mach numbers of about one. This result is at first startling since it implies that only the relative Mach number of the two layers determines the growth rate. However, if one does a Galilean transformation to follow the vortex structures at their average speed the relationship to convective Mach number makes more sense.

In the case of the confined mixing layer no experimental studies have been performed to correlate confinement with shear-layer growth. On the theoretical side, Tam and Wu[4] recently reported on the linear stability of confined,

*This research is supported by the Office of Naval Research under Contract No. N00014-87-K-0174
†Assistant Professor, Department of Aeronautics and Astronautics.
‡Professor, Department of Mechanical Engineering.
§Graduate Research Assistant, Department of Aeronautics and Astronautics.
¶Graduate Research Assistant, Department of Applied Mathematics

three-dimensional, spatially developing shear layers. His conclusions are that in a confined layer reflected Mach waves can interact such that perturbation growth is reinforced. An interpretation of this is that pressure fluctuations can be brought out of phase with the disturbance, as is natural in subsonic flows, if the reflected pressure waves are out of phase. This interesting result is also found in this study and is reported in Greenough, et al.[5].

The Galilean transformation into a moving frame of reference can be a convenient tool. Then, the time history of a single structure can be traced from its creation (see fig. 1). If one simplifies further and assumes the structure is periodic, i.e. it exists in equal magnitude ahead and behind, then the problem reverts to that of a temporally growing shear layer. The temporal shear layer is much simpler to study since boundary conditions are simplified and computational requirements are reduced significantly. In this study the two and three-dimensional temporal shear layers are studied in both subsonic and supersonic flows.

Linear stability analysis for the two-dimensional, unbounded inviscid, compressible, vortex sheet has been studied by Landau[6], Hatanaka[7], and Pai[8]. All three arrived at the important result that, for identical streams of fluid, the layer would remain stable above a relative Mach number of $\sqrt{8}$. Note that this Mach number is the Mach number difference across the layer, which implies that the streams have a Mach number of $\pm\sqrt{2}$. This is in contrast to the convective Mach number which, for identical gases in both streams, is one-half of the relative Mach number. Miles[9] confirmed the result and, by solving the eigenvalue problem, found that below $M = \sqrt{8}$ there is at most one unstable mode. Extensions to continuous velocity profiles have been made by Blumen[10], Blumen et al.[11], and Drazin et al.[12]. The three papers introduce three modes of instability, the first corresponding to Miles result. A second instability appears which is actually a pair of modes with equal and opposite signed phase speeds. This instability, however, is an order-of-magnitude smaller than the first. The paper by Drazin et al. identifies yet a third instability which provides a complicated picture of stability of the unbounded mixing layer. The important result, however, is that for any Mach number there exists unstable modes, although their growth rates may be extremely small.

Linear stability analysis and direct simulations of the Euler equations are both used to investigate compressibility effects on shear layers. The stability analysis is used as a guide to the types of instabilities possible, their initial characteristics, etc., to provide comparisons for initial linear growth rates and to provide appropriate eigenfunctions for starting the nonlinear, numerical simulations of the confined layers. The direct numerical simulations give the nonlinear development after the initial linear growth. The simulations are performed for both the bounded and the unbounded case.

Discussion

The numerical simulations make use of the two or three-dimensional, non-steady Euler equations governing the motion of inviscid, non heat-conducting gases. The two-dimensional Euler equations in cartesian coordinates are written

$$\frac{\partial Q}{\partial t} + \frac{\partial F}{\partial x} + \frac{\partial G}{\partial y} = 0$$

where,

$$Q = \begin{pmatrix} \rho \\ \rho u \\ \rho v \\ e \end{pmatrix}; \qquad F = \begin{pmatrix} \rho u \\ \rho u^2 + p \\ \rho uv \\ u\,(e+p) \end{pmatrix}$$

$$G = \begin{pmatrix} \rho v \\ \rho uv \\ \rho v^2 + p \\ v\,(e+p) \end{pmatrix}$$

$$e = \rho\varepsilon + \frac{1}{2}\rho\left(u^2 + v^2\right)$$

where, ϵ is the internal energy per unit mass, e is the total energy per unit volume and the pressure p is determined from the Equation of State

$$p = (\gamma - 1)\left(e - \frac{1}{2}\rho(u^2 + v^2)\right).$$

In three-dimensions a z-component is added to the fluxes and a fifth, z-momentum, equation is added.

The equations are normalized, as in Soetrisno et al.[13], for simplification and lead to new variables defined by

$$x^* = \frac{x}{\theta} \qquad y^* = \frac{y}{\theta} \qquad \rho^* = \frac{\rho}{\rho_\infty}$$

$$u^* = \frac{u}{c_\infty} \qquad v^* = \frac{v}{c_\infty} \qquad p^* = \frac{p}{\rho_\infty c_\infty^2}$$

$$e^* = \frac{e}{\rho_\infty c_\infty^2} \qquad t^* = \frac{t}{\frac{\theta}{c_\infty}}$$

$$\theta = \int_{y_1}^{y_2} |\frac{2\bar{u}}{M}| \left(1 - |\frac{2\bar{u}}{M}|\right) dy$$

$$M = \frac{\sqrt{(\bar{u}_1^2 + \bar{v}_1^2)}}{c_\infty} - \frac{\sqrt{(\bar{u}_2^2 + \bar{v}_2^2)}}{c_\infty}$$

where M is the Mach number difference between the two stream, c is the sonic velocity and θ is here taken to be the momentum thickness of the initial mixing layer. $\bar{u}$ is the averaged streamwise velocity. Since the two streams are identical gases, the $(\,)_\infty$ values can be taken from either stream. Hereafter the superscript $(*)$ is dropped, and all variables used are assumed to be nondimensionalized variables.

Numerical Method

Studies of the large scale structure evolution in free-shear flows require a robust scheme with minimal diffusion. The Euler equations are cast in conservation law form so that any shock waves and contact surfaces are captured as part of the solution without special treatment. This work follows that of Soetrisno et al.[13] where the Yee, Warming and Harten[14] second-order, total variation diminishing (TVD) algorithm is used. The scheme is total variation diminishing in the nonlinear scalar and constant coefficient system cases, consistent with entropy inequality, and consistent with conservation laws. Since it is TVD, the algorithm guarantees not to generate spurious oscillations.

The only difference between this work and Soetrisno et. al.[13] is that a Cartesian form of the algorithm is used in this study. An explicit scheme is chosen to resolve the time evolution of the large scales in turbulent flow fields. A CFL number of 0.2 is used to insure numerical stability and to resolve the time evolution. The Yee, Warming and Harten scheme is second-order accurate in space and second-order accuracy for the time integration is obtained using a second-order Runge-Kutta method.

Note that during the course of the study comparisons have been made with spectral numerical calculations for shock-free flows and the results were nearly identical. Also, grid refinement studies for the temporal shear layer showed consistent results for grid resolutions 64×64 or greater. Comparisons of linear growth rates predicted from the simulations agree within a few percent to the linear stability analysis also adding to our confidence. Higher-order schemes are being studied to ensure that diffusion and dispersion are minimized, although we do not think that these factors have significant bearing on this particular study.

One reason for retaining the second-order TVD algorithm over the others we have tried is its efficiency. By solving the two-dimensional Euler equations in cartesian coordinates, rather than generalized coordinates, the memory requirement is reduced to 8 pieces of data and 297 calculations per grid point. Larger simulations are possible on our limited computational resources by using this efficient algorithm.

The mean flow for the two-dimensional simulations is initialized with the following properties,

$$\rho = 1; \qquad p = \frac{1}{\gamma}; \qquad \bar{v} = 0$$

$$\bar{u} = \frac{M}{2} tanh\left(\frac{y}{2\theta}\right)$$

where θ is the initial momentum thickness. The stagnation energy per unit volume, e, is calculated from p, ρ and u. No three-dimensional simulations have been completed to date.

The initial perturbation functions used for the confined layer are obtained from the linear stability solutions. The following section outlines the linear stability theory which is used to predict initial growth rates and to determine the correct, unstable, perturbation function. In general, the most unstable eigenfunction solution of the Rayleigh equation, together with the first subharmonic of this mode, are superimposed on the mean velocity profile.

Linear Stability Analysis

The linear stability analysis applied to the bounded, temporal layer is discussed in a paper by Greenough et al.[5]. Briefly, the continuous profile problem is solved for flow in a channel. The fluid is assumed to be inviscid, non heat-conducting, and adiabatic. The equations solved are thus the Euler equations given above except that the equation of state and energy are replaced by the isentropic relation

$$\frac{p}{\rho^{\gamma}} = constant.$$

The uniform flow conditions are perturbed and substituted into the governing equations. Linearizing these equations and assuming a normal mode formulation gives a system representing a nonlinear eigenvalue problem. The eigenvalue is the complex phase speed, $c_k = c_r + ic_i$. The problem is solved with a fourth-order Runge-Kutta shooting method coupled with a Newton-Raphson iteration. This procedure gives the flow field perturbations for both the two and three-dimensional simulations.

Perturbations for the two-dimensional, unbounded layer are of the form

$$u_j^p = A_1 u_f(y) cos\left[k(x+\theta)\right] + A_2 u_s(y) cos\left(\frac{1}{2}kx\right) \tag{1}$$

where $2\pi/k$ is the wavelength of the fundamental mode, θ is is the phase shift between the fundamental and subharmonic modes, u_f and u_s are chosen as the most unstable eigenfunctions for the given wavenumber and normalized to a maximum value of 1. A_1 and A_2 are the amplitudes of oscillation of the harmonics. These are chosen so that the disurbance is 1% of the mean flow energy for the numerical simulations when used to compare with the linear analysis and is 10% when the simulations are used to explore the nonlinear behavior. The fundamental mode wavelength, the wavenumber, k, and the amplitudes are given as solutions to the eigenvalue problem for the stability theory. The wave number chosen can be the one found by the eigenvalue problem for fastest intial growth, or any other wave number (e.g. 1) of interest.

2D Results – Unbounded

Numerous numerical simulations of the unbounded shear layer have been performed. Much of this work was recently presented in a paper by Soetrisno et al.[13]. Figure 2 shows the predicted growth rate of the unbounded shear layer as a function of relative Mach number for a fixed wavelength. As predicted by Miles[9] the layer is stable above a relative Mach number of $\sqrt{8}$. Figure 3 is a contour plot of spanwise vorticity after pairing for a $M = 0.5$ layer. The behavior of the vortices is essentially the same as for the incompressible, unbounded layer.

The higher Mach number cases, however, show quite different results. Soetrisno performed calculations for many relative Mach numbers and found that, as the relative Mach number increases, the vortices become more elongated along the streamwise axis. Figure 4 shows the vorticity contours for a simulation at a relative Mach number of 2.25. The layer evenually rolls up but at a much slower rate than the lower Mach numbers. In Soetrisno's calculations the growth stops for layers with relative Mach numbers of about $\sqrt{8}$ and above.

2D Results – Bounded

The two-dimensional, bounded shear layer has introduced several interesting features not found in the unbounded case. In particular, additional unstable modes appear with relative Mach numbers above about 2. We call these modes "wall modes" and they have also been identified in a paper by Tam and Wu[4] for the three-dimensional spatially developing shear layer.

All the calculations presented in this paper on the two-dimensional, confined shear layer have a channel half-width 20 times the initial momentum thickness, i.e. $2d/\theta = 40$. Only symmetric channels, where the channel half-width above and below are equal, are presented here. (Results for asymmetric channels can be found in Greenough et al.[5])

The growth rates as a function of relative Mach number, with streamwise wavenumber $k = 1$, are shown in fig. 5. The most striking result is the additional peaks above a relative Mach number of 2. The series of peaks represent a reinforcing Mach wave system created by the initial perturbation. These Mach waves reflect off the walls and then interact with the perturbation to produce an instability.

Each of the peaks can be characterized as being either symmetric or asymmetric disturbances, where symmetry pertains to the magnitude of the pressure eigenfuction about the flow centerline. Also it should be noted that symmetry implies a zero real phase speed, i.e. there is no oscillation in time associated with the exponential linear growth. The asymmetric modes, therefore, travel in time since they have non zero real phase speed. With $k = 1$ fixed, both symmetric and asymmetric modes exist as alternating peaks beginning with the symmetric modes at the lowest Mach number. For symmetric channels, if only the most unstable disturbances for each Mach number are considered, the symmetric perturbations are the important ones. But, for a fixed wavenumber, k, there are some Mach numbers where the Mach wave system travels in order to give instability.

The direct numerical simulations have been performed on a variety of cases. However only three Mach numbers are considered here. Each case is for $k = 1$ and the predicted growth rates are shown on fig. 5. The first simulation is for a relative Mach number 1.5. We call this a transonic convective Mach number case. The transonic convective Mach number occurs when each stream is subsonic but is accelerated to supersonic speeds as the layer rolls up. Figure 6 shows the calculation during the nonlinear growth period. The layer is excited with only the fundamental mode, $k = 1$, yet a triplet of vortices begins to grow quickly. Spectral analysis shows that the three mode ($k = 3$) has been highly excited. This is a nonlinear self-excitation of the three mode and may provide interesting avenues of further study. These vortices ultimately aglomerate and the fundamental mode dominates. Clearly, there is an atypical energy cascade, with respect to incompressible temporal mixing layers, in that energy is seen to flow to small scales and then back to large scales. Note that since each stream is initially subsonic we believe the roll up is Kelvin-Helmholtz in nature instead of a wall-mode that relies on a system of Mach waves.

The cases for supersonic convective Mach numbers illustrate the physical significance of both symmetric and asymmetric disturbance wall modes. Figure 7 is a Mach 2.9 numerical simulation of an asymmetric mode and fig. 8 is a Mach 4.975 simulation of a symmetric mode. The basic evolution of the two types of modes is the same except that the asymmetric mode has a standing wave character in addition to the growth. The initial layer is seen to develop into a sawtooth-like pattern which ultimately fills the channel. There is no roll up behavior that we can

detect. Since the streams are supersonic shock waves form due to the flow deviation. In the Mach 4.975 case, these shock waves start obliquely and then become stronger as the layer grows. Eventually they become normal shocks at which time they dramatically pinch the layer which then proceeds to grow quickly 180° out of phase. At this time we are still unsure of why this unusual situation occurs.

3D Results

Linear stability analysis and direct simulations have also been performed for three-dimensional shear layers. There is significant doubt in the community that the large scale structures in a three-dimensional compressible shear layer are two-dimensional as in the incompressible counterpart. However, a Squire's theorem analogy for compressible flows can be made which says that any three-dimensional instability can be obtained from a two-dimensional problem at a reduced Mach number. The details of this analogy and its consequences are given in Greenough et al.[5]. The theorem says that an instability in three-dimensional flow oriented at angle θ in wave space from the streamwise, k, direction can be solved as a corresponding two-dimensional problem at Mach number $M\cos\theta$. Or, conversely, the two-dimensional problem can be solved and applied to any three-dimensional field by computing θ and using an inverse transformation. This result can be conveniently used when solving the three-dimensional eigenvalue problem. The results that illustrate and justify this approach will now be discussed.

Figure 9 is a contour plot of growth rates in k, l wavenumber space at Mach 0.5 for a bounded shear layer, where k is the streamwise wave number and l is the spanwise wave number. In this figure it is clear that the maximum growth rate occurs on the k axis which signifies that the primary instability is two-dimensional in nature. Thus we find that the compressible, but subsonic, case is similar to the incompressible case in how it transitions to turbulence.

Figure 10 is a contour plot for the Mach 1.5 confined, temporal layer. The peak has moved off of the k axis. This means that the primary instability leading to growth in a three-dimensional, supersonic shear layer is truely three-dimensional in nature. The peak, in fact, moves off of the k axis when the relative Mach number first becomes supersonic. This instability has the characteristics of a Kelvin-Helmholtz instability.

Lastly, fig. 11 shows yet a higher Mach number, well above the unbounded, two-dimensional limit of $\sqrt{8}$. This result at $M = 2.975$ shows that the maximum growth rate has moved significantly off the k axis. The fastest growing disturbance is now very oblique to the main, streamwise direction. The interesting feature to note in this plot are the regions of zero growth and the additional, local maximums at higher wave numbers in k. These correspond to the wall modes shown in the two-dimensional analysis. These wall modes have growth rates that are smaller in magnitude yet still of the same order as the fastest growing disturbances, which are Kelvin-Helmholtz at oblique angles. Therefore, in the three-dimensional layer wall modes should be explored since they might have interesting consequences.

Conclusions

Many new ideas and new presentations of old ideas have been presented in this paper. First, in the two-dimensional mixing layer some interesting, unexpected results are found. The transonic simulation shows self-excitation of the third harmonic and atypical energy tranfer. The "wall-modes," also found by Tam and Wu[4], have some fascinating features when they become nonlinear. The instabilities grow to fill the channel width but never give any indication that they will roll up. The "wall-modes" are either asymmetric, which gives a non zero phase speed, or symmetric, which gives zero phase speed for certain modes (e.g. $k = 1$) but are always symmetric when $k = kmax$, i.e. the wave number for maximum growth is used. In all cases the nonlinear simulations reproduce the linear results exactly but

develop the more interesting features during the nonlinear growth period.

The three-dimensional, linear stability analysis demonstrates that the primary instabilities are indeed three-dimensional for supersonic shear layers. These primary instabilities are of the Kelvin-Helmholtz type. In addition, the "wall-modes" appear as both two and three-dimensional instabilities.

The results shown in this paper are only a few of the cases run at the University of Washington. These specific cases are the most interesting and/or show the most typical characteristics of the problems tested. Numerical solutions of three-dimensional shear layers are important for studying the nonlinear growth of a layer after its initial linear growth.

References

[1] Brown, G. L., Roshko, A., "On Density Effects and Large Structure in Turbulent Mixing Layers," **J. Fluid Mech.**, vol.64, 1974, pp.775-816.

[2] Winant, C. D., Browand, F. K., "Vortex Pairing, the Mechanism of Turbulent Mixing Growth at Moderate Reynolds Number," **J. Fluid Mech.**, vol.63, 1974, pp.237-255.

[3] Papamoschou, D., Roshko, A., "Observations of Supersonic Free Shear Layers," AIAA-86-0162, 1986.

[4] Tam, C., Wu, F., "Instabilities of Supersonic Mixing Layers Inside a Rectangular Channel," **Proceedings of the First National Fluid Dynamics Congress**, (AIAA 88-3675) Cincinnatti, July 1988.

[5] Greenough, J. A., Riley, J. J., Soetrisno, M., Eberhardt, S., "The Effects of Walls on Compressible Mixing Layer," AIAA-89-0372, Jan. 1989.

[6] Landau, L., C. R. Acad. Sci. USSR., Vol 44, 1944.

[7] Hatanaka, H., **J. Soc. Sci. Culture**, Vol 2, 1949.

[8] Pai, S. I., **J. Aero. Sci.**, Vol 18, 1951.

[9] Miles, J., "On the Disturbed Mothion of a Plane Vortex Sheet," **J. Fluid Mech.**, vol.4, part 5, 1958, pp. 538-551.

[10] Blumen, W., "Shear Layer Instability of an Inviscid Compressible Fluid," **J. Fluid Mech.**, vol.40, part 4, 1970, pp.769-781.

[11] Blumen, W., Drazin, P. G., Billings, D. F., "Shear Layer Instability of an Inviscid Compressible Fluid. Part 2," **J. Fluid Mech.**, Vol 71, 1975, pp 305-316.

[12] Drazin, P. G., Davy, A., "Shear Layer Instability of an Inviscid Compressible Fluid. Part 3," **J. Fluid Mech.**, Vol 82, 1977, pp 255-260.

[13] Soetrisno, M, Eberhardt, S., Riley, J. J., McMurtry, P., "A Study of Inviscid, Supersonic Mixing Layers Using a Second-Order TVD Scheme," **Proceedings of the First National Fluid Dynamics Congress**, (AIAA 88-3676) Cincinnatti, July 1988.

[14] Yee, H. C., Warming, R. F., Harten, A., "Implicit Total Variation Diminishing (TVD) Schemes for Steady State Calculations." **J. of Comp. Phys.**, vol.57, 1984, pp.327-360.

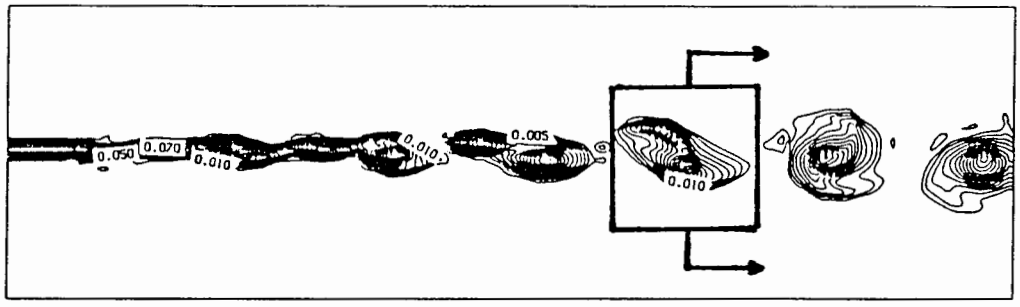

Fig. 1. Relationship of spatial and temporal shear layers.

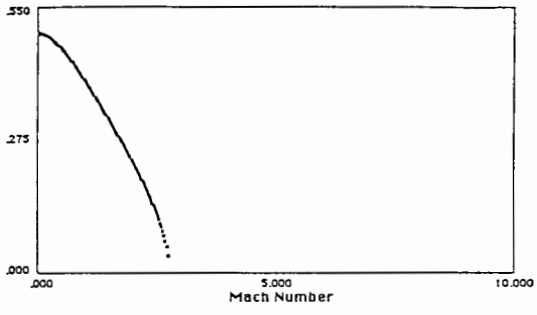

Fig. 2. Growth rate verses Mach number for unbounded vortex sheet.

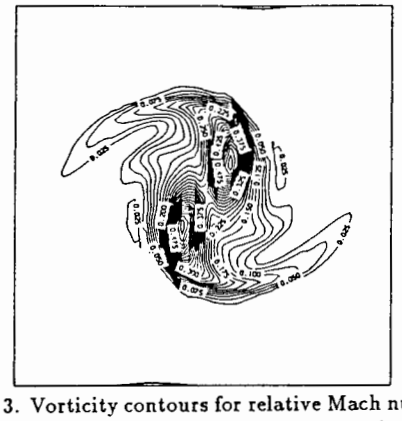

Fig. 3. Vorticity contours for relative Mach number 0.5 at T = 22.5 for the unbounded temporal shear layer.

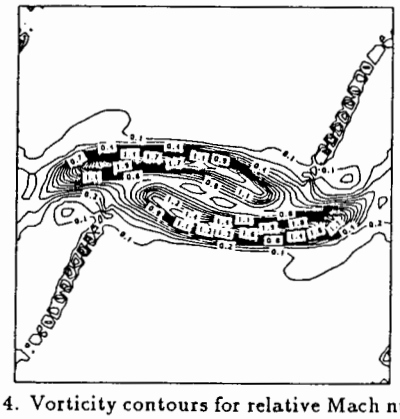

Fig. 4. Vorticity contours for relative Mach number 2.25 at T = 22.5 for the unbounded temporal shear layer.

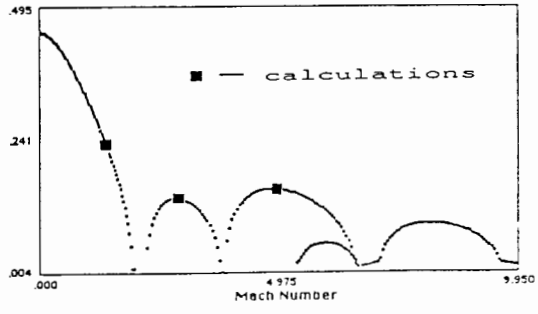

Fig. 5. Growth rate verses Mach number for a symmetric channel with $\frac{d}{\theta} = 40$.

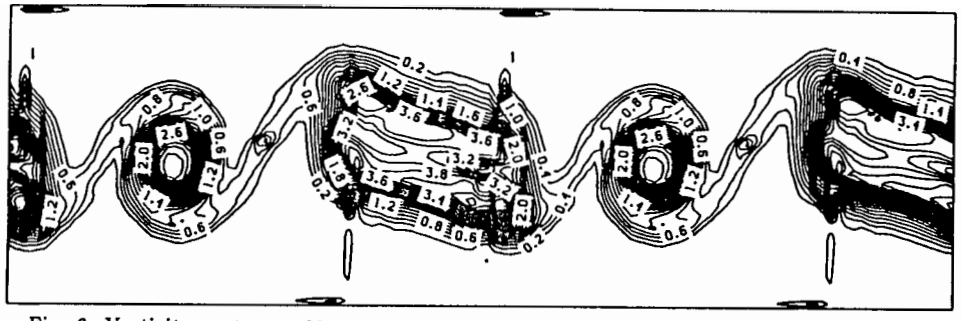

Fig. 6. Vorticity contours of bounded layer at $M = 1.5$ showing "three-mode" instability.

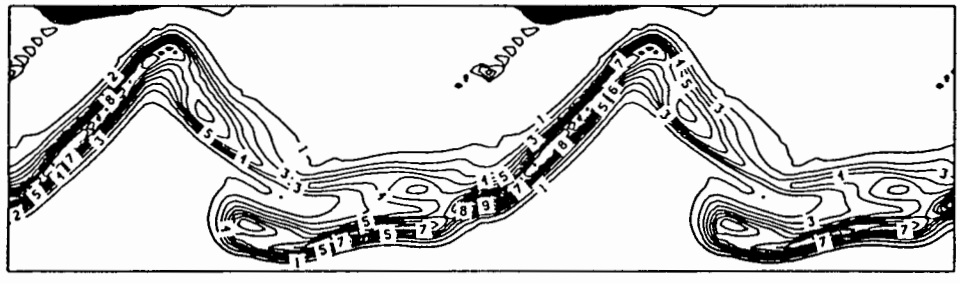

Fig. 7. Vorticity contours of bounded layer at $M = 2.9$ showing the growth of an asymmetric wall mode.

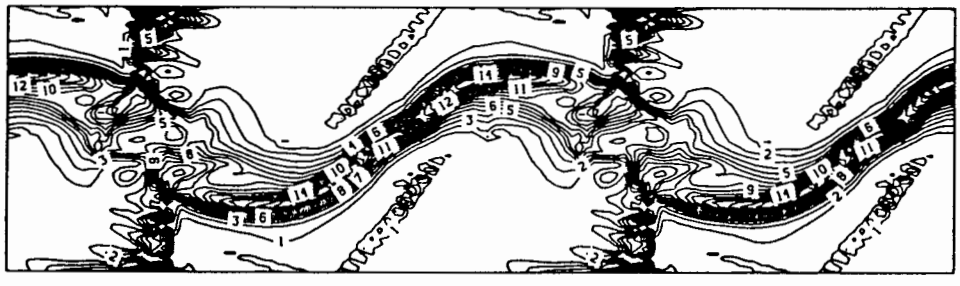

Fig. 8. Vorticity contours of bounded layer at $M = 4.975$ showing the growth of a symmetric wall mode just as the shock waves pinch the layer.

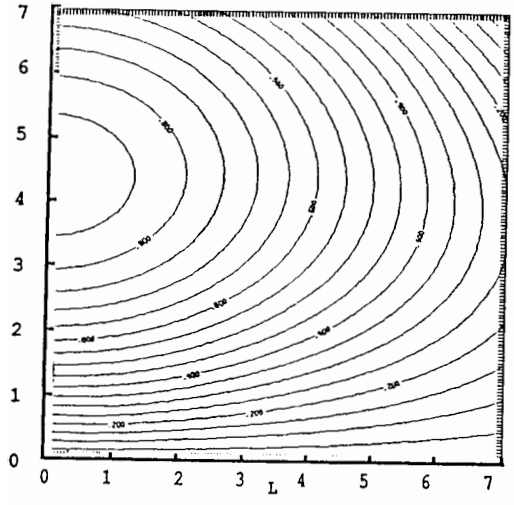

Fig. 9. Growth rate contours in $k - l$ space at relative Mach number 0.5.

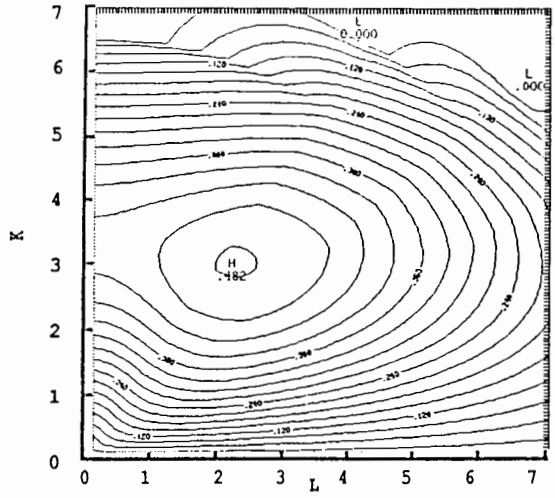

Fig. 10. Growth rate contours in $k - l$ space at relative Mach number 1.5.

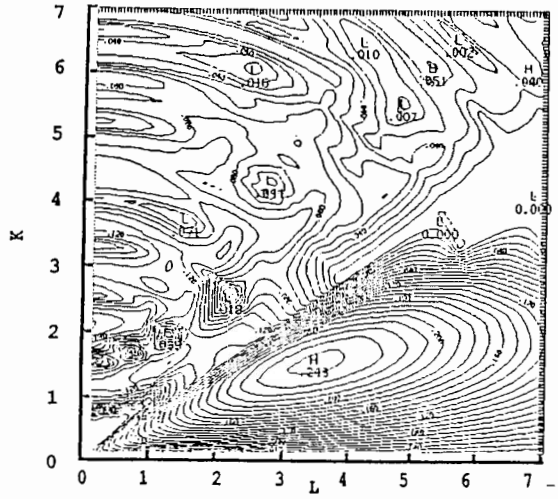

Fig. 11. Growth rate contours in $k - l$ space at relative Mach number 2.975.

SIMULATION OF SHOCK AND VORTEX INTERACTIONS

Janet L. Ellzey* and Elaine S. Oran
Laboratory for Computational Physics and Fluid Dynamics
Naval Research Laboratory
Washington, D.C. 20375

I. Introduction

Previous experimental and theoretical studies have shown that unstable subsonic shear layers evolve into a pattern of large-scale vortices which engulf fluid as they rotate in the flow field. In many cases, these large vortices break down even further due to conditions in the flow that allow new instabilities to develop. This convective mixing process is particularly important in combustors in which ignition of the premixed gases depends upon adequate mixing of the hot and cold fluids. In supersonic mixing layers, the structure of the shear layer can resemble what we see in subsonic mixing layers if the relative Mach number between the two layers is subsonic. However, the presence of shock waves may have a significant effect on the vortices and on the large-scale mixing process.

Both experimental and numerical studies on the effect of a shock on the mixing process have been conducted previously. Andronov et al. (1,2) measured the turbulent mixing zone between two gases of different density and showed that the width of the mixing zone increases rapidly after the passage of a shock. Numerical simulations of a shock passing over a single low-density bubble (3) show that vorticity is generated at the boundary of the bubble and rolls up into a vortex filament pair. This agrees with experimental observations of a shock wave interacting with a flame (4) and with a gas inhomogeneity (5). Passot and Pouquet simulated a shock passing through a turbulent field and suggest that the individual vortices may be flattened by the shocks, vortices may be formed behind the shock, or vortices may be formed in strong colliding shocks (6).

In this paper, we present numerical simulations of a single element of the mixing process: the interactions between a shock and a single vortex representative of those found in mixing layers. The effects on two vortices of different strengths will be examined.

II. Numerical Model and Method

$$\frac{\partial \rho}{\partial t} + \nabla \cdot \left(\rho \vec{V}\right) = 0 \tag{1}$$

$$\frac{\partial \rho \vec{V}}{\partial t} + \nabla \cdot \left(\rho \vec{V} \vec{V}\right) = -\nabla P \tag{2}$$

* Berkeley Research Associates, Springfield, VA

$$\frac{\partial E}{\partial t} + \nabla \cdot \left(E\vec{V}\right) = -\nabla \cdot P\vec{V} \tag{3}$$

These equations are solved assuming that the gases obey the thermal equation of state,

$$P = nkT \tag{5}$$

and that the relation between internal energy, e, and pressure, P, is given by

$$e = \frac{P}{\gamma - 1} \, . \tag{6}$$

This set of equations is rewritten in terms of finite-difference approximations on an Eulerian mesh. The solution to the convection of conserved quantities is obtained with the Flux-Corrected Transport (FCT) algorithm which is an explicit, finite-difference algorithm with fourth-order phase accuracy. FCT has been used extensively in supersonic flows, and has shown excellent agreement with theory and experiment (7).

The geometry for the simulations is shown at the top of Figure 1. The inflow conditions on the left are determined from the normal shock relations. The top, bottom, and right boundaries are reflecting. In each simulation, the shock propagates from the left boundary to the right and then reflects off the wall. The shock Mach number is 1.5 and the pressure ratio across the shock is 2.45. The fluid velocity behind the shock is 236 m/s.

A vortex is initialized on the left side of the computational domain. The velocity field consists of two regions: an inner region where the velocity is described by solid body rotation of the form

$$v(r) = \frac{v_{max}}{r_1} r \, , \tag{7}$$

and an outer region where the velocity decays to zero according to

$$v(r) = Ar + \frac{B}{r} \, . \tag{8}$$

where v_{max} is the maximum velocity, occuring at $r = r_1$, and equals 10 m/s or 236 m/s for the two cases presented in this paper. Constants A and B are chosen such that the velocity matches that determined by equation 7 at $r = r_1$ and decays to zero at $r = r_2$. The inner radius, r_1, equals 0.75 cm and the outer radius, r_2, equals 1.75 cm. Test runs with different inner and outer radii did not reveal qualitatively different behavior.

III. Results

Weak Vortex

Figure 1 shows a sequence of pressure and vorticity distributions for a shock with a pressure ratio of 2.45 passing over a vortex with $v_{max} = 10$ m/s. The shock is not visibly deformed by the interaction at $t = 0.06$ ms, but the vorticity is significantly redistributed.

The maximum vorticity has increased by a factor about 2.5 from its initial value at $t = 0$ to its value immediately after the shock interaction at $t = 0.06$ The vortex is compressed into an ellipse and is convected with the flow behind the shock until $t = 0.26$ m/s. The shock reflects off the right wall and passes over the vortex again at $t = 0.29$ ms, bringing the background flow velocity to zero and increasing the maximum vorticity by about 30%. The vortex then continues to rotate by stopes moving across the system.

Figure 2a shows v_y along the centerline of the domain. Initially, at the centerline $v_x = 0$ and $v_y = v_{max}$. At $t = 0.06$ ms the shock is passing over the vortex and increases the maximum velocity to approximately 1.5 times v_{max}. The line connecting v_{max} with $-v_{max}$ remains straight during and after the shock passes indicating that the core is behaving as a rotating solid body with v proportional to r, but the inner radius has been decreased due to the compression of the vortex. The maximum velocity decays after the shock has passed and is approximately 1.2 times its original value. Figure 2b is the same as Figure 3a except that more time steps have been plotted. This clearly shows the initial amplification of the maximum velocity at $t = 0.06$ ms. Between 0.09 ms and 0.26 ms, the vortex is convected with the flow but the maximum velocity and the shape of the profile does not change. At $t = 0.29$ ms, the reflected shock passes over the vortex a second time and the maximum (negative) velocity increases by a factor of 1.3 but rapidly decays.

Very Strong Vortex

The final simulation shows the interaction of a shock with a very strong vortex. In this case, the maximum rotational velocity of the vortex is equal to the velocity behind the shock. The pressure contours in Figure 3 show that the shock front is extremely distorted as it passes over the vortex at $t = 0.06$ ms. The vortex is rotating in a counter-clockwise direction, and the local velocity is decreased which retards the shock propagation on the upper half of the vortex. The pressure difference across the shock increases in this region; and the shock velocity increases due to the change in local conditions, returning the shock to a nearly planar front at $t = 0.15$ ms. The reverse process occurs on the lower half of the vortex, where the shock is initially accelerated. Comparison with the first simulation indicates that the shock velocity has not been significantly affected by the interaction. The reflected shock is distorted somewhat when it passes over the vortex.

The maximum vorticity increases again by a factor of approximately 2.5 after the shock passes the vortex at $t = 0.09$ ms. The vortex is compressed into an ellipse and rotates about its axis until the shock passes it again at $t = 0.26$ ms where there is another 60% increase in maximum vorticity.

Figure 4 shows v_y along the centerline of the domain for several timesteps during the simulation. At $t = 0.06$ ms, the maximum velocity has increased by a factor of 1.2 which is less than that observed for the weak vortex. The maximum velocity decays rapidly and

then starts increasing again at $t = 0.15$ ms, but this is due to the rotation of the "elliptical" vortex. The velocity through the central core is linear with r, as for solid body rotation, but the velocity does not decrease as rapidly at $t = 0.15$ ms because the major axis of the ellipse is now aligned with the centerline and the fluid further from the center is moving faster.

IV. Conclusions

Our major conclusions are:

1. A shock passing through a vortex increases the rotation rate of the vortex and affects the weaker vortex more than the stronger vortex.
2. Either a strong or a weak vortex is compressed into an ellipse which then rotates about its central axis.
3. The shock front itself is not distorted by a weak vortex and is only temporarily distorted by a very strong vortex.

Acknowledgments

This work was sponsored by the Naval Research Laboratory through the Office of Naval Research and by the Defense Applied Research Projects Agency in the Applied and Computational Mathematics Program.

References

1. Andronov, V.A., Bakharkh, S.M., Meshkov, E.E., Mokhov, V.N., Nikiforov, V.V., Pevnitskii, A. V., and Tolshkmyakov, A. I., Turbulent Mixing at Contact Surface Accelerated by Shock Waves, *Sov. Phys. JETP*, vol. 44, no. 2, 424–427, 1976.
2. Andronov, V.A., Bakharkh, S.M., Meshkov, E.E., Nikiforov, V.V., Pevnitskii, A.V., and Tolshkmyakov, A. I., An Experimental Investigation and Numerical Modeling of Turbulent Mixing in One-Dimensional Flows, *Sov. Phys. Dokl.*, bf 27, 5, 393–396, 1982.
3. Picone, J.M., Oran, E.S., Boris, J.P., and Young Jr., T.R., Theory of vorticity Generation by Shock Wave and Flame Interactions, *Dynamics of Shock Waves, Explosions, and Detontation*, edited by J.R. Bowen, N. Manson, A.K. Oppenheim, and R.I. Soloukhin, Vol. 94 of Progress in Astronautics and Aeronautics, 1985.
4. Markstein, G.H., Experimental Studies of Flame-Front Instability, *Nonsteady Flame Propagation, AGARDograph No. 75*, Permagon Press, Oxford, 75–100, 1964.
5. Haas, J.F., and Sturtevant, B., Interaction of Weak Shock Waves with Cylindrical and Spherical Gas Inhomogeneities, *J. Fluid Mech.*, vol. 181, 41–76, 1987.
6. Passot, T., and Pouquet, A., Numerical Simulation of Compressible Homogeneous Flows in the Turbulent Regime, *J. Fluid Mech.* vol. 181, 441–466, 1987.
7. Oran, E.S., and Boris, J.P., *Numerical Simulation of Reactive Flow*, Elsevier, New York, 1987.

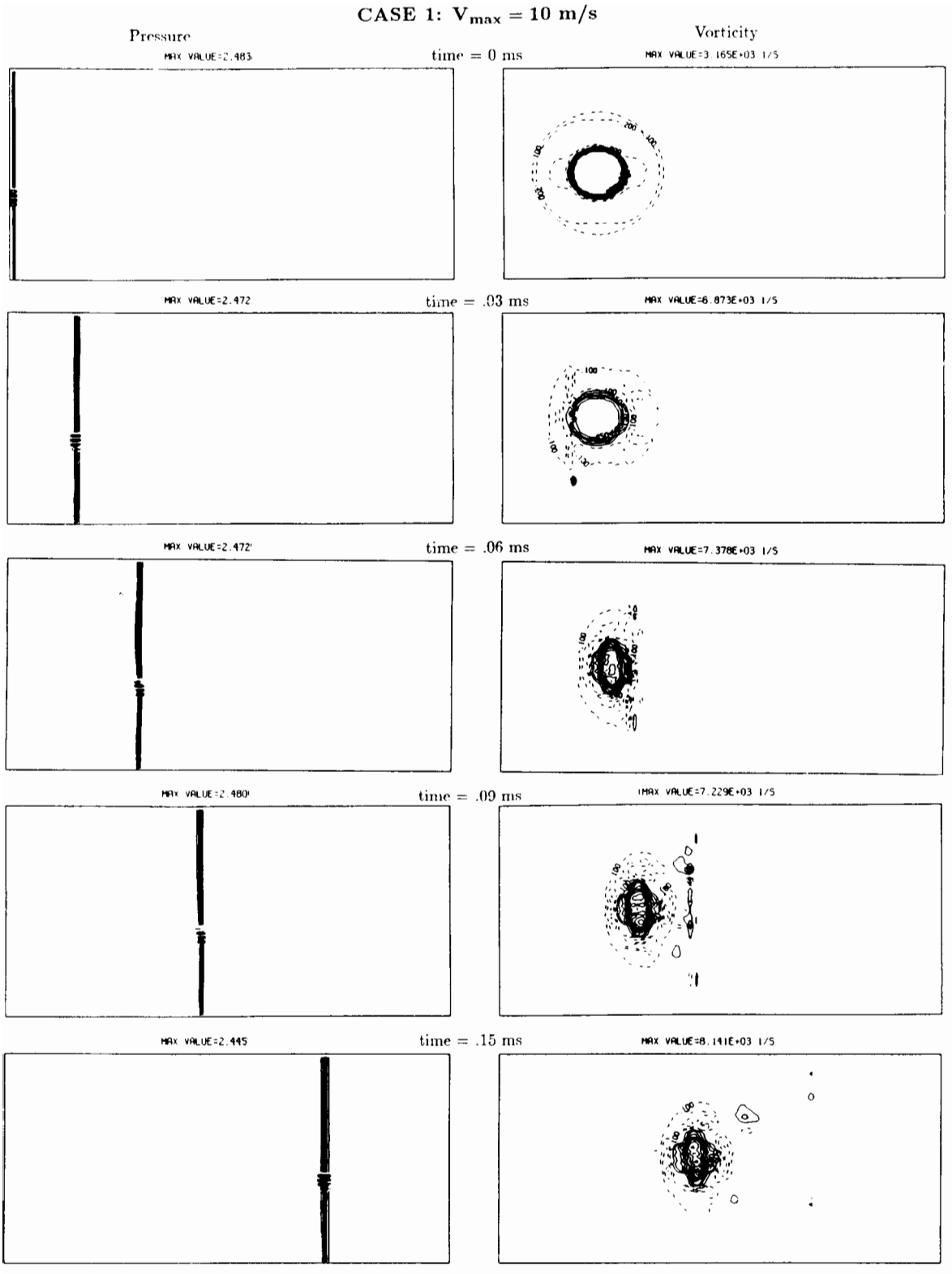

Figure 1. Contours of pressure difference, $(p - p_{atm})/p_{atm}$, and vorticity (1/s) for several time steps with $v_{max} = 10m/s$ (continued on next page).

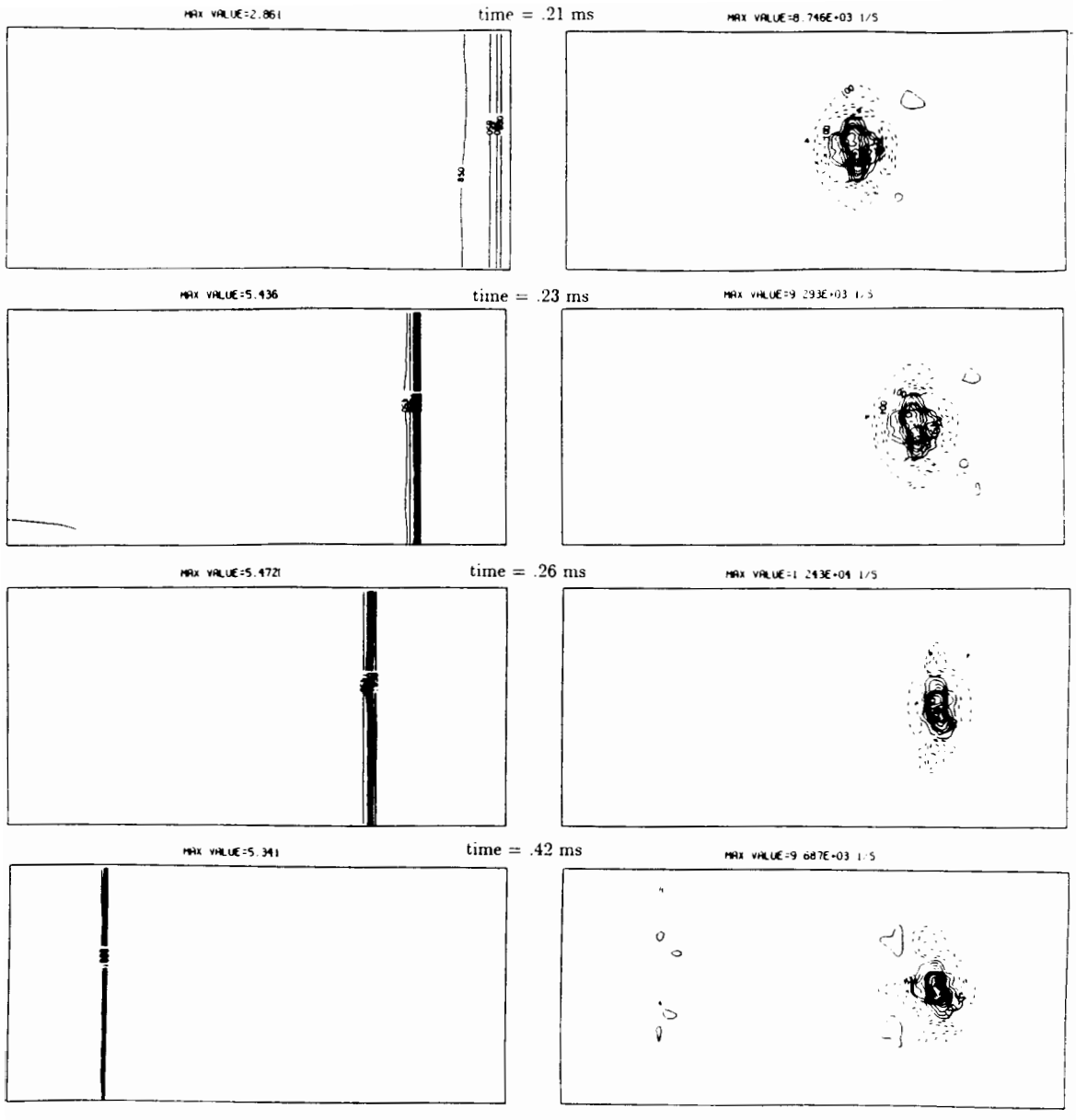

Figure 1. *(continued)*

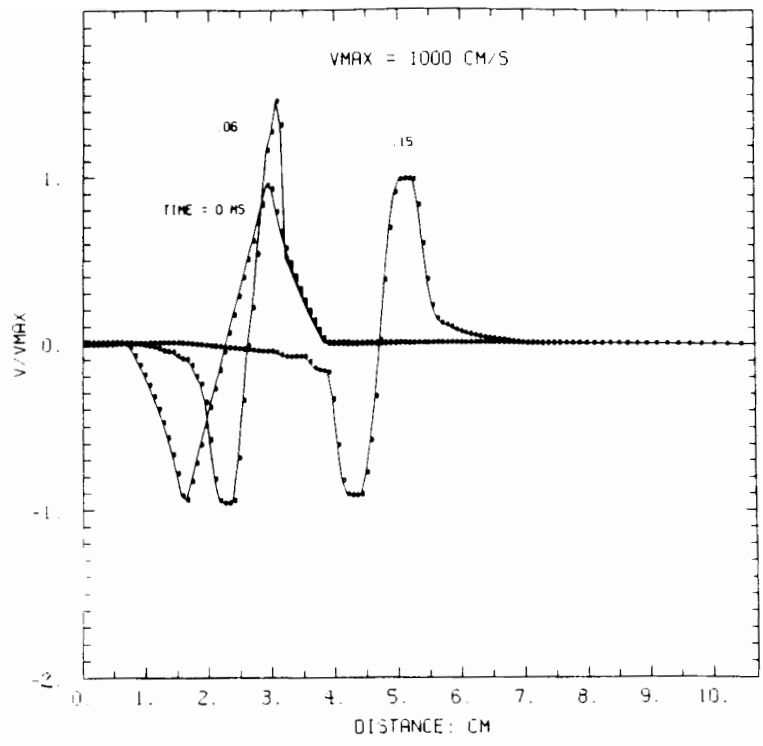

Figure 2a. v_y/v_{max} along centerline of domain for v_{max} = 10 m/s at t = 0.0, 0.06, 0.15 ms.

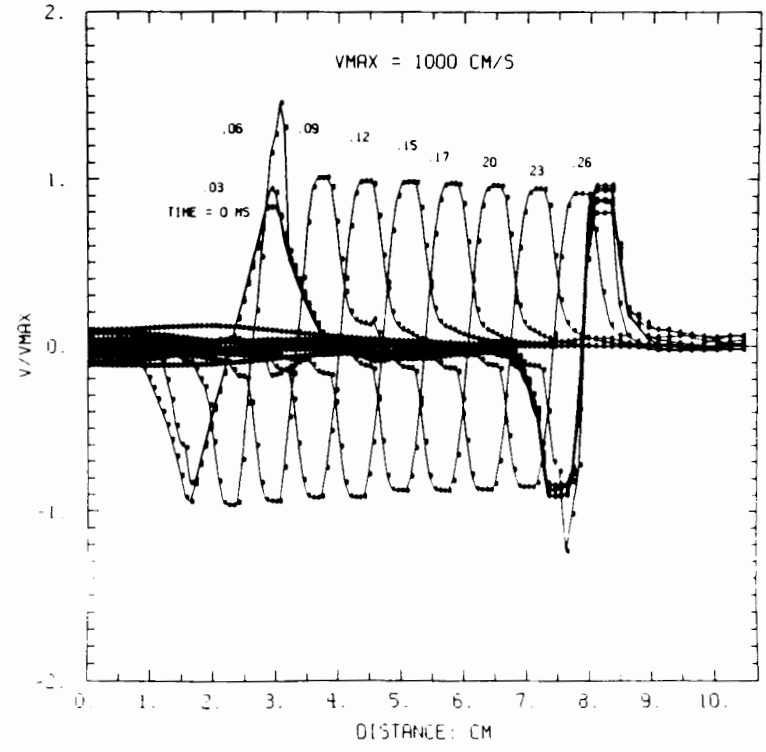

Figure 2b. v_y/v_{max} along centerline of domain for v_{max} = 10 m/s at several time steps.

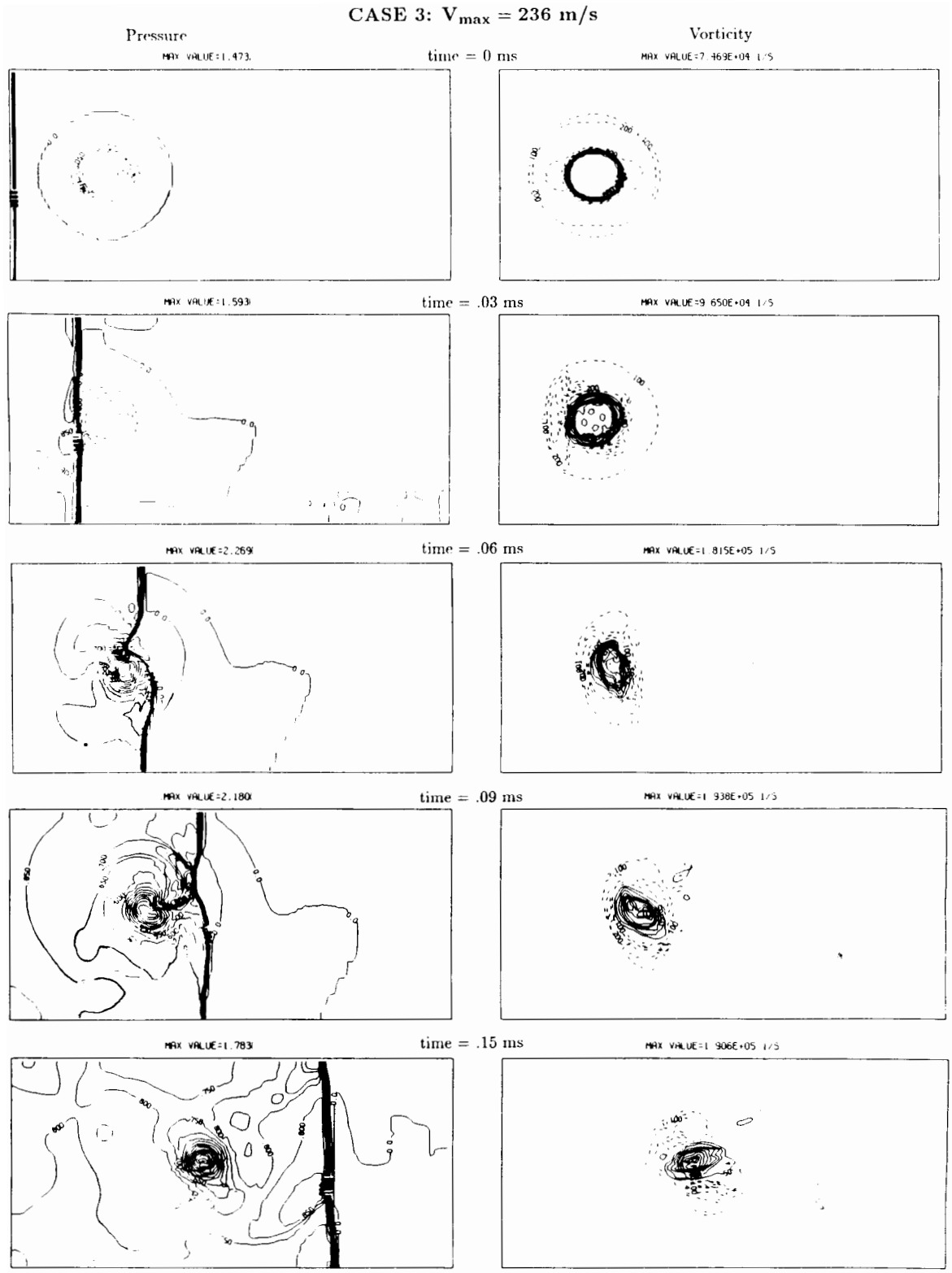

Figure 3. Contours of pressure difference, $(p - p_{atm})/p_{atm}$, and vorticity (1/s) for several time steps with v_{max} = 236 m/s (continued on next page).

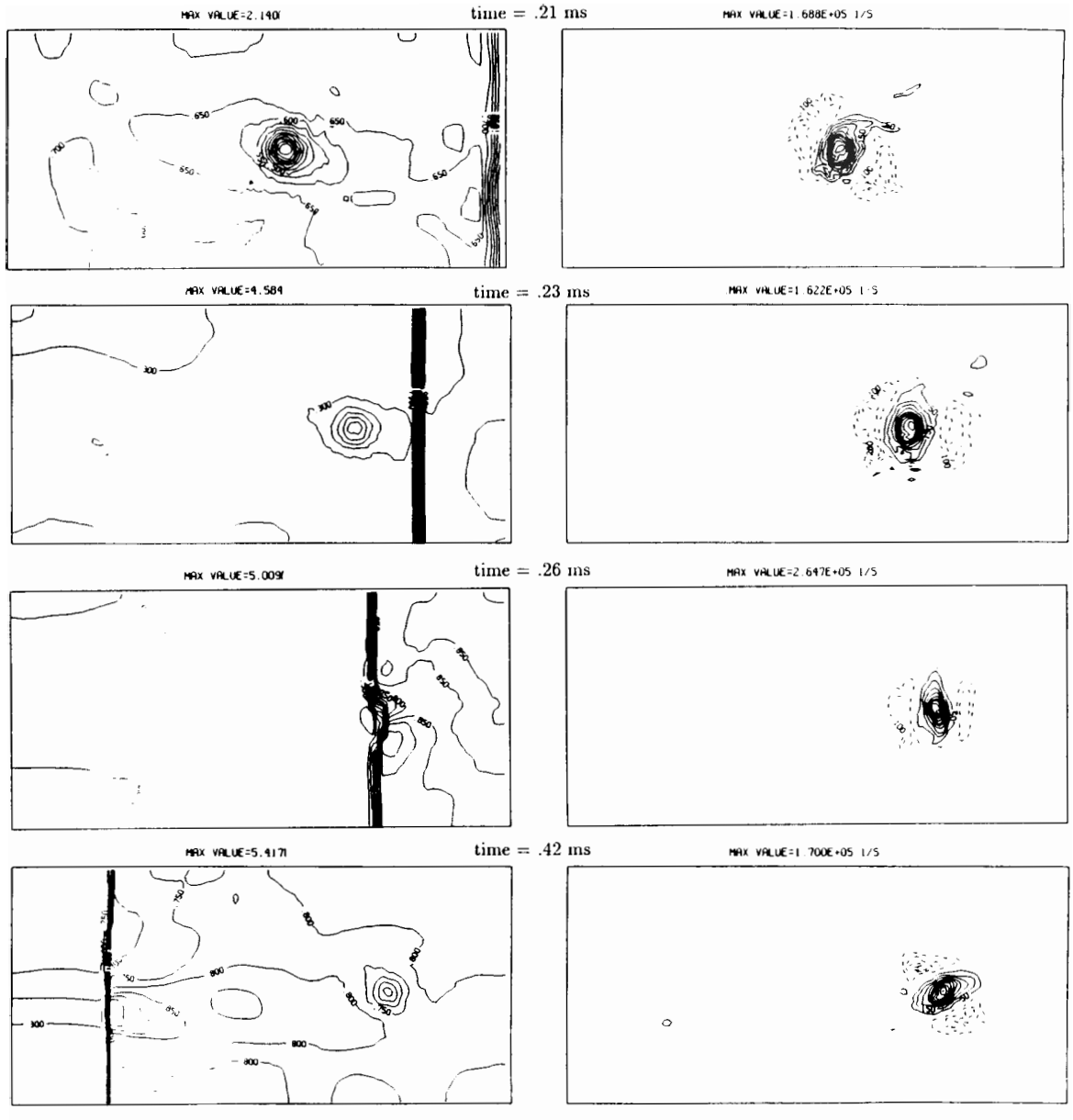

Figure 3. *(continued)*

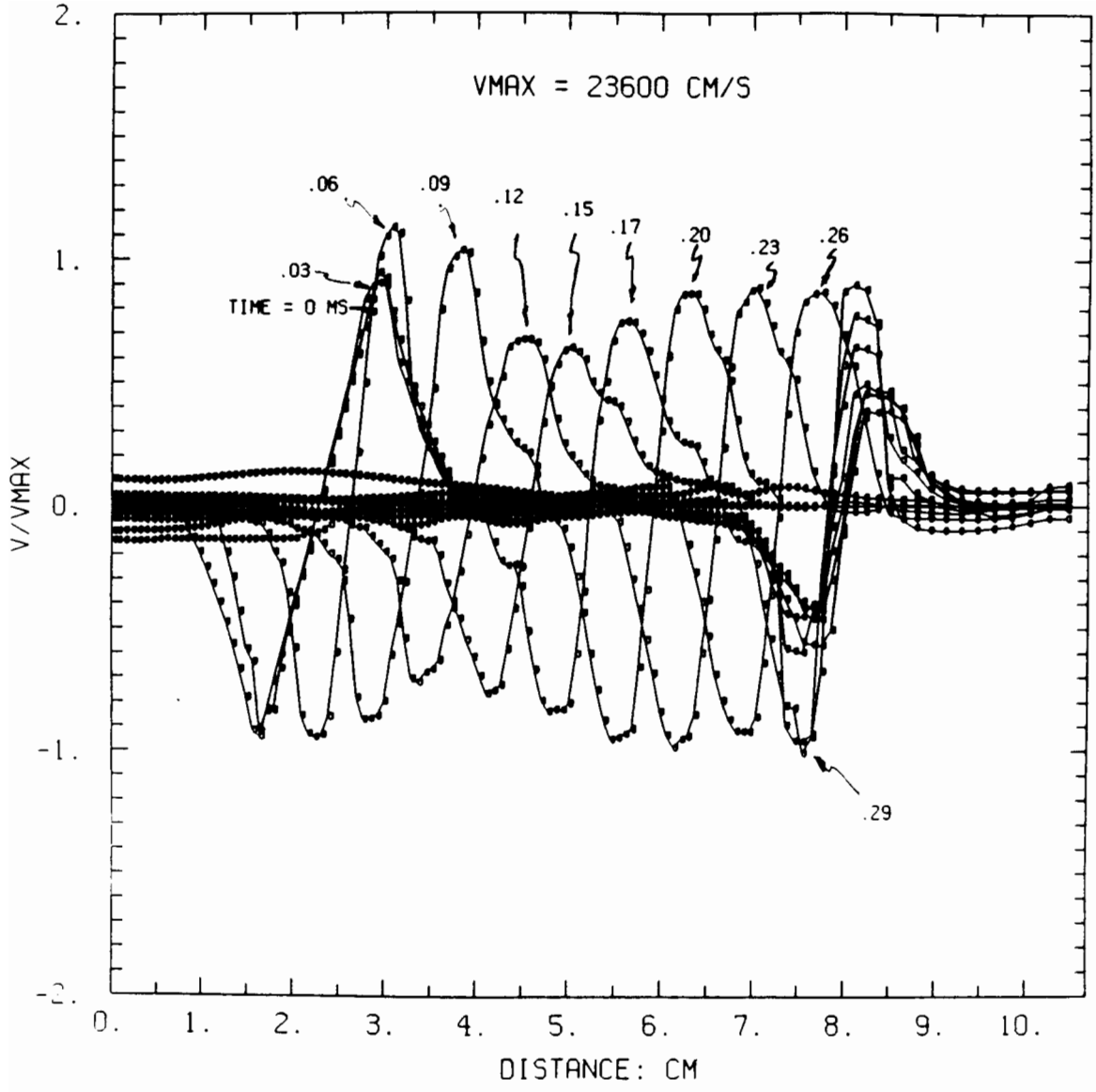

Figure 4. v_y/v_{max} along centerline of domain for $v_{max} = 236$ m/s at several time steps.

MIXING PATTERNS AND THE GENERATION OF VORTICITY IN A DENSITY STRATIFIED SHEAR LAYER

Ahmed F. Ghoniem and Anantha Krishnan
Department of Mechanical Engineering
Massachusetts Institute of Technology
Cambridge, MA 02139

ABSTRACT

Numerical solutions of the unsteady inviscid, two-dimensional vorticity and mass conservation equations for an incompressible density-stratified flow in a Lagrangian, grid-free form are used to investigate the effects of vorticity generation due to baroclinicity on the development of the Kelvin-Helmholtz (K-H) instability beyond the linear range. Continuous, although sharply-decaying, density stratification is considered, and large overall density ratios are assumed. Solutions are also obtained for the corresponding linear stability problem and are used to complement the numerical solution within the initial stages of the instability.

Results show that the generation of baroclinic vorticity due to the acceleration of fluid elements in a non-uniform density field imparts certain asymmetry on the structures that develop due to the K-H instability. This asymmetry is associated with the convective motion of the structure in the direction of the heavy fluid but towards the light fluid, and causes a bias in the composition of the fluid within the structure towards the light fluid.

I. INTRODUCTION

Density-stratified flows are of utmost importance fundamentally and in practical applications. Fundamentally, the presence of a density gradient in an otherwise incompressible flow is the first deviation from the incompressible, uniform-density limit. In this paper, we study the effect of density stratification on the growth of the Kelvin-Helmholtz instability in which the vorticity layer and the density gradient layer initially coincide and are of the same thickness. This flow is a good, while not perfect, model of a mixing layer, defined as a shear layer which exists between two streams of different fluids. For the purpose of studying these flows, we have developed a numerical scheme based on vortex methods to compute the generation and transport of vorticity and of a scalar, in this case the density, in the inviscid limit. The algorithm used to compute the transport of scalars is a grid-free Lagrangian method constructed on the basis of the relationship between the distortion of the flow map and the gradients of a passive scalar.

We also present comparisons with the corresponding linear stability theory for small amplitude perturbations to: (1) provide preliminary information on the possible effects of baroclinic vorticity generation on the flows of interest; and, (2) obtain a rigorous check on the accuracy of the numerical methods by comparing their results on the growth of the perturbations to those obtained analytically. The accuracy of the results during the non-linear stages can only be ascertained by using numerical convergence criteria, i.e., refining the numerical parameters until the results are shown to be independent of the choice of these parameters. Experimental results are also used to validate the results of the numerical computations.

II. FORMULATION AND NUMERICAL SCHEMES

II.1. GOVERNING EQUATIONS

The appropriate form of the governing equations when vortex methods are considered is the vorticity transport form. For an incompressible, inviscid, density-stratified flow in two dimensions, the governing equations can be written in the following form:

$$\frac{d\omega}{dt} = -\frac{\nabla\rho}{\rho} \times (\mathbf{a}) \tag{1}$$

$$\frac{d\rho}{dt} = 0 \tag{2}$$

$$\mathbf{u}_\omega(\mathbf{x}) = \int \mathbf{K}(\mathbf{x}-\mathbf{x}')\,\omega(\mathbf{x}')\,d\mathbf{x}' \tag{3}$$

where $\mathbf{a} = d\mathbf{u}/dt$ is the material acceleration, $\mathbf{u} = (u,v)$ is the velocity, u and v are defined in the x and y directions, respectively, $\mathbf{x} = (x,y)$ is the space coordinate, x and y are the streamwise and cross-stream directions, respectively, $d/dt = \partial/\partial t + \mathbf{u}\cdot\nabla$ is the material, or Lagrangian derivative, $\nabla = (\partial/\partial x, \partial/\partial y)$, t is time, $\omega\,\mathbf{k} = \nabla \times \mathbf{u}$ is the vorticity, ρ is the density, $\mathbf{k}$ is the unit vector in the direction normal to the x-y plane, and $\mathbf{K} = -1/2\pi r^2(-y,x)$, is the kernel of the Poisson equation, where $r^2 = x^2 + y^2$.

Equation (1) is derived from the momentum equation: $\rho\,\mathbf{a} = -\nabla p$. This allows the computation of the source term in the vorticity transport equation without explicitly computing the pressure. The velocity $\mathbf{u}_\omega$ is solenoidal, $\nabla\cdot\mathbf{u}_\omega = 0$, and is due to the vorticity distribution within the computational domain. To obtain the total velocity, $\mathbf{u}_\omega$ is complemented with another velocity component to satisfy the boundary condition if the domain is not the free space, i.e., $\mathbf{u} = \mathbf{u}_\omega + \mathbf{u}_p$, and $\nabla\cdot\mathbf{u} = 0$ from incompressibility. This model implicitly assumes that the Mach number of the flow is very small and thus spatial pressure variations and density variations are uncoupled (see Rehm and Baum [1]).

For the shear layer, the reference velocity is: $U_o=(U_1-U_2)/2$ where U_1 and U_2 are the free-stream velocity in the high-speed and low-speed sides, and the

reference length is $L_o = \Delta S/2$ where ΔS is the vorticity thickness. We assume an infinite domain in the y-direction and apply periodic conditions in the x-direction. The potential component of the velocity, u_p, due to these periodic boundaries is obtained by summing over the sister vortices outside the computational domain.

II.2. THE VORTEX ELEMENT METHOD

In the vortex method for an incompressible, uniform density flow, $d\omega/dt = 0$, the vorticity field is discretized into a number of vortex elements of finite and overlapping cores:

$$\omega(\mathbf{x},t) = \sum_{i=1}^{N} \Gamma_i \, f_\delta(\mathbf{x}-\chi_i(\mathbf{X}_i,t)) \qquad (4)$$

where $\Gamma_i = \omega_i h^2$ is the total circulation of an element, N is the total number of vortex elements, h is the average distance between the centers of neighboring elements in two principal directions, $h^2=h_x h_y$, δ is the core radius of a vortex element, and $f_\delta = 1/\delta^2 \; f(r/\delta)$ is the core function. The importance of the core function in stabilizing vortex computations was realized, among others, by Chorin and Bernard [2] and was shown to be necessary for the convergence of the method by Hald [3] and Beale and Majda [4].

The accuracy of the discretization depends on: (1) the choice of the core function f; (2) the initial distribution of the particles that will be used to transport the vorticity; (3) the method of determining the initial values of values of ω_i or Γ_i, i = 1, 2, ... , N; and, (4) the ratio of δ/h. For details on the four points, see Ghoniem, Heidarinejad and Krishnan [5].

The velocity field of a distribution of vortex elements is given by:

$$\mathbf{u}(\mathbf{x},t) = \sum_{i=1}^{N} \Gamma_i \, \mathbf{K}_\delta(\mathbf{x}-\chi_i(\mathbf{X}_i,t)) \qquad (5)$$

where

$$\frac{d\chi_i}{dt} = \mathbf{u}(\chi_i(\mathbf{X}_i,t),t) \qquad (6)$$

where $\mathbf{K}_\delta(\mathbf{x}) = \mathbf{K}(\mathbf{x}) \; \kappa(r/\delta)$, and $\kappa(r) = 2\pi \int_0^r f(r') \; r' \; dr'$.

The generation of strong strain with the growth of perturbations into the non-linear stages increases the distance between neighboring elements, $\delta\chi$, beyond the "target" value of h. To avoid this problem, more elements are introduced in areas where $\delta\chi > \beta h$ where $\beta \sim 1.5$, and the circulation of the original elements is locally redistributed among the newly introduced elements. The redistribution of circulation is accomplished by dividing the value of h^2 of the original element equally among the newly generated elements and the original element.

For consistency, and to satisfy the condition of conservation of vorticity, $d\omega/dt = 0$, the value of δ^2 should also be adjusted so that the ratio of δ^2/h^2 is maintained constant in Equation (4). This helps minimize the numerical diffusion

which may accumulate to unacceptable levels if the area on which the vorticity exists is allowed to grow beyond its original size.

The numerical scheme is extended to the incompressible, density-stratified flow by allowing the strength of the vortex elements to change with time according to the source term in Equation (1). At each time step, and after vortex elements have been transported by the local velocity field, their strength, $\Gamma_i(t)$, is updated according to the following equation:

$$\frac{d\Gamma_i}{dt} = - \frac{\nabla\rho_i}{\rho_i} h_i^2 \times (\frac{du}{dt})_i \qquad (7)$$

The material acceleration of an element is computed by numerically differentiating its velocity between two time steps, and the local value of the density gradient is computed using the transport element method.

II.3. THE TRANSPORT ELEMENT METHOD

Given that ρ is a conserved scalar described by Equation (2), the equation governing the transport of its gradient $\mathbf{g} = \nabla\rho$ is:

$$\frac{d\mathbf{g}}{dt} = - \mathbf{g} \cdot \nabla\mathbf{u} - \mathbf{g} \times \boldsymbol{\omega} \qquad (8)$$

showing $\mathbf{g}$ changes due to the straining and rotation of the material lines by the local strain field and vorticity. If the material is exposed to a strong strain in the direction normal to the gradient, the value of g must increase by the same amount as the stretch in the material element. This can be seen by deriving an equation that governs $g = |\mathbf{g}|$. To do this, Eq. (8) is expanded in terms of $g\,\mathbf{n}$, implementing kinematical relations that describe the variations of $\mathbf{n} = \mathbf{g}/g$, the unit normal vector to the iso-scalar line. After some lengthy manipulations (see Ghoniem et al [6] for details), we get:

$$\mathbf{g}_i(t) = \frac{\delta\rho_i \; \delta\mathbf{l}_i(t)}{h_i^2} \mathbf{n}_i(t) \qquad (9)$$

where $h_i^2 = \delta\mathbf{l}_i . \delta\mathbf{n}_i$, and $\delta\rho_i$ is the initial density variation across the line $\delta\mathbf{l}_i$. $\delta\mathbf{l}_i$, the length of the material element is given by $\delta\mathbf{l}_i(t) = (\chi_{i+1} - \chi_{i-1})/2$ and $\mathbf{n}_i \cdot \mathbf{l}_i = 0$. These relations can be used to construct a scheme which is compatible with the vortex method to compute the evolution of the density field. The density gradient field is discretized among a number of elements which are transported along particle paths while the gradients vary according to equation (9). Thus;

$$\mathbf{g}(\mathbf{x},t) = \sum_{i=1}^{N} \mathbf{g}_i(t) \; h^2 \; f_\delta(\mathbf{x} - \chi_i(\mathbf{X}_i,t)) \qquad (10)$$

Given the location and strength of the transport elements, the scalar concentration is computed by direct integration over the fields of the transport elements:

$$s(\mathbf{x},t) = \sum_{i=1}^{N} q_i(t)\, h^2 \cdot \nabla G_\delta(\mathbf{x}-\chi_i(X_i,t)) \qquad (11)$$

where $\nabla G_\delta(\mathbf{x}) = (x,y)/2\pi r^2\, \kappa(r/\delta)$. Note that this formulation is fully compatible with the vortex method since all the information needed to compute the scalar transport are already a part of the vortex computations, including all the expressions for the Green functions. For extended derivations, discussions and validations, see Ghoniem et al. [5,6].

III. NUMERICAL SIMULATION OF THE KELVIN-HELMHOLTZ INSTABILITY

We have run computations for density ratio $r_\rho = \rho_1/\rho_2 = 1$, 2, 3, and 4. In all cases, the high-density fluid is on top, in the fast stream, and the low density stream is on the bottom, the slow stream. All results were obtained with the shear layer initially perturbed at a wavelength $\lambda = 6.6\ \Delta S$ using a sinewave displacement of the vortex elements with an amplitude $\varepsilon = 0.01\ \lambda$. This wavenumber is very close to the most unstable wavenumbers for all the density ratios considered. The initial vorticity and density distributions are Gaussians with standard deviation $\sigma = \Delta S/2$.

The results of the linear analysis for this problem are shown in Figures 1 and 2. The linear growth rate of the shear layer as a function of the wavenumber is plotted in Figure 1 for different values of r_ρ. Figure 2 shows the phase velocity as a function of wavenumber for the corresponding cases. The symbols shown in the two figures represent the results of numerical simulations. It is seen that the maximum growth rate in all the cases is almost independent of the density ratio. There is a small increase in the wavenumber of the most unstable mode with increasing density ratio. Moreover, perturbations with longer/shorter wavenumbers than that of the most unstable mode behave differently; they grow faster/slower as the density ratio increases. In Figure 2, we see that the phase velocity of the waves increases with density ratio. Thus, Kelvin-Helmholtz waves in a density stratified flow are dispersive, with longer waves propagating at higher phase speeds.

Figures 3(a) and 4(a) show the location and velocity of all the transport elements used in the computations for $r_\rho = 1$ and 3 respectively and figures 3(b) and 4(b) show the corresponding streamlines. The non-dimensional times are t= 5.5, 16.5 and 24.0. The growth of the initial vorticity perturbation leads to the roll-up of the vorticity layer into a coherent elliptical structure that entrains all the initial vorticity within the layer and, for $r_\rho > 1$, engulfs the newly generated vorticity. Contrary to the case of $r_\rho = 1$, the vorticity generated by baroclinicity, the only extra dynamic process in the density stratified flow, causes a definite asymmetry in the developing structures, and advances the structure at a finite velocity in the direction of the high-density stream.

Now we turn our attention to the streamline plots shown in Figures 3(b) and 4(b). A structure resembling a "cat's eye" forms due to the roll-up of the vorticity into a single coherent structure. The maximum volume of fluid entrained

into the structure is reached with the maximum growth of the instability, around time t = 20 for the r_ρ = 1 case. Beyond this stage, fluid start to leak out of the structure and join the original free streams. The total volume of fluid within the structure can be estimated by the value of the stream function at the core. The bounding streamline of the structure is set to zero in all the cases. At t=24, the values of the streamfunction at the core are 2.96 and 3.26 for r_ρ = 1 and 3 respectively. This clearly indicates the increase in total volumetric entrainment into the eddy with increasing density ratio. Also, the beginning of the collapse stage is delayed for the density stratified eddies. Thus, the vorticity generated due to acceleration, or inertia effects, results in the formation of a stronger eddy that can entrain more fluid and survive longer before it collapses and fluid starts to leak out in the flow direction.

The distribution of vortex elements indicate that more light fluid is being entrained into the structure than heavy fluid, which is shown by the presence of a deeper tongue of lighter fluid than that of the heavy fluid. This asymmetric entrainment has been observed in experiments [7]. We note that all these effects are dynamic consequences of the generation of vorticity by the baroclinic torque due to the interaction between the pressure field and the density gradient. Thus, we plot the contours for the light fluid concentration and the vorticity for the two cases in Figures 5 and 6 respectively. A clear picture of the asymmetric entrainment is depicted in the plots of the concentration contours showing how the motion of the eddy in the direction of the heavy fluid promotes the entrainment of more light fluid into the core of the eddy.

The vorticity contours reveal that as the eddy grows, a layer of intense negative vorticity forms on the right side of the $\chi(\lambda/2,y,t)$ point while positive vorticity is forming on the left side of the same point. The negative vorticity is constantly being entrained into the core of the eddy while the positive vorticity forms a "wing" on the top side of the eddy. The positive vorticity concentrated on the top side of the eddy leads to a net positive velocity component at the center of the eddy. Notice that the vorticity intensity is increasing in the eddy core and this helps its coherence beyond the maximum entrainment stage.

In summary, all representations of the flow indicate that: (1) the structure moves horizontally in the direction of the high density fluid attaining a constant velocity beyond the linear range. Meanwhile, it moves vertically towards the light fluid. By inspecting experimental data on a spatially-growing mixing layer, Dimotakis [7] suggested the following formula for determining the structure velocity:

$$U_c = (1 + r_u s^{1/2}) / (1 + s^{1/2}) \qquad (12)$$

where r_u and $s = 1/r_\rho$ are the velocity ratio and density ratio across the layer, respectively. This formula can be used to predict the structure velocity in a temporal frame of reference and the resulting expression is:

$$U_{ct} = 1 - 2 s^{1/2} / (1 + s^{1/2}) \qquad (13)$$

The convective velocity of the structure in the temporal frame of reference is plotted as a function of $s=1/r_\rho$ in Figure 7 using expression (13). The results of the numerical simulations are represented by symbols. Dimotakis [7] also obtained an empirical expression for the volumetric entrainment ratio as a function of the density ratio and the velocity ratio in a spatial shear layer. This expression is given as:

$$E_v = s^{1/2} (1.0 + 0.68 (1 - r_u)/(1 + r_u))) \qquad (14)$$

'E_v' is defined as the ratio of volume of fluid entrained from the heavier top stream to that entrained from the lighter bottom stream. For a temporal shear layer the velocity ratio, r_u is close to unity and the above expression is simplified as:

$$E_v = s^{1/2} \qquad (15)$$

This expression is plotted as a function of $s=1/r_\rho$ in Figure 8. The symbols represent the entrainment ratio estimated from the numerical simulations at a non-dimensional time of 24.0. It is observed that the results of the numerical simulations compare very well with the empirical results of Dimotakis.

The temporal picture of a mixing layer has been shown to be a good representation of the forced spatially-growing mixing layer, except for the fact that the latter exhibit one more mechanism of growth asymmetry. This mechanism is associated with the difference in velocity across the layer which again biases the growth towards the high speed stream.

IV. CONCLUSIONS

The Vortex-Transport element method has been used to study the development of the K-H instabiliity in a density stratified shear flow. The results obtained are validated using the linear theory in the initial stage of the growth of the perturbation and comparisons with experimental and theoretical work are used to support the results in the non-linear regime. The generation of vorticity due to baroclinicity in a density stratified temporal shear layer leads to the asymmetric development of the large scale structure and simultaneously imparts an extra convective velocity to the eddy in the direction of the heavier stream. The entrainment ratio and the convection velocity of the eddy calculated from the numerical simulations compare well with experimental results. Since the entrainment ratio is found to be a strong function of the density ratio, the effect of baroclinicity becomes very important in studying and understanding chemical reactions occuring in flows dominated by large scale structures. These structures serve to entrain the reactants and bring them into contact with each other thus promoting mixing and hence the reaction. Therefore the relative entrainment of the respective fluids will have an important effect on the reaction.

REFERENCES

1. Rehm, R. and Baum, H., N.B.S.J. Res., 83, 3, 1978, pp. 297-308.

2. Chorin, A. and Bernard, P., J. Comput. Phys., 13, pp.423-28 (1973).

3. Hald, O.H., SIAM J. Num. Anal., 16, 726 (1979).

4. Beale, T.J. and Majda, A., Math. Comput., 39, 29 (1982).

5. Ghoniem, A.F., Heidarinejad, G. and Krishnan, A., The United States-France Joint Workshop on Turbulent Reactive Flows, Proceedings: Volume III, July 6-10, 1987, Rouen, France, 10:1-41.

6. Ghoniem,A.F., Heidarinejad, G. and Krishnan, A., AIAA 26th Aerospace Sciences Meeting, January 11-14, 1988/Reno, NV, AIAA-88-0729.

7. Dimotakis, P., AIAA Journal, 24, pp. 1791-96 (1986).

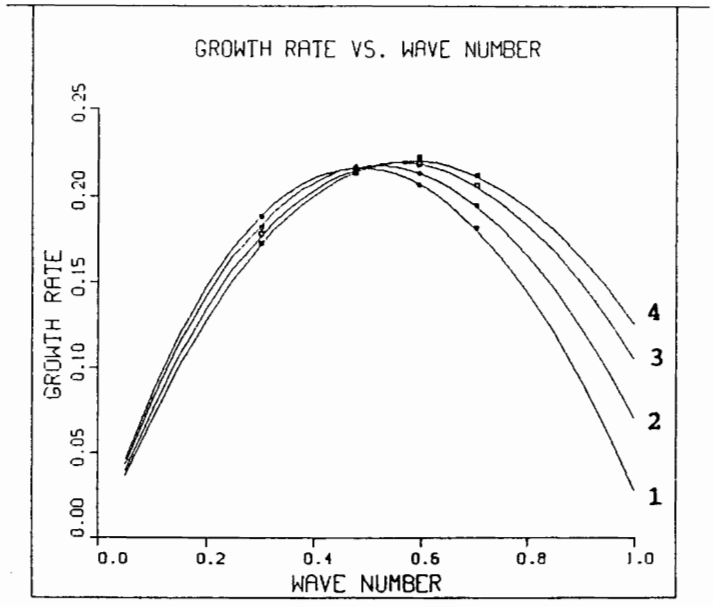

Figure 1. Plot of linear growth rate versus the wavenumber for the K-H instability. Curves 1, 2, 3 and 4 represent values of r_ρ = 1, 2, 3 and 4 respectively. The symbols represent results of numerical simulation.

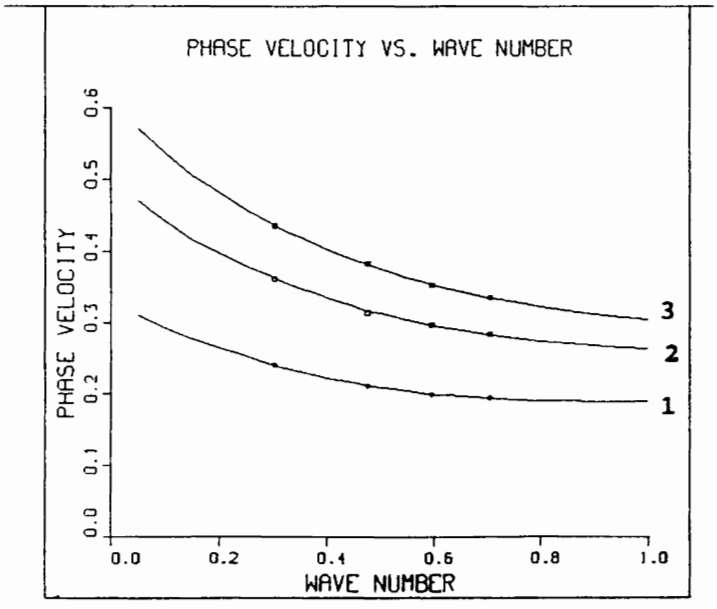

Figure 2. Plot of real part of the phase velocity versus the wavenumber for the K-H instability. Curves 1, 2 and 3 represent values of r_ρ = 2, 3 and 4 respectively. The symbols are the results of numerical simulation.

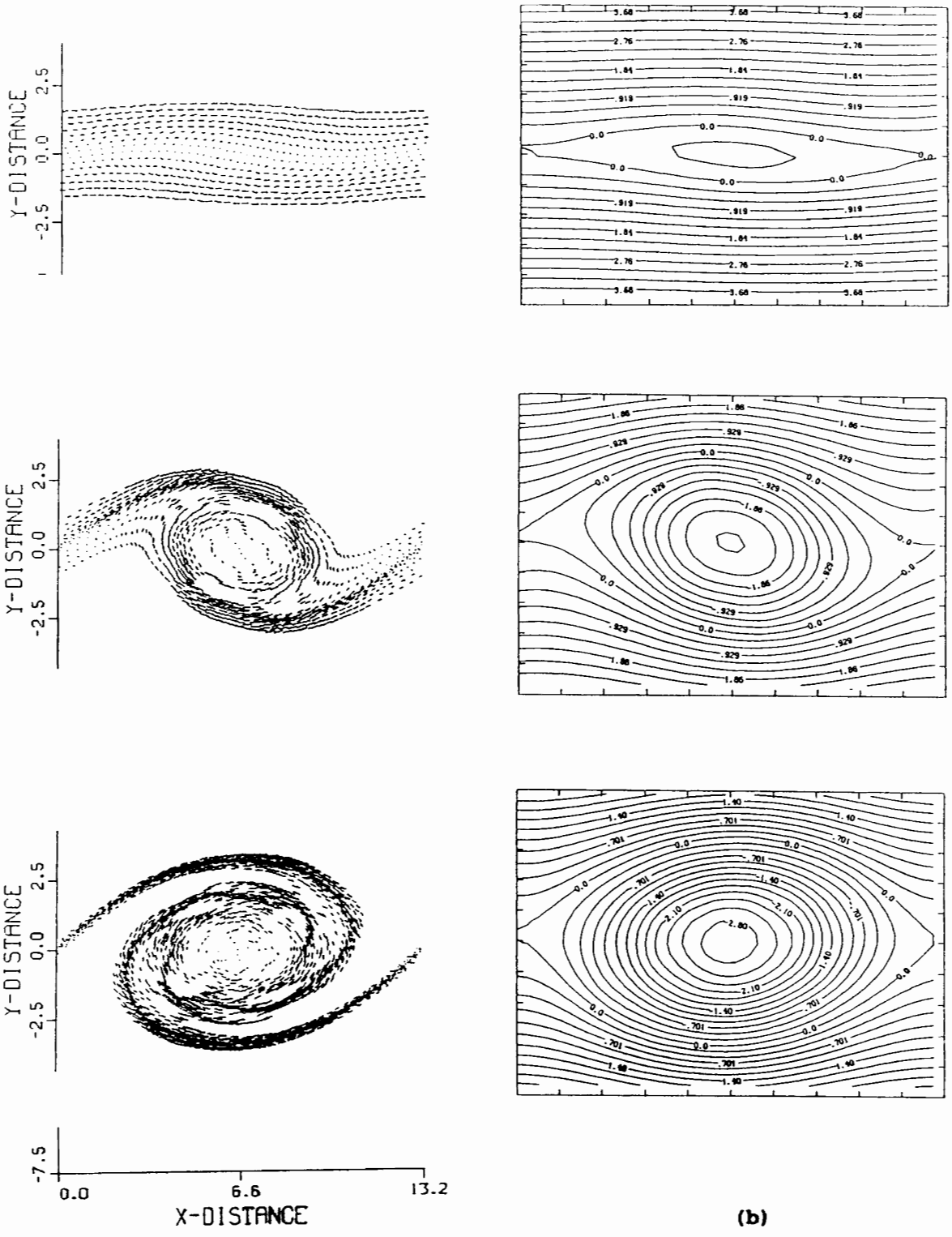

Figure 3. (a) Transport element location and velocity vectors for the K-H instability for $r_0 = 1$ at t=5.5, 16.5 and 24.0 respectively. (b) the streamline plots corresponding to the case in (a).

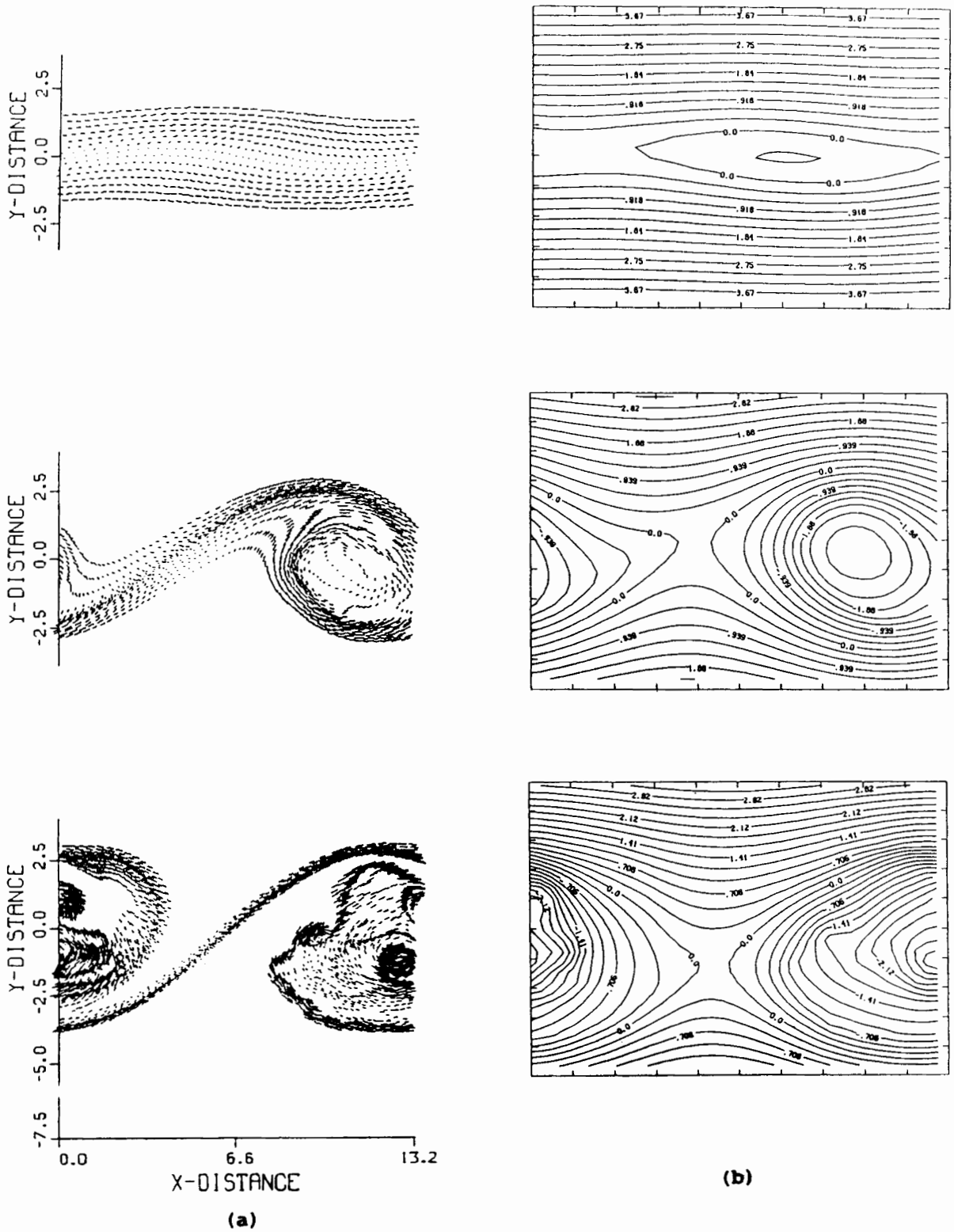

Figure 4. (a) Transport element location and velocity vectors for r = 3 at t= 5.5, 16.5 and 24.0 respectively. (b) the streamlines corresponding to the case in (a).

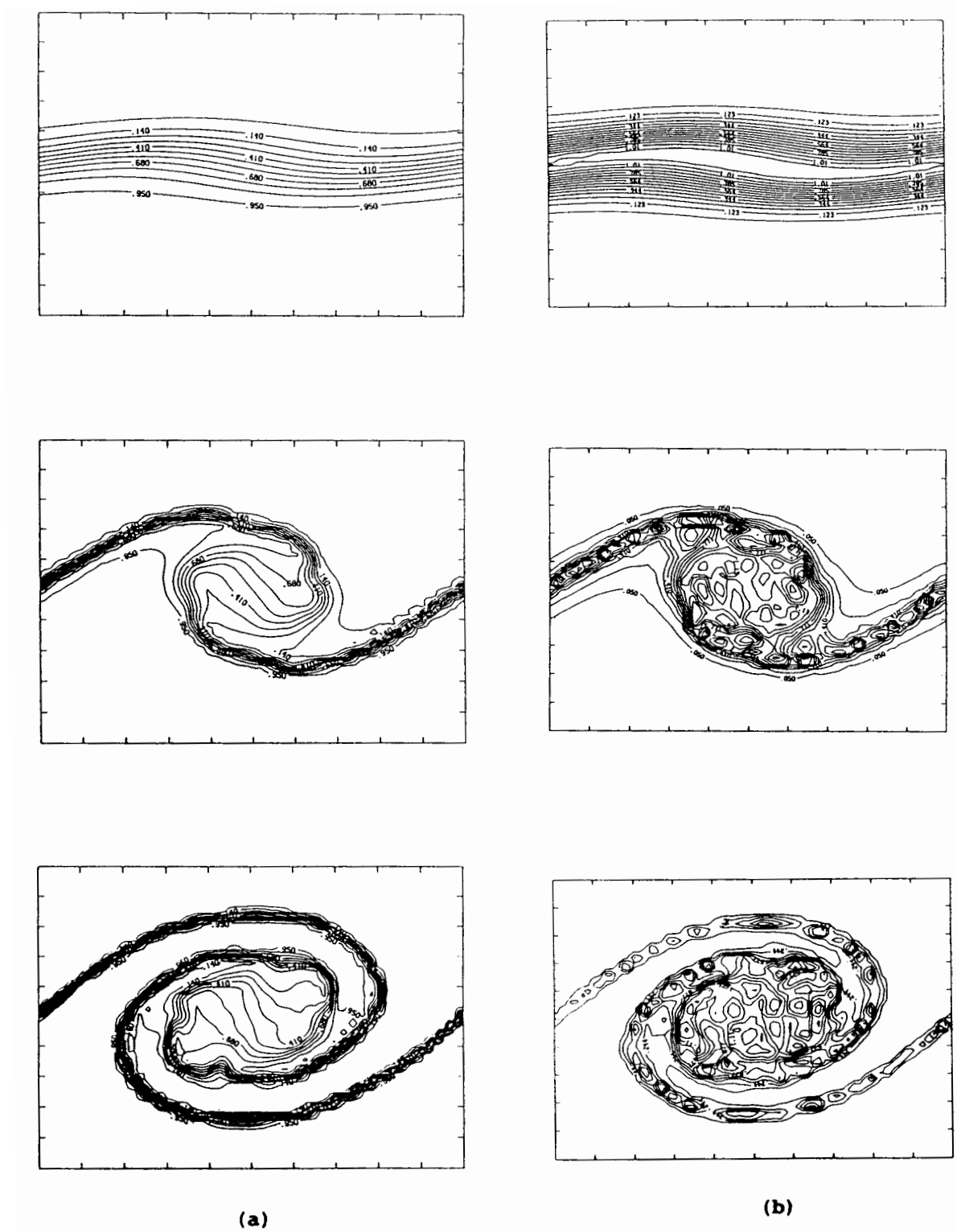

Figure 5. (a) The light fluid concentration (or normalised temperature) contours for $r_\rho = 1$ at t= 5.5, 16.5 and 24.0. (b) the corresponding vorticity contours.

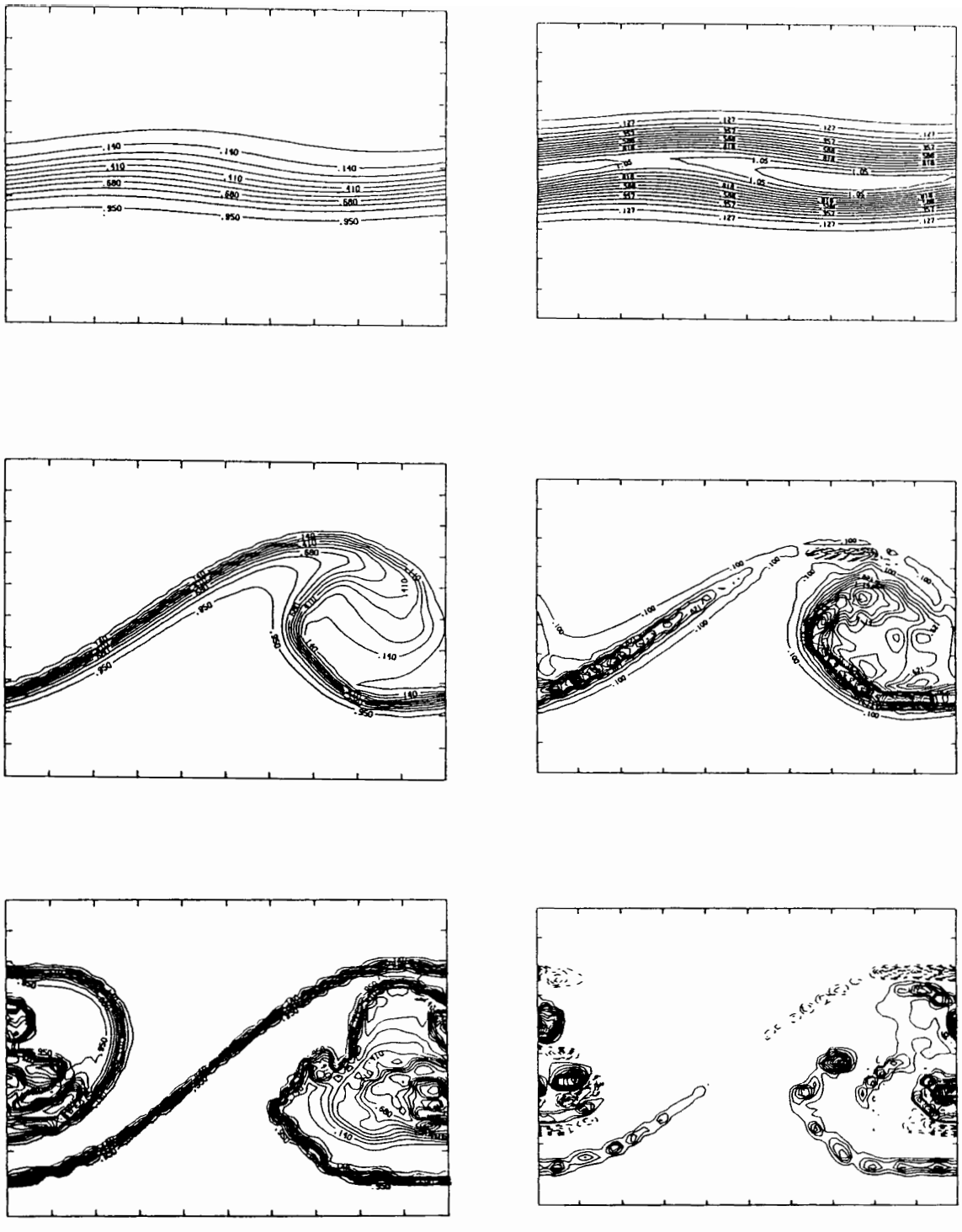

(a) (b)

Figure 6. (a) The light fluid concentration contours for $r_o = 3$ at t= 5.5, 16.5 and 24.0 (b) the corresponding vorticity contours (the dashed contours represent positive vorticity and the continuous contours the negative vorticity).

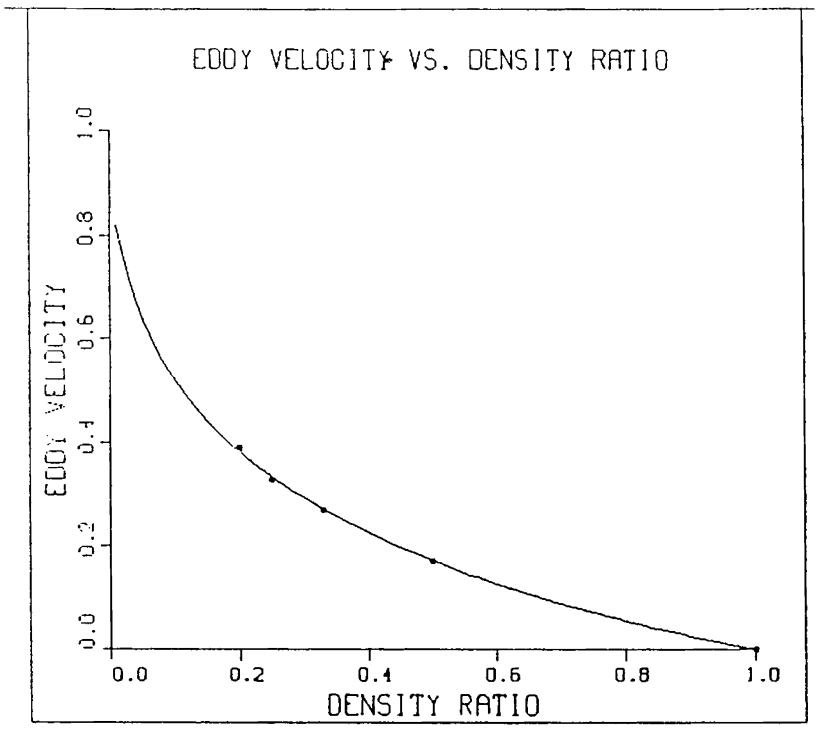

Figure 7. Plot of eddy convective velocity versus $s= 1/r_\rho$. The symbols represent results of numerical simulation.

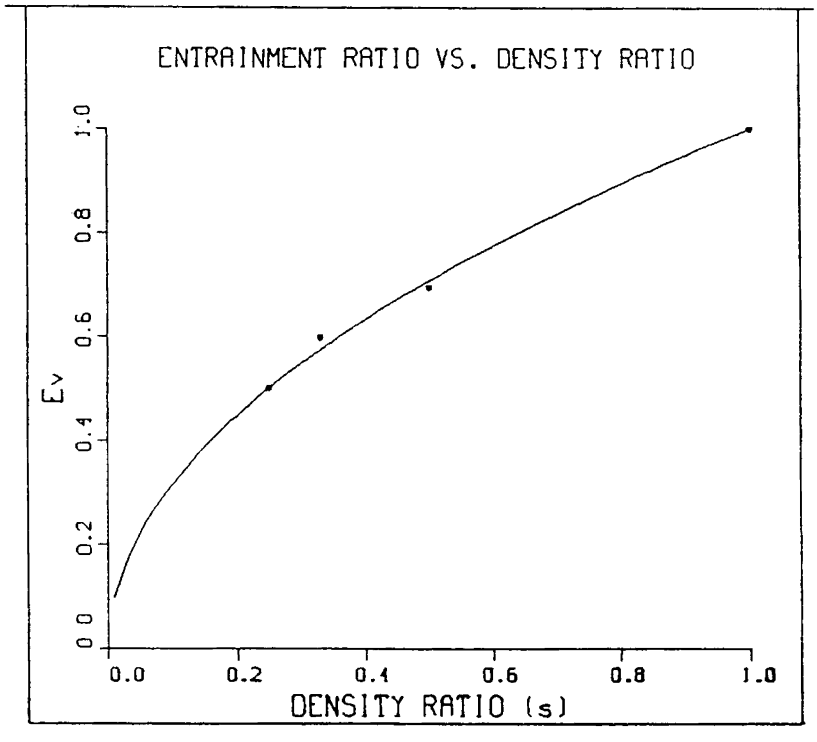

Figure 8. Plot of entrainment ratio versus $s= 1/r_\rho$. The symbols represent results of numerical simulation.

VORTEX SHEDDING AND MERGING IN HIGH-SPEED CONFINED SHEAR FLOWS

K. Kailasanath, J.H. Gardner, E.S. Oran, and J.P. Boris
Laboratory for Computational Physics and Fluid Dynamics
Naval Research Laboratory, Code 4410
Washington, D.C. 20375

Abstract

We describe a series of numerical simulations of a confined axisymmetric jet in which the inflow Mach number is varied, but the geometry and properties of the gas are held fixed. Of particular interest is how the acoustic-vortex interactions change as the inflow velocity varies from 50 to 300 m/s, corresponding to Mach numbers from 0.15 to close to one. When the velocity is increased, the natural instability frequency of the shear layer increases. If the gas properties and the geometry of the system are fixed, the acoustic frequencies remain essentially the same. Thus by varying the inflow velocity, we can examine the coupling between the acoustics and the flow instabilities. We find that when a dominant acoustic frequency is near the natural instability frequency, the shear layer first rolls up at the acoustic frequency. However, when these frequencies are very different, the shear layer rolls up at the natural instability frequency. In all cases, the acoustic frequencies strongly affect the downstream vortex mergings.

Introduction

A characteristic feature of the geometric configuration of many propulsion systems is an abrupt increase in cross-sectional area. The flow separates at this location and the separated shear layer is usually turbulent. Such transitional shear layers are characterized by large-scale coherent vortical structures. Interactions among these structures can generate acoustic waves, and the interactions themselves can be affected by the acoustic waves imposed on the system by, for example, the geometry or outside driving.

The geometry we are considering is shown in Figure 1. A premixed gas flows through a cylindrical inlet into a chamber of larger diameter, and then exits through a choked nozzle at which the the flow becomes sonic. For this system, the quarter-wave mode of the inlet is 150 Hz, the first longitudinal acoustic frequency is 450 Hz, and the transverse acoustic frequency is 2960 Hz.

Earlier studies of the effects of acoustic forcing in this particular geometry [1–3] showed that forcing at the first longitudinal acoustic mode of the chamber induces vortex rollup near the entrance to the chamber at the forcing frequency. However, in these simulations, the frequency of the first longitudinal mode of the chamber was close to the initial vortex-rollup frequency observed in the unforced calculations. Comparisons of calculations with and without forcing [3] also showed that the predicted vortex-rollup frequencies were in good agreement with experimental observations [4]. There was also an overall low-frequency at which the entire confined flow was periodic, and this low frequency is determined by the acoustics of the inlet [5]. The effects of independently changing the acoustics of the inlet and the chamber have also been studied [5]. In all of the cases simulated, vortex rollup near the inlet-chamber junction occurs at the first longitudinal mode of the chamber. The merging pattern of the vortices in the chamber is, however, significantly different in the different cases. These merging patterns result from an interaction of phenomena occurring at the vortex-rollup

frequency and the frequency of the quarter-wave mode of the inlet. In all of these studies, the inflow velocity was kept constant at Mach number 0.153.

In this paper, we discuss the effects of increasing the Mach number of the incoming gas. We have effected this by increasing the inflow velocity while maintaining the same pressure and density, thus varying the natural shedding frequency of the shear layer. This approach was taken so that the acoustic frequencies of the system are essentially held fixed, but we can vary the shear-layer instability frequency through changes in the velocity. Hence this study provides a way to probe the interaction between the acoustic frequencies and the natural instability frequencies of the system.

The Numerical Model

The numerical model solves the compressible, time-dependent, conservation equations for mass, momentum and energy in a two-dimensional axisymmetric geometry. The algorithm used for fluid dynamic convection is Flux-Corrected Transport (FCT) [6], a conservative, monotonic algorithm with fourth-order phase accuracy. FCT algorithms can be constructed as a weighted average of a low-order and a high-order finite-difference scheme. During a convective transport timestep, FCT first modifies the linear properties of the high-order algorithm by adding diffusion. This prevents dispersive ripples from arising, and it ensures that all conserved quantities remain monotonic and positive. Then FCT subtracts out the added diffusion in regions away from discontinuities. Thus it maintains a high order of accuracy while enforcing positivity and monotonicity. With various initial and boundary conditions, this algorithm has been used to solve a wide variety of problems in both supersonic reacting flows [7–9] and subsonic turbulent shear flows [1,3,5,10,11].

The calculations presented below are inviscid, that is, no explicit term representing physical viscosity has been included in the model. Also, no artificial viscosity is needed to stabilize the algorithm. There is a residual numerical diffusion present which effectively behaves like a viscosity term for short-wavelength modes on the order of the zone size. Unlike most numerical methods, however, the damping of the short-wavelength modes is nonlinear. Thus the effects of this residual viscosity diminish very quickly for the long wavelength modes, which result in a high effective Reynolds number. In the problem considered in this paper, we are primarily interested in the interaction of the acoustic modes with large-scale vortex structures, which is essentially an inviscid interaction.

The calculations reported here are essentially large-eddy simulations which model the fluid instabilities leading to a transition to turbulent flow. Although a subgrid turbulence model is not explicitly included in these calculations, the nonlinear cutoff of high-frequency modes by the FCT algorithm acts as a subgrid model. The question of exactly how this high frequency filter acts is currently a topic of research.

The choked outflow conditions force the flow to become sonic at the throat of the exit nozzle. At the solid walls, the normal flux is set to zero and the pressure is extrapolated to the normal stagnation condition. At the inflow, the pressure is allowed to fluctuate, but the mass flow rate and the inflow velocity are specified. These conditions allow the acoustic waves to reflect without amplification or damping at the inflow. These inflow boundary conditions could be modified to damp the acoustic waves originating downstream. More detailed discussions and tests of the boundary conditions have been presented in earlier papers [1,3,12].

The computational cell spacing was set up at the beginning of the calculation and then held fixed in time. Fine zones were used near the entrance to the step in the larger chamber in both the radial and axial directions. In both directions the cell sizes gradually increased away from the dump plane.

The effects of numerical resolution were checked by comparing calculations with different grids and these results have been reported elsewhere [1,3,12]. In the calculations described in this paper, a 60 × 120 grid is used.

Results and Discussion

The numerical simulations predict values of the density, momentum, and energy for each of the computational cells as a function of time. From this information, we can selectively generate the various physical diagnostics. In this presentation, we use the Fourier analysis of local, time-dependent velocity fluctuations at various locations in the flow and instantaneous velocity streamlines to provide flow visualization. Streamlines are a useful visual diagnostic of the structure of the flow and they also allow us to correlate and track the coherent structures and their mergin patterns.

Inflow Mach Number 0.31, An Intermediate Value

The series of instantaneous velocity streamlines shown at intervals of 1000 timesteps in Figure 2 show that vortex shedding occurs at approximately every 2000 timesteps, corresponding to a frequency of about 1330 Hz, and two of these merge at about every 4000 timesteps, corresponding to a frequency of about 665 Hz. Figure 2 also shows vortices growing by entraining the surrounding fluid and merging with other vortices. For example, the vortex shed at step 123,000 grows by entraining the surrounding fluid before it merges with another vortex.

Because it is difficult to determine the vortex shedding and merging frequencies from streamlines shown at every 1000 timestep intervals, it is useful to look at fluctuations of the physical variables such as pressure or velocity to determine the more global features of the flow more precisely. Figure 3 shows Fourier analyses of velocity fluctuations at two locations close to the step. At the distance 0.57 D downstream, there is one dominant line, 1380 Hz, which is the passage frequency of vortices at this location and also corresponds to the vortex-shedding frequency of the shear layer at the step. At the distance 1.63 D, the strongest line is at 690 Hz, the first subharmonic of the vortex-shedding frequency and the passage frequency of the larger vortex formed by the first merging of vortices that occurs upstream. Therefore, based on these Fourier analyses and on the instantaneous streamlines, we conclude that vortex shedding occurs with a frequency of about 1380 Hz and these vortices merge within 2 D at a frequency of about 690 Hz.

In these simulations, the momentum thickness is 0.106 cm. Using this thickness and a frequency of 1380 Hz, the Strouhal number is 0.015. In laboratory experiments [13], an initially laminar shear layer rolls up at St_θ = 0.012 when the theoretical value is 0.017 [14]. From this analysis, we estimate that the natural instability frequency of the shear layer in the simulations is 1380 Hz.

Vortex mergings further downstream become highly erratic. Occasionally a merging is seen at 450 Hz, but mergings are also seen at 442, 295, 884, 662, and 531 Hz. The frequency of 884 Hz is close to the passage frequency following the first vortex-merging, 690 Hz, and the 662 and 531 Hz lines are beat frequencies between this and the quarter wave mode frequency of the inlet, 150 Hz. The 442 and 295 Hz lines are close to the first longitudinal frequency of the chamber and a beat frequency between the inlet and chamber frequencies.

In summary, the first vortex roll-up and merging behaves as if the jet is free and rolling up at the natural instability frequency of the shear layer. Vortex mergings in most of the chamber occur at frequencies resulting from the interaction between the vortex shedding frequency and its subharmonics and the dominant acoustic frequencies of the system.

Inflow Mach Number 0.15, A Low-Speed Case

In this case, the natural instability frequency is 700 Hz and because this is considerably closer to the acoustic frequency of 450 Hz, we expect some coupling between the two. The Fourier analyses of velocity fluctuations shown in Figure 4a at 0.98 D from the step shows that 450 Hz is the dominant frequency but that there are also weaker lines at 550 Hz and at 150 Hz. Streamlines of this system confirm that vortex shedding no longer occurs at one frequency. In contrast to the case higher Mach-number case discussed above, here the acoustics influence the vortex shedding process: there is shedding at three frequencies, two acoustic frequencies, 450 and 150 Hz, and at a beat frequency, 550 Hz. It appears that the acoustic mode has suppressed the natural mode.

The Fourier analyses of velocity fluctuations shown in Figures 4b and c are at two locations further downstream in the chamber between which frequent vortex mergings are observed. Two dominant frequencies in the spectra are 150 and 300 Hz, frequencies close to either acoustic frequencies of the system or beat frequencies of acoustic modes. At 1.97 D, there is no distinguishable line at 450 Hz but the 300 and 400 Hz beat frequencies appear and the inlet frequency, 150 Hz, is still strong. The 400 Hz line is a beat between one of the shedding frequencies, 550 Hz, and the 150 Hz mode. Even further downstream at 3.04 D, only the 150 and 300 Hz lines remain strong.

Note that in a slightly different calculation that was made for a case in which the natural instability frequency was equal to the first longitudinal mode, the 450, 300, and 150 Hz lines dominate and the beat frequencies are not seen. These conditions were created in the calculation by changing the natural shedding frequency by adjusting the shear-layer thickness.

In contrast to the previous case with a higher Mach number and larger separation between the acoustic and natural frequencies, now vortex shedding takes place primarily at the first longitudinal mode of the chamber. The trend illustrated by this case is consistent with the conclusions of a paper describing a case for which the two frequencies essentially equal [3]. In both that and the case described here, the acoustics played an important part in determining the frequency of the first vortex rollup. When the frequencies were very close, the effect was even stronger and beat frequencies were suppressed.

Mach Numbers above 0.60

Figure 5 shows the Fourier of velocity fluctuations for the case of Mach number 0.61, corresponding to an inflow velocity of 200 m/s. Close to the step, at 0.57 D, the dominant frequency is 2960 Hz, which is close to the transverse acoustic frequency and natural vortex-shedding frequency of 2760 Hz. At 1.3 D, the dominant frequency is 1360 Hz, the passage frequency of the first vortex merging. Thus, near the step, the flow is qualitatively similar to that seen in the first case when Mach number was 0.31. In both cases, vortex shedding occurs at the natural shedding frequency and an initial vortex merging occurs within 1.5 D from the dump plane. However, the spectra are noisier and there are other frequencies almost equally as strong that appear as the flow becomes more and more compressible.

Figures 5b and c, velocity-fluctuation spectra at two and three diameters downstream, show three dominant frequencies: 430, 580 and 730 Hz. These are close to either acoustic frequencies of the system or beat frequencies of acoustic modes at 150 Hz and 450 Hz. There are also fluctuations at 1360 Hz corresponding to the passage frequency of the first merged vortex.

As in the first case considered, the downstream spectra are very noisy and there are many frequencies that usually correspond to beat frequencies between the acoustic and natural instabilitity modes.

The vortex shedding and the first vortex merging are not affected by the acoustics of the system for these high-speed flows. In simulations for even higher Mach numbers, for example, 0.90, the same trend appears, and there is even less order in the spectra far from the step.

Summary and Conclusions

In this paper, we have presented numerical simulations of vortex shedding and merging in an chamber whose flow is fed by a relatively long channel and choked at the exit. The purpose of the paper was to examine the effects on the structure and merging patterns in the flow by varying the inflow Mach numbers, while keeping fixed the acoustics of the system, the thermodynamic properties of the gas, and the momentum thickness of the shear layer. The effect then was to vary the natural instability frequency of the shear layer by varying the velocity of the flow. Flow velocities ranging from 50 to 300 m/s were considered, which corresponded to Mach numbers ranging from 0.15 to 0.90.

The calculations show complex interactions among the natural instability frequency of the shear layer at the inlet of the chamber and the acoustic frequencies of both the inlet and the chamber. For the highest Mach number cases, vortex shedding occurs at the natural instability frequency of the shear layer and the first vortex merging occurs at the first subharmonic of the shedding frequency. That is, the shear layer near the inlet to the chamber (within about 1.5 D) is not affected significantly by the acoustics of the system. This is perhaps because the dominant acoustic frequencies of the system are significantly lower than the shear-layer instability frequency and its first subharmonic. However, even for these two cases, the acoustic frequencies of the system do affect the vortex dynamics downstream from the step. The dominant low-frequency oscillation observed in earlier simulations [1,3,5] did not appear at high Mach number, probably because the chamber is not long enough to accomodate the mergings which are required to attain low frequencies from the high vortex-shedding frequencies.

At low Mach number, the acoustic frequencies are more important. For Mach number 0.15, vortex shedding occurred primarily at the first longitudinal frequency of the chamber, which is similar to previous numerical simulations [1,3,5]. For this case and for the earlier simulations, the first longitudinal mode frequency is close to the natural instability frequency of the shear layer, and the acoustic mode of the inlet remains important.

From this series of calculations, we conclude that the shear layer in a confined chamber rolls up at either its natural instability frequency or at a dominant acoustic frequency of the system, if that frequency is nearly equal to or greater than the natural instability frequency. In all the simulations, the acoustic frequencies strongly affect the vortex mergings occurring within the chamber.

Acknowledgements

This work was sponsored by the Office of Naval Research and the Naval Air Systems Command. The support and encouragement from Dale Hutchins at NAVAIR , Robert J. Hanson at ONR and Douglas Davis at AFWAL is greatfully acknowledged.

References

1. Kailasanath, K., Gardner, J.H., Boris, J.P. and Oran, E.S., "Acoustic-Vortex Interactions in an Idealized Ramjet Combustor," *Proceedings of the 22nd JANNAF Combustion Meeting, Pasadena, CA,* CPIA publication 432, Vol. 1, Oct. 1985, pp. 341-350.
2. Jou, W.H. and Menon, S., "Large Eddy Simulations of Flow in a Ramjet Combustor," *Proceedings of the 22nd JANNAF Combustion Meeting, Pasadena, CA,* CPIA publication 432, Vol. 1, Oct. 1985, pp. 331-339.

3. Kailasanath, K., Gardner, J., Boris, J. and Oran, E., "Interactions Between Acoustics and Vortex Structures in a Central Dump Combustor," AIAA paper 86-1609, also see *J. Prop. Power*, Vol. 3, Nov-Dec. 1987, pp. 525-533.
4. Schadow, K.C., Wilson, K.J., Crump, J.E., Foster, J.B. and Gutmark, E., "Interaction Between Acoustics and Subsonic Ducted Flow with Dump," AIAA paper No. 84-0530, presented at the AIAA 22nd Aerospace Sciences Meeting, Jan. 1984.
5. Kailasanath, K., Gardner, J.H., Boris, J.P., and Oran, E.S., "Acoustic-Vortex Interactions and Low Frequency Oscillations in Axisymmetric Combustors," AIAA paper 87-0165, presented at the AIAA 25th Aerospace Sciences Meeting, Reno, Jan. 1987 (also submitted to AIAA J. Prop. Power.)
6. Boris, J.P. and Book, D.L., "Solution of Continuity Equations by the Method of Flux Corrected Transport," *Methods of Computational Physics*, Academic Press, New York, 1976, Vol. 16, Chapter 11.
7. Oran, E.S., Young, T.R. and Boris, J.P., "Application of Time-Dependent Numerical Methods to the Description of Reactive Shocks," *Seventeenth Symposium (International) on Combustion*, The Combustion Institute, Pittsburgh, 1979, p. 43.
8. Kailasanath, K., Oran, E.S., Boris, J.P. and Young, T.R., "A Computational Method for Determining Detonation Cell Size," AIAA paper No. 85-0236, presented at the AIAA 23rd Aerospace Sciences Meeting, January 1985.
9. Guirguis, R.H., Grinstein, F.F., Young, T.R., Oran, E.S., Kailasanath, K., and Boris, J.P., "Mixing Enhancement in Supersonic Shear Layers," AIAA paper 87-0373, presented at the AIAA 25th Aerospace Sciences Meeting, Reno, Jan. 1987.
10. Boris, J.P., Oran, E.S., Gardner, J.H., Grinstein, F.F., and Oswald, C.E. "Direct Simulations of Spatially Evolving Compressible Turbulence, *Ninth International Conference on Numerical Methods in Fluid Dynamics*, pp. 98-102. Springer-Verlag, 1985.
11. Grinstein, F.F., Oran, E.S. and Boris, J.P., "Direct Simulation of Asymmetric Mixing in Planar Shear Flows,"*J. Fluid Mech*, Vol. 165, 1986, pp. 201-220.
12. Kailasanath, K., Gardner, J.H., Boris, J.P., and Oran, E.S., "Numerical Simulations of the Flow Field in a Central Dump Ramjet Combustor–I. Tests of the Model and Effects of Forcing," NRL Memorandum Report 5832, Naval Research Laboratory, Washington, D.C., 20375.
13. Zaman, K.B.M.Q., and Hussain, A.K.M.F., "Vortex Pairing in a Circular Jet Under Controlled Excitation. Part 1. General Jet Response," *J. Fluid Mech.*, Vol. 101, 1980, pp. 441-449.
14. Michalke, A., "On Spatially Growing Disturbances in an Inviscid Shear Layer,"*J. Fluid Mech.*, Vol. 23, 1965, pp. 521-544.

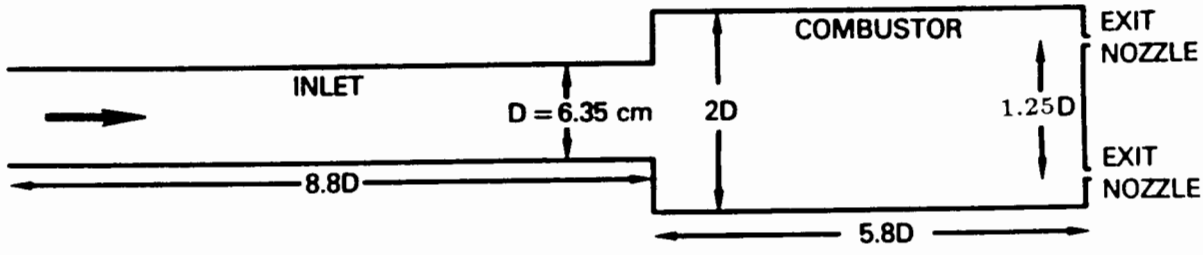

Figure 1. Schematic of the axisymmetric configuration described in the simulations. Flow through a long inlet cylinder exits into an axisymmetric, confined chamber. The flow exit is a choked, annular region. The initial chamber pressure is 188 kPa.

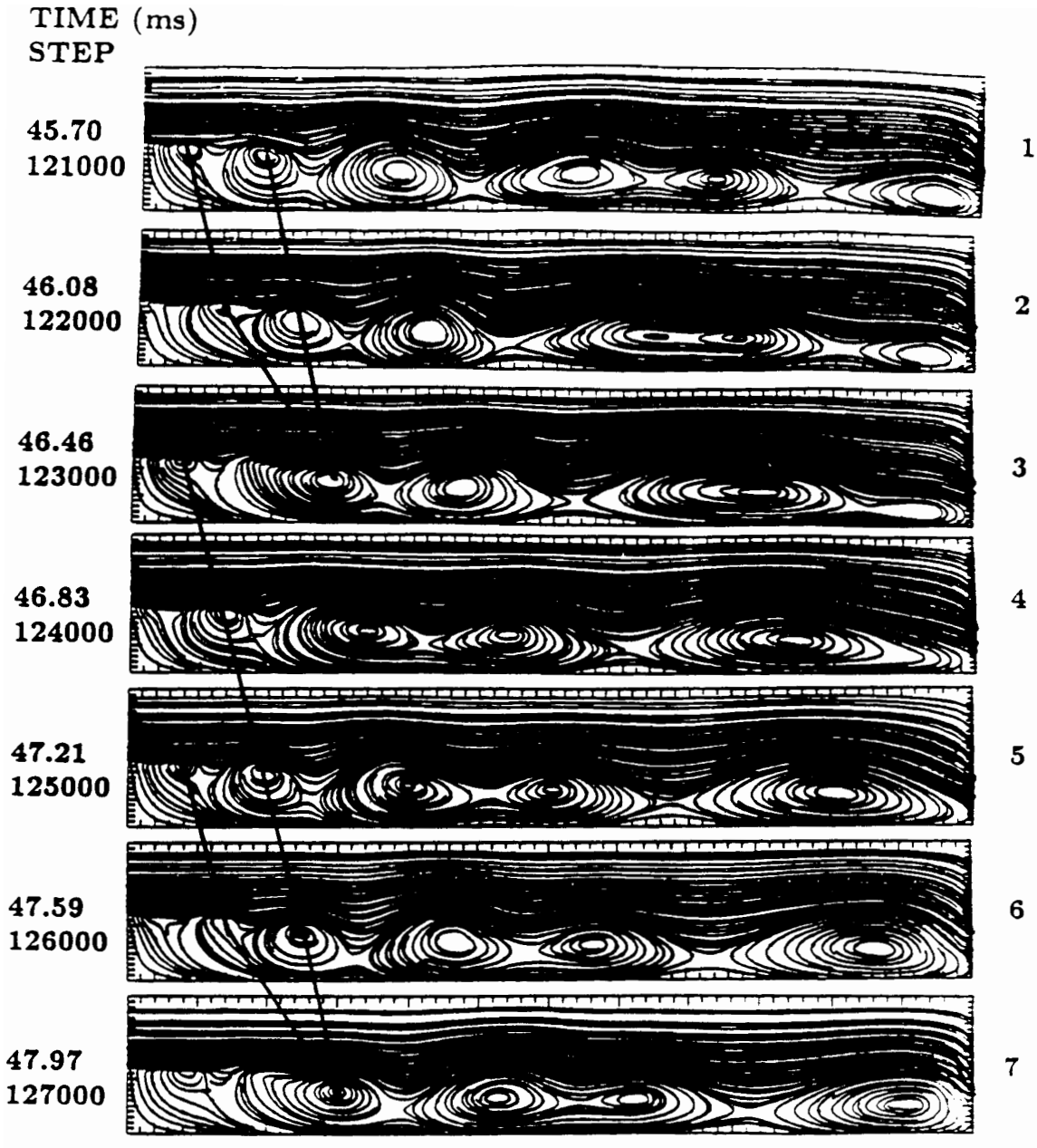

Figure 2. Sequence of instantaneous velocity streamlines for inflow Mach number 0.31, showing vortex shedding and merging near the step in the chamber.

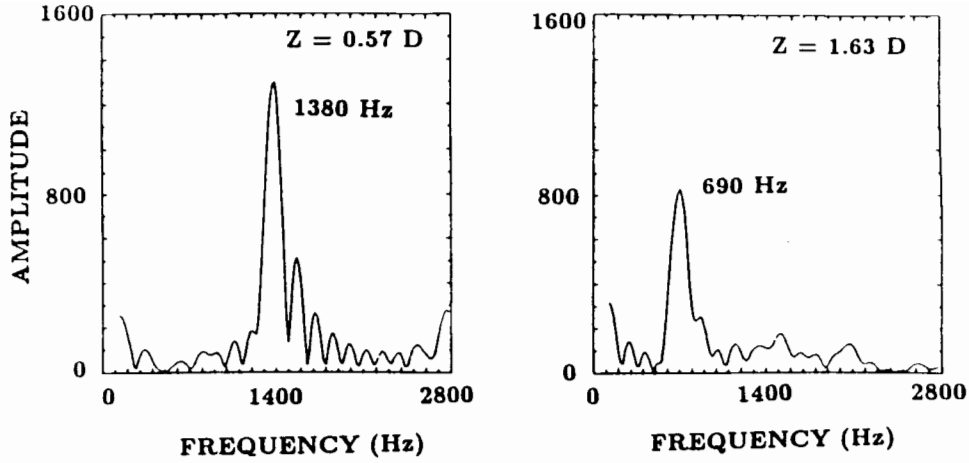

Figure 3. Frequency spectra of velocity fluctuations in the shear layer at two locations near the step in the chamber for Mach 0.31 flow.

Figure 4. Frequency spectra of velocity fluctuations in the shear layer at three locations in the chamber for Mach 0.15 flow.

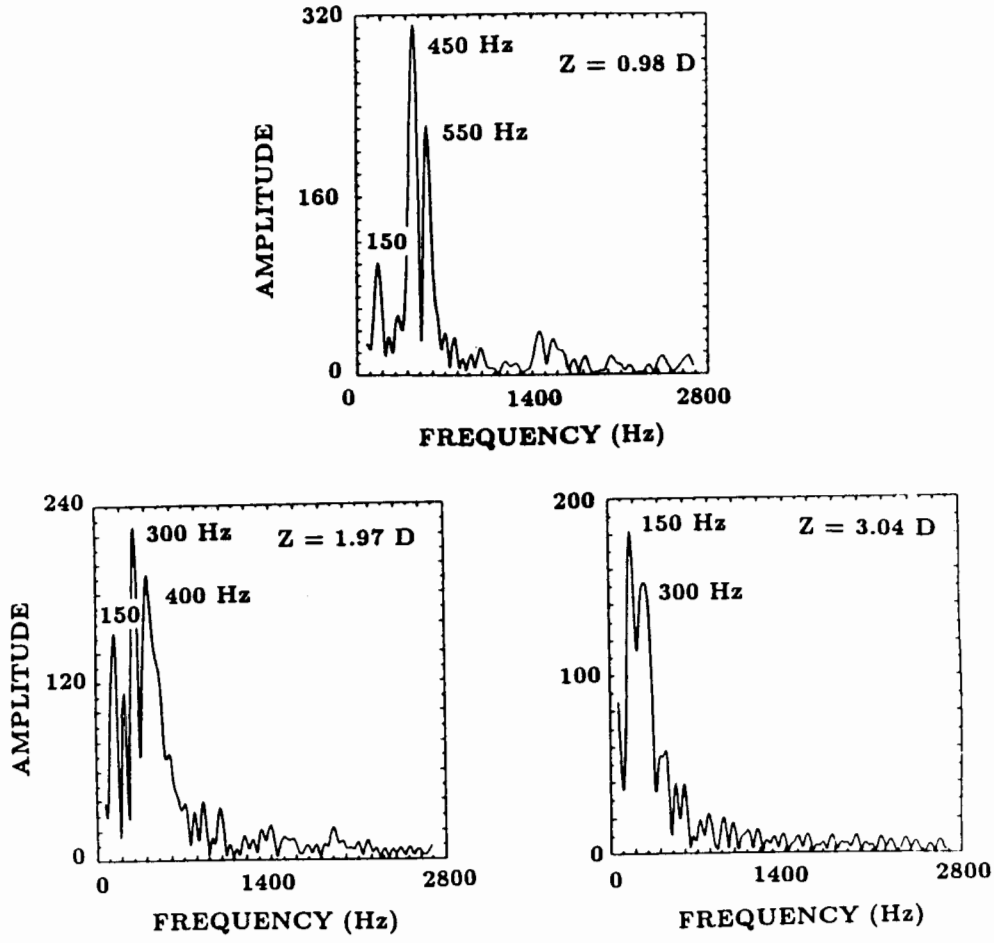

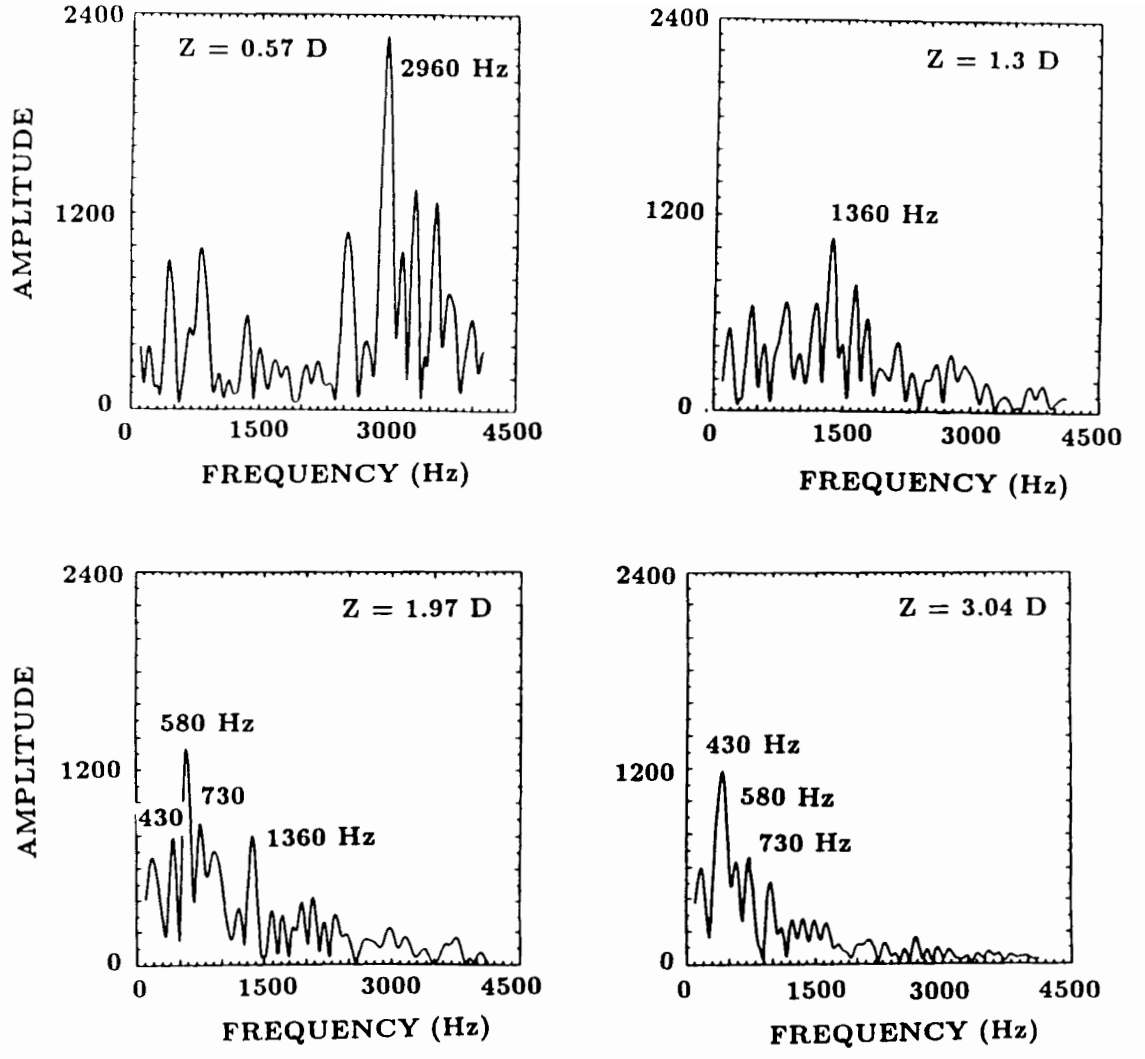

Figure 5. Frequency spectra of velocity fluctuations in the shear layer at four locations in the chamber for Mach 0.61 flow.

EXTENSION OF SECOND-MOMENT TURBULENCE MODELS IN CASES WITH LARGE DENSITY NON-UNIFORMITY

Jordan M. MacInnes
M.A.E. Dept., Princeton University
Princeton, NJ 08544

ABSTRACT

The paper provides an assessment of the turbulence modeling of incompressible non-reacting flows and focuses on the main physical processes associated with the density non-uniformity in such cases. Experimental evidence from plane mixing layers under various conditions is used to deduce some controlling mechanisms and to arrive at a proposed modeling to represent those mechanisms.

Introduction

MacInnes [1985] made an extensive examination of the modeling of each term in the exact transport equations for the second moments. The performance of the models was judged in comparison with data from self-preserving non-reacting and incompressible flows with sustained density gradients resulting from either a variation in molecular weight or a large temperature variation in gas flow. Each of the cases considered showed behavior which the standard models failed to capture even qualitatively. After assessing the possible influence of each of the terms in the moment equations associated with density non-uniformity, it could be firmly concluded that none of these terms could help to explain the experiments.

A more promising prospect for bringing agreement with the experiments was found to lie in the modeling of the dissipation rates of both the turbulence kinetic energy and the scalar property variance. New terms may reasonably be introduced into the modeled dissipation rate equations to represent the effects of density non-uniformity. The focus of the paper is on the new terms in the dissipation equations. Before discussing the dissipation modeling, a brief overview of the key experimental evidence is given, followed by a summary of how density non-uniformity enters into the second-moment modeling generally.

Guiding experiments

There are few reports of measurements in flows with large density non-uniformity that are at the same time sufficiently simple to provide solid guidance in the modeling. Obtaining good measurements in flow with variations in both velocity and density is extremely difficult. It is perhaps not surprising, therefore, that only three experimental studies are directly helpful in developing models and that each has settled on measuring just the mean field quantities. The first two, Brown and Roshko [1974] and Rebollo [1973], employ the same apparatus at Caltech to study the plane turbulent mixing between helium and nitrogen gas streams. The density ratio between the two gas streams is 1:7 and various velocity ratios are tested.

Two cases are representative of the basic phenomena observed throughout the various data sets. The case measured by Rebollo in which the low-density helium flows at about three times the speed of the nitrogen shows two striking features: the rate of spreading of the mean velocity profile is about 25% greater than for the uniform-density mixing layer (in this case the value used for the uniform-density limit is that measured in the same rig for nitrogen mixing with air) and the turbulent Schmidt number drops from around 0.6 to 0.7 in the uniform density mixing layer to around 0.2. These observations are reinforced by the other case reported in Brown and Roshko in which the helium stream is the slowest moving of the two, having only about one third the speed of the nitrogen stream. Here, the spreading rate drops by about 30% relative to the uniform density case and the Schmidt number increases to around 0.8. These results are summarized in Table 1 for reference since they are the central guiding facts in the present study.

A third and much different flow case is considered in MacInnes [1985]. Mean temperature distributions in a highly heated plane thermal mixing layer were measured with a fine-wire thermocouple probe. The flow is formed by passing a hot and an ambient air stream through a turbulence grid and allowing mixing to proceed beyond the grid. The mean velocity is uniform and hence no important augmentation of the turbulence energy created in the vicinity of the grid can occur.

Measurements in three cases of density ratio between the two streams are reported: 1.03, or approximately uniform density, 1.26, and in the case of greatest heating 1.95. The results for the thermal layer growth are shown in Figure 1. The data are plotted so that the virtual origins coincide (theoretical considerations dictate that the layer width increase as the one-half power of the downstream distance). The striking feature displayed by the data is an increase in the growth rate of the layer width with density differential. In the case with medium heating the layer width is 23% greater than with passive heating, in the case of maximum heating it is 43% greater. From the latter increase one can infer an approximate doubling of the turbulent diffusivity level.

Modeling

A turbulence model intended for application in combusting and compressible flow must be capable of simulating the gross effects outlined above. This section presents a brief overview of second-moment level modeling highlighting the possible roles that density non-uniformity could play.

In variable density flows the most common method of decomposing the instantaneous variables is to use density-weighted means for all variables except pressure and the density itself. As is widely known, this approach leads to equations which are nearly identical in form to the uniform-density ones, but written in terms of the density-weighted quantities. The simplicity of the equations is often construed as a sign that density-weighting is the "natural" way to form averages and models developed in uniform-density flows are commonly translated into a variable-density form by simply replacing the standard un-weighted mean quantities with the weighted ones. However, no solid justification has been given for such a scheme.

The other approach of using standard mean values is adopted here, as it was in MacInnes [1985]. Of course, the two decompositions are equivalent expressions of the conservation laws and modeling developed under one decomposition scheme can in principle be converted to the other scheme.

In the following, attention is restricted to flows which are steady in the mean as this allows simplification in presentation and is applicable to all experimental cases considered. The mean equations for momentum, scalar, and mass conservation are

$$\frac{\partial(\rho U_j+\overline{\rho' u_j})U_i}{\partial x_j} = -\frac{\partial P}{\partial x_i} - \frac{\partial \rho\overline{u_i u_j}+\overline{\rho' u_i}U_j+\overline{\rho' u_i u_j}}{\partial x_j}$$

$$\frac{\partial(\rho U_j+\overline{\rho' u_j})C}{\partial x_j} = -\frac{\partial \rho\overline{u_j c}+\overline{\rho' c}\,U_j+\overline{\rho' c u_j}}{\partial x_j} \qquad (1)$$

$$\frac{\partial \rho U_j+\overline{\rho' u_j}}{\partial x_j} = 0$$

C is the mean value of the scalar quantity and c denotes its fluctuation about the mean. Generally, upper case letters designate the mean while lower case letters designate the fluctuation. An exception is made for Greek letters in which case the fluctuation is designated by a prime, eg ρ is mean density, ρ' is the fluctuation about the mean. As a result of

density fluctuations an additional four correlations enter the set of mean equations joining the two, $\overline{u_i u_j}$ and $\overline{u_j c}$, found in uniform density.

MacInnes [1985] reports the influence of including the triple moments which occur in equations (1) and finds only minor alterations to the calculated mean profiles and turbulence quantities in the shear flows examined. Note that the mass flux $\overline{\rho' u_j}$ appearing in the convection terms is important in the direction transverse to the main flow direction since then the mean velocity is small. (In the thin flows considered here $\overline{\rho' u_j}$ does not need to be explicitly introduced into the calculations, as it can be eliminated using mass continuity.)

The models for $\overline{u_i u_j}$ and $\overline{u_j c}$ employed are at what is termed second-moment level. This means that the second moments are found by solving modeled versions of their exact transport equations. Higher moments are modeled with at most algebraic formulas. To sketch briefly what is involved in modeling the second moments the exact form of the $\overline{u_i u_j}$ equation will be considered.

$$\frac{\partial(\rho U_k + \overline{\rho' u_k})\overline{u_i u_j}}{\partial x_k} = P_{ij} - \rho\varepsilon_{ij} + \phi_{ij} + D_{ij} \tag{2}$$

where the terms on the right-hand side represent the terms providing production, dissipation, pressure smearing, and diffusion of the $\overline{u_i u_j}$ components, respectively. These are

$$P_{ij} = -(\rho\overline{u_i u_k}\frac{\partial U_j}{\partial x_k} + \rho\overline{u_j u_k}\frac{\partial U_i}{\partial x_k})$$
$$-(\overline{\rho' u_i u_k}\frac{\partial U_j}{\partial x_k} + \overline{\rho' u_j u_k}\frac{\partial U_i}{\partial x_k}) + U_k(\overline{\rho' u_i}\frac{\partial U_j}{\partial x_k} + \overline{\rho' u_j}\frac{\partial U_i}{\partial x_k})$$

$$\rho\varepsilon_{ij} = -\overline{\tau_{ik}'\frac{\partial u_j}{\partial x_k}} - \overline{\tau_{jk}'\frac{\partial u_i}{\partial x_k}}$$

$$\phi_{ij} = \overline{p(\frac{\partial u_i}{\partial x_j} + \frac{\partial u_j}{\partial x_i})} \tag{3}$$

$$D_{ij} = -\frac{\partial}{\partial x_k}(\rho\overline{u_i u_j u_k} + \overline{pu_i}\delta_{jk} + \overline{pu_j}\delta_{ik} - \overline{u_i\tau_{jk}'} - \overline{u_j\tau_{ik}'})$$
$$-\frac{\partial}{\partial x_k}(\overline{\rho' u_i u_j u_k} - \overline{\rho' u_k}\,\overline{u_i u_j} + U_k\overline{\rho' u_i u_j})$$

There are a number of new terms relating to interactions with the mean flow incorporated in P_{ij}. These turn out to be less than about 10% compared with the main terms and do not play an important role. The pressure correlation may be analyzed using the quasi-isotropic model (QIM) of Naot et al [1973] and developed in Launder et al [1975]. The pressure fluctuation is represented in terms of mean and fluctuating velocity (and density) using the solution to its Poisson equation formed from the fluctuating part of the momentum equation. Substitution for p in ϕ_{ij} leads to an integral expression involving two-point correlations. The QIM amounts to assuming the two-point correlations to have properties strictly true only in isotropic turbulence but allowing the one-point limit to be anisotropic.

MacInnes [1985] has examined the QIM path with regard for density fluctuation and has derived the series of new terms which are implied. Test calculations show that, much as the non-uniform density P_{ij} terms make little impact on the calculations, the refinements in ϕ_{ij} modeling are not very important in the flows considered. One indication of that study, however, seems to be that the practice of translating the pressure models by just rewriting them in terms of density-weighted variables, Jones [1980], is probably acceptable. The extra QIM terms are incorported into the density-weighted averages.

The diffusion terms, D_{ij}, are unlikely to hold much sway over the calculated $\overline{u_i u_j}$. Even in uniform density flows of the thin, unidirectional sort examined here these terms are of little importance. It is interesting, however, to note the appearance of a quadruple moment. Vandromme and Kollmann [1982] introduced modeling for the quadruple moments to account for the quite steep gradients in second moments in calculations of the Caltech mixing layers.

None of the effects due to density non-uniformity mentioned up to this stage proves to have much effect on either the calculated rate of spread or the Schmidt number level in a mixing layer. The values calculated will be essentially those which are calculated with uniform density. One must evidently turn to modeling the dissipation rates of $\overline{u_i u_j}$ and $\overline{c^2}$ in order to capture the observed behavior. It is reasonable to expect ε_{ij} to be isotropic since the eddy sizes in which this term is important are far removed from the small wave number spectra where the mean flow gives the turbulence an orientation. Thus, $\varepsilon_{ij}=2/3\varepsilon\delta_{ij}$ may be used, leaving only ε together with ε_c, the dissipation rate of $\overline{c^2}$, to be found.

Dissipation rate modeling

Rather than model the actual dissipation process one models the process by which the large scale motions are converted, by stretching, into smaller and smaller scales, to the point where molecular dissipation becomes important. It is the spectral transfer which must be described by the model and not the actual dissipation associated with sharp velocity gradients

or scalar gradients.

Model transport equations for ε and ε_c are constructed by using invariant parameters depending on the mean field variables and the turbulence correlations. For ε

$$\frac{\partial(\rho U_j+\overline{\rho' u_j})\varepsilon}{\partial x_j} = \rho\frac{\varepsilon^2}{k}\psi_\varepsilon + D(\varepsilon) \tag{4}$$

where $D(\varepsilon)$ represents the rate of change of ε due to diffusion processes and is usually modeled using a gradient diffusion hypothesis. The crucial element of the model is the dimensionless source/sink function ψ_ε. This term should naturally act to increase the dissipation rate (spectral transfer rate) when turbulence generation increases but to decrease it as the dissipation rate grows. The form commonly used to represent these effects is

$$\rho\frac{\varepsilon^2}{k}\psi_\varepsilon^0 = \frac{\varepsilon}{k}C_1\frac{P_{kk}}{2} - \rho\frac{\varepsilon}{k}C_2\varepsilon \tag{5}$$

The '0' superscript on ψ_ε emphasizes that this is a model for uniform density flow. The same sort of approach can be used to develop an equation for ε_c. More terms enter into the ψ_{ε_c} function since the spectral transfer of scalar fluctuation depends not just on the scalar fluctuation processes of generation and dissipation but also on the same parameters that make up ψ_ε since scalar fluctuations depend on the state of the turbulent motions. Such an equation has been developed by Newman et al [1981] and is being used in this study.

In order to extend the model to include density effects one must consider the possible ways in which the density non-uniformity might affect the way turbulent eddies are stretched. There appear to be two main influences. The first is associated with the presence of density fluctuation, even when mean gradients of density are locally absent. The idealized picture is in Figure 2. Solid and open circles represent heavy and light elements of fluid respectively. In Figure 2*a* the elements are shown evenly distributed in a region of the fluid. Imagining now that the fluid in this region is in rotational motion, caught up in an eddy motion, the heavy elements will be forced through centrifugal action to the outer regions of the eddy, the light ones to the center, as illustrated in Figure 2*b*. With the mass concentrated on the outer rim of the eddy the angular speed must decrease in order for angular momentum to be conserved. The slower eddy rotation causes a reduction in induced lift and the consequent stretching of the eddy, which in effect means the eddy will be stabilized. The result is reduced transfer of energy to smaller-scale eddies. This process can be used to explain the observed higher levels of turbulent transport in the thermal mixing layer experiments, the density non-uniformity acting to reinforce the turbulent motions against erosion

into smaller scale motions.

The second effect is more global in nature, having to do with mean spatial variation in density. When a large eddy is aligned with its rotation axis perpendicular to the mean density gradient, the eddy is influenced by centrifugal forces in a rather more complicated way. Again, an idealized picture is useful to understand what results. Figure 3 shows an eddy region in which high density fluid and low density fluid mutually entrain (the density gradient, which is downwards, is perpendicular to the axis of the eddy motion which is outward). At the interfaces between the two fluids there will be either a stable or an unstable balance depending on the curvature. In the illustration, sections of the interface subject to destabilization are indicated by an irregularly drawn line while stabilized interface is designated with a smooth line. Since the largest eddies will be most prone to this effect, the indication is that the eddy will be destabilized and broken down into small scale motions in the low density region, while the break-down will be suppressed on the high-density side. Correspondingly, turbulence energy should be more rapidly transferred spectrally and, hence, dissipated in the low density region and less rapidly on the high density side. While the first effect described would always tend to increase the level of turbulence regardless of the orientation of the mean density and the mean velocity gradients, the second may be expected to lead to an overall increase or decrease in the turbulence level depending on the mean flow conditions. Hence, the second effect may be able to account for the opposite result found in the Caltech mixing layers when the density gradient is reversed.

Many possible terms can be imagined with which to represent the above effects in the ψ_ε and the ψ_{ε_c} functions. All terms appear to be of two main types as far as their behavior in boundary layer type flows is concerned. One type of term maintains the same sign across the entire layer and corresponds to the first effect. The other type reverses sign and could be used to represent the second effect. For the purposes of initial explorations, a model composed of two terms which are the most convenient from a computational point of view are chosen to represent the two effects in the ψ_ε functions. The new terms

$$\psi_\varepsilon^\rho = C_{\rho 1}\frac{k^3}{\rho^2\varepsilon^2}\left(\frac{\partial \rho}{\partial x_i}\right)^2 + C_{\rho 2}\frac{k^3}{\rho\varepsilon^2}\frac{\partial \rho^2}{\partial {x_i}^2} \tag{6}$$

are added to ψ_ε^0 to represent the two processes.This additive function has been used with the same coefficient values $C_{\rho 1}$ and $C_{\rho 2}$ in both the ε and ε_c equations in calculations of the Caltech mixing layers. It was found that the coefficients could, indeed, be selected to bring perfect agreement with the observed layer growth rates in the two cases. The second term produced a greater spreading rate in one case than in the other, though as the gap widened the spreading rates of both cases were underpredicted. The first term was needed to increase

the growth rate in both cases in order to bring agreement with the experiments. The Schmidt number, on the other hand, is predicted as before -- nearly equal to the uniform-density value in both cases. This indicates that the coefficients need to be selected independently for the ε and the ε_c equations. This step has yet to be taken.

Summary

An overview of the second-moment modeling of non-uniform density but incompressible turbulent flows has been made, giving strong support for modifying the dissipation rate equations. Two mechanisms whereby the density non-uniformity influences the spectral transfer rates have been described and corresponding addition terms in the dissipation rate equations representing these mechanisms have been presented. The limited amount of testing which has at present been completed indicates the model can bring agreement with the observed spreading rates of mixing layers. However, it cannot be determined whether the observed variation of the turbulent Schmidt number can be accounted for by the model until tests are carried out in which the model coefficients in the scalar and kinetic energy dissipation equations are adjusted independently.

References

Brown, G.L. and A. Roshko, 1974, "The effect of density difference on the turbulence mixing layer", J. Fluid Mech., Vol. 64, pp. 775-816.

Jones, W.P., 1980, "Models for turbulent flows with variable density and combustion", in Prediction Methods for Turbulent Flows, ed. W. Kollmann, Hemisphere.

Launder, B.E., G.J. Reece, and W. Rodi, 1975, "Progress in the development of a Reynolds-stress turbulence closure", J. Fluid Mech., Vol. 68, pp. 537-566.

MacInnes, J.M., 1985, "Turbulence modelling of flows with non-uniform density", Ph.D. Thesis, University of Manchester Institute of Science and Technology.

Naot, D., A. Shavit, and M. Wolfshtein, 1970, "Interaction between components of the turbulent velocity correlations tensor due to pressure fluctuations", Israel J. Tech., Vol. 8, pp. 259-269.

Newman, G.R., B.E. Launder, and J.L. Lumley, 1981, J. Fluid Mech., Vol. 111, p217.

Rebollo, M.R., 1973, "Analytical and experimental investigation of a turbulent mixing layer of different gases in a pressure gradient", Ph.D. thesis, California Institute of Technology.

Vandromme, D. and W. Kollmann, 1982, "Second order closure for variable density free shear layer", Turbulent Shear Flows 3, Springer-Verlag.

Table 1. Experimental findings in variable density mixing layers.
(Subscript '0' indicates uniform density value.)

Case	ρ_A/ρ_B	U_A/U_B	$\frac{d\delta_{19}}{dx}/(\frac{d\delta_{19}}{dx})_0$	Sc_t/Sc_{t_0}
I	7.0	0.38	1.25	0.31
II	7.0	2.63	0.71	1.23

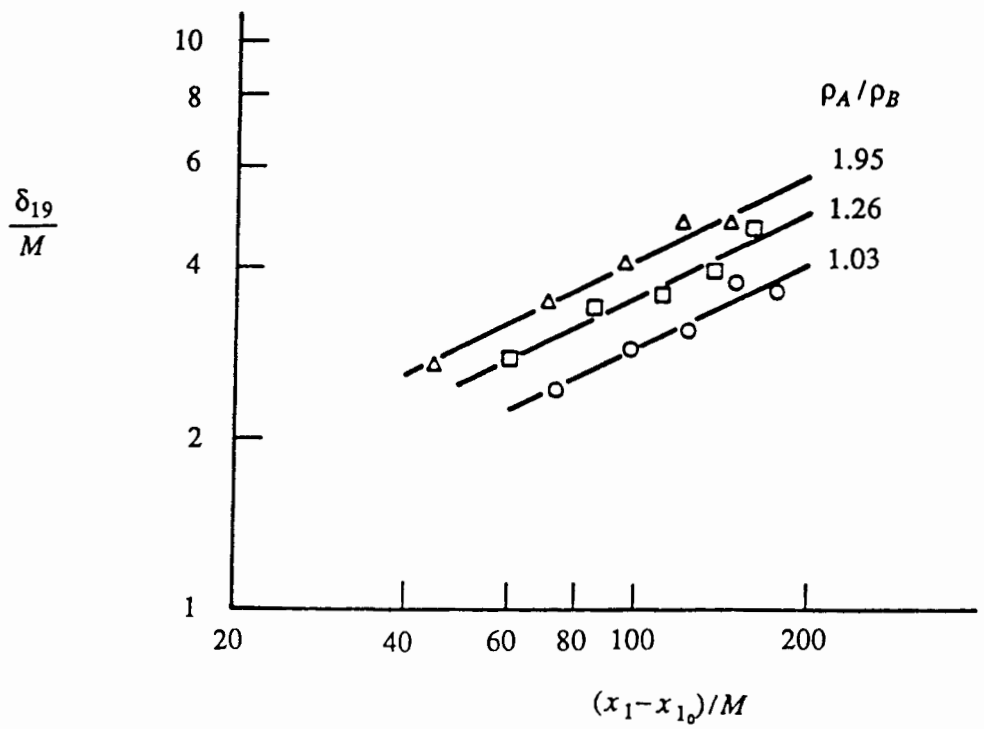

Figure 1. Thermal layer growth for three density ratios. M is the distance between grid wires and x_{1_0} is the virtual origin of the thermal layer.

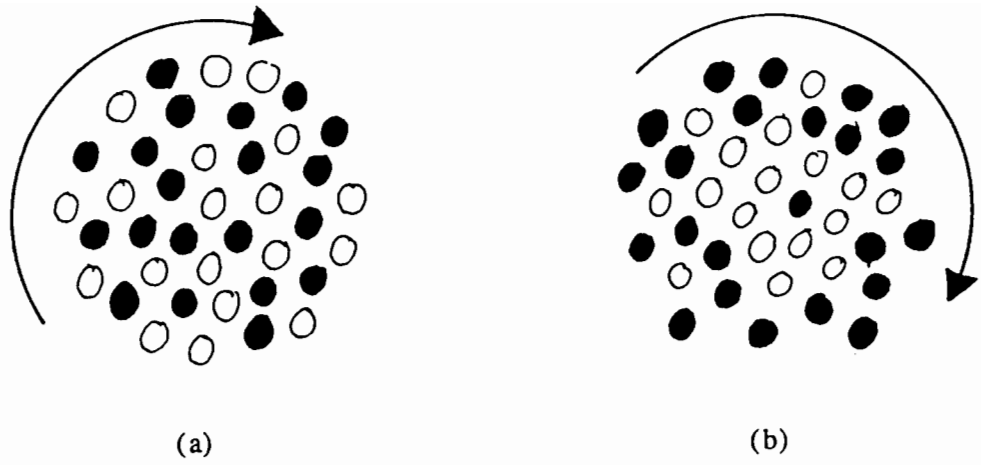

Figure 2. Centrifuge mechanism operating in non-uniform density turbulence. Uneven distribution of density in fluid caught up in an eddy motion leads to heavy elements of fluid (●) concentrating at the rim of the eddy leaving light elements of fluid (0) in the center.

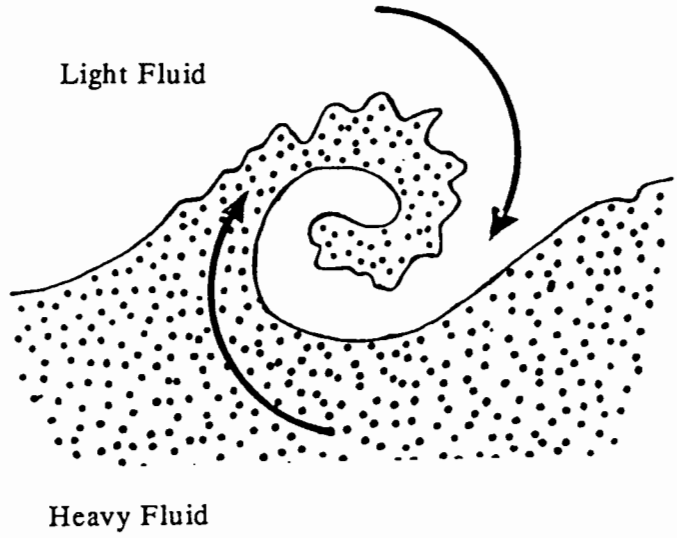

Figure 3. An idealized eddy that has its rotation axis perpendicular to the direction of mean density gradient. Light and heavy fluid mutually entrain, as shown, producing stabilization or destabilization at the interface.

"INSTANTANEOUS VELOCITY PROFILES AND DENSITY CROSS SECTIONS IN SUPERSONIC SHEAR LAYERS"

R. Miles, A. Smits, E. Markovitz, J. Connors, G. Roth, P. Howard
M. Smith, V. Kumar, and W. Lempert
Department of Mechanical & Aerospace Engineering
PRINCETON UNIVERSITY
Princeton, New Jersey 08544

ABSTRACT

A new method of nonintrusive diagnostics in air based on vibrational excitation of oxygen, laser-induced fluorescence and Rayleigh scattering, is applied to a supersonic axisymmetric free jet and a supersonic Mach 3 boundary layer to generate instantaneous velocity profiles and density cross sections. The velocity profiles give a quantitative measure of the velocity across the jet at any location downstream of the nozzle exit. Numerous such images are taken at several locations to generate average velocity profiles as well as turbulence intensity and axial velocity correlations across the turbulent free shear layer. Simultaneous Rayleigh scattering gives a two-dimensional cross section of the density. In the boundary layer, Rayleigh scattering is used to generate instantaneous density cross sections, two-dimensional density correlations, and probability density distribution functions of the density. This new measurement technique introduces a promising method to make quantitative comparisons with computational models.

DISCUSSION

Our newly developed capability of writing lines into air flows (1) gives us a unique tool for measuring instantaneous velocity profiles and determining the statistics of the turbulent flow in shear layers. Lines are tagged and interrogated by Raman Excitation and Laser-Induced Electronic Fluorescence (RELIEF). Vibrational tagging occurs during a 10 nsec interval by simultaneously passing two high-power pulsed laser beams colinearly through the flow region. These beams are separated in frequency by the vibrational frequency of oxygen and, consequently, write a line of vibrationally excited oxygen by stimulated Raman excitation. Since the oxygen molecules are excited to the same rotational state from which they came, there is virtually no heating associated with this tagging mechanism.

The vibrational lifetime of oxygen is in excess of 100 μsec in air, so the line persists in the flow until it is interrogated by laser-induced electronic fluorescence using a far UV argon-fluoride laser. The interrogation also occurs over approximately 10 nsec, and the fluorescence is imaged with a high-sensitivity video camera. The displacement of the line between tagging and interrogation

gives a quantitative measure of the velocity profile. If the interrogating laser is expanded into a thin sheet of light passing through the flow field, the Rayleigh scattering can be simultaneously imaged to give a two-dimensional cross section of the density.

Two experiments are reported in this paper. The first is the measurement of velocity profiles, turbulence intensities, and correlations in the free shear layer of an underexpanded sonic jet. The second experiment shows preliminary measurements of density cross sections in a Mach 3 supersonic boundary layer. Work on velocity tagging in the boundary layer is currently underway, and is not included in this paper.

Free Jet Experiment

A diagram of the underexpanded supersonic jet is shown in Fig. 1. This jet was run with a pressure ratio of 10.2 to 1 into a one atmosphere chamber, leading to a maximum Mach number of 4.06 at the Mach disk, and a maximum flow velocity of 621 meters/sec. Table I shows the computed velocity, pressure, temperature, Mach number, and density as a function of distance from the orifice (2). The orifice was 6.35 mm in diameter (.25"), and the Mach disk was located approximately two orifice diameters downstream of the exit. Figure 2 shows the image of a single line which was written across the supersonic expansion 2 μsec before the picture was taken. The line was written approximately 2 mm upstream of the Mach disk, which can be seen in the figure due to the large difference in Rayleigh scattering associated with the change in density. Other features including the reflected shock, the barrel shock, and the turbulent free shear layer are also apparent in this figure.

By placing a far UV-blocking filter over the camera, only the fluorescence from the marked line is visible. Figure 3 is a close-up view of four separate images showing four examples of the instantaneous turbulent structure. By observing hundreds of such images, the average velocity profile and the turbulence intensity across the free shear layer can be determined. Furthermore, since each individual image contains the instantaneous profile of the axial velocity component, these images may be used to find the correlation of the axial velocities across the free shear layer. Figure 4 shows the computed velocity profile, turbulence intensity, and the correlation with the axial velocity at the center of the free shear layer. Figure 5 is a composite indicating the growth of the free shear layer as a function of the distance from the nozzle exit to the Mach disk. Each inset shows the turbulence intensity and the transverse correlation of the axial component of the velocity. Figure 6 shows a plot of the width of the shear layer versus distance

from the exit, and Fig. 7 shows the normalized integral length scale taken from the correlations as a function of distance from the exit. The velocity along the centerline of the jet was also measured, and Fig. 8 shows a plot of the measured center velocities compared with the computed values (2). The velocity uncertainty in this figure is caused by inaccuracies in the measurement of the line position due, largely, to the finite resolution of the camera. The position uncertainty reflects the distance the line moved between tagging and interrogation.

Supersonic Boundary Layer Experiment

Preliminary measurements were also made in a the boundary layer of a small Mach 3 wind tunnel facility. A time-frozen Rayleigh scattering cross section of that boundary layer is shown in Fig. 9. The brightness is a direct measurement of the density. The density is lowest near the wall where the temperature is high, and highest in the free stream where the temperature is low. The flow is from right to left, the Reynold's number is 15,000 based on the boundary layer momentum thickness, and the boundary layer is 5 mm thick. Many such images can be combined to generate the average density variation, and the spatial fluctuations of the density can be correlated to generate a two-dimensional density correlation function which shows the shape and extent of the turbulent structure. Figure 10 shows three correlations in the boundary layer where the correlation points have been chosen at a y/δ of 0.4, 0.6, and 0.8. High brightness indicates strong correlations and the dark lines indicate constant correlation contours. Note that the angle of the correlation at $y/\delta = 0.4$ agrees with the structure angles measured by hot wire probes (3).

By changing the wind tunnel orientation, a plan form view of the boundary layer can also be taken at selected heights above the wall. Figure 11 shows the picture of a plan form view at a y/δ of 0.6. Since the brightness is a measure of the density, a probability density distribution function of the density can be created from each plan form image. The variation of that probability density distribution function with distance from the wall is shown in Fig. 12. An expanded view at $y/\delta = 0.6$ is shown in Fig. 13. These curves are similar to the probability density distribution of mass-flux fluctuations measured by Hayakawa et al. (4) in a similar flow, giving indirect support to the Strong Reynolds Analogy. In Fig. 14 a 16° angle wedge has been placed in the flow to show the dynamics of shockwave boundary layer interactions.

Work is currently underway to better quantify the probability density functions of the density as well as the density correlations. By marking lines in the boundary layer we also expect to be able to see the correlation between velocity and density

fluctuations. By crossing the tagging laser beams, small football-shaped volume elements can be written into the flow and tracked to give three-dimensional velocity and vorticity vectors. We expect that the development of this new technique will open the door to volumetric measurements of both low-speed and high-speed flows.

ACKNOWLEDGEMENT

This work was sponsored by the Air Force Office of Scientific Research.

REFERENCES

1. R. Miles, C. Cohen, J. Connors, P. Howard, S. Huang, E. Markovitz, and G. Russell, "Velocity Measurements by Vibrational Tagging and Fluorescent Probing of Oxygen," Optics Letters 12, 861, (November 1987).

2. S.M. Dash in "Tactical Missile Aerodynamics," Progress in Astronautics and Aeronautics, Vol. 104, Edited by M.J. Hemsch and J. N. Nielsen (AIAA, New York 1986), pp. 778-841.

3. E.F. Spina and A.J. Smits, "Organized Structures in a Compressible, Turbulent Boundary Layer," J. Fluid Mech. 182, 85 (1987).

4. K. Hayakawa, A.J. Smits, and S.M. Bogdonoff, "Hot-Wire Investigation of an Unseparated Shock-Wave/Turbulent Boundary-Layer Interaction," AIAA Journal 22, 1984, page 579.

TABLE I
CENTERLINE PARAMETERS (CALCULATED)

P_o = 1.03 x 10^6 pascal (150 psia), T_o = 250 K,
$P_{ambient}$ = 1.01 x 10^5 pascal (14.7 psia),
Exit Diameter = 6.35 mm (.25")

LOCATION (mm)	VELOCITY (m/sec)	PRESSURE (pascal)	TEMP. (K)	MACH #	DENSITY g/cc
.127	292	5.40 x 10^5	208	1.01	.00906
2.69	433	2.02 x 10^5	157	1.72	.00449
5.23	529	5.95 x 10^4	111	2.51	.00187
7.80	576	2.33 x 10^4	85	3.13	.00096
MEASUREMENT LOCATION--10.3	604	1.12 x 10^4	68	3.64	.00057
MACH DISK----------12.6	621	6.27 x 10^3	58	4.06	.00038
MEASUREMENT LOCATION--13.5	134	1.06 x 10^5	241	.43	.00153

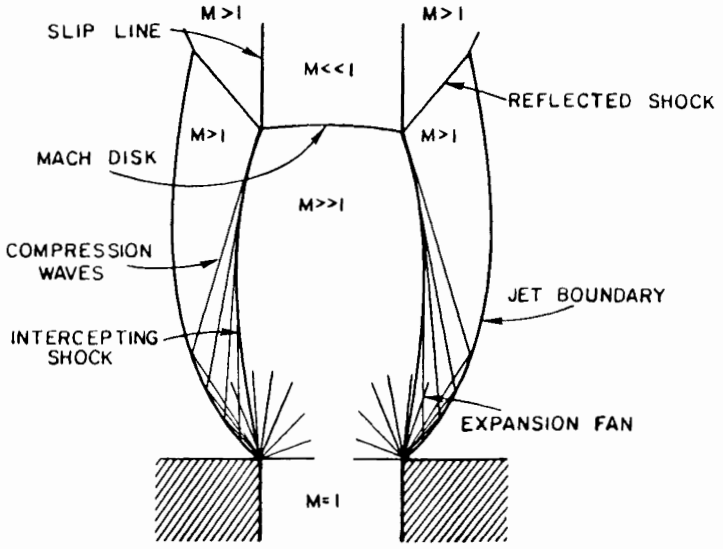

Figure 1. Structure of an underexpanded sonic jet.

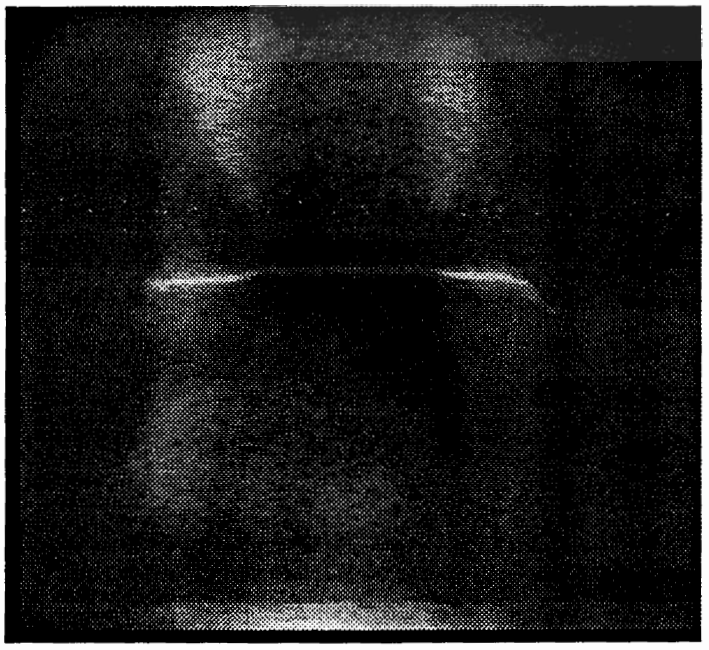

Figure 2. Density cross sections of an underexpanded sonic jet with a line tagged before the Mach disk. Flow is from bottom to top.

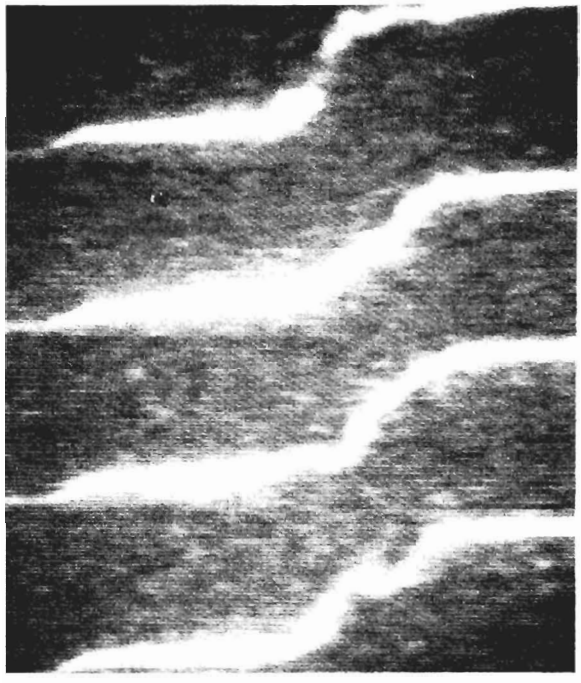

Figure 3. Composite picture of four separate recorded images of lines across the free shear layer 2.2 mm before the Mach disk.

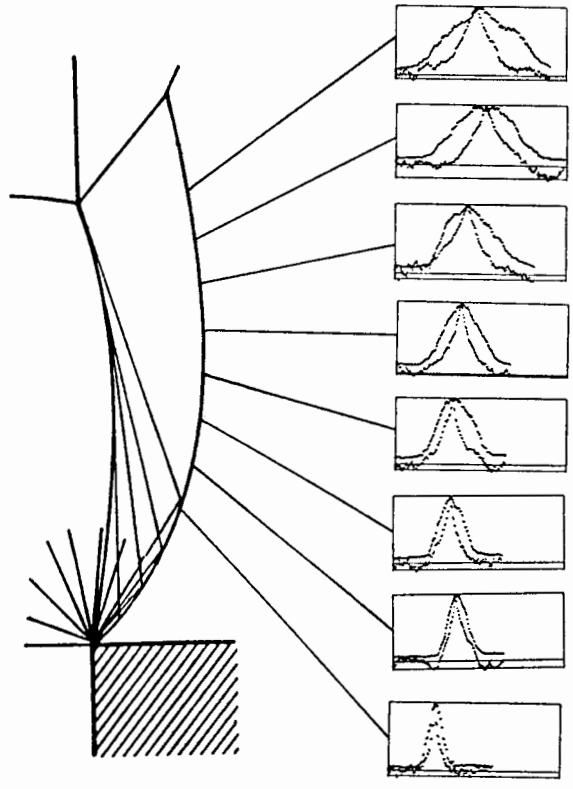

Figure 5. Turbulence intensity and velocity correlation across the free shear layer.

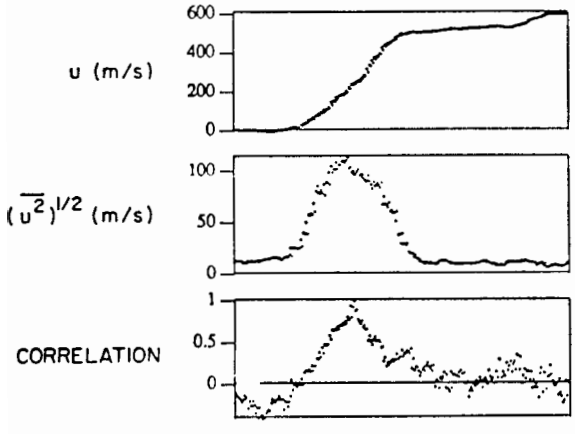

Figure 4. Measured velocity, turbulence intensity, and correlation function 2.2 mm upstream of the Mach disk.

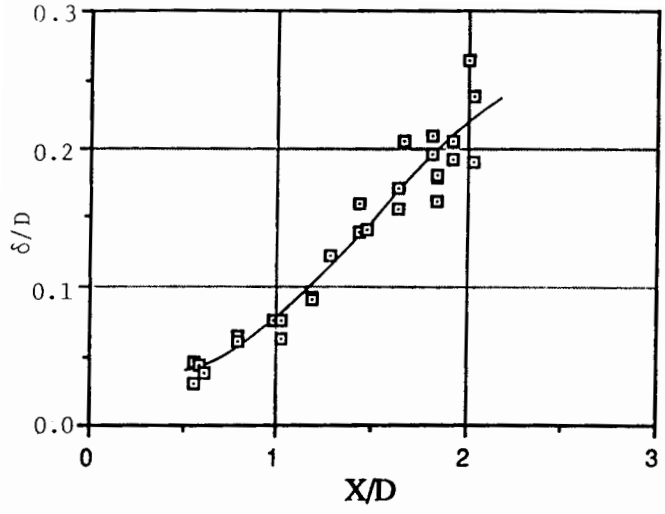

Figure 6. Width of shear layer versus distance from exit.

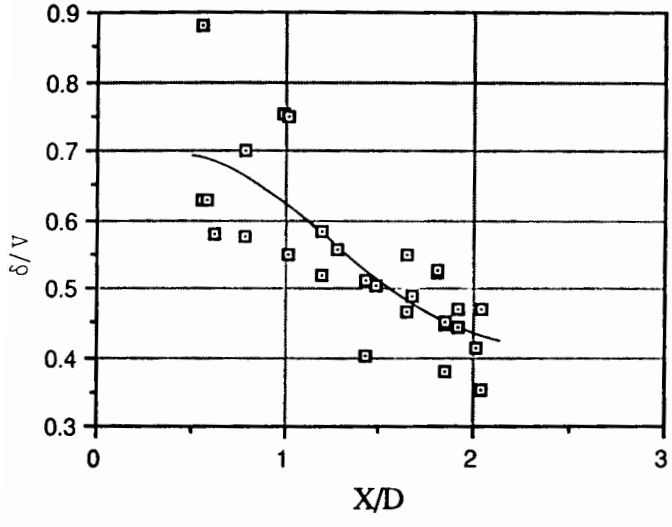

Figure 7. Integral scale normalized by shear layer width.

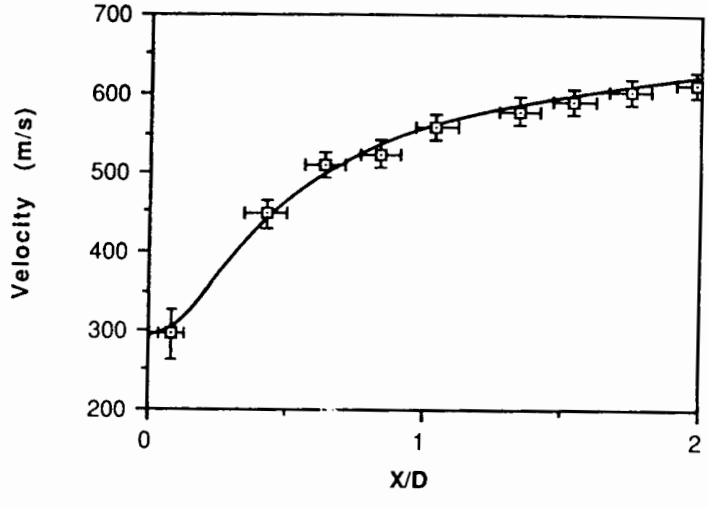

Figure 8. Centerline velocity downstream of the nozzle. The points are measured values and the line is computed.

Figure 9. Instantaneous density cross section of a Mach 3 turbulent boundary layer. Flow is from right to left.

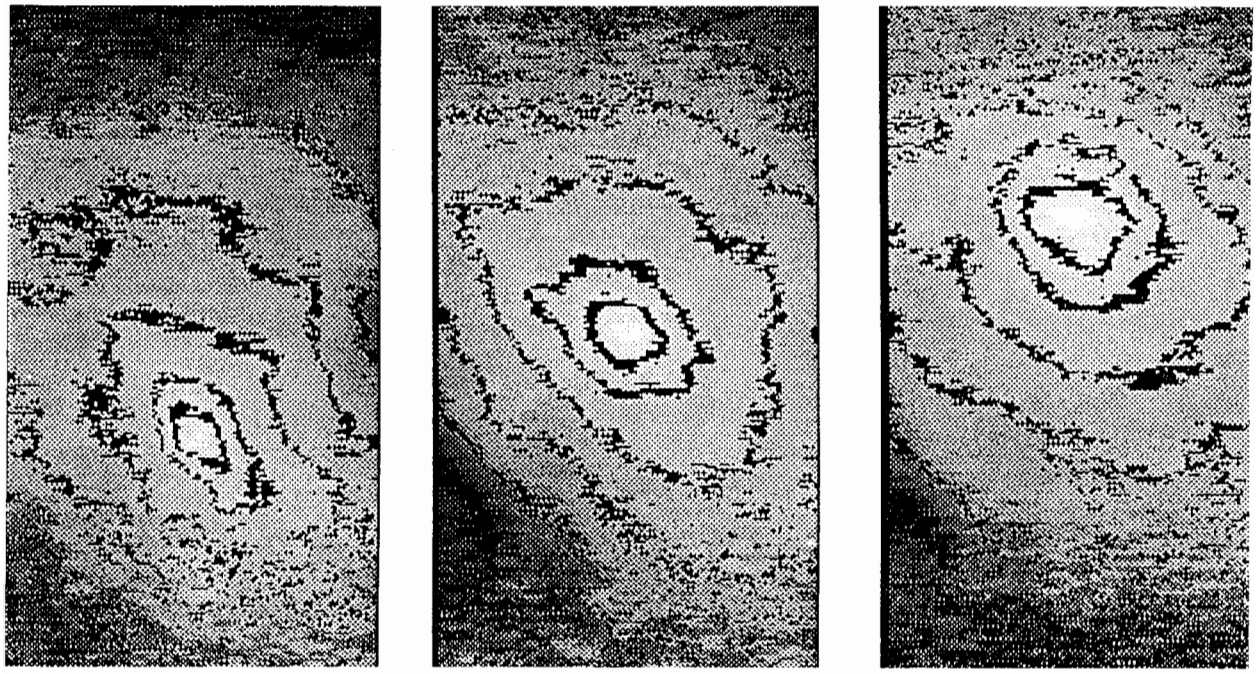

10(a) 10 (b) 10(c)

Figure 10. Density correlation at $y/\delta=0.4$, 0.6, and 0.8 in a Mach 3 turbulent boundary layer. Flow is from right to left.

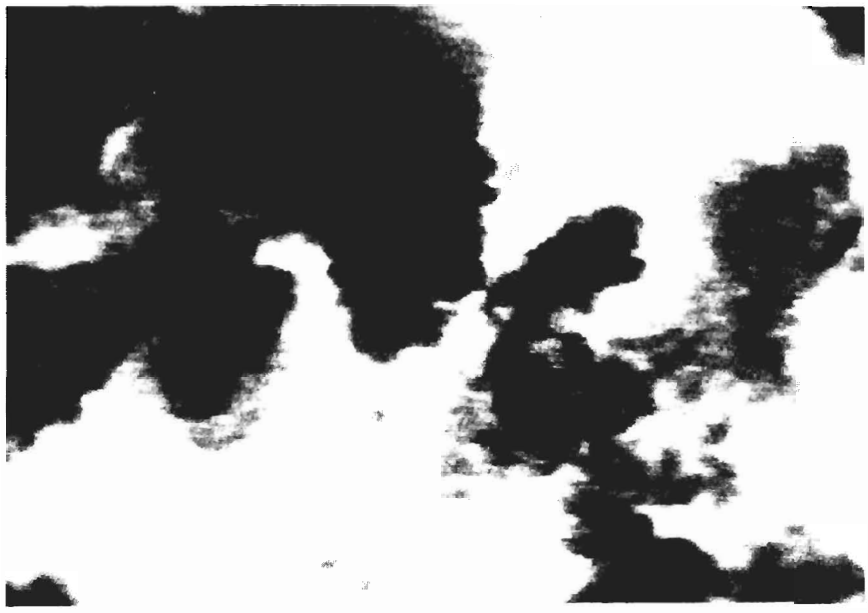

Figure 11. Instantaneous density cross section in a Mach 3 turbulent boundary layer. Plan form view at $y/\delta = 0.6$.

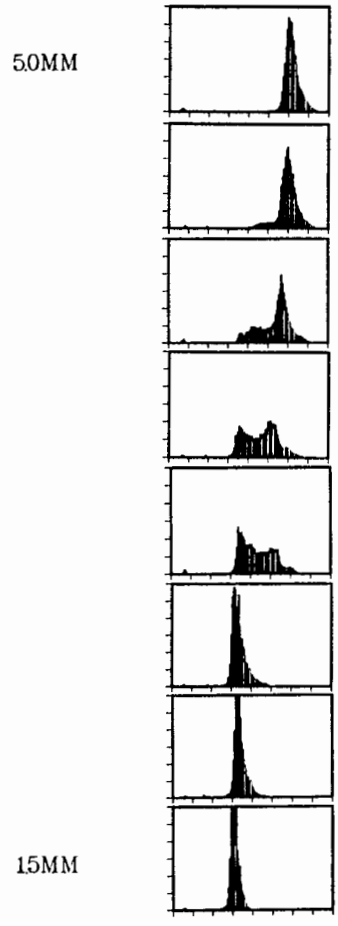

Figure 12. Probability density distribution functions of the density at y/δ=0.3, 0.4, 0.5, 0.6, 0.7, 0.8, 0.9, and 1.0.

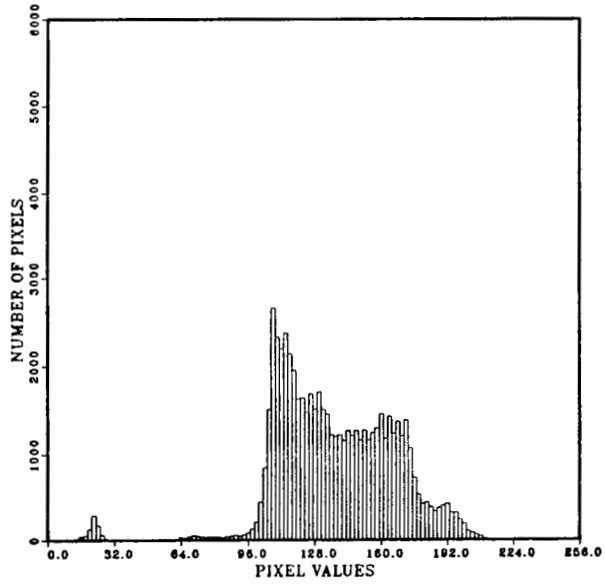

Figure 13. Probability density distribution function of the density at $y/\delta = 0.6$ (expanded view).

Figure 14. Shock wave/boundary layer interaction in a Mach 3 flow with a 16° angle wedge.

NUMERICAL SIMULATION OF THE FORMATION OF VORTEX STREETS IN A COMPRESSIBLE FLUID

C. D. Munz
Kernforschungszentrum Karlsruhe, Institut für Neutronenphysik und Reaktortechnik,
Postfach 36 40, D-7500 Karlsruhe, FRG

L. Schmidt
Universität Karlsruhe, Institut für Angewandte Mathematik,
Englerstr. 2, D-7500 Karlsruhe, FRG

S. Schöffel
Universität Kaiserslautern, Mechanische Verfahrenstechnik und Strömungsmechanik,
Postfach 30 49, D-6750 Kaiserslautern, FRG

Introduction

The mechanism of the formation of vortex streets in the wake of a bluff body can be studied by considering the interaction of two infinite vortex sheets which are initially a fixed distance apart. This idea was conceived by Abernathy and Kronauer [1] who, by this consideration, succeeded in explaining essential features of the mechanism in an inviscid incompressible fluid. In this paper, we take up this idea in order to study the formation of vortex streets in a compressible fluid at different Mach numbers. This is done by direct numerical simulations based on the two-dimensional compressible Navier-Stokes equations. To follow the development of the vortex sheets we combined the numerical simulation of the flow field with a marker particle algorithm. At the beginning of our calculations the vortex sheets are marked by a set of particles. They are advected during the calculation in a Lagrangean fashion according to the calculated flow field. The formation of the vortex street is then visualized by graphically displaying these marker particles, similar to streaklines in experiments. While in practice flows usually develop streamwise, in our numerical calculations we assume two infinite vortex sheets which are periodically disturbed in space and the results show the development of vortex streets in time. This flow model enables us to perform large-scale computations with good resolution, and the solution does not leave the computational domain.

It is obvious that the numerical approximation of nonlinear instabilities is a very difficult problem. Any disturbance introduced may rapidly increase and it is a hard task to determine the meaning of small-scale details revealed by the simulations. The main limitation of the direct simulation of instabilities and the transition to turbulence is given by the grid. Structures which are smaller than a few grid zones cannot be captured. Hence, either physical viscosity must be large enough to suppress "subgrid-scale structures" or a statistical treatment of these structures must be incorporated. The second way implies a difficult problem because numerical dissipation or dispersion acts on these scales. Furthermore, each statistical treatment reduces the possibility of finding coherent structures. We decided to adopt the first way. To obtain a clear physical meaning we required in our calculations the

following features. The numerical scheme should be stable for all inviscid problems which admit a stable solution. This guarantees that calculations with high Reynolds numbers can be performed without introducing numerical instabilities and no physical viscosity is consumed to stabilize the numerical scheme. Nevertheless, the inherent numerical dissipation should be one order of magnitude smaller than the real viscous terms. Increasing the Reynolds number this requires a drastic mesh-refinement and large-scale computations can be performed only on super-computers. If these requirements had been satisfied, the calculations of stable problems produced quite similar results for different mesh sizes.

Governing Equations and Numerical Method

We consider the two-dimensional compressible Navier-Stokes equations, written in conservation form

$$(1) \qquad U_t + F(U)_x + G(U)_y = R(U)_x + S(U)_y\,, \quad U = (\rho, \rho u, \rho v, e)^T$$

where U is the vector of the conserved variables, ρ is the density, u and v are the velocity components in x- and y-direction and e is the total energy per unit volume. The functions F(U), G(U) are the Euler fluxes, while the functions R(U), S(U) stand for the dissipative terms:

$$(2) \qquad F(U) = \begin{bmatrix} \rho u \\ \rho u^2 + p \\ \rho uv \\ u(e+p) \end{bmatrix}, \quad G(U) = \begin{bmatrix} \rho v \\ \rho uv \\ \rho v^2 + p \\ v(e+p) \end{bmatrix}, \quad R(U) = \begin{bmatrix} 0 \\ \tau_1 \\ \tau_2 \\ u\tau_1 + v\tau_2 + q^x \end{bmatrix}, \quad S(U) = \begin{bmatrix} 0 \\ \tau_2 \\ \tau_3 \\ u\tau_2 + v\tau_3 + q^y \end{bmatrix}$$

with

$$\tau_1 = (2\mu + \lambda)u_x + \lambda v_y\,, \qquad \tau_2 = \mu(u_y + v_x)\,, \qquad \tau_3 = (2\mu + \lambda)v_y + \lambda u_x\,,$$

$$q^x = \gamma \frac{\mu}{Pr}\, \epsilon_x\,, \qquad q^y = \gamma \frac{\mu}{Pr}\, \epsilon_y\,.$$

Here, p denotes the pressure, μ and λ are the coefficients of shear viscosity and bulk viscosity, respectively, ϵ is the specific internal energy, γ denotes the adiabatic exponent and Pr the Prandtl number. We assume a polytropic equation of state $p = (\gamma\text{-}1)\rho\epsilon$. Furthermore, we assume that the viscosity coefficients are constant and we use Stokes' hypothesis $\lambda = -2\mu/3$.

For fluid flow at high Reynolds and Mach numbers strong gradients or shock waves may occur and the Euler terms dominate the dissipative terms. In numerical calculations it is important to approximate the Euler terms very accurately. The equations (1) should be considered as an inviscid hyperbolic system with a small parabolic perturbation. Our numerical method for the compressible Navier-Stokes equations is a difference scheme based on a "High Resolution Scheme" for the Euler equations and the usual central differencing of the dissipative terms. The high resolution schemes which have been developed recently are shock-capturing schemes with the following properties: They are at least second-order accurate on smooth parts of the flow, but they sharply resolve discontinuities without generating spurious oscillations. The main building block is an upwind scheme which incorporates into

the numerical solution the direction of nonlinear wave propagation as given by the direction of the characteristics. This upwind differencing establishes the shock-capturing property of the scheme. The high resolution scheme used in the calculations below is a MUSCL-type scheme with upwind differencing based on the flux-vector splitting of van Leer; a detailed description is given in [4].

For high resolution schemes the discretization error is reduced to a level such that any numerically introduced dissipative terms are very small. In a range where the vortex streets are laminar and stable we obtained in calculations with different mesh sizes quite similar results and the results seemed to converge, when the mesh sizes tend to zero. For higher Reynolds numbers the development of the interfacial instabilitites and the formation of the vortex street tend to a chaotic system. In the inviscid limit convergence cannot be achieved. On a finer grid smaller structures are captured, the number of small vortices increases and due to the different interactions of these vortices the solutions disagree after a short time. In this chaotic state, noise which is always introduced from roundoff or truncation errors will rapidly grow, no matter what computational method is applied. Small disturbances in the initial data produce quite different solutions. The large-scale solutions may be similar again. Hence, for a practical problem the solution should be given in terms of statistical probabilities rather than in a deterministic way. But what can we learn from deterministic calculations? These calculations provide insight into the interaction of vortices and the mechanism of the transition to turbulence. Two-dimensional direct simulation can resolve very small structures which may be impossible with three-dimensional calculations even with the next generation of supercomputers. On the other hand, if turbulence starts in a two-dimensional vortex street, then three-dimensionality may evolve and become important.

Numerical Results

In the low Reynolds number regime a laminar and stable Karman vortex street develops in the wake of a bluff body. The vortices decay slowly due to viscous dissipation and no turbulent motion will exist. If the Reynolds number is increased, transition from the laminar vortex street to a turbulent wake will start (see, e.g. [5], [6]). Abernathy and Kronauer [1] explained the formation of a vortex street in an incompressible fluid by the interaction of two sinusoidally disturbed parallel shear layers. It is considered that the bluff body has the role only to generate the shear layers. In our numerical calculations the shear layers are idealized as vortex sheets. A diagram of the initial values and the computational region is given in Fig. 1. A fluid flow to the right is separated by a jet flowing to the left. Density and pressure are unity in the whole domain. The velocity into y-direction is sinusoidally disturbed inside the whole jet

$$(3) \qquad v_0 = v_0(x) = 0.1 \sin(4\pi x) \quad \text{in B}\,.$$

At the right-hand and left-hand side of the computational domain we prescribed periodic boundary conditions, at the upper and lower boundary outflow conditions. The disturbance of mode 2 as given by (3) needs finer grids than a mode 1 disturbance, but has the advantage that a breakdown of periodicity may be recognized.

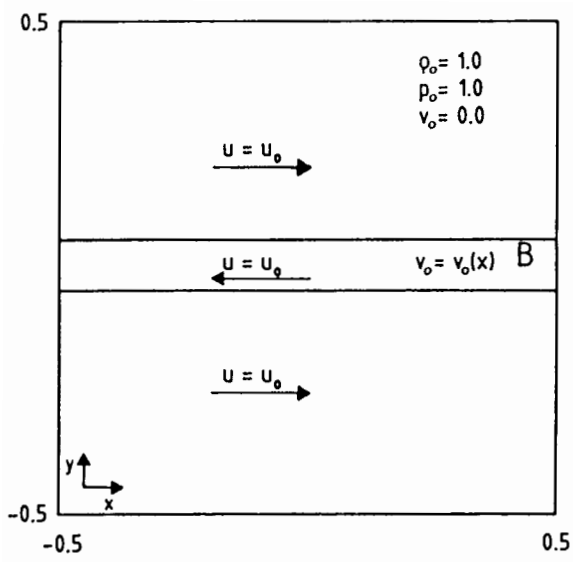

Fig. 1: Computational domain and initial values

The Mach and Reynolds numbers of the jet are defined by

$$(4)\quad M = \frac{2u_0}{c_0},\quad R = \frac{2u_0\ \lambda\ \rho_0}{\mu}$$

where $2u_0$ is the initial relative velocity of the shear flow and c_0 the sound velocity $\sqrt{\gamma\ p_0/\rho_0}$. The characteristic length λ is chosen to be the wavelength of the perturbation : $\lambda = 0.5$. All calculations were performed with $\gamma = 1.4$ and Pr = 0.712. We will show numerical results for Reynolds numbers R = 1475, 5900, 11800, 59000. With increasing Reynolds number we refined the grid from 200 x 200 to 500 x 500 grid zones. Each vortex sheet is marked by 20000 Lagrange points, which are restricted to a purely passive tracer role. These Lagrange points are advected in each time step according to the flow field. The advection velocities are determined by bilinear area weighting interpolation (see [4]).

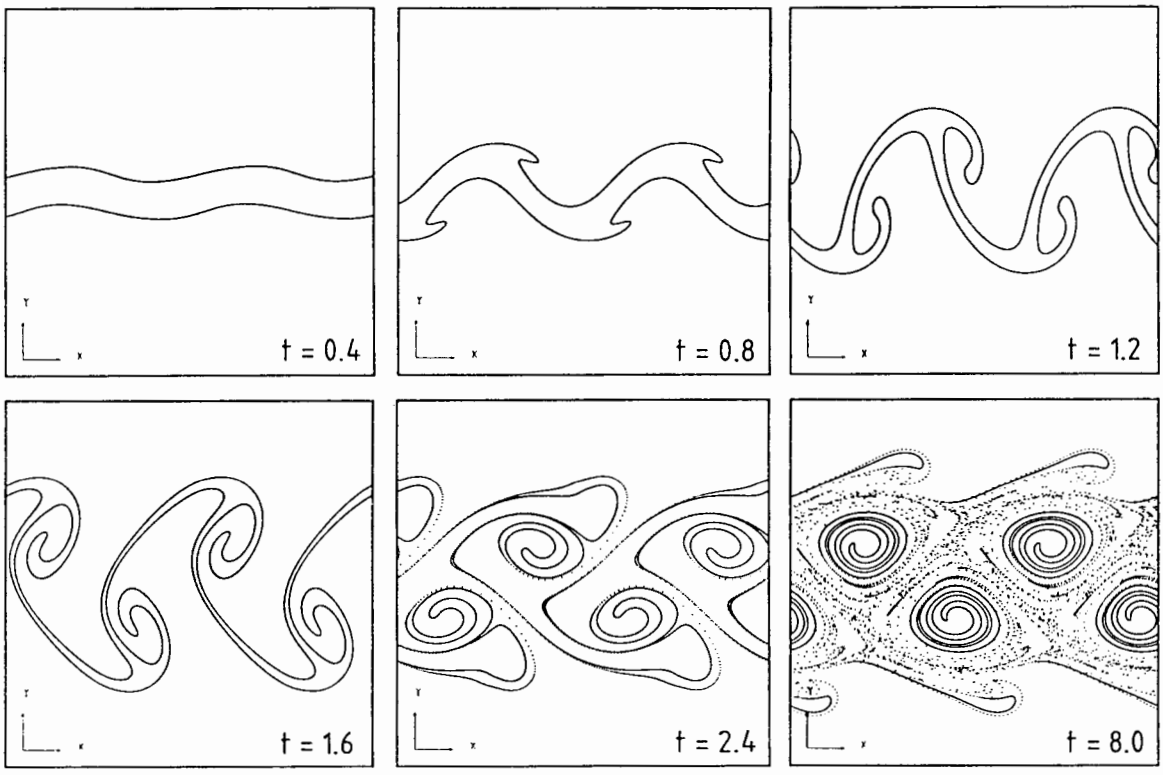

Fig. 2: Mach number M = 1, Reynolds number R = 1475

At first we will present results for Mach number M = 1. Fig. 2 shows the temporal development of the vortex sheets at Reynolds number R = 1475, graphically visualized by the marker particles. Initially, the disturbance of the velocity inside the jet leads to a sinusoidal geometric disturbance of the jet. Then a laminar roll-up of the shear layers starts and two parallel rows of staggered vortices develop. At this Reynolds number the Karman vortex street is stable for large time spans. If the Reynolds number is increased to 5900, aditional secondary vortices occur during roll-up (Fig. 3). But they are rapidly entrained and merge with the primary large eddies. The overall structure of the flow is quite similar to that at R = 1475. At Reynolds number R = 11800 eight small vortices occur in addition to the four big ones. The first plot at t = 0.4 indicates that, besides the growth of the sinusoidal disturbance, small wavelength disturbances arise and grow more rapidly than the long wavelength disturbance. The small disturbances are initiated by approximation errors. Due to the Kelvin-Helmholtz instability of the shear layer, small-scale errors introduced will rapidly grow. The classical linearized stability analysis for the inviscid equation predicts exponentially exploding modes. Because viscosity has a stabilizing effect, disturbances of a certain magnitude grow, while stability for disturbances of smaller wavelength is established.

The influence of the Kelvin-Helmholtz instability becomes much more obvious at R = 59000. Fig. 5 shows that small-scale disturbances arise. These disturbances rapidly grow and besides the four large eddies introduced by the long sinusoidal wavelength perturbation 12 smaller vortices are created. Figs. 4 and 5 show the development of an asymmetric street of cloudy vortex lumps each of which consisting of a number of smaller vortices. The vortices inside these clouds interact and rotate round each other. Due to damping by viscosity, the smaller vortices may decrease and, finally, merge with the big ones. This situation occurs at Reynolds number 11800 where the large-scale solution is a stable vortex street similar to those obtained at lower Reynolds numbers. At R = 59000 the interaction of the different vortices leads to a breakdown of the calculations, because vortices are swept outside the computational domain. The wake seems to become completely turbulent.

The results at Mach number M = 1 are quite similar to experimental results for an incompressible fluid. The streaklines and the geometry of the vortex street correspond well to results of water flowing past a cylinder (see, e. g. [3], [5], [6]). In this case the Reynolds number is usually defined by choosing the diameter of the cylinder as characteristic length and the freestream velocity as characterstic velocity. They determine the wavelength of the disturbance of the shear layers. We observed that the so-defined cylinder Reynolds number R_d is about 20 times smaller than the Reynolds number used within this context. Hence, the numerical results may be compared with incompressible experimental results for the range of cylinder Reynolds numbers from 80 up to 4000. The experimental results show that at R_d = 40 to 150 a regular vortex street is formed. After a transition stage the irregular range begins at about 300 in which turbulent fluctuations accompany the periodic formation of vortices. At Reynolds numbers up to the critical one $R_d = 2 \cdot 10^5$ periodic arrangements of vortices are observed experimentally in a turbulent ground flow. In our results the spacing ratio of the vortex street is in the range 0.34 ... 0.38 which exceeds the classical Karman ratio of 0.28 for an invisicid potential flow. This is in accordance with experimental observations and may be explained by the finite-size viscous core of the eddies. Compressibility effects become visible by the plots of the flow field of the laminar vortex street in Fig. 6. A 20 per cent density drop in the vortex centers is observed. The pressure drop is of the same

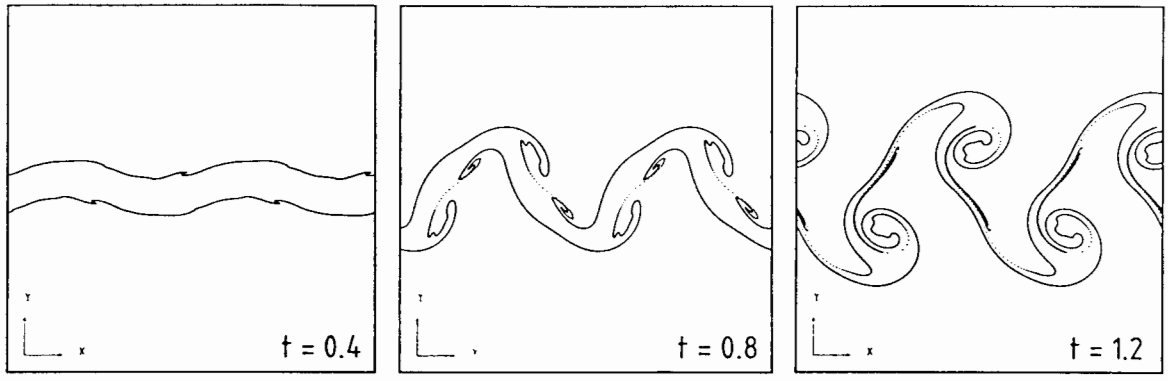

Fig. 3: Mach number M = 1, Reynolds number R = 5900

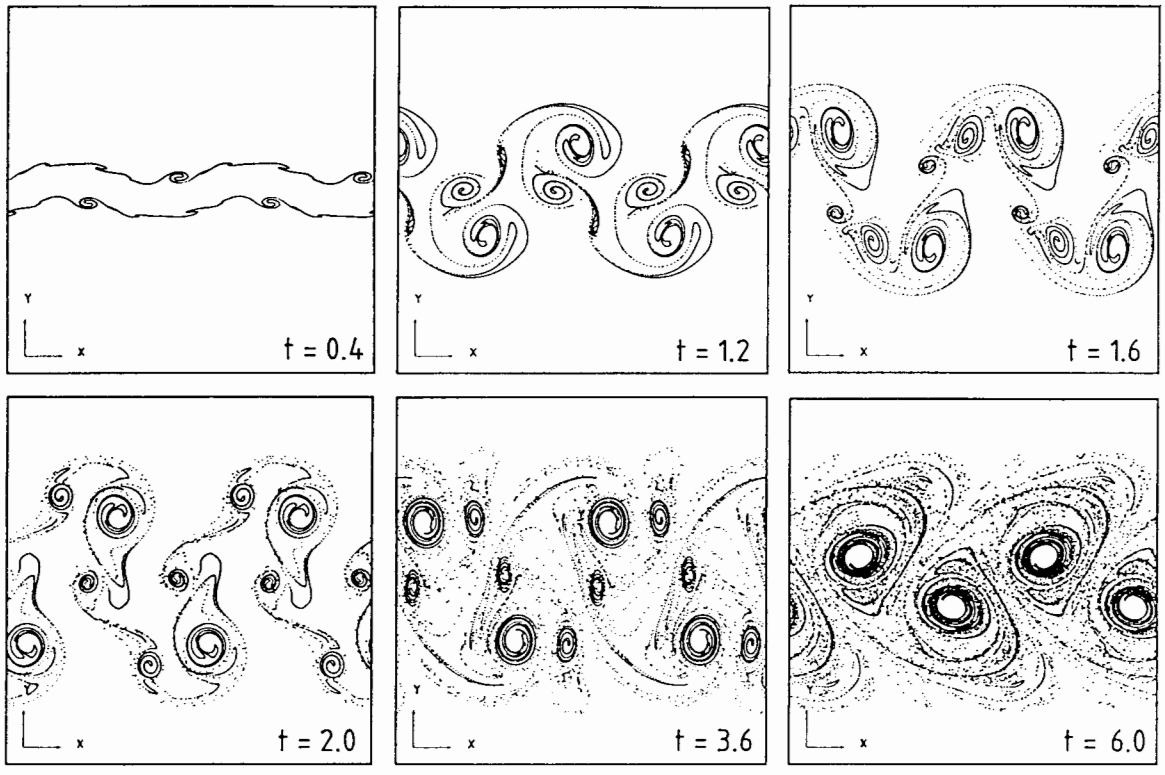

Fig. 4: Mach number M = 1, Reynolds number R = 11800

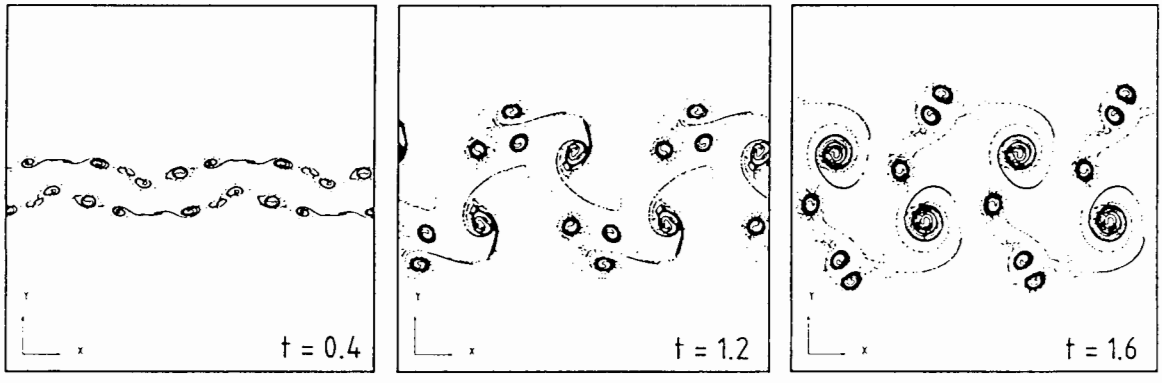

Fig 5: Mach number M = 1, Reynolds number R = 59000

magnitude and the turning point of the pressure profiles indicates the size of the vortex core. The vortices have a circumferential velocity distribution which is aptly modelled by a Hamel-Oseen vortex. The expansion in the centers caused by the roll-up is an irrevessible process which can also be recognized at the entropy distribution. The contourlines of the entropy have the same shape as the streaklines. Besides the wavelength of the disturbance another length-scale is the initial width of the jet. We observed that a change of the width does not affect the spacing ratio of the vortex street. Futhermore, defining a Strouhal number as the product of the shedding frequency of the large vortices and the characteristic time t_0 ($t_0 = d_0/2u_0$, d_0 initial jet width), the numerical results indicate that this number is also largely not affected by changes of d_0. A decrease in jet width is accompanied by an inversely proportional increase of the vortex propagation velocity and shedding frequency of the evolving Karman vortex street.

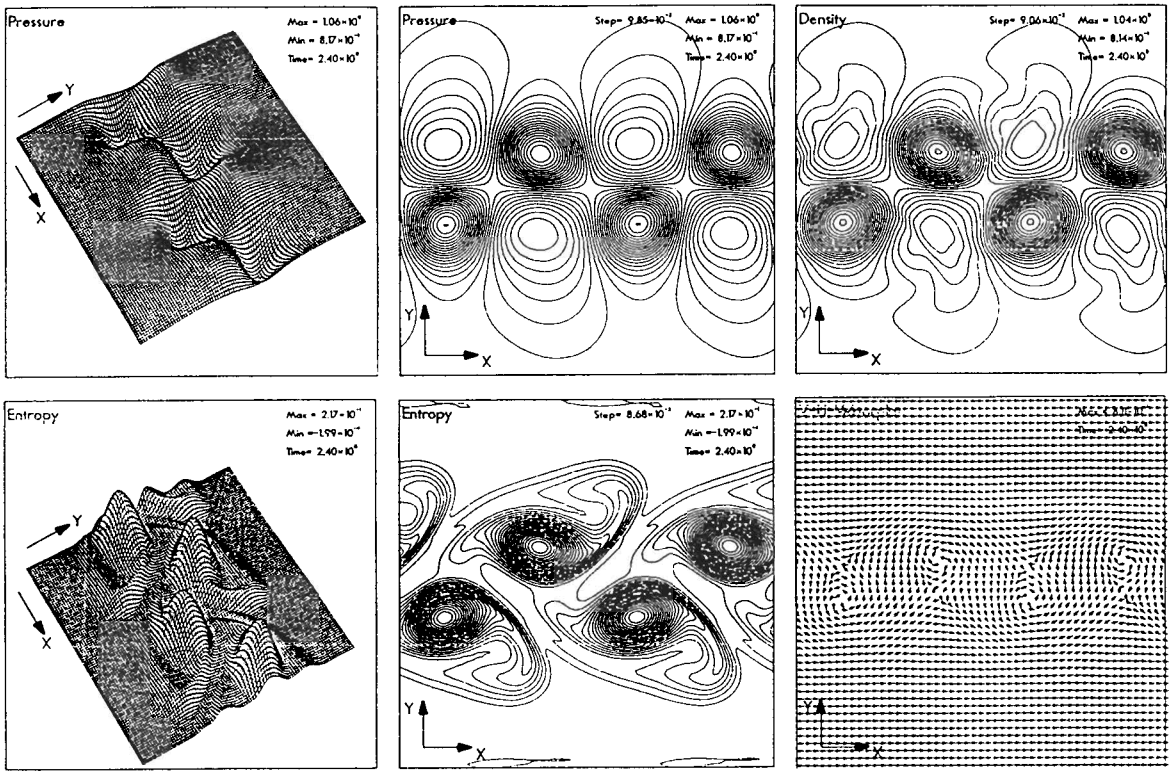

Fig. 6: Mach number M = 1, Reynolds number R = 1475

The classical linearized stability analysis for the single vortex sheet predicts stability for Mach numbers $M > 2\sqrt{2}$. However, Artola and Majda [2] - induced by numerical results obtained by Woodward - showed that nonlinear instabilities arise. Via asymptotic analysis by a high frequency perturbation expansion they found nonlinear kinks appearing on the slipstream surface. These kink modes grow in time, collide and interact; ultimately, enough vorticity ist generated through nonlinear interaction of the kink modes so that the compressible vortex sheet rolls up. Our calculations bear out that supersonic vortex sheets are unstable and that the mechanism of vortex sheet roll-up and vortex street formation changes for higher Mach numbers. They clearly demonstrate that a Karman vortex street may also arise at high Mach numbers by nonlinear interaction of two vortex sheets. The vortex street is more stable in

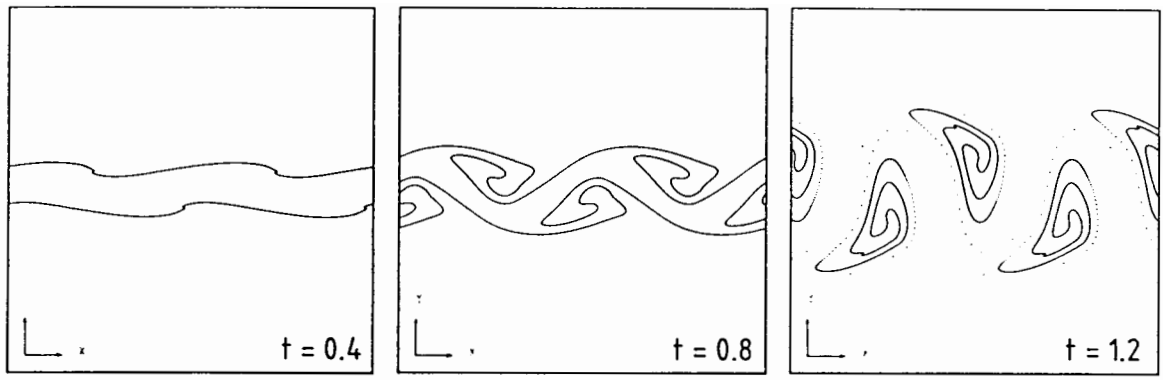

Fig. 7: Mach number M = 3, Reynolds number Re = 4425

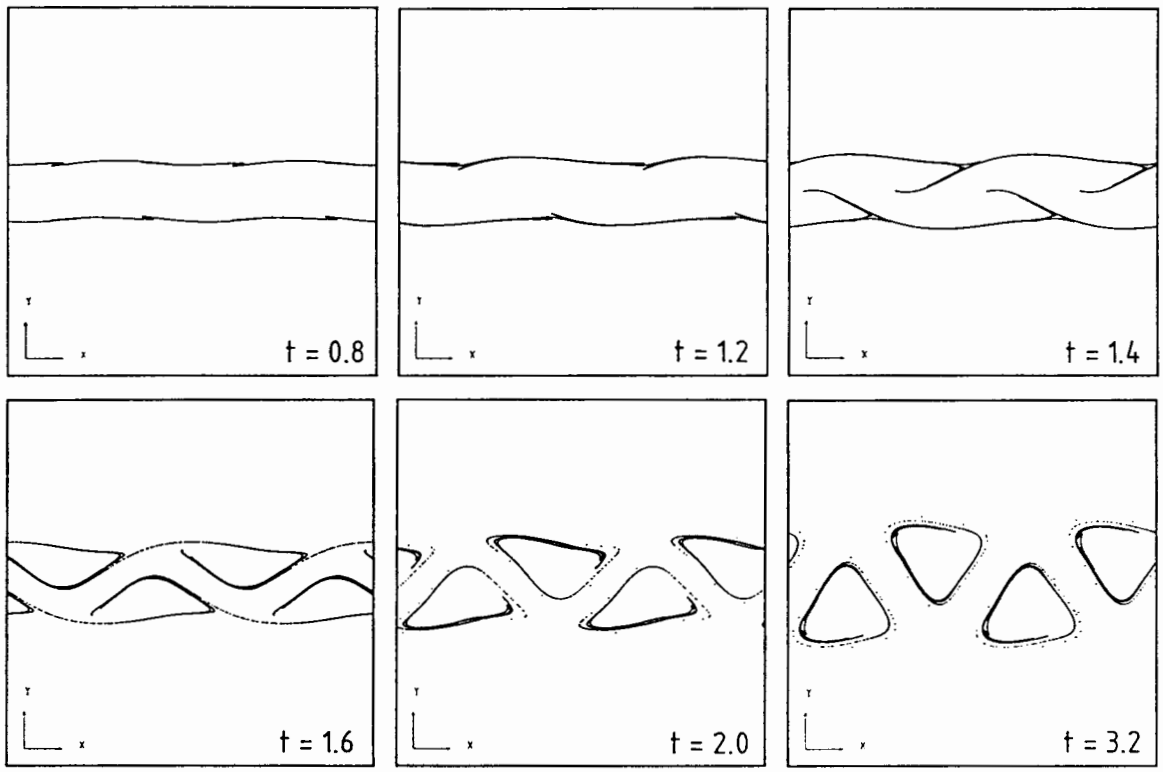

Fig. 8: Mach number M = 5, Reynolds number Re = 7375

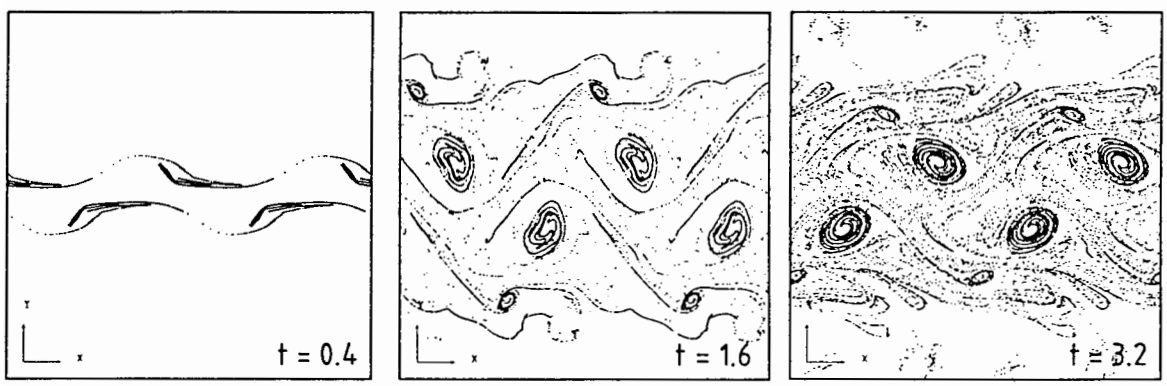

Fig 9: Mach number M = 5, Reynolds number Re = 59000

the sense that secondary disturbances are more strongly damped. It seems that the wave patterns stabilize the vortex street. Steaklines of the flow at M = 3 and R = 4425 are shown in Fig. 7. The sinusoidal disturbance of the jet increases much slower than at M = 1. The spreading rate of the wake increases monotonously to a smaller value. That the instability of the vortex sheets must have another origin becomes more obvious at higher Mach numbers. Figs. 8 and 9 show results for Mach number M = 5. At R = 7375 no clear sinusoidal displacement of the vortex sheets appears, and only the width of the wake increases. At t = 0.3 small disturbances of the vortex sheets appear as kinks which do not roll up to small vortices at once. Two different kinds of kink modes seem to emerge. At t = 0.8 they are visible as a clear kink and as a thickening, respectively. Both move to the right and left. At time t = 1.2 they collide and then a roll-up inside the wake takes place. A Karman vortex street ist formed consisting of vortices with a triangular shape, moving to the right. At higher Reynolds numbers the instability increases more rapidly. At R = 59000 a number of kinks in the streaklines appear at t = 0.2. At this time a sinusoidal displacement of the vortex sheets occurs. Fig. 9 shows the streaklines at time t = 0.4 where a chaotic roll-up of the shear layers starts. Shortly afterwards four big and for small vortices appear. Later on the flow becomes more regular and a stable vortex street is formed. At t = 3.2 the small vortices besides the big ones are still visible. They merge with the big eddies and disappear.

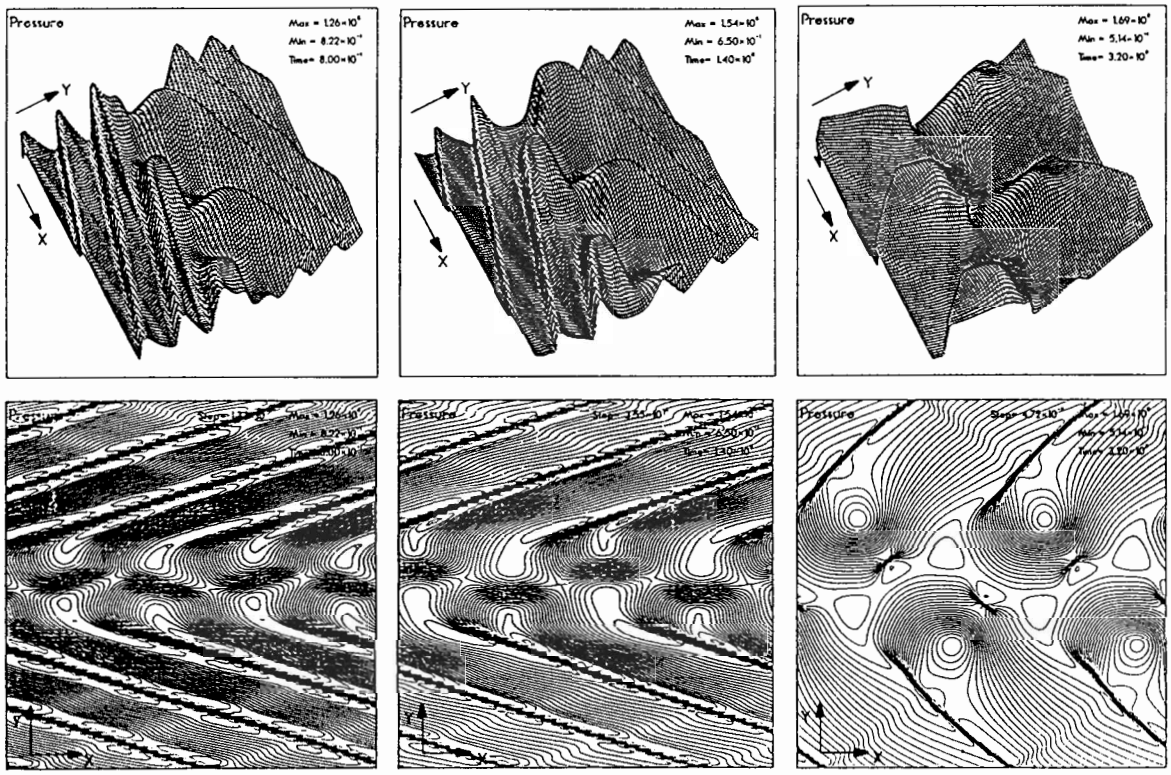

Fig. 10: Pressure distribution for M = 5, R = 7375, t = 0.8, 1.4, 3.2

Fig. 10 shows the contour lines and 3-D plots of the wake at M = 5, R = 7375 for three different times. Due to the disturbance waves are initially created inside and outside the wake travelling parallel to the vortex sheets. The outside waves leave the computational region at about t = 0.4, and are followed by an asymmetric regular pattern of Machwaves. These form an angle of inclination of about

20^0. This angle increases up to 60^0 when the roll-up process begins and the vortices have evolved further to the right. This is due to the decrease of relative velocity between wake boundary and outer flow. At about t = 5.6 the Machwaves leave the computational region. When the vortices are formed at about t = 2.0 the inside wake structure shows shocklets orthogonal to the vortex contours. They disappear at about t = 4.0

Conclusions

We considered the mechanism of the formation of a vortex street in a compressible fluid by interaction of two infinite vortex sheets. The numerical results were obtained by direct numerical simulations. At relatively low Mach numbers they correspond well to experimental observations for incompressible fluid flow. The calculations were performed for the range of Reynolds numbers where systematic arrangements of vortices have been experimentally observed in the wakes of bluff bodies. For increasing Reynolds number the numerical results show laminar-turbulent transition and interaction of the asymmetric long wavelength disturbance with fine-grained turbulence. The results at high Mach numbers indicate that the mechanism of the instability of shear layers changes and kink modes appear as predicted by Artola and Majda [2]. Our results demonstrate that at high Mach numbers a stable Karman vortex street is formed as well. The shock wave patterns support the formation of the vortex street. All calculations have been performed on a Fujitsu VP 50 vector processor. The computational effort varied between about 15 minutes and 5 hours depending on grid size, Mach and Reynolds number.

Acknowledgement

We would like to thank Rupert Klein for many helpful discussions.

References

[1] Abernathy, F.H., Kronauer, R.E.: The formation of vortex streets, J. Fluid Mech. 13 (1962), 1 - 20

[2] Artola, M., Majda A.J.: Nonlinear development of instabilities in supersonic vortex sheets, I.: The basic kink modes, Physica D 28D (1987), 253 - 281

[3] Dyke, M. van: An Album of Fluid Motion, Parabolic Press, Stanford California, 1982

[4] Munz, C.D., Schmidt, L.: Numerical simulations of hydrodynamic instabilites with high resolution schemes, to appear in Proc. of 2nd Int. Conf. on Hyperbolic Systems, Aachen 1988, R. Jeltsch, J. Ballmann (Eds.)

[5] Roshko, A.: On the development of turbulent wakes from vortex streets, NACA-Report 1191 (1954)

[6] Wille, R.: Karman vortex streets, Advances in Applied Mechanics 6 (1960), 273 - 287

Outstanding Issues In the Area of Compressible Mixing

By Dimitri Papamoschou

Graduate Aeronautical Laboratories, California Institute of Technology, Pasadena, CA 91125

Issues that arose from the experimental investigation of the turbulent compressible shear layer in a variable-gas, variable-Mach number facility are explored. In that investigation, the growth rates were correlated with the convective Mach number M_c, i.e., the Mach number in the frame of reference of the large-scale structure. Initially, M_c was obtained theoretically, using arguments which give it approximately the same value on the two sides of the layer. The growth rate, normalized by its incompressible value, versus M_c falls on a universal curve that decreases with M_c. Implications of that curve, as well as possible intuitive scenarios for the growth-reduction mechanism, are discussed. Recent double-exposure photos of the flow reveal that, at high compressibility, M_c has substantially different values on the two sides of the layer. Reasons for this difference between experiment and theory are suggested. The effect of the walls and the possible three-dimensionality of the flow are identified as open questions whose resolution is very important.

Introduction

The mixing layer between two parallel compressible streams (Fig.1) represents an interesting and challenging area of fluid mechanics. The unique nature of compressibility renders it a very different problem from that of its incompressible counterpart. Lately, it has attracted a lot of attention because of applications such as supersonic-combustion (scramjet) engines and chemical lasers.

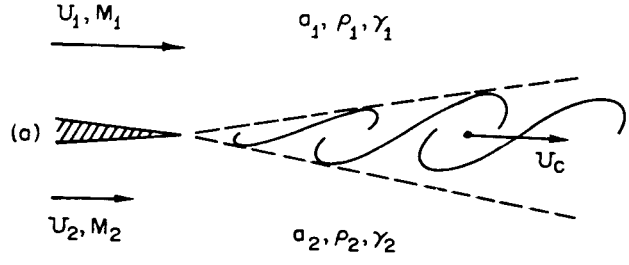

Fig. 1 Shear-layer geometry.

Recent experimental studies of plane turbulent shear layers [1,2] indicate that compressibility has a strong stabilizing effect on the flow, the growth rate at high compressibility being one-fifth of the incompressible one. These studies have advanced the concept of the *convective Mach number* as a compressibility-effect parameter. It is the Mach number in a coordinate system in which the large-scale structure is stationary. Its use for the turbulent case was first proposed by Bogdanoff [3]. The shear-layer

growth rate, normalized by its incompressible value, versus convective Mach number collapses on a nearly-universal curve, as shown on Fig. 2. Similar universal trends are apparent in recent inviscid linear instability analyses [4,5], where normalized amplification rates were correlated with the convective Mach number based on the phase speed of the disturbance. In fact, long before these analyses were performed, Mack [6] had shown that the linear instability problem can be formulated in terms of a single parameter, the convective Mach number based on the local mean values of velocity and speed of sound and the complex phase speed.

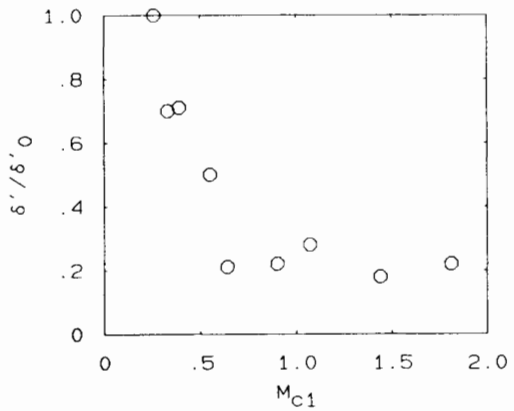

Fig. 2 Normalized growth rate versus convective Mach number. From Ref. 2.

Although the above correlations are very useful for engineering applications and for describing the gross features of the flow, more light needs to be shed on the mechanism by which compressibility inhibits mixing. Knowledge of that mechanism will not only give us a much better perspective on the problem, it may also enable us to control mixing, via passive or active methods, and perhaps to enhance it in ways that do not introduce large losses in the system. The exploration of this subject, however, must be done simultaneously with the exploration of fundamental and intertwined issues that are largely unanswered: is the flow basically two- or three-dimensional? Does the presence of solid boundaries significantly alter the flow field from the unconfined case? Is the existing theoretical model for computing convective Mach numbers accurate for all ranges of compressibility? The last question stems from recent exeriments where the convective Mach number was measured experimentally [7].

Open Questions

The purpose of this report is to suggest some of the framework in which the above issues may be addressed. The effects of compressibility may be divided into two basic categories. First, compressibility is associated with density gradients in the mean flow. This is not an exclusive property of compressibility, as density gradients can be produced by incompressible mixing of gases with different densities and/or temperatures. In the laminar case, the problem of a shear flow with density gradients can be reduced to one with uniform density by coordinate stretching such as the Howarth [8] transformation. In the turbulent case, the effect of density ratio on shear-layer growth rate has been measured by experiments, such as those of Brown & Roshko [9], and is relatively-well established.

Second, compressibility may cause hindrance of communication among parts of the flow. This is a unique property that can drastically change the character of the flow. To illustrate this effect, consider a shear flow where, at a given streamwise location, fluid element A moves supersonically with respect to another fluid element B. Element B does not "know" what element A is doing, and vice-versa, in the

same manner that an observer on the ground cannot hear a supersonic airplane approaching him. It is this impeded and sometimes absent interaction between parts of the flow that is largely responsible for the low mixing rate. This abstract notion, although intuitively useful, needs to be supplemented by a more detailed description of the flow interactions in order to have a well-defined picture of the physics of the problem.

Finally, density and pressure gradients, stemming from the above two basic effects, produce a source of vorticity not commonly present in incompressible flows. It is represented by the $\nabla p X \nabla \rho$ term on the right-hand side of the compressible vorticity equation, often called the "baroclinic torque" term. Its effect is largest in flows with strong shock waves and large density ratios.

These two basic effects of compressibility are reflected in the plot of growth rate versus convective Mach number shown on Fig. 2. The experimentally-determined growth rate, δ', is normalized by the incompressible growth rate, δ_0', at the same density and velocity ratios. This normalization removes, at least to first order, the effects of density and velocity ratios and gives a quantity that is primarily a function of compressibility. Now, it is assumed that the mixing process is governed by a dominant instability wave, taken to be the large-scale structure with a constant velocity of propagation, U_c (Fig. 1). The Mach numbers in the frame of reference of this wave are

$$M_{c_1} = \frac{U_1 - U_c}{a_1} \tag{1}$$

for the high-speed side, and

$$M_{c_2} = \frac{U_c - U_2}{a_2} \tag{2}$$

for the low-speed side, where U_1, a_1 and U_2, a_2 are the freestream velocities and speeds of sound for the high-speed and low- speed sides, respectively.

In the works of Papamoschou & Roshko [1,2], M_{c_1} and M_{c_2} were calculated using a conjecture that the total pressures of the two streams in the convective frame be equal. It was assumed that, in that frame, a stagnation point exists between any two structures, at which fluid from the two freestreams comes to rest isentropically (Fig. 3). The suitability of this assumption for flows with high convective Mach numbers will be examined later in this paper.

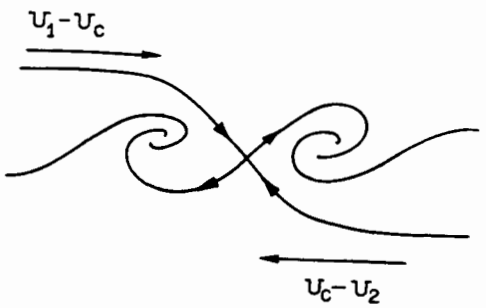

Fig. 3 Model of large-scale structure.

This model gives that M_{c_1} and M_{c_2} are equal for streams with same specific-heat ratio and only slightly different otherwise. The fact that M_{c_1} and M_{c_2} are, in theory, very close or equal, suggested to the above

authors that either of them could be used for expressing compressibility associated with the large-scale structure. In their work, M_{c_1} was chosen for correlating the growth rate. In the discussion that follows, however, it is not necessary to assume any relation between M_{c_1} and M_{c_2} except that arising from their definitions, (1) and (2). The symbol M_c will be used to denote the convective Mach number for unspecified side of the shear layer.

It is important to underline the differences between flow fields with $M_c<1$ and those with $M_c>1$. For $M_c<1$, a disturbance that originates in the main flow decays exponentially with distance away from the layer. Such disturbance is classified as "subsonic". For $M_c>1$, a disturbance propagates largely unattenuated along Mach lines originating at the structure, therefore it penetrates a long distance into the surrounding flow field. Such disturbance is classified as "supersonic". When a disturbance is supersonic, energy is radiated away from the main flow that could otherwise have been used for amplification of that disturbance. This can be stated more precisely by writing the conservation equation for the disturbance kinetic energy

$$k = \frac{1}{2}\left[\overline{u'^2} + \overline{v'^2} + \overline{w'^2}\right]$$

For highly-turbulent flows with large Reynolds numbers, such as those usually dealt with, the viscous terms in the equation for k are very small. Thus, its inviscid version should be a good approximation:

$$\frac{Dk}{Dt} = -\rho\,\overline{u'v'}\,\frac{du}{dy} - \left[\overline{u'\,\frac{\partial p'}{\partial x}} + \overline{v'\,\frac{\partial p'}{\partial y}} + \overline{w'\,\frac{\partial p'}{\partial z}}\right] \tag{3}$$

Depending on whether the right-hand side of (3) is negative, zero, or positive, a disturbance is decaying, neutral, or amplifying. The first term of the right-hand side is commonly referred to as "turbulent production" and represents the transfer of energy from the mean flow to the disturbance via the Reynolds stress $\tau_R = -\rho\overline{u'v'}$. Since τ_R is generally positive, so is this term, thus energy is supplied from the mean flow to the disturbance. Note that, since du/dy vanishes at the edges of the shear layer, this term is confined to the mean flow. The second term of the right-hand side, although negligible for incompressible flow, becomes important for compressible flow. For $M_c>1$, the quantities involved in the correlations propagate unattenuated away from the layer. In that case, this term is not confined to the mean flow and represents the radiation of disturbance energy from the shear layer. The growth-rate versus M_c correlation of Fig. 2 suggests that the magnitude of this term (without the minus sign) increases with M_c, thus decreasing the magnitude of the entire right-hand side of (3). It also suggests that, at high M_c, the right-hand side reaches some limit value, small but positive, corresponding to the plateau of the curve in Fig. 2. It is worth noting that the Reynolds-stress distribution may also be very different from that in subsonic flows. For $M_c>1$, it will also exhibit radiative behavior and will be finite at large distances away from the layer. Lees & Lin [10] and Gropengiesser [11] discuss (3) in more detail.

Obviously, it would be very beneficial to know the distribution of the terms of (3) and how it changes with increasing compressibility. Experimentally, the velocity-pressure gradient correlations would be extremely-difficult to obtain. However, analytical and computational methods should be in a position to provide valuable information on these correlations.

In most of the experimental and theoretical works in the literature, it is assumed that the disturbance is spanwise coherent. Departures from two-dimensionality may significantly alter the effect of compressibility on the flow. The instability of a disturbance propagating at an angle θ to the mean flow is governed by $M_c \cos\theta$, rather than by M_c. For large θ, a disturbance that would have been supersonic if it were two-dimensional, may now be effectively subsonic. Morkovin [12] suggests that, at high compressibility, the flow would prefer such oblique disturbances rather than two-dimensional ones. It is therefore imperative to ascertain experimentally whether and to what extent the compressible shear layer is three-dimensional.

Given the unique nature of a supersonic disturbance, i.e. that it radiates away from the layer, the presence of walls within which the flow is confined could be of non-trivial consequences. Waves emanating from such a disturbance would reflect from the solid boundary and impinge back on the shear layer. How that would affect mixing is not currently known. Recent theoretical studies by Tam & Hu [13] suggest that the confined compressible shear layer exhibits several additional instability modes to those of the unconfined case. It is very difficult to conceive of an experiment where a supersonic shear layer is formed without any surrounding walls. If such apparatus were devised, however, it would be very valuable for researching the differences between confined and unconfined flows.

The convective velocity of the large-scale structure (U_c) has recently been investigated experimentally using a double-exposure schlieren system [7]. Results indicate that when M_c exceeds a value of about 0.7, U_c tends to be very close to one of the freestream velocities. Fig. 4 shows a double-exposure photo of a shear layer formed by helium at M=1.7 and nitrogen at M=2.8. The time interval between the two exposures is 25.4 μs. Arrows indicate features of the large-scale structure and their displaced position in that time interval. Notice the difference between the theoretical value of U_c (770 m/s) and the experimental one (640 m/s). This trend of U_c to be close to either U_1 or U_2, depending on the test case, makes the convective Mach numbers M_{c_1} and M_{c_2} very different from each other. This is in

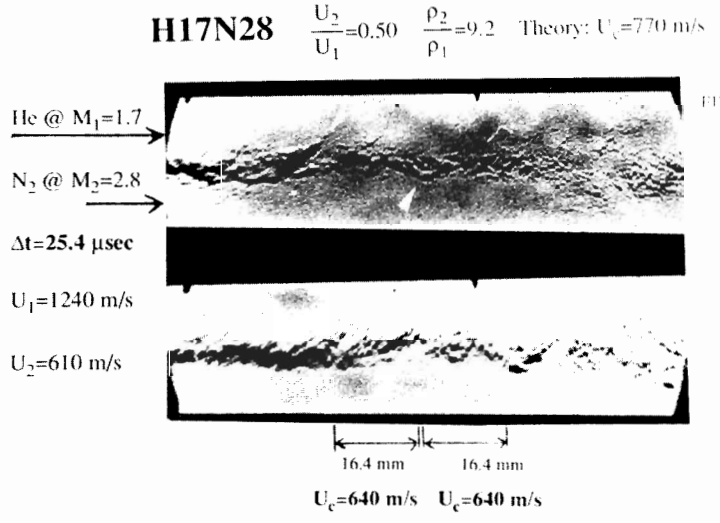

Fig. 4: Double-exposure photo of turbulent turbulent shear layer. From Ref. 7.

contrast to the theoretical model, outlined above, that predicts them to be very close or equal.

It must be emphasized that the theoretical model does not take into account the existence of shock waves formed on the structure when M_c becomes supersonic. This omission could be responsible for the difference between theoretical and experimental M_c, because the shock waves generate total-pressure losses not accounted for in the existing model. The presence of solid boundaries in the flow could also affect the determination of U_c: unless completely canceled by surrounding expansion waves, shock waves originating from the structure will reflect back on the shear layer, possibly altering the "boundary condition" by which M_c and U_c were computed. Resolution of this issue is very important because U_c determines the entrainment ratio, which in turn controls the mixing and combustion processes.

Note that the deviation of experiment from theory starts where the plot of growth rate versus M_c reaches the plateau of about 0.2. Thus, the growth rate still collapses on a universal curve when correlated with the highest of the two experimentally-determined M_c's [7].

Conclusion

Several issues related to compressible mixing are identified whose resolution is crucial for making worthwhile progress in this field. There is a need for a great amount of experimental work directed toward answering fundamental questions that remain open, such as three-dimensionality of the flow field, effect of the walls, and dynamics of the large-scale structure. Not all questions can, however, be addressed by experiment only. There is also a need for theoretical and computational studies, which should focus in providing physical explanations of the processes involved in compressible mixing. The turbulent correlations that govern instability and mixing would be great candidates for such studies.

Acknowledgements

The experimental work mainly referred to in this paper (Refs. 1, 2, and 7) has been supported by a grant from the Rockwell International Foundation Corporation Trust and by Contract No N00014-85-K-0646 of the U. S. Navy Office Of Naval Research.

References

1. Papamoschou, D. & Roshko, A. 1986 Observations of Supersonic Free Shear Layers. *AIAA-86-0162*.

2. Papamoschou, D. & Roshko, A. The Compressible Turbulent Shear Layer: an Experimental Study. To appear in the *Journal of Fluid Mechanics*.

3. Bogdanoff, D.W. 1983 Compressibility Effects in Turbulent Shear Layers. *AIAA J.*, **21(6)**, 926-927.

4. Ragab, S. A. & Wu, J. L. 1988 Instabilities in the Free Shear Layers Formed by Two Supersonic Streams. *AIAA-88-0038*.

5. Zhuang, M., Kubota, T. & Dimotakis, P.E. 1988 On the Instability of Inviscid Compressible Shear Layers. *AIAA-88-3538*.

6. Mack, L. 1975 Linear Stability Theory and the Problem of Supersonic Boundary-Layer Transition. *AIAA J.*, **13(3)**, 278-289.

7. Papamoschou, D. 1989 Structure of the Compressible Shear Layer. To be presented at the *AIAA 27th Aero. Sci. Meeting.*

8. Howarth, L. 1948 Concerning the Effect of Compressibility on Laminar Boundary Layers and their Separation. *Proc. Roy. Soc. London,* **A 194**, 16-42.

9. Brown, G.L. & Roshko, A. 1974 On Density Effects and Large Structures in Turbulent Mixing Layers. *J. Fluid Mech.*, **64(4)**, 775-781.

10. Lees, L. & Lin, C.C. 1946 Investigation of the Stability of a Laminar Boundary Layer in a Compressible Fluid. *NACA TN 1115.*

11. Gropengiesser, H. 1970 Study of the Stability of Boundary Layers in Compressible Fluids. *NASA-TT-F-12.*

12. Morkovin, M.V. 1987 Transition at Hypersonic Speeds. *NASA CR 178315, ICASE Interim Rep. 1.*

13. Tam, C.K.W. & Hu, F.Q. 1988 Instabilities of Supersonic Mixing Layers Inside a Rectangular Channel. *AIAA-88-3675.*

EFFECT OF PARTICULATE ADDITIVES ON HEAT TRANSFER FROM A SHOCK-INDUCED TURBULENT BOUNDARY LAYER

G.T. Roberts, R.A. East, N.H. Pratt
Department of Aeronautics and Astronautics
University of Southampton

Introduction

Evidence exists that significant reductions in gun barrel wall heat flux (and hence extension of the barrrel life) can be effected by adding particulate matter to the non-steady, turbulent boundary layer which develops behind the moving projectile. The mechanisms causing the heat transfer reduction are uncertain but may be related to the phenomenon, noted in incompressible turbulent boundary layer flows, where additives (either in the form of long chain molecules of length comparable to the Kolmogorov scale of turbulence in the case of water flows, or solid particulates in the case of gaseous flows) reduce the wall skin friction.

In order to investigate further the heat flux reduction phenomenon, the present work was undertaken to measure the wall heat flux from a non-steady, turbulent boundary layer in a shock tube, where the freestream Mach number was supersonic and the wall was initially coated with a thin layer of talc particles of mean diameter D = 4.5μm.

Experimental Conditions

The shock tube experiments were performed at Southampton University (AASU) and at the Australian National University (ANU) under conditions of similar freestream speeds and temperatures, but the experiments at ANU were made at higher pressures and densities. The data shown here were obtained using an inert gas (argon) and the particle Reynolds numbers,based on the estimated mean wall shear velocity, were in the range 60 to 600. Apart from varying pressure (and hence density), the main variable in the experiments was the initial loading (mass per unit area) of the particles deposited on the wall prior to the run. A summary of the main experimental conditions for the two sets of experiments are given in Table 1.

Results

In Figure 1, which was obtained from experiments performed at AASU, the rate of heat transfer ($\dot{q}_w$) is shown as a function of time for the clean flow and for two cases of dusty flow in which the initial particle loading (m_p) was 2.2 and 8.3 gm^{-2} respectively.

In the case of the clean flow, the rise in heat transfer at about 20μs following the passage of the shock indicates transition from laminar to turbulent boundary layer flow,

corresponding to a transition Reynolds number of about 10^6. The rate of heat transfer then fell with time in accordance with the expected turbulent boundary layer growth.

In the case of the dusty flows, large reductions in heat transfer are shown to occur with the experimental records showing large intermittency. The greatest reductions in heat transfer occurred with the larger particle loading. However, beyond about 160μs following shock transit the dusty results tend to approach the clean flow data. The heat flux signals have been frequency analysed (not shown here) and indicate marked changes in spectrum with changes in the initial loading of the particles. However because of the limited dynamic response of the thin film heat transfer gauges and associated circuitry ($10^2\,Hz < f < 10^6\,Hz$), it is not possible to arrive at any firm conclusions regarding the significance of the observed change in spectrum.

Figure 2 shows the variation in total heat flux (Q), found by integrating q_w over the run time of 200 μs, with changes in initial particle loading. For the experiments performed at AASU, the heat flux reduces as the initial loading increases and appears also to be dependent on the freestream (and hence wall) gas density: for a given loading of particulate the reduction in heat flux decreases as the gas density increases [Ref 1].

Also shown in Figure 2 are data obtained from experiments at ANU which, although exhibiting much greater scatter, confirm that the heat flux reduces with increasing loading of particulate. However, unlike the AASU data, the ANU data do not indicate any strong dependence on gas density. In fact the heat flux reductions observed in the ANU experiments were much greater than anticipated from extrapolation of the trends shown by the AASU data, leading to the tentative hypothesis that the mechanisms of heat transfer reduction may be stronger at the higher gas densities [Ref 2].

Discussion and Conclusions

These results indicate that the large changes in the rate of wall heat transfer, which occur when the boundary layer wall is coated with a uniform distribution of particulate, can only satisfactorily be explained in terms of a strong interaction between the particulate and the turbulence structure in the boundary layer, with consequent changes in the mean velcotity profile. The information gained from the changes in the frequency spectrum of the fluctuations in wall heat transfer rate in the AASU experiments are not regarded as sufficiently reliable to confirm that a shift in turbulence spectrum to lower frequencies occurred between the 'clean' flow and the 'dusty' flow experiments, which would have been interpreted as indicative of a change in the dissipation process.

Laser beam attenuation measurements confirmed that particulate was rapidly lifted from the walls and some particles even jumped outside the boundary layer. The greatest concentration of particulate was, however, seen closer to the wall. It may be conjectured that the particles performed certain random trajectories, in which they were initially lofted

from the surface by the action of shear, but subsequently impacted and rebounded from the surface, displacing further particulate material from the surface layer as they did so.

The process described here is similar to that of saltation [Ref 3] and although the details of the interaction of these lifting particles from the 'wall' with the turbulence structure in the boundary layer are still not clearly understood, nevertheless the resulting changes in the wall shear stress, the effective roughness height, and the mean velocity profile have close analogies with what we estimate are the overall physical processes present in our experiments, even though the combination of shear velocities and gas densities were far in excess of the range normally considered necessary for saltation of particles, of the given size and density, to occur.

Although many attempts have been made to model the results obtained in these experiments both analytically, following the work on dusty gas flows by Saffman [Ref 4] and Lumley [Ref 5], and numerically [Refs 6 and 7], we believe that further work is needed to model correctly this flow field interaction where the particulate size, D, is typically many times larger than the scale of the near wall turbulent structures present in the 'clean' wall case and is, in particular, much greater than the microscales of the turbulence.

Acknowledgements

The experimental work was carried out with the support of the Procurement Executive, Ministry of Defence. The authors are indebted to Professor G.M. Lilley for his many helpful discussions in preparing this paper and for presenting the work at the Workshop on the Physics of Compressible Turbulent Mixing, Princeton, October 1988.

References

[1] Roberts, G.T., East, R.A. and Pratt, N.H. "Surface heat transfer measurements from a turbulent dusty boundary layer" in Proc. 14th Int. Symposium on Shock Tubes and Waves, Sydney, 1983.

[2] Roberts, G.T. et al "Shock tube measurements of convective heat transfer from a high Reynolds number, particle-laden turbulent non-steady boundary layer " in Proc. 15th Int. Symposium on Shock Tubes and Waves, Berkeley, 1985.

[3] Owen, P.R. "Pneumatic transport". J Fluid Mechanics, 39, part 2, pp407-432, 1969.

[4] Saffman, P.G. "On the stability of a laminar flow of a dusty gas". J. Fluid Mechanics, 13, Part 1, pp 120-128, 1962.

[5] Lumley, J.L. "Two-phase, and non-Newtonian flows" in 'Topics in Applied Physics, Volume 12 : Turbulence, 2nd edition. Bradshaw, P (ed). Springer-Verlag, pp 289-324, 1978.

[6] Buckingham, A.C. "Turbulent boundary layer thermochemical attack on coated walls" in Proc. 1984 Jannaf Propulsion Meeting, New Orleans.

[7] Ludwig, J.C., Rhodes, N. and Tatchell, D.G. "Numerical modelling of the flow of a hot, particle-laden gas" in Proc. 7th Int. Symposium on Ballistics, The Hague, 1983.

	AASU	ANU
Freestream pressure (bar)	3-15	40-120
Freestream temperature (K)	2700-3000	2600-3000
Freestream density (kgm^{-3})	0.6-2.4	8-20
Freestream velocity (ms^{-1}) (shock fixed)	450	450
Freestream velocity (ms^{-1}) (Laboratory coordinates)	1350	1350
Wall shear velocity (ms^{-1})	50	40
Particle Reynolds number $Re = u_\tau D/\nu_w$	60	600
Heat flux (Wm^{-2}) (clean flow)	$0(10^7)$	$0(10^8)$

Table 1: Experimental Conditions.

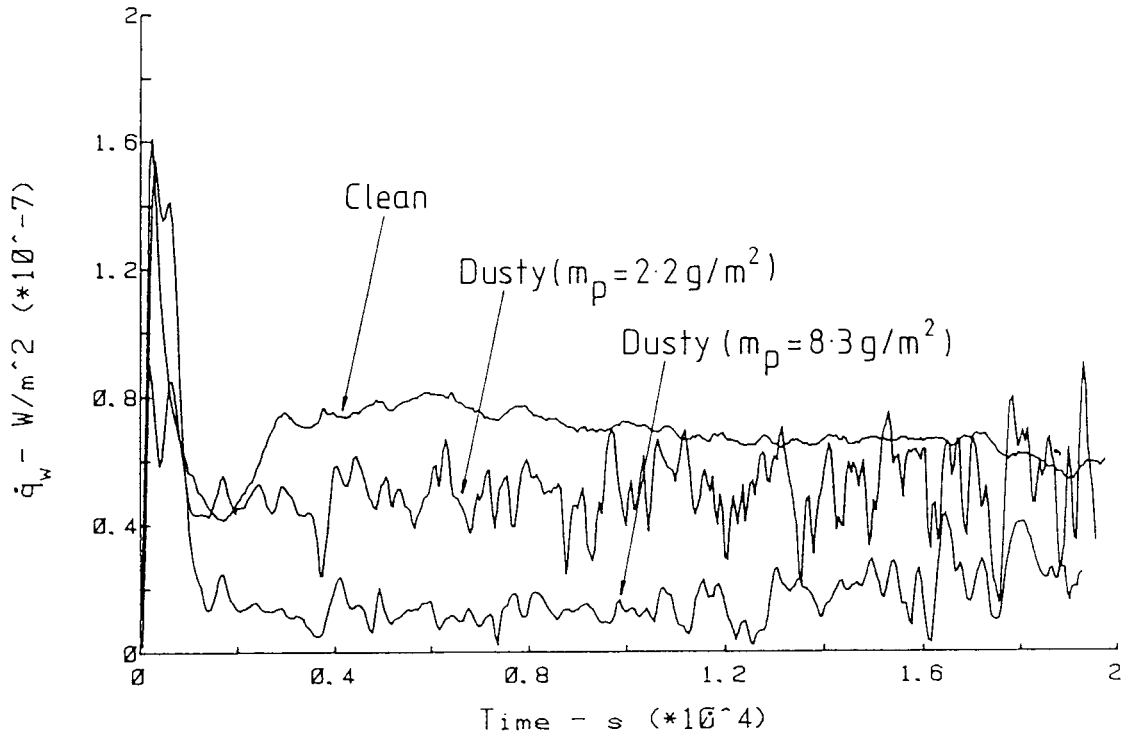

Figure 1; Typical dusty/ non-dusty heat flux profiles - AASU experiments

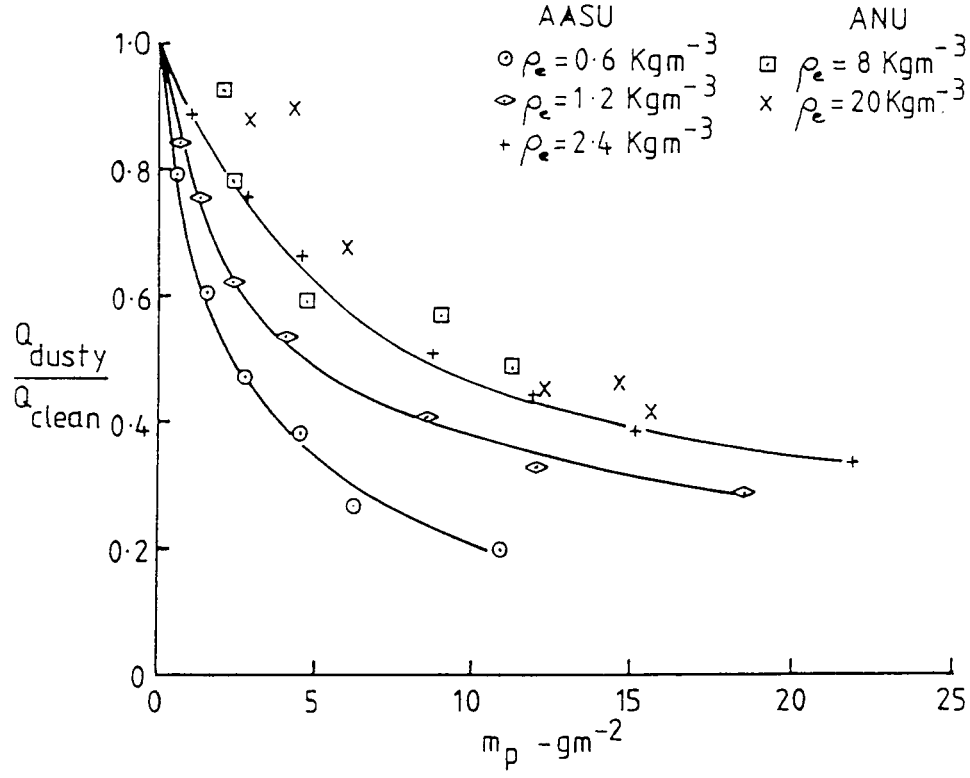

Figure 2; Heat flux reduction vs particle mass loading

PERIODIC SLOT BLOWING OF A SUPERSONIC TURBULENT BOUNDARY LAYER

Michael S. Selig, Alexander J. Smits and Emerick M. Fernando

Department of Mechanical and Aerospace Engineering
Princeton University
Princeton, NJ 08544 U.S.A.

1. INTRODUCTION

The present investigation was initiated to help improve our understanding of unsteady shock-wave/boundary layer interactions, with the specific aim of determining the effect of the unsteady shock movement on the boundary layer turbulence. An unsteady shock-wave/boundary-layer interaction was produced on a flat plate by introducing periodic blowing through a spanwise slot in the wall at frequencies up to 5kHz. The incoming flow conditions were $M_\infty = 2.84$, $Re_\infty/\ell = 6.5 \times 10^7$, and $\delta_o = 26$ mm. Measurements of the fluctuating mass flux and wall pressure were made, and the unsteady flowfield was visualized through stroboscopic schlieren videography. Since the blowing was periodic, phase-averaging could be used to identify the downstream effect of the shock oscillation. The results suggest that the main effect of the unsteady shock motion is to displace the incoming boundary layer flow without affecting the turbulence levels significantly. More interestingly, the speed of the upstream and downstream shock movement was found to be only a small fraction of the freestream velocity, and it was not strongly affected by the amount of blowing, or by the frequency of blowing.

2. EXPERIMENTAL FACILITY, APPARATUS, AND TEST CONDITIONS

The experiments were performed in the Princeton University 203 x 203 mm (8 x 8 in.), Mach 3, blowdown wind tunnel. For all tests, the nozzle-wall boundary layer was used. At the position of the injection slot, 1.95 m downstream of the throat, the layer was typical of a zero-pressure gradient fully turbulent boundary layer, and it obeyed both the law of the wall and law of the wake (Taylor 1984; and Settles et al., 1976). Its characteristics are summarized in Table I.

The freestream Mach number was fixed by the nozzle geometry at 2.84 ± 1%, and the stagnation pressure was held fixed at 0.69×10^6 Pa ± 1% (100 psia). The stagnation temperature remained fairly constant over the test period at 270 K ± 2%. The freestream turbulence level was about 1 to 1.5% (Spina & Smits 1987).

The periodic blowing apparatus operates somewhat like a siren in that a stream of air is clipped periodically to produce a high-frequency, pulsed jet of air issuing through a spanwise slot in the floor of the test section (see figure 1). The slot is opened and closed by a hollow slotted drum, spinning within a pressurized plenum chamber. The frequency of the blowing was controlled by the speed of the drum and

could be safely set as high as 5 kHz. The amount of air injected through the injection slot into the boundary layer was controlled by varying the supply pressure in the plenum chamber and by varying the width of the slot. Since the flow mostly responded to the net amount blowing rather than how it was achieved, the slot width was fixed at 3.2 mm (1/8 inch), and only the plenum chamber pressure was varied to control the blowing flow rate.

The static pressure variations were measured using miniature differential pressure transducers manufactured by Kulite Semiconductor Inc., Model XCQ-062-25-D. In this study the transducers were used primarily to reveal the dynamic character of the low-frequency shock motion (500 Hz to 10 kHz) and the limited frequency response of the pressure transducers was of no great concern. The transducers were positioned along the centerline of the tunnel floor, with a minimum spacing of 4.2 mm. No wall-pressure measurements were made downstream of the slot.

The fluctuations in the boundary layer mass flux were measured using a DISA 55M10 constant-temperature hot-wire anemometer, according to the technique described by Smits et al. (1983). To reduce the temperature sensitivity of the anemometer, so that the output was sensitive only to variations in mass flux, the probe was operated at an overheat ratio of 0.8, yielding an uncertainty in the measured $<(\rho u)'>/(\rho U)$ of -5% to 9% (Smits & Dussauge 1988). The frequency response was always in excess of 100 kHz.

In digitizing, the anemometer output signal was split into two components, a fluctuating and a mean. The mean was obtained by low-passing the signal at 10 Hz and sampling at a relatively low rate. The fluctuating part of the signal was obtained by high-passing the signal at 10 Hz. This fluctuating signal was amplified to fill the range of the A/D converter, filtered at a cut-off point of 250 kHz, then sampled at 500 kHz or 1 MHz. The signal from the drum encoder was also recorded so that the data could be phase-averaged using the blowing cycle phase.

Every run was visualized using a schlieren videography system. The spark source of the schlieren system was strobed slightly out of phase with the periodic blowing frequency to reveal the flow response in stroboscopic "slow motion." In this way, the conventional video camera was converted into a psuedo-high-speed camera to provide 'movies' of the flow (see Selig 1988 for further details).

3. RESULTS

With the amount of blowing fixed at 9% of the freestream mass flux, that is, $(\rho V)_{slot}/(\rho U)_\infty = 0.09$, the flow was examined for blowing frequencies of 1,2,3, and 4 kHz. Wall-pressure data were taken upstream of the slot for each case, and mass-flux data were taken downstream for the 2 kHz case only. Flow visualization using the schlieren videography system demonstrated that the flow structure depends on the frequency of blowing. At low frequencies an oblique shock forms as the incoming

flow is deflected by the blowing. As the blowing continues, this shock travels upstream at a speed of the order of 50 m/s to reach a maximum position upstream of the slot. When the blowing stops, the shock dissipates as it is convected downstream at a speed of the order of 120 m/s. The sequence is repeated with the start of the next blowing cycle. As the blowing frequency increases, a critical frequency is reached (between 2 and 3 kHz) at which the downstream-moving shock just reaches the slot as a new blowing cycle begins. At still higher frequencies the shock does not reach the slot before the new blowing cycle starts. As a result, the blowing triggers the formation of a second shock which itself travels upstream and intersects the first shock. The two shocks merge into one, move upstream to a maximum position, and on returning downstream encounter another shock produced by the next blowing cycle, and so on. At the higher frequencies, disturbances travelling along the shock are observed. These disturbances deform the shock into a wave-like shape (see figure 2).

Wall-pressure time histories for the 1 kHz and 4 kHz cases are shown in figure 3. At the lower frequency, a relatively steep rise in the mean wall pressure is seen with the passage of the shock upstream, followed by a more gradual reduction of the wall pressure as the shock passes back downstream. Behind the shock at x = -12.7 mm (x is measured positive downstream from the back edge of the slot), the normalized pressure rise for this 1 kHz case is roughly 1.75, which at this Mach number corresponds to an 8^{o} turning of the flow with a shock angle of 27^{o}. This estimated shock angle is in good agreement with that measured from the flow visualization. At the higher frequency, the pressure at x = -12.7 mm never returns to its upstream value, indicating that a shock wave is always located upstream of that point.

The mean wall-pressure data, given in figure 4, shows that the mean pressure distribution is virtually independent of the blowing frequency. The rms wall-pressure levels (figure 5) begin to rise further downstream as the blowing frequency increases; at lower frequencies there is more time for the shock to penetrate upstream before the blowing stops. As the blowing frequency increases, the blowing period approaches the time constant of the shock motion, and as a result the maximum fluctuation level decreases at higher frequencies.

The mass-flux turbulence intensity profiles for the 2 kHz case are given in figure 6, and the spectra for two locations are given in figure 7. The peak in the turbulence intensity profile at x = 12.7 mm is in the region of the shock oscillation and should not be considered as 'true' turbulence. Discounting this shock-induced peak, the turbulence intensities in the outer part of the boundary layer downstream of the slot are very similar to the upstream levels, except for an outward displacement of about 5 mm, probably due to the intermitent presence of the thin separated zone near the wall.

The mass-flux spectra show a spike at the blowing frequency throughout the

boundary layer, indicating that the periodic motion of the shock makes a small contribution to the turbulence. The phase-averaged results indicated that for stations downstream of x = 12.7 mm the periodic component contributes less than 25% to the mean square intensity (see figure 8).

4. CONCLUSIONS

Periodic blowing was found to have relatively little effect on the flat plate boundary layer except for a small displacement away from the wall. The speed of the shock motion in both the upstream and downstream directions was only a small fraction of the freestream velocity, and it was not strongly affected by the level of blowing. Andreopoulos & Muck (1987) in their study of compression ramp flows found that the mean frequency of the shock oscillation was constant for corner angles from 16° to 24°. However, since the zone of shock oscillation increases with corner angle, and the results from periodic blowing showed there were limits on the shock speed, the frequency should not be constant but vary inversely with an amplitude or the range of shock oscillation, that is, the frequency should be higher for smaller turning angles. Indeed Dolling (1987), using a sophisticated conditional-sampling method developed by Narlo (1986), found that the mean frequency of the oscillation increased with decreasing ramp angle.

ACKNOWLEDGEMENTS

This work was supported by the U. S. Army Research Office, under Contract DAAG29-K-0255, monitored by Dr. T. L. Doligalski.

REFERENCES

Andreopoulos, J. and Muck, K. C. (1987), "Some new aspects of the shock wave boundary layer interaction in compression ramp flows," J. of Fluid Mech., Vol. 180, pp. 405-428.

Debieve, J. F. and Lacharme, T. P. (1985), "A shock-wave/free turbulent interaction," IUTAM Symposium on Turbulent Shear Layer/Shock Wave Interaction, Palaiseau, France, Sept. 9-12. Published by Springer-Verlag, Berlin, 1986, ed. J. Delery.

Dolling, D. S. (1985), "Unsteadiness of shock wave-induced turbulent boundary layer separation - A review," IUTAM Symposium on Turbulent Shear Layer/Shock Wave Interaction," Palaiseau, France, September.

Fernholz, H. H., Smits, A. J., Dussauge, J. P. and Finley, P. H. (1988), "A survey of measurements and measurement techniques in rapidly disturbed compressible flows," AGARDograph 315.

Narlo, J. C. (1986), "Experimental investigation of the driving mechanism of separation shock wave motion in interaction flows," M.Sc. Thesis, The University of Texas at Austin.

Selig, M. S. (1988), "Unsteadiness of shock-wave/turbulent boundary layer with dynamic control," M.Sc. Thesis, Department of Mechanical and Aerospace Engineering, Princeton University.

Settles, G. S. (1975), "An experimental study of compressible turbulent boundary layer separation at high Reynolds numbers," Ph.D. Thesis, Department of Aerospace and Mechanical Sciences, Princeton University.

Settles, G. S., Vas, I. E. and Bogdonoff, S. M. (1976), "Incipient separation of a supersonic turbulent boundary layer at high Reynolds numbers," AIAA J., Vol. 14, No. 1, pp. 50-56.

Smits, A. J. and Dussauge, J. P. (1988), refer to Chapter 5 of Fernholz et al. (1988).

Smits, A. J., Hayakawa, K. and Muck, K. C. (1983), "Constant temperature hot-wire anemometer practice in supersonic flows, Part I - The normal wire," Experiments in Fluids, Springer-Verlag.

Spina, E. F. and Smits, A. J. (1987), "Organized structures in a compressible turbulent boundary layer," Journal of Fluid Mechanics, Vol. 182, pp. 85-109.

Taylor, M. W. (1984), "A supersonic turbulent boundary layer on concavely curved surfaces," M.Sc. Thesis, Mechanical & Aerospace Engineering Department, Princeton University.

Test Conditions		
p_o	=	0.69 $\times 10^6$ Pa (100 psi)
T_o	=	270 K
M_∞	=	2.84
Re_∞/ℓ	=	6.5 $\times 10^7$/m
δ_o	=	26 mm
δ^*	=	6.4 mm
θ_o	=	1.3 mm
C_{f_o}	=	0.00115

Table I. Boundary layer characteristics and incoming flow conditions.

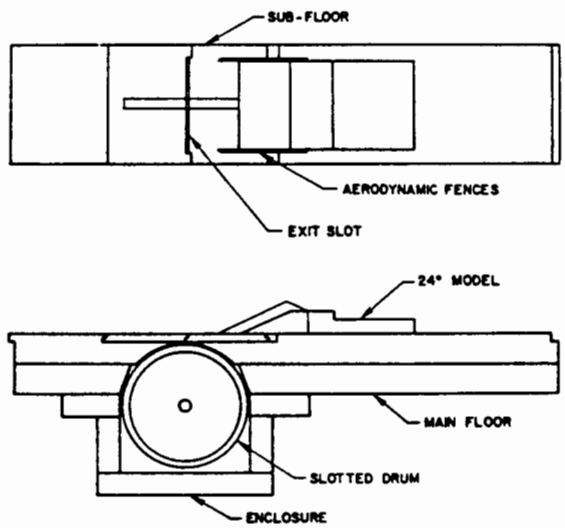

Fig. 1 Periodic blowing apparatus.

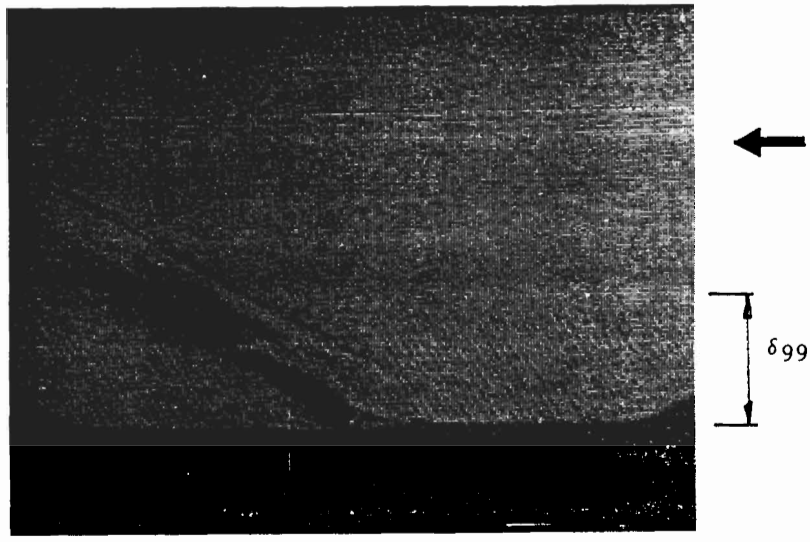

Fig. 2 Videograph of 5khz case showing disturbances travelling along shock.

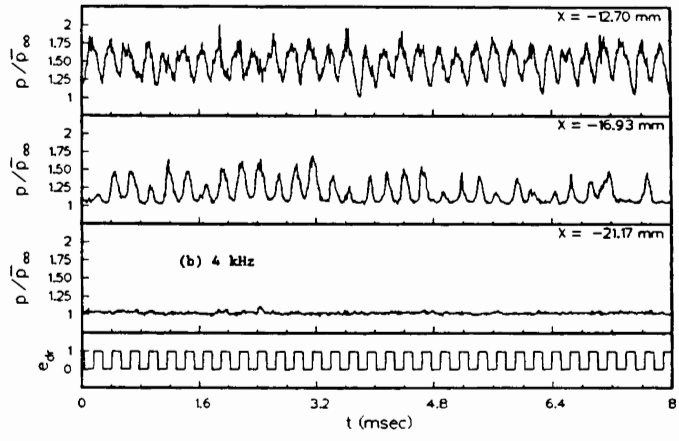

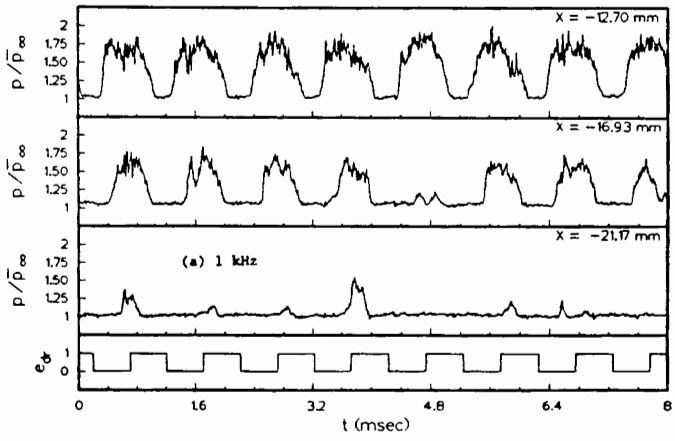

Fig. 3 Wall-pressure time histories. Blowing frequency: (a) 1 kHz, (b) 4 kHz.

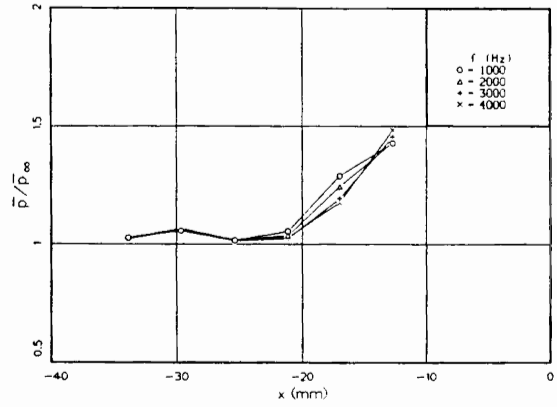

Fig. 4 Mean wall-pressure distributions. Blowing frequency: 0, 1kHz; Δ, 2kHz; +, 3kHz; X, 4khz.

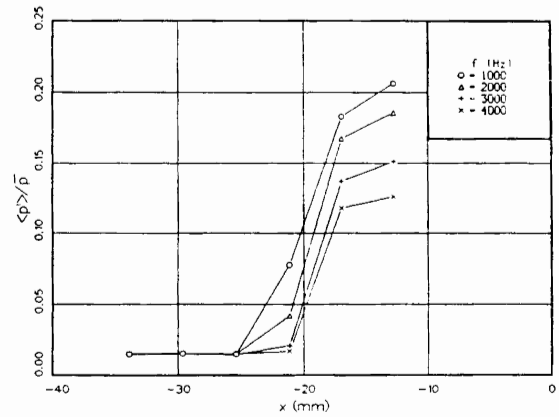

Fig. 5 Rms wall-pressure distributions. Blowing frequency: 0, 1kHz; Δ, 2kHz; +, 3kHz; X, 4kHz.

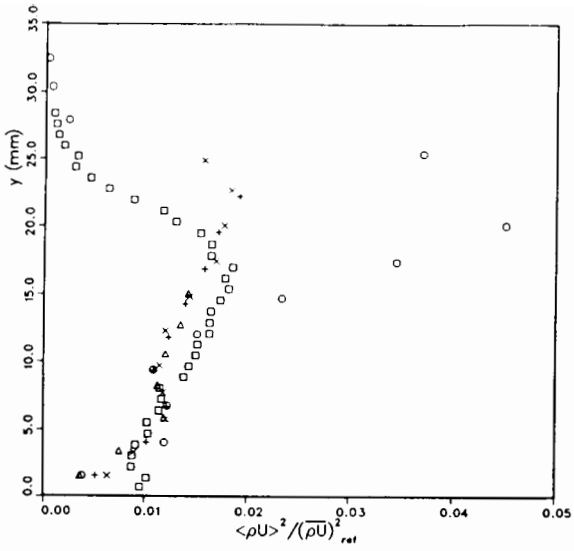

Fig. 6 Mass-flux turbulence intensity profiles, 9% blowing at 2 kHz: 0, x = 12.7 mm; Δ, x = 25.4 mm; +, x = 38.1 mm; X , x = 50.8 mm.

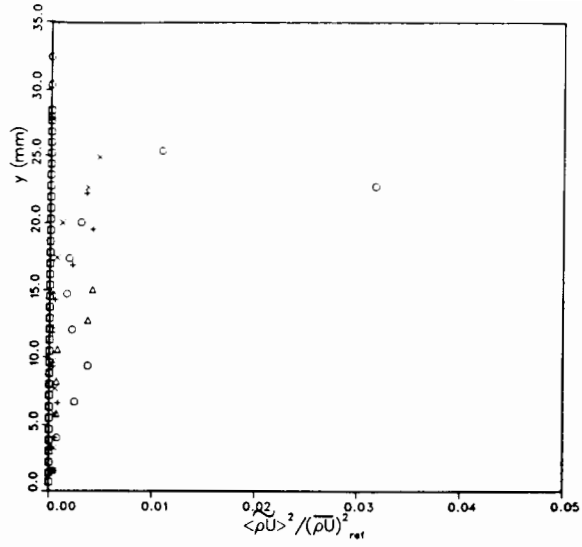

Fig. 8(a) Phase-averaged mass-flux turbulence intensity profile, 9% blowing at 2kHz: 0, x = 12.7 mm; Δ, x = 25.4 mm; +, x = 38.1 mm; X , x = 50.8 mm.

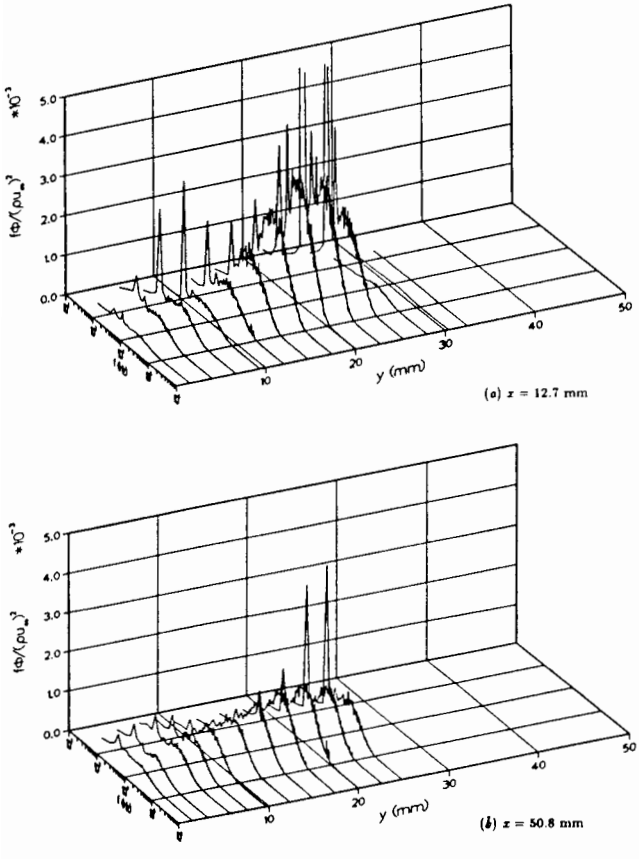

Fig. 7 Energy spectra of the mass flux. Blowing at 2 kHz: (a) x = 12.7 mm; (b) x = 50.8 mm.

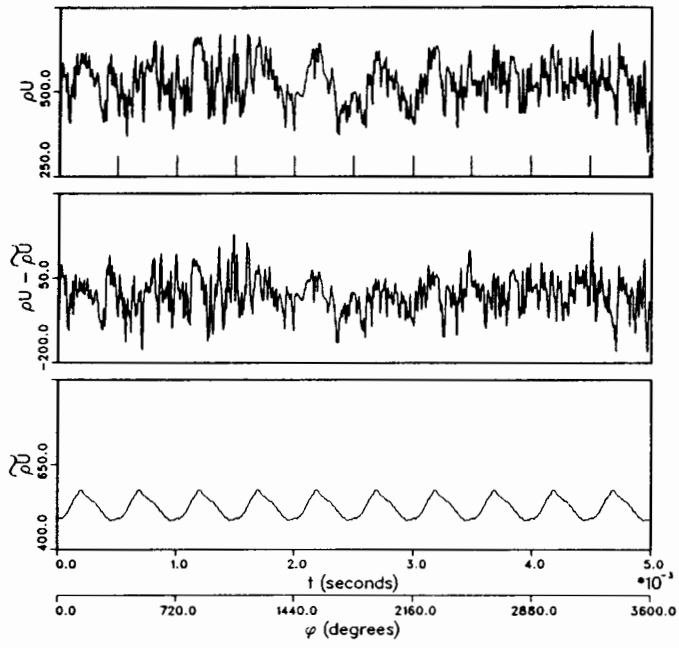

Fig. 8(b) Time traces of instantaneous mass-flux showing broad-band $(\rho u)'$ and phase-averaged component $(\rho u)'$ at x = 51 mm, y = 23 mm (9% blowing at 2kHz).

Compressible, Fully De-aliased, Two-dimensional Spectral Method Simulations of Fluid and Magneto-Fluid Turbulence

John V. Shebalin
NASA Langley Research Center, MS 490, Hampton VA 23665

David Montgomery
Department of Physics & Astronomy, Dartmouth College, Hanover, NH 03755

Abstract

A fully de-aliased, two-dimensional Fourier spectral method simulation is described. This numerical method is used to study the spectral distribution of relative compressible and magnetic energy versus initial rms Mach number for decaying turbulence. Results from fluid (Navier-Stokes) simulations are compared with magneto-fluid (MHD) simulations. Future applications of the numerical procedure are also discussed.

Introduction

As is well known, compressible turbulence and mixing plays an important role in many different phenomena: atmospheric reentry, scram-jet engines, aerosol dispersal, explosion dynamics and in the enhancement of chemical kinetics, to name a few. In all these highly compressible processes, several generic features occur and interact with one another: shocks, turbulence, boundary influences, multiple reaction species, ionization, magnetism and complex thermodynamic effects. These highly non-linear processes are directly susceptible to few analytic approaches, but instead must be understood through observation in either physical or numerical experiments.

Here, we would like to describe a fairly general two-dimensional numerical experimental apparatus which can handle both fluid and magneto-fluid problems. Initially, we consider only density, velocity and magnetic field dynamics, the pressure being determined by a polytropic equation of state; the capability to handle other generic processes will be added incrementally, as will an extension of the codes to three-dimensionality. Following a brief description of the fluid and magneto-fluid codes, we will examine, in a magneto-fluid context, a phenomenon uncovered by Passot and Pouquet [1] in Navier-Stokes fluids: the qualitative difference between flows at low and high Mach numbers, with respect to the relative amount of

compressible energy and its spectral distribution. Then, we will examine the spectral distribution of magnetic energy and its relation to compressibility. Finally, we will conclude with possible future extensions and uses of the codes.

Computational Procedure

As we have mentioned, a polytropic equation of state is used, obviating the need for an energy (temperature) equation; in its place we have added a magnetic field evolution equation to the basic Navier-Stokes equations. The basic, non-dimensional equations are:

$$\frac{\partial \lambda}{\partial t} + \mathbf{v}\cdot\nabla\lambda = -\nabla\cdot\mathbf{v} \qquad (1a)$$

$$\rho\left(\frac{\partial \mathbf{v}}{\partial t} + \mathbf{v}\cdot\nabla\mathbf{v}\right) = -\beta\nabla p + \mathbf{j}\times(\mathbf{B}_o+\mathbf{b}) + \nabla\cdot\left[\mu\left(\nabla\mathbf{v} + \frac{1}{3}\mathbf{I}\nabla\cdot\mathbf{v}\right)\right] \qquad (1b)$$

$$\frac{\partial \mathbf{a}}{\partial t} = \mathbf{v}\times(\mathbf{B}_o+\mathbf{b}) + \eta\nabla^2\mathbf{a}\,, \quad \mathbf{b}=\nabla\times\mathbf{a}\,, \quad \mathbf{j}=\nabla\times\mathbf{b} \qquad (1c)$$

where motion takes place in the x-y plane, and all variables are functions of x, y and the time t only. The velocity $\mathbf{u}$ and magnetic field $\mathbf{B}$ are measured in terms of reference values U_o and B_o, respectively, while the reference values for length and time are L_o and T_o, respectively. The magnetic field consists of two parts, $\mathbf{B}=\mathbf{B}_o+\mathbf{b}$, *i.e.*, an externally produced mean part $\mathbf{B}_o$ and the internal, turbulent part $\mathbf{b}$. Furthermore, other quantities and their (units) are:

$\rho=e^{\lambda}$: mass density (ρ_o)

$p=\rho^{\gamma}$: pressure (p_o), $\gamma\equiv$constant

$\mu=\rho\nu$: viscosity, $\nu\equiv$constant (L_o^2/T_o)

η : electrical resistivity (L_o^2/T_o)

$\beta \equiv \dfrac{p_o}{\rho_o U_o^2}$: a measure of compressibility

$\mathbf{a}=a\mathbf{e}_z$: magnetic potential (B_oL_o)

$\mathbf{I}=\mathbf{e}_i\mathbf{e}_i$: unit 2nd rank tensor

In those situations when the magnetic energy is comparatively small, U_o may be an rms fluid velocity $U_o=\sqrt{[u^2]}$, while in the case where the magnetic energy is comparatively large, $U_o=V_A\equiv B_o/\sqrt{4\pi\rho_o}$ (cgs units);

B_o is either the mean field strength, or the rms value of **b** and V_A is the *Alfven velocity.* If the magnetic and kinetic energies are comparable, $V_A \approx \sqrt{[u^2]}$, and U_o can represent either one.

The numerical procedure we use is a de-aliased spectral transform method of the Orszag-Patterson type [2,3]. Also, note that we use the natural logarithm of the density rather than the density iself as the computational variable; this insures that any numerical time-integration scheme will not produce negative values of density.

In the numerical procedure, the dynamical fields are expanded in Fourier series:

$$\lambda(\mathbf{x},t) = \sum_{|\mathbf{k}|\le K} \lambda(\mathbf{k},t)e^{-i\mathbf{k}\cdot\mathbf{x}}, \qquad \mathbf{v}(\mathbf{x},t) = \sum_{|\mathbf{k}|\le K} \mathbf{v}(\mathbf{k},t)e^{-i\mathbf{k}\cdot\mathbf{x}}, \qquad a(\mathbf{x},t) = \sum_{|\mathbf{k}|\le K} a(\mathbf{k},t)e^{-i\mathbf{k}\cdot\mathbf{x}}$$

Here, the position vector is $\mathbf{x}=(x,y)$, the wave vector is $\mathbf{k}=(k_x,k_y)$ and K is the maximum modulus of $\mathbf{k}$. This yields a set of many hundred or thousand ordinary, coupled differential equations. Time integration is performed by a second order Runge-Kutta method with the dissipative terms being evaluated implicitly.

Aliasing is avoided in the formation of high-order products in

$$\rho, \quad \rho^{\gamma}, \quad \rho^{-1}$$

through the use of the expansion

$$\rho^{\alpha} = e^{\alpha\lambda} = 1 + \alpha\lambda + \{\alpha\lambda,\frac{\alpha\lambda}{2}\} + \{\{\alpha\lambda,\frac{\alpha\lambda}{2}\},\frac{\alpha\lambda}{3}\} + \cdots$$

The n^{th} term in the series is a fully de-aliased quadratic product formed from the the preceding term and $\alpha\lambda/n$, and summation continues until machine accuracy is reached. The curly brackets {a,b} signify that a single, de-aliased quantity has been formed from a and b by the Patterson-Orszag transform method [3].

Finally, the arrays which contain dynamic variables, their derivatives and products are *minimal arrays*, rather than full FFT arrays (of which there are only two in the code). In a Patterson-Orszag de-aliasing method [3], the FFT arrays are somewhat sparse, a 2-D array containing 30% zeros and a 3-D array containing 56% zeros. The

minimal array consists of only the non-zero FFT array elements; mapping to and from the FFT arrays is accomplished by a bit-vector or order array. Mapping into the minimal array also serves the purpose of isotropic truncation, as required by the Patterson-Orszag method [3].

It should also be noted that the viscosity μ we use here, in equation (1b), is linearly related to the density. This form is a great simplification of theory [4] and is chosen since the scalar viscosity of a fully ionized plasma (*i.e.*, magneto-fluid) is believed to vary as $T^{5/2}$ [4]; with a polytropic equation of state, $T=\rho^{\gamma-1}$, so that using $\gamma=7/5$ (as would be the case for a diatomic gas), we have $\mu=\rho\nu$, where ν is constant. If this form of the viscosity is heuristically adopted in the Navier-Stokes case also, it removes the constraint imposed by density fluctuations which limited the time-step of Passot and Pouquet [1]. In the MHD case, however, the presence of the Lorentz force term requires that this constraint be retained.

We have used this algorithm to study numerically [5] theoretical predictions made earlier by Montgomery, *et al.*, [6] to explain the observed spectral structure of small amplitude turbulent density fluctuations in the interstellar medium [7]. The theoretical predictions made by Montgomery, *et al.*, [6] followed from the assumption that interstellar density fluctuations were inherently related to the *magnetohydro*dynamics rather than just the *hydro*dynamics of the interstellar medium. The prediction was, in effect, that the total pressure (magnetic plus thermodynamic) was essentially constant at the smaller spatial scales. Assuming (among other things) that the statistical behavior of both kinetic and magnetic energy spectra was described by $k^{-5/3}$ led to the conclusion that the omnidirectional density fluctuation spectrum behaved as $k^{-5/3}$, which agreed quite well with experimental observations [7] (which spanned 12 spatial orders of magnitude); in contrast, a long-standing, purely hydrodynamic argument [8] lead to a predicted $k^{-7/3}$ behavior. The numerical work [5] verified, in turn, that the theory also matched data generated by direct numerical simulation, even when the Reynolds numbers are not large enough to expect inertial range power laws.

In the next section we use our algorithm to explore the evolution of the relative compressible energy spectra in homogeneous fluids and magneto-fluids with respect to initial rms Mach number. We also

report on the effects of compressibility on the evolution of turbulent magnetic energy spectra.

Numerical Results

The numerical results we present here are broken into two sets: First, we allowed the Navier-Stokes (N-S) and MHD versions of our code to run for relatively long times on a 64x64 grid with $\mathbf{B}_o=0$ and $\gamma=1.4$, for many values of β; here, we show results for $\beta=12.5$ and 8. In all runs, the time step size satisfied the usual *CFL* criteria (in the MHD code this value was divided at each iteration by the maximum grid value of ρ^{-1}, the previously mentioned constraint of Passot and Pouquet [1].) The initial condition of all the 64x64 N-S runs was to have the same purely solenoidal (*i.e.*, $\nabla\cdot\mathbf{v}=0$ at $t=0$) velocity field; initially, $\Sigma|\mathbf{v}(\mathbf{k})|^2$ was normalized to an rms value of unity and $|\mathbf{v}(\mathbf{k})|^2$ varied as $e^{-(k-5)^2/2}$ with the $\mathbf{v}(\mathbf{k})$ having random phase. In the MHD runs, an initial magnetic field $\mathbf{b}(\mathbf{k})$ of the same spectral characteristics as this initial $\mathbf{v}(\mathbf{k})$ (but independently random phase) was also used. In these 64x64 runs, $\nu=\mu=0.005$ and the maximum computed dissipation wave number was around 50, while the microscale Reynolds #'s typically started around 40 but fell to about 15.

Since the initial rms velocity field was unity, the initial rms Mach #, *Ma*, was $Ma=(\beta\gamma)^{-1/2}$; thus, the rms initial Mach #'s corresponding to $\beta=12.5$ and 8 are $Ma=0.239$ and 0.299, respectively. These values are representative of a larger range we used to bracket $Ma=0.3$, the threshold value that Passot and Pouquet [1] had observed, above which the relative compressible energy in the smaller scales of N-S flow became markedly larger. In Figure 1, we give a graphical comparison between the N-S and MHD cases. Here, we add up various energies within three equi-areal, concentric and contiguous annuli in $\mathbf{k}$-space in order to get a measure of their relative proportions in the large, medium and small scales of flow. We define the large, medium and small scales as those for which $0\le k\le K/3$, $K/3<k\le 2K/3$ and $2K/3<k\le K$, respectively.

(The energies we are concerned with here are

$$E_s=\left[\mathbf{p}_s\cdot\mathbf{u}_s/2\right] : \textit{solenoidal}\ \text{part of kinetic energy}$$

$$E_c=\left[\mathbf{p}_c\cdot\mathbf{u}_c/2\right] : \textit{compressible}\ \text{part of kinetic energy}$$

$E_I=\left[\beta\rho(\rho^{\gamma-1}-1)/(\gamma-1)\right]$: internal energy $\qquad E_B=\left[\mathbf{b}\cdot\mathbf{b}/2\right]$: magnetic energy

$E_K = E_s + E_c$: total kinetic energy $\qquad E_{com} = E_I + E_c$: total compressible energy

$$E = E_K + E_I + E_B = E_{com} + E_s + E_B \text{ : total energy}$$

while two other important quantities are

$$\Omega\equiv\left[(\nabla\times\mathbf{u})^2\right] \text{ : enstrophy} \qquad J\equiv\left[(\nabla\times\mathbf{b})^2\right] \text{ : Mean square current}$$

The square brackets signify a volume average over the computational box:

$$[Q]\equiv\frac{1}{(2\pi)^2}\int_0^{2\pi}dx\int_0^{2\pi}dy\ Q(x,y)$$

and the solenoidal and compressible parts of the momentum are, $\mathbf{p}_s\equiv\{\rho\mathbf{u}_s\}$ and $\mathbf{p}_c\equiv\{\rho\mathbf{u}_c\}$, respectively.)

The second set of computations we wish to present were done on a 256x256 grid and consisted of two N-S runs (γ=1.4, β=25 and β=1) and two MHD runs (γ=1.4, β=25 and β=1). The initial conditions for all these runs were the same: at t=0, all the energy was in the solenoidal part of the velocity field, which had random phase and an energy spectrum which varied as $e^{-(k-10)^2/64}$; furthermore, $[v^2]$=1 at t=0, so the initial Ma corresponding to β=25 and β=1 were 0.169 and 0.845, respectively. In the two MHD runs, there was no initial turbulent magnetic field energy, but there was a mean magnetic field $\mathbf{B}_o=0.05\mathbf{e}_x$ present. The interaction of the velocity with the mean field resulted in the generation of a turbulent magnetic field $\mathbf{b}$, as seen in Figure 2, which shows the time behavior of the total energies, enstrophy and mean square current for these four runs. In these 256x256 runs, $\nu=\mu=0.002$ and the maximum computed dissipation wave number was around 75, while the microscale Reynolds #'s typically started around 44 and fell to about 32.

In Figure 2, we also compare the energy spectra for these four runs at similar times in their evolution. There are two time scales inherent in these simulations; one is set by dissipation and the the other by compressibility. Variation of the 'solenoidal' energy

$E_{sol} = E_s + E_B$ occurs on a 'dissipation time scale' while E_{com} varies on a 'compression time scale'. We choose to standardize in terms of the time it takes a sound wave to cross a unit distance; thus, $T_o \equiv C_s^{-1}$, where $C_s=\sqrt{\beta\gamma}$ is the sound speed. (If the E_B and J curves were removed from the plots in Figure 2, what remains is essentially the N-S results.) Finally, in Figure 3, we show physical space contour plots for the 256x256, MHD, $\beta=1$ run.

Discussion

Compressibility has some interesting effects on MHD turbulence. First, as shown in Figure 1, the effect observered by Passot and Poquet [1] is mitigated in the case of MHD: there is both more compressible energy at small scales for low Ma and less at high Ma than in the corresponding N-S flows. Second, as seen in Figure 2, magnetic energy appears predominant at small scales, although predominance decreases with increasing compressibility (Ma). This small scale magnetic predominance manifests itself in the many intense current filaments seen in Figure 3c. These observations reinforce earlier results [5,6], in that they underscore the importance of magnetic field fluctuations in the dynamics of a compressible, turbulent and conducting fluid.

As a final point, we note that if $\mathbf{B}_o \neq 0$, magnetic dynamo processes appear possible, as indicated by the behavior of E_B and J in Figure 2(a,b), even in two dimensions. (No 'anti-dynamo' theorem can be proved in the presence of even a small dc mean field $\mathbf{B}_o$.) This is a point we plan to explore numerically by introducing mechanical forcing into our MHD code. In addition, we plan to add a temperature equation, using $\tau = \ln(T)$ as our primary variable, rather than directly using the temperature T.

References

[1] T. Passot & A. Pouquet, **J. Fluid Mech, 181**, 441, 1987.
[2] S. A. Orszag, **Stud. Appl. Math., 50**, 293, 1971.
[3] G. S. Patterson & S. A. Orszag, **Phys. Fluids, 14**, 2538, 1971.
[4] S. I. Braginskii, "Transport processes in a plasma", in **Reviews of Plasma Physics, v.1**, M. A. Leontovich, ed., Consultants Bureau, New York, 1965.
[5] J. V. Shebalin & D. Montgomery, **J. Plasma Phys., 39**, 339, 1988.
[6] D. Montgomery, M. R. Brown & W. H. Matthaeus, **J. Geophys. Res., 92**, 282, 1987.
[7] J. W. Armstrong, J. M. Cordes & B. J. Rickett, **Nature, 291**, 561, 1981.
[8] M. J. Lighthill, **Proc. Roy. Soc. Lon., A, 211**, 564, 1952.

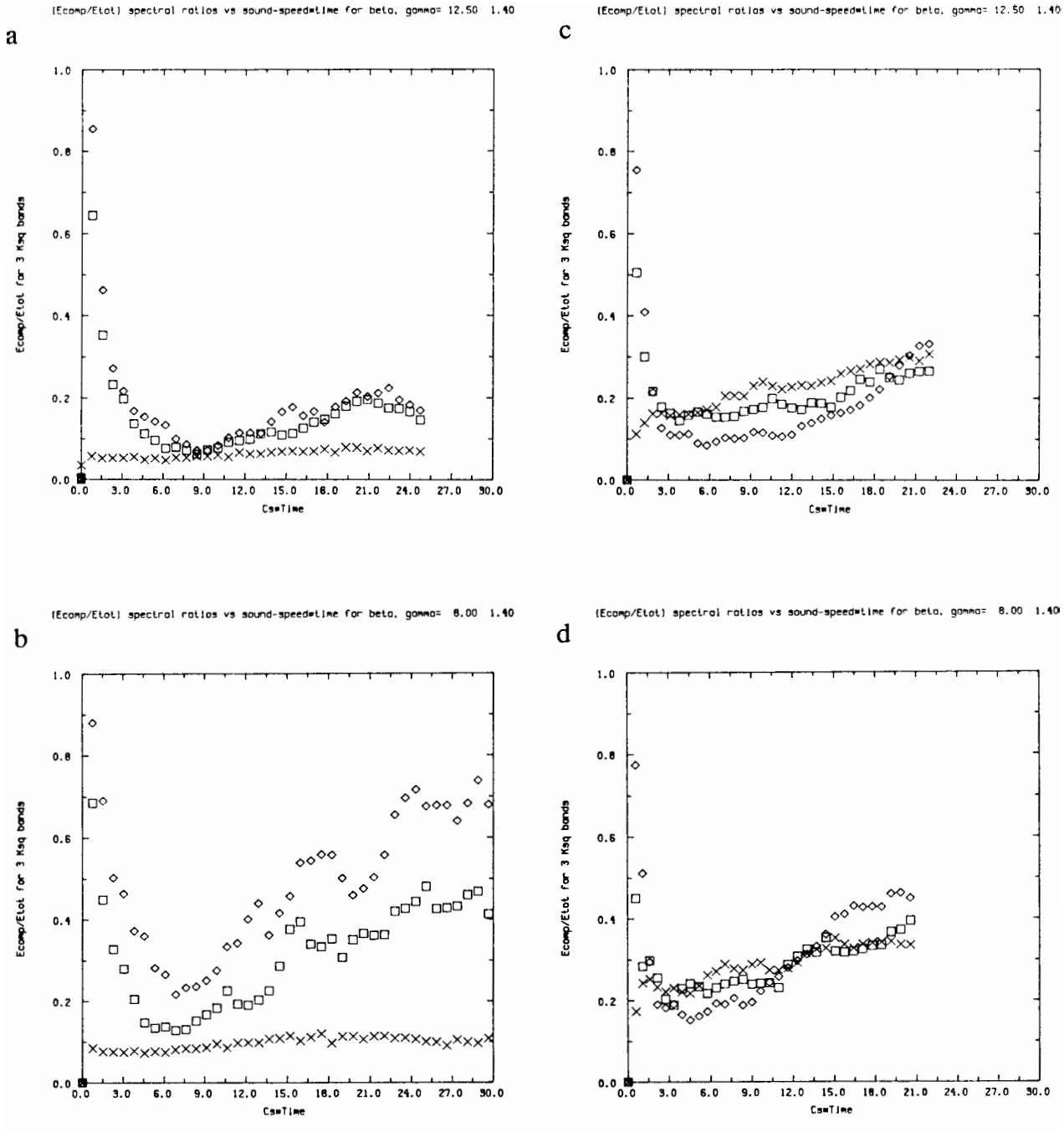

Figure 1. 64x64 runs: $E_{com}/(E_{com}+E_s)$ vs time for large (×), medium (□) and small (◇) scales, for N–S with initial *Ma* : a) 0.239, b) 0.299; for MHD with initial *Ma* : c) 0.239, d) 0.299.

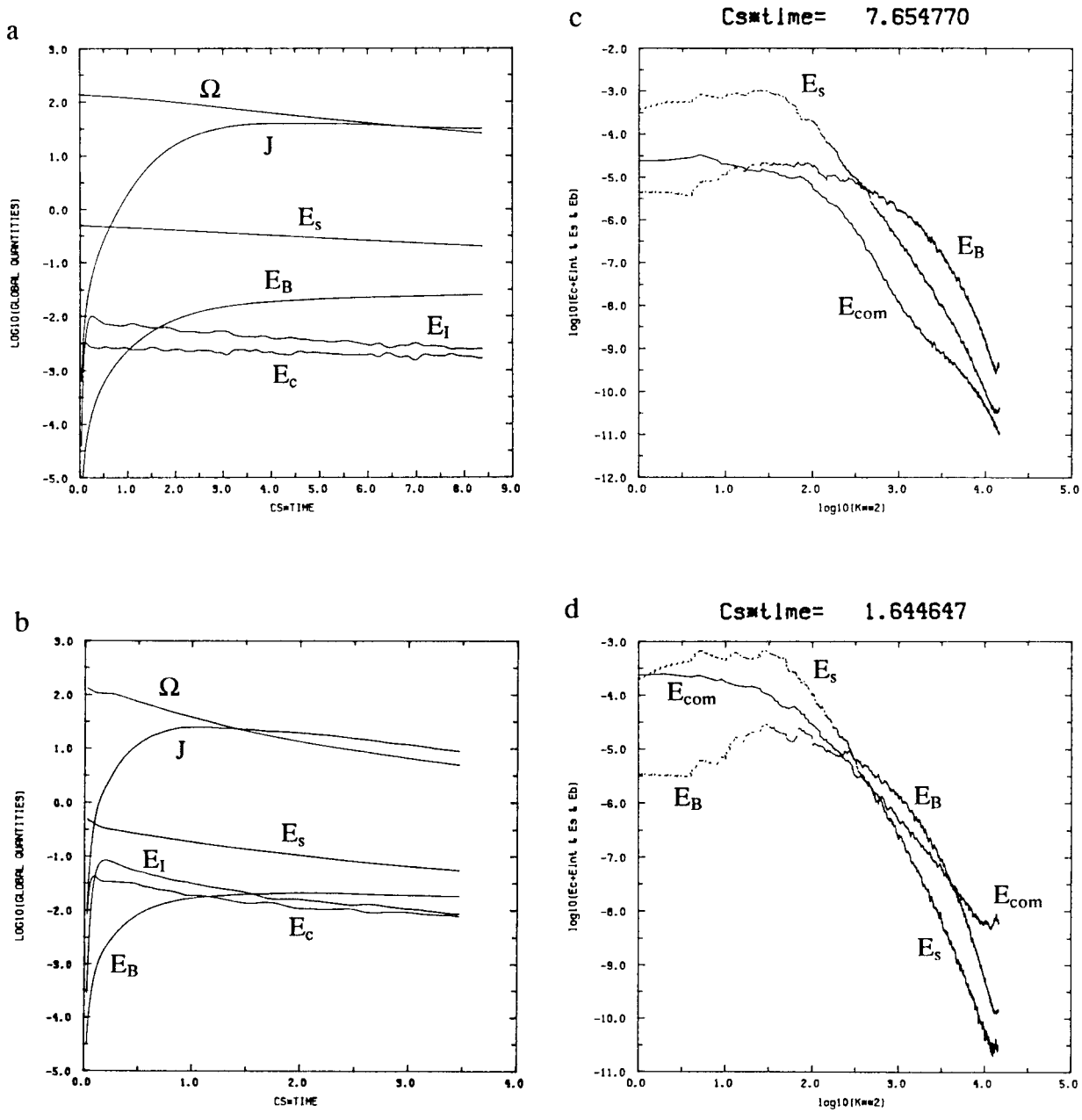

Figure 2. Energies, enstrophy (Ω) and mean square current (J) for 256x256 MHD runs with initial *Ma* : a) 0.169, b) 0.845; energy spectra shortly after $J \approx \Omega$ for these same runs: c) initial *Ma* =0.169, d) initial *Ma* =0.845.

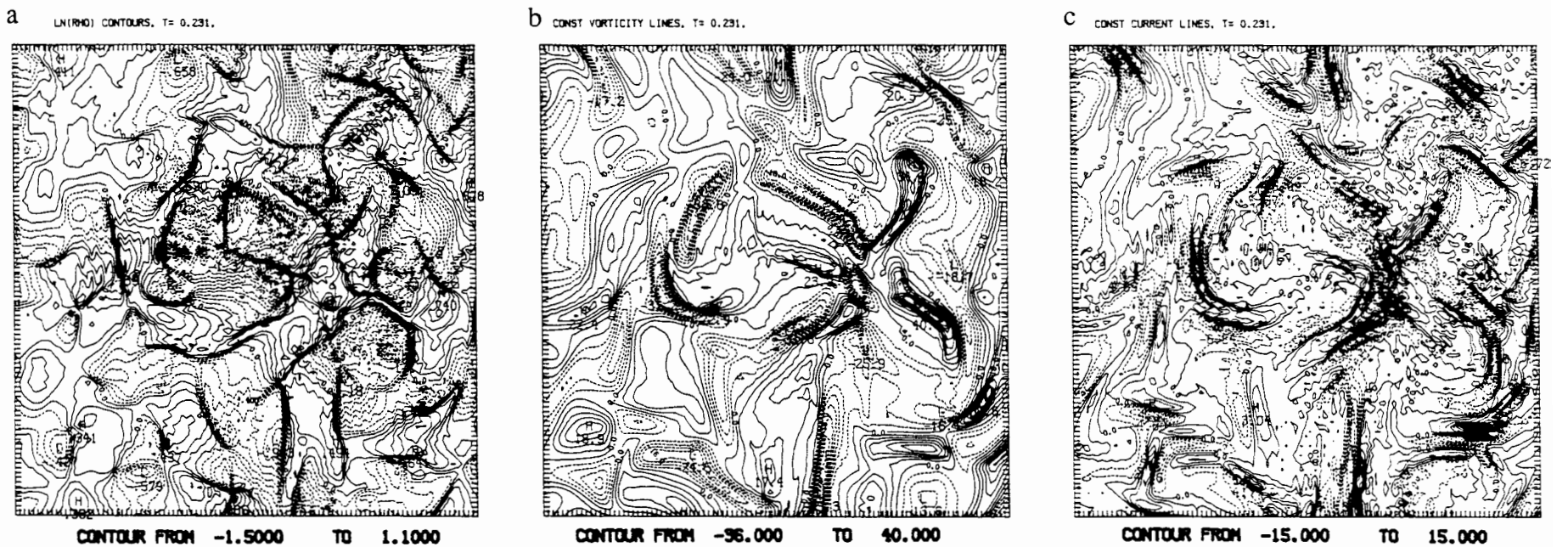

Figure 3. **x**-space contour plots of lower left 100x100 section of 256x256 grid for MHD run with initial Ma =0.845, close to maximum E_{com} : a) ln(ρ), b) $\omega=\nabla\times\mathbf{v}$, c) $\mathbf{j}=\nabla\times\mathbf{b}$.

EULER EQUATION OF ONE-DIMENSIONAL COMPRESSIBLE GAS AND LOCALLY-EQUILIBRIUM MOLECULAR DYNAMICS

Ya. G. Sinai
Landau Institute of Theoretical Physics
Academy of Sciences, USSR
ul. Kosygina, dom 2, Moscow 117334 USSR

1. FORMULATION OF THE PROBLEM

The problem which we intend to consider in this talk can be described as the study of relations between microscopical properties of matter and their macroscopical manifestation. One of the final goals, which is still unfortunately very far from us, is to understand whether turbulent motions may be thought as collective motions of some modes having a thermodynamic origin. We shall make several speculations about this at the end of this talk.

The matter which we shall deal with here is classical. It means that we neglect quantum effects. This seems to be reasonable for normal thermodynamic conditions. Another restriction which we impose is more serious. We intend to consider only one-dimensional gases but we shall take into account their properties of compression and heat conductivity. The advantage or disadvantage of the one-dimensional systems is due to the fact that the local changes of form of the infinitesimal volumes are also one-dimensional, i.e., they are reduced only to the change of the scale but not to the change of form which does not even exist in the one-dimensional situation.

We assume that the motion of the one-dimensional gas takes place on the circle S^1. It will be most convenient for us to take as an independent variable the Lagrangian variable ξ where ξ is the mass of the gas counted starting with some fixed point, O, at the initial moment of time. Its connection with the usual coordinate χ follows from the equality

$$\int_0^{\chi} \rho(y;0)\,dy = \xi$$

where $\rho(y;t)$ is the density at the point $y \in S^1$ at a time, t. The whole mass, $\int_0^1 \rho(y;0)\,dy = 1$, which is certainly nothing other than some normalizing condition. Introduce the hydrodynamical variables $\varepsilon(\xi,t)$, $v(\xi,t)$, $r(u,t)$, where $\varepsilon(\xi,t)\,d\xi$ is the total internal energy of particles which initially were in the interval $(\xi, \xi+d\xi)$. $v(\xi,t)$ is the hydrodynamical velocity of the same particles, and $r(\xi,t)$ is the mean distance between particles, i.e., $r^{-1}(\xi,t)$ is the density. The system of Euler equations takes now a divergence-like form (see [1])

$$\frac{\partial\varepsilon(\xi,t)}{\partial t} = \frac{\partial T^{(1)}(\xi,t)}{\partial \xi}; \qquad \frac{\partial v(\xi,t)}{\partial t} = \frac{\partial T^{(2)}(\xi,t)}{\partial \xi}; \qquad \frac{\partial r(\xi,t)}{\partial t} = \frac{\partial T^{(3)}(\xi,t)}{\partial \xi} \tag{1}$$

Here $T^{(1)}$, $T^{(2)}$, $T^{(3)}$ are the components of the energy-momentum tensor. In particular, $T^{(2)}(\xi,t) = -p(\xi,t)$ where p is the pressure, $T^{(3)}(\xi,t) = v(\xi,t)$, $T^{(1)}(\xi,t)$ has a more complicated form.

We also shall need conjugate variables $\beta(\xi,t)$, $\gamma(\xi,t)$, $\mu(\xi,t)$ where

$$\frac{\partial h(\beta,\gamma,\mu)}{\partial \beta} = \varepsilon, \qquad \frac{\partial h(\beta,\gamma,\mu)}{\partial \gamma} = v, \qquad \frac{\partial h(\beta,\gamma,\mu)}{\partial \mu} = r, \tag{2}$$

Here h is the Gibbs free energy. In the one-dimensional case h is always a strictly convex function of its variables and therefore the usual difficulties related to the Legendre transformation do not appear. Certainly the system of Euler equations can be written in terms of variables ö, q, m but we do not need their exact form. We use only the Duham-Gibbs equality (see [1])

$$\frac{dh(\beta,\gamma,\mu)}{dt} = \varepsilon(\xi,t)\frac{\partial T^{(1)}(\xi,t)}{\partial \xi} + v(\xi,t)\frac{\partial T^{(2)}(\xi,t)}{\partial \xi} + r(\mu,t)\frac{\partial T^{(3)}(\xi,t)}{\partial \xi} \tag{3}$$

The system of Euler Eq. (1) determines the one-parameter group of transformations $\{\varepsilon^t\}$ acting in the space of 3-tuples $[\varepsilon(\xi), v(\xi), r(\xi)]$. Namely $\varepsilon^t\{\varepsilon(\xi), v(\xi), r(\xi)\} = \{\varepsilon(\xi,t), n(\xi,t), r(\xi,t)\}$. We shall not concern ourselves here with various problems related to the existence and uniqueness of solutions of (1). Locally these properties are satisfied and, at this point, this is enough for us. To be more precise we shall assume that initial data and all $\varepsilon^t\{\varepsilon(\xi), v(\xi), r(\xi)\}$, $|t| \le t_o$ are well-defined and belong to a bounded domain of the space $C^2(S^1)$.

The microscopical description of the non-uniform but locally-equilibrium distribution of parameters ε, v, r is well-known (see [2], [3]). Consider the system of N particles of mass 1 on the line having the coordinates and velocities q_i, v_i, $1 \le i \le N$, $q_i \le q_{i+1}$. The interaction is pairwise with the potential U(r). The usual assumption is that it has a hardcore, i.e., $U(r) = \infty$ for $r \le r_o$, and a short range, i.e., $U(r) = 0$ for $r \ge r_1$. Between r_o and r_1 U is twice-differentiable. Let $\beta(\xi)$, $\gamma(\xi)$, $\mu(\xi)$ be three C^2-functions on S^1. Take the Hamiltonian of the system in the form

$$H_{\beta,\mu,\gamma}(\{q_i,v_i\}) = \sum_{i=1}^{N}\left[\beta\left(\frac{i}{N}\right)\varepsilon_i + \gamma\left(\frac{i}{N}\right)v_i + \mu\left(\frac{i}{N}\right)r_i\right]$$

Here

$$r_i = q_{i+1} - q_i, \qquad \varepsilon_i = \frac{1}{2}\left[v_1^2 + U(q_{i+1} - q_i) + U(q_i - q_{i-1})\right]$$

and the periodic boundary conditions are imposed, $q_{N+i} = q_i + N$. Introduce the locally-equilibrating Gibbs distribution $P_{\beta,\gamma,\mu}$ having the density

$$Z^{-1}_{\beta,\gamma,\mu}\exp\left\{-H_{\beta,\gamma,\mu}(\{q_i,v_i\})\right\} \tag{4}$$

where $Z_{\beta,\gamma,\mu}$ is the partition function

$$Z_{\beta,\gamma,\mu} = \int \exp\left\{-H_{\beta,\gamma,\mu}(\{q_i, v_i\})\right\}\prod_{i=1}^{N} dq_i\,dv_i$$

It is not difficult to show that

$$\lim_{N\to\infty}\frac{1}{N}\ \ell n\ \ Z_{\beta,\gamma,\mu}=\int_0^1 h\left[\beta(\xi),\ \mu(\varepsilon),\ \gamma(\varepsilon)\right]\delta\xi$$

Here h is the Gibbs free energy which was mentioned previously. The last formula also shows the usefulness of the Lagrangian variable ξ.

The equations of motion for the whole array of particles have the form

$$\frac{dr_i}{d\tau}=v_{i+1}-v_i\ ,\ \frac{dv_i}{d\tau}=U'(r_i)-U'(r_{i-1})$$

$$\frac{d\varepsilon_i}{d\tau}=U'(r_i)\frac{v_i+v_{i+1}}{2}-U^1(r_{i-1})\frac{v_i+v_{i-1}}{2}$$

Denote by $\varepsilon_i(\tau)$, $v_i(\tau)$, $r_i(\tau)$ the solution of these equations and $\{S^\tau\}$ is the corresponding group of transformations of the phase space. The $U^\tau P_{\beta,\gamma,\mu}$ is the probability distribution in the phase space having the density

$$Z^{-1}_{\beta,\gamma,\mu}\exp\left\{-H_{\beta,\gamma,\mu}\left[S^{-\tau}\{(q_i,v_i)\}\right]\right\} \tag{5}$$

The partition function $Z_{\beta,\gamma,\mu}$ is not changed due to Liouville theorem,

$$H_{\beta,\gamma,\mu}\left[S^{-\tau}\{(q_i,v_i)\}\right]=\sum_{i=1}^{N}\left\{\beta\left(\frac{i}{N}\right)\varepsilon_i(-\tau)+\gamma\left(\frac{i}{N}\right)v_i(-\tau)+\mu\left(\frac{i}{N}\right)r_i(-\tau)\right\}$$

The hydrodynamical time and the microscopical time are related to each other through the formula $tN = \tau$. We can consider the probability distribution (4) as some distribution which can be prepared in advance in a laboratory. The main problem which we intend to discuss here concerns the question in what sense the probability distribution (5) is locally-equilibrating for hydrodynamical times τ. Certainly it does not have the

form of (4) with changed β , γ, μ. But local equilibrium can be defined in a more mild form. To do this take a test function $\phi(x,y,z) \varepsilon C_0^{\infty}(R^3)$ and consider the average

$$I[\{q_i, v_i\}, t] = \frac{1}{N} \sum_{i=1}^{N} \varphi\{\varepsilon_i(tN), v_i(tN), r_i(tN)\}$$

If (5) is, in a sense, locally equilibrating then $I[\{q_i, v_i\}, t]$ should be close to $J(t) = \int_0^1 \varphi\{\varepsilon(\xi,t), v(\xi,t), r(\xi,t)\}\, d\xi$ where $\{\varepsilon(\xi,t), v(\xi,t), r(\xi,t)\} = E^t\{\varepsilon(\xi), v(\xi), r(\xi)\}$. We shall say that (5) is locally-equilibrating in a weak sense if for $\delta > 0$

$$\lim_{N\to\infty} P_{\beta,\gamma,\mu}\left(\left| I\{(q_i, v_i), t\} - J(t) \right| > \delta \right) = 0 \qquad (6)$$

Now our main question can be formulated as follows: Given the probability distribution (4), what is the interval of hydrodynamical time during which we can guarantee (6). There are some partial results for several degenerate models which are discussed in particular in [3]. The importance of our problem increased recently in connection with the famous work of Frisch, Hasslacher and Pomeau [4] where the authors constructed the system of cellular automata modeling the Navier- Stokes equations. However, as far as I know at this time, there were no general results related to the whole problem. In the next section we develop a new approach which might lead to some progress in the case which we consider.

2. THE MAIN INEQUALITY AND ITS COROLLARIES

Take a microscopical time τ_o and for any $\beta(\xi)$, $\gamma(\xi)$, $\mu(\xi)$ put

$$\frac{d\, U^{\tau_o} P_{\beta,\gamma,\mu}}{d\, P_{E^{-\tau_o/N}(\beta,\gamma,\mu)}} = \exp\left[F_{\beta,\gamma,\mu}\{(q_i, v_i)\} \right]$$

The form of $F_{\beta,\gamma,\mu}$ will be written below.

Assume that (β, γ, μ) is an arbitrary 3-tuple of functions on the circle belonging to a bounded domain of $C^2(S^1)$.

The main inequality. For $\tau_o > 0$ one can find $B = B(\tau_o) > 0$ such that for all $A > 0$

$$P_{E^{-\tau_o N}(\beta,\gamma,\mu)}\left[F_{\beta,\gamma,\mu}\{(q_i, v_i)\} > A\right] \le \exp\left(-NA^2 B^{-1}\right)$$

and $B(\tau_o)\, \tau_o^{-2} \to 0$ as $\tau_o \to \infty$.

A weaker form of this inequality appeared in [5]. Now we can formulate our main result.

Theorem. If the main inequality is valid then there exists a hydrodynamical time $t_o = t_o(\tau_o, B)$ such that for all t, $|t| \le t_o$, the local equilibrium (6) holds.

The proof of the theorem is given in the Appendix. Here we shall write down the exact expression for F:

$$\begin{aligned}
F_{\beta,\gamma,\mu}\{(q_i, v_i)\} = \frac{1}{N}\sum_{i=1}^{N} \Bigg[& -\frac{\partial\beta}{\partial\xi}\left(\frac{i}{N}\right) \int_{-\tau_o}^{0} \left\{ T_i^{(1)}(s) - T^{(1)}\left(\beta\left(\frac{i}{N}\right), \gamma\left(\frac{i}{N}\right), \mu\left(\frac{i}{N}\right)\right)\right\} ds \\
& -\frac{\partial\gamma}{\partial\xi}\left(\frac{i}{N}\right) \int_{-\tau_o}^{0} \left\{ T_i^{(2)}(s) - T^{(2)}\left(\beta\left(\frac{i}{N}\right), \gamma\left(\frac{i}{N}\right), \mu\left(\frac{i}{N}\right)\right)\right\} ds \\
& -\frac{\partial\gamma}{\partial\xi}\left(\frac{i}{N}\right) \int_{-\tau_o}^{0} \left\{ T_i^{(3)}(s) - T^{(3)}\left(\beta\left(\frac{i}{N}\right), \gamma\left(\frac{i}{N}\right), \mu\left(\frac{i}{N}\right)\right)\right\} ds \\
& -\tau_o \left[\frac{\partial\beta}{\partial\tau}\left(\frac{i}{N}; 0\right)\left\{\varepsilon_i - \varepsilon\left(\beta\left(\frac{i}{N}; 0\right), \gamma\left(\frac{i}{N}; 0\right), \mu\left(\frac{i}{N}; 0\right)\right)\right\}\right. \\
& +\frac{\partial\gamma}{\partial t}\left(\frac{i}{N}; 0\right)\left\{v_i - v\left(\beta\left(\frac{i}{N}; 0\right), \gamma\left(\frac{i}{N}; 0\right), \mu\left(\frac{i}{N}; 0\right)\right)\right\} \\
& \left. +\frac{\partial\mu}{\partial t}\left(\frac{i}{N}; 0\right)\left\{r_i - r\left(\beta\left(\frac{i}{N}; 0\right), \gamma\left(\frac{i}{N}; 0\right), \mu\left(\frac{i}{N}; 0\right)\right)\right\}\right] \Bigg]
\end{aligned}$$

We denoted $T_i^{(1)}(s) = \frac{v_{i+1}(s)\, U^1\{r_i(s)\} - v_i(s)\, U^1\{r_{i-1}(s)\}}{2}$, $T_i^{(2)}(s) = U^1\{r_i(s)\}$, $T_i^{(3)}(s) = v_i(s)$.

It is worth mentioning that the main inequality takes into account only the dynamics during a fixed interval of the microscopic time. It means that we do not need any information concerning ergodic or mixing properties of the system with the fixed N. This seems to be quite natural because the local equilibrium is a quite common phenomenon which should not be connected with such refined properties. From another side, the estimation which enters the main inequality is of the type of large deviation estimations in probability theory. Sometimes the main contributions to the corresponding probabilities comes from or nontypical configurations or nontypical dynamics involving some collective motions. The form of these collective motions is unclear. It cannot be excluded that they are somehow connected with turbulence. In our opinion, an analysis of the main inequality deserves a very thorough study.

REFERENCES

1. Zubarev, D. N., "Non-Equilibrium Statistical Mechanics", Moscow, Nauka, 1971, p. 416.

2. Spohn, H., "Kinetic Equations for Hamiltonian Systems: Markovian Limits", Rev. Modern Phys. **52**, (3), 1980, p. 569-616.

3. Dynamics Systems — 2. In the Series: Fundamental Directions in Mathematics. Consultant-Editor - Sinai Ya. G., VINITI Press, Moscow, 1985.

4. Frisch, U., Hasslacher, B., Pomeau, Y., "Lattice-Gas Automata for the Navier-Stokes Equation", Phys. Rev. Letts. **56**, (14), 1986, 1505-1508.

5. Sinai, Ya. G., "Dynamics of Locally-Equilibrating Gibbs Distribution and Euler Equations", in Problems of Modern Statistical Physics, Naukova Dumka, Kiev, 1985, p. 287.

APPENDIX. PROOF OF THE MAIN THEOREM

We reproduce here with minor modifications and corrections the proof given in [5]. We start with the following lemma well-known from probability theory.

Lemma. For any $\delta > 0$ there exists $f(\delta) > 0$ such that for all considered β, γ, μ and t

$$P_{E^t(\beta,\gamma,\mu)}\left[\left| I\{(q_i, v_i); 0\} - \int_0^1 \varphi\{\varepsilon(\xi,t), v(\xi,t), r(\xi,t)\}\, d\xi \right| > \delta\right] < \exp\{-N f(\delta)\}$$

Its proof is omitted. But

$$\frac{d\, U^{(k\tau_0)} P_{\beta,\gamma,\mu}}{d\, P_E{}^{-k\tau_0/N(\beta,\gamma,\mu)}} = \exp\left\{U^{k\tau_0} L_k\right\}$$

Then

$$\frac{d\, U^{((k+1)\tau_0)} P_{\beta,\gamma,\mu}}{d\, P_E{}^{-(k+1)\tau_0/N(\beta,\gamma,\mu}} = \frac{d\, U^{\tau_0}\left(U^{k\tau_0} P_{\beta,\gamma,\mu}\right)}{d\, P_E{}^{-(k+1)\tau_0/N(\beta,\gamma,\mu)}}$$

$$= \frac{d\, U^{\tau_0}\left(e^{U^{k\tau_0} L_k} P_E{}^{-k\tau_0/N}{}_{\beta,\gamma,\mu}\right)}{d\, P_E{}^{-(k+1)\tau_0/N(\beta,\gamma,\mu)}}$$

$$= \exp\left\{U^{(k+1)\tau_0} L_k + F_E{}^{-k\tau_0/N(\beta,\gamma,\mu)}\right\},$$

i.e.,

$$U^{(k+1)\tau_0} L_{k+1} = U^{k\tau_0} L_k + F_{E^{-\tau_0 N(\beta,\gamma,\mu)}}$$

Further, put for any $A > 0$

$$C_k = \left\{ (q_i, v_i) \;\middle|\; L_k \geq k\,A,\ P_{\beta,\gamma,\mu}(C_k) = \pi_k \right\}$$

then

$$\pi_{k+1} \leq \pi_k + \int_{\substack{L_k < kA \\ L_{k+1} \geq (k+1)A}} d\,P_{\beta,\gamma,\mu} = \pi_k + \int_{\substack{L_k < kA \\ L_{k+1} \geq (k+1)A}} e^{-H_{\beta,\gamma,\mu}} \prod_{i=1}^{N} dq_i\, dv_i$$

$$= \pi_k + \int_{\substack{U^{(k+1)\tau_0} L_k < kA \\ U^{(k+1)\tau_0} L_{k+1} \geq (k+1)A}} e^{-U^{(k+1)\tau_0} H_{\beta,\gamma,\mu}} \prod_{i=1}^{N} dq_i\, dv_i = \pi_k$$

$$+ \int_{\substack{U^{(k+1)\tau_0} L_k < kA \\ U^{(k+1)\tau_0} L_{k+1} \geq (k+1)A}} e^{U^{(k+1)\tau_0} L_k + F_k}\; d\,P_{E^{-(k+1)\tau_0 N(\beta,\gamma,\mu)}} \leq \pi_k$$

$$+ \exp\{kA\} \int_A^{\infty} \exp\{x\}\, d\,G(x)$$

where G is the probability distribution function of the random variable $F_{E^{-k\tau_0 N(\beta,\gamma,\mu)}}$ found with the help of $P_{E^{-(k+1)\tau_0 N(\beta,\gamma,\mu)}}$. The integration by parts and the main inequality of § 2 give

$$\int_A^{\infty} \exp\{x\}\, dG(x) \leq \int_A^{\infty} \exp\{x\}\, dx \int_x^{\infty} dG(u)$$

$$\leq \int_A^{\infty} \exp\left\{ x - \frac{Nx^2}{B} \right\} dx \leq \exp\left\{ A - \frac{NA^2}{B} \right\}$$

Thus $\pi_{k+1} \le \pi_k + \exp\left\{(k+1)A - \frac{A^2 N}{B}\right\}$. Assuming that t is $Nt\,\tau_0^{-1}$ is an integer we get

$$\pi_{Nt\,\tau_0^{-1}} \le Nt\,\tau_0^{-1} \exp\left\{Nt\,\tau_0^{-1} A - A^2 N B^{-1}\right\}$$

Take any $\delta > 0$ and find $f(\delta) > 0$ in view of the lemma. It is easy to see that $f(\delta) \to 0$ as $\delta \to 0$. Choose firstly large A so that $A^2 B^{-1} \ge f(\delta)$ and then large t_0 so that $t_0 A \tau_0^{-1} \le \frac{1}{2} f(\delta)$. Then

$$P_{\beta,\gamma,\mu}\left\{C_{Nt\,\tau_0^{-1}}\right\} \le \exp\left\{-\frac{1}{3} f(\delta) N\right\}$$

for sufficiently large N and

$$P_{\beta,\gamma,\mu}\left\{\left|\{(q_i, v_i); t\} - J(t)\right| > \delta\right\}$$

$$\le P_{\beta,\gamma,\mu}\left\{\left|\{(q_i, v_i); t\} - J(t)\right| > \delta \cap \overline{C}_{Nt\,\tau_0^{-1}}\right\}$$

$$+ P_{\beta,\gamma,\mu}\{C_{Nt\,\tau_0^{-1}}\} \le \exp\left\{-\frac{1}{3} f(\delta) N\right\}$$

$$+ \int_{\substack{|J(0) - I(0)| > \\ U^{Nt\tau_0^{-1}} L_{Nt\tau^{-1}} < Nt\tau_0^{-1} A}} \exp\left\{- U^{Nt\tau_0^{-1}} H_{\beta,\gamma,\mu}\right\} \Pi\, dq_i\, dv_i \le \exp\left\{\frac{1}{3} f(\delta) N\right\}$$

$$+ \exp\left\{Nt\,\tau_0^{-1} A\right\} P_{E\{\beta,\gamma,\mu\}}\left\{\left|I\{(q_i, v_i); 0\} - J(0)\right| > \delta\right\}$$

$$\le 2 \exp\left\{-\frac{1}{3} f(\delta) N\right\} \to 0, \quad \text{as } N \to \infty .$$

THE STRUCTURE OF SUPERSONIC TURBULENT BOUNDARY LAYERS: WHAT WE KNOW AND WHAT WE THINK WE KNOW

A. J. Smits
Dept. Mechanical & Aerospace Engineering
Princeton University

INTRODUCTION

A considerable amount of turbulence data has been obtained in supersonic boundary layer flows. Virtually all data up to 1980 which could be considered "functionally complete" that is, well-documented, were compiled by Fernholz and Finley (1980), and this listing was recently brought up to date by Fernholz et al. (1988). Measurements of $\langle u' \rangle$, $\langle (\rho u)' \rangle$ and $\langle T' \rangle$ are widely available, but unfortunately measurements of $\langle v' \rangle$ and $-\overline{u'v'}$ are not. Even more unfortunately, few measurements of higher order moments have been made, and spectral data, probability density distributions, and correlations have only been obtained in very few cases. In this respect, the most complete data sets for zero pressure gradient flat plate boundary layers are those by Owen and Horstman (1972), Owen, Horstman and Kussoy (1975), Robinson (1986), Fernando (1988), Spina (1988) and Smits et al. (1988). In the present contribution, we present a review of this work to assess the significance of variable density on the structure of high speed turbulent boundary layers. For the purpose of comparison with the subsonic case we use the results from Alving (1988) because of the wide variety of data obtained in that flow. The flow conditions for all cases are summarized in Table I. Not all quantities were measured by every investigator, and therefore it is not always possible to make a clear distinction between Mach and Reynolds number effects.

Before considering the results, it is useful to summarize the type of data measured by these investigators and how they were obtained. In all four cases, the data were obtained using hot-wire anemometry. In the study of Flow 3 by Owen and Horstman (1972), autocorrelations, spectra and space-time correlations in the streamwise and transverse directions were obtained using the fluctuating component of the hot wire voltage. Since they used a constant-temperature system, operated presumably at a high overheat ratio, the fluctuating voltage is proportional to $(\rho u)'$ if the fluctuations are small (Smits et al. 1983). In their later work, Owen et al. (1975) used constant-current anemomety to obtain the integral scales and microscales, the probability density distributions, the skewness and flatness, and estimates for the turbulence lifetimes for both the fluctuating mass-flux and total temperature . In Flow 2, Robinson (1986) used a constant-temperature anemometer operated at high overheat ratio to obtain $(\rho u)'$, and he measured the flatness profile, the correlations in the direction normal to the wall, and did some preliminary

conditional sampling using the VITA technique. All the work done in Flow 1 was done using constant temperature anemomety, and the primary data were time histories of $(\rho u)'$ and v'. The vertical velocity fluctuations v' can be measured directly in supersonic flow (Fernando et al. 1987) but fluctuations in mass-flux and total temperature cannot be decomposed into density, pressure, temperature and u' velocity fluctuations without additional measurements or assumptions (for a more extensive discussion of this problem see Owen et al. 1975, or Smits et al. 1988). In contrast, the data in subsonic flows are always in terms of u' and v'.

	Subsonic flow	Supersonic flow 1	Supersonic flow 2	Supersonic flow 3
M_∞	0.1	2.9	2.97	6.7
U_{ref}	31 m/s	565 m/s	594 m/s	1110 m/s
C_f	.00283	.00114	.00166	.00080
R_θ	5000	80,000	15000	8500
δ	19.3 mm	28 mm	12 mm	33 mm

Table 1. Experimental conditions for the supersonic boundary layers investigated by Spina (1988) and Fernando (1988) (Flow 1), Robinson (1986) (Flow 2), and Owen et al. (1975) (Flow 3), and the subsonic boundary layer investigated by Alving (1988).

In supersonic Flows 1 and 2, the freestream Mach number is in the range where Morkovin's hypothesis should apply over most of the boundary layer thickness. The Mach number gradient near the wall, however, is very high (for example, in Flow 1 the sonic line is located at approximately $y = 0.005\delta = 0.13mm = 75\ \nu_w/u_\tau$), and it may be expected that the fluctuating Mach number can exceed unity in the region of maximum turbulence production, and Morkovin's hypothesis may break down in the near-wall region.

2. Statistical Evidence

The simplest comparison between the turbulence behavior in subsonic and supersonic boundary layers is to compare the distributions of $\langle u' \rangle$. When normalized by u_τ ($= \sqrt{\tau_w/\rho_w}$), the distributions appear to show a strong Mach number effect (see, for example, Schlichting 1968, p. 659). However, if the results for Mach numbers less than 5 are normalized by a velocity scale derived using the wall stress and the local density ($= \sqrt{\tau_w/\rho}$), as suggested by Morkovin, the Mach number dependence is no longer evident. At a Mach number of 6.7, however, Owen et al. found that this transformation did not seem to collapse the data, indicating that hypersonic flow may display strong compressibility effects. It is also known that the flatness profile in supersonic flows is more constant than in the corresponding subsonic case

(see figure 1). One definition of intermittency is I = (3/Flatness), where Flatness = $\overline{u'^4}/(\overline{u'^2})^2$, and the results imply that the intermittency profile is fuller in supersonic flows. In contrast, the flow visualization of density cross sections by Smith at Princeton (private communication) reveals that the boundary layer has a very similar appearance to that seen in subsonic flows (see figure 2), and it may be possible that the flatness profiles of $(\rho u)'$ do not give an accurate picture of the intermittency. Recent measurements of the intermittency function from the $(\rho u)'$ signal by Selig (1988) seem to support this idea.

What is even more interesting is that the shear correlation coefficient R_{uv} ($= -\overline{u'v'}/\langle u'\rangle\langle v'\rangle$) is different (figure 3). The subsonic data reveal a higher correlation across the boundary layer with a nearly constant value of 0.45 for $0 < y/\delta < 0.8$, while the supersonic correlation decreases steadily as y/δ increases. Differences were also observed in the distribution of the structure parameter $a_1 = -\overline{u'v'}/q^2$ (not shown). In these same studies, however, Fernando and Alving found similar anisotropy ratios, suggesting that the difference in character of the R_{uv} distribution is caused by a change in the shear stress, that is, the organized motions, not by a change in u' or v' alone. These changes are clearly evident in the joint probability density distributions of u' (or $(\rho u)'$) and v', shown in figure 4. The contributions to $-\overline{u'v'}$ are organized differently; as a basis for comparison, it may be seen that the major axes of these approximately elliptical distributions are aligned more closely with the horizontal axis when the flow is supersonic.

A wide variety of two-point space-time correlation data is available, including mass-flux $(\rho u)'$ (or velocity u') correlations in the streamwise, normal, and spanwise directions (x,y, and z, respectively). To begin the discussion of the results, consider the time records of $(\rho u)'$ obtained in the zero pressure gradient boundary layer from three hot wires (figure 5). The signals exhibit a very similar character, indicating the passage of organized motions of a scale larger than the separation distance between the top and bottom wires. The space-time correlations for one supersonic and one subsonic flow are shown in figure 6. For both cases, the peak values of the correlations are quite high, reaching a maximum of 0.65 near the middle of the boundary layer. The correlation frictions for the supersonic boundary layer are considerably narrower than for subsonic layer. Furthermore, the dimensionless delay time corresponding to the peak of the space-time correlation, τ_{max}, decreases from 0.4 (= 20 $\pm$ 0.5μs) at the floor to nearly zero at the edge of the boundary layer.

The high peak level of the correlation and the non-zero value of the time delay imply that both wires are detecting the same "disturbance", and that one wire is detecting it before the other. Since the time shift was applied to the upper wire,

the peak at negative time delay means that the upper wire detects the disturbance first, that is, the disturbance leans downstream. Accordingly, an angle θ can be defined for this "front" by using the value of τ_{max} along with the wire separation distance, ξ, and the local convection velocity. That is,

$$\theta = \tan^{-1}\left[\frac{\xi}{U_c \tau_{max}}\right]$$

The angle θ may be called an "average structure angle," in that it is associated with an average large-scale motion. Figures 10 and 11 show that the structure angle depends on the distance between the two measurement points, and that the distribution for supersonic flow is different from that in subsonic flow. In the supersonic case for small values of ξ (ξ/δ = 0.09 ,say), the structure angle is approximately constant at a value between 45° and 50° for $0.2 < y/\delta < 0.8$. For $\xi/\delta \geq 0.2$, the structure angle becomes insensitive to variation in the separation distance, and it varies from about 40° at y/δ = 0.2 to about 60° at y/δ = 0.8. In the subsonic case, however, small values of ξ give larger values of θ, and large values of ξ gives smaller values of θ than those observed in the supersonic case. For example, Alving found that for ξ/δ = 0.1, the structure angle was approximately at a value of 60° for $0.2 < y/\delta < 0.8$, whereas for $\xi/\delta \geq 0.2$, θ varied from about 20-30° to about 50° over the same interval in y. Note that the uncertainty in the convection velocity will not affect these results significantly: when θ = 45°, 0% error in U_c leads to an error in θ of only 2-3°. These results help to explain the differences seen in the correlation functions (figure 6). Since the average large-scale structure is more upright in a supersonic boundary layer, the space-time correlation is apt to fall off at shorter time delays since the extent of the structures in the mean flow direction will be smaller.

Using the same upstream flow conditions used by Spina and Smits for the zero pressure gradient layer discussed above, Donovan and Smits (1987) investigated the mean structure angle distribution following a short region of concave surface curvature using two different flow models: one which turns the flow through 8° with a radius of curvature of 1270 mm (δ/R = .022), and the other turns the flow 16° with δ/R = .08. Fernando and Smits (1987) made similar measurements on a flat plate following a short region of adverse pressure gradient. In that case, the pressure gradient was generated by a contoured plate, designed so that the pressure distribution matched that of the 8° model using by Donovan and Smits. The general shape of the distribution remained the same as in the zero pressure gradient case. However, there appeared to be a small increase in the structure angle after each of the three perturbations. Furthermore, the structure angle after the stronger curvature was slightly higher than after the weaker curvature. Donovan and Smits suggested that the perturbation rate was too rapid in the stronger curvature model

to allow readjustment of the large-scale motions, and thus the angle of inclination is affected. It appears that the same preliminary conclusion can be drawn for all three of the flow perturbations, since they all exhibit the same trend.

While the present study traverses two "detection probes" through the boundary layer at a fixed separation distance (small compared to δ), most other measurements of this kind have used one detection probe fixed at the wall (a hot wire, a shear stress gauge, or some similar device) and another probe which was traversed through the boundary layer, thereby varying the separation distance. The fixed separation method used here results in a typical mean structure angle of 45^{o} in supersonic flow and about 30^{o} in subsonic flow. While the variable separation method seems to give a lower characteristic value; in supersonic flow Robinson (1986) found 30^{o} and in incompressible flows Brown and Thomas (1977) found 18^{o}, whereas Rajagopalan and Antonia (1979) found 12.5^{o}, and Robinson (1985) found 16^{o}. The advantage of the present method is that the slope of the structure is determined locally, instead of being inferred from a large-scale measurement.

A superposition of peak time delays on the "mean structure shape" was used to produce iso-correlation contours for the supersonic case using $\xi = 0.09\delta$ and 0.30δ (figure 9). The "mean structure shape", the solid curve drawn through the center of the contours, was constructed from an extrapolation of the mean structure angle from one measurement location to the next (with the first location supplying the appropriate inclination from the origin). The peak of the cross-correlation at each mean wire position was then shifted so that it was coincident with the curve delineating the mean structure shape. The contours give a good indication of the extent of the field around the identified structure. The same mean structural characteristics are evident in all of the contours, as well as those determined by Robinson. Similar contour plots were derived for the subsonic boundary layer studied by Alving and they are given in figure 10. The differences in mean structure angle that exist between supersonic and subsonic flows (figures 7 and 8) are readily apparent in figures 9 and 10, as are the much greater streamwise extent of the large-scale structures in the subsonic boundary layer.

In addition to the measurements made at two points separated in the direction normal to the wall, measurements were taken at a variety of spanwise spacings in both the supersonic and subsonic cases. The space-time correlation for a spanwise spacing of 0.09δ is shown in figure 11 for several locations across the supersonic boundary layer. The corresponding results for the subsonic boundary layer are given in figure 12. The peak values are somewhat lower than in the supersonic case, although the correlations are much broader. In both cases, however, the character and strength of the correlations is similar to those found for the vertical separ-

ations, except that the peak occurs at zero time delay in this case. Since the correlation between wires spaced 0.09δ apart is similar for both the spanwise and vertical alignments, a similarity of the structures is suggested in the y- and z-directions for small distances in both cases. As determined from the peak values of the correlation functions, it appears that the spanwise scales are slightly smaller than the vertical scales.

A comparison of the length scales based entirely upon the peak values of the correlations is not conclusive, however. Therefore, the transverse scales were further explored with the aid of iso-correlation contours which give the behavior of the entire correlation curve, not just the peak value. The space-time correlations were reflected about $\xi = 0$ for each y-position (this is valid since the spanwise correlations are symmetric), and iso-correlation contours were drawn from the resulting surfaces (figures 13 and 14). As with the vertical correlations, the time delay was normalized by outer-layer variables, and by Taylor's hypothesis can be interpreted as a streamwise distance. The plots then give (pseudo) x-z cross-sections of the boundary layer at three different y-locations. What is very striking is that the spanwise extent of the large-scale motions in subsonic and supersonic flows are almost identical (and in good agreement with the results of Kovasznay et al. 1970), whereas the streamwise scale differs by a factor of about two. In addition, the spanwise scale of the detected structures increases away from the wall. Since the overall size of the structures increases with y/δ this behavior is not surprising. The spanwise scale of the detected organized structures should therefore increase as we move farther from the wall.

4. Summary and Conclusions

All the measurements presented here indicate that despite broad similarities, the turbulence structure of supersonic and subsonic boundary layers display significant differences. Some of these differences, such as the change in the flatness profile, have been observed in previous studies, and are now relatively well known. Structure parameters have not been widely studied in supersonic flows, however, and the new measurements presented here indicate that strong differences exist. For example, the length scales derived from space-time correlations indicate that the spanwise scales are almost identical but that the streamwise scales in the subsonic flow are about half the size of those in supersonic flow. The large-scale structures in the subsonic boundary layer also appear to move slightly slower, and lean more towards the wall, than those observed in supersonic flows, and their shear stress content is distributed differently among the four quadrants. All these observations suggest that there may be fundamental differences between the structure of subsonic and supersonic boundary layers. It is possible that the density gradients in a supersonic shear layer affect the large scale structure, and

that there exists a damping effect of Mach number on the turbulent motions which may be important even for turbulence away from the wall. In some sense it would not be surprising to find differences between compressible and incompressible boundary layers since the vorticity transport equation describes the transport of vorticity per unit mass, rather than the absolute vorticity. Density gradients must therefore affect the vorticity dynamics to some extent, and the extent of this influence will vary with Mach number.

Acknowledgement

The financial support of AFOSR under Grant 88-0120 is gratefully acknowledged.

References

Alving, A. E. 1988, Ph.D. Thesis, Princeton Univ., Princeton, NJ.

Brown, G. L. and Thomas, A. S. W., 1977, Physics of Fluids, Vol. 20(10), p. 243.

Donovan, J. F. and Smits, A. J. 1987, AIAA Paper 87-1285.

Fernando, E. M. and Smits, A. J. 1987, AIAA Paper 87-1286.

Fernando, E. M. 1988 , Ph.D. Thesis, Princeton Univ., Princeton, NJ.

Fernando, E. M., Donovan, J. F. and Smits, A. J. 1987, Proc. ASME Symp. on Thermal Anenometry, Cincinnatti, OH.

Fernholz, H. H. and Finley, P. J. 1980, AGARDograph No. 253.

Fernholz, H. H., Smits, A. J., Dussauge, J. P. and Finley, P. J. 1988, AGARDograph No. 315.

Kovasznay, L. S. G., Kibens, V. and Blackwelder, R. F. 1970, J. Fluid Mech. 41, 283.

Morkovin, M. V. 1962, Int. Symp. on the Mechanics of Turbulence 367. C.N.R.S., Paris.

Owen, F. K. and Horstman, C. C. 1972 , J. Fluid Mech. 53: 611-636.

Owen, F. K., Horstman, C.C. and Kussoy, M. I. 1975, J. Fluid Mech. 70, 393.

Rajagopalan, S. and Antonia, R. A. 1979, Physics of Fluids, Vol. 22(4), p. 614.

Robinson, S. K. 1985, Chem. Eng. Communications, Vol. 43, p. 347.

Robinson, S. K. 1986, AIAA Paper 86-1130.

Schlichting, H., 1968, "Boundary Layer Theory", McGraw-Hill, 6th Edition.

Selig, M. S., 1988, M. Sc. Thesis, Princeton Univ., Princeton, N.J.

Smith, M. W. and Smits, A. J. 1988, AIAA Paper 88-0500.

Smits, A. J., Muck, K. C. and Hayakawa, K. 1983, Experiments in Fluids 1, 83.

Smits, A. J., Alving, A. E., Smith, R. W., Spina, E. F., Fernando, E. M., and Donovan, J. F. 1988, 11th Symp. on Turbulence, Univ. Missouri-Rolla, Missouri.

Spina, E. F. 1988, Ph. D. Thesis, Princeton Univ., Princeton, NJ.

Spina, E. F. and Smits, A. J., Journal of Fluid Mechanics, Vol. 182.

Tran, T. T. 1987, Ph.D. Thesis, Princeton Univ., Princeton, NJ.

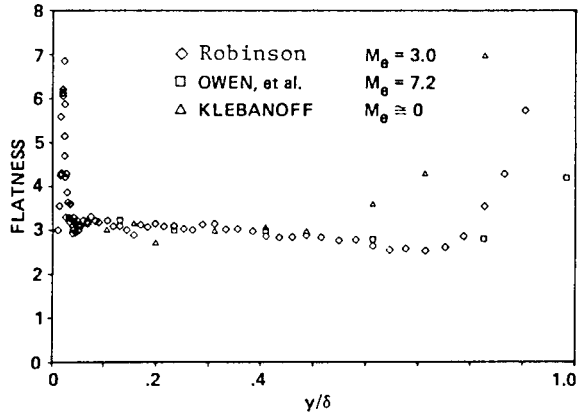

Fig. 1. Comparison of the flatness profiles for different Mach numbers (from Robinson 1986).

Fig. 2 Cross-section of density field in turbulent boundary layer with R_θ = 15,000 and free stream Mach number of 3. Visualization is by M. W. Smith [private communication] using UV Rayleigh scattering from an Ar-Fl laser sheet (see Miles et al. 1988 in Proceedings of this Conference). Flow is from right to left. Exposure time is 10 nanosec.

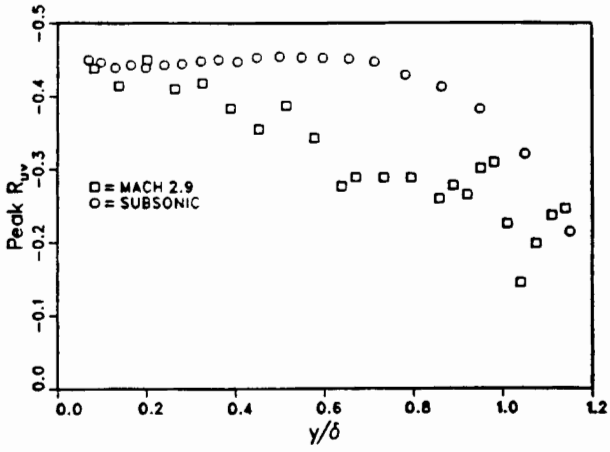

Fig. 3 Comparison of the shear correlation coefficient ($R_{uv} = \overline{u'v'}/\langle u'\rangle\langle v'\rangle$) in supersonic (Fernando 1988) and subsonic (Alving 1988) turbulent boundary layers.

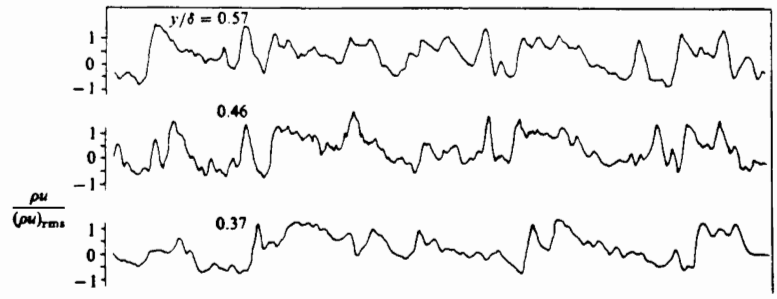

Fig. 5. Three simultaneously measured, instantaneous mass-flux signals (Flow 1, Spina and Smits 1987).

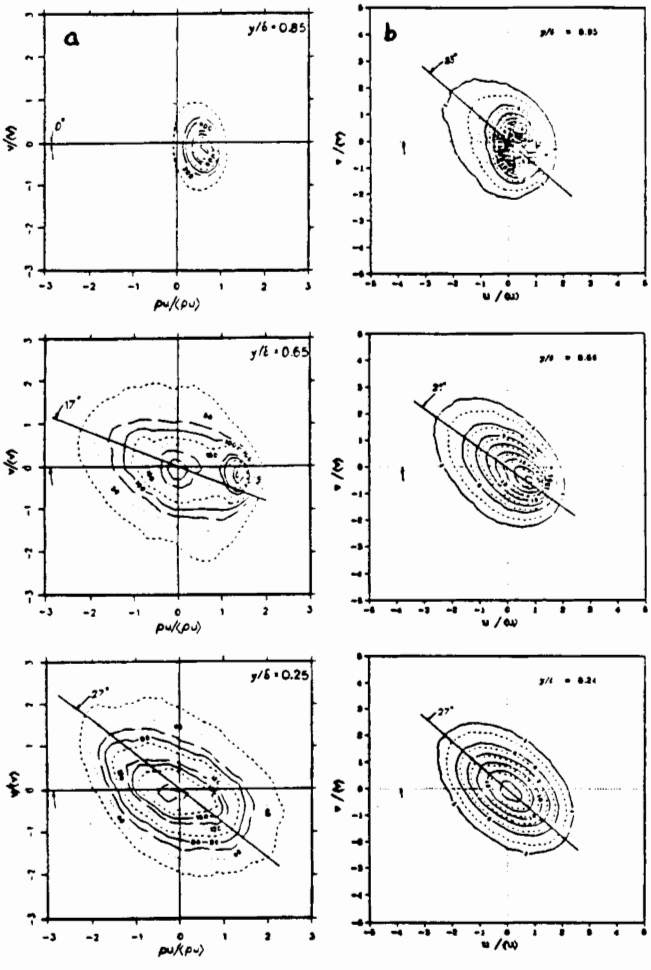

Fig. 4. Probability density function for (a) $\overline{(\rho u)'v'}$ from Fernando (1988), and (b) $\overline{u'v'}$ from Alving (1988).

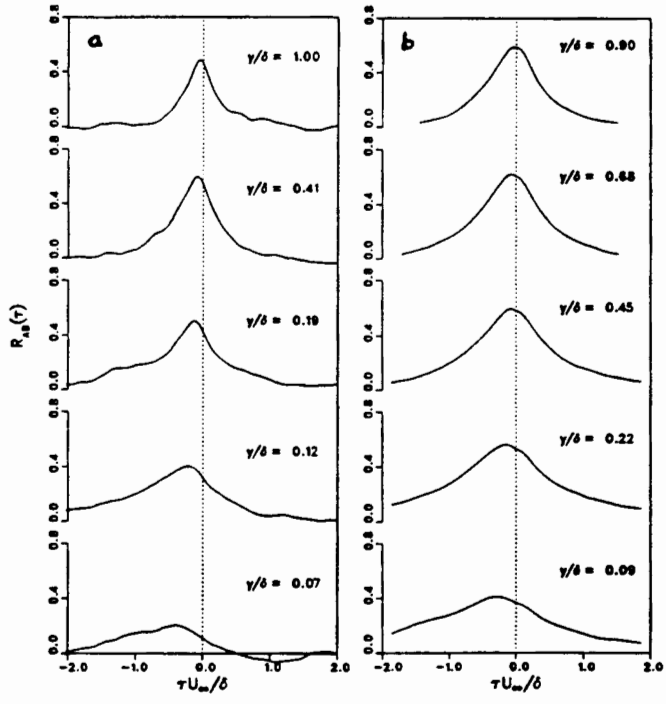

Fig. 6(a) Cross-correlation measurements in the supersonic boundary layer, $\xi/\delta_{99} = 0.09$. From Spina (1988).

Fig. 6(b) Cross-correlation at several positions in the subsonic boundary layer, $\xi/\delta_{99} = 0.10$. From Alving (1988).

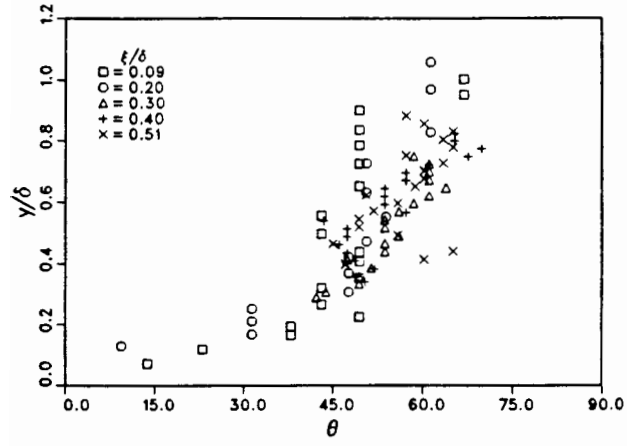

Fig. 7. Large-scale structure angle in the supersonic boundary layer for different wire separation distances (from Spina 1988).

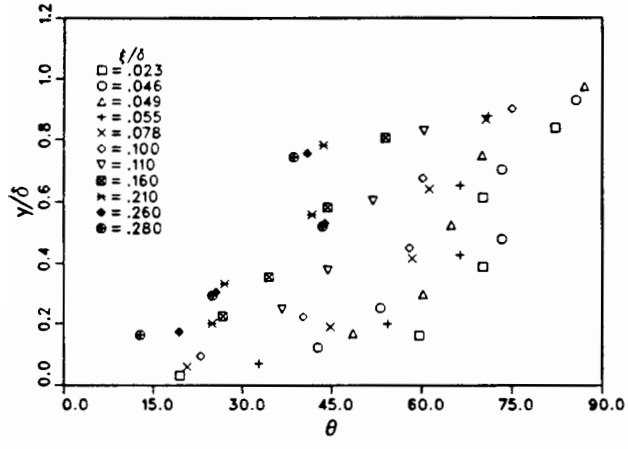

Fig. 8. Large-scale structure angle in the subsonic boundary layer for different wire separation distances (from Alving 1988).

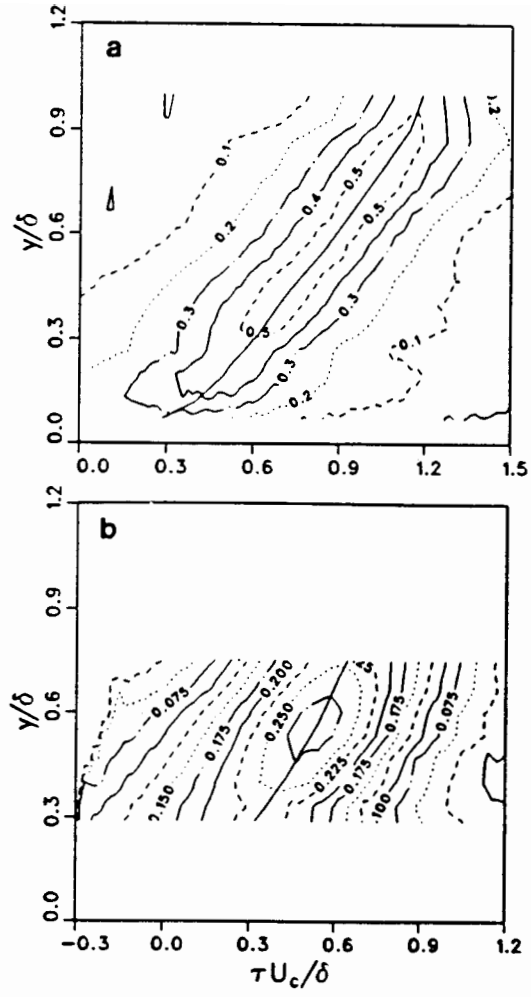

Fig. 9 Equi-value space-time correlation contours from vertically separated mass-flux signals in a supersonic boundary layer: a) $\xi = 0.09\delta$, b) $\xi = 0.30\delta$ (from Spina 1988).

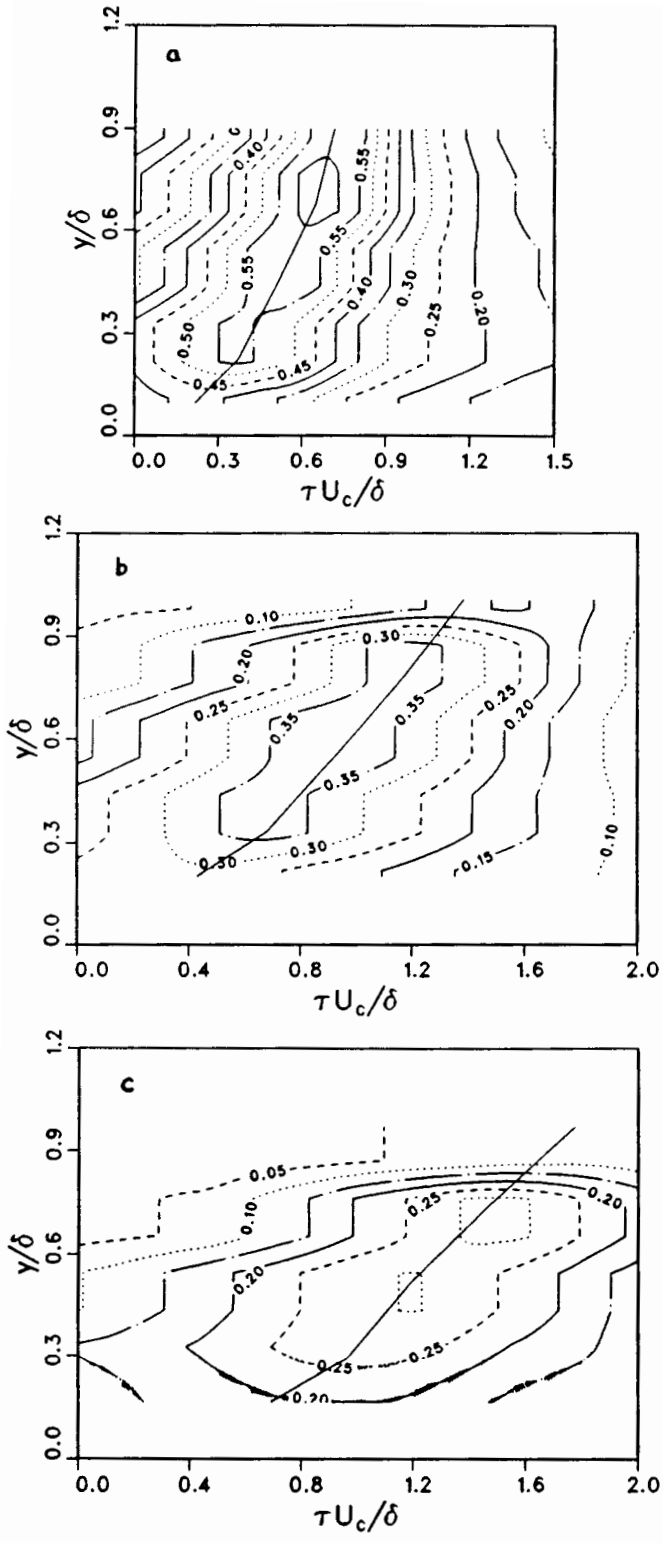

Fig. 10 Equi-value space-time correlation contours from vertically separated velocity signals in the subsonic boundary layer studied by Alving (a) ξ = 0.10, (b) ξ = 0.21, (c) ξ = 0.29.

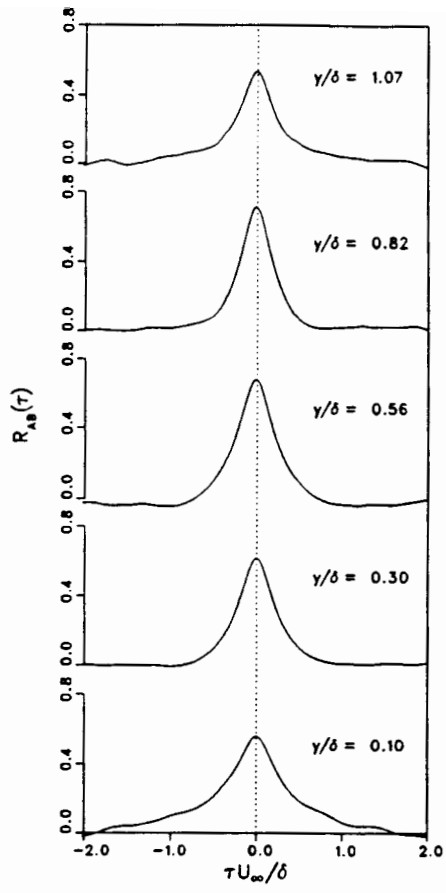

Fig. 11. Space-time correlation between spanwise separated mass-flux signals for several locations in a supersonic boundary layer; ξ = 0.09δ (Spina 1988).

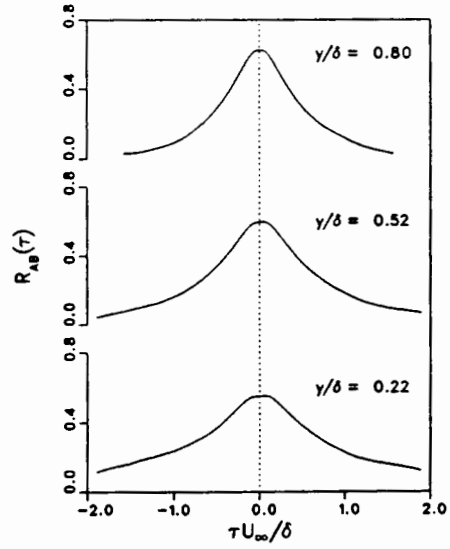

Fig. 12. Space-time correlation between spanwise separated velocity signals for several locations in the subsonic boundary layer studied by Alving; ξ = 0.09δ.

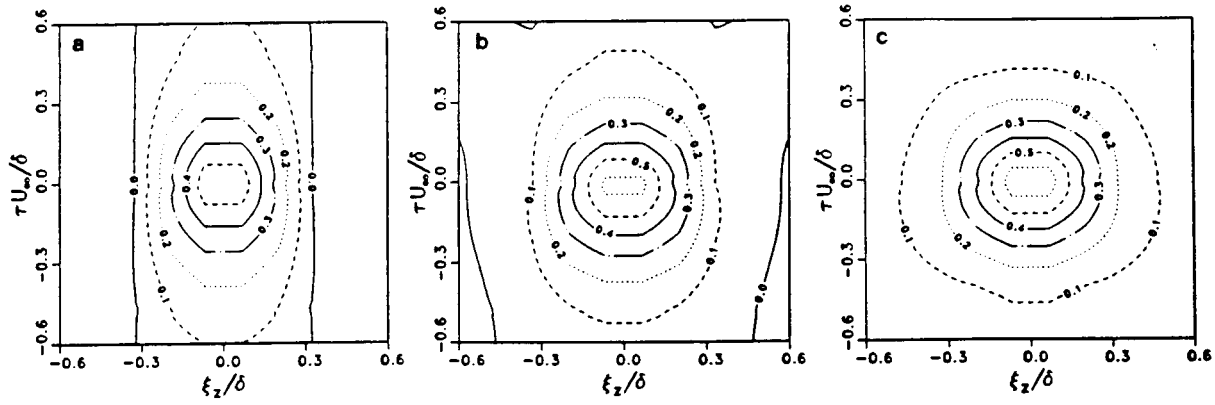

Fig. 13 Equi-value space-time correlation contours from spanwise separated mass-flux signals in the supersonic boundary layer a) y/δ = 0.20, b) y/δ = 0.51, c) y/δ = 0.82 (Spina 1988).

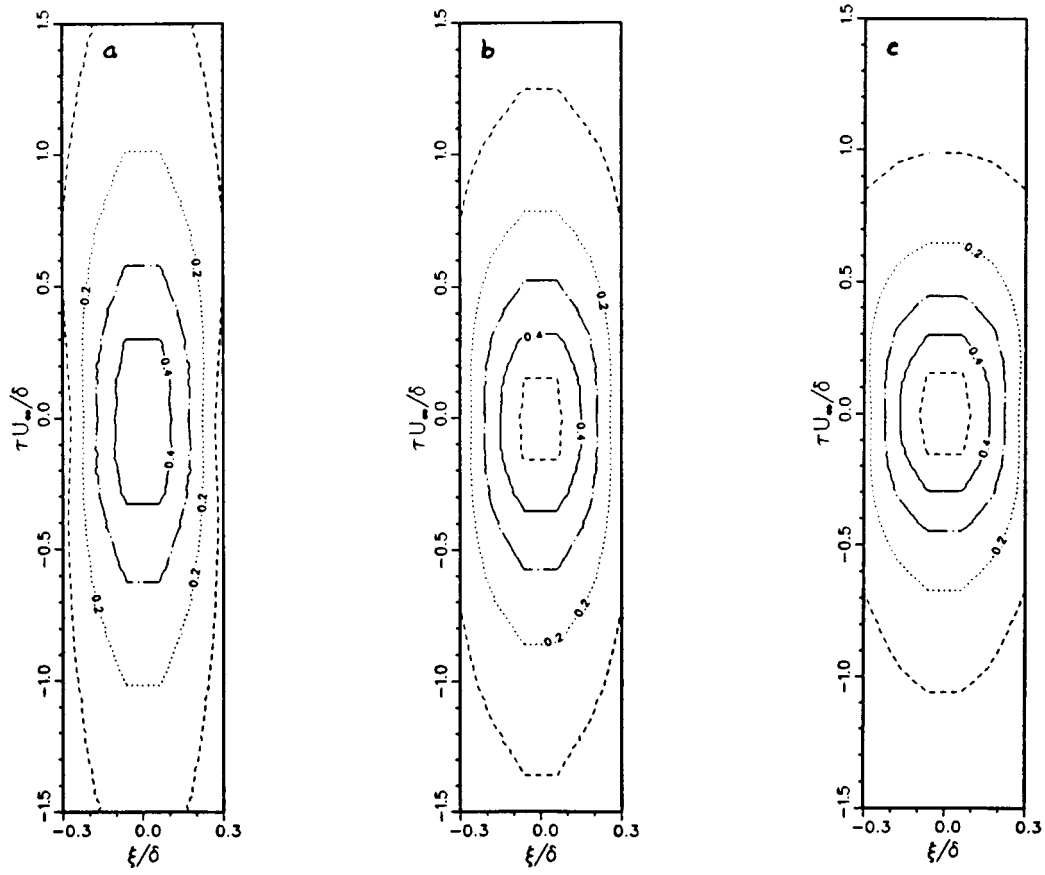

Fig. 14 Equi-value space-time correlation contours from spanwise separated velocity signals in the subsonic boundary layer studied by Alving: a) y/δ = 0.22, b) y/δ = 0.52, c) y/δ = 0.80.

Navier-Stokes Simulation of Supersonic Free Shear Layer Flows

W. Tang, L.N. Sankar and N.M. Komerath
School of Aerospace Engineering
Georgia Institute of Technology, Atlanta, GA 30332

ABSTRACT

The behavior of supersonic free shear layers has been analyzed through numerical solution of the 2-D compressible Navier-Stokes equations. A modified McCormack scheme that is fourth order accurate in space and second order accurate in time was used. It was found that small amplitude normal velocity disturbances introduced into the flow field grew as they were convected downstream and eventually led to organized vortical structures. The growth rate of these disturbances was found to depend on the convective Mach number. It was also found that streamwise and spanwise velocity disturbances introduced into the shear layer did not grow as rapidly as the normal velocity disturbances did.

INTRODUCTION

During the past several years, within the aerospace community there has been an increased interest in a class of propulsion systems called SCRAMJET engines. In these systems, the high speed supersonic air stream captured by the inlet is slowed down through a series of shock waves to low supersonic speeds before entering the combustion chamber. For efficient and reliable performance, and to keep the overall length and weight of the system small, it is imperative that this high speed air stream mixes well with fuel and reacts rapidly. Because normal injection of the fuel stream into the air stream produces good mixing at the expense of significant total pressure loss, researchers have begun to consider configurations where the mixing of parallel or oblique streams of fuel and air will occur.

Unfortunately, the shear layer which forms at the juncture of the supersonic air and fuel streams tends to grow at a much slower rate than its subsonic counterpart. Spark Schlieren photographs taken by Papamoschou [Ref. 1, 2] show the growth rate of supersonic shear layers to be less than 1/3 that of an incompressible shear layer, for a wide range of combinations of fuel-air ratio, specific heats, Mach numbers, temperatures and densities. Similar experimental results were also observed by Chinzei et al. [Ref. 3]. Therefore there is some interest in the use of passive and active control techniques which will promote mixing.

The passive and active control techniques are based upon the following principle. If vorticity is introduced into the shear layer, it will interact with the shear layer, grow as it is convected downstream, increase the turbulence level within the shear layer, and lead to an overall improvement in mixing. Guirguis [Ref. 4] and Drummond et al. [Ref. 5] considered the effect of a bluff body placed in the middle of the shear layer. Kumar et al. [Ref. 6] considered the effects of vorticity produced by a pulsating shock wave on the growth characteristics of shear layers.

In the present work, we investigate active control techniques for the promotion of mixing between supersonic fuel and air streams. Sinusoidally varying velocity disturbances are introduced at the initial, laminar mixing region of the shear layer. These disturbances grow with time as they are convected downstream and eventually lead to well organized vortical structures. These vortical structures are responsible for increase in the mixing between the fuel and air streams, in a manner similar to that in subsonic shear layers.

Streamwise, normal and spanwise disturbances are considered as suitable candidates for promoting mixing in this work. The 2-D and quasi 3-D compressible Navier-Stokes equations in a strong conservation form are numerically solved, using a modified MacCormack scheme that is second order accurate in time, and fourth order accurate in space. This scheme is suitable for studying phenomena such as propagation of acoustic waves, boundary layer instability, and shear layer instability and has been previously used by several authors [Ref. 7-9]. It is our experience that higher order schemes such as these are more suitable for the present application than conventional second order schemes based on an ADI formulation [Ref. 10].

NUMERICAL FORMULATION

The behavior of 2-D supersonic free shear layers, and that of 3-D supersonic free shear layers subject to the infinite sweep assumption, are both governed by a system of partial differential equations of the following form:

$$\mathbf{q}_t + \mathbf{F}_x + \mathbf{G}_y = \mathbf{R}_x + \mathbf{S}_y$$

Here **F** and **G** are the inviscid flux terms and account for the transport of mass moment and energy, and for the influence of pressure. The terms **R** and **S** are the viscous stress terms. The above set of equations are parabolic with respect to time, and may be solved using a variety of stable time marching schemes. For 2-D flows there are four equations. In the case of 3-D flows subject to infinite-sweep assumption, there are five equations, the additional equation corresponding to the conservation of spanwise momentum.

In this work the above equation was solved using a splitting approach. That is, the solution was advanced from one time level 'n' to the next 'n+2' through the following sequence of operations:

$$q^{n+2} = (L_x \, L_y \, L_{xv} \, L_{yv} \, L_{yv} \, L_{xv} \, L_y \, L_x) \, q^n$$

where, for example, the **Lx** operator involves solution of the following 1-D equation:

$$q_t + F_x = 0$$

This 1-D equation was solved through the following predictor-corrector sequence, recommended by Bayliss et al. [Ref. 7]:

Predictor Step:

$$q_{i,j}^{*} = q_{i,j}^{n} - \frac{\Delta t}{6 \Delta x} \left[7 F_{i,j} - 8 F_{i-1,j} + F_{i-2,j} \right]^n$$

Corrector Step:

$$q_{i,j}^{n+1} = \frac{1}{2} \left(q_{i,j}^{n} + q_{i,j}^{*} \right) + \frac{\Delta t}{12 \Delta x} \left[7 F_{i,j} - 8 F_{i+1,j} + F_{i+2,j} \right]^*$$

When the above equations are applied at nodes close to the left and right side boundary, a fourth order accurate extrapolation procedure was used to extrapolate the flux vectors **F** and $\mathbf{F}^*$ needed at nodes outside the computational domain.

The **Ly** operator requires solution of the equation

$$q_t + G_y = 0$$

using a similar approach.

The operators **Lxv** and **Lyv** correspond to numerical solution of 1-D equations such as

$$q_t - R_x = 0$$

The above equation was solved through the following two-step sequence:

$$q_{i,j}^{*} = q_{i,j}^{n} + \frac{\Delta t}{\Delta x}\left[R_{i+\frac{1}{2},j} - R_{i-\frac{1}{2},j} \right]^{n}$$

$$q_{i,j}^{n+1} = \frac{1}{2}\left(q_{i,j}^{n} + q_{i,j}^{*}\right) + \frac{\Delta t}{2\Delta x}\left[R_{i+\frac{1}{2},j} - R_{i-\frac{1}{2},j} \right]^{*}$$

The viscous terms are thus updated only to second order accuracy in space. It may be shown that the above scheme has very little artificial dissipation inherent in it, and is fourth order accurate in space, as far as the inviscid part is concerned.

BOUNDARY CONDITIONS

The computational domain is shown in Figure 1, along with some of the relevant flow properties. For the numerical simulations performed, the boundary conditions are as follows. At the upstream boundary, the flow is supersonic for both the air and fuel stream. Thus, all the flow properties may be prescribed at this boundary, and may include any velocity and pressure disturbances externally imposed on the shear layer. At the downstream boundary, for the small amplitude velocity disturbances encountered in this work, the flow remains supersonic, and may be extrapolated from the interior. Alternatively, the governing equations themselves may be applied if the streamwise diffusion terms **Rx** are suppressed at the downstream nodes.

At the lateral boundaries, it was assumed that the flow is confined by smooth, flat walls. In order to avoid resolving the boundary layers that grow on these plates, and to avoid any influence of these boundary layers over the shear layer, slip boundary conditions are used at these side walls. These walls are considered adiabatic, and the normal derivatives of density and pressure are also set to zero.

In the present work, all the calculations have been performed for cold flows. Furthermore, it was assumed that the species above and below the shear layer have the same ratio of specific heats, and moleculer weight.

RESULTS AND DISCUSSION

A 221x61 uniform grid, with grid spacing equal to 0.01 millimeter in both directions was used. The Reynolds number of the flow (using the speed of sound of the upper stream as the reference velocity) was 1000 per millimeter. The calculations were carried out, starting with step velocity, density and temperature profiles everywhere in the computational domain, and marching in time until an asymptotic steady state shear layer evolved. Next, streamwise, normal, or spanwise velocity disturbances varying sinusoidally with time were

imposed at the upstream boundary. Calculations were carried out for several cycles of imposed oscillations to ensure that these disturbances introduced at the upstream boundary had enough time to travel through the length of the computational domain and leave through the downstream boundary. Four typical cases calculated with normal velocity disturbances are shown in Table 1.

Because the supersonic shear flow problem involves at least 10 flow parameters (5 flow properties on each side of the shear layer), it is desirable that these parameters be combined to give one or two nondimensional parameters of importance. Papamoschou [Ref. 1] has used the convective Mach number as the single parameter that ties all his experimental observations together. This parameter is simply the Mach number of dominant vortical structures within the shear layer with respect to, say, the upper stream. If the upper and lower stream both have the same ratio of specific heat then the velocity of convected disturbances will be given by:

$$U_c = \frac{a_1 U_2 + a_2 U_1}{a_1 + a_2}$$

and the convective Mach number is

$$M_c = \frac{U_1 - U_c}{a_1} .$$

Note that the subscript 1 and 2 correspond to conditions on either side of the shear layer. In Table 1, the convective Mach numbers are tabulated according to Papamoschou's formula, and also based on our own numerical simulations. To compute the convective Mach number from our numerical simulation, the vorticity contours were plotted at adjacent time levels and the distance travelled by vortical disturbances during that interval were computed, in a manner shown in Figure 2. It was found that the convective Mach number from our simulation was always equal to or lower than that from Papamoschou's formula. Thus, the present calculations show the convected vortices to travel at speeds closer to the faster stream.

In Figures 3 through 6, the calculated vorticity contours are shown for the mean flow, as well as for the cases with imposed normal velocity disturbances. The inflow Mach number combinations are shown in Table 1. And the amplitudes of disturbance velocity were 2% of the corresponding streamwise component. The following conclusions may be drawn from an examination of these contours:

(a) Small amplitude normal disturbances introduced upstream grow rapidly, and eventually lead to well organized vortical structures.

(b) As the convective Mach number computed according to Papamoschou's formula increases, the growth rate of the shear layer decreases. It should be noted that this observation is in agreement with Papamoschou's experimental observations, and with linear stability theory.

(c) A comparison of vorticity contours of the steady shear layer (without disturbances) and excited shear layer indicates that the small amplitude normal velocity disturbances introduced lead to a pronounced increase in the shear layer growth rate.

In Figure 7 and 8, the vorticity contours are shown for shear layers with imposed streamwise or spanwise velocity disturbance, both with the same amplitude as those in the normal direction. The inflow boundary conditions were the same as in case-1. It is seen that these disturbances are not as effective in increasing the growth rate of the shear layer as exciting the normal velocity component by the same amount.

CONCLUDING REMARKS

A technique for enhancing the growth rate, and hence the mixing characteristics of supersonic shear layers has been described. A numerical procedure was used to study the spatial and temporal growth of sinusoidal disturbances introduced into the shear layer. It was found that a near linear growth with respect to x in the amplitude of these disturbances results. Highly organized vortical structures could be found in the shear layer, which are expected to improve mixing between the air and fuel streams.

ACKNOWLEDGEMENTS

This work was supported by the Office of Naval Research under contract No. N00014-87-K-0132. Dr. S.G. Lekoudis was the Technical Monitor. Computer time was provided by the University of Pittsburgh Supercomputing Center.

REFERENCES

1. Papamoschou, D., "Experimental Investigation of Heterogeneous Compressible Shear Layers," Ph. D. Dissertation, California Institute of Technology, 1986.

2. Papamoschou, D. and Roshko, A., "Observations of Supersonic Free Shear Layers,", AIAA Paper 86-0162, January 1986.

3. Chinzei, N., Masuya, G., Komuro, T., Murakami, A. and Kudou, K., "Spreading of Two-Dimensional Supersonic Mixing Layers," Physics of Fluids, Vol. 29, No. 5, pp 1345-1347, May 1986.

4. Guirguis, R.H., "Mixing Enhancement in Supersonic Shear Layers: III. Effect of Convective Mach Number," AIAA Paper 88-0701, January 1988.

5. Drummond, J.P. and Mukunda, H.S., "A Numerical Study of Mixing Enhancement in Supersonic Reacting Flow Fields," AIAA Paper 88-3260, July 1988.

6. Kumar, A., Bushnell, D.M. and Hussaini, M.Y., "A Mixing Augmentation Technique for Hypervelocity Scramjets," AIAA Paper 87-1882, July 1987.

7. Bayliss, A., Maestrello, L, Parikh, P. and Turkel, E., "Numerical Simulation of Boundary Layer Excitation by Surface Heating and Cooling," AIAA Journal, Vol. 24, No. 7, July 1986.

8. Bayliss, A. and Maestrello, L., "Simulation of Instabilities and Sound Radiation in a Jet," AIAA Journal, Vol.9, No. 7, July 1983.

9. Hariharan, S. and Lester, H., "A Finite Difference Solution for the Propagation of Sound in Near Sonic Flows," NASA TM-84663, July 1983.

10. Sankar, L.N., Tang, W. and Komerath, N.M., "Numerical Simulation of Supersonic Free Shear Layers," International Conference on Computational Engineering Science, April 1988.

case	M_1	M_2	U_1	U_2	M_c Papamoschou's formula	M_{vortex} Present results
1	4.0	2.3	4.00	3.51	0.20	0.2
2	4.0	2.0	4.00	3.05	0.38	0.2
3	4.0	1.3	4.00	1.98	0.80	0.2
4	5.0	1.3	5.00	1.98	1.20	0.6

Table 1. Cases Presented

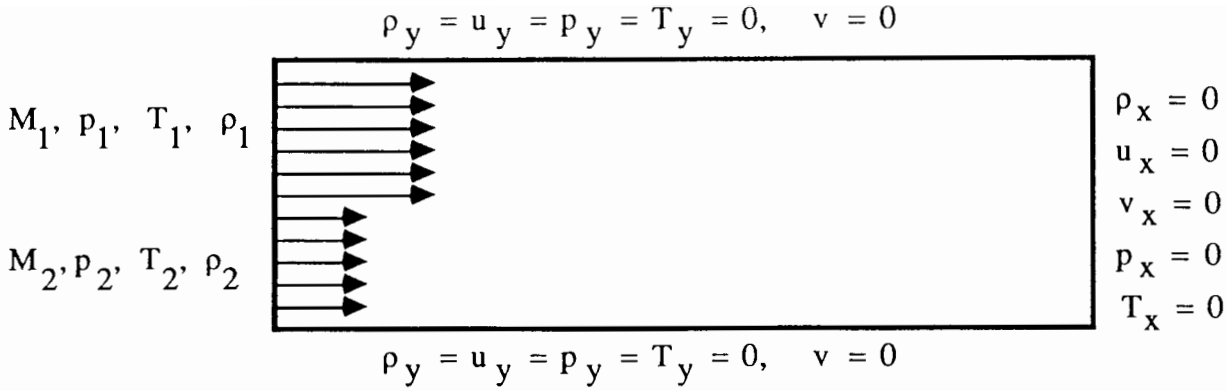

Figure 1. Boundary conditions for supersonic free shear layer

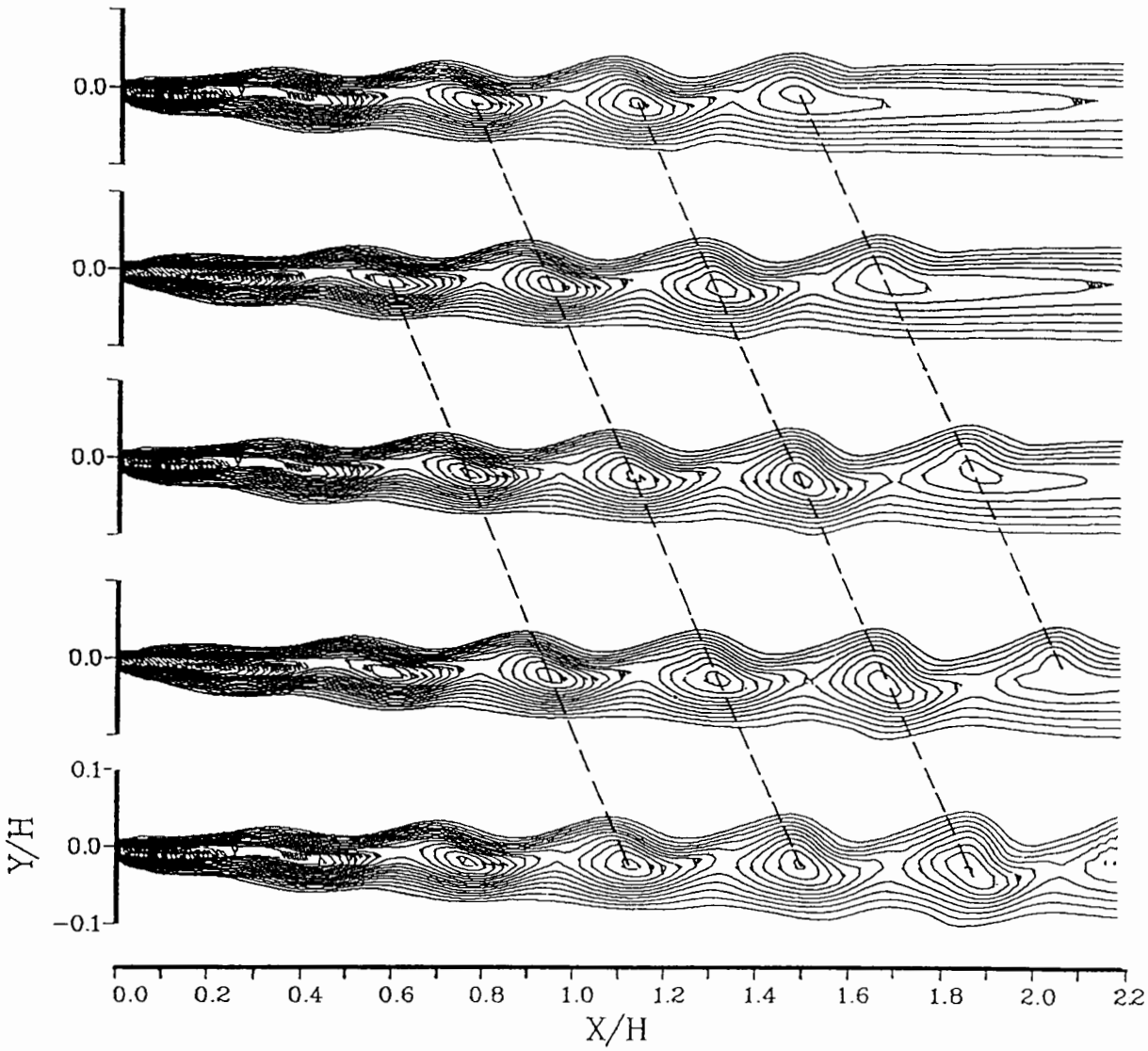

Figure 2. Vorticity contours at different time levels for case-2. $M_1 = 4.0$, $M_2 = 2.0$, $M_c = 0.38$.

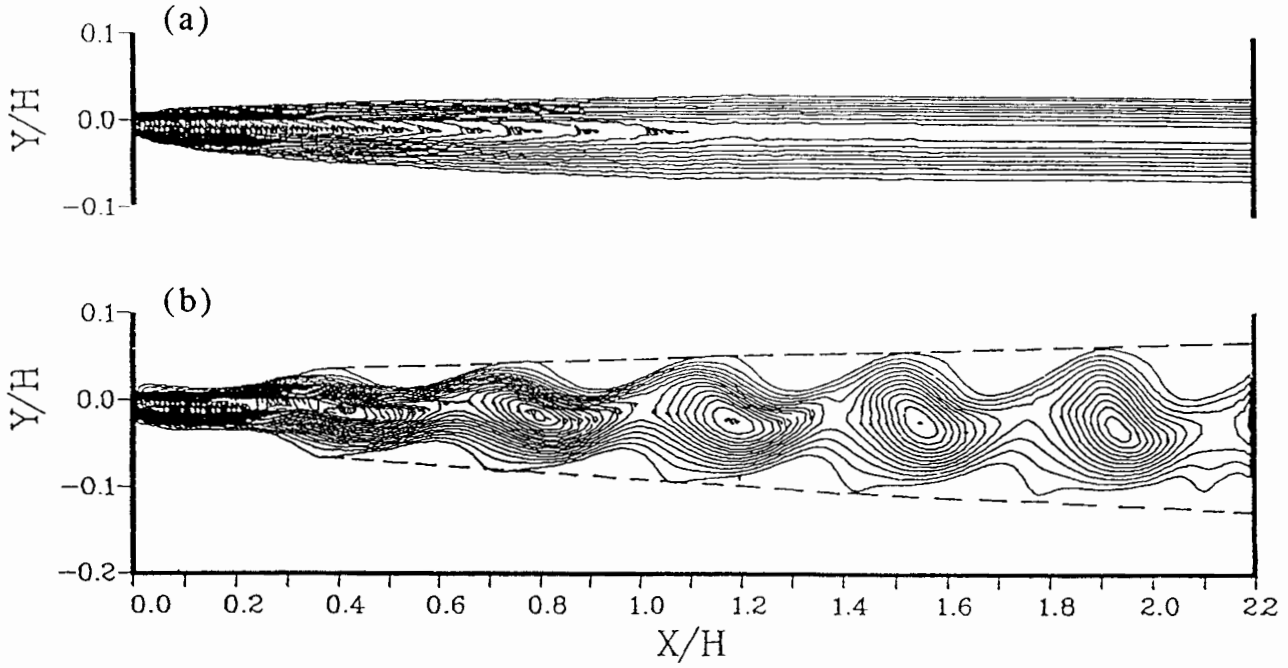

Figure 3. Vorticity contours for case-1, $M_1 = 4.0$, $M_2 = 2.3$, $M_c = 0.2$.
(a) without disturbance. (b) with disturbance in the normal direction.

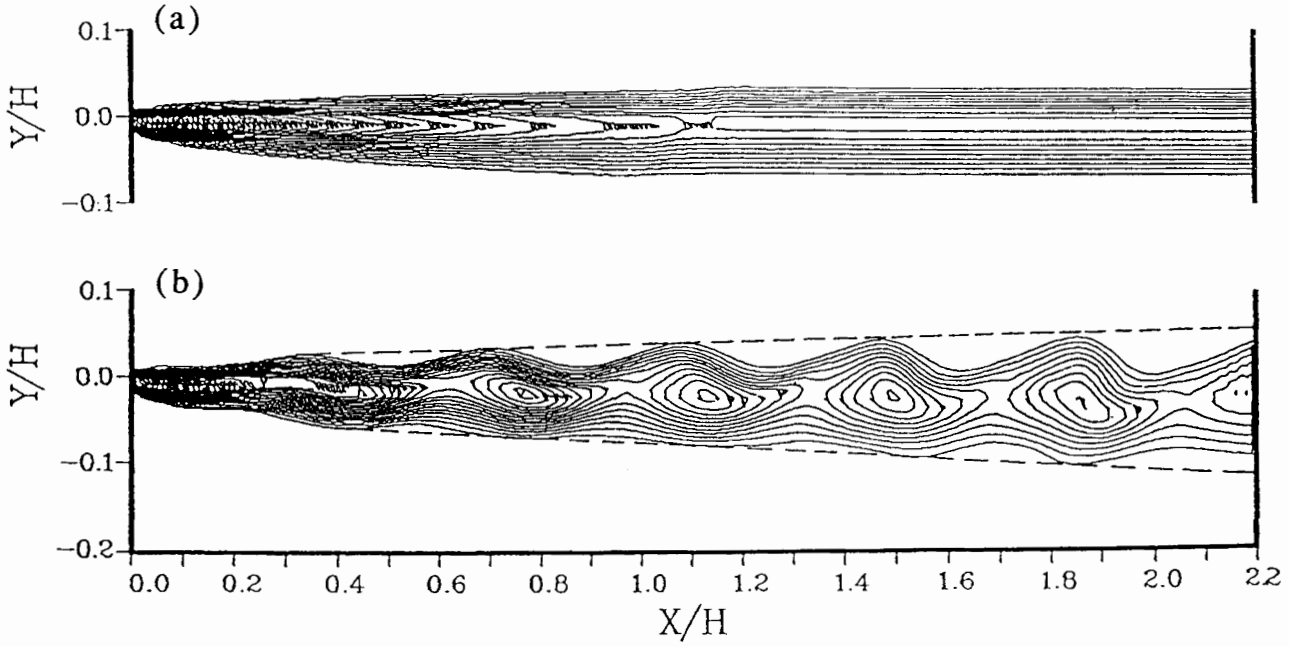

Figure 4. Vorticity contours for case-2, $M_1 = 4.0$, $M_2 = 2.0$, $M_c = 0.38$.
(a) without disturbance. (b) with disturbance in the normal direction.

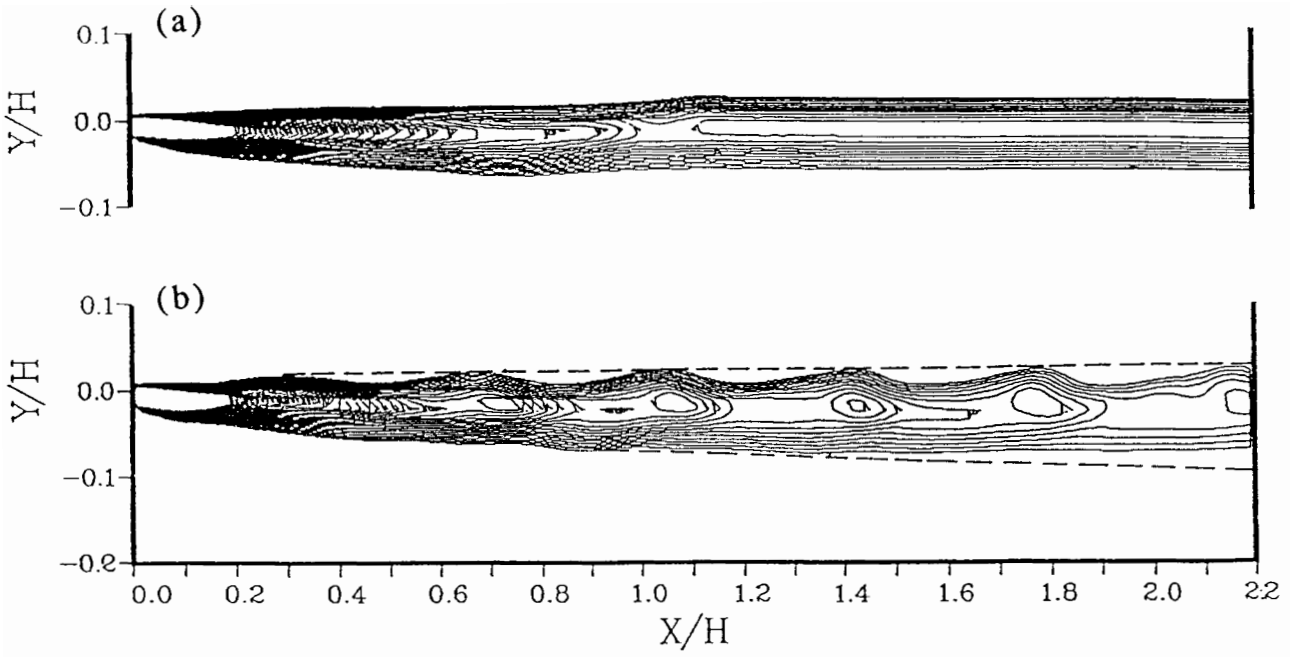

Figure 5. Vorticity contours for case-3, $M_1 = 4.0$, $M_2 = 1.3$, $M_c = 0.8$.
(a) without disturbance. (b) with disturbance in the normal direction.

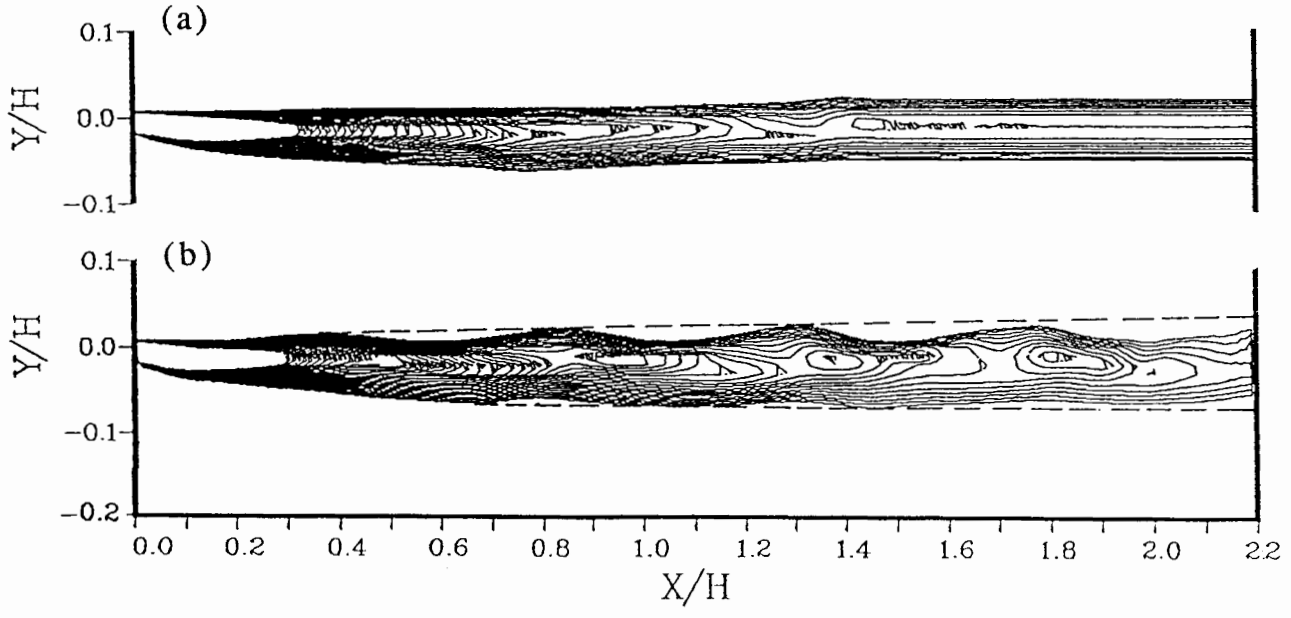

Figure 6. Vorticity contours for case-4, $M_1 = 5.0$, $M_2 = 1.3$, $M_c = 1.2$.
(a) without disturbance. (b) with disturbance in the normal direction.

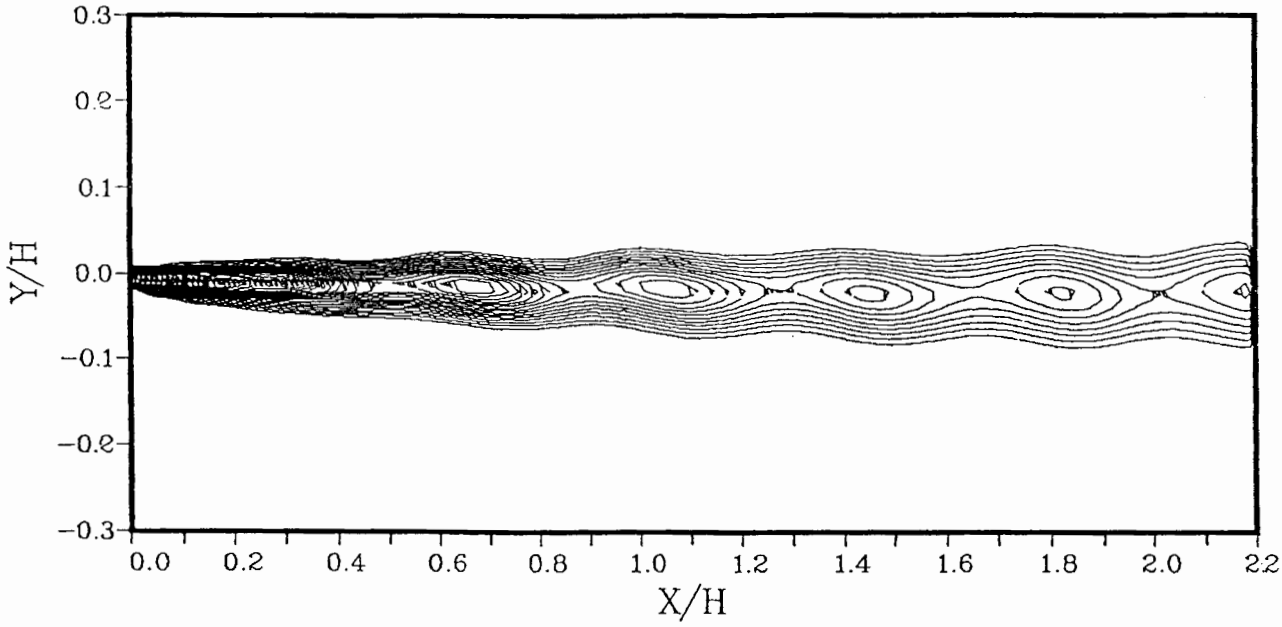

Figure 7. Vorticity contours for case-1, $M_1 = 4.0$, $M_2 = 2.3$, $M_c = 0.2$, with disturbance in the streamwise direction.

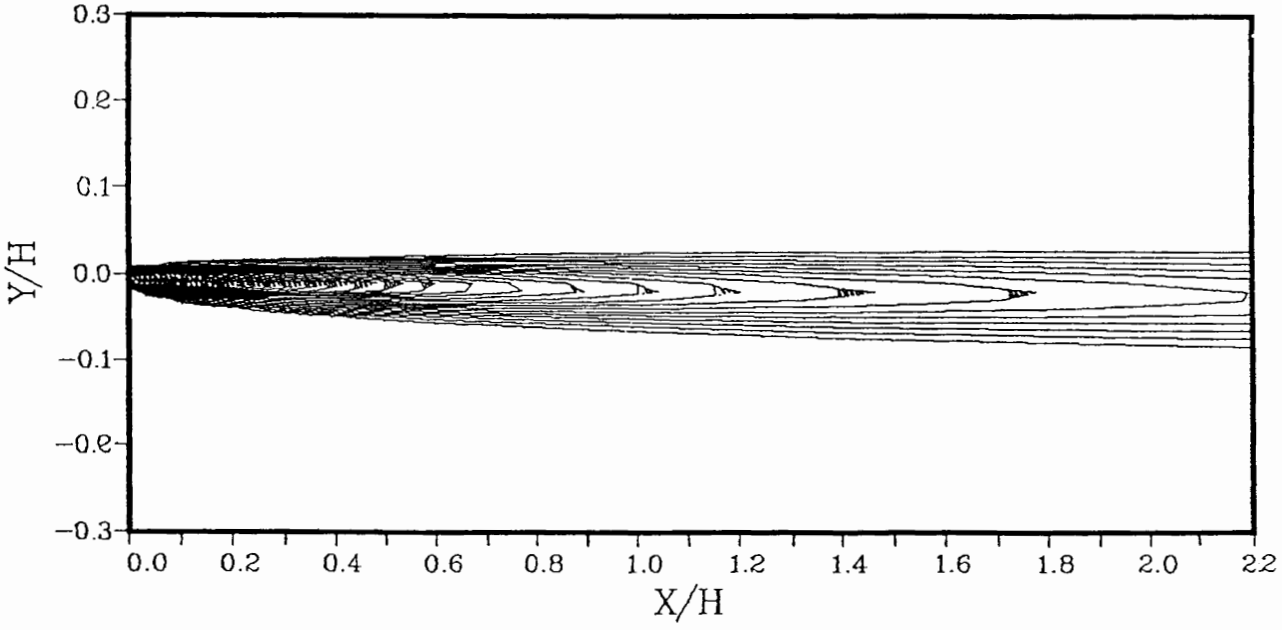

Figure 8. Vorticity contours for case-1, $M_1 = 4.0$, $M_2 = 2.3$, $M_c = 0.2$, with disturbance in the spanwise direction.

NUMERICAL SIMULATION OF ENHANCED MIXING AND TURBULENCE IN SUPERSONIC FLOWS

Thomas A. Zang, J. Philip Drummond, and Ajay Kumar

Computational Methods Branch
NASA Langley Research Center
Hampton, Virginia 23665

Introduction

The fundamental issues involved in compressible turbulence are of great technological importance and present severe challenges for analytical, numerical, and empirical predictive methodologies. One pressing application is to hypersonic flight, especially for the internal flow in combustors. A principal objective is to optimize the efficiency of the fuel-air mixing occurring in the engine. In the very high speed vehicle configurations currently being considered, achieving a high combustor efficiency is particularly difficult. This is a consequence of the fact that with increasing vehicle Mach number, the average Mach number in the combustor also increases. As the combustor Mach number increases the degree of fuel-air mixing that can be achieved through natural convective and diffusive processes is reduced, leading to an overall decrease in combustion efficiency and thrust.

Numerical methods for supersonic (and reacting) flow have matured to the point at which they are playing a key role in exploring machanisms for enhancing mixing and turbulence in compressible flow. In this paper some representative illustrations of recent work directed towards mixing enhancement in supersonic combustors will be presented.

Numerical Methods

This decade has witnessed rapid progress in numerical methods for supersonic and hypersonic flow. Upwind-biased schemes of increasing sophistication and accuracy have passed rapidly from academic circles to large production codes at national laboratories and in industry. Most practitioners have their own pet suite of test problem. In this section we provide a brief discussion of the progress made on two of our favorites.

The ideal shock-capturing numerical method would capture shock-waves and slip lines in 2 grid points with no smearing or spurious oscillations while at the same time retaining high accuracy on small-scale flow field features. A problem which is ideally suited for putting schemes to this particular test is the interaction of turbulence with a shock. A schematic is provided in Fig. 1. At time $t = 0$ an infinite, normal shock at $x = 0$ separates a rapidly moving, uniform fluid on the left from the fluid on the right, which is in a quiescent state except for some specified fluctuation. The initial conditions are chosen so that, in the absence of any fluctuation, the shock moves uniformly in the positive x direction with a specified Mach number (relative to the fluid on the

right). In the presence of the fluctuations, the shock front will develop ripples and waves will be established behind the shock. The particular case illustrated in the figure pertains to a Mach 8 shock encountering a plane shear wave inclined at an angle of 30° to the undisturbed shock front.

Linear theory predictions for the wave amplitudes behind the shock have been available since the 1950's ([1,2]). Zang, Hussaini, and Bushnell [3] have tested these in the nonlinear regime using shock-fitting methods. Figure 2 is a typical result of that work. The amplitude of a vorticity wave generated behind the shock by a downstream shear wave is plotted as a function of the angle of inclination of the wave. (Results for both finite-difference and spectral shock fitting calculations are shown.) For small angles the agreement with linear theory is very good, whereas near the critical angle (beyond which the waves behind the shock decay), the linear prediction is unreliable. At small angles of inclination, however, the linear result is a very good measure of the actual solution. Thus linear theory can be used to calibrate numerical methods for this test problem.

Since in the shock-fitting method the shock front is a boundary of the computational domain, the difficulties associated with differencing across the shock are not present. Although shock-fitting methods have produced impressive results on simple flows they are not a practical tool for the complicated flows that must be analyzed in many engineering problems.

A wide variety of upwind-biased difference schemes are currently available. Shu and Osher [4] have applied a particular upwind scheme, known as the ENO method, to this problem. The simplest relevant example of theirs involves a pure density fluctuation at zero angle of inclination. This reduces to a one-dimensional problem. Figure 3 displays the result of sixth-order ENO with 300 grid points for an incoming wave with a 20% fluctuation in the density. The solution to this problem involves both an acoustic wave and an entropy wave behind the shock. Both contribute density fluctuations, with the acoustic contributions having longer wavelength and faster propagation speed. The solid line comes from a highly-resolved ENO calculation. The high-order scheme does a very impressive job of capturing the shock and resolving both the acoustic and entropy waves. The result of a shock-fitted calculation are shown in Fig. 4. A second-order MacCormack method was employed. There are two features in the shock-fitted results which are not reflected in the ENO results. One is the oscillations near the upstream peaks of the acoustic wave and the other is the small-scale fluctuations near the the two upstream peaks due to the entropy wave. Results from a spectral domain decomposition shock-fitted code (Kopriva, 1988, private communication) suggest that these are real elements of the solution; the former arises from transients generated when the shock suddenly encounters the incoming wave and the latter occurs because of the superposition of the acoustic and entropy responses. Evidently, the ENO scheme does eliminate these real features from the flow. Nevertheless, this particular upwind scheme does an impressive job of replicating the large- and medium-scale flow features of this simple one-dimensional test problem.

A second simple test problem involves the interaction of a shock with a vortex. This problem, too, has been computed by shock-fitting ([5]). The problem is most challenging when the vortex is sufficiently strong to create a secondary shock along with a triple point. Figure 5, taken from [6], shows a typical experimental result. Here, the shock is moving from right to left and has just passed over the vortex. Note the two triple points in the figure.

Figure 6 shows the numerical results [7] obtained from a second-order upwind method. The calculation used a 132×122 grid. The close agreement between the primary shock, the secondary shock and the triple points is encouraging.

Mixing Enhancement From Oscillating Shocks

One technique for mixing enhancement that has been explored recently is based on utilizing either natural or forced shock oscillations to enhance turbulence. Kumar, Bushnell, and Hussaini [8] devised a simple two-dimensional model problem for this study. It consists of Mach 3 inviscid flow past a 10° compression ramp. The shock oscillations are forced by utilizing an oscillatory inflow boundary condition on the Mach number M of the form

$$M = M_\infty[1 + A(y)\ sin(2\pi ct)] \tag{1}$$

where

$$A(y) = \begin{cases} \sqrt{0.45y} & 0 \le y \le 0.05 \\ .15e^{-25(y-.05)} & y \ge 0.05. \end{cases} \tag{2}$$

The Mach number oscillations are concentrated near the lower wall, with a maximum amplitude of 5% of the free stream Mach number at y = 0.05 . The frequency c was the free parameter in this study. Kumar, et al examined frequencies between 1 and 10. This covers the relevant range of turbulence frequencies.

The numerical simulations of this problem were performed with a second-order upwind method. Results over one period for c = 5 are shown in Figure 7. The disturbance introduced at the foot of the shock propagates along the shock into the free stream flow. The induced free stream oscillations should enhance mixing. The Reynolds stress created by the shock oscillation are displayed in Figure 8. Note that the amplitude of the Reynolds stresses decreases as the frequency of the shock oscillation increases. Hence, low frequency shock oscillations should be the most effective ones.

In a real combustor shock oscillations can arise from unstable flow fields. Potential sources are from fuel injection, unsteady boundary-layer separation regions, boundary-layer turbulence, and from in-stream bodies.

Mixing Enhancement From Temperature Control

A useful idealization of the fuel-air mixing problem is sketched in Fig. 9. A splitter plate on the left separates the initial fuel (top) and air (bottom) streams. The air stream is presumed at rest, whereas the fuel stream has a specified Mach number M_∞. The ratio of the air to fuel temperatures is denoted by β_T. A free shear layer develops downstream of the splitter plate. This, of course, is unstable and linear stability theory can describe the initial stages of the instability.

Macaraeg & Street [9] have performed a parametric study of the temporal stability of the self-similar, non-reacting mixing layer. The compressible linear stability equations were solved with a spectral method using on the order of 100 points. Figure 10 displays typical dependicies of the growth rates, denoted by ω_i, upon Mach number, temperature ratio, and Reynolds number Re. The decrease in growth rate with increasing Mach number is familiar and underlies the necessity of increasing the mixing at higher speeds. The modest dependence of the growth rate upon Reynolds number reflects the essentially inviscid character of the instability. The strong dependence of the growth rate upon the temperature ratio suggests that mixing can be enhanced by proper tuning of the fuel temperature. Fortunately, the greater instability of the shear layer with decreasing fuel temperature is favorable to hypersonic combustors: the air entering the combustor will be very hot and the fuel can be relatively cold.

Of course, most of the flow in combustors is in the strongly nonlinear regime. Numerical investigations of all but the initial stages require full simulations. Drummond and co-workers have developed a comprehensive capability for simulating spatially-developing, reacting, viscous shear layers. A recent description of this capability is provided in [10]. Second- and fourth-order central difference methods are used for the numerical solution of the Navier-Stokes, energy, and species continuity equations. Finite-rate chemical reactions are included.

A number of numerical simulations of such shear layers have been conducted. Drummond and Mukunda [10] have studied the effect of curved shocks upon the mixing efficiency. Figure 11 illustrates the conditions of a simple comparison. The left part of the figure shows the benchmark case, which is the shear layer which develops from a fuel and air stream initially separated by an infinitely thin splitter plate. The physical domain was 0.1 m long and 0.1 m high. The computational grid was 201×51, with a strong concentration of grid-points within the shear layer. The simulation of this case was begun with static conditions in the flow domain and it was conducted for 0.1 ms. This time represented 14 computational sweeps of the flow field and was sufficient for a temporally periodic solution to develop. The right part of Figure 11 shows the conditions for the companion simulation which included a square cylinder (0.0012 m high and 0.002 m long) a distance 0.02 m behind the trailing edge of the splitter plate. This body induces a bow shock, which has strong curvature in the immediate neighborhood of the body.

The numerical results for both cases are shown in Figure 12. The water mass fraction is displayed because it is a useful tracer of the mixing. The benchmark case exhibits slow mixing, with the flow remaining laminar for the first 0.08 m downstream of the splitter plate. The familiar Kelvin-Helmholtz instability develops, but there is an insufficient length in the region of interest for the instability to evolve significantly. The effect of the obstacle is quite dramatic. When the high velocity gradient region of the mixing layer is processed by the curved shock in front of the square cylinder, vorticity is produced. The vorticity is then convected downstream where it produces enhanced macromixing of fuel and air. The velocity field becomes unstable near the trailing edge of the interference body and the thickness of the shear layer grows rapidly with increasing streamwise coordinate. The shear layer thickness defined by water mass fraction is significantly greater downstream of the obstacle than it is in the benchmark case.

Figure 13 provides a quantitative measure of the mixing efficiency in the two cases. The mixing efficiency (a number between 0 and 1) denotes the amount of fuel that could react at any x station if chemical reaction was taking place. The efficiency values for the two cases should be viewed in a relative sense because there are significant regions of fuel and air that can never mix since they are located at large transverse distances from the mixing layer. After the 0.02 m station (where the obstacle is located), there is a significant growth in mixing efficiency due to the obstacle. Near the outflow station, the mixing efficiency is roughly four times that of the benchmark case. This figure also contains results for a shear layer interacting with a pair of straight, oblique, intersecting shocks. They produce relatively little mixing enhancement for a shear layer which is still laminar. Thus, it is the curvature of the shock that is crucial for increasing the mixing.

This comparison demonstrates that the introduction of curved shocks into a mixing layer is beneficial. In a real engine the use an obstacle introduced solely for the purpose of producing a curved shock is not practical. The total pressure loss caused by the extra bow shock is a disadvantage. Moreover, aerodynamic heating would also pose a problem. Ideally, one should take advantage of a shock that is already present.

Drummond and Mukunda [10] next examined a configuration closer to an actual combustor. The top part of Figure 14 shows a conventional strut in a scramjet engine. Fuel can be injected both parallel to and transverse to the air stream. Transverse injection predominates over parallel injection when the engine is operating in the high Mach number regime to hasten fuel-air mixing. At lower Mach numbers, more parallel injection is used in order to produce slower mixing. Transverse injection takes place following a rearward-facing step that provides improved flameholding, and parallel injection occurs at the strut base. The transverse jet induces a bow shock. In the conventional design the flow from the parallel jet does not interact with this bow shock. The results of the comparison above suggested that a relocation of the transverse injection might improve the mixing. The bottom part of Figure 14 shows a strut which has been modified to take advantage of this mixing enhancement mechanism. Here the parallel injector is re-located so that it interacts with the the transverse jet (and its resulting bow shock). The same amount of fuel is introduced by each injector.

Figure 15 shows the numerical results for both the old strut and the modified strut. The old strut was operated with only parallel injection, whereas the modified strut produced both parallel and transverse injection. The effect of the interaction of the parallel jet with the bow shock is apparent in the water mass fraction contours. The unenhanced parallel jet behaves much like the unenhanced mixing layer described earlier. The growth of the jet was quite modest. For the modified strut, however, the interaction of the parallel jet with the curved bow shock ahead of the transverse jet indeed produced significant vorticity and results in increased mixing. Figure 16 shows the mixing efficiencies of the two cases. Efficiencies of over 90% are achieved after 0.04 m for the modified strut, whereas 0.075 m are required to achieve this level for the old strut.

Conclusions

Modern numerical methods have produced a significant improvement in the capability to simulate mixing in compressible flows. Upwind schemes provide sharp shocks and high-order schemes permit many small-scale flow features to be computed reliably.

Several examples of two-dimensional computations of mixing enhancement have been presented. They suggest that combustor designs can take advantage of oscillating and curved shocks as well as of enhanced instability due to temperature gradients across a shear layer. The natural extension of these investigations is to three-dimensional flows.

Acknowledgments

It is a pleasure to acknowledge that many individuals who have contributed to the results presented here: Dennis Bushnell, Mark Carpenter, Yousuff Hussaini, David Kopriva, Michele Macaraeg, Kristine Meadows, Chi-Wang Shu, and Craig Streett.

References

1. Moore, F. K.: Unsteady Oblique Interaction of a Shock Wave with a Plane Disturbance, NACA 1165, 1954.

2. Ribner, H. S.: Shock-Turbulence Interaction and the Generation of Noise, NACA 1233, 1955.

3. Zang, T. A.; Hussaini, M. Y.; and Bushnell, D. M.: Numerical computations of turbulence amplification in shock wave interactions, AIAA J., Vol. 22, pp. 13-21, 1984

4. Shu, C.-W.; and Osher, S.: Efficient Implementation of Essentially Non-oscillatory Shock Capturing Schemes II, ICASE Report 88-24, 1988.

5. Pao, S. P.; and Salas, M. D.: A Numerical Study of Two-Dimensional Shock-Vortex Interaction, AIAA Paper 81-1205, 1981.

6. Naumann, A.; and Hermanns, E.: On the Interaction Between a Shock Wave and a Vortex Field, AGARD-CP-131, 1973.

7. Meadows, K. R.; Kumar, A.; and Hussaini, M. Y.: A Computational Study on the Interaction Between a Vortex and a Shock Wave, presented at AIAA 12th Aeroacoustics Conference, April 10-12, 1989.

8. Kumar, A.; Bushnell, D. M.; and Hussaini, M. Y.: A Mixing Augmentation Technique for Hypervelocity Scramjets, AIAA Paper No. 87-1882, 1987.

9. Macaraeg, M. G.; and Streett, C. L.: A Spectral Collocation Solution of the Compressible Stability Eigenvalue Problem, NASA TP 2858, 1988.

10. Drummond, J. P.; and Mukunda, H. S.: A Numerical Study of Mixing Enhancement in Supersonic Reacting Flow Fields, AIAA Paper 88-3260, 1988.

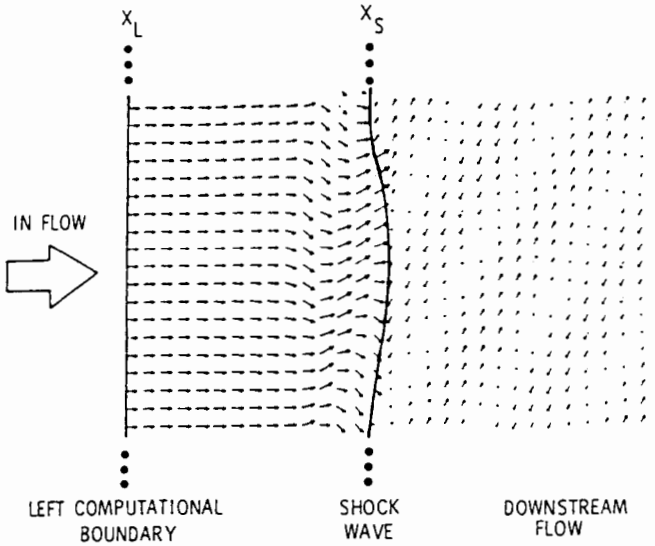

Figure 1. Typical shock-fitted time-dependent flow model for shock/turbulence interaction.

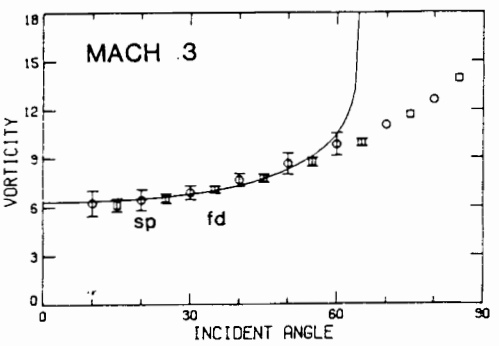

Figure 2. Vorticity response to vorticity waves incident upon a Mach 3 shock from both spectral (SP) and finite-difference (FD) shock-fitting codes.

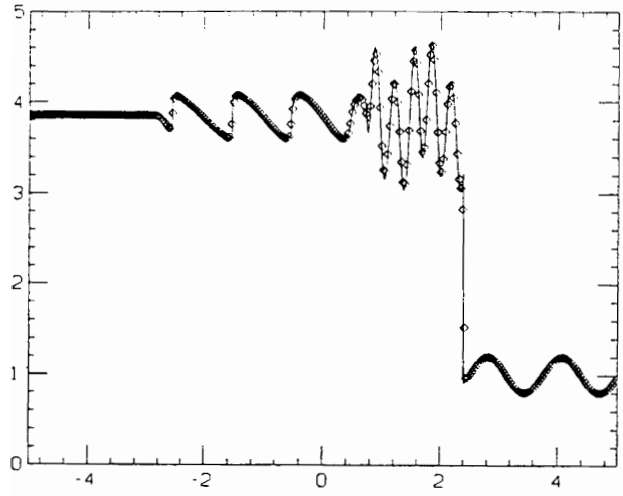

Figure 3. ENO solution for a fluctuating density incident upon a Mach 3 shock.

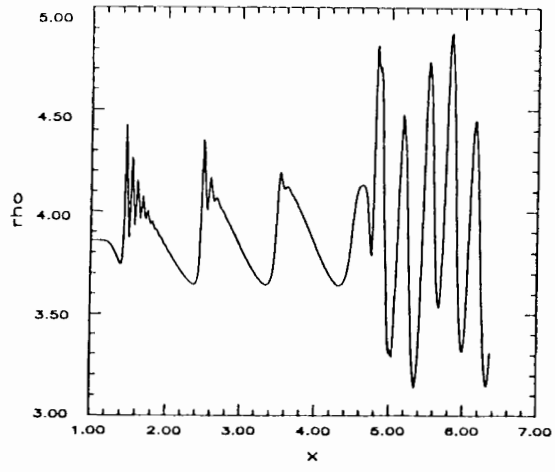

Figure 4. Shock-fitted solution for a fluctuating density incident upon a Mach 3 shock.

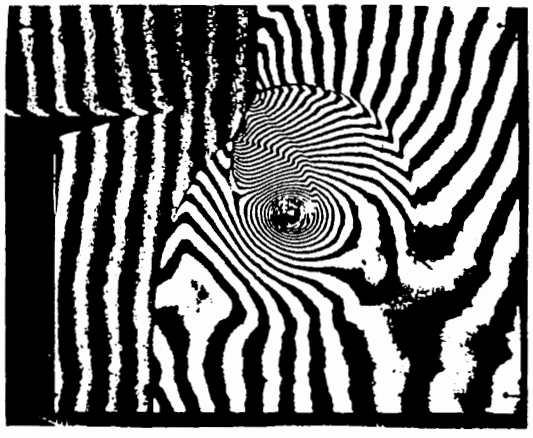

Figure 5. Mach-Zehnder interferogram for a strong vortex interacting with a shock.

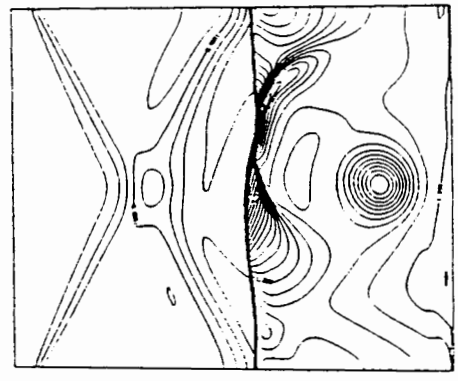

Figure 6. Density contours from a second-order upwind method for the shock/vortex interaction.

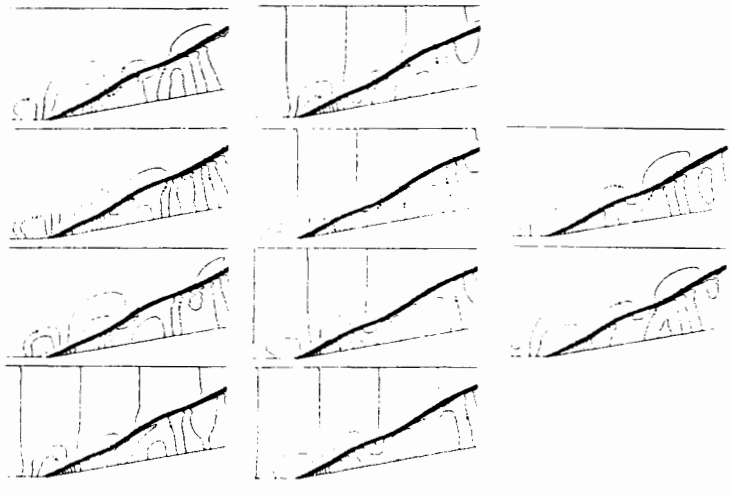

Figure 7. Pressure contours showing shock motion over one period for c = 5.

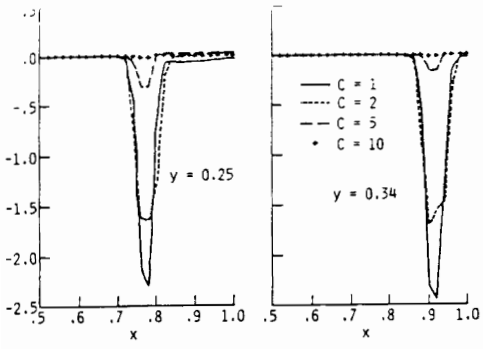

Figure 8. Time-averaged Reynolds stresses.

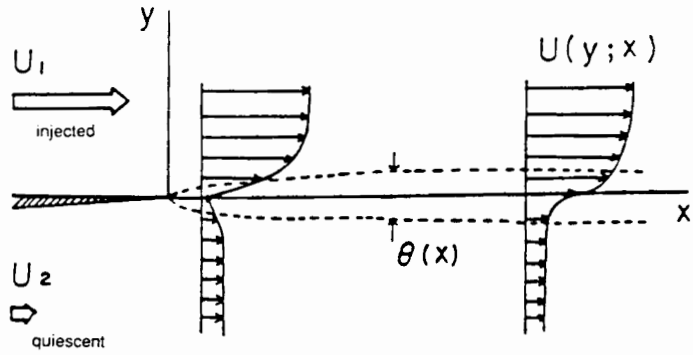

Figure 9. Schematic of the mixing layer.

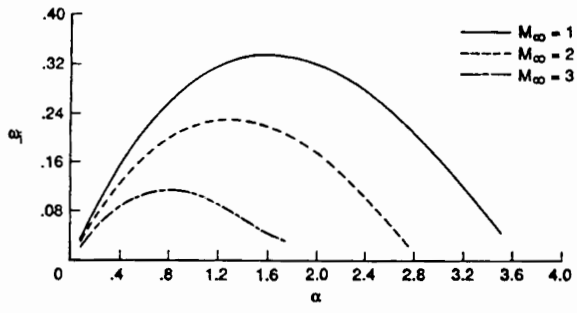

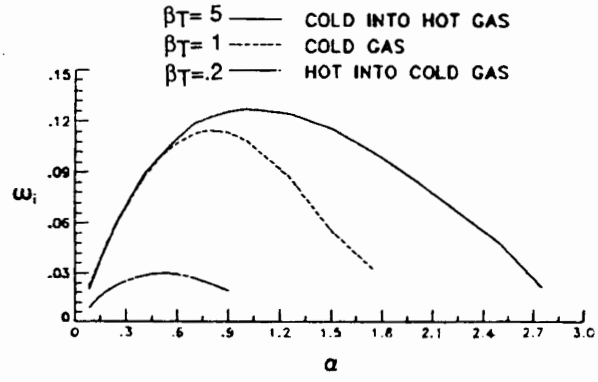

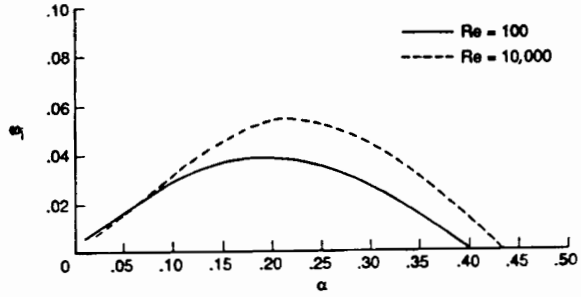

Figure 10. Parametric dependencies of the mixing layer.

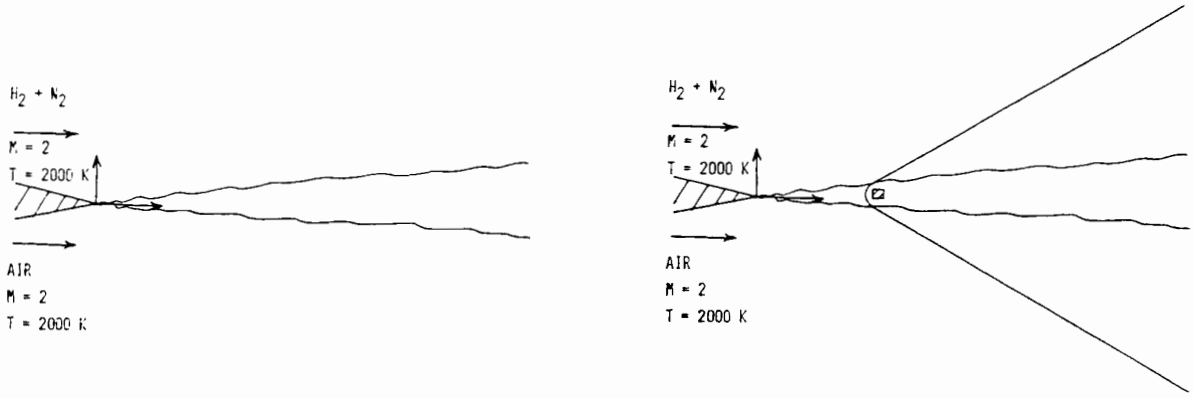

Figure 11. Schematic of the benchmark supersonic reacting mixing layer (left) and the mixing layer containing a square obstacle (right).

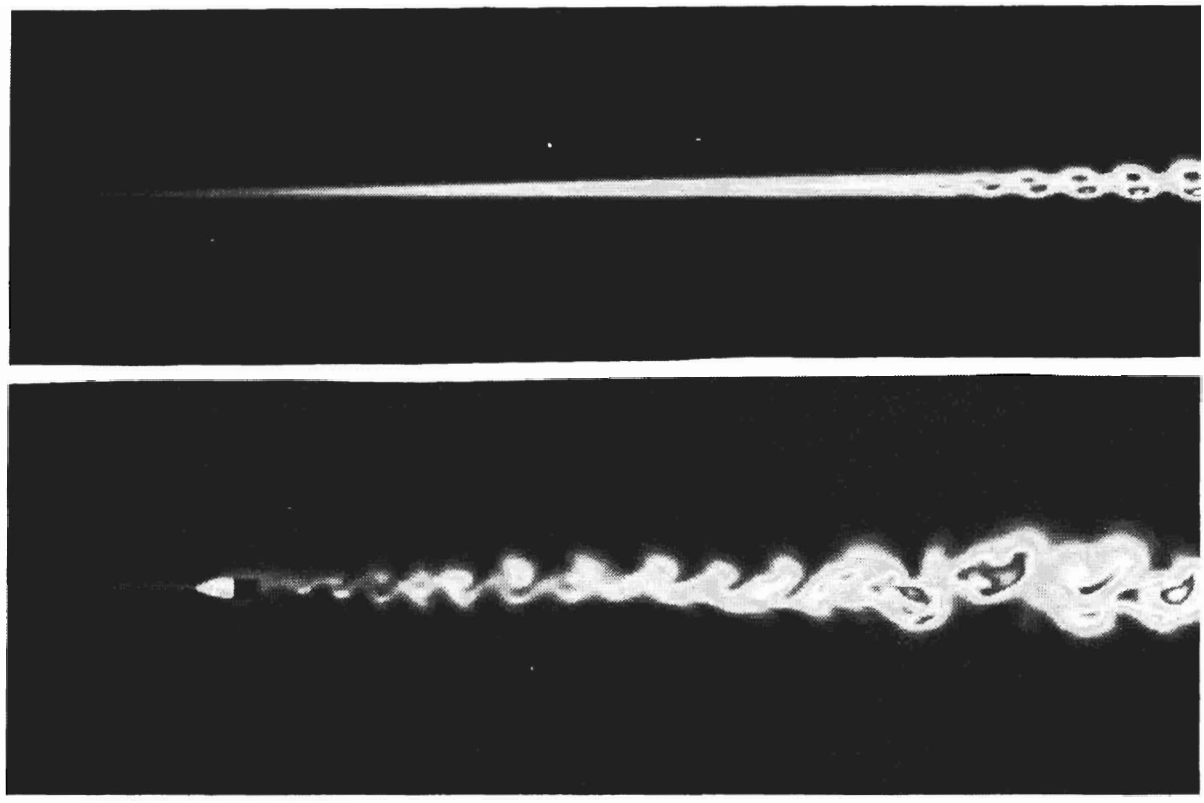

Figure 12. Water mass fraction contours for the benchmark mixing layer (top) and the mixing layer containing a square obstacle (bottom).

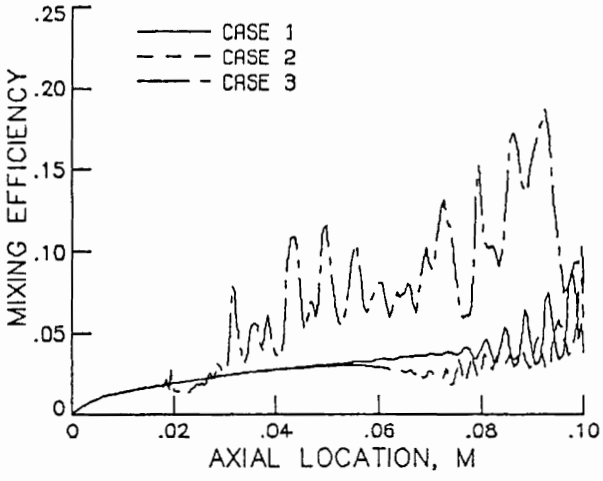

Figure 13. Mixing efficiencies for the benchmark mixing layer (Case 1), the mixing layer containing two oblique shocks (Case 2), and the mixing layer containing a square obstacle (Case 3).

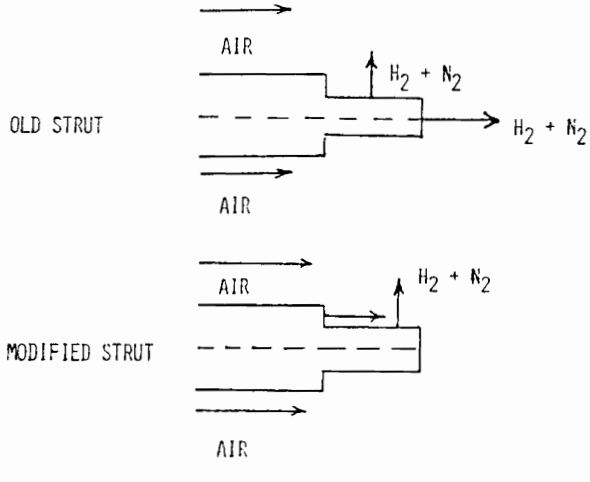

Figure 14. Schematic of conventional and modified fuel injector strut configurations.

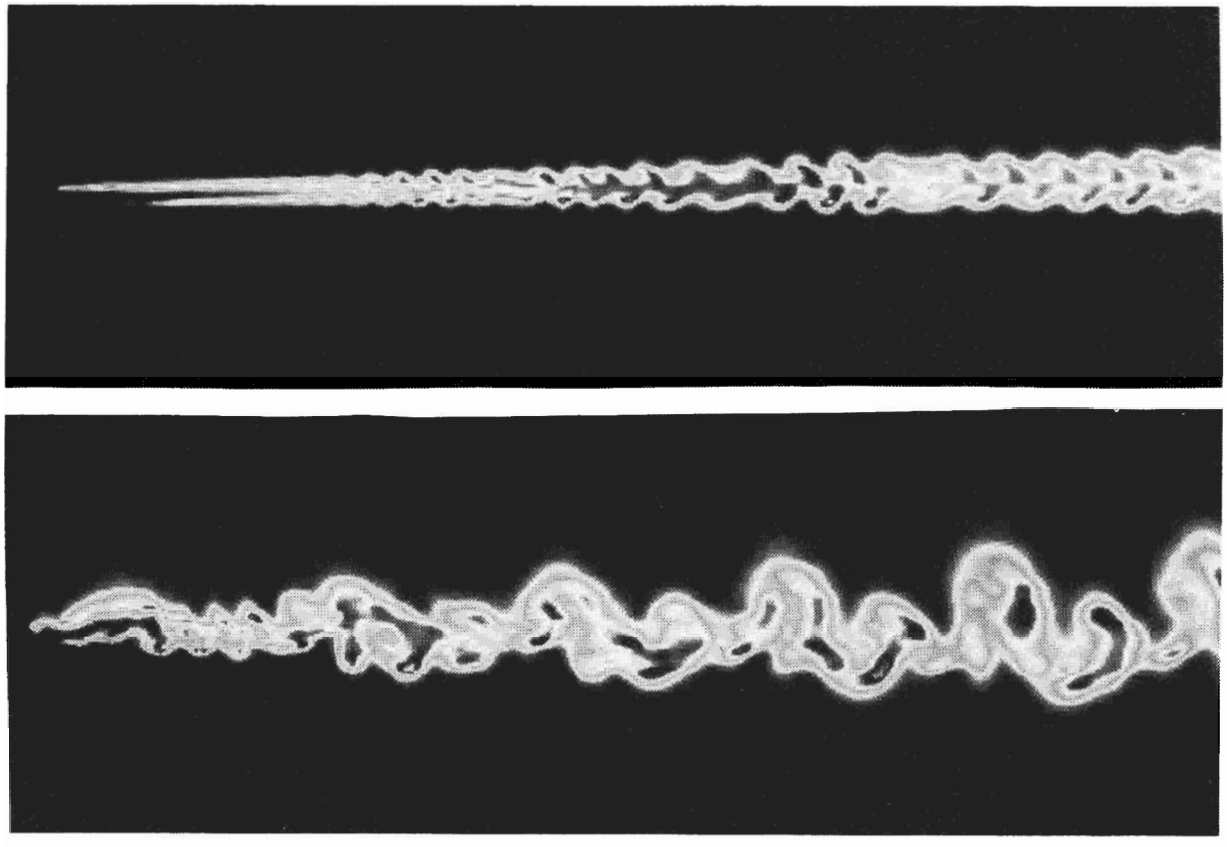

Figure 15. Water mass fraction contours for the conventional strut (top) and the modified strut (bottom).

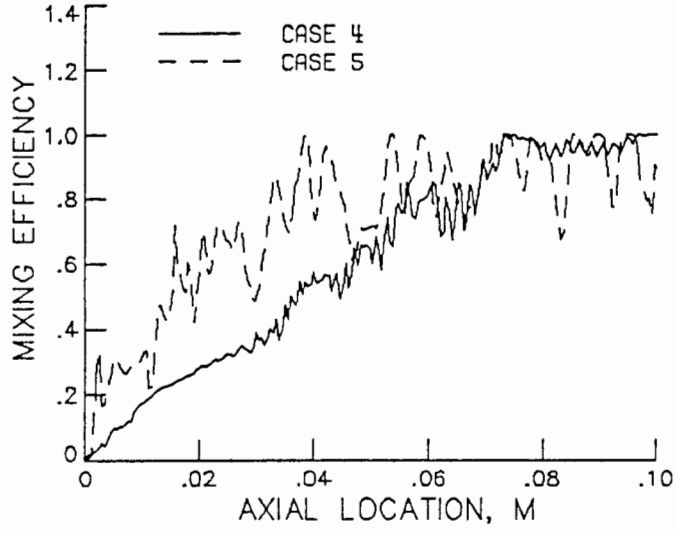

Figure 16. Mixing efficiencies for the conventional strut (Case 4) and the modified strut (Case 5).

III. Strongly Coupled Compressibility

MEASUREMENTS OF TURBULENT, ANISOTROPIC DENSITY FLUCTUATIONS IN A ROCKET EXHAUST PLUME BY A CROSS BEAM THREE-AXIS CORRELATION TECHNIQUE

G.J. BALL
Department of Aeronautics and Astronautics
University of Southampton

Introduction

Theoretical predictions of chemically reacting flows are sensitive to the assumptions made concerning the level of fluctuations of scalar variables such as density and temperature. There is need for experimental data to test modelling assumptions. The measurement of fluctuating density and temperature in the high temperature exhaust plume of a rocket motor poses several daunting technical problems.

The use of optical non-intrusive techniques is one means of obtaining such data and this paper describes the use of the Crossed Beam Correlation method (CBC) to obtain localised measurements of the mean square density fluctuations within a rocket exhaust plume. The method uses robust, low cost optical components and is relatively insensitive to vibration and chemical contamination and requires no flow seeding.

Theory and Development of CBC

A narrow beam of light traversing a flow is refracted at each refractive index gradient it encounters and the emerging ray therefore diverges from its original path. The deflection of the beam is a measure of the refractive index gradients, within the flowfield, integrated along the beam path. Wilson and Damkevala (1970) made use of a pair of orthogonal intersecting beams in order to obtain localised information. They demonstrated that the covariance of the time varying deflections of the two beams can be used to obtain the mean square density fluctuations at the intersection point, under the assumption of isotropy of the turbulent density field. Kalghatgi (1980) showed that, in the presence of an anisotropic density field, additional information is required concerning the ratio of the anisotropic length scales of the turbulence, and that this information can be derived with the aid of a third orthogonal beam. The three-beam CBC therefore provides a diagnostic tool for the measurement of density fluctuations in anisotropic turbulent flows, and it is this system that was used in obtaining the present measurements.

Instrumentation

Measurements reported here were made using a crossed beam correlator (see Wilson and Damkevala 1970) as modified by Kalghatgi (1980). The three beams are provided by three 4mW HeNe lasers which intersect at the measurement point (see figure 1). Each transmitted beam is directed onto a position sensitive photodiode which measures the

angular deflection induced by density gradients in the flow (bandwidth 0-20kHz). The deflections are cross-correlated in order to obtain localised information from the beam intersection. The mean square density fluctuation is obtained, together with the ratios of three orthogonal length scales of the density field.

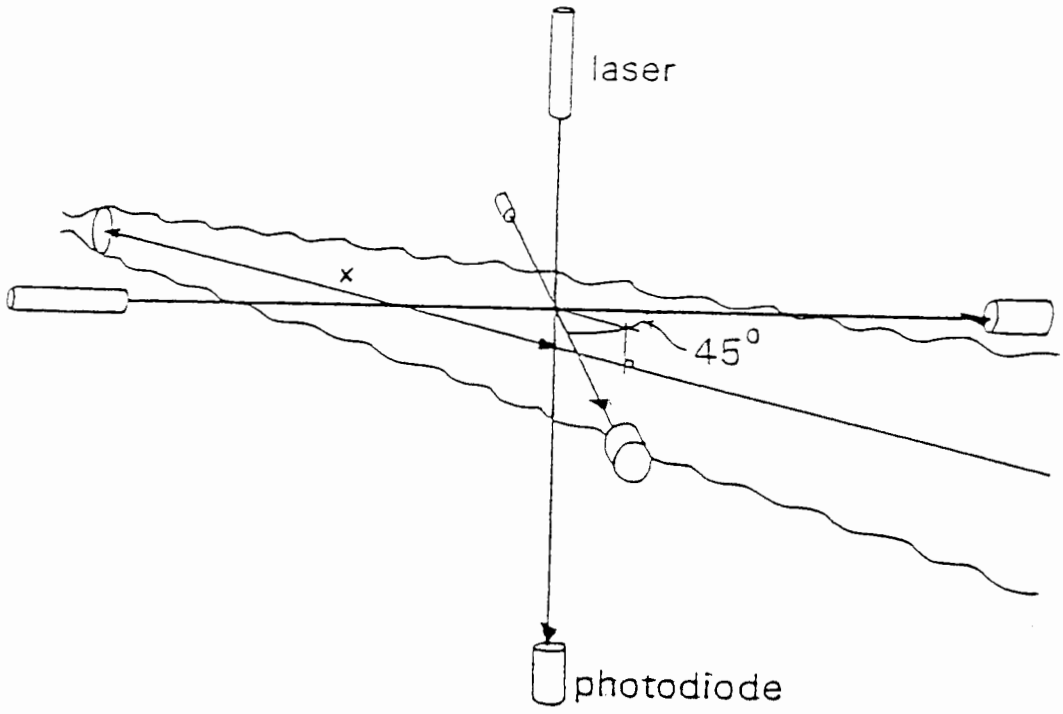

FIGURE 1: Optical configuration for CBC measurements in the rocket plume.

Rocket Plume measurements

Measurements were made of the density fluctuations in the near-field exhaust plume of a stationary liquid fuelled rocket motor. The plume gases were exhausted from a 72.65 mm nozzle, having a throat of 40 mm, at approximately 2200 m/s at an exit temperature of 2000 K. The chamber pressure was 60 atmosphere. The plume was under expanded with an exit plane pressure of 4 atmospheres. This resulted in the formation of barrel shock cells as shown in Figure 2. Noise levels close to the plume exceeded 140 dB. The oxidant employed was red fuming nitric acid, quantities of which were expelled as a fine mist at the end of each firing. These factors served to create in the plume vicinity a hostile environment for the measuring optics. Nevertheless the apparatus survived approximately 200 firings each of 10 seconds duration without serious failures.

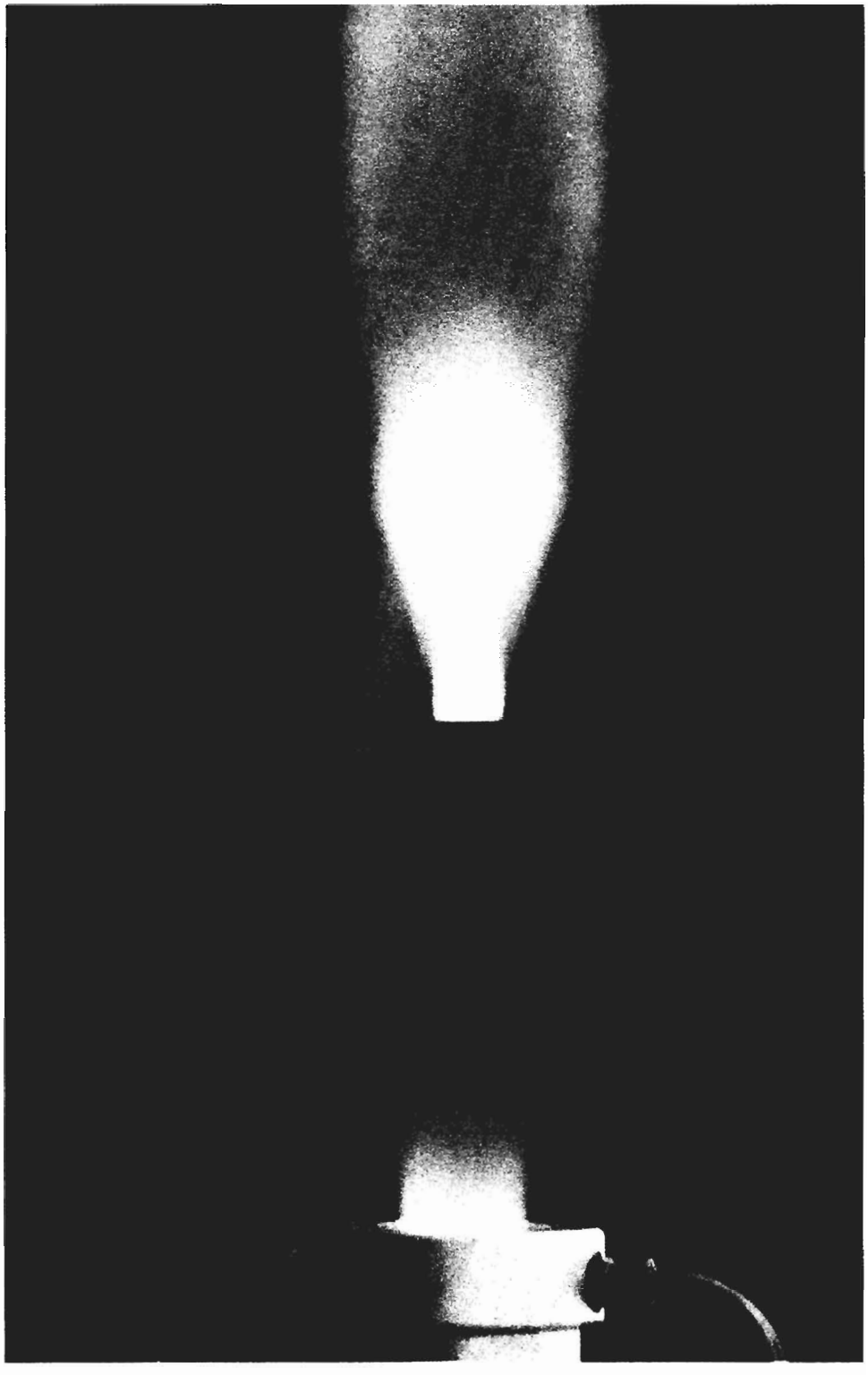

Figure 2. The rocket plume.

Results

A large number of measurements of the density fluctuations at various stations along the length of the plume were made. (For reference to all the measurements see Ball (1984)).

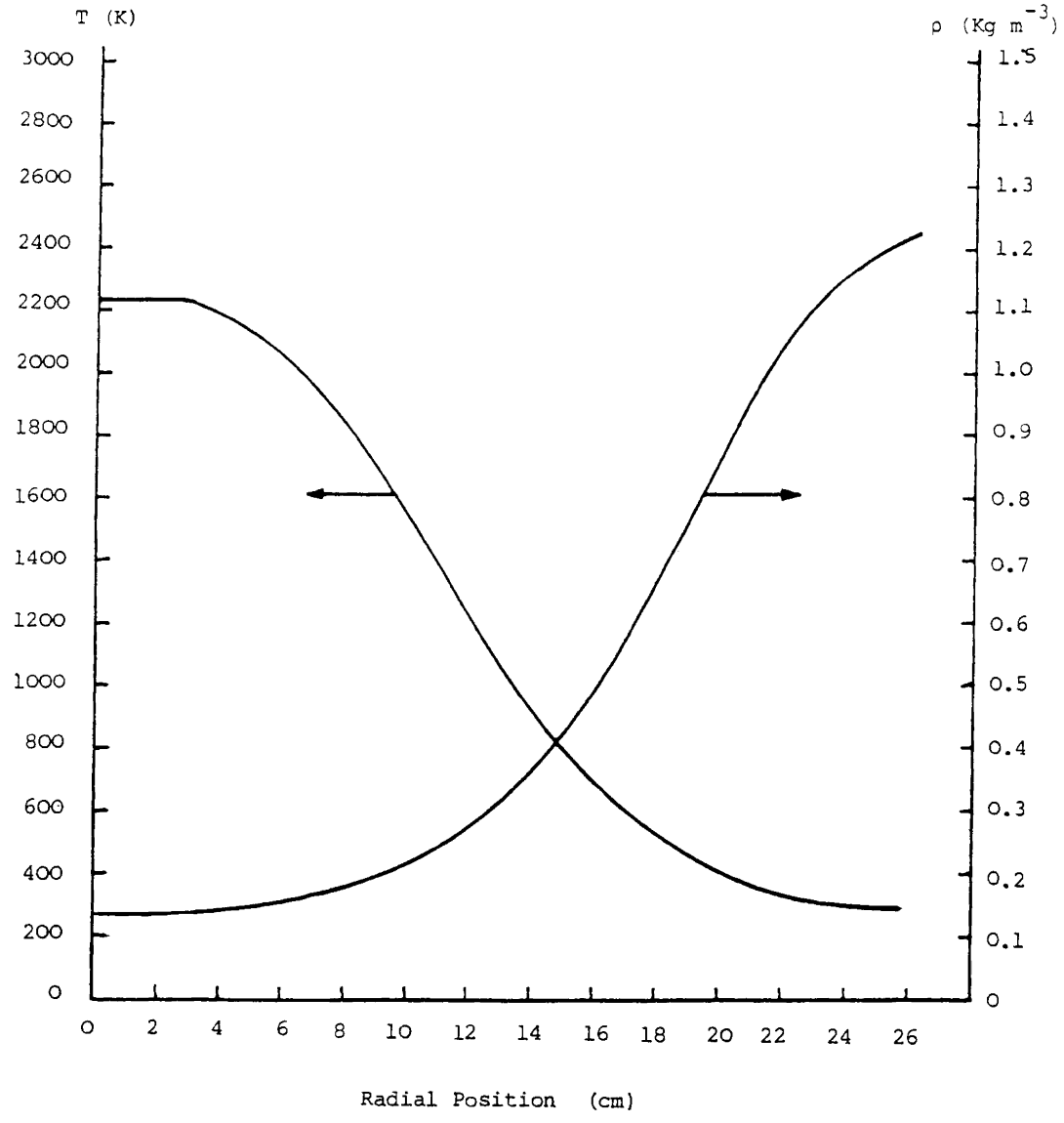

FIGURE 3: Predicted time mean profiles of temperature and density 1.0 metres from the nozzle exit.

Computer predictions of the mean density and temperature at 1.0 m from the nozzle exit are shown in Figure 3, while Figure 4 shows measured values of the root mean square density fluctuations at this same station.

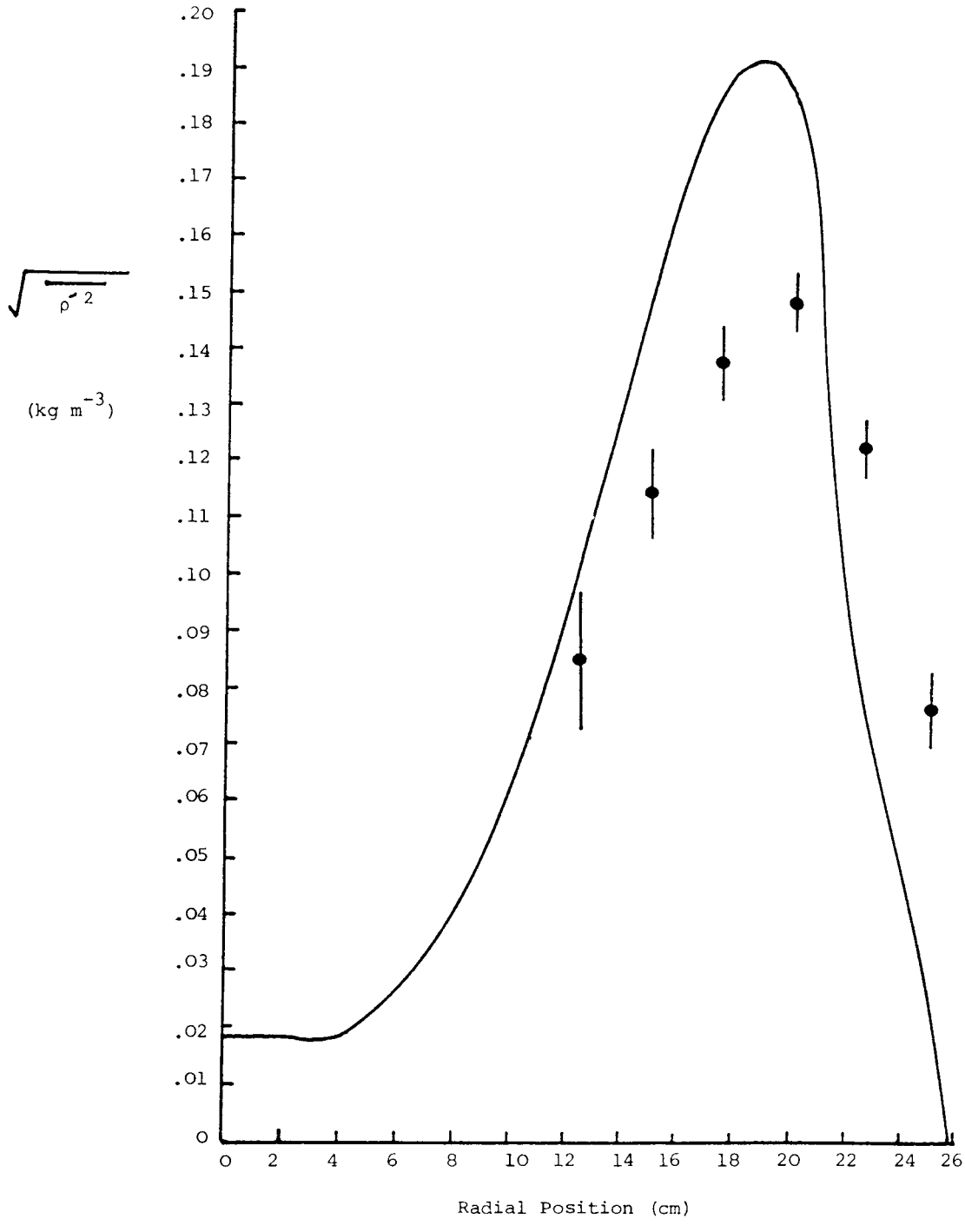

FIGURE 4: Predicted and measured profiles of density fluctuation 1.0 metres from the nozzle exit.

Discussions and Conclusions

The estimated errors for each deflection covariance are of the order of ± 10%.

Although the 3 beam CBC technique proposed by Kalghatgi has been shown to yield plausible results in a field of gross anisotropic turbulence, the density variance obtained relies heavily on the assumed model of the spatial correlation function for density fluctuations used by Kalghatgi. Ball (1984) showed that only one orientation of the 3 beams can give complete correction for the effects of anisotropy, when the beams are not so aligned some loss in accuracy is expected. Ball (1984) and Ball and Bray (1985) include proposals for modifications to the 3-beam CBC to overcome this problem. In its present form the CBC technique is shown to be a relatively simple and inexpensive method for the determination of the density fluctuations in hostile flow fields.

Acknowledgements

The author is indebted to Professor G M Lilley for presenting this work at the workshop and for assistance in preparing this paper. This work was supported by the UK Ministry of Defence.

References

Wilson L.N., Damkevala R.J., Journal of Fluid Mechanics, Vol. 43, 1970, pp 291-303.

Kalghatgi G.T., AASU Technical Memo 80/3, University of Southampton 1980.

Kalghatgi G.T., Cousins J.M., Bray K.N.C., Combustion and Flame, Vol. 43, 1981, pp 51-67.

Ball G.J., Ph.D. Thesis, University of Southampton, 1984.

Ball G.J., Bray K.N.C., AIAA 85-1255, 1985.

EXPERIMENTAL OBSERVATIONS OF SHOCK STABILITY AND SHOCK-INDUCED TURBULENCE

Robert F. Benjamin
Los Alamos National Laboratory
Los Alamos, NM, USA 87545

Abstract

We observe the Richtmyer-Meshkov (RM) instability of a perturbed, shock-accelerated interface between different gases. Instability growth of a singly shocked interface is observed to be consistent with previous experimental data. Late-time growth visually appears nonlinear but the growth rate remains the same as during linear growth. Re-shocking the interface produces additional RM growth and substantial profile broadening, which does not show the effect of local vorticity generation.

Introduction

Shock acceleration of an interface between fluids of different density produces a hydrodynamic instability similar to the well-known Rayleigh- Taylor instability of an accelerated interface. Perturbations at the shocked interface grow and eventually produce mixing of the fluids. Re-shocking the interface enhances the rate of mixing, and may be viewed as promoting a transition from instability to turbulence. We examine the physics of this transition experimentally by taking shadowgraphs of the flow pattern during the re-shocking of the perturbed interface. We also report measurements of the amplitude growth of a singly-shocked, perturbed interface.

Growth of the shock-induced instability in gases when the initial amplitude of the perturbation is small was first studied theoretically by Richtmyer[1] and experimentally by Meshkov.[2] Hence, the shock-induced instability is often called the "Richtmyer-Meshkov" (RM) instability. The RM unstable interface is a perturbed contact discontinuity subjected to normal shock acceleration. Using a shock tube and optical diagnostics to study the shocked interface between different gases, Meshkov measured the growth rate for the amplitude of a single-wavelength perturbation to be considerably smaller than predicted by Richtmyer's analytical approximation. Our measurements for amplitude growth rates are slightly higher than Meshkov's results, but significantly less than those given by Richtmyer's

formula. Measurements of instability growth in gases at much higher Mach number were recently reported.[3]

By contrast with these experiments with gases in which the measured values are lower than analytic estimates, experimental results with liquids[4] are higher than the analytic expression derived from Taylor's and Richtmyer's analyses.

Several investigators[5-9] have studied the growth of a *planar* interface evolving into a mixing zone as a consequence of multiple shocks and rarefactions. Although these interfaces are nominally planar, they have uncharacterized perturbations that lead to instability and mixing. Recent results[9] suggest that earlier measurements may have been dominated by boundary layer effects that obscured the interfacial region of bulk mixing. All of these experiments measured the mixing (or perhaps boundary layer effects) induced by shocking a nominally flat interface between the fluids, but they did not carefully examine the details of the first re-shock to the interface, which is when the growth rate changes most abruptly. Our goal is to investigate this transition experimentally and to develop a database that describes this transition and related phenomena.

Instability growth from a single shock

Richtmyer considered the case of a shock wave moving from a lower- density fluid, having density ρ_L, into a higher-density fluid, ρ_H. He derived the following analytic expression for the growth rate of a small- amplitude, single-mode (i.e., single wavelength) perturbation:

$$d\eta/dt = k\,\eta'_o\,U_I\,\{(\rho_H - \rho_L)/(\rho_H + \rho_L)\} \qquad (1)$$

where: η = amplitude of the perturbation (η_o is the initial amplitude.)
η'_o = the initial, *shock-compressed* amplitude
k = wavevector of the perturbation = $2\pi/\lambda$
U_I = interface velocity
$(\rho_H - \rho_L)/(\rho_H + \rho_L)$ = Atwood number

Richtmyer also performed a numerical calculation for this light-to-heavy case and found that Eq. (1) is a good approximation to the numerical computation provided one uses shock-compressed values for the Atwood number and initial amplitude. However, Sturtevant[8] pointed out that there is ambiguity about the value of the amplitude compression of the perturbation. Meshkov estimates the compression with an expression involving velocities, whereas Sturtevant suggests alternative

expressions using density compressions. For purposes of comparing Meshkov's results and the present work, we use Meshkov's expression.

Experimental details

Both the single-shock and re-shock experiments were performed in a horizontal shock tube having inside square cross section with dimensions 75 x 75 mm. The sinusoidal perturbation of the interface between the test gases was produced by a 0.5-μm-thick cellulose nitrate membrane clamped in a sinusoidal shape characterized by wavelength λ=37.5 mm and initial amplitude η_o = 2.4 mm. These dimensions give an initial (uncompressed) value of $k\eta_o = 0.40$.

We diagnose the interfacial instability by side-viewing the interfacial region with either of two shadowgraph systems. One system is used to take a flash shadowgraph that gives one high-resolution frame per event. The frame duration, determined by the light source, is about 2 μs. This shadowgraph gives a detailed view of the flow patterns. The other system uses a multi-frame camera[10] to measure growth rates. The camera produces 12 frames equally spaced in time, but having less spatial resolution. The interframe time set by the camera is 18.5 μs, and a long-pulse (i.e., several ms) light source is used.

Observations for a singly-shocked interface

Our measurements of the singly shocked, corrugated interface are qualitatively in agreement with Meshkov's results, but slightly different quantitatively. We examined two systems in which the shock wave moved from:

air into SF_6 (light-to-heavy);

air into helium (heavy-to-light).

In the light-to-heavy experiment, the shock wave moves from the lower-density gas into the higher-density gas, and vice versa for the heavy-to-light. The qualitative agreement with Meshkov's results is seen in Fig. 1. The perturbed interface is observed to be unstable in both the light-to-heavy and the heavy-to-light cases, since large growth of the amplitude occurs when the interface is subjected to a single shock in either direction. The amplitude grows immediately in the light-to-heavy case, whereas in the heavy-to-light case, one observes a phase inversion at early time and growth at later time. During the phase inversion the amplitude appears to be stabilizing, but its later growth shows that the velocity field in the flow is characteristic of the instability. These qualitative features were observed by Meshkov[2] and are confirmed by our present results.

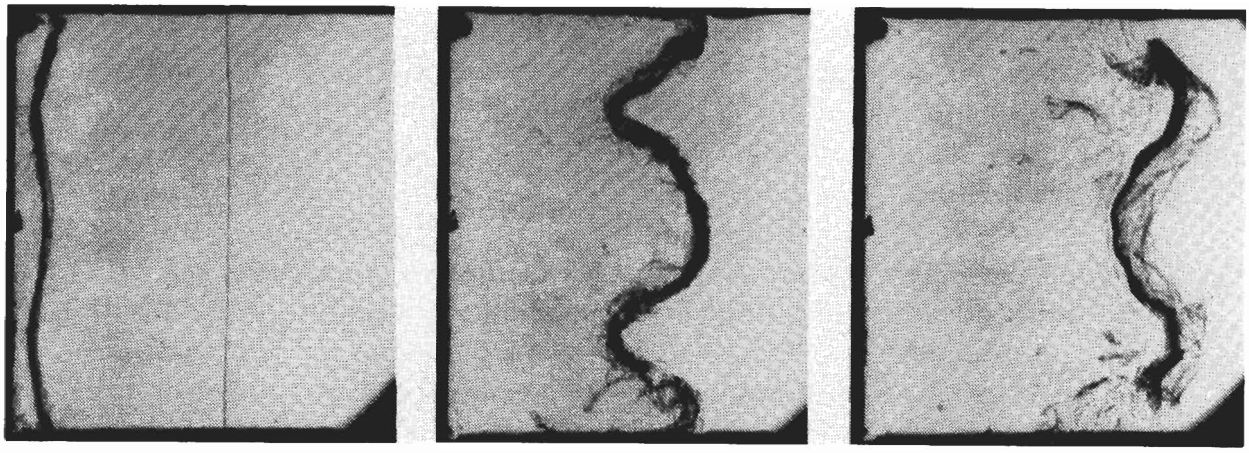

A *B* *C*

Figure 1. These three flash shadowgraphs show the effects of different density gradients across the interface. In all three cases the interface is accelerated by a shock wave moving from air on the left into the downstream gas on the right side of the sinusoidal membrane. ***A****:* The downstream gas is air, so the perturbed interface is stable, although the amplitude is shock-compressed. The transmitted shock front (moving left to right) is seen to the right of the perturbed interface. ***B****, light-to-heavy case:* The downstream gas is SF_6, which is about five times more dense than air. The perturbation's amplitude is observed to grow without inverting phase. ***C****, heavy-to-light case:* The downstream gas is helium, and the amplitude is observed to invert phase and grow. Note that the transmitted shock wave is out of the viewing area in ***B*** and ***C***.

Our multi-frame shadowgraphs provide time-resolved data from which we measure the growth rate $d\eta/dt$. We find that the amplitude η grows linearly in time, even at later times when the visual appearance of the interface takes on the spike-and-bubble configuration associated with nonlinear growth.

We make quantitative measurements of $d\eta/dt$ by time-resolving the shadowgraphs with an electronic framing camera that takes a series of twelve frames per event, having an interframe time = 18.5 μs. For an incident shock wave of Mach 1.24 in air, the measured growth rates of the amplitude are:

Air --> SF_6 (light-to-heavy) $d\eta/dt = 7.9$ m/s ($U_I = 81$ m/s)
Air --> He (heavy-to-light) $d\eta/dt = 19$ m/s ($U_I = 185$ m/s)

Using Meshkov's method to estimate the compression of the initial amplitude, we compare the air/SF_6 growth rate with Eq. 1:

$$(d\eta/dt)_{LANL} / (d\eta/dt)_{Eq.\ 1} = 0.46 .$$

By contrast, Meshkov's interpolated result for the Atwood Number corresponding to air/SF_6 ($\rho_H/\rho_L = 5.1$) gives a growth rate:

$$(d\eta/dt)_{Meskov} / (d\eta/dt)_{Eq.\ 1} = 0.35 .$$

Thus, the present results are somewhat higher than Meshkov's experiments, but substantially lower than the growth rate given by Eq. 1 using Meshkov's estimate for the initial compression.

Observations for a re-shocked interface

When an air/SF_6 interface is re-shocked after its amplitude has grown into the nonlinear regime, the profile of the interface appears to broaden substantially and the mean profile of the interface undergoes RM growth. The broadened interfacial region, denoted "mixing zone," contains a mixture of air, SF_6 and membrane debris. These features are seen in Fig. 2. The shock wave reflected from the endwall is moving from the higher- density SF_6 into the lower-density air, which is the "heavy-to-light" case of RM, so the interface's amplitude inverts phase before growing. Thus, the re-shocked interface momentarily appears to be stabilizing as it passes through the inversion phase, but later growth of its profile is clearly observed.

We observe in Figs. 2B and 2C that there appears to be no enhancement of the width of the mixing zone in the two regions where the vorticity production is greatest. These regions are where the pressure gradient of the shock, ∇p, and the density gradient of the interface, $\nabla \rho$, have the greatest included angle; i.e., where $\nabla p \times \nabla \rho$ is greatest. These regions occur where the interface profile is nearly perpendicular to the shock front. The growth of the mixing zone appears to be independent of the local angle between the shock front and the interface.

The wave reflected back into the SF_6 appears to be a rarefaction fan, and the wave transmitted into the air appears to be a sharp discontinuity characteristic of a shock wave. The rarefaction has a mottled appearance.

The visual appearance of the interface profile shows many well-resolved features, as seen in Fig. 2, but we observe blurring of a substantial amount of this region. The blurring is distinct from the broadening of the mixing zone; i.e., part of the broadening is well-resolved and part is blurred. The blurring suggests that the refractive index gradients are so steep that ray-crossing occurs before the shadowgraphic system's probe beam reaches the film, which is only a few mm from the window.

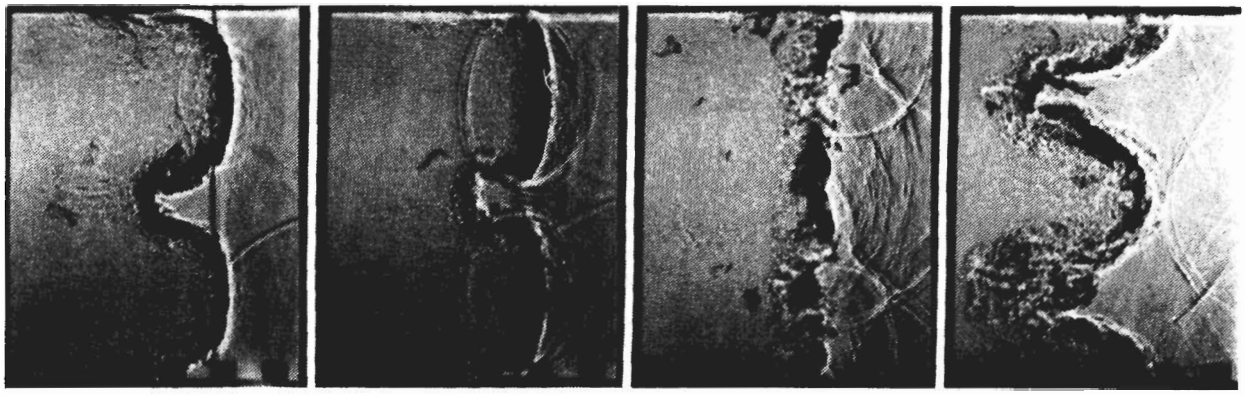

A ***B*** ***C*** ***D***

Figure 2. These four flash shadowgraphs, recorded on different events, show the evolution of a re-shocked interface. The interface was initially accelerated by a shock wave moving from air on the left toward SF_6 on the right side of the corrugated interface. ***A:*** The shock wave reflected from the endwall is beginning to compress the interfacial region, which had grown into nonlinear (i.e., spike-and-bubble) appearance. The reflected shock is moving right to left. The reflected rarefaction wave (moving back into the SF_6) has begun at the two regions of contact between the shock front and the interface. ***B:*** Later, part of the reflected shock wave is transmitted into the air where it accelerates, but the portion of the shock (at the center) that is still in the SF_6 is undergoing a complex interaction with the shock wave refracted into the SF_6 and the rarefaction. ***C:*** Later, the interface appears to have stabilized, but it is really inverting. At this moment the amplitude is quite small. ***D:*** Still later, the mean profile of the interface inverts phase and grows in amplitude, as expected by the Richtmyer-Meshkov instability. The profile appears much broader because of mixing of gases and wall effects (i.e., the interaction between the boundary layer and the reflected shock). The shock wave transmitted into the air is out of view on the left.

Interpretations

The results of the singly shocked interface are consistent with Meshkov's previous experiment. The measured growth rates stated above are within experimental uncertainties of each other. However, both sets of data are significantly less than the growth rate predicted from Eq. 1. The source of this difference between experiment and theory is unknown, although strength effects of the membrane are suspected.

We interpret the qualitative features of the re-shock experiments in terms of two superposed velocity fields, the mean-flow field and the fluctuations. If we assume that the mean position of the interface is determined by the mean-flow field,

then this field appears to undergo the "heavy-to-light" RM instability, as expected. The fluctuating field is manifest as broadening the interfacial region. The broadening is observed to increase following the re-shock, as seen clearly in Figs. 2C and 2D. However, in those regions where we expect the vorticity generation to be greatest, i.e., where the angle between density gradient and pressure gradient is greatest, we fail to observe substantially greater broadening. Since the broadening appears to be independent of the local angle between shock front and interface, the vorticity generated by the re-shock does not seem to be manifest locally as increased broadening. It appears that such vorticity is either associated primarily with the mean-flow field or it diffuses rapidly in the broadened profile.

The observed mixing zone consists of: (1) the bulk mixing of gases, (2) the boundary layer (i.e., "wall effect"), and (3) membrane fragments. Related experiments[9] suggest that the boundary layer's signature may dominate, so interpretation of mixing-zone growth cannot be made until further experiments distinguish between bulk and wall effects. If further experiments determine that we are indeed observing the mixing zone, then the re-shock data, such as growth of the mixing width, can be interpreted as a measure of the effects of shock-wave interaction with pre-existing turbulence and/or with membrane fragments.

The presence of the rarefaction wave reflected back into the SF_6 demonstrates that the shock impedance of the membrane is not influencing the mean-flow field. However, membrane fragments may be influencing the mixing. The mottling of the rarefaction may be a signature of the length scales present in the mix region.

Conclusions

Our observations of singly shocked interfaces between different gases are consistent with the previous work of Meshkov, but the difference between experimental data and Eq. 1 persists. Also, the persistence of the linear growth rate into the regime of visual nonlinearity is unexplained. The phenomena of a re-shocked interface show simultaneous RM growth and broadening. Strength effects of the membrane on the mean-flow velocity field are negligible, although inertial effects on the broadening may persist. Structure in the mixing region and on the reflected rarefaction may be useful in characterizing the onset of turbulent mixing if further experiments determine that the observed broadening is not a wall effect.

Acknowledgements

We gratefully acknowledge useful discussions and encouragement from John Shaner, Frank Harlow, and Brad Sturtevant, and the technical assistance of Clinton Findley, Vivian Gurule, and Dan Bannerman. This work has been supported by the US Department of Energy.

References

1. R. D. Richtmyer, Commun. Pure Appl. Math. **13**, 297 (1960).

2. Meshkov, Izv. Akad. Nauk. SSSR Mekh. Zhidk. Gaza **4**, 151 (1969) [Russian: Izv. Acad. Sci. USSR Fluid Dynamics **4**, 101 (1969)].

3. A. M. Vassilenko, O. V. Buryakov, V. F. Kuropatenko, V. I. Olkhovskaya, V. P. Ratnikov, and V. G. Jakovlev, "Experimental research of gravitational instability and turbulization of flow at the noble gases interface," to appear elsewhere in these Proceedings of the International Workshop on the Physics of Compressible Turbulent Mixing, 24-27 October 1988 at Princeton.

4. Robert F. Benjamin and Joseph N. Fritz, Phys. Fluids **30**, 33 (1987).

5. V. A. Andronov, S. M. Bakhrakh, E. E. Meshkov, V. N. Mokhov, V. V. Nikiforov, A. V. Pevnitskii, and A. I. Tolshmyakov, Sov. Phys. JETP **44**, 424 (1976). [Russian: Zh. Eksp. Teor. Fiz. **71**, 806 (August 1976).]

6. V. A. Andronov, S. M. Bakhrakh, E. E. Meshkov, V. V. Nikiforov, A. V. Pevnitskii, and A. I. Tolshmyakov, Sov. Phys. Dokl. **27**, 393 (1983). [Russian: Dokl. Akad. Nauk SSSR **264** (1), 76 (1982).]

7. S. G. Zaitsev, E. V. Lazareva, V. V. Chernukha, and V. M. Belyaev, Teplofizika Vysokikh Temperatur (English translation) **23**, 435 (1985). [Russian: Teplofizika Vysokikh Temperatur **23**, 535-541 (1985).]

8. B. Sturtevant, Proceedings of the 16th International Symposium on Shock Tubes and Waves, p. 87 (Aachen, 1987).

9. Martin Brouillette and Bradford Sturtevant, "Shock induced Rayleigh-Taylor instability at a continuous interface," to appear elsewhere in these Proceedings of the International Workshop on the Physics of Compressible Turbulent Mixing, 24-27 October 1988 at Princeton; also to appear in the Proceeding of the Advances in Fluid Turbulence Conference, May 1988 at Los Alamos.

10. Model Imacon 790 streak/framing camera manufactured by Hadland Photonics, Ltd.

ANALYSIS OF SHOCK-INTERFACE AND SHOCK-TURBULENCE INTERACTIONS BY DIRECT SIMULATION AND TURBULENCE TRANSPORT MODELING

Didier Besnard and Jean-Francois Haas
Centre d'Etudes de Limeil-Valenton, BP 27,
94190, Villeneuve-St-Georges FRANCE
and
Rick Rauenzahn
Los Alamos National Laboratory, Group T-3, MS B216
Los Alamos N.M. 87545 USA

ABSTRACT:

We present three methods of analyzing shock-interface and shock-turbulence interaction: direct simulation, turbulence transport with a full Reynolds tensor, variable density transport model, and a newly developed "k-ε-ρ'^2" model. Using direct simulations performed with the 2D FCT code EAD, we discuss here the structure of the flow produced by a shock-interface interaction as well as shock-mixed region interaction, as obtained in shock-tube experiments. Boundary layer effects, a prominent feature of such experiments, are examined using the 2D ALE CAVEAT code, in which the simplified model mentioned above was implemented.

I-INTRODUCTION

Turbulence modeling has long been an indispensible tool for examining complex flows. More recently their applications have been extended to circumstances involving several compressible materials. As a result, Reynolds-stress transport closure models have evolved /1,2/. Quantitative assessment of these models in general flows is still quite limited, primarily due to their complexity and the questionable improvement in performance over that of standard "k-ε" models and their derivatives. This paper is an attempt to look at shock-interface and shock-turbulence interaction by combining the two approaches of turbulence modeling and highly resolved direct simulations.

Originally, this effort was directed at comparisons between our turbulence model, called BHR, and some direct simulations using EAD, a 2D Eulerian code /3,4/ of shocks interacting with a random, multimode interface between air and helium. BHR is derived, as most turbulence transport models, from the mean and fluctuating Euler equations for a variable density flow. Closures of higher-order correlations are accomplished in either the standard, "diffusive" modeling popularized in the 1970's, or by means of "two-field-like" closures that retain the description of directed interpenetration /4/. This latter feature is crucial to the proper treatment of the current problem of shock interface interactions since turbulence is initially absent from the problem. BHR initializes the turbulence in the flow by describing interactions of the density inhomogeneities, characterized by levels of ρ'^2 , and the mean flow presure gradient. This term, which is not modeled but emerges directly from the derivation, drives the turbulent interpenetration from a quiescent start. We propose here a new derivation, starting from BHR, of a hybrid "k-ε-ρ'^2" model that contains some of its essential features. This model is more tractable than BHR for multidimensional engineering flows. This model has been implemented in CAVEAT /5/, a 2D ALE code, and has computed shock-interface and shock-turbulence interactions generated in a prototype shock-tube experiment similar to some experiments performed at Marseille /6/. They show the crucial importance of the boundary layers developing in the shock-tube. Future calculations will be directed at precise comparisons between calculations and experimental data.

Some general concepts concerning comparison of direct simulation results, such as those from EAD, and predictions from turbulence transport modeling are discussed. These are exemplified in the analysis of a simulation of a generic shock-tube experiment /7/. We also extend our view of the EAD results presented earlier /4/ by discussing spanwise spectra of the velocity field, and their relationship to the initial definition of the interface.

II-DERIVATION OF A "k-ε-ρ'^2" MODEL

BHR furnishes a rather complete framework for studying unsteady, anisotropic turbulence. It also allows for circumstances such as instability-induced turbulence (Rayleigh-Taylor, Richtmyer-Meshkov, Kelvin-Helmholtz, referred later respectively as RT, RM, and KH).

However, its rather complex formulation makes it hard to use to simulate real flows for which the mean flow is multidimensional. For such engineering flows, we use a simplified model, that can be derived from BHR, and retains some of its most important features. In the case of constant density, this model reduces to the well-known "k-ε" model. The derivation also shows that the "k-ε" model is, in principle, only valid for "small" mean gradients, in a sense that will be detailed below (see also Besnard et Bonnefille /8/ for details). The full BHR model equations have been reported elsewhere, and we start here only with the necessary ones, which are the equations for the Reynolds stress tensor K^{ij} and its dissipation D^{ij}, the turbulent mass flux a_i, and its dissipation Da^i.

We then consider idealized circumstances for which a steady-state turbulent flow has been achieved, for which the turbulence is isotropic. There is therefore a balance between production and dissipation of turbulence. In the equations, we lump together all the terms balancing the dissipation term into a "source" term F^{ij} that evolves on the time scale of the turbulence $s/\sqrt{k}$, in which s is the turbulence length scale. We now introduce small perturbations in the flow, due to a mean velocity gradient, and an acceleration. The length scales associated with these perturbations are assumed to be much larger than s and the initial flow length scale. For sake of simplicity, we take the perturbations length scales to be both of order L, with L much larger than s. We consider these equations in a non-dimensional form, which involve the variables

$$
\begin{aligned}
t &= t_0\ t^*, \\
x_k &= L\ x_k^*, \\
K^{ik} &= \kappa\ K^{ik*}, \\
D^{ik} &= \kappa/s^2\ D^{ik*}, \\
a^i &= \alpha\sqrt{\kappa}\ a^{i*}, \\
\nabla P &= \rho_0\ g\ \nabla^* P^*, \\
\rho &= \rho_0\ \rho^*, \\
B &= \alpha^2\ \rho_0\ B^*, \\
u_i &= V\ u_i^*\ , \\
D_B &= B\ D/K\ , \qquad (1)
\end{aligned}
$$

D^{ij} and K^{ij} contracting respectively into D and K.

In Eq.(1), V is a measure of the intensity of the velocity jump which pertubates the initial flow, L is its gradient length, and g is a measure of the acceleration superimposed on the flow on the length scale

L; α measures the density fluctuations intensity. The time scale t_0 is chosen to be L/V, which is assumed to be much larger than the turbulence time scale. The resulting equations are

$$\frac{Vs}{L\sqrt{\kappa}}\frac{\partial K^{ij}}{\partial t} + \frac{Vs}{L\sqrt{\kappa}}u^k\frac{\partial K^{ij}}{\partial x_k} + \frac{Vs}{L\sqrt{\kappa}}\left(K^{ik}\nabla_k u^j + K^{jk}\nabla_k u^i\right)$$

$$= C_{k1}\sqrt{D}\left(\frac{\delta^{ij}}{3}K - K^{ij}\right) + \alpha\frac{sq}{\kappa}\frac{1}{\rho}\left(a^i\nabla_k P^{jk} + a^j\nabla_k P^{ik}\right)$$

$$+ \frac{1}{\rho}\frac{s^2}{L^2}\nabla_k\left(\alpha_k\frac{\rho K}{\sqrt{D}}\nabla_k K^{ij}\right) - C_k K^{ij}\sqrt{D} + F^{ij}{}_k\,, \qquad (2a)$$

$$\frac{Vs}{L\sqrt{\kappa}}\frac{\partial D^{ij}}{\partial t} + \frac{Vs}{L\sqrt{\kappa}}u_k\nabla^k D^{ij} + \frac{Vs}{L\sqrt{\kappa}}\frac{1}{\rho}\left(D^{ik}\nabla_k u^j + D^{jk}\nabla_k u^i\right)$$

$$= C_{D1}\sqrt{D}\left(\frac{\delta ij}{3}D - D^{ij}\right) + \alpha\frac{sq}{\kappa}\frac{1}{\rho}\left(D_a{}^i\nabla_k P^{jk} + D_a{}^j\nabla_k P^{ik}\right)$$

$$+ \frac{s^2}{L^2}\frac{1}{\rho}\nabla_k\left(\alpha_D\frac{\rho K}{\sqrt{D}}\nabla^k D^{ij}\right) - CD\sqrt{DD}^{ij} + F^{ij}{}_D, \qquad (2b)$$

$$\frac{Vs}{L\sqrt{\kappa}}\frac{\partial a^i}{\partial t} + \frac{Vs}{L\sqrt{\kappa}}u_k\nabla^k a^i + \frac{s}{\alpha L}K^{ik}\frac{1}{\rho}\nabla_k\rho - \alpha\frac{s}{L}\nabla_k a^i a^k$$

$$- \alpha\frac{s}{L}a^k\nabla_k a^i + \frac{Vs}{L\sqrt{\kappa}}a^k\nabla_k u^i = \frac{s^2}{L^2}\frac{1}{\rho}\nabla_k\left(\alpha_a\,\rho\,\frac{K}{\sqrt{D}}\nabla^k a^i\right)$$

$$+ \alpha\frac{qs}{\kappa}B\frac{1}{\rho^2}\nabla_k P^{ik} - C_a\sqrt{D}\,a^i, \qquad (2c)$$

$$\frac{Vs}{L\sqrt{\kappa}}\frac{\partial D_a{}^i}{\partial t} + \frac{Vs}{L\sqrt{\kappa}}u_k\nabla^k D_a{}^i + C_{Da1}\frac{s}{\alpha L}D^{ik}\frac{1}{\rho}\nabla_k\rho$$

$$= \frac{s^2}{L^2}\frac{1}{\rho}\nabla_k\left(\alpha_{Da}\,\rho\,\frac{K}{\sqrt{D}}\nabla^k D_a{}^i\right) - \frac{Vs}{L\sqrt{\kappa}}D_a{}^k\nabla_k u$$

$$+ C_{Da2} \frac{\alpha g s}{\kappa} \frac{BD}{\rho^2 K} \nabla_k P^{ik} - C_{Da}\, D_a{}^i \sqrt{D} \,, \qquad (2d)$$

where we have dropped the *'s for convenience.

In these equations, three main non-dimensional parameters appear: the first one is the ratio of the turbulence length scale s to the hydrodynamic length scale L associated with the mean velocity gradient perturbing the flow; it can be clearly identified as the Knudsen number of the turbulence Kn_s, s describing a mean-free-path for the colliding eddies. The second one is $Vs/L\sqrt{\kappa}$, that describes the relative strength of the perturbative shear and the internal shear due to eddies rubbing against each other (it could be rewritten as the product of $Kn_s{}^2$ by a Reynolds number based on the perturbation scales L and V, and the turbulent viscosity $s\sqrt{\kappa}$). The third one is sg/κ, which can be interpreted as the Richardson number Ri_s of the turbulence, that compares the relative intensities of the velocity created by the acceleration g and the shear velocity in the direction of this acceleration (here, it is the shear created at scale s).

We want to obtain an approximation for Eqs.(2a-d) that accounts for both shear and acceleration effect. To do so, we assume that Kn_s is small. The relative intensity of the perturbative acceleration, Ri_s is assumed to be comparable to Kn_s, in order to simplify the expansion in terms of the small parameter Kn_s; we also assume that $Vs/L\sqrt{\kappa}$ is comparable to Kn_s, which implies that $V/\sqrt{\kappa}$ is not greater than 1, and that the parameter α is of order 0 with respect to Kn_s.
We now expand K^{ij}, D^{ij}, a^i, and Da^i in terms of Kn_s, and denote, for each of the four variables, the two first terms in the expansion by using the subscripts 0 and 1.

To the lowest order, both $K^{ij}{}_0$ and $D^{ij}{}_0$ are not affected by the perturbations, as expected. The same result is true for $a^i{}_0$ and $Da^i{}_0$, which stay at their zero initial value.

To the next highest order, we can solve directly for $a^i{}_1$, $Da^i{}_1$, and $D^{ij}{}_1$, and obtain

$$a^i{}_1 = \frac{1}{C_a \rho \sqrt{D_0}} \left(- \frac{1}{\alpha} K^{ik}{}_0 \nabla_k \rho + \alpha \frac{gL}{\kappa} \frac{B}{\rho} \nabla_k P^{ik} \right) \qquad (3a)$$

$$Da^i{}_1 = \frac{1}{C_{Da} \rho \sqrt{D_0}} \left(- \frac{C_{Da1}}{\alpha} D^{ik}{}_0 \nabla_k \rho + C_{Da2}\, \alpha \frac{gL}{\kappa} \frac{BD}{\rho K} \nabla_k P^{ik} \right) \qquad (3b)$$

$$D^{ij}{}_1 = - \frac{1}{C_D+C_{D1}} \frac{\sqrt{D_0}}{3} \frac{V}{\sqrt{\kappa}} \left(\frac{4}{9} \frac{\delta^{ij}}{C_D} \left(C_{D1} - \frac{C_D}{2} \right) \nabla_m u^m + \nabla_i u^j + \nabla_j u^i \right) \qquad (3c)$$

Inserting the expression ontained for $D^{ij}{}_1$ in the first order equation for $K^{ij}{}_1$, we obtain that

$$K^{ij}{}_1 = - \frac{1}{C_K+C_{K1}} \frac{K_0}{3\sqrt{D_0}} \frac{V}{\sqrt{\kappa}} \; X$$
$$\left(\nabla^i u^j + \nabla^j u^i + \frac{2}{3} \left(\frac{C_{K1}}{C_K} \left(1 - \frac{C_K}{3C_D} \right) - \frac{C_K}{3C_D} \right) \nabla^m u^m \, \delta^{ij} \right) \qquad (3d)$$

Keeping now the lowest order terms for respectively the isotropic and anisotropic parts of the Reynolds tensor K_{ij}, we obtain the well-known Boussinesq approximation, when the result is restricted to divergence free flows.

Next, using the approximations (3a-d), together with the definitions

$$k = K/2 \; ,$$
$$\varepsilon = C_k K\sqrt{D}/2, \qquad (4)$$

we obtain a "k-ε" model. However, the above approximations were derived under the assumption that the mean gradients perturbing the flow were small. When applying the model to more demanding circumstances, we must introduce some additional safeguards. To do so, we recognize that any diagonal component of the Reynolds stress, and the corresponding dissipation stress must remain positive and smaller than the trace of the tensor itself. This results in a constraint on the ratio k/ε, which reads

$$k/\varepsilon < \text{Min } (\lambda_1,\lambda_2,\lambda_3,\lambda_4,\lambda_5,\lambda_6),$$

with

$$\lambda_i = \text{Max } (\lambda \geq 0 \; , \; 0 \leq 2/3 + (\lambda - 1/3) S_k{}^{ii}/S_k{}^{jj} \leq 1) \; , \; i=1,2,3 \; ,$$
$$\lambda_{i+3} = \text{Max } (\lambda \geq 0 \; , \; 0 \leq 2/3 + (\lambda - 1/3) S_\varepsilon{}^{ii}/S_\varepsilon{}^{jj} \leq 1) \; , \; i=1,2,3 \; ,$$
$$S_k{}^{ij} = Kn_s \; K^{ij}{}_1{}^{(-)} \; ,$$
$$S_\varepsilon{}^{ij} = \frac{\varepsilon}{k} S_k{}^{ij} + \frac{C_K{}^2 k^2}{2\varepsilon} S_D{}^{ij},$$
$$S_D{}^{ij} = Kn_s \; D^{ij}{}_1{}^{(-)} \; , \qquad (5)$$

where (-) indicates that the terms are now expressed in terms of the dimensional variables (we use now k and ε instead of K and D).

Considering now the case of Rayleigh-Taylor instability induced turbulence, we must enforce the fact that no turbulence is ever created in the stable case, whenever the initial interface is nearly in the linear regime (i.e. small amplitude to wavelength ratio). To show this, we consider circumstances when the turbulence is RTI driven, and keep only the driving terms in K^{ij} and a^i equations. Differentiating Eq.(2a) with respect to time , and using Eq.(2b), we obtain that K^{mm} shows no growth in the stable case. We therefore truncate the density gradient terms to zero in Eqs.(3a) and (3b), whenever stability is achieved. In the unstable case we retain only part of the exact solution, neglecting its exponentially vanishing part. This should not be to worrisome, as long as we consider circumstances that do not depend strongly on initial conditions, such as self-similar, fully developed turbulence regimes. The resulting equations read

$$\frac{\partial k}{\partial t} + 2\nabla_m u_l \; S_k{}^{ml} = \frac{1}{\rho} A_k{}^m \; \nabla_l P_m{}^l - \varepsilon + \nabla_l \left(2 \; \alpha_k C_K \; \rho \; \frac{k^2}{\varepsilon} \; \nabla^l k \right) ,$$

$$\frac{\partial \varepsilon}{\partial t} + \nabla_m u_l \; S_\varepsilon{}^{ml} = \frac{1}{\rho} A_\varepsilon{}^m \; \nabla_l P_m{}^l - \left(1 + \frac{C_D}{2C_K} \right) \frac{\varepsilon^2}{k} + \nabla_l \left(2 \; \alpha_k C_K \; \rho \; \frac{k^2}{\varepsilon} \; \nabla^l \varepsilon \right) ,$$

with

$$A_k{}^i = \frac{Kn_s C_K k}{C_a \varepsilon} \left(- \left(\frac{2}{3} \frac{k}{\rho} \; \delta^{il} \; \nabla_l \rho \right)^{<} + \frac{B}{\rho^2} \; \nabla_l P^{il} \right) ,$$

$$A_D{}^i = \frac{Kn_s}{C_{Da} C_K k} \left(- \left(\frac{2}{3} \; C_{Da1} \; \delta^{il} \; \frac{\varepsilon}{\rho} \; \nabla_l \rho \right)^{<} + C_{Da2} \; \frac{B\varepsilon}{2C_K \rho^2 k^2} \; \nabla_l P^{il} \right) ,$$

$$A_\varepsilon{}^i = \frac{\varepsilon}{k} A_k{}^i + \frac{C_K{}^2 k^2}{2\varepsilon} \; A_D{}^i \; , \qquad (6)$$

where $<$ indicates that the bracketed expression is truncated to zero if $\nabla_l \rho \nabla_k P^{lk}$ is positive.

III-2D DIRECT SIMULATIONS OF SHOCK-INTERFACE INTERACTION

1-Description of the numerical experiments

By performing high resolution calculations, we are able to extract very useful information usually not attainable by experiments, such as

statistical correlations predicted by turbulence transport models. To do so in the RMIM and RTIM cases, as an example, the interface between two materials is defined by a sum of cosines waves which amplitudes are sampled from a gaussian probability distribution function. The mesh is chosen such that the smallest wavelength and the interface rms are described by a large enough number of cells (typically 25 and 10, respectively), and the largest mode is contained in the calculation box. The analysis of the results relies heavily on a number of diagnostics generated by a post-processor code to EAD. It includes maps of pressure, density, velocity in the interface reference frame, as well as vorticity and compression. In addition, Schlieren and shadowgraphs are generated, that can be compared directly with experiments. A detailed study of the flow structure is provided by the pseudo-spectral decomposition of the flow, allowing for the description of mode coupling in the mixing region. The other diagnostics include all the statistical correlations involved in the transport model BHR. From these 1D profiles, we obtain a time evolution of integral quantities such as the interpenetration length (MZT), and the total fluctuating energy contained in the mixing zone (ZFKE) and across the computation grid (TFKE). All the results presented here are for the same two materials, respectively air (shocked first), and helium (shocked second); the shock Mach number in air is 1.3, with one exception at 1.2.

2-Averaging procedure

A number of comments must be made concerning the relationship of the 1D diagnostics to the correlations obtained through the BHR model. First, the interfaces that are chosen here are not fully random. Because we want to resolve each initial mode in the interface, we consider wavelengths that are harmonics of 2h, where h is the vertical size of the box. We impose mirror conditions at the top and the bottom of the computation box. The largest wave length described here is .4h, about 20 percent of the total box height. This means that, at late times in the calculation, one should notice the effect of this particular wavelength that grows more slowly than the other ones (convergence of mushrooms at that scale). Eventually through nonlinear coupling, even larger ones appear.

Second, there are several possible averaging techniques. For our problem, the simplest possible is to take a spanwise strip average across the mesh. This corresponds to an ensemble average over all

possible phase shifts for a given set of cosine functions defining one interface, if the interface were to be infinitely long. Its length is finite, but the hope is that its main statistical features are present in this particular segment. All the transverse fluctuations are removed by this procedure. If we now want to obtain results that do not depend upon the detailed structure of the interface but rather upon a statistical quantity such as the interface variance, we would, in principle, average our results on all possible interfaces of a given variance. Translated in terms of spatial average, this means we would average streamwise on a thickness nearly equal the interface variance. Therefore, any diagnostic obtained from horizontal integration across the mixing zone, such as the jump of the fluctuating kinetic energy due to a shock-interface interaction, or the mixing zone thickness (MZT), (both in RT and RM cases) gives information that is somewhat independent of the detailed shape of the interface. However, such an average (which would be here on about 10 cells streamwise) smooths out all details on any scale smaller that the interface variance. No structure smaller than the interface rms can be studied in terms of statistics related to the rms. As an example, outside the interface region, the shock is only a few cells wide (3 or 4 for this FCT code). However, we can restrict ourselves to the sub-ensemble consisting of, for a given set of wavelengths and amplitudes, the realizations produced by vertical phase shifts. This is consistent with a 1-cell vertical strip averaging procedure. The 1D statistical model we use here is based on averages over an ensemble of realizations having the same initial 1D profiles obtained by strip averaging. This ensemble is much richer than the phase-shift invariant ensemble used in the 2D code. We still compare here our model in its 1D version with the averaged 2D results obtained with EAD, but we make sure that its initialization uses the actual 2D interface to get the 1D initial profiles through the same average than for extracting diagnostics from the 2D results. The additional constraint is that both the 2D code and the 1D model must use the same horizontal mesh.

3-Convergence of the calculations and numerical diagnostics:

To have any confidence into our numerical results, we must check that all the large scale features of the flow are well resolved. To do so, we ran three different calculations, with the same initial interface (referred to as case K), but with respectively a mesh size of 0.01,

0.0125, and 0.02 cm. Notice that, if the initial interface is rather well resolved for all three cases, this is not the case for its rms, physically 1/4 of the initial thickness. In the RM case, because the shock is going here from heavy to light, all the modes on the interface undergo a phase reversal leading at peak contraction to a thickness (of about five cells in the coarsest case) that may not be well resolved. Therefore, we cannot expect a good result in the third case for large times.

Figure 1 shows the interface region in each of these cases, at 60μs and 180μs, well beyond the shock passage (the curved line just to the left of the interface is an artifact).

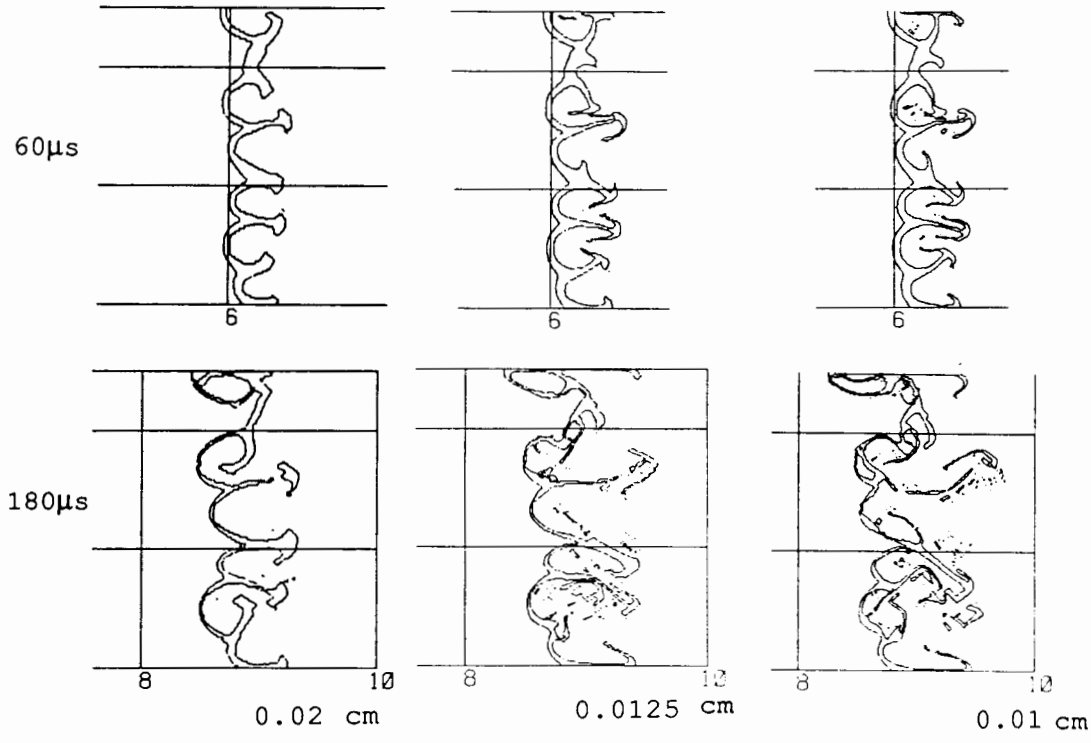

Figure 1: Interface at 60μs and 180μs, for three cell sizes.

At 60μs, the large scale structures are similar on the two finer grids. They are still rather well indicated on the coarse mesh, but one can notice significant differences with the two other interfaces at this early time. The mixing zone thicknesses are respectively .66, .64, and .57 cm as measured from the interface plots. These measures have an

error bar of about one cell. If we now calculate the thickness associated to a departure of 0.5% of the mass concentration from 0 or 1 (MZT), we get the values .66, .62, and .54 cm respectively. Notice here that ,due to a ratio of 1 to 7.3 between the shocked densities of the two gases, MZT starts when 9 (respectively 7 and 4) helium filled cells (on the average) are encountered in the strip average on the air side. In contrast, well before an amount corresponding to a single cell of air is detected on the helium side, the concentration threshold is reached. Taking now into account the highly different morphologies of the bubbles and spikes, these numbers indicate that the uncertainty on the location of the mixing zone is about 1-2 cells on the air (bubble) side and 1 cell on the helium (spike) side. As we currently use MZT for estimating integrated quantities across the mixing layer, this shows there can be an uncertainty on the results such as the fluctuating kinetic energy at minimum MZT.

There are also inherent uncertainties due the numerical scheme itself. First, the smoothing of the shock on 3-4 cells induces uncertainty in its position and the timing of its interaction with the different modes in the interface, which do not have the same amplitude. Secondly, the interface treatment introduces another uncertainty of the order of 1-2 cells (SLIC prevents excessive diffusion by retaining a given material until it has filled the entire cell). If we estimate the absolute error to be 4 cells, we can then put error bars on the MZT (as an example), to get respectively .66±.04, .62±.05, and .54±.08 cm . If we test now the minimum value of MZT (in time, coresponding to peak contraction of the layer), we obtain respectively .14±.04, .13±.05, and .1±.08 cm, which shows that the results obtained from that last case must be considered with the greatest caution. These numerical errors affect such sensitive results as the quantity of fluctuating kinetic energy created by the shock-interface interaction. A linear argument probably does not hold here because of the nonlinear interactions between the different modes in the interface and the shock. When we plot the values of $TFKE_{max}$ (this peak value is attained at about the time the shock leaves the interface) and $TFKE_{60\mu s}$ as a function of the mesh size, and take a linear extrapolation from the three points given by the calculation, we obtain an extrapolated value roughly 20% larger than the one obtained with the finest mesh we used. This is connected to the uncertainty of the minimum value of MZT; this is expected, because this smallest value is attained during the actual shock-interface interaction, when the shock deformation is the most closely related to

the interface shape.

At 180μs (Figure 1), the three results are quite different:the amount of energy created by the shock in the interface region decrases with the number of cells, inducing less additional mixing through nonlinear turbulent diffusion and stronger numerical dissipation of vorticity. This may lead to significant errors: the three bottom spikes, do not seem to converge for the coarsest mesh, which they do in the two other runs.

4-Estimate of shock-induced fluctuating kinetic energy creation

Our simulations furnish the amount of FKE created during the shock-interface interaction, both in the mixing zone and in the entire computation box. These results can be used to normalize a theoretical estimate /9/, that is based on a statistical average, over all modes contained in the interface, of the single-mode, linear result of Richtmyer. The comparison between theory and simulation was performed previously /4/, and we give here only an update that takes into account our above comments.

The theoretical estimate reads

$$FKE = \beta \langle \eta^2 \rangle^{1/2} U^2 At (\rho_{0+}-\rho_{0-})/4, \qquad (7)$$

where $\langle \eta 2 \rangle^{1/2}$ is the interface variance, β the factor introduced by the cut-off for high wavenumbers, U the jump in velocity, At the Atwood number, and ρ_{0+}, ρ_{0-} the densities of the two materials after the shock passage.

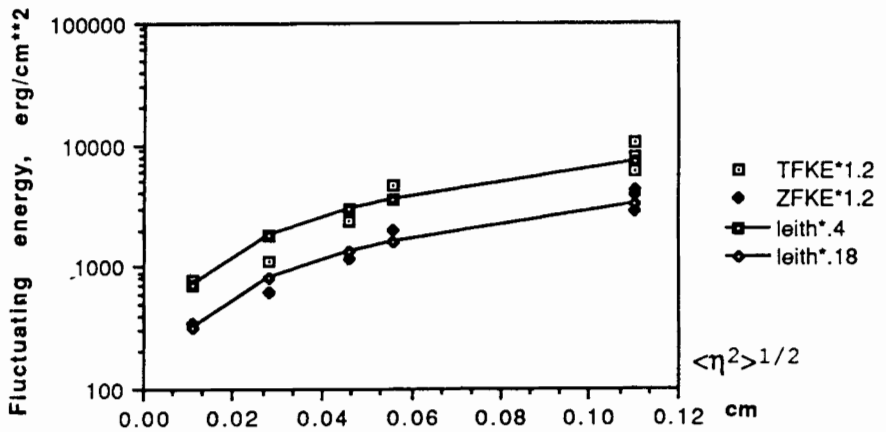

Figure 2: Fluctuating kinetic energy at peak value vs $\langle \eta^2 \rangle^{1/2}$.

The choice of the cut-off (i.e. β) is difficult from theoretical arguments, and we use here the extrapolated EAD results (for a mesh size going to zero) for guidance. Figure 2 indicates (following /9/) that the cut-off wavelength appears to be around $1.25\langle\eta^2\rangle^{1/2}$ or $.5\langle\eta^2\rangle^{1/2}$ (β being respectively .4 and .18), depending of the choice of TFKE or ZFKE as the proper value to be compared with the estimate /9/.

5-Time evolution of TFKE, ZFKE, and MZT

We analyze here two different runs. The first one (case K) was already considered above; the second one (case L) is a simulation of a Rayleigh-Taylor instability induced mixing shock tube experiment, that can be said to describe a generic numerical experiment representative of current experiments /7/.

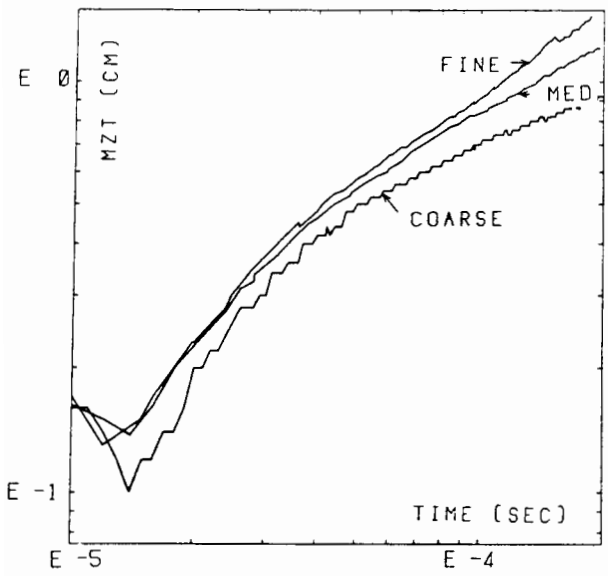

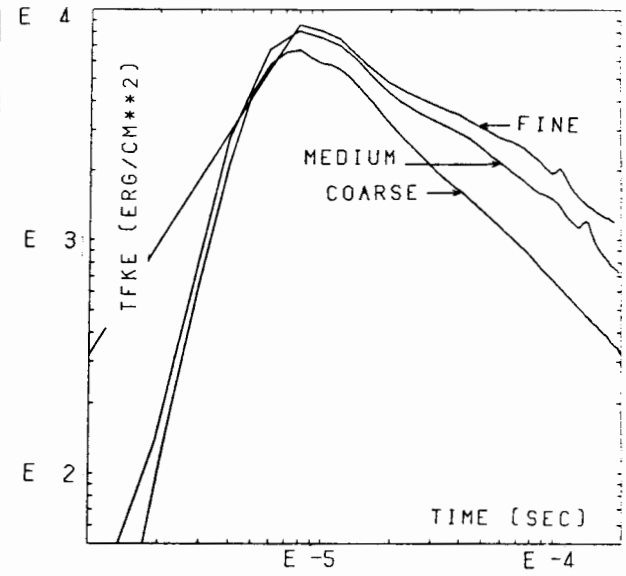

Figure 3: MZT vs time (log scale). Figure 4: TFKE vs time (log scale)

In run K, we plotted, for the three different meshes, MZT, TFKE, ZFKE, and the ratio of ZFKE to the directed energy contained in the mixing zone. They are displayed respectively on Figures 3, 4, 5 and 6. Three main phases show on these figures. The first one, lasting until the shock leaves the interface, corresponds to the inversion of the interface, as shown by a decrease of MZT on Figure 3, and the appearance of jets, evolving into vortices, corresponding to the rapid increase of

TFKE shown on Figure 4.

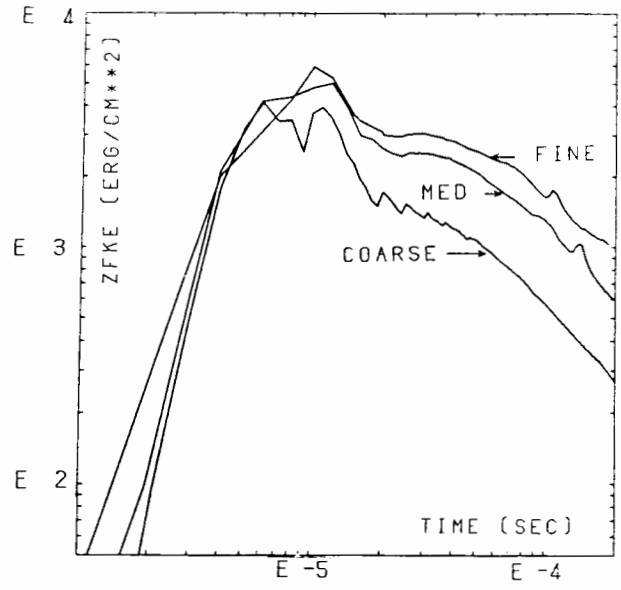

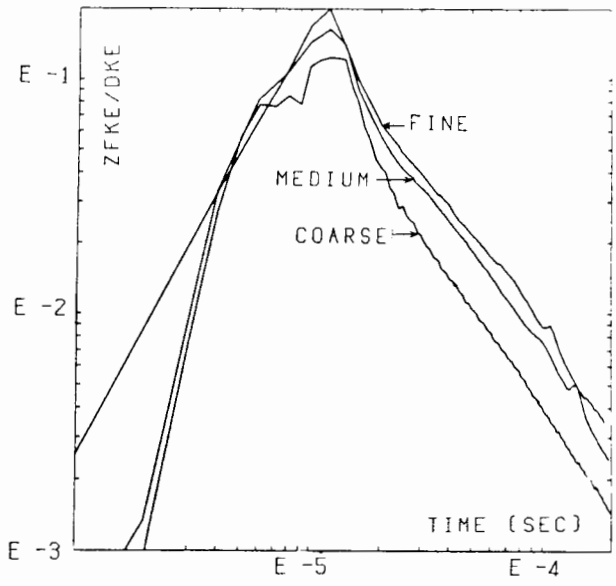

Figure 5: ZFKE vs time (log scale). Figure 6: ZFKE/DKE vs time (log).

A rapid decrease of ZFKE follows, as shown on Figure 5, that lasts until the rarefaction wave leaves the interface /4/. The last phase shows a more gentle decrease of the fluctuating kinetic energy, as shown on Figures 4 and 6. The two first phases have been somewhat examined previously /4/, and in the above section. Regarding the third phase, one is most interested to know if the behavior displayed on Figures 3-6 is universal, in terms of rate of decay of fluctuating energy, and rate of thickening of the mixing zone. This question is related to the possible existence of a self-similar regime for the spanwise averaged variables. Unfortunately, at this stage of our study, no definite answer can be given. There is first a linear contraction and expansion up to 40μs, typical of the RM process in the early phase. From Figure 3, a time power-law fit of the mixing zone thickness (after 50μs) gives an exponent that varies linearly with the cell size: .43, .6, and .7 for the coarse, medium and fine mesh respectively (linearly extrapolated for zero cell size, one gets a growth rate of about 1). The MZT time evolution may depend upon the two length scales that can be associated to the problem. The first one, Ut, is built out of the shock velocity jump U , and the second one, $E^{1/3}t^{2/3}$ /9/, out of the total fluctuating kinetic energy FKE_{max}(=E) created by the shock interface interaction, neglecting dissipation. At this point, it is not possible to decide which trend MZT follows.

In our calculations, we are certainly relatively far from a regime independent of the initial conditions. In this low Mach number regime (behind the shock), incompressible theory can be safely applied and shows that the linear development of any mode leads to a flowfield whose spatial extension is of the order of the wavelength of the perturbation. At the end of the calculation, the mixing zone thickness is of the order of 2cm (extrapolated), which is only twice the largest wavelength initially present in the interface. This largest mode is therefore still marginally in the nonlinear regime. We can then safely conclude that we are still far from a regime independant of initial conditions.

The time rates of evolution (after 50μs) of TFKE for the three cases K (Figure 4), and L are -1.07 (coarse), -.86 (medium), -.71 (fine), and -.76 respectively. Simulations K (medium) and L were performed with the same cell size, the same modes being initially present in the interface, but having different amplitudes (the initial thickness is .37 cm for case K, and .2 cm for case L).

Figure 5 gives the rate of decay of the fluctuating energy in the mixing zone, ZFKE. The rates are -1.03, -.88, -.7, and -.61 (case L). At late times, the fluctuating Reynolds tensor is not too far from isotropy in the mid-part of the mixing region, as shown on Figure 7.

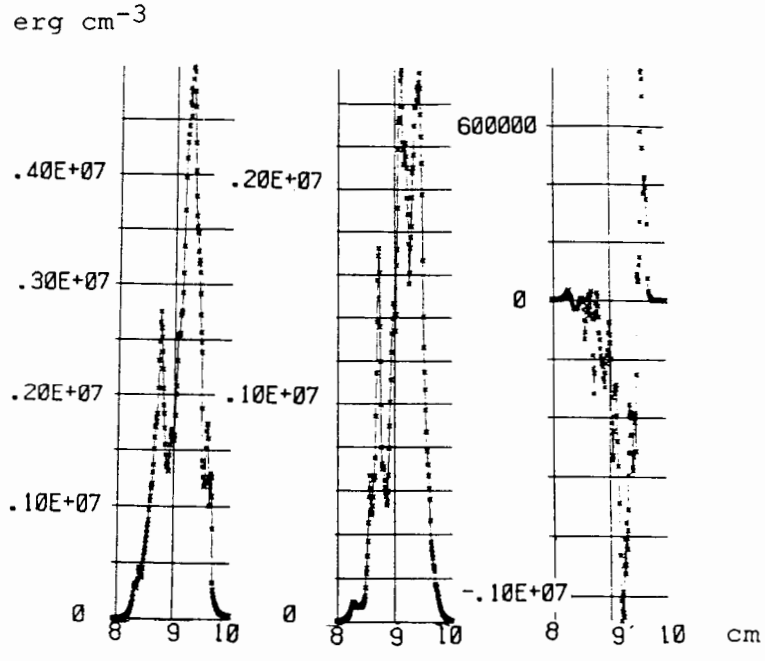

Figure 7: Diagonal components of the Reynolds stress tensor at 180μs vs space; streamwise, left; spanwise, center. Off-diagonal, right.

Assuming homogeneity, which is a rough approximation, one can try to compare the obtained results with theoretical ones on homogeneous isotropic turbulence.

Dimensional arguments in modeling show that the rate of growth m of MZT, and the rate of decay n of ZFKE, are related by m=1-n/2. This is not satisfied here; this due in part to the fact that the simulations are not in a fully self-similar regime, as noticed above, and that the fluctuating energy is not really homogeneous across the mixing zone.

6-Spectra

A full quasi-spectral decomposition is currently planned, but, at this stage of this study, we only have performed spanwise spectral decomposition of the flow (i.e. streamwise and spanwise velocities, as well as density). Much improvement is needed in term of smoothing of the results through averaging on a few subsequent time steps, or neighbouring cells. However, a flavor of the results obtained from case K, fine mesh, is given on Figures 8 to 10. We chose two characteristic times in the calculation. The first one is during the shock-interface interaction (at about 50μs), and the other one is at late times, close to the end of the calculation (at about 180μs). Figure 8 shows streamwise and spanwise velocity signals, the associated spectra, at 50μs. It indicates that the modes initially present in the interface are all excited, as expected.

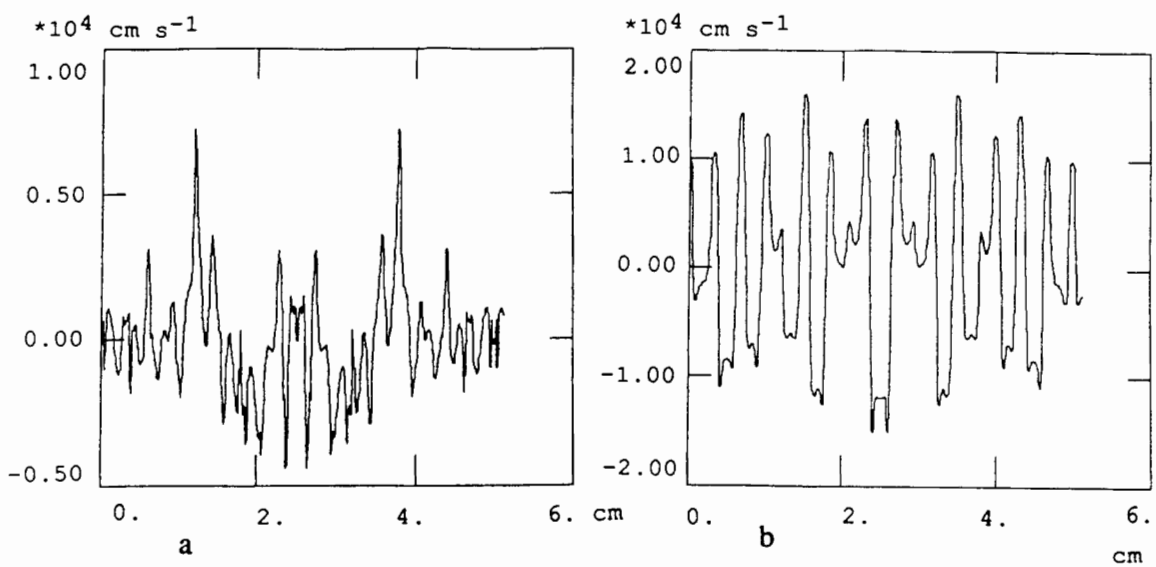

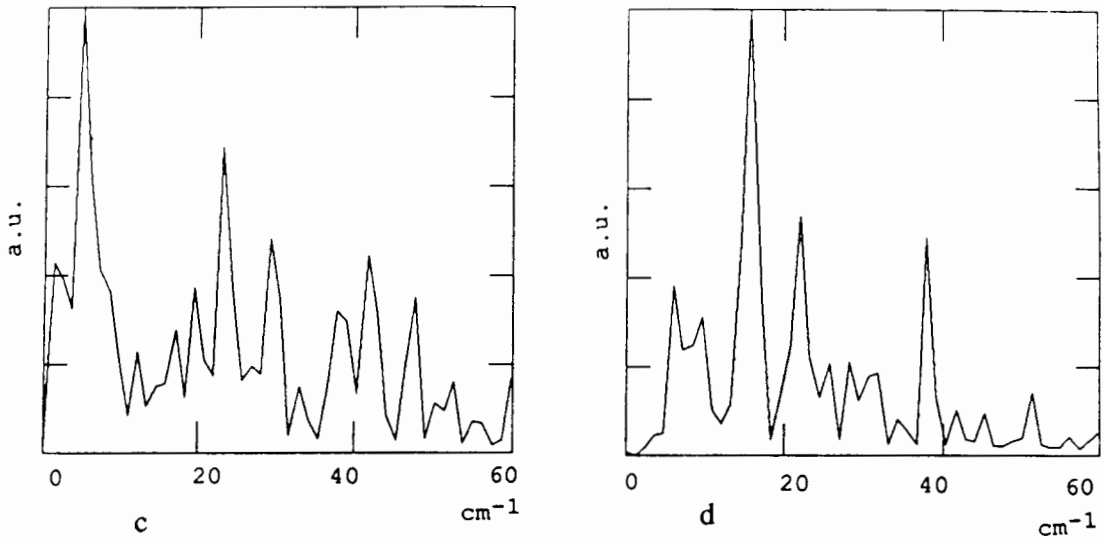

Figure 8: Streamwise (a), and spanwise (b) velocity signals vs vertical distance; corresponding spectra (c,d); t=50μs; center of the zone.

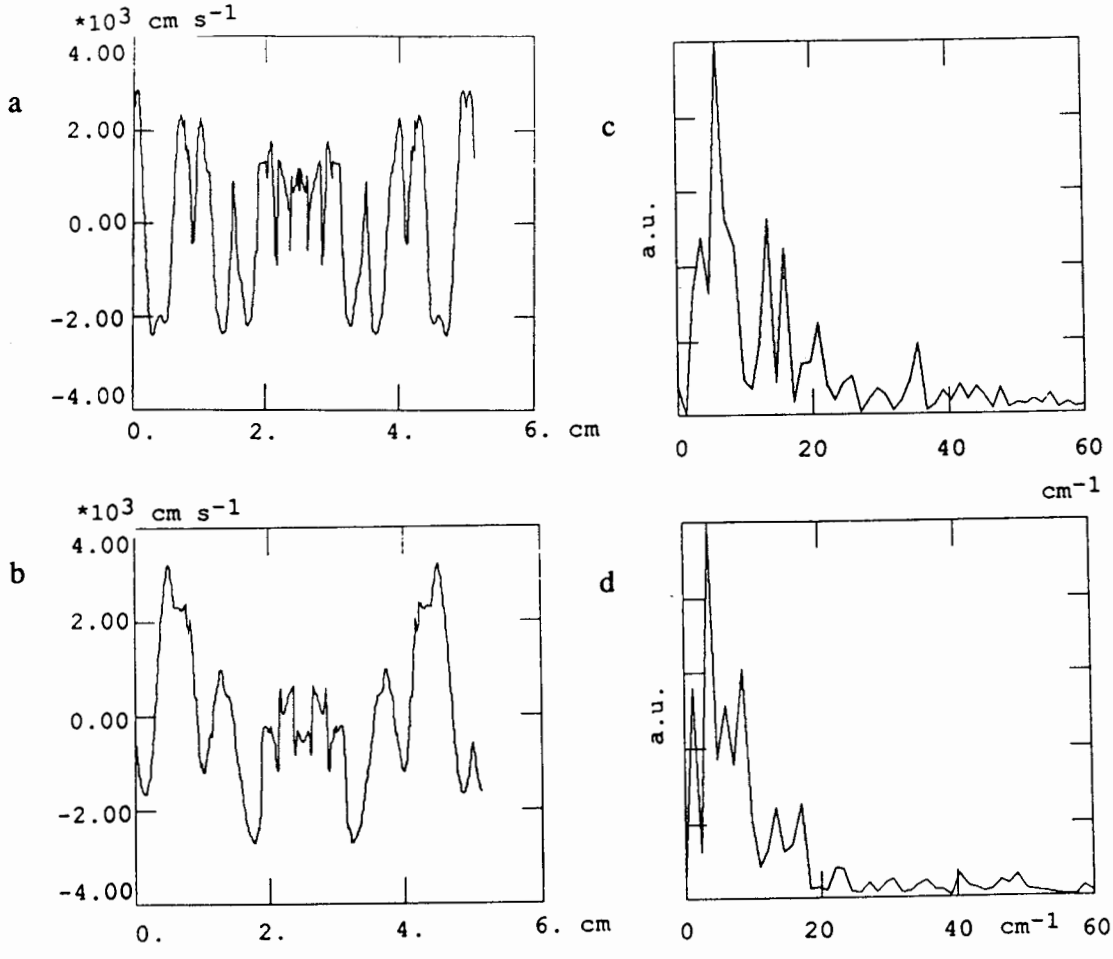

Figure 9: same as Figure 8; t=180μs.

Following the spectra with time (see for example Figure 9, showing velocity signals and spectra at 180μs, about in the middle of the mixing region), one notices a transfer of energy toward smaller wavenumbers, demonstrating what could be visually seen on pressure and density maps /4/, namely the occurrence of bubble coalescence. Further work is needed to evaluate numerically the time rate of change of each mode.

Near the edge of the mixing region, the flowfield is smoother, as shown by Figure 10. Although clearer than the other spectra, no analysis has been done yet.

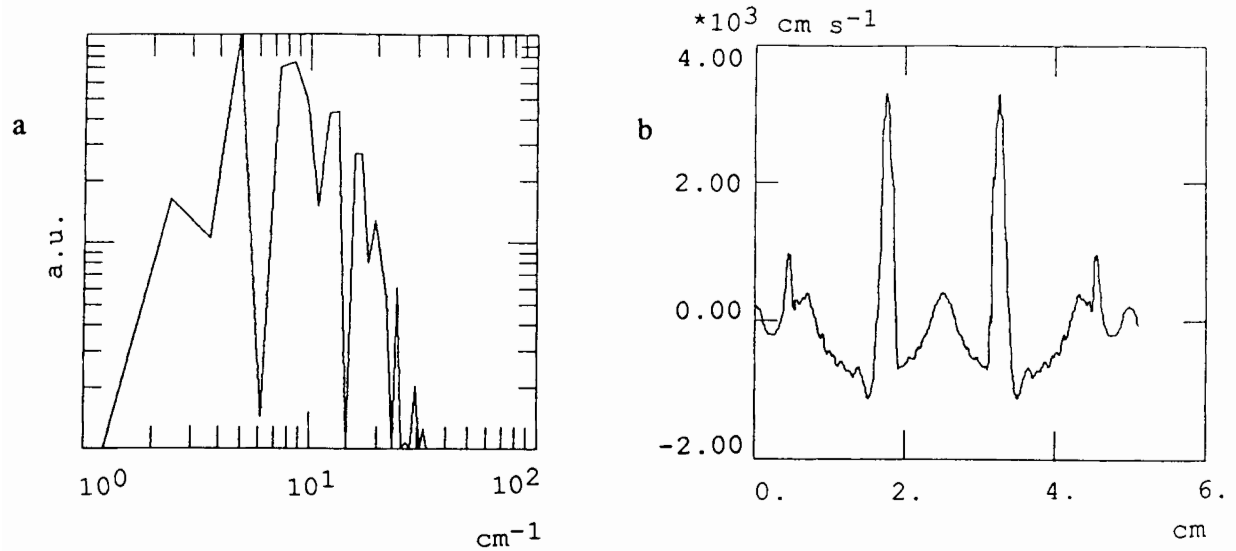

Figure 10: Streamwise velocity spectrum and signal; t=180μs; edge of the mixing zone.

7-Multiple shock-mixing zone interactions simulations

As mentioned above, run L simulates a generic shock-tube experiment of mixing zone formation between air and helium, due to the multiple reflections of a shock on the endwall of the tube /2,7/. Plates 1 and 2 display density and pressure maps from the simulation. The computation box is 2.5 cm (200 cells) high and 15 cm (1250 cells) long with a length of helium of 8.3 cm to the right of the interface. Photograph 1a shows the initial shock position about 1 cm to the left of the interface. Photograph 1b exhibits the result of RMI shape reversal with emerging spikes and bubbles at 52 μs i.e. 25 μs after the interaction. Note the density variations between the interface and the

rarefaction to the left. The spikes and bubbles are well developed on photograph 1c at 134 μs (110 μs after interaction). Their shapes appear distorted at 200 μs, i.e. 40 μs after the first reflected shock (moving to the left on photograph 1d) decelerates the interface translation. This shock, and all subsequent ones, propagate now from light to heavy and should increase interface perturbations. This appears as a stretching of the pre-existing air spikes to the right, into pure helium and the development of new spikes to the left in the bubbles. The first ones eventually pinch off, while the second ones collide on the left boundary of the bubbles. This process is illustrated on photographs 1e,f and g recorded at 300, 400 and 500 μs, respectively 30 μs after the second reflected shock and during the passage of the third and fourth reflected waves, which by now must be weak compression waves. Photograph 2a (25 μs after interaction) displays the regular pattern of the pressure field between the transmitted shock (right), and the reflected rarefaction (left) which still reflects the initial shape of the interface (indicated here by the corrugated white line). At 200 μs (photograph 2b), we observe the more random pressure field between the first reflected shock in air (left) and a wide compression wave in helium (right). Finally one distinguishes on photograph 2c the pattern of reflected wavelets during the passage of the third reflected shock through the mixing region at 400 μs.

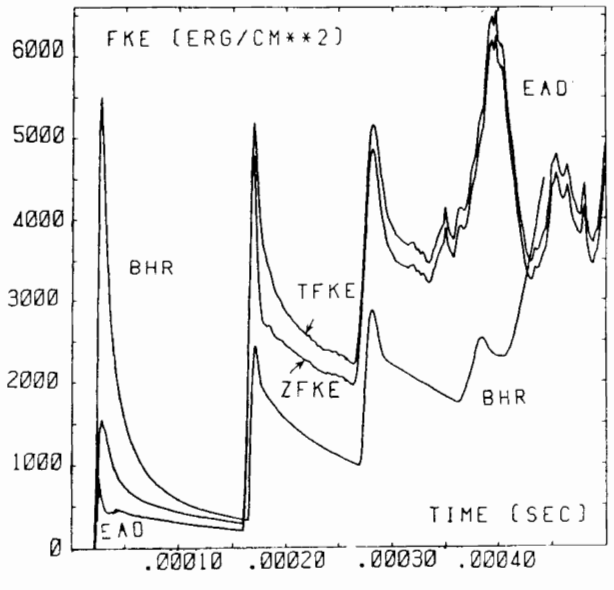

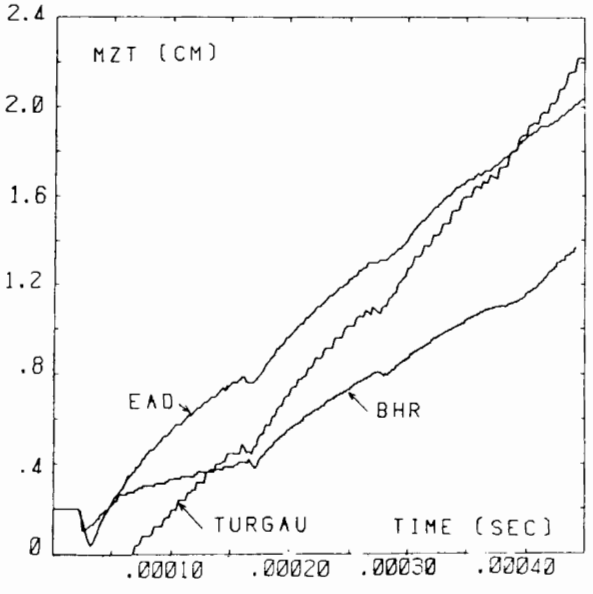

Figure 11: FKE vs time (EAD and BHR). Figure 12: MZT vs time.

We will now examine the time evolution of FKE and MZT, and their comparison with the results obtained from transport models (Figures 11 and 12). In Figure 11, the FKE value presented for BHR must be divided by two for consistency. ZFKE and TFKE approach each other at late times because all the fluctuations reside in the mixing zone. Figure 12 shows that the growth obtained with BHR is smaller than with EAD. There are two possible explanations for this: first, there is some uncertainty in the way the initial length scale is initialized in BHR. Some of EAD calculations of single shock-interface were used to define a procedure for this initialization, but there is still some concern about the universality of the rule that was obtained, especially for late time simulations. Second, BHR, is intended to model 3D situations, and EAD is only a 2D code. This may not be crucial for early times /4/, but certainly for late times, for which we expect the inverse cascade to dominate in the 2D calculation, and therefore the growth of the mixing zone thickness to be larger for EAD than for BHR. Inversely, TURGAU overestimates the growth of the mixing zone. Because this 1-equation model intends to describe fully developed turbulent flows, its formulation does not allow for the simulation of the interface inversion, and it has to be initialized after the shock has crossed the interface. This procedure is described elsewhere /10/. The explanation for its behavior is not clear at this time, but may be due to a too strong coefficient in the RT source term appearing in the evolution equation for the fluctuating energy, and to the underdeveloped nature of the flowfield. Despite these differences, it is reassuring to notice that, between the shocks, the behaviors obtained from the calculation and the two models are quite similar. The same rate of change can certainly be obtained through an optimization of the coefficients in the models, but one must keep in mind that the models have been fitted on experimental data, and that the EAD simulations are only generic experiments, because the initialization used here does not reflect the physics of the membrane break-up (which has not been documented experimentally).

IV-CAVEAT SIMULATIONS OF SHOCK-TUBE EXPERIMENTS

The k-ε-$\overline{\rho'^2}$ model described earlier has been implemented in CAVEAT, a 2-D Godunov-based ALE code used extensively at Los Alamos National Laboratory. CAVEAT also contains a second-order advection

algorithm and a mixed cell scheme. For these calculations, however, the mixedness of a cell was tracked by a concentration variable. This comparison was motivated by the recent experiments conducted by Houas et al. /6/ at Marseille, examining the effect of passing a strong shock (M = 3.7 - 4.2) in CO_2 over an interface into helium or argon (which fills initially a 1.27 meters long section of the tube). Interfacial mixing and development of boundary layers ensues along the shock tube walls, which remain at approximately constant temperature. However, the initially low pressures in the shock tube permit significant boundary layer growth to occur by the time of shock reflection from the end wall.

This experiment serves as a reasonable test of the turbulence model because it addresses inhomogeneity-induced mixing along an initially quiescent interface, development of nonequilibrium boundary layers in shocked material, and multimaterial and compressibility effects. Furthermore, extensive development of temperature and concentration diagnostics using CO_2 temperature-dependent infrared emission and absorption for these experiments have produced time- and space-resolved data for comparison purposes. As a basis for assessing the accuracy of the calculations, we expect to find qualitative agreement with the boundary layer growth rates quoted by Houas et al.

Rather than use the complete model outlined above, we have chosen to approximate $\overline{\rho'^2}$ by its two-field value /4/ throughout the mesh:

$$\overline{\rho'^2} = \alpha_1\alpha_2(\rho_1 - \rho_2)^2$$

Because turbulence is generated by the nonhomogeneity source term in Eq.(6), the values of k and ε are initially zero in these calculations. Now, the levels of turbulence produced depend on the densities of the two materials but also to some extent on mesh resolution.

As a preliminary test of the model, a Mach 3.68 shock in argon was established in a frame of reference where the shock is at rest. Since the walls of the shock tube are moving with the initial shock velocity (U_S = 1180 m/s, initial pressure = 2000 Pa), a turbulent boundary layer develops above the shock (Figure 13, horizontal velocity contours), induced by initializing $\overline{\rho'^2}$ along the tube wall to simulate effects of wall roughness.

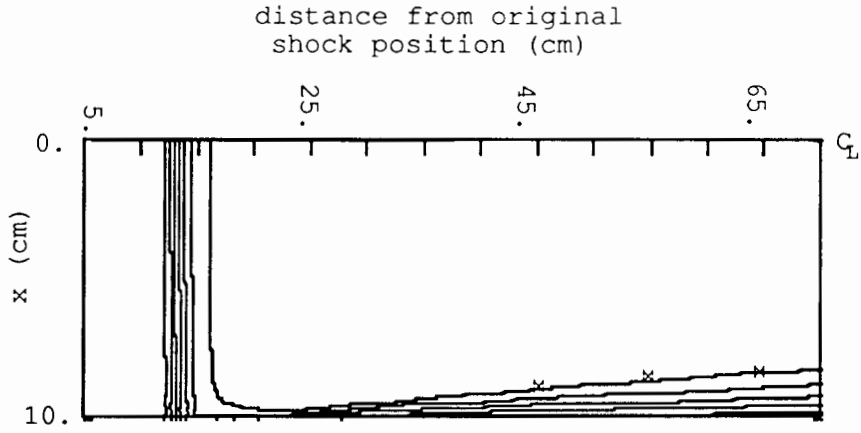

Fig. 13. Horizontal velocity contours for approximately steady-state shock in argon (M = 3.68). x's denote boundary layer thickness according to theory of Mirels /11/. Note that wall is moving with original shock speed (U_s = 1180 m/s).

The growth of the boundary layer for known freestream conditions has been reported by Mirels /11/, assuming that the boundary layer thickness is much less than the tube half-width. In the region above the shock, the boundary layer growth compares well with the x's marking the theoretical estimate (Figure 13). As a consequence of the boundary layer growth, the shock moves upward from its initial position at y = 10 cm. Thus, the shock speed in the laboratory frame would be slower than expected from one-dimensional arguments, in qualitative agreement with previous experimental observations. However, a quantitative expression for shock deceleration is not provided by Mirels /11/.

Turbulence calculations for a M = 3.7 shock in CO_2 interacting with an argon interface in a shock tube with constant temperature walls are presented next. The computational diagnostics shown are contours of mass concentration of CO_2, velocity vector plots and trajectories of the shocks and contact surface on an x-t diagram. The x-t diagram given by Ramdani /12/ from the Marseille experiments this calculation is modeled after is repeated in Figure 14a and shows two fairly straight line trajectories for the shock and the CO_2-Ar contact surface.

The x-t diagram in argon from our run exhibits some distinct differences with the experimental results (Figure 14b) and from the behavior expected in the shock tube configuration analyzed by Mirels. In the latter, it was the primary contact surface between the driver gas (here He or H_2) and the test gas that was considered.

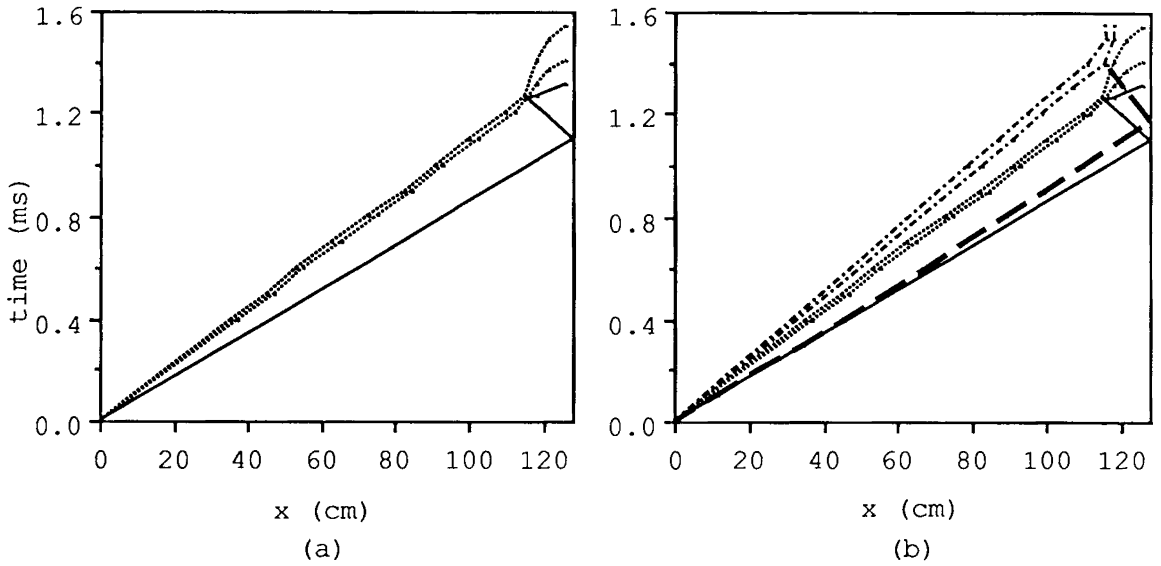

Fig. 14. x-t diagrams from Marseille shock tube experiments and simulation. Experimental contact surface (dashed line) and shock (solid line trajectories are shown on the left, and simulated shock and contact surface lines have been added on the right. Note that the experimental shock and contact surface interact earlier than predicted.

In this case, that contact surface originates about 5 meters upstream from the test section of interest. Thus, in order to replicate the Marseille experiments faithfully, we would account for the actual flow in CO_2 produced by the rupture of the primary diaphragm containing the driver gas and the ensuing boundary layer development during the 5 meter run of the shock in CO_2. Here we have chosen to ignore the departures from one-dimensionality in the CO_2 and concentrate on the behavior in argon. We initially placed the contact surface at y = 10 cm from the inlet and specified constant inflow conditions corresponding to a 3.7 Mach number shock in CO_2.

The calculated contact surface velocity maintains the value expected from simple 1-D analysis, whereas the experimentally observed contact surface immediately departs from the classical results and continues on a straight path. Conversely, the reported shock path displays no departure from its normally expected behavior, whereas the calculated shock line begins to decelerate due to the effect described above and by Mirels at about 500 to 600 μs after meeting the argon contact surface. Given that the observed compression of argon exceeds a factor of four, on average, the leakage of argon to the boundary layer must have been more substantial than we are predicting. Furthermore, the

apparently ideal shock line in the experimental data does not conform with Mirels' observations for nonideal shock tubes. Evidently, this situation is complicated by the presence of two contact surfaces and the development of a boundary layer in the CO_2 before the shock meets the second contact surface.

Since the observed shock seems to perform nearly ideally and the contact surface is traveling faster than expected right from the start, the inflow conditions used must be called into question For this case, maintaining constant inflow at the bottom of the mesh for all time is not accurate. If exact corespondence with experiments were desired, we would replicate the entire experiment, commencing with the rupture of the primary diaphragm. However, one of the major features of interest concerns the interaction of the shock and the contact surface after shock reflection from the endwall.

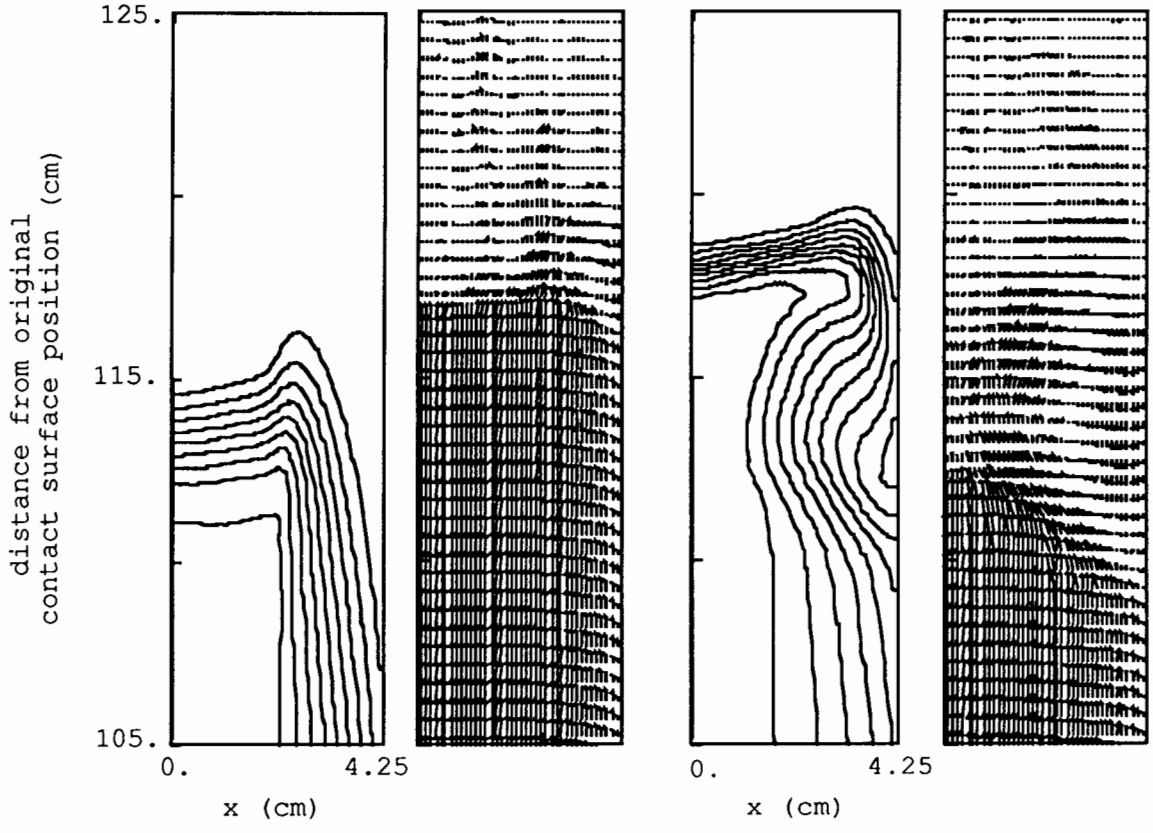

Fig. 15. Concentration contours and velocity vector plots near the end of the shock tube at 1400μs (left) and 1600μs (right) after shock-contact surface interaction. The rapid expansion of the mixing region noticed in the experiment is likely due to the swirl developing below the contact surface.

In the experiment, the contact surface thickness grows quickly and appears to fill the end of the tube. Here again, the two-dimensional nature of the flow plays a major role. As the shock returns, the calculation shows that a vortex develops along the rigid wall (Figure 15) and enhances the mixing rate over that expected in an experiment without significant boundary layer effects. The vortex induced just below the contact surface in the CO_2 causes the argon originally trapped in the boundary layer to swirl toward the centerline and enhance the mixing process greatly. Because the emission diagnostic is focused near the center of the tube, this swirl of mixed material would appear as a growth of the mixing layer. The generation of vorticity can be qualitatively explained by the interaction of the density gradient in the boundary layer and the reflected shock (the corresponding source term appears in the vorticity equation). This process is analogous to the shock-bubble interactions described by Haas and Sturtevant /13/, and discussed and simulated by Picone and Boris /14/.

Notice that the interface never reaches the end of the shock tube in the calculations, probably because we are underpredicting its speed throughout the entire simulation. In fact, the nominal interface actually is somewhat compressed by the return shock and never re-expands within the simulation time. One would not expect the interface to grow rapidly, since the post-shock Atwood number is only about -.26. Therefore, the mixing that was actually observed in the experiment is likely primarily due to two-dimensional effects and not to shock-induced interfacial mixing at the contact surface.

V-CONCLUSION

This paper presents the current state of our study of shock-interface and shock-turbulence interaction. The analysis of our direct simulation leads to a good hold of the physical processes occurring in this interaction, at least for the early phases. The late phase of fully developed mixing will require some additional calculation and modeling to further settle the question of the universality of the MZT growth, and FKE decay. Full shock tube experiments can clearly be simulated through direct simulations, as long as boundary layer effects are not crucial. In that case, one must turn to modeling, and CAVEAT calculations show, in the case of high Mach number experiments, the

crucial importance of the boundary layer treatment. Some precise comparisons of the numerical and experimental results will be presented in the near future.

References:

1-D.C. Besnard, R.M. Rauenzahn, and F.H. Harlow, in "Computational Fluid Dynamics", G. de Vahl Davis and C. Fletcher Editors, North Holland (1988), 295-304.
2-V.A. Andronov et al., Sov. Phys. Dokl., 27 (1982) 5.
3-C.Coste et al., Joint CEA-LANL Conference on hydrodynamic instabilities, Los Alamos, in: Computing Methods in Applied Science and Engineering, Glowinski and Lions, eds. (North-Holland, 1982).
4-D.C. Besnard, J.F. Haas, and R.M. Rauenzahn, Proceedings of the CNLS Workshop "Advances in Fluid Turbulence", Los Alamos, May 1988, in print.
5-F.L. Addessio et al., LA 10613-MS, Los Alamos National Laboratory report.
6-L. Houas, A. Fahrat, and R. Brun, Phys. Fluids 31, 4 (1988)
7-R. Benjamin, private communication.
8-D.C. Besnard, M. Bonnefille, "Une formulation tensorielle covariante pour le modele BHR; Derivation d'un modele simplifie "k-ε-ρ'^2", CEA Note, in preparation.
9-C.E. Leith, Lawrence Livermore National Laboratory working paper (1985).
10-D.C. Besnard et al, Shock Waves and Shock Tubes, Proceedings of the 16th ISSWST, H. Gronig, ed., (VCH Verlagsgesellshaft) 1988.
11-H. Mirels, AIAA J., 22, 8 (1983) 1042-1047. See also AIAA J., 2, 1 (1963) 84-93.
12-A. Ramdani, "Determination de grandeurs caracteristiques d'une zone de melange creee par l'interaction d'une onde de choc et d'une interface gazeuse", Thesis, University of Provence (1988).
13-J-F. Haas, and B. Sturtevant, J.F.M., 181 (1987) 41-76.
14-M. Picone, and J. Boris, J.F.M., 189 (1988) 23-51.

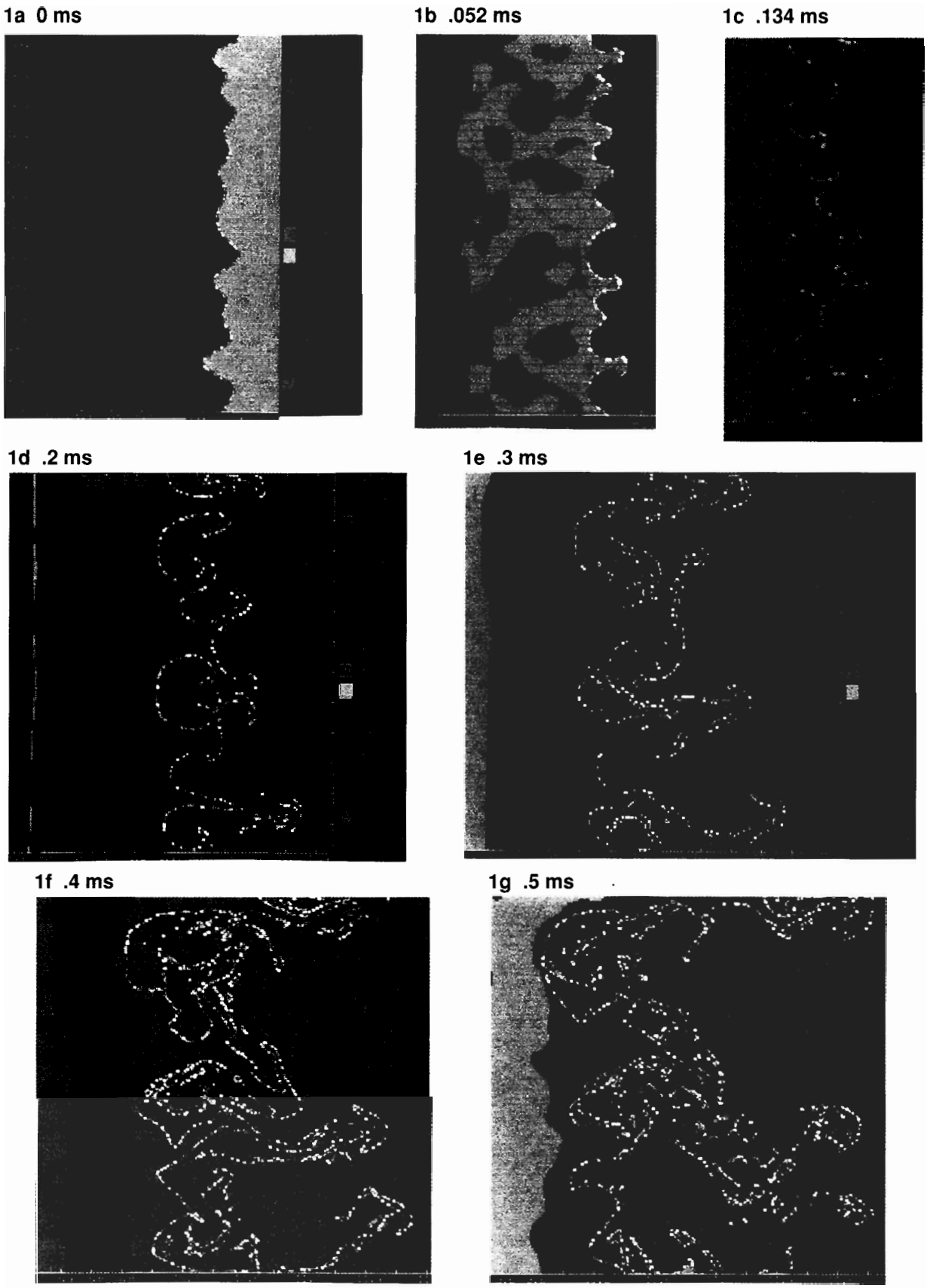

Plate 1. Density plots for the multiple interaction problem (case L).

2a .052 ms

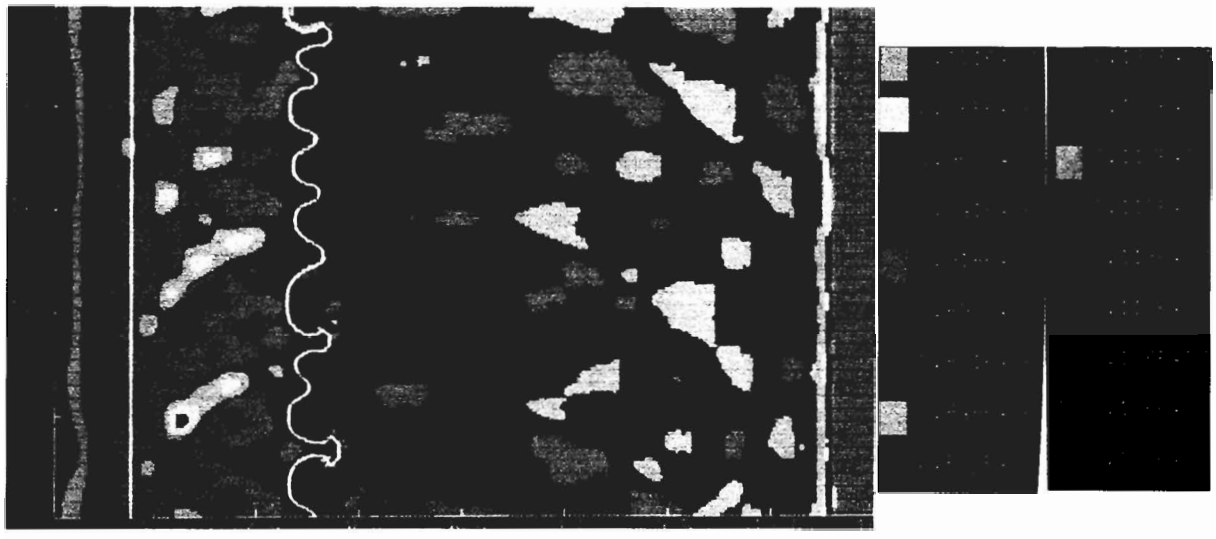

2b .2 ms

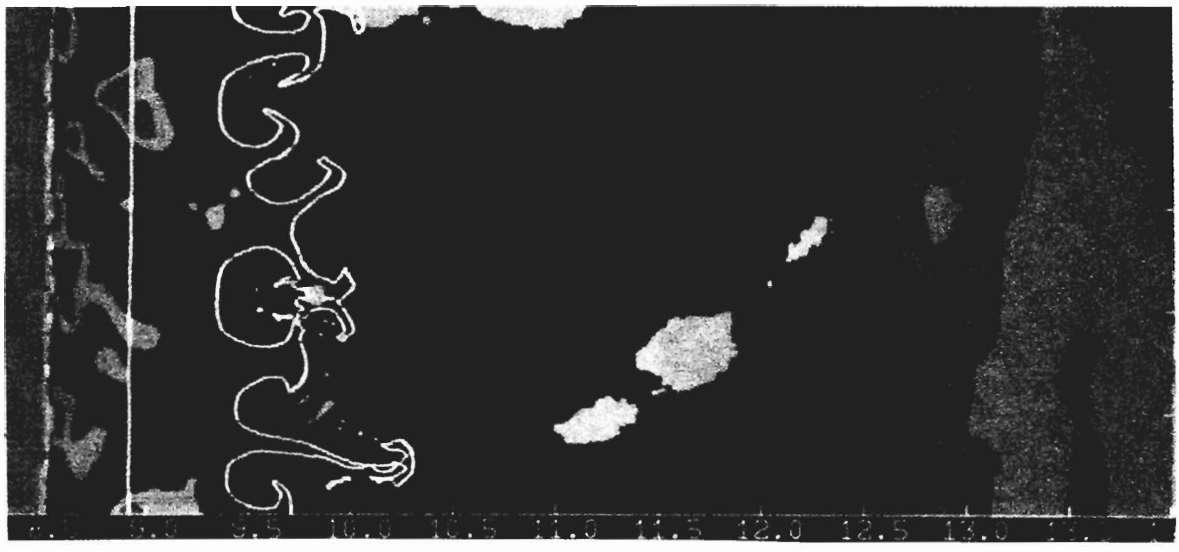

2c .4 ms

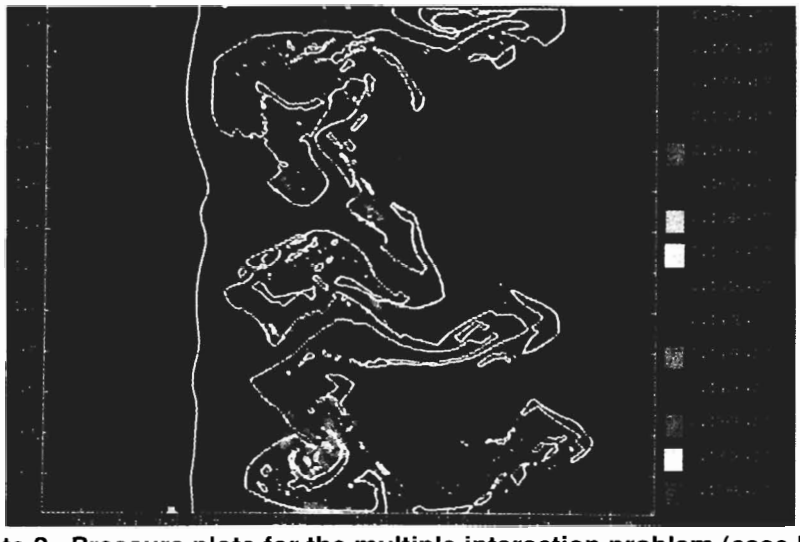

Plate 2. Pressure plots for the multiple interaction problem (case L).

Numerical Simulation of Compressible Homogeneous Turbulence

G. A. Blaisdell*, N. N. Mansour†, W. C. Reynolds*†
*Stanford University
†NASA - Ames Research Center

Direct numerical simulations of compressible decaying isotropic turbulence have been performed on a 64^3 grid. The simulations include a passive scalar with and without a mean scalar gradient. The balances for the equations of second order statistics are used to evaluate the effect of compressiblility on the turbulence. We find that the development of the fluctuations of density and of the dilatational portion of the velocity field are dependent on the initial conditions, and that the compressible terms in the balances vanish rapidly at the Reynolds numbers considered.

INTRODUCTION

Our goal is to aid the development of turbulence models for highly compressible flows by using direct numerical simulations. Much of the data required for modeling is not available experimentally. However, some of this needed data can be generated numerically by solving the time dependent compressible Navier-Stokes equations. Because such simulations can only be performed for simple flows we have chosen to study the case of homogeneous turbulence. This is an idealized case, but it is useful in developing turbulence models for two reasons. First, the statistical quantities needed in the averaged Navier-Stokes equations can be obtained directly by averaging over the computational domain. Second, homogeneous flows such as shear flow and strained flow can be thought of as basic building blocks of more complicated flows. Numerical simulation of homogenous turbulence has been useful in the development of turbulence models for incompressible flows and we believe this will be a useful approach for improving compressible turbulence models as well.

In order for the turbulence to be homogeneous the mean fields must satisfy certain restrictions. The mean density and pressure must be uniform; the mean velocity field must be linear, $\tilde{u}_i = A_{ij}(t)x_j$, with A_{ij} evolving in time according to $\dot{A}_{ij} + A_{ik}A_{kj} = 0$; and the mean passive scalar must be linear, $\tilde{\theta} = M_j(t)x_j$, with M_j obeying $\dot{M}_j + M_i A_{ij} = 0$. Some specific solutions for $A_{ij}(t)$ are given by Dang and Morchoisne [1] who studied isotropic turbulence. The case of shear flow was studied by Feiereisen [2]. In the current paper, only the case of decaying isotropic turbulence, in which $A_{ij}(t) = 0$, is considered. The scalar field, however, is solved with and without a mean gradient. The numerical procedure used to simulate the isotropic case is described next.

NUMERICAL METHOD

The Navier-Stokes equations are solved in strong conservation form using ρ, ρu_i, and ρE as the dependent variables where $E = e + \frac{1}{2}u_i u_i$ is the total energy per unit mass. An ideal gas with constant specific heats is assumed and the ratio of the specific heats, γ, is taken to be 1.4.

Viscosity is allowed to be temperature dependent and follows a power law, $\mu/\mu_0 = (T/T_0)^{0.67}$. The Prandtl number and Lewis number are assumed constant and are taken to be 0.7 and 1.0 respectively. The equations are nondimensionalized using a length scale L_0 equal to the computational box size divided by 2π and a velocity scale $c_0 = \sqrt{\gamma R T_0}$ where T_0 is the mean temperature of the initial field. Density is nondimensionalized by ρ_0 equal to the mean density of the initial field and the viscosity is nondimensionalized by $\mu_0 = \mu(T_0)$.

Two scalars are solved for simultaneously — one with a mean gradient and one without. Since the turbulence is isotropic only one scalar with a mean gradient is needed. The scalar θ_1 has a mean gradient $\partial\tilde{\theta}_1/\partial x_1 = M_1$ and is nondimensionalized by $M_1 L_0$. The second scalar θ_2 does not have a mean gradient and is nondimensionalized by the standard deviation of the initial θ_2 field.

The equations of motion are solved using a pseudo-spectral Fourier method. Time advancement is done in physical space using a compact storage third order Runge-Kutta scheme (Wray [3]) while fast Fourier transforms are used to evaluate the spatial derivatives.

Initial conditions are specified by using random Fourier coefficients with a specified power spectrum for the fields of density, velocity, temperature and scalar θ_2. The scalar θ_1 has no initial fluctuations. The magnitude of the velocity fluctuations are fixed by specifying ${M_0}^2 = \overline{u_i u_i}$. Since the velocities are scaled by c_0, M_0 is an approximation to the initial fluctuating Mach number. The velocity field is further parameterized by the ratio of energy in the dilatational part of the field to that in the solenoidal part given by E^d/E^s similar to Passot and Pouquet [4].

For the simulations done to date a square pulse spectrum which has energy for $8 \leq k \leq 16$ as shown in Fiqure 1a has been used to generate the initial fields. The simulations use 64^3 grid points while a simulation with 128^3 grid points has been used to assess the numerical errors.

SIMULATION RESULTS

Two simulations of decaying isotropic turbulence will be discussed. The parameters describing the initial conditions are given in Table 1. Results from simulation II are described in detail below and differences with simulation I are noted.

Simulation	$(\overline{\rho'\rho'})^{\frac{1}{2}}$	M_0	E^d/E^s	$(\overline{T'T'})^{\frac{1}{2}}$	$\mathrm{Re}_{\lambda\ 11}$	Re_0
I	0.0	0.3	0.0	0.0	20	365
II	0.1	0.3	0.1	0.1	20	395

Table 1. Initial condition parameters for simulations I and II.

Figure 1a shows the initial velocity spectrum $E(k)$ from simulation II. It has been decomposed into a solenoidal velocity spectrum, $E^s(k)$, and a dilatational velocity spectrum, $E^d(k)$. Figure 1b shows the decomposed velocity spectrum at $t = 3.0$. (For reference, the initial conditions have a time scale $\tau = \frac{1}{2}\overline{\rho u_i'' u_i''}/\epsilon = 1.3$.) The spectrum $E(k)$ has smoothed out and is proportional to k^2 at lower wave numbers. No inertial subrange exists because the energy containing scales and the dissipation scales are not separated at these low Reynolds numbers. It is

interesting that the pulse structure persists in $E^d(k)$. In general the energy cascade to low and high wavenumbers removes any discontinuities in the spectrum. The reason for the persistance of the discontinuity in $E^d(k)$ is not known. Simulation I builds a smooth $E^d(k)$ spectrum that lies at a low level.

The history of the rms and maximum Mach numbers is given in Figure 2. The simulation decays toward low Mach numbers so that any strong effects due to compressibility can be expected to be limited to early times during the simulation. Unfortunately the simulation takes time to develop away from the artificial initial conditions into true turbulence. In order to determine when the simulation has developed sufficiently some standard measures of validity have been examined. The velocity derivative skewness goes from 0.0 to -0.4 by $t = 0.2$ and then decays as the Reynolds number drops. The Taylor microscales decrease slightly and then start growing linearly after $t = 1.5$. Thus the simulation takes about one initial turbulence time scale τ to develop.

The symbols shown in Figure 2 show the points where flow fields were stored on tape so that detailed statistics could be calculated. In order to provide some information that may be useful to turbulence modeling the balances for second order statistics were calculated. In the equations below the variables are split into mean and fluctuating components either as $\phi = \tilde{\phi} + \phi''$ where $\tilde{\phi} = \overline{\rho\phi}/\bar{\rho}$ is a mass weighted average or as $\phi = \bar{\phi} + \phi'$ where $\bar{\phi}$ is a normal Reynolds averaged quantity.

The equation for the turbulent kinetic energy in homogeneous turbulence can be written as

$$\frac{\partial}{\partial t}\left(\frac{1}{2}\overline{\rho u_i'' u_i''}\right) = \overbrace{p\frac{\partial u_i''}{\partial x_i}}^{①} - \frac{\tilde{\mu}}{Re_0}\overbrace{\frac{\partial u_i''}{\partial x_k}\left(\frac{\partial u_i''}{\partial x_k} - \frac{\partial u_k''}{\partial x_i}\right)}^{②} - \frac{4}{3}\frac{\tilde{\mu}}{Re_0}\overbrace{\frac{\partial u_k''}{\partial x_k}\frac{\partial u_i''}{\partial x_i}}^{③}$$

$$-\frac{1}{Re_0}\overbrace{\mu''\frac{\partial u_i''}{\partial x_j}\left(\frac{\partial u_i''}{\partial x_j} + \frac{\partial u_j''}{\partial x_i} - \frac{2}{3}\frac{\partial u_k''}{\partial x_k}\delta_{ij}\right)}^{④}.$$

Compared to the incompressible case, this equation has three additional terms. The viscous dissipation, ϵ, has been broken into three parts and can be rewritten as

$$\epsilon = \frac{\tilde{\mu}}{Re_0}\overbrace{\overline{\omega_i'\omega_i'}}^{②} + \frac{4}{3}\frac{\tilde{\mu}}{Re_0}\overbrace{\overline{\frac{\partial u_i''}{\partial x_i}\frac{\partial u_j''}{\partial x_j}}}^{③} + \frac{1}{Re_0}\overbrace{\overline{\mu''\frac{\partial u_i''}{\partial x_j}\left(\frac{\partial u_i''}{\partial x_j} + \frac{\partial u_j''}{\partial x_i} - \frac{2}{3}\frac{\partial u_k''}{\partial x_k}\delta_{ij}\right)}}^{④}.$$

The first term is proportional to the enstrophy and is the only term for a constant viscosity, incompressible flow. The second term is proportional to the mean squared fluctuating dilatation. The last term is a correlation involving fluctuating viscosity.

Figure 3a shows the balance for the turbulent kinetic energy equation. Symbols corresponding to Term 1, Term 2, etc. represent the terms as they appear left to right on the right hand side of the equation. The symbols marked RHS give the sum of the terms on the right hand side of the equation and D()/Dt corresponds to the time derivative on the left hand side of the

equation. The discrepancy between D()/Dt and RHS is a measure of the numerical error. We find the balance is still dominated by dissipation rate. Term 4, the correlation involving fluctuating viscosity, is negligible even with temperature fluctuations of ten percent. It may, however, play a role for more highly compressible flows. The relative size of Term 3 compared to Term 2 is dependent on the initial condition parameter E^d/E^s. Term 1, the pressure-dilatation correlation, is small compared to the other terms. It is seen to exhibit erratic behavior early in the simulation after which it becomes positive, acting as a gain term.

Writing an equation for the exact dissipation would be difficult because of the temperature dependent viscosity. However equations can be written for the enstrophy and the mean squared fluctuating dilatation. The enstrophy equation for homogeneous turbulence can be written as

$$\frac{\partial}{\partial t}\overline{\omega_i'\omega_i'} = \overbrace{\overline{\omega_i'\omega_j'\left(\frac{\partial u_i''}{\partial x_j}+\frac{\partial u_j''}{\partial x_i}\right)}}^{①} - \overbrace{\overline{\frac{\partial u_j''}{\partial x_j}\omega_i'\omega_i'}}^{②}$$

$$+\overbrace{\frac{2}{Re_0}\overline{\left(\varepsilon_{ijk}\frac{\partial \omega_k'}{\partial x_j}\right)\frac{1}{\rho}\frac{\partial}{\partial x_\ell}\left[\mu\left(\frac{\partial u_i''}{\partial x_\ell}+\frac{\partial u_\ell''}{\partial x_i}-\frac{2}{3}\frac{\partial u_m''}{\partial x_m}\delta_{i\ell}\right)\right]}}^{③} + \overbrace{2\,\overline{\omega_i'\varepsilon_{ijk}\frac{1}{\rho^2}\frac{\partial p}{\partial x_k}\frac{\partial \rho}{\partial x_j}}}^{④}.$$

Figure 3b shows that the dominant terms are the viscous dissipation term and the vorticity-vorticity-strain correlation, which acts to produce enstrophy by vortex stretching. The enstrophy-dilatation correlation is erratic at early times and then becomes negligible. The term corresponding to the baroclinic torque in the vorticity equation is negligible throughout the simulation.

The large discrepancy between D()/Dt and RHS at early times in Figure 3b caused some concern. It was found that the error was due to poor spatial resolution during the early portion of the simulation. A 128^3 simulation with the same initial condition parameters as simulation II was carried out to $t = 0.6$. Balances for the 128^3 simulation evaluated at $t = 0.2, 0.4, 0.6$ showed a discrepancy of less than 1 percent of the largest term. The qualitative results from the 64^3 simulation were unchanged. The lack of spatial resolution in the 64^3 simulations can be clearly seen by examining the spectra of the enstrophy for the two simulations. Figure 4a shows the poor resolution of the small scales for the 64^3 simulation while Figure 4b shows that the high wave numbers are well resolved for the 128^3 simulation. From this we have found two diagnostic tools for judging the resolution of a simulation. The enstrophy spectrum should fall off sufficiently at high wave numbers and the equations for higher order statistics of interest should balance.

The other part of the dissipation consists of the mean squared fluctuating dissipation. The equation for this quantity in homogeneous turbulence is

$$\frac{\partial}{\partial t}\overline{\left(\frac{\partial u_i''}{\partial x_i}\frac{\partial u_j''}{\partial x_j}\right)} = \overset{①}{\overline{\frac{\partial u_i''}{\partial x_i}\frac{\partial u_j''}{\partial x_j}\frac{\partial u_k''}{\partial x_k}}} - 2\overset{②}{\overline{\frac{\partial u_i''}{\partial x_j}\frac{\partial u_j''}{\partial x_i}\frac{\partial u_k''}{\partial x_k}}} - 2\overset{③}{\overline{\frac{\partial u_k''}{\partial x_k}\frac{\partial}{\partial x_i}\left(\frac{1}{\rho}\frac{\partial p}{\partial x_i}\right)}}$$

$$- \frac{2}{Re_0}\overset{④}{\overline{\frac{\partial}{\partial x_i}\left(\frac{\partial u_k''}{\partial x_k}\right)\frac{1}{\rho}\frac{\partial}{\partial x_j}\left[\mu\left(\frac{\partial u_i''}{\partial x_j} + \frac{\partial u_j''}{\partial x_i} - \frac{2}{3}\frac{\partial u_\ell''}{\partial x_\ell}\delta_{ij}\right)\right]}}.$$

Figure 3c shows the balance for this equation. The obvious point here is that each term is significant so that no term can be neglected in the model.

We thought it might be possible to model the fraction of the dissipation due to the mean squared fluctuating dilatation if one had a knowledge of E^d/E^s. Figure 5 shows the history of E^d/E^s and the ratio of the mean squared fluctuating dilatation to the enstrophy. The two curves start together but then develop differently so that E^d/E^s could not be used to model the dissipation due to the mean squared fluctuating dilatation. We see that after the initial period the dissipation due to dilatation increases so that at the end of the simulation 21 percent of the dissipation is directly due to a compressible term. This is surprising since the rms Mach number at this time is so low.

The passive scalars were included in the simulation in order to study mixing. Because the scalar θ_1 has a mean gradient it develops a flux, $\overline{\rho u_1'' \theta_1''}$, shown in Figure 6a. The equation for this flux in homogeneous turbulence can be written

$$\frac{\partial}{\partial t}\overline{\rho u_1'' \theta_1''} = \overset{①}{\overline{p\frac{\partial \theta_1''}{\partial x_1}}} - \frac{1}{Re_0}\overset{②}{\overline{\mu\left(\frac{\partial u_1''}{\partial x_k} + \frac{\partial u_k''}{\partial x_1} - \frac{2}{3}\frac{\partial u_\ell''}{\partial x_\ell}\delta_{1k}\right)\frac{\partial \theta_1''}{\partial x_k}}}$$

$$- \frac{Le}{Re_0 Pr}\overset{③}{\overline{\mu\frac{\partial u_1''}{\partial x_k}\frac{\partial \theta_1''}{\partial x_k}}} - \overset{④}{\overline{\rho u_1'' u_1''}} - \frac{Le}{Re_0 Pr}\overset{⑤}{\overline{\mu\frac{\partial u_1''}{\partial x_1}}}.$$

The balance for this equation is shown in Figure 6b. Term 4 is the production term from the mean scalar gradient. All the other terms act to reduce the flux. The only noticable difference in this balance between simulations I and II is that the pressure-scalar gradient term is larger in simulation II.

CONCLUSIONS

Direct numerical simulations of compressible decaying isotropic turbulence have been performed on a 64^3 grid. Rapid changes are seen to take place during the early portion of the simulation when the flow is developing away from the initial conditions. During this time the 64^3 grid does not adequately capture all the scales of motion, but it gives correct qualitative results (as seen by comparison with a 128^3 simulation) and is accurate after this initial period.

In order to perform full simulations at higher Reynolds numbers or under conditions that show more of a compressibility effect it will be necessary to use larger grids.

Our results show that the magnitude of the density fluctuations and of the dilatational velocity field are dependent on initial conditions. Simulation I, which had no initial density or temperature fluctuations and no energy in the dilatational part of the velocity field, did develop density and dilatational velocity fluctuations; however, they were an order of magnitude smaller than those of simulation II which had initial fluctuations of these quantities. Similarly, the compressible terms in the equations for the turbulent statistics were present to a much greater degree in simulation II than in simulation I. However, in neither case did they have a large influence.

One problem with decaying turbulence is that the compressible terms in the equations are large only at early times when the turbulence is developing away from the initial conditions. In order to overcome this problem and to study flows more closely related to those of engineering interest our future plans include inserting a mean shear that will produce turbulence. We hope these simulations will provide information useful in developing compressible turbulence models.

ACKNOWLEDGMENTS

This research has been supported by the Air Force Office of Scientific Research under F49620-86-K-0022. The authors are very grateful for the use of the computer facilities at NASA Ames Research Center.

REFERENCES

1. Dang, K. and Morchoisne, Y. F.,"Numerical Simulation of Homogeneous Compressible Turbulence," Proc. 2nd Int. Symp. on Transport Phenomena in Turbulent Flows, Tokyo, 1987, pp. 723–734.

2. Feiereisen, W. J., Reynolds W. C. and Ferziger, J. H.,"Numerical Simulation of Compressible Homogeneous Turbulent Shear Flow," Rept. TF–13, Mech. Eng. Dept., Stanford Univ., 1981.

3. Wray, A. W.,"Very Low Storage Time-Advancement Schemes," unpublished paper, NASA Ames Research Center, M.S. 202A-1, Moffett Field, CA 94035.

4. Passot, T. and Pouquet, A.,"Numerical Simulation of Compressible Homogeneous Flows in the Turbulent Regime," J. Fluid Mech., vol. 181, pp. 441-466, 1987.

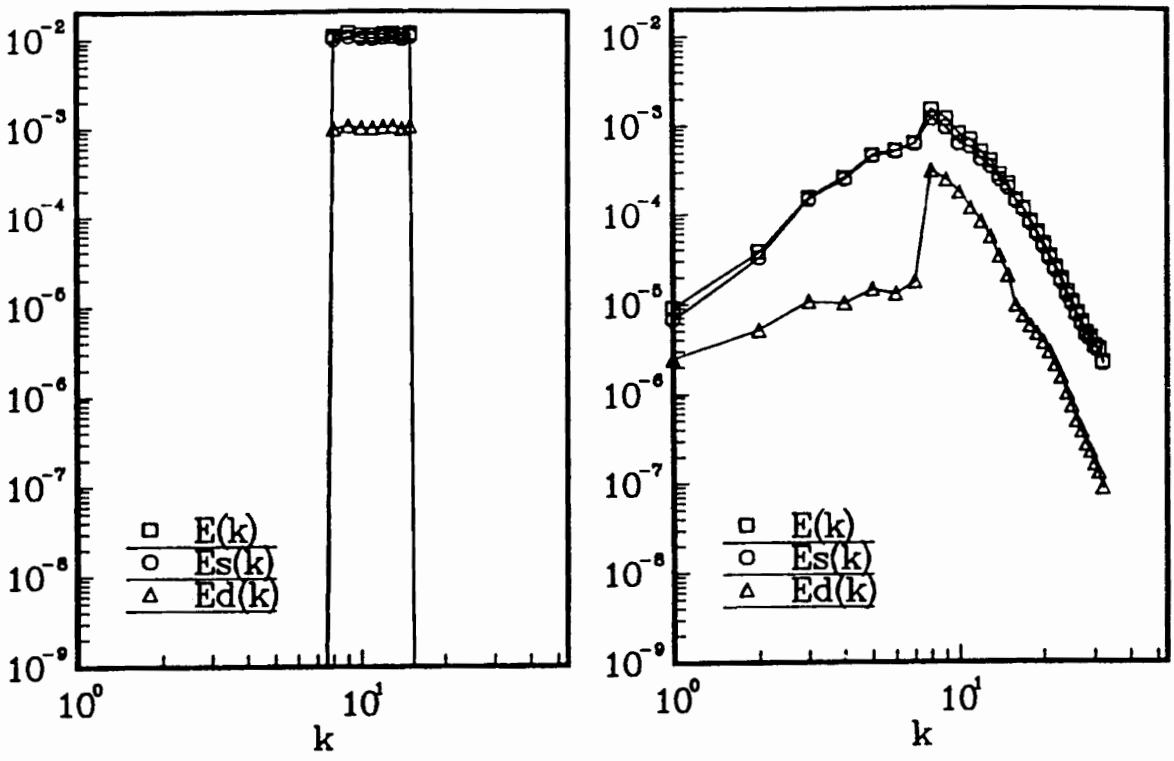

Figure 1. Decomposed velocity spectra (a) at $t = 0.0$ and (b) at $t = 3.0$. $\mathrm{E}^s(k)$ is the solenoidal velocity spectrum, $\mathrm{E}^d(k)$ is the dilatational velocity spectrum.

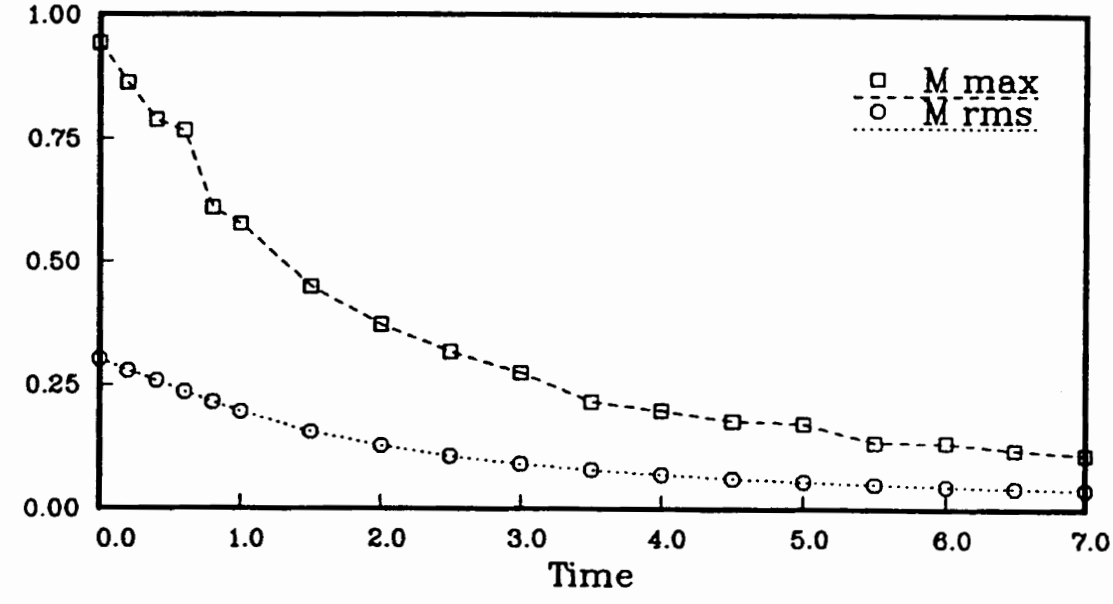

Figure 2. Maximum and rms Mach number history.

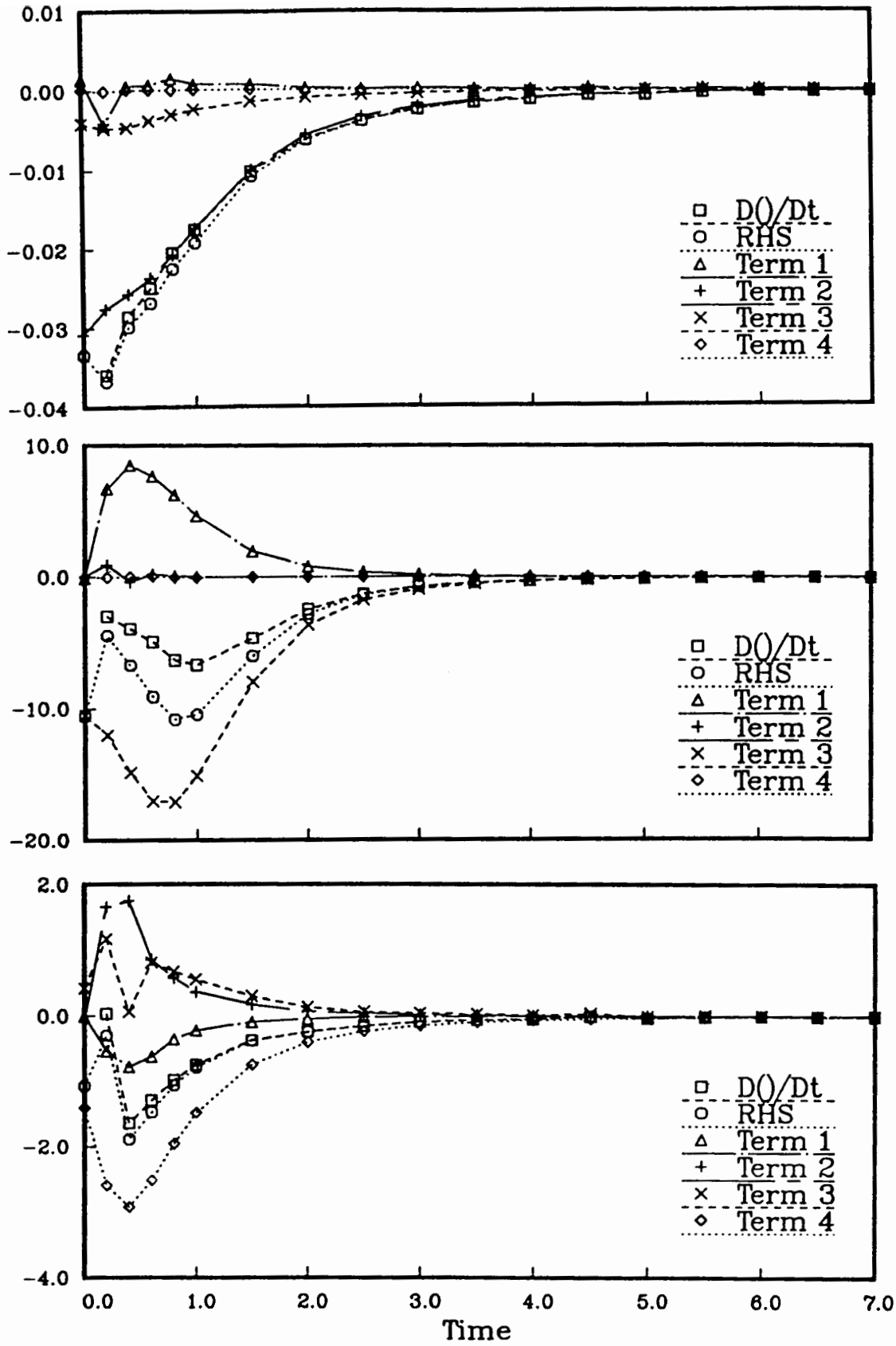

Figure 3. Balances for the equations of (a) turbulent kinetic energy, (b) enstrophy, and (c) mean squared fluctuating dilatation.

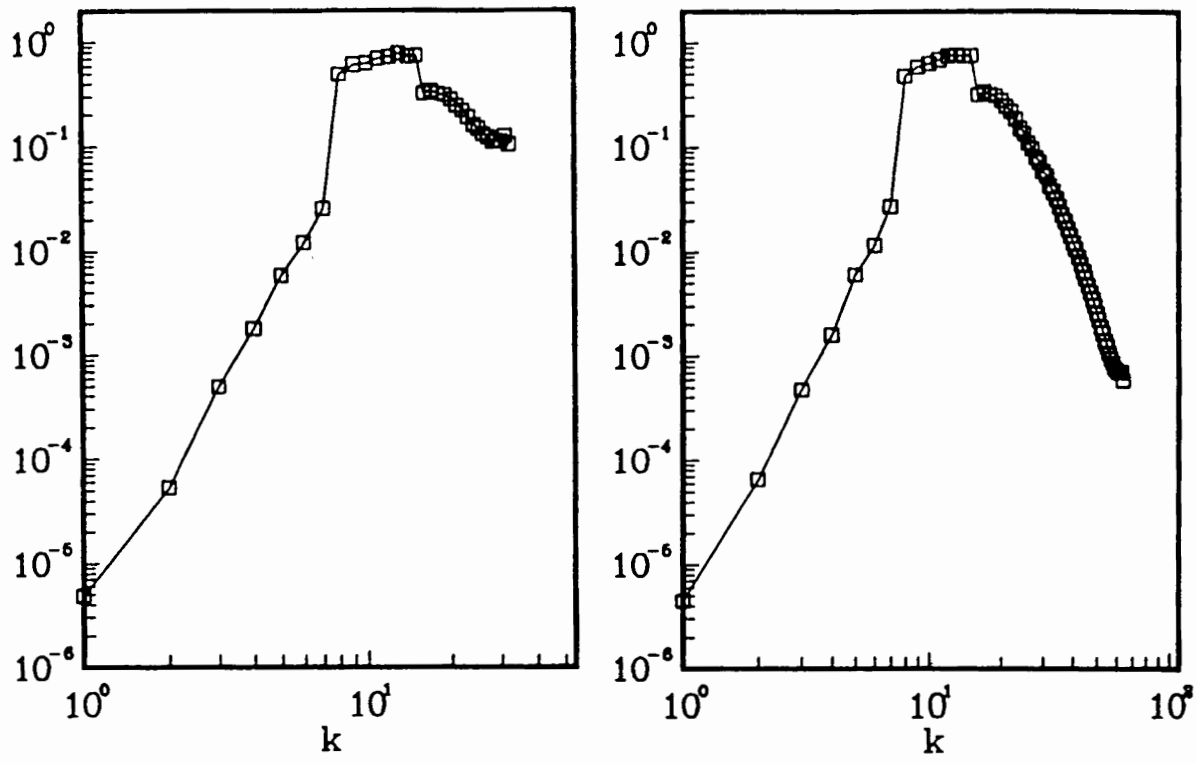

Figure 4. Enstrophy spectra at $t = 0.6$ for simulations with (a) 64^3 grid points, and (b) 128^3 grid points.

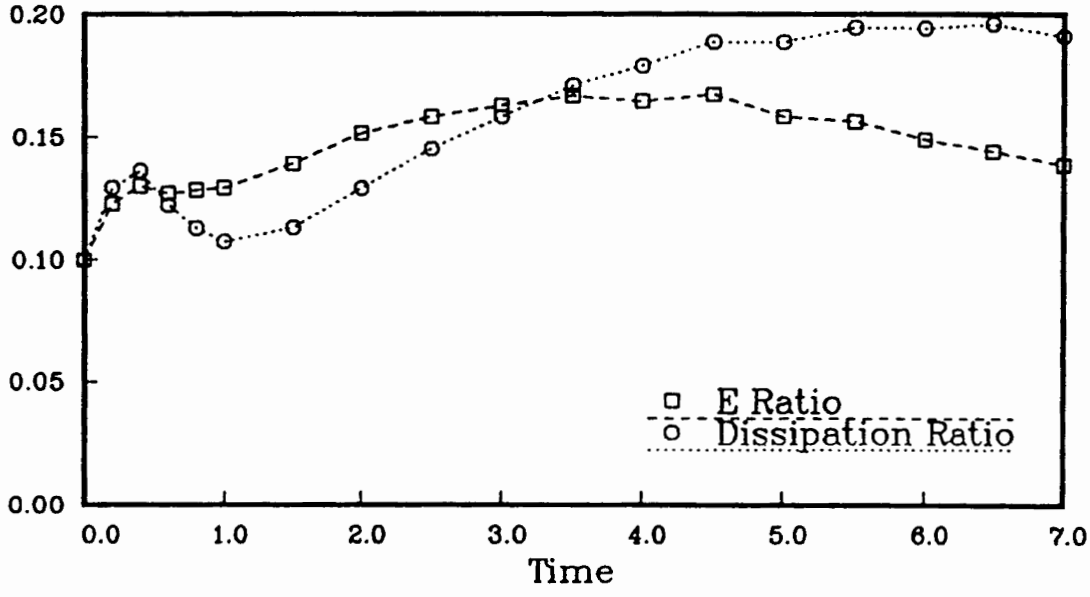

Figure 5. History of the ratio of energy in the dilatational and solenoidal velocity fields and the ratio of mean squared fluctuating dilatation to enstrophy.

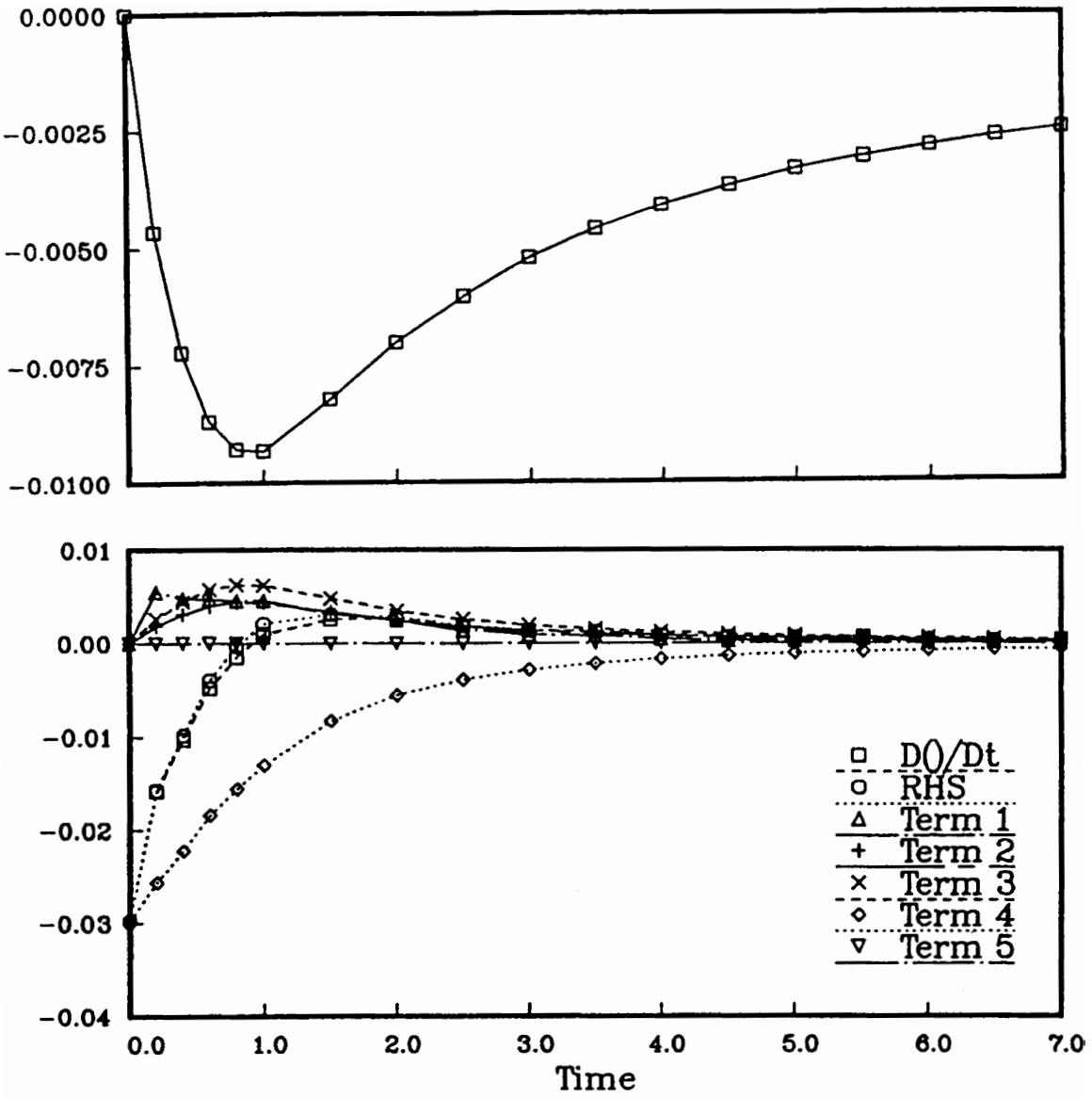

Figure 6. (*a*) History of the scalar flux. (*b*) Balance of the scalar flux equation.

TURBULENT JUMP RELATIONS IN THE INTERACTION OF A SHOCK WAVE WITH A TURBULENT REGION .

Michel Bonnet°, Serge Gauthier°, Bernard Sitt * & Patrick Spitz°
°C.E.A/Centre d'Etudes de Limeil-Valenton BP 27
94190 Villeneuve-St-Georges France
*C.E.A/Centre d Etudes de Vaujours-Moronvilliers BP 7
77181 Courtry France

ABSTRACT

When a shock wave crosses a turbulent region, it can be assumed that there exists an equivalent average shock front, through which average flow variables, turbulent transport fluxes and source terms undergo jumps that satisfy modified turbulent Hugoniot conditions, independently of the closure model. These relations are presented and additional kinematic jump relations are also derived, so that the Richtmyer-Meshkov turbulent source effect can be described quantitatively.With the help of the K- ε turbulent mixing model presented in the companion paper /1/, the results of numerical tests of these relations performed on a classical Air-Helium shock tube computer experiment are presented and discussed.

I - INTRODUCTION

When a shock front enters a region of fully developed compressible turbulence and propagates through it, it undergoes strong local distortions due to refraction by flow field random inhomogeneities of all scales, and also by the creation and multiple reflection of shocklets in the case of heterogeneous turbulent mixing. Therefore, instead of being a single, abrupt transition governed by molecular transport and established over a distance of a few particle mean free paths, the overall shock process is spread over a much larger distance such that average dissipation can take place, that is, a few Kolmogorov scalelengths.

But, if the incident shock is strong enough, namely if its characteristic propagation time is much less than the time scale of the smallest eddies (quasi-frozen turbulence), one can postulate that its effect on the turbulent flow is equivalent to that of a single, randomly perturbed shock. In particular, the flow variables, including turbulent fluxes, undergo jumps that, in view of the classical conservation properties, must satisfy a set of relations that should generalize the usual Rankine-Hugoniot jump relations.

Our purpose in this study is to determine the general form of these relations and the role of the average turbulent variables (kinetic energy, transport fluxes, source terms).

Of particular interest is the quantitative description of the expected amplification(or creation) of anisotropy through the average front, following the intuitive view that, in a first approximation, transverse velocity components should not be strongly affected, while the axial (normal to the average front) average and fluctuating velocity components should be compressed in order to conserve the flow rate.

Besides their physical interest, turbulent jump relations can be simulated numerically with a hydrodynamic code using any turbulent closure model. One can thus explore the physical conditions under which these relations are relevant and, in a correlated way, test the adequacy of a given model for the treatment of strong discontinuities with the attendant turbulent production, to be modeled by "turbulent Richtmyer-Meshkov" source terms.We establish in sections II and III the general average jump relations derived from the usual conservation laws, as well as two additional ones for the axial and transverse turbulent kinetic energy. We then use a K- ε turbulent model /1/ to compute the development of the turbulent mixing zone in a classical Air-Helium shock tube problem and to perform numerical tests on the associated set of jump relations.

II - GENERAL INSTANTANEOUS AND AVERAGE CONSERVATION LAWS

For a mixture of two (say) non heat-conducting species, the conservation laws can be expressed under the usual conservative form, using standard notations:

$$\frac{\partial \rho_\alpha}{\partial t} + \nabla \cdot \left(\rho_\alpha \vec{u}_\alpha \right) = 0 \quad , \qquad \alpha = 1, 2 \quad , \qquad (1.1)$$

$$\frac{\partial \rho}{\partial t} + \nabla \cdot \left(\rho \vec{u} \right) = 0 \quad , \qquad (1.2)$$

$$\frac{\partial}{\partial t} \left(\rho \vec{u} \right) + \nabla \cdot \left(p \bar{\bar{1}} - \bar{\bar{\sigma}} + \rho \overline{\vec{u}\vec{u}} \right) = 0 \quad , \qquad (1.3)$$

$$\frac{\partial}{\partial t} \left\{ \rho \left(e + \frac{|\vec{u}|^2}{2} \right) \right\} + \nabla \cdot \left\{ \left(e + \frac{|\vec{u}|^2}{2} + \frac{p}{\rho} \right) \rho \vec{u} - \bar{\bar{\sigma}} \cdot \vec{u} \right\} = 0 . \qquad (1.4)$$

where, denoting by ρ_α, c_α, $\vec{u}_\alpha$, e_α, respectively, the α-species mass density, concentration ρ_α/ρ, velocity and internal energy, one has:

$$\rho = \sum_\alpha \rho_\alpha \quad , \quad \vec{u} = \sum_\alpha c_\alpha \vec{u}_\alpha \quad , \quad e = \sum_\alpha c_\alpha e_\alpha \quad ,$$

and p is the total static pressure, given by some constitutive law for the mixture, assuming an arbitrary equation of state for each species.

Now, introducing the decomposition of every flow quantity Q into its mass-averaged and fluctuating parts:

$$Q = \tilde{Q} + Q' \quad , \qquad \tilde{Q} = \frac{\overline{\rho Q}}{\bar{\rho}} \quad ,$$

one can obtain the turbulent flow general equations, again under conservative form:

$$\frac{\partial \bar{\rho}_\alpha}{\partial t} + \nabla \cdot \left(\bar{\rho}_\alpha \tilde{\vec{U}} + \overline{\rho c_\alpha \vec{u}'} \right) = 0 \quad , \qquad (2.1)$$

$$\frac{\partial \bar{\rho}}{\partial t} + \nabla \cdot \left(\bar{\rho} \tilde{\vec{U}} \right) = 0 \quad , \qquad (2.2)$$

$$\frac{\partial}{\partial t}\left(\bar{\rho} \tilde{\vec{U}} \right) + \nabla \cdot \left(\bar{p} \bar{\bar{1}} + \bar{\rho}\, \tilde{\vec{U}} \tilde{\vec{U}} + \overline{\rho \vec{u}' \vec{u}'} \right) = 0 \quad , \qquad (2.3)$$

$$\frac{\partial}{\partial t}\left(\bar{\rho} \tilde{E} \right) + \nabla \cdot \left\{ \bar{\rho} \left(\tilde{E} + \frac{\bar{p}}{\bar{\rho}} \right) \tilde{\vec{U}} + \tilde{\vec{U}} \cdot \overline{\rho \vec{u}' \vec{u}'} + \overline{\rho e' \vec{u}'} + \overline{\rho k \vec{u}'} + \overline{p \vec{u}'} \right\} = 0 \quad . \qquad (2.4)$$

where $k = 1/2 \left| \vec{u} \right|^2$ is the turbulent kinetic energy, and $\tilde{E} = \tilde{e} + 1/2 \left| \tilde{\vec{U}} \right|^2 + \tilde{k}$ is the average total energy per unit mass.

III - JUMP RELATIONS FROM CONSERVATION LAWS

III.1-Instantaneous jump relations.

Consider a general conservation law, in a scalar or vector form:

$$\frac{\partial q}{\partial t} + \nabla \cdot \vec{F} = 0 \qquad \text{or} \qquad \frac{\partial \vec{v}}{\partial t} + \nabla \cdot \bar{\bar{T}} = 0 \qquad (3)$$

assumed to be valid in the weak sense (i.e. for distributions). One can show in a rather simple way that, at any propagating discontinuous front $\Sigma(t)$, with unit normal $\vec{n}$ and celerity D along $\vec{n}$, denoting the jump through Σ as:

$$[Q] = Q_+ - Q_- \quad ,$$

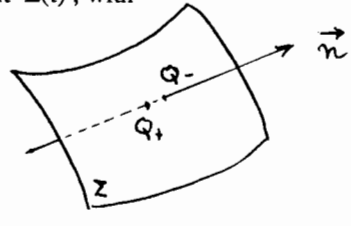

one has the associated jump relation:

$$D\left[g\right] - \vec{n}\cdot\left[\vec{F}\right] = 0 \qquad \text{or} \qquad D\left[\vec{v}\right] - \left[\vec{\vec{T}}\right]\cdot\vec{n} = 0. \quad (4)$$

Now, straightforward application of formulas (4) to flow equations (1) gives relations which are valid at any instant and for any shock distortion and reflection, provided that shock transition is strong enough:

$$D\left[\rho_\alpha\right] = \vec{n}\cdot\left[\rho_\alpha \vec{u}_\alpha\right], \quad (5.1)$$

$$D\left[\rho\right] = \vec{n}\cdot\left[\rho\,\vec{u}\right], \quad (5.2)$$

$$D\left[\rho\vec{u}\right] = \left[p\right]\vec{n} - \left[\vec{\vec{\sigma}}\right]\cdot\vec{n} + \left[\rho\,(\vec{u}\cdot\vec{n})\,\vec{u}\right], \quad (5.3)$$

$$D\left[\rho\left(e + \frac{|\vec{u}|^2}{2}\right)\right] = \vec{n}\cdot\left[\rho\left(e + \frac{|\vec{u}|^2}{2} + \frac{p}{\rho}\right)\vec{u} - \vec{\vec{\sigma}}\cdot\vec{u}\right]. \quad (5.4)$$

III.2 - Average turbulent Rankine-Hugoniot jump relations

The next step now consists in introducing the mean plus fluctuating variable decomposition into relations (5) and taking their ensemble average. But this procedure induces the appearance of second or third-order correlation products that are usually not modeled, since they involve front fluctuation terms D' and $\vec{n}'$, and are certainly difficult to take into account. To make the analysis more tractable, we then assume that the overall flow field transition is set up by a single, randomly distorted shock with celerity and unit normal:

$$D(t) = \overline{D}(t) + D'(t), \qquad \vec{n}(t) = \vec{\overline{n}}(t) + \vec{n}'(t).$$

Since this relation already incorporates strong local perturbations, it also does not seem unreasonable to assume that shock fluctuations $(D', \vec{n}')$ about its average $(\overline{D}, \vec{\overline{n}})$ are weak. Then, neglecting first-order and higher-order perturbation terms in (5) after averaging leads to the following set of relations (the average flow through the front is along the normal $\vec{\overline{n}}$, with average and fluctuating velocity components $\tilde{U}$ and u').

$$\bar{D}\left[\bar{\rho}_\alpha\right] = \left[\bar{\rho}_\alpha \tilde{U}\right] + \left[\overline{\rho c'_\alpha u'}\right] \qquad (6.1)$$

$$\bar{D}\left[\bar{\rho}\right] = \left[\bar{\rho}\tilde{U}\right] \qquad (6.2)$$

$$\bar{D}\left[\bar{\rho}\tilde{U}\right] = \left[\bar{p} + \overline{\rho u'^2} + \bar{\rho}\tilde{U}^2\right] \qquad (6.3)$$

$$\bar{D}\left[\bar{\rho}\tilde{E}\right] = \left[\bar{\rho}\left(\tilde{E} + \frac{\bar{p} + \overline{\rho u'^2}}{\bar{\rho}}\right)\tilde{U}\right] + \left[\overline{\rho e' u'}\right] + \left[\overline{\rho h u'}\right] + \left[\overline{p u'}\right] \qquad (6.4)$$

The first remark to be made is that these relations can also be obtained by application of jump formulas (4) to average flow equations (2): this shows the consistency of the approximations made above. First-order terms, not shown here, all give the incidence of shock velocity fluctuations on transverse momentum terms and fluxes. Unfortunately, these terms are usually not modeled, and are not considered in the present work.

If one introduces the average mass flow rate through the front:

$$\tilde{m} = \bar{\rho}_+\left(\tilde{U}_+ - \bar{D}\right) = \bar{\rho}_-\left(\tilde{U}_- - \bar{D}\right),$$

relations (6.2) to (6.4) can also be written:

$$\left[\tilde{U}\right] = \tilde{m}\left[\bar{V}\right], \qquad (7.1)$$

$$\left[\bar{p} + \overline{\rho u'^2}\right] = \tilde{m}\left[\tilde{U}\right], \qquad (7.2)$$

$$\tilde{m}\left[\tilde{e} + \tilde{k}\right] + \left\langle \bar{p} + \overline{\rho u'^2} \right\rangle \left[\tilde{U}\right] + \left[\overline{\rho e' u'} + \overline{\rho k u'} + \overline{p u'}\right] = 0. \qquad (7.3)$$

where: $\bar{V} = \frac{1}{\bar{\rho}}$ and $\langle Q \rangle = 1/2\,(Q_+ + Q_-)$. The close analogy to the classical Rankine-Hugoniot relations /2/ and the role of additional turbulent jumps are quite clear:

-to the static pressure $\bar{p}$ is added a dynamic pressure term $\overline{\rho u'^2}$ created by axial velocity fluctuation u' only.

- to the internal energy $\tilde{e}$ is added the kinetic energy of fluctuations $\tilde{k}$, which therefore plays the role of an equivalent additional internal energy.

- the generalized internal energy relation (7.3) includes further modifications due to the additional jumps of:

- the internal energy flux term $\overline{\rho e' u'}$,
- the turbulent kinetic energy flux term $\overline{\rho k u'}$,
- the pressure-velocity correlation term $\overline{p u'}$.

(note that the sum of the first and third contribution is just equal to the enthalpy flux term $\overline{\rho h' u'}$).

It is important to remark that these relations are perfectly independent of turbulent closure models, so that any model can be implemented for numerical tests.

Now, these relations are not complete, in the sense that they give no separate information on the jump of kinetic energy terms. Such an information can actually be obtained from instantaneous dynamic relations (5.3).

III.3 - Turbulent kinetic energy jump relations

Introducing the transverse velocity component $\vec{u}'_\perp$ through the relation: $\vec{u} = (\tilde{U} + u')\vec{n} + \vec{u}'_\perp$ in (5.3), and neglecting the first-order and higher-order perturbation terms, one readily obtains instantaneous jump relations for axial and transverse momentum:

$$\bar{D}\left[\rho(\tilde{U} + u')\right] = \left[\bar{p} + p'\right] - \left[\vec{n}\cdot\bar{\bar{\sigma}}\cdot\vec{n}\right] + \left[\rho(\tilde{U}+u')^2\right], \quad (8.1)$$

$$\bar{D}\left[\rho \vec{u}'_\perp\right] = -\left[(\bar{\bar{\sigma}}\cdot\vec{n})_\perp\right] + \left[\rho(\tilde{U} + u')\vec{u}'_\perp\right]. \quad (8.2)$$

In (8.1), the axial viscous stress can be neglected with respect to the axial Reynolds stress. (8.2) shows that the transverse velocity discontinuity $\left[\vec{u}'_\perp\right]$ is generated by the discontinuity of the transverse component of the axial viscous stress $\left(\bar{\bar{\sigma}}\cdot\vec{n}\right)_\perp$. Multiplying the above two relations respectively by $< \tilde{U} + u' >$ and $< \vec{u}'_\perp >$, one gets, after some algebra, separate jump relations for the axial and transverse kinetic energy $\tilde{k}_\parallel = \frac{1}{2}\frac{\overline{\rho u'^2}}{\bar{\rho}}$ and $\tilde{k}_\perp = \frac{1}{2}\frac{\overline{\rho |\vec{u}'_\perp|^2}}{\bar{\rho}}$:

$$\tilde{m}\left[\tilde{k}_\parallel\right] + \left[\overline{\rho k_\parallel u'}\right] + \left[\overline{p u'}\right] - \overline{<p>\left[u'\right]} + <\overline{\rho u'^2}>\left[\tilde{U}\right] = 0, \quad (9.1)$$

$$\tilde{m}\left[\tilde{k}_\perp\right] + \left[\overline{\rho k_\perp u'}\right] + \overline{<(\bar{\bar{\sigma}}\cdot\vec{n})_\perp>\cdot\left[\vec{u}'_\perp\right]} - \vec{n}\cdot\left[\overline{\bar{\bar{\sigma}}\cdot\vec{u}'_\perp}\right] = 0. \quad (9.2)$$

Adding up the two equations, one gets the jump relation for the turbulent kinetic energy $\tilde{k} = \tilde{k}_\parallel + \tilde{k}_\perp$ where the viscous contribution is indeed negligible:

$$\tilde{m}\left[\tilde{k}\right] + \left[\overline{\rho k u'}\right] + <\overline{\rho u'^2}>\left[\tilde{U}\right] + \left[\overline{p u'}\right] - \overline{<p>\left[u'\right]} = 0 \quad (10)$$

These three relations give the general form of the production terms for $\tilde{k}_\parallel$, $\tilde{k}_\perp$ and $\tilde{k}$ through a shock front. Subtracting Eq.(10) from the energy relation (7.3), one obtains the internal energy jump relation:

$$\tilde{m}\left[\tilde{e}\right] + \langle \bar{p} \rangle \left[\tilde{U}\right] + \overline{\langle p \rangle \left[u'\right]} + \left[\overline{\rho e' u'}\right] = 0, \quad (11)$$

which is the strict generalization of the classical shock adiabatic modified essentially by the discontinuity of the turbulent thermal flux and of the pressure-velocity correlations. It also appears that, within our approximation concerning the fluctuations of the front, the dominant production terms across the shock ("turbulent Richtmyer-Meshkov" source terms) create axial kinetic energy only.

IV - NUMERICAL TESTS ON TURBULENT JUMP RELATIONS.

All the discontinuity relations established above can be tested with any hydrodynamic code including a more or less sophisticated turbulent model, provided that the right average transport and production terms are accounted for and computed.

We therefore choose the compressible k-ε two-species model and code developed at CEA/CEL-V /1/, which includes a production term accounting for turbulence induced by Rayleigh-Taylor instability, and we consider the associated set of jump relations (6.1-3), (10) and (11), to be analyzed numerically.

We have taken as a first test problem a high Mach number shock tube simulation, where a shock at a pressure of 20 bars is impinging upon an immaterial interface between air and helium at standard temperature and pressure, with an Atwood number equal to 0.758. The interface is then subject to the Richtmyer-Meshkov instability and, as is well-known experimentally, multiple shock reflections between the tube end and the interface induce the development of a turbulent mixing zone (TMZ) between air and helium. As seen in Fig.1, the initial TMZ superimposed at time t=0.27 10^{-3}s is made fairly wide, in order to facilitate numerical measurements of the flow discontinuity through the shock reflected from the tube end. The analysis is done at time t=0.315 10^{-3} s when the shock is approximately in the middle of the TMZ. Spatial profiles of the average density and pressure are shown on Fig.2 and 3, and clearly indicate the position of the front. The $\bar{\rho}$ profile serves for the identification of the mesh zones defining the upstream (-) and downstream (+) boundaries of the shock wave structure, between which the jumps are to be computed. Relation (6.2), which does not depend explicitly on turbulent fluxes, is used to compute shock celerity from the mass flow rate and density jumps: D= 77.8 cm s^{-1}. This value is then used to check the other jump relations. For instance, (6.3) is written down as an equality between an upstream and downstream quantity:

$$D\,\bar{\rho}_+\tilde{U}_+ - \bar{p}_+ - \overline{\rho_+ u'^2_+} - \bar{\rho}_+\tilde{U}^2_+ = D\,\bar{\rho}_-\tilde{U}_- - \bar{p}_- - \overline{\rho_- u'^2_-} - \bar{\rho}_-\tilde{U}^2_-$$

Taking the ratio of the numerical value of the the left hand side to the right one and comparing it to 1 therefore gives the accuracy of the momentum jump relation, which is found to be true within 3.6% in the present case. Similarly, the accuracy of the concentration jump relation (6.1) is found to be 14%. The first figure is fairly satisfactory, thanks to the fact that the jump of the turbulent axial momentum flux $\overline{\rho u'^2}$ is fairly well defined, as can be seen on Fig.4. This is less so for the jump of the turbulent concentration flux (Fig.5) and accordingly for relation (6.1). Although other turbulent fluxes and source terms also experience measurable jumps (see for instance the profile of the enthalpy flux on Fig. 6), these are not as steep as would be required to obtain an accurate check of relations (10) and (11). Therefore, further simulations with higher shock strengths will be necessary to obtain stronger flow discontinuities that will allow more precise numerical tests.

V - CONCLUSION

We have obtained, under reasonable assumptions, a generalization of the Rankine-Hugoniot jump relations through a shock front, including the effect of turbulent flux and production terms, independently of any turbulence modelling.

Therefore, with high shock strength numerical experiments, one can perform tests of both the adequacy of our underlying assumptions and the ability of any given closure model to treat strong discontinuities.

REFERENCES

1 - M. Bonnet, S. Gauthier, P. Spitz, Numerical Simulations with a k-ε Mixing Model in the Presence of Shock Waves, paper presented at this Workshop.

2 - Ya. B. Zel'dovich, Yu. P. Raizer, Physics of Shock Waves and High-Temperature Phenomena, Vol. 1, p. 50 (1966).

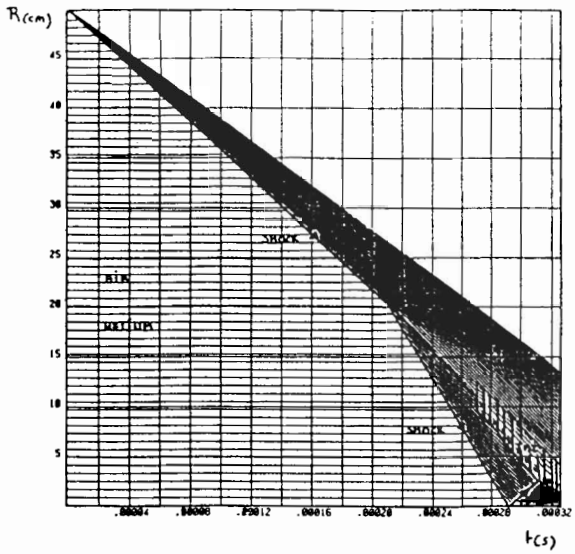

Fig. 1 - R-T diagram of shock propagation and turbulent mixing zone initialization and development

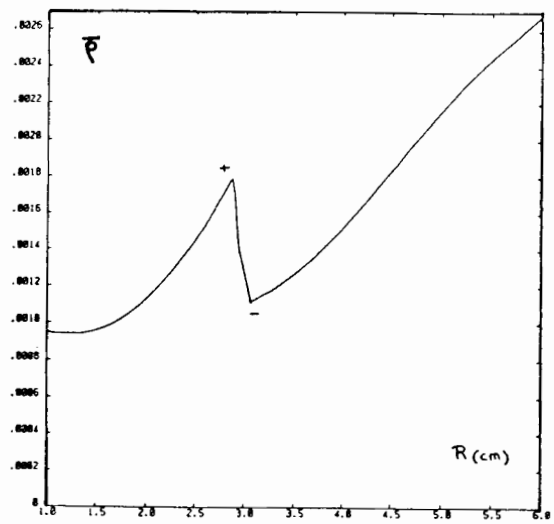

Fig. 2 - Space profile of average density $\bar{\rho}$ at time $0.315\ 10^{-3}$ s

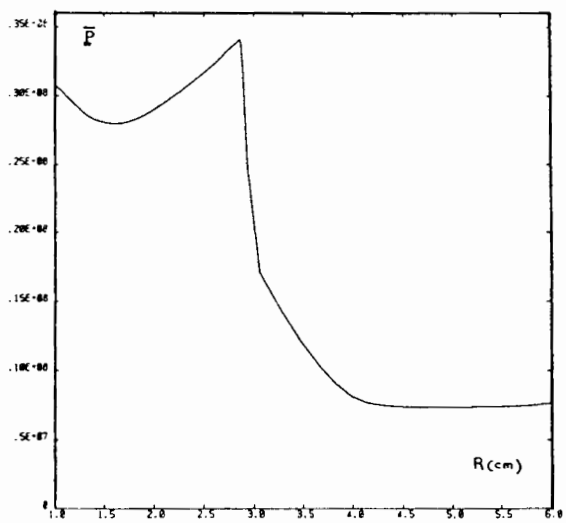

Fig. 3 - Space profile of average pressure $\bar{p}$ at time $0.315\ 10^{-3}$ s

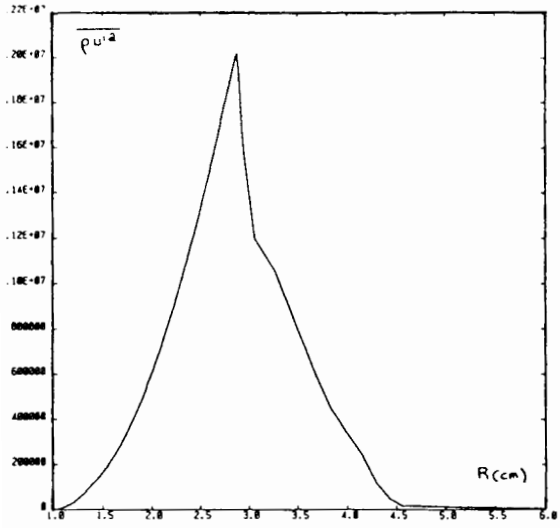

Fig. 4 - Space profile of turbulent momentum flux $\overline{\rho u'2}$ at time 0.315 10^{-3}s

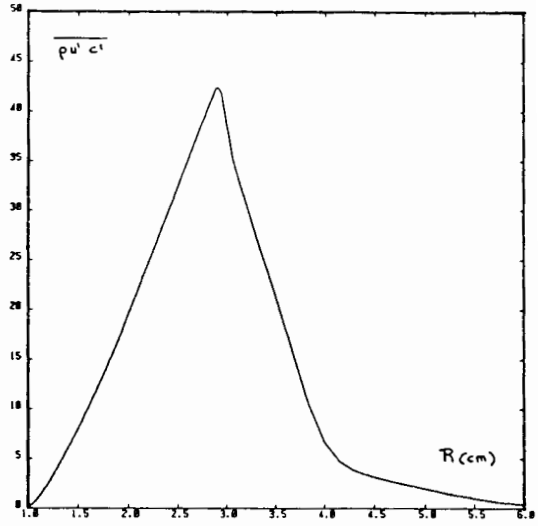

Fig. 5 - Space profile of turbulent concentration flux $\overline{\rho\, c'\, u'}$ at time 0.315 10^{-3}s

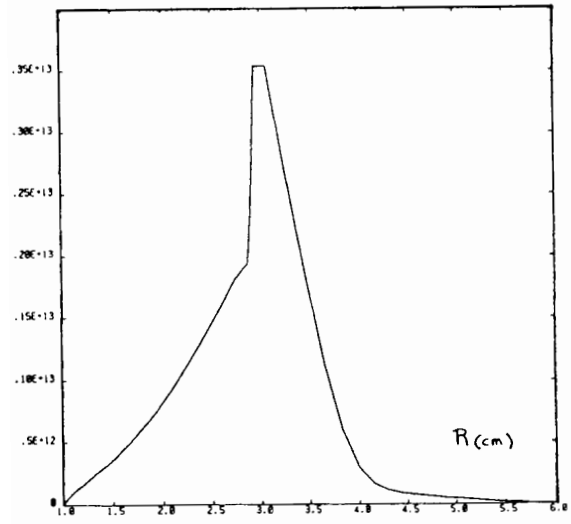

Fig. 6 - Space profile of turbulent enthalpy flux $\overline{\rho\, h'\, u'}$ at time 0.315 10^{-3}s

NUMERICAL SIMULATIONS WITH A 'k-ε' MIXING MODEL IN THE PRESENCE OF SHOCK WAVES

Michel Bonnet, Serge Gauthier & Patrick Spitz
Centre d'Etudes de Limeil-Valenton BP 27
94190 Villeneuve-St-Georges France

I - INTRODUCTION:

Rayleigh-Taylor and Richtmeyer-Meshkov instabilities occuring in the context of inertial confinement fusion have been the object of a growing interest in the recent years. While the linear growth of small perturbations on the interface between layers of different densities is relatively well understood, the non-linear stage and the subsequent turbulent phase are poorly understood. Some insights in the non-linear growth can be done by numerical simulations as opposed to the fully developed turbulent phase where models are needed. In the context of interest, the challenge was to build a 1D mixing model which had to be imbedded in a 1D production hydrocode. As in the Andronov et al's pioneering work [1], we used closure models which are probably the only way to work out, despite the weaknesses of such an approach. Later on, these authors also published a more sophisticated model [2] with evolution equations for every second order quantities. In the same time, turbulent mixing models became fashionable on the West and simple models [2-4] and then more elaborated models were built up [1]. Nevertheless, it is not clear yet what informations are brought by n-equation models.

However, when using closure models in unsteady situations, we are faced up to some major difficulties. The first one is the need of giving an initial turbulent state. This necessity comes from the basic assumptions where variables are splitted into a mean part and a fluctuating one. In other words, statistical models are unable to describe transition mechanisms. As a result, the final state is slightly sensitive to the initialization procedure. A second difficulty arises when simulating the interaction of turbulence with a shock wave. The numerical treatment of strong discontinuities requires a numerical dissipation in order to smear out shock waves and smooth gradients, which makes them artificially less efficient in producing turbulent kinetic energy. It follows some dependence on the spatial resolution. A third difficulty is encountered when setting up the closure assumptions. They often assume a weak dependence of the n^{th} correlation versus the $(n-1)^{th}$ one. Under shock wave influence, such an hypothesis is no longer valid and closure assumptions have to be supplemented by some relationships to produce meaningfull results. Last but not least, closure assumptions are not accounting for inhomogeneity.

In view of this application, a one-equation turbulent model has been developed at Limeil and sucessfully used to numerically simulate turbulent mixing at an interface [3]. In this model the characteristic length was assumed to be the mixing length which is a global quantity. In order to remove these unsatisfactory global quantities we added an equation for the dissipation rate ε.

In section II we present the model, numerical applications are given in the third section.

II - THE k-ε MIXING MODEL:

II.1 MODEL EQUATIONS

Our model is based on the assumptions that the two fluids are miscible, the thermal equilibrium is reached and the turbulence in the plane normal to the shock propagation direction is statistically homogeneous.

It follows that the mixing flow can be described only by the mean quantities ρ, T, P, u and $c=\rho_1/\rho$, where these symbols have their usual meaning. By means of the classical Favre's average, it is straigthforward to derive evolution equations for the mean quantities ρ, c, u, e and k. The equation for ε is usually built by comparison with the k-equation. Following Launder and Spalding [5], we assume that source terms are equal to the k-equation source terms up to a dimensional factor of the form $C^{st}\ k/\varepsilon$. Adding a diffusion term and a production one due to the compressibility effect, we finally obtain an evolution equation for ε. The set of equations reads

Continuity equation

$$\frac{D\bar{\rho}}{Dt} = -\bar{\rho}\,\frac{\partial \tilde{u}_n}{\partial n}$$

Concentration equation

$$\bar{\rho}\,\frac{D\tilde{c}}{Dt} = -\frac{\partial}{\partial n}\,\overline{\rho c' u_n'}$$

Momentum equation

$$\bar{\rho}\,\frac{D\tilde{u}_n}{Dt} = -\frac{\partial \bar{P}}{\partial n} - \frac{\partial}{\partial n}\,\overline{\rho u_n'^2}$$

Energy equation

$$\bar{\rho}\,\frac{D\tilde{e}}{Dt} = -\bar{P}\,\frac{\partial \tilde{u}_n}{\partial n} + \overline{w}\,\frac{\partial \bar{P}}{\partial n} + \frac{\partial}{\partial n}\left(\frac{C_D}{\sigma_e}\,\bar{\rho}\,\frac{\tilde{k}^2}{\tilde{\varepsilon}}\,\frac{\partial}{\partial n}\left(\tilde{e} + \frac{\bar{P}}{\bar{\rho}}\right)\right) + \bar{\rho}\,\tilde{\varepsilon}$$

Turbulent kinetic energy equation

$$\bar{\rho}\,\frac{D\tilde{k}}{Dt} = -\overline{\rho u_n'^2}\,\frac{\partial \tilde{u}_n}{\partial n} - \overline{u'}\,\frac{\partial \bar{P}}{\partial n} - \frac{\partial}{\partial n}\,\overline{\rho k' u_n'} - \bar{\rho}\,\tilde{\varepsilon}$$

Dissipation rate equation

$$\bar{\rho}\,\frac{D\tilde{\varepsilon}}{Dt} = -C_{\varepsilon_1}\,\frac{\tilde{\varepsilon}}{\tilde{k}}\,\overline{\rho u_n'^2}\,\frac{\partial \tilde{u}_n}{\partial n} - C_{\varepsilon_3}\,\bar{\rho}\,\tilde{\varepsilon}\,\frac{\partial \tilde{u}_n}{\partial n} - C_{\varepsilon_0}\,\frac{\tilde{\varepsilon}}{\tilde{k}}\,\overline{w}\,\frac{\partial \bar{P}}{\partial n} + \frac{\partial}{\partial n}\left(\frac{C_D}{\sigma_\varepsilon}\,\frac{\tilde{k}^2}{\tilde{\varepsilon}}\,\bar{\rho}\,\frac{\partial \tilde{\varepsilon}}{\partial n}\right)$$
$$- C_{\varepsilon_2}\,\bar{\rho}\,\frac{\tilde{\varepsilon}^2}{\tilde{k}}$$

As assumed in the standard 'k-ε' turbulent fluxes are computed from first gradient law where diffusion coefficients are built from the two basic local quantities k and ε. However, on the shock

wave these formulae have to be supplemented by algebraic relations in order to satisfy realizability conditions. For example, the radial turbulent kinetic energy has to satisfy the obvious inequalities

$$0 < \overline{\rho u_r'^2} < 2\,\bar{\rho}\,\tilde{k}. \qquad (2.1)$$

Therefore, on strong discontinuities, we use the classic invariant closure

$$-\overline{\rho u'^2} = 2\mu_t \frac{\partial \tilde{u}_r}{\partial r} - \frac{2}{3}\bar{\rho}\tilde{k} - \frac{2}{3}\bar{\rho}\mu_t \frac{\partial \tilde{u}_r}{\partial r} \quad \text{with} \quad \lambda_m \bar{\rho}\tilde{k} < \overline{\rho u'^2} < \lambda_M \bar{\rho}\tilde{k} \qquad (2.2)$$

where λ_m and λ_M have been respectively chosen equal to 0.10 and 1.25 and $\mu_t = c_d \bar{\rho}\tilde{k}^2/\tilde{\varepsilon}$
In the same way approximating the turbulent mass flux $\overline{\rho' u'}$ by the density gradient may lead to very high unphysical values under a shock wave. On the other hand, this flux has to satisfy the Scharwz inequality

$$\overline{\rho' u'} < \overline{\rho'^2}^{1/2}\ \overline{u'^2}^{1/2} \qquad (2.3)$$

The momentum mass flux being bounded by the total turbulent kinetic energy and the variance of density fluctuations is assumed to be bounded by the mean density itself, we finally write the turbulent mass flux as

$$\overline{\rho' u'} = D_\rho \operatorname{grad} \bar{\rho} \quad \text{with the realizability condition} \quad \overline{\rho' u'} < \alpha\ \lambda_M^{1/2}\ \bar{\rho}^{1/2}\ \tilde{k}^{1/2}$$

where α is equal to 0.67.

The closure relations for f= c, e and k are now simply written as

$$\overline{\rho f' u'} = D_f \operatorname{grad} f \qquad \text{with} \qquad D_f = \mu_t/\sigma_f\, \tilde{k}^2/\tilde{\varepsilon}$$

II.2 MODEL CONSTANTS

We consider the following set of key experiments connecting experimental data to model constants, for calibration purposes:

- turbulence decays according to a power law in time with the exponent n . Consistency requires:

$C_{\varepsilon 2} = (1+n)/n$ with $n = 1.1$

-in self induced diffusion of turbulence from a steady source of turbulence at a plane in a fluid [6], experiments show that the turbulent intensity decays exponentially away from an effective source plane. Assuming:

$k(x) \propto x^{-m}$ and $\varepsilon(x) \propto x^{-n}$, we have :

$\sigma_\kappa = (3\, c_d\, \beta^2\, m^2)/2$ and $\sigma_\varepsilon = (c_d\, \beta^2\, (2+3m)\,(1+2m))/2\, c_{\varepsilon 2}$

with $\beta = 0.846$ and $m = 3$ [6]

-experiments on nearly homogeneous turbulent shear flow. In such a stationary flow [7], the k-ε model reduces to :

$$\rho u \frac{dk}{dx} + \overline{\rho u'v'} \frac{du}{dy} + \rho \varepsilon = 0$$

$$\rho u \frac{d\varepsilon}{dx} + c_{\varepsilon_1} \frac{\varepsilon}{k} \overline{\rho u'v'} \frac{du}{dy} + c_{\varepsilon_2} \rho \frac{\varepsilon^2}{k} = 0$$

with du/dy=constant. An exact solution may be exhibited. More interesting is its asymptotic behavior leading to the relation: $c_d = \tau^2 (c_{\varepsilon 1} - 1)/(c_{\varepsilon 2} - 1)$ linked to the experimental value τ=0.34 with $c_{\varepsilon 2}=(1+p)/p$ where p is an asymptotic exponent for decaying turbulence.

-boundary layer flows yield the well-known relation :

$c_{\varepsilon 1} = c_{\varepsilon 2} - \chi^2 / \sigma_\varepsilon c_d^{1/2}$ with $\chi = 0.41$

-rapid isotropic compression of homogeneous turbulence. There is little experimental evidence to test the compressible aspects of a k-ε model . Nevertheless, ignoring the Reynolds turbulent stress and dissipation the model equations become :

$$\rho \frac{Dk}{Dt} + \overline{\rho u'^2} \frac{\partial u}{\partial x} = 0$$

$$\rho \frac{D\varepsilon}{Dt} + c_{\varepsilon_1} \frac{\varepsilon}{k} \overline{\rho u'^2} \frac{\partial u}{\partial x} + c_{\varepsilon_3} \rho \varepsilon \frac{\partial u}{\partial x} = 0$$

or $$\frac{D}{Dt} Log \left(\frac{k}{\varepsilon}^{\frac{3 c_{\varepsilon_3} + 2 c_{\varepsilon_1}}{2}} \right) = 0$$

Assuming an invariant eddy viscosity coefficient $c_d k^2 / \varepsilon$ /3/, we have: $c_{\varepsilon 3} = 2 (2 - c_{\varepsilon 1})$.

The set of above relations gives a consistency equation on c_d which writes :

$$C_D^{5/2} - \left(\frac{\eta^2 p}{n} \right) C_D^{3/2} + \frac{2 \eta^2 \chi^2 p (1+n)}{n \beta^2 (2+3n)(1+2n)} = 0$$

The classic value c_d=0.09 given by numerical optimisation for years can be obtained from this equation by setting p=1.652. In that particular case, we must mention an another solution c_d=0.115 is associated with c_d=0.09.

Now, an attempt is made in order to connect $c_{\varepsilon 0}$ with σ_ρ by regarding turbulence decaying in a stratified stationary incompressible fluid .The k-ε model reduces to :

$$\rho u_0 \frac{dk}{dx} + \frac{\overline{v'\rho'}}{\rho} \frac{d\rho}{dy} + \rho \varepsilon = 0$$

$$\rho u_0 \frac{d\varepsilon}{dx} + c_{\varepsilon_0} \frac{\varepsilon}{k} \overline{v'\rho'} \frac{d\rho}{dy} + \rho c_{\varepsilon_2} \frac{\varepsilon^2}{k^2} = 0$$

setting $N=\left(\frac{g}{\rho}\frac{d\rho}{dy}\right)^{1/2}$, assuming $\gamma=\frac{1}{\rho}\frac{d\rho}{dy}$ and defining $\phi=\varepsilon/k$, the set of equations becomes :

$$\frac{d\phi}{dx}+\left(\frac{C_{\varepsilon_2}-1}{u_0}\right)\phi^2+\frac{C_D N^2(1-C_{\varepsilon_0})}{\sigma_\rho u_0}=0$$

The asymptotic behavior of the solution is :

$$c_{\varepsilon 0} = 1+ \left((c_{\varepsilon 2} - 1) \sigma_\rho \varepsilon^2(\infty)\right) / N^2 c_d k(\infty)$$

Using the experimental data from Ref.[8], an estimate can be made that yields : $c_{\varepsilon 0}=0.2\sigma_\rho+1$ with $c_{\varepsilon 2}=1.9$ and $c_d=0.09$.

Conventional choices are made for σ_c and σ_e :

$\sigma_c=0.7$ passive scalar mixing

$\sigma_e=0.9$ heat transfer experiments

Finally, the set of model constants used for numerical applications is :

$C_{\varepsilon 0}$	$C_{\varepsilon 1}$	$C_{\varepsilon 2}$	$C_{\varepsilon 3}$	σ_κ	σ_ε	σ_c	σ_e	C_d	σ_ρ
1.065	1.47	1.90	0.35	0.87	1.30	0.70	0.90	0.09	0.325

III - NUMERICAL APPLICATIONS:

The model is numerically solved by the Richtmeyer scheme. K and ε diffusion terms are handled in a coupled implicit manner while Rayleigh-Taylor source terms are discretized in an explicit way.

The canonical Andronov et al's experiment has been simulated with our k-ε model. The 1.3 Mach number shock wave was produced by a constant pressure at one boundary. We used the perfect gas equation of state. The initialization was done by using the Mikaelian's model [9] and the mix model was turned on at t=800 μs. We have displayed on Fig. 1-2 the interface velocity profile and its spatial derivative. It is clear that the velocity gradient is applied for a short time - 10μs - compared to the characteristic time of diffusion which is of the order of 700μs, in other words, shock waves act as a rapid distorsion which is essentially governed by linear effects [10]. This conclusion is enforced by looking at Fig.11 where the return time to isotropy is of the order of 10μs and the turbulence decaying time is of the order of 200μs (Fig.3). It follows that the dominant behavior is essentially a diffusion one, and model responses are weakly non-linear.

The time evolution of the total turbulent kinetic energy is displayed on Fig.3. It is easy to notice the effect of shock wave on turbulence: it increases the turbulent kinetic energy by one order of magnitude, for the first shock. As shock waves become more and more attenuated after some reflections on the wall, the enhancement of turbulent kinetic energy is smaller and smaller. By looking at any typical quantity such as the turbulent kinetic energy, the dissipation rate or turbulent fluxes, we observe the same kind of behavior: the quantity is strongly enhanced by shock waves and decays over a large characteristic time. We notice that the Mach number of the two first shocks Ma_c are greater than one. But the Mach number of the flow, computed by $Ma_f=u/c_s$, is never greater than 0.60 (Fig.5), and the maximum decreases as time goes on. The Mach number of the fluctuating velocity, computed by $Ma_t=k^{1/2}/c_s$ (Fig.6), is largely less than the unity: velocity fluctuations are strongly subsonic. Fig.7 shows the evolution of both experimental and calculated mixing zone boundaries.The mixing thickness is displayed on Fig.8 and is in good agreement with the experimental data. It clearly appears

that the mixing penetrates more rapidly in the light fluid than in the heavy one.

On Fig.8 we have plotted the evolution of the characteristic length $k^{3/2} / \varepsilon$ at different locations of the mixing zone together with the mixing zone width. It appears that they are not proportional as assumed in a one equation model. In other words, the size of largest eddies saturates as shock waves attenuate.

In the experiment described in [11] a shock wave in CO_2 accelerates a CO_2/helium or argon contact surface thus creating a turbulent mixing zone which is then decelerated by a reflected shock. The initial pressure of gases is 2000 Pa or 1500 Pa. So, three experimental combinations are carried out. The comparison between calculated and experimental turbulent mixing zone thicknesses are presented on Figures 13-15. Using the same initialization procedure as for the Andronov et al's experiment, a value of σ_ρ of about 0.32-0.33, yields satisfying simulations of the turbulent thickening. This result emphasizes the turbulent model ability to simulate different Atwood and Mach number experiments.

Finally, we must mention and recall that a part of the discrepancy between experimental and calculated values is probably due to non negligible boundary layer effects. The Marseilles k-ε simulations are now under way and a detailed analysis will be published later on.

IV - CONLUSION:

We have developed a k-ε model for handling situations characterized by high values of the turbulent flux Richardson number. Closure relations have been supplemented in order to be valid under strong discontinuities. Calibration has been done by classic experimental available data and by studying the k-ε model in some special cases. Simulations on several shock tube experiments agree fairly well with available experimental data.

ACKNOWLEDGMENTS: We would like to thank A. Grimaldi for her help in preparing the manuscript.

REFERENCES:

1 - V. A. Andronov et al. JETP Lett. **29**, 1 (1979) and Sov. Phys. Dokl.,**27** , 5 (1982).
2 - S. Gauthier, CEA Limeil-Valenton Internal Report (1982).
3 - M. Bonnet, S. Gauthier, P. Spitz, CEA Limeil-Valenton Internal Report (1987).
4 - C. E. Leith Preprint-Livermore (1987).
5 - B. E. Launder and D. B. Spalding, Comp. Meth. in Applied Mech. and Eng., 3, 1974.
6 - A. Sonin, Phys. Fluids **26**, 10, 1983.
7 - F. C. Champagne et al., J. Fluid Mech., **41**, 81, 1970.
8 - E.C. Itswere et al, J. Fluid Mech., **162**, 299, 1986.
9 - K. O. Mikaelian, Phys. Rev. Lett. **54**, 5 (430) 1985.
10 - J. Mathieu, Bréau-Sans-Nappe Summer School (1982).
11 - L. Houas et al., 15 th International Symposium on shock waves and shock tubes. Stanford University Press (1986).

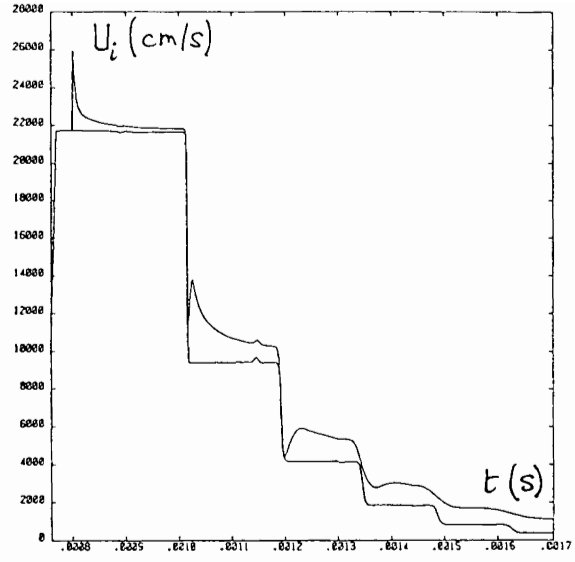

Fig. 1 - Interface velocity profile with and without mixing.

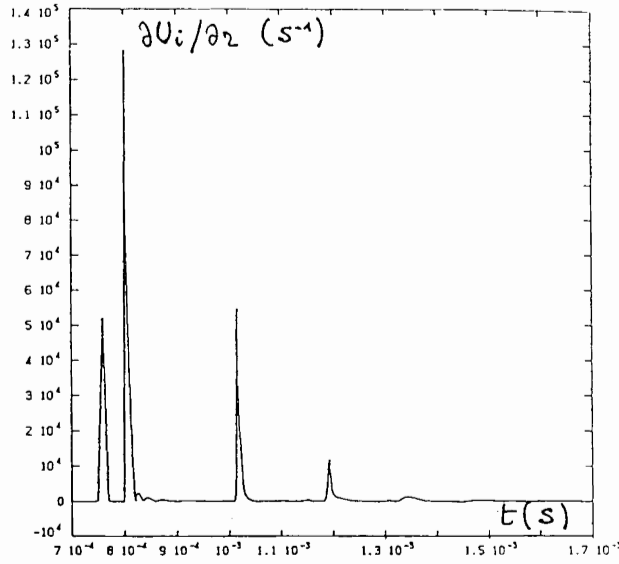

Fig. 2 - Interface velocity gradient profile.

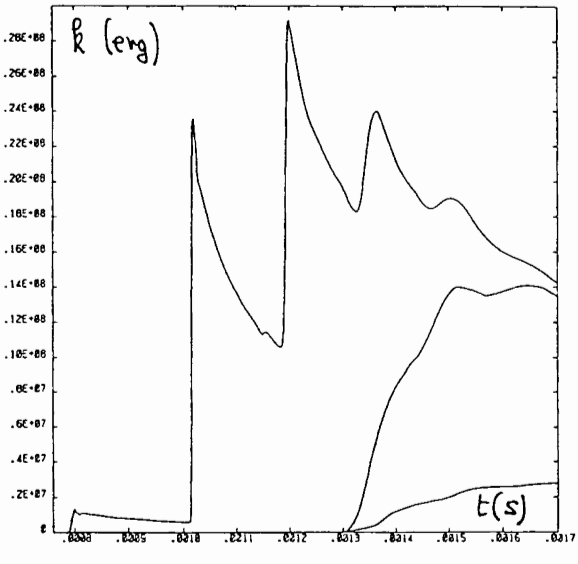

Fig. 3 - Evolution of the turbulent kinetic energy at three different locations.

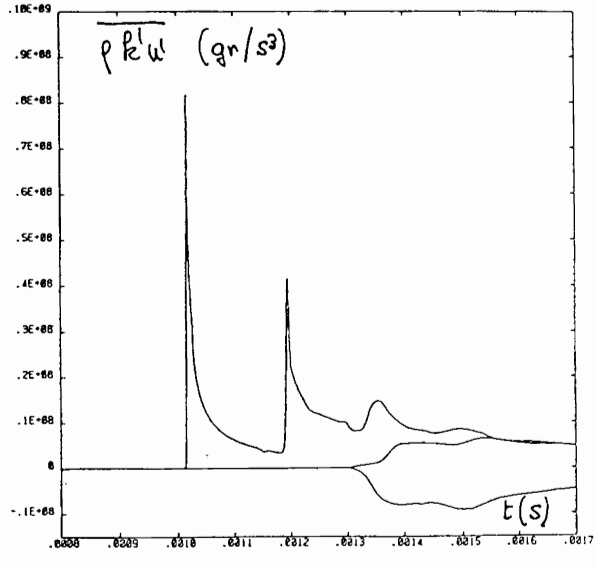

Fig. 4 - Evolution of the turbulent kinetic energy flux (same locations as in Fig.3).

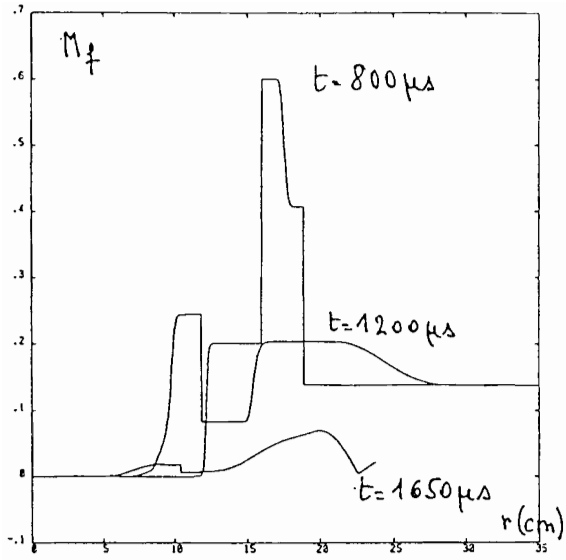

Fig. 5 - Flow Mach numbers.

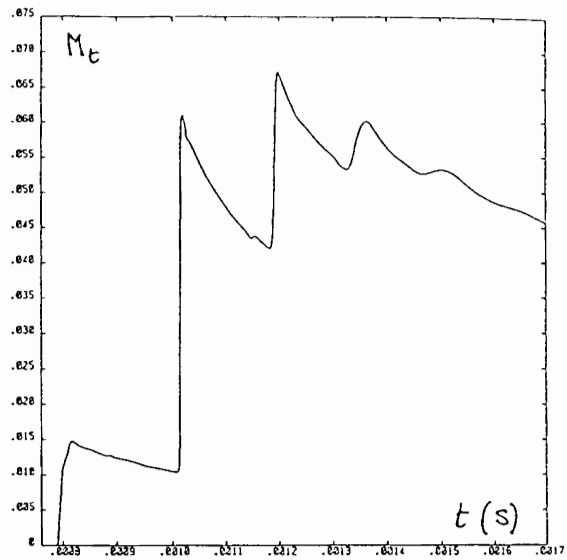

Fig. 6 - Turbulent Mach number of the interface.

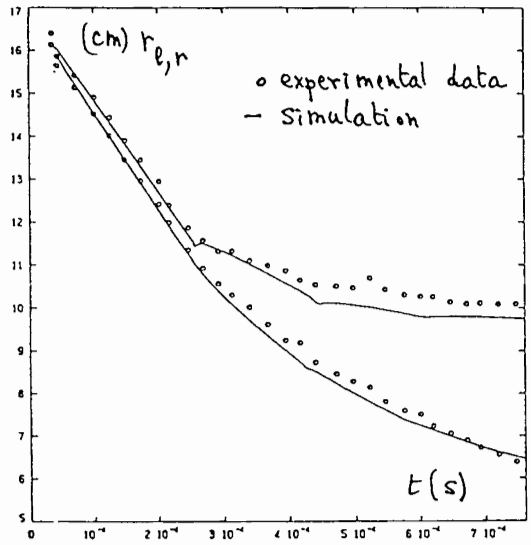

Fig. 7 - Turbulent mixing zone boundaries.

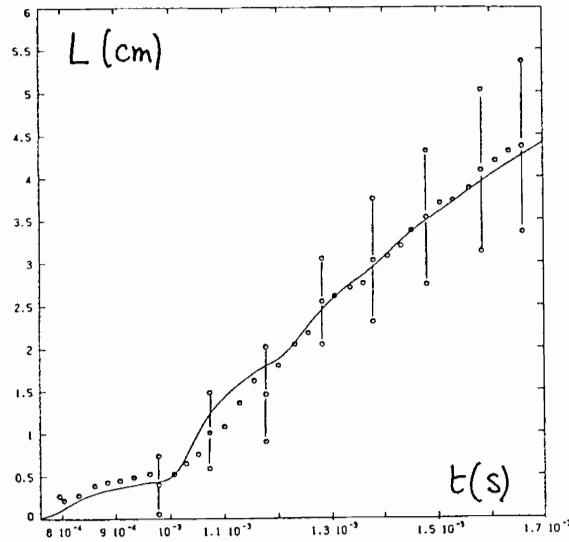

Fig. 8 - Thickness of the turbulent mixing zone.

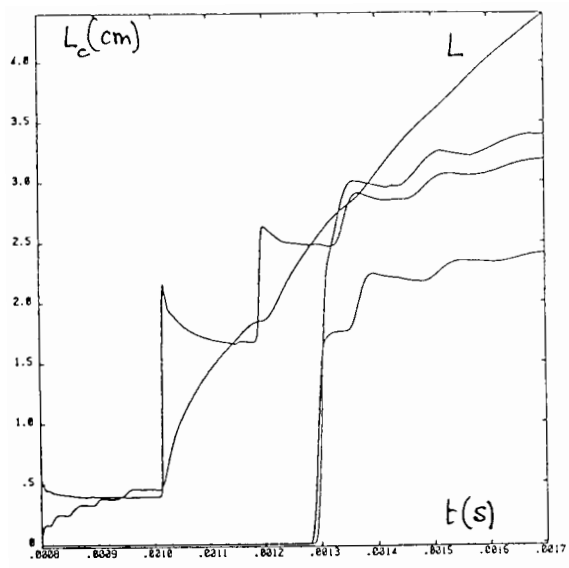

Fig. 9 - Evolution of the characteristic length $k^{3/2}/\varepsilon$ at three different locations (same as in Fig.3) with the turbulent zone thickness

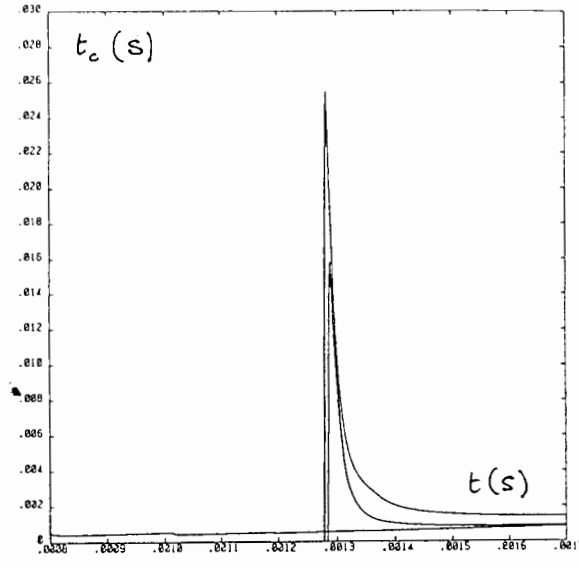

Fig. 10 - Turbulent characteristic time k/ε (same locations as in Fig.3).

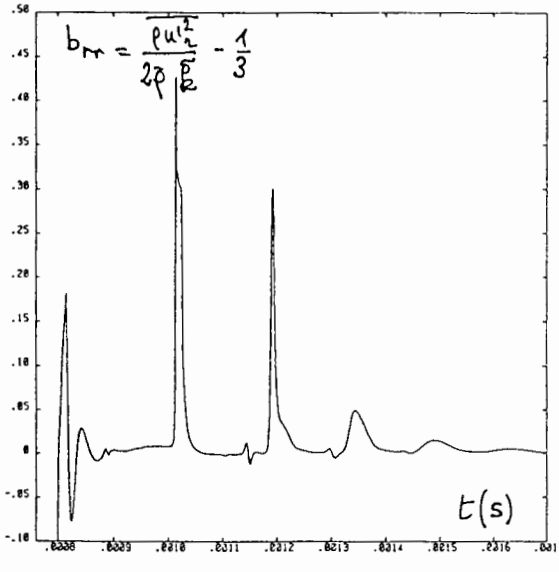

Fig. 11 - Radial part of the Reynolds stress tensor deviator.

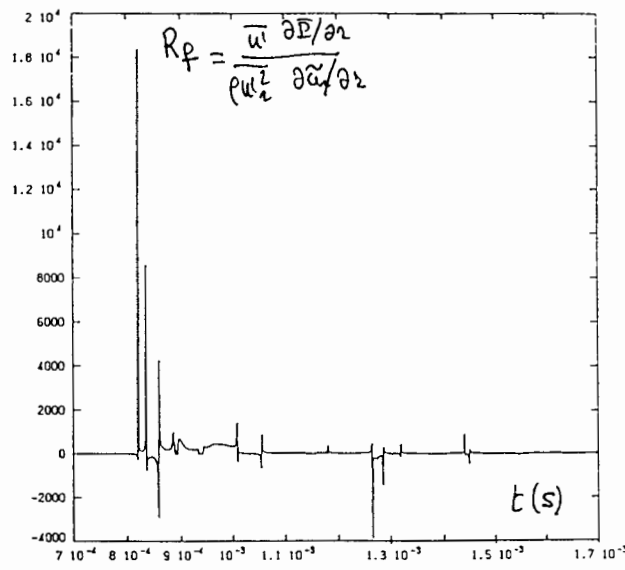

Fig. 12 - Turbulent flux Richardson number.

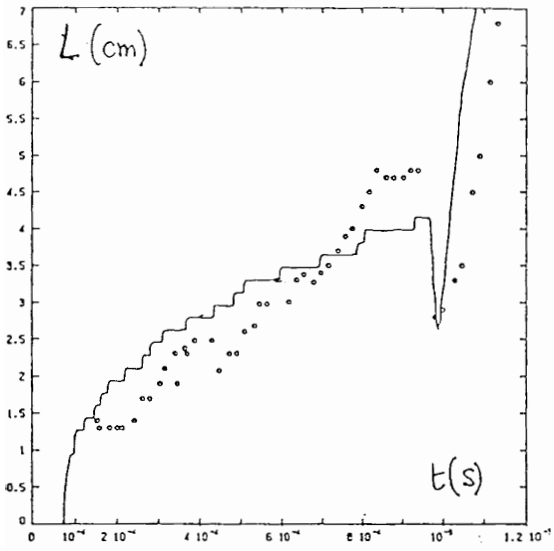

Fig. 13 - He/CO_2 - $P_{initial}$=2000 Pa thickness of the TMZ.

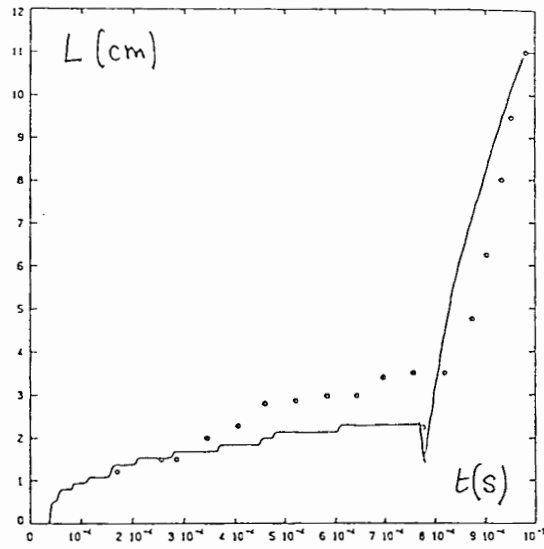

Fig. 14 - He/CO_2 - $P_{initial}$=1500 Pa thickness of the TMZ.

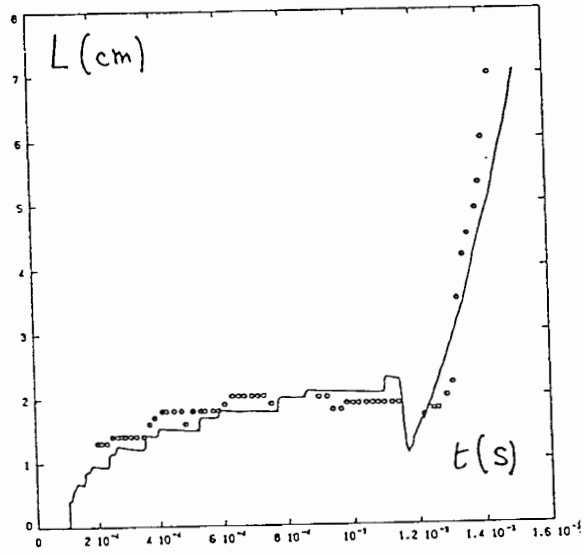

Fig. 15 - Ar/CO_2 - $P_{initial}$=2000 Pa thickness of the TMZ.

A SECOND-ORDER CLOSURE FOR SUPERSONIC TURBULENT FLOWS APPLICATION TO THE SUPERSONIC MIXING

J.P. DUSSAUGE & C. QUINE

INSTITUT DE MECANIQUE STATISTIQUE DE LA TURBULENCE
Unité Mixte Université-CNRS N° 380033
12 Avenue du Général Leclerc, 13003 Marseille (France)

INTRODUCTION

The classical second-order closures are generally well adapted to the computation of supersonic flows in which non-linear effects due to compressibility are weak for moderate supersonic Mach numbers (Dussauge, Gaviglio,1987).

For higher Mach numbers, the structure of turbulence in boundary-layers seems altered (Laderman, Demetriades, 1979). The measurements involved are difficult, but some conclusions of this analysis are in agreement with the recent work of Smits et al. 1988. A good example of the effects of compressibility is given by supersonic free shear flows, which cannot be computed with low-speed turbulence models. This is probably due to the large density fluctuations produced by the high speeds. For example, a classical $k-\varepsilon$ model does not reproduce the spreading rate of the supersonic free shear layer. An analysis is proposed in the present paper to take in account small departures from incompressibility caused by density fluctuations. An algebraic stress model is deduced and is used to compute free shear layers. The results are compared to measurements of mean and fluctuating quantities.

ANALYSIS

It is known from experiment that the spreading angle of supersonic free shear layers is a decreasing function of the Mach number. The reasons of the reduction of the turbulent mixing are not clearly identified, but some salient features of supersonic shear layers can be recalled, and used as guidelines to find the compressibility effects involved.

Firstly, as the flow is nearly parallel, the mean divergence can be neglected: the mean flow reduces practically to a pure shear, and the observed phenomena cannot be understood as an effect of mean compressibility or mean velocity divergence. Secondly, the density fluctuations can be very large. For flows without heat sources, their order of magnitude is given by the

"Strong Reynolds Analogy" (SRA) relation :

$$\rho'/\overline{\rho} \cong (\gamma - 1)\, M^2\, (u'/\overline{u}) = (\gamma - 1)\, Mm \qquad (1)$$

$\overline{u}$ is the longitudinal mean velocity, ρ the density, M the mean Mach number, $m = u'/a$ is the Mach number of the fluctuations, $\gamma = C_p/C_v$. Formula (1) essentially assumes that the total temperature fluctuations are smaller that the temperature fluctuations (Debieve, Gouin, Gaviglio, 1983), and that the density (or temperature) fluctuations are isobaric, as in zero pressure gradient turbulent boundary-layers (Laufer, 1968).

This relation shows that even at $M = 1$, density and velocity fluctuations have comparable intensities. High density fluctuations may change the properties of turbulence. For example for subsonic flows, some closures can be derived from the incompressibility of the fluctuating motion. It is then useful to have some hint about the generality of this hypothesis. For small fluctuations, the divergence of the fluctuating velocity is given by :

$$\mathrm{divu}' = -\frac{1}{\gamma}\left(\frac{d}{dt}\frac{p'}{\overline{p}}\right) - \left(\overline{u_i' \frac{\partial}{\partial x_i}\frac{p'}{\overline{p}}}\right) - \frac{\varepsilon}{C_p \overline{\theta}}\frac{\theta'}{\overline{\theta}} - \frac{\varepsilon_\theta}{\gamma \overline{\theta^2}}\frac{\theta'}{\theta} \qquad (2)$$

θ is the temperature and ε_θ the rate of dissipation of temperature variance. Dussauge, Debiève and Smits (1988) noticed that the pressure terms in eq.(2) can be neglected of the level of p'/p is small compared to $\theta'/\overline{\theta}$ and if the characteristic time scale of pressure fluctuations is not too small, compared to the time scale of the other quantities. With these assumptions they found that the ratio $\mathrm{divu}'/(\partial u_i' / \partial x_j)$ is proportional to $m^3 M(1 + CM^2)$, where C is a constant. This result is valid only in cases where divu' is caused by heating through viscous dissipation and heat conduction. It suggests that in many supersonic (but not hypersonic) flows, divu' is probably small, and the fluctuating field is nearly solenoïdal. Such a situation occurs probably only when m is much less than 1. If $m \sim 1$, the turbulent motion may produce a significant number of shocklets. In this case, the pressure term of eq.(2) cannot be neglected and the previous result does not hold. In many flows without heat sources at moderate supersonic Mach numbers ($M \sim 2$, say), it seems that m is much less than 1, but the density fluctuations are not small. Then, for such flows, it may be assumed that the velocity field is solenoïdal but the turbulent diffusion of momentum, kinetic energy, etc... and the return to isotropy can be modified by the density fluctuations. Brown and Roshko (1974)

pointed out, from dimensional reasoning and from order of magnitude estimates, that the pressure fluctuations should depend on the Mach number. They supposed that essentially the "pressure transport" terms were affected by this effect. In the present work it is supposed that the pressure-strain terms in the Reynolds stress equation should be modified as well. Indeed, the decrease of the spreading rate indicates that the turbulent diffusion (and the Reynolds stress $\overline{u'v'}$) becomes smaller with increasing Mach number. Then, the influence of density fluctuations on the pressure-strain terms has to be examined, as previously suggested by Bonnet (1981). The present paper underlines this aspect of the problem, but we must have in mind that the effect of pressure-transport is to be also considered in a more complete model.

A temptative illustration of the modification of the return-to-isotropy process by density fluctuations can be proposed by reconsidering the scheme used by Rotta (1951), for constant enthalpy evolutions : a lump of incompressible fluid is pinched in the longitudinal direction by a fluctuation of velocity u'_1 . Because of incompressibility, it is stretched in the other directions, producing u'_2 and u'_3 fluctuations.

If now the fluid is compressible with a constant total enthalpy the pinching in direction 1 produces u'_1 and ρ' fluctuations ; u'_2 and u'_3 are then not the same as in the incompressible case. Moreover the S.R.A. indicates that u'_2 and u'_3 are not linearly associated with density fluctuations. From this point of view, u'_1 and u'_2 or u'_3 do not play symmetrical roles.

The order of magnitude analysis shows (Quine, 1986) that for an incompressible field with non constant density and zero mean pressure gradient, the simplified equation for pressure reads :

$$-\Delta p' = 2\,\overline{\rho}\,\frac{\partial \overline{u_j}}{\partial x_i}\frac{\partial u'_i}{\partial x_j} + \overline{\rho}\,\frac{\partial u'_i}{\partial x_j}\frac{\partial u'_j}{\partial x_i} + \frac{\partial \rho'}{\partial x_i}\left(\frac{\partial u'_i}{\partial t} + \overline{u_j}\,\frac{\partial u'_i}{\partial x_j} + u'_j\,\frac{\partial \overline{u_i}}{\partial x_j}\right)$$

$$+ \text{higher order terms.}$$

The quadratic terms involving density fluctuations are :

$$\frac{\partial \rho'}{\partial x_i}\left(\frac{\partial u'_i}{\partial t} + \overline{u_j}\,\frac{\partial u'_i}{\partial x_j} + u'_j\,\frac{\partial \overline{u_i}}{\partial x_j}\right) \qquad (3)$$

If the three terms in brackets are of the same order, their magnitude can be obtained by considering the second one $\dfrac{\partial \rho'}{\partial x_i}\,\overline{u_j}\,\dfrac{\partial u'_i}{\partial x_j}$.

It is of the order of $(\gamma - 1)\, M^2\, \overline{\rho}\, \frac{\partial u_i'}{\partial x_j}\, \frac{\partial u_j'}{\partial x_i'}$ if relation (1) holds and if the space scales for density and velocity fluctuations are of the same order. Therefore, these terms cannot be neglected in supersonic flows. Their contribution to the pressure-strain terms is modeled in the following way :

$$\Pi_{ij,\rho}(\vec{x}) = \frac{1}{4\pi}\, \overline{u_k} \int_{vol} \frac{\partial \rho'(\vec{x}+\vec{r})}{\partial x_l}\, \frac{\partial u_l'(\vec{x}+\vec{r})}{\partial x_k} \left(\frac{\partial u_j'}{\partial x_i}(\vec{x}) + \frac{\partial u_i'}{\partial x_j}(\vec{x}) \right) \frac{dvol}{r}$$

By analogy with Rotta's model for the return-to-isotropy, $\Pi_{ij,\rho}$ is supposed of the form :

$$\Pi_{ij,\rho} = \overline{u_l}\, \frac{\varepsilon}{k}\, T_{ij}^1 \qquad (3)$$

where T_{ij}^1 is a function of the arguments $\overline{\rho' u_i'}$, $\overline{\rho' u_i' u_j'}$, etc... Only the argument of lowest order $\overline{\rho' u_i'}$ is retained here. As the isotropic value of $\overline{\rho' u_i'}$ is zero an expansion to the first order with respect to $\overline{\rho' u_i'}$ is made. As the turbulent field is nearly incompressible, the condition $\Pi_{ii,\rho} = 0$ can be used. Applying the conditions of symmetry and incompressibility, the expression of T_{ij}^1 is found :

$$T_{ij}^1 = \alpha \left[\overline{\rho' u_l'} \delta_{ij} - \frac{3}{2} \left(\overline{\rho' u_j'} \delta_{il} + \overline{\rho' u_i'} \delta_{jl} \right) \right] \qquad (4)$$

where α is a constant to be determined from experiment.

For flows with constant total enthalpy, the turbulent mass flux can be related to the Reynolds stress through relations similar to (1). For example, Debièvet al. (1983) and Dussauge and Gaviglio (1987) use

$$\frac{\overline{\rho' u_i'}}{\overline{\rho}} = k(i)\, (\gamma - 1)\, M^2\, \frac{\overline{u'_1 u_i'}}{\overline{u}} \qquad (5)$$

with $k(i)$ are functions of the correlation coefficients between velocity components or between velocity and density, $k(1) = 0.8$ and $k(2) = 1.5$.

Relations (3), (4) and (5) are used together with the A.S.M. proposed by Rodi (1976). Modified algebraic expressions are deduced :

$$\begin{cases} \dfrac{\overline{u'_1u'_1}}{k} = \dfrac{(\overline{u'_1u'_1}/k)_o}{1 - 2\,\beta\,k(1)\,M^2} \\ \dfrac{\overline{u'_2u'_2}}{k} = \left(\dfrac{\overline{u'_2u'_2}}{k}\right)_o \left[1 - \dfrac{\beta\,k(1)\,M^2}{1 - 2\,\beta\,k(1)\,M^2}\left(\dfrac{\overline{u'_1u'_1}}{\overline{u'_2u'_2}}\right)_o\right] \\ \dfrac{\overline{u'_1u'_2}}{k} = \left(\dfrac{\overline{u'_1u'_2}}{k}\right)_o \dfrac{1}{1 - (3/2)\,\beta\,k(2)\,M^2} \end{cases} \qquad (6)$$

with

$$\beta = \frac{\alpha\,(\gamma - 1)}{(C_1 - 1) + P/\varepsilon}$$

The subscript o indicates the value for incompressible (zero Mach number) flows.

$\gamma = C_p/C_v = 1{,}4$; $C_1 = 1.5$ is the constant in Rotta's model for the return-to-isotropy; P is the production per unit mass of turbulent kinetic energy k and ε its dissipation rate.

In particular the ratio $C_\mu = \left(\dfrac{\overline{u'_1u'_2}}{k}\right)^2$ used in eddy viscosity formulations can be determined :

$$C_\mu = C_{\mu_o} \frac{1}{(1 - (3/2)\,\beta\,k(2)\,M^2)^2} \qquad (7)$$

with

$$\nu_T = C_\mu\,k^2/\varepsilon \qquad (8)$$

A simplified model was also tested, by replacing in (6) the Mach number by its external value M_e :

$$C_\mu = C_{\mu_o} / (1 - (3/2)\,\beta'\,k(2)\,M_e^2)^2 \qquad (9)$$

β' is a constant

Calculations of mixing layers were performed with different models. Firstly the high Reynolds number part of the model of Jones and Launder (1971) was used; this model uses relation (5) with $C_\mu = 0.09$ (model I). Secondly, formula (4) was used to determine C_μ ; the value of α had to be determined (model II). Thirdly, (model III), the simplified formulation (6) was tested. The parabolic set of equations was solved by the numerical procedure of Patankar and Spalding (1970).

RESULTS

The rate of spread $s = d\delta/dx$ was calculated to determine the constants α and β'. The recommendations of the Stanford Conference (1980) were followed to define the thickness of the layer δ : δ was determined between the points where the velocity is $\sqrt{0.1}\ U_e$ and $\sqrt{0.9}\ U_e$.

For subsonic flows (Me<0.1) it was found that the three models give a satisfactory spreading rate , $s = 0.13$. For higher speeds, model I keeps s unchanged and does not follow the experimental data. Model II with $-1.35 \leqq \alpha \leqq -0.8$ and model III with $\beta' = -0.05$ give satisfactory predictions of s (Fig. 1). A better agreement for high Mach numbers is obtained for large values of $-\alpha$, but the evolution at low Mach number is too rapid. As the model is not expected to be adequate in the hypersonic regime, the value $\alpha = -0.8$ seems to be a better compromise.

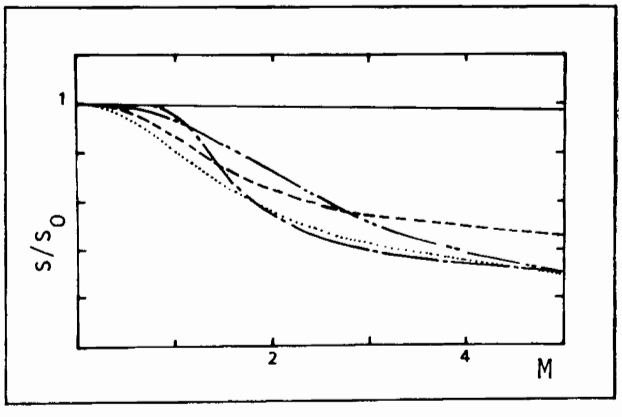

Figure 1:
Computed rate of spread of the supersonic mixing layer
—— - —— experiments
—— model I ;
- - - model II $\alpha = -0.8$;... $\alpha = 1.35$
— - - — model III

Figure 2 presents the evolution of the maximum value of the shear stress $-\overline{u'_1u'_2}/U^2_\infty$. The experimental data are very scattered; it seems however that $-\overline{u'_1u'_2}$ decreases with increasing Mach number. Model I is not able to reproduce this trend while model II and III find results qualitatively

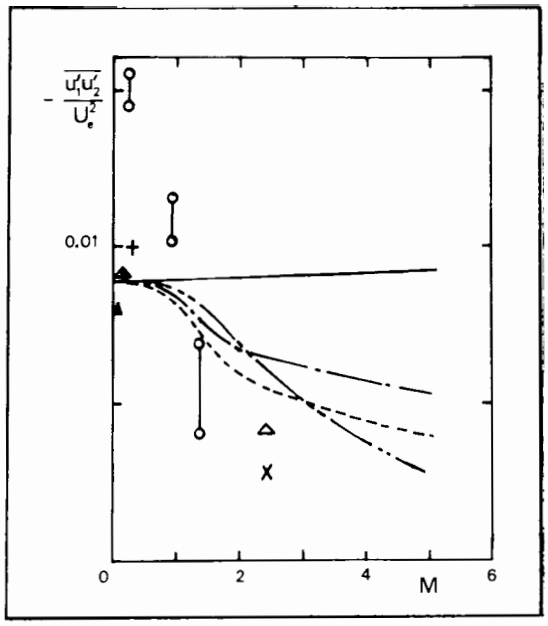

Figure 2 :

Maximum value of the shear stress in supersonic mixing layers

Model I —— ;

Model III —— - - —— ; $\beta' = -0.05$

Model II: —— - —— $\alpha = -0.8$

--------- $\alpha = -1.35$

▲ Liepmann, Laufer 1947;

Δ Wygnanski, Fiedler 1970;

\+ Bradshaw, 1966;

X Ikawa Kubota 1975 ;

o Lau et al. 1979;

Δ Samimy et al. 1986.

similar. The same comments can be made for the maximum value of $\overline{u'_1{}^2}/U^2_\infty$ (Figure 3).

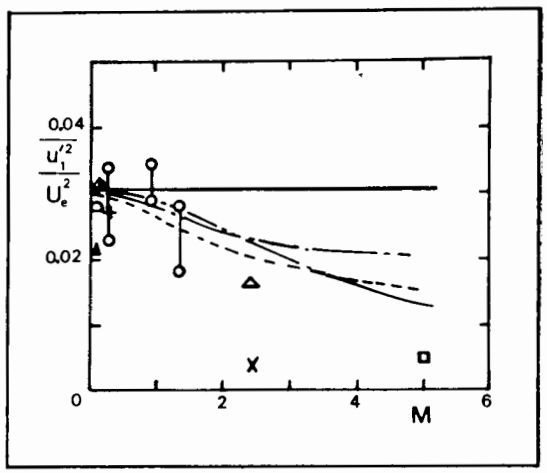

Figure 3 :

Evolution of the maximum value of $\overline{u'_1{}^2}$ in supersonic mixing layers.

Champagne, Pao, Wygnanski, 1976 ;

Wagner, 1975

Other symbols as in Figure 2

Figure 4 shows the results about the maximum value of the variance of transversal velocity fluctuations $\overline{u'_2{}^2}/U^2_\infty$.

The computations indicate that $\overline{u'_2{}^2}/U^2_\infty$ increases, but no clear trend can be deduced from measurements which are particularly difficult for this component. Then the computation finds that the anisotropy of the turbulent stresses is strongly changed, while the ratio k/U^2_∞ remains nearly constant:

the effect of the model is to transfer energy from $\overline{u_1^2}$ to the other components. Moreover it was found that the ratio $-\overline{u'_1u'_2}/\overline{u'^2_1}$ is a weak function of the Mach number.

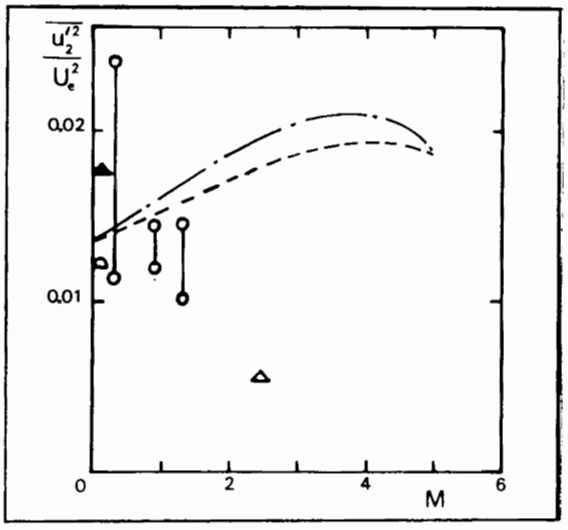

Figure 4 :

Maximum values of $\overline{u'^2_2}/U^2_\infty$ in supersonic mixing layers.

Symbols as in Figure 3

Computations using Model II and III predict that the correlation coefficient $-R_{12}$ between the longitudinal and transversal velocity fluctuations is a decreasing function of the Mach number. Although the complete calculation of a boundary layer was not performed with the present models, it was tempting to compare them with some recent measurements of correlation coefficient in a boundary layer at Mach 3 (Fernando 1988, Smits et al. 1988).

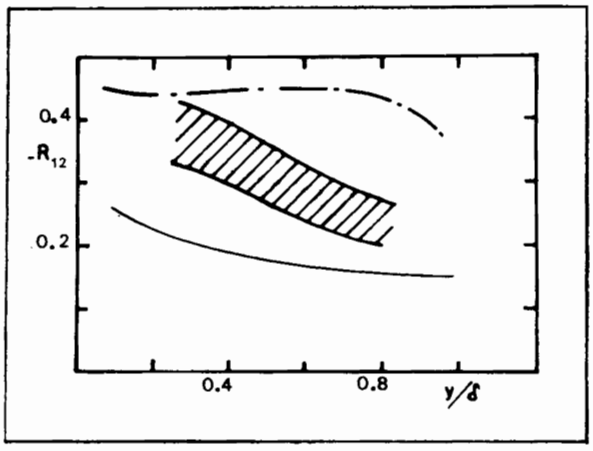

Figure 5 :

Velocity correlation coefficient in subsonic and supersonic boundary layers

—— - —— Subsonic boundary layer (Alving 1988)

/// Supersonic (M_e = 3) boundary layer (Fernando 1988 and Smits, private communication, 1988)

—— Model II

Model II was applied with $P/\varepsilon = 1$. The comparison with the experiments is given in Figure 5. The results of Model II are lower than the experimental value, but it is striking that the right trend was obtained i.e. values significantly smaller than the subsonic ones, although the ratio $P/\varepsilon = 1$ is a good choice only in the inner part of the layer.

CONCLUSIONS

It has been proposed to explain the anomalous rate of spread of the supersonic mixing layer by the influence of density fluctuations on the turbulent fluxes. The turbulent motion was supposed incompressible with a constant total enthalpy. A modification to the modeling of the return-to-isotropy is proposed. Correct values of the spreading rate of the mixing layer have been obtained, but the present models can probably be improved by taking in account the influence of compressibility on turbulence diffusion and pressure transport, without changing the qualitative trends found in the present version. The more striking result is a drastic change in the structure of turbulence and in the anisotropy of the Reynolds stresses. A first evidence is that the small number of measurements of $\overline{u'_2{}^2}$ and their limited accuracy preclude any firm conclusion on the ability of the model to calculate this component. The particular evolution of the anisotropy implies a reduction of $\overline{u'_1{}^2}$ and an increase of $\overline{u'_2{}^2}$ and $\overline{u'_2{}^3}$.

If the proposed mechanism gives a correct description of turbulence in supersonic flows, an important conclusion is that the motions with longitudinal vorticity can be reinforced by compressibility.

ACKNOWLEDGEMENTS

The authors are indebted to Dr J.P. BONNET for stimulating discussions and for the useful references he indicated to them.

REFERENCES

A.E. Alving, 1988, Ph. D. Thesis, Princeton Univ., Princeton, N.J., USA.

J.P. Bonnet, 1981, AFOSR-HTTM Stanford Conference Proceedings,Vol.3,pp 1408-1410.

P. Bradshaw, 1966, J. Fluid Mech., 26, pp 225-236.

G.L. Brown, A. Roshko, 1974, J. Fluid Mech., Vol. 64, part 4, pp 775-816.

F.H. Champagne, Y.H. Pao, I.J. Wygnanski, 1976, J. Fluid Mech., Vol. 74, part 2, pp 209-250.

J.F. Debiève, H. Gouin, J. Gaviglio, 1983, "Momentum and temperature fluxes in a shock-wave/turbulence interaction", Proceedings of the ICHMT/IUTAM, Dubrovnick 1980, Hemisphere Pub. Corp., Washington.

J.P. Dussauge, J.F. Debieve, A.J. Smits, 1988, "Rapidly distorted compressible boundary layers" in AGARDograph 315, H.H. Fernholz, A.J. Smits, J.P. Dussauge, P.J. Finley, To be published.

J.P. Dussauge, J. Gaviglio, 1987, J. Fluid Mech., Vol. 174, pp 81-112.

E.M. Fernando, 1988, Ph. D. Thesis, Princeton Univ., Princeton, N.J., USA.

H. Ikawa, T. Kubota, 1975, AIAA J., Vol. 13, N°5, pp 566-572.

W.P. Jones, B.E. Launder, 1971, Int. J. Heat Mass Transfer, Vol. 15, pp 301-314.

A.J. Laderman, A. Demetriades, 1979, AIAA J., Vol 17, N°7, 736-743.

J.C. Lau, P.J. Morris, M.J. Fisher, 1979, J. Fluid Mech., Vol 93, part 1,1-27.

J. Laufer, 1968, AIAA Paper N° 68-41, AIAA 6th Aerospace Science Meeting, New-York.

M.W. Liepmann, J. Laufer, 1947, N.A.C.A., T.N. N°1257.

S.V. Patankar, D.B. Spalding, 1970, "Heat and mass transfer in boundary layers, a general calculation procedure", Intertext book, London.

C. Quine, 1986, Mémoire de D.E.A., I.M.S.T., Univ. Aix-Marseille II.

W. Rodi, 1976, Z.A.M.M., 56.

J.C. Rotta, Z. Phys., Vol. 129, 547.

M. Samimy, H.L. Petrie, A.L. Addy, 1986, AIAA J., Vol 24, N°2.

A.J. Smits, A.E. Alving, R.W. Smith, E.F. Spina, E.M. Fernando, J.F. Donovan, 1988, "A comparison of the turbulence structure of subsonic and supersonic boundary layers", 11th Symposium on Turbulence, Univ. Missouri - Rolla, USA.

R.D. Wagner, 1975, N.A.S.A., T.N. D - 7366.

I. Wygnanski, H.E. Fiedler, 1970, J. Fluid Mech., Vol 41, 327-361.

1980-1981, AFOSR - HTTM - Stanford Conference, Vol I, S.J. Kline, B.J. Cantwell, G.M. Lilley Ed., Stanford University, Ca.

EVIDENCE OF RAYLEIGH-TAYLOR INSTABILITIES IN TRI-LAYER TARGETS

D. Galmiche, P. A. Holstein, B. Meyer, M. Rostaing, N. Wilke
Centre d'Etudes de Limeil-Valenton
BP 27, 94190 Villeneuve S^{t} Georges, France

INTRODUCTION

In laser fusion, the Rayleigh-Taylor (RT) instability represents a major obstacle by destroying the spherical symmetry of the imploding shell, thus leading to a degradation of target performance [1,2,3,4]. During implosion process, this instability may occur at the ablation layer on the outer surface, at an internal interface, or at the fuel-pusher interface during the deceleration phase. If the instability grows enough, it will buckle or break the shell and will cause fuel mix.

Experiments have been carried out at Limeil on P102 laser system in order to investigate the problem of target stability under ablative acceleration and to get direct evidence of RT instability [5]. Main experimental results are reported here.

Numerical simulation have been performed with the 1-D hydrocode FCI1 coupled with a simple mixing model. We present, in the following text, part of our numerical investigations which support the occurrence of a mixed layer.

I - EXPERIMENTS

I.1 - Experimental set-up

Tri-layer targets Au/Al/Au are accelerated by a main laser beam. The RT instability is thought to occur at the rear interface Al/Au where the pressure and density gradients are opposed. The front Au layer function is to smooth the energy deposition and to avoid a straight heating of the Al layer by the laser.

To evidence an Al-Au mixing, the rear surface composition of the target is diagnosed by using a probe laser beam being delayed with respect to the main beam. If the Al-Au mixing is quite developed,this probe beam heats up the rear mixing boundary; Al X-ray lines are excited and are observed with a spectrograph [6].

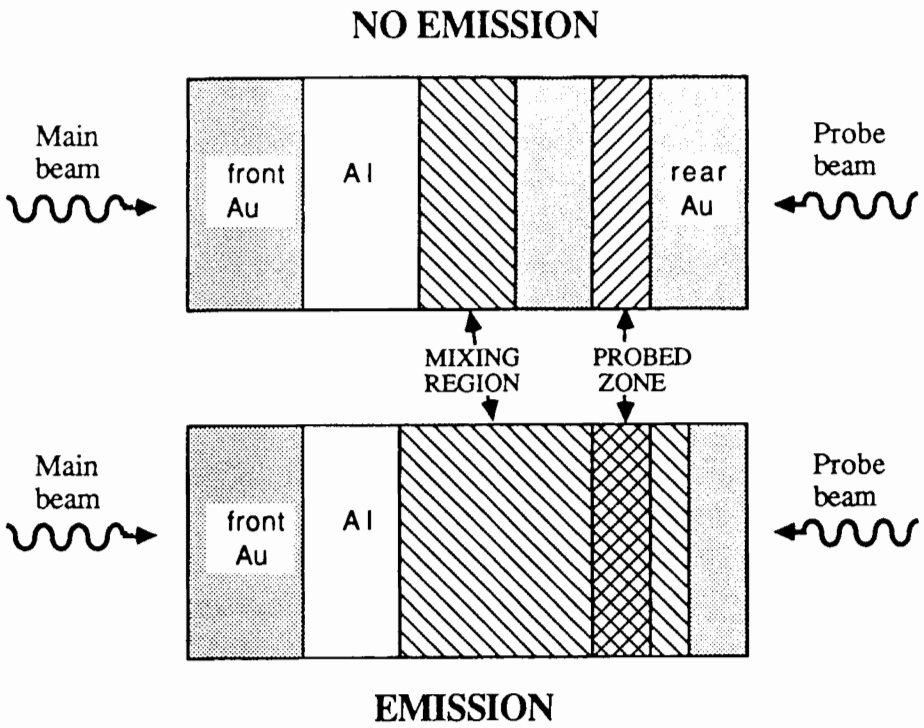

FIGURE 1
Schematic of experiment principle : Al emission is observed when the mixing region is well developed.

The main laser beam is at 0.35 μm and is focused from 10^{13} to 10^{14} W/cm^2 on target in a 180 μm diameter spot (its energy ranges from 1 to 11 J). The pulse is a sum of two gaussians with a 0.8-1 ns FWHM (full width at half maximum).

The probe beam is at 1.06 μm and is focused to 3 10^{13} W/cm^2 in a 180 μm diameter spot (its energy is 11 J); it is delayed by 1 ns relative to the main beam, and has a similar pulse shape with a 900 ps FWHM.

The X-ray spectrum from the rear target surface is measured in the range 1.4-2.7 keV with two spectrometers : the first one (TIS) temporally integrates the Al-lines, and the second one (TRS) gives the temporal resolution.

Typically the thickness is 0.3 μm for Au foils and 1 or 2 μm for Al foil.

I.2 - Benefit of time-resolved spectrometer (TRS)

The TRS supplies us with the intensity of lines emissions in the range 1.5-1.7 keV for Al ions and in the range 2.3-2.5 keV for Au ions; in addition, it gives us the durations and the shift between both emissions. Only the intensities higher than the detection threshold are experimentally observed.

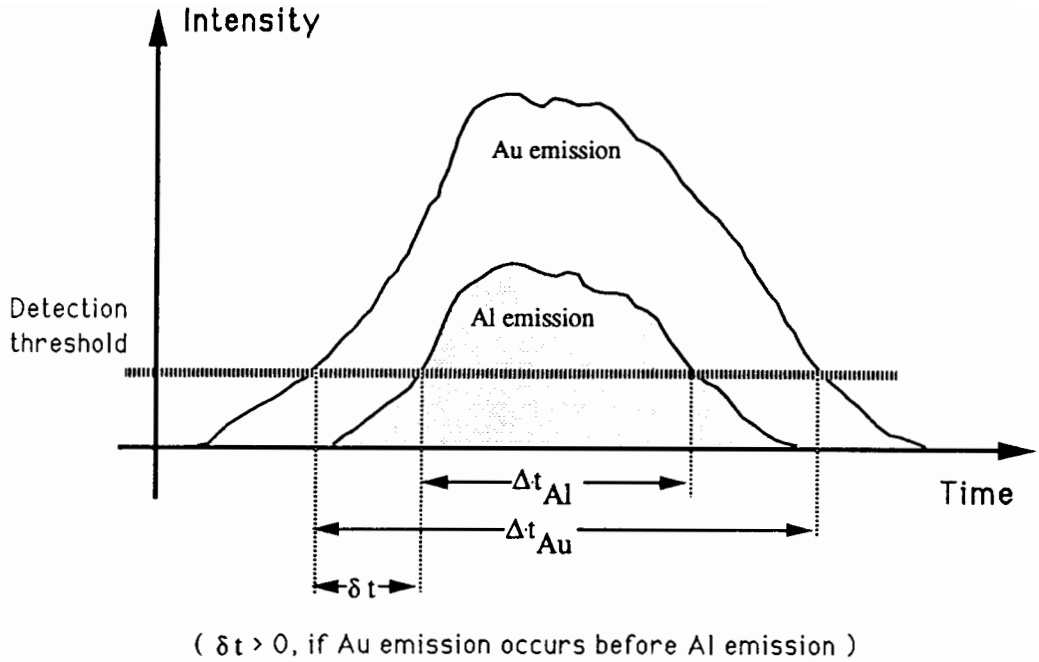

FIGURE 2
Schematic illustration of experimental data obtained with the time-resolved spectrograph (TRS).

The temporal shift δt gives informations about the depth of the mixing zone : δt is all the higher as the non-polluted Au thickness is large. For a small unmixed Au layer, the Al line emission may start before the Au emission, so that δt is negative.

X-ray lines emissions should enable us to get an evaluation of the mixing zone composition. To this end, it has been necessary to calibrate the intensity of emission for mixed Al and Au samples of which ions ratios were known. This step was followed by an other set of samples covered with Au, in order to point out the effect of a non-polluted Au layer.

Emission durations may drive numerical simulations. Comparisons between experiments and computations require the knowledge of emission threshold, and are proving hard to deal with.

Au emission in the Al lines range has to be subtracted. As signals are noisy, this systematic correction is approximate and we have to be very cautious in temporal shifts and lines intensities interpretation.

The advantage we should reap from TRS is illustrated at Figure 3 where results obtained with three samples are presented :

- two mixed Al-Au samples with different ions ratios are well characterized by emission levels and by temporal shift.
- two identical mixed Al-Au samples, one of which is covered with a Au layer, yield very different results.
- in spite of similar emissions, the temporal shift let us differentiate the (20%Al, 80%Au) sample to the (50%Al, 50% Au)+0.04 μm Au sample.

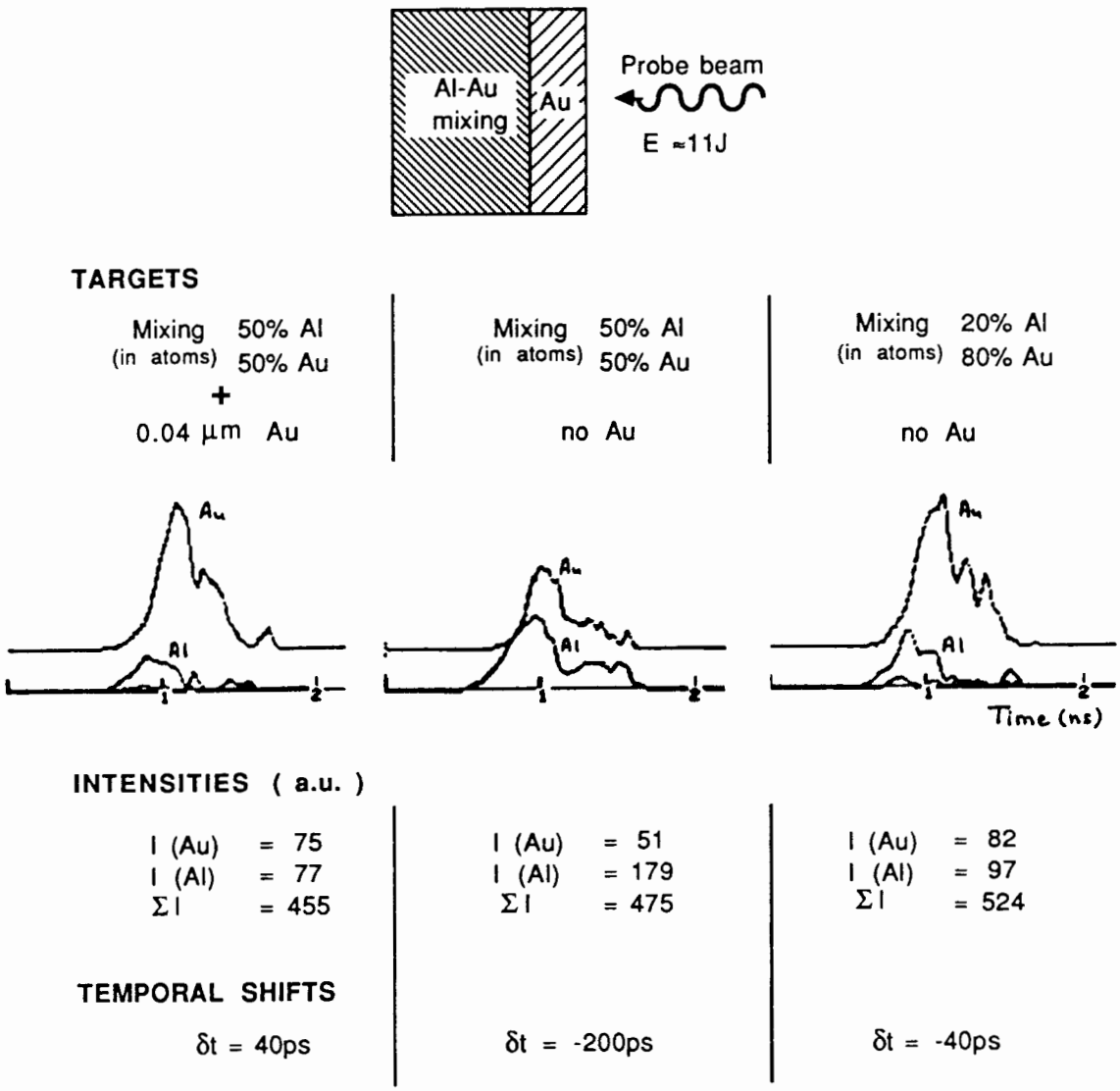

FIGURE 3
Experimental spectra obtained with the TRS. The intensities of Au emission, Al emission and the whole emission, and the temporal shift between Au and Al emissions are given for three different targets.

I.3 - Experimental results

The front gold layer prevents the Al layer from a direct heating and smooths the energy deposition by radiation. Former experiments carried out at Limeil have shown that for a 0.3 μm gold layer the pressure asymmetries at the ablation surface are reduced by a factor 3-4 [7], which may ensure the absence of large-scale instabilities due to irradiation non-uniformity. In the present experiment, optical smoothing with the "Random Phase Plates" technique (RPP) has been realized during last shots; as results obtained with and without RPP are similar, it has confirmed that large-scale illumination non-uniformities are not responsible for the apparent mixing.

Preliminary experiments have been realized to determine the ablation depth in order to make sure that, in the initial configuration, the Al layer cannot be heated by the probe laser beam. Two-layer targets have been irradiated with the probe beam : over 0.1 μm gold thickness, the Al He_α line emission is below the experimental threshold. A 0.3 μm rear gold thickness assures us that there will be no emission in the absence of mixing.

Figure 4 gives the Al line energy versus the main laser energy with a 2 μm Al foil tri-layer target. Despite the 0.3 μm gold thickness, the Al line appears, therefore some mixing occurs. Dispersion of the data is due to the very small signals receive on the spectrograph. Al line emission, which is our mixing signature, appears between 2 and 4 J, and increases with the main beam energy.

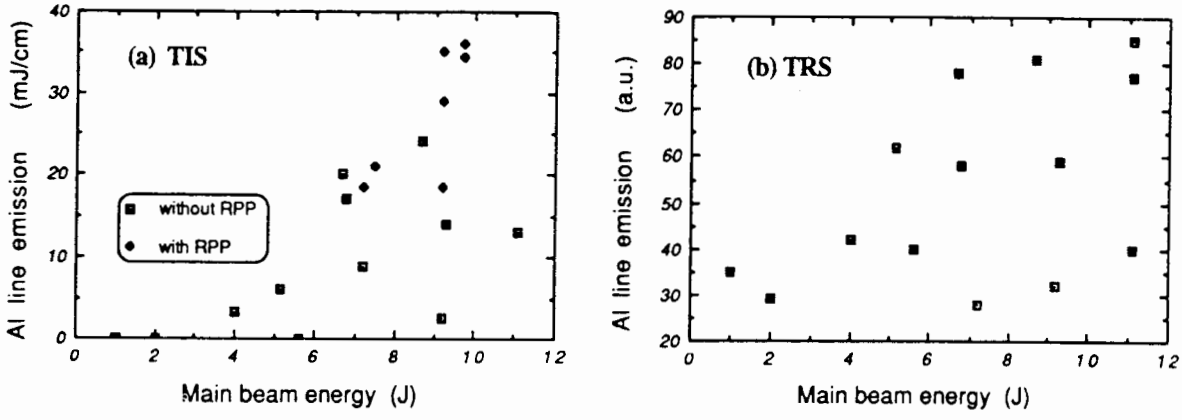

FIGURE 4
Al line energy versus main laser energy : experimental results obtained from the TIS (a) and the TRS (b) (for the TRS, Au emission has not be subtracted so that emission is not zero at small energy).

Temporal shifts between Au and Al emissions obtained with the TRS scatter close to $\delta t = 0$, which means that both emissions occur quite simultaneously whatever is the main beam energy.

In order to assess quantitatively the mixing composition, we measured the Al line emission by irradiating samples with pre-made mixing layers of variable Al-Au ions densities. As the rear Au layer may

be non-totally polluted, we made measurements again with these samples coated with Au. With the help of TRS signals, for a main beam energy in the region of 10 J, the composition of the probed zone seems to correspond to a 20 % Al ions density mixing zone with a Au layer in the range 0-40 nm.

We made another set of experiments with 1 μm Al foils instead of 2 μm. Data obtained with these tri-layer targets exhibit an opposite behavior : the mixing becomes smaller as the main energy increases from 5 to 10 J. In the same time, the temporal shift grows: Al emission starts before Au emission at low energy , in a less and less marked way as the energy increases, till the Au emission occurs first at high energy.

The distinct behaviors of 1 μm and 2 μm are analysed in the next section.

II - NUMERICAL RESULTS

Numerical simulations have been performed with the monodimensional hydrocode FCI1 coupled with a mixing code which is a rough modeling of ordered energy conversion into disordered energy. This mixing code is a static model and evaluates masses of mixed Al and Au as a postprocessor at each step of the calculation.

FCI1 is run with the ionization model MM (Mixed Model /8/) to obtain relevant Au emission.

The temporal shape of the interface velocity depends strongly on the energy and on the shape of both laser pulses, and on the delay of the probe beam. Typical interface velocity and acceleration plots are shown in Figures 5 and 6. In this case, the Al layer thickness is 2 μm and main and probe beam energies are respectively 6.7 J and 10.7 J.

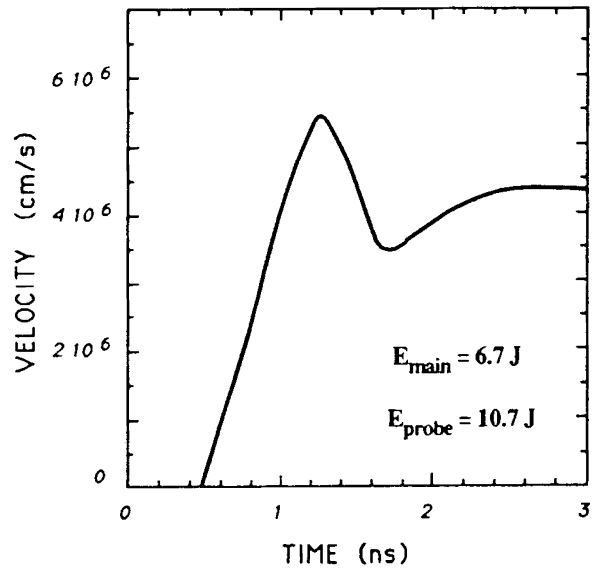

FIGURE 5
Al/rear Au interface velocity versus time.

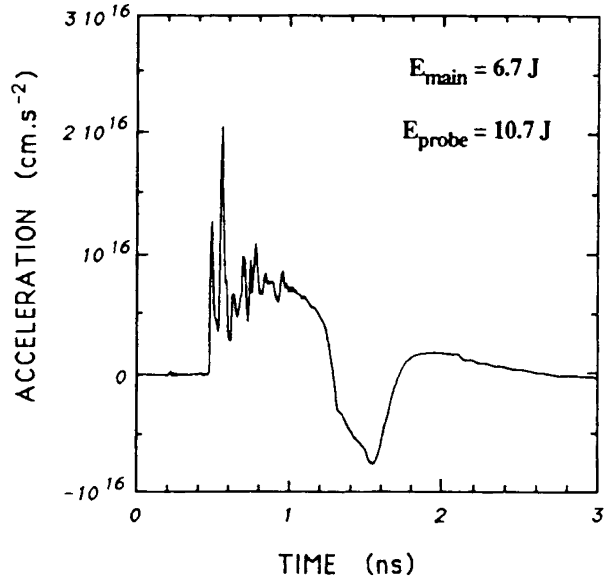

FIGURE 6
Al/rear Au acceleration versus time.

The probe beam is responsible for the deceleration; this slowing down of the interface is followed by another positive acceleration phase due to the decompression of target material related to the deposition of rear Au X-ray energy. The Richtmyer-Meshkov (RM) stage (when the shock goes across the interface) is short, and the RT stage plays a prominent part. As long as the velocity increases, we may consider that the acceleration process is RT unstable. We recall that we do not use grooved targets, but the instability growth originates from the interface roughness. As the probe beam is delayed, perturbations have time to develop and induce turbulent mixing.

The evolution of mixed materials masses is shown in Figure 7. The unstable phase starts as soon as the first strong shock goes across the interface. The rear Au pollution expands very quickly and is almost entire. The Al pollution develops more slowly and affects half of the whole Al layer.

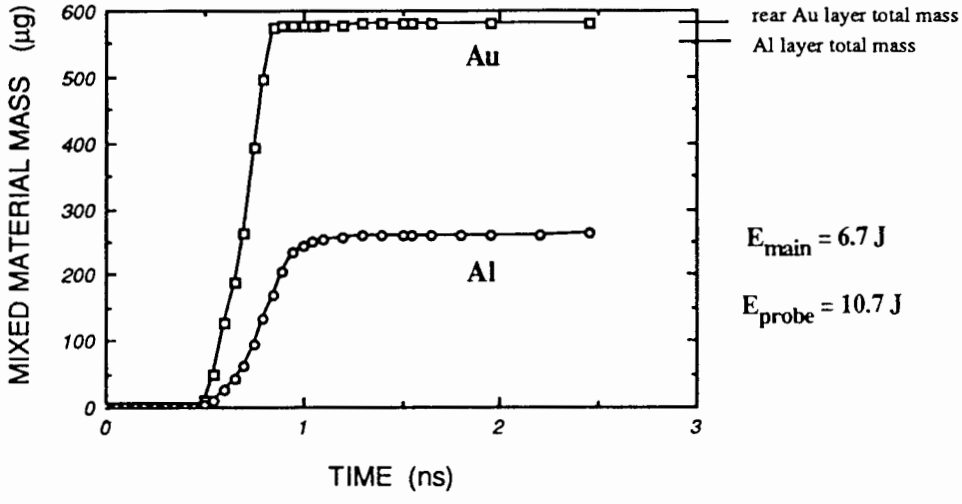

FIGURE 7
Temporal evolution of masses of mixed Au and Al.

The X-rays coming from the front Au layer induces a more or less important preheating, so the matter expands and the mixing is reduced as material density is decreased, although Atwood number has not much changed. Simulations pointed out that this radiation preheating, which is very sensitive to the pulse rise time, can become large enough when the beam energy is increased so that the rear Au expands very much and the mixing mass is reduced. Main beam energy and radiative preheating are strongly correlated but have opposite influence on the growth of the mixing, as the first one increases the acceleration of the target and the other lessens the material densities.

Our numerical investigations lead us to the following remarks :

- the mixing process is not much sensible to the main beam pulse shape as long as we consider gaussian (or sum of gaussians) pulses (i.e. smooth pulses)
- the delay of the probe beam is a major factor; it is all the more determinant as the main beam energy is small, because the unstable phase starts later and develops more slowly
- Al and Au emission levels are very sensitive to the value of the probe energy.

For 2 μm Al tri-layer targets, the rear Au layer is nearly wholly polluted in the range of energy 2 J to 12 J : entire mixing for 12 J, and some nanometers of the initial Au layer unmixed for 2 J. The disappearance of this unmixed layer could validate the experimental growth of Al emission as the energy is increased.

The weak scattering in temporal shift δt data is relevant too as pollution of rear Au layer is quite complete in most cases : for low energies, a small non-polluted Au layer may induce a little delay of Al emission; for high energies, front Au radiative preheating may set before the Au emission. Both behaviors could explain a non-modified shift between emissions.

Numerical results for various main beam energies gives a remarkably stable mixing composition. Assuming an homogeneous mixing layer, the composition is close to 25 % Au ions and 75 % Al ions densities. It is quite the reverse of the experimental proportion, but in the experiment only a small region of the mixing layer is probed. The existence of a concentration gradient is a possible explanation.

Experiments with 1 μm Al layer, performed without the probe beam, displayed that front Au X-rays can go through the target. Simulations assert the major role of front Au preheating with these structures. With both laser beams, numerical spectra obtained at the rear side of the tri-layer targets exhibit precursory signals connected to front Au radiation. This supports the experimental increase of the temporal shift δt.

From the mixing code, according to the growing reduction of Al layer density, polluted Al mass is shown to lessen when the main beam energy is increased; in the same time, Au layer mixing is not much disturbed and remains total. Therefore the experimental decrease of Al emission is coherent.

The competition between radiative preheating and target acceleration drive the opposite behavior observed with 2 μm and 1 μm Al foil tri-layer targets.

III - CONCLUSIONS

Tri-layer experiments assert the validity of X-ray spectroscopy measurements as experimental method to investigate the problem of target stability under ablative acceleration. A mixing zone is evidenced and general trends of mixing development versus target acceleration are coherent with numerical simulations (emission level, shift between emissions).

Results obtained with optical smoothing demonstrate that the apparent mixing is not due to large-scale illumination non-uniformities. As numerical simulations have confirmed, the Rayleigh-Taylor instability seems to be the dominant process responsible for the mixing.

Benefit of time-resolved spectroscopy appears very attractive and should supply us with a real knowledge of the mixing layer (span and composition). Its ability to discriminate between distinct mixing compositions with or without remaining Au layer is most valuable. Yet, under our present experimental conditions, especially dispersion of the data, it remains difficult to make full use of this diagnostic. We got

an estimate of the probed zone composition which is consistent with our numerical results. More numerical runs are necessary, and we intend to realize an additive set of simulations with other turbulence models.

Improving this experiment needs more beam energy in order to get higher emission intensities. Acquisition of repetitivity should enable us to get real quantitative results : with reproductive shots, by varying the probe energy, we could probe the mixing zone at different depths, and display (perhaps!) a concentration gradient.

REFERENCES

[1]	K. Tanaka, E.I. Thorsos	Appl. Phys. Lett. **35**, 853 (1979)
[2]	M.H. Key et al.	Appl. Phys. Lett. **36**, 269 (1980)
	M.H. Key et al.	Phys. Rev. Lett. **45**, 1801 (1980)
[3]	J.S. Wark et al.	Appl. Phys. Lett. **48**, 969 (1986)
[4]	H. Azechi et al.	Phys. Rev. Lett. **59**, 2635 (1987)
[5]	P.A. Holstein et al.	C.R. Acad. Sci. Paris, t. 307, Série II, p. 211 (1988)
[6]	A. Raven et al.	Phys. Rev. Lett. **47**, 1049 (1981)
[7]	J. L. Bocher et al.	Phys. Rev. Lett. **52**, 823 (1984)
[8]	M. Busquet	Phys. Rev. A **25**, 2302 (1982)

SHOCK-WAVE/SHEAR LAYER INTERACTION IN CIRCULAR SUPERSONIC JETS

E. Gutmark, S. Koshigoe, and K. C. Schadow
Research Department
Naval Weapons Center
China Lake, CA 93555-6001

Abstract

The interaction between shock-waves and large coherent structures in a turbulent compressible jet flow, is studied experimentally. The results are compared qualitatively with trends predicted by the linear stability theory. The techniques developed for analyzing the stability of circular jets are extended to include the shock-cell interaction with the instability waves. The controlling effect on the shear layer evolution, of the turbulent initial conditions, the shape of initial mean velocity profile, and Reynolds and Mach numbers are investigated. The shock wave strength is varied as well as the shear layer parameters, i.e., mean and turbulent velocity distribution, thickness, etc. These parameters determine the extent of penetration of the shock into the shear layer, the compression/expansion pattern, the diffusion rate of the shocks, and the shear layer instability characteristics. A possible feedback which is generated by the sound emitted from the shock/vortices interaction locations and subsequently excites the roll-up of vortices in the shear-layer, is discussed.

Introduction

The present study is concerned with understanding the behavior of a supersonic jet shear layer in the presence of shocks. This is related to the understanding of the mixing process in the supersonic jets which become more stable with increasing Mach number [1]. Similar to the subsonic, incompressible flows, the supersonic shear flow dynamics are governed by large-scale coherent structures. Their development, starts from selective amplification of initial disturbances into vortices and continues with subsequent vortex interaction. The role of large-scale structures and their generation by flow instabilities were studied extensively in subsonic shear flow both experimentally [2] and theoretically [1]. Similar studies in sonic and supersonic flows were done mainly in low Reynolds number flow (up to 10^5) [3] and some in high Reynolds number ($>10^6$) [4]. Evidence on the existence of large-scale structures in supersonic flows of both low and high Reynolds numbers was presented in these works. Efforts to increase the mixing by acoustic excitation, similar to the mixing enhancement method used for subsonic flows, encountered problems due to the difficulty to produce sufficient acoustic energy in the high frequency range required for supersonic jets [5]. When the flow contains shock waves, as in over or underexpanded jets, the shear

layer interaction with the shock can produce enough acoustic energy to excite the shear layer. This mechanism was shown to have the potential to significantly enhance mixing [6]. The objective of this work is to study the mechanism of the interaction between the shock cells and the shear layer in a circular configuration.

Experimental Arrangement

The jet system consisted of a cylindrical settling chamber, 24.1 cm long and 10.8 cm in diameter. The nozzle section was attached to the converging section of the settling chamber with an area ratio of 32. Two different nozzles were used to obtain jets with different initial momentum thickness. One jet was discharged through a pipe, with a thicker momentum thickness of $\theta = 0.6$ mm. The second nozzle was an orifice plate with sharp edges, yielding a thin momentum thickness of $\theta = 0.16$ mm. Experiments were done in underexpanded conditions. The initial turbulence level at the exit was 2% in the circular jet. The stagnation pressures, p_o, for the underexpanded jet were 29 to 40 psia. These pressures correspond jet Mach numbers of $M_j = 1.09$ to 1.33, for a fully expanded isentropic flow. The Reynolds number for the largest M_j was $Re = U_o D_e/\nu = 5.7 \cdot 10^5$. The flow field measurements were done using a hot-wire anemometer, with frequency response of 50 kHz. The hot-wire scanned the flow field using a computer controlled three-axes traverse mechanism. Each scan consisted of 250 measurement points. Calibration, data acquisition, and analysis were performed using a VAX 750 computer. Spark Schlieren photography was used to visualize the shock structures of the jets.

Results and Discussion

Shock Cell Structures

The effect of the initial shear layer thickness on the shock cell structure is studied by comparing the jet issued from a pipe nozzle to the orifice jet which has a very thin initial momentum thickness. The two jets are visualized using spark Schlieren photography in Figure 1, for $M_j = 1.3$ and in Figure 2 for $M_j = 1.6$. The photograph in Figure 1 covers the first 10 diameters of the jets. The differences in the near flow field of $x/D < 3$ are especially in the shock cell structures which are larger for the orifice jets. The far field difference is related to the jet's shear layer structure. Large, helical coherent structures develop in the pipe flow at $x/D > 3$, while the orifice jet retains a predominantly symmetric behavior. Consequently, the pipe jet is spreading more than the orifice jet at these conditions. For a slightly higher $M_j = 1.6$, the differences in the initial shock-cell structure are more pronounced (Figure 2). The initial

shock cell is larger for the orifice jet relative to the pipe jet, resulting in a different size of the normal shock and the angles of the oblique shocks. The pipe jet has a section of a normal shock, with slip lines downstream of the intersection of the oblique and normal shocks. The orifice jet does not have any normal shock and the intersection occurs between two oblique shocks, with a very weak slip line. Subsequently, the slip-line shear layer has different velocity ratio across it and the mean velocity characteristics will vary.

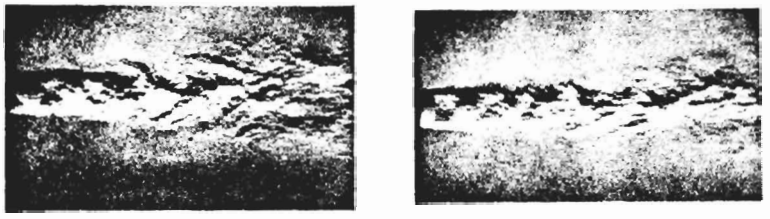

Figure 1. Schlieren photograph of jets discharging with a circular pipe profile thick momentum thickness (θ) (a); and a top-hat profile thin θ (b). $M_j = 1.3$.

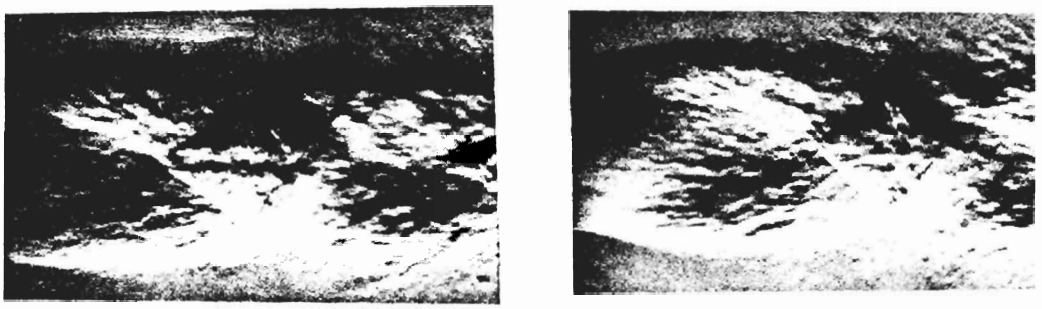

Figure 2. Same as 1, $M_j = 1.6$.

For increasing Mach numbers, M_j, the shock-cell length ($L_{S.C.}$) was shown to be growing as $a\beta^b = a(M_j^2 - 1)^{b/2}$, where a and b are experimental coefficients. Figure 3 shows this behavior for the two jets. The jet with the larger initial shear layer thickness has shorter shock cell length up to $M_j < 2.2$ The difference between them is reduced with increasing M_j, until they become equal for $M_j > 2.2$. The curves deviate slightly from the above linear logarithmic dependence of the shock length on β for the nearly sonic M_j which correspond to $\beta = 0.46$. The slope (b) is larger for the pipe jet.

Linear stability theory is used to calculate the shock-cell and spatial instability modes for supersonic round jets with finite momentum thickness. The shock-cell eigenmodes are determined from the zero-frequency limit of the regular instability equations. The experimental results (Figure 3) are in good qualitative agreement with the instability analysis calculations. Figure 4 shows the effect of the momentum thickness on the real part, α_r, of the shock cell eigenvalues when Mach number is taken as parameter for

the fundamental eigenmode of the shock cells. α_r is inversely proportional to the shock-cell wavelength. As evident from the figure, increasing momentum leads to reduction of the shock cell spacing for all eigenmodes in a wide range of Mach numbers. This effect is more eminent in the low Mach numbers range.

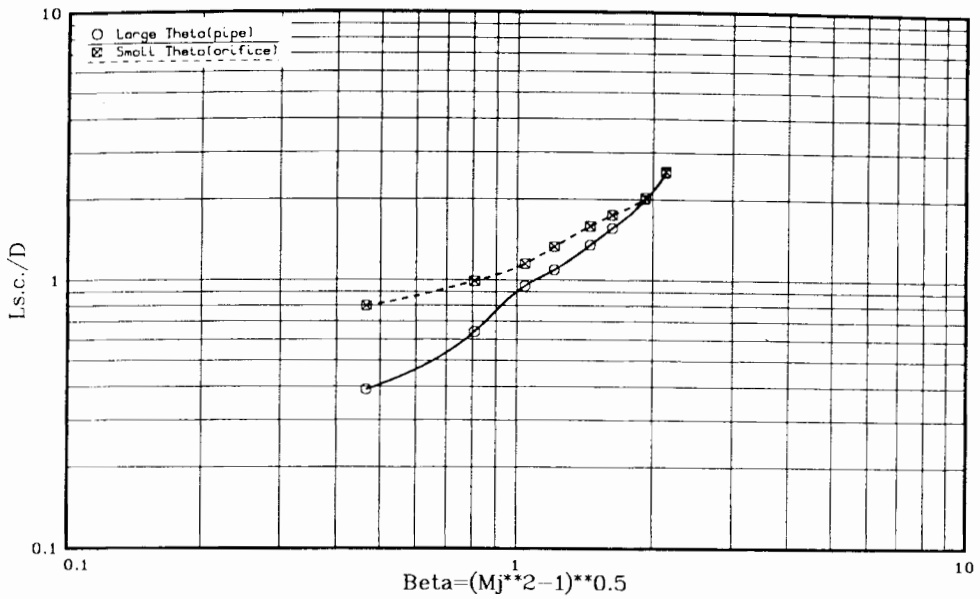

Figure 3. Shock cell spacing versus Mach number. Pipe jet (——), orifice jet (- - -).

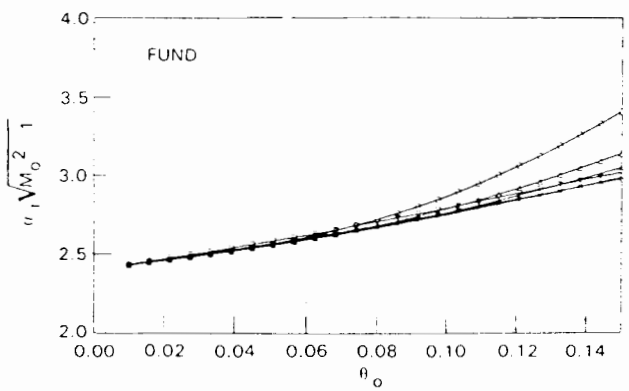

Figure 4. Real shock cell eigenvalues variation with θ for fundamental mode. M = 1.1, 0; 1.2, Δ; 1.3, +; 1.5, X; 2.0, ◊; 2.5, ∇.

Mean and Turbulent Flow Field

The pipe and orifice jets flow fields were measured using hot-wire probes for three exit Mach numbers, M_j = 1.09, 1.21, and 1.33. The initial shear layer surrounding the jet's potential core was mapped. For these fully expanded jet conditions, the jet behavior is similar to subsonic flow with linear spreading rate. The maximum turbulence intensity is not reached at the center of the shear layer, where the velocity drops to 50% of the centerline value as in subsonic jets, but in the inner section closer to the jet centerline (Figure 5a). This location corresponds to a shift of the velocity profile inflection point into the jet, to smaller radial positions relative to the subsonic jets due to the effect of the shock cells. Similar behavior was measured for the other turbulence intensity components v' and w', (not shown here) which had about half the intensity of the axial component. The orifice jet at the same conditions had an initial thin momentum thickness, but further downstream a similar mean velocity field, with a similar pattern of turbulence intensity distribution (Figure 5b).

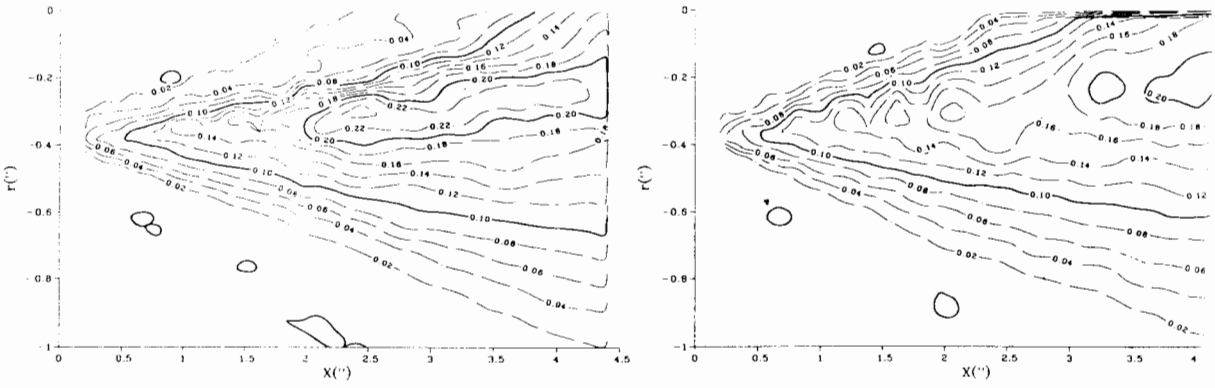

Figure 5. Contours of axial turbulence intensity of the pipe jet (a), and in the orifice jet (b), at M_j = 1.09.

The flow structure was substantially altered when the shock waves became stronger as the pressure ratio increased. For M_j = 1.33 (Figure 6a), the contours in the outer part of the shear layer are deflected into the flow with a subsequent reduction in the jet's spreading rate. The velocity profile gets distorted with multiple inflection points, which leads, according to stability theory, to additional instability in the flow field. Consequently, the intensity of the axial turbulence component is increased more than twice (Figure 6b) relative to the lower M_j. Similar trends were measured for the other components of the turbulence intensity. An indicator of the presence of shock-cells in the shear layer are the Reynolds stresses $\overline{u'v'}$ shown in Figure 7. Four maxima in the contour plot correspond to the location of the shock cells. The peak values of these maxima are reduced in the downstream location with the decreased strength of the shock waves.

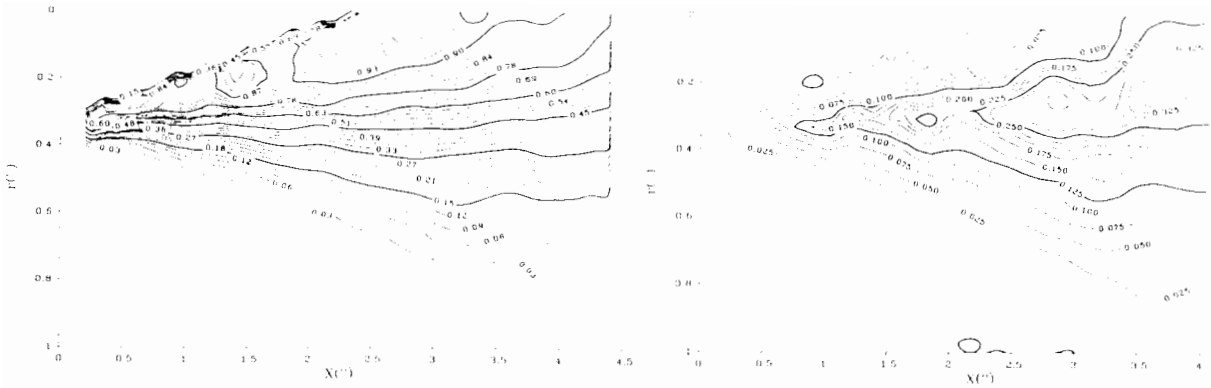

Figure 6. Contours of mean axial velocity and turbulence intensity of the pipe jet, at $M_j = 1.33$.

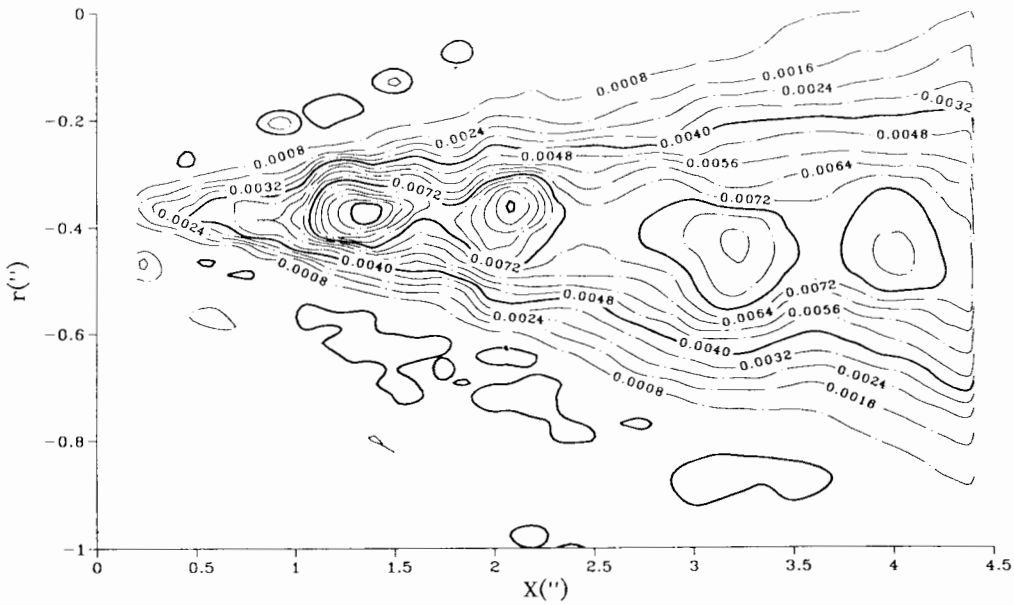

Figure 7. Contours of Reynolds stresses, $\overline{u'v'}$,of the pipe jet, at $M_j = 1.33$.

The effect of M_j on the spreading rate of the two jets is summarized in Figure 8, where $R_{0.05}$ is plotted as a function of the axial distance. $R_{0.05}$ is the radial distance from the centerline where the mean velocity drops to 5% of the center line value. This is a measure of the total radial extent of the jet. This specific criterion is chosen because the effect of the shocks on the mean velocity field of the shear layer is most prominent in the outer sections of the shear layer. For $M_j = 1.09$, both the pipe and orifice jets exhibit similar linear spread. As M_j is increased, the jet width is reduced, and several steps are measured in the spread curve, especially at $M_j = 1.33$. These steps correspond to the deflection of the streamlines by the compression/expansion waves. The variation of the momentum thickness in the downstream

direction was measured for the two jets. In spite of the initially thicker momentum thickness of the pipe jet ($R/\theta = 16$ relative to 60 for the orifice jet), the two curves, for the pipe and orifice jets, nearly overlap further downstream. There is no significant change as the jet Mach number is increased.

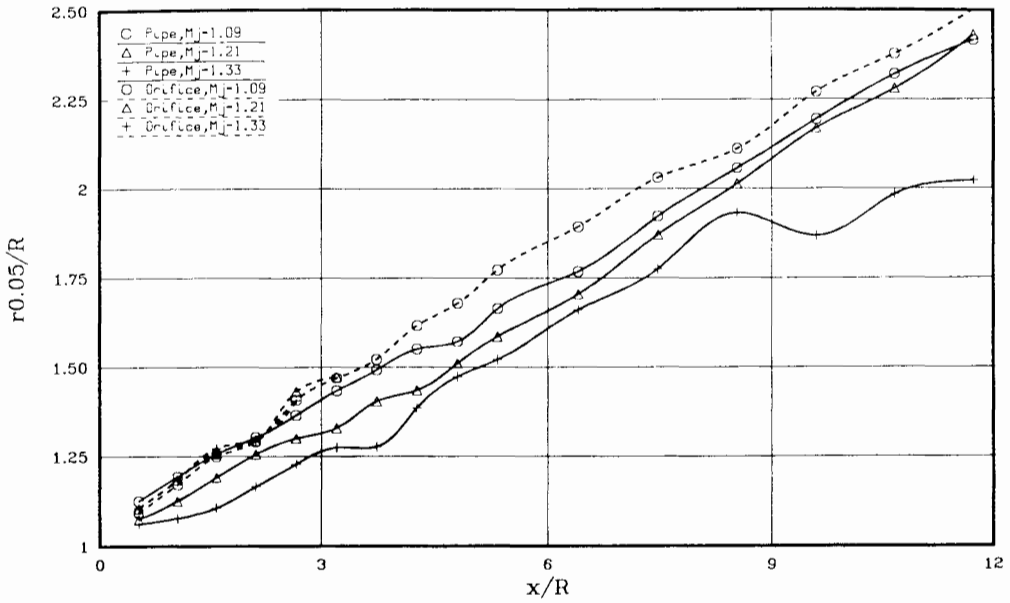

Figure 8. Spreading rate of the pipe and orifice jets for various M_j.

Instability Considerations and Turbulence Amplification

Instability analysis of circular jets [1] shows that as the Mach number increases the jet becomes more stable. This behavior is shown in Figure 9, for thin ($\theta/R = 0.02$, solid line) and thick ($\theta/R = 0.08$, dashed line) initial momentum thickness. The lines without circles show the maximum amplification rate of the shear layer instability waves as a function of M_j.The thinner shear layer is less stable than the thicker one. Both cases become more stable with increased M_j, with very weak dependency on this variable. This analysis is valid for fully expanded jet flows without the presence of shock cells in the flow. When the jet operates at off-design conditions, shock cells are interacting with the large-scale structures in the jet's core. The interaction results in a modification of the instability characteristics. As shown in Figure 9 (circle symbols), an increase of the pressure ratio, or increased difference between M_j and M_d (design Mach number) results in an increase of the amplification rate related to the shock cells interaction with the shear layer structures. This increase rate is highly dependent on M_j. Similar to the fully expanded jet, the

amplification rate of the thin shear layer is higher than for the thick one. For the off-design conditions the difference is much more significant. In both cases, the shock cell-shear layer interaction destabilizes the flow and contributes to larger amplification of disturbances.

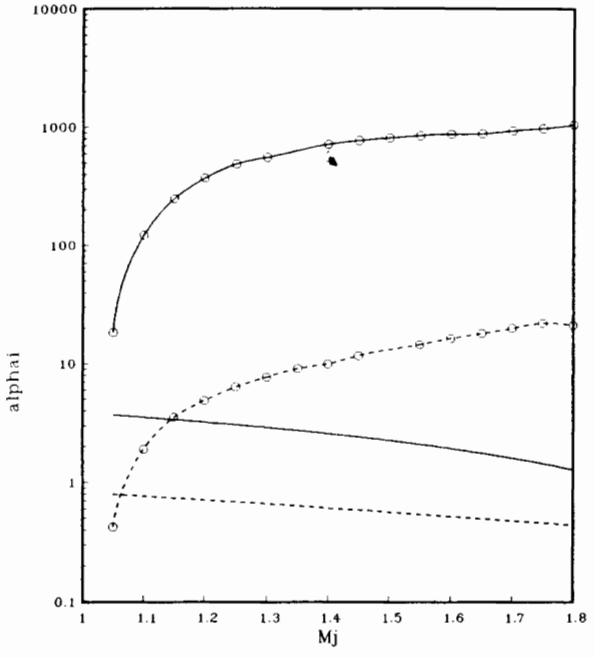

Figure 9. Dependence of the maximum amplification rate of the shear layer instability waves in a fully-expanded jet and in an underexpanded jet (circles), corresponding to the shock-cell shear layer interaction. Solid lines correspond to $\theta/R = 0.08$, dashed lines to $\theta/R = 0.02$.

The stability analysis can explain the experimental observation shown along the shear layer center (Figure 10). In this figure the maximum values of the axial turbulence intensity are plotted as a function of X. The turbulence intensity for $M_j = 1.33$ is more than double relative to $M_j = 1.09$. Similar results were obtained along the centerline of the jet.

The variation of the peak value of the Reynolds stresses, $\overline{u'v'}$, along the axial direction is given in Figure 11 for $M_j = 1.09$ and 1.33. For the lower Mach number the variation is relatively smooth with few undulations, which could correspond to the appearance of weak shock cells. At $M_j = 1.33$ sharp periodic peaks in the $\overline{u'v'}$ curve, suggest that the shock waves produce high shearing stresses in the shear layer, which can be related to the generation of strong acoustic waves from the underexpanded jet.

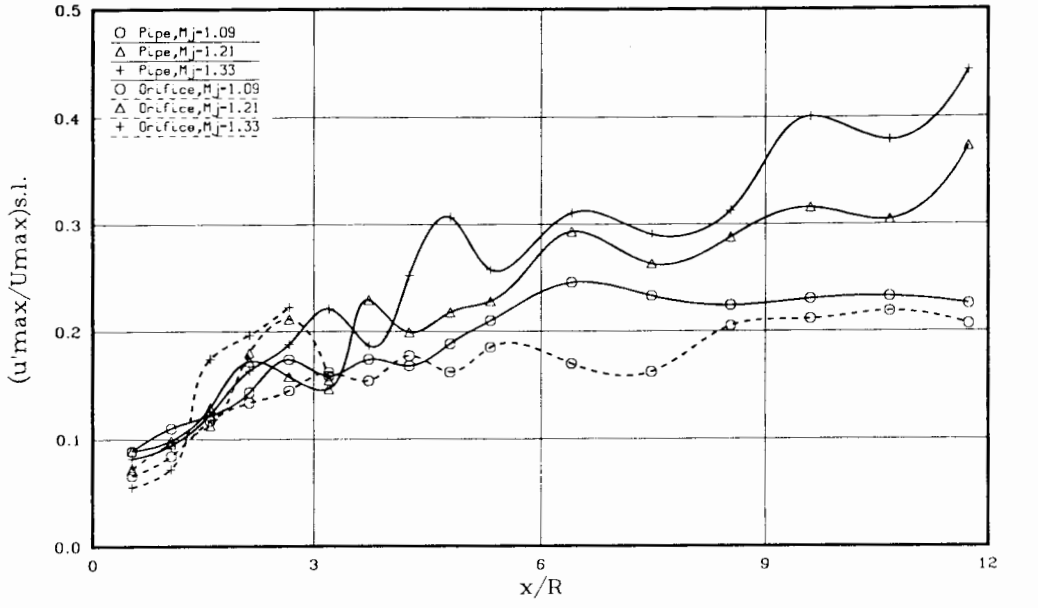

Figure 10. Axial turbulence intensity along the jet's shear-layer for the pipe and orifice jets at different M_j.

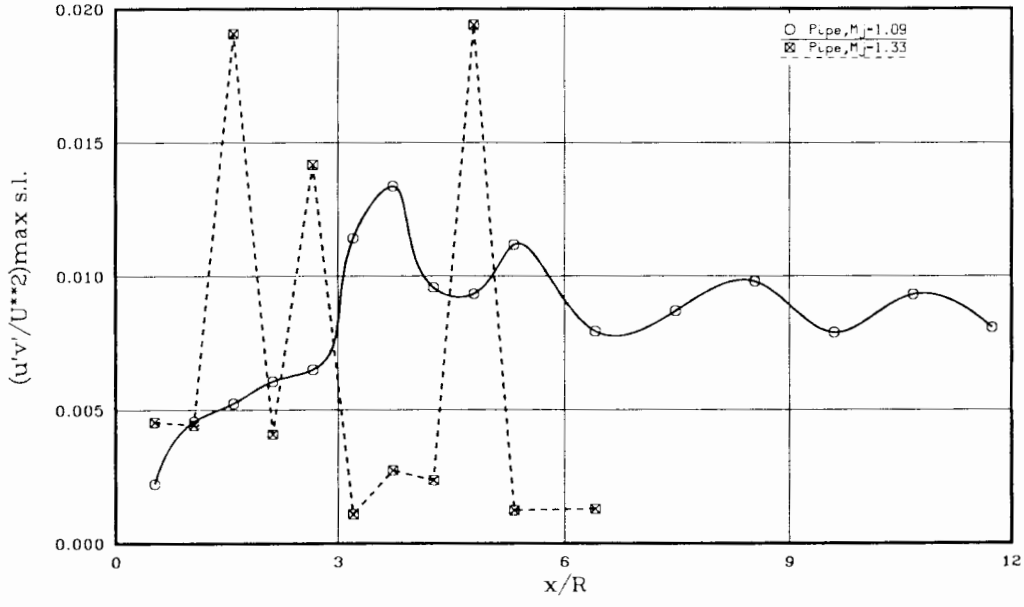

Figure 11. Variation of peak Reynolds-stress ($\overline{u'v'}$) values along the pipe jet's shear layer for M_j = 1.09 and 1.33.

Conclusions

The interaction between shock waves and shear layer structure was studied in a supersonic underexpanded circular jet. It is shown that the shock behavior and the shear layer flow field are mutually affected in this flow configuration. The gas dynamics equations for compression/expansion wave behavior are not sufficient to describe the shock-cell structure. The flow initial conditions, i.e., momentum thickness and initial turbulence level determine the shock orientation and strength. In the low Mach numbers range, when the shock strength is not overcoming the shear flow dynamics, the thicker shear layer is reducing the shock cell length which is equivalent to reducing the effective Mach number, since the shock cell spacing grows proportionally to the jet's exit Mach number. The thicker shear layer causes faster dissipation of the shock waves. The flow field in the shear layer is altered by the compression/expansion waves. At the intersection with these waves the mean flow field is deflected inside or outside the flow depending on the wave type. This deflection modifies the mean velocity profile, and generates new inflection points, resulting in additional flow instability. Thus, the turbulence production is enhanced. Of specific interest are the Reynolds shear stresses, which reach a high sharp peak at the locations where the shocks are intersecting the shear layer. The time dependent change in these stresses are sources for acoustic radiation of the supersonic jets. It is possible, as was previously shown, that this sound is exciting the initial shear layer and modified its structure and evolution, to enhance its spreading rate.

References

1. A. Michalke. "The Instability of Free Shear Layers," Prog. Aerospace Sci., 12, Pergamon-Press, pp. 213-239, 1972.

2. C. M. Ho and P. Huerre. "Perturbed Free Shear Layers," Ann. Rev. Fluid Mech., Vol. 16, pp. 365-424, 1984.

3. G. L. Morrison and D. L. McLaughlin. "Instability Process in Low Reynolds Number Supersonic Jets," AIAA J., Vol. 18, No. 7, pp. 793-800, 1980.

4. J. M. Seiner, J. C. Manning, and M. K. Ponton. "The Preferred Spatial Mode of Instability for a Mach 2 Jet," AIAA Paper No. 86-1942, July 1986.

5. K. K. Ahuja, J. Lepicovsky, and W. H. Brown. "Some Unresolved Questions in Hot-Jet Mixing Control Through Artificial Excitation," AIAA Paper No. 86-1956, July 1986.

6. D. R. Glass. "Effect of Acoustic Feedback on the Spread and Decay of Supersonic Jets," AIAA J., Vol. 6, No. 10, October 1968.

CREATION AND ENHANCEMENT OF TURBULENT MIXING ZONES DUE TO HIGH MACH NUMBER SHOCK-INTERFACE INTERACTION

L. Houas, A. Ramdani and J. Fortes

U.A. CNRS 1168, SETT, Département des milieux hors d'équilibre, Université de Provence, Avenue Escadrille Normandie Niemen, 13397 Marseille cedex 13, FRANCE.

The birth and growth of turbulent mixing of two gases having different densities after acceleration and deceleration by high Mach number shock waves are investigated in a double diaphragm shock tube. The gases are initially separated by an interface materialized by a thin plastic membrane. When a high Mach number shock wave accelerates the interface, this one is subjected to the Richtmyer-Meshkov instability. Different measurement techniques have been used and adapted to observe the created turbulent mixing zone : heat transfer gauges for the study of the incident mixing zone front, infrared absorption of a CO_2 vibrational-rotational laser line which provides temperature and density profiles in the mixing zone and infrared emission of CO_2 which gives the evolution of the mixing zone thickness.

I. INTRODUCTION

In the context of nuclear fusion by inertial confinement, a fundamental problem apears : the creation and development of a turbulent mixing zone between the shell material and the thermonuclear combustible. This mixing zone, initially due to the Rayleigh-Taylor instability, contributes to reduce the efficiency of the nuclear reaction by an early break-up of the shell and a cooling of the combustible. The aim of the present work is to study in the simpler shock tube environment the evolution of the mixing zone created by the interaction of a high Mach number shock wave and a gaseous interface (initially at rest).

Experiments are conducted in a double diaphragm shock tube. It has a square cross section (8.5 x 8.5 cm) and its total length is about 9 m. The test section (the third one) is about 1.5 m long. The gases, carbon dioxyde upstream and helium or argon downstream, are initially separated by a thin plastic film (0.5 - 1.5 - 19 µm) which corresponds to the second diaphragm. When a shock wave accelerates the interface, this one is subjected to the impulsive Rayleigh-Taylor instability also called Richtmyer-Meshkov instability. When the membrane is initially planar, only the random small spatial scales created by the membrane break-up are excited and the turbulent mixing occurs soon. With an initial bulge of the membrane set by pressure difference between the gases, this turbulent mixing ,arising from the small scales, is superposed to a large scale Richtmyer-Meshkov instability (in its non linear phase) which can also be described as a baroclinic gradient of the shock and density gradient of the non planar interface.

The three dimensional turbulent mixing zone is later decelerated by one or several shock waves reflected from the end wall of the shock tube. Using two gas pairs, CO_2/He and CO_2/Ar, allows to analyse the more precise influence of the Atwood number ($|A_t|_{CO2/He} \approx 0.8$ and $|A_t|_{CO2/Ar} \approx 0.3$) on the instability and subsequent turbulent mixing zone.

The CO_2 is used for its spectroscopic properties and He and Ar because they present no infrared emission or absorption in the domain of our experiments, and also because their densities are respectively very different and close to the CO_2 one.

Measurements are based on infrared emission or absorption of shock heated CO_2 and enable us to obtain the trajectory and the thickness of the mixing zone as well as average temperature, CO_2 density and concentration profiles within.

These techniques require strong shocks (Mach 3.5 - 6.5 in CO_2 and Ar, 1.5 - 3 in He) and therefore the velocities behind the shock (1000-2000 m/s) are well into the compressible range (see Table 1). Thus it is expected that mixing should be different from that obtained in the experiment of ref. 1 where a Mach number 1.3 shock interacts with an air/He interface, and more similar to recent experiments of ref. 2 where, for example, a Mach number 3 shock interacts, with He/Ar or Ar/He interfaces.

However, high Mach number shocks and low initial pressures lead to thicker boundary layers on the shock tube side walls and thus viscosity effects are always combined with the development of the instability.

II. EVOLUTION OF THE TURBULENT MIXING ZONE FRONT

Large scale deformation of the turbulent mixing zone front have been measured using an array of five platinum heat transfer gauges located at the same abscissa and at different ordinates perpendicular to the flow[3].

For each gas pair, three kinds of experiments have been done. Two when the interface is initially bulged and one when it is plane. The interface is said to be positively or negatively bulged when the initial pressure of the CO_2 filling the second chamber is greater or smaller, respectively, than that of the gas in the third chamber (He or Ar). When the pressure difference is equal to zero the interface is initially plane.

The aim of these experiments is to evaluate the shape of the incident front of the mixing zone in the presence of a boundary layer and to compare it with the linear theory predictions[3]. The growth of a sinusoidal deformation of the mixing zone front is (assuming $(2\pi a/\lambda) \ll 1$)

$$\frac{da}{dt} = \frac{2\pi}{\lambda} a_0 A_t U_I \left(1 - \frac{U_I}{U_S}\right)$$

where a_0 is the amplitude of the initial deformation, λ_0 its wavelength, A_t the Atwood number and U_I and U_S the absolute velocities of the mixing zone and shock wave respectively.

The amplitude evolution of the mixing zone front deformation appears on figure 1 for the two gas pairs (ref. 3), where "Linear theory" means the linear evolution of the Richtmyer-Meshkov instability, and numerical simulation corresponds to calculations made with EAD, a 2D Eulerian non viscous code from the Centre d'Etudes de Limeil Valenton (C.E.A.).

In the case when the shock wave propagates from the heavy gas to the light one, the linear theory predicts that the interface front must reverse (crossing of the time axis fig.1). The results presented in ref. 3 show that when the interface is initially negatively bulged ($a_0 = -13$ mm) its reversal is observed but with a delay which is more important in the CO_2/He case. Viscosity effects act, in this case, at later time but in the same sense as the vorticity effects and both cause the reversal. When the interface is initially positively bulged ($a_0 = +11$ mm), vorticity

effects tend to decrease the bulge in the beginning as predicted by the linear theory, but later, boundary layer effects completely prevent the interface reversal.

With an initially plane interface, large scale deformation of the mixing zone will be only due to the boundary layer effects. These are the conditions of the experiments described hereafter for the determination of the thickness of the mixing zone and the temperature and density profiles within.

III. EVOLUTION OF THE MIXING ZONE THICKNESS

A. Present measurements

Measurements of the infrared emission (centered at 4.3. μm) of shock heated CO_2 provide the time evolution of the quantity $\rho(CO_2)\, Ev_3(T)$ where $Ev_3(T)$ is the average specific energy corresponding to the third mode of vibration of the CO_2 molecule and $\rho(CO_2)$ the density of CO_2. The optical set up is such that the infrared detector records the emission of a small volume of fluid at the center of the shock tube[4]. A typical signal from 2 detectors looking at positions on the shock tube 15 cm apart is shown on figure 2. The rise indicates the passage of the mixing zone CO_2/Ar in front of the detector. The plateau corresponds to the emission from pure CO_2 with pertubations due to boundary layer effects and rarefaction waves. The final decay is caused by the arrival of the driver gas (H_2). Platinum heat transfer gauges mounted flush at the walls are used to record the propagation of the shock waves. Using several wall gauges and infrared detectors (two or three) per shock tube run and combining the measurements from several runs at the same conditions enable us to construct (x, t) diagrams of the shock waves and mixing zone trajectories such as the ones shown in figures 3 and 4. The rise time of the signals from the infrared detectors provides the thickness history of the mixing zone. Figures 5 and 6 show the evolution of the mixing zone thickness L for the 2 pairs of gases and different initial pressures and for different incident shock Mach numbers. Error bars on the thickness have been estimated to ± 2 mm. The (x, t) diagrams (figures 3 and 4) show the transmitted shock in the rare gas, the reflected shock from the end wall and the waves resulting from its interaction with the mixing zone. x = 0 corresponds to the initial position of the Mylar membrane.

The mixing zone trajectory is plotted from a distance of 20 cm from the initial position of the separating membrane (here 1.5 μm Mylar). We can notice that the lines connect only data points from different runs and do not represent corresponding variations of velocity during the same test.

Beyond 30-50 cm, the mixing zone velocity is fairly constant and higher than predicted by the Rankine-Hugoniot relations based on the measured shock velocity. This is a well known boundary layer effect in high Mach number shock tube experiments and we found it more pronounced for the CO_2/He case. The behavior of the CO_2/Ar mixing zone after its deceleration by the reflected wave reveals the complex 3-dimensional shock wave interaction whith a mixing zone in the presence of boundary layers as indicated in figure 7, where the passage of the two feet of the shock is clearly visible as well as the separated zone inducing a decrease of the heat transfer. The mixing zone is accelerating after the interaction, which is contrary to the behavior observed for low Mach number experiments and non viscous numerical simulations.

Figure 5 shows that the CO2/Ar mixing zone is thin and thickens very slowly after 400μs (i.e. beyond 40 cm from the initial position), but the unmeasured initial thickening rate must have been larger. The reflected shock causes first a compression and after a very rapid thickening. The CO2/He mixing zone (figure 6) thickens at an important rate up to the compression by the reflected wave and thickens again very quickly afterwards.

B. Comparison with Zaitsev's experiments

Zaitsev's experiments were made with similar incident shock Mach numbers (3 vs 3.7 and 4 in our experiments) and shock tube cross section (7 vs 8.5 cm). Their separating membrane : 2 μm Lausan or Dacron might have mechanical properties close to those of our 1.5 μm Mylar film. We have found that thicker (and stronger) membranes lead to thicker mixing zones (figure 8) and we expect that our membranes have a larger influence on the mixing zone compared to the experiments of Andronov et all and of Caltech[5] where films were used. Our measurement technique also differs from the schlieren photographs of the other experiments. As stated above and confirmed by our own preliminary photographs taken close to the initial membrane position, the thickness obtained from IR emission from the center of the channel is 30% smaller than the thickness photographically obtained. Another important difference between Zaitsev's experiments and ours is the length of the test section : 37 vs 127 and 152 cm in our case.
Zaitsev's results are summarized in two formulas for the thickening rate (dL / dt) of the mixing zone before and after the reflected shock as a function of the velocity jump and the Atwood number A_t (calculated after shock compression).

- before reflected shock :

$$\frac{1}{U_I}\frac{dL_1}{dt} = 0.02 + 0.07\left|A_{t_1}\right|$$

for $A_{t1} < 0$ and when U_I is the measured mixing zone velocity.

- after reflected shock :

$$\frac{1}{\Delta U_R}\frac{dL_2}{dt} = 0.05 + 0.85\left|A_{t_2}\right|$$

for $A_{t2} > 0$ and when ΔU_R is the calculated velocity jump due to the reflected wave.

Table 1 gives the relevant data for our experiments. In this table, At_0 is the initial Atwood number, M_I and M_T are respectively the incident (in CO_2) and transmitted (in He or Ar) shock Mach numbers, U is the contact surface velocity obtained from the Rankine-Hugoniot relations. Note that the experiments performed at lower M_I (3.7) have about 10% of air by volume mixed with the rare gas which significantly altered the density and speed of sound of "helium". Non dimensional thickening rates $(1 / U_I)(dL_i / dt)$ in the initial phase (up to 200 μs on figures 5 and 6) and $(1 / U_I)(dL_1 / dt)$ are compared with Zaitsev's estimate : $0.02 + 0.07\,|A_{t1}|$ and $(1 / \Delta U_R)(dL_2 / dt)$ with the other estimate : $0.05 + 0.85\,|A_{t2}|$.

The comparison shows that the thickening rate (dL_1 / dt) is lower than predicted by Zaitsev's formula but the poorly measured initial rate (dL_i / dt) is close.The thickening rate after reflected wave interaction (dL_2 / dt) is also close to Zaitsev's formula in 3 cases. However the value obtained for helium at 2000 Pa being too high.

IV. AVERAGE TEMPERATURE AND DENSITY PROFILES IN THE MIXING ZONE.

We present in this paper results obtained with a CO_2 laser absorption technique which have already been presented in ref. 4, but we use here a new data reduction process.

The most important differences between the present results and those given on the paper of ref. 4. are the following : Now, we do not assume that the profile of the line is Lorentzian and calculations are made with a Voigt profile which corresponds better to the physical reality ; also we take into account the hot bands of CO_2. Thus, a more rigourous method has been developed, and will be presented in detail in a future paper.

Without rewriting all the equations, we remind here the principle of the measurements. The absorption by the test gas CO_2 in the mixing zone of two continuous CO_2 laser lines, corresponding to transition beween the vibrational levels 00°1 --> 10°0 (about 10.6 µm wavelenght) yields average profiles of density temperature and CO_2 mass concentration in the mixing zone. Typical profiles obtained at a distance of 940 mm from the initial position of the interface, approximately 770 µs after shock acceleration of the CO_2/He interface (36 mm thick) and 1020µs for the CO_2/Ar one (26 mm thick), and just before the arrival of the reflected shock, are shown in figures 9 to 14. Initial conditions are those indicated in Table 1 column 2 for CO_2/Ar and column 4 for CO_2/He. Calculated values in pure gases are presented in Table 2.

Experimental values, outside the mixing zone, are in fairly good agreement with calculations obtained with a Rankine-Hugoniot one dimensional model. The asymmetry of the CO_2/He density profile (compared to the CO_2/Ar one) might be due to the spike and bubble pattern typical of the interpenetration of gases with large density differences. These results can be compared with numerical simulations. We can note, for example, that the fact that the CO_2/He mixing zone is more turbulent than the CO_2/Ar one, shown by local emission measurements in ref. 6, does not appear clearly with absorption measurements probably because these last ones are averaged across the tube section.

Error bars have been estimated to ± 8% and the fiability of our results appear clearly on each concentration profile since this quantity must be included between 0 and 100%.

V. CONCLUSION

High Mach number shock-interface interaction experiments lead to three dimensional flows which are difficult to describe in the framework of the simple Rayleigh-Taylor instabilities. The results do not agree also with simulations using non viscous hydrodynamic codes. However they are in rough agreement with previous high Mach number experiments.

We will use the same methods to investigate the turbulent mixing zone behaviour for other values of the Atwood and Mach numbers, and we will complete the present data with Schlieren flow visualisations, which will provide more information on the three-dimensional nature of this turbulent mixing in high Mach number shock tube flows.

ACKNOWLEDGMENTS

This work is supported by the Centre d'Etude de Limeil-Valenton (C.E.A.) and we are particularly indebtead to Dr. J. F. Haas for many helpful discussions.

REFERENCES

1. V.A. ANDRONOV, S.M. BAKHRAKH, E.E. MESHKOV, V.V. MOKHOV, V.V. NIKOFOROV, A.V. PEVNITSHII and A.I. TOLSHMYAKOV, "Turbulent Mixing at Contact Surface Accelerated by Shock Waves, Sov, Phys, JETP, 44, 424 (1976).
2. S.G. ZAITSEV, E.V. LAZAREVA, V.V. CHERNOUKHA and V.M. BELYAEV, "Intensification of Mixing at the Interface Between Media of Different Densities Upon the Passage of Shock Wave Trough It, Sov, Phys, Dokl, 30, 576 (1985).
3. L. HOUAS, A. FARHAT and R. BRUN, "Shock Induced Rayleigh-Taylor Instability in the Presence of a Boundary Layer", The Pysics of Fluids, Vol. 31, N°4, (1988).
4. L. HOUAS, A. FARHAT, A. RAMDANI, J. FORTES and R. BRUN, "Concentration and Temperature Profiles in a Shocked Gaseous Interface", Proceedings of the 16th International Symposium on Shock Waves and Shock Tubes, ed, H. Grönig, RWTH, Aachen, p. 831 (1987).
5. B. STURTEVANT, "Rayleigh-Taylor Instability in Compressible Fluids", Shock Waves and Shock Tubes" Proceedings of the 16th International Symposium on Shock Waves and Shock Tubes, ed, H. Grönig, RWTH, Aachen, p.89 (1987).
6. L. HOUAS, R. BRUN and M. HANANA, "Experimental Investigation of Shock-Interface Interaction", AIAA J. Vol. 24, N°8, p.1254 (1986).

	Conditions 1	Conditions 2	Conditions 3	Conditions 4
Gases	CO_2/Ar	CO_2/Ar	CO_2/He	CO_2/He
Test section length (cm)	127	152	127	152
Initial pressure (Pa)	1500	2000	1500	2000
M_I	4.2	3.7	4.2	3.7
M_T	4	3.7	2.4	1.95
U (m/s)	817	632	1236	914
U_I (m/s)	1030	970	1700	1240
A_{t0}	- 0.0476	- 0.06	- 0.833	- 0.75
A_{t1}	- 0.48	- 0.42	- 0.86	- 0.795
$\frac{dL_i}{dt}$ (m/s)	50	65	70	75
$\frac{1}{U_I}\frac{dL_i}{dt}$	0.048	0.067	0.056	0.06
$\frac{dL_1}{dt}$ (m/s)	7.7	10	38	50
$\frac{1}{U_I}\frac{dL_1}{dt}$	0.0075	0.010	0.023	0.04
$0.02 + 0.07 \lvert A_{t1} \rvert$ (Zaitsev)	0.054	0.049	0.08	0.075
ΔU_R (m/s)	1040 - 200 - 840	815 - 140 - 675	1680 - 820 - 840	115 - 560 - 555
A_{t2}	0.67	0.59	0.92	0.86
$\frac{dL_2}{dt}$ (m/s)	530	400	850	900
$\frac{1}{\Delta U_R}\frac{dL_2}{dt}$	0.63	0.59	1.012	1.62
$0.05 + 0.85 \lvert A_{t2} \rvert$ (Zaitsev)	0.62	0.55	0.832	0.781

Table 1 : Summary of velocity and thickening rates measurements.

Table 2 : Theoritical values corresponding to results of figures 9 to 14.

Gases	CO_2/Ar	CO_2/He
Conditions (Table:1)	2	4
T_{CO2} (K)	765	637
D_{CO2}(kg/m^3)	0.17	0.08
T_{He} (K)		548
D_{He} (kg/m^3)		0.0072
T_{Ar} (K)	1230	
D_{Ar} (kg/m^3)	0.01	

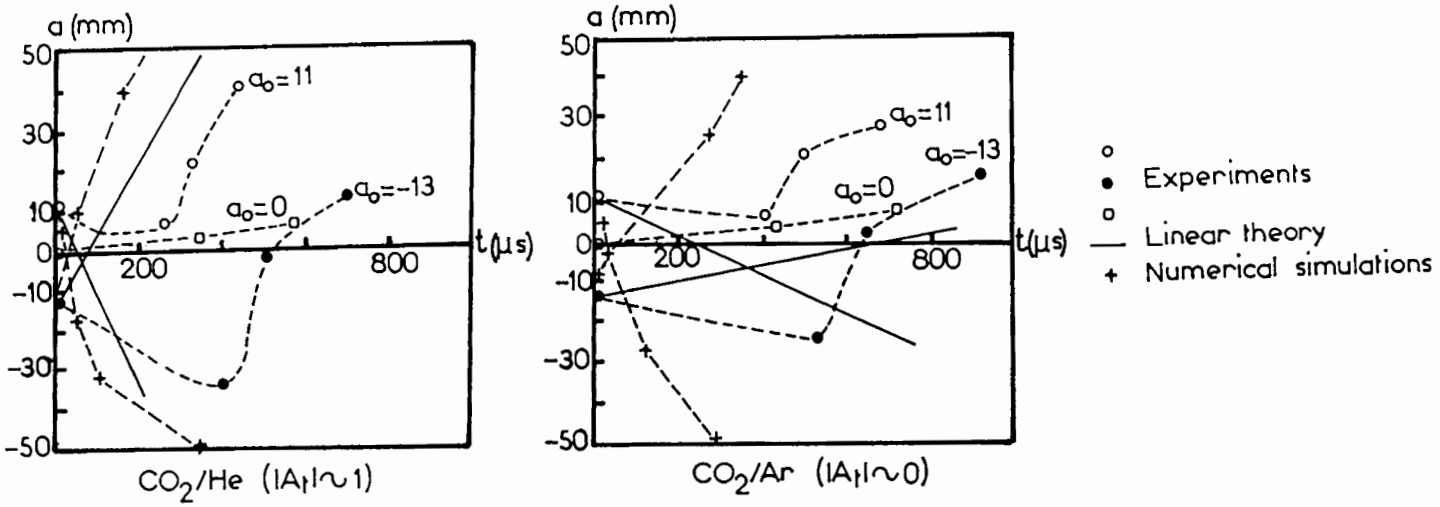

Figure 1 : Evolution of the amplitude a of the mixing zone front deformation.

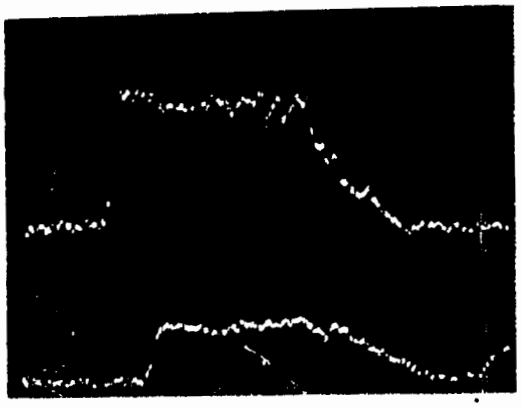

Figure 2 : Example of oscillographic emission records for CO_2/Ar mixing zone thickness determination.

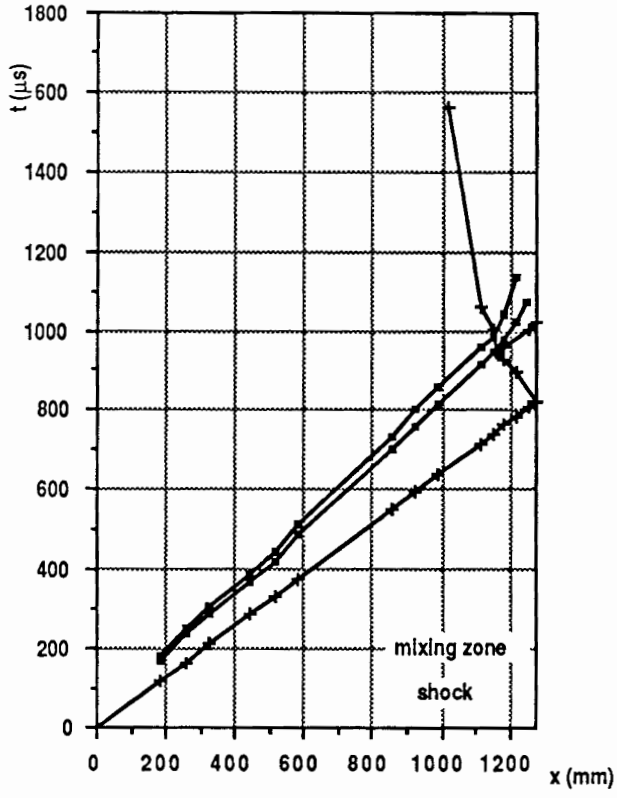

Figure 3 : Experimental (x, t) diagram for CO_2/He mixing zone (conditions 4).

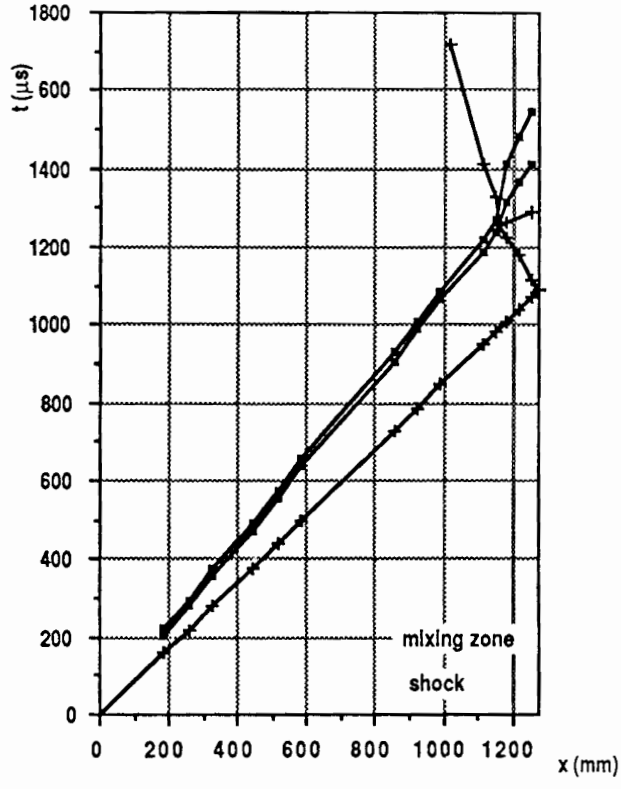

Figure 4 : Experimental (x, t) diagram for CO_2/Ar mixing zone (conditions 2).

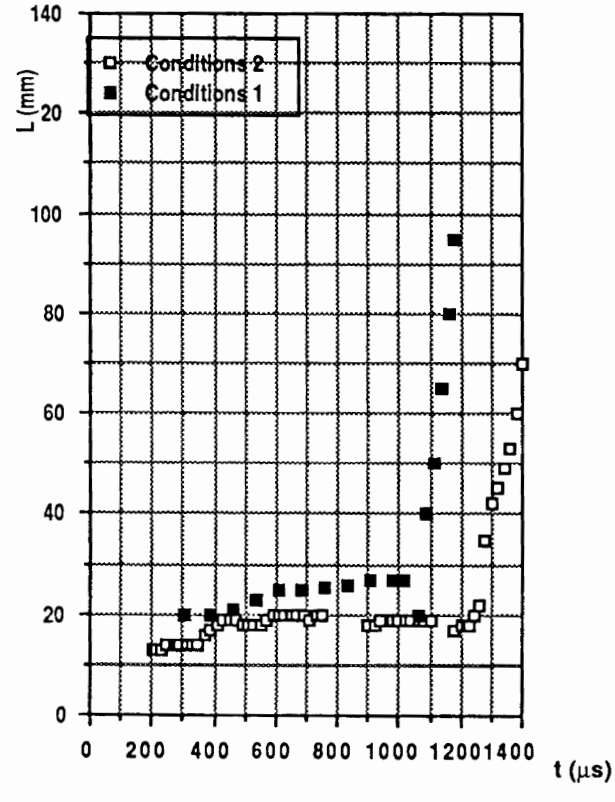

Figure 5 : CO_2/Ar mixing zone thickness.

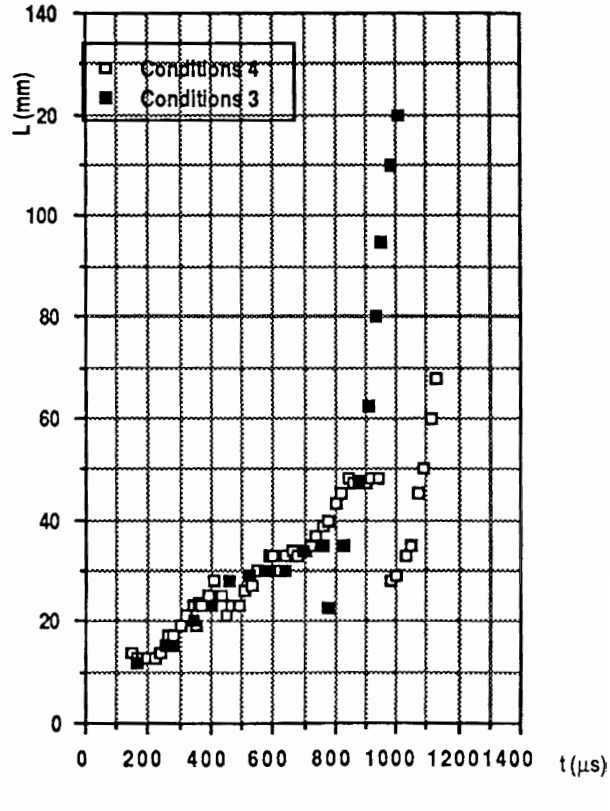

Figure 6 : CO_2/He mixing zone thickness.

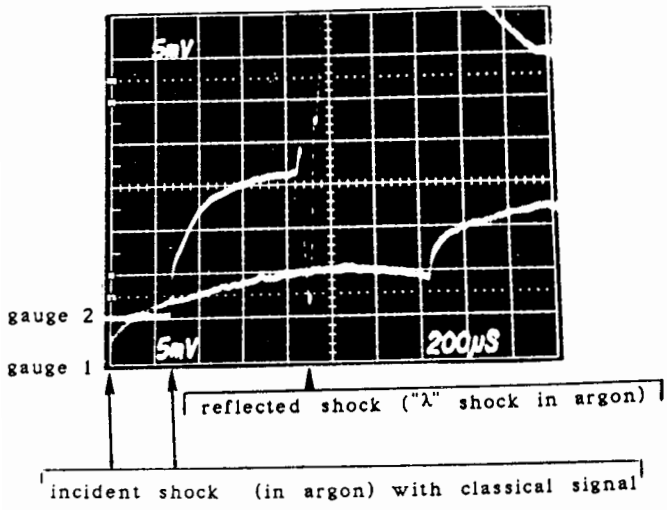

Figure 7 : Example of "λ" shock detected by wall heat transfer gauges.

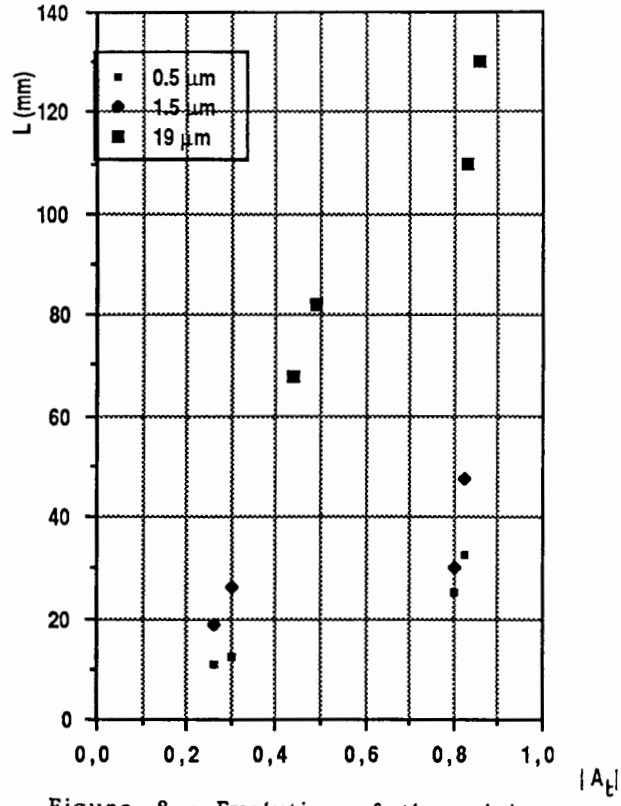

Figure 8 : Evolution of the mixing zone thickness for different membranes.

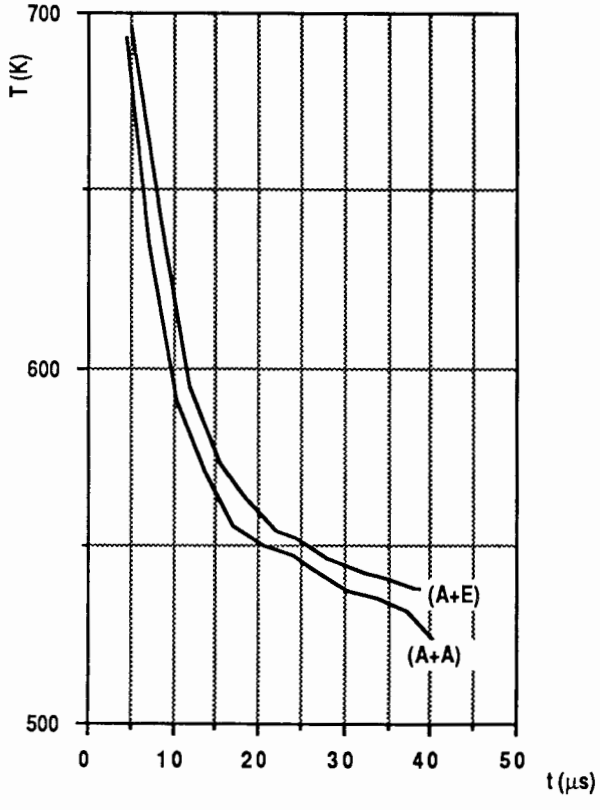

Figure 9 : Average Temperature profile in the CO_2/He mixing zone.

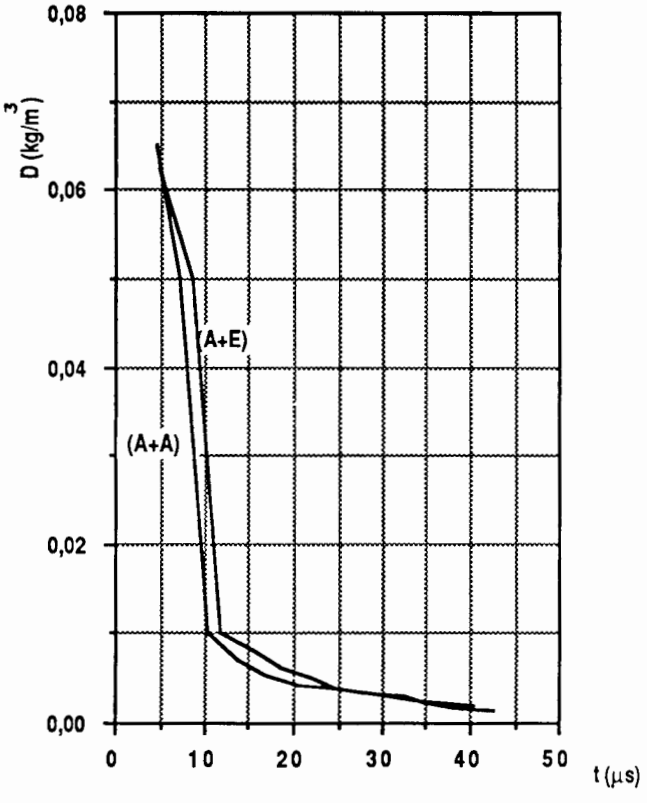

Figure10 : Average Density profile in the CO_2/He mixing zone.

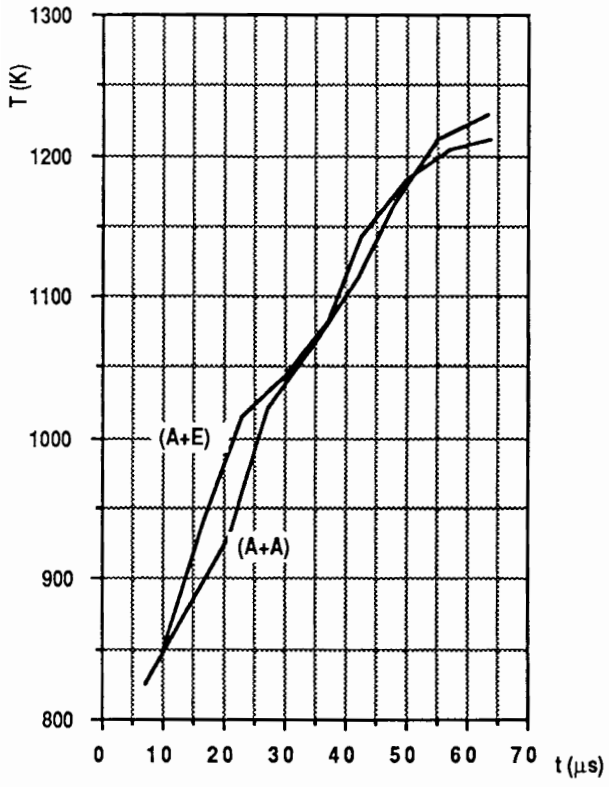

Figure11 : Average Temperature profile in the CO_2/Ar mixing zone.

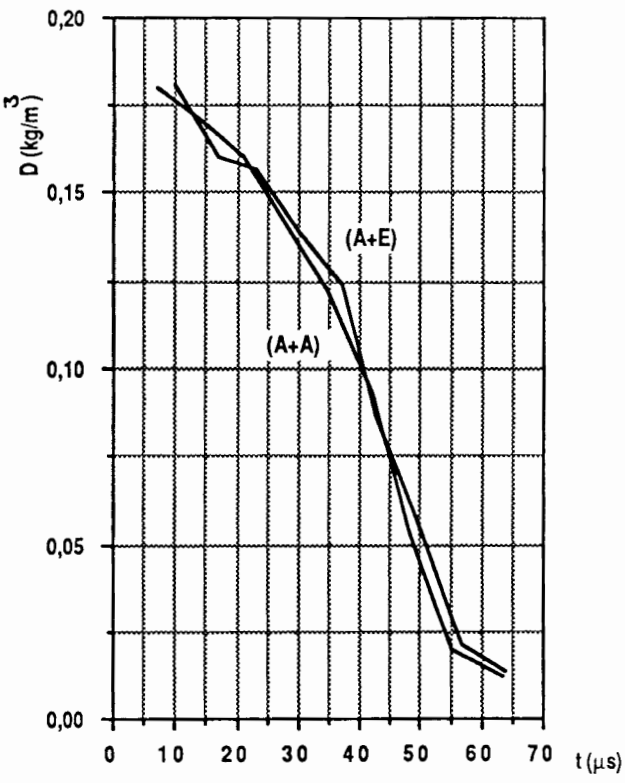

Figure12 : Average Density profile in the CO_2/Ar mixing zone.

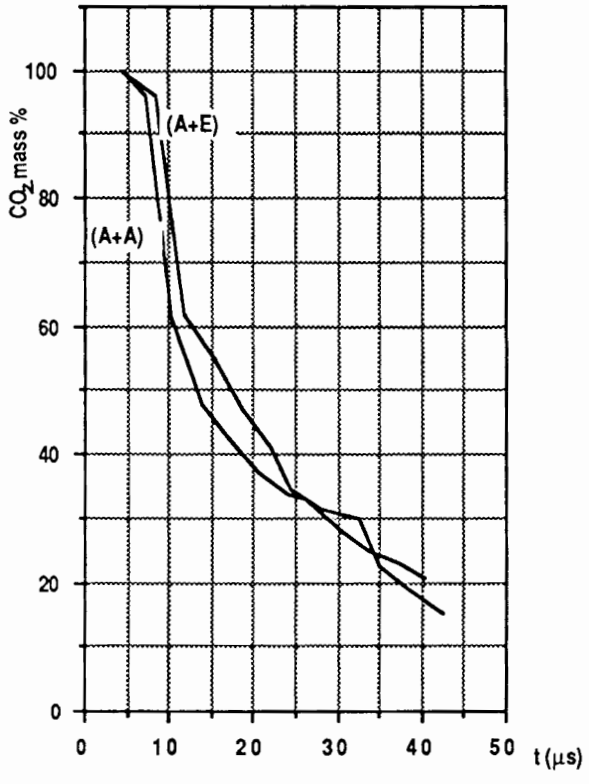

Figure13 : CO_2 Mass Concentration profile in the CO_2/He mixing zone.

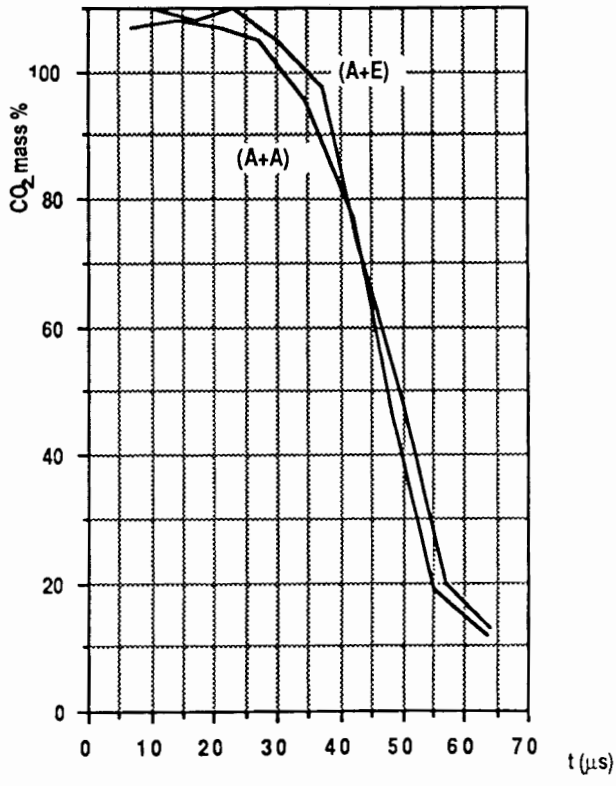

Figure14 : CO_2 Mass Concentration profile in the CO_2/Ar mixing zone.

PRELIMINARY DATA ON THE DYNAMICS OF TURBULENT SHOCKLETS

J. A. Johnson III, L. E. Johnson, J. Zhang, Y. Zhang
Department of Physics, The City College, CUNY
New York, NY 10031 USA

Substantial interest exists in the coherent structures produced by supersonic free shear layers. Coherent structures play an important role when nonequilibrium and nonlinear behavior is dominated by mass and momentum transfer effects. Some have argued that the mass and momentum transfer is produced by merging coherent structures.[1] Hence, if one knows how to manipulate the structures, the entrainment can be controlled.[2] Our work focuses on the formation and evolution of coherent structures in the supersonic free shear layer using non-obtrusive optical diagnostics. We are specifically interested here in the turbulent shocklets which are thought to be associated with these structures. We present our first preliminary data on the shocklet profile, velocity, and production frequency; we also suggest some properties of the turbulence associated with these entities.

The tube wind tunnel used is an elaboration of the configuration originally proposed by Ludwieg.[3] A conventional shock tube is modified by inserting a layer-spilling asymmetric supersonic nozzle into the section upstream from the diaphragm (the high pressure section). When the diaphragm breaks, an expansion wave moves upstream into the high pressure section through the nozzle causing the local pressure, density and gas velocity to change with time and as a function of distance from the diaphragm's location. At a time determined by the ratio of the nozzle's throat area to its exit area, the nozzle is choked, i.e., the mass flow rate is frozen, and stable supersonic flow is established in the exit region. The steady period's duration is determined by the round-trip time for the head of the expansion wave to travel from the nozzle's throat to the high pressure section's upstream end. In the literature, one can find derivations of the formulas relating the nozzle's parameters to the initial conditions of the tube.[4] With this kind of device, high Reynolds numbers (resulting from high stagnation pressures) can be maintained in the exit region under conditions of steady supersonic flow for more than 10 ms.

The low pressure section of our Ludwieg tube has two parts: a 6 in. diameter 5 ft. long cylindrical end piece and a 3 ft. long

transition piece that changes from a 6 in. diameter circular cross section to a 3.6x3.6 in. square at the diaphragm. The transition piece has a hand operated plunger for rupturing the diaphragm. The high pressure section has five parts: a 6 ft. long 3.6x3.6 in. square test section with five optical ports on each face and corresponding pressure ports; a 3 ft. long transition piece for the change from a 3.6x3.6 in. cross section to the 6 in. diameter cylindrical piece; and two pieces that are each quarter circle arcs of 2 ft. radius with 6 in. diameter cross sections. The curved sections conveniently extend the overall length of the high pressure section and thereby increase the duration of the period of steady supersonic flow. The overall thickness is roughly 0.3 in. throughout.

The starting processes are conventional. The integrity of the boundary layer which produces the free shear layer was confirmed by exhaustive pitot gauge studies. The nozzle's flow Mach number is calibrated by using wedges inserted in the flow and measuring the angles of the shock waves produced by the wedges. A 5 ft. long, 6 in. diameter cylindrical piece was added upstream of the circular arcs in order to increase the steady flow time. For each desired value of p_4 (the initial pressure in the high pressure section), we determined the value of p_1 (the initial pressure in the low pressure section) for which smooth (i.e., free of either expansion waves or shock waves) flow is achieved at the edge of the nozzle; this procedure defines the the operating ratio p_4/p_1 for the given value of p_1 (and therefore the Reynolds number) at which measurements will be made. By thereby avoiding back pressure effects, we have created flow environments which can be generalizable.

The optical systems are suggested in Fig. 1(a). An argon ion laser and a mecury-arc lamp are used as our light sources. We used three different diagnostic techniques.

In line absorption measurements, the light from the mecury lamp is split into four parallel small beams; each is 1 mm in diameter, separated from its nearest neighbor by 1 mm along the downstream direction. This is defined as the x-direction, with the direction perpendicular to the flow and to the surface of the nozzle being defined as the y-direction. The absorbed light signals are collected by photomultiplier tubes. This line-averaged measurement gives us line-averaged density history.

We also use crossed beam measurements. The same light source is employed; the four split beams are arranged so that they cross, two each, at right angles as indicated in Fig. 1(a). That is, two beams are separated by 1 mm along x and parallel to the y-direction; the other two beams are parallel to the z-direction. The points of intersection are inside the free shear layer and a little bit off the x-axis. This technique can give us the point density fluctuation signals.

The third optical diagnostic is the fluorescence measurement. The 2 W 488.0 nm blue light from the argon ion laser is expanded and then split into three small beams with the same size and separation used in the first and second techniques just described. The beams are sent through the free shear layer along the y direction and separated in the x direction. A small admixture of NO_2 (roughly 3% in N_2) provides a target for the laser light and is the source of the fluorescent light. The fluorescence signals from the three points inside the free shear layer are collected by photomultiplier tubes. The three signals come from three points with a separation of 1 mm along the x-axis on the y-axis or three points of separation of 1 mm along the x-axis and 1 mm off the x-axis. This kind of measurement allows a precise point density history.

Static pressure ports along the test section use conventional Kistler gauges. Total pressure operating conditions are monitored and controlled using a Baratron pressure transducer system. The signals from the photomultiplier tubes are amplified and digitized with Nicolet ADC's. The system runs at room temperature. A thermocouple is fixed at the high pressure section so as to check the temperature drop when the high pressure section is filled with the NO_2 and N_2 mixtures. Generally, our typical operating conditions are: Mach numbers between 1.6 and 2.5; unit Reynolds numbers between 10^6 and 10^7 /cm; typical pressures in the high pressure section between 33 psia and 80 psia and between 20 Torr and 110 Torr in the low pressure section. In this paper, we focus on one configuration at a Mach number of 2.0 and a Reynolds number (based on measurements 1 cm into the free shear layer) of 4×10^6.

Evidence for the existence of turbulent shocklets is found in all of our optical diagnostics. This supports our previous report on the evidence from shadowgraph photography and the correlation of shocklet

strength with Reynolds number.[5] In Fig. 1(b), we show typical results using the crossed beam set-up for point r.m.s. density fluctuations in the free shear layer. Here there is a signature in the density fluctuations at the shocklet front from the edge of the wedge, 1.7 cm and 2.7 cm respectively from the edge. In each case, the effective duration of the shocklet front is less than 0.005 msec. These data indicate that a very strong localized increase in density fluctuations takes place at the turbulent shocklet, on a scale much larger than the fluctuations either just before or just after the shocklet. Relatively speaking, there also does not seem to be much of a change in the intensity of the turbulent fluctuations from one side of the shocklet to the other. Fig. 1(b) also shows that the duration or thickness of the shocklet is consistent with the expected values for a shock wave phenomenon.

The same qualitative features are confirmed in the point density histories from fluorescence and the line-averaged blue light absorption. Samples of these data are shown in Fig. 2. Fig. 2(a) show fluorescence data from two measurements separated from each other by 1 mm along the x-axis and parallel to the centerline, 1 mm away from it in the y direction. Fig. 2(b) shows results from a similar configuration, using the line-averaged blue light absorption. In both cases, the standard signature for a shock wave is unmistakable.

From these data, we have determined some of the dynamical properties of the shocklets. The local velocity of shoocklets in the region where we are making these measurements is 86±35 m/s; the shocklet production frequency is at least as high as 6 KHz providing a Strouhal number (based on the local mean flow velocity of 512.0 m/s) of at least 0.12. We also notice that the prominence of the signal in the line-averaged data suggests a strongly two-dimensional character in these shocklets.

The spectral properties in the turbulent fluctuations do not seem to be influenced by the turbulent shocklet. Typical examples of this are shown in Fig. 3. Fluorescence data from one Ludwieg tube firing, off axis measurements at consecutive stations 1 mm apart, show FFT spectra before and after the shocklet which are typically turbulent but apparently unchanged by the shocklet. This is confirmed by studies of velocity fluctuation measurements take from PHACO velocimetry[6] on the line averaged data using the previously published

analytical procedures as shown in Fig. 4(a). These FFT data along with the apparent insensitivity of the turbulent intensity to the shocklet seems to imply an important limitation in the impact of the turbulent shocklet on the strength of the turbulence.

However, the shocklet does seem to have some influence on the structure of the turbulence. This is implied by the data in Fig. 4(b); the turbulent correlation length scale seems to be changed by the shocklet. In Fig. 5 (taken from the same fluorescence data as Fig. 3) this is unambituously confirmed. The effect of the turbulent shocklet is that of causing a significant distortion in the characteristic length scale, by as much as a factor of two.

Notice that this correlation scale would probably determine the extent to which a local turbulence can couple into a local chemical reaction. Thus, these preliminary results indicate that the turbulent shocklets: (1) do not change the turbulence; (2) might influence the relative impact of turbulent mixing processes (since the shocklets should effect the local mean flow while leaving the turbulent strength unchanged); and (3) might effect the progress of a nonequilibrium molecular process.

This work was supported in part by NASA Grant NAG-1-377.

1. Winant, C. D., Brownand, F. K., J. Fluid. Mech., 63, 237-255 (1974).
2. Ho, C.-H., "Mixing Processes in Free Shear Layers," AIAA Paper AIAA-86-0234, (1986).
3. Ludwieg, H., "Tube Wind Tunnel: A Special Type of Blow Down Tunnel," NATO Headquarters, Scheveningen, Holland, AGARD Rept. 143, June, 1952.
4. Cable, A. J., Cox, R. N., The Aero. Quart., Vol. XIV, Pt. 2, 143-157 (1973).
5. Johnson, J. A. III, Zhang, Y., Johnson, L. E., AIAAJ, 26, 502-504 (1988).
6. Johnson, J. A. III., Johnson, L. E., Chen, S.-C., Rev. Sci. Instr., 56, 1831-33 (1985).

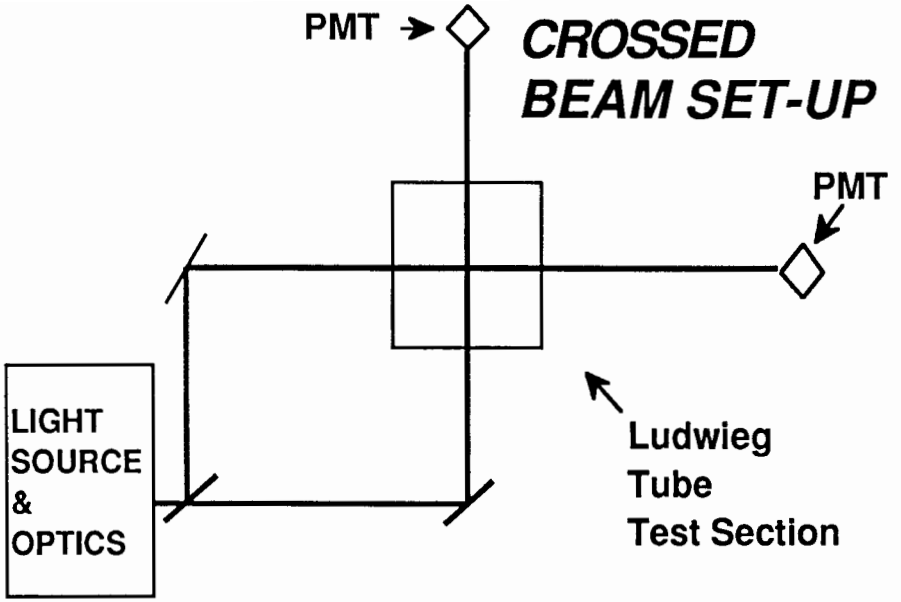
PMT
CROSSED
BEAM SET-UP
PMT
LIGHT
SOURCE
&
OPTICS
Ludwieg
Tube
Test Section

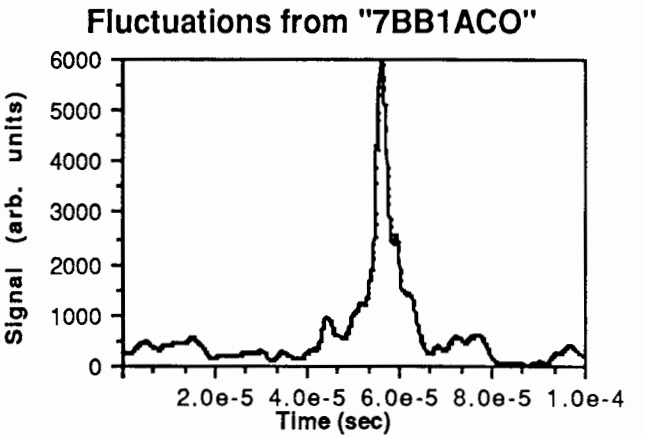
Fluctuations from "7BB1ACO"
Signal (arb. units)
6000
5000
4000
3000
2000
1000
0
2.0e-5 4.0e-5 6.0e-5 8.0e-5 1.0e-4
Time (sec)

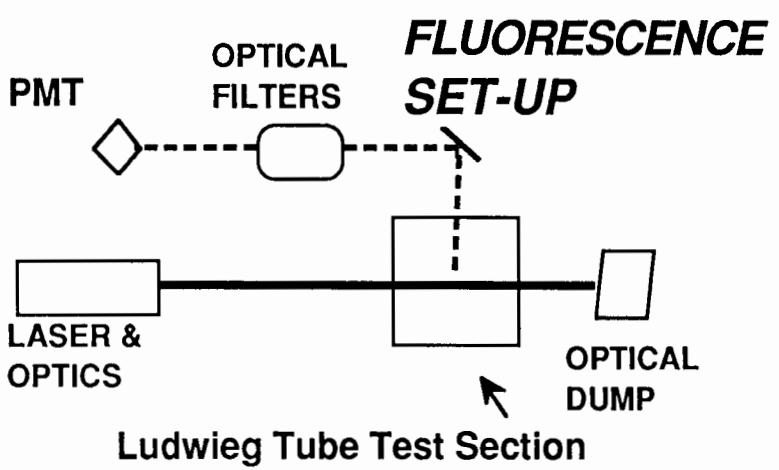
PMT
OPTICAL
FILTERS
FLUORESCENCE
SET-UP
LASER &
OPTICS
OPTICAL
DUMP
Ludwieg Tube Test Section

(a)

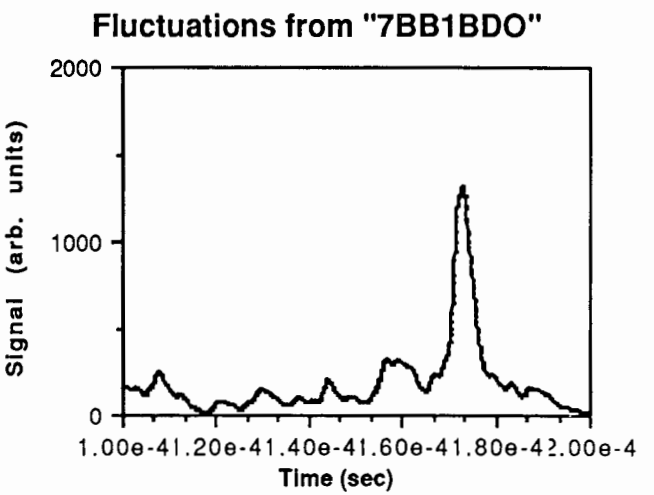
Fluctuations from "7BB1BDO"
Signal (arb. units)
2000
1000
0
1.00e-4 1.20e-4 1.40e-4 1.60e-4 1.80e-4 2.00e-4
Time (sec)

(b)

Figure 1.

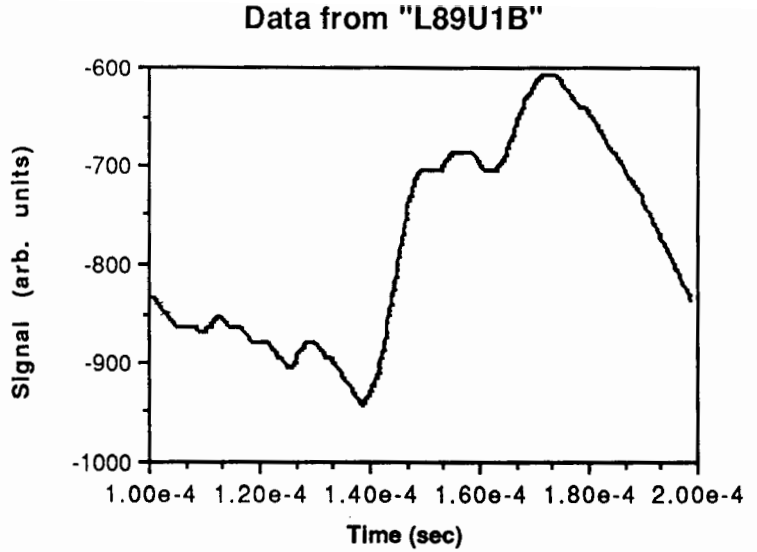
Data from "L89U1B"
Signal (arb. units)
-600
-700
-800
-900
-1000
1.00e-4 1.20e-4 1.40e-4 1.60e-4 1.80e-4 2.00e-4
Time (sec)

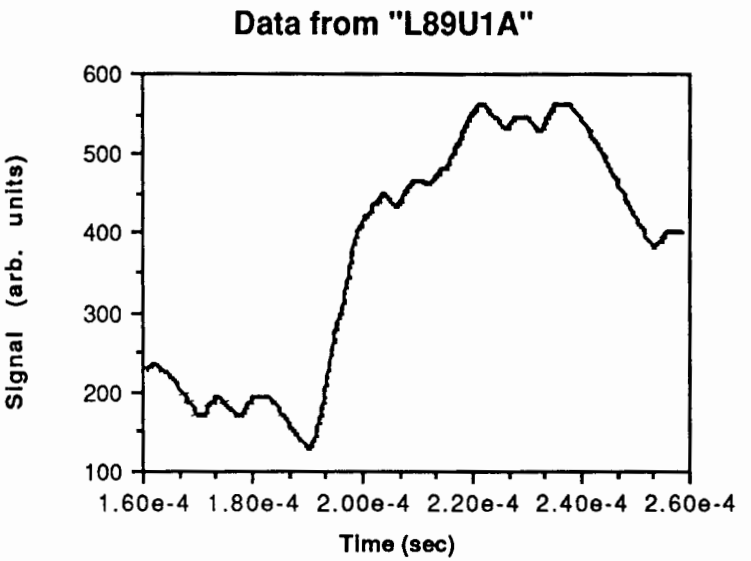
Data from "L89U1A"
Signal (arb. units)
600
500
400
300
200
100
1.60e-4 1.80e-4 2.00e-4 2.20e-4 2.40e-4 2.60e-4
Time (sec)

(a)

(b)

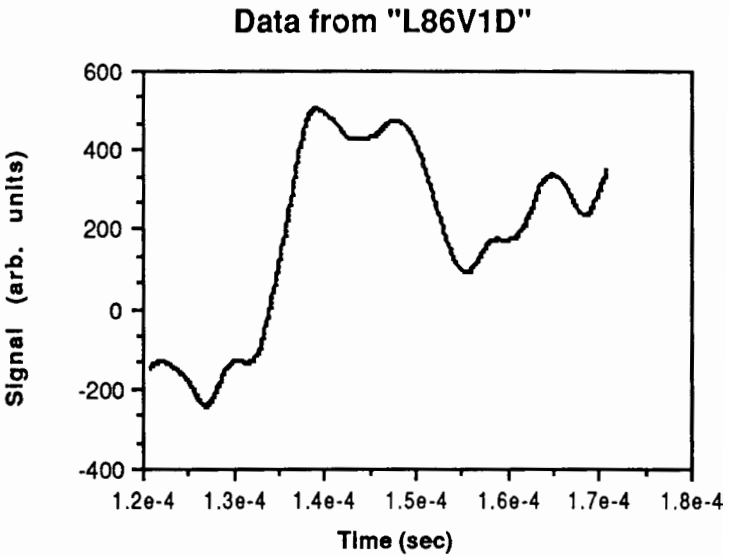
Data from "L86V1D"
Signal (arb. units)
600
400
200
0
-200
-400
1.2e-4 1.3e-4 1.4e-4 1.5e-4 1.6e-4 1.7e-4 1.8e-4
Time (sec)

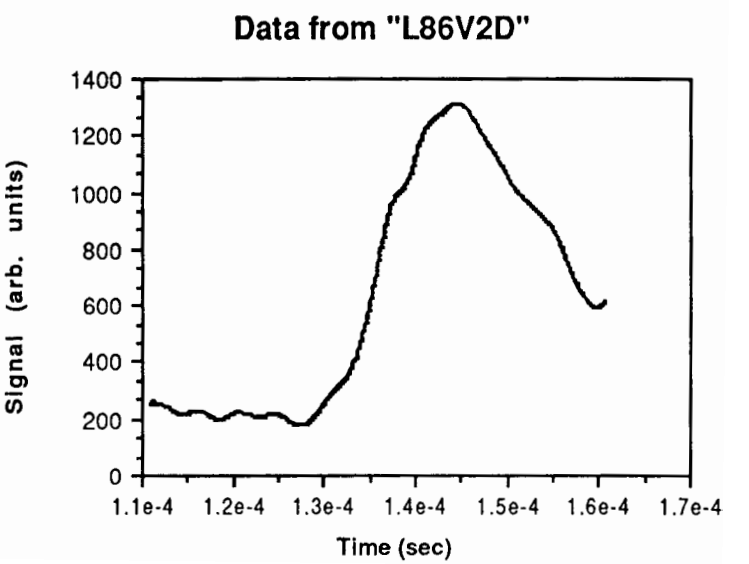
Data from "L86V2D"
Signal (arb. units)
1400
1200
1000
800
600
400
200
0
1.1e-4 1.2e-4 1.3e-4 1.4e-4 1.5e-4 1.6e-4 1.7e-4
Time (sec)

Figure 2.

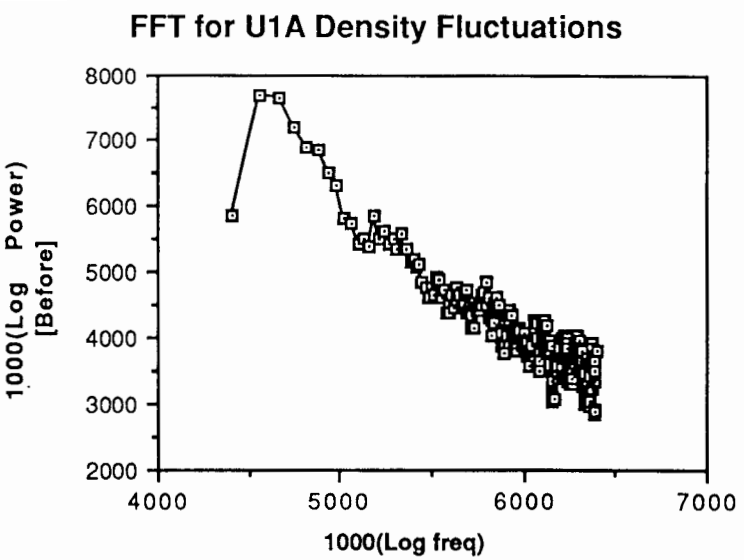
FFT for U1A Density Fluctuations
1000(Log Power) [Before]
1000(Log freq)
8000
7000
6000
5000
4000
3000
2000
4000
5000
6000
7000

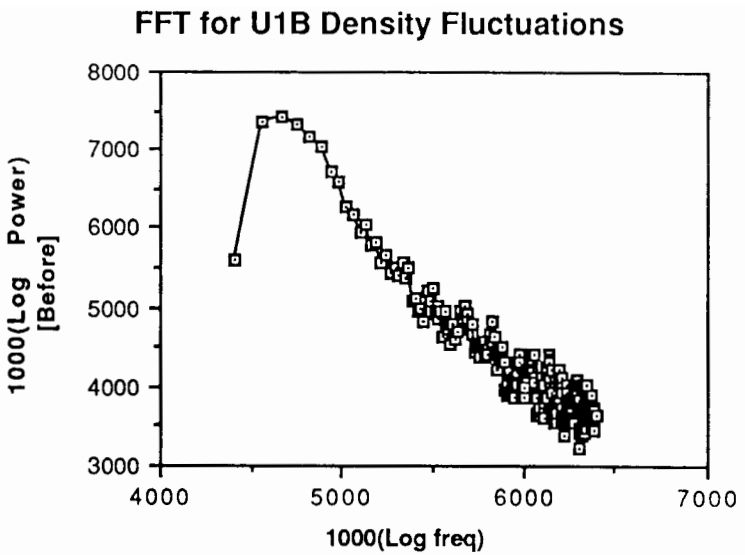
FFT for U1B Density Fluctuations
1000(Log Power) [Before]
1000(Log freq)
8000
7000
6000
5000
4000
3000
4000
5000
6000
7000

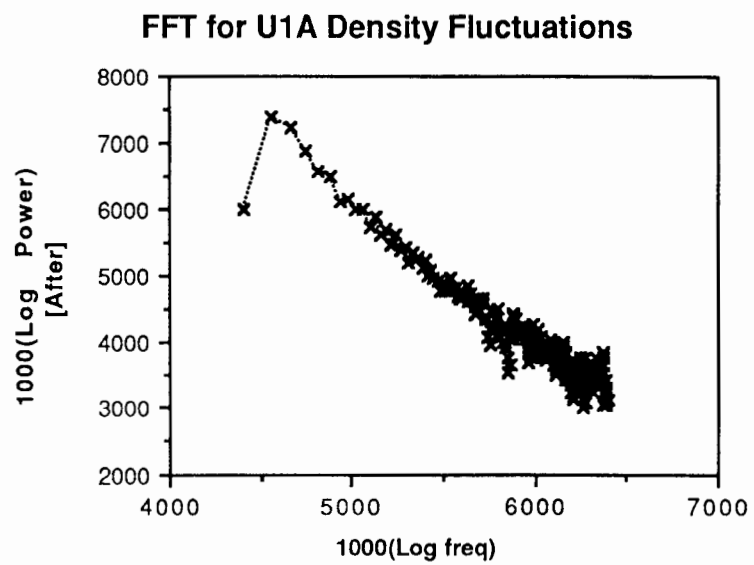
FFT for U1A Density Fluctuations
1000(Log Power) [After]
1000(Log freq)
8000
7000
6000
5000
4000
3000
2000
4000
5000
6000
7000

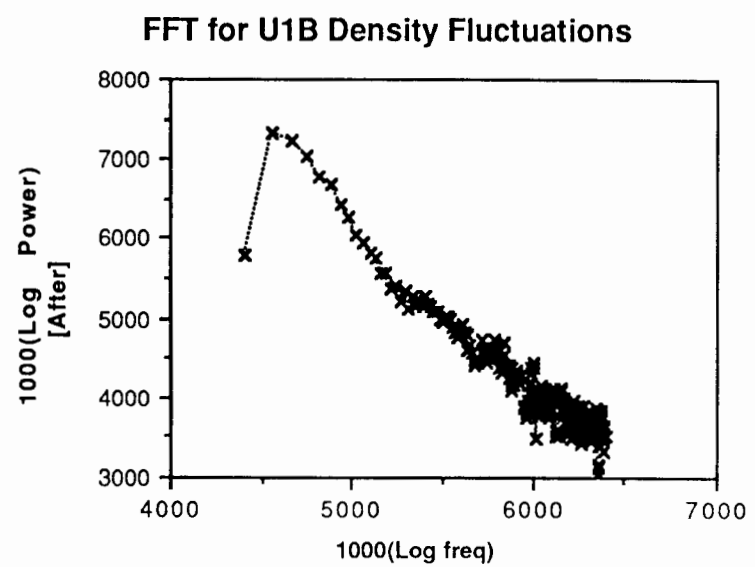
FFT for U1B Density Fluctuations
1000(Log Power) [After]
1000(Log freq)
8000
7000
6000
5000
4000
3000
4000
5000
6000
7000

Figure 3.

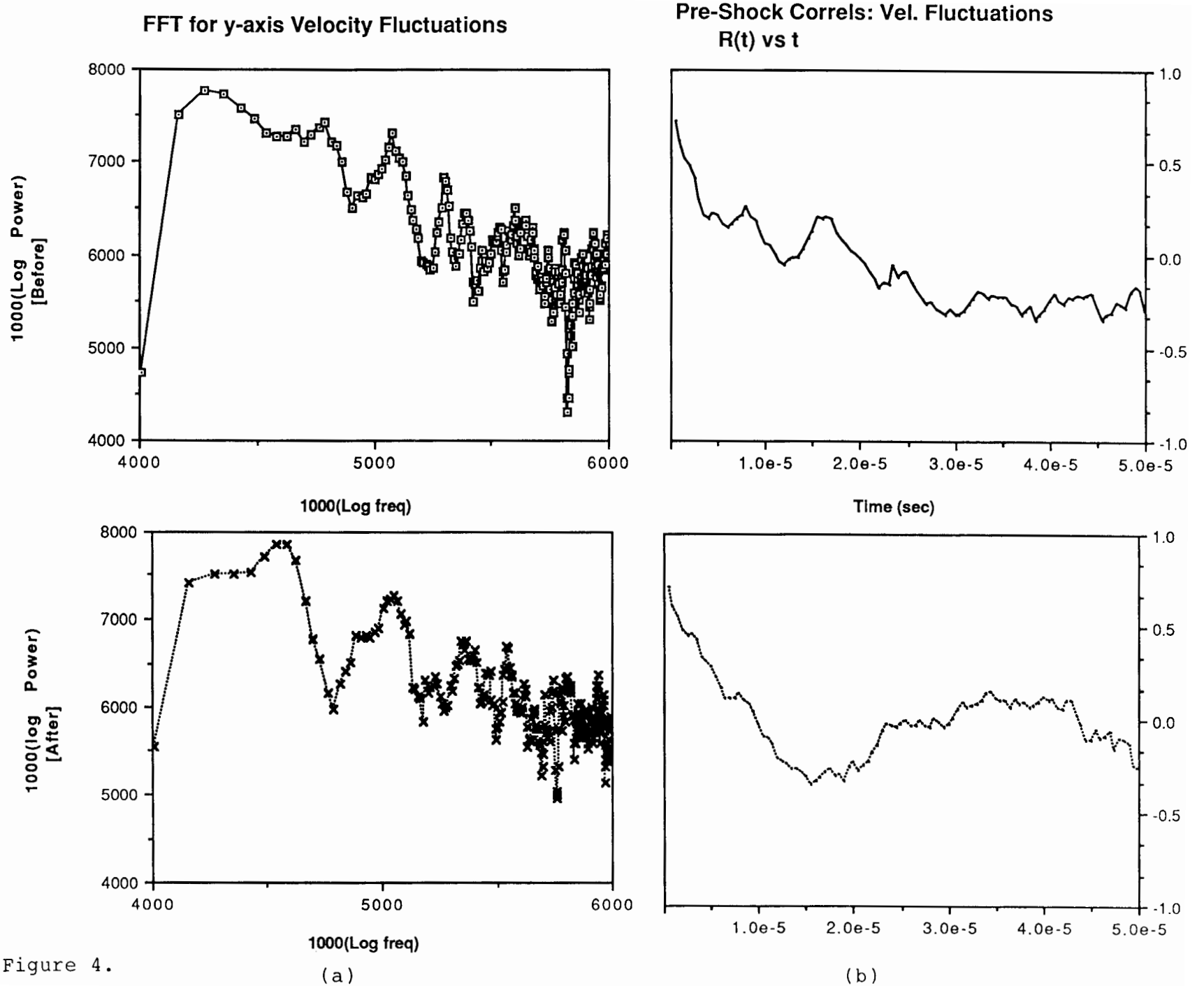
FFT for y-axis Velocity Fluctuations
1000(Log Power) [Before]
8000
7000
6000
5000
4000
4000
5000
6000
1000(Log freq)
Pre-Shock Correls: Vel. Fluctuations
R(t) vs t
1.0
0.5
0.0
-0.5
-1.0
1.0e-5
2.0e-5
3.0e-5
4.0e-5
5.0e-5
Time (sec)
1000(log Power) [After]
8000
7000
6000
5000
4000
4000
5000
6000
1000(Log freq)
1.0
0.5
0.0
-0.5
-1.0
1.0e-5
2.0e-5
3.0e-5
4.0e-5
5.0e-5

Figure 4.

(a) (b)

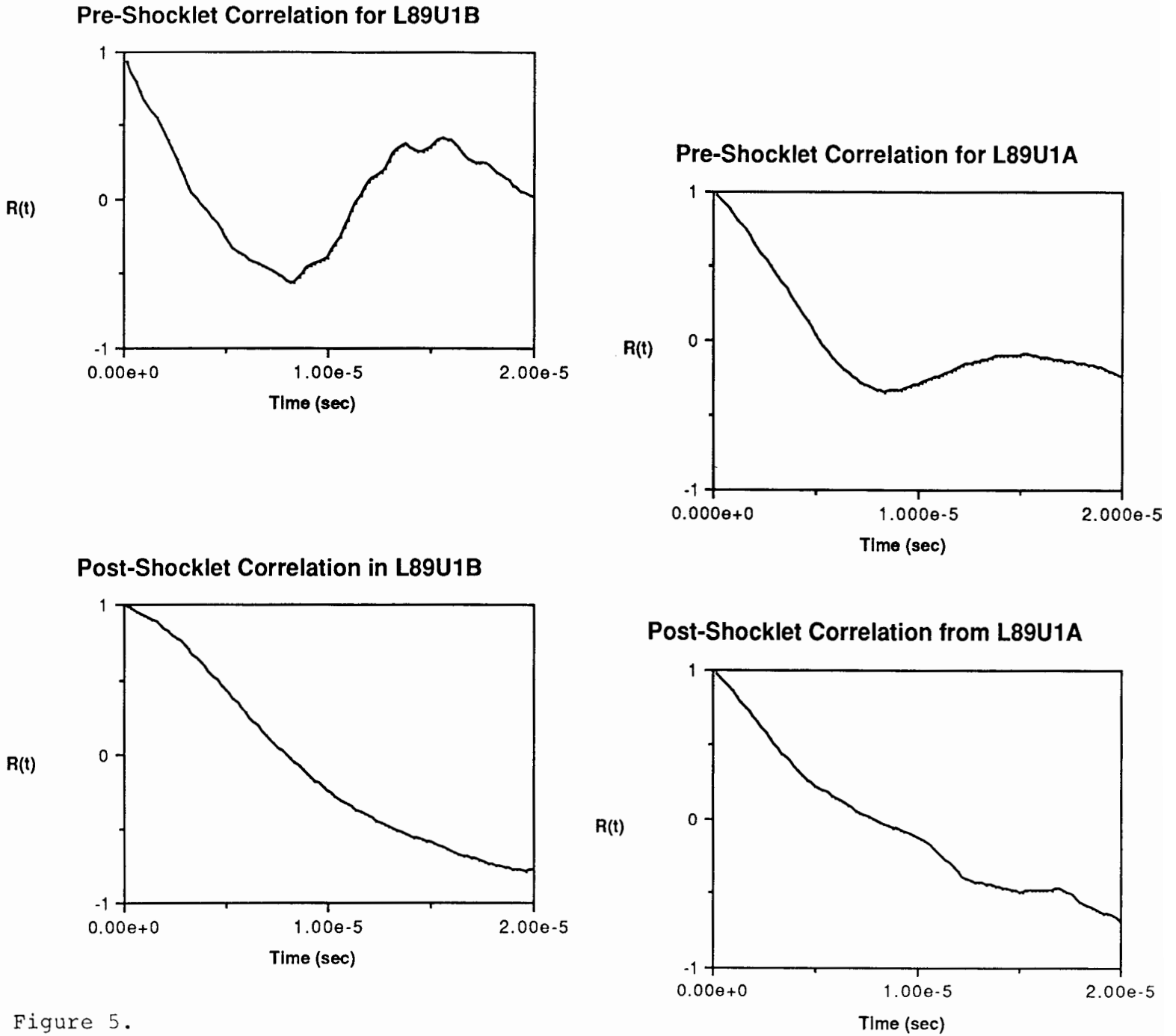
Pre-Shocklet Correlation for L89U1B
R(t)
1
0
-1
0.00e+0
1.00e-5
2.00e-5
Time (sec)
Pre-Shocklet Correlation for L89U1A
R(t)
1
0
-1
0.000e+0
1.000e-5
2.000e-5
Time (sec)
Post-Shocklet Correlation in L89U1B
R(t)
1
0
-1
0.00e+0
1.00e-5
2.00e-5
Time (sec)
Post-Shocklet Correlation from L89U1A
R(t)
1
0
-1
0.00e+0
1.00e-5
2.00e-5
Time (sec)

Figure 5.

THE INTERACTION OF A SUPERNOVA REMNANT WITH INTERSTELLAR CLOUDS USING HIGH ORDER LOCAL ADAPTIVE MESH REFINEMENT METHODS

Richard I. Klein
Lawrence Livermore National Laboratory
and
Department of Astronomy, University of California at Berkeley
Philip Colella
Lawrence Livermore National Laboratory
and
Department of Mechanical Engineering, University of California at Berkeley
Christopher F. McKee
Departments of Physics and Astronomy
University of California at Berkeley

I. INTRODUCTION

The interaction between supernova remnants (SNR) and interstellar clouds in the galaxy is known to play a major role in determining the structure of the interstellar medium (ISM). We know that the ISM is highly inhomogeneous, consisting of both diffuse atomic clouds (T~100K) and dense molecular clouds (T~10K) surrounded by a low density warm ionized gas(T~10^4K) and by a very hot coronal gas (T~10^6K). Next to radiation directly from stars, supernova explosions represent the most important form of energy injection into the ISM; they determine the velocity of interstellar clouds, accelerate cosmic rays, and can compress clouds to gravitational instability, possibly spawning a new generation of star formation.[1] The shock waves from supernova remnants can compress, accelerate, disrupt and render hydrodynamically unstable interstellar clouds, thereby ejecting mass back into the intercloud medium. Thus, while the interaction of the SNR blast wave with cloud inhomogeneities can clearly alter the appearance of the ISM, the cloud inhomogeneities can similarly have a profound effect on the structure of the SNR.

Given the importance of the interaction of the supernova shocks with clouds for understanding the structure and the dynamics of the ISM as well as the potential importance of the interaction as a means of triggering new star formation, the problem has been studied both analytically and numerically over the past decade. Even when idealized as the interaction of a strong shock with a spherically symmetric cloud embedded in a less dense intercloud medium, the problem represents an extremely complex non-linear hydrodynamic flow encompassing a rich family of shock-shock interaction phenomena. The multi-dimensional nature of the evolution of the disrupted cloud is such as to make a detailed analytic calculation intractable. The first serious attempt to follow the interaction numerically was made by Woodward[2], who used a combined Eulerian-Lagrangian approach to follow the interaction of the shock from a spiral density

wave with a galactic cloud. These results showed the start of both Rayleigh-Taylor and Kelvin Helmholtz type instabilities; however, the calculation was not carried out far enough to ascertain the final fate of the cloud. A subsequent attempt to investigate this problem by Nittman et al.[3] used a flux-corrected transport approach and was very unresolved. Recently, Tenorio-Tagle and Rozyczka[4] attempted to follow the evolution with a second order accurate hydrodynamic scheme, but again the calculation was under-resolved and clearly showed the effects of strong numerical diffusion at the interface of the cloud boundary and the intercloud medium. This made it impossible to disentangle the mixing of cloud-intercloud matter due to physical instabilities from mixing due to numerical effects. All of the previous work on this important problem leave unanswered several questions of key importance: What is the ultimate fate of clouds that have been impacted by SNR shocks? What is the total momentum delivered to the cloud? How much mass is lost from the cloud? To what extent is the cloud disrupted? How do the results scale with cloud density, shock Mach number and cloud size? Is the cloud driven to gravitational instability or is the cloud destroyed? What is the effect of the interstellar magnetic field on the evolution? What are the observable consequences of the interaction?

As we shall see, highly complex shock-shock interactions play a major role in determining the morphology of the cloud. Instabilities and shear flow motions are crucial to track accurately. These physical phenomena place an enormous constraint on the capabilities of most conventional numerical methods for solution in 2-D. Even high order accurate approaches such as PPM[5] with fixed Eulerian grids would require at least 10^6 grid points to follow the evolution accurately enough to answer the questions posed above. Clearly, one has a great need to evolve solutions in 2-D with a great enough accuracy to deal with physical constraints and at the same time do so economically in both storage and time.

II. METHODOLOGY

To address these difficulties, we have used the local adaptive mesh refinement techniques with second order Godonov methods developed by Berger and Colella.[6] This first important problem will be the forerunner of a broad-based program we are developing to use adaptive mesh refinement to study astrophysical gas dynamics. We employ a second order finite difference solution of the Euler equations on a square grid in a cylindrically symmetric geometry. The numerical integration of the Euler equations is accomplished using an operator split version of a second order Godunov method (Van Leer,[7] Colella and Woodward[8]). The Godunov method conserves mass, momentum and total energy. We use a γ law equation-of-state, with the cloud and intercloud medium potentially having differing γ. The resulting method is second order accurate in space and time, and captures shocks and other discontinuities with minimal numerical overshoot and dissipation.

The fluid interface is modeled using the SLIC[9] algorithm. In this approach the fraction f of the cell occupied by the cloud is determined for each grid cell through which the cloud interface passes. At the end of every timestep a simple picture of the interface consisting entirely of vertical and horizontal line

segments is reconstructed from the volume fraction information. This picture is then used to determine how much of each fluid is convected out of the cell into adjacent cells at this time step and an update of the partial volumes associated with each cell is obtained. A possible difficulty of this approach is that in a region of expansion or compression, both fluids in a multi-fluid cell will be expanded or compressed equally, regardless of the difference in compressibility between them. To correct this difficulty, we use a scheme in which the equations of motion are rewritten to include extra evolution equations for the volume fraction, total energy of each fluid, and mass density of each fluid in multi-fluid cells. This takes into account the fraction of each fluid component in the cell in such a way as to ensure the correct relative expansion or compression of each fluid component.

From the point of view of being able to resolve detailed complex physical structures with reasonable amounts of supercomputer time and memory, the most important feature of our code is that it employs a dynamic regriddng strategy known as Adaptive Mesh Refinement (AMR)[6] to dynamically refine the solution in regions of interest or excessive error. This is effected by placing a finer grid over the region in question with the grid spacing reduced by some even factor (typically 4). The boundary of the refined grid is always chosen to coincide with cell edges of the coarser grid. Multiple levels of grid refinement are possible with the maximum number of nested grids supplied as a parameter in the calculation. Typically our calculations employ two nested grids over the initial coarse (level 1) grids. In our present work, we determine those regions which require refinement by estimating the local truncation error in the density and refining those regions where the error is greater than some initially specified amount. In addition, we require the maximum level of refinement in the neighborhood of all cells containing cloud material. Special care is taken to ensure the correct fluxes across boundaries between and fine grids. This dynamic adaptive gridding approach is a crucial factor in our ability to economically resolve important features in the cloud shock interaction.

An important feature of our method is that the mesh is locally refined in space-time by $r=\Delta X_{l-1}/\Delta X_l$ on all grids, where ΔX_l is the grid spacing on level l. This implies that the explicit difference scheme remains stable on all grids. In our approach, refined regions appear and disappear in time as they are needed. Given that high resolution second order Godunov schemes are necessary to resolve key features of the interaction, but may still be expensive, AMR concentrates the computational effort in regions where it is most needed without sacrificing accuracy anywhere else. This is in contrast to moving grid approaches. Here one is pulling grid-lines into one region at the expense of sacrificing accuracy elsewhere, giving a fixed cost for the most accurate solution. Grid moving methods have inherent difficulties. There are problems maintaining smooth grids; regularity terms and penalty functions for grid regularization can be complicated and expensive, and one must initially guess at the adequate number of grid points necessary to resolve features that may appear. On contrast, AMR obtains a fixed accuracy at minimum cost. Grid points are added or removed as is necessary to maintain a desired accuracy.

III. CLOUD SIZE SCALES

As the SNR expands through the ISM, it drives a shock into any cloud it encounters. Assuming that these are strong shocks, the pressure behind the blast wave and the pressure behind the transmitted cloud shock are comparable, and one finds that (McKee and Cowie)[10]

$$v_s \approx (\rho_i/\rho_c)^{1/2}\, v_b \ , \tag{1}$$

where v_s and v_b are the cloud shock and blast wave velocities and ρ_c and ρ_i the cloud and intercloud densities, respectively. Following McKee[1], we define characteristic timescales for the cloud-shock interaction. Let $\chi \equiv \rho_c/\rho_i$ be the density and assume that $\chi >> 1$. Assume that the cloud is a sphere with radius a at a distance R from the supernova explosion. The blast wave in the Sedov-Taylor phase will expand as $R_b \propto t^{2/5}$. We can define the cloud crushing time,

$$t_{cc} \equiv \frac{a}{v_s} = \frac{\chi^{1/2}\, a}{v_b} \tag{2}$$

the intercloud crossing time,

$$t_{ic} \equiv \frac{2a}{v_b} \tag{3}$$

and the age of the SNR,

$$t \equiv \frac{dR_b}{dt} = \frac{2}{5}\frac{R_b}{v_b} \tag{4}$$

The cloud is destroyed by thermal evaporation or by hydrodynamic instabilities in a time of order $t_d \sim \chi^{1/2}\, t_{cc}$, which is comparable to the time for drag forces to bring the cloud to rest in the intercloud medium.

In this paper, we will consider only clouds that can be characterized as "small", so that the SNR does not evolve significantly during the time for the cloud to be crushed: and we find that

$$t > t_{cc} \Rightarrow a < \frac{0.4R}{\chi^{1/2}} \tag{5}$$

Indeed, we shall focus on the case in which the cloud is "very small", so that $t >> t_d$, and $a << 0.4R/\chi$. In either case, we have $a << R$ so that the blast wave may be treated as a planar shock. In the opposite limit of a shock interaction with a large cloud the SNR blast wave will undergo substantial weakening over the time it takes to cross the cloud. We expect substantial disruption for the small clouds, but only impulsive effects for large clouds.

IV. RESULTS

Since there are no intrinsic scales in the problem, it is parameterized by the Mach number of the SNR blast wave M and the density ratio χ. Our calculations assumed 2-D axisymmetry for an inviscid fluid with no magnetic field. Two cases were considered for the cloud: $\gamma=1.1$ and $\gamma = 5/3$. The intercloud gas was assumed to have $\gamma = 5/3$. Several calculations have been made for Mach numbers in the range $10\text{-}10^3$ and density ratios $10\text{-}10^2$.

It is useful to follow the morphological evolution of the cloud through several cloud crushing times to obtain a sense of the different stages of development. We present the time-development of the isodensity contours of the cloud for the case γ (cloud) = γ (intercloud) = 5/3, χ=10, M=10. At $t=0.84t_{cc}$ (Fig. 1), the transmitted shock is compressing the cloud from the front, secondary shocks have enveloped the sides of the cloud as the blast wave passes over the cloud, and a reflected bow shock moves upstream into the intercloud medium. The reflected shock becomes a standing bow shock and eventually a weak acoustic wave carrying away a small amount of energy from the supernova shock (Spitzer, 1982). At $t=1.05t_{cc}$ (Fig. 2) the blast wave behind the cloud reflects off the axis giving rise to a Mach reflected shock back into the cloud. After $t=1.26t_{cc}$ (Fig. 3), behind the cloud, a double Mach reflection with the appearance of two triple point interactions occurs. This classic oblique shock interaction[12,13] shows evidence of a strong supersonic vortex ring far behind the cloud. The vortex ring may have interesting observational consequences for SNR (see below), but plays no role in the continued dynamical evolution of the cloud. The reflected shock and the transmitted shock undergo a strong interaction at $t=1.68t_{cc}$ (Fig. 4) resulting in a initial flattening of the cloud. We also note the beginning of a strong shear flow. The vorticity is efficiently produced by strong components of $\nabla\rho X\nabla P$ at the interface. Substantial flattening of the cloud is observed at $t=2.1t_{cc}$ from the strong shocks which have squeezed it like a vise. The pressure maximum on the nose of the cloud exceeds the pressure minimum on the sides and the cloud begins to expand laterally[3] (Fig. 5). We note the growth of Richtmyer-Meshkov[13] instabilities on the cloud nose which grow more slowly than the classic Rayleigh Taylor modes. At $t=2.5t_{cc}$, we see evidence of Kelvin Helmholtz instabilities, on the sides of the cloud; weak shocks still residing in the cloud interior dissipate their energy (Fig. 6). At $3.78t_{cc}$ a prominent shear layer exists through the cloud. This shear is caused by a combination of the effects of the downstream reflected shock keeping high pressure in the center of the cloud relative to the sides, the effects of the cloud moving through the ICM, and the development of Kelvin-Helmholtz instabilities. The shear produces copious vortex rings along the shear flow layer and leads to substantial Kelvin Helmholtz instabilities which break up the arms (Fig. 7). The cloud consists of a distorted unstable axially flattened core component and a severely disrupted halo of cloud material. Over 70% of the original cloud mass is in small fragments which, in the absence of cooling, should merge with the intercloud medium. The unstable break up is dominated by large scale differential shear. Finally, at $t=9.7t_{cc}$ the cloud is essentially destroyed. The cloud consists of multitudes of small fragments distributed along a halo structure with an aspect ratio of about 6, with no evidence of a core component (Fig. 8).

Let us consider the characterization of the evolution of the interstellar cloud in more detail. In Table 1, we display the results of adiabatic calculations for three models where γ=1.67 in both the cloud and ICM for all cases. The calculations are done for two models of M=10 and 100 for density contrast χ =10 and one model M=100 and density contrast 100. The first entry in the table is the time normalized to the intercloud crossing time. The second entry gives the time normalized to the cloud crushing time and the drag time, $t_d = \chi^{1/2}\, t_{cc}$. The next column is the sound speed behind the cloud shock normalized to the blast wave velocity. It can be shown that the initial cloud shock can accelerate the gas up to 3/4 v_s for non-radiative shocks, so the next entry is a measure of the fraction of the velocity currently in the cloud to its maximum possible velocity; in the frame of the shocked intercloud gas, this is a measure of cloud deceleration. The next column is a characterization of the cloud's aspect ratio in the radial and axial direction weighted by its half mass distribution. Here $r_{1/2}$ is the radial half-mass distance and $Z_{1/2}$ is the axial half-mass distance. The last column gives the radial $\dot{r}_{1/2}$ and axial $\dot{Z}_{1/2}$ dispersion velocities of the cloud to quantify the amount of stretching the cloud undergoes as it is subjected to shearing. These velocities are computed by using the half mass distance distributions at the two final times in the calculation.

Several conclusions can be drawn from these results. Comparing the results at the same normalized "final" time t=4.2t_{cc} for clouds of the same density χ=10, but subjected to blast waves of different Mach number 10 and 100, we note that both clouds have decelerated to about 0.15 of their initial velocities. Thus, these clouds have almost stopped, leading to a small pressure differential between the front of the cloud surface and the sides so that there is little force driving further radial expansion; hence the clouds have a radial dispersion velocity $\dot{r}_{1/2} \approx 0$. The strong shear flow in the cloud is still dominant, however, and both clouds are supersonically shearing apart at about the same axial dispersion velocity $\dot{Z}_{1/2}$ of 3 times the cloud velocities. The physical extent of the stretching in both the radial and axial direction

$$\frac{r_{1/2}(t)}{r_{1/2}(0)}, \frac{Z_{1/2}(t)}{Z_{1/2}(0)}$$

when compared to the characteristics cloud size initially is essentially the same. The remarkable agreement of these features of the clouds leads one to suspect that the cloud evolution may scale similarly with the Mach number of the SNR shock. In fact, if we look at the isodensity contours of both clouds at t=4.2t_{cc}, we clearly see the evolution is similar (Fig. 9a,b). This Mach scaling can be clearly seen if we scale the time, velocity and pressure as $t' = t/M$, $v' = vM$ and $P' = PM^2$. Substituting these scaled quantities into the Euler equations, we find that Euler equations are invariant under this transformation. Thus, we find that for fixed γ and density, the morphological evolution is a function of t/t_{cc} only in the limit of large M. At t=3.78t_{cc} (Fig. 7), the cloud is experiencing a large drag due to the lateral increase in its surface area associated with the highly flattened core component. This results in the large deceleration as the cloud is slowed to .16 of its maximum velocity. At the final time t=9.7t_{cc} in the calculation, the cloud has

essentially been destroyed (Fig. 8). We note that the cloud has decelerated to 0.07 of its original velocity and has essentially stopped expanding axially as well as radially. The final fate of this cloud consists of a quasi-static halo of fragments of which 50% of the mass resides in an axially elongated distribution stretched out 5-6 times its initial shape, and the rest of the mass resides in a multitude of fragments much less dispersed. If we consider the case with χ=100, we note that the cloud has a large aspect ratio and appears to be substantially more radially compressed than the lower density cloud. This can be understood by considering that the shock passes over the cloud far more rapidly than the cloud shape can change, and a quasi-steady flow is established around the cloud with a pressure maximum at the front of the cloud and a pressure minimum on the sides. The gas passes through a sonic point point as it flows past the cloud. A rarefaction wave moves into the shocked cloud (Nittmann and Falle[3]) producing velocities of the order of the sound speed so that the cloud expands laterally at the sound speed. It is easily shown that the sound speed

$$c \propto \left(\frac{\rho_i}{\rho_c}\right)^{1/2} v_b \ ,$$

so for the higher densities the cloud expands much more slowly and appears radially compressed. These clouds have less drag and so experience less deceleration than the less dense clouds. We also note that at $t=4.3t_{cc}$, the cloud is still axially supersonically shearing. As remarked above, the destruction time for the cloud t_d is comparible to the drag time $\frac{a\chi}{v_b}$ and our simulation confirms that the small clouds experience substantial ablation after a few drag times.

We have performed calculations for several similar models for γ=1.1 in the cloud.[15] This softer equation-of-state is more representative of clouds that are radiative, although it should be pointed out that truly radiative clouds can get rid of their stored energy efficiently, and we would expect substantially more shock compression than the models considered here. We note that these "radiative" clouds move substantially more rapidly than their γ=1.67 counterparts. These clouds are significantly more radially compressed, and thus experience far less drag than the γ=1.67 clouds. This can again be understood by consideration of the sound speed in these clouds. We find that the scaling of sound speed c with γ is such that $c(\gamma=1.1) << c(\gamma=5/3)$, so that these "radiative" clouds expand laterally more slowly. We note that the high density "radiative" cloud is still experiencing large supersonic axial shearing. As with the previous models Mach scaling appears to be established.

An outcome of these calculations that may be potentially very important for observations of SNR is the discovery of the copious production of vortex rings distributed along the strong shear flow layer (Fig. 10). In this graph of iso-vortex contours at $t=5.0t_{cc}$ we see formation of many points of high vorticity. Approximating the rotation of these vortices by rigid body rotation, we can relate the vorticity ω in an individual vortex ring to the pressure differential across the vortex ΔP, and we find that

$\omega = (8\Delta P/\rho)^{1/2}\ 1/r$. This appears to be an excellent approximation when compared to our detailed calculations. Recent high resolution radio observations of the Cas A SNR(Tuffs[16]) have revealed several hundred intense compact radio emission peaks distributed throughout the remnant. We have demonstrated that strong shear flows associated with shock cloud interactions result in the production of many supersonic vortex rings. These vortex rings can be expected to wind up ambient magnetic fields present in the interstellar clouds until equipartition between the energy in the field and the vortex is achieved. It is quite possible that the resulting intense wound up magnetic field could account for the synchrotron emission of electrons, thus explaining the observations in Cas A. Chevalier[17] (1976) postulated the presence of turbulent vortices, acting as magnetic scattering centers in SNR's to explain particle acceleration by a second-order Fermi mechanism. We conjecture that the radio hot spots may indeed be indirect observational evidence of the presence of vortex rings produced behind the shocked clouds.

V. CONCLUSIONS

We have performed, for the first time, second order accurate high resolution local adaptive mesh refinement calculations of the interaction of a supernova shock with interstellar clouds. These extremely powerful hydrodynamic techniques have enabled us to calculate exceedingly complex flows much more rapidly and much more accurately and much further in time than previous work with standard fixed grid hydrodynamics. We have followed the evolution of interstellar clouds well into the regime of fragmentation. Our calculations have demonstrated high accuracy with 80,000 grid cells in the cloud that would only be achievable with fixed grid high order accurate hydrodynamic schemes with >1,000,000 grid cells. We find:

1) Small interstellar clouds are efficiently destroyed in a few cloud drag times by combined Rayleigh-Taylor and Kelvin Helmholtz instabilities dominated by large scale shear flow. Clouds that have the same density but are enveloped by strong shocks of differing Mach number exhibit scaling behavior in their morphological evolution.
2) Small clouds are highly fragmented. Cloud fragments will most likely feed their mass back into the ISM by thermal conduction.
3) Small clouds fragment to such an extent that it is unlikely that fragments large enough to become gravitationally unstable and form stars will survive. This conclusion is based on the present adiabatic calculations and may not apply to radiative clouds or clouds which are not "small".
4) Clouds evolve toward a elongated structures with aspect ratios of five to six consisting of multitudes of fragments.
5) Our calculations indicate the copious production of supersonic vortex rings. Those rings with large aspect ratio may be subject to non-axisymmetric instabilities and break up into yet smaller vortex structures.[18] "Fat" rings, with small aspect ratio, are likely to remain intact. These vortex rings may be effective in winding up the ambient magnetic field in clouds, increasing the magnetic field strength and enhancing the synchrotron emission of cosmic ray electrons. This could explain the recent observations of numerous compact radio hot spots in Cas A.

In the future, we will be using adaptive mesh refinement hydrodynamic techniques to investigate a broad range of astrophysical gas dynamical phenomena.

ACKNOWLEDGEMENTS:

The calculations presented in this paper were performed on the XMP416 at the Lawrence Livermore National Laboratory. This work was also performed in part under the auspices of a special NASA astrophysics theory program which supports a joint Center for Star Formation studies at NASA Ames Research Center, University of California, Berkeley, and University of California, Santa Cruz.

Table 1

	t/t_{ic}	t/t_{cc} t/t_{drag}	c/v_b	$\frac{4}{3}(v_c/v_b)$	$r_{1/2}(t)/r_{1/2}(0)$ $Z_{1/2}(t)/Z_{1/2}(0)$	$\dot{r}_{1/2}/v_b$ $\dot{Z}_{1/2}/v_b$
$\frac{\chi=10}{M=10}$	6.7	4.2 1.3	0.18	0.16	1.8 3.2	~0.0 0.35
	15.3	9.66 3.0		0.074	2.38 5.69	~0.0 ≤0.045
$M=100$	6.7	4.2 1.3	0.18	0.14	2.0 2.6	~0.0 0.32
$\frac{\chi=100}{M=100}$	21.3	4.3 0.43	.056	0.25	3.7 8.4	~0.0 0.42

BIBLIOGRAPHY

1. McKee, C. F., 1988, IAU Coll.101, Supernova Remnants and the Interstellar Medium, Ed. R. S. Roger and I. L. Landecker, Comb. Univ. President, 205.

5

2. Woodward, P., 1976, Ap.J., 207, 464.

3. Nittman, J., Falle, S., and Gaskell, P., 1982, N.N.R.A.S., 201, 833.

4. Tenorio-Tagle, G., and Rozyczka, M., 1986, Astron. Astrophys., 155, 120.

5. Woodward, P. and Colella, P., 1984, J. Comp. Phys., 54, 115.

6. Berger, M. J., and Colella, P., 1989, to appear in J. Comp. Phys.

7. Van Leer, B., 1979, J. Comp. Phys. 32, 101.

8. Colella, P. and Woodward, P., 1984, J. Comp. Phys. 54, 174.

9. Noh, W. F. and Woodward, P., 1976, UCRL Preprint No. 77651.

10. McKee, C. F. and Cowie, L. L., 1975, Ap.J., 195, 715.

11. Spitzer, L., 1982, Ap.J., 262, 315.

12. Hornung, H., 1986, Ann. Rev. Fluid Mech., 18, 33.

13. Glaz, H. M., Colella, P., Glass, I.I., Deschambault, R. L., 1985, Proc. Ray. Soc. Lond. A 398, 117.

14. Richtmyer, R.D., 1960, Comm. Pur. Appl. Math., 13, 297.

15. Klein, R. I., Colella, P. and McKee, C. F., 1989, Ap. J. in preparation.

16. Tuff, R. J., 1986, M.N.R.A.S., 219, 13.

17. Chevalier, R. A., 1976, Ap.J., 207, 450.

18. Saffman P. G., Baker, G. R., 1979, Ann. Rev. of Fluid Mech. 11, 95.

Density, $t=0.84t_{cc}$

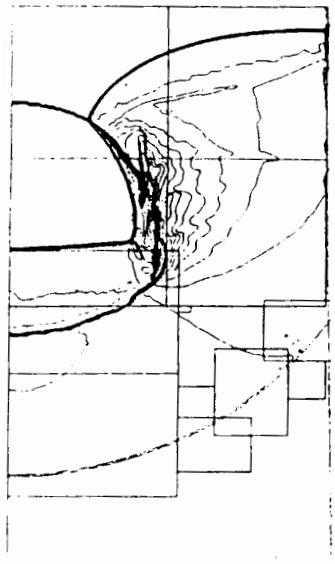

Figure 1

Density, $t=1.05t_{cc}$

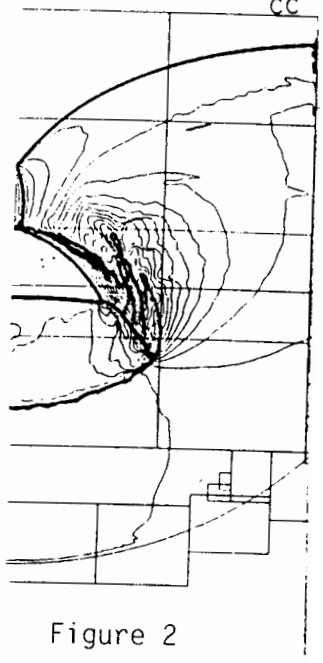

Figure 2

Density, $t=1.26t_{cc}$

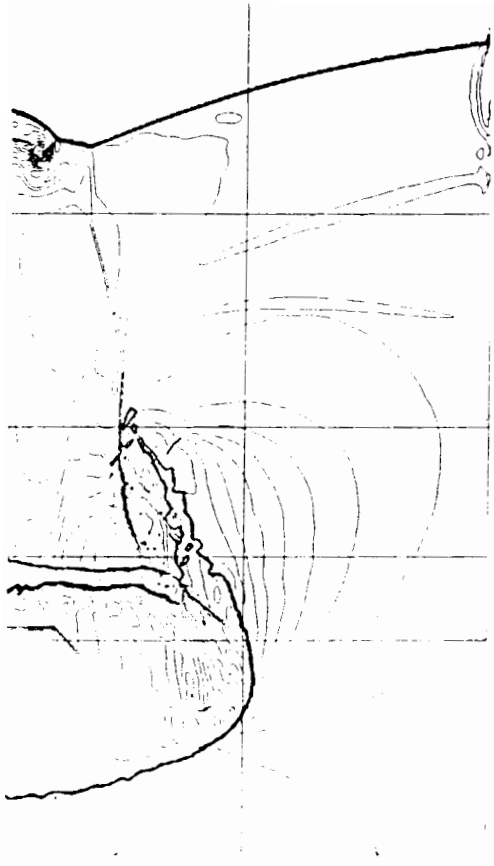

Figure 3

Density, $t=1.68t_{cc}$

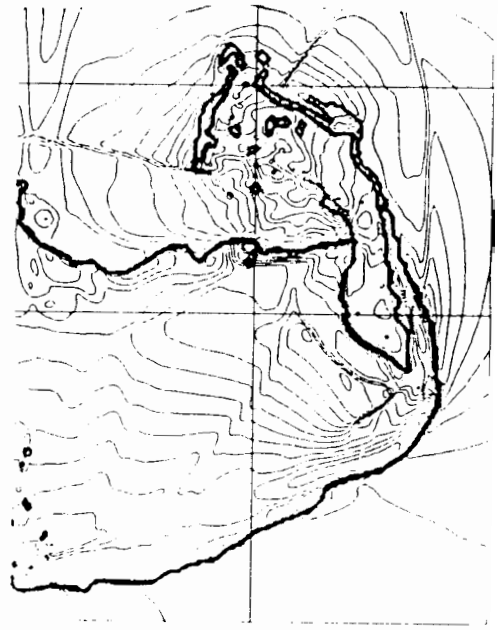

Figure 4

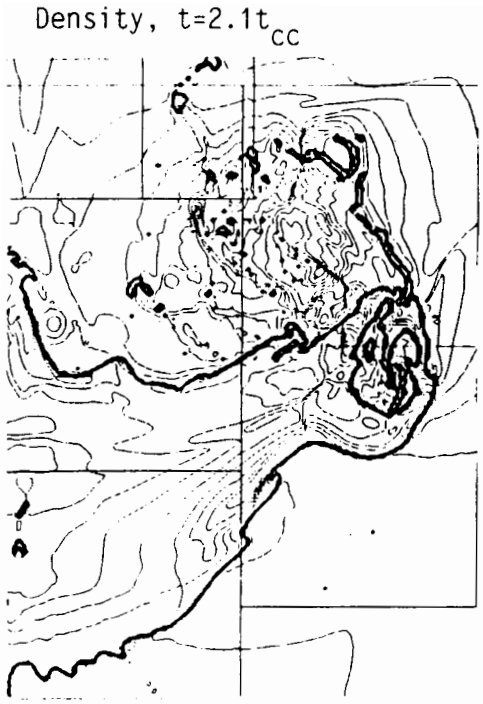

Figure 5

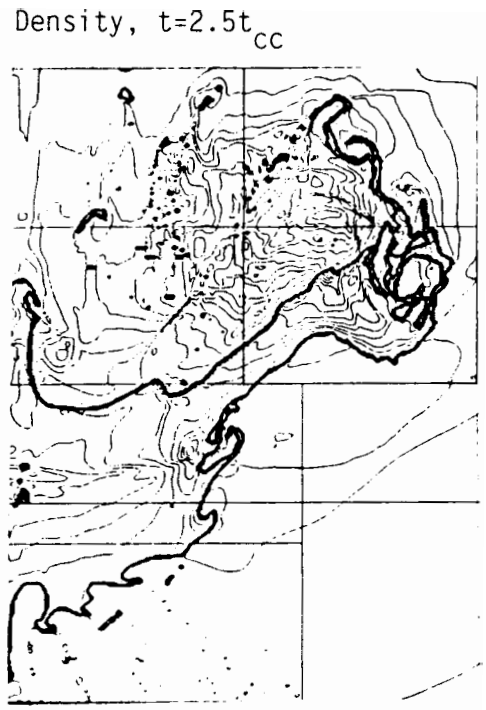

Figure 6

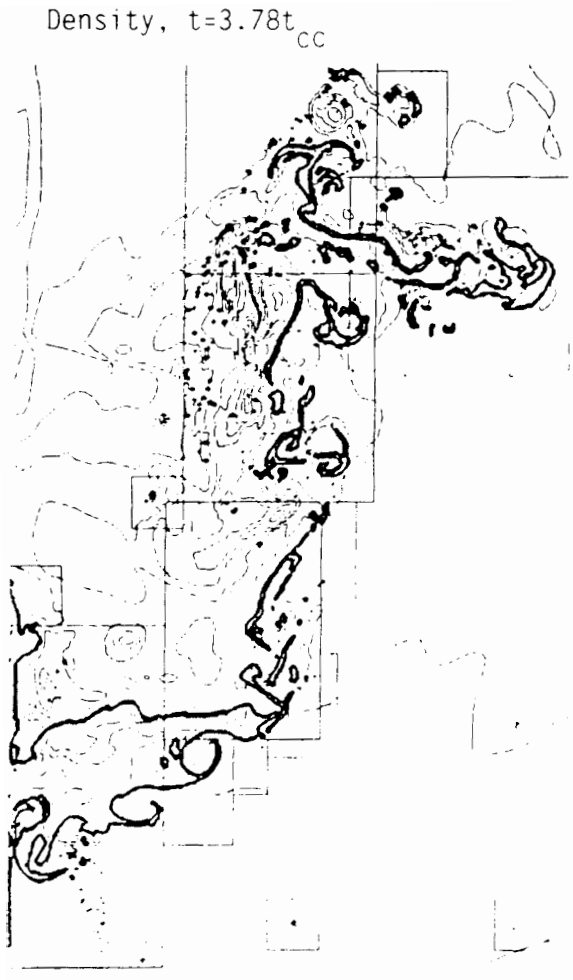

Figure 7

Figure 8

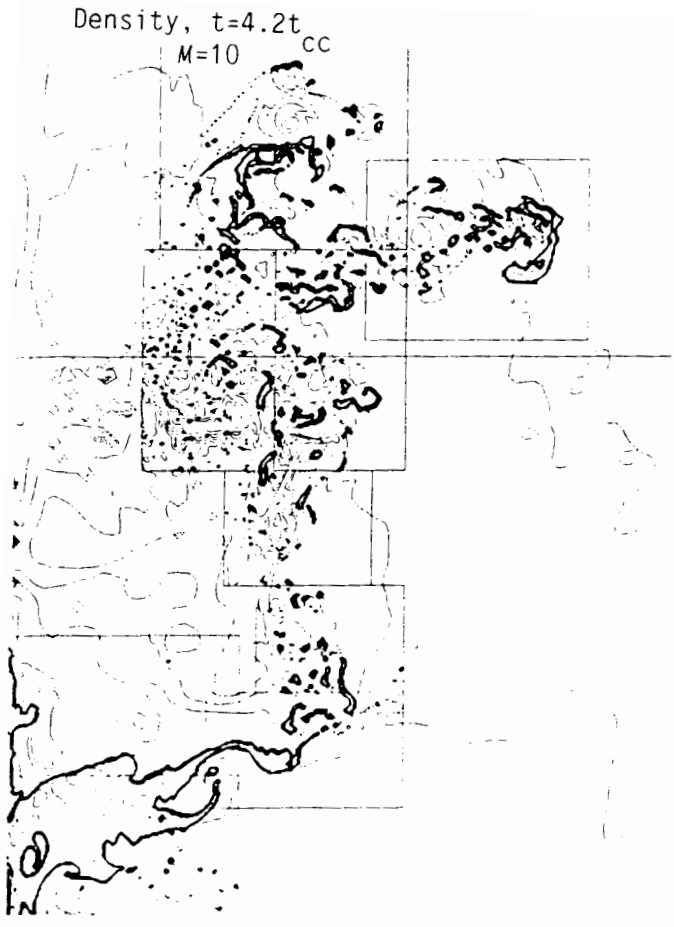

Figure 9a

Figure 9b

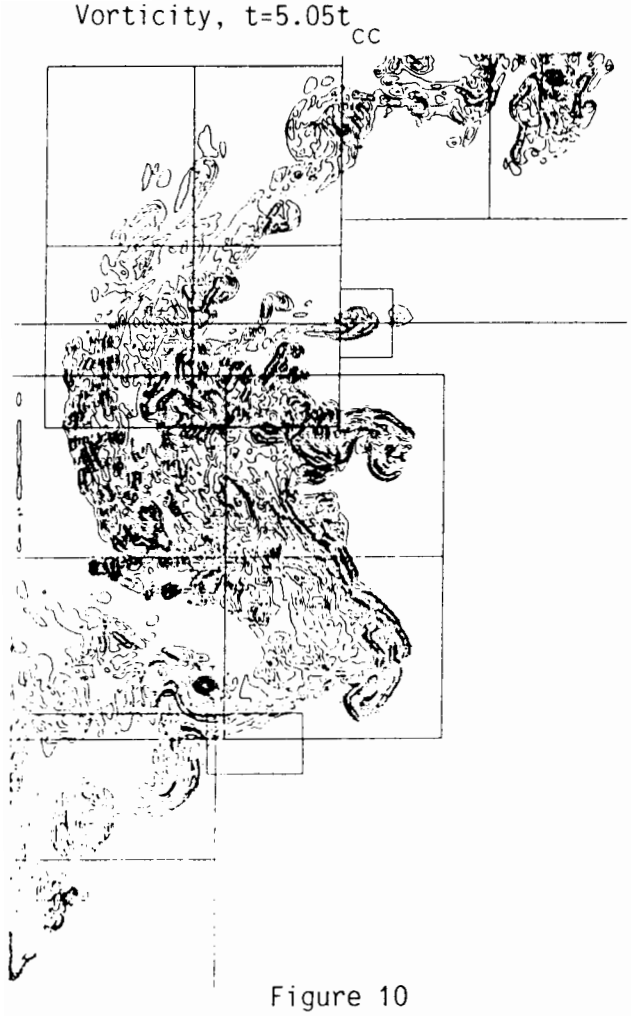

Figure 10

INSTABILITY OF SHOCK-ACCELERATED INTERFACE BETWEEN TWO MEDIA

E. E. Meshkov
Moscow

Experimental results on shock tube studies of the instability of a shock-accelerated interface between two gases are presented in this review. Turbulent mixing appears after instability development when the interface is accelerated by a series of plane stationary waves. Nonlinear effects are described, which accompany the development of distortions, that are reflected and refracted at the shock wave/expansion wave interface. A local cumulation phenomenon caused by shock reflection at the perturbed interface is described.

INTRODUCTION

Let us consider the following case: two gases of different densities are separated by a generally flat but slightly perturbed interface. The perturbations are sinusoidal. A plane stationary shock passes from one gas to the other through the interface. The interface experiences a pulsed acceleration. In this case the interface appears to be unstable. The initial distortion starts to grow and continues to grow with time. This pulse-initiated instability is independent of the shock direction; that is,. it is unstable to pulsed motion from a light gas to a heavy one (L → H) [1,2] or from a heavy gas to a light one (H → L) [2]. If the interface is accelerated by a series of wave pulses, the initial perturbations may develop nonlinearly into turbulence with consequent turbulent mixing of the two gases [3].

Incident shock passage through the distorted interface appears to generate refracted and reflected secondary shock waves in both directions (L → H) and (H → L). The evolution of the interface perturbations and

secondary shock wave refraction and reflection is accompanied by other nonlinear effects. Breaks are formed at shock fronts. Behind the perturbed shock front, the lateral material flow may be accelerated sufficiently to form localized, laterally distributed, secondary shock waves [4,5]. During this period the initially perturbed shock shape may become more distorted and disturbance subharmonics may be simultaneously generated which, in turn, grow with time [6,7]. Along the distorted interface, vorticity generation sites may develop [6]. Instability development coincides with the cumulation of these localized sites. At these specific "hot" spots the pressure and temperature scales may substantially exceed average levels by more than an order of magnitude [8,9]. Experimental results illustrating these effects in gases are described in this report.

These events have been studied in condensed media in the experiments described in [32,33]. In [34] the peculiarities of instability development [1,2] in systems with many different densities were considered.

2. INSTABILITY OF AN INTERFACE, ACCELERATED BY A SHOCK WAVE

2.1 The experiments were conducted in an air shock tube. Its design is analogous to that described in [15]. The test section of the tube had a rectangular cross-section, 40 x 120 mm^2 (Fig. 1). It was divided by a thin plastic film with areal density (3 to 4) $\cdot 10^{-5}$ g/cm^2. The sections upstream and downstream of the film were filled with different gases. The prescribed initial interface distortion was of the form $Y = a_0 \cdot \cos \kappa x$, or in the form of mated circular arc segments at the interface examined. A flat stationary shock wave was propagated into the test section. Shadowgraph photos provided the flow visualization in the test section following the passage of the shock wave over the disturbed interface.

2.2 Figures 2 a,b are graphic sketches prepared from the photos which display the phenomena of the developing interface disturbances. Air (ρ_0 = 1.205 g/ℓ, γ = 1.4) and refrigerant-12 (ρ_0 = 5.1 g/ℓ, γ = 1.138) are the gases in these illustrations. Each of these photos corresponds to a

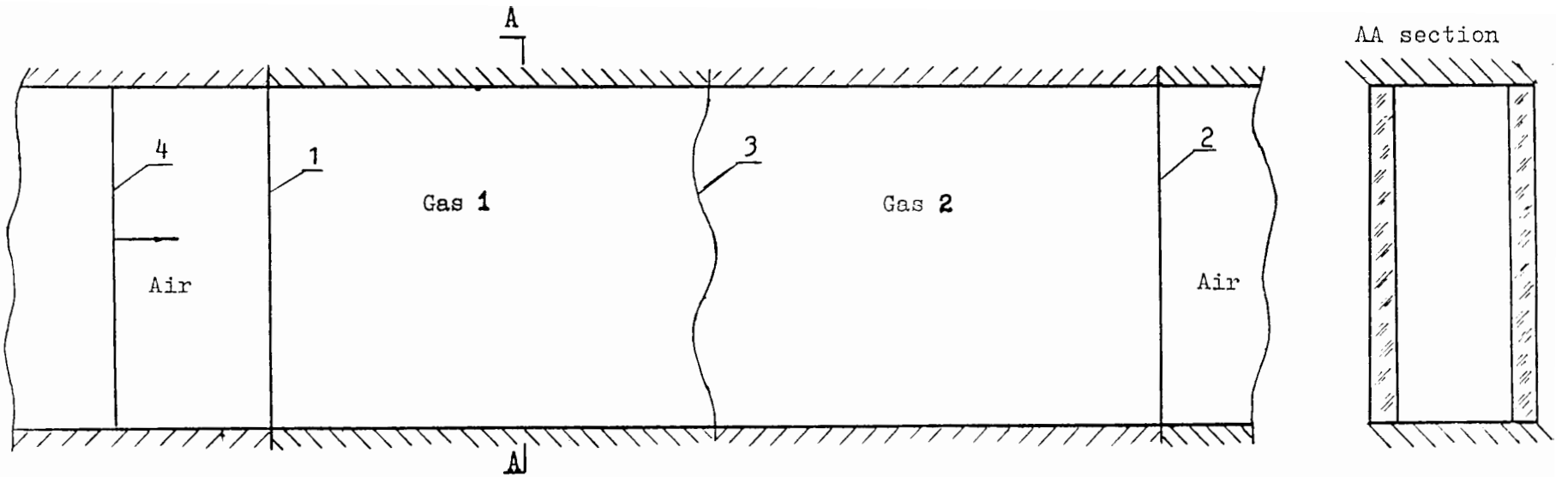

Fig. 1 The arrangement of the shock tube measuring section in the experiments on the stability of the disturbed separation interface of two gases with different densities, accelerated by a shock wave.

1,2 A thin film, separating the jointed blocks of the measuring section;

3 An interface studied;

4 A plane, stationary shock wave.

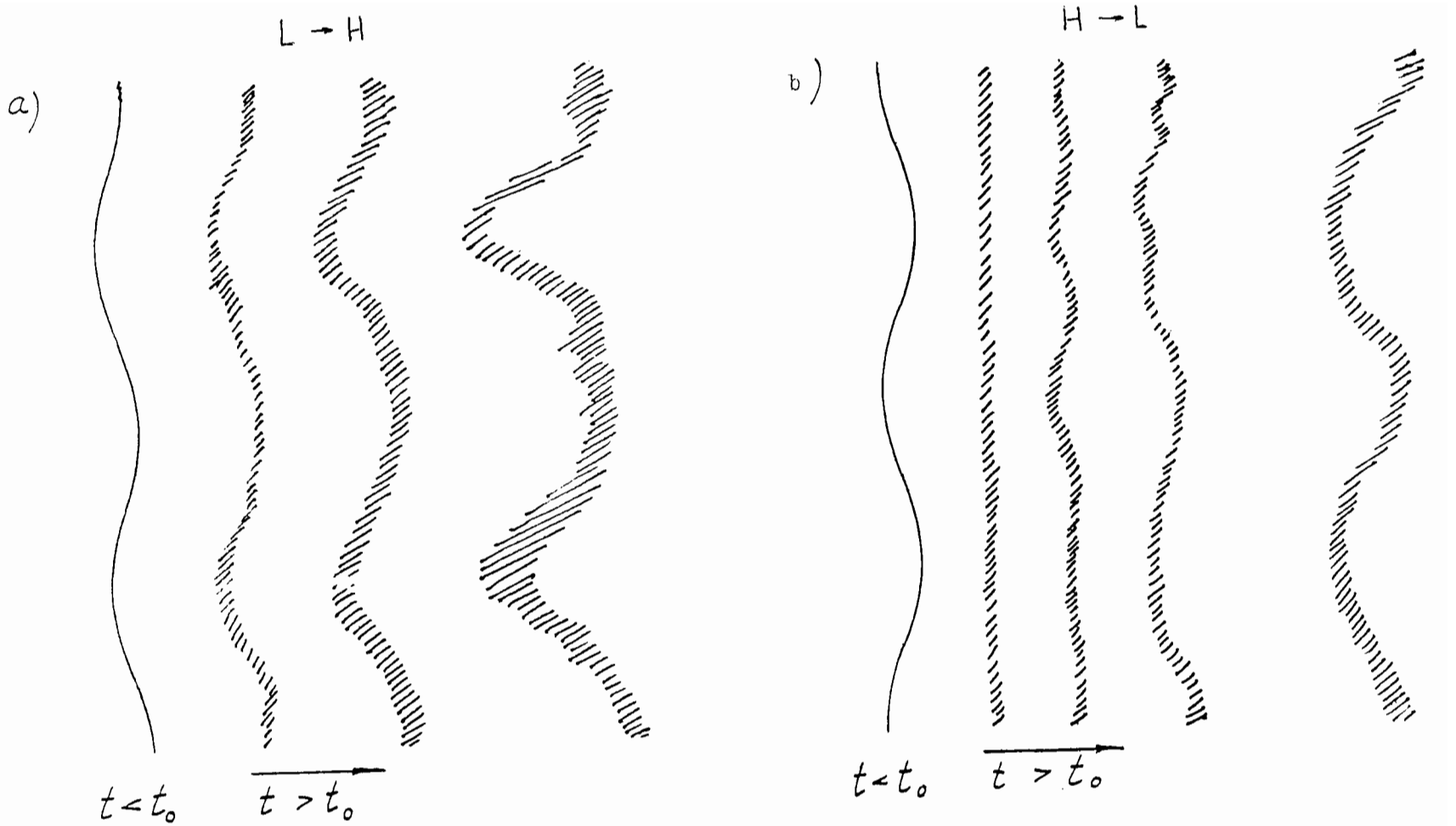

Fig. 2 Variation of the disturbed interface amplitude and form, when accelerated by a shock wave during its movement. (a) air to refrigerant-12; (L → H case); (b) refrigerant-12 to air (H → L case); $t = t_0$, — time at arrival of a shock wave through an interface. In the figure, the graphical sketches of the interface are based on photos of some tests at the specified times. The sketches are in a fixed-coordinate system.

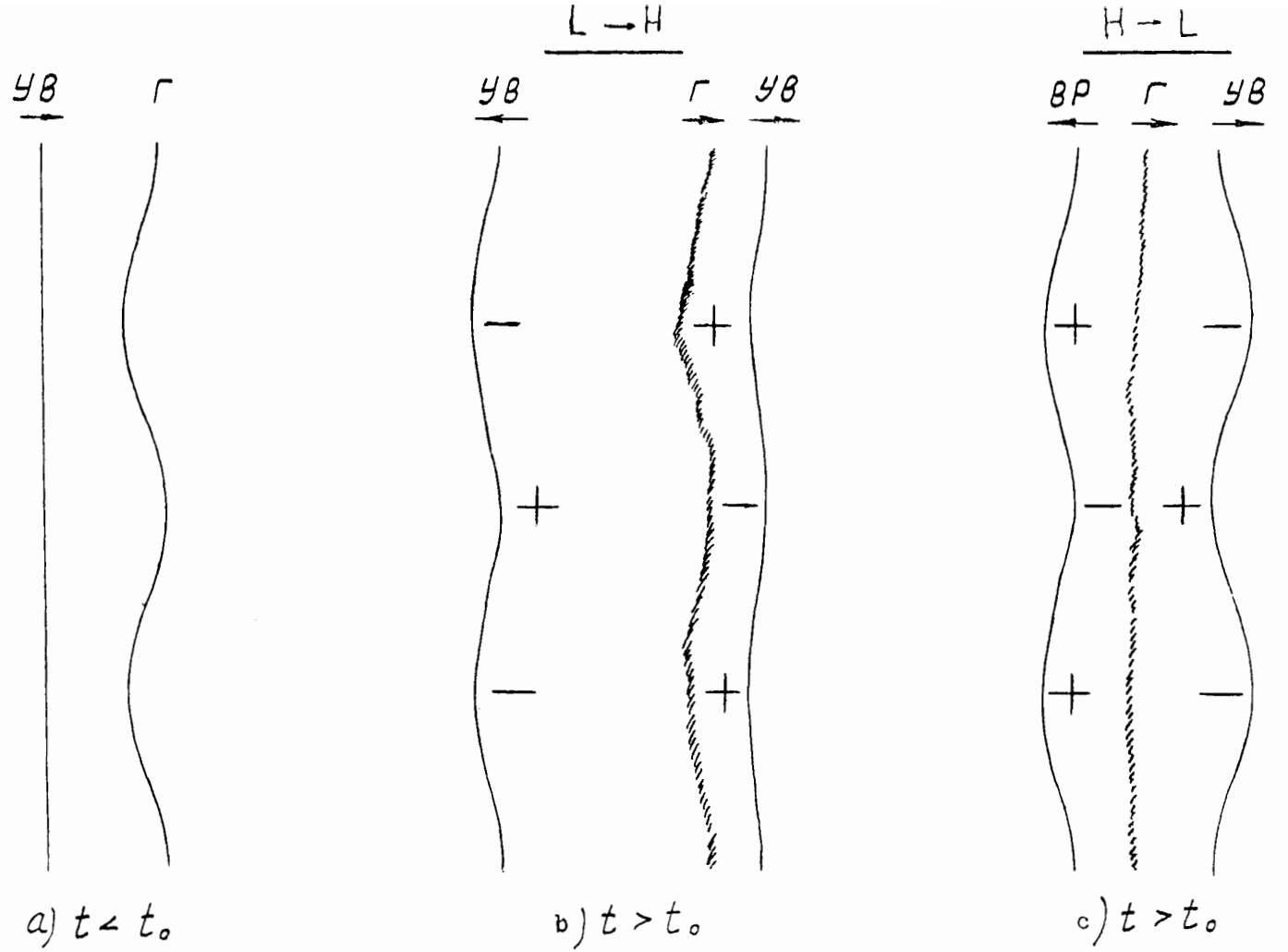

Fig. 3 The distribution of high (+) and low (-) pressure zones relative to an average level behind the wave fronts. (a) initial geometry; Γ is the interface studied, YB is the shock wave; (b) sketch of a photo of the initial flow phase in air → refrigerant-12 test; (c) sketch of a photo of the initial flow phase in refrigerant-12 → air test. BP is the refraction wave. Arrows show the direction of wave and interface motion.

there is a negligible influence at the interface from the lateral diverging waves. These lateral wave propagation processes are interconnected with the primary reflected and refracted shock-wave processes.

In case H - L, the reflected expansion wave is perturbed in phase and the refracted shock wave in antiphase relative to the interface distortion (Fig. 3). The high and low pressure zones behind the perturbed expansion wave evolve in phase opposition relative to the distribution of perturbations behind the shock wave front. The high pressure zone appears where the expansion wave diverges locally and vice versa. The pressure gradient initiates and supports a lateral flow along the interface. The interface distortion undergoes phase cancellation, changes sign, and then grows monotonically. At the distortional curvature sites on the interface, vorticity is generated, local vortex concentration zones are formed and develop (Fig. 4). The higher the amplitude of the initial disturbance and the ratio of gas densities, the earlier the vortex zones appear and develop. The initial distortion influences the early period of vortex evolution. The shear, originating with the vanishing tangential flux at the wall-surface boundaries, also results in local vorticity generation.

2.3 The instability reported in [1,2] is related to the more general phenomenon of Rayleigh-Taylor gravitational instability [17]. In the case L - H with constant acceleration, g, the small initial distortions of the contact interface grow exponentially in time. If the initial distortion is given in the form, $y = a_o \cdot \cos \kappa x$, $\kappa = 2\pi/\lambda$ (and $a_o << \lambda$), and if both media are ideal incompressible liquids with densities ρ_1 and ρ_2; the following differential equation describes the disturbance amplitude growth [17]:

$$\frac{d^2a}{dt^2} = \omega^2 a, \qquad a(0) = a_o \left.\frac{da}{dt}\right|_{t=o} = 0 \qquad \omega^2 = g\kappa\frac{\rho_2 - \rho_1}{\rho_2 + \rho_1} \equiv g\kappa \cdot A , \tag{1}$$

where A is known as the Atwood Number.

In case H → L, under the same assumptions, the initial distortion oscillates with time.

The following equation defines disturbance amplitude growth for impulse (δ-function) acceleration [1]:

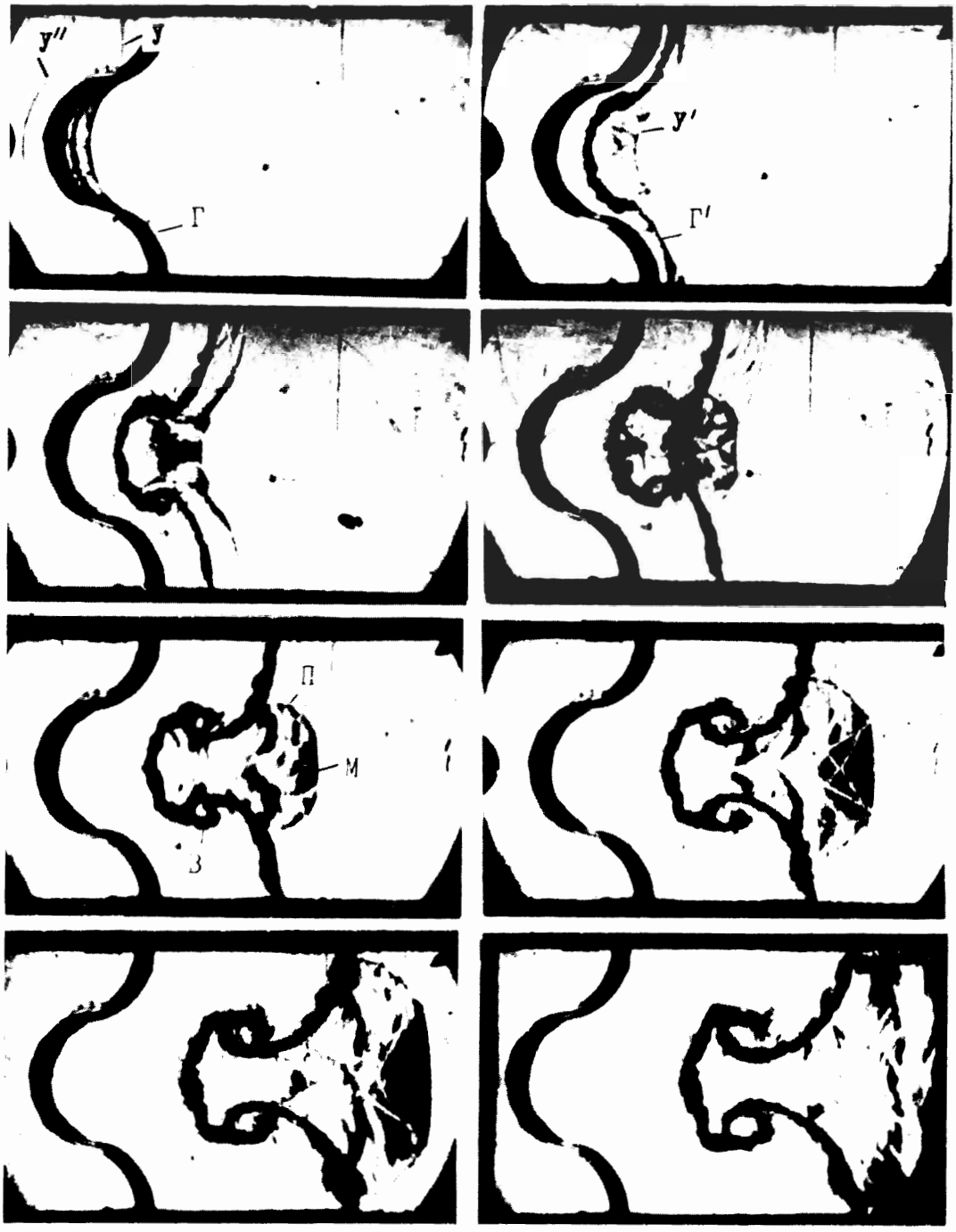

Fig. 4 Photo frames of disturbed interface acceleration by a shock wave (M = 1.42). The initial boundary disturbance is in the form of adjoining circles. y, y', y" = incident, transmitted, and reflected shock wave; Γ is the initial interface location; Γ' is a film, separating gases; π is the transverse wave; M is a Mach wave; B is vortex.

$$\frac{da}{dt} = a_o \cdot \kappa \cdot u \cdot A \qquad (2)$$

where u is the stationary interface velocity resulting from the impulse acceleration.

As the computations and experiments [1,2,7,10,12] showed, when the shock wave accelerates the interface (L - H), equation (2) describes the asymptotic disturbance growth, with reasonable accuracy, provided that parameter values from the region behind the wave front, define a_o and A. The distortion amplitudes a_o and a are measured from crest to trough. Dependence (2) may be used to estimate disturbance growth in case H - L, as well, but only under the same assumptions as those for case L - H. However, for case H - L, the disturbance amplitude, a_o, is defined as an amplitude averaged before and after shock passage across the interface [12].

The following equation [7] expresses distortion growth velocity with impulsive interface acceleration, including the effects of viscosity (with the assumption that only one of the gases is viscous)

$$\frac{da}{dt} = a_o \cdot A \cdot u \cdot \kappa \cdot e^{-0.9126 \cdot \nu \cdot \kappa^2 \cdot t} \qquad (3)$$

Here, ν is the kinematic viscosity of the viscous gas. It is obvious, that when $t \to \infty$, viscosity stabilizes disturbance growth, $\frac{da}{dt} \to 0$ completely, provided the degree of stabilization continues to increase with ν growing and with $\lambda = \frac{2\pi}{\kappa}$ decreasing.

The two-dimensional computations [7,10,12,13] and linear approximation computations [1,7] are needed to estimate interface distortion growth accurately. Here, we show the experimental and computational results for the pair of gases: helium (ρ_o = 0.167 g/ℓ, γ = 1.63) - air (ρ_o = 1.205 g/ℓ, γ = 1.4) (Fig. 5) and air - helium (Fig. 6).

We show the numerical results and the experimental results combined graphically. Here, 1 denotes the linear approximation computation [7]; 2 denotes the analytical computation according to [1]; 3 denotes the two-dimensional computation [12]; 4 denotes the two-dimensional computation [7] by the "Sigma" method [18], which is, in the main, the technique

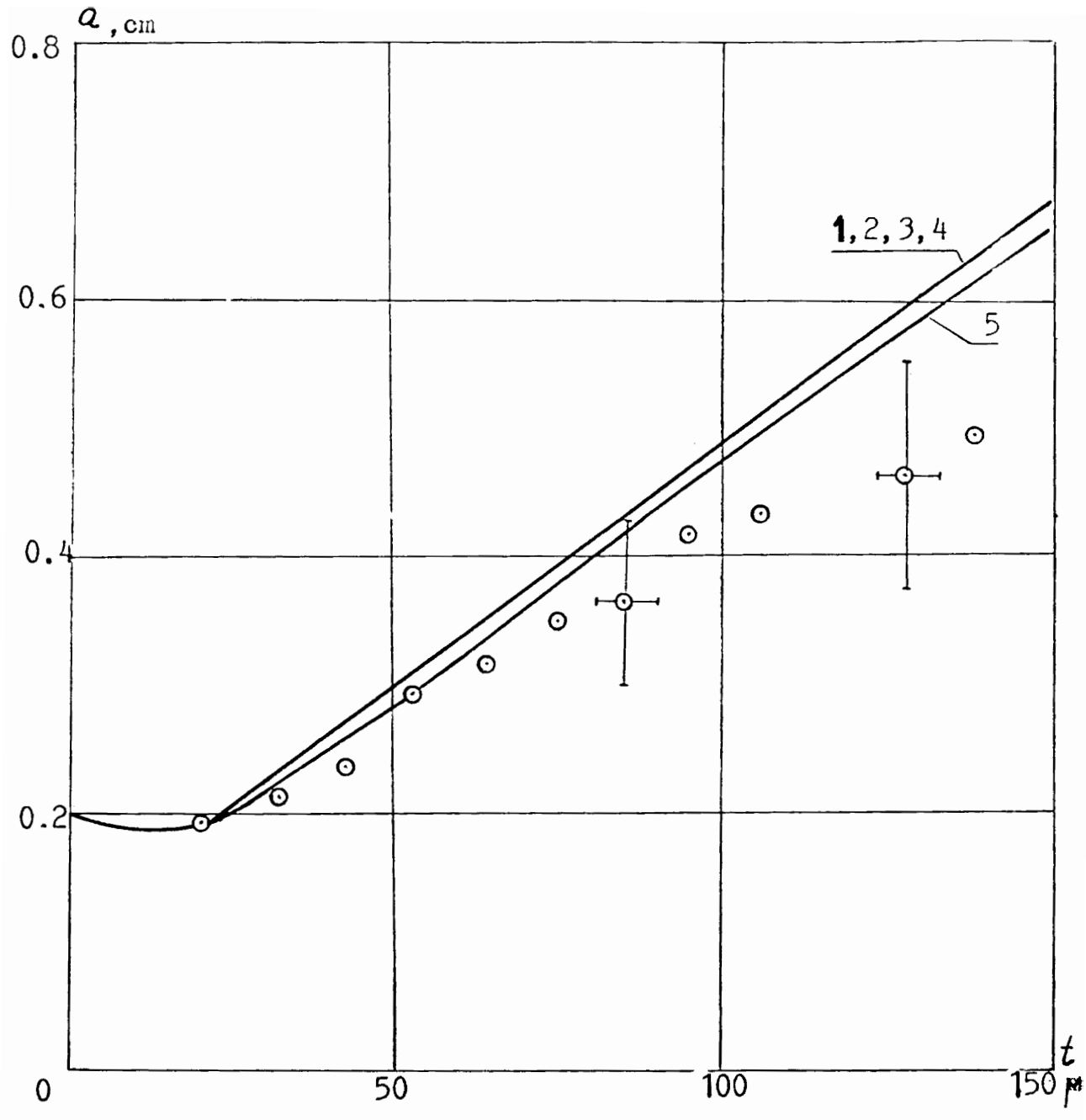

Fig. 5 Dependence of the amplitude of helium-to-air (L → H) interface distortion on shock-wave acceleration. Points are the experiment, curves are the computations, shock wave propagating in a shock-tube channel at M = 1.51.

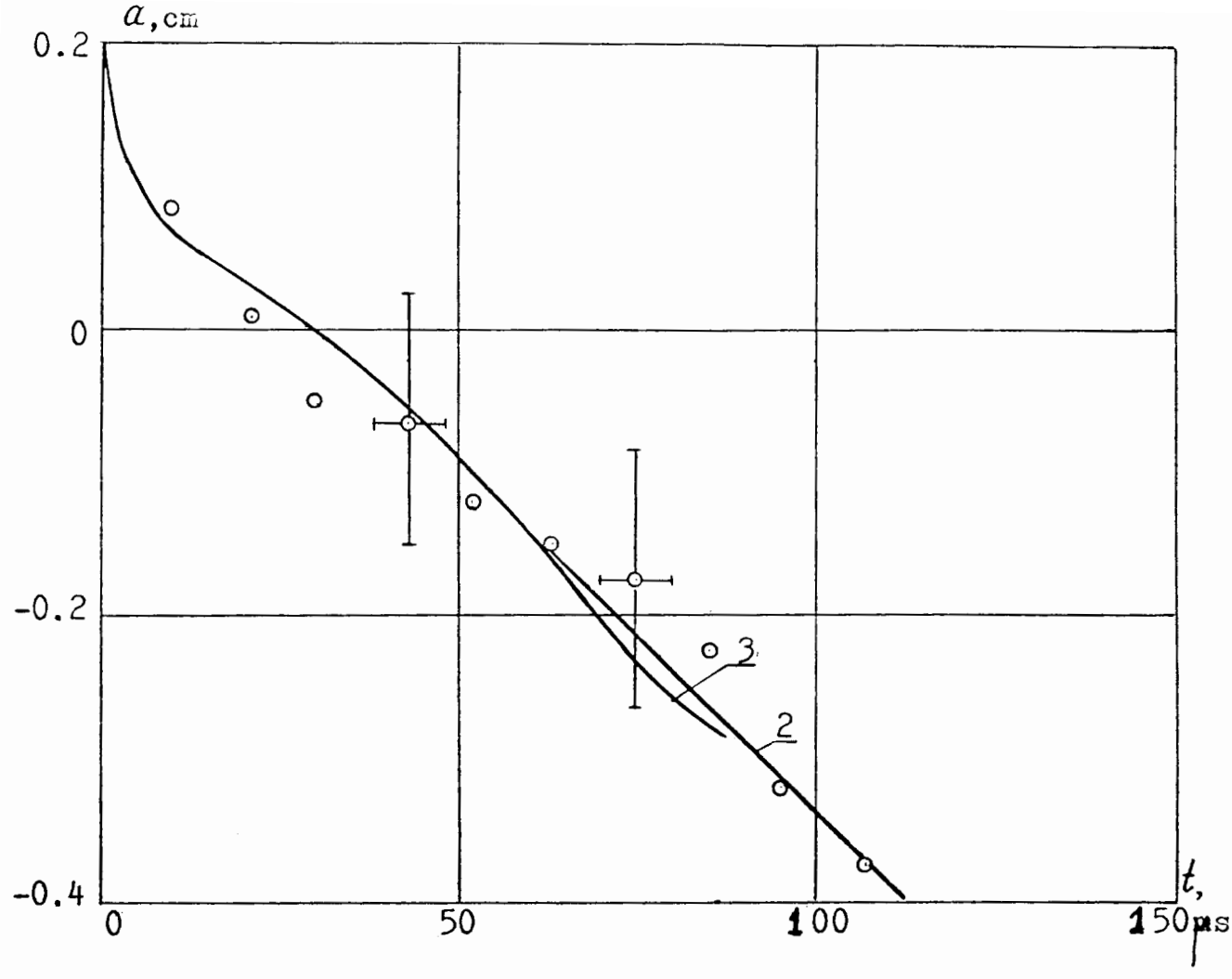

Fig. 6 Dependence of the amplitude of air-to-helium interface distortion (H → L) on shock-wave acceleration (M = 1.51). Points are the experiment, curves are the computations.

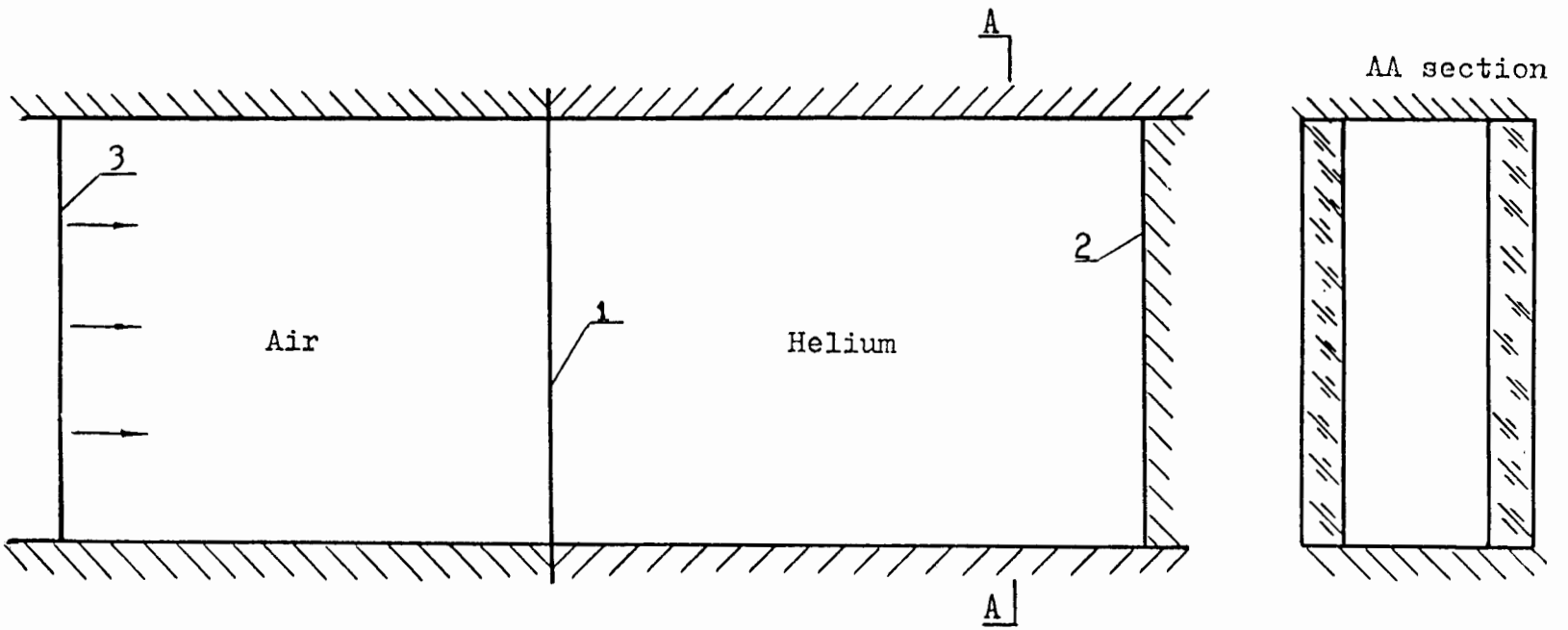

Fig. 7 The schematic of the experiment with turbulent mixing at the interface of two gases (air to helium), accelerated by a shock wave. (1) A thin film, separating gases; (2) A plug with a flat face; (3) A shock wave.

described in [19]; while 5 denotes the two-dimensional computation [7] by "ZGAK" method [20].

In these figures (5 and 6), we present the results of the experiments in which the initial distortion scale (a_0 and λ) was prescribed to be three times the value assigned to the initial two-dimensional computation data. It is difficult, if not impossible, to assign a unique value to the experimental distortion amplitude, ao. This necessitated this decision on, at least, a consistent prescription relative to the computations. Values of λ and a_0 were varied over a wide range during the experiments. The results showed that, within the assumed accuracy, these experiments demonstrated similarity in growth rate. That is, data for different λ and a_0 coincide in growth with dimensionless similarity variables, $a(t)/a_0$ and $S(t)/\lambda$. Where a(t) is the current disturbance amplitude, and S(t) is the current distance traveled by the interface.

In case L $\rightarrow$ H, the experimental results show a somewhat lower disturbance growth rate in comparison to the computations. The presence of the film, initially separating the gases may be the cause of it. This factor was not taken into account in the computations. Film mass is small, in comparison to characteristic gas masses included in the calculated motion. For this reason, it is assumed to have almost negligible influence on the character of distortion evolution. This assumption is supported by the results of direct calculations as well [7]. On the other hand, aside from the mass-inertial influence, the elasticity and strength of the film may influence the rate of interface disturbance growth. The proposed mechanism for this influence is as follows. During the initial stage, the disturbance amplitude growth increases film tension. This results in the creation of a tensile force which counters the amplitude increase. This tensile force acts to oppose film surface expansion. In this sense, it is analogous to the surface tension force. This force continues to act until the film is torn. The estimates [7] suggest that, in the foregoing situation, this factor may decrease the disturbance amplitude growth rate by about 15%.

In case H - L (Fig. 6) the tensile influence of the film is not appreciable. It is believed that this is connected with the fact that in the initial stage the disturbance changes in sign. The film surface area does not increase, but instead decreases, suggesting that the film strength is

not influential during this phase. Later, when the interface disturbance amplitude becomes equal to the initial one (after undergoing a change in the phase of the disturbance and a corresponding sign change), the film surface may be broken as a result of the formation of occasional small-scale distortions. The ruptured film cannot support a tensile stress and thereby has no further direct influence on the growth rate. Subsequently, however, remnants of the film may act as perturbation sources in the later evolution of the mixing zone velocity field.

It should be noted that in the experiments and in the calculations, disturbance amplitude growth takes place according to linear theory (2) even when the amplitudes grow to be comparable with the wave length. This is well beyond the limit of applicability predicted by the linear theory. Simultaneously, the interface surface comparatively quickly acquires a nonsinusodial form, in contrast to the sinusoidal form predicted according to the linear theory. This means that, in addition to the basic harmonic growth, the interface exhibits formation and evolution of complementary, phase-shifted harmonic amplitudes, $\cos \frac{2\pi}{m} x$, with wave lengths $m = \lambda/2, \lambda/3$ and so on [7].

3. TURBULENT MIXING AT THE CONTACT INTERFACE, ACCELERATED BY SHOCK WAVES

As a consequence of the late time nonlinear instability development, the flow in the vicinity of the interface becomes turbulent with resultant turbulent mixing (see, for example, [21]). When the interface is accelerated by a single shock, the prescribed initial distortion of the interface may grow in amplitude considerably (by a factor of 10-20), local vorticity concentrations are created, but the process as a whole has an ordered character. When the surface is accelerated by a series of stationary shock waves the distortion growth rate (in L - H case) approaches exponential behavior [11]. Experimentally we found that if the series of stationary shock waves accelerates the flat interface between two gases, turbulent mixing of the contact gases takes place [3].

The experiments were conducted in the shock tube previously discussed. The test section end of the shock tube (Fig. 7) had transparent lateral walls and consisted of two matched gas volumes, separated by a thin film. The channel end was plugged by a stopper with a flat face. The closed volume was filled with helium in the test section with air in the upstream side of the film at atmospheric pressure. A flat stationary shock wave crossed the surface (H - L case) and accelerated it. After the reflection from the flat-plug face which acted as a rigid wall, the reflected shock wave passed through the contact surface again in a reversed direction (L - H). Then it reflected from the contact discontinuity at the L - H interface. After that it reflected from the wall once again, and so on. Thus, a series of stationary shocks of consequently decreasing amplitude crossed the film surface (in direction L - H) and it was impulsively broken up, a process which continues until motion ceases.

Immediately after the start of motion, the interface begins to smear due to the small-scale disturbance growth. The small-scale disturbances have characteristic scales that are below the resolution limits of the photographic flow visualization technique (Fig. 8). The primary sources of these small-scale disturbances may be the variations in thickness of the film (± 50% of the average thickness) and equally small-scale folds along the interface surface. Gradually the interface distortions smear and thicken until the interface zone becomes a region of turbulent mixing with nonuniform edges. The characteristic scale of zone edge distortions grow with time. The picture of mixing zone has a cellular structure, typical of the shadowgraph flow visualization of turbulent flow. The film, which initially separated the gases, breaks into tiny pieces. While originally flat, these pieces later turn into thickened clumps. When their form becomes more compact, their drag decreases. They acquire a velocity equal to the mass averaged gas velocity after the initial shock, and they are weakly dragged by the subsequent shock waves. Thus, the film clumps pass through the mixing zone and later are advected from this zone into the light gas region. First, a simple phenomenological model of turbulent mixing in Rayleigh-Taylor instability was developed in [22]. Later in [3,14,23] other variants of semi-empirical models were suggested to describe gravitational turbulent mixing as well as the acceleration of the interface by stationary shocks [3,14]. The model described in [14] seems

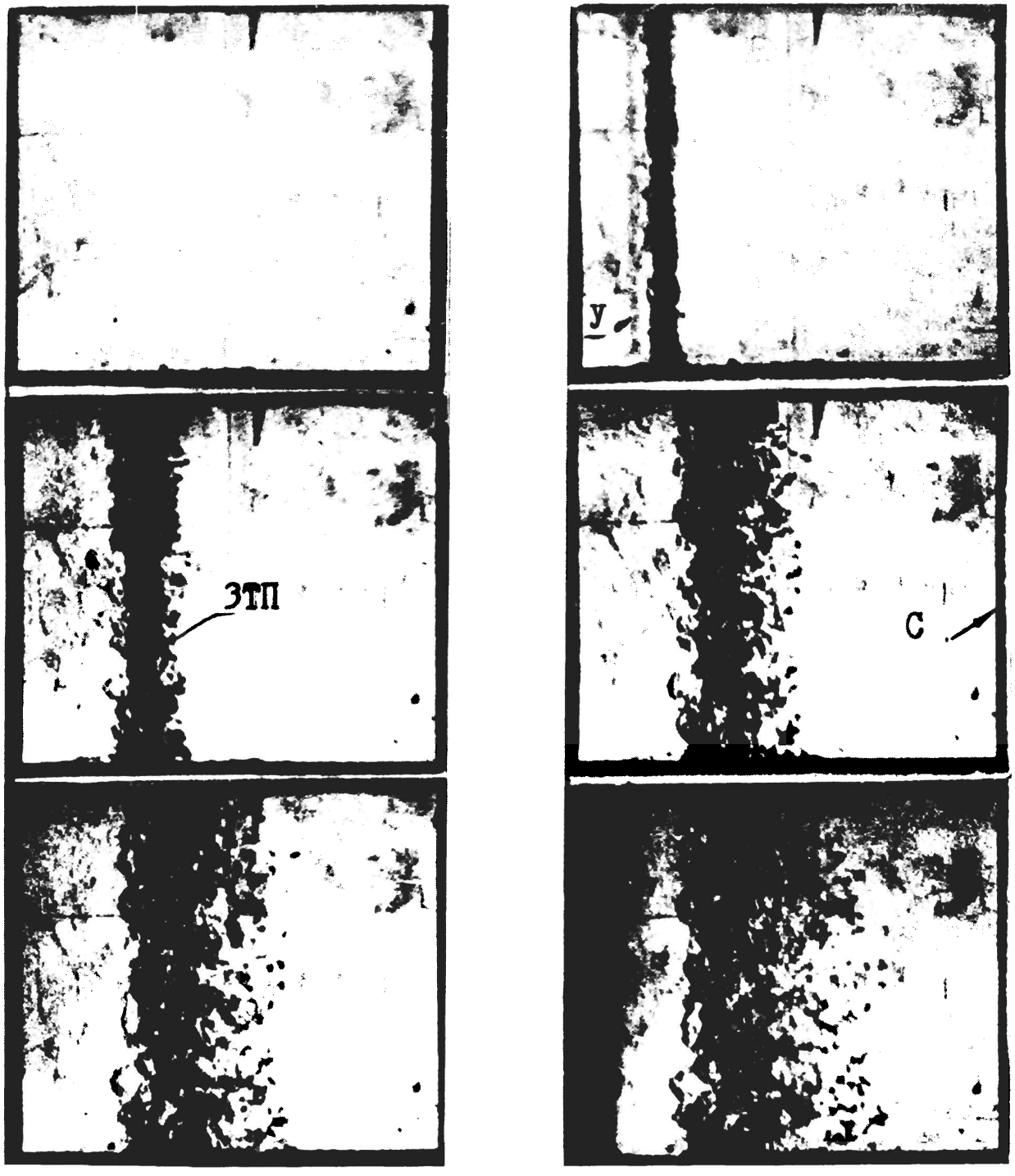

Fig. 8 The evolution of turbulent mixing zone at the interface of gases (air to helium), accelerated by a shock wave (M = 1.3), 3TII is the turbulent mixing zone, y is a shock wave; C is a a rigid wall.

to be a more satisfactorily complete and descriptive model for this process.

In Fig. 9 the averaged data of nine tests and the calculated results are compared for the experimental arrangement described previously [14]. The absolute width of the mixing zone at a fixed time differs slightly from test to test due to the difference in the levels of intermittent distortions which appear at the moment of film breakage. Nevertheless, the rate of zone width growth, especially that at late times, appears to be practically equal in all tests. The computations [14] agree well with the test results.

Mixing zone width grows continuously in time,. Its growth accelerates when shocks pass through the zone. It is related to the disturbance evolution mechanism in the case of the L - H instability [1,2]. Another essential mechanism may be present as well. In the mixing zone, density pulsations exist, that are the result of intrusions of more light or more heavy gas compared with the mean background level. When the shock wave passes through the gas with lighter intrusions, the latter are observed to be accelerated up to a velocity, which exceeds the mean background level [24]. If the density intrusions are relatively heavy, the opposite situation appears. The heavier intrusions are left behind the mean background mixing region. Thus, when the shock wave passes through the mixing zone, heavier gas intrusions tend to collect in the region occupied formerly by the light gas while the lighter gas penetrates the region formerly occupied by the heavier gas. At the acceleration of such density intrusions by a shock wave, vortex rings are created at their edges [35].

4. NONLINEAR EFFECTS OF DISTORTIONS EVOLVING AT THE SHOCK AND EXPANSION WAVES

During shock passage through the disturbed contact interface, disturbance generated shock waves and expansion waves are formed. In certain cases it is interesting to define the laws of this disturbance evolution. Usually the problems of stability and evolution of small distortions in gas dynamics are studied by the solution of (analytic or

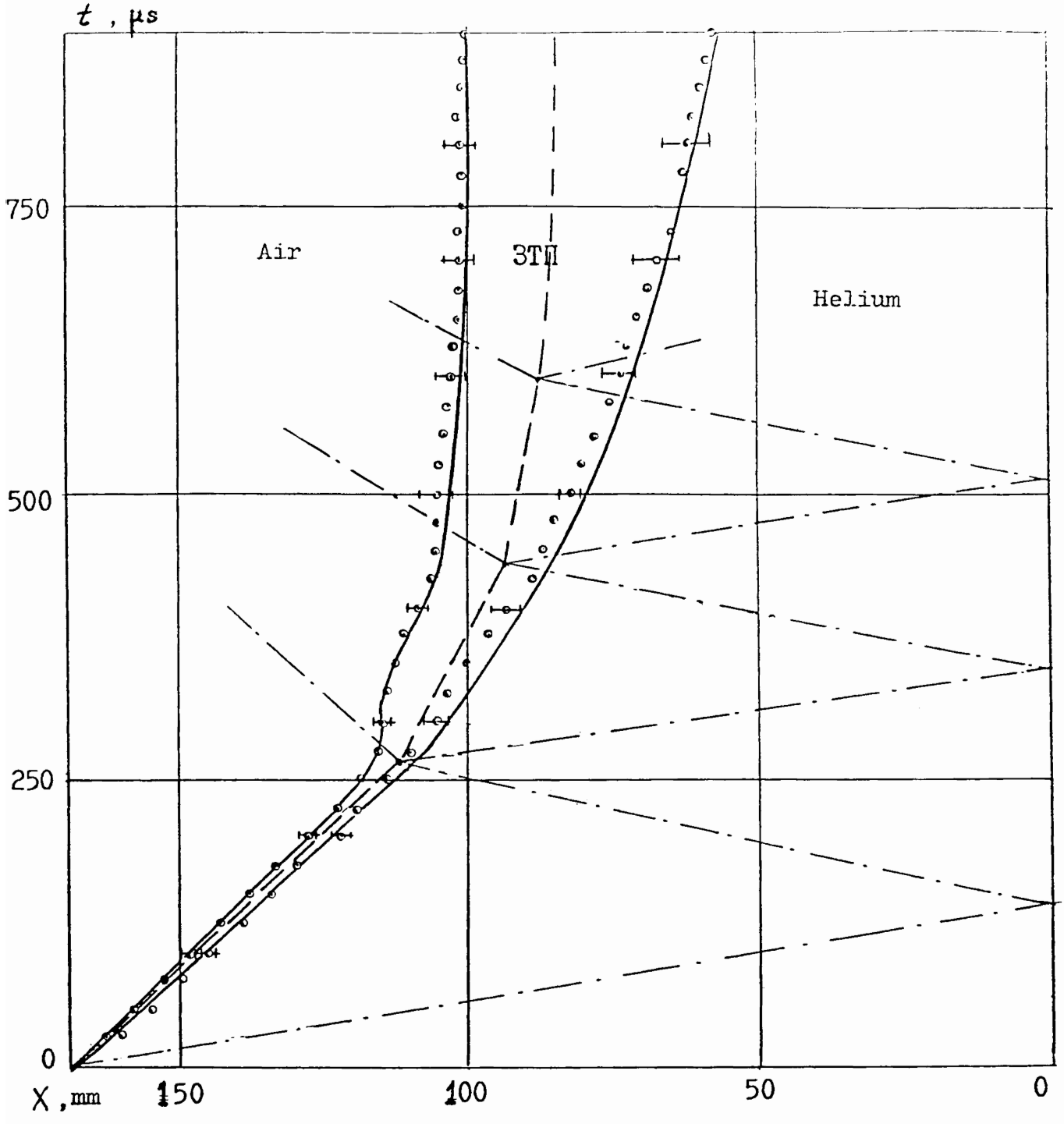

Fig. 9 X - t diagram of air-to-helium interface and of the mixing zone evolution. Here, points are the experiment, solid curves are the calculation [14]; dashed and dot-dashed lines are the shock wave and interface trajectories, respectively, in the computation without accounting for mixing.

numerical) linearized equations. In such cases the initial disturbance is often given in form $y = a_0 \cdot \cos \kappa x$ and is solved as $y = a(t) \cdot \cos \kappa x$, where a(t) is a certain instantaneous amplitude value. Applicability of the linear approximation is usually determined by the relative smallness of the distortion dimension. In particular, it is usually applicable if a(t) has the length,

$$a(t) \cdot \kappa << 1 \qquad (4)$$

However, in some cases the linear approximation appears to be invalid, even if relation (4) is satisfied.

Immediately following, experimental results [4,5] are presented, which illustrate the nonlinear effects limiting applicability of the linear approximation. This process is most evident and is dramatically illustrated in the evolution of expansion wave distortions. In the linear approximation, strictly speaking, the initial disturbance amplitude $\Delta_0 = 2a_0$ must be infinitesimally small. It does not change with time, i.e., $\Delta(t) = \Delta_0 =$ Constant. As the experiment shows, in the case of a small, but finite distortion of the expansion front, another situation appears.

The experiment was arranged as shown in Fig. 1. The first closed volume of the shock tube (gas 1) was filled with carbon dioxide ($\rho_0 = 1.85$ g/ℓ, $\gamma = 1.30$) and the second volume filled with air ($\rho_0 = 1{\cdot}205$ g/ℓ, $\gamma = 1.40$). Hence, this is a case of H - L. In Fig. 10 the photo of the expansion distortion pattern is presented. At the initial motion the disturbance amplitude of the reflected expansion wave is [1 + (c - u)/D] times greater than the initial amplitude of interface disturbance. Here, D is the velocity of the incident shock wave, while u and c are the particle and sound speeds, respectively, behind the front in carbon dioxide. Each point of the wave front moves at the local sound velocity. Since the flow behind the incident plane shock wave is homogeneous, all points of the expansion front are shifted with the same velocity. It follows that evolution of the wave front form with time must proceed, in accordance with Huygens' classical principle of optics. As interpreted here, this means that each subsequent front location represents the envelope of spherical waves, originating from the points on the previous one. This is well confirmed by the experiment.

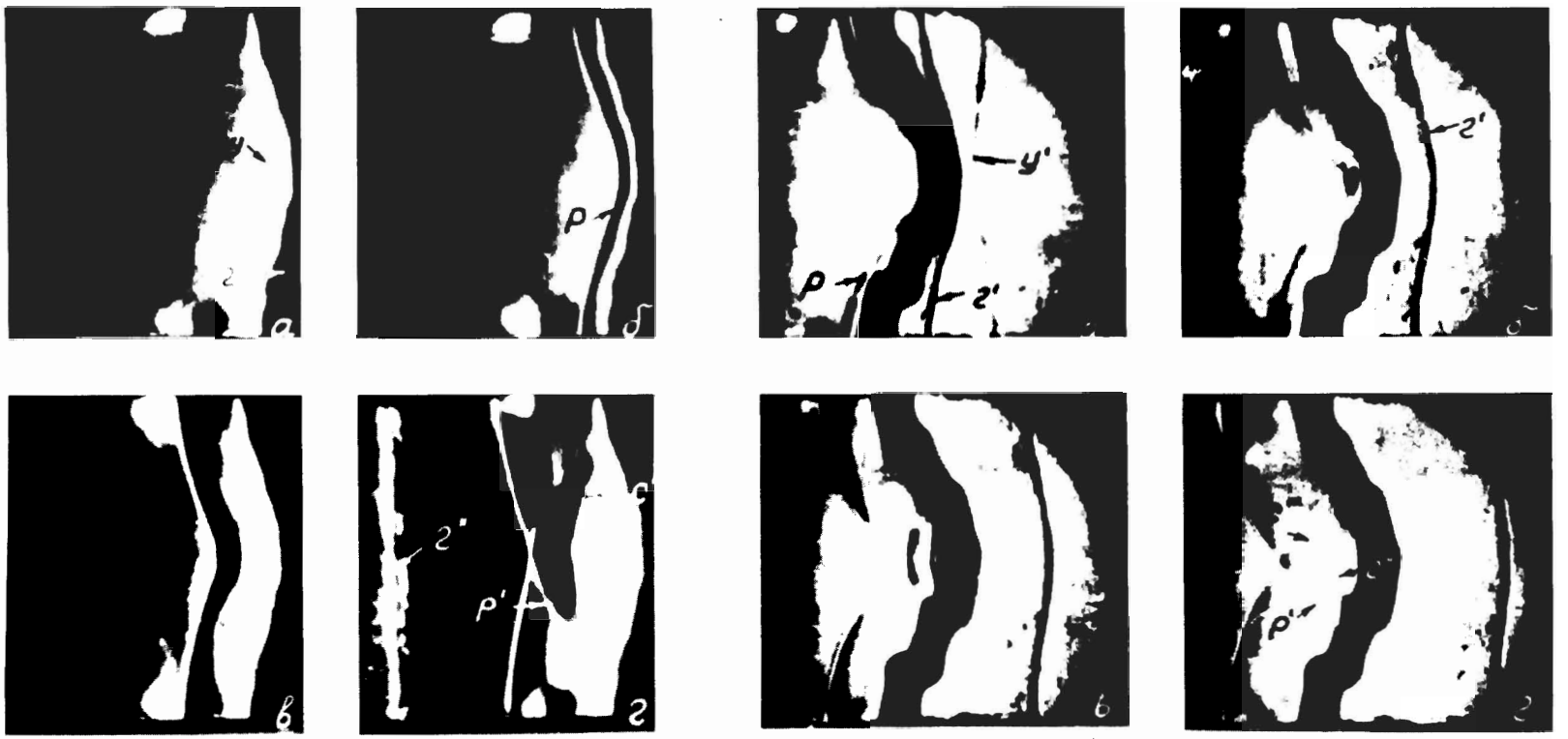

Fig. 10 Disturbance evolution of the expansion wave, originating at the shock-wave passage (M = 1.42) through the gas interface: carbon dioxide to air. Initial interface distortion $y = a'_0 \cos(2\pi/120 \cdot x)$, x in mm (1) a_0 = 6 mm; (2) a_0 = 12 mm; Γ is the initial location of the interface: carbon dioxide to air; Γ' is the interface: carbon dioxide to air; Γ'' is the interface: air to carbon dioxide; y is the incident shock wave; y' is the transmitted shock wave; P is the the reflected expansion wave; P' is the secondary expansion wave; C', C'', C''' are secondary compression waves.

This evolution is characterized by a singular point, where the continuous curvature of the wave front is broken into two segments. It should be noted, that this singular behavior is not the result of excessive disturbance magnitude. Based on geometrical considerations one may show that such points must appear early or later for any finite distortion, no matter how small. The distortion amplitude does not change, until the singularity in the wave front appears. Following the appearance of these points, secondary waves P' originate in the flow behind the front. These are extensions of the primary front fields (see Fig. 10.1). In this situation the continuous wave front disintegrates into a group of intersecting arcs. The front P' is characterized by the fact, that it is formed at all points at different times. Discontinuities in the density spread along the front with a finite velocity. This is evident from Fig. 10.1. When the initial amplitude of the expansion wave distortion increases, the discontinuous front profile and origination of the secondary wave occurs earlier (see Fig. 10.2). Secondary compression waves are correspondingly formed in the flow behind the expansion front.

In either case, when the singularity appears, the front wave disturbance amplitude, Δ, begins to decrease and asymptotically tends to zero. When time periods are sufficiently large, the form of the diverging wave profiles becomes cylindrically symmetrical and appears insensitive to influences of their initial form. Under this assumption of insensitivity, it is not difficult to show that the expansion wave-front disturbance amplitude changes according to $\Delta \simeq$ constant $\cdot\, t^{-1} \simeq$ constant $\cdot\, s^{-1}$, at $t \to \infty$, where t is time, and s is the path of a wave.

The shock wave disturbance evolution is accompanied not only by the wave front change, but also by the appearance of discontinuities in the curvature of the transverse shock wave fronts formed in the flow behind the primary front. A series of shadowgraph photos of the shock wave evolution on reflection in air against a rigid wavy wall, placed at the end shock tube test section, is shown in Fig. 11. In these experiments we varied the disturbance amplitude of the wavy wall at a fixed distortion wave length.

In all the cases the reflected wave front form deviates from the initial sinusoidal form increasingly with time. In particular, the formation of discontinuities in the front curvature, seen in Fig. 11,

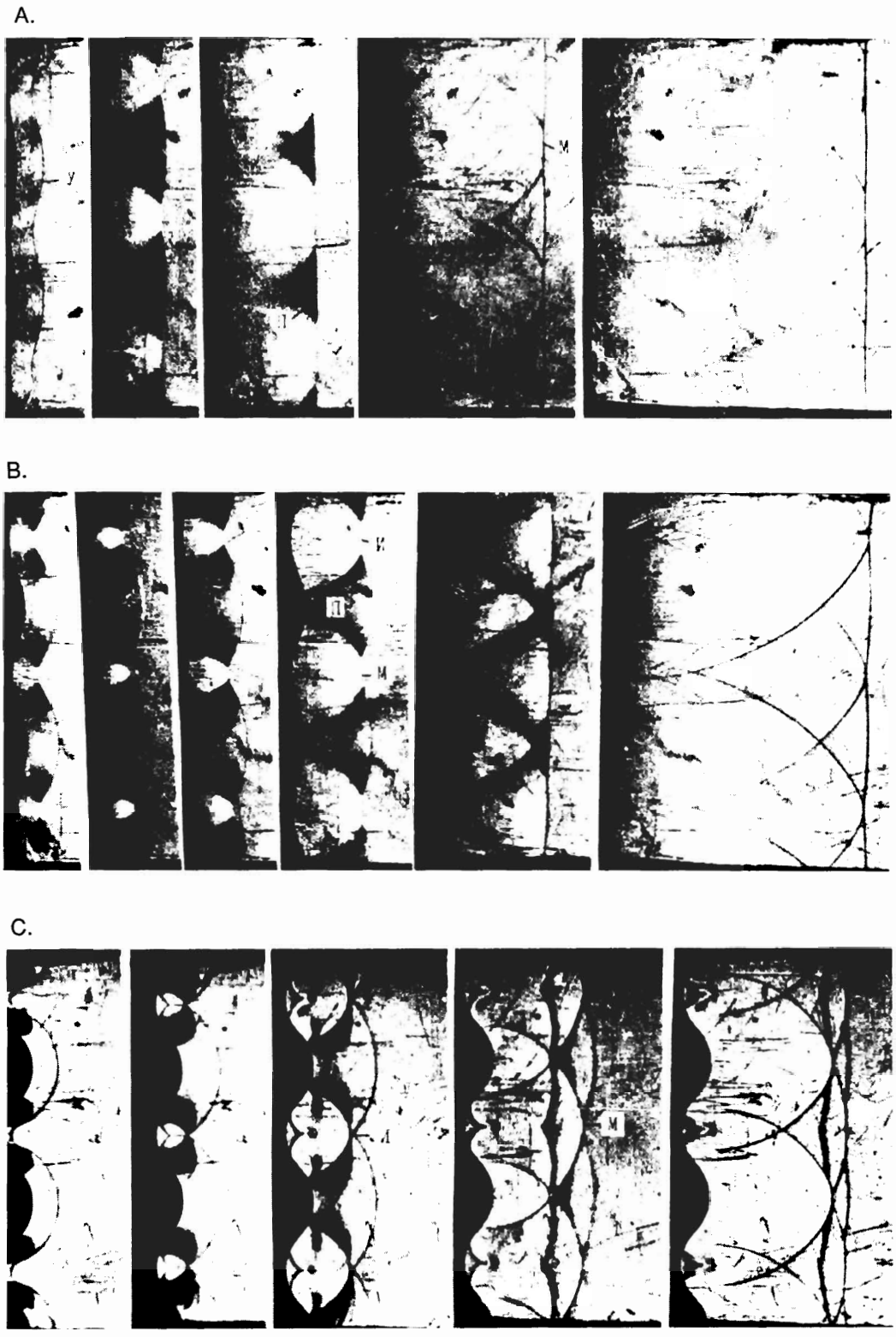

Fig. 11 Disturbance evolution at the shock wave front, reflected from a rigid wavy wall. (a) $a_0k = 0.2$ ($a_0 = 0.025\ \lambda$); (b) $a_0k = 0.4$ ($a_0 = 0.05\ \lambda$); (c) $a_0k = 0.8$ ($a_0 = 0.01\ \lambda$); y is the reflected shock wave; H is the breakage point of a shock wave front; II is the transverse wave front; M is the Mach wave.

illustrate this process. Simultaneously, discontinuities are formed at the fronts of the transverse waves in the flow behind the front of the reflected wave. Initially the density in the flow is smoothly distributed. The early smearing of the transverse waves is observed in the shadowgraph photos. Subsequently, the fronts sharpen with time and their photo visualizations consequently become more distinct and clearer. As the amplitude of the initial disturbance decreases, the formation of singularities in front curvature and deviations from sinusoidal form diminishes. Ultimately, one similar class of nearly sinusoidal perturbations survives in the field of continuously interacting Mach waves, M.

In the foregoing situation, the small distortion evolution under the necessary small amplitude criterion (4), is not sufficient to establish applicability of the linear approximation. The criterion of small time must also be satisfied [5]

$$t << t_* = \left(c_o a_o \kappa^2\right)^{-1}$$

where c_o is characteristic sound velocity. It follows that care should be taken to define the limits for use of the asymptotic formulas [25-31], which are based on the linear approximation when computing a finite value of distortion.

5. LOCAL CUMULATION PHENOMENON

Transverse flow initiated in the plane of the distorted interface by streamwise shock passage through the interface, may produce significant nonuniformity in the local energy concentration. Experiments on shock wave reflections from rigid, concave: (a) cylindrical and (b) spherical walls [8,9], illustrate the scale of such concentrations. In case (a) the experiment was done in a shock tube within the measuring region of the rectangular test section. A plug whose inner surface had a concave

cylindrical shape was placed at the end of the test section (Fig. 12a). The lateral walls of the test section were made of optical glass. We obtained the shadowgraph photos of the reflection of a flat, stationary shock wave from the concave wall as well as optical-slit resolution of the flow (x-t diagrams) in the horizontal plane of chamber symmetry. In Fig. 13 we present the photos of flow pattern variations with changes in wall concavity. The changes in wall concavity are characterized by the nondimensional parameter $\eta = \frac{h}{R}$, where h is the depth of the concavity and R is cavity radius of curvature (Fig. 12A).

At small values of $\frac{h}{R}$ (e.g., $\frac{h}{R}$ = 0.085), (Fig. 13A), the reflected wave y acquires a cylindrical shape in the area near the symmetry plane of the shock tube channel. In this case the initial radius of this wave is ~ $\frac{1}{2}$ R. This section cylindrically and symmetrically converges to the axis, located at distance ~ $\frac{1}{2}$ R from the wall. The symmetrical convergence of the central area of the reflected wave is interrupted by the collapse of transverse compression wave II, which advances from the periphery to the symmetry plane. These transverse waves develop from the tangential flow, which originates during the shock wave reflection, at the inclined wall sections.

As the compression waves advance, their fronts steepen and they coalesce into shock waves. At the collapse of the transverse waves on the symmetry axis, the front velocity of the reflected wave increases impulsively. Here, the wave configuration becomes that, which corresponds to an irregular reflection of the shock wave with an apparent formation of a central Mach wave, "M".

When $\frac{h}{R}$ is sufficiently high (e.g., $\frac{h}{R}$ = 0.3), (Fig. 13B), from the very beginning the transverse waves are shocks. This can be seen from the sharp, discontinuous images of their fronts and by the characteristic envelope focus which originates at the reflected wave front. The intersection point of the reflected and transversal waves moves along line Э (as designated in Fig. 13B). This line marks separation between the regions of two- and three-fold compression. This line also is the tangential contact discontinuity, which separates regions of different entropy and density.

At $\frac{h}{R}$ = 0.53, (Fig. 13C), the distinguishing characteristics of the previous case are repeated, in general, but are displaced in intensity,

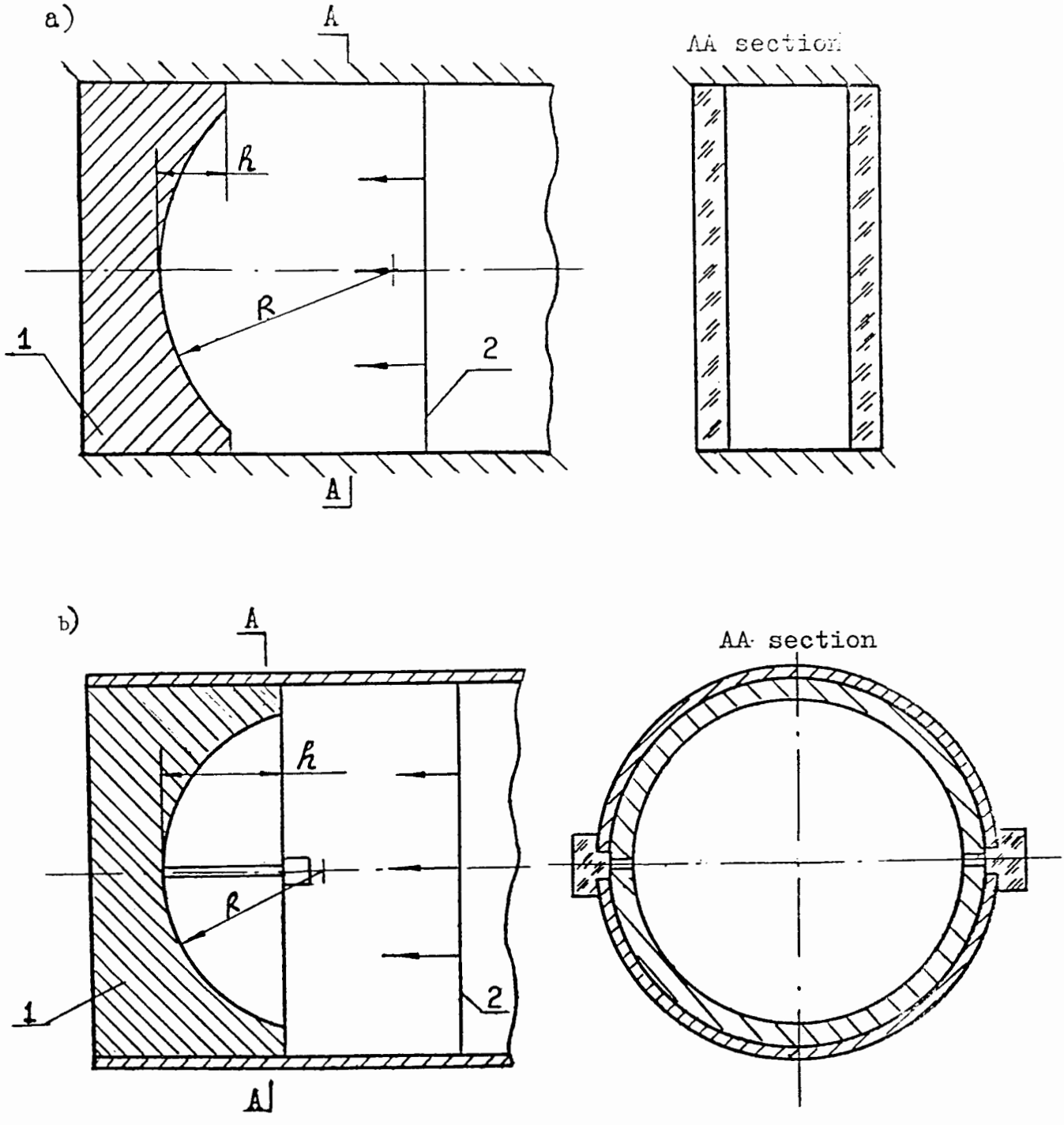

Fig. 12 Experiment arrangement to study the shock-wave reflection from
a) cylindrical
b) spherical concave wall.
1 - a plug in the channel end of a shock tube;
2 - a front of a stationary shock wave.

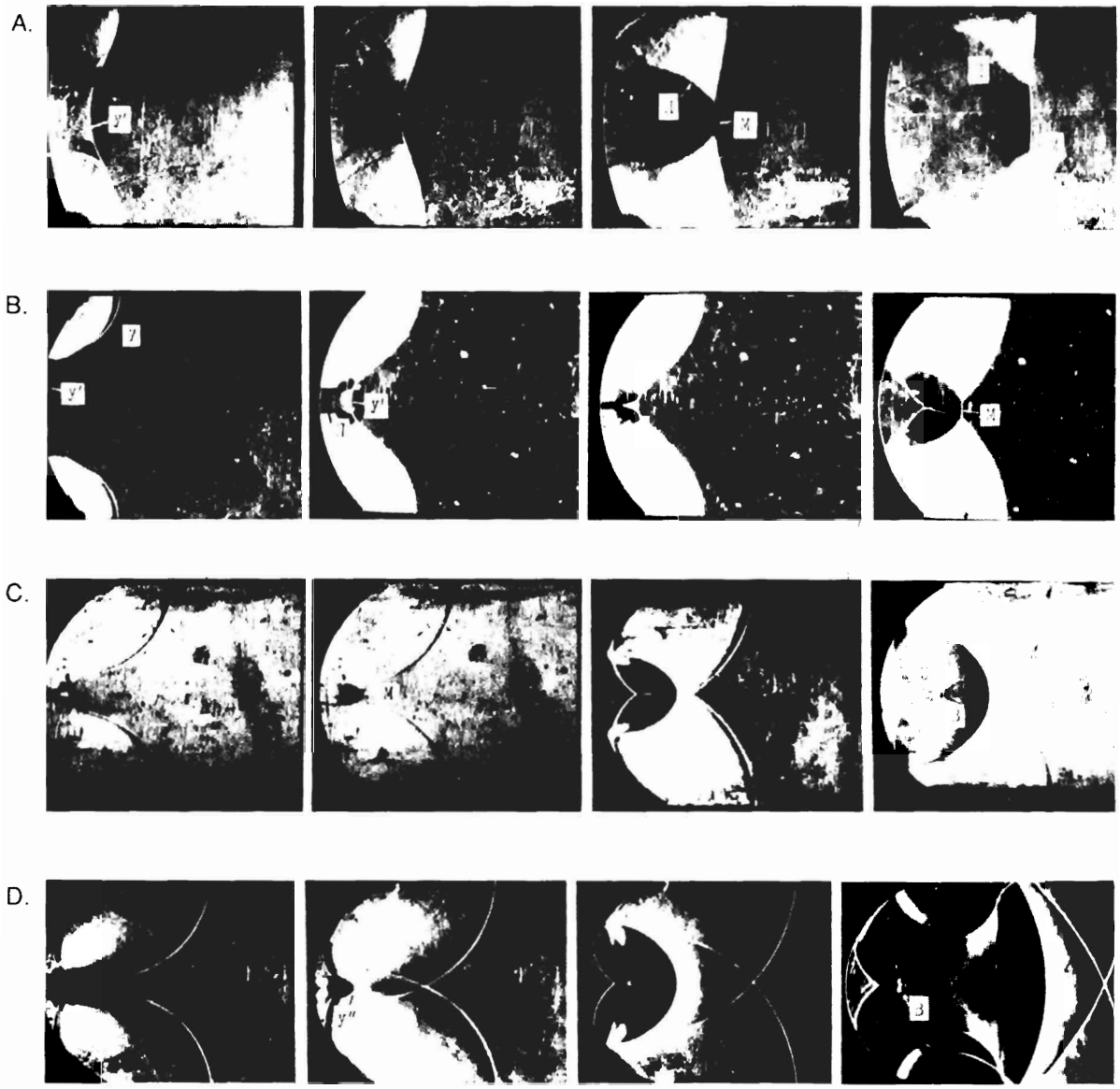

Fig. 13 The shadowgraph photos of the flow, appearing at the shock-wave reflection from a cylindrical concave wall with M = 1.27; (A) $\frac{h}{R}$ = 0.085; (B) $\frac{h}{R}$ = 0.3; (C) $\frac{h}{R}$ = 0.53; (D) $\frac{h}{R}$ = 0.89. y — a reflected wave front; y' — a central, cylindrically symmetrical region of a reflected wave; II — a transverse wave; M — Mach wave; Э — entropy trace, tangential breakage; B — vortex zone, y" — a front of a shock wave, diverging from a higher pressure zone.

time, and position. However, following Mach wave M formation in the central region, the flow character changes abruptly in comparison with the previous case. The lateral branches of reflected wave y collapse on the symmetry plane, the phase speed of their intersection is higher than the front velocity of the reflected wave. Subsequently, their trajectories diverge from the central region of the high pressure area (the dark zone) which is the locus of points reached during transverse wave collapse. The energy concentration is sharply localized to a finite, but small, central region. A comparatively small gas fraction acquires a rotational velocity, significantly larger than that of the surrounding gas. Consequently, vortex, B, appears.

In case $\frac{h}{R} = 0.89$ (Fig. 13D) the lateral branches of the shock wave y collapse on the symmetry plane continuing until the transverse waves collapse. Hence, the higher pressure area is left far behind the reflected wave front. In this case the front velocity of wave y from the highest reflected pressure region appears to be the maximum of the several cases examined. .By means of flow tracing (x-t diagram) in the symmetry plane, we find an indication of the possible appearance of a shock wave, diverging from the high pressure region.

The parameters of the flow after the incident shock wave and the state equation of medium (in this case it is an ideal gas with $\gamma = 1.4$) are known. Hence, one may estimate the parameters of the state after the reflected wave front, diverging from the high pressure zone. In Fig. 14, we record the dependence of the relation of maximal attained temperature T_{max} in the "hot" zone to the temperature behind the incident shock wave front T_1 at the $\frac{h}{R}$ values for the cases considered (curve 1). In this case the attained temperatures are comparatively low; approximately 1.5 times the temperatures which appear at the reflection from the flat wall.

This effect was more in evidence when the primary wave was reflected from a spherical concave wall. In Fig. 12B the test arrangement diagram is shown. The end of the test section of the cylindrical shock tube is closed off with a plug whose inner face has been given a spherical groove. In the plug, a narrow slit was cut. Its plane coincides with the tube axis. In the tube walls, two narrow windows of high optical-quality glass were placed. The slit plane in the plug was aligned with the windows. Thus, it was possible to obtain slit scanned-flow images along

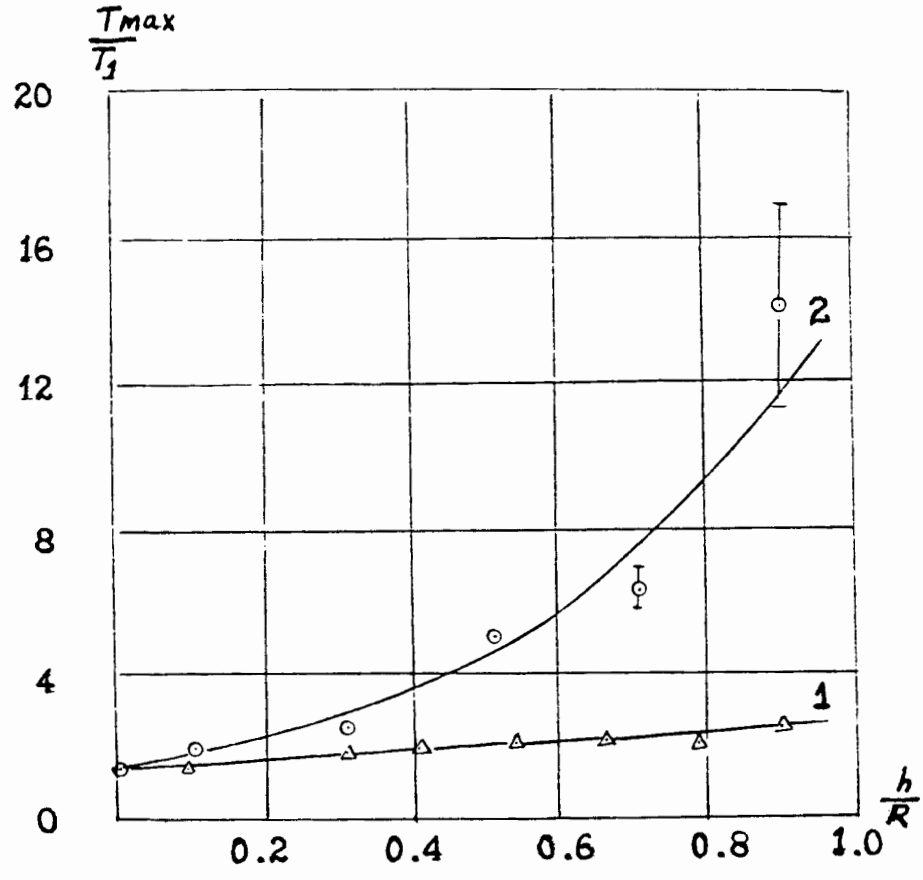

Fig. 14 The dependence on the degree of wall cavity $\frac{h}{R}$ of temperature rise, T_{max}, behind reflected shock to temperature behind incident shock, T_1. Curves:
1 - reflection from cylindrical wall;
2 - reflection from spherical wall.
Incident shock Mach No., M = 1.27.

the tube axis. The quality of the coincident matching of the x-t diagram of the flow to the shadowgraph evidence, described previously, suggests the satisfactory level of comparison in the flow patterns deduced from the two independent diagnostic techniques applied.

Curve 2 of Fig. 14 shows the computed maximum temperatures based on the measured experimental wave velocities and the thermodynamic state assumptions previously described. The curve indicates that, under these circumstances, temperatures may develop which are an order of magnitude or more higher than those generated behind a shock reflected from a plane wall. These substantially increased temperature levels indicate that the converging transverse waves are cylindrical. That is, it is only by the convergence of cylindrical waves on the axis of a spherical groove that temperature increases of this magnitude can be produced under these circumstances.

REFERENCES

1. R.D. Richtmyer, Communs. Pure and Appl. Math., Vol. 13, 1960, pp. 297-319.

2. Ye. Ye. Meshkov, Bulletin of the Academy of Sciences of the USSR, Fluid and Gas Mechanics, No. 5, 1969, pp. 151-158.

3. V.A. Andronov, S.M. Bakrakh, Ye. Ye. Meshkov, V.N. Mokhov, V.V. Nikiforov, A.V. Pernitskiy, A.I. Tolshmyakov, Journal of Experimental and Theoretical Physics, Vol. 71, 8, 1976, pp. 806-811.

4. B.A. Klopov, Ye. Ye. Meshkov, Combustion and Explosion Physics, Vol. 18, 4, 1982, pp. 93-96.

5. Ye. Ye. Meshkov, V.N. Mokhov, Combustion and Explosion Physics, V. 18, No. 4, 1982, pp. 96-100.

6. Ye. Ye. Meshkov, Computer-Aided Study of Hydrodynamic Stability. Collection of scientific works edited by K.I. Babenko. Preprint of the Institute of Problems of Mechanics, 1981, pp. 163-190.

7. S.M. Bakhrakh, G.A. Grishina, N.P. Kovalev, Ye. Ye. Meshkov, A.I. Tolshmyakov, Uy. V. Yanilkin, Computational Methods of the Mechanics of a Continuous Medium, Vol. 9, No. 5, 1978, pp. 5-12.

8. Ye. Ye. Meshkov, Bulletin of the Academy of Sciences of the USSR, Fluid and Gas Mechanics, Vol. 4, 1970, pp. 33-39.

9. B.A. Klopov, Ye. Ye. Meshkov, A.I. Tolshmyakov, Journal of Applied Mechanics and Technical Physics, No. 4, 1976, pp. 33-37.

10. N.N. Anuchina, S.M. Bakhrakh, A.V. Zabrodin, L.A. Pliner, I.D. Sofronov, Computer-Aided Study of Hydrodynamic Stability. Collection of scientific works edited by K.I. Babenko. Preprint of the Institute of Problems of Mechanics, 1981

11. R.M. Zaydel', Bulletin of the Academy of Sciences of the USSR, Fluid and Gas Mechanics, Vol. I, 1972, p. III.

12. K.A. Meyer, P.J. Blewett, Phys. of Fluids, Vol. 15, No. 5, 1972, pp. 753-759.

13. N.N. Anuchina, Computational Methods of the Mechanics of a Continuous Medium, Vol. I, 1970, p. 4.

14. V. A. Andronov, S.M. Bakhrakh, Ye. Ye. Meshkov, V.V. Nikiforov, A.V. Pevnitskiy, A.I. Tolshmyakov, Report Lectures of the USSR Academy of Sciences, Vol. 264, No. 1, 1982, pp. 76-82.

15. H. Schardin, L. Agnew, Math. Phys., Vol. 9, No. 5/65, 1958, pp. 606-621.

16. G.T. Chang, Phys. of Fluids, Vol. 2, No. 6, 1959, p. 656.

17. G.I. Taylor, Proc. Roy. Soc., Ser. A, Vol. 201, No. 1065, 1950, pp. 192-196.

18. M.V. Batalova, S.M. Bakhrakh, O.A. Vinokurov, V.L. Zaguskin, L.N. Ivanova, A.I. Kolmanovich, I.D. Shinderman, Works of the All-Union Seminar on Computational Methods of Viscous Fluid Mechanics, Novosibirsk, 1969, pp. 283-286.

19. I.D. Sofronov, N.A. Dmitriyev, L.V. Dmitriyev, Ye. V. Malinovskaya, Computational Methods of Two-Dimensional Non-Steady Problems of

Gas Dynamics in Lagrange Variables, Preprint of the Institute of Problems in Mechanics, 1976.

20. S.M. Bakhrakh, Yu. P. Glagoleva, M.S. Samigulin, V.D. Frolov, N.N. Yanenko, Yu. V. Yanilkin, Report Lectures of the USSR Academy of Sciences, Vol. 257, No. 3, 1981.

21. N.N. Anuchina, Yu. A. Kucherenko, V. Ye. Neuvazhayev, V.N. Ogibin, L.I. Shibarshov, V.G. Yakovlev, Bulletin of the Academy of Sciences of the USSR, Fluid and Gas Mechanics, Vol. 6, 1978, p. 157.

22. S.Z. Belenkiy, E.S. Fradkin, Transactions of the Physics Institute of the Academy of Sciences of the USSR, Vol. 29, 1965, p. 207.

23. V.E. Heuvazhayev, V.G. Yakovlev, Journal of Applied Mechanics and Technical Physics, Vol. 7, 1976, p. 74.

24. G. Rutinger, L. M. Somers, J. Fluid Mech., Vol. 7, 1960, p. 161.

25. N.C. Freeman, Proc. Roy. Soc. A, Vol. 228, 1955, p. 341.

26. R.M. Zaydel', Applied Mathematics and Mechanics, Vol. 24, No. 2, p. 219.

27. S.V. Iordanskiy, Applied Mathematics and Mechanics, Vol. 21, No. 4, 1957, p. 465.

28. R.M. Zaydel', Journal of Applied Mechanics and Technical Physics, Vol. 4, 1967, p. 30.

29. Yu. M. Nikolayev, Applied Mathematics and Mechanics, Vol. 29, 1965, p. 658.

30. G.A. Grishina, R.M. Zaydel', O.M. Zotova, Applied Mathematics and Mechanics, Vol. 30, No. 5, 1966, p. 975.

31. A.A. Kovitz, M.G. Brisco, J. Acoust. Soc. America, Vol. 45, No. 5, 1969, p. 1157.

32. R.F. Benjamin, R.G. McQueen, S.P. Marsh, J.W. Shaner, "Shock Waves in Condensed Matter - 1983", Proc. of the Amer. Phys. Soc. Topical Conf., Santa Fe NM, July 18-21, 1983, p. 259.

33. R.F. Benjamin, H.E. Trease, J.W. Shaner, Phys. Fluids, Vol. 27, No. 10, 1984, p. 2390.

34. K.O. Mikaelian, Phys. Rev. A, Vol. 31, No. 1, 1985, p. 410.

35. M.M. Evans, F.H. Harlow, B.D. Meixner, Phys. Fluids, Vol. 5, No. 6, 1962, p. 651.

NUMERICAL SIMULATION OF TURBULENT MIXING IN SHOCK-TUBE EXPERIMENTS

Karnig O. Mikaelian
Lawrence Livermore National Laboratory
Livermore, California

We have carried out a number of 2D numerical simulations on an ALE code for shock-tube experiments in which a shock crosses one or more contact discontinuities and, after traveling through a homogeneous medium, reflects off a rigid wall at the end of the shock-tube and re-crosses the contact discontinuity (Fig. 1). As indicated in Fig. 1, we have considered two-fluid and three-fluid experiments: the first fluid, which carries the original shock, is air; the other fluids are helium, freon, SF_6, or air again. Helium is lighter than air, while freon and SF_6 are heavier than air. The interface(s) between the fluids serve as contact discontinuities and are subjected to the original shock, the re-shock, and subsequent rarefactions/compressions. Figure 1 also shows the velocity histories of the interface for two cases: when the test section is 60 cm long and filled with helium, and when it is 30 cm long and filled with freon. When the incoming shock has M_s=1.2, it takes a little over 1 ms and 2 ms for the re-shock in the 60 cm helium and the 30 cm freon cases, respectively. Subsequent reverberations of the shock are weaker and act to slow down the interface at later times.

We have carried out numerical simulations for five types of experiments as indicated in Fig. 1. Single-scale/single-interface experiments are of the classical type considered theoretically by Richtmyer[1] and experimentally by Meshkov.[2] Perturbations of amplitude η and wavelength λ evolve according to $d\eta/dt = \eta(0)(2\pi/\lambda)A\Delta v$ where A is the Atwood number and Δv is the jump velocity of the interface. Perturbations grow for both positive A and negative A as considered by Richtmyer and Meshkov, respectively. Figure 2 shows the air/helium case. As expected, when A<0 the amplitude goes through zero (second frame in Fig. 2) and grows with the opposite phase. The reflected shock, indicated by the arrow, sees a positive A and increases the growth rate without changing phase. To cover multiple shocks, we extended Richtmyer's formula by adding $\dot{\eta}(0)$ to it, so that after each shock the amplitude evolves according to (Ref. 3)

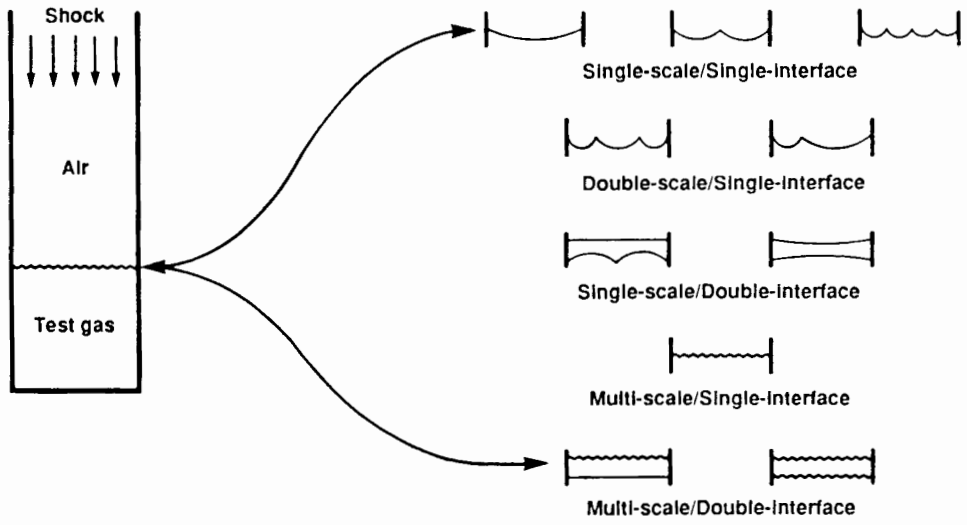

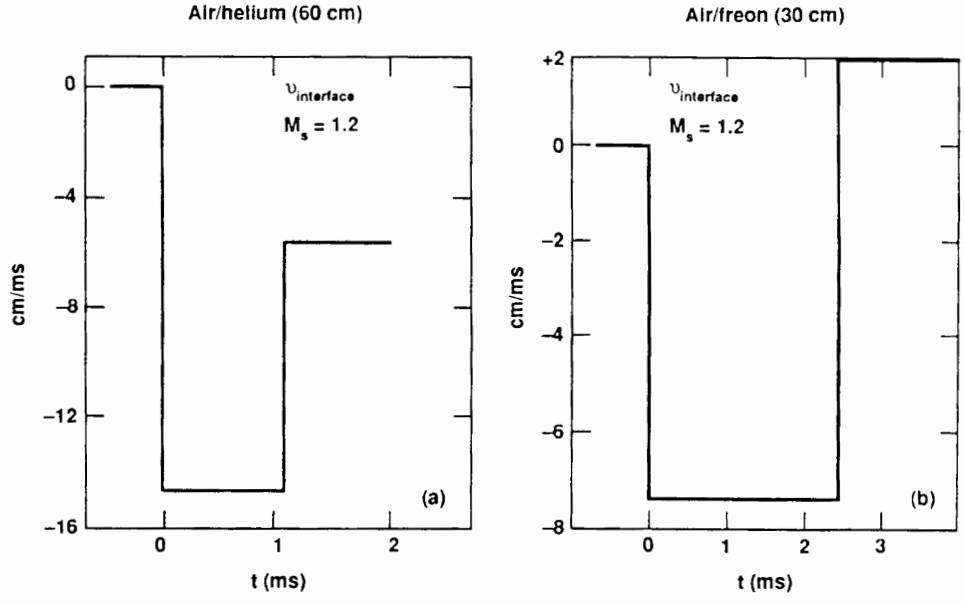

Figure 1

$$\eta(t) = \eta(0)[1 + \frac{2\pi}{\lambda} A\Delta v t] + \dot{\eta}(0)t \quad . \tag{1}$$

Several interesting cases arise in two-shock systems, as discussed in Ref. 3, particularly when $\rho_{test\ gas} > \rho_{air}$ as in the air/freon case. The perturbations go through zero and reverse phase when the original shock relfects off a rigid end-wall to re-cross the interface

($\Delta v_2 > \Delta v_1$). However if the strength of the shock can be reduced ($\Delta v_2 < \Delta v_1$), then the amplitude can be "frozen-out" by proper shock-timing. The time when η goes through zero, or the shock-timing necessary to freeze η, depend on the strength of the shocks via Δv_1 and Δv_2, but are independent of the original amplitude with which the experiment starts. This independence from initial amplitude makes the experiments much easier to carry out, but they have not been performed yet.

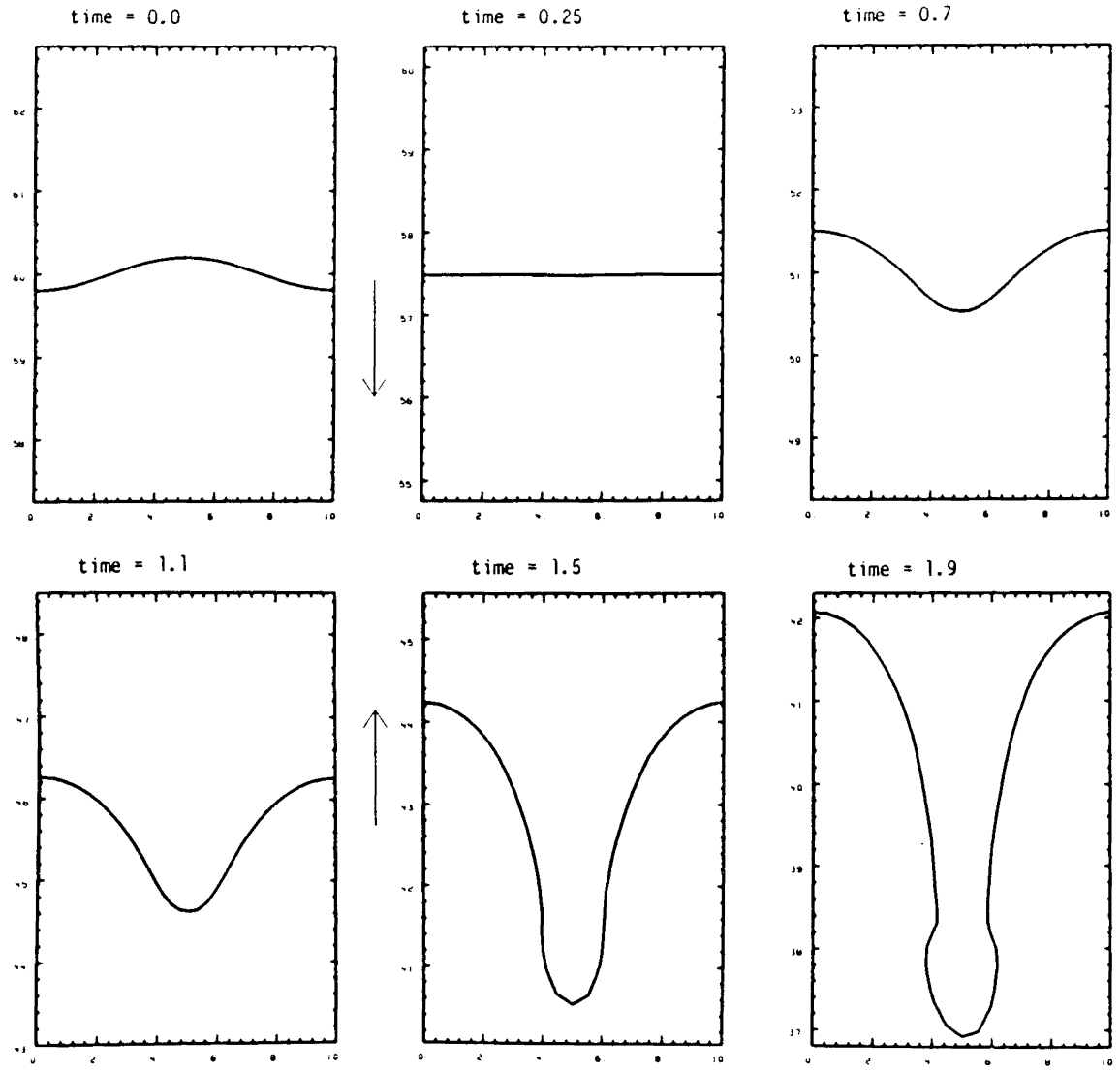

Figure 2

The second type of experiments we simulated have double-scale perturbations at a single interface. All of our simulations are reported

in Ref. 4 and here we summarize our results very briefly. We see that in the problem of competition between bubbles and spikes of different sizes, a bubble that is twice as large as other bubbles both in wavelength and amplitude moves slightly ahead of the smaller bubbles, but the late time evolution of a bubble that is twice as large as others in wavelength only is similar to the evolution of the smaller bubbles.

The third type of experiment we simulated was a three-fluid experiment with single-scale perturbations, an example of which is shown in Fig. 3. A Mach 1.2 shock moves from air into a 4 cm thick layer of freon and after emerging from the lower (perturbed) side of freon it enters another layer of air, 60 cm long. The perturbations change phase soon after the shock leaves the freon (second frame in Fig. 3). About 2.8 ms after the first shock the freon layer is re-shocked and the perturbations grow faster. The case where there are no large scale perturbations but only small amplitude random perturbations is shown in Fig. 4. This fourth type of experiments has been recently carried out by N.C. Stearman and the results are in good qualitative agreement with our simulations reported in Ref. 4. The perturbations develop first on the upper surface of freon, which is shocked first, but after re-shock the perturbations on both interfaces are comparable.

The fifth type of simulations involve random perturbations at a single interface. The results of several calculations are reported in Ref. 4 for air/helium and air/SF_6. The emphasis was on a) sensitivity to initial conditions and b) time-evolution of the mix layer or of the "turbulent mixing zone" as defined in the experiments of Andronov et al.[5] and Zaitsev et al.[6] From our simulations we can draw only qualitative conclusions because many more zones are required to resolve small scale structures, and because the code uses an artificial viscosity for numerical stability. Typically 100x250 zones were used in the simulations and in the few cases where the mesh was refined by a factor of 2 the mixing width increased by about 20%. Nevertheless, our calculations suggest that the late time evolution of the mix layer depends weakly on initial conditions. In Fig. 5 we show the interface in the air/SF_6 case at t=3 ms by which time it has been reshocked. The frames labeled A, B, and C started with initial random perturbations of

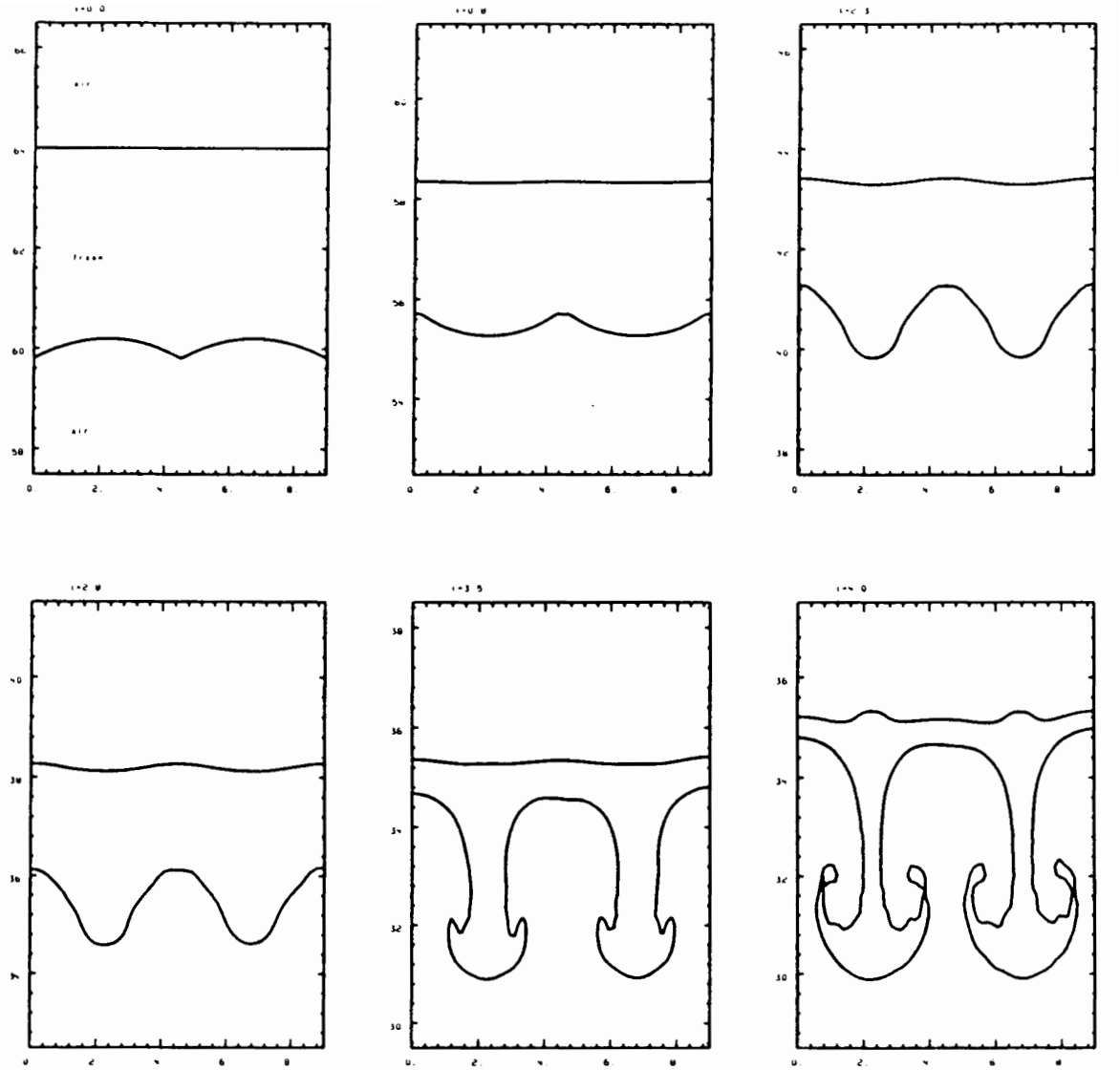

Figure 3

0.05 cm, 0.10 cm, and 0.20 cm, while frame D started with multi-scale perturbations which had longer wavelengths but the same maximum amplitude of 0.20 cm. The total width of the mixed region appears to be insensitive to such variations in initial conditions. Experimental results on this issue was reported only at this workshop by B. Sturtevant, and appear to support this notion of universality. In a related process, mix generated by the Rayleigh-Taylor instability (constant acceleration), there is both numerical and experimental evidence of universality presented in the work of Read and Youngs.[7] Based upon their result, we suggested[8] that the mixing width into the heavier fluid evolves as

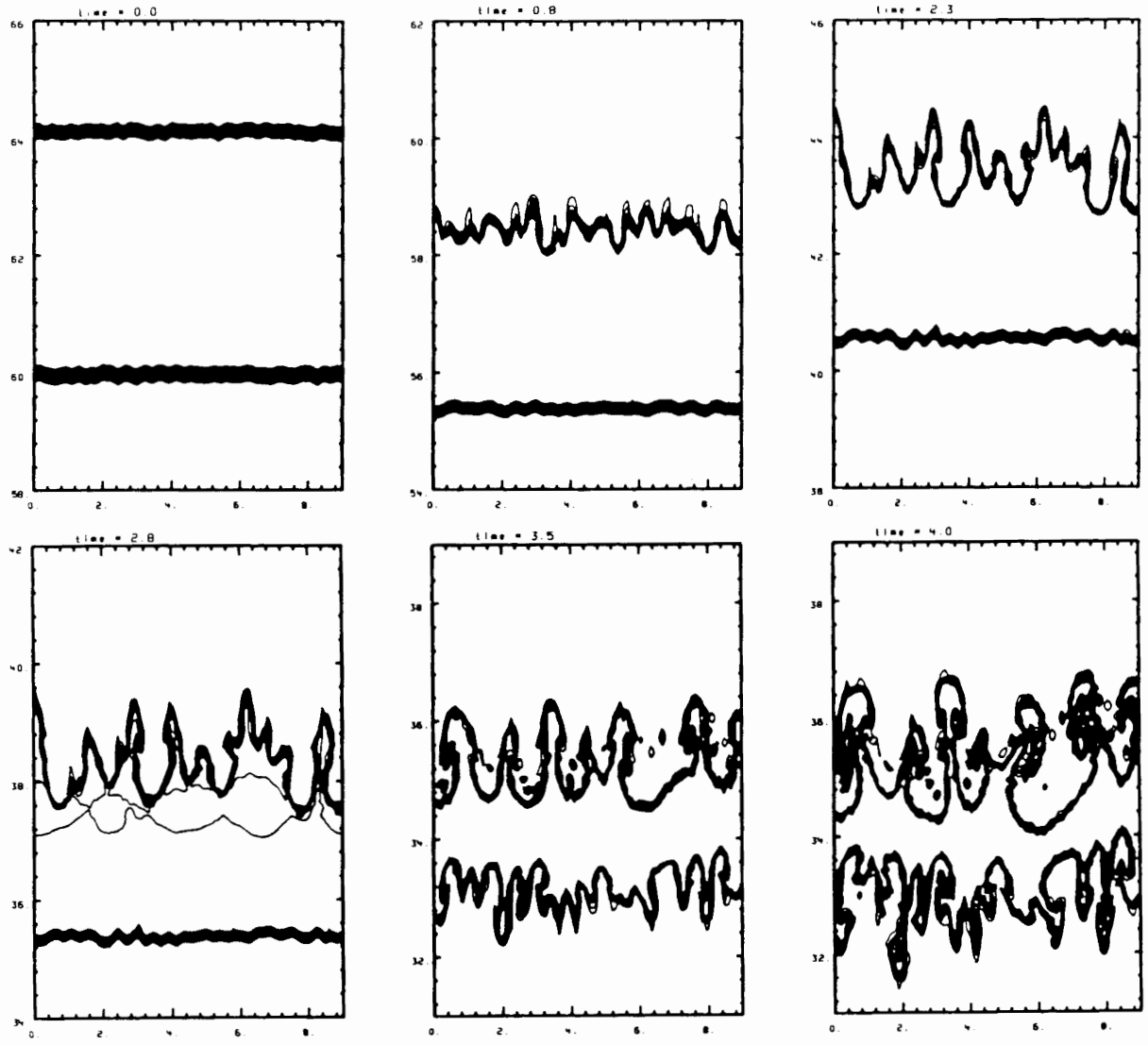

Figure 4

$$h = 0.14\ A\Delta vt \qquad (2)$$

in the case of a shock. In our simulations the mixing width grows not quite linearly in time but at a slower rate. We suspect that the artificial viscosity in the code slows the late time growth, but we have no direct support for this view, except the scaling argument that independence from initial conditions directly implies that $h \sim \Delta vt$. If we admit dependence on an initial length scale $h(0)$, then of course any functional dependence on time is possible. We hope future experiments will throw light on this issue.

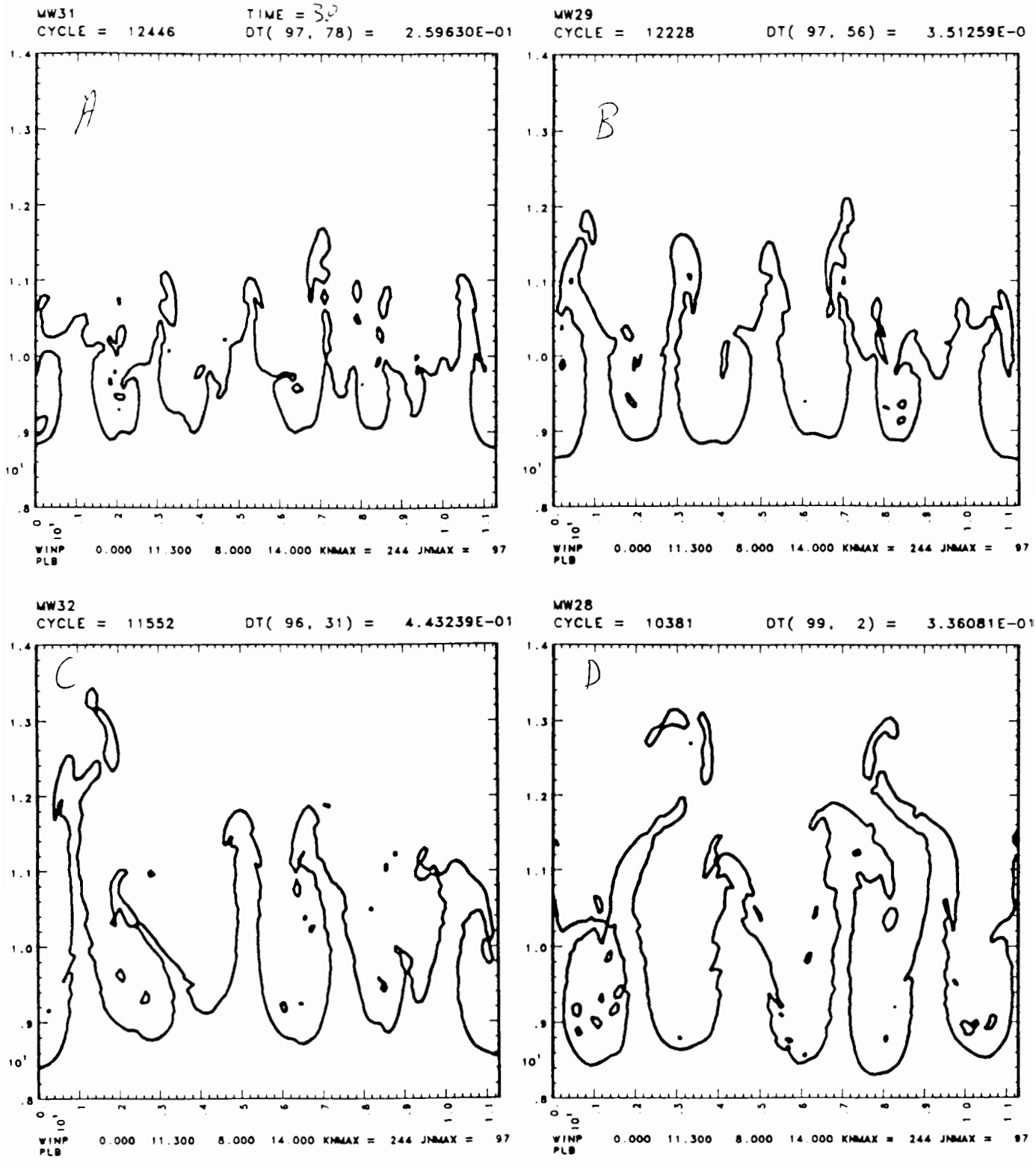
MW31
CYCLE = 12446
TIME = 3.0
DT(97, 78) = 2.59630E-01
A
WINP 0.000 11.300 8.000 14.000 KMAX = 244 JMAX = 97
PLB
MW29
CYCLE = 12228
DT(97, 56) = 3.51259E-0
B
WINP 0.000 11.300 8.000 14.000 KMAX = 244 JMAX = 97
PLB
MW32
CYCLE = 11552
DT(96, 31) = 4.43239E-01
C
WINP 0.000 11.300 8.000 14.000 KMAX = 244 JMAX = 97
PLB
MW28
CYCLE = 10381
DT(99, 2) = 3.36081E-01
D
WINP 0.000 11.300 8.000 14.000 KMAX = 244 JMAX = 97
PLB

Figure 5

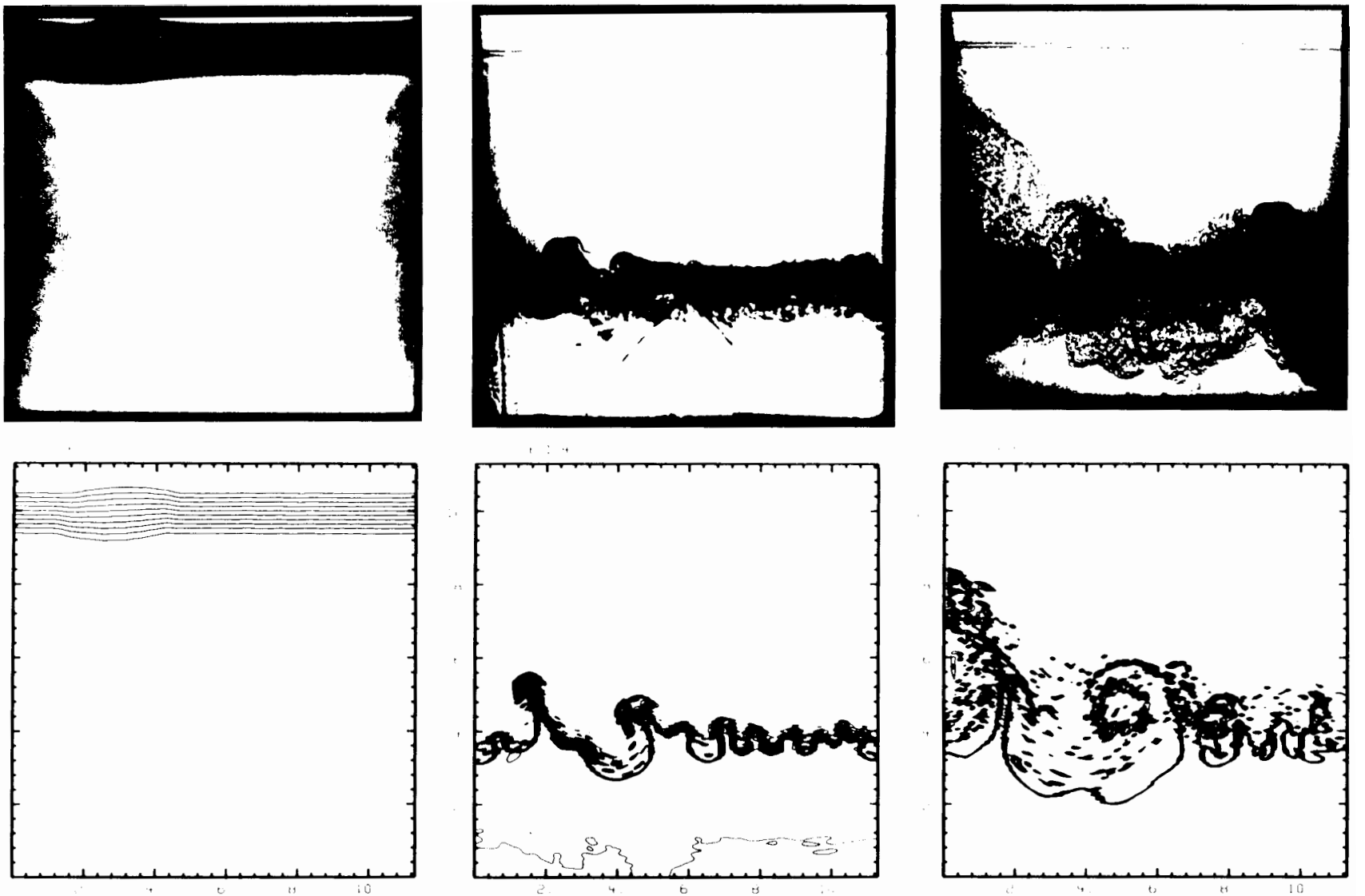

Figure 6

The last simulation that we performed was of an actual experiment carried out by B. Sturtevant.[9] A Mach 1.3 shock passes from air into SF_6 and reflects off the end-wall of a 10 cm long test section. The initial air/SF_6 interface is diffuse and contains a bump because of gravity waves set up when a plate is withdrawn just before shock arrival. The re-shock and subsequent rarefactions/compressions stop the bulk motion of the two gases, but mixing continues at a rate which is approximately linear in time. As shown in Fig. 6, our simulations agree quite well with the experimental results, even though we have slip conditions on the two side walls and cannot reproduce the wall boundary layer seen in the experimental photographs.

The simulations reported here and in Ref. 4 were conducted on the Livermore Cray computers. The longest runs were the problem just discussed (M_s=1.3 to t=5.7 ms) and another air/helium problem (M_s=1.7 to t=1.9 ms). None of them took more than 15 Cray-hours. I am grateful to G. Burke for support and encouragement, and to B. Sturtevant for sharing his experimental results. This work was performed under the auspices of the U. S. Department of Energy by the Lawrence Livermore National Laboratory under contract number W-7405-ENG-48.

References

1. R. D. Richtmyer, Commun. Pure Appl. Math. 13, 297 (1960).
2. E. E. Meshkov, Izv. Akad, Nauk. SSSR, Mekh. Zhidk. Gaza 5, 151 (1969).
3. K. O. Mikaelian, Phys. Rev. A31, 410 (1985).
4. K. O. Mikaelian, "Simulation of the Richtmyer-Meshkov Instability and Turbulent Mixing in Shock-Tube Experiments," Lawrence Livermore National Laboratory Report UCID-21328 (January 1988).
5. V. A. Andronov, et al., Sov. Phys. JETP 44, 424 (1976).
6. S. G. Zaitsev, et al., Sov. Phys. Dokl. 30, 579 (1985).
7. D. L. Youngs, Physica 12D, 32 (1984); K. I. Read, ibid 12D, 45 (1984). See also D. L. Youngs in the Proceedings of this Workshop.
8. K. O. Mikaelian, "Turbulent Mixing Generated by Rayleigh-Taylor and Richtmyer-Meshkov Instabilities," Lawrence Livermore National Laboratory Report UCRL-93499 (September 1985).
9. B. Sturtevant, "Shock Waves and Shock Tubes," proceedings of the 16th International Symposium on Shock Waves and Shock Tubes, ed. H. Gronig, RWTH, Aachen, Germany, p. 89 (1987).

COMPUTATIONS OF SUPERSONIC FLOWS: SHEARS, SHOCKS, AND DETONATIONS

Elaine S. Oran, Jay P. Boris, and K. Kailasanath
Laboratory for Computational Physics and Fluid Dynamics
Naval Research Laboratory
Washington, D.C. 20375

Abstract

This paper describes some of the basic features of and physical mechanisms controlling two types of supersonic flows: detonations and supersonic shear layers. Gas-phase detonations are supersonic flows in which a leading shock is driven through an energetic material by local energy release. The material behind the leading shock front of a detonation is highly disturbed and contains many interacting shocks, shears layers, and rection zones that produce cell-like patterns on the chamber containing the flow. Supersonic shear layers often are extremely irregular and noisy and show strong interactions between shocks and vortical structures. This paper first discusses the roll of shocks in suppressing mixing and vortex merging in shear flows, and then discusses the effects of shock interactions on pattern formation and vorticity generation behind propagating detonations.

Numerical Model

The detonation and shear-flow calculations described here were performed with numerical models that solve the time-dependent two-dimensional Euler equations using nonlinear, fully compressible Flux-Corrected Transport (FCT) algorithms [1]. FCT is an explicit, conservative, finite-volume method designed to ensure that all conserved quantities remain monotonic and positive. It has proven particularly effective in maintaining steep gradients and generally accurate solutions in both supersonic and subsonic flow calculations. The particular direction and time-split version used here and a number of related calculations performed with it are described in some detail by Oran and Boris [2].

The FCT solutions are more accurately described as large-eddy simulations of the Navier-Stokes equations in which the subgrid turbulence model is the nonlinear high-frequency filter in FCT itself. This nonlinear filter, designed to maintain positivity and monotone flow profiles, does not effect large-scale structures but diffuses the smallest-scale structures that cannot be adequately described with the grid resolution chosen. Provided that the computational grid is fine enough to resolve the large-scale features of the flow, the residual numerical viscosity of the algorithm mimics the behavior of small-scale turbulent diffusion at high Reynolds number by smoothing small-scale structures on the order of a few computational cells without smoothing adjacent regions where there is no flow. There are no appreciable smoothing effects at scales greater than a few cells. The ability of the nonlinear filter to simulate the effects of physical viscosity, for example, was recently shown by Grinstein [3,4].

Supersonic Shear Layers

The linear theory for a periodic shear flow with equal and opposed velocities shows that the Kelvin-Helmholtz instability at low velocities is stabilized when the Mach number becomes large enough. Though compressibility allows additional modes of flow that can change the stability properties, the speed of the flow becomes so fast that there is little interaction between the two streams. The usually destabilizing pressure drops associated with the Bernoulli-effect are cancelled by the pressure rises required to deflect each high-speed stream past transverse displacements of the other stream. However, it has now become important to try to determine how to mix the two high-speed streams in times compatible for chemical reactions to occur. To investigate this, numerical simulations are needed to extend the calculations beyond the linear theory, to represent the behavior of the coherent structures, and describe the effects of chemical reactions in the regions of mixing.

A number of simulations of supersonic shear layers in a laboratory coordinate system have been performed to determine those properties of the system that most influence mixing and to investigate the structure of the shear layer itself [5]. Figure 1 compares the large-scale features of a subsonic and a supersonic mixing layer. Figure 1a is an experimentally generated shadowgraph of the mixing layer between two subsonic streams [6], in which the top stream is nitrogen flowing at 10 m/s and the bottom stream is a mixture of helium and argon flowing at 3.5 m/s. The shadowgraph highlights the interface between the two streams and shows well-defined, organized, and linearly growing large coherent structures in the flow. Figure 1b is a numerical shadowgraph showing mixing contours and thus the regions of large gradients in the species densities. This was taken from a calculation of a underexpanded confined shear layer in which the upper air stream was moving at Mach 4.5 and the lower stream was moving at Mach 1.5 when they enter the system. Again, there are well-defined large structures, but they are neither as organized nor as coherent as those shown in the subsonic shear layer. In addition, there is not nearly as much mixing between the layers as occurs in a subsonic flow with a similar velocity ratio.

Figure 2 shows important feature of supersonic flows: the presence of shocks throughout the flow. In underexpanded or overexpanded flows, the shear layer is initially deflected from the centerline and sets up another shear layer across which the pressures are equal. In addition, there are reflected shock waves and rarefaction waves that influence the mixing layer and are important in triggering instabilities that lead to mixing. However, in these flows, there are high-pressure regions with shocks actually separating the relatively low-pressure vortices. From this observation, it appears that the shocks play a major role in the structure of the flow. The high-pressure regions appear to form an effective barrier between the vortices, possibly inhibiting merging and the growth of the shear layer.

A Localized Supersonic Shear Layer

Numerical simulations of laboratory shear flows are difficult because of the inflow-outflow boundary conditions that characterize most real systems and because of the very extensive

calculations needed to accumulate flow and mixing statistics over long enough times. To circumvent this problem, periodic boundary conditions in the streamwise direction are an often-used numerical idealization in shear-layer mixing calculations. These conditions localize the shear-layer development to the computational domain, but they do not exactly correspond to laboratory flows. The uncertainty of how to treat inflow and outflow boundaries is replaced by the question of how to interpret periodic calculations in terms of experimentally realizeable fluid dynamic systems.

Some of the problems with inflow and outflow boundary conditions are mitigated in supersonic flow calculations, often to be replaced by other numerical difficulties involved with adequately resolving multiple shock interactions and shock-vortex interactions. However, the vortices in a supersonic shear-flow calculation in a laboratory frame of reference form and move quickly out of the computational domain. To study their interactions with shocks and with each other, it would be most useful to focus on a small, localized region of the flow.

In order to isolate the mechanism of shear-layer suppression observed in previous simulations of supersonic shear layers, we have performed a series of calculations in the geometry shown in Figure 3, in which two uniform parallel streams of equal and opposite velocity are separated by a thin plate with a slot in the center [7]. The fluid above and below the plates interact in the region of the slot, and the velocity of the fluid varies from subsonic to supersonic. This geometry was chosen because the region of interaction is localized to the vicinity of the slot which does not move in space. The geometry is similar to periodic flows, but the simulations themselves are spatially evolving because they have inflow and outflow boundary conditions at the edges of the computational domain.

The simulations showed three flow regimes that occurred as the free-stream velocities were varied in the Mach-number range 0.6 to 2.4. In the low Mach-number regime, the flow in the slot initially behaves very much like a periodic temporal simulation, but then evolves into a nearly stationary potential flow. In the high Mach-number regime, a supersonic shear layer results with the formation of strong shocks. Very little mixing occurs between the two streams because the shocks to inhibit vortex formation and growth. In an intermediate transition regime, there are two shocks in the slot whose strength and position vary in time. The two shocks form a roughly antisymmetric configuration bounding a high-pressure region containing a time-varying amount of circulation. In this case, there is more mixing between the layers than in the fast supersonic case or the subsonic case.

Figure 4 shows the evolution of the vorticity during the first 20,000 steps for a flow in the low Mach-number regime (Mach number 0.6 and velocity 200 m/s). The flow initially behaves like a temporally evolving simulation with periodic boundary conditions. Four small vortices form in the slot, two of these move towards the center of the system and two become attached to the edges of the slot. Eventually the two vortices in the center merge to form one large vortex and small asymmetries appear in the flow. By step 12,000, the large vortex has moved from the center and by step 20,000, the vortex has been blown out of the system leaving essentially a potential flow. Pressure contours (not shown) show that weak shocks form in the

vicinity of the plate, even at inflow speeds as low as of 200 m/s. This same general flow evolution and final state is seen up to speeds of approximately 400 m/s, although the shocks near the plates become stronger as the velocity increases.

Figure 5 shows vorticity and pressure contours for the case where the free-stream velocity is 800 m/s, corresponding to a Mach number of 2.4. At these supersonic flow velocities, the streams do not appear to interact strongly even though essentially all the vorticity in the slot initially stays there during the course of the calculation. The flow speed is so high that each stream cannot change direction enough to turn around the edge of the slot, as occurred in the lower-speed cases. The streams are somewhat deflected because of low-pressure regions that form near the plate edges, but this displacement causes a strong shock to form in the oncoming stream from the other direction. The pressure increase of this shock prevents the deflection from growing enough for a potential flow to form.

Thus the dynamics of the flow itself continually act to restore the shear layer. As in unsteady flows at lower velocities, when a vorticity layer thins there is a natural tendency for the layer to roll up. This motion here would lift the thickening knot of vorticity into the supersonic stream. However, this displaced vortex layer now collides with the fast flow above it and forms a strong shock. The high-pressure region corresponding to this shock drives the shear layer back toward its equilibrium position. Even far from the slot edge, the velocity associated with the vortical structures is not high enough to overcome the restoring forces generated by the flow. The vortical structures that do form are driven back into line by the high-pressure associated with the strong shocks. Thus the vorticity in the slot stays there with the net effect that the shear layer bounces up and down slightly. The resulting flow does not seem to approach a steady state, but very little mixing is observed because the vorticity cannot separate into coherent structures. Then the shocks rapidly weaken and vorticity moves downstream. This process, in which high-pressure regions keep vortices from moving in the transverse direction, is one mechanism by which vortex merging is inhibited.

The Role of Turbulence in Detonations

A detonation is a shock wave driven by local energy release. The energy can come from exotheromic chemical reactions in the material itself, or it can come from, for example, laser-energy deposition. Generally, the front of a detonation is not a single planar shock wave, but instead a system of dynamically evolving and interacting incident shocks, Mach stems, and transverse shocks. The region immediately behind the incident shocks and Mach stems is extremely noisy and looks very turbulent. Only in the most ideal cases is it very ordered and regular. Recently the role of turbulence in detonations has become a subject of some discussion. Turbulence could be important in 1) the shock-to-detonation transition, 2) the deflagration-to-detonation transition, and 3) detonation propagation itself. How and if turbulence can affect detonations is potentially important for understanding detonation phenomena and the potential role of detonations in reacting shear layers such as those discussed above. Here we briefly discuss each of these and leave a more detailed discussion to a future paper [8].

The fundamental physical mechanisms in detonation propagation are convection and energy release from chemical reactions. In addition to these, molecular and thermal diffusion are also fundamental mechanisms in flame propagation. In a deflagration-to-detonation transition, the characteristic energy release rates and flow velocities are fast enough that the diffusion processes must become negligible. This transition can occur through a number of mechanisms. One mechanism is very similar to that described above in a shock-to-detonation transition: hot spots can form behind a flame front and these spots generate pressure waves that result in an increase in flame velocity, eventually leading to detonation. The pressure waves could directly accelerate the flame by increasing the pressure behind the front. They can indirectly cause the flame front to become distorted, so that its surface area is increased, more energy is released, and the flame front seems to move faster. These mechanisms are the result of pressure disturbances generated by a noisy or turbulent flow behind the flame and these disturbances directly or indirectly accelerate the flame front.

The final issue is the effect of turbulence generated by a propagating detonation. The question here is where is the turbulence and what can its effects be. In the regions behind the leading shock fronts, there is a spectrum of pressure fluctuations in both the fully reacted material and the reaction zones. A major effect of such perturbations is to accelerate the initiation process. They provide a mechanism of reinitiation of the triple points by causing hot spots in either the reaction zones behind the Mach stem or incident shock or by speeding up the reactions in any unreacted gas pockets cut off by transverse waves.

A source of some of these fluctuations could be Kelvin-Helmholtz instabilites at slip lines behind the shock fronts. The major effect here would not necessarily be convective mixing, which is normally associated with such shear-layer instabilities, but the noise generated by the compressible turbulent flow. It is not yet clear, however, how important these fluctuations are relative to fluctuations generated by the chemical-acoustic processes in nonequilibrium flows.

Acknowledgments

This work was sponsored by the Naval Research Laboratory through the Office of Naval Research and by the Defense Advanced Research Projects Agency in the Applied and Computational Mathematics Program in the Defense Advanced Research Projects Agency and done in consultation and collaboration with John Gardner, Theodore Young, Raafat Guirguis, and Bakhtier Farouk.

References

1. J.P. Boris and D.L. Book, Solution of the Continuity Equation by the Method of Flux-Corrected Transport, *Methods in Computational Physics*, 16: 85–129, 1976.
2. E.S. Oran and J.P. Boris, *Numerical Simulation of Reactive Flow*, Elsevier, New York, 1987.
3. F.F. Grinstein and R.H. Guirguis, to be submitted to *J. Comput. Physics*, 1989.
4. F.F. Grinstein, R.H. Guirguis, J.P. Dahlburg, and E.S. Oran, Three-Dimensional Numerical simulation of Compressible, Spatially Evolving Shear Flows, to appear in *Proceedings of the Eleventh International Conference on Numerical Methods in Fluid Dynamics*, Springer, New York, 1988.

5. R. Guirguis, F. Grinstein, T. Young, E. Oran, K. Kailasanath, and J. Boris, Mixing Enhancement in Supersonic Shear Layers, AIAA Paper No. 87-0373, 1987.
6. A. Roshko, *AIAA J.*, 14, 1349, 1976.
7. J.P. Boris, E.S. Oran, J.H. Gardner, K. Kailasanath, and T.R. Young, Jr., Computational Studies of a Localized Supersonic Shear Layer, AIAA Paper No. 89-0125, AIAA, Washington, DC, 1989.
8. E.S. Oran, The Role of Turbulence in Detonations, in preparation, 1988.
9. K. Kailasanath and E.S. Oran, 1983, Ignition of Flamelets behind Incident Shock Waves and the Transition to Detonation, *Combust. Sci. Tech.* 34, 345.

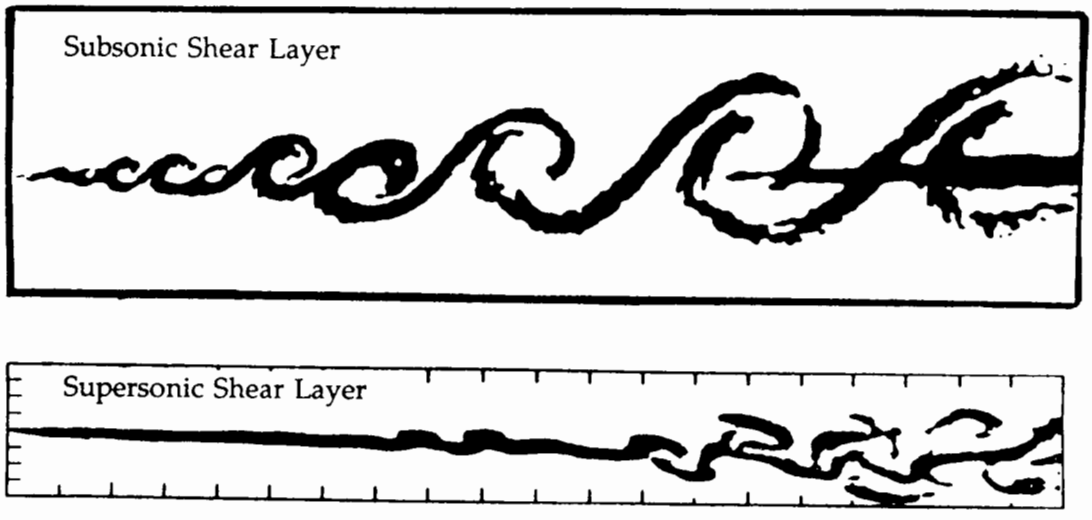

Figure 1. Comparison of an experimental shadowgraph of a subsonic mixing layer [6] and a numerical calculation of the mixing ratio in a supersonic mixing layer [5].

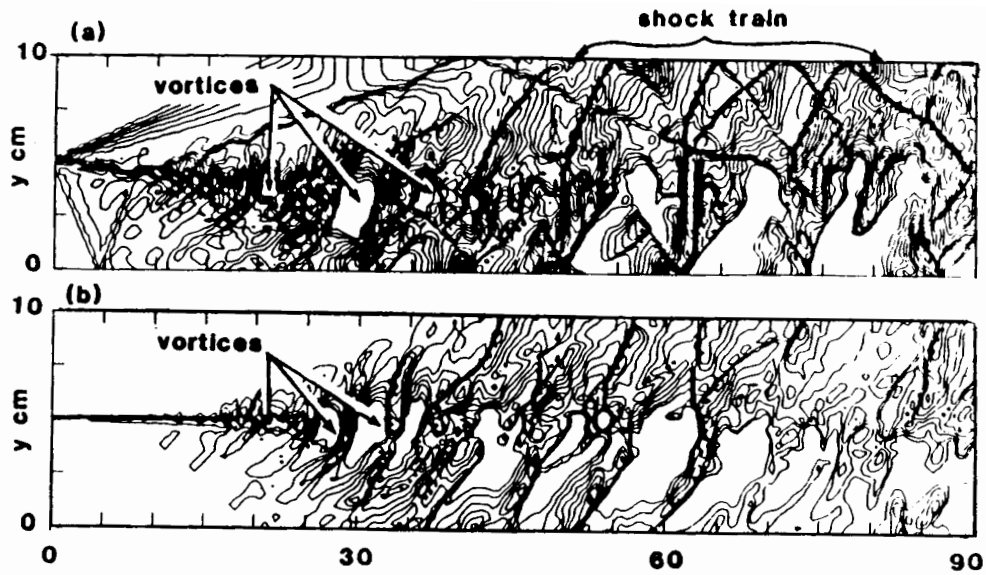

Figure 2. Calculated density contours for an (a) underexpanded confined and (b) an equal pressure unconfined supersonic shear layer [5].

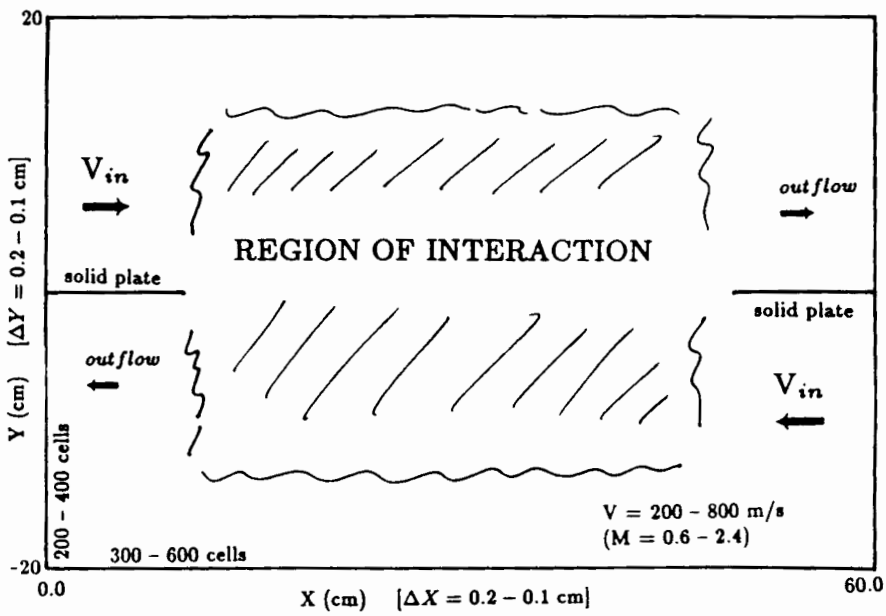

Figure 3. Schematic of the computational region of the localized shear layer simulation.

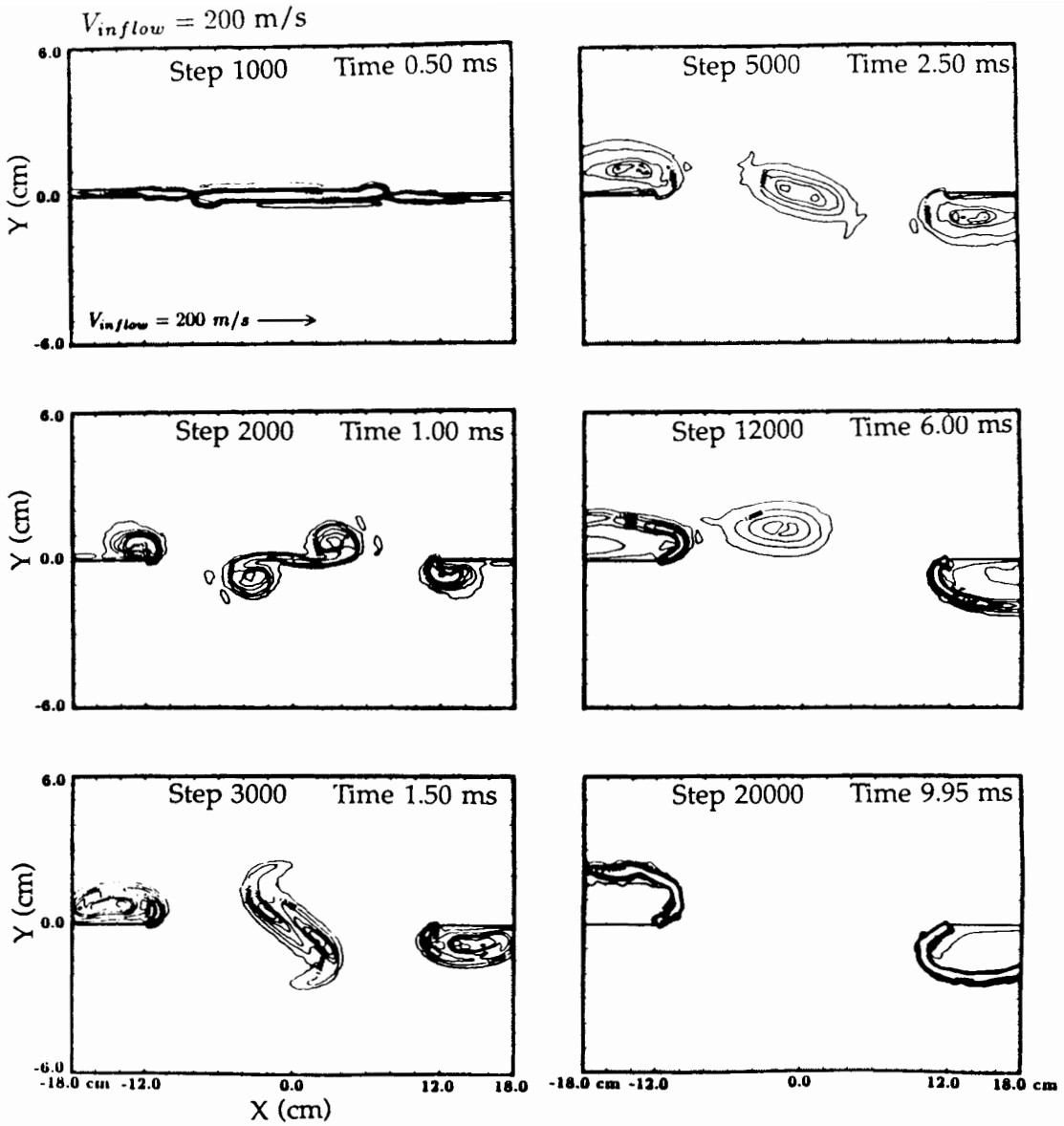

Figure 4. Computed vorticity contours for the subsonc localized shear layer.

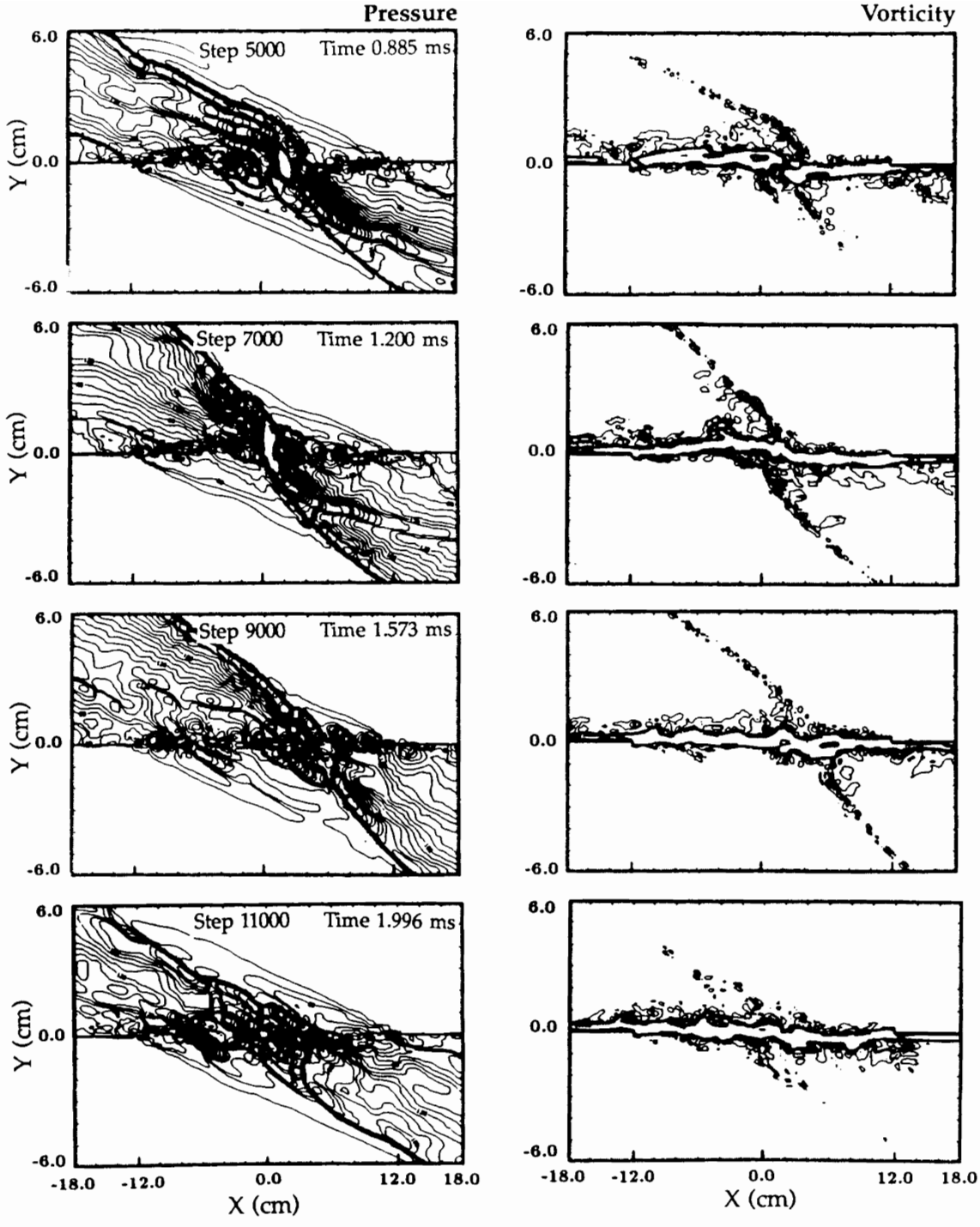

Figure 5. Computed pressure and vorticity contours for the high-speed supersonic localized supersonic shear layer.

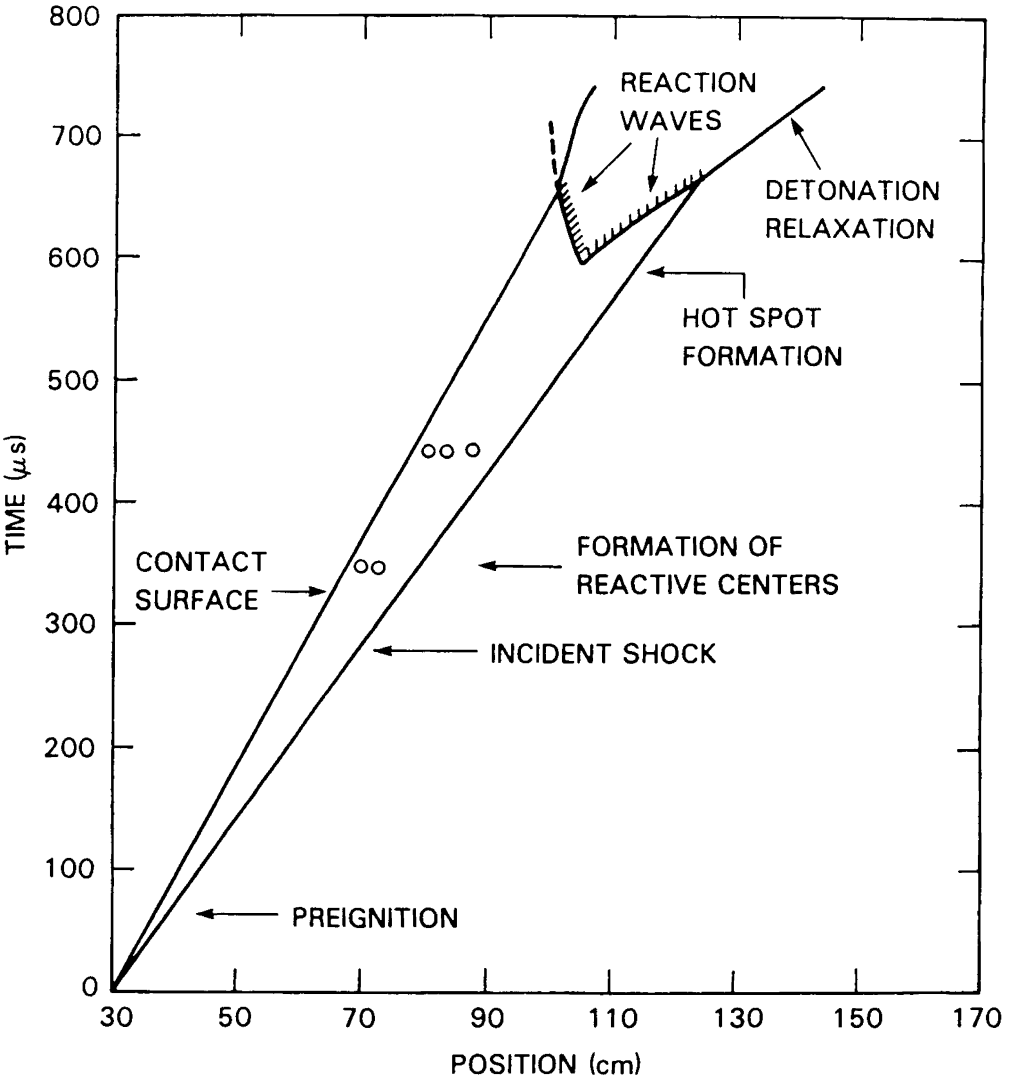

Figure 6. Time-history of the important waves in the system in a computation of a bursting diaphragm shock in a hydrogen-oxygen mxiture [9]. A circle between the incident shock wave and the contact surface represents the location of reactive centers or hot spots, one of which eventually becomes a reaction wave and then a detonation.

ESSENTIALLY NON-OSCILLATORY SHOCK CAPTURING METHODS APPLIED TO TURBULENCE AMPLIFICATION IN SHOCK WAVE CALCULATIONS

Stanley Osher[1]
Department of Mathematics
University of California
Los Angeles, CA 90024

Chi-Wang Shu[2]
Division of Applied Mathematics
Brown University
Providence, RI 02912

ENO (essentially non-oscillatory) schemes can provide uniformly high order accuracy right up to discontinuities while keeping sharp, essentially non-oscillatory shock transitions. Recently we obtained an efficient implementation of ENO schemes based on fluxes and TVD Runge-Kutta time discretizations. The resulting code is very simple to program for multi-dimensions. ENO schemes are especially suitable for computing problems with BOTH discontinuities AND fine structures in smooth regions, such as shock interaction with turbulence, for which results for one dimensional and two dimensional Euler equations are presented. We observe much better resolution by using third order ENO schemes than by using second order TVD schemes for such problems.

Efficient Implementation of ENO Schemes

The solutions to systems of hyperbolic conservation laws of the type

$$\mathbf{u}_t + \sum_{i=1}^{d} \mathbf{f}_i(\mathbf{u})_{x_i} = 0 \quad (\text{or } = g(\mathbf{u}, \mathbf{x}, t), \text{ a forcing term}) \tag{1.1a}$$

$$\mathbf{u}(\mathbf{x}, 0) = \mathbf{u}^0(\mathbf{x}) \tag{1.1b}$$

where $\mathbf{u} = (u_1, \ldots, u_m)^T$, $\mathbf{x} = (x^1, \ldots, x^d)$, and for real $\xi = (\xi_1, \ldots, \xi_d)$, the combination $\sum_{i=1}^{d} \xi_i \frac{\partial \mathbf{f}_i}{\partial \mathbf{u}}$ is assumed to have m real eigenvalues and a complete set of eigenvectors, may develop discontinuities (shocks, contact discontinuities, etc.) regardless of the smoothness of the initial condition. Examples of (1.1) include Euler equations of gas dynamics. ENO schemes, originally constructed by Harten, Osher, Engquist and Chakravarthy [1-4], use a local adaptive

[1]Research supported by NSF Grant No. DMS85-03294, DARPA Grant in the ACMP Program, ONR Grant N00014-86-K-0691, NASA Langley Grant NAG-1-270
[2]Research supported by NSF Grant No. DMS88-10150

stencil to obtain information automatically from regions of smoothness when the solution develops discontinuities. As a result, approximations using these methods can obtain uniformly high order accuracy right up to discontinuities, while keeping a sharp essentially non-oscillatory shock transition. The original ENO schemes in [1-4] used a cell-average framework which involved a reconstruction procedure to recover accurate point values from cell averages, and a Lax-Wendroff procedure (replacing time derivatives by space derivatives, using the P.D.E.) for the time discretization. This can become a bit complicated for multi-dimensional problems [1]. For ease of implementation we constructed [7, 8] ENO schemes applying the adaptive stencil idea to the numerical fluxes and using a TVD Runge-Kutta type high order time discretization. These ENO schemes skip the reconstruction step and the Lax-Wendroff time discretization procedure, hence the resulting code is simple for multi-space dimensional problems.

Let us describe our scheme first in scalar, one dimensional case ($d = m = 1$ in (1.1)). The scheme, in its method-of-lines form, is

$$\frac{du_j}{dt} = L(u)_j \equiv -\frac{1}{\Delta x}(\hat{f}_{j+\frac{1}{2}} - \hat{f}_{j-\frac{1}{2}}) \tag{1.2}$$

where the numerical flux $\hat{f}_{j+\frac{1}{2}}$ approximates $h(x_{j+\frac{1}{2}})$ to a high order, with $h(x)$ defined by

$$f(u(x)) = \frac{1}{\Delta x}\int_{x-\frac{\Delta x}{2}}^{x+\frac{\Delta x}{2}} h(\xi)d\xi \tag{1.3}$$

We first obtain the primitive function of $h(x)$:

$$H(x) = \int_{-\infty}^{x} h(\xi)d\xi \tag{1.4}$$

at $x_{j+\frac{1}{2}}$ by

$$H(x_{j+\frac{1}{2}}) = \int_{-\infty}^{x_{j+\frac{1}{2}}} h(\xi)d\xi = \sum_{k=-\infty}^{j}\int_{x_{k-\frac{1}{2}}}^{x_{k+\frac{1}{2}}} h(\xi)d\xi = \Delta x \sum_{k=-\infty}^{j} f(u_k), \tag{1.5}$$

then construct polynomials interpolating $\{H_{j+\frac{1}{2}}\}$ in an ENO fashion, i.e. by obtaining a locally "smoothest" stencil starting from one or two points, then adding one point to the stencil at each stage by comparing two divided differences and choosing the one which is smaller in absolute value. $\hat{f}_{j+\frac{1}{2}}$ is then taken as the derivative of this interpolating polynomial evaluated at $x_{j+\frac{1}{2}}$. "Upwinding" is achieved by the initial choice in the stencil-choosing process, and it is also crucial for the evident stability of these methods. We also need an entropy fix in any "expansion shock cell". For details, see [7, 8].

The time discretization of (1.2) is implemented via a class of TVD Runge-Kutta type methods [7]. For example, the third order case is

$$u^{(1)} = u^{(0)} + \Delta t L(u^{(0)}) \tag{1.6a}$$

$$u^{(2)} = \frac{3}{4}u^{(0)} + \frac{1}{4}u^{(1)} + \frac{1}{4}\Delta t L(u^{(1)}) \tag{1.6b}$$

$$u^{(3)} = \frac{1}{3}u^{(0)} + \frac{2}{3}u^{(2)} + \frac{2}{3}\Delta t L(u^{(2)}) \tag{1.6c}$$

$$u^{(0)} = u^n, \; u^{n+1} = u^{(3)} \tag{1.6d}$$

This class of Runge-Kutta methods was shown to have the property that the total variation of the spatial part is not increased during the time discretization under a suitable restriction on $\frac{\Delta t}{\Delta x}$.

For multi-dimensions the right-hand-side of (1.2) is applied to each of the terms $f_i(u)_{x_i}$ in (1.1a), keeping all other variables fixed. The Runge-Kutta methods such as (1.6) can still be applied.

For nonlinear systems, we simply apply the algorithms in each local characteristic field. We take an 1-dimensional system to exemplify this process. Let $A_{j+\frac{1}{2}}$ be some "average" Jacobian at $x_{j+\frac{1}{2}}$. Examples include $A_{j+\frac{1}{2}} = \frac{\partial \mathbf{f}}{\partial \mathbf{u}}\big|_{\mathbf{u}=\frac{1}{2}(\mathbf{u}_j+\mathbf{u}_{j+1})}$ or, in the case of Euler equations of gas dynamics $A_{j+\frac{1}{2}} = \frac{\partial \mathbf{f}}{\partial \mathbf{u}}\big|_{\mathbf{u}=\mathbf{u}^{(\mathrm{Roe})}_{j+\frac{1}{2}}}$ where $\mathbf{u}^{(\mathrm{Roe})}_{j+\frac{1}{2}}$ is the Roe average of $\mathbf{u}_j$ and $\mathbf{u}_{j+1}$ [6]. We then use the eigenvalues of $A_{j+\frac{1}{2}}$, project to the local characteristic fields: and finally apply our scalar algorithms in each of these fields. See [8] for more details.

2. Numerical Tests – Shock Interaction with Turbulence

Example 1. We start with one dimensional Euler equations of gas dynamics for a polytropic gas, i.e. (1.1) with $d = 1$, $m = 3$, and

$$\mathbf{u} = (\rho, M, E)^T, \quad \mathbf{f}(\mathbf{u}) = q\mathbf{u} + (0, P, qP)^T \tag{2.1a}$$

where

$$P = (\gamma - 1)(E - \frac{1}{2}\rho q^2), \quad M = \rho q \tag{2.1b}$$

We use $\gamma = 1.4$, and an initial condition

$$\begin{cases} \rho = 3.857143; & q = 2.629369; \quad P = 10.333333 \quad \text{when } x < -4 \\ \rho = 1 + \varepsilon \sin 5x; & q = 0; \quad P = 1 \qquad\qquad\quad \text{when } x \geq -4 \end{cases} \tag{2.2}$$

If $\varepsilon = 0$, this is a pure Mach $= 3$ shock moving to the right.

For a detailed linearized analysis see [5]. This linearized analysis, predicts fine structures for the density profile because of the different propagation speeds of entropy and acoustic waves. For

ε small (say $\varepsilon = 0.05$) we observe results close to linearized analysis. For $\varepsilon = 0.2$ we can observe nonlinear effects such as additional small shocks in the density profile.

This is a good test problem because both shocks and fine structures in smooth regions exist. Traditional high order methods will develop oscillations near shocks, and TVD methods, while nonlinearly stable, will lose resolution for the fine structures because of the degeneracy to first order accuracy at smooth critical points.

In Figure 1-4, the solid lines are numerical solutions of third order ENO scheme (henceforth shortened to ENO-3) with 1600 grid points. This can be regarded as a converged solution. From Figure 1, we see that ENO-3 with 400 points almost gives a converged solution, while TVD-2 (a second order MUSCL type TVD scheme) with 800 points just has roughly the same resolution as ENO-3 with 200 points. On the other hand, the improvement of ENO-3 over TVD-2 is not so significant for the velocity and pressure profiles (Figure 2), because they both lack any detailed structure.

To further exemplify the advantage of higher order methods, we increase the spatial order of our ENO scheme and compare density and entropy profiles with 300 grid points using ENO-3, 4, 5, 6. We clearly observe better resolution by going to higher spatial orders (Figure 3). In Figure 3 the time discretization is third order (1.6) with Δt decreased for high spatial orders. When we use higher order time discretizations as well we observe further improvements in resolution (pictures not included).

We finally test the effect of physical viscosities by solving the Navier-Stokes equation, i.e. (1.1)-(2.1) with a right-hand-side

$$(0, \frac{4}{3} \cdot \frac{1}{\mathrm{Re}} q_{xx},\ \frac{1}{\mathrm{Re}} \cdot \frac{2}{3}(q^2)_{xx} + \frac{1}{(\gamma-1) \cdot P_r \cdot \mathrm{Re} \cdot M^2}(\frac{E}{\rho} - \frac{1}{2}q^2)_{xx})^T \tag{2.3}$$

We used $Pr = 1,\ M = 3$ and gradually increased the Reynolds number Re. Clearly we observe (Figure 4) convergence to Euler's result as the physical viscosity goes to zero ($\mathrm{Re} \to \infty$). To verify the theory (rigorously proven by Kreiss) that for wave lengths $> c \cdot \frac{1}{\sqrt{\mathrm{Re}}}$ the problem is viscosity dominated and otherwise essentially inviscid, we re-ran our result with a different frequency for the sine wave. We do observe the correctness of the above theory with $c \approx 3$ in our scaling. The pictures are omitted.

Example 2. Next we come to two dimensional Euler equations, i.e. (1.1) with $d = 2,\ m = 4$, and (we use $\mathbf{f}, \mathbf{g}, x, y$ instead of $\mathbf{f}_1, \mathbf{f}_2, x_1, x_2$):

$$\begin{gathered} \mathbf{u} = (\rho, M_x, M_y, E)^T, \quad \mathbf{f}(\mathbf{u}) = \mathbf{q}_x \mathbf{u} + (0, P, 0, q_x P)^T \\ \mathbf{g}(\mathbf{u}) = q_y \mathbf{u} + (0, 0, P, q_y P)^T \end{gathered} \tag{2.4a}$$

where

$$P = (\gamma - 1)(E - \frac{1}{2}\rho q^2), \quad q^2 = q_x^2 + q_y^2, \quad M_x = \rho q_x, \quad M_y = \rho q_y \tag{2.4b}$$

The test problem we choose is a moving shock interacting with compressible turbulence [9, 10]. At $t = 0$, a Mach 8 shock at $x = -1.0$ is moving into a state with $P_R = 1, \quad \rho_R = 1$ and $q_x = -\frac{C_R}{P_R}\sin\theta_r \cos(xk_R\cos\theta_R + yk_R\sin\theta_R), \quad q_y = \frac{C_R}{P_R}\cos\theta_R\cos(xk_R\cos\theta_R + yk_R\sin\theta_R)$ where $k_R = 2\pi, \theta_R = \frac{\pi}{6}$, and $C_R = \sqrt{\frac{\gamma P_R}{\rho_R}}$. We display the results at $t = 0.20$ in Figure 5. Notice that in [9, 10] similar results were obtained using a shock-fitting rather than a shock capturing method. This is actually a two dimensional analogue of Example 1 – a combination of shocks and fine structures in smooth regions. Hence it is again a good test problem for the high order ENO schemes. The successful computation of this example shows that ENO schemes have excellent potential for shock-turbulence computations.

Acknowledgements: We thank David Gottlieb, Ami Harten, Lawrence Sirovich and Thomas Zang for many helpful discussions and suggestions.

References

[1] A. Harten, Preliminary results on the extension of ENO schemes to two-dimensional problems, in Proceedings of the International Conference on Hyperbolic Problems, Saint-Etienne, January 1986.

[2] A. Harten and S. Osher, Uniformly high order accurate non-oscillatory schemes, I, SIAM J. Numer. Anal., 24 (1987), pp. 279-309.

[3] A. Harten, B. Engquist, S. Osher and S. Chakravarthy, Uniformly high order accurate essentially non-oscillatory schemes, III, J. Comput. Phys., 71 (1987), pp. 231-303.

[4] A. Harten, S. Osher, B. Engquist and S. Chakravarthy, Some results on uniformly high order accurate essentially non-oscillatory schemes, J. Appl. Numer. Math., 2 (1986), pp. 347-

[5] J. McKenzie and K. Westphal, Interaction of linear waves with oblique shock waves, Phys. Fluids, 11 (1968), pp. 2350-2362.

[6] P. Roe, Approximate Riemann solvers, parameter vectors, and difference schemes, J. Comput. Phys., 43 (1981), pp. 357-372.

[7] C.-W. Shu and S. Osher, Efficient implementation of essentially non-oscillatory shock capturing schemes, J. Comput. Phys., 77 (1988), pp. 439-471.

[8] C.-W. Shu and S. Osher, Efficient implementation of essentially non-oscillatory shock capturing schemes, II, ICASE Report 88-24, J. Comput. Phys., to appear.

[9] T. Zang, M. Hussaini and D. Bushnell, Numerical computations of turbulence amplification in shock-wave interactions, AIAA J., 22 (1984), pp. 13-21.

[10] T. Zang, D. Kopriva and M. Hussaini, Pseudospectral calculation of shock turbulence interactions, in Proceedings of Numerical Methods Conference, C. Taylor et al, eds., Pineridge Press, Swansea, U.K., (1984), pp. 210-221.

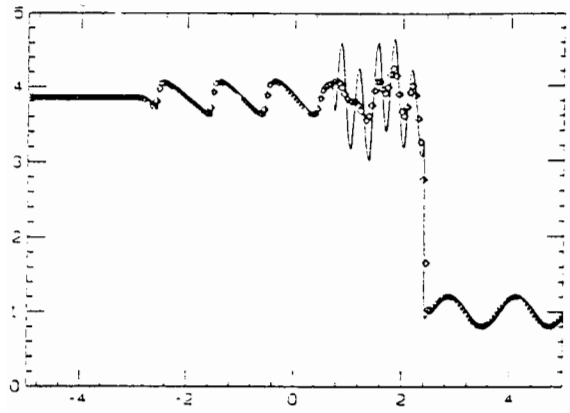

1(a): ENO-3 with 200 points

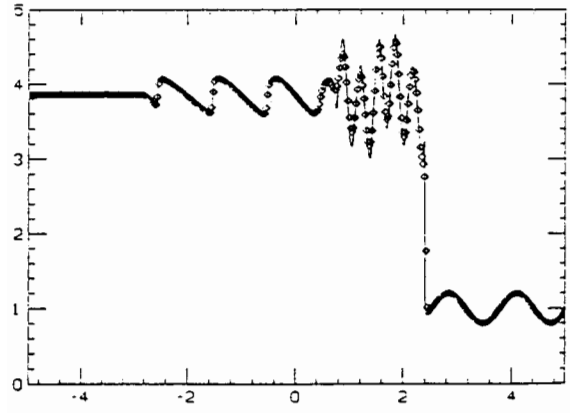

1(b): ENO-3 with 400 points

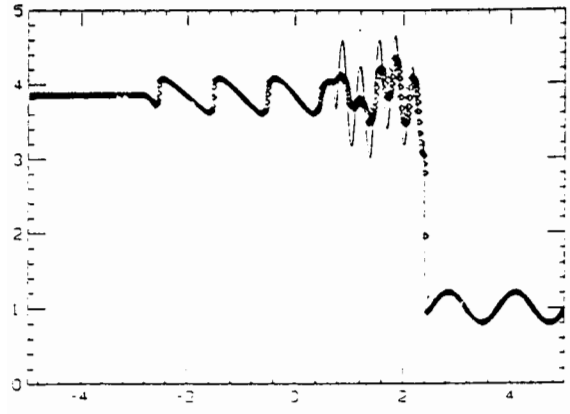

1(c): TVD-2 with 800 points

Figure 1: density

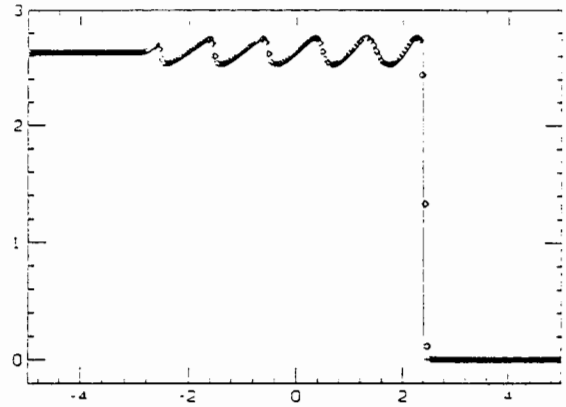

2(a): ENO-3, velocity

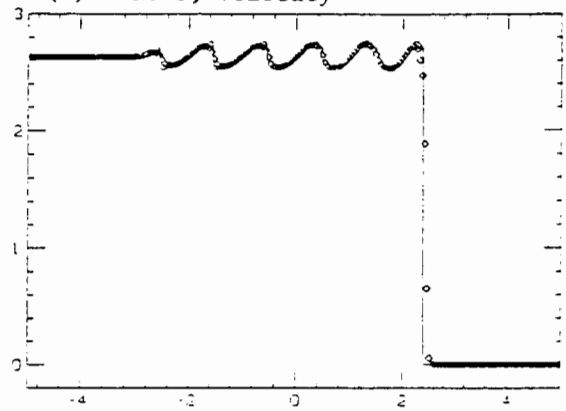

2(b): TVD-2, velocity

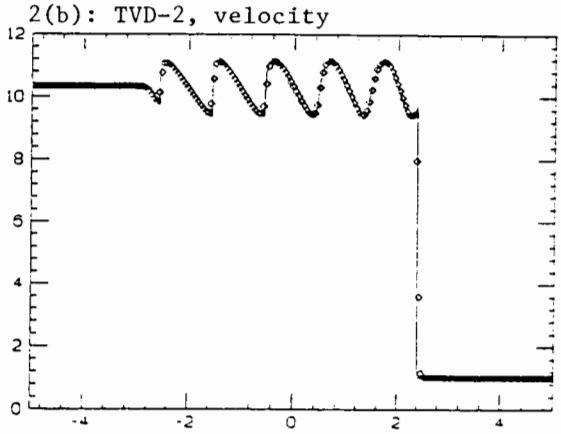

2(c): ENO-3, pressure

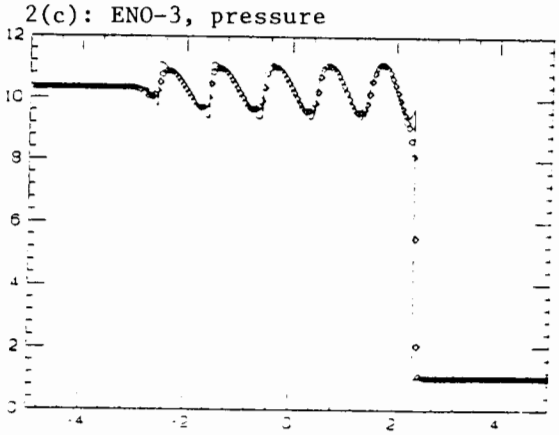

2(d): TVD-2, pressure

Figure 2: 200 points

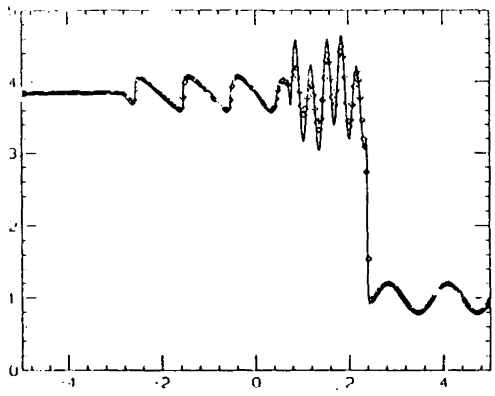

3(a): ENO-3

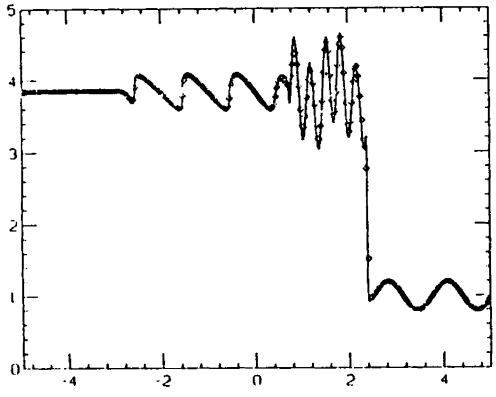

3(b): ENO-4

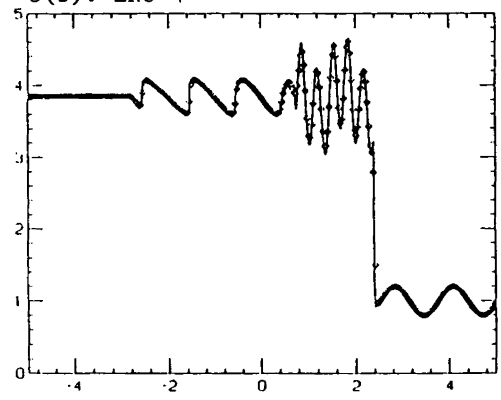

3(c): ENO-5

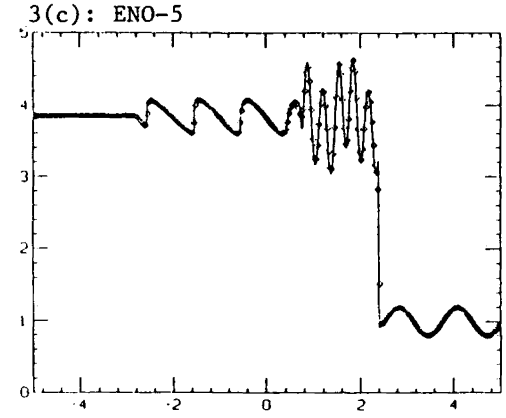

3(d): ENO-6

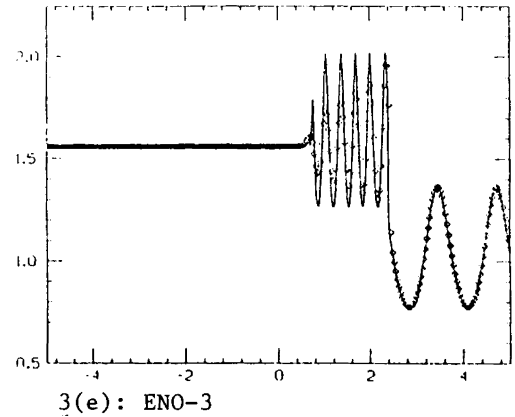

3(e): ENO-3

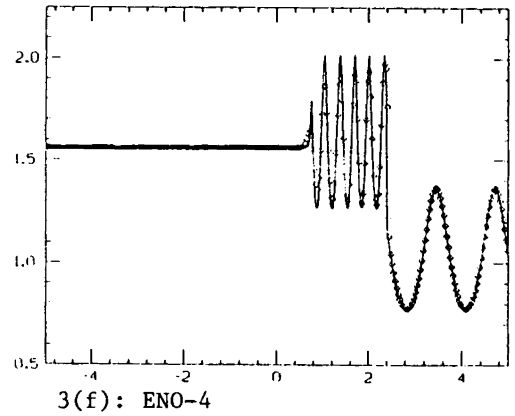

3(f): ENO-4

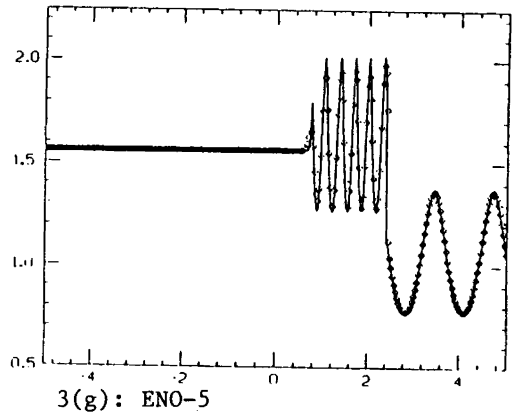

3(g): ENO-5

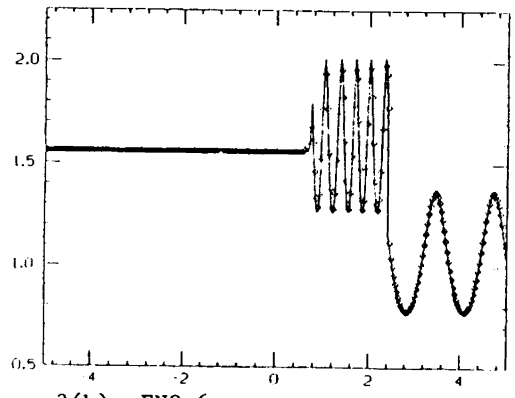

3(h): ENO-6

Figure 3: 300 points, density (left) and entropy (right)

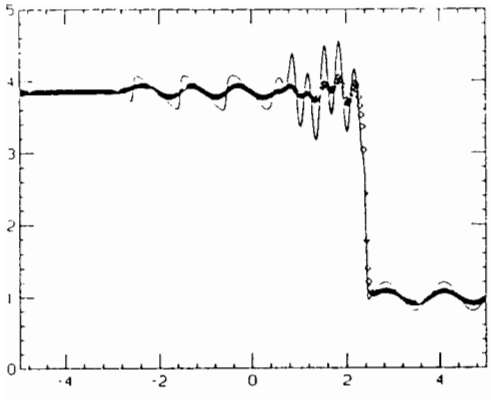

4(a): Re = 10

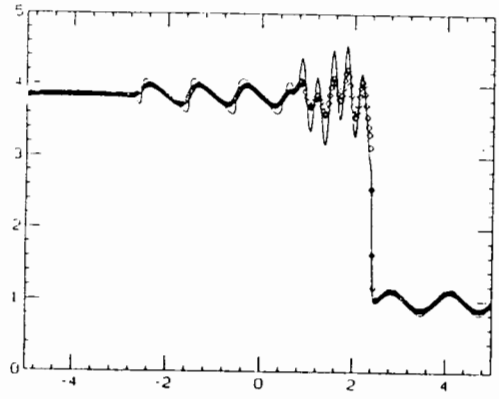

4(b): Re = 20

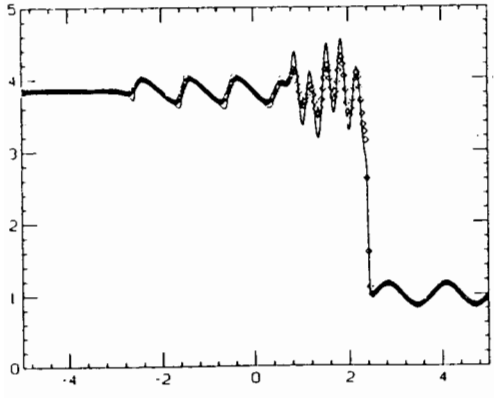

4(c): Re = 30

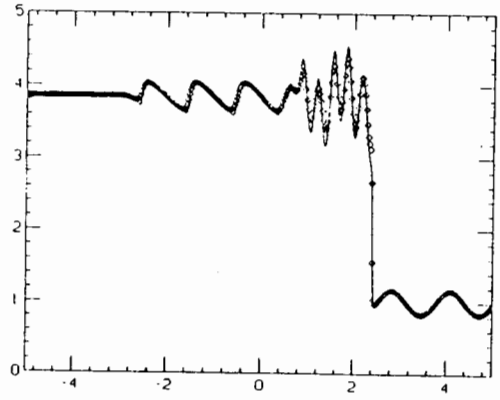

4(d): Re = 50

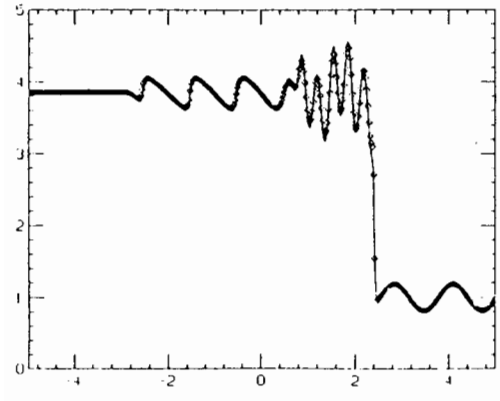

4(e): Re = 100

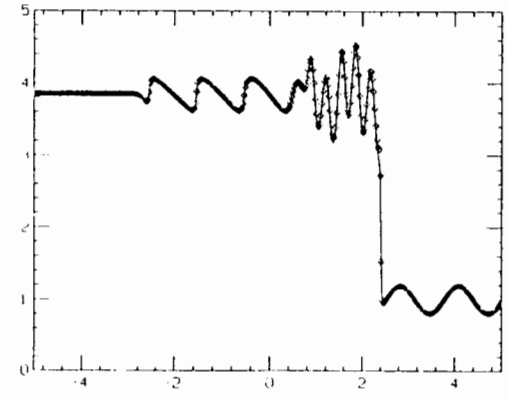

4(f): Re = 200

Figure 4: ENO-3 with 400 points for Navier-Stokes equation.
The solid line is for the solution of Euler's equation.

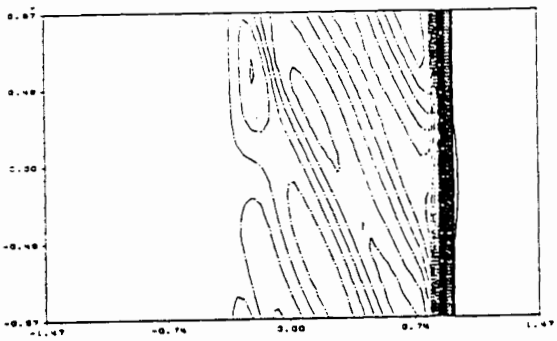

5(a): 60 x 40 points, pressure

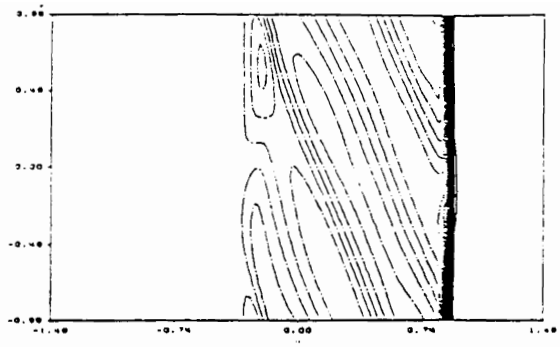

5(d): 120 x 80 points, pressure

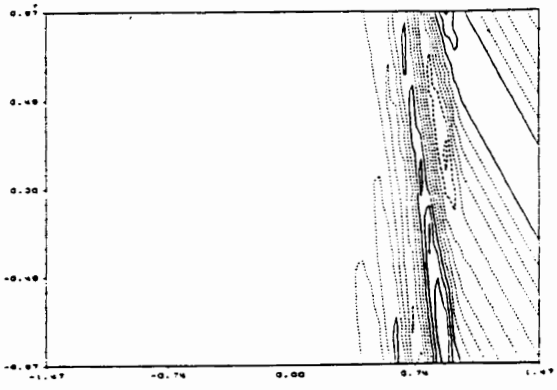

5(b): 60 x 40 points, vorticity

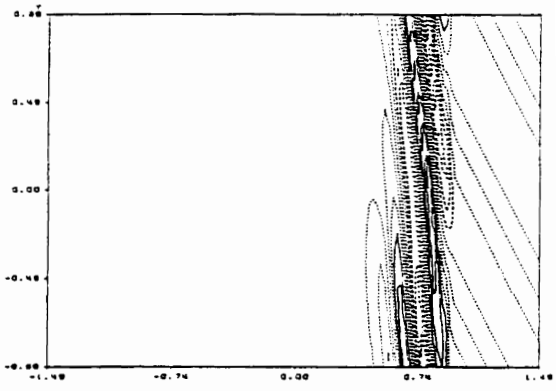

5(e): 120 x 80 points, vorticity

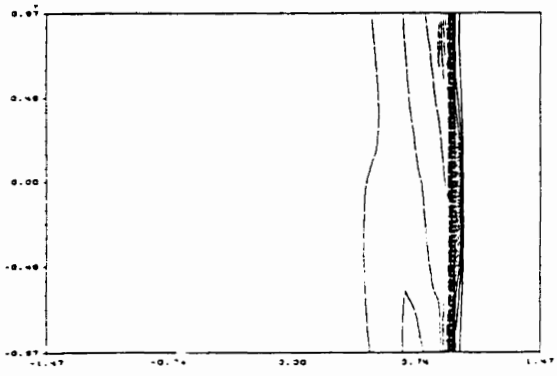

5(c): 60 x 40 points, entropy

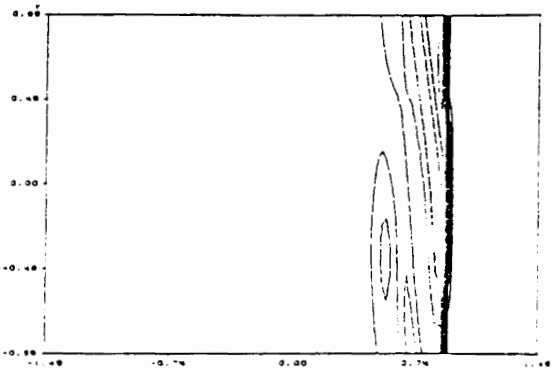

5(f): 120 x 80 points, entropy

Figure 5: ENO-3

SHOCK-GENERATED TURBULENCE

J. M. Picone and J. P. Boris
Laboratory for Computational Physics and Fluid Dynamics
Naval Research Laboratory, Washington, D. C. 20375

Abstract

We review our theoretical and numerical results on the initiation of turbulence by shocks. Problems which have been addressed include turbulent cooling of laser and electric discharge channels in a gas, shock-flame interactions, and shock propagation through inhomogeneous fluids. The central issue is the identification of a nonlinear mechanism underlying the production of turbulence in an inviscid medium by flows that are initially irrotational with local density and pressure gradients aligned. The basis for our theory is the observation that vorticity is generated when the local pressure and density distributions are misaligned. The theory is nonlinear and supersedes linear treatments of shock-flame and shock-bubble interactions. In the case of hot, gaseous channels, no appropriate theory had existed beforehand. As an example, we present numerical simulations and analytic models which have given useful descriptions of evolving, hot, gaseous channels. This work has led to a successful method of suppressing turbulence in channels produced by lasers.

I. Introduction

Experimental data on a variety of transient, compressible flows in inhomogeneous gases have shown that long wavelength disturbances occur at the boundaries of fluid structures near which shocks have been produced or through which shocks have propagated. As time passes, these disturbances can evolve into one or more vortex structures, and smaller scale disturbances and turbulent motion become superposed on the structures. In addition, mixing with the ambient gas can occur on time scales that are much shorter than nonturbulent diffusive processes would allow. This further supports the interpretation that the motion has become turbulent. Examples of such phenomena include the turbulent cooling of lightning, laser, and laboratory discharge channels in a gas [1, 2], shock-flame interactions [3], and shock propagation through inhomogeneous, compressible fluids [4].

In all of the above cases, the central question has concerned how turbulent flows can be produced by flows that are initially irrotational with local density and pressure gradients aligned. Prior to our work, linear stability theory formed the basis for most theoretical analysis. For interactions of a planar shock with a flame or bubble, an analogy to the impulsive Rayleigh-Taylor or "Richtmyer-Meshkov" instability [5, 6, 7] provided some insights, although other methods had been attempted [4]. In the classical Richtmyer-Meshkov problem, a planar shock strikes a rippled interface separating materials of different density. For the present case, the upstream surface of the bubble corresponds to one-half wavelength of the rippled interface.

Now consider a hot, roughly cylindrical volume of gas heated by a laser pulse or a transient electric discharge and eventually expanding to pressure equilibrium. Gas of progressively lower density is thus accelerating radially against the denser ambient gas. This observation led to an

unsuccessful analogy with the classical, linear (not impulsive) Rayleigh-Taylor instability [8, 9]. The Rayleigh-Taylor problem involves two fluids of different density which are in contact at a perturbed interface. Instability occurs when the lighter fluid accelerates the heavier fluid in a direction normal to the interface. Textbook treatments usually assume that the acceleration is constant over a long period of time.

These approaches have several flaws. First, bubbles deviate significantly from the rippled interface of the Richtmyer-Meshkov problem. In the case of the gaseous channels, the acceleration stage is of finite duration and is followed by a deceleration stage, so that the classical Rayleigh-Taylor picture does not apply. In addition, the physical situations do not involve infinitesimal perturbations, either spatial or temporal, with which linear stability theory begins. These shortcomings imply that a fully nonlinear picture based on the inviscid equation for the evolution of the vorticity $\boldsymbol{\omega}$ is necessary:

$$\frac{D\boldsymbol{\omega}}{Dt} + \boldsymbol{\omega}\nabla \cdot \mathbf{v} = \boldsymbol{\omega} \cdot \nabla \mathbf{v} + \frac{\nabla\rho \times \nabla P}{\rho^2} \ . \tag{1}$$

Here $\mathbf{v}$ is the fluid velocity, P is the pressure, and ρ is the mass density. When the local pressure and density distributions are geometrically misaligned, the baroclinic source term $\mathbf{S} = (\nabla\rho \times \nabla P)/\rho^2$ is nonzero and the generation of vorticity occurs.

The spatial scale of the vorticity distribution is that of the asymmetry between the density and pressure in the flow field, and sizable residual vorticity remains after the driving asymmetry disappears [10]. The subsequent evolution of the fluid to a turbulent state, in which many spatial scales are excited, will not depend on $\mathbf{S}$ unless further asymmetries or shock interactions occur. The theory described below thus treats the *initiation* of turbulence by compressible phenomena. This is an essential part of analyzing the resulting turbulent state in a realistic system.

Direct analytic integration of Eq.(1) in two dimensions with some simplifying assumptions has yielded useful analytic expressions for the residual circulation or vortex strength for each of the phenomena that have been studied [1, 10, 11, 12, 13]. Several categories of vorticity-generating phenomena have emerged during the course of our work on nonmagnetized fluids:

(1) irregular reflections of shock waves from surfaces or nonlinear interactions among shocks,
(2) gas expansion into or wave propagation through a region of nonuniform mass density (e.g., shock-bubble interactions), and
(3) expansion of a heated irregular volume of gas, produced, for example, by asymmetric energy deposition.

To demonstrate the stages of initiation and development of a turbulent state in a realistic, compressible fluid, the next section presents experimental data on turbulent laser or discharge channels in a gas. This falls under the third category, although features of the other categories are present. Section III describes our theoretical approach based on Eq.(1) in greater detail for the example of hot, gaseous channels. Section IV then presents numerical simulations used to calibrate and verify the analytic results.

II. Hot, Turbulent Channels in a Gas

Figure 1 shows a series of Schlieren photographs of electric discharges of duration $\sim 3\mu$s and length 20 cm in air (published previously in references 1 and 2). The numbers below each photograph give the time elapsed (in μs) between firing the discharge and taking the photograph. Each photograph corresponds to a separate discharge. By 8 μs, a hot, smooth channel with a radius of 1.4 cm has formed, and the accompanying shock wave appears as a sharp line at the channel boundary. By 30 μs, the shock is easily identifiable and propagates out of the field of view at a time somewhat greater than 100 μs. At approximately 100 μs, the interior temperature of the channel is $\sim$ 5000 K, the gas density is $\sim 10^{18}$ cm^{-3}, and the electron density is $\sim 10^{14}$ cm^{-3}. The channel remains stable up to that time. By 250 μs, however, density fluctuations are evident at the boundary. The photograph at 900 μs shows that these distortions become more pronounced as more cool air mixes into the channel. The average radius has increased to $\sim$ 2 cm, indicating an increase of $\sim$ 100% in the volume of the channel due to entrainment of the surrounding air. As the time from discharge initiation increases, smaller scale (turbulent) structure appears and by 10 ms the channel has begun to disappear.

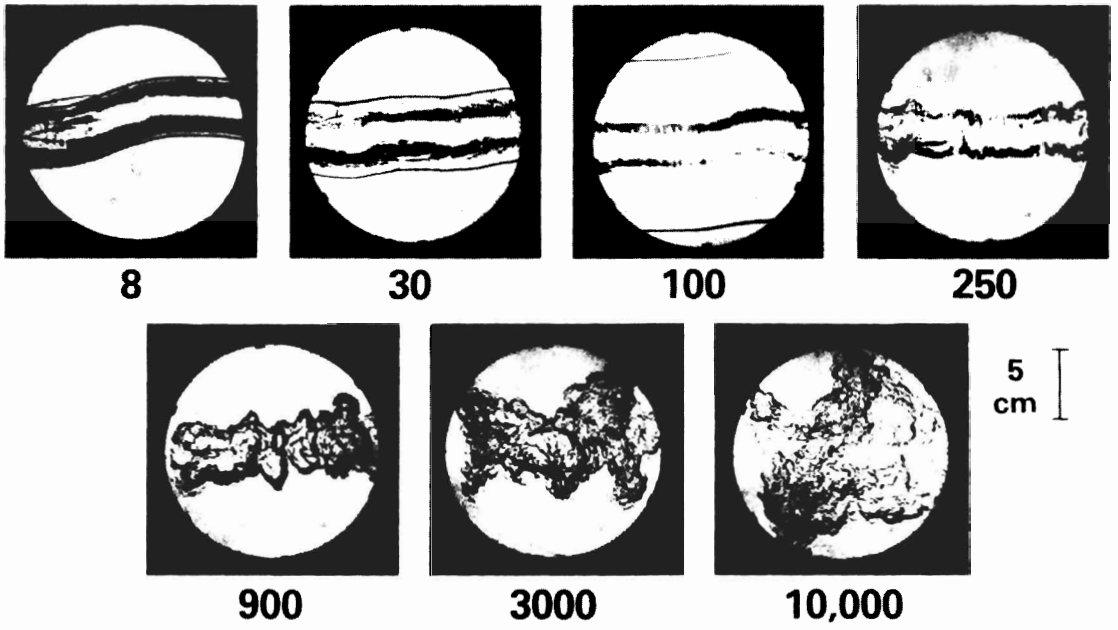

Fig. 1. Series of separate, nominally identical electric discharges in air. The energy deposition before expansion occurred was ~ 40 J/cm^3.

The sequence of events is similar for CO_2 laser channels in nitrogen [2]. Both discharge and laser channels expand diffusively after reaching pressure equilibrium, following the equation

$$R^2(t) = R^2(\tau) + 4\alpha(t - \tau) \quad , \tag{2}$$

where R is the average radius of the cross section at time t, pressure equilibration occurs at time τ, and α is the effective diffusivity. For the electric discharges, $\alpha \sim 500$ cm^2/s, and for the laser

channels, $\alpha \sim 250$ cm^2/s. The kinematic viscosity for air at room temperature is $\nu \approx 0.3$ cm^2/s. This disparity between observations and the nonturbulent diffusivity supports the interpretation that turbulence is present and entrains ambient gas into the channels.

III. Theoretical Approach [10]

To develop a theoretical expression for the effective diffusivity in a hot turbulent channel, one must first estimate the residual vortex strength produced during the expansion of the channel to pressure equilibrium. This requires integration of Eq.(1) for evolving pressure and density distributions which are appropriate to the channel expansion. Such models depend on assumptions about the type of geometrical asymmetry responsible for the generation of vorticity. We have investigated four classes of asymmetry for this problem and others that are closedly related: (1) curvature of the axis along which energy is deposited, as in Fig. 1, (2) deviations from azimuthal (circular) symmetry in the transverse plane, (3) nonuniform energy deposition (i.e., "hot spots") within a roughly circular envelope in the transverse plane, and (4) noncollinear energy deposition by two successive pulses.

To model the evolving density and pressure distributions for the various asymmetry classes, we use the geometrical properties of the density and pressure during and after expansion to pressure equilibrium. The expansion produces a pressure field (shock wave) which has circular symmetry or rapidly approaches it, as verified by numerical simulation [10]. The density field retains the geometrical asymmetry of the initial state, although the various physical proportions are altered and the distribution has expanded. Smooth energy deposition with an elliptical cross section, for example, results in an approximately circular shock wave and a elliptical region of reduced density.

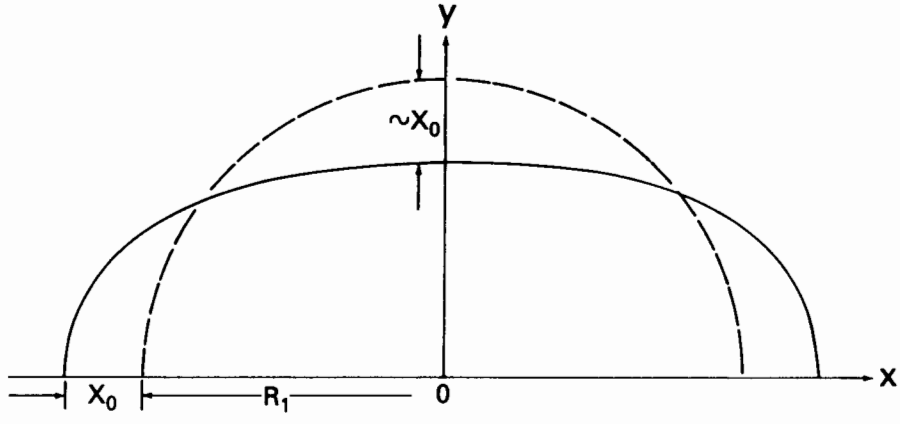

Fig. 2. This schematic shows the upper half of our model flow field for energy deposition with elliptical contours. The solid line shows the envelope of the mass density distribution while the dashed line shows the shape of the model velocity field and pressure distributions. (Published previously in [1])

For this case, Fig. 2 shows that our model uses a time dependent radial flow field and

pressure distribution (dashed line) with an expanding elliptical density distribution (solid line). The expanding flow first accelerates to some maximum speed and then decelerates to zero at pressure equilibrium. Integration of Eq.(1) under these assumptions has shown that the residual flow field can then be represented in terms of one or more pairs of vortices of strength $\pm\kappa$, where

$$\kappa = U[R(\tau) - R(0)] \ln(\rho_\infty/\rho_0)\ f \quad . \tag{3}$$

In Eq.(3), U is a characteristic velocity of expansion to pressure equilibrium; the ambient density is ρ_∞; the density at the center of the channel at time $t = \tau$ is ρ_0; and the form factor $0 \leq f \leq 1$ measures the degree of asymmetry in energy deposition.

As indicated earlier, Eq.(3) describes the initiation of turbulent motion by creating vorticity on the length scale of the asymmetry between the density and pressure fields. The experimental result of Eq.(2), however, is consistent with expansion in a homogeneous turbulent field containing a range of length scales. For the cooling of laser and electric discharge channels, we have derived effective turbulent diffusivities in good agreement with experiment by assuming the following:

(1) A compressible fluid in an unstable state for which the rotational flow is confined to the large scales at early times will evolve into a turbulent state containing a broad spectrum of momentum scales, of which the smallest are determined by dissipative phenomena, such as that due to viscosity.

(2) A coupling exists between the large scale motion and disturbances on the smallest scales, at which dissipation takes place.

(3) The large scale motion determines the rate at which energy is dissipated, in accordance with the simple picture of Kolmogorov and Obukhov (e.g., [14]).

Given these assumptions, the effective diffusivity is [11]

$$\alpha \sim \kappa/4\pi \quad . \tag{4}$$

Equations (3) and (4) along with supporting numerical simulations have provided estimates of the experimental turbulent diffusivity that are accurate to within factors of 50% or better.

IV. Numerical Simulations of a Laser Channel

The most interesting and difficult case was that of a laser pulse with an approximately circular envelope [15]. If the initial energy deposition were truly uniform over the pulse, the form factor f would be zero, since the pressure and density gradients would be aligned during channel expansion to pressure equilibrium. However, the data have given $\alpha \sim 250$ cm^2/s. This led us to postulate the existence of "hot spots" within the envelope, for which we performed the numerical simulation shown in Fig. 3.

For this calculation, we used the code FAST2D, which is based on the Flux-Corrected Transport (FCT) algorithm [16] in conjunction with operator splitting. The grid was Cartesian

with 100 × 100 square cells. Figure 3 shows a central region, consisting of 50 × 50 square cells, where energy was deposited. The cell dimensions increased geometrically outside the uniform central region, so that the boundary was far from the channel. A renormalization of the pressure after shock passage from the region containing the pulse permitted the use of large time steps and reduced the cost of the calculation in following the residual fluid motion [15].

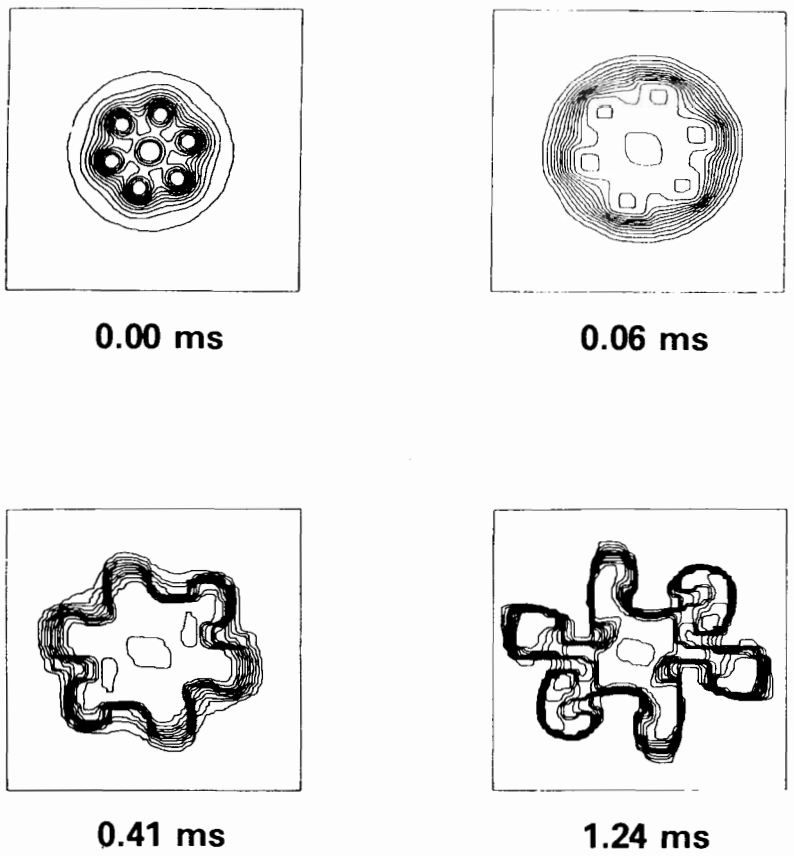

Fig. 3. Numerical simulation of air heated by a laser pulse travelling perpendicular to page and containing "hot spots". The first diagram shows contours of constant pressure just after the pulse has passed through the plane. The remaining diagrams show contours of constant mass density.

All variables except the pressure and internal energy were initially constant and uniform. The diagram at $t = 0$ shows contours of constant pressure. While the envelope was circular, the pressure fluctuated weakly enough in the interior to be at most marginally detectable by laboratory burn patterns. The hot spots produced weak shocks, each of which interacted with the other shocks and swept through the density depressions at the positions of the other hot spots, generating vorticity according to Eq.(1).

The remaining diagrams show contours of constant density at later times. Notice that the

density retains the original asymmetries found in the initial pressure distribution. By $t = 60\mu$s, the shocks passed out of the region, leaving behind a vortex pair near each of the six outer hot spots. The outward motion and interactions of the vortex pairs then distorted the channel and increased its apparent dimensions. By $t = 1.24$ ms, the apparent envelope (as viewed from the side) included a significant amount of ambient gas and the average temperature had decreased on the timescale with which the vortex pairs propagated outward. This calculation indicated that a form factor of $f \sim 1$ was appropriate in Eq.(3); the resulting value of κ gave good agreement with experiment.

The most exciting aspect of the above calculation was the prediction that turbulence could be significantly *suppressed* if nonuniformities in the cross section of the laser pulse were eliminated. Subsequent experiments significantly reduced transverse variations by permitting only axial modes in the pulse. The resulting channel remained "stable" for several milliseconds, giving an effective diffusivity of $\alpha \sim 3$ cm^2/s. This reduction in turbulent mixing by two orders of magnitude confirmed our predictions [2] and demonstrated the practical utility of the theory outlined above.

V. Summary

We have outlined a theoretical approach for determining the initiation of turbulent motion by asymmetric energy deposition within a compressible fluid and by shock interactions with fluids having nonuniform density distributions. Our examples have come from the former category, which is less well known to the fluid dynamics community. The latter work has dealt the interactions of a shock with a flame or bubble, a research area which has experienced a surge in interest over the last few years (e.g., [17]).

In the case of hot, gaseous channels, numerical simulations and experimental data have confirmed our theory for the initiation of turbulent motion and our estimates of the associated turbulent diffusivity in laboratory experiments. The theory also permits the identification of key factors for suppressing turbulence, a potentially valuable capability.

While we were able to obtain useful estimates of the experimental turbulent diffusivities, accurate modeling of the evolution to a turbulent state in a compressible fluid is necessary if better estimates are to be obtained. This calls for detailed analysis of the turbulent spectrum in a compressible fluid, both experimentally and theoretically. Each will require a significant effort. Our work represents an essential first step, providing the "initial conditions" from which the fully turbulent state forms.

Acknowledgements

The authors thank R. B. Dahlburg for a thorough reading and suggestions for improving the manuscript. In addition, we acknowledge J. P. Dahlburg, J. H. Gardner, R. Löhner, and E. S. Oran for helpful discussions and contributions to the overall research effort. The Defense Advanced Research Projects Agency supported the calculations on hot, gaseous channels, and the Office of Naval Research supported projects on shock interactions with flames and bubbles.

References

1. J. M. Picone, J. P. Boris, J. R. Greig, M. Raleigh, and R. F. Fernsler, J. Atmos. Sci. **38**(9), 2056 (1981).
2. J. R. Greig, R. E. Pechacek, and M. Raleigh, Phys. Fluids **28**(8), 2357 (1985).
3. G. H. Markstein, in *Nonsteady Flame Propagation, AGARDograph No. 75*, ed. by G. H. Markstein (Pergamon, Oxford, 1964), 75.
4. J.-F. L. Haas and B. Sturtevant, J. Fluid Mech. **181**, 41 (1987).
5. G. H. Markstein, J. Aero. Sci. **24**, 238 (1957).
6. R. D. Richtmyer, Commun. Pure Appl. Math. **23**, 297 (1960).
7. Y. Y. Meshkov, NASA TT F-13, 074 (1970).
8. S. Chandrasekhar, *Hydrodynamic and Hydromagnetic Stability* (Dover, New York, 1981), 428.
9. M. Lampe, private communication (1980).
10. J. M. Picone and J. P. Boris, Phys. Fluids **26**(2), 365 (1983).
11. J. M. Picone, J. P. Boris, J. H. Gardner, J. R. Greig, M. Raleigh, M. Lampe, and R. E. Pechacek, in *Beams '83: Proceedings of the Fifth International Conference on High-Power Particle Beams*, ed. by R. J. Briggs and A. J. Toepfer (LLNL, Livermore, California, 1984), 378.
12. J. M. Picone, E. S. Oran, J. P. Boris, and T. R. Young, Jr., in *Dynamics of Shock Waves, Explosions, and Detonations*, ed. by J. R. Bowen, N. Manson, A. K. Oppenheim, and R. I. Soloukhin, Progress in Astronautics and Aeronautics, Vol. 94 (AIAA, New York, 1985), 429.
13. J. M. Picone and J. P. Boris, J. Fluid Mech. **189**, 23 (1988).
14. L. D. Landau and E. M. Lifshitz, *Fluid Mechanics* (Pergamon, New York, 1959), Chapter 3.
15. J. M. Picone and J. P. Boris, in *Proceedings of the Eighth International Conference on Numerical Methods in Fluid Dynamics*, ed. by E. Krause (Springer-Verlag, New York, 1982), 408.
16. J. P. Boris and D. L. Book, in *Methods in Computational Physics, Vol. 16* (Academic Press, New York, 1976), 85.
17. K.-H A. Winkler, J. W. Chalmers, S. W. Hodson, P. R. Woodward, and N. J. Zabusky, Physics Today **40**(10), 28 (1987).

NUMERICAL SIMULATIONS OF TURBULENT SUPERSONIC FLOWS

A. Pouquet* and T. Passot**
*GTP/HAO/MMM, National Center for Atmospheric Research†
P.O. Box 3000, Boulder, Colorado 80307, U.S.A.
**Department of Mathematics, University of Arizona,
Tucson, Arizona 85721, U.S.A.
Both on leave from Observatoire de Nice, B.P. 139, Nice Cedex 06003, France.

ABSTRACT

Compressible flow calculations are reported using periodic boundary conditions, with r.m.s. Mach number of order unity. In the turbulent regime, the temporal evolution of the Mach number is mild, the flow retaining some of its compressible character for long times, with strong small-scale vortices visible in the two–dimensional case, forming in the vicinity of shocks. In the non–acoustic regime, large scales are dominated by shear motions, and small scales by shocks, with substantial inequipartition. The inertial range spectral index in dimension two for the compressible component of the velocity is close to –2, reminiscent of observations in several molecular clouds which are the site of star formation. One clear feature of three–dimensionality is the marked appearance of regions of low density.

1. INTRODUCTION

Although incompressible flows have been studied in quite a wealth of details, such is not the case in the compressible regime. Pioneer studies, both in the analytical and the numerical framework were performed, for example by Lighthill, Richmyer and von Neumann, and often restricted to one space dimension. There is now a resurgence of interest for such problems among which one can cite: i) technological and industrial developments, in particular the hypersonic plane and the space shuttle; ii) the accrued possibilities of present–day computers, in particular through either a gain in available semi–fast memory by two orders of magnitude, or through the development of semi–easily programmable highly parallelised computers; iii) recent ground–based and spatial observations of several astrophysical objects indicating that they are in a regime of homogeneous compressible turbulence. Prevalent among them are the molecular clouds, observed for example in ammonia or carbon–dioxyde lines in the galactic plane, and which are the site of star formation. Recent ameliorations in observational techniques, in particular in the radio wavelength part of the spectrum because of very large base interferometry, allow a detailed study of these clouds with a spatial dynamical

† The National Center for Atmospheric Research is sponsored by the National Science Foundation.

range of more than 10^3. Scaling laws clearly appear (Larson, 1981; Myers, 1983; Perrault, 1987) both for the velocity and for the density versus scale, with inertial indices compatible with a Kolmogorov law, although somewhat steeper, and also compatible between themselves with virial equilibrium between potential and kinetic energy at all scales. They read (Falgarone and Perrault, 1986) :

$$\sigma_v = 0.4\ kms^{-1}\ (R/1Pc)^{0.5} \quad \text{and} \quad M = 1_{sm}(R/1Pc)^{2.0} \tag{1}$$

where σ_V is the velocity dispersion measured in km/s, R is the scale measured in parsecs, where ρ is the density and where sm means solar mass. Such laws need to be interpreted in a turbulent context, because of the huge Reynolds numbers involved in these astrophysical flows (see Scalo, 1985; Passot et al., 1988).

Previous analytical works of compressible flows have been mostly restricted to the acoustic regime. Particular attention has been paid to the far–field emission of sound, as well as to the production of vorticity in boundary layers, due to vortex shedding induced by large–scale acoustic waves (see for example Howe, 1984). Analytical works concerning the interaction of turbulence and sound for small Mach numbers have been reviewed elsewhere (see for example Passot and Pouquet, 1987). They mostly deal with phenomenological evaluations of the various characteristic times of competing phenomena, of their ordering, and of the subsequent regimes that arise, leading to various predictions of the possible energy spectra for both the acoustic part and the solenoidal part of the velocity written as $u = u^c + u^s$, as proposed for example in Moyal (1952). Another approach consists in applying some closure scheme to the primitive equations. The earliest works dealt with the Quasi–Normal Approximation (QNA) on the equations with self–gravity (Chandrasekhar, 1951; Sasao, 1973). Weiss (1976) applied the eddy–damped markovian QNA to a model of subsonic flow, and more recently Hartke et al. (1988) used the Direct Interaction Approximation on a model of compressible convection (see also Marion, 1988). In the latter cases, one finds that the compressible velocity mode is dominated at all scales by the vortical part of the velocity field. However, this may be due in fact to the underlying hypothesis in deriving the model used before applying the closure scheme. In numerical simulations in the two–dimensional case as well as in the three–dimensional one the longitudinal modes are dominant in the small scales, due to shocks, as soon as one leaves the acoustic regime. Two–scale analysis of large scale instabilities due to small–scale helicity (Moiseev et al, 1983) indicate the possibility in the barotropic case of an inverse cascade leading to the development of large scale coherent structures in compressible flows. The analysis, using white–noise forcing, has not as yet been extended to the non–isentropic case, for which the conservation of helicity probably does not hold, except in regions where the Ertel potential is zero (Gaffet, 1985).

We describe here the main results of a numerical study of homogeneous flows in the supersonic regime for fully developed turbulence in two– and three–dimensional geometry. We shall in this paper concentrate on the differences in behavior between the two–dimensional

and the three-dimensional cases for homogeneous flows using random initial conditions and periodic boundary conditions.

2. THE NUMERICAL METHOD

The method we use is that of collocation: space-derivatives are computed in Fourier space, and non-linear products of variables in configuration space. Such methods, widely used in the turbulence context for incompressible flows, are not necessarily the first choice for compressible ones when shocks are bound to develop, and Gibbs phenomena will appear. However, provided the flow remains smooth through a proper choice of the diffusion parameters, in fact the spectral method will retain its polynomial high degree of spatial accuracy. For that purpose, shocks will have to be spread on roughly five points. Other methods exist to simulate such flows, which often use the Euler equation and some sort of artificial viscosity to smooth out the flow. Another source of concern when simulating compressible flows is the low values reached by the density, particularly when the flow is self-gravitating. One possible way out is to use a coefficient of diffusion of mass, but no such term will be used here. Aliasing may also develop, as described for example in Alecian and Léorat (1988), but these errors can be prevented by adequate resolution, with spectra several orders of magnitude smaller in the small scales than they are in the energy-containing scales.

The equations, in adimensionalised form, are:

$$
\begin{aligned}
&\partial_t \rho + \nabla \cdot (\rho u) = 0, \\
&\partial_t \rho u + \nabla \cdot (\rho u u) = -(\gamma - 1)\nabla(\rho e) + \frac{1}{Re}\left(\nabla^2 u + \frac{1}{3}\nabla \cdot (\nabla \cdot u)\right), \\
&\partial_t E + \nabla \cdot (Eu + (\gamma - 1)\rho e u) = \frac{1}{Re}\nabla \cdot (\tau \cdot u) + \frac{1}{(\gamma - 1)PrReM^2}\nabla^2 T,
\end{aligned}
\tag{2}
$$

where three dimensionless parameters appear: the Mach number $M = U_0/C_0$, the Reynolds number $Re = p_0 U_0 L/\mu$ and the Prandtl number $Pr = \mu C_p/k$ where C_p is the constant-pressure specific heat and k is the coefficient of thermal conductivity. In the above equations, $e = C_v T$ is the internal energy where C_v is the constant-volume specific heat, and $E = \rho e + u^2/2$ is the total energy. Finally, τ_{ij} is the viscous stress tensor, defined as $\tau_{ij} = \eta \nabla \cdot u \delta_{ij} + \mu(\partial_j u_i + \partial u_j)$, where δ_{ij} is the Kronecker symbol and where $\eta = \mu/2$, with the choice of a zero volumetric viscosity coefficient. These equations conserve mass, momentum, and total energy (for the barotropic case, see Léorat et al., 1984).

A purely explicit temporal scheme was used in the two-dimensional simulations, and a partially implicit scheme in the three-dimensional case, because of the low values of the minimum of the density, which can be 10^{-3} that of the mean density. In that case, the dissipation term would become prohibitive to compute explicitely, and we use a splitting method (Passot, 1987).

3. TEMPORAL EVOLUTION

For an incompressible flow, the two–dimensional case differs strongly from the three–dimensional one, because of the supplementary conservation law of vorticity, rendering the energy dissipation extremely weak. However, as soon as shocks can form, this represents the dominant mode of energy dissipation whatever the spatial dimension, and one can thus expect a similar temporal behavior for the kinetic energy and related quantities. In all that follow, the unit time is the eddy turnover time of the large scales, which is of the same order than the shock–formation time. In figure 1, we show the time evolution of the *rms* Mach number, for a 3D (solid line) and 2D (dashed line) flow at a Reynolds number of 120. The 2D–3D distinction may therefore not be so stringent in the compressible case, compared to the incompressible one.

For a wide range of initial ratio of compressive to solenoidal energies E^C/E^S including when it is unity, the flow rapidly evolves towards a state where the large scales are dominated by the solenoidal part of the velocity component, and the small scales by the shocks provided the rms Mach number is above a critical value of 0.3 which does not seem to depend strongly on dimension: even for flows at or around Mach one, coupling between sound and vortices differs in intensity at different scales.

We performed one run at a Reynolds number of 60 for a time long compared to the eddy turnover time, and comparable to the sound crossing time of the computational box. In figure 2, we show the evolution of the ratio of compressible to kinetic energy (% value) for this run. The oscillations, clearly visible in the 2D case at Reynolds numbers of 200, are here also quite marked, and their period correspond to the acoustic time of the large scales. On average, in 3D as in 2D, this ratio tends to settle around 10%. We show in Figure 3 the temporal evolution of the characteristic wavenumbers of the solenoidal (solid line) and compressive (dashed line) part of the energy spectrum; their increase (slight in the former case) corresponds to the energy transfer to small scales and to shock formation, the following decrease being due to the finite value of the dissipation. Not far from the acoustic regime, it has been determined numerically (Feireisen et al., 1981; Zang, private communication) that the skewness factor which measures in a non–dimensionalised way the triple moments of the velocity field, remains close to its incompressible value. Finally, in Figure 4, we give the time variation of the three directional components of the kinetic energy where we can note that isotropy is reached in a few eddy turn–over times.

4. CHARACTERISTIC STRUCTURES

What follows is only a brief account of the structures that develop in the flow. When performing cuts within the flow, these structures are quite similar to their 2D counterparts. For example, in figure 5, we show a cut in the density field for a run in which initially the turbulent Mach number is 2.2 , (with a local maximum of 4.9), and the characteristic wavenumber is 1.5, where the minimum wavenumber k_{min} is taken equal to unity. The cut

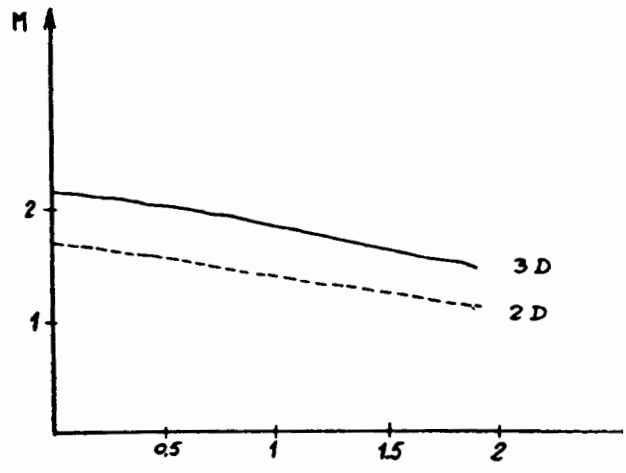

Figure 1: Temporal evolution of the Mach number

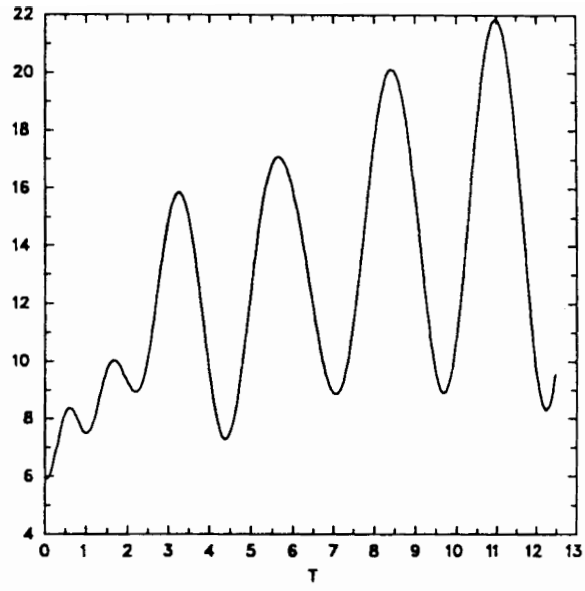

Figure 2: Kinetic energy in its compressive mode

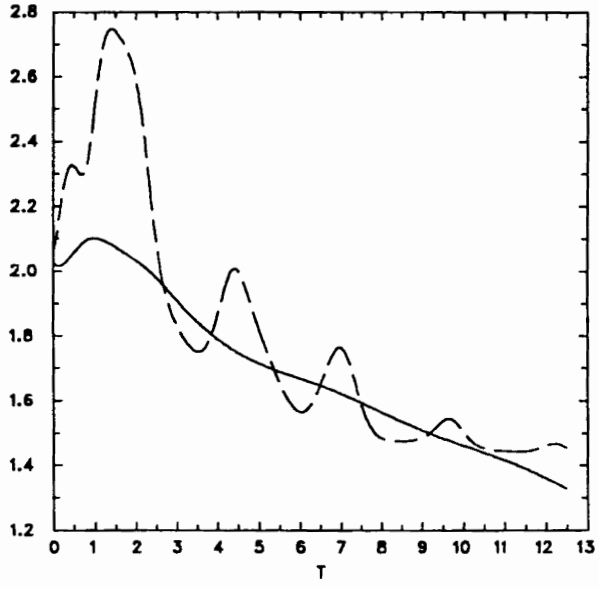

Figure 3: Time evolution of integral wavenumbers

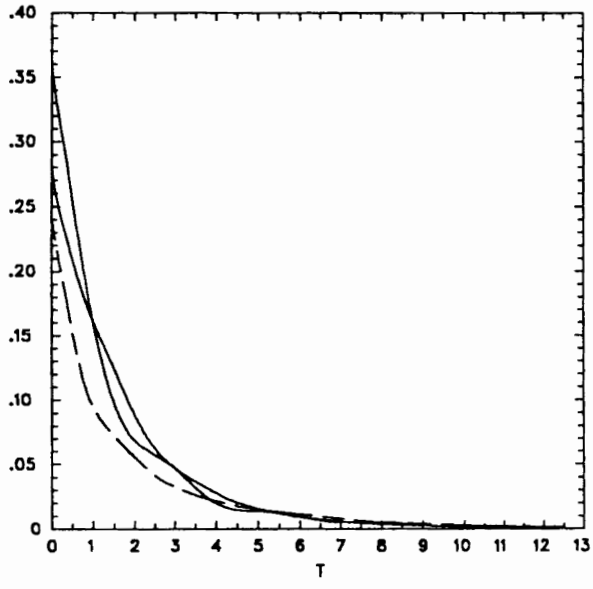

Figure 4: The three components of the kinetic energy

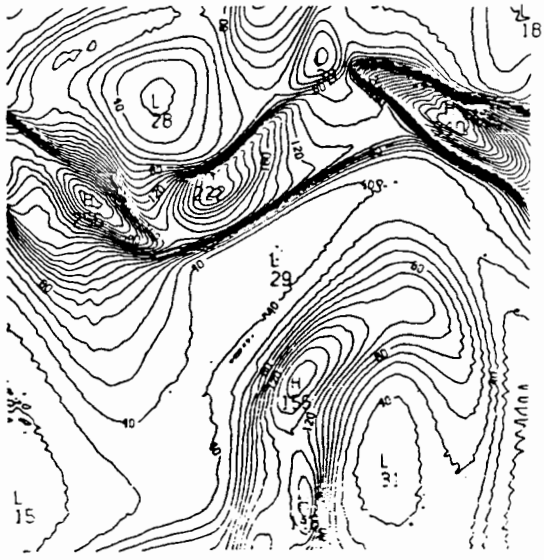

Figure 5: Horizontal cut of the density field

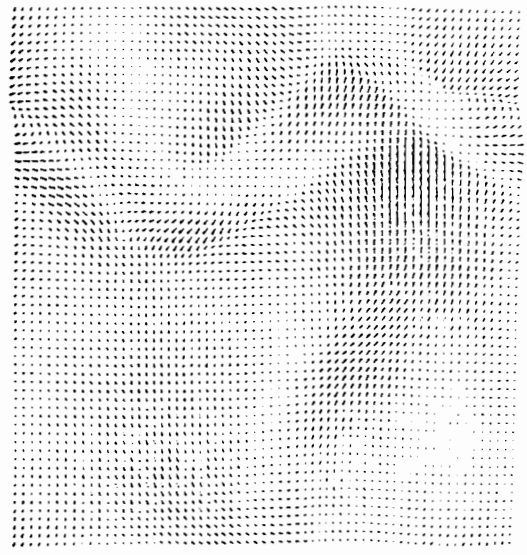

Figure 6: Same as fig.5 for the horizontal velocity

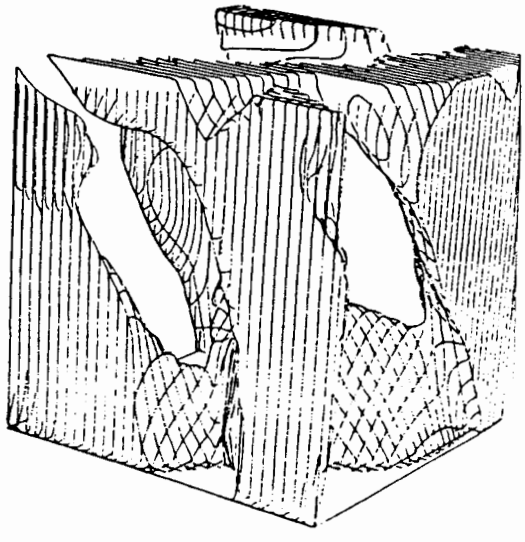

Figure 7: Density when above 20% of its maximum

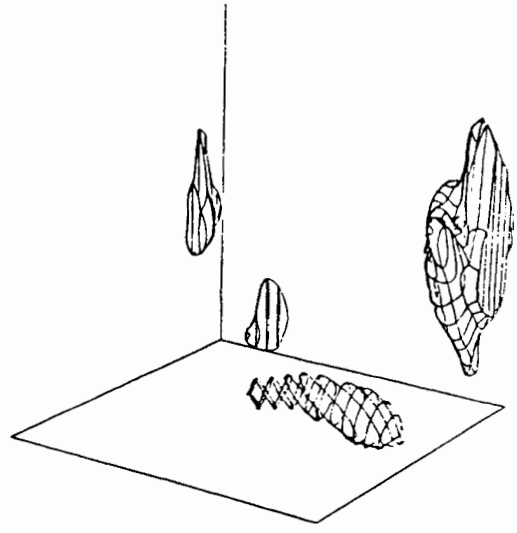

Figure 8: Same as fig.7 for a 50% threshold

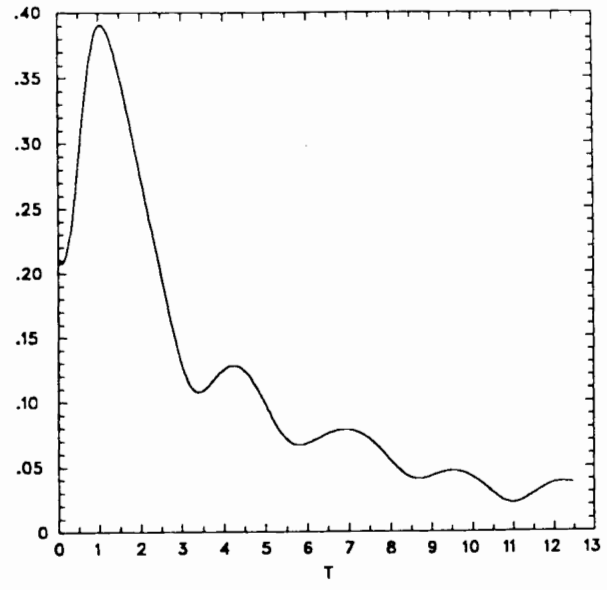

Figure 9: Density fluctuations as a function of time

is performed at $t = 1.9$ at altitude $z = 80$, with $z_{max} = 128$ (in units of grid increments) corresponding to the total length of the box. In the course of the computation, density reaches extrema values of respectively 7.6 and 0.14 . At the time at which the cut is shown, the Mach number is 1.5 and the temperature is 1.27 its initial value. The corresponding horizontal velocity field is shown in figure 6. Similar features develop for flows with various initial conditions. Comparing the evolution with the 2D case, it seems that the formation of shocks here is a smoother process in three dimensions.

A clear feature of the 3D case, not present in the 2D one, is the possibility of having regions of low density (1% of the mean value) in some regions of the flow. For example, for a run in which initially the Mach number is equal to unity, and the ratio of the typical wavenumber to k_{min} is now 3.8 , sharp density contrasts (ratio of maximum to minimum density within the whole volume) develop, up to 100 , with the minimum density reaching a value of .07 its mean, and with relative density fluctuations $\delta\rho/\rho \sim 0.6$. In the two–dimensional case, at similar Reynolds numbers, the minimum density is more like 10% the mean and the density contrast remains close to 4 . This may alter in a significant way the collapse of a cloud under its own gravity, where it should be noted that for evident reasons the two–dimensional geometry is the one most commonly investigated numerically. These regions of low density are presumably associated with strong shocks, but this point will require further investigation. We finally show typical perspective plots of the density; in this run, the initial Mach number is unity, the integral wavenumber is 2 , the ratio of compressible to total kinetic energy is 50% , and the Reynolds number is 105 . In Figure 7, the density is plotted at time $t = 1.2$ when it is above 20% of its maximum, and in figure 8 when it is above 50% of its maximum. This roughly indicates the location of shocks.

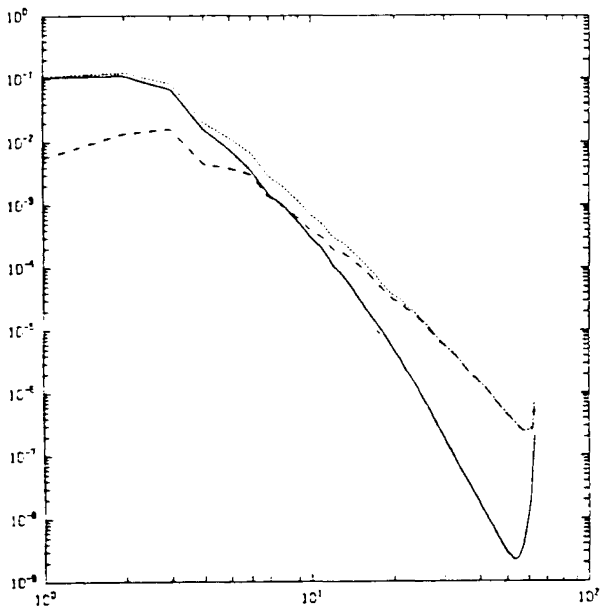

Figure 10: Energy spectra at t=1.

In figure 9 is shown the temporal evolution of the density fluctuations for the run already mentionned in figures 2 to 4. As time evolves, one enters the acoustic regime (the faster, the lower the Reynolds number) but determination of spectral indices would be meaningless because at those times the Reynolds number is barely above unity. We show in figure 10 the compressible (dashed line) and solenoidal (solid line) spectra for a run computed on a 128^3 grid at $t = 1.9$ mentionned before (same run as fig. 5). The total kinetic energy is represented by the dotted line. The flow is not sufficiently resolved, as the high wavenumber tail shows, but this numerical error, possibly due to time differencing, remains within reasonable bounds, with a relative energy six order of magnitudes below the large-scale energy. Spectra are quite steep, but this in no way represents a determination of possible inertial ranges for that problem, it only represents a lack of sufficient resolution. We expect that the compressible part of the energy spectrum will undergo a -2 power law, because it is dominated by pseudo-discontinuities in the flow. On the other hand, the solenoidal part is expected to follow a law steeper than the $-5/3$ Kolmogorov range, and presumably for strongly compressible flows will also follow a -2 law. This would allow for an equipartition between the compressible and solenoidal modes to develop, as predicted by Kraichnan (1953) on the basis of a statistical argument. For the moment, we can only say that the lack of equipartition between the two components of the velocity field is as pronounced as in the two-dimensional case, at a given Reynolds number. To help determine what possible power-law ranges develop, one can use an hyper-viscosity to artificially lengthen the domain of wavenumbers in which the non-linear transfer prevails over dissipation. One may also look at steady-state solutions, for which time-averaging may provide a sufficient smoothing effect.

5. DISCUSSION

This paper presents preliminary results of numerical experiments on three–dimensional compressible homogeneous isotropic turbulent flows. The 2D and 3D cases do not differ substantially, and certainly not as much as in the incompressible case. This in fact is an encouraging factor to pursue detailed analysis of various configurations using the two–dimensional approximation. However, the one striking difference concerns the development of regions of low density in the vicinity of shocks.

Further study is needed, to scan parameter space. One aspect we investigate at the present is the possible influence of oligotropy defined as $\sigma = \omega \cdot \nabla s$, where ω is the vorticity and s the entropy (note that the Ertel's potential vortex can be defined from the oligotropy as $\mathcal{E} = \sigma/\rho$, and is a Lagrangian invariant). Indeed, kinetic helicity $< \omega \cdot u >$ is conserved locally in space where the oligotropy is zero (Gaffet, 1985), and may induce large–scale instabilities (Moiseev et al., 1983). Since regions of initial zero oligotropy remain so, this property is bound to play a role in the dynamical evolution of the flow.

One 2D feature not revealed in 3D is the production of strong localised vortices when two strong shocks collide. Such features were only observed in the 2D case at resolutions higher than those presented here, so we cannot conclude at the present time. It certainly represents one of the points that could be investigated with different numerical methods that modelise in some way the small scales, possibly using for example some parametrisation, through either artificial viscosity, or hyper–viscosity. For spectral methods, one could extend the hyperviscosity analysed in Passot and Pouquet (1988) for the 2D case, that preserves positivity of the dissipation at all grid points. One could also use the transport coefficients derived from closure methods (Chollet and Lesieur, 1981) which provide in a unifying way a time-dependent and velocity-dependent parametrisation of small scales; however, the large number in the compressible case of transport coefficients representing the eddy–diffusivities due to the various coupling between the compressive and vortex part of the spectra may prove prohibitive, unless some simplifying assumptions are introduced.

ACKNOWLEDGEMENTS

Part of the computations reported here were done on the Cray–2 of the CCVR (Palaiseau, France), and parts on the Cray–XMP at NCAR. Partial support for this research was through CNRS grants, from the ATP on Numerical Geophysical Flows and from the RCP on Astrophysical Flows in the Supersonic Regime.

REFERENCES

Alecian G. and Léorat J. (1988) Preprint Observatoire de Meudon.

Chandrasekhar S. (1951) Proc. Roy. Soc. **A210**, 26.

Chollet J.P. and Lesieur M. (1981) J. Atmos. Sci. **38**, 2747.

Feircisen W.J., Reynolds W.C. and Ferziger J.H. (1981) NASA Report **TF-13**, Stanford University.

Gaffet B. (1985) J. Fluid Mech. **156**, 141.

Falgarone E. and Perrault M. (1986) *Physical Processes in Interstellar Clouds*, eds. G. Morfil and M. Schola, Reidel.

Hartke G. J., Canuto, V. M., and Alonso, C. T. (1988) Phys. Fluids **31**, 1034.

Howe M.S. (1984) 187, Academic Press.

Kraichnan R.H. (1953) J. Acoust. Soc. of America **25**, 1096.

Larson R.B. (1981) Monthly Not. Roy. Astron. Soc. **194**, 809.

Léorat J., Pouquet, A. and Poyet, J.P. (1984) *Problems of Collapse and Numerical Relativity*, M. Bancel and M. Signore eds., Reidel.

Marion J.D. (1988) Thèse (Mécanique), Ecole Centrale de Lyon.

Moiseev, S.S., Sagdeev, R.Z., Tur, A.V., Khomenko, G.A. and Yanovskii, V.V. (1983) Sov. Phys. JETP **58**, 1149.

Moyal J.E. (1952) Proc. Camb. Philos. Soc. **48**, 329.

Myers P.C. (1983) Astrophys. J. **270**, 105.

Passot Th. (1987) Nouvelle Thèse (Physique), Université de Paris VII.

Passot Th. and Pouquet A. (1987) J. Fluid Mech. **181**, 441.

Passot Th. and Pouquet A. (1988) J. Comp. Phys. **75**, 300.

Passot Th., Pouquet A. and Woodward P. (1988) Astron. and Astrophys., **197**, 228.

Perrault M. (1987) Thèse d'Etat (Astrophysique), Université de Paris VII.

Sasao T. (1973) Pub. Astr. Soc. Jap. **25**, 1.

Scalo, J. (1985) *Protostars and Planets*, **2**, D. Black and M. Matthews eds., University of Arizona Press, p. 201 *sq.*

Weiss J. (1976) PhD Thesis, University of New-York.

SHOCK ENHANCEMENT OF A TURBULENT FLOW

Doug Rotman
Lawrence Livermore National Laboratory
Livermore, CA. 94550

Introduction

Presented here are calculations describing the enhancement of turbulence caused by the passing of a shock wave. This field is of interest to those investigating the Richtmyer-Meshkov instability, supersonic combustion, fusion and many others. Experiments involving shocks and turbulence (Sturtevant, et. al. 1980, Smits and Muck 1987, Trolier and Duffy 1984) show that the turbulence level following a shock wave can be as much as 3 times higher then that before the shock. Predictions from linear theory (McKenzie and Westphal 1968 and Anyiwo and Bushnell 1982) show very similar shock enhancements. Recent calculations involving nonlinear effects (Kumar et. al. 1987 and Viecelli 1988) show promise in explaining how this enhancement is obtained. This study will use a shock tube type calculation domain to investigate the effect of a shock wave on pre-existing turbulence

Calculations

The computational domain involves a square box with a grid of size 100 X 100. Within this, a pre-existing random (turbulent) flow pattern is placed, as shown in figure 1. This flow was obtained by choosing random numbers from a Gaussian random number generator and imposing those on a secondary staggered grid within the box. Assigning those numbers as stream functions, a divergence free velocity field was obtained by using spatial derivatives of the stream functions. From experiments it is known that shock waves tend to decrease the scales of turbulence, thus to obtain larger scale initial turbulence a diffusive operator was applied to the velocity field to finally give the field as shown in figure 1.

The numerical scheme used for all the calculations is a second order Godunov scheme solving the two dimensional Eulers equations of motion using a gamma law gas equation of state (Colella and Glaz 1985). Two systems have been investigated: one of low initial turbulence and the other of high initial turbulence levels. In each case the imposed shock wave had a pressure ratio of 4.9 and a density ratio of 2.78. The shock was imposed by setting three of the domain boundaries as reflecting while the last having an inflow condition. This results in a shock moving from the far wall towards the inflow boundary. Contours of the shock wave appear in figure 2.

Results

The first case investigated is the low turbulence level, one of 0.04%. This represents the ratio of the energy of the turbulence divided by the energy of the incoming flow. The fluctuating velocity field is seen in figure 3. Here we see the shock moving into the initial large scale turbulence and leaving behind a turbulent field of much smaller scale. The calculated turbulent kinetic energy (one half the square of the fluctuating velocity) is 5.2 times higher behind the shock as before it on a per unit volume basis or 1.9 times higher on a per unit mass basis. Figure 4 presents the pressure contour for this system. It shows that the turbulence is weak enough that it does not influence the shock wave and thus it stays straight.

The second case investigated is the high turbulence level, one of 2.0%. Figure 5 shows the fluctuating velocity field and again we see the smaller scale behind the shock, but the difference is not as obvious. In this case the turbulent kinetic energy is only 4.5 times higher per unit volume or 1.6 times higher per unit mass. But in figure 6 we see that the turbulence level is now becoming high enough so that the flow is starting to affect the shape of the shock wave. The shock now appears to form curves as it moves through the turbulence.

Discussion

The decrease in the turbulence scale size following a shock is similar to the shock tube results of Sturtevant, although the experiments are done at a lower pressure ratio. These smaller scales then result in higher fluctuations in velocity and thus higher turbulent kinetic energy. Using arguments involving the conservation of angular momentum, Viecelli shows that in the limit of zero viscosity and zero initial turbulence this enhancement of turbulent kinetic energy goes as the square of the density compression ratio. Furthermore, going to higher and higher initial turbulent kinetic energies, the enhancement becomes a smaller and smaller fraction of the density compression ratio. Results shown here present exactly these trends. In addition to conservation of angular momentum, the reduction in turbulence scales could be caused by the breakup of individual eddies. When a shock interacts with an eddy, an initially round eddy will deform to an ellipse shaped eddy. It is possible that a weak eddy could then split into two individual eddies, thus creating smaller scales of turbulence.

Examined in this study are only two cases of a long list of possible flows systems. Future work will investigate the effect of pressure ratio, density ratio, and initial turbulent field on the enhancement of the turbulence. Also, the division of energy between the rotational, acoustic and entropy modes will be considered to see how each of these are affected.

Acknowledgements

I thank Chuck Leith, Phil Colella, Bill Ashurst and Alfred Buckingham for their many helpful discussions. This work was performed for the U.S. Department of Energy under contract No. W-7405-Eng-48 by the Lawrence Livermore National Laboratory

References

Sturtevant, B., Hesselink, L., and Haas, J. F., "Propagation of Shock Waves in Random Media," in Proc. of the 12th International Symposium on Shock Tubes and Waves (1980), pp. 359-365

Smits, A.J. and Muck, K.L., "Experimental Study of Three Shock Wave/Turbulent Boundary Layer Interactions," J. Fluid Mech., 182 271 (1987)

Kumar, A., Bushnell, D.M., and Hussaini, M.Y., "A Mixing Augmentation Technique for Hypervelocity Scramjets," presented at the AIAA/SAE/ASME/ASEE 23rd Joint Propulsion Conference, San Diego, California, June26-July 2, 1987, AIAA-87-1882

Colella, P and Glaz, H.M.,"Efficient Solution Algorithms for the Riemann Problem for Real Gases," J. Comp. Physics, 59 264 (1985)

Trolier, J. W. and Duffy, R. E. "Turbulence Measurements in Shock-Induced Flows," presented at the AIAA 13th Aerodynamics Testing Conference, San Diego, California, March 5-7, 1984, AIAA-84-0631

McKenzie, J. F. and Westphal, K. O., "Interaction of Linear Waves with Oblique Shock Waves," The Physics of Fluids 11, no. 11, 2350 (1968)

Anyiwo, J. C. and Bushnell, D. M., "Turbulence Amplification in Shock-Wave Boundary-Layer Interaction," AIAA Journal 20, no. 7, 893 (1982)

Viecelli, J. A., "Material Mixing Geometry Produced by Shock Compressed Two-Dimensional Turbulence," UCRL-98994, Lawrence Livermore National Laboratory, 1988

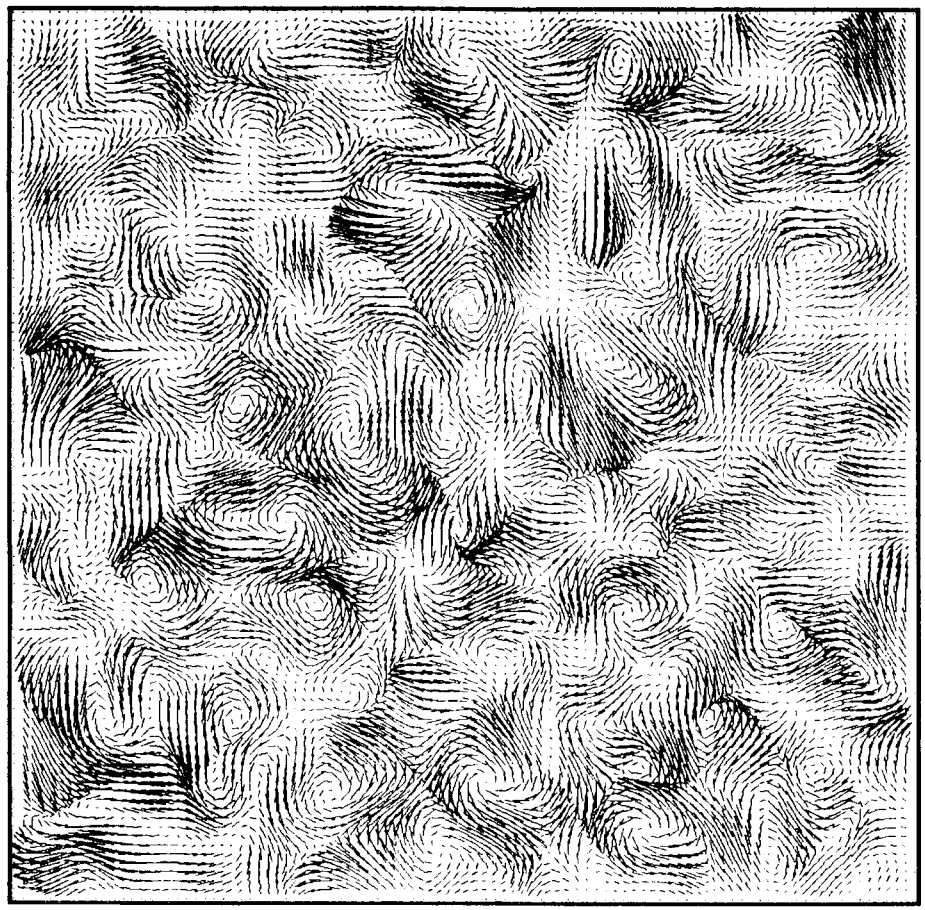

Figure 1. Initial Turbulent Velocity Field

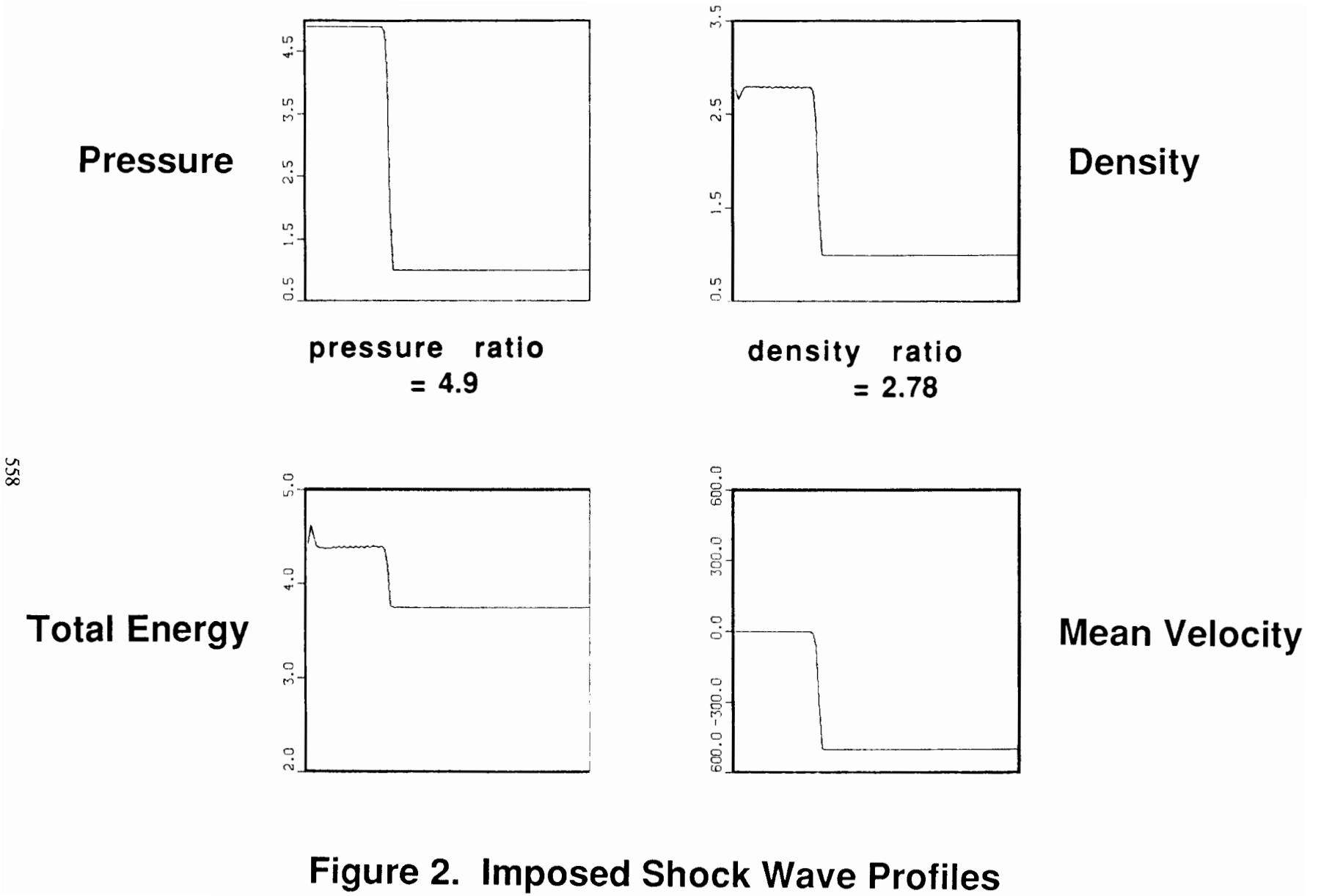

Figure 2. Imposed Shock Wave Profiles

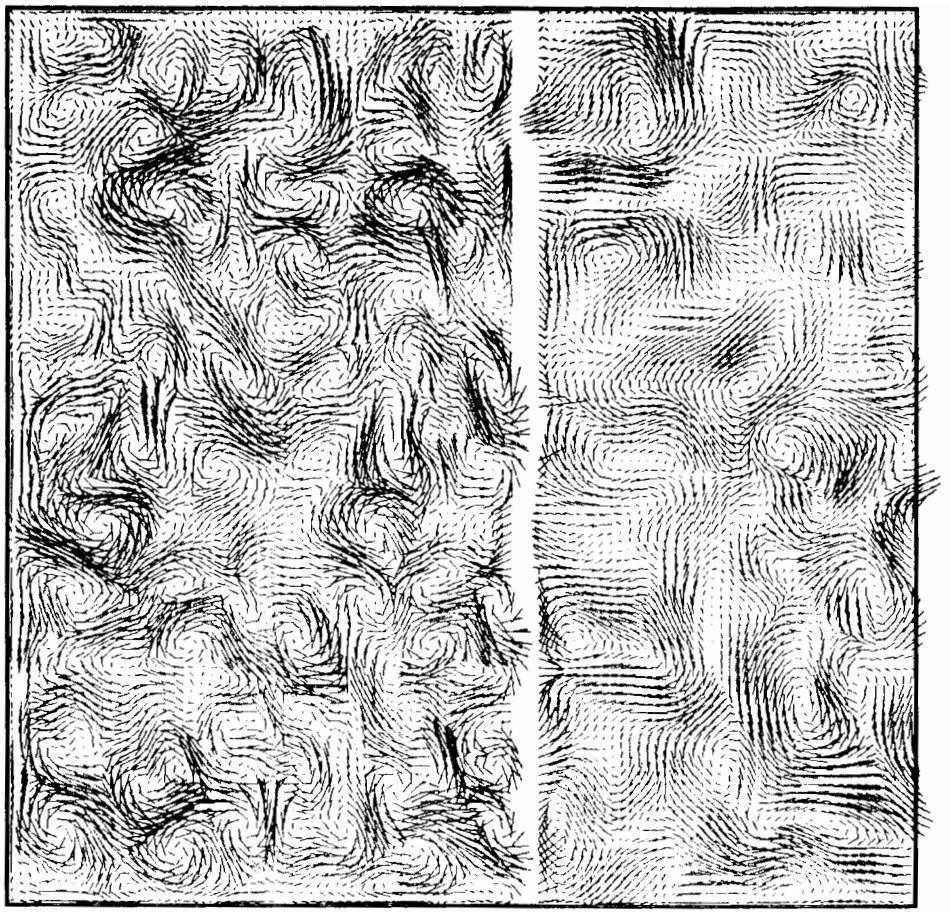

Figure 3. Velocity Field for Low Turbulence

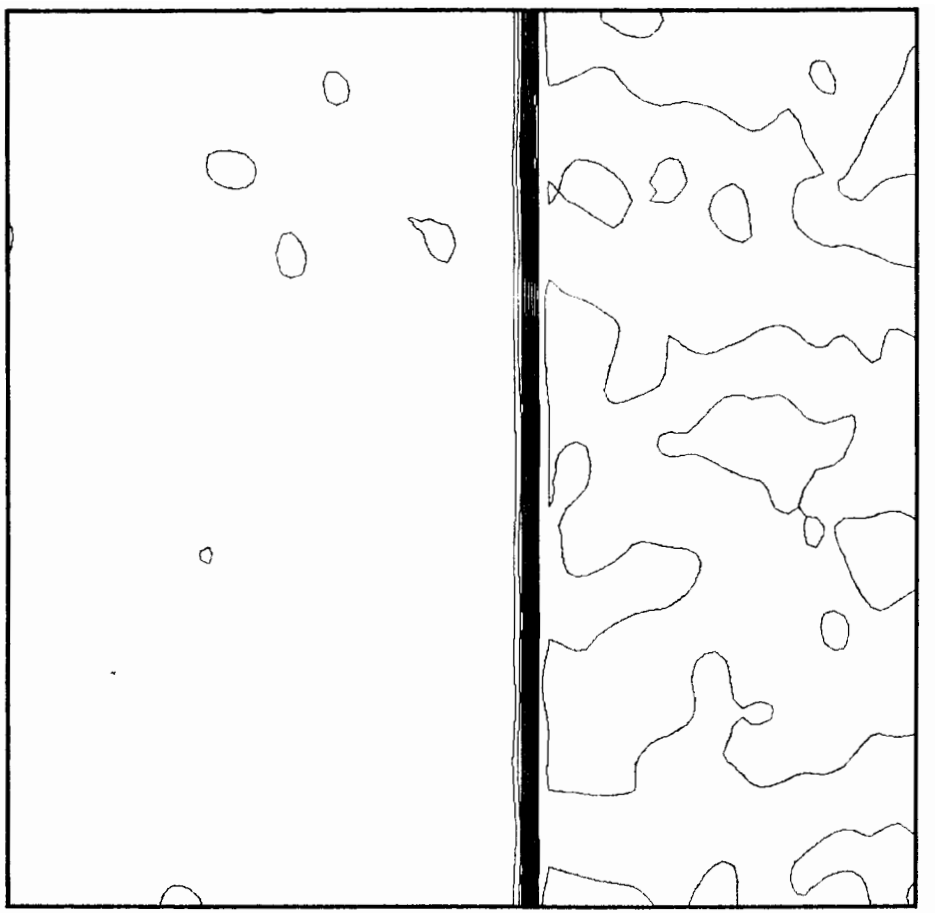

Figure 4. Pressure Contours for Low Turbulence

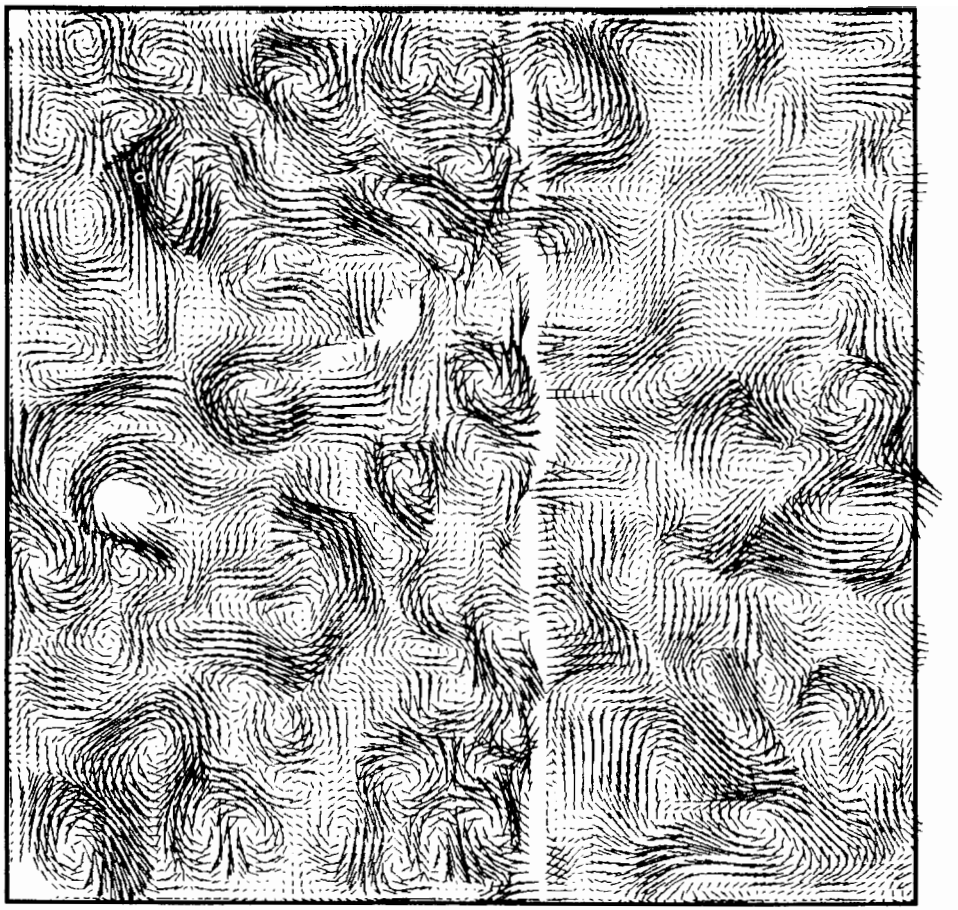

Figure 5. Velocity Field for High Turbulence

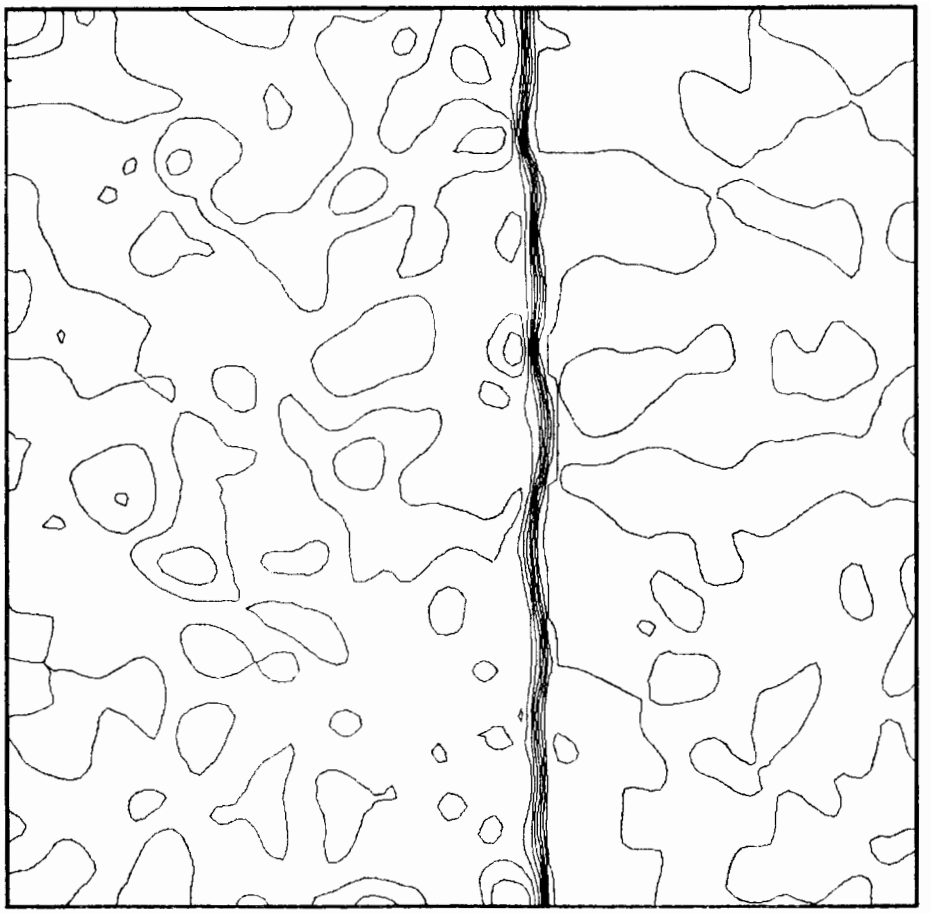

Figure 6. Pressure Contours for High Turbulence

NOVA MIX EXPERIMENTS

V. C. Rupert, J. D. Kilkenny, P. G. Skokowski
Lawrence Livermore National Laboratory
P.O. Box 808, Livermore, CA 94550

The NOVA mix experiments are designed to study mix between two dissimilar materials subjected to strong (M ~50) shocks and variable accelerations in a direction normal to their common boundary. The main purpose of the experiments is to provide a data base with which predictive models can be compared and normalized. Together with shock tube experiments[1], which explore a different regime, the current NOVA tests investigate the shock induced source terms in our model[2] and the evolution of both Rayleigh–Taylor stable and unstable interfaces.

In these experiments, a laser pulse of 1/3 μm wavelength and 1 ns duration is used to generate a radiation source which is more uniform that the original laser beams. This source heats the front surface of a material of density ρ1, which ablates and expands back towards the source. Momentum conservation causes a shock to propagate through the material away from the source and through the interface of the ablator with a material of density ρ2. The evolution of the interface between the two materials is studied to determine the extent and composition of the mixed region. On some experiments a tamper has been used to hold the sample in place. This results in an additional interface through which mix can occur. To date the experiments have been geared towards diagnosing only the ablator interface, although simulations do provide a prediction of the mix through the tamper boundary as well.

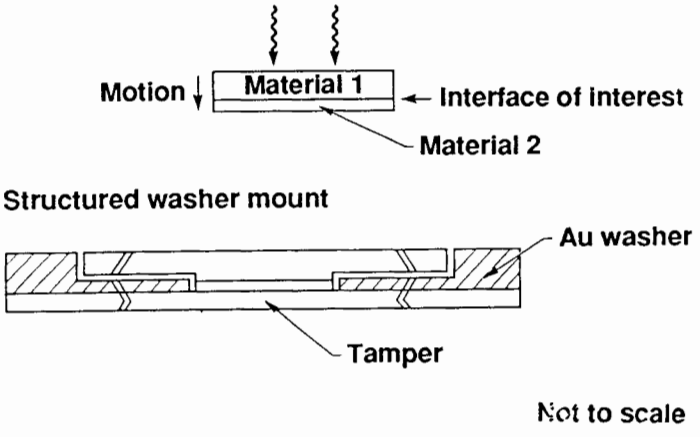

Fig. 1 Nominal Nova mix sample and mounting scheme.

The sample used in these experiments is shown in Figure 1. Selection of the materials is based on:

the requirement for high mix ($\rho_1 \neq \rho_2$) or low mix ($\rho_1 \sim \rho_2$);

their spectral signature, for diagnostic purposes; and

the ease of fabrication.

Current samples use a polypropylene sulfide ablator (PPS), with molybdenum (Mo) or Parylene C (PyC) for the second material, and Parylene N (PyN) for tamper. Although the most recent shots have not

included the tamper, the data presented herein were obtained with tamped samples as shown in Figure 1. Nominal dimensions of these samples are 50 to 60 μm thick PPS, 1.5 to 2 μm thick Mo or 15 μm thick PyC and 3 μm PyN. The nominal target diameter (at the interface) is of the order of 200 μm.

The ideal experiment would have the materials moving only in a direction normal to the original interface. Figure 2 shows the trajectories of various parts of the target for a NOVA shot at 7 kJ. Ablation of the front part of the PPS layer sends a shock through the sample. When the shock breaks out at the back of the tamper, the later expands into the surrounding vacuum. The concomitant rarefaction wave propagating back through the sample produces a small additional acceleration of the PPS/Mo interface in the same direction as the shock impulse. Figure 3a shows the density distribution through the sample 7ns after the start of the laser pulse, and Figure 3b shows its variation in time across the PPS/Mo interface. The latter shows a change in densities prior to shock arrival (at ~ 1 ns) due to a slight preheat of the materials

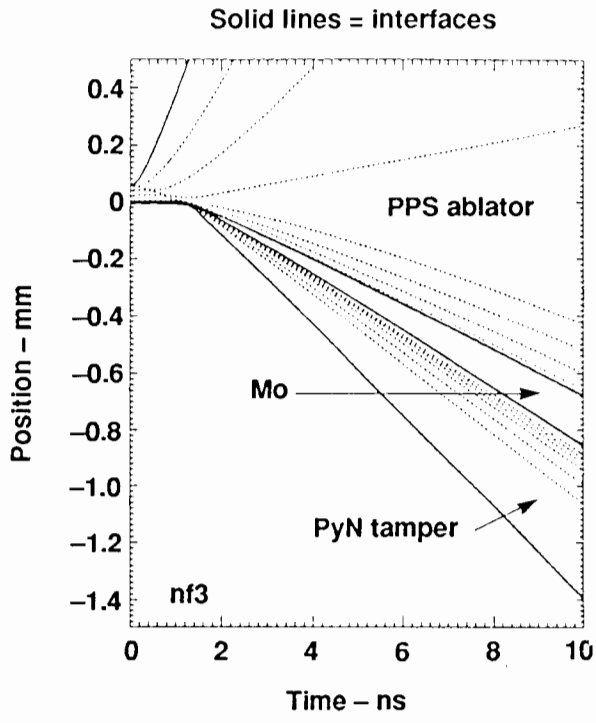

Fig. 2 Trajectories of various parts of a high mix sample.

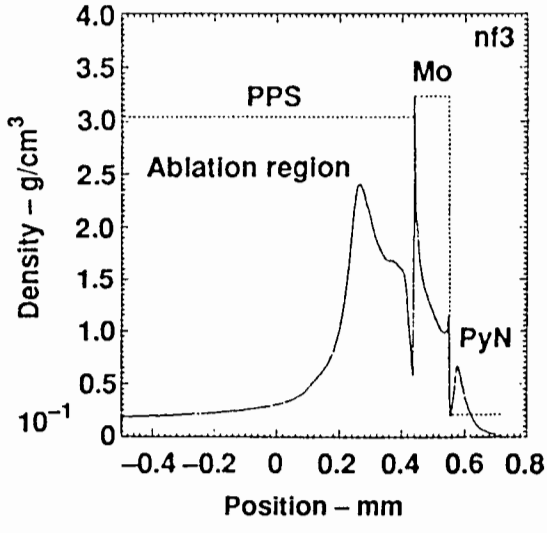

Fig. 3a Density distribution along the sample at 7ns - dashed lines show the locations of the different materials.

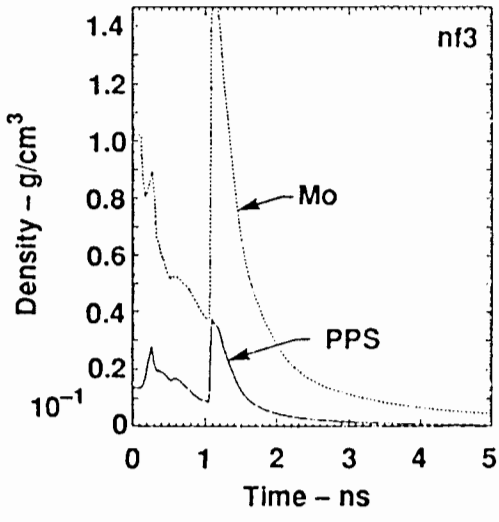

Fig. 3b Density variation across the PPS/Mo interface.

Mix calculations using the kε model[2,3] implemented in our hydrodynamic code imply that most of the mix occurs just after shock passage both at the Rayleigh Taylor unstable (PPS/Mo) and stable (Mo/PyN) interfaces. While the mass of mixed material changes insignificantly thereafter, the width of the mixed layer increases as the materials expand (Figure 2). At times of the order of 6ns, the width is sufficient to be observable with diagnostics of 10 to 20 μm resolution.

Point projection spectroscopy (Figure 4) is used to image the sample and unambiguously determine the extent of the different materials in the instrument's line of sight. The system is currently configured to probe the 2 to 3.2 keV range which encompasses the sulphur k edge (in PPS), the Molybdenum L_I to L_{III} edges, and the Chlorine K edge (in PyC). The tamper (PyN) is not highlighted in this energy range. Figure 4 shows an image which would be obtained for an unmixed sample.

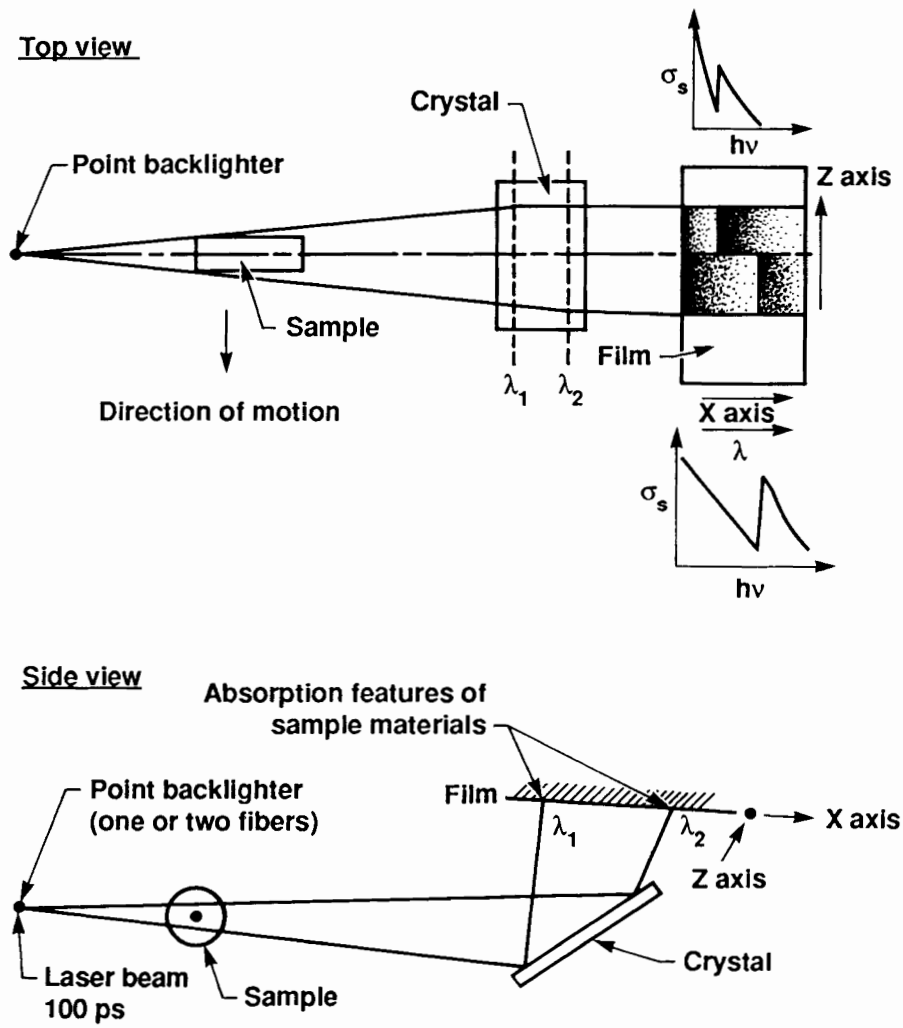

Fig. 4 Point projection spectroscopy principle.

If the sample did indeed move only in a direction normal to the original interfaces, any overlap of the material spectral features (lines or edges) would indicate mix, and the mixed region width could be determined. In practice, as soon as the sample moves out of it's mounting washer, lateral expansion occurs and two dimensional effects need to be accounted for.

Figure 5 shows a 2 dimensional calculation of a low mix target with no mix model invoked. A 1-D calculation of the same configuration shows that 10-20 μm of mix could be expected at 7ns between the PPS ($\rho \sim 1.36$) and the PyC ($\rho \sim 1.29$), or the PyC and PyN ($\rho = 1.26$). Figure 5 clearly shows the lateral expansion of the target (original diameter 200 μm), the jetting tendency of the ablator around the rest of the target, and the lag of the target edges due to the restraining effect of the large diameter tamper. Note that the part of the tamper shielded by the gold washer remains cold and dense so that the tamper just appears to stretch around the expanding PPS and PyC. This figure also shows that the bulk of the material interfaces remains fairly planar and normal to the initial target axis. The same general behavior is observed for high mix targets, although the jetting of the ablator around the Mo is more pronounced. These computations indicate that the apparent mix (overlap of spectroscopic features), due to the non planarity of the (unmixed) interfaces, should be within instrumental error for the current experiments, since, in the outer regions, the densities drop rapidly, and the overlap widths in the direction of observation are small. One dimensional calculations incorporating mix models should adequately describe the observed mix width. Two dimensional calculations such as those shown in Figure 5 are fraught with difficulties, even in the absence of mix, and are expensive in both computer memory usage and time. They cannot be used for parameter studies inherent in experimental design or repeated for each realization of the experiments. They have been used mainly to study the mounting schemes which, experimentally, appeared the best (minimum target curvature), and provide guidelines to the correlation of experiments and one dimensional calculations with mix.

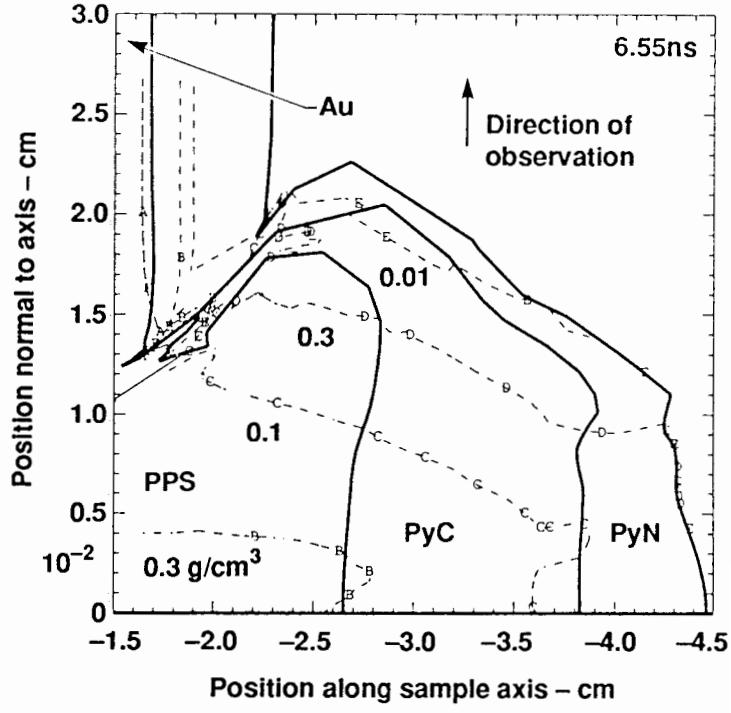

Fig. 5 Two dimensional calculation of a low mix type target.

Experiments have been conducted for two classes of targets. The "low mix targets" use materials with closely matched densities. Since the mix process depends on the Atwood number, little mix should occur for these samples. Figures 6a and b show the experimental data, and a simulated radiograph from a 1-D calculation for a low mix shot at 8 kJ. Both simulated and experimental data clearly show a sulphur edge shifting to higher energy in the heated PPS on the ablative side (bottom of picture), and the 1s-3p line of sulphur like chlorine, followed by the chlorine edge. The overlap of the sulphur and chlorine features translate to 14 μm in the simulated data. The experimental overlap of 40 μm is consistent with this value when motion blurring (200 ps snapshot) and instrumental resolution are taken into account.

Since the simulated radiograph was obtained from a 1-D calculation, it does not display the shadow of the mount. In fact it is possible to "see", inside the washer, the hot ablating PPS. Note that the opacity data used to obtain Figure 6b represents an average ion at the density and temperature of the material at the given position, so all the fine details of the experimental spectrum are not recorded.

The oval shapes seen in Figure 6 (and 7) are due to the reduced chord length at the edge of the target (Figure 4 side view).

Results for the low mix shot contrast sharply with those for a high mix shot shown on Figures 7a and 7b. Here an overlap of the order of 150 μm is obtained experimentally and matched by one of the mix models. Several heated (Ne like) sulphur lines are clearly visible, in particular the 1s-2p line at 2.3 kev. Closer to the mixed region the cooler (Si or P like) 1s-3p sulphur line at 2.449 keV

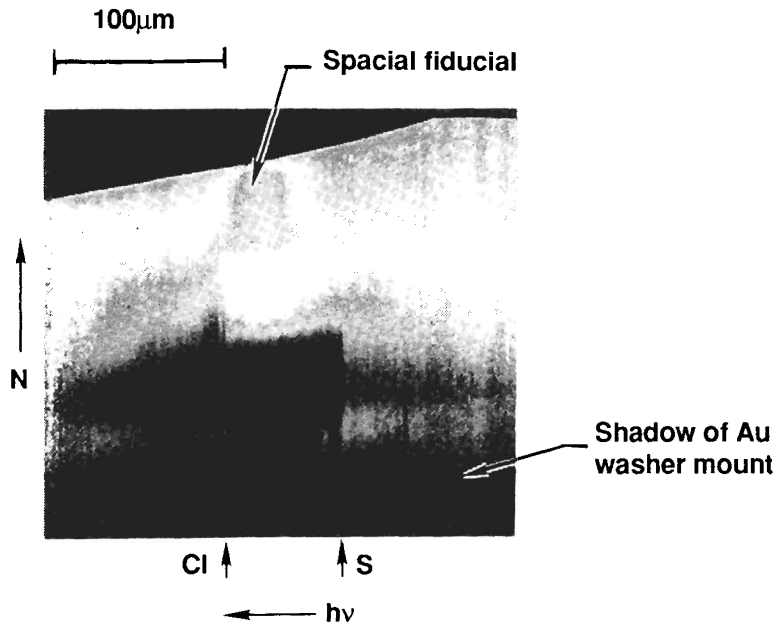

Fig. 6a Experimental radiograph – low mix shot

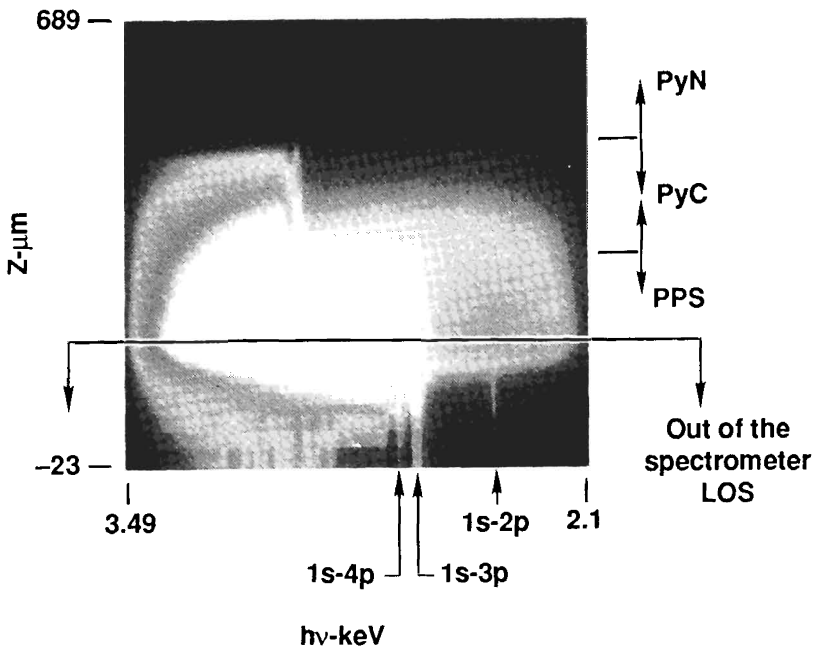

Fig. 6b Simulated radiograph – low mix shot

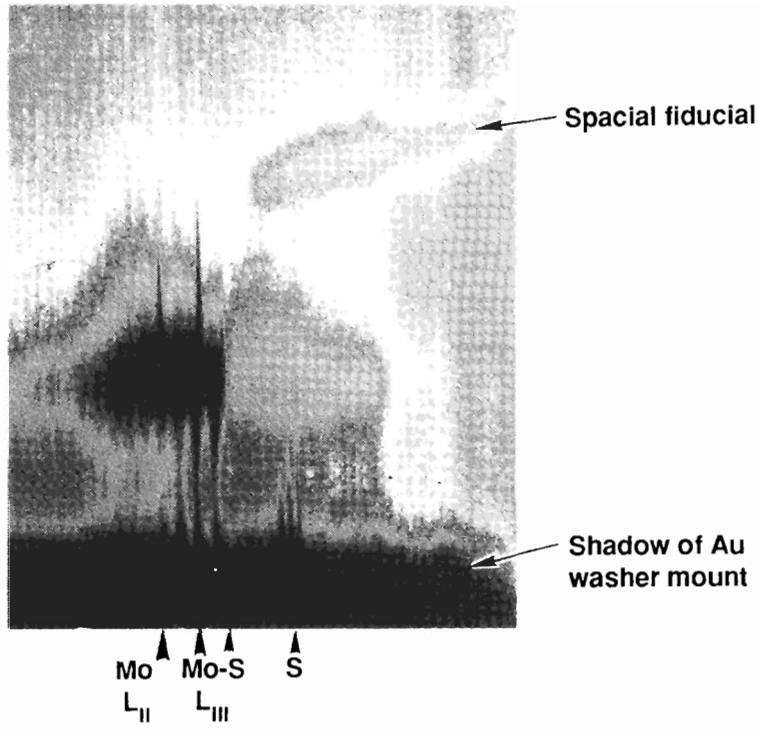

Fig. 7a. Experimental radiograph – high mix shot

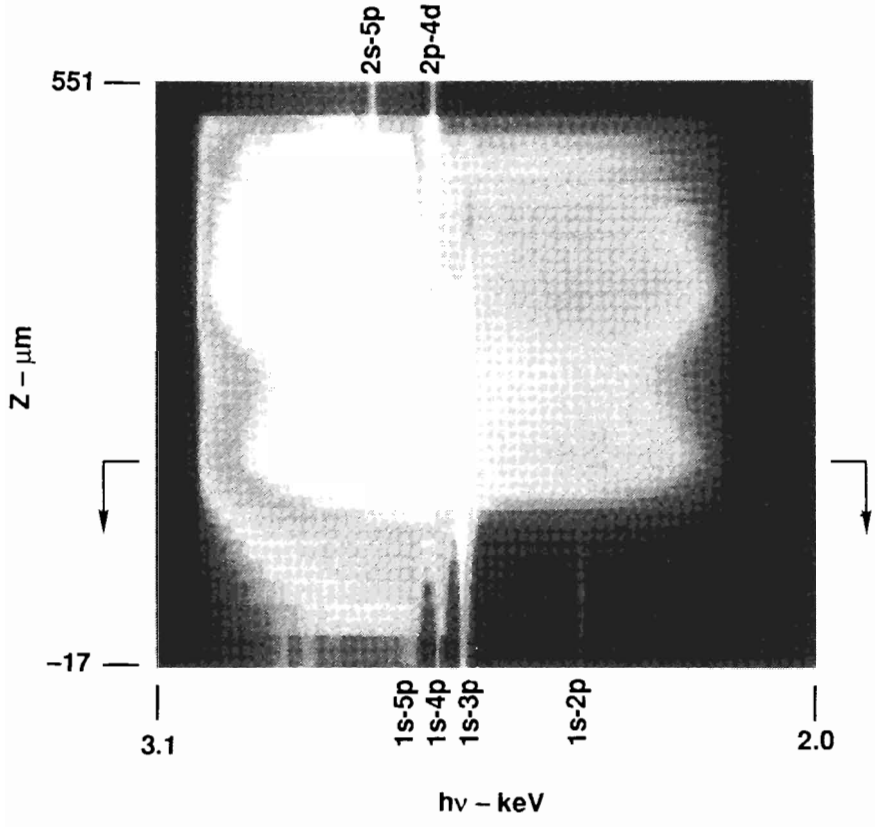

Fig. 7b. Simulated radiograph – high mix shot

dominates the spectrum, while the dominant line for the Molybdenum is the 2p-4d Zr like line at 2.55 keV. The experiment had been designed specifically to maintain the sulphur sufficiently cold within the mixed region to avoid overlap of the 1s-4p S line and the 2p-4d Mo line: such an overlap, which invalidated the diagnostic method, had been observed in experiments with a thin ablator for early time snapshots.

It is interesting to note that on the experimental radiograph the region of minimum backlighter transmission lies entirely within the mixed layer, and the ablator, as evidenced by the S 1s-3p line, extends beyond it. Computationally such a behavior is difficult to simulate as, in general, the high opacity of the Mo overwhelms the density distribution, which shows a peak in the PPS region, and leads to the minimum transmission region extending outward of the mix region throughout the Mo. Only one set of parameters in the mix model, out of many, resulted in a material distribution as shown in Figure 7b, which resembles the experimental data.

Under some broad assumptions about opacities, the areal mass of the different materials versus axial position can be extracted from the experimental data as shown in Figure 8.

These data can then be compared with calculated density distributions. Note that the mix calculations are one dimensional, and, to compare with the experimental data, some constant "effective sample diameter" at snapshot time is implicitly assumed. The two dimensional calculations show that such an assumption is not strictly correct; moreover, the narrow range around the nominal unmixed interface where 2-D calculations show material overlap within the instrument line of sight (no mix) is not simulated by the 1-D calculations. Hence at this time, only qualitative comparisons of the density distribution can be made between experiment and calculations. The total material overlap is not dependent on the various assumptions underlying either the experimental data reduction or the 1-D calculations, and quantitative comparisons are possible.
Comparison of Figure 7 and 9a show

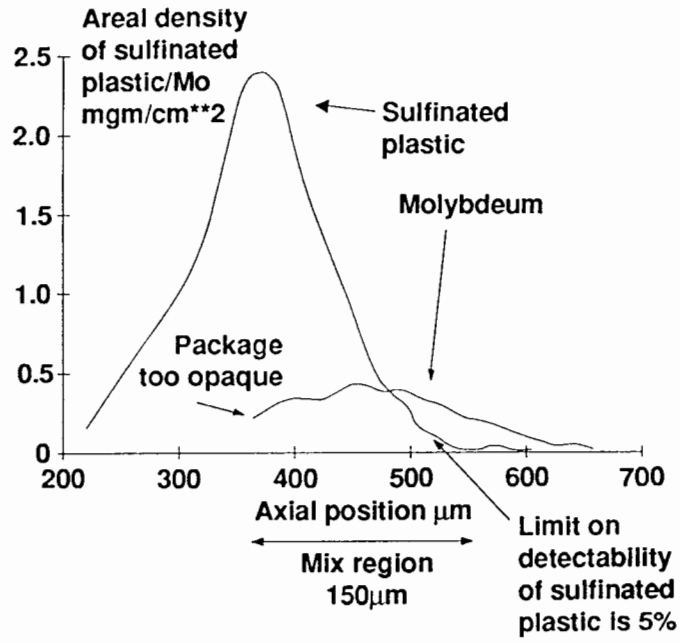

Fig. 8 High mix package - estimate of experimental mass distribution

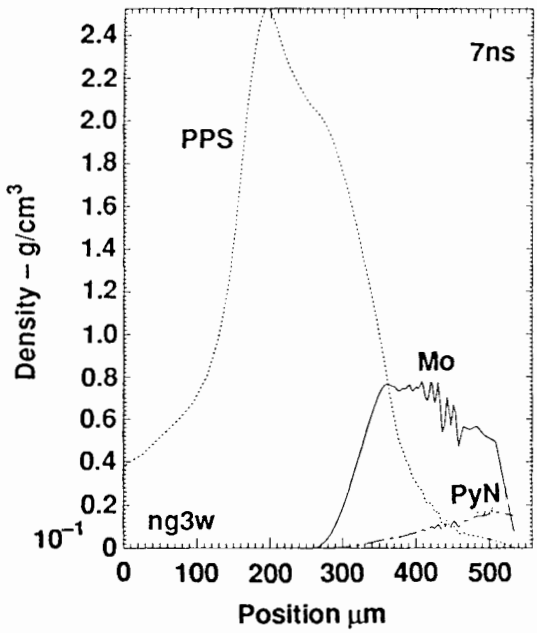

Fig. 9a Simulated density distribution - high mix package

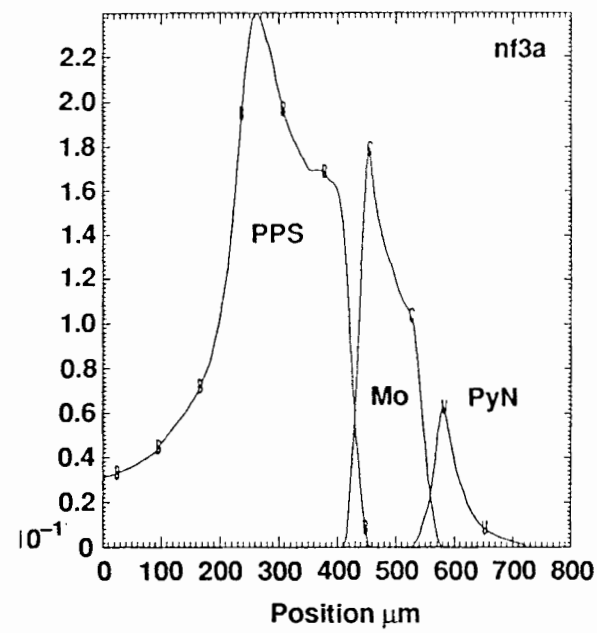

Fig. 9b Simulated density distribution - high mix package

that some appropriate choice of model parameters gives the correct mix width and also reproduces fairly well the axial mass distribution. Figure 9b shows poor results obtained from a different set of model parameters.

Calculations, such as those shown on Figure 9, show that the experiments are indeed providing data useful for normalizing our mix models. Many of the model parameters used to analyze NOVA data are identical to those used for the shock tube results.[1,2] More data from both sets of experiments are needed to uniquely define all the model parameters.

Development of the experimental techniques at NOVA have reached fruition, and we are ready to start a comprehensive experimental series where a single target configuration will be tested at various times with double backlighters.

ACKNOWLEDGEMENTS

The NOVA mix experiments are a cooperative effort between AWE and LLNL. Dr. P. Fieldhouse and his colleagues have been conducting a number of similar experiments with the Helen laser and providing timely information to aid in conducting and interpreting the NOVA experiments. We wish to acknowledge in particular the contributions of T. Goldsack and J. Hansom.

RAYLEIGH TAYLOR INSTABILITY OBSERVATIONS OF SHOCK ACCELERATED GASES

N C Stearman
Atomic Weapons Establishment, Foulness,
Essex, SS3 9XE, United Kingdom

The initial aim of this work was to reproduce the work of Meshkov et al (1) by using a shock tube of 8x2 inch cross section to produce high acceleration gradients in gases initially at atmospheric pressure and thus observe the growth of Rayleigh Taylor instabilities. The work has since diversified and has to date included two interface geometries and also isolated bubble studies. In both cases the interaction of refrigerant 12 (freon), density 5.36 gm/litre, with both air, 1.2 gm/l, and helium, 0.18 gm/l, has been observed using shadowgraphy (fig 1) and compared with 1-D and 2-D computer simulations.

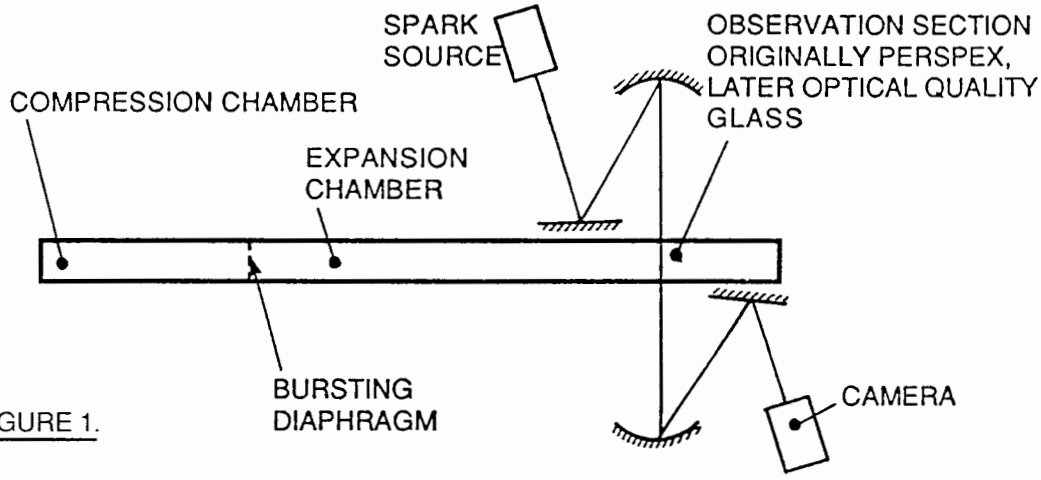

FIGURE 1.

PLANE GEOMETRY

Gas separation in the first case was achieved by the use of a thin membrane produced by pouring a solution of basically nitrocellulose on to a water surface and allowing the solvents to evaporate. The thickness of the resulting membrane may be ascertained from the colours reflected, (as with oil on water). Most of the membranes used reflected no colour at all indicating that the thickness is less than half a wavelength of visible light, ie approximately 0.2 microns.

Photographs obtained from three tests of each of air/freon/air and air/freon/helium are shown in figs 4a,b. Flat topped air shocks of approximately 0./6 bar overpressure, (fig 2), were incident on the layer. Two dimensional numerical simulations of the situations are shown in figs 5a, b and a correspondence is clearly visible in many distinctive features.

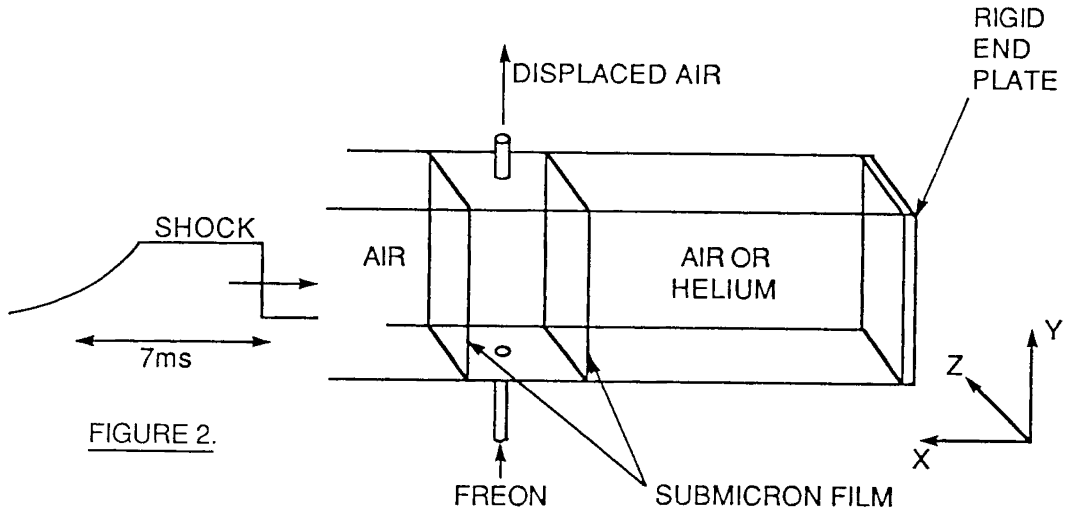

FIGURE 2.

In order to be able to compare such chaotic behaviour it is necessary to study the general effect rather than specific features. Therefore the maximum width of the mix region predicted and observed was compared. At early times the visual estimates of the width of the mixed regions in the experiments may be affected by edge effects. Figure 6 shows the results of 1 dimensional Lagrangian calculations. With no mixing the solid lines show the positions of the interfaces. Also shown are the observed mix widths from the tests. Figure 7 shows the limits of the mixed region predicted by a two dimensional calculation using a technique described by Youngs (2) with a perturbed interface such that:

$$\text{perturbation, } \zeta(y) = s \sum_{n=n_1}^{n_2} a_n \cos \frac{n\pi y}{w}$$

where y = vertical height

n_1 = 2 n_2 = 20

w = width of computational region = 10 cm

a_n = random number chosen from [-1,+1]

s = scaling factor chosen so $[\langle\zeta^2\rangle]^{0.5} = \sigma$ = 0.2 mm

These are the conditions that applied for figs 5a,b. Calculations for air/freon/helium were also performed.

Comparison of the code simulations and the experimental results reveals a consistent under-estimation of mix growth. At late time the ratio of observed to calculated mixed region width is about 1.4. The size of the mix features is less than the internal width of the shock tube and this allows growth in 3-D, thus it might be supposed that the extra degree of freedom promotes more thorough mixing. The results show good general agreement nonetheless.

BUBBLE EXPERIMENTS

The bubble experiments were of a broadly similar nature, (fig 3), and again shadowgraphs and numerical simulations of the conditions were compared, (figs 8 and 9). Shock overpressures in these experiments were around 0.3 bar. The bubbles

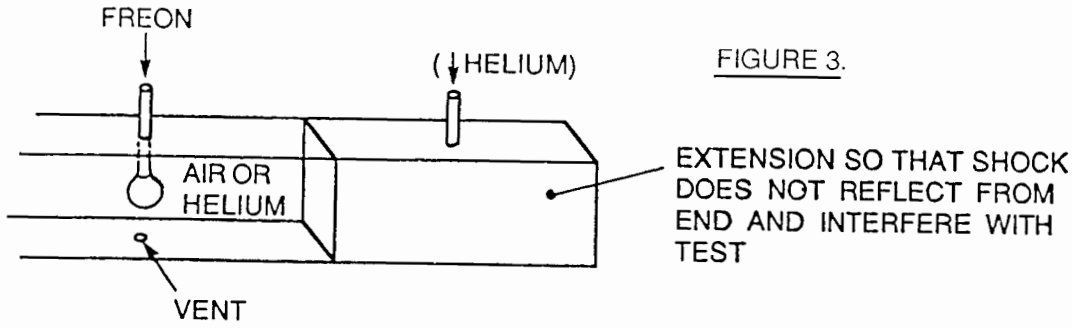

FIGURE 3.

were blown in a solution of Expandol, a fire fighting foam, as this was found to produce long lived bubbles and did not allow diffusion of freon. As may be seen from fig 8 the bubbles were attached to the generating stem at the time of shock impact but this appeared to have little bearing on subsequent development. They are also not truly spherical. The heavy gas inside the bubble causes it to adopt a raindrop shape but the bottom half was close to hemispherical.

This problem was particularly acute with freon in helium and continuous bubble generation was tried to alleviate the problem. This met with some success but the bubbles were still small and thick walled. The results from these experiments are distinctly different, as expected from computer simulations, fig 9, but are questionable and show the need for refinement of technique. They are not to date suitable for quantitative analysis. Experiments using freon bubbles in air were also described by Haas (3). The aim of the present experimental programme is to investigate late time effects and high density ratios.

Comparison between observation and 2-D calculation should ideally involve the position of the centre of mass. This is not determinable from shadowgraphs and so the position of the leading edge of the bubble has been used for comparison as this is a readily identifiable feature. In order to allow for slightly different shock strengths and bubble diameters dimensionless parameters have been used. (fig 10).

Note that the predicted locus in fig 10 refers to a 15.0mm diameter bubble, (slightly less than the mean experimental value of 16.2mm), because the prediction was from a single calculation performed in advance of the tests.

Good agreement is seen and the tendency for the experimental data to lie above the predicted locus may be accounted for by the constraining nature of the shock tube. The bubbles are of a similar size to the tube width, (34mm dia cf 51mm tube width), and so may restrict the flow and thus become accelerated quicker.

FURTHER WORK

Further experiments whereby a measure of the gas density may be determined at a given point have commenced. These utilise bromine as a colouring agent in the freon. The mixing is then observed by high speed cine photography. With uniform back lighting this technique lends itself to densitometry analysis and thus contours of average volumetric mix ratios along the z-axis may be determined.

Bromine gas has a higher density (7.59gm/l), than freon 12 but is only used

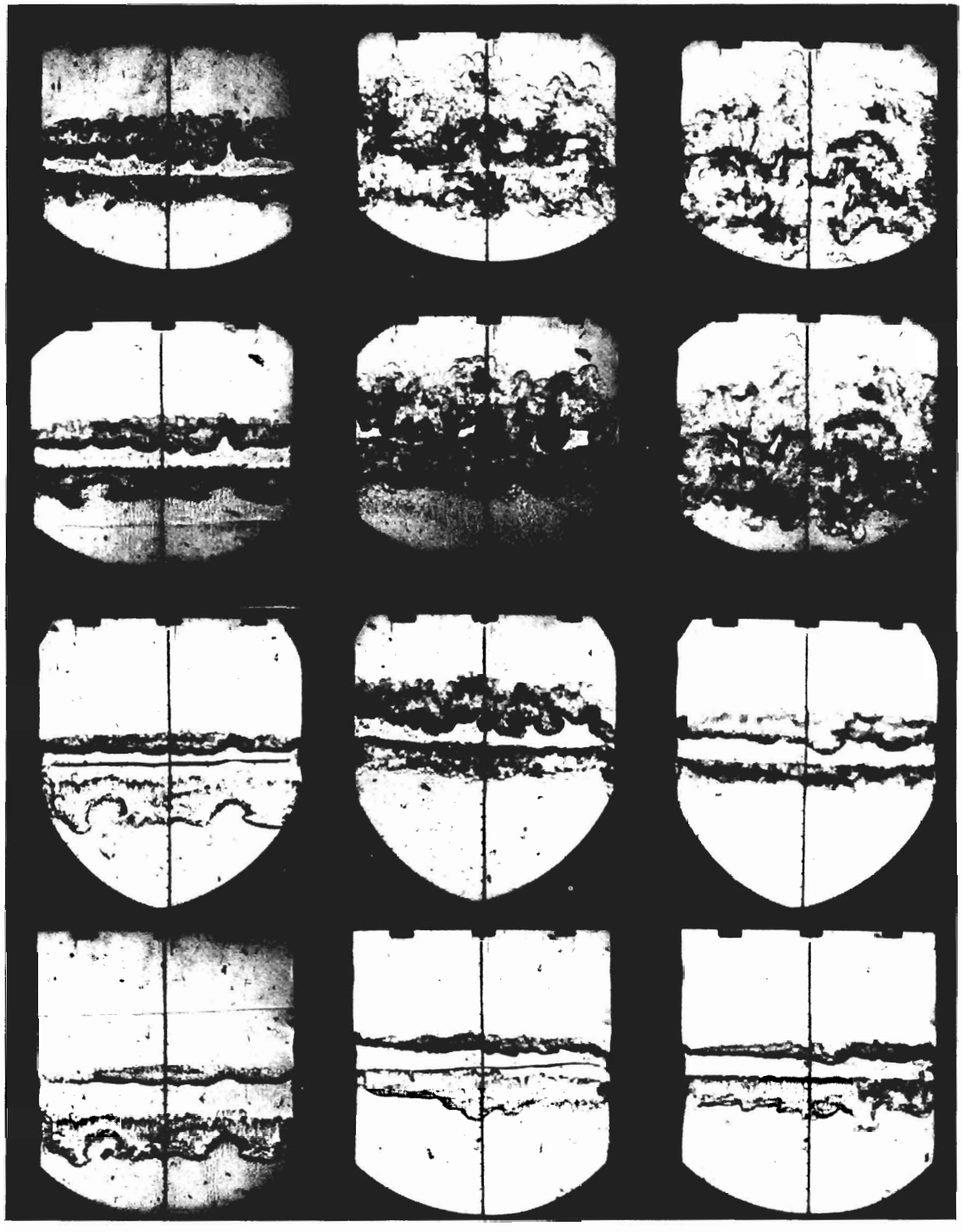

FIGURE 4a Air/Freon/Air Interactions

2.07	2.27	2.47	2.67	ms after shock
2.37	2.97	3.57	4.17	arrival at first
2.37	2.67	4.67	4.97	membrane

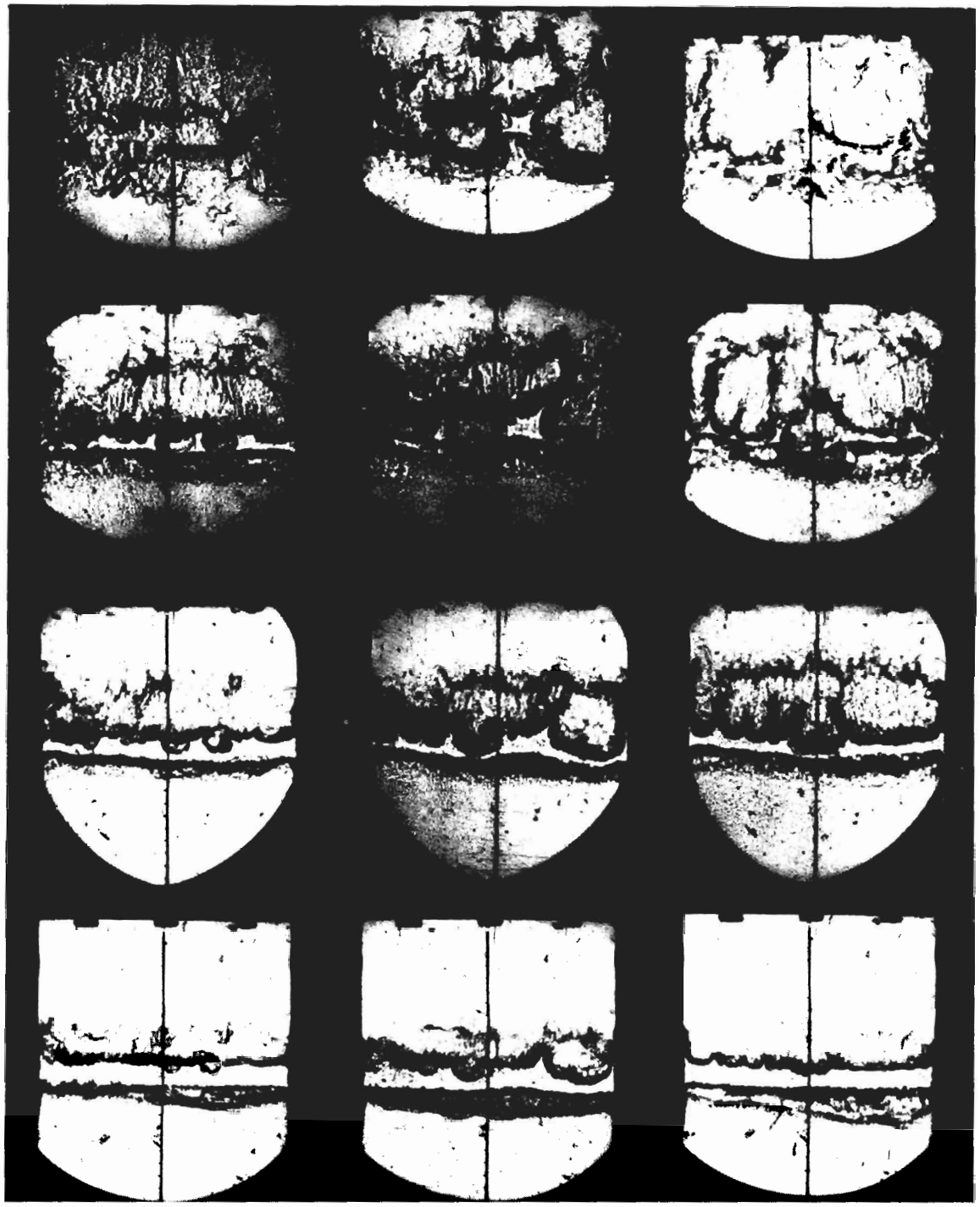

FIGURE 4b Air/Freon/Helium Interactions

2.07	2.36	2.56	4.57	ms after shock
2.07	2.37	2.67	2.98	arrival at first
2.06	2.56	3.06	3.56	membrane

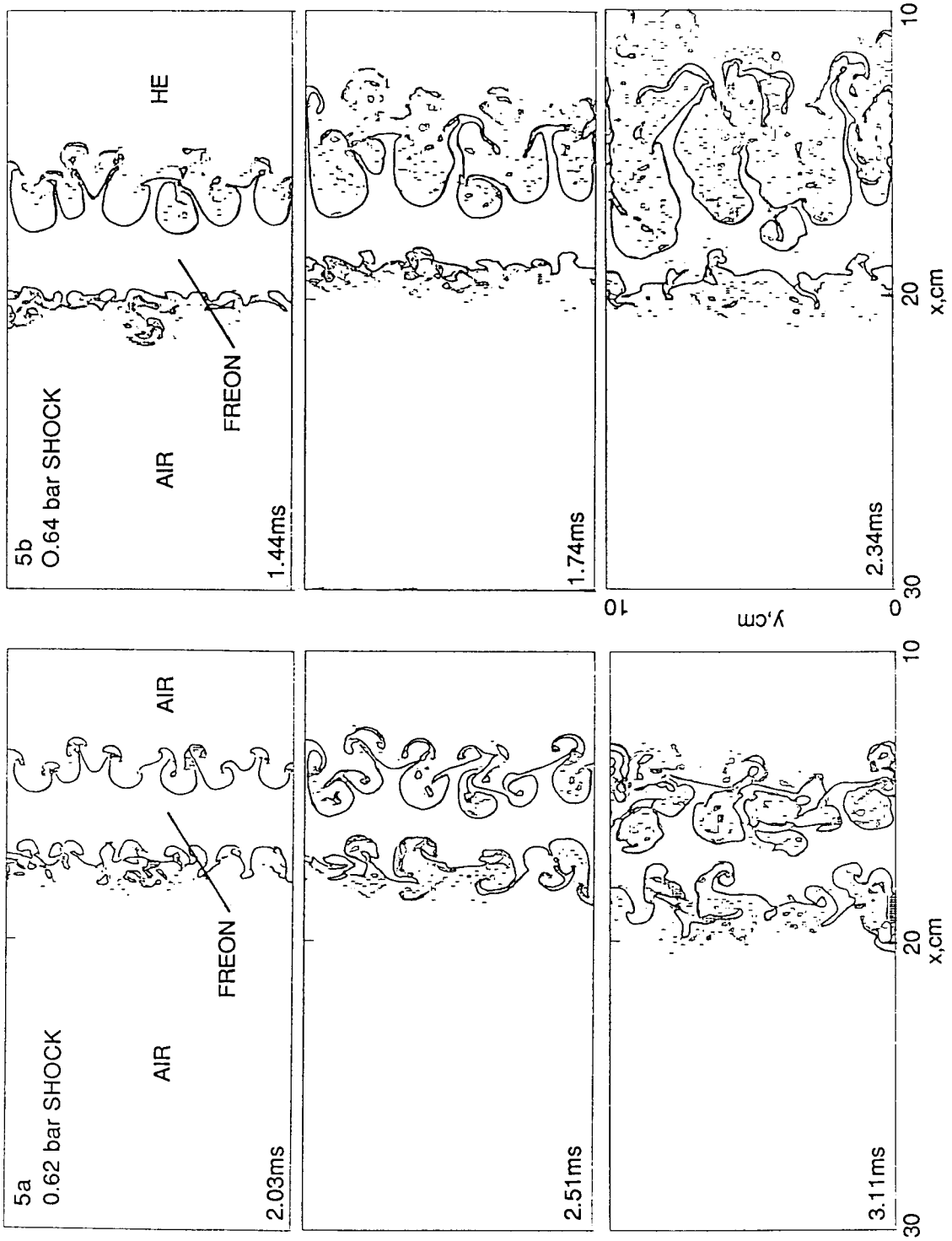

FIGURE 5. INTERACTION PREDICTED BY 2D CODE

in concentrations of a few per cent. Early tests with the double interface experiments have shown that, unless they are made so thick that they do not break up on shock impact, the membranes allow the small bromine molecules to pass through

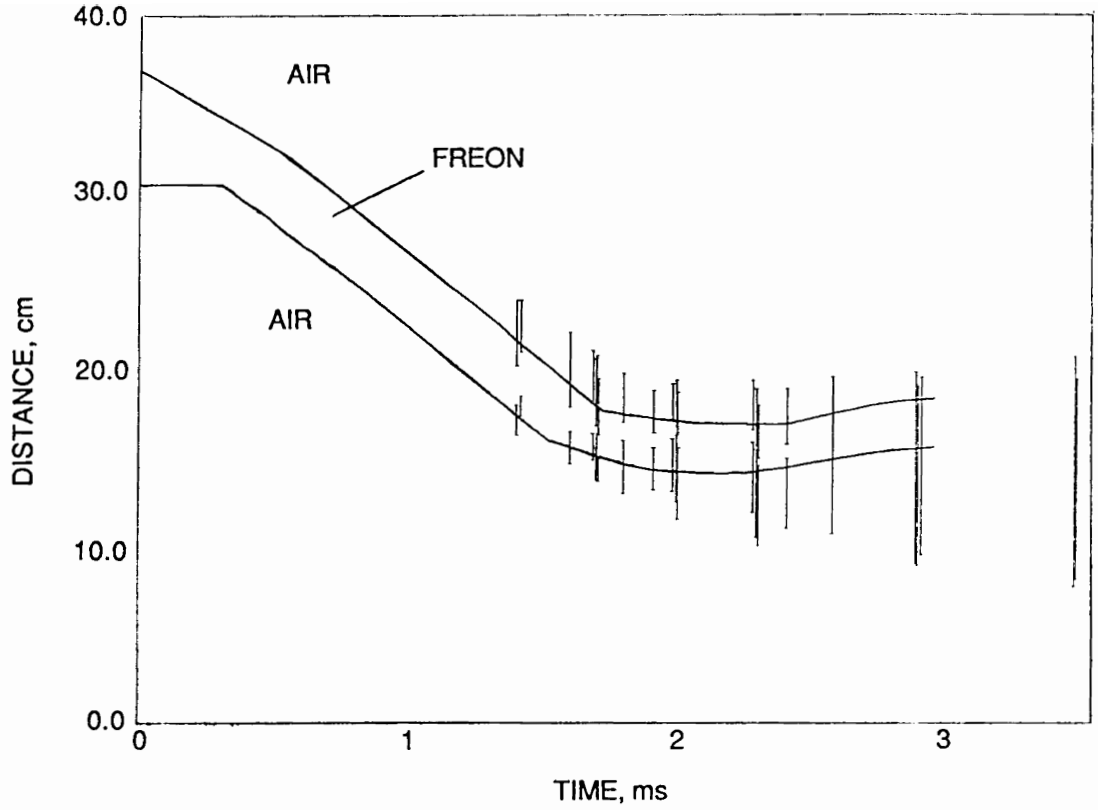

FIGURE 6a. I-D LAGRANGIAN CALCULATION AND OBSERVED MIX WIDTHS

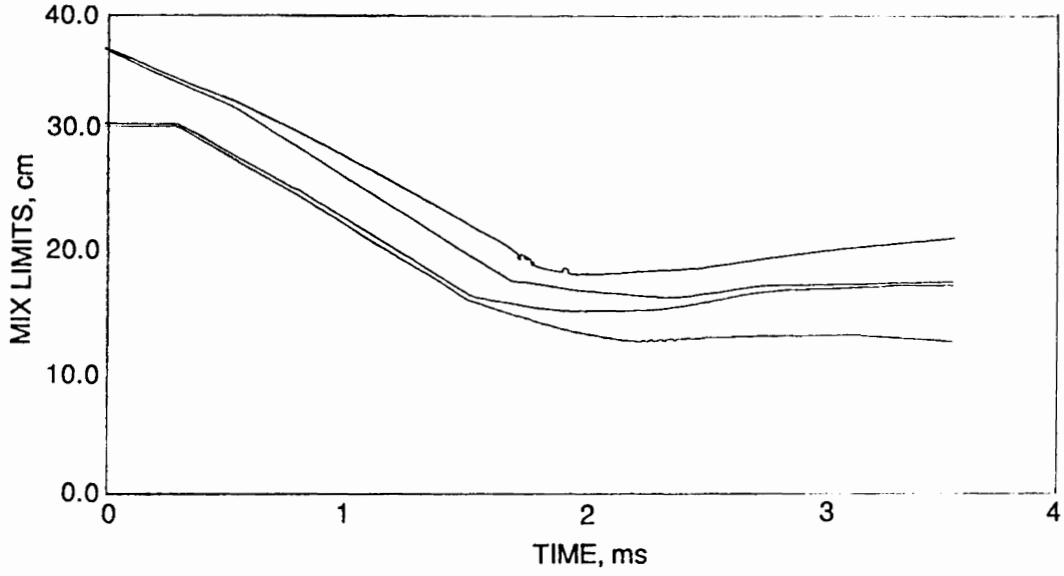

FIGURE 7a. 2-D NUMERICAL SIMULATION

them. Diffusion also prevents any bubble experiments with bromine tracing. Tests replacing the membranes with aluminium foils less than one micron thick have shown that diffusion through the foil is not a problem and makes the proposition feasible.

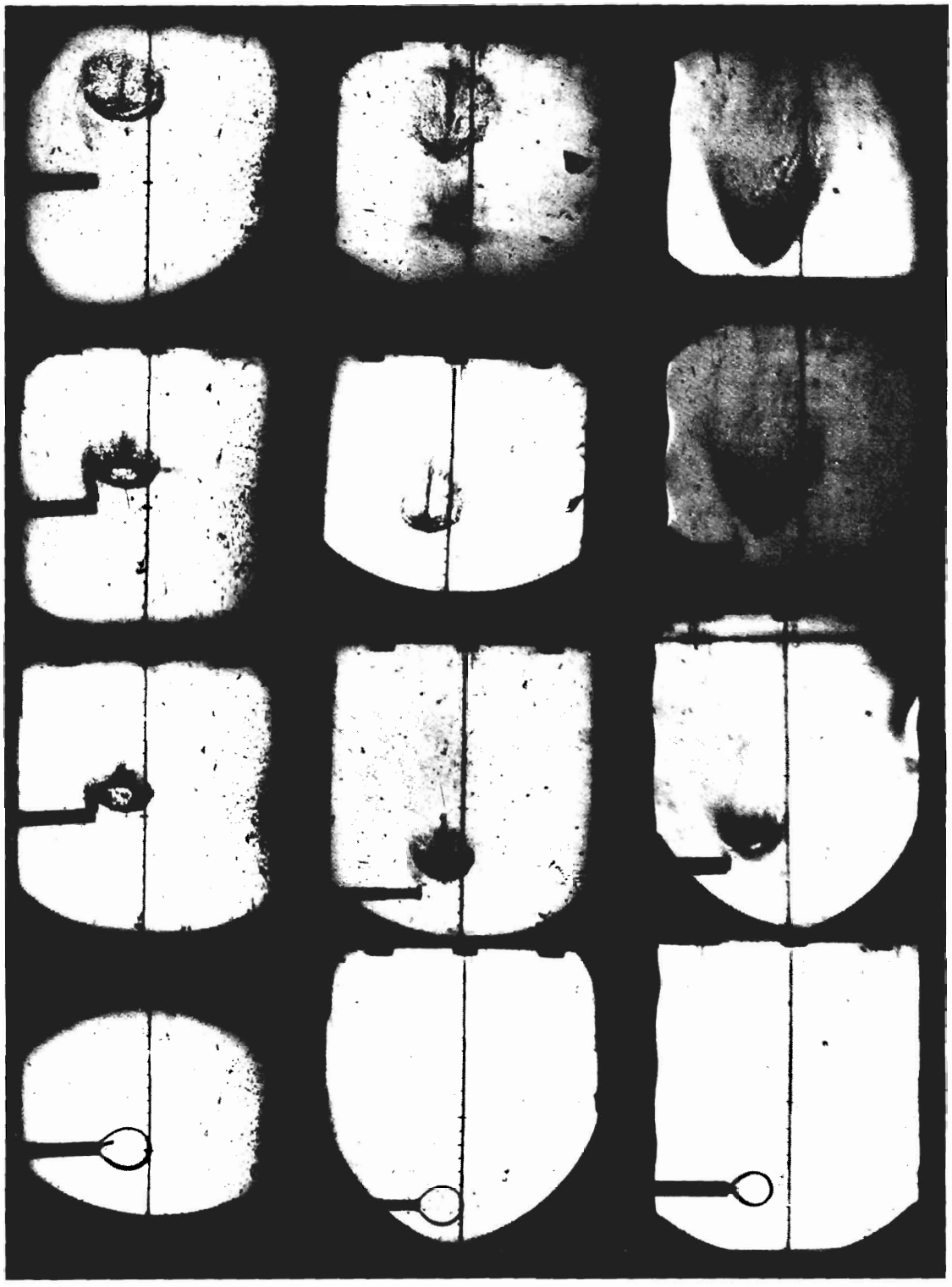

FIGURE 8 Freon Bubble in Air and Helium

Air	-0.80	0.70	1.00	1.70	ms after shock
	-0.53	0.97	1.97	2.97	arrival at leading
	-0.05	0.75	1.16	1.36	edge of bubble

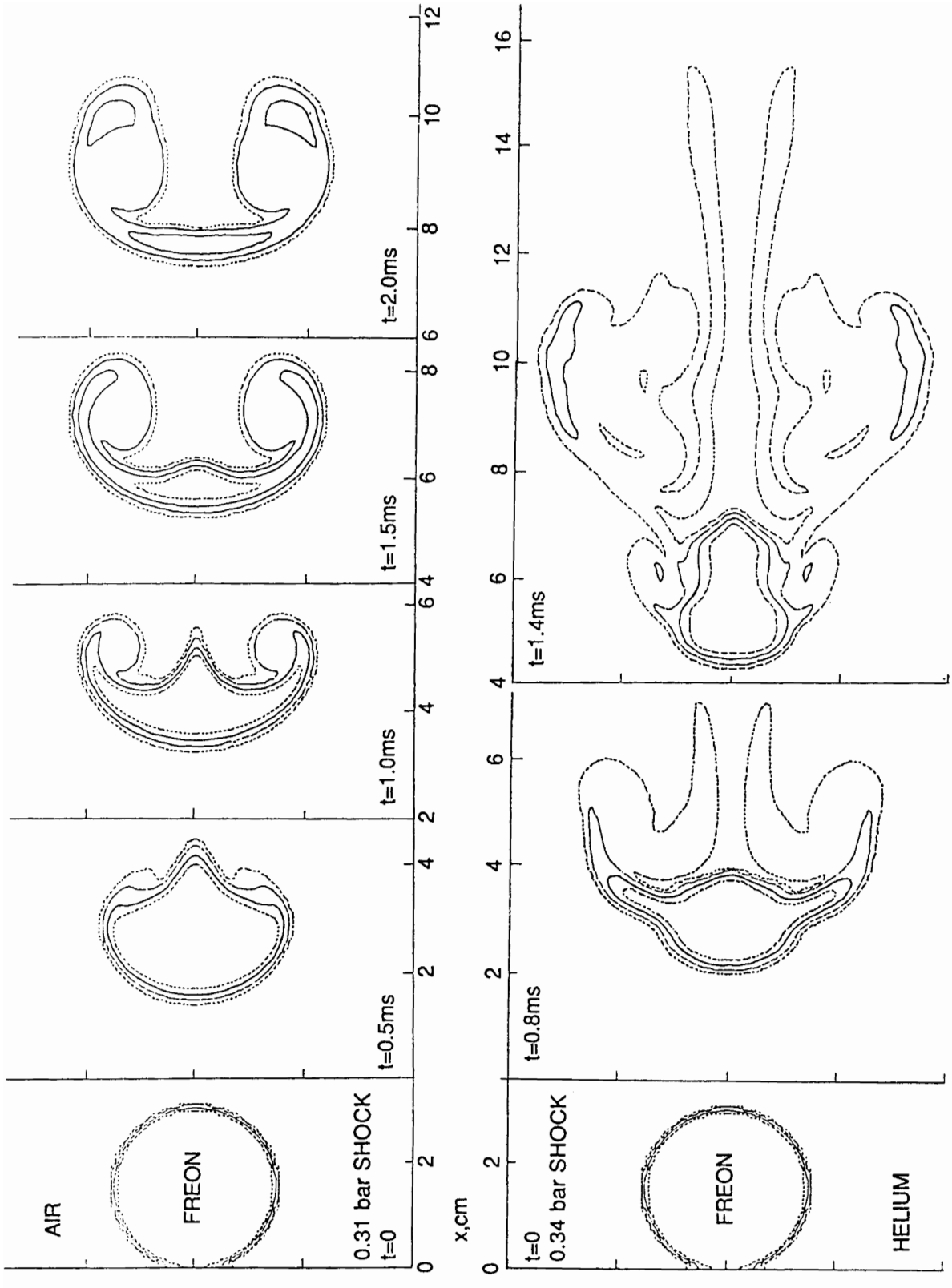

FIGURE 9. 2D CALCULATIONS OF BUBBLE BEHAVIOUR

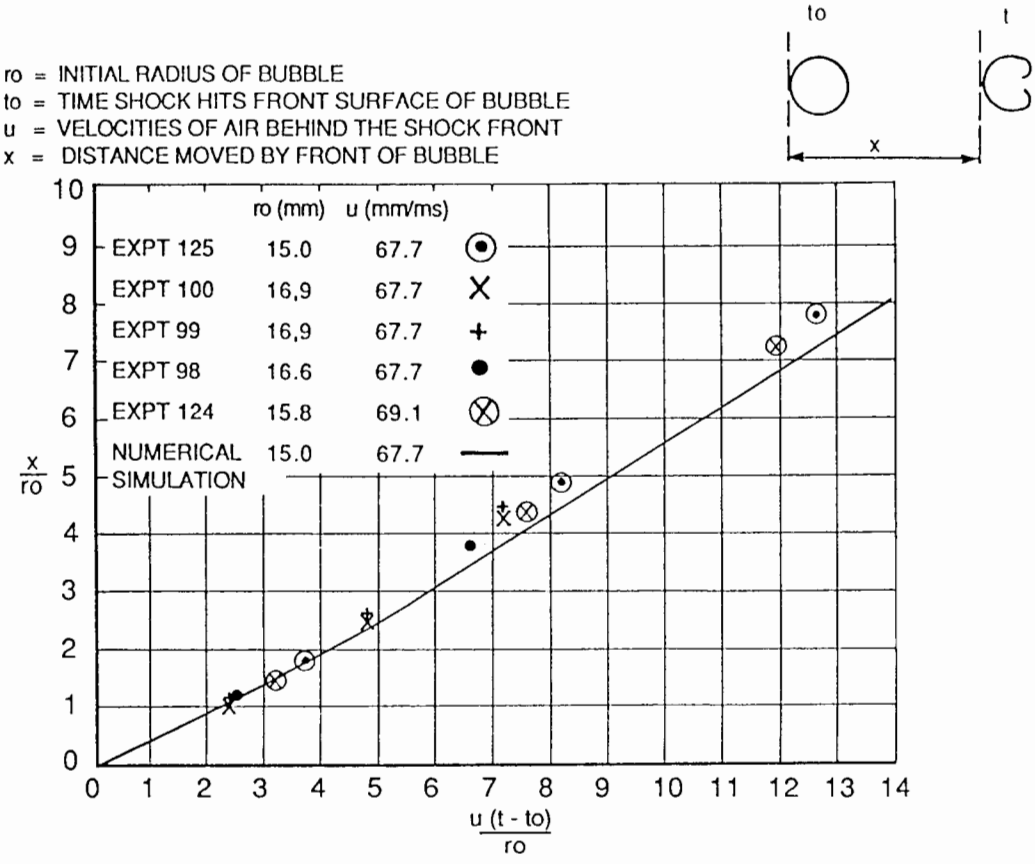

FIGURE 10. COMPARISON OF PREDICTED AND OBSERVED DISPLACEMENT OF FREON BUBBLE IN AIR

Handling the foils is most difficult as they are far more brittle than the nitrocellulose membranes.

Future experiments replacing shadowgraphy by holography to study various instability interactions are to take place in Nov 88. Both absolute and differential interferometric techniques will be employed.

ACKNOWLEDGEMENTS

Numerical simulations performed by N W Cowperthwaite.

REFERENCES

1. V Andronov, S M Bakhrakh, E E Meshkov, V N Mokhov, V V Nikiforov, A V Pevnitsvii and A I Tolshmayakov, Sov. Phys JETP 44 p424-427 (1976)

2. D L Youngs, Physica 12D, p32 (1984)

3. J F Haas, B Sturtevant, J Fluid mech 181 p41 (1987)

EXPERIMENTAL RESEARCH OF GRAVITATIONAL INSTABILITY AND TURBULIZATION OF FLOW AT THE NOBLE GASES INTERFACE

A. M. Vasilenko, O. V. Buryakov, V. F. Kuropatenko,
V. I. Olkhovskaya, V. P. Ratnikov, V. G. Jakovlev

INTRODUCTION

A special type of turbulence — gravitational turbulence appears at the interface of media having different densities under nonstationary motion because of Taylor instability [1]. This phenomenon takes place, for example, when nonstationary shockwaves pass through nonhomogeneous media.

Theoretical description of the development of small interface perturbations is of no difficulty but in the process of experimental work it came out [2-4], that the growth of finite perturbations, comparable with the wave length, leads to the distortion of their initial form and complicates the analytical examination of this problem [5].

Gravitational turbulent mixing theoretical research made by Belyenkii and Fradkin [6] and some other authors [7-9] is of semi-empirical character. In some works [10-13] gravitational instability numerical research on the ground of Euler nonstationary equations with two spatial variables was carried out.

Experimentally this problem is also poorly investigated. There are few works [14-16] devoted to this question.

The aim of this work is the experimental research of turbulization process of interface perturbations for gases having different densities under the influence of the strong decelerating shockwave under the condition of essential compressibility of initial substance.

The noble gases choice was made in terms of the equality of their adiabatic compressibility. This sufficiently simplifies the experimental analysis.

I. EXPERIMENTAL METHOD

1.1 The Description of the Experiment

The experiments were carried out in the electromagnetic shock tube which is shown in Fig. 1.1. Shock tube frame is made of textolite plates in the form of compartments of different length and purpose. This allows change to not only the total tube length, but also the compartment's position.

Shock tube channel with the cross section of 100 x 100 mm^2 was partitioned off at the joints by two nitrocellulose diaphragms, 0.4 mm thick, into three compartments filled with various noble gases, as shown in Fig. 1.1.

Such a system of gas layers was subjected to the action of decelerating shockwave. As a result, this caused the state of gravitational instability at the second interface, between Krypton and Helium, in accordance with Taylor criterion [1]. Acceleration at the interface was created by unloading wave defining the flow deceleration. The use of noble gases permitted retention of the initial gas density ratio after the rupture disintegration at the stable interface. The first interface was stable and served for shock-wave intensification in order to create necessary conditions for rapid nitrocellulose diaphragm destruction. These conditions were considered to be satisfied in case the temperature of one of the gases at the interface exceeded nitrocellulose flash temperature.

At the second interface, sinusoidal perturbations were artificially set on lateral sides of the sectional aluminum frame then the nitrocellulose diaphragm was fixed between the sinusoidally preformed frame sections. The profile on the frame is formed by conjugate circle arcs, which is a quite satisfactory approximation to the sinusoidal profile. To avoid significant distortion of set perturbation form on the frame, because of film tension, it was fixed to fifteen nichrome wires 0.12 mm thick, stretched along the profile generator.

In experiments the development of three initial perturbations was examined, namely: α_o = 1 mm, λ = 25 mm, α_o = 1 mm, λ = 50 mm, α_o = 2.5

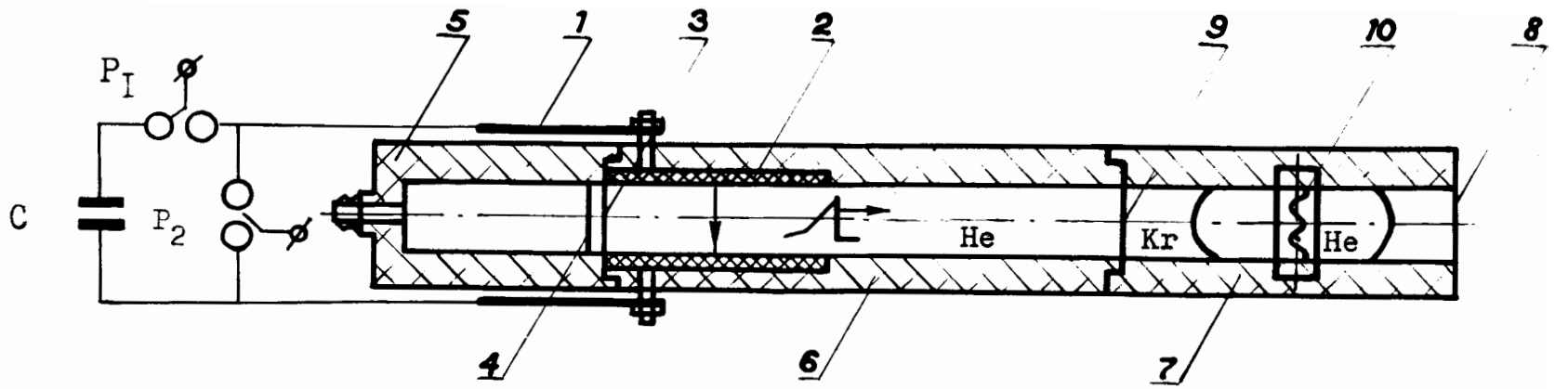

Fig. 1.1 Schematic representation of the electromagnetic shock tube.C - capacitor bank: P_1, commutative discharger; P_2, short-circuiting discharger; 1, collector busbar; 2, accelerating electrode; 3, additional diaphragm; 4, principal diaphragm; 5, vacuum compartment; 6, discharge compartment; 7, measuring compartment; 8, diaphragm; 9, joint for thin film mounting; 10, joint in the measuring compartment for the mounting of the frame with a film.

mm, λ = 50 mm. (α_0 - initial amplitude, λ - wave length). Recording of the perturbations development was carried out by means of a shadow device IAB-451 optically coordinated with two SFR cameras operating in the mode of stop-motion photography and photochronography.

1.2 Main Characteristics of the Electromagnetic Shock Tube

Shock-wave generation was obtained as a result of the discharge of a capacitor bank consisting of 90 capacitors of IS-6.65-20 type. Total inductance of the electromagnetic shock tube circuit equals 223 nH. The electromagnetic shock tube is equipped with a short-circuiting discharger P_2 (see Fig. 1.1). This permits formation of single pulses of the discharge current.

The distinctive feature of the given electromagnetic shock tube [17-19] is a vacuum compartment (5 in Fig. 1.1) which forms the flow behind the front of a rather long shock wave. The front is not distorted by the secondary shock wave. The secondary shock wave appears in the electromagnetic shock tube when forming a single discharge current impulse because of oscillation of a vacuum region formed when the flow layer separates from the shock tube "bottom" under the influence of the intrinsic discharge magnetic field. The flow, forming in the electromagnetic shock tube, is analogous under such conditions to the flow forming in the automodel problem about the short-term shock upon a free gas surface [20]. The flow forming is characterized by the limiting value of shock wave deceleration for the given conditions of experiments.

The vacuum compartment is separated from the shock-tube channel by two thin mylar diaphragms destroyed at the discharge current initial stage.

The first diaphragm had five thin strips of an aluminum foil; each was 2 mm wide and 10 mm thick. They were needed for the electric breakdown between electromagnetic shock-tube accelerating electrodes.

1.3 Calculations for the flow in the electromagnetic shock tube were carried out in accordance with the program "VOLNA" (WAVE) which is intended for mathematic modeling of one-dimensional unsteady motions of compressible ideal media [21].

Physical model realized in the program VOLNA is based on partial differential equations which are a consequence of laws of conservation of mass, momentum, and energy in the Lagrangian coordinate system.

In a common case a domain, where the solution must be found, consists of several regions, each characterized by its own equation of state, by its own speed, and by its thermodynamic parameters set at the initial moment of time. Regions are separated from each other by interfaces or vacuum gaps. Boundary conditions are pistons where either speed or initial pressure is set. Nonuniform differential method is used for numerically integrating of set of equations for a given physical model. This method permits tracing the following elements and features:

1. Smooth solutions.
2. Strong, weak and contact ruptures.
3. Phase transformation front — strong or weak rupture on the surface at which the matter phase state changes.
4. Arbitrary rupture disintegration.
5. Strong rupture emergence out of the initially smooth solution.
6. Interaction of strong rupture with initially smooth solution.

To determine the flow parameters at the strong rupture front, the Hugoniot relation is solved in common with the equation for the changing values of velocity along the rupture surface. The equation is of the following form:

$$\frac{d[P]}{dt} + \frac{C^2}{W} \cdot \frac{d[U]}{dt} + A = O,$$

where:

$$A = \frac{(\alpha - 1)\, U + V_+ C^2}{U} + \frac{C_+^2 - W^2\, \alpha(r^{\alpha-1})}{W} \cdot \frac{\delta P}{\delta t} + \frac{C^2}{W} \cdot \frac{dU}{dt}. \qquad (1.1)$$

Where [P], U represent sudden changes of pressure and velocity on the surface of strong rupture; C is the sound speed; W is the mass velocity of the strong rupture surface; α is the problem symmetry index; r is a spatial coordinate; t is the time. Values with the mark "-" denote the state

"before", and values with the mark "+" denote the state behind the rupture surface.

For the velocity of the shock wave, W, this equation will have the following form:

$$\frac{dW}{dt} + \frac{1}{[U]}\left[\left(\frac{C_+^2}{W} + W\right)\frac{d[U]}{dt} + A\right] = O \qquad (1.2)$$

Nonuniform differential method realized in WOLNA program uses a regular difference grid for the regions of integrating with smooth solutions and "blurred" features, and also uses a feature refining the grid which is superposed on the regular grid.

Difference schemes included in the nonuniform differential method are obvious and have the first order of approximation in time, and the second order in space on the uniform grid.

In a given case, the impulse of pressure is set on the left gas boundary which corresponds to the beginning of the shock tube. The impulse form is defined by the first semiperiod of the current discharge.

$$P = \begin{cases} P^* \exp(-2t/\tau) \cdot \mathrm{Sin}^2 2\pi t/T \; n\rho u & 0 \le t \le \frac{T}{2}, \\ 0 & n\rho u \; t > \frac{T}{2} \end{cases} \qquad (1.3)$$

where:

P^* = parameter which corresponds to effective pressure of the magnetic piston;

T = 75 ms — the period of the bankery discharge;

τ = 78 ms — parameter which characterizes the electric discharge attenuation.

In the calculations according to the WOLNA program, P^* was selected proceeding from the condition of reaching the coordinate X = 1993 mm by the shock wave front at τ = 522 μs. We could observe this front in the experiments with helium atmosphere.

P^* was obtained as a result of few calculations for various P which, following interpolation, equaled 140.2 bar.

It is worth mentioning that the flow description with due regard for the secondary shock wave is possible in case of substituting the condition of stopping this boundary (V = 0) for the boundary condition on the left gas boundary after terminating the action of the impulse of pressure.

At this moment the secondary shock wave is being formed considering that it corresponded to the left gas boundary which collided with the vacuum compartment "bottom."

Usually, such a procedure was not used because, in this experiment, the process of interaction of the secondary shock wave with the interface was not studied.

The calculations of flow for the description of the gases gravitational instability experiments were carried out in accordance with the specific scheme of gas disposal in the shock-tube channel (see Table 1.1).

TABLE 1.1

N	Gas	γ	ρ g/cm^3	Interface Coordinate mm
1	Helium	1.63	$1.6 \cdot 10^{-4}$	1087
2	Krypton	1.689	$3.364 \cdot 10^{-3}$	1327
3	Helium	1.63	$1.6 \cdot 10^{-4}$	2500

In the Table: γ — Poisson adiabatic index,
ρ — gas density.

Gas parameters were determined according to table data [22] and were computed at the experimental conditions. Average atmospheric pressure of gases was 0.984 bar.

Confidence of the results of calculations of the flow in the electromagnetic shock tube is shown in X, t-diagram, Fig. 1.2, where the comparison of the trajectory of the shock-wave front movement with experimental results was carried out. Standard deviation of experimental points from the computed curve was equal to 1.2%. This is in the range of the experimental data scattering.

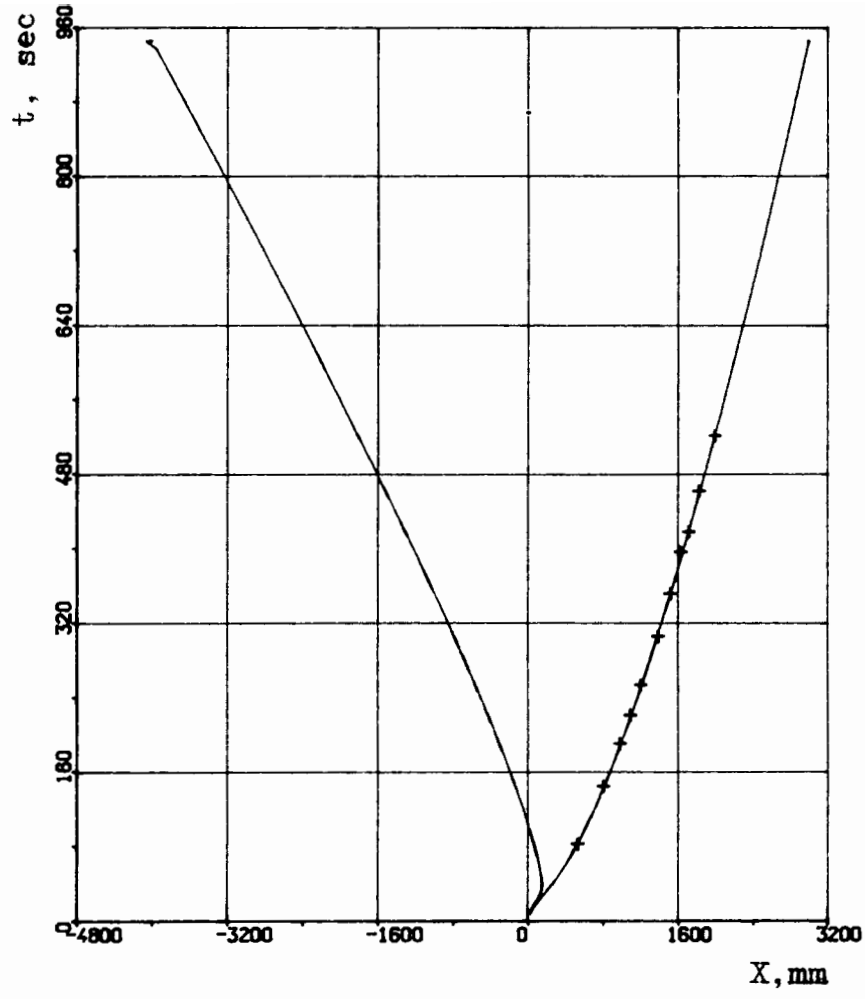

Fig. 1.2 X, t - diagram of the flow in the shock-tube channel in helium atmosphere,- - calculations, + - experiment.

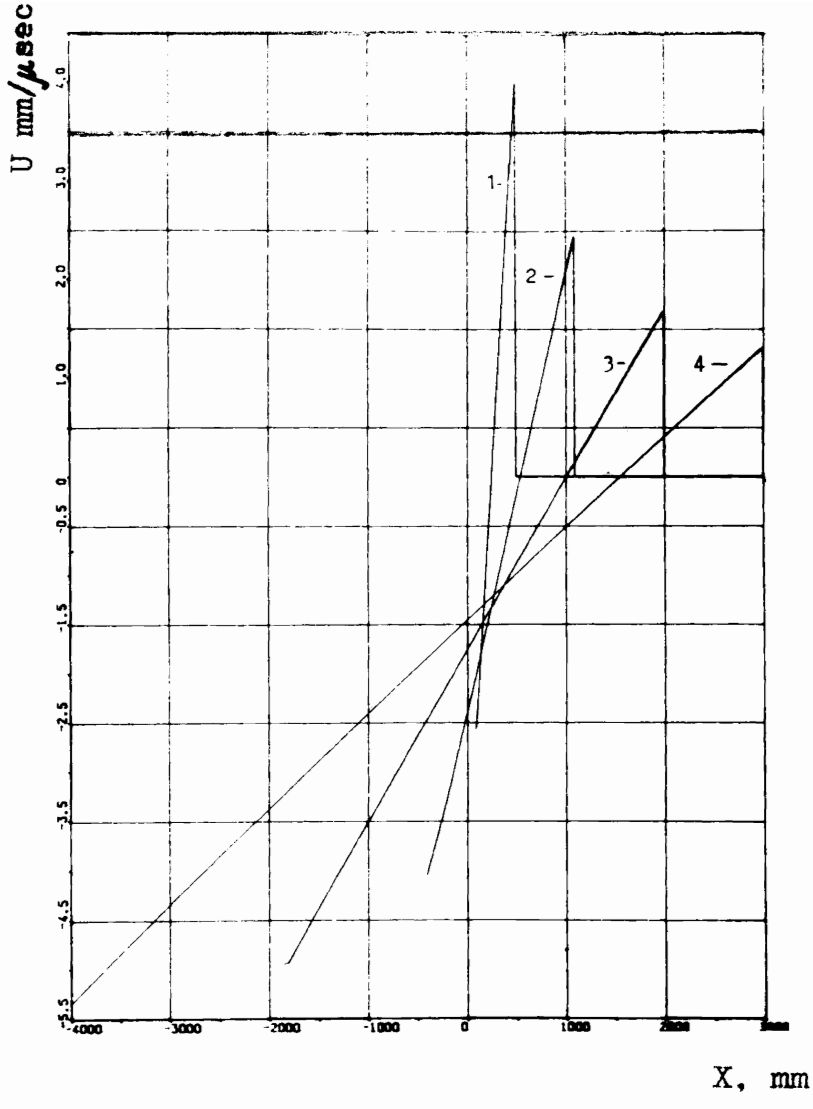

Fig. 1.3 He velocity profiles in the shock tube channel at different moments of time.1 - 80 μsec, 2 - 283.9 μsec, 3 - 522 μsec, 4 - 946.6 μsec.

The current layer shift, caused by the discharge's magnetic field and determined by accelerating electrodes erosion, equals 140 mm. This satisfactorily agrees with the computed shift of 150.9 mm on the left gas boundary.

Gas mass velocity profiles shown in Fig. 1.3 have linear form that demonstrates the approaching of flow to the regime which is close to automodel flow in the problem about short-term shock upon the free gas surface.

2. EXPERIMENTAL RESULTS

2.1 Preliminary analysis of physical conditions at the interface was carried out on the basis of the results of one-dimensional gas flow calculations in the electromagnetic shock tube. Just after the rupture disintegration, the pressure at the interface was P = 3.687 bar and the velocity of the shock wave falling upon the interface was W_1 = 0.8114 mm/ms. Initial mass velocity of gases was V_o = 0.94 mm/μs; gas density ratio was 13.75. Breaking distance connected with the unloading wave influence was determined by the formula

$$S = U_o \hat{t} - \hat{x}, \qquad (2.1)$$

where: $\hat{t}$ - time with respect to the moment when the shock wave reaches the interface;

$\hat{x}$ - distance passed by the interface with respect to the initial position.

Maximum value of the interface deceleration is g = 10^6 m/s^2. By the end of the boundary observation, at the time t = 1151 μs, gas pressure decreases to 2.07 bar, and velocity to 0.487 mm/μs.

2.2 The process of the development of the interface gravitational instability and gas turbulent mixing can be conditionally divided into three stages: regular, transitional and turbulent. The regular stage includes the stage of the exponential growth of perturbations in accordance with the linear theory (see [1]) and nonlinear stage, where

deceleration of perturbations growth and the distortion of their form take place, but spatial structure of perturbations is not distorted.

In the transitional stage the distortion of perturbations spatial structure takes place and the regions of flow vorticity arise.

In the turbulent stage intensive initial substance mixing takes place. The experimental results have been analyzed in accordance with such a classification of the stages of the interface instability development. The shadow photographs of the experiments are presented in Fig. 2.1 - 2.3.

2.3 The regular stage was revealed when comparing the experimental results with analytical solution which was obtained by one of the authors for the case of ideal fluids under condition of successive influence of shock and permanent accelerations upon the interface similar to how it happens in the experiment. The development from infinitesimally small perturbations is described by the following equations [23]

$$\frac{d^2\alpha(t)}{dt^2} = A\kappa g \qquad (2.2)$$

with initial conditions:

where $A = \frac{\rho_2 - \rho_1}{\rho_2 + \rho_1}$ – Atwood number,

ρ_2, ρ_1 - heavy and light liquids densities, respectively;

$$\kappa = \frac{2\pi}{\lambda} \qquad (2.3)$$

Solution has the following form:

$$\alpha = \alpha_o \left[\cosh wt - (U_o/W) \cdot \mathrm{Sinh}\, wt \right],$$

where

$$w = \sqrt{Agk}\,; \qquad W = \sqrt{g/Ak}$$

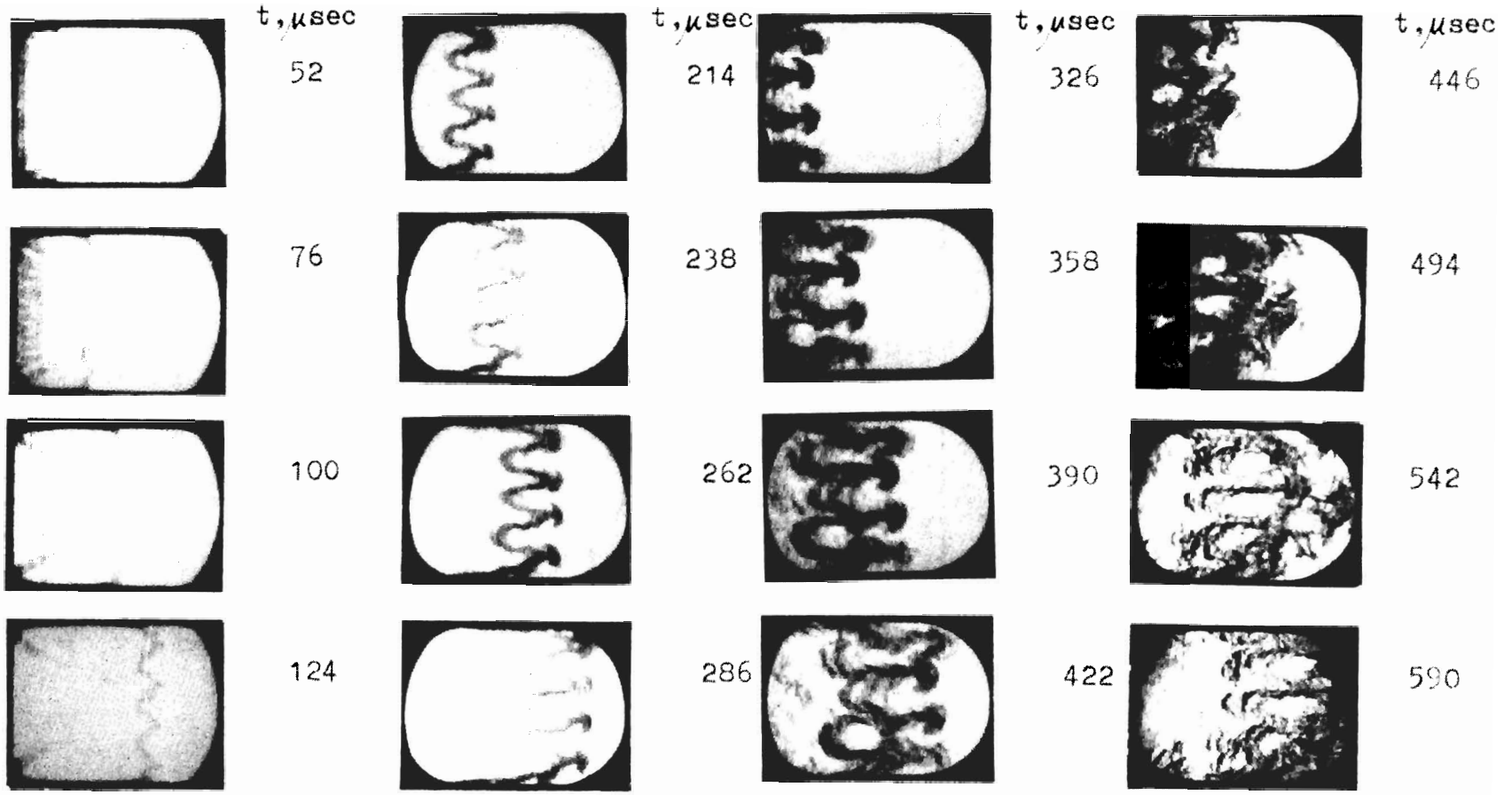

Fig. 2.1 Perturbation development at Kr - He interface with the initial perturbation a_0 = 1.0 mm, λ = 25 mm.

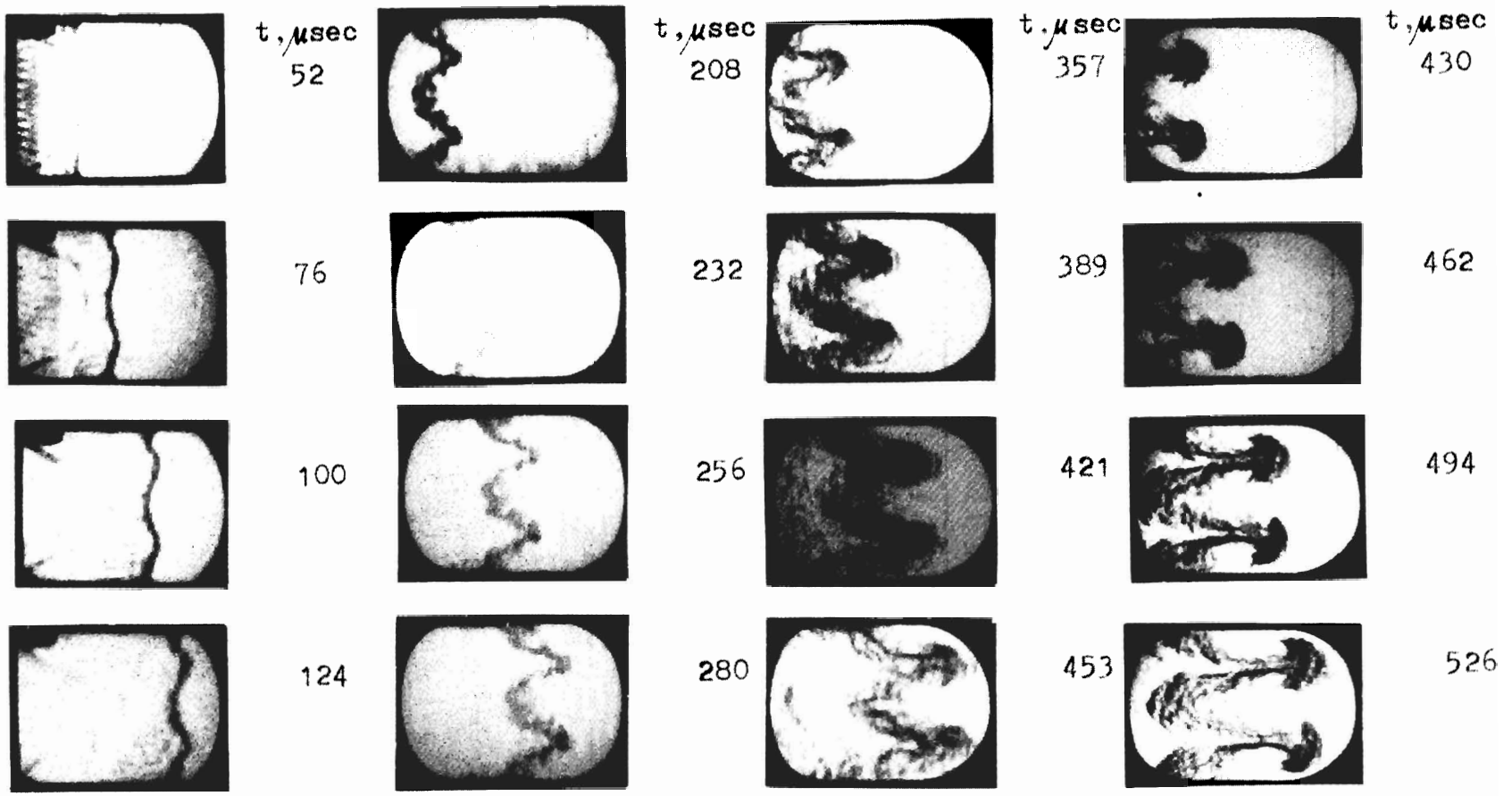

Fig. 2.2 Perturbation development at Kr - He interface with the initial perturbations α_0 = 1.0 mm, λ = 50 mm.

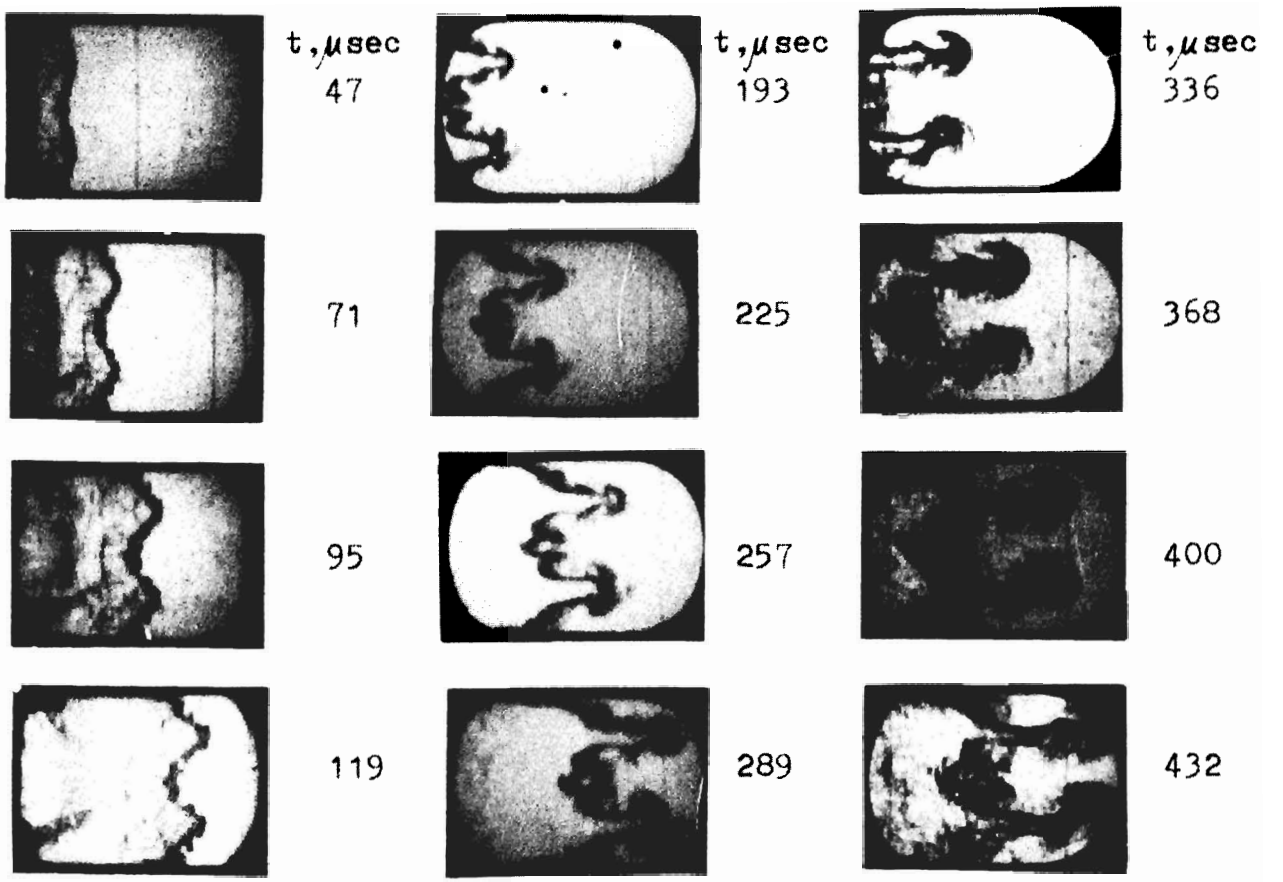

Fig. 2.3 Perturbation development at Kr - He interface with the initial perturbation α_0 = 2.5 mm, λ = 50 mm.

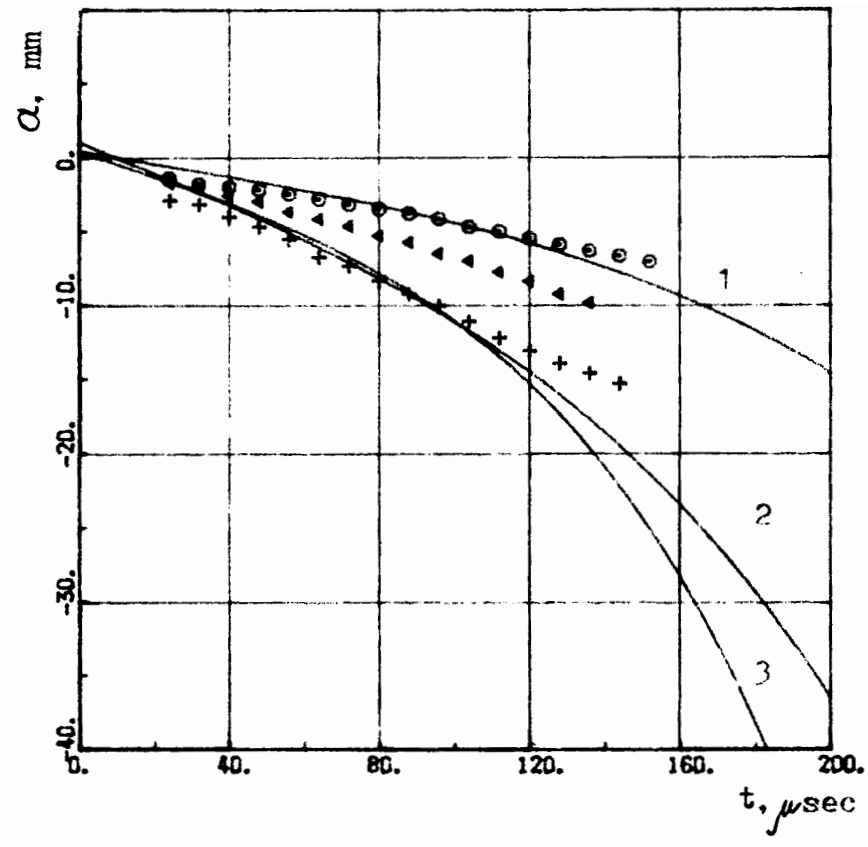

Fig. 2.4 The development of the perturbation amplitudes at the gas interface in the regular stage.

o - α_0 = 1.0 mm, λ = 50 mm;

‣ - α_0 = 1.0 mm, λ = 25 mm;

\+ - α_0 = 2.5 mm, λ = 50 mm;

1,2,3, - linear impulse theory for perturbations o, ‣ , + accordingly.

Taking into account the change of the initial perturbation amplitude because of the gas compressibility [24] the solution has the following form:

$$\alpha(t) = \frac{\alpha_o}{2}\left[1 + \left(1 - \frac{U_o}{W_1}\right)\right]\left[\cosh wt - \frac{U_o}{W}\,\mathrm{Sinh}\, wt\right] \qquad (2.4)$$

where: W_1 is the shock wave front velocity before incidence upon the interface.

The gravitational instability development at the process initial stage reveals linear dependence of the perturbations amplitude on time up to the moment $t \sim 130$ μs, which is characteristic of the interface shock acceleration [23] and is connected with small role of quasi-stationary acceleration at the initial stage.

Comparison of experimental results with analytical solution (Eq. 2.4) gives every reason to consider that up to the amount $t^* \approx 130$ μs for perturbation with $\lambda = 50$ mm and up to the moment $t^* \approx 30$ μs for perturbations with $\lambda = 25$ mm, in the range of 10%-deflection satisfactory agreement of linear impulse theory with experiment is observed. It is worth mentioning that the perturbations amplitude is 5-6 times the initial one. Earlier divergence of the experiment with theory for the perturbations with $\lambda = 25$ mm is explained by evident distortion of sinusoidal profile because of a less number of frame wires per perturbation wave length. As can be seen in the photos 2.1 and 2.2, the influence of these wires upon the process of instability development is not observed. Their indirect influence reveals itself in the distortion of more wide helium jets for the perturbation with $\alpha_0/\lambda = 0.05$ (see Fig. 2.3), which is caused, perhaps, by the nonsmooth character of the initial perturbation form.

Thus, taking into account the satisfactory agreement of experimental results with analytical solution at the considerable period of development up to t^* we can ascertain the satisfactory preparation of experiments. We also can assert that the use of the nitrofilm 0.4 μm thick does not influence the instability development significantly relative to the process

as a whole, because the systematic distortion of experimental results could have been expected, especially in the initial stage of this phenomenon because of additional film mass involved in the motion. Because of these arguments, any possible doubts concerning the experimental results confidence at later stages of the instability development have no grounds.

2.4 Further development of perturbations leads to distortion of their sinusoidal profiles and to the forming of narrow krypton jets and wider helium jets. The profile distortion begins approximately with t^*, that agrees with the value of W^{-1}, which characterizes the application limit of the linear theory.

At this stage of the perturbation development it is revealed as the result of the asymmetry of gravitational instability, which is characterized by a deeper penetration of krypton jets into helium in comparison with helium jets, penetrating into krypton.

The nonlinear stage of the perturbation development is accompanied by the appearance of vortex regions at the top of krypton jets. The appearance of the vortex regions means the occurrence of a new factor, which did not take place earlier as well as the destruction of the initial spatial structure of perturbation and the transition to the flow turbulization. The flow turbulization in the perturbation zone is accompanied by increasing krypton jet instability that is revealed in their tortuosity. Increasing vortices lead to their closing up with the neighbor ones. That, in its turn, leads to the chaotic state of the flow and to formation of a zone with a complex flow picture on the part of helium. This gas mixing zone can be interpreted, probably, as the zone of the gas turbulent mixing. Full value of this mixing zone reaches 100 mm.

By this time, while observing the interface in a direction, perpendicular relative to the generator of the sinusoidal profile, it was observed that there developed sufficiently significant distortions of perturbation zone front. This demonstrates the destruction of the initial two-dimensional perturbation structure.

Penetration of helium into krypton evolves in the form of wide jets, which are analogous to bubbles in Lewis' experiments [2]. Periodical structures present do not disintigrate even at late times in observing this

phenomena ($\hat{t} \approx 600$ μs, S = 140 mm). However, the boundaries of helium jets are blurred by a low-scale turbulence which reaches a mean scale of ≈ 40 mm at $\hat{t}$ = 500 μs. Meanwhile, development of the low-scale turbulence displays evident signs of dependence upon an initial perturbation amplitude. When the initial amplitude rises, blurring of jet interface is decreased.

The development of gas jet flow (krypton jets are especially significant), which proceeds from the laminar flow through the transient one to turbulent flow, is analogous to turbulization of free turbulent jets [25]. It demonstrates the commonality of some features of gravitational and shearing turbulences, namely: chaotic state, periodic structure, component mixing, independence from initial conditions.

One can see the nearly periodic regions where krypton jet boundaries are distorted. Chaotic state and gas mixing are observed in the region of turbulent flow on the boundary with helium. There appears a new feature, namely, a gravitational mixing anisotropy, which becomes apparent in the jet structure of the mixing zone.

The process of transition to the turbulent stage of mixing is characterized by large variety of flows, which depend upon precisely fixed conditions of the experiment conducted. But the asymptotic turbulent stage, in consequence to its insensitivity to initial conditions, does not depend upon conditions of the experiment conducted.

It is practically impossible to realize the asymptotic stage of mixing in the experiment because of finite dimensions of the installation and the short-term acceleration action.

Therefore, for fulfilling the analysis of experimental results, it is necessary to take into account those or other theoretical considerations about the character of dependence of the studied process upon experimental conditions.

Results of our experiments for researching the development of the mixing zone are analyzed on the assumption of a quadratic law of dependence of mixing zone width upon the time, which is described in the works [6,7]. In consequence to inconsistency of the deceleration value of the interface, this analysis was conducted on the assumption of

proportionality of mixing zone width, L, to breaking distance, S, in the following relation:

$$L = \beta f(N) \cdot 2S , \qquad (2.5)$$

where: β is a constant;

N is an interface gas density relation.

The influence of initial perturbations of interface upon mixing zone dimensions was taken into consideration during processing experimental data in the coordinate plane $(\sqrt{L}, \sqrt{2S})$ proceeding from the dependence, proposed in [8],

$$\sqrt{L} = \sqrt{L_o} + \sqrt{\hat{L}} , \qquad (2.6)$$

where: L_o is the initial turbulent mixing zone width;

$\hat{L}$ is the transient width of the mixing zone.

The concept of mixing intensity is introduced for describing the process of the gravitational turbulent mixing:

$$J = \frac{dL}{d2S} \qquad (2.7)$$

Data processing was conducted on the assumption, that the value of each uncontrolled perturbation of a flow is a random value in that sense, that the combined ensemble of flow perturbations, which have statistical influence on the experiment, are realized during each controlled experiment.

Therefore data processing results, obtained in different experiments, were averaged and the average of them was adapted as the most probable outcome.

Dependence of $\sqrt{L}$ on $\sqrt{2S}$ (see Fig. 2.5 - 2.7) has a linear form not only for the combined data of each separate experiment, but for all experiments as a whole. At $S \geq 10$ mm, this corresponds to measurements at $\hat{t} > 150$ μs. The average correlation coefficient is $R(\sqrt{L}, \sqrt{2S}) = 0.996$.

The transition to the linear dependence is more clearly observed for the largest perturbations ($\alpha_o/\lambda = 0.05$). This is connected apparently with

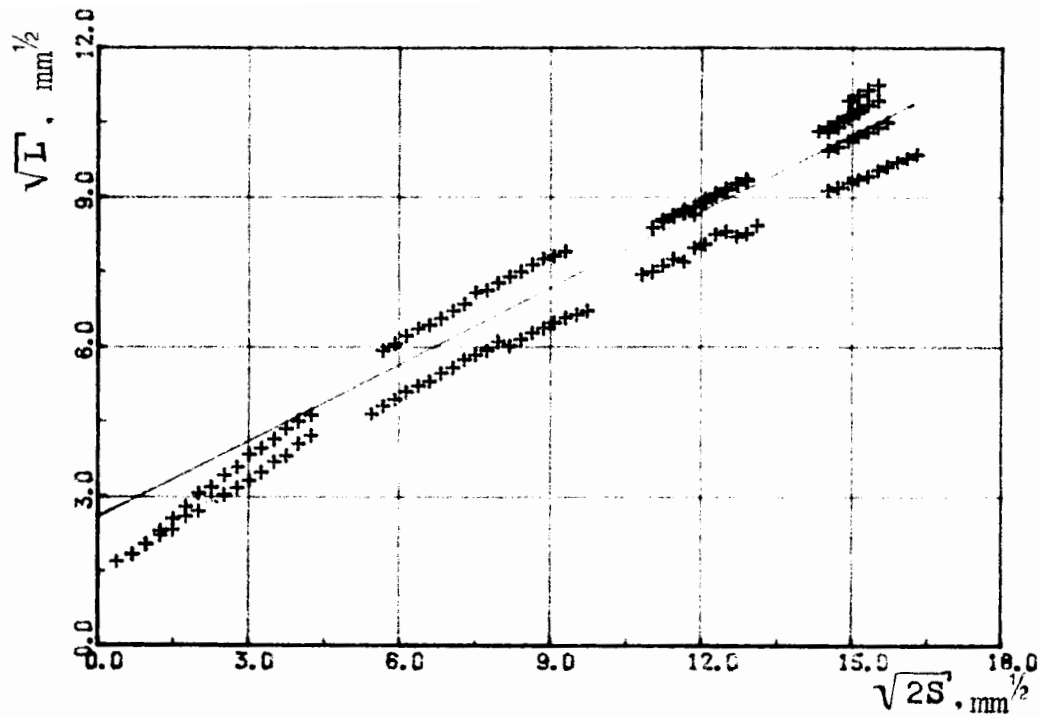

Fig. 2.5 The development of the gas mixing zone width versus braking distance in the turbulent stage.+ - experimental results with the initial perturbation α_0 = 1.0 mm, λ = 25 mm; — - the results of processing experimental dates by the method of least squares. J = 0.26, L_0 = 6.7 mm.

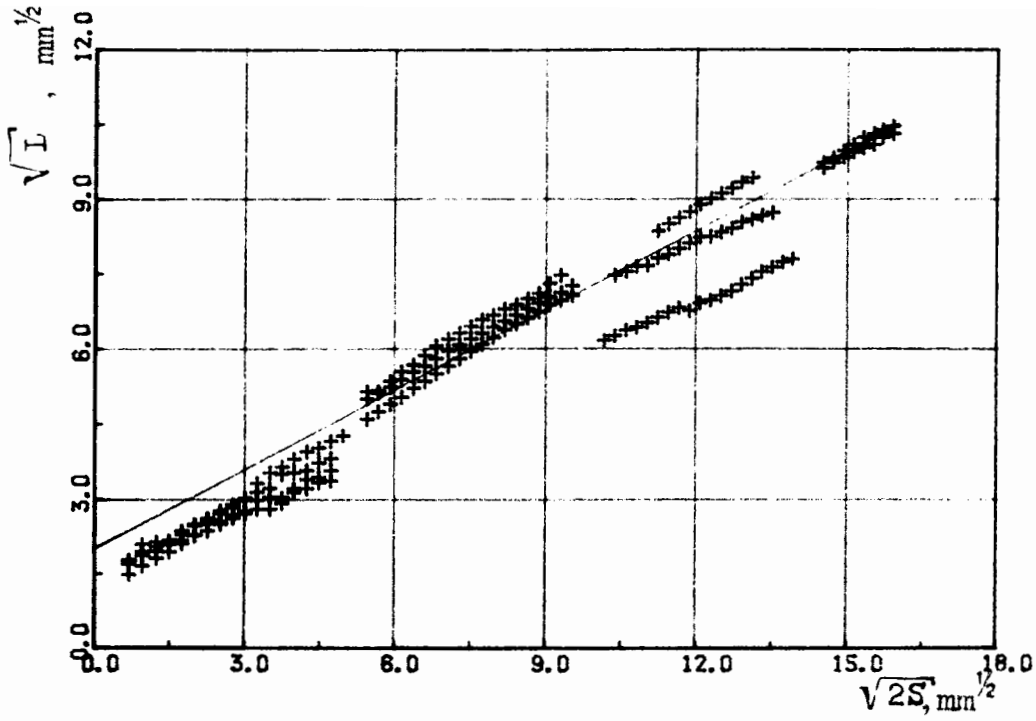

Fig. 2.6 The development of the gases mixing zone width versus braking distance in the turbulent stage.+ - experimental results with the initial perturbation α_0 = 1.0 mm, λ = 50 mm; — - the result of processing experimental dates by the method of least squares. J = 0.28, L_0 = 4.05 mm.

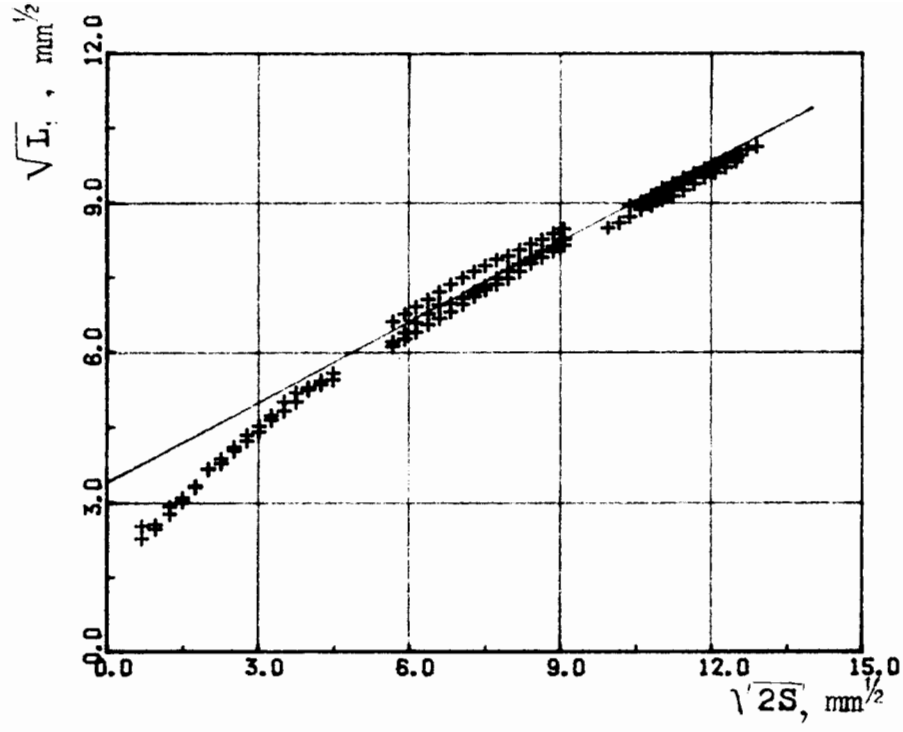

Fig. 2.7 The development of the gases mixing zone width versus braking distance in the turbulent stage.+ - experimental results with the initial perturbation α_0 = 2.5 mm, λ = 50 mm. — - the result of processing experimental dates by the method of least squares. J = 0.29, L_0 = 11.6 mm.

the decreasing significance of uncontrollable perturbations and increasing dominance of periodic distortions of the interface.

When the initial sinusoidal perturbation amplitude is decreasing, the whole mixing zone width is also decreasing, but the intensity of mixing (see Table 2.1) remains constant. It is observed that the proportionality of the relative roughness of interface α_o/λ with the effective initial mixing zone width L_o demonstrates effectiveness of this method of experimental result processing.

The "ignoring" of initial conditions in the given case is revealed in the relation that the value of J remains constant in spite of the fact that the whole acceleration, which is acted on the interface, depends appreciably on the character of the shock wave action:

$$g(t) = U_o\, \delta(t) - \hat{g}\,. \tag{2.8}$$

where: $\delta(t)$ - Dirac's function and

$\hat{g}$ - acceleration, which is created by the unloading wave

TABLE 2.1

Statistical processing results of experimental data

Series of Experiments	Number of Experiments	α_o/λ	J	ΔJ	L_o
1	8	0.02	0.28	0.04	4.05
2	6	0.04	0.26	0.02	6.70 ± 1
3	10	0.05	0.29	0.01	11.60

Data spread ΔJ is given with confidence probability P = 0.95.

Mixing intensity constancy, at sufficiently large changes in initial perturbations of interface, can be interpreted as establishing the turbulent stage of mixing. The observation, that the periodic structure of initial perturbations have not been destroyed at the end, is connected

apparently, with establishment of certain large-scale, periodic mixing features, which are characteristic of this phenomenon.

An additional argument in favor of such a supposition is the agreement of mixing intensity data with the results of numerical computations, which simulate the development of turbulent mixing of fluids for the case of full width of the mixing zone [9], while using two-dimensional methods.

Experimental data allow determination of the empirical constant of the gravitational turbulent mixing "β" in the dependence, as suggested in the work [7].

$$L = \beta \frac{\rho_2 - \rho_1}{\rho_2 + \rho_1} \cdot 2S, \qquad (2.9)$$

where: $\beta = 0.32 \pm 0.010$.

The error of measuring the value of "β" has a confidence probability of 0.95.

It must be noted that in experiments conducted with fluids [14,16], one can observe a mixing intensity which is less by approximately a factor of two. Such a discrepancy of results cannot be completely explained by essential compressibility of the media based on data from experiments with gases.

It is possible that forces of surface tension exert a certain influence upon the development process of turbulent mixing of liquid media that, in its turn, can result in capillary instability of jets, whereas this factor is fully excluded in experiments with gases.

REFERENCES

1. Taylor, G., Proc. Roy. Soc. Ser. A, 1950, Vol. 201, N 1065, p. 192-196.

2. Lewis D., Proc. Roy. Soc. Ser. A, 1950, Vol. 202, p. 81-96.

3. Ratafia, M., Phys. Fluids, 1973, Vol. 16, N 8, p. 1207-1210.

4. Meshkov, E. E., "Some Experimental Research Results of Gravitational Instability of Interfaces of Media with Different Densities", Preprint. Keldish Inst. Appl. Math., Ac. Sci. USSR, 1981.

5. Emmons, H. W., Journ. Fluid Mech., 1960, Vol. 7, Part 2, p. 177-193.

6. Belyenkii, S. Z., Fradkin, E. S., "Theory of Turbulent Mixing Transact.", Phys. Inst. Ac. Sci. by name of Lebedev, Vol. 29, p. 207-238, 1965.

7. Neuvazhaev, V. E., "To the Theory of Turbulent Mixing", Rep. Ac. Sci. USSR, 1975, Vol. 222, N 5, p. 1053-1056.

8. Neuvazhaev, V. E., Yakovlev, V. G., "About Mixing of Interface Decelerated by Stationary Shock Waves", J. Appl. Mech. and Tech. Phys., 1981, p. 85-89.

9. Andronov, V. A., Bahrah, S. M., et al., "Numerical Simulation of Some Turbulent Flows in Approximation to Two-Dimensional Turbulence", Proc. Ac. Sci. USSR, Fluid Mech., N 6, 1984, p. 20-27.

10. Anuchina, N. N., Ogibina, V. N., "Numerical Research of Gravitational Instability of Interface of Media with Different Densities", Physical Mechanics of Nonuniform Media Trans. Edited by T. V. Gadijak. Ac. Sci. USSR, Sib. Dept., Inst. Teor. and Appl. Mech., Novosibirsk, 1984.

11. Anuchina, N. N., Ogibina, V. N., "Computerized of Hydrodynamic Instability Transact.", edited by Babenko, K. J., Keldish Inst. Appl. Math., Ac. Sci., USSR, Moscow, 1981.

12. Neuvazhaev, V. E., "Model Characteristics of Turbulent Mixing of Interface of Accelerated Fluids with Different Densities", J. Appl. Mech. and Tech. Phys., 1983, N 5, p. 81.

13. Neuvazhaev, V. E., "Diffusion of Mixture Turbulent Layer", J. Appl. Mech. and Tech. Phys., 1988, N 2, p. 46.

14. Anuchina, N. N., Kucherenko, Y. A., Neuvazhaev, V. E., et al., "Turbulent Mixing on Accelerating Interface of Fluids Having Different Densities", Proc. Ac. Sci. USSR, Fluid Mech., 1978, N 6, p. 157-160.

15. Andronov, V. A., Bahrah, S. M. et al., "Turbulent Mixing on the Contact Surface, Accelerated by Shock Waves", J. Exp. and Ther. Phys., 1976, N 7 (Issue 218).

16. Read K. J., Physica, 1984, p. 45-58.

17. Makarov, Y. V., Chekalin, E. K., "Physical Processes in Electromagnetic Tube.", Atomisdat, 1986.

18. Buzhinskii, O. I., Volkov, L. P., "Investigation of Shock Waves Excited in Electromagnetic Shock Tube.", J. Tech. Phys., 1972, Vol. 42.

19. Keck, J., Phys. of Fluids, 1964, 7, N 11, p. 186-197.

20. Zeldovich, Y. B., Raizer, Y. P., "Physics of Shock Waves and High-Temperature Hydrodynamic Phenomena", Academic Press, New York, 1967.

21. Kuropatenko, V. F., Potapkin, B. K., "Experience of Creating Large Programs of Serial Count after the Example of the Program 'RAND'", Complexes of Mathematical Physics Programs, Trans. Novosibirsk, 1972.

22. Kay, J., Laby, T., "Tables of Physical and Chemical Constants", Publishing House "Nauka" (Phys. Math.), 1962.

23. Meyer, K. A., Blewett, P., Phys. Fluids, 1972, Vol. 15, N 5, p. 753-759.

24. Richtmyer, R. D., Comm. Pure and Appl. Math., 1960, Vol. 13, N 2, p. 297-319.

25. "Turbulence Principles and Applications", Edited by Frost, U., Mowlden, T., Moscow, "MIR," 1980, p. 9-32.

EXPERIMENTAL INVESTIGATION OF TURBULENT MIXING BY RAYLEIGH-TAYLOR INSTABILITY

David L Youngs

Atomic Weapons Establishment, Aldermaston,
Reading, RG7 4PR, United Kingdom

1. INTRODUCTION

A key feature of compressible turbulent mixing is the generation of vorticity via the $\nabla p \times \nabla(1/\rho)$ term. This source of vorticity is also present in incompressible flows involving the mixing of fluids of different density, for example Rayleigh-Taylor unstable flows. This paper gives a summary of an experimental investigation of turbulent mixing at a plane boundary between two fluids, of densities ρ_1 and ρ_2 ($\rho_1 > \rho_2$) due to Rayleigh-Taylor instability. The two fluids are near incompressible and mixing occurs when an approximately constant acceleration, g, is applied normal to the interface with direction from fluid 2 to fluid 1. Full details of the experimental programme are given in a set of three reports [1,2,3]. Some of the earlier experiments are also described by Read [4].

Previous experimental work [5-10] and much of the theoretical research has concentrated on studying the growth of the instability from a single wavelength perturbation rather than turbulent mixing. Notable exceptions are published in the Russian literature [11-13]. A related process, turbulent mixing induced by the passage of shock waves though an interface between fluids of different density is described by Andronov et al [14]. The major purpose of the experiments described here was to study the evolution of the instability from small random perturbations where it is found that large and larger structures appear as time proceeds. The acceleration of the interface was chosen to be high enough for surface tension and viscosity to have a small effect on the overall growth rate of the mixed region. A novel technique [4] was used to provide the desired acceleration. The two fluids were enclosed in a rectangular tank, the lighter fluid 2 initially resting on top of the denser fluid 1. One or more rocket motors were then used to drive the tank vertically downwards. The aim of the experimental programme is to provide data for the calibration of a turbulence model used to predict mixing in real situtions [19].

2. BASIC PICTURE OF THE MIXING PROCESS

In the absence of viscosity, surface tension or other stabilising mechanisms, the growth in the amplitude, a, of a small perturbation of wavelength λ is given by [15],

$$\frac{d^2a}{dt^2} = n_\lambda^2 \, a \qquad \ldots (1)$$

where $n_\lambda^2 = \dfrac{2\pi g A}{\lambda}$ and $A = \dfrac{\rho_1 - \rho_2}{\rho_1 + \rho_2}$ (Atwood number)

Hence short wavelength small perturbations grow more rapidly than long wavelength small perturbations. When the amplitude of the perturbation becomes significant compared to its wavelength the rate at which the instability penetrates the denser fluid approaches a limiting value proportional to $\sqrt{g\lambda}$ see Lewis [5] and Layzer [16]. Short wavelength perturbations then grow more slowly than long wavelength perturbations. The result of this behaviour is that one expects small structures to appear first. As time proceeds larger and larger structures should dominate the flow. The dominant length scale, λ_d, increases by a process of bubble competition as proposed in [16] and observed in [7].

According to (1) n_λ increases without limit as $\lambda \to 0$. In reality, mechanisms such as viscosity, surface tension or finite initial density gradient limit n_λ to a maximum value ($= n_m$), corresponding to the most unstable wavelength λ_m. If viscosity alone is present [15],

$$\lambda_m \simeq 4\pi \left\{\frac{\nu^2}{gA}\right\}^{1/3} \quad \text{and} \quad n_m = \left\{\frac{\pi g A}{\lambda_m}\right\}^{1/2} \qquad \ldots (2)$$

where $\nu = (\mu_1 + \mu_2)/(\rho_1 + \rho_2)$ is the mean kinematic viscosity.

If surface tension is the main stabilising mechanism, then [15]

$$\lambda_m = 2\pi \left\{\frac{3T}{g(\rho_1 - \rho_2)}\right\}^{1/2} \quad \text{and} \quad n_m = \left\{\frac{4\pi g A}{3\lambda_m}\right\} \qquad \ldots (3)$$

If instead of a sharp initial interface the density drops from ρ_1 to ρ_2 over a distance Δ then [17]

$$n_\lambda \simeq \left\{\frac{2\pi g A}{\lambda + \pi\Delta}\right\}^{1/2} \quad \text{so that} \quad n_m = \left\{\frac{2gA}{\Delta}\right\}^{1/2} \qquad \ldots (4)$$

Hence the growth of larger and larger structures is likely to begin with the appearance of perturbations with wavelength of order λ_m. These arguments suggest that the evolution of Rayleigh-Taylor instability at a plane boundary from a low initial perturbation should proceed as follows [18]:-

Stage 1: A perturbation of wavelength $\sim\lambda_m$ appears. This should happen after a time of order 10 τ_m where $\tau_m = 1/n_m$.

Stage 2: The perturbation of wavelength λ_m saturates and longer wavelength perturbations begin to grow more rapidly. Larger and larger structures evolve.

Stage 3: λ_d grows from about 10 λ_m to infinity. The stabilising mechanisms, viscosity surface tension etc now have little effect and growth by bubble competition suggests that the average properties of the mixed region should lose dependence on the initial conditions. For a given density ratio the mixing process is described by a similarity solution with length scale proportional to gt^2. Two-dimensional numerical simulation, [18] indicated penetration of fluid 1,

$$h_1 = \alpha A\, gt^2 \qquad \ldots (5)$$

with $\alpha \sim 0.04$, to 0.05 and h_2/h_1 = (penetration of fluid 2)/(penetration of fluid 1) an increasing function of density ration ρ_1/ρ_2.

Neuvazhaev and Yakovlev [12] also described the turbulent mixing process by a similarity solution with length scale proportional to gt^2. The width of the mixing zone was given by

$$L \approx \alpha_o^2 \left[1 + 0.05 \log \frac{\rho_1}{\rho_2}\right] \log \left[\frac{\rho_1}{\rho_2}\right] gt^2 \qquad \ldots (6)$$

Whether or not loss of memory of initial conditions occurs, as assumed in (5) and (6), is of major importance. If it does the problem of making predictions in real applications is very greatly simplified. As already noted the dominant wavelength λ_d should increase with time. A necessary requirement for loss of memory of initial conditions to occur in stage 3 is that the structures of wavelength λ_d should have evolved from the interaction between smaller structures rather than from an initial perturbation of wavelength λ_d. Equations (5), (6) will not apply if large amplitude long wavelength perturbations are present initially.

3. EXPERIMENTAL RESULTS

3.1 The Apparatus Used

The Rocket-Rig apparatus, Read [4], is shown in figure 1. A rectangular tank contains the two fluids, with the lighter fluid 2 initially resting on top of the denser fluid 1. An unstable situation is created by driving the tank vertically downwards using one or two small rocket motors. The tank is attached by four PTFE bushes, two on either side of the tank, to a pair of guide rods. This ensures vertical motion. The accelerations achieved are high enough to make the effects of surface tension and viscosity small.

Acceleration is measured by accelerometers attached to the tank. A distance scale is fixed to the rig in the plane of the front of the tank so that measurements of distance moved and instability growth may be obtained by photography. Photographs of the tank motion are obtained using two Vinten 35 mm framing cameras operating at a nominal 200 frames per second and with a frame exposure time of 0.14 ms. The duration of each experiment is of order 100 ms. Backlighting was provided by a bank of diffused photoflood bulbs.

The tanks used to contain the fluids are essentially glass walls within a metal framework of internal dimensions H X W X D, where H is the height of the tank, W is the width and D is the depth in the viewing direction. Four tank sizes have been used all of which have W = 150 mm:-

(a) The "2D" tank 150 x 150 x 25 mm
(b) The 3D tank 150 x 150 x 150 mm
(c) The long tank 250 x 150 x 25 mm
(d) The pressurised tank 200 x 150 x 50 mm

For tank (a) which has D << W the late stages of the mixing process were to some degree constrained to be two-dimensional. Tank (b) allowed three dimensional instabilities to develop without constraint. This was more difficult to use than the

"2D" tank and because of the extra weight gave lower accelerations. The results obtained showed the two-dimensional tank (a) did not give a noticeable reduction in instability growth. The long tank(c) was used for tilted-rig experiments where a larger value of H was needed to observe the features at the sides of the tank. The pressurised tank (d) enabled compressed gas/liquid combinations to be used. Overpressures of up to 10 bar could be used. Then with fluid combinations such as SF_6/pentane density ratios ρ_1/ρ_2 of order 20 were achieved. The types of experiment performed, together with the definitions of the measured quantities are shown in figure 2. Results will be discussed in the following subsections.

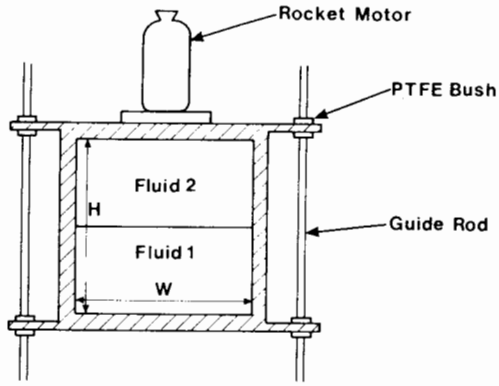

Figure 1: The Rocket-Rig apparatus

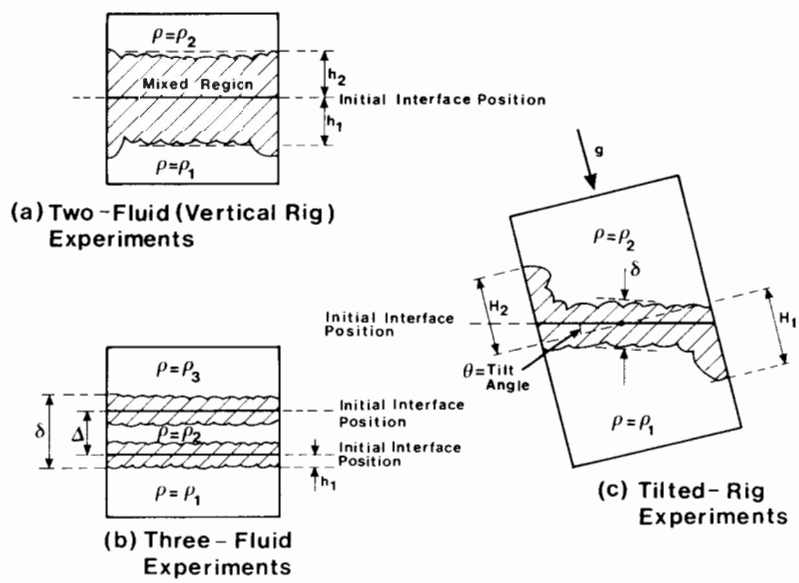

Figure 2: Types of experiment performed

3.2 The Quadratic Growth Law

The main purpose of the experimental programme was to perform experiments with no deliberately imposed initial perturbations ie to observe the growth of the instability from small random perturbations and investigate the validity of the quadratic growth law (5).

Experiments have been performed at a wide range of density ratios by using liquid/liquid, liquid/air (1 bar) and liquid/compressed SF_6 (up to 10 bar) combinations. Examples of the photographic records are shown in figures 3 to 6.

Figure 3 shows an example of an experiment using NaI solution/hexane in the 3D tank with ρ_1/ρ_2 = 2.8. The two fluids have very difficult refractive indices. hence the mixed region appears dark on the photographs. The first frame shows the difficulty in analysing the results obtained with the 3D tank. Very little mixing has occurred at this time. The apparent mix region is due to the fact that the camera is looking up at the interface from below. Parallax corrections, as described in [1] are therefore necessary. Similar corrections are made for the pressurised tank [3]. Parallax effects are considered small enough to neglect for the "2D" tank. This makes the results much easier to analyse.

Figure 4 shows an experiment using NaI solution/water in the "2D" tank, with ρ_1/ρ_2 = 1.89. In this case the fluids used are miscible. All other fluid combinations used were immiscible. Phenolphthalein and HCl were added to the water and KOH was added to the NaI solution. The concentrations of KOH and HCl were chosen so that the indicator (initially clear) would turn red when about 6% of fluid 1 was mixed with fluid 2. The red product was observed in the colour photographs, showing that significant mixing at a molecular level occurs. Unfortunately darkening of the photographs was due to refractive index fluctuations in the mixed region as well as the chemical reaction. Hence the film density could not be used to quantify the amount of molecular mixing. The alternative approaches of Linden and Redondo [21] should give quantitative estimates of molecular mixing in Rayleigh-Taylor flows, for the case ρ_1/ρ_2 close to unity.

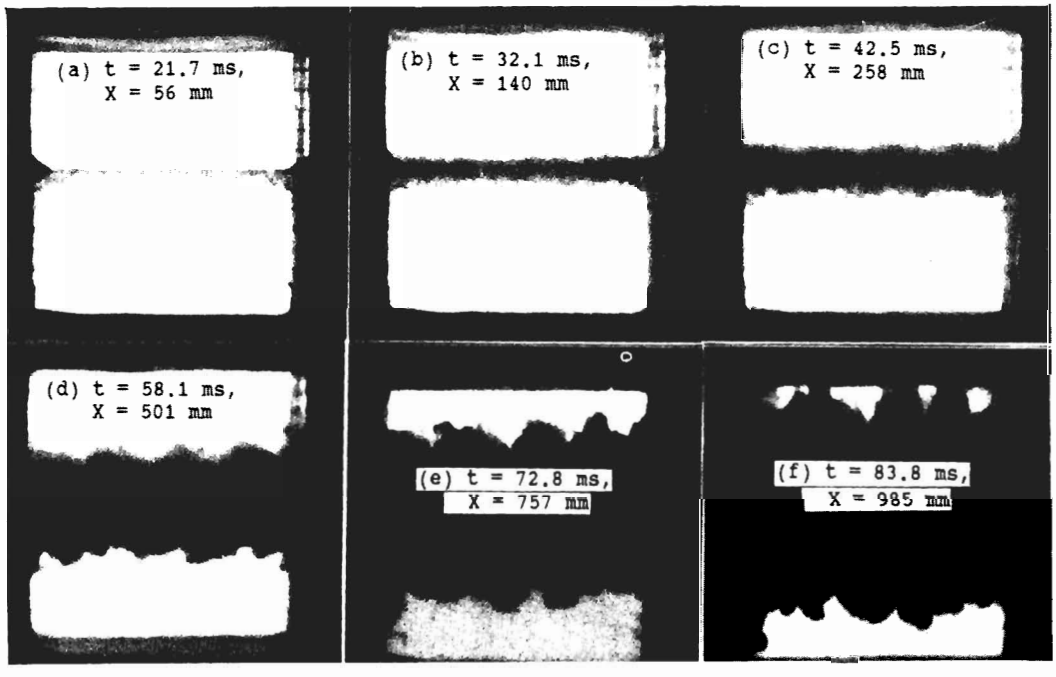

Figure 3: Experiment 62, NaI solution/hexane, 3D tank, ρ_1/ρ_2 = 2.8

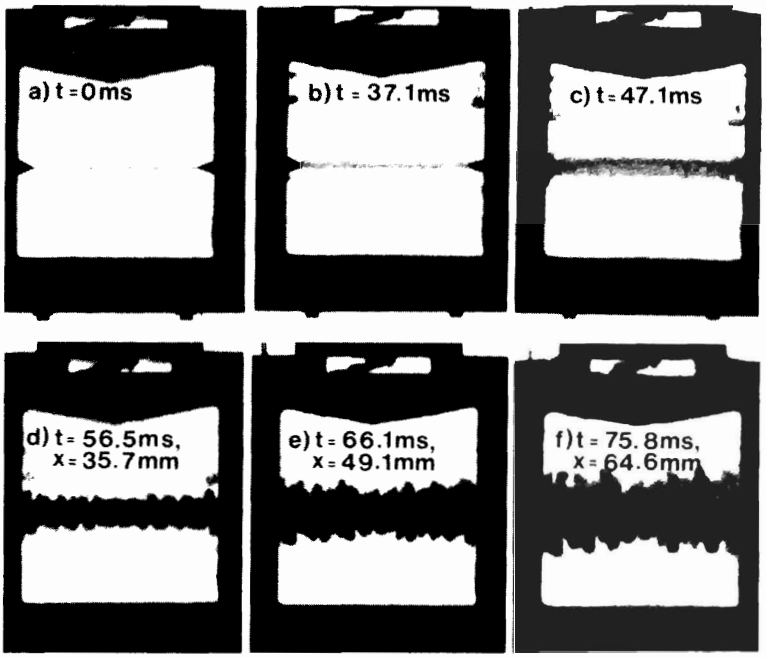

Figure 4: Experiment 112, NaI solution/water, 2D tank, $\rho_1/\rho_2 = 1.89$

Figures 5 and 6 show results obtained with the pressurised tank. The fluids used are compressed SF_6 gas and pentane. The SF_6 pressure is adjusted to give $\rho_1/\rho_2 = 8.5$ (figure 5) and $\rho_1/\rho_2 = 29.1$ (figure 6). The perturbation due to the meniscus present at t = 0 has some effect on the results. A thin film of liquid is seen to climb the front and back walls of the tank. The effect of the meniscus perturbation is greatest in the tank corners. For the higher density ratio experiment (figure 6) large bubbles formed in the tank corners. Similar, but more pronounced, effects to these were observed in the liquid/air experiments at relatively low acceleration of Emmons et al [7]. These edge effect are ignored when h_1 and h_2 are estimated. Measurements are made in the darkest area in the central region of the tank, see figures 5(f) and 6(f).

For the two compressed/SF_6 experiments shown in figures 5 and 6, the photographs show that show that the instability begins with the appearance of a perturbation of wavelength λ ~4 mm. The most unstable wavelength, according to linear theory, which is dominated by surface tension in this case, is (3)

$$\lambda_m = 2\pi \left\{ \frac{3T}{g(\rho_1 - \rho_2)} \right\}^{\frac{1}{2}} = \begin{array}{l} 4.5 \text{ mm for experiment 105} \\ 4.3 \text{ mm for experiment 114} \end{array}$$

The value used for the surface tension of pentane, 13.7 mNm^{-1}, does not allow for the presence of the compressed SF_6. Nevertheless it is apparent that a perturbation with wavelength close to λ_m appears first. Then as time proceeds the photographs clearly show the appearance of larger and larger bubbles.

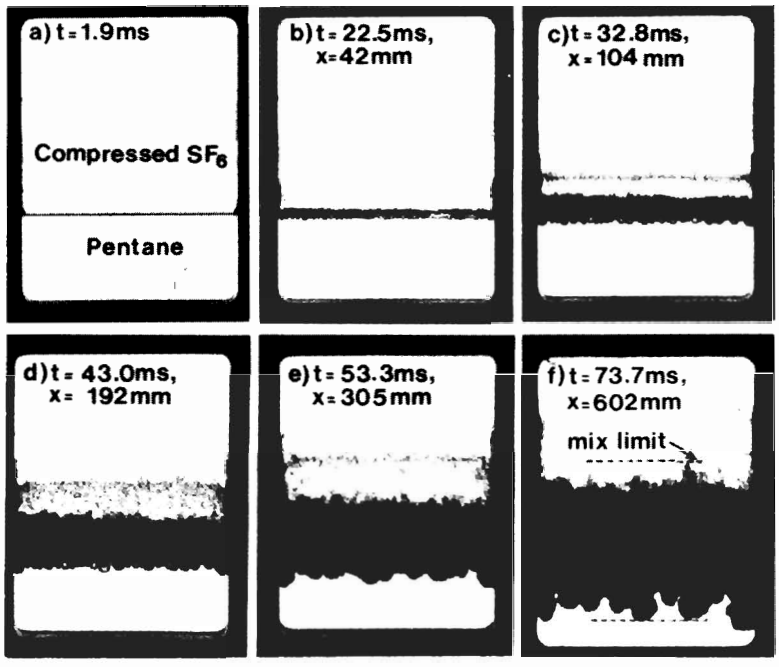

Figure 5: Experiment 105, Pentane/compressed SF_6, ρ_1/ρ_2 = 8.5

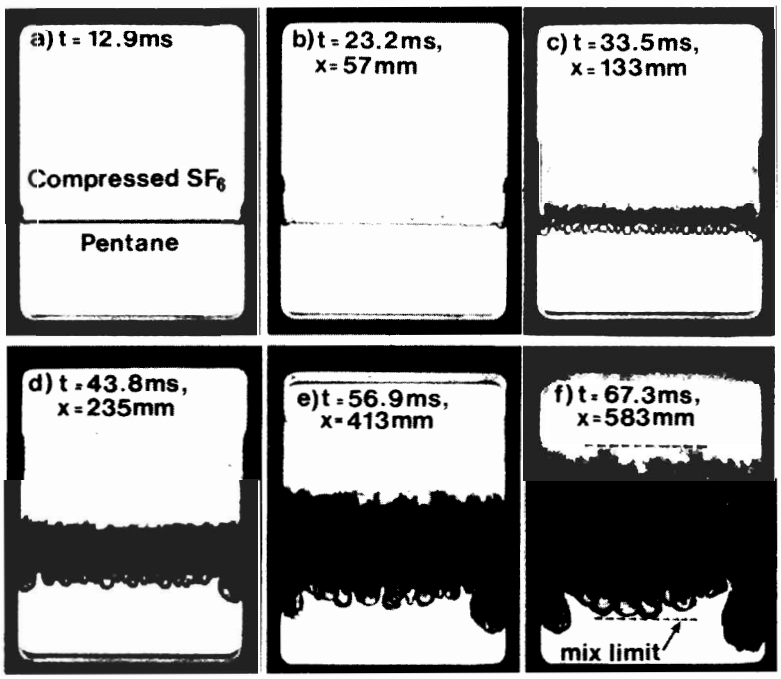

Figure 6: Experiment 114, Pentane/compressed SF_6, ρ_1/ρ_2 = 29.1

The photographs show that the bubble penetration, h_1, is more clearly defined than the spike penetration. Hence experiments have been analysed by plotting h_1 against Agt^2. The tank acceleration is approximately constant. However there is some variation with time. To correct for this the distance variable used is chosen to be proportional to $(\int n dt)^2$, ie the square of the number of exponential growth periods for a given wavelength. As $n \propto g^{\frac{1}{2}}$ (neglect surface tension and viscosity) h_1 is plotted against

$$X = A \left\{ \int_0^t \left[g(t') \right]^{\frac{1}{2}} dt' \right\}$$

In this integral $g = g_1 - g_0$, where g_1 is the tank acceleration and g_0 is the acceleration due to gravity. It is evaluated from the accelerometer record of g_1 versus t, scaled to give the distance moved by the tank measured on the photographs.

For each experiment the data is fitted by the linear law

$$h_1 = \alpha(X - X_0)$$

where the constant X_0 represents a time delay or an over-shoot. Tables 1 and 2 record the values of α deduced. The values quoted for g are approximate mean values. For the compressed SF_6 experiments, table 2, estimates of h_2/h_1 are also noted.

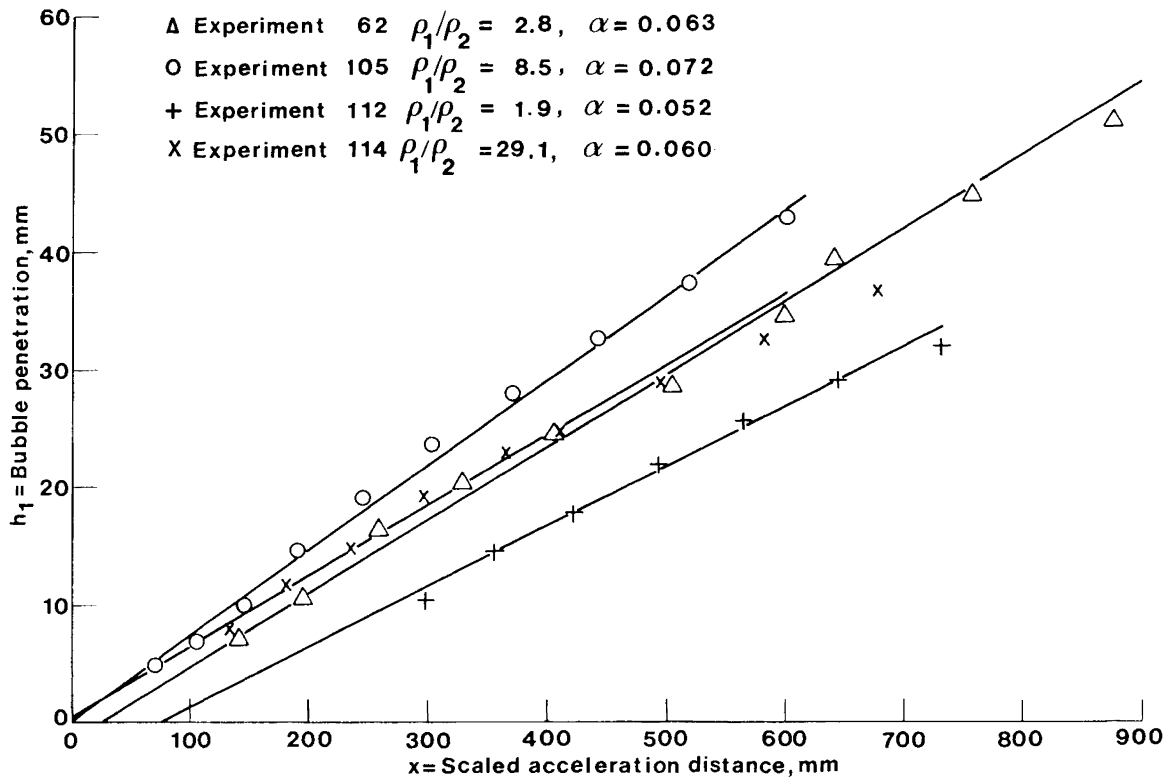

Figure 7: Bubble penetration versus scaled acceleration distance

Table 1: Growth Rate Summary

	$\frac{\rho_1}{\rho_2}$	Mean Acceleration g	Experiment Number	α	Report Reference
Two-dimensional tank alcohol/air	600	49 g_o 44 g_o 38 g_o 48 g_o	26 34 40 56	0.065 0.062 0.063 0.058	1 1 1 2
Two-dimensional tank NaI solution/pentane	3.0	51 g_o 49 g_o 40 g_o	23 36 42	0.060 0.064 0.061	1 1 1
Two-dimensional tank NaI solution/hexane	2.8	39 g_o 45 g_o 42 g_o	57 61 85	0.061 0.057 0.053	2 2 2
Two-dimensional tank NaI solution/water	1.89	39 g_o	112	~0.052	3
Two-dimensional tank NaCl solution/pentane	1.75	47 g_o	52	0.069	2
Two-dimensional tank $CaCl_2$ solution/hexane	1.73	47 g_o 45 g_o 44 g_o 45 g_o 43 g_o	54 66 71 93 94	0.065 ~0.055 0.063 0.050[1] 0.051[1]	2 2 2 3 3
Two-dimensional tank water/pentane	1.6	48 g_o	50	0.058	1
Three-dimensional tank alcohol/air	600	23 g_o 39 g_o 43 g_o	29 39 58	0.073 0.076 0.077	1 1 2
Three-dimensional tank NaI solution/pentane	3.0	27 g_o 31 g_o	33 35	~0.066 0.071	1 1
Three-dimensional tank NaI solution/hexane	2.8	28 g_o 32 g_o 48 g_o	60 62 72	0.070 0.063 0.056	2 2 2

Notes: (1) Calculated from the $\bar{f}_1$ versus z profiles obtained by densitometer analysis. h_1 is measured to the point where $f_1 = 0.95$.

The range of values for α is 0.050 to 0.077. Some of the lower values are affected by a limited set of data points or by a different definition of h_1 (experiments 93 and 94). It is likely that the highest values are influenced by additional perturbations. There does not appear to be any significant variation with density ratio. The values of α for the 3D tank are on average higher than those obtained with the "2D" tank. However, there is overlap in the data and it is not clear that this difference is significant. On the basis of the data given here the value $\alpha = 0.06$ is recommended for all density ratios.

Table 2: Growth Rate Summary for the Compressed SF_6 Experiments, reference [3]

Experiment	$\frac{\rho_1}{\rho_2}$	Mean acceleration g	α	$\frac{h_2}{h_1}$	Comments
Water/SF_6					
91	13.6	16 g_o	0.057	1.8	
98	13.1	16 g_o	0.055	1.7	
99	13.5	17 g_o	0.057	>1.7	h_2/h_1 was increasing at the end of the experiment
102	19.6	17 g_o	0.050	2.0	Large corner bubbles present
103	31.3	16 g_o	0.059	>1.8	h_2/h_1 was increasing at the end of the experiment. Large corner bubbles present.
Pentane/SF_6					
97	9.2	17 g_o	0.060	1.8	
101	10.7	16 g_o	0.063	1.6	
104	18.4	16 g_o	0.068	1.9	Long wavelength perturbation present.
105	8.5	15 g_o	0.072	1.5	
114	29.1	15	0.060	2.3	Large corner bubbles present.

Experimental results are quoted in [13], for ρ_1/ρ_2 = 3 and 20, and are expressed in the form of equation (6). At ρ_1/ρ_2, $\alpha_o^2 = 0.041$. This gives similar growth rate to that quoted here. However, the value $\alpha_o^2 = 0.023$ at $\rho_1/\rho_2 = 3$ gives significantly less growth than reported here. The reason for this discrepancy is not understood.

Examples of the plots of h_1 versus X are given in figure 7. Reasonably good linear correlations are obtained. For three of the four experiments shown the line passes close to the origin. However, for experiment 112 (miscible liquids) there is a delay in the onset of mixing, $X_o \sim 80$ mm. For this experiment there was not a sharp interface at t = 0. The initial thickness was estimated, very approximately to be $\Delta = 3\frac{1}{2}$ mm. Then using equation (4) gives $\tau_m \sim 3.9$ ms. Now X_o = 80 mm corresponds to t = 26 ms. Hence the delay of 7 τ_m ties in with linear theory.

Figure 8 shows a plot of h_2/h_1 versus ρ_1/ρ_2 for the compressed SF_6 experiments. The point $h_2/h_1 = 1.3$ at $\rho_1/\rho_2 = 3$ estimated for NaI solution/hexane see [1], is added. There is considerable spread in the results, to some extent due to the uncertainty in defining h_2. At $\rho_1/\rho_2 = 20$, h_2/h_1 is about 2.

Consider the following argument for predicting the variation of h_2/h_1 with density ratio. let R be the radius corresponding to the dominant bubble or spike size. R increases in proportion to the width of the mixed region. The bubble and

spike velocities, $V_1 = h_1$ and $V_2 = h_2$, may be estimated by equating buoyancy force to drag, ie,

$$\frac{4}{3}\pi R^3 (\rho_1 - \rho_2) g = C_D \cdot \pi R^2 \cdot \rho_1 V_1^2 = C_D \cdot \pi R^2 \cdot \rho_2 V_2^2$$

whence

$$\frac{h_2}{h_1} = \frac{\int V_1 dt}{\int V_1 dt} = \left(\frac{\rho_1}{\rho_2}\right)^{1/2}$$

Inertial effects are neglected as the accelerations V_1, V_2 are somewhat smaller than g. Then $h_2/h_1 = 4.5$ at $\rho_1/\rho_2 = 20$. This is far greater than the observed value of about 2, and shows that the argument above needs to be modified. The photographs indicate that the spikes are more diffuse than the bubbles. Possible reasons for the low values of h_2/h_1 are:-

(a) R for the spikes is smaller than R for the bubbles.

(b) The spikes have entrained a large amount of the lower density fluid, ie, the effective value of $\rho_1 - \rho_2$ in the buoyancy force term is lower on the spike side than on the bubble side.

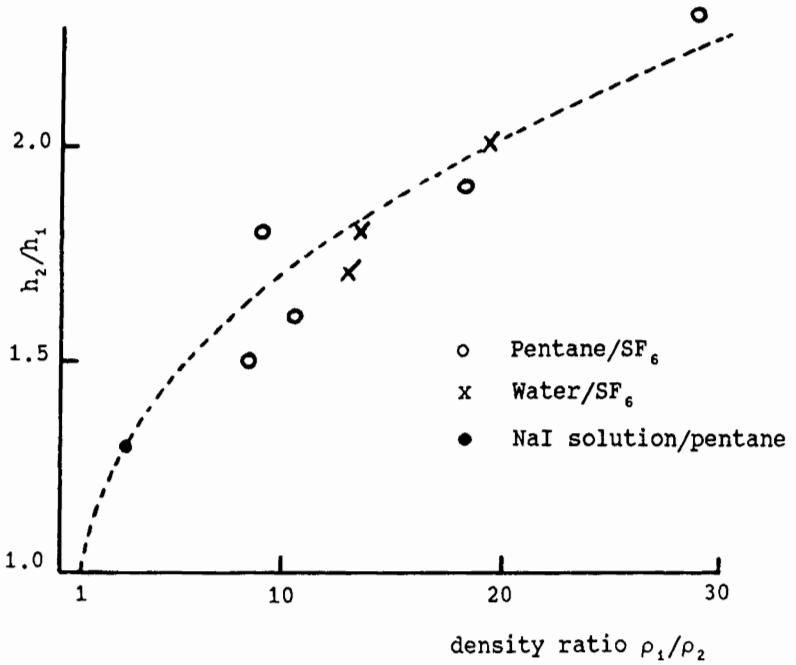

Figure 8: Variation of h_2/h_1 with density ratio

3.3 Additional Experiments

The main purpose of the experimental programme was to measure α and h_2/h_1 at a range of density ratios. However, the Rocket-Rig apparatus proved to be useful for performing additional types of experiment, three of which are described here.

Experiments with matched refractive indices.

If two fluids of very different refractive index are used the mixed region appears black on the photographs and no details of the structure within the mixture can be seen. As an alternative, a series of experiments [2,3] has been performed using $CaCl_2$ solution/hexane, in which the salt concentration was adjusted so that the two fluids had the same refractive index. Dye was added to the aqueous solution. Then if the refractive index match is perfect, there is no scattering of light due to refractive index flucations and the dyed fluid acts as a pure absorber of the backlight. Densitometer analysis of the photographic negatives may then be used to measure the amount of dyed fluid. The dye concentration was chosen to give a linear variation of film density (d) with volume fraction f_1. The variation of $\bar{f}_1$, f_1 averaged over a horizontal layer, with height could then be estimated

$$\bar{f}_1 = \frac{\bar{d}_{max} - \bar{d}}{\bar{d}_{max} - \bar{d}_{min}}$$

where $\bar{d}$ = film density averaged over a horizontal layer

$\bar{d}_{min}$ = value of $\bar{d}$ for dyed fluid immediately below the mixed region.
$\bar{d}_{max}$ = value of $\bar{d}$ for undyed fluid immediately above the mixed region.

Photographs for one of these experiments is shown in figure 9 and results of the film analysis are shown in figure 10, this shows an approximately linear variation of $\bar{f}_1$ with z. However, the profiles should not be regarded as of high accuracy because of the difficulties in obtaining uniform backlighting and a perfect refractive index match.

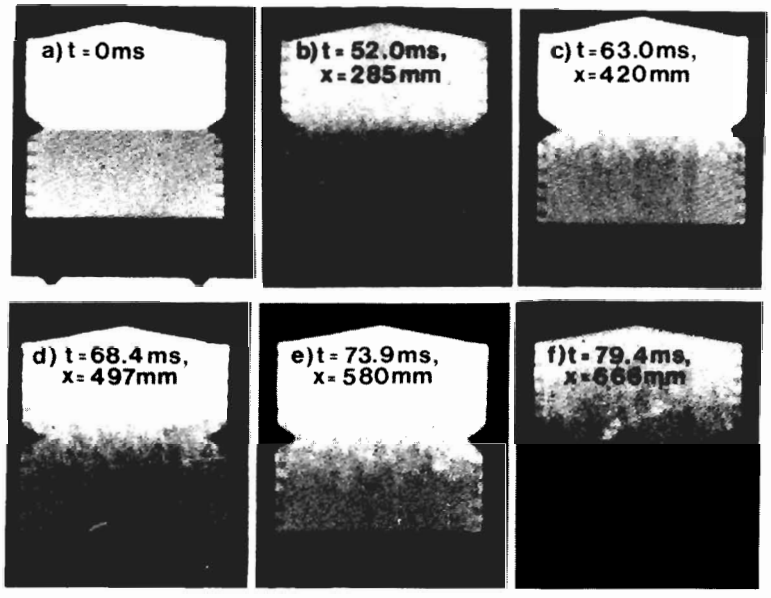

Figure 9: Experiment 94, $CaCl_2$ solution (dyed)/hexane, $\rho_1/\rho_2 = 1.7$

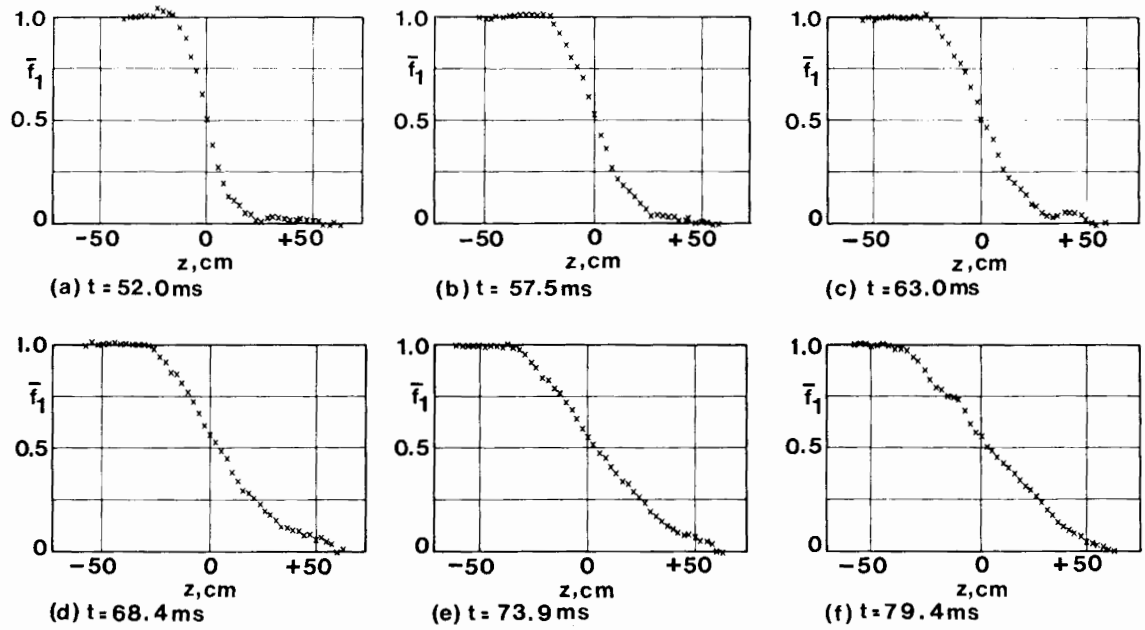

Figure 10: Experiment 94, volume fraction distributions

Tilted-rig experiments

In some experiments the rig was tilted by an accurately measured angle, θ, as shown in figure 2. This gave a way of generating a two-dimensional (on average) flow from precisely known initial conditions. The purpose of these experiments was to provide data for two-dimensional turbulence models. Similar experiments at a density ratio ρ_1/ρ_2 close to unity are described by Andrews [22].

The tank acceleration g remains aligned with the sides of the tank. Hence the experiment is equivalent to using a vertical rig with a linear initial perturbation.

$$\zeta(x,0) = a_o \left[1 - \frac{2x}{W}\right] = \frac{8a_o}{\pi^2} \sum_{r=0}^{\infty} \frac{\cos(2r+1)\,\pi x/W}{(2r+1)^2}$$

where $a_o = \frac{1}{2}W \tan\theta$.

The small amplitude linear theory for Rayleigh-Taylor instability may be used to give an indication of the early time behaviour. At time t the perturbation is given by

$$\zeta(x,t) = \frac{8a_o}{\pi^2} \sum_{r=0}^{\infty} \frac{\cos(2r+1)\,\pi x/W}{(2r+1)^2} \cosh nt \qquad \ldots (7)$$

where n is the coefficient of exponential growth for perturbations of wave number $k = (2r+1)\,\pi/W$. If viscosity and surface tension are neglected $n \to \infty$ as $k \to \infty$ and the series (7) diverges for $t > 0$. However, if a small amount of viscosity is added the singularity is removed. Numerical summation of the series shows that narrow jets are formed at $x = 0$ and $x = W$.

Figures 11 and 12 show experimental photographs for two experiments at ρ_1/ρ_2 = 2.9 and 19.6. For the lower density ratio, jets forming at the sides of the tank are clearly seen at the beginning of the experiment. Non-linear effects soon set in and mushrooming out of the jets occurs. As time proceeds the features at the side of the tank increase in size and a gross overturning motion occurs. Figure 13 shows plots of the instability penetrations measured for this experiment. At early time the variation of the width of the mixed region in the centre of the tank, δ, is close to that expected for $\theta = 0$, ie

$$\delta = 0.06\ (1 + h_2/h_1)X = 0.06\ .\ 2.4\ .\ X = 0.144\ X$$

At late time the graph of δ versus X flattens off. At the higher density ratio, figure 11, the behaviour is markedly different. As before jets form at the sides of the tank. However, the feature at x = W develops into a large bubble whereas the feature at x = 0 forms a narrow spike.

Two-dimensional numerical simulation of these two experiments, Youngs [19], reproduced both the behaviour at the side walls and the gross overturning motion seen in these experiments.

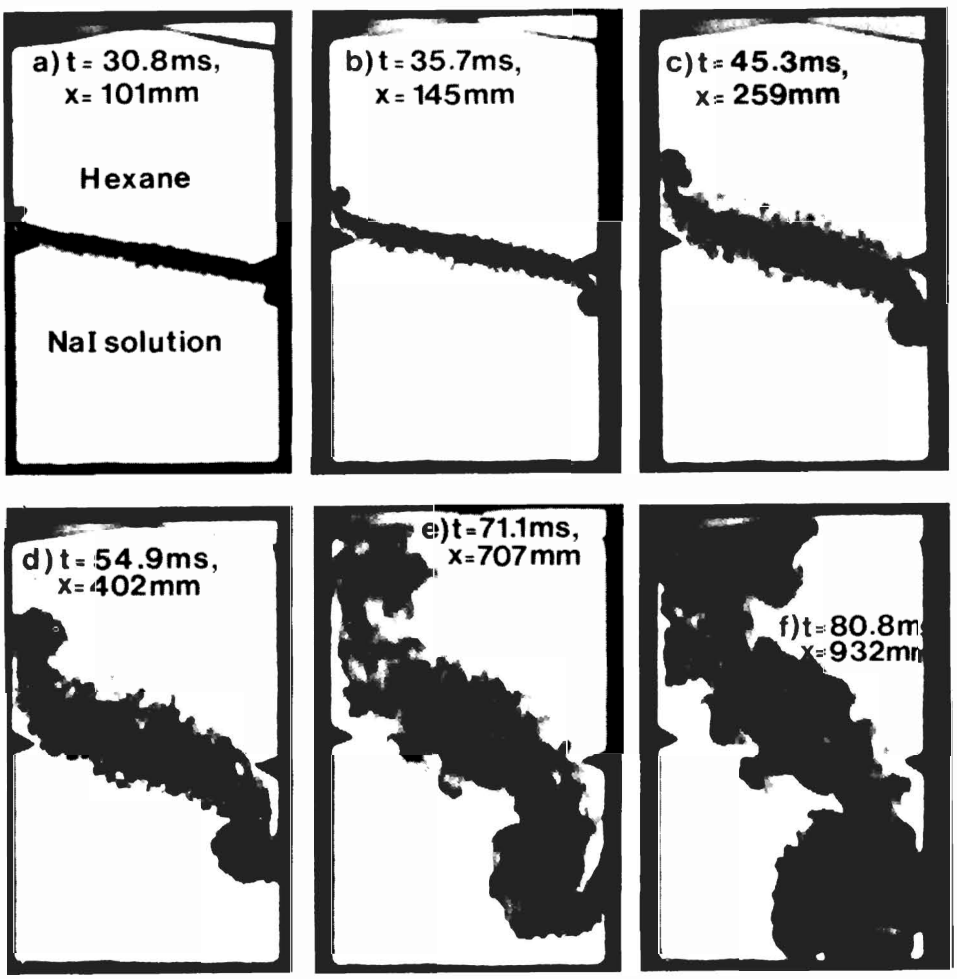

Figure 11: Experiment 110, NaI solution/hexane, ρ_1/ρ_2 = 2.9, $\theta = 5^{\circ}46'$, g ≈ 35 g_0

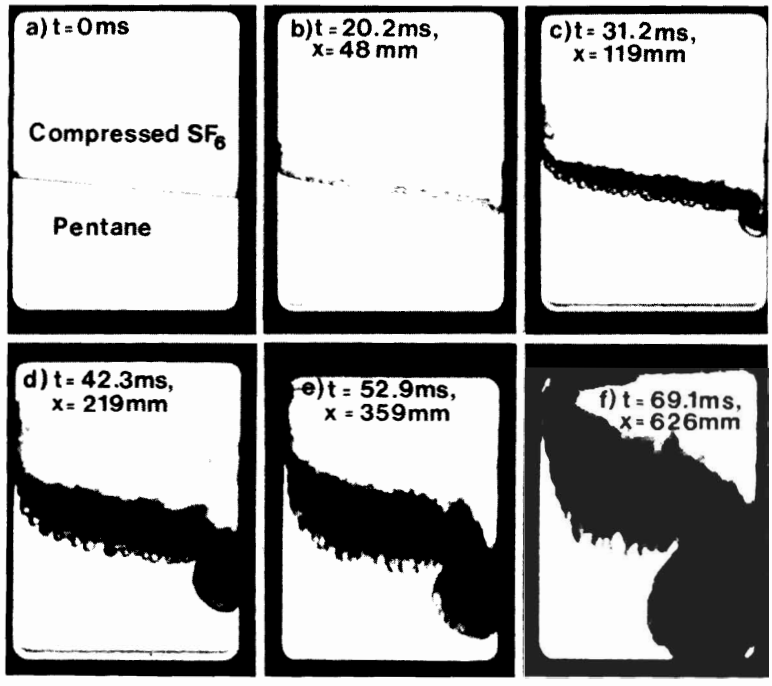

Figure 12: Experiment 115, pentane/compressed SF_6, ρ_1/ρ_2 = 19.6, $\theta = 5^{o}9'$, g ≈ 16 g_0

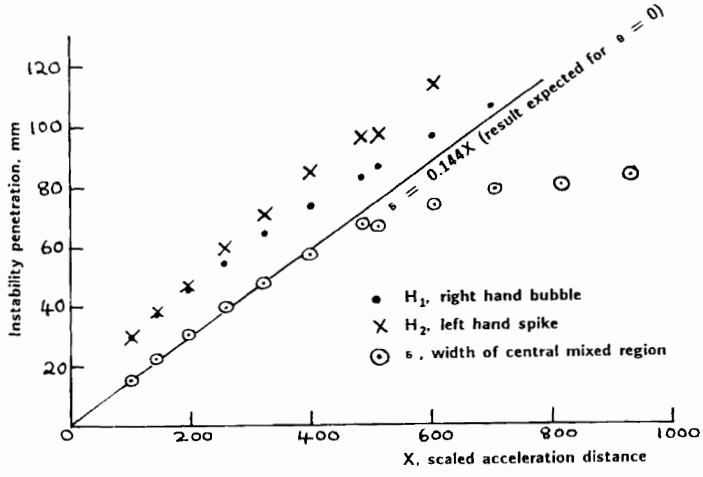

Figure 13: Instability penetrations for experiment 110.

Three fluid experiments

In many problems where Rayleigh-Taylor instability has an important effect, such as the implosion of Inertially Confined Fusion capsules, several layers of material with different densities may be present and in some cases thin layers of material will become fully mixed. Hence there is a need for turbulence models to treat the mixing of more than two materials. Three-fluid experiments have been carried out using the Rocket-Rig apparatus [2,3]. A series of experiments has been performed using carbon tetrachloride/NaCl solution/hexane with densities ρ_1 ρ_2 ρ_3.

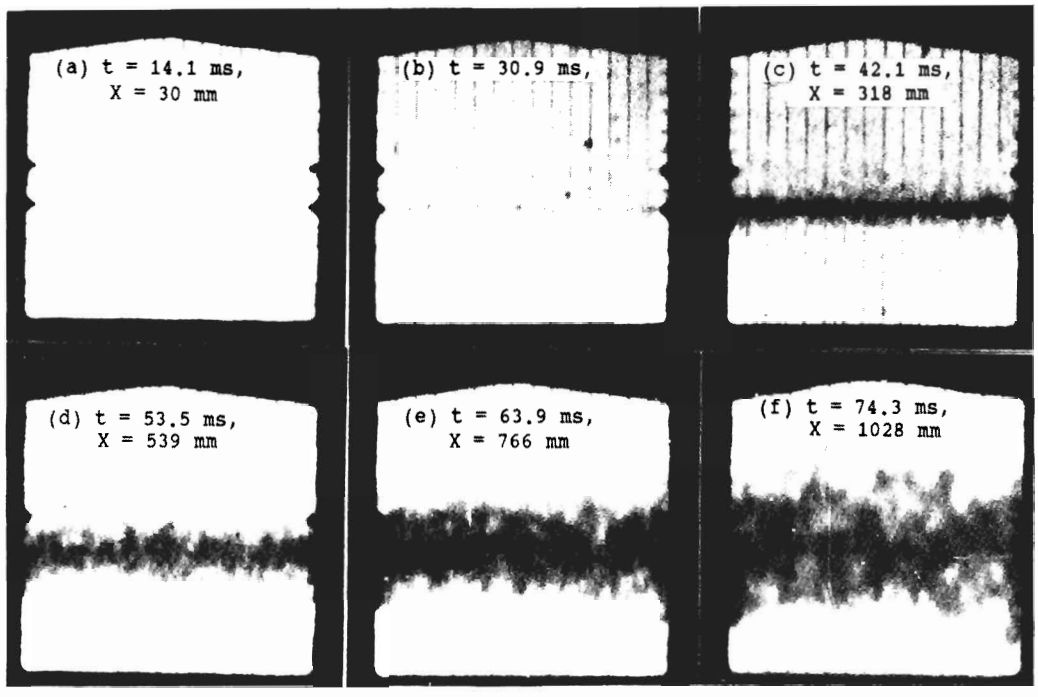

Figure 14: Experiment 59, carbon tetrachloride/NaCl solution/hexane, thickness of middle layer = 20 mm

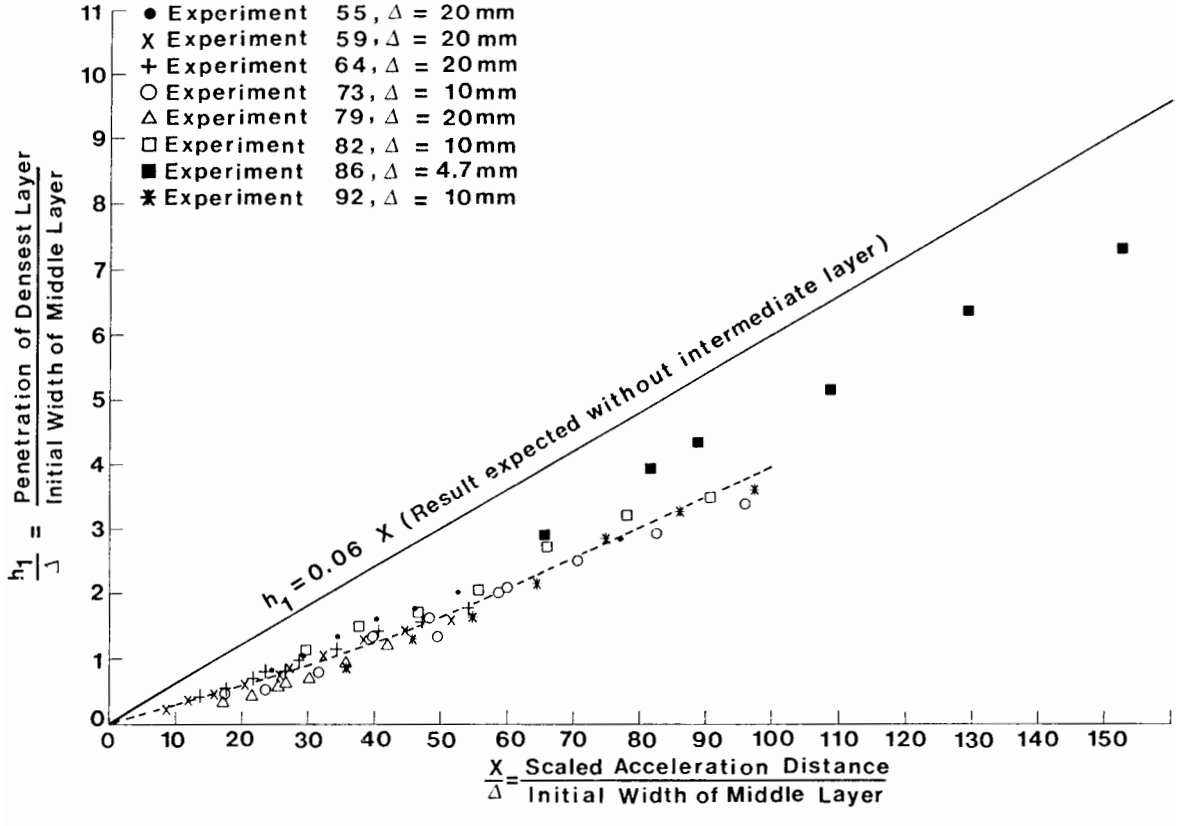

Figure 15: Analysis of the three-fluid experiments

The concentration of the salt solution was adjusted to make the density of the intermediate layer $\rho_2 = \sqrt{\rho_1 \rho_3}$. Experiments were performed with intermediate layer thicknesses of Δ = 5, 10 and 20 mm. Photographs for one such experiment are shown in figure 14. Instability growth is related to the parameter

$$\frac{X}{\Delta} = \frac{\rho_1 - \rho_2}{\rho_1 + \rho_3} \frac{gt^2}{\Delta}$$

A non-dimensional plot is obtained by plotting h_1/Δ against X/Δ, see figure 15. h_1 is the penetration of the densest fluid, as defined in figure 2. Results for the smallest value of Δ, 5 mm, are not considered accurate; it appears that the perturbation due to the meniscus at the top and bottom of the intermediate layer enhanced instability growth. At early time, before the layer of fluid 2 has broken up h_1 is about half that expected with no intermediate layer. This is a consequence of the reduced Atwood number. At late time the effect of the intermediate layer should be negligible and h_1 should be given by

$$\frac{h_1}{\Delta} = 0.06 \left[\frac{X}{\Delta} - B \right]$$

where B is a constant. It is not possible to give a precise estimate. However, figure 15 suggests that B is probably about 2½. Hence the effect of the intermediate layer is to reduce h_1 by about 2½Δ at late time.

4. COMPUTER SIMULATION

Two dimensional computer simulation [18,19] has indicated α ~0.04 to 0.05 and h_2/h_1 a slowly increasing function of density ratio ρ_1/ρ_2. A calculation at ρ_1/ρ_2 = 20 [19] gave h_2/h_1 ~2.3 in fair agreement with the experimental estimate of 2.0, figure 8. Hence the simulations also indicate high drag on the spikes. The 2D estimates of α tend to be somewhat less than the observed values. Recently 3D calculations have begun using a restricted mesh. The numerical method is an extension to 3D of the compressible technique used by Youngs [18]. The 3D version was developed by Rowse et al [20]. The sound speeds were chosen to be high enough to give an almost incompressible flow. Calculations have been performed at a density ratio ρ_1/ρ_2 of 3. In some of the calculations an interface tracking technique was used to follow the boundary between the two fluids. Plots of the interface are useful for visualising bubble formation. However, in reality the sharp interface is broken up by small scale eddies and mixing at a molecular level occurs. Other calculations have used a single fluid with an initial density step. The density discontinuity is then smeared by numerical diffusion. As fine scale mixing indeed occurs there seems no reason for believing that this simpler approach is less accurate.

The calculations used an initial interface perturbation

$$\zeta(x,y) = S \sum_{m,n=0}^{N} a_{mn} \cos \frac{m\pi x}{W} \cos \frac{n\pi y}{D}$$

where a_{mn} is a random number chosen from a Gaussian distribution,

S is a scaling factor chosen to give $\{<\zeta^2>\}^{1/2} = \sigma$ the required initial amplitude,

$a_{oo} = a_{io} = a_{oi} = 0$.

3D calculations with interface tracking used 32 x 32 x 40 zones, W = D = 1, N = 12 and σ = 0.002. Calculations were performed without interface tracking using 32 x 32 x 60 zones and the same initial perturbations. For comparison 2D calculations were performed with only the n = 0 modes present and mesh sizes of 32 x 40 (interface tracking) and 32 x 60 (no interface tracking). To show the effect of mesh size, the 2D calculations without interface tracking were repeated using 96 x 180 zones, N increased to 36 and σ reduced to 0.0007. The acceleration g was chosen to give n_w = 1.0. All calculations used zero normal velocity boundary conditions.

Figure 16 shows a sequence of interface plots for one of the 3D calculations with interface tracking. Two views are given, a side view and a view of the bubbles forming. The fluid 1 volume fraction averaged over a horizontal layer is defined to be

$$\bar{f}_1 = \frac{\bar{\rho} - \rho_2}{\rho_1 - \rho_2}$$

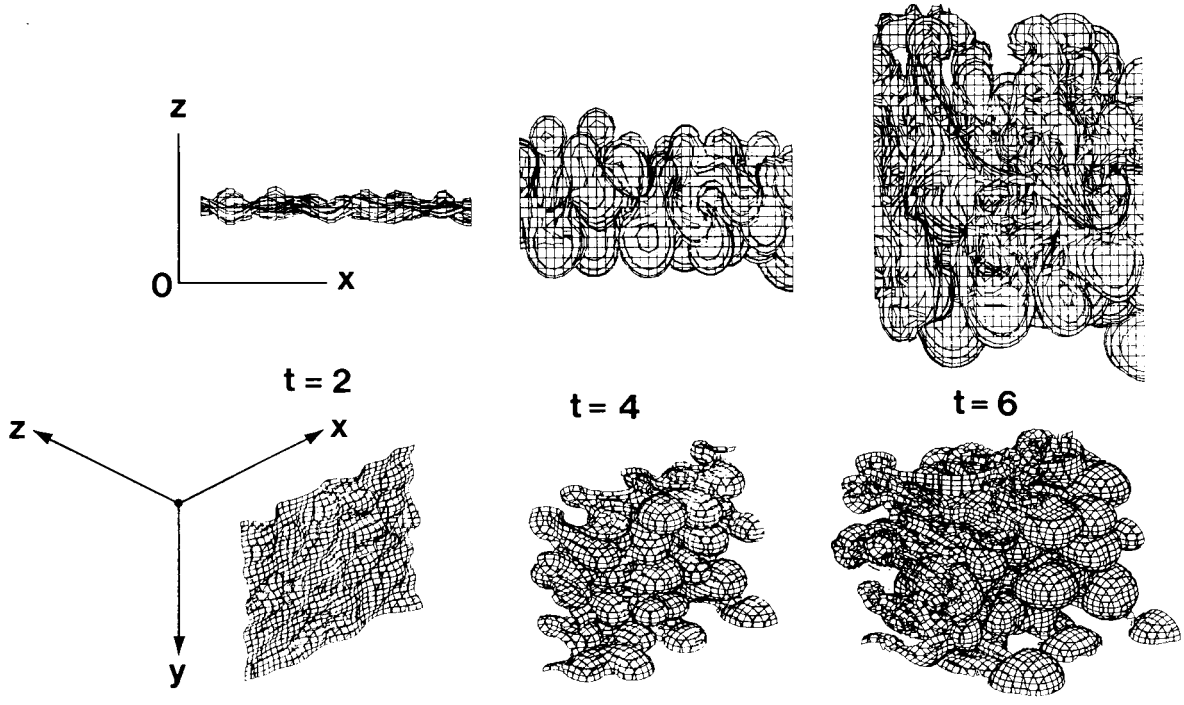

Figure 16: Interface plots obtained by 3D numerical simulation

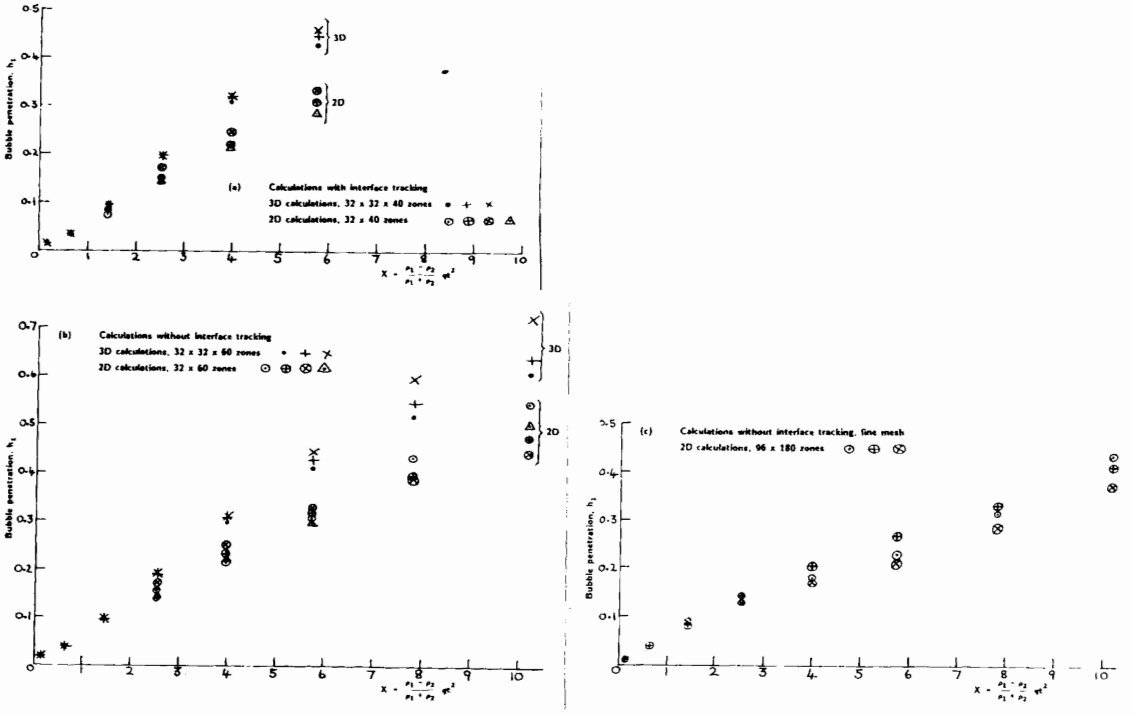

Figure 17: Instability penetration obtained from 2D and 3D numerical simulation

The instability penetration, h_1, is then measured to the point where $f_1 = 0.95$. Plots of h_1 against Agt^2 are shown in figure 16. Each type of calculation has been repeated using different random initial perturbations.

Comparison of 3D calculations and 2D calculations with the same mesh size show that the 3D growth rate is about 30% greater than the 2D growth rate. The 2D calculations with the finer mesh show that the slope of the h_1 vs X curve has not yet settled down to its limiting value. Hence the 3D calculations need to be repeated with a finer mesh before definitive statements can be made about the 3D value of α. Nevertheless, the 2D estimate of $\alpha \sim 0.04$ to 0.05 together with the somewhat higher growth rate in 3D seems consistent with the observed estimate of $\alpha \sim 0.06$.

5. CONCLUSIONS

Experiments performed at a wide range of density ratios show that if mixing evolves from small random pertubations, then the depth to which the instability penetrates the denser fluid is given by

$$h_1 = \alpha \frac{\rho_1 - \rho_2}{\rho_1 + \rho_2} gt^2$$

A value of α of approximately 0.06 is recommended for all density ratios. The ratio (spike penetration)/(bubble penetration) = h_2/h_1 is a slowly increasing function of ρ_1/ρ_2. At $\rho_1/\rho_2 = 20$, h_2/h_1 is approximately 2.

The overall growth rate of the mixed region has been measured and shown to fit into a simple pattern. The mean volume fraction distribution has been estimated

at low density ratios. However, there are major gaps in the data even for this simple situation; for example the proportion of the turbulence kinetic energy generated which is dissipated and the degree to which the fluids mix at a molecular level have yet to be quantified.

The simple quadratic law is obtained when the mixing process loses memory of the initial conditions. In many real applications large amplitude long wavelength will be present and loss of memory of the initial conditions may not occur. It would be useful to have a model relating the non-linear growth of the mixed region to the initial perturbation spectrum.

REFERENCES

1. K I Read, D L Youngs, AWRE report 011/83 (1983).
2. K D Burrows, V S Smeeton, D L Youngs, AWRE Report 022/84 (1984).
3. V S Smeeton D L Youngs, AWE Report 035/87 (1988).
4. K I Read, Physics 12D, p45 (1984).
5. D J Lewis, Proc Roy Soc, 202A, p81 (1950).
6. J Allred and G Blount, Los Alamos report LA-1600 (1953).
7. H W Emmons, C T Chang and B C Watson, J Fluid Mech, 7, p177 (1960).
8. R E Duff, F H Harlow and C W Hirt, Phys Fluids, 5, p417 (1962).
9. R L Cole and R S Tankin, Phys Fluids, 16, p1207 (1973).
10. R Popil and F L Curzon, Rev Sci Instr 50, p1291 (1979).
11. S Z Belen'kii, E S Fradkin, Tr Fiz Inst Akad Nauk SSSR, 29, p207 (1965).
12. V E Neuvazhaev and V G Yakovlev, Zh Vychisl Mat Fiz 16, No. 2 (1976).
13. N N Anuchina, Yu A Kucherenko, V E Neuvazhaev, V N Ogibina, L I Shibarshov and V G Yakolev, Izv Akad Nauk SSSR, Mekh Zh Gaza, No. 6, p157 (1978).
14. V Andronov, S M Bakhrakh, E E Meshkov, V N Mokhov, V V Nikiforov, A V Pevnitskii and A I Tolshmyakov, Sov Phys JETP, 44, p424 (1976).
15. S Chandrasekhar, "Hydrodynamic and Hydromagnetic Stability", OUP (1961).
16. D Layzer, Astrophysical J 122, p1 (1955).
17. R LeLevier, G J Lasher and F Bjorklund, UCRL 4459 (1955).
18. D L Youngs, Physica 12D, p32 (1984).
19. D L Youngs, submitted to proceedings of "Advances in Fluid Turbulence" Conference, Los Alamos (1988).
20. D P Rowse, B J Parker, D Boulton, private communication.
21. P F Linden, J Redondo: these proceedings.
22. M J Andrews, these proceedings.